COMPOSITE CONSTRUCTION IN STEEL AND CONCRETE VIII

Proceedings of the Eighth International Conference on Composite Construction in Steel and Concrete

Edited by Gian Andrea Rassati, Jerome F. Hajjar, and Roberto T. Leon

July 29 – August 2, 2017
SPRING CREEK RANCH
Jackson Hole, Wyoming, U.S.



COMPOSITE CONSTRUCTION IN STEEL AND CONCRETE VIII

Proceedings of the Eighth International Conference on Composite Construction in Steel and Concrete

Edited by Gian Andrea Rassati, Jerome F. Hajjar, and Roberto T. Leon

July 29 – August 2, 2017
SPRING CREEK RANCH
Jackson Hole, Wyoming, U.S.





© AISC 2020

by

American Institute of Steel Construction

All rights reserved. This book or any part thereof must not be reproduced in any form without the written permission of the publisher.
The AISC logo is a registered trademark of AISC.

ISBN 978-1-56424-062-0

The information presented in this publication has been prepared following recognized principles of design and construction. While it is believed to be accurate, this information should not be used or relied upon for any specific application without competent professional examination and verification of its accuracy, suitability and applicability by a licensed engineer or architect. The publication of this information is not a representation or warranty on the part of the American Institute of Steel Construction, its officers, agents, employees or committee members, or of any other person named herein, that this information is suitable for any general or particular use, or of freedom from infringement of any patent or patents. All representations or warranties, express or implied, other than as stated above, are specifically disclaimed. Anyone making use of the information presented in this publication assumes all liability arising from such use.

Caution must be exercised when relying upon standards and guidelines developed by other bodies and incorporated by reference herein since such material may be modified or amended from time to time subsequent to the printing of this edition. The American Institute of Steel Construction bears no responsibility for such material other than to refer to it and incorporate it by reference at the time of the initial publication of this edition.

Printed in the United States of America

Cover image © Wright Runstad & Co., provided by Magnusson Klemencic Associates.

Abstract: These proceedings summarize the state-of-the-art in composite construction worldwide, as presented at the eighth international conference on *Composite Construction in Steel and Concrete* held at Spring Creek Ranch (Jackson Hole, Wyoming, USA) from July 29 to August 2, 2017. The papers contained in this volume cover a wide variety of topics, including innovative composite structural systems, composite columns, composite slabs, shear connectors, fire and seismic resistance of composite structural systems, composite bridges, and practical applications.

Preface

These proceedings summarize the state-of-the-art in composite construction worldwide, as presented at the international conference on Composite Construction in Steel and Concrete held at Spring Creek Ranch in Jackson Hole, Wyoming (USA) in July 2017. This is the eighth in a series of conferences on this topic organized by the United Engineering Foundation (then Engineering Conferences International and now by Continuing and Professional Education @ Virginia Tech) aimed at assessing and synthesizing the most recent advances in research and practice in the area of composite steel-concrete construction. This conference was preceded by those held in Henniker, New Hampshire, USA (1987), Potosi, Missouri, USA (1992), Irsee, Germany (1996), Banff, Canada (2000), Kruger National Park, South Africa (2004), Tabernash, Colorado, USA (2008), and Palm Cove, Australia (2013).

The papers contained in this volume cover a wide variety of topics, including innovative composite structural systems, composite columns, composite slabs, shear connectors, fire and seismic resistance of composite structural systems, composite bridges, and practical applications. Seventy-six participants from seventeen countries participated in four days of presentations, panel discussions, and dialogue addressing all aspects of composite construction. The conference was organized and co-chaired by Dr. Roberto Leon, Virginia Tech, Dr. Jerome F. Hajjar, Northeastern University, and Dr. Gian Andrea Rassati, University of Cincinnati, U.S.A. The conference was generously supported by the American Institute of Steel Construction (AISC) and the Virginia Tech Charles E. Via Department of Civil and Environmental Engineering (VT/CEE).

The papers in the proceedings were peer reviewed as per the guidelines used for the *AISC Engineering Journal*. The review process was administered by the editors of the proceedings, who would like to thank all the authors and reviewers for their contributions. The publication of the proceedings was supported by the AISC.

The editors will like to thank the staff of Continuing and Professional Education at Virginia Polytechnic Institute and State University and particularly Ms. Kathy Laskowski, Director of Facilities/Operations and Major Grants Coordinator at VT/CEE, for all their help in organizing and coordinating the conference.

Gian Andrea Rassati, Jerome F. Hajjar, and Roberto T. Leon
April 2020



Conference Participants

Organizing Committee

Chairs:
Roberto T. Leon, Virginia Polytechnic Institute and State University, Blacksburg, VA, USA
Jerome F. Hajjar, Northeastern University, Boston, MA, USA
Gian Andrea Rassati, University of Cincinnati, Cincinnati, OH, USA

Scientific Committee

Ulrike Kuhlmann, University of Stuttgart, Germany
K. C. Tsai, NCREE, Taipei, Taiwan
Brian Uy, University of Sydney, Sydney, Australia
Jim Harries, Harris and Associates, Denver, Colorado, USA
Toko Hitaka, University of Kyoto, Kyoto, Japan
Larry Griffis, W.P. Moore and Associates, Austin, Texas, USA
Kent Harries, University of Pittsburgh, Pittsburgh, Pennsylvania, USA
Yan Xiao, Hunan University, Hunan, China
Oreste Bursi, University of Trento, Trento, Italy
Mario Fontana, ETH, Zürich, Switzerland
Wolfgang Kurz, University of Kaiserslautern, Kaiserslautern, Germany
Dennis Lam, University of Leeds, Leeds, United Kingdom
Robert Tremblay, Ecole Polytechnique, Montreal, Canada

TABLE OF CONTENTS

Composite Construction Design Codes and Structures

Rainier Square-concrete filled composite plate shear wall high-rise tower, Seattle, WA **1**
Brian Morgen, Hee Jae Yang, Ron Klemencic and John Hooper

G.T. Land Plaza: using composite structure for solving the challenges and complexities of a tall, long and slender tower **13**
Mark Sarkisian, Neville Mathias, John Gordon and Joanna Zhang

Multifunctional commercial buildings in steel and composite construction **25**
Richard Stroetmann and Lukas Hüttig

Building scale composite systems **38**
Aaron Mazeika and Ashpica Chhabra

Towards the use of high strength steel and concrete in high-rise construction **50**
Richard Liew, Yan-Bo Wang and Du Yong

Development of a new push test for Eurocode 4 **62**
Stephen Hicks, Adrian Ciutina and Christoph Odenbreit

Development of European design guidance for steel-concrete (SC) structures in nuclear power plant **74**
Bassam Burgan and Eleftherios Aggelopoulos

The new Australia/New Zealand Standard on composite steel-concrete buildings, ASNZS2327 **86**
Brian Uy, Stephen Hicks, Won Hee Kang, Huu-Tai Thai and Farhad Aslani

The new joint Australian and New Zealand Design Standard for steel and composite bridges AS/NZS 5100.6 - Part 6: Steel And Composite Construction **98**
Stephen Hicks, Brian Uy and Won-Hee Kang

Shear Connectors

Shear connections by headed studs close to the concrete edge **109**
Ulrike Kuhlmann, Jochen Raichle and Ana M. Pascual

Considerations on composite beam connection due to plastic deformation capacity and strength ratio **121**
Yuko Shimada and Satoshi Yamada

Behaviour of composite dowels positioned close the surface of concrete slabs **132**
Wolfgang Kurz, Yannick Broschart and Joanna Gajda

Pin shear connectors for steel-concrete composite constructions **144**
Maik Kopp, Kevin Wolters, Markus Feldmann, Martin Claßen and Johannes Schäfer

Behavior of a new type of shear connectors for U-shaped steel-concrete hybrid beams **157**
Pisey Keo, Clémence Lepourry, Hugues Somja and Franck Palas

Shear performance of nonparallel type twin perfobond steel plate shear connectors: FEM analysis and experimental verification 169
Hai Chen, Yang Liu, Zixiong Guo, Yong Ye and Bahram Shahrooz

Composite Floor, Slab, and Diaphragm Systems

Experimental studies of composite slim floor beams 181
Dennis Lam, Therese Sheehan and Xianghe Dai

Slim-floor construction - deformation and load carrying behaviour 194
Johannes Schorr, Ulrike Kuhlmann and Gunter Hauf

Experimental and numerical study on mechanical behaviour of composite slabs with closed profiled sheeting 206
Guochang Li, Xiao Zhang, Zhijian Yang and Fengwei Guo

Role of the floor system in the cyclic response of composite steel gravity framing 217
Sean Donahue, Michael Engelhardt, Patricia Clayton, Eric Williamson and Todd Helwig

A design approach for the serviceability limit state of composite steel-concrete slabs 228
Gianluca Ranzi

Longitudinal shear resistance of ComFlor 210 239
Roland Abspoel and Jan Stark

Behavior of a sustainable composite floor system with deconstructable clamping connectors 251
Lizhong Wang, Mark Webster and Jerome Hajjar

Preliminary assessment of a composite flooring system for reuse 263
Martin Nijgh, Mareike von Arnim, Marko Pavlović and Milan Veljković

Seismic collectors in composite steel deck diaphragms 274
Robert Fleischman, Anshul Agarwal, Haitham Ayyad, Richard Sause, Jim Ricles and Chia-Ming Uang

Evaluation of strength and stiffness predictions for steel deck diaphragms with structural concrete fill 286
Patrick O'Brien, W. Samuel Easterling and Matthew Eatherton

Composite Beams

Review of plastic moment resistance for composite beams 298
Markus Schäfer

Influence of the composite action on the load bearing and deformation behavior of composite beams with and without profiled steel sheeting 310
Florian Eggert and Ulrike Kuhlmann

Effect of post-welding residual stresses on distortional buckling of steel-concrete composite beams 322
Marian Gizejowski, Radoslaw Szczerba, Marcin Gajewski and Wioleta Barcewicz

Strength of lateral-torsional buckling of a composite steel beam subjected to reverse curvature bending 334
Satoshi Kitaoka, Ryoichi Kanno, Satoru Hiroshima, Koji Hanya, Keiichi Takada and Fumihisa Yoshida

Deformation-based reliability concept for composite beams 346
Wolfgang Kurz, Karsten Geißler, Natali Kostadinova and Gregor Korpas

Effects of composite slab on shear strength of steel plate girders 358
Peter Wang and Maria Garlock

Composite Columns and Column Bases

Structural reliability of steel-concrete composite columns and frames 369
Mark Denavit

Calibration of the elastic flexural rigidity from ambient vibration measurements for a building with encased composite columns 381
Tiziano Perea, Miguel A. Garcia, Manuel Ruiz-Sandoval, Roberto T. Leon, Mark D. Denavit and Jerome F. Hajjar

Pushing the envelope of composite column design using high-strength materials 392
Amit Varma and Zhichao Lai

Strength of CFT Columns with Various Material Strengths and Sectional Slenderness 404
Ho-Jun Lee and Hong-Gun Park

Buckling resistance of hybrid steel-concrete columns 416
Pisey Keo, Hugues Somja, Quang-Huy Nguyen and Mohammed Hjiaj

The seismic stability and ductility of steel columns interacting with concrete footings 428
Hiroyuki Inamasu, Amit Kanvinde and Dimitrios Lignos

Performance based evaluation of a multiple CFT bridge pier with buckling restrained bracings 440
Chi-Ho Jeon, Dong-Wook Kim and Chang-Su Shim

Seismic performance of an innovative composite column with replaceable steel slit dampers: FEM analysis and design method 450
Yang Liu, Yifan Liao, Zixiong Guo, Yingting Lu, Xiaojuan Liu and Bahram Shahrooz

Life-cycle performance of concrete-filled steel tubular column subjected to corrosion and impact 462
Lin-Hai Han and Chuan-Chuan Hou

Research on deformation limits of SRC columns based on experiment data 474
Jing Ji, Lei Zhang, Xiaolei Han, Tao You and Yuan Cao

Composite Connections

Update of design provisions for moment-resisting joints between steel beams and reinforced concrete columns 486
Luis Fargier-Gabaldon, Paul Cordova, Gustavo Parra-Montesinos and Gregory Deierlein

Innovative slip-critical blind bolts and connections for concrete-filled RHS columns 502
Wei Wang, Mingxiao Li, Yiyi Chen and Xiaogang Jian

Braced frame connections with square CFT columns penetrated by gusset plates 513
Peng Wang, Jianrong Pan, Jingmin Liang, Huashen Xie and Zhan Wang

Influence of composite slab on the nonlinear response of extended end-plate beam-to-column steel joints 526
Roberto Tartaglia, Mario D'Aniello, Gian Andrea Rassati and James Swanson

Numerical investigation of moment-resisting slim-floor beam-to-column connections 538
Cristian Vulcu, Rafaela Don, Adrian Ciutina and Dan Dubina

Improved beam-column connection for partially encased composite structure 550
Yiyi Chen, Guanghong Chuan and Jie Li

Girder-wall connections using concrete anchors in composite construction 561
Jian Zhao and Bo Yang

Steel-to-concrete joints with large anchor plates under shear loading 574
Jakob Ruopp and Ulrike Kuhlmann

Seismic column base connections: experiments, simulations, component and building models, and design implications 586
Amit Kanvinde

Moment-rotation characteristics for deconstructable flush end plate composite joints 597
Mark Bradford, Abdolreza Ataei and Xinpei Liu

Composite Lateral Force Resisting Systems

The influence of a composite slab on the seismic behavior of moment resisting frames 607
Roberto Tartaglia, Mario D'Aniello, Gian Andrea Rassati and James Swanson

Concrete-filled steel tube dual lateral-force resisting system 619
Johnn Judd and Nipun Pakwan

An introduction to coupled composite core wall systems for high-rise construction 631
Amit Varma, Zhichao Lai and Jungil Seo

In-plane cyclic testing of concrete-filled sandwich steel panel walls with and without boundary elements 643
Michel Bruneau and Yasser Alzeni

Cyclic shear behavior of steel-plate composite walls for high-rise buildings 655
Xiaodong Ji, Xiaowei Cheng and Xiangfu Jia

Experimental study on the seismic performance of new hybrid coupling wall subassemblies with replaceable steel coupling beam 667
Yang Liu, Hao Lin, Zixiong Guo, Hongsong Hu and Bahram Shahrooz

Numerical investigation of composite detachable short links 678
Mariana Zimbru, Mario D'Aniello, Aurel Stratan, Raffaele Landolfo and Dan Dubină

Direct Analysis for structures made of high strength steel 690
Sw Liu, Sl Chan and Tj Li

Fire and Progressive Collapse

Performance of composite beams in fire: pre-test analysis of full-scale experiments 702
Joseph Main, Fahim Sadek, Jonathan Wigand, Jian Jiang, Lisa Choe, Selvarajah Ramesh, Matthew Hoehler, Mina Seif and John Gross

Towards an engineering method for fire design of concrete-filled steel tube columns with solid steel core 714
Martin Neuenschwander, Markus Knobloch and Mario Fontana

Fire behavior of blind-bolted connections to concrete filled tubular columns under tension 726
Ana M. Pascual and Manuel L. Romero

Robustness design and possible collapse mechanisms of building frames in a fire 738
Kei Kimura, Fuminobu Ozaki and Ryoichi Kanno

Progressive collapse analysis of composite steel frames under elevated temperature 750
Hussam Mahmoud and Chao Qin

Progressive collapse: the case of composite steel-concrete frames 762
Riccardo Zandonini, Nadia Baldassino, Fabio Freddi and Giacomo Roverso

Bridges

Concrete filled steel tubes for bridge applications 775
Charles Roeder and Dawn Lehman

Hot-dip galvanizing in steel and composite bridge constructions 787
Dieter Ungermann, Svenja Holtkamp and Dennis Rademacher

Operational testing of composite railway bridges with innovative composite dowels 800
Daniel Pak, Maik Kopp and Günter Seidl

Integral vs. seismic control in composite deck bridges 812
Uwe E. Dorka and Andrea Klarendic

TABLE OF CONTENTS (continued)

Authors' Index.....825

Keyword Index.....827

RAINIER SQUARE: CONCRETE FILLED COMPOSITE PLATE SHEAR WALL HIGH-RISE TOWER, SEATTLE, WA

Brian Morgen
Magnusson Klemencic Associates
Seattle, Washington USA
bmorgen@mka.com

Hee Jae Yang
Magnusson Klemencic Associates
Seattle, Washington USA
hyang@mka.com

Ron Klemencic
Magnusson Klemencic Associates
Seattle, Washington USA
rklemencic@mka.com

John Hooper
Magnusson Klemencic Associates
Seattle, Washington USA
jhooper@mka.com

ABSTRACT

AISC 341-16 includes expansion of Section H Composite Braced-Frame and Shear-Wall Systems to include Concrete Filled Composite Place Shear Walls (CF-CPSWs). This paper and presentation focuses on the design of a high-rise building in Seattle that employs a CF-CPSW coupled core wall lateral force-resisting system.

Recent high-rise office building construction has commonly utilized reinforced concrete core walls for lateral resistance with composite steel floor framing. This mixture of concrete and steel trades results in the concrete core construction being on the critical path of the overall project schedule. The use of a CF-CPSW lateral system offers a potential alternative to concrete core walls where the steel erector can install the floor framing concurrent with the erection of the dual plate steel core and allow for the wall concrete to be infilled with the pouring of the composite decks in a trailing sequence reducing the overall construction schedule. In addition, the steel dual plate wall modules can be pre-fabricated in a shop and field spliced with the face plates serving a permanent formwork for the concrete fill.

The Rainier Square project in Seattle is a 58-story, 850-feet tall, 1.4 million square foot mixed-use office and residential tower with over 750,000 square feet of office space, approximately 200 residential units, 30,000 square feet of retail, and parking for over 1,000 vehicles. The implementation of the CF-CPSW core was utilized to accelerate the construction schedule by several months.

INTRODUCTION

The 2016 edition of AISC 341 includes a new and expanded specification Section H7 for the design of Concrete Filled Composite Plate Shear Wall (CF-CPSW) systems (American Institute of Steel Construction, 2016). Composite plate shear walls are comprised of structural steel face plates, tie-rods linking the face plates, and concrete infill. Composite action between the plates and concrete fill can be achieved using either tie bars or a combination of tie bars and shear studs.

The use of concrete filled composite plate shear walls in construction can provide a cost-effective alternative to special reinforced concrete shear wall construction and reduce overall project construction durations of the primary structural frame. Recent high-rise office building construction has commonly utilized a reinforced concrete core wall for lateral resistance with composite steel floor framing. This commonly results in the construction time of the concrete core being on the critical path of the overall project schedule. The use of a CF-CPSW lateral system offers a potential alternative to concrete core walls where the steel erector can install the floor framing concurrent with the erection of the composite plate steel core and allow for the wall concrete to be infilled with the pouring of the composite decks in a trailing sequence reducing the overall construction schedule. In addition, the steel dual plate wall modules can be pre-fabricated in a shop and field spliced with the face plates serving a permanent formwork for the concrete fill.

Research over the past decade on the construction of dual-plate sandwich panel construction has shown, with proper detailing of the face plate thickness and tie bar spacing, that the CF-CPSW systems have a high strength and stiffness (similar to or greater than a similarly proportioned reinforced concrete shear wall) and have a highly ductile seismic performance (Alzeni & Bruneau, 2014) (Ramesh, Kreger, & Bowman, Behavior and Design of Earthquake-Resistant Dual-Plate Composite Shear Wall Systems, 2013). Other positive system characteristics include:

- The steel plate face plates and tie-rods act as permanent formwork for the concrete infill;
- The steel boundary elements and panels can be shop prefabricated and field spliced, reducing construction time;
- The un-concreted panel assembly has the ability to carry the steel gravity floor framing self-weight, allowing the shear wall and floor framing to advance several levels ahead of the concrete infill operation;
- The steel face plates and tie-rods act as confinement for the unreinforced concrete, increasing the confining pressure and permitting development of the full composite capacity, with stable seismic energy dissipation;
- The concrete core and tie-rods provide plate stability and limit plate buckling enhancing ductility of the composite wall system.

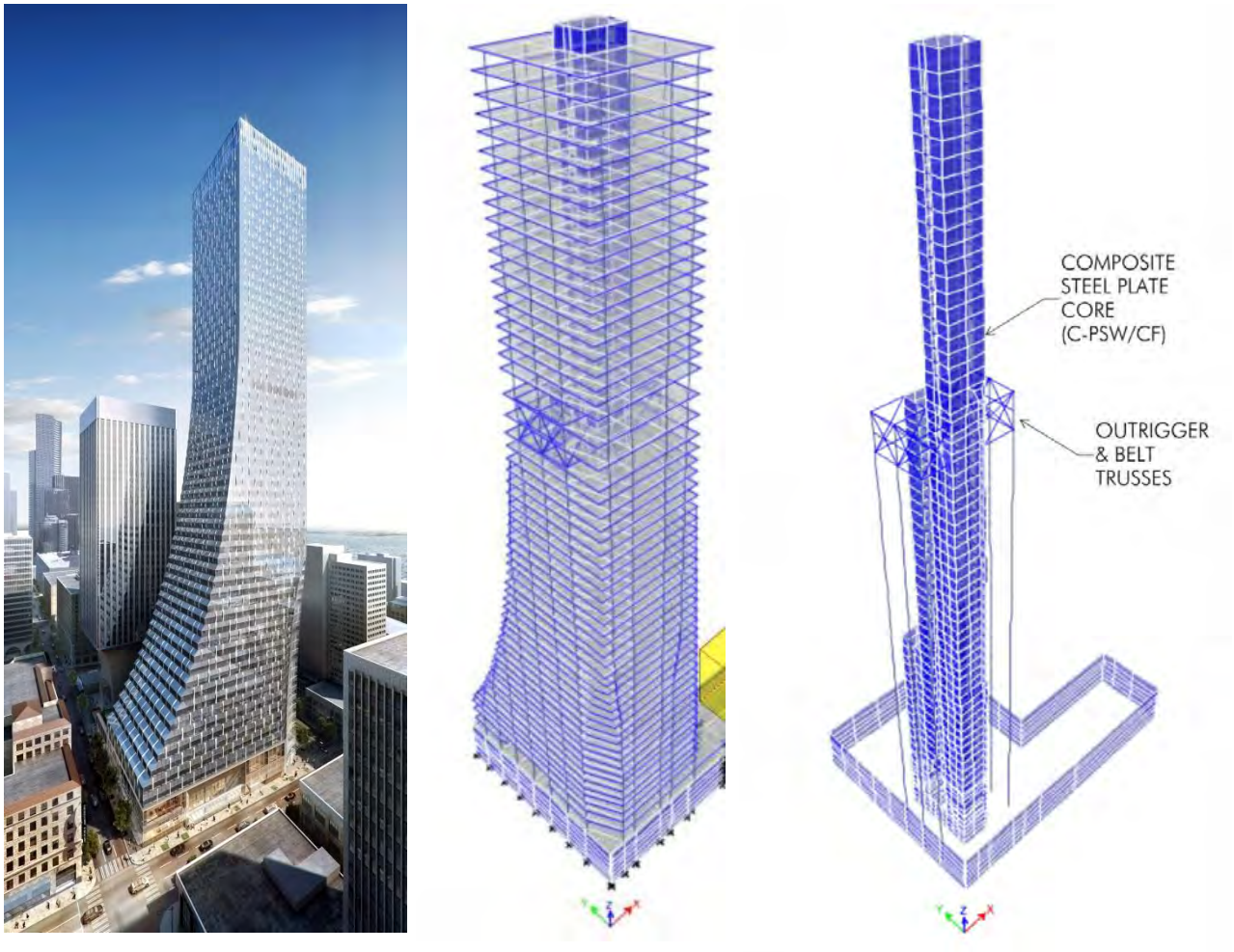
TALL BUILDING APPLICATION

The Rainier Square project in Seattle, Washington USA is a 58-story, 850-feet tall, 1.4 million square foot mixed-use office and residential tower with over 750,000 square feet of office space, approximately 200 residential units, 30,000 square feet of retail, and parking for over 1,000 vehicles. At projected completion in 2020, the project is slated to be Seattle's second tallest building.

The structural design was performed in accordance with the 2012 International Building Code and City of Seattle Amendments, utilizing a non-prescriptive seismic design methodology (Pacific Earthquake Engineering Research Center, Tall Building Initiative (PEER TBI), 2010)

since selected code provisions are taken as exceptions, including allowable building height for the proposed seismic lateral force-resisting system. A performance-based seismic design procedure as allowed by the IBC and ASCE 7 is used to provide a level of safety and overall building ductility equivalent to or greater than that of a prescriptively-designed building.

As illustrated in Figure 1, the building lateral resistance to wind and seismic lateral demands is provided by a coupled shear wall core placed around the central elevator and stair core of the tower supplemented by mid-height Buckling-Restrained Brace (BRB) outriggers and belt trusses to enhance the overall stability and stiffness of the tower.



(a) (b) (c)

Fig 1. – Rainier Square Tower: (a) Architectural Rendering (courtesy Wright Runstad & Company), and (b) & (c) ETABS computer model graphics

To demonstrate that the design is capable of providing code-equivalent seismic performance, a three step analysis and design procedure was performed. The first phase of design is the preliminary design phase where structural components are designed for code-level demands (wind and seismic). For structural components that are anticipated to and detailed to yield based on code-level seismic demands, they are proportioned to satisfy the minimum strength requirements of the IBC. For structural components that are designated to remain elastic, an initial design is performed based on estimated amplification factors to account for strength demands coming from the maximum considered earthquake (MCE) analysis.

The second phase of the building design is a serviceability analysis for a service-level earthquake (SLE) where evaluation of the primary system responses characteristics (such as story drift) and structural components (such as coupling beams, shear walls, and buckling-restrained braces) to demonstrate that the structure is serviceable when subjected to a response spectrum corresponding to a 43-year return period. The final phase of the design includes a nonlinear response history analysis verification of three-dimensional nonlinear computer models considering the MCE event. As part of the MCE verification, acceptance criteria are selected and established for Collapse Prevention performance under the MCE-level demands.

Given the unique nature of the proposed lateral system and the limited use in building construction, an independent peer review panel of experts in this building construction research was employed by the Seattle Department of Construction and Inspections (SDCI) to assist in the building permit review.

CF-CPSW CORE WALL DETAILING

Early schematic designs for the project included the central core being constructed of reinforced concrete. Based on early pricing and schedule studies of the mid-height outrigger and belt truss connections to the core, an alternate core construction utilizing composite plate shear walls was introduced. Based on the construction schedule savings of several months, the project moved forward with the CF-CPSW core construction system for the tower (see Figure 2).

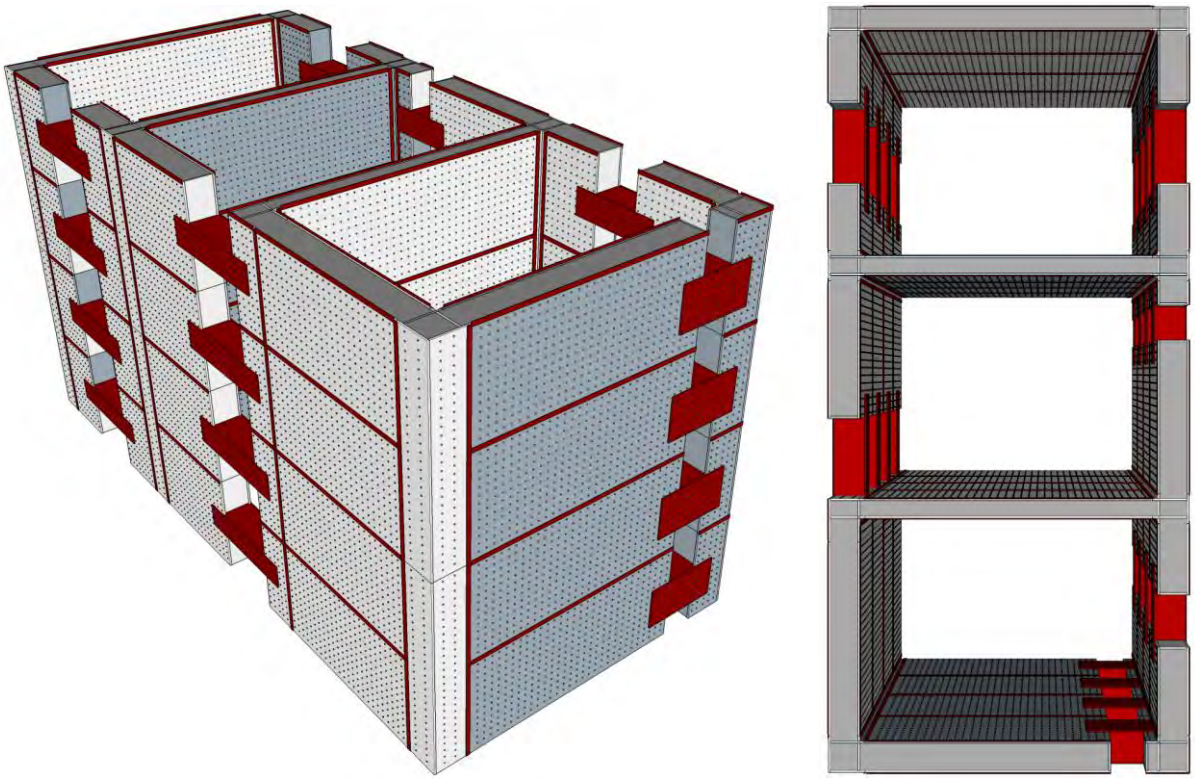


Fig. 2 – CF-CPSW Multi-Cell Core Wall

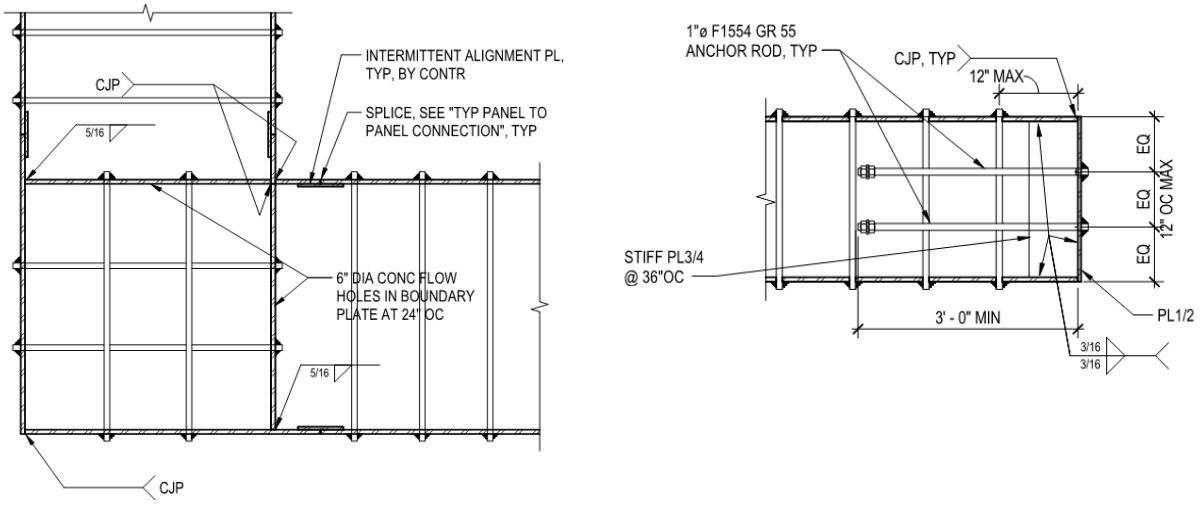
The CF-CPSW wall system consists of a three-cell core at the building base which tapers to a two-cell at the top of the office programming. Above the outrigger and belt-truss levels, a single cell core extends through the residential programming to the roof. Composite wall thicknesses range from 45” at the base to 21” thick at the top of the building. Face plates are 1/2-inch minimum with more highly stressed regions as much as 3/4-inch thick. Tie-rods are specified as 1-inch diameter F1554 Grade 55 anchor rods and are spaced at 12-inch on center both horizontal and vertical resulting in a tie-rod spacing-to-steel plate thickness ratio ranging from 16 to 24 and a tie reinforcing ratio of 0.55%. A ratio of 24 is less that the maximum recommended tie-rod spacing-to-steel plate ratio limit of 30 as observed to match the high-ductility performing test specimens from (Eom, Park, Lee, Kim, & Chang, 2009).

Also, the tie spacing of 12-inches each way is conservatively below the maximum limit for tie-rod spacing-to-thickness ratio specified by AISC 341-16 equation (H7-1), with $E = 29000\ ksi$, $F_y = 50\ ksi$, and $t = 0.5\ inches$, which results in the following:

$$w_1 = 1.8t\sqrt{\frac{E}{Fy}} = 21.7\ inches\ maximum$$

The 1-inch diameter ASTM F1554 Grade 55 tie-rods meet the requirements of AISC 341-16 equations (H7-4), (H7-5), and (H7-6) and have welded connections to the face plates which develop the full tension strength of the tie-rod.

As illustrated in Figure 3, the core wall corners, wall intersections, and wall ends are detailed as tie-rod confined boundary elements to limit the onset of plate buckling and provide concrete confinement. Research on concrete confined by rectangular steel tubes/plates with tie-rods indicates increased ultimate strength and ductility of the section similar to that of added cross-tie and confinement reinforcement in reinforced concrete detailing (Long & Cai, 2013).



(a) (b)

Fig. 3 – CF-CPSW Boundary Element Detailing: (a) Core Wall Corner Intersection, (b) Wall End

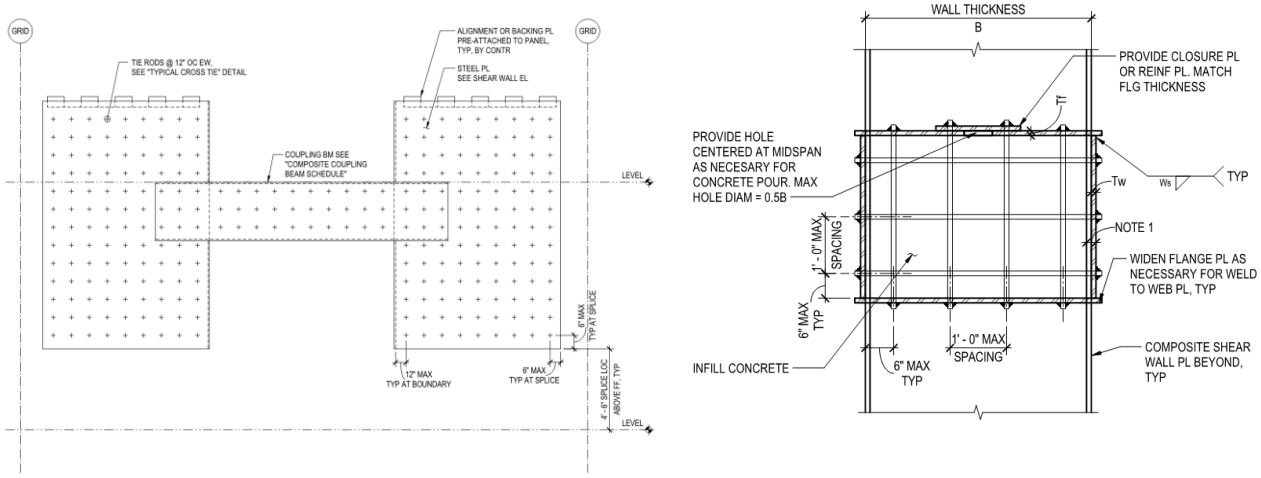
Much of the existing research on CF-CPSW systems to date has utilized planar wall systems with and without boundary elements at the wall ends. To enable greater building lateral strength and stiffness or to extend the system to greater building heights, planar walls are often needed to be extended to flanged walls and/or core wall configurations where the introduction of doorways into and out of the core for building services are required (stairs, elevator lobbies, back of house, etc.). To maintain stiffness of the core, introduction of composite link beams over

the doorways are utilized to couple the wall panels and increase the overall core stiffness, strength, and ductility.

Experimental research programs utilizing coupled wall panels with composite coupling beams indicate ductile nonlinear performance (Eom, Park, Lee, Kim, & Chang, 2009). Plastic stress distribution methods for calculating plastic moment capacity of the composite steel and concrete cross section were found to be in good agreement with the load-carrying capacities of the tested coupled wall specimens. The test results showed that CF-CPSW systems had excellent load-carrying capacities, but in order to ensure ductile behavior of the system, detailing to prevent early fracture of the welded connections at the coupling beam-to-wall interface is critical.

Subsequent experimental studies of concrete-filled composite plate coupling beams had similar findings where the fracture of the web and flange plates at the interface of the coupling beam-to-wall pier was identified as the critical limit state impacting ductility (Hu, Nie, & Eatherton, 2014), (Nie, Hu, & Eatherton, 2014). To avoid welds at the critical demand interface at the coupling beam-to-wall interface, the Rainier Square project utilizes detailing for the concrete-filled composite plate coupling beams as illustrated in Figure 4.

The coupling beam web plates are lapped to the sides of the wall panel with the welded connection away from the interface and location of maximum moment demand. The top and bottom flange plates extend horizontally into the wall panel are welded to the inside face of side plates to develop the capacity of top and bottom plates into the adjacent composite wall elements.



(a) (b)

Fig. 4 – Composite Coupling Beam: (a) Elevation of Pre-Fabricated Coupling Beam Wall Panel, (b) Coupling Beam Section

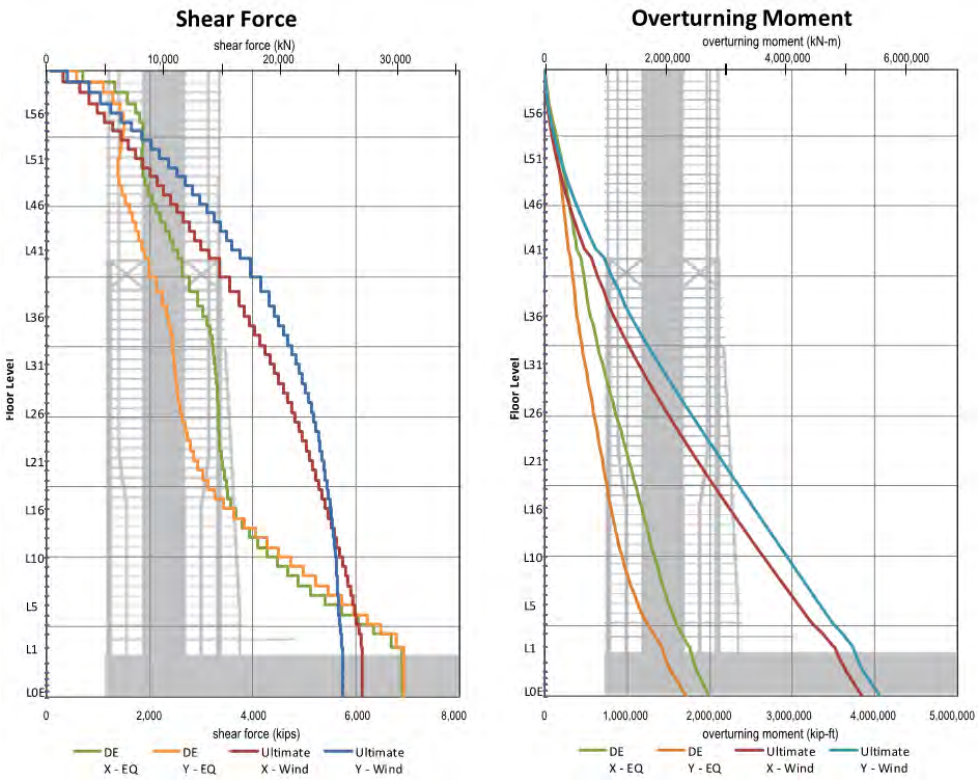
CODE-LEVEL ELASTIC STRENGTH DESIGN

The linear elastic analysis and design of the lateral force-resisting system subjected to the design earthquake (DE) and wind loading is the first stage of the three-stage design and verification process. The initial design is governed by the envelope of strength demands and performance criteria for the DE and design wind loads. This step ensures that a minimum strength for the building similar to that of traditional code-level demands is provided. The overall objectives for the DE-level design are: (a) to proportion the members of the lateral system to provide sufficient stiffness and strength to resist the DE demands, (b) to provide an initial design for the core wall face plates, (c) to provide an initial design for the core wall coupling beams, and (d) to provide an initial design for the buckling-restrained braces (BRBs) as part of the core

wall outrigger system. This design stage considers an elastic response spectrum analysis for the DE-level event.

Given the height of the structure, a linear elastic design for ultimate wind demands ensures that sufficient lateral system strength is provided to withstand the recommended wind demands as provided by a site-specific wind tunnel testing study. The proportioning for the lateral force-resisting elements is provided to satisfy the strength design requirements for the enveloped strength demands from the DE and wind analyses. A comparison of the building shear and overturning demands from the DE and wind demands is illustrated in Figure 5. As can be observed, the wind demands generally control the proportioning of the lateral force-resisting system with the overturning moment demand due to code wind strength demands being twice that of the code seismic demands. Shear demands of the core generally follow this trend, except for noted locations at lower floor levels where the DE demands exceed the accumulated wind shear demand.

This observation, where wind demands are much larger than the DE demands and control the proportioning of the core wall face plates, coupling beams, and BRBs, suggests that the building lateral system and CF-CPSW core will likely exhibit limited yielding when subjected to MCE demands. The nonlinear verification analyses confirmed this early design proportioning observation as discussed later in this paper.



(a) (b)

Fig. 5 – Code-Level Building Demands: (a) Building Shear, (b) Building Overturning Moment

The linear elastic design for service-level earthquake (SLE) is the second stage of the three-stage design and verification process of the lateral system. This step provides a second method of providing a minimum strength for the lateral system. Acceptance criteria are selected such that essentially elastic behavior of the structure is anticipated. The recommendations from the PEER TBI (Pacific Earthquake Engineering Research Center, Tall Building Initiative (PEER

TBI), 2010) are utilized as a baseline for the design. The overall objectives for the SLE design are: (a) to provide a second method for proportioning the members of the lateral system such that sufficient strength and stiffness are provided and that the building is expected to behave in an essentially elastic manner under a more frequent earthquake and (b) to verify that the initial design for the lateral force-resisting system performed at the DE/wind analysis is satisfactory for SLE demand levels.

NONLINEAR VERIFICATION

To achieve the objectives of the verification and design phases, a nonlinear computer model of the structure is built where member sizes, material, and elastic and inelastic behaviors are modeled as accurately as practical. The model is subjected to ground shaking, and the results are analyzed. The nonlinear verification phase is utilized to illustrate that that lateral force-resisting system meets at a minimum a Collapse Prevention performance objective. The nonlinear analysis results are compared to a set of predefined acceptance criteria that are selected such that nonlinear behaviors remain with limits established by testing or limits typically deemed acceptable by the structural engineering profession.

The nonlinear verification model is constructed utilizing CSI Perform-3D (Computers and Structures, Inc., 2016). The model includes inelastic member properties for ductile-detailed elements that are anticipated to be loaded beyond their elastic limits under MCE demands. These include the core wall axial/flexural response behavior, coupling beam rotational demands, and outrigger BRB bracing element axial yielding. CF-CPSW shear resistance, diaphragm slabs, and outrigger columns are desired to remain elastic under MCE demands, and are designed and detailed as a force-controlled element action and are modeled with effective stiffness elastic properties.

Inelastic vertical fiber elements are used for composite core walls to capture nonlinearity of moment and axial load interaction. The fiber element is comprised of both concrete and steel fibers. Coupling beams are modeled as nonlinear shear hinges with element stiffness, yield, and degradation characteristics that are matched to composite coupling beam experimental testing programs (Nie, Hu, & Eatherton, 2014). The following acceptance criteria as illustrated in Table 1 were selected for a Collapse Prevention performance objective under the MCE-level demands for a Risk Category III structure, which includes a 0.8 adjustment factor to adjust from common Risk Category II acceptance criteria.

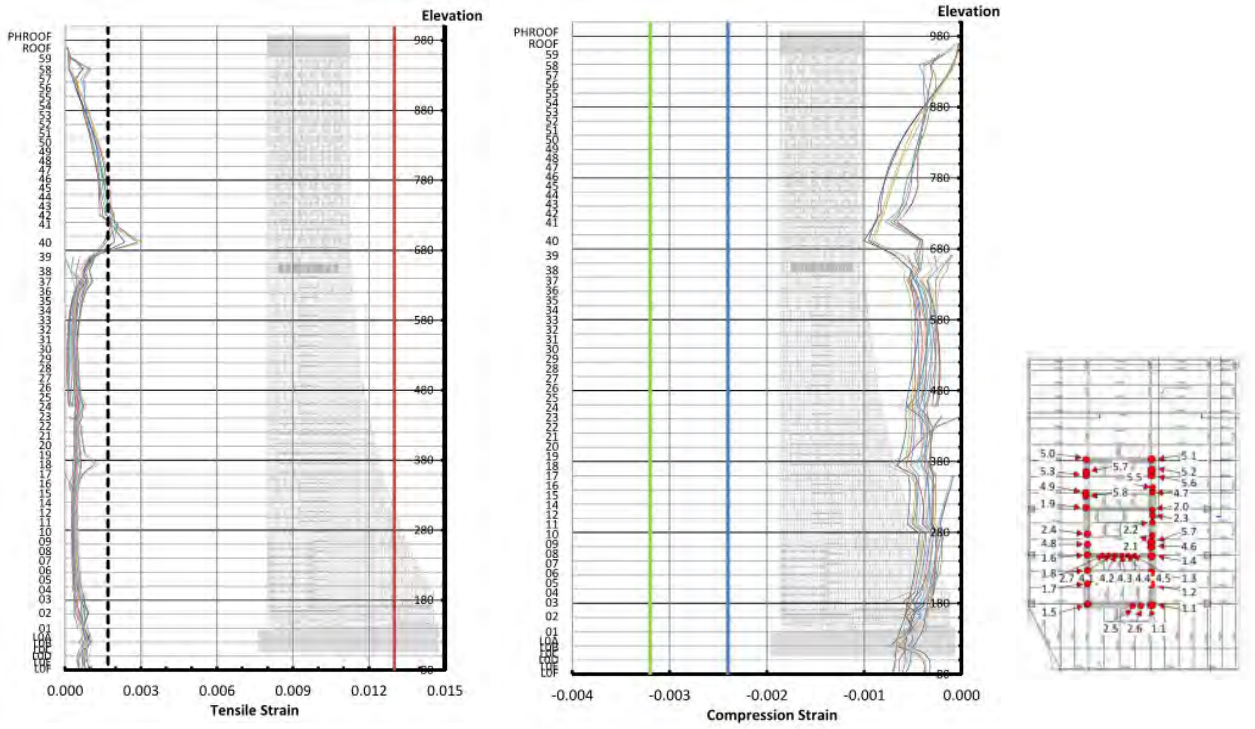
Response Parameter	Acceptance Criteria Value
Story Drift	3.0 x 0.8 = 2.4 percent taken as the average of 11 analyses; 4.5 x 0.8 = 3.6 percent maximum from any single analysis.
Residual Story Drift	1.0 x 0.8 = 0.8 percent taken as the average of 11 analyses; 1.5 x 0.8 = 1.2 percent maximum from any single analysis.
Coupling Beam Rotation	0.025 x 0.8 = 0.020 radian rotation limit, taken as the average of 11 analyses.
CF-CPSW Steel Plate Axial Strain	0.016 x 0.8 = 0.013 in tension, and matching concrete compression limit, taken as the average of 11 analyses.
CF-CPSW concrete Compression Strain	Based on confinement model by (Long & Cai, 2013), the strain limit is set as the strain at 80% of the peak stress on the descending branch of the confinement curve. Confined concrete strain limit of 0.0040 x 0.8 = 0.0032, taken as the average of 11 analyses.
BRB Deformation	2.5% x 0.8 = 2.0% compression and tension deformation, taken as the average of 11 analyses.

Table 1 – MCE Acceptance Criteria for Deformation-Controlled Actions

The nonlinear verification model was subjected to two suites of 11 pairs of site specific ground motions determined using the conditional mean spectrum approach. One suite characterizes relatively short period motion (corresponding to the primary 2nd/3rd mode of vibration), and the other suite characterizes long period motion (corresponding to the primary 1st mode of vibration).

As was observed in the detailed elastic design phase, the Rainier Square lateral system proportioning was governed by wind design considerations, with the wind elastic strength demands double or more of that of the design earthquake demands. The proportioning results in an inherent seismic overstrength beyond designing solely for code-level earthquake strength demands and suggested that limited system yielding might be observed in the nonlinear MCE analyses. Figure 6 plots the average maximum tension and compression strains recorded in the nonlinear responses at monitored locations at each wall end and wall intersection along the height of the tower. The peak measured CF-CPSW face plate tension strain was approximately 0.003 in/in which is more than a factor of four below the target acceptance criteria (0.013 in/in) and only about 1.5 times plate yield strain, which indicates an essentially elastic behavior of the core face plates in flexure-induced tension demands.

The peak measured CF-CPSW concrete compression strains were approximately 0.001 in/in which is observed to be well below the target acceptance limit of 0.0032 in/in. Peak concrete compressive strain of 0.001 in/in is within the elastic range of stress-strain behavior for both a confined concrete and an unconfined concrete condition, indicating an elastic response behavior of the composite core wall in compression.

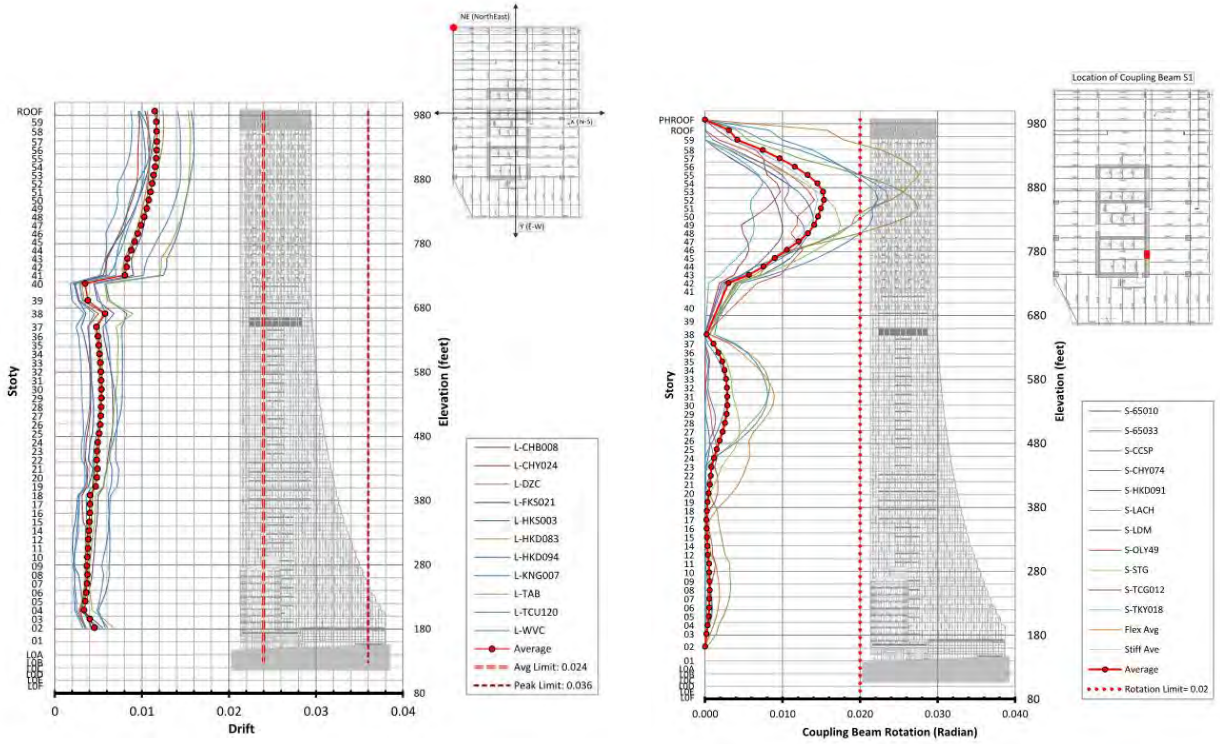


(a) (b)

Fig. 6 – CF-CPSW Maximum Strains: (a) Tension Strains, (b) Compression Strains

Other building response parameters also indicated limited nonlinear response for the lateral force-resisting system under the MCE demands. As illustrated in Figure 7(a), the average maximum inter-story drift of the building below the outrigger and belt truss level falls within similar magnitude ranges. A similar trend for the drifts above the outrigger and belt truss level is observed. The measured range of building floor plate corner drifts below the outrigger level are approximately bounded by 0.25% to 0.75% whereas the measured range above the outrigger level are approximately bound by 0.75% to 1.50% inter-story drift. For building response in the short core direction, the outrigger level provides a stiff restraint limiting core and building demands below the outrigger level. For building response in the long core direction, above the outrigger level the core wall drops from a two-cell core to a single-cell core to the roof.

The single core above the outrigger level is less stiff than the lateral system of the building below the outrigger level resulting in larger inter-story drifts in the building residential levels, but still well below the targeted acceptance criteria of 2.4% under the MCE ground motion records.



(a) (b)

Fig. 7 – Representative Building Responses: (a) Maximum Building Inter-Story Drift, (b) Coupling Beam Rotation

Figure 7(b) provides a representative coupling beam inelastic rotational response for a single coupling beam bay up the height of the tower. It is observed that very limited rotational demands are present in the core coupling beams below the outrigger level. This is supported by the observation in Figure 7(a) with limited building drift demands in the lower portions of the building. Above the outrigger level, coupling beam rotations are more pronounced, with average maximum rotations approaching 1.5%, but falling well below the target acceptance criteria of 2.0%.

Overall, as was suspected during the elastic design phase, the building response under MCE demands undergoes very little inelastic deformation demands and responds in an ‘essentially elastic’ response.

For building response parameters desired to remain elastic under MCE demands, they are designed and detailed as a force-controlled element action as described in PEER TBI, with appropriate response parameter criticality definition and strength reduction factors.

Specific to the CF-CPSW system, the design shear strength ϕV_{ni} is determined utilizing AISC 341-16 equation (H7-7) as follows:

$$\phi V_{ni} = \kappa F_y A_{sw}$$

where $\phi = 0.90$, F_y is the specified minimum yield stress of the face plates, and $A_{sw}$is the area of the steel face plates. Given the configuration of concrete fill thickness and area of steel face plates utilized on the Rainier Square project, the κ-factor as defined by AISC 341-16 equations (H7-8) and (H7-9) is nearly unity, with range of 0.97 to 1.0 depending on wall configuration.

Figure 8 plots the average maximum shear wall panel stresses for two representative shear wall panels along the building height. Both average demands and average demands amplified by a criticality factor of 1.5 are presented. The allowable shear stress of approximately 38 ksi is indicated as being above the amplified shear wall demands with face plate thickness of 1/2-inch nominal and more highly stressed regions near the building base and the outrigger levels at 3/4-inch. The allowable shear stress is calculated by taking the allowable design shear strength ϕV_{ni} and multiplying by a factor of 0.8 to account for the adjustment from Risk Category II to Risk Category III acceptance criteria.

Overall, the MCE nonlinear analysis verified the preliminary elastic SLE, DE, and Wind design, indicating the lateral force-resisting system meets at a minimum a Collapse Prevention performance objective and provides a level of safety and overall building ductility equivalent to or greater than that of a code prescriptive designed building.

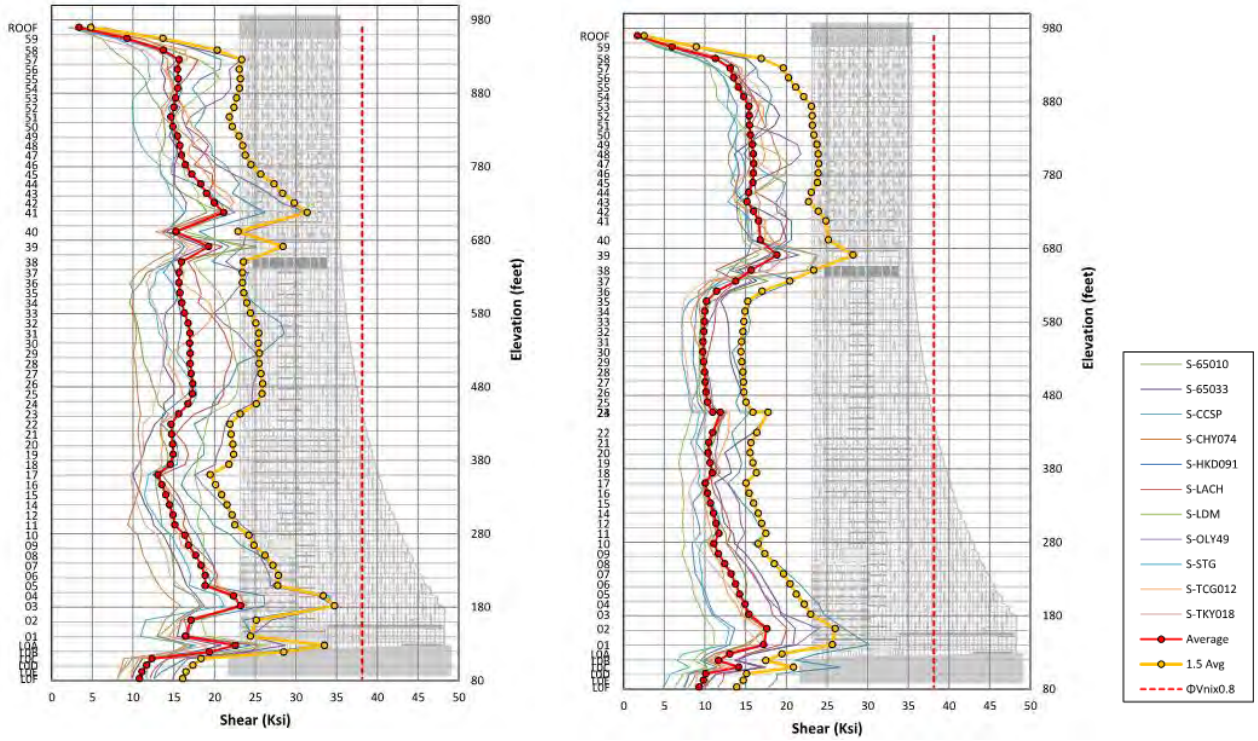


Fig. 8 – Representative CF-CPSW Normalized Wall Shear Stresses

SUMMARY

The Rainier Square project in Seattle is a 58-story, 850-feet tall mixed-use office and residential tower that utilizes a concrete filled composite plate shear wall (CF-CPSW) system for the central core component of an outriggered core lateral force-resisting system. The use of prefabricated steel plate panels allows for construction schedule savings when compared to a more traditional reinforced concrete core wall system. A detailed design and nonlinear verification analyses of the proposed Rainier Square lateral force-resisting system suggests that the lateral system once designed to remain elastic under the governing ultimate wind demands, will likely have limited inelastic demands under the MCE earthquake.

REFERENCES

Alzeni, Y., & Bruneau, M. (2014). *Cyclic Inelastic Behavior of Concrete Filled Sandwich Panel Walls Subjected to In-Plane Flexure.* MCEER-14-0009.

American Institute of Steel Construction. (2016). *Seismic Provisions for Structural Steel Buildings (ANSI/AISC 341-16).* Chicago, IL USA.

Eom, T.-S., Park, H.-G., Lee, C.-H., Kim, J.-H., & Chang, I.-H. (2009). Behavior of Double Skin Composite Wall Subjected to In-Plane Cyclic Loading. *Journal of Structural Engineering, 135*, 1239-1249.

Hu, H.-S., Nie, J., & Eatherton, M. R. (2014). Internal Force and Deformation of Concrete-Filled Steel Plate Composite Coupling Beams. *Journal of Constructional Steel Research, 92*, 150-163.

Long, Y.-L., & Cai, J. (2013). Stress-Strain Relationship of Concrete Confined by Rectangular Steel Tubes with Binding Bars. *Journal of Constructional Steel Research, 88*, 1-14.

Nie, J.-G., Hu, H.-S., & Eatherton, M. R. (2014). Concrete Filled Steel Plate Composite Coupling Beams: Experimental Study. *Journal of Constructional Steel Research, 94*, 49-63.

Pacific Earthquake Engineering Research Center, Tall Building Initiative (PEER TBI). (2010). *Guidelines for Performance-Based Seismic Design of Tall Buildings, Version 1.0.*

Ramesh, S., Kreger, M. E., & Bowman, M. D. (2013). *Behavior and Design of Earthquake-Resistant Dual-Plate Composite Shear Wall Systems.* West Layfayette, Indiana: School of Civil Engineering, Purdue University.

Razvi, S., & Maatcioglu, M. (1999). Confinement Model for High-Strength Concrete. *Journal of Structural Engineering*, 281-289.

G.T. LAND PLAZA: USING A COMPOSITE STRUCTURE TO ADDRESS THE CHALLENGES OF A COMPLEX SLENDER TOWER

Mark Sarkisian, PE, SE, LEED
Partner, Skidmore, Owings & Merrill LLP
San Francisco, California
mark.sarkisian@som.com

Neville Mathias, PE, SE, LEED AP
Associate Director, Skidmore, Owings & Merrill LLP
San Francisco, California
neville.mathias@som.com

John Gordon, PE, SE, CEng MIStructE
Associate Director, Skidmore, Owings & Merrill LLP
San Francisco, California
john.gordon@som.com

Joanna Zhang, PE, SE, LEED AP
Associate, Skidmore, Owings & Merrill LLP
San Francisco, California
joanna.zhang@som.com

ABSTRACT

The G.T. Land Plaza project occupies a 37 hectare site within the new Central Business District of Hangzhou in China. The mixed-use development comprises three independent building structures that extend over much of the site, including a 43-story office and hotel tower (Tower A), a 26-story residential tower (Tower B), and a retail podium building up to seven stories high (Building C).

The architectural massing of Tower A defines a narrow rectangular bar building, 165 m by 33 m in plan and 200 m tall to the top of the parapet. Various architectural features vary the regularity of the building geometry, enhance the spatial experience for different building programs, and present particular challenges in structural design. While the structure is predominantly of reinforced concrete, structural steel elements and composite elements are integrated where appropriate to deal with certain special features.

In addition to the typical static gravity and lateral analyses, response spectrum seismic analysis, non-linear time-history seismic analysis, non-linear push-over seismic analysis, wind tunnel study, vibration analysis, staged-construction analysis and thermal analysis were performed on the building. To satisfy the Chinese regulations, the project underwent and passed a seismic Expert Panel Review. Through a rigorous approach to the structural design, close collaboration between design disciplines, and the strategic use of concrete, steel and composite structural components, it was possible to provide a coordinated structural solution that satisfies both the target performance goals for the overall structure and enhanced performance goals for critical elements.



Figure 1: Architectural rendering

INTRODUCTION

The G.T. Land Plaza occupies a 37 hectare site within the new Central Business District of Hangzhou, located 5 km east of the city's legendary West Lake and 700 m from the north bank of the Qian Tang River. The site is flat, generally square in plan, and is occupied by a canal along the north-east (project east) boundary. The mixed-use development comprises three independent building structures that extend over much of the site, that are separated from each other by seismic movement joints above grade. Tower A is a 43-story, 200 m tall building that will be the focus of discussion in this paper. Tower A accommodates a hotel, office spaces and serviced apartments, and provides retail spaces in the first five levels. Tower A is rectilinear in plan, with its broad face aligned with the canal and the north-east (project east) boundary of the site (Figure 2). Adjacent to it, fronting the north-west (project north) boundary, Tower B is a 26-story, 110 m

tall, rectilinear building, accommodating retail in the first five levels above grade and serviced apartments above. Occupying much of the remainder of the site, to the south of the two towers, Building C is a retail podium building, up to seven stories tall. The roof over the center of Building C supports a garden with an extensive water feature, symbolically evoking the West Lake as the defining geographical feature of the city of Hangzhou.

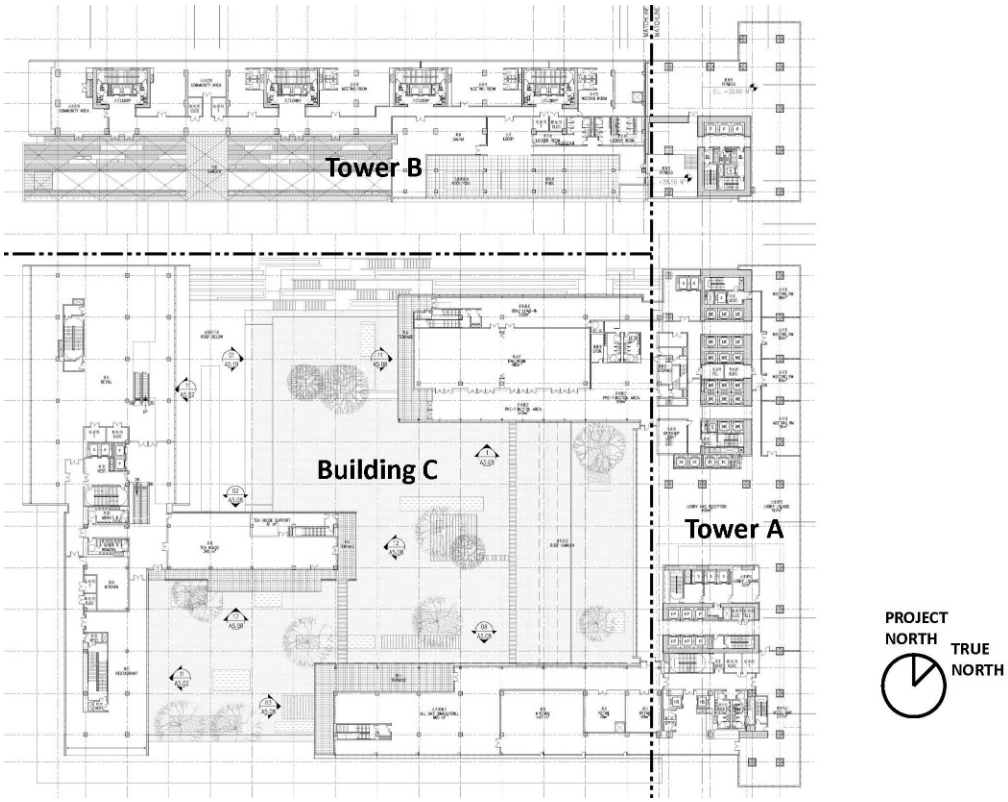


Figure 2. Plan of the project at level 6, showing the three buildings

STRUCTURAL SYSTEM

The architectural massing of Tower A defines a long rectangular bar building, 165 m by 33 m in plan and 200 m tall to the top of the parapet. Various architectural features vary the regularity of this shape, and these will be described. The structure is predominantly of reinforced concrete, with structural steel elements and composite elements integrated where necessary to deal with certain special features.

Resistance to lateral wind and seismic loads is provided through a combination of reinforced concrete core shear walls and reinforced concrete moment resisting frames. Reinforced concrete shear walls are typically located within three distinct core areas surrounding the mechanical rooms, stairwells and elevators. All major building columns participate in the moment resisting frames, and these are typically located at 9.0 m on center along the broad face, and at 7.25 m / 9.50 m / 7.25 m on center in the narrow direction. The outermost lines of columns in this direction are centered 24 m apart, and these define the width of the lateral system. Only a portion of the core at the north end of the building extends beyond this zone. To limit column sizes as well as to provide good ductility, composite steel reinforced concrete columns are provided in the lower levels at certain locations.

The gravity system typically comprises reinforced concrete beams at 3 m on center, supporting one-way spanning reinforced concrete floor slabs. Long span cantilever beams support the floor

slabs beyond the perimeter column lines. The reinforced concrete core shear walls and moment resisting frames also resist gravity load.

Below grade, all three independent buildings share a common three-story deep basement that extends over the entire site. The buildings are founded on a pile-supported reinforced concrete mat foundation that varies in thickness. Delayed pour settlement joints are incorporated into the basement and foundation structures, to accommodate the planned construction sequencing of the individual buildings and the varying settlements that are expected to occur. The 3.0 m thick mat under Tower A is supported by 840 no. 1000 mm diameter base-grouted bored piles. 690 of these piles extend approximately 40 m below grade into a sand and gravel layer, while 150 more heavily loaded piles under the north end of the tower extend approximately 65 m below grade into bedrock.

SPECIAL FEATURES

Several major and complex architectural features exist that present particular challenges in the structural design of Tower A:

Vertical slots. Two 13.5 m wide, multi-story tall vertical slots penetrate the building on its broad face (Figure 3). These slots serve to subdivide the program elements of the mixed-use building and allow more natural light to enter these spaces. In general, the program within the building is subdivided vertically, with the serviced apartments, office and hotel occupying the northern, central and southern portions respectively. The floors up to level 5 are largely occupied by retail.

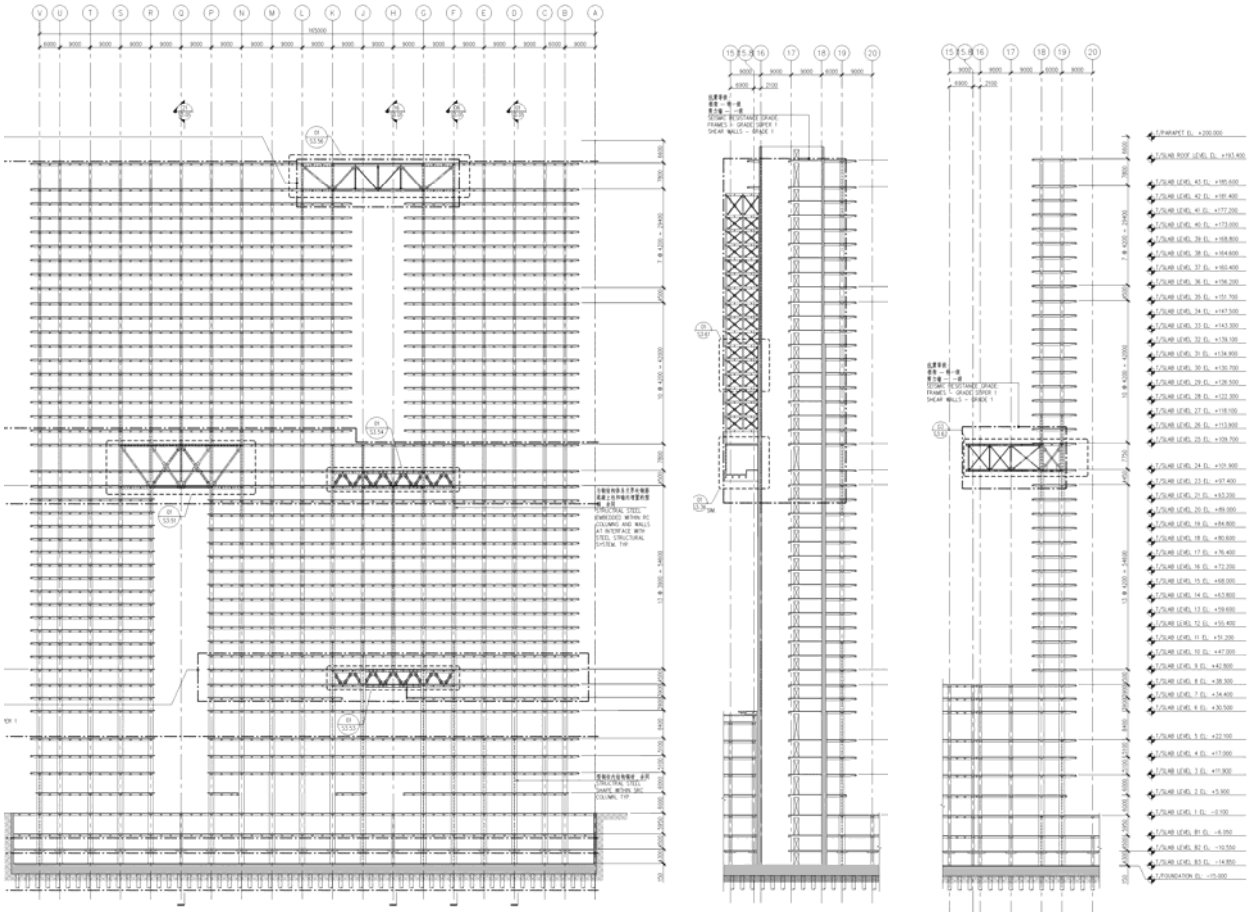


Figure 3. Sections through Tower A

North slot with transfer trusses. The first of the two slots is located in the northern half of the building, between level 1 and the underside of level 23, a slot height of 96.4 m. The location of the slot provides a natural separation between the serviced apartments and the office space. Provision of this slot involves eliminating a single line of columns below level 23, necessitating a transfer system to support the columns above.

The single line of four columns is transferred by a series of two-story high, built-up steel transfer trusses, located between levels 23 and 25, at the bottom of the column stacks (Figure 4). The floors at these levels accommodate mostly mechanical space, and the higher floor-to-floor heights provide a well-proportioned transfer truss system that is 12.3 m high and spans 18.0 m between supports.

The primary transfer system is a simple A-frame, with two built-up steel box diagonals in compression and a series of steel plates resisting the tension in the bottom chord. A secondary transfer system is provided for redundancy. This takes the form of an inverted A-frame, superimposed over the primary system, with built-up steel H-shape diagonals supporting the tension forces induced by the column transfer. Compression forces in the top chord are resisted by built-up steel H-shapes embedded within and acting compositely with the reinforced concrete floor framing.

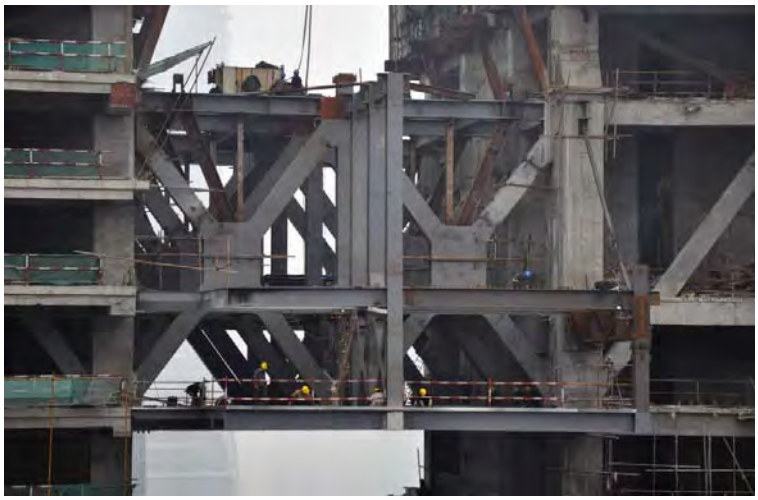


Figure 4. Construction photo of the transfer truss between levels 23 and 25

Four transfer trusses are provided to support the four columns. The innermost two trusses are supported directly by steel columns embedded within the reinforced concrete walls of the north core and central core. The steel columns extend one story above and below the height of the transfer trusses. In addition, the bottom chord of each truss is extended one bay further on each side through the use of steel shapes embedded within the core walls at level 23. The outermost two trusses are supported by steel columns embedded within the reinforced concrete building columns. As with the inner trusses, the steel columns extend one story above and below the height of the trusses. Additionally, all members of the outer trusses extend one bay further each way, with a single tension diagonal in the end bays.

At levels 23 and 24, within the 18.0 m wide zone defined by the clear span of the trusses, the floor framing comprises steel beams supporting one-way spanning reinforced concrete floor slabs. At level 25 and all floors above, the floor framing reverts to reinforced concrete beams and one-way spanning slabs.

South slot with coupling trusses. The second of the two slots is located in the southern half of the building, between level 25 and the underside of level 43, a height of 74.8 m, and separates

the office space from the hotel guest rooms. Two adjacent lines of columns are eliminated to create this slot, which although only 13.5 m wide on the east face, widens to 23.4 m on the west face.

A single 7.8 m tall story (level 43) occurs above this slot, above which is the main roof of the tower. The floor space in this area is occupied by hotel program, mostly restaurants, kitchens, and other back-of-house elements. Four single-story (7.8 m) high built-up steel trusses, spanning 27.0 m between supports, are employed to support the floor framing at level 43 and roof level (Figure 5). These act as a coupling structure, connecting the building on each side of the slot.

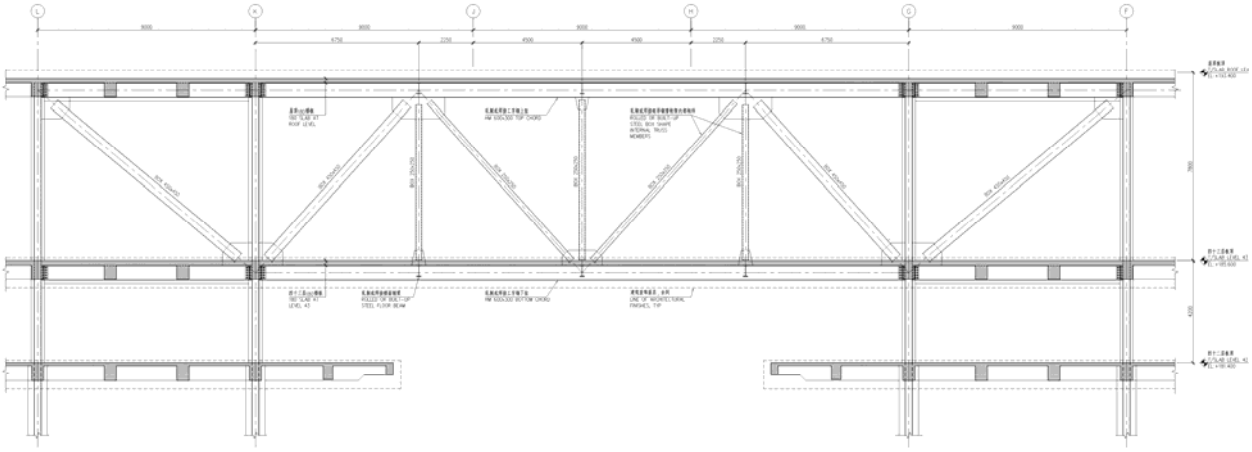


Figure 5. Coupling truss between level 43 and roof level

The trusses adopt a configuration similar to a Warren truss, typically with 4 bays of 6.75 m each. The two inner trusses are supported by steel columns embedded within the reinforced concrete columns and walls of the central core and south core. The two outer trusses are similar, but are supported by steel columns embedded within the reinforced concrete building columns. These trusses also extend one 9 m wide bay further each way. The steel columns supporting all trusses extend down one story below the underside of the truss, to level 42. At level 43 and roof level, within the 27.0 m wide zone defined by the clear span of the trusses, the floor framing comprises steel beams supporting one-way spanning reinforced concrete floor slabs.

Long-span floors. To accommodate large open spaces within the hotel entrance lobby at level 1 and the two-story tall hotel reception area at level 6, a single line of columns is eliminated between level 1 and the underside of level 8. All floors between these two levels are required to span 18.0 m, with the deeper floor framing being accommodated within the higher floor-to-floor heights at the lower levels of the tower. Above level 8, however, the lesser floor-to-floor heights determine that these columns remain, requiring a further transfer system. Fortuitously, the columns to be transferred are located under the building slot that separates the office space from the hotel guest rooms in the upper levels of the tower, and as such these columns extend no higher than level 25.

The primary transfer system takes the form of four single-story tall, built-up steel transfer trusses, located between levels 8 and 9. This 4.5 m high story is occupied mainly by mechanical rooms. The configuration of diagonals within the trusses closely resembles a Warren truss, and the relatively shallow truss depths combined with the need to support seventeen floor levels determine that the sizes of the diagonal and chord members are substantial. The two inner trusses are supported by steel columns embedded within the reinforced concrete building columns. The two outer trusses are similar, but extend one 9 m wide bay further each way. The steel columns supporting all trusses extend one story above and below the height of the trusses.



Figure 6. Construction photos of the transfer truss between levels 8 and 9

A secondary transfer system is provided for redundancy. This system is a near identical arrangement of transfer trusses located within the 4.5 m high mechanical floor near the top of the transferred column stack, between levels 23 and 24. As such, the secondary system supports the transferred columns as hangers, and steel column shapes encased within the reinforced concrete columns are provided to accommodate the tensile forces of a hanging system. The steel column shapes connect the primary and secondary transfer systems at levels 9 and 23 respectively.

At levels 8, 9, 23 and 24, within the 18.0 m wide zone defined by the clear span of the two truss systems, the floor framing comprises steel beams supporting one-way spanning reinforced concrete floor slabs. At floor levels in-between, the floor framing reverts to reinforced concrete beams and one-way spanning slabs.

Cantilever trusses at hotel guest rooms. The architectural design extends the building beyond the typical 33 m width, at two bays to the west of the south core, between levels 25 and 42. This results in floors that extend approximately 10 m into column free space beyond the face of the core. The floors are to accommodate hotel guest rooms that face west, with blank walls to the north and south.

The original structural concept was to provide a series of vertical hanging steel truss frames, aligned with the supporting walls and columns of the south core, to form the support structure on the north and south sides of this space. To incorporate redundancy into the system, this developed into X-braced hanging steel truss frames with the diagonal members resisting tension or compression (Figure 7). The area within the space is column free. Floor framing spanning 18 m between trusses comprises steel beams supporting a composite metal deck floor slab. The hanging trusses are supported by steel columns embedded within the wall and column elements of the south core.

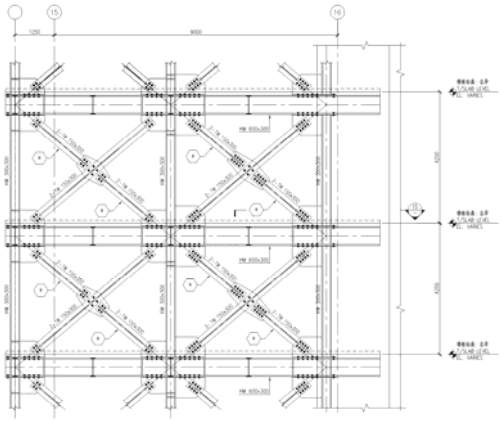


Figure 7. Cantilever trusses between levels 25 and 42

Long cantilever floor. Between levels 23 and 25, the building width extends to the west to create a long, two-story high shelf. This extension occurs along much of the west elevation, between the north and south cores. The depth of the extension matches that at the south core above level 25. The extended space at level 24 is intended to accommodate hotel amenities and conference rooms, whilst level 23 accommodates MEP equipment rooms.

Within the northern half of this extended space, the structural system typically incorporates a series of 2.0 m deep reinforced concrete beams at level 24 that cantilever 10.5 m from each column line. The 7.25 m backspan beam is similarly 2.0 m deep. These beams support conventional reinforced concrete floor framing at level 24. Steel posts, located at the tips of the cantilever beams, support steel framing with a composite metal deck slab at level 25. Similarly, steel hangers supported at the underside of the cantilever beams support steel framing with a composite metal deck slab at level 23.

At the north end, the extended space interfaces with the transfer trusses that span across the north slot (described previously). At this location, the cantilever and backspan beams that would have been supported by the transferred column line are replaced by a 4.5 m high, single-story cantilever and backspan truss between levels 23 and 24. This is in turn supported by two of the transfer trusses.

Within the southern half of the extended space, the reinforced concrete cantilever beams support a swimming pool at level 24 (Figure 8). The structural system is similar to that in the northern half, although the lower beams dictated by the pool's depth eliminates level 23 below. In addition, the cantilever and backspan beams taper at their common support to engage the main floor at level 23 and eliminate the short column.

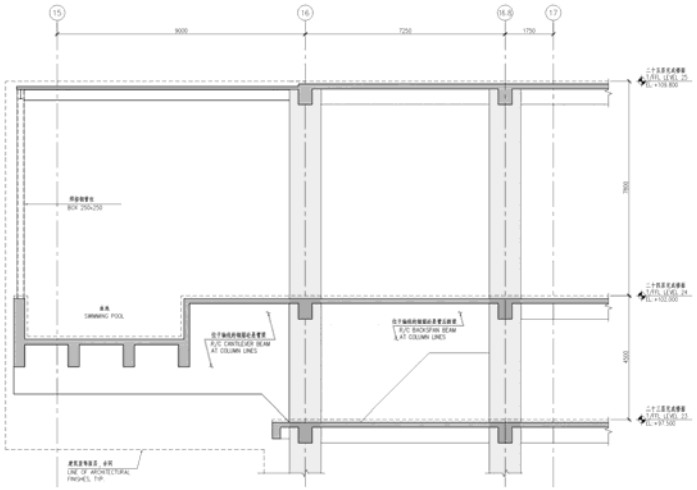


Figure 8. Long cantilever beam supporting swimming pool at level 24

Similar to the structure at the north end, one of the cantilever and backspan beams supporting the swimming pool are supported by the transfer trusses that support the long-span floors (described previously).

Long cantilever trusses at hotel spa. At its southern end, the width of tower narrows from 33 m typically to only 13.5 m. This occurs over a 29 m length of the building beyond the south core. Two lines of columns in the narrow direction are spaced only 6 m apart. A single east-west shear wall replaces one of the columns in this area, to help mitigate the effects of lateral and torsional loads.

Typically, this area of the tower is occupied by hotel guest rooms. The 7.8 m tall story at level 24, however, accommodates hotel amenities, some of which have already been described. At the southern end, between levels 24 and 25 only, the tower width extends dramatically from 13.5 m to 33 m to match the typical tower width elsewhere. This extended area accommodates the hotel spa treatment rooms.

The structural system in this area provides two single-story tall built-up steel trusses between levels 24 and 25 that cantilever to the west of the main building structure (Figure 9). The first of these trusses cantilevers 22.2 m from the nearer support column, and engages the second support column 6 m behind it. The second truss cantilevers 19.5 m from the edge of the 6 m wide shear wall which it fully engages with steel truss members embedded within. Both steel trusses incorporate cross-braced panels to ensure redundancy, with vertical members at truss nodes. Steel column shapes embedded within the supporting columns and walls extend one story above and below the truss depths.

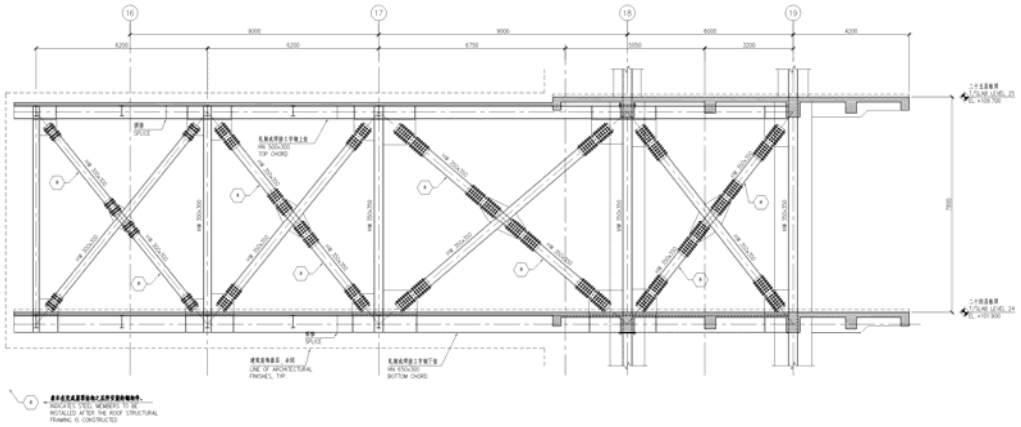


Figure 9. Long cantilever truss supporting hotel spa at level 24

In the area supported by the trusses at levels 24 and 25, floor framing comprises steel beams supporting composite metal deck floor slabs. Steel cross-bracing on plan is provided to ensure that the diaphragm forces are adequately transferred to the main structure and the lateral resisting elements.

SPECIAL ANALYSES

The structural design was performed in accordance with the requirements of the relevant Chinese codes and standards, including those for Zhejiang province. Building structures in Hangzhou are designed for seismic design intensity 6 which represents a moderate seismic level. Considering the height, length and slender form of Tower A, 100 year return basic wind pressure was used for both the strength and drift code design checks. In addition to the code defined wind pressures, the results of the wind tunnel study was also considered. Because of the various structural irregularities resulting from the architectural design, certain special studies and analyses were carried out. Some of these studies and analyses were mandated as a result of the seismic expert panel review (EPR) process as a precondition to fulfilling the requirements for Design Development approval. They included:

Wind tunnel test. The wind tunnel test and wind vibration analysis were conducted by College of Civil Engineering and Architecture, Zhejiang University. The wind tunnel test was performed, from 0° to 360° in 10° increments around the building. Both scenarios with and without future buildings were modeled. (Lou, 2009) The wind loads from wind tunnel test were compared with the wind load from the code and the most critical cases have been used for the structural design.



Figure 10: Wind environment simulation at the wind tunnel test (Lou, 2009)

Wind acceleration check. The accelerations at the highest occupied floor due to a 10-year return wind were checked to ensure compliance with the 0.15 m/s^2 code specified limit for residential usage.

Vertical seismic force checks. The following elements were designed to resist a vertical seismic force equivalent to 10% of seismic gravity load:

- The long cantilever trusses supporting the hotel spa at level 24.
- The cantilever trusses supporting the hotel guest rooms between levels 25 and 42.
- The cantilevered swimming pool structure at level 24.
- The coupling truss at level 42.

Seismic performance in the moderate earthquake. Certain key elements that are critical to the performance of the building were designed to meet a higher seismic design standard than conventional structural members. The following were designed to remain elastic in a moderate earthquake (475-year return period):

- All transfer trusses.
- The long cantilever trusses supporting the hotel spa at level 24.
- The cantilever trusses supporting the hotel guest rooms between levels 25 and 42.
- The coupling truss at level 42.

Non-linear pushover analysis. A non-linear pushover analysis was performed for Tower A, using the PERFORM-3D program. Various lateral load distribution scenarios were considered. It was found that the inter-story drift ratio along the height of the building during a rare earthquake event (2,475-year return period) was much less than 1% at all floors for the x- and y- directions.

Diaphragm slab stress analysis. To strengthen the tower structure above and below the two large vertical slots in the building, the slabs over the entire floor at levels 1, 23, 24, 25, 43 and roof level were increased to 180 mm thick. The slabs at levels 8 and 9 at the location of the transfer truss over the hotel lobby were also increased to 180 mm. thick. Slab diaphragms in critical areas were analyzed using semi-rigid diaphragms. Principal stresses were checked, and where the allowable tensile stresses were exceeded, additional reinforcing bars, sufficient to resist full tension load, were provided at slab mid-depths. In addition, reinforcing bars in all slabs in critical areas were designed not to yield in the moderate earthquake.

Floor vibration check. The vibration performance of the following elements was checked for compliance with the requirements of AISC Design Guide 11 “Floor Vibrations due to Human Activity”:

- The long cantilever trusses supporting the hotel spa at level 24.
- The cantilever trusses supporting the hotel guest rooms between levels 25 and 42.
- The coupling truss at level 42.

In all cases, the estimated peak acceleration corresponding to the first vertical mode was considerably less than the recommended limit of 0.5% g. This is because of the large participating mass associated with vibration modes when compared to the walking excitation forces.

Core shear wall optimization. As the architectural design of Tower A developed, so did the configuration of the lateral resisting system, in particular the shear walls. The extreme rectilinear plan of the tower (165 m long by 33 m wide) determined that torsion control would be a major feature of the structural design. Together with the high aspect ratio of the structure, it was apparent that identifying a suitable configuration of shear walls would be paramount.

To minimize the impact on space within the tower, shear walls were arranged as much as possible around and within the building cores (Figure 10). Three distinct core areas were established (north core, central core and south core) to serve the three zones of the tower subdivided by the vertical slots. To adequately resist torsion, the north and south cores were enhanced, through the addition of an east-west wall extension to the west of the north core, as well as an isolated east-west shear wall located south of the south core. Wall thicknesses were optimized as necessary, to bring the centers of mass and rigidity as close as possible to each other. Similarly, where the provision of walls was detrimental to the lateral performance of the structure, these walls were minimized as much as possible or removed altogether. This is evident in the central core where walls along the south and west sides of the core have been replaced by columns.

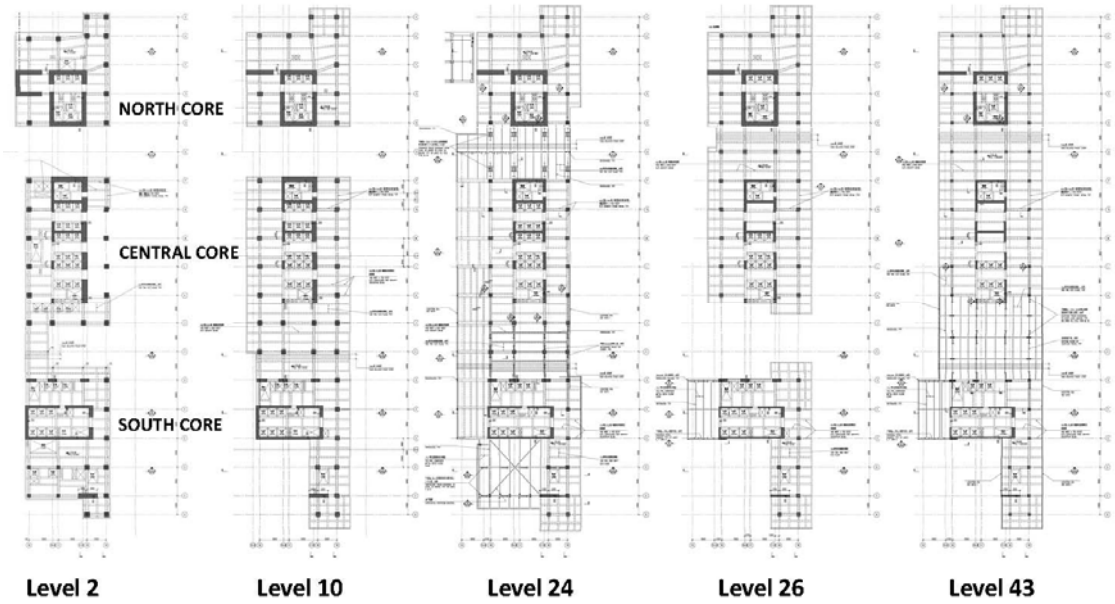


Figure 11. Core shear wall and floor framing configurations at various floor levels

Thermal analysis. An analysis was performed on Tower A to investigate the effects of thermal variations on the behavior of the structure. The study also considered the effects of shrinkage strains, in addition to thermal loads. Since the thermal demands on the structure depend on the temperature at the time of construction, specifically at the time the delayed pour strips provided

to reduce shrinkage strains were poured, multiple construction scenarios with different construction starting dates were considered. The thermal and shrinkage strain demands at various points in time, during and after construction completion, with corresponding temperature conditions which result from the governing scenarios, were then used to perform a structural analysis of the full building model using the computer program ETABS. Various references were used to compute the demands on structural elements considering thermal load and shrinkage, and to estimate the implications of those demands on the structure including prediction of whether cracking might occur and to propose localized strengthening of certain areas in order to control cracking and/or improve strength resistance. Recommendations from those references were evaluated in conjunction with results from the structural analysis of the building, which takes into account the unique geometry and structural configuration of the building.

From the analysis results, it was found that the stresses caused by thermal changes were relatively small, and were generally smaller in magnitude than those caused by shrinkage. It was also found that the use of delayed pour strips was expected to reduce shrinkage strains by about 40%. The obtained stresses due to the combined effect of shrinkage and thermal loads were generally very low throughout the building, and the highest tensile stresses generally occurred at levels where the building slab was continuous from end to end which occurs at the floors near the middle and top of the building. Tensile stresses were generally under 1.25 MPa, and on this basis, no cracking would be expected in the slab under tension.

CONCLUSION

When considering only its rectilinear shape, the tall, long and slender Tower A is, by itself, a challenging structure to engineer. In addition, the structure of the building exceeded several prescriptive limits defined in the Chinese design codes causing it to require an expert panel review (EPR) which was undertaken and passed.

The architectural design of Tower A called for radical formal moves that resulted in a complex structure. Through a rigorous approach to the structural design and close collaboration between all design disciplines, and a strategic use of concrete, steel and composite elements, it was possible to provide coordinated structural solutions that met and exceeded the structural performance and overall building structural design goals.

REFERENCE

Lou, W. J., Shen, G. H., & Wang, X. (2009). *Wind Tunnel Test Report of G. T. Land Plaza.* Hangzhou, China: College of Civil Engineering and Architecture, Zhejiang University.

MULTIFUNCTIONAL COMMERCIAL BUILDINGS IN STEEL AND COMPOSITE CONSTRUCTION

Prof. Dr.-Ing. Richard Stroetmann
Institute of Steel and Timber Construction, Technical University of Dresden
Dresden, Germany
Richard.Stroetmann@tu-dresden.de

Dipl.-Ing. Lukas Hüttig
Institute of Steel and Timber Construction, Technical University of Dresden
Dresden, Germany
Lukas.Huettig@tu-dresden.de

ABSTRACT

In the life cycle of commercial buildings the user requirements are changing usually manifold. In addition to changing within a utilization form, e.g. office use, also different types of use, for instance residential use, hotel and retail, may also be relevant. This requires a suitable building design, which makes due to its supporting structures and façades, the floor plan layout and building accesses, these kinds of usage possible. The following article presents results of the ongoing research project P1118 "Multifunctional residential and commercial buildings in steel and composite construction" (Stroetmann et al., 2015). This includes the ecological and economic assessment of the buildings taking into account the convertibility, the use of steel and composite constructions and the consideration of façades in the design and optimization according to sustainability criteria.

1 INTRODUCTION

A relatively high vacancy rate of office buildings can be found in Germany and in many other European countries (Figure 1). Especially in major cities, vacancy may become a visible problem. While, until the 70s of the last century, buildings were characterized by predominantly robust structures, which were planned for long-term use. In the subsequent time, increasingly cost-effective investment properties were developed for special uses and early amortization of investments. Negative consequences of this development are the lack of adaptability to changing requirements, decreasing marketability with possible structural vacancy and demolition of the buildings.

The office and commercial building of the future should be planned in a way that the consequences of social and sociological changes within its life cycle can be incorporated with low monetary resources to avoid the vacancy of the property and to achieve a higher profitability. For this, it is necessary to design the buildings for different types of uses. It requires a "robust" primary structural system that allows the integration of a wide variety of uses without major structural interventions.

The design of the structures gives the boundary conditions for the mechanical installations and building finishing. Variable buildings are characterized by the fact that they require no or only

minor modifications of the structures when the type of use changes. Steel and composite construction provides advantages related to conventional concrete structures because, besides large spans and fewer columns, a reduction of building materials can be achieved. This leads to less demand of building material and improves the ecological performance.

In the research project P881 the sustainability of steel and composite constructions for office and administration buildings were investigated (Mensinger et al., 2016). Guidelines and planning tools, such as component catalogs and design software for office buildings were developed. By planning of buildings under defined design conditions, involving the relevant scenarios of office configurations, the ecology and economy of the bearing structures was optimized. Hence, multifunctional office and commercial buildings are the subject of the ongoing research project P1118 (Stroetmann et al., 2015). Based on the project P881, various types of usage, e.g. as office building, different types of residential, retail, hotel and gastronomy, will be considered in the design and optimization.

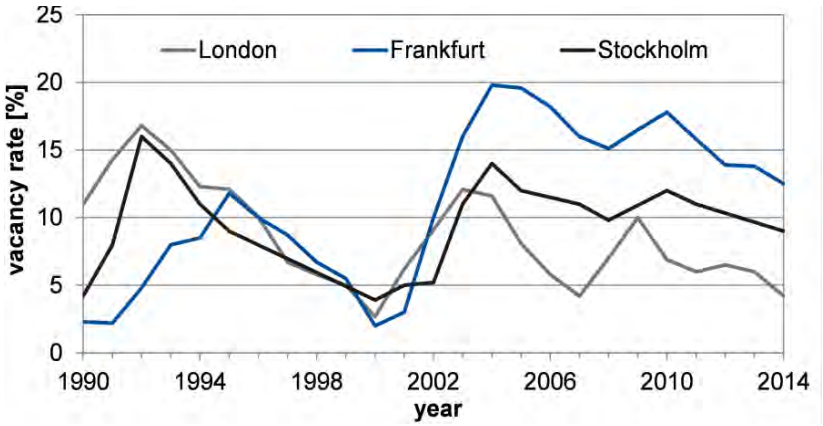


Fig. 1 – Changes in the vacancy rates of office space in selected European cities (Stroetmann & Hüttig, 2016).

2 ASSESSMENT OF SUSTAINABILITY

The assessment of sustainability takes place by various certification systems. The British system BREEAM and the US system LEED are the international leading systems. In Germany, the equivalent systems DGNB (Deutsches Gütesiegel für Nachhaltiges Bauen) for public buildings and BNB (Bewertungssystem Nachhaltiges Bauen für Bundesgebäude) for federal buildings have been developed. Compared to BREEAM and LEED an equal rating of the three aspects ecology, economy, socio-cultural and functional quality is taken by DGNB and BNB. Thus, the German systems are also referred as systems of the second generation. In addition, the technical and the process quality are taken into account as in all areas relevant properties. Meanwhile, in addition to office and administration buildings other types of buildings, such as hotels, commercial buildings, education centers, industrial buildings and parking garages can be assessed.

2.1 ECOLOGICAL SUSTAINABILITY

The evaluation of the ecological quality follows by the Life Cycle Assessment (LCA) of buildings and its components. This includes the phases of product manufacturing, construction, the use stage and disposal. In addition credits and debits beyond the life cycle for reuse, recovery and recycling will be considered. The environmental indicators (e. g. global warming potential and

primary energy demand) for building materials and products are collected in databases and environmental product declarations (EPD). An overview is given in (Stroetmann et al., 2016). In several EPD only the phase of manufacturing and the credits and debits at the end of life are considered. For the phases of erecting, use and disposal a lack of data can be observed. An estimation can carried out from the construction processes and transportation distances.

The Assessment of buildings according to DGNB and BNB is carried out by defined reference, target and limit values for the individual criteria. By comparison with the values of the assessed building points will award. To determine the degree of the ecological quality, environmental indicators will weighted by factors of importance. The reference, target and limited values are defined for entire buildings but not for individual components or building systems. A similar procedure, as applied for buildings, is possible for the evaluation of components and building systems (Mensinger et al., 2016). Thereby, it is necessary to define the functional unit and to determine target and limit values for the variations of relevant constructions. This allows classifying the quality of the given solution. By using the factors of importance for the individual criteria, the ecological performance can be determined similar to the systems of BNB and DGNB. The principles of the method used in the research project P881 are shown in the Figure 2.

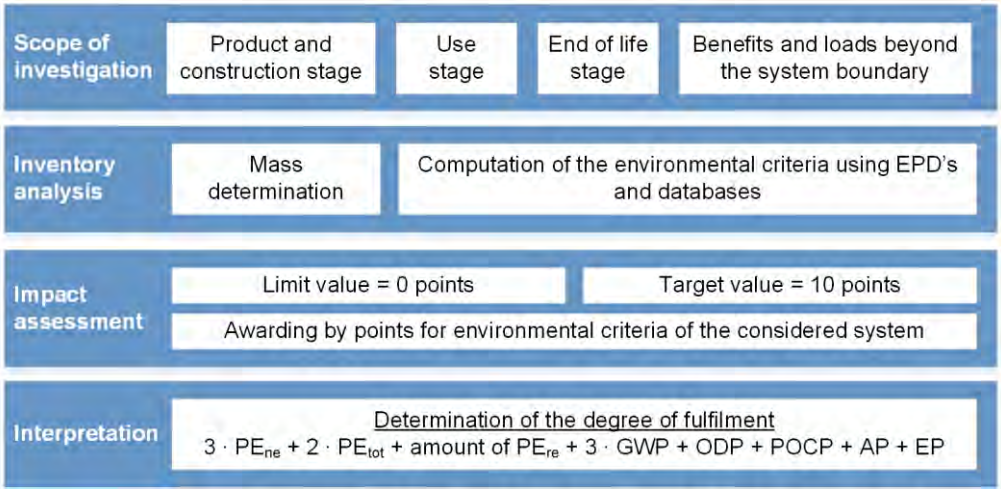


Fig. 2 – Life cycle assessment of structures in the context of the research project P881 (Mensinger et al., 2016).

2.2 Economical sustainability

The economic assessment takes into account the building-related life cycle costs (LCC) as well as the efficiency, adaptability and the intrinsic value. Table 1 provides an overview of the criteria given by BNB and DGNB for office and administration buildings and their shares in the overall assessment. The construction costs of the buildings become less importance. The influence of the follow-up costs as well as the efficiency, flexibility and intrinsic value increases. The efficient use of buildings to the intended purpose is measured by the area efficiency factor F_{eff}, which will determined by the ratio of main usable area to gross floor area. At BNB the target value is $F_{eff} = 0.75$, the limit value is $F_{eff} < 0.48$. The intrinsic value of a building increases by its adaptability to different scenarios of use. Scopes of the evaluation are criteria like

- clear story height and building width,
- vertical access of the building,
- floorplan design (size of units, space for mechanical services, emergency exits etc.)
- construction of inner- and partition walls

- level of imposed loads and their reserves
- technical equipment for air condition, building automatization, building installation centers
- possibility of space use in small units, possibility to use renewable energies.

Depending on the type of building different requirements are placed on the mentioned criteria. Space efficiency and adaptability can be achieved by appropriate floorplan design, building width, clear story heights, building access, including relevant usage scenarios and appropriate revisable technical installations. Flexible buildings are characterized by floors without or at least optimal positioned inner columns involving various usage scenarios. Related to the construction, the adaptability by BNB is rated positive, if at least 80 % of the inner walls are movable and at least 50% of the floors are designed for an imposed load of ≥ 5 kN/m². Partition walls should be connectable in each axis of the façade grid, not extend into the floor and ceiling structure, dust-free mountable and reusable.

Under the conditions for a space-efficient and flexible building and the assumption that the costs for operating and maintenance are largely independent on the bearing structures, the optimization and comparison of building structures can be made on the manufacturing costs. Prices for building materials, performance values for productivity and salaries depending on regional, temporal and economic fluctuations. In the research project P881, a compilation of manufacturing costs and work processes for bearing structures of buildings was made. This is based on researches and experience of various companies from the German-speaking countries. The results of the parametric studies were rated as a percentage of the respective peak value (100 %). This corresponds to a relative comparison, disposing the effect of these variations on the results as far as possible. This applies as long as the relations of the expenses remain at the compared systems.

Table 1. Criteria of the economic quality of office buildings (cf. BNB, DGNB).

content	BNB	DGNB
building-related life cycle costs	11,25 %	9,64 %
profitability, intrinsic value, performance	space efficiency 3,75 %	flexibility and conversion feasibility 9,64 %
	adaptability 7,5 %	marketability 3,21 %

3 DESIGN OF BEARING STRUCTURES

From the building requirements and the specified grids of façades and columns, the boundary conditions and design parameters for the bearing structures arises. This includes the spans of slabs and beams, floor heights, imposed and additional dead loads, fire protection, the design of components and installation spaces. A selection of appropriate construction systems, components and design principles, which fulfill the requirement under consideration of sustainability criteria in an optimum, has to be taken.

A systematic procedure for the design of the building structures is to deduce the essentials parameters of the relevant usage scenarios. The choice of scenarios should consider the building location (e.g. city center or suburb) and the current and future needs. Furthermore, it is preferable to distinguish between floors within the building because certain uses preferable positioned in certain floors. Typical positioning's are underground parking and storage areas in the basement, retail on the ground floor, office, residential and hotel uses on the upper floors. Specific requirements resulting from the type of use, e. g., the width of the building, story height, im-

posed loads, access to the building and technical equipment. Vice versa, the suitability of the building parameters to specific usage can be carried out. According to the previous descriptions, in P1118 the essential characteristics of building parameters for the design of bearing structures were examined. Some individual parameters are explained in the following.

The assumptions for dead and imposed loads are carried out in Europe by EN 1991-1-1 and the country-specific national annexes. Figure 3 shows a comparison of the imposed loads, which are applicable with a surcharge for partition walls for different types of usage taking into account the German national annex. Floors for office, residential and hotel usage can be designed for a relatively low imposed load (≤ 3.0 kN/m²). For retail, convention centers and gastronomy areas, imposed loads up to 5.0 kN/m² have to be considered. Storage and archive space requiring even higher loads. The amount of additional dead load depends on the ceiling construction. The use of suspended ceilings and double floors creates a high degree of flexibility for the technical installations and subsequent use changes. If the floors are rented to different users, the combination of both systems may be relevant.

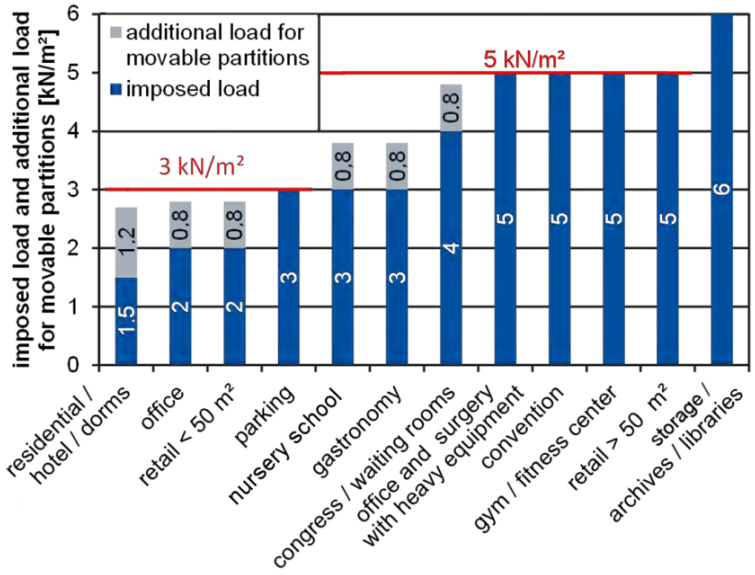


Fig. 3 – Imposed loads and additional loads for partition walls for various types of use.

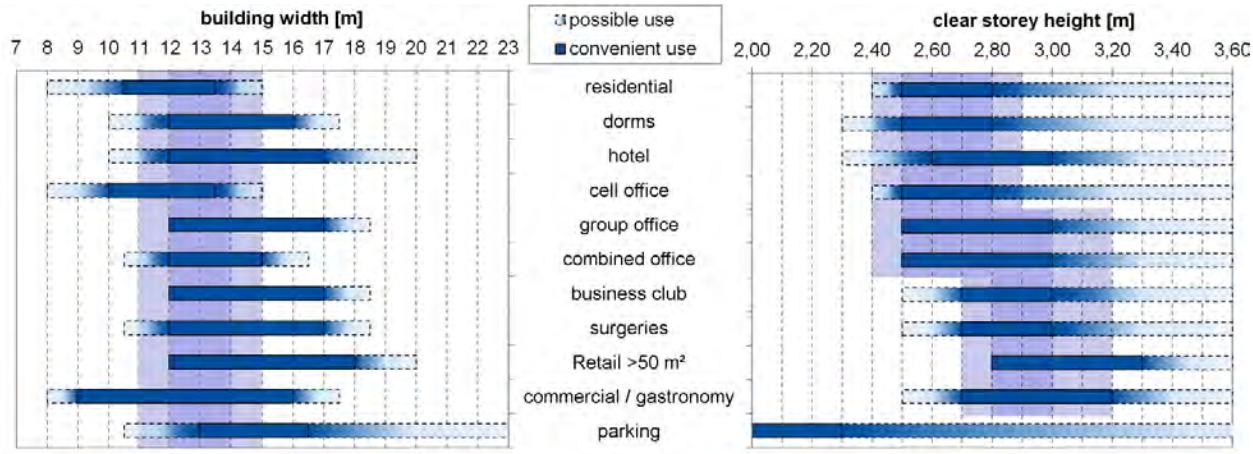


Fig. 4 – Convenient and possible building width and clear story height of various types of use.

Figure 4 shows convenient and possible building widths and story highs for various types of usage. The left diagram indicates that a building width of 12 to 14 m allows several types of use. The ceiling structures may design with or without internal columns. By positioning inner columns the material consumption and the width of the floor constructions may be reduced, on the other hand the flexible usage will be restricted. Looking at the clear story height, considerable differences as a result of the various usage requirements can be found. Parking levels can be built with a clear height of ≥ 2 m. For residential and office uses clear heights ≥ 2.50 m are suitable. For retail larger clear story heights are necessary depending on the sales areas.

4 DESIGN AND EVALUATION OF REFERENCE BUILDINGS

Based on the results of the research project P881, in the project P1118 buildings with different degrees of variability will be optimized according to ecological and economic criteria. The investigations include the supporting constructions and foundations, the structural fire protection as well as the façades. The assessment takes into account, in particular, the influence of variability and the resulting improvement of marketability for a longer period of use. It will be proved, to what extent a greater variability of the buildings leads to more effort in the supporting and façade constructions. Furthermore, the impact to the ecological and economic balance over the life time of the building is in the focus of the examination. In the following, studies on a building with high variability and the influence of the supporting and façade constructions on the ecological performance are described.

Figure 5 shows the cross-section of the reference building with a high variability of use. A selection of floor systems without inner columns will be accessed. Due to the clear story heights of 3.2 m and imposed loads of 5.0 kN/m² in all upper floors, common usage types such as office, residential, hotel use, medical practices and retail are made possible. The ground floor offers due to its larger clear story height optimal conditions for the usage as a sales area. The two lower floors serve as parking and storage areas. They will be included in the examinations at a later stage. The following evaluations refer to the ground floor and the upper floors.

Multifunctional reference building with three different floor systems (see Figure 6):

- downstand beams with composite slabs,
- additive floor with integrated beams (IFB)
- TOPfloor® Integral system.

Input variables:

- loads: dead load of construction,
  additional dead load 1.5 kN/m²
  imposed load 5.0 kN/m²
- construction steel grade: S460
- reinforcing steel grade: BSt500
- column spacing: 5.4 m

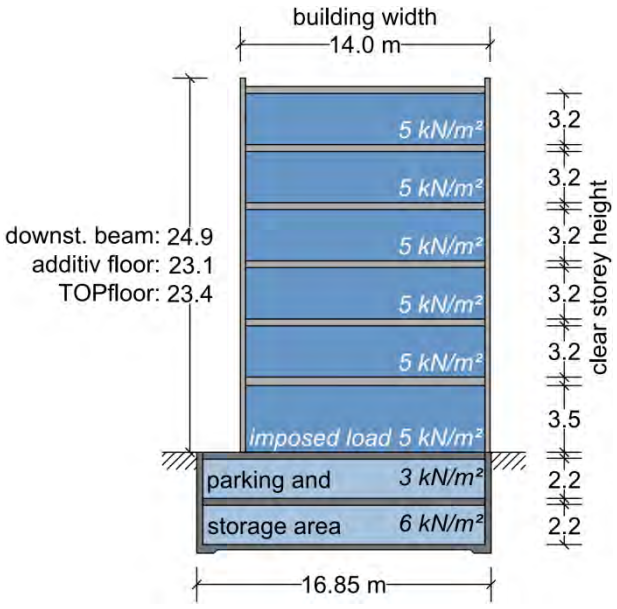


Fig. 5 – Cross section of a multifunctional reference building with clear story heights and total building height with the floor systems of Figure 6.

For the reference building, three composite floor systems with a span of approximately 13.0 m in transverse direction of the building were selected. This spans the building width without inner columns. Figure 6 shows the positioning of the columns and beams in the floor plan as well as a longitudinal and cross-sections of the floor systems. Figure 7 compares the demand of building material for the supporting constructions. The quantities are shown separately for the different types of materials with relationship to a square meter gross floor area (GFA). The mass of concrete has to multiply by a factor of 10. In the case of structural steel, the proportions of the columns and beams are shown separately. The columns are hot rolled sections from the HEM-, HEA- and HEB-series. Even if they have only a small portion of the building materials, its visibly clear that the quantity of the column steel also increases as the floor weight increases.

The composite floor with downstand beams offers the advantage of high material efficiency and low construction weight. This is particularly evident in the low demand for sectional steel. Because of the relatively large spans of 5.4 m, intermediate supports of the profile sheets are necessary during concreting works.

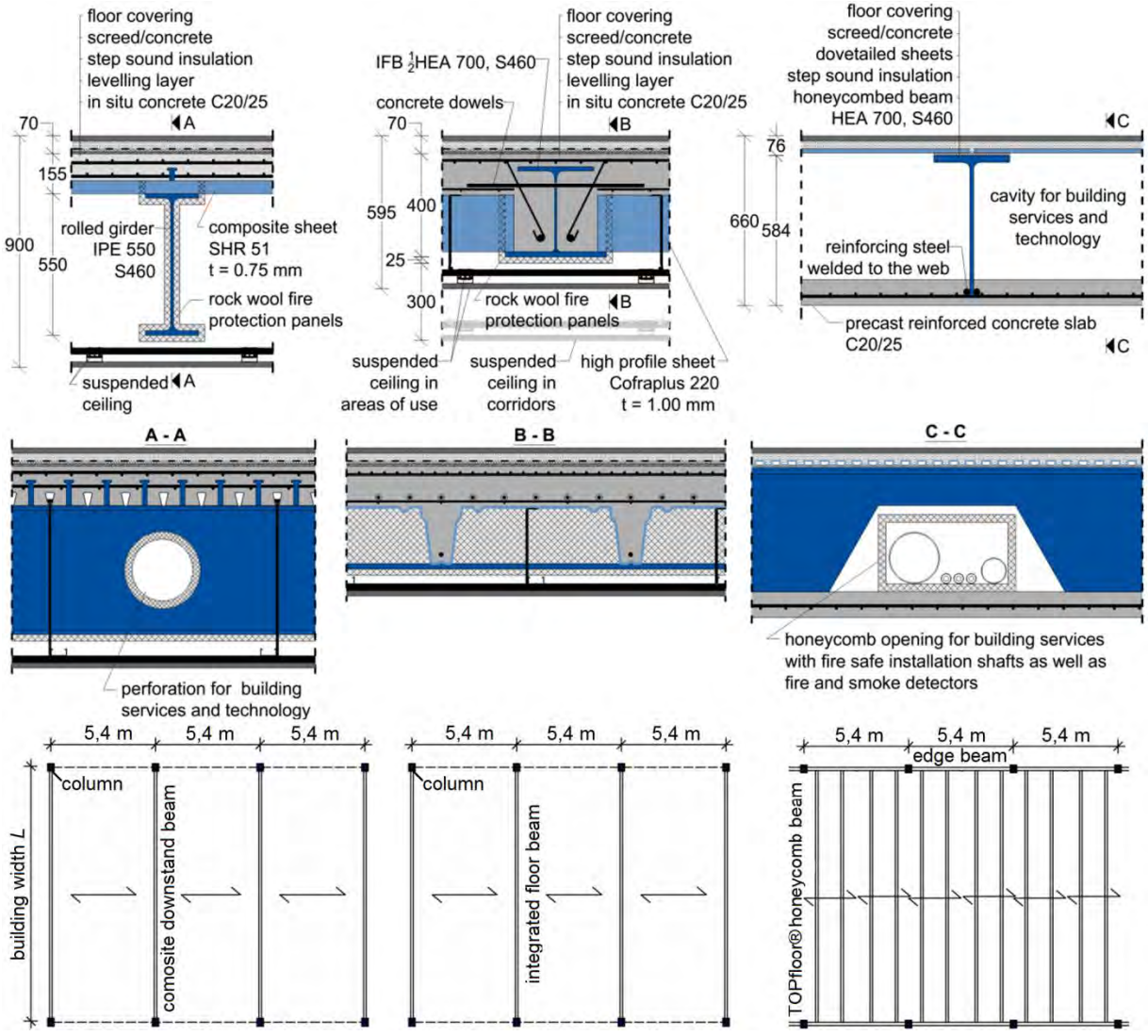


Fig. 6 – Composite floor systems: Left – downstand beams with composite slabs; middle – additive floor with integrated floor beams (IFB); right – TOPfloor® Integral system.

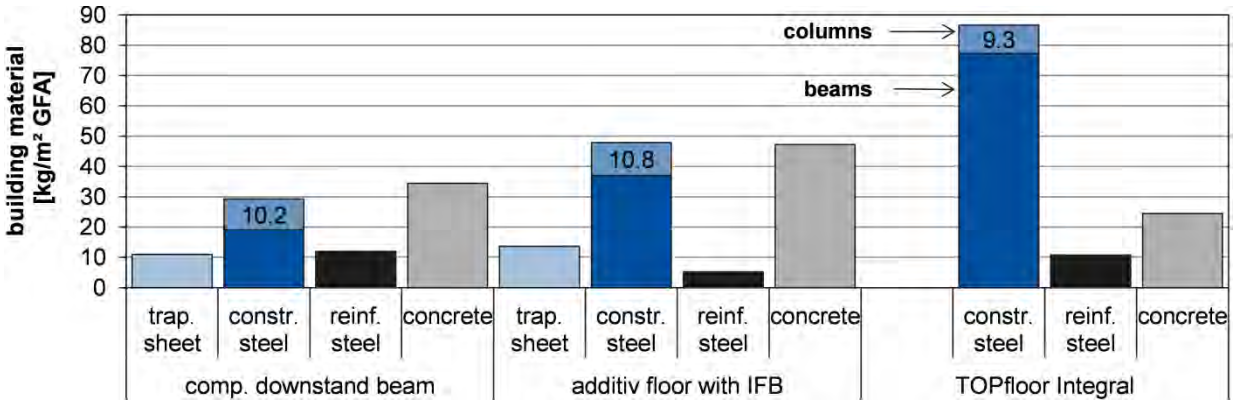


Fig. 7 – Demand of building material for the different constructions (concrete in [10^{-1} kg/m²]).

The second variant is a slim floor system with integrated floor beams (IFB). High trapezoidal metal sheets without composite effects and in-situ concrete (additive floor) was considered to allow concreting without intermediate supports. The composite effect between the steel beams and the in-situ concrete will reached by means of drilled web holes and through-mounted reinforcement. The additive floor system can be designed with a construction height of only 40 cm.

For the composite floors with downstand beams and slim floor systems typical additional components for residential, office and commercial buildings, like floor screed and footfall sound insulation, will be considered. Downwards, the structures are covered by suspended ceilings. In the case of composite floors with downstand beams the technical installation can be integrated in the level of the beams. To cross the beams the webs have openings in the regions of low shear forces. In the case of the additive floors, the clear room height in the corridor area is reduced by a suspended ceiling, above which the technical installation is located. The steel sections are clad with 2.5 cm thick stone wool plates to achieve a fire resistance of 90 minutes.

The third variant is the TOPfloor® Integral system of the Swiss Wetter AG. The prefabricated elements consist of two half honeycombed beams and a thin reinforced concrete slab. The composite effect is reached by reinforcing bars welded on both sides to the web. The transportable elements have a width of 2.5 to 2.7 m, the distance of the beams is between 1.25 and 1.35 m. After laying, shear connectors between the elements will welded and the gaps between the elements will grouted. The system can be carried out with the reinforced concrete slab in upper or the lower position (negative position). Although the negative position leads, in particular for long spans, to significant higher steel demand compared to the other floor systems, but this has two essential advantages. On the one hand, the underlying concrete slab protects the overlying steel beams against fire. Furthermore, the building technology can be accommodated in the resulting cavity floor. A change of user does not require any intervention in the underlying story of the building. The technical installation happens in cable ducts which are equipped with fire protection. As a result, no further fire protection measures for the honeycomb beams are necessary.

On the basis of the building materials demand, the environmental impacts caused by the supporting constructions can be determined. Table 2 shows the primary energy demand and the global warming potential of typical building materials. The ecological balances are made available in environmental product declarations and databases, such as ÖKOBAUDAT. In these balances the phases considered in the lifecycle are reported according to EN 15643-2.

Figure 8 shows the primary energy demand and the global warming potential of the accessed floor systems and columns related to a square meter gross floor area (GFA). The efficient ma-

terial utilization of the composite floor with downstand beams results in a low demand of building materials, which has a positive effect on the ecological balance. In contrast, the TOPfloor® integral system results in significantly less favorable LCA values due to the small beam distances, additional edge beams, the lower construction height and the steel chords in the compression zone. In addition to the sectional steel and reinforcement, the galvanized composite and trapezoidal sheets have also a considerable impact in the ecological balance of the composite and additive floors.

Table 2 – Primary energy demand and global warming potential of building materials.

building material	PE_{ges} [MJ/t]	GWP [kg CO_2/t]	sources	lifecycle phases
trapezoidal sheet	18808	1020	IFBS,2013	A1-A3, C4, D
			Ökobaudat,2015	A4, A5
steel sections and plates	12065	808.0	bauformunstahl e.V.,2013	A1-A3, D
			Ökobaudat, 2015	A4, A5, C1, C2
reinforcement	12753	760.8	Ökobaudat, 2015	A1-A5, D
concrete C20/25	465.8	73.7	InformationsZentrum Beton GmbH, 2013	A1-A5, C1-C4*, D
*includes waste transport and separation of concrete, reinforcement and trapezoidal sheet				

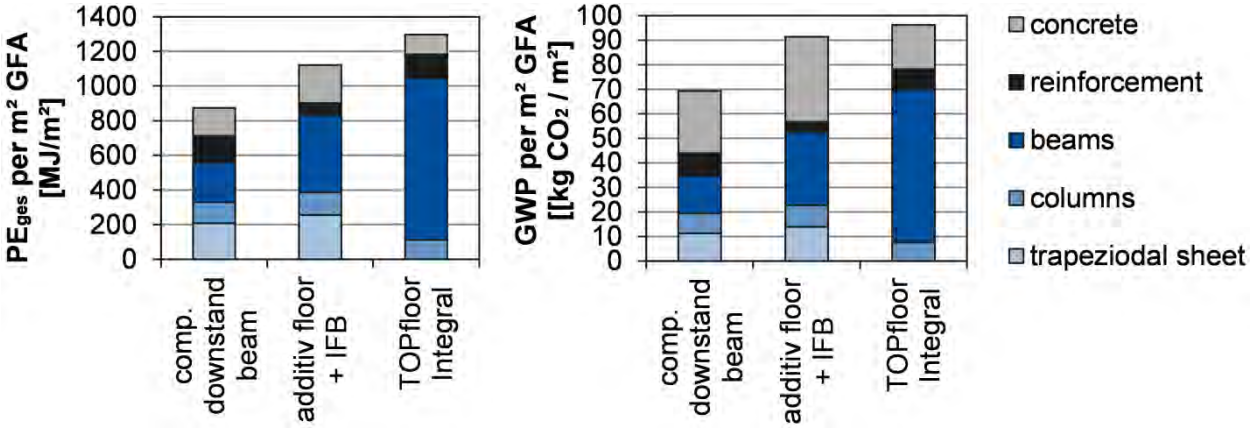


Fig. 8 – Primary energy demand and global warming potential of the supporting constructions.

5 SUSTAINABILITY AND INFLUENCE OF FACADE SYSTEM

Modern buildings impress with their exterior design with innovative façade solutions. The trend is increasingly moving away from conventional perforated facades to strip and element facades with a small proportion of opaque surfaces up to all-glass façades. Particularly for multifunctional buildings in steel and composite construction, element façades are preferred solutions because of the adaptability to changing user requirements.

The choice of the façade influences the ecological performance of a building, especially during its use phase. Depending on the heat transfer coefficient of the façade system as well as the size of the façade area, the heating and cooling energy demand increases or decreases. While in the past all-glass and element façades have been classified as ecologically harmful, modern systems with coated multi-pane insulation glazing and improved frame constructions can

achieve a heat transfer coefficient that is far below the allowed value and is comparable with perforated façades.

In addition to the utilization phase, the construction and dismantling phases as well as the recycling potential of the materials also influence the ecological balance of buildings. Up to now, there are hardly any official data for façades available. In Table 3 preliminary data of four elementary facades for office and commercial buildings are listed. Figure 9 shows a comparison of the non-renewable and total primary energy demand (PE_{ne}, PE_{ges}) as well as the global warming potential (GWP). Three all-glass façade systems with frame constructions out of timber, steel and aluminum as well as an element facade with aluminum cladding are considered. The ecological data are basing on information from facade manufacturers and environmental product declarations.

The comparison shows the sum of the expenses for the lifecycle phase's construction, dismantling and recycling. As expected, the glass façade with timber frame shows the lowest ecological impact due to the sustainable frame material. The all-glass facades with steel or aluminum frames are significant less favorable. Furthermore, the higher aluminum content of the elementary façade leads to even higher values compared to the other systems. The total primary energy demand in the phases A1 to A5 and C1 to C4 is almost twice as high as the all-glass façade. However, the recyclability of the aluminum leads to the fact that the additional impact is limited to approx. 1/3 compared to the all-glass façade with steel or aluminum frame. For the all-glass façade with timber frames the EPD assumes in the End of life phase that 90 % of the metals can be recycled and 100 % of the timber will be used for thermal utilization.

Tab. 3 –Primary energy demand and global warming potential of different façade systems.

façade system	phase of production and disposal		recycling phase		Source
	PE_{ges} [MJ/m²]	GWP [kg CO_2/m²]	PE_{ges} [MJ/m²]	GWP [kg CO_2/m²]	
all-glass façade, timber frames	1358.3	64.35	-215,0	-12,60	(UniGlas, 2015 BGT, 2012)
all-glass façade, steel frames	2155.3	121.03	-805.8	-47.90	(ift, 2012)
all-glass façade, aluminum fra.	2190.0	140.00	-847.4	-45.01	(Eichhorn, 2010)
elementary façade, aluminum cladding and fra.	3830.0	225.00	-1998.5	-105.94	

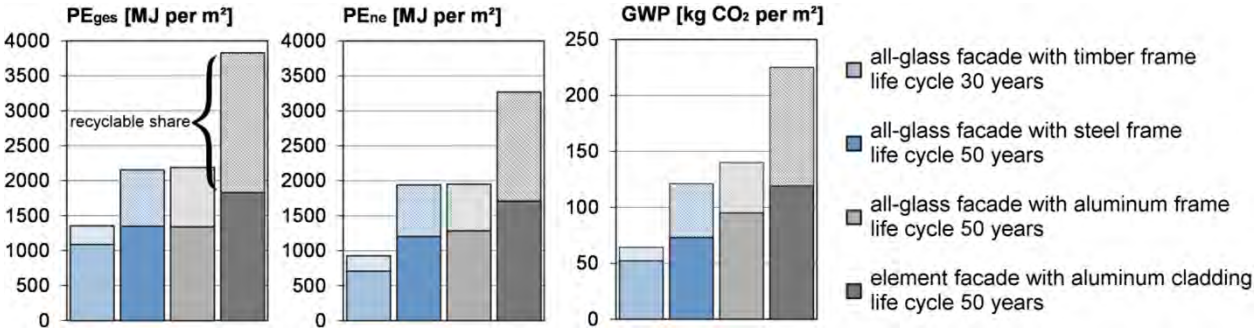


Fig. 9 – Primary energy demands and global warming potential of different façade systems in the life cycle phases A1 – A5, C1 – C4 and D (recycling).

When evaluating the façade systems, the operating life up to a necessary replacement should also be considered. According to the manufactures specifications the considered timber frame facade has only an estimated operating life of 30 years, while the steel and aluminum facades can achieve a life cycle of 50 to 60 years. In view of the high adaptability of the systems and the physical properties, which are far above current legal requirements, longer life cycles are possible.
Figure 10 shows the primary energy demand of the various façade systems and supporting structures for the reference building of Figure 6. The different construction heights of the floor systems lead to different building heights and façade surfaces and their proportions in the ecological balance (Table 4 and Figure 10). This is between 1/3 and 2/3 of the total primary energy demand in the phases of construction, dismantling and recycling.

Figure 11 shows with the left graph a comparison of the ecological performance of the supporting structures for the different floor systems. The use of composite floors with downstand beams leads to the best performance with a clear distance from the other systems. Considering the various façade systems in the life cycle assessment in addition leads to a reduction of the distance. Consequently, the selection of floor systems with a low construction height results in savings of facade area, which leads to an improvement in the ecological balance.

Tab. 4 – Ratio of façade to gross floor area of the reference building for different floor systems.

floor system	building height	façade area	GFA_{ges}	FA/GFA_{ges}
composite slab, downstand beams	23.7 m	4731 m²	6804 m²	0.695
additive floor with IFB	21.9 m	4389 m²		0.645
TOPfloor® Integral system	22.2 m	4438 m²		0.652

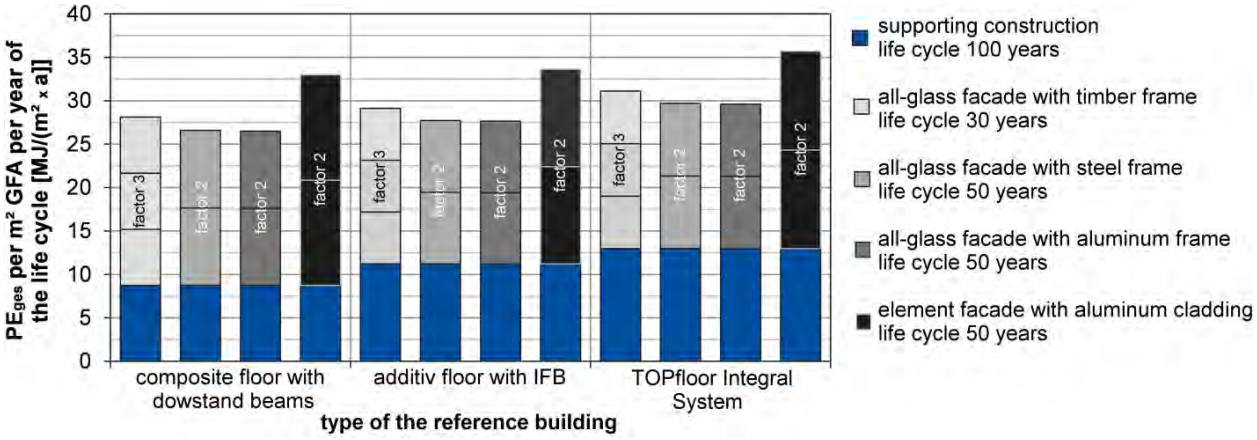


Fig. 10 – Primary energy demand per year of life cycle for different combinations of supporting constructions and façade system (total life cycle = 100 years).

6 CONCLUSION

Examples of changing social conditions are the demographic change and the growing awareness of sustainability, which affect the user requirements of buildings. The development of the vacancy rates shows that lots of commercial and office buildings are insufficient flexible for adaptation to the changing user requirements. Resource conservation, recyclability, life cycle costs

and conservation of value, even under changing property conditions, are more in the focus of planning.

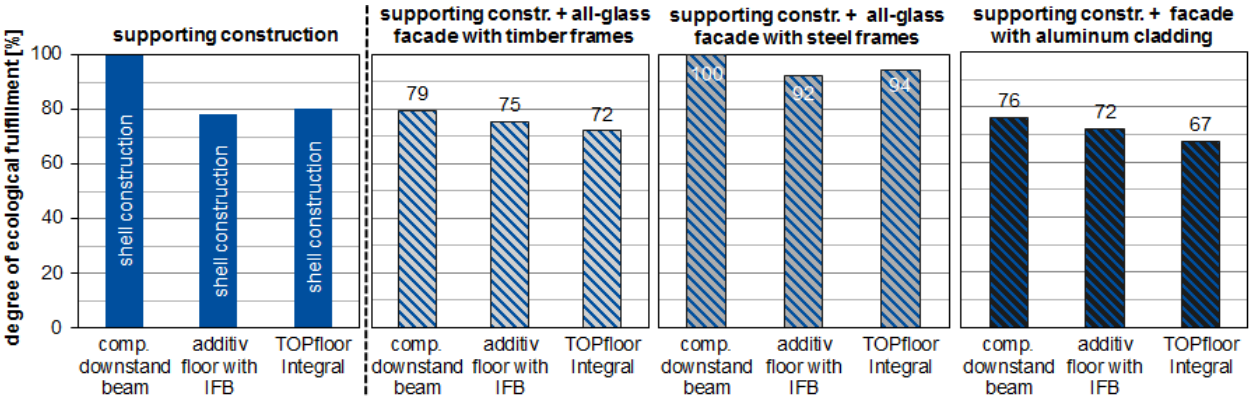


Fig. 11 – Degree of ecological fulfillment of different supporting constructions and their combinations with façade systems for a 100-year life cycle.

Steel and composite constructions offer significant advantages to increase the sustainability related to conventional building structures. The comparatively low construction weights and demand of building materials have positive effects on the structures up to the building foundations. This leads to reductions of the expenses for construction, transportation, erection and waste at the end of building life.

Subject of the ongoing AIF FOSTA research project P1118 is the sustainability of office and commercial buildings by using steel and composite constructions. Aims and results are the quantification of the environmental and economic sustainability of the supporting structures and the development of recommendations, guidelines and tools for planning of these building types.

7 REFERENCES

bauforumstahl e. V. (2013). *Environmental product declaration - Baustähle: Offene Walzprofile und Grobbleche*. Institut Bauen und Umwelt e. V. (Ed.). Declaration-number: EPD-BFS-20130094-IBG1-DE. Valid until: 24th October 2018.

BGT Bischoff Glastechnik AG (2012) *Environmental product declaration - Mehrscheibenisolierglas*. ift Rosenheim GmbH (Ed.). Declaration-number: M-EPD-MIG-001021. Valid until: 1st May 2017.

Eichhorn, D. (2010) *Kurzfassung - Ökobilanzierung der Lindner ECO® Fassade*. Lindner Fassaden GmbH (Ed.). Arnstorf.

EN 1993-1-2 (2010). *Eurocode 3: Design of steel structures – Part 1-2: General rules – Structural fire design; German version EN 1993-1-2:2005 + AC:2009*.

IFBS (2013): *Environmental product declaration - Profiltafeln aus Stahl für Dach-, Wand- und Deckenkonstruktionen*. Institut Bauen und Umwelt e.V. (Ed.). Declaration-number: EPD-IFBS-2013211-D. Valid until: 13th January 2018.

ift Rosenheim GmbH (2012) E*nvironmental product declaration – Muster-EPD Stahl-/Edelstahlfassaden*. ift Rosenheim GmbH (Ed.). Declaration-number: M-EPD-SFA-XXX. Valid until: 1st November 2017.

InformationsZentrum Beton GmbH (2013): *Environmental product declaration - Beton der Druckfestigkeitsklasse C 20/25*. Institut Bauen und Umwelt e.V. (Ed.). Declaration-number: EPD-IZB-2013411-D. Valid until: 25th Juley 2018.

Stroetmann R., Faßl Th., Hüttig L. (2016). *Nachhaltige Geschossbauten in Stahl- und Verbundbauweise*. In Stahlbaukalender 2016, Abschnitt 10, Seite 571 – 665. Berlin: Wilhelm Ernst & Sohn.

Mensinger, M., Stroetmann, R., Feldmann, M., Eisele, J., Zink, J., Lingnau, V., Kokot, K. (2016). *Nachhaltige Büro- und Verwaltungsgebäude in Stahl- und Stahlverbundbauweise (Final Report Research Project FOSTA P881)*. Düsseldorf: Verlag und Vertriebsgesellschaft mbH.

Ökobaudat (n.d.). Retrieved December 16, 2015, Information portal for sustainable building of the German Federal Ministry for the Environment, Nature Conservation, Building and Nuclear Safety, http://www.oekobaudat.de/en/

Stroetmann, R., Eisele, J., Schach, R., Hüttig, L., Trautmann, B.; Harzdorf, A. (2015) *Einflüsse der Stahl- und Verbundbauweise auf die Lebenszykluskosten und Vermarktungsfähigkeit multifunktionaler Büro- und Geschäftshäuser*. IGF-Project-No. 18659 BG; FOSTA P1118. Manuscript in preparation.

Stroetmann, R, & Hüttig, L. (2016) Multifunctional commercial buildings in steel and composite construction*. Report of IABSE Congress Stockholm – Challenges in Design and Construction of an Innovative and Sustainable Built Environment*, 482-489.

UniGlas GmbH & Co. KG (2015) *Environmental product declaration - Konstruktion der UNIGLAS Facade.* ift Rosenheim GmbH (Ed.). Declaration-number: EPD-UGF-0.01. Valid until: 1st May 2017.

BUILDING SCALE COMPOSITE SYSTEMS

Aaron Mazeika, PE SE AIA
Skidmore, Owings & Merrill LLP
Chicago, USA
aaron.mazeika@som.com

Ashpica Chhabra, PE SE
Skidmore, Owings & Merrill LLP
Chicago, USA
ashpica.chhabra@som.com

ABSTRACT

Composite construction is often defined at the component level, with individual structural members being composite elements, or with the selection of different materials for each element based on specific structural demands. This paper will instead focus on composite structural systems at the building- and multi-building scale. A selection of building design solutions will be discussed where conventional structural components have been employed in innovative configurations resulting in large scale composite structural systems that offer distinct structural and economic advantages over more conventional design solutions.

CONVENTIONAL COMPOSITE CONSTRUCTION

Composite materials have been in use in building construction for thousands of years, from wattle and daub walls that were used as far back as the Neolithic period, through to modern carbon fiber reinforced polymers that have been introduced to building structures in just the past few years. For the most part during this period, composite construction has developed with a focus on the micro scale. The interaction of materials of different properties resulting in a material with an amalgam of the properties of its constituent parts (wattle and daub, steel reinforced concrete, glass fiber reinforced polymer, etc.). Composite construction can also be considered as a structural system at the building component level. Composite steel floor framing beams and concrete filled steel tube columns being examples of this application. This paper is intended to highlight the use of composite construction at the macro or building system scale.

COMPOSITE BUILDING CORE

In high rise building construction it is common for the building core to reduce in size up through the height of the tower, as certain core components drop off. A three zone direct elevatored office building requires three elevator banks from the ground to the top of zone 1, two from the top of zone 1 to the top of zone 2, and one from the top of zone 2 to the highest floor. This erosion of the building core with height typically allows floor area used for the core below to be returned to rentable office space at the upper floors, however there are limitations to this approach. Office space that is too far from the building façade will receive insufficient natural daylight and will not be useful as rentable office space. While in office buildings this space can be useful for other functions, such as file storage etc., in other program types this space can be without value. A

specific example of this would be the common building typology of a mixed used tower with a hotel constructed atop an office tower. This program mix is increasingly commonplace with many examples built around the world. What makes this program stacking difficult is the combination of different core requirements and different lease span (distance from core to façade) requirements of the two different programs. The office levels typically have high core requirements due to the large occupancy populations that need to be transported at peak arrival, departure and lunch time. The office levels also typically favor a lease depth of 12-13m. A hotel floor plate by contrast has a much smaller core requirement due to lower and less concentrated elevator traffic, and a preferred lease depth of approximately 10m. The trivial solution to these conflicting requirements would be a step change in the building width, with a narrower hotel tower sitting atop a wider office tower. A more elegant form may be a tapered tower, but this introduces a new problem of variable depths to the hotel rooms, an issue that complicates the work of the hotel operators and interior designers. This design problem was elegantly solved in the design of the Jin Mao Tower in Shanghai, China. This 420m tall composite tower consists of 52 stories of office floors beneath a 36 story tall 5-star hotel. To address the different core requirements, rather than taper or step the perimeter of the tower, the design team instead elected to hollow out the core and turn the unused space into a dramatic 30 story tall atrium (see figure 01).

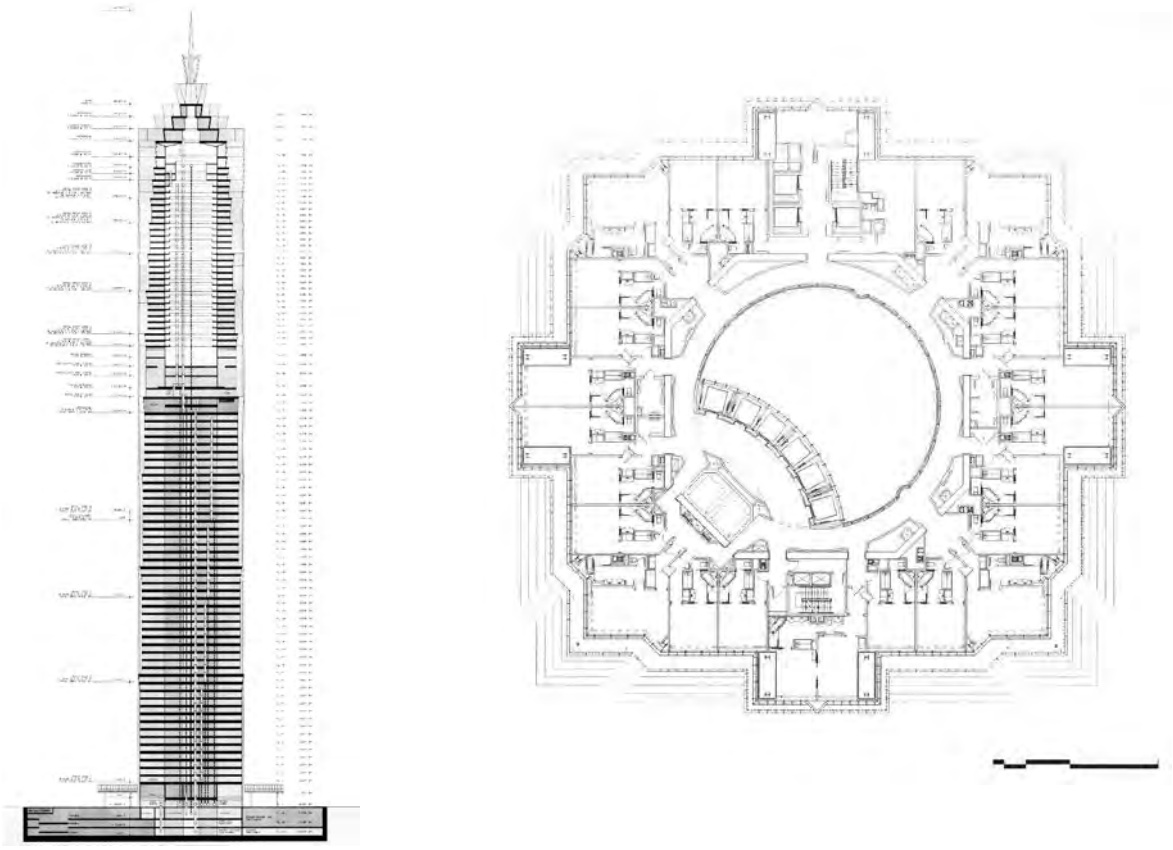


Figure 01-Jin Mao Tower Section (Left); Typical Hotel Level Plan (Right)

For the Wujiang Greenland Tower, in Suzhou, China, this concept of an upper level atrium hotel was developed one stage further. The lower level barrel shaped office floor plan sat beneath a hotel floor plan consisting of two curved single-loaded hotel bars facing north and south (see figure 03). This arrangement allowed for the middle third of the core to be eroded forming an atrium which passed completely from the west side to the east side of the building, giving the building its signature 'eye of the needle' form (See figure 02). The resulting atrium has dramatic views out to the west and east. While adding an important architectural element, the atrium in this configuration resulted in the core being split in two, greatly reducing its structural stiffness in the upper half of the tower. To correct this the two isolated building cores in the upper half of the building are laced together using structural steel bracing to form a composite 'coupled core'.

Wujiang Greenland Structural System

The lateral force resisting system for the tower consists of a 'frame shear-wall' structure supplemented by structural steel outriggers and belt trusses. It consists of reinforced concrete walls around vertical circulation and mechanical service zones at the center of the floor plate, and a moment resisting frame, with columns located at the perimeter of the floor plate.



Figure 02- Architectural Rendering

The reinforced concrete core is separated into two portions in the upper levels of the building by the hotel lobby (see figure 03 for building section). These two portions of the core are laced together using a structural steel diagonalized truss, which allows the two portions of the core to act compositely as one overall rectangular section. The moment resisting frame consists of steel spandrel beams and encased composite columns at hotel levels and reinforced concrete beams and encased composite columns at the office levels.

Floor framing consists of structural steel beams supporting composite metal deck slabs at hotel levels and conventional reinforced concrete beams and slabs at office levels. Two of the columns on each of the longer faces of the building are connected to the reinforced core with structural steel outrigger trusses at mechanical levels and stiffen the tower lateral force resisting system in the weak axis of the building. Belts Trusses are provided at these levels to engage axial stiffness contributions of all perimeter columns. Core walls will vary from 1800mm thick at the base to 350mm thick at the top, with column sizes varying from 2100mm diameter to 800mm diameter.

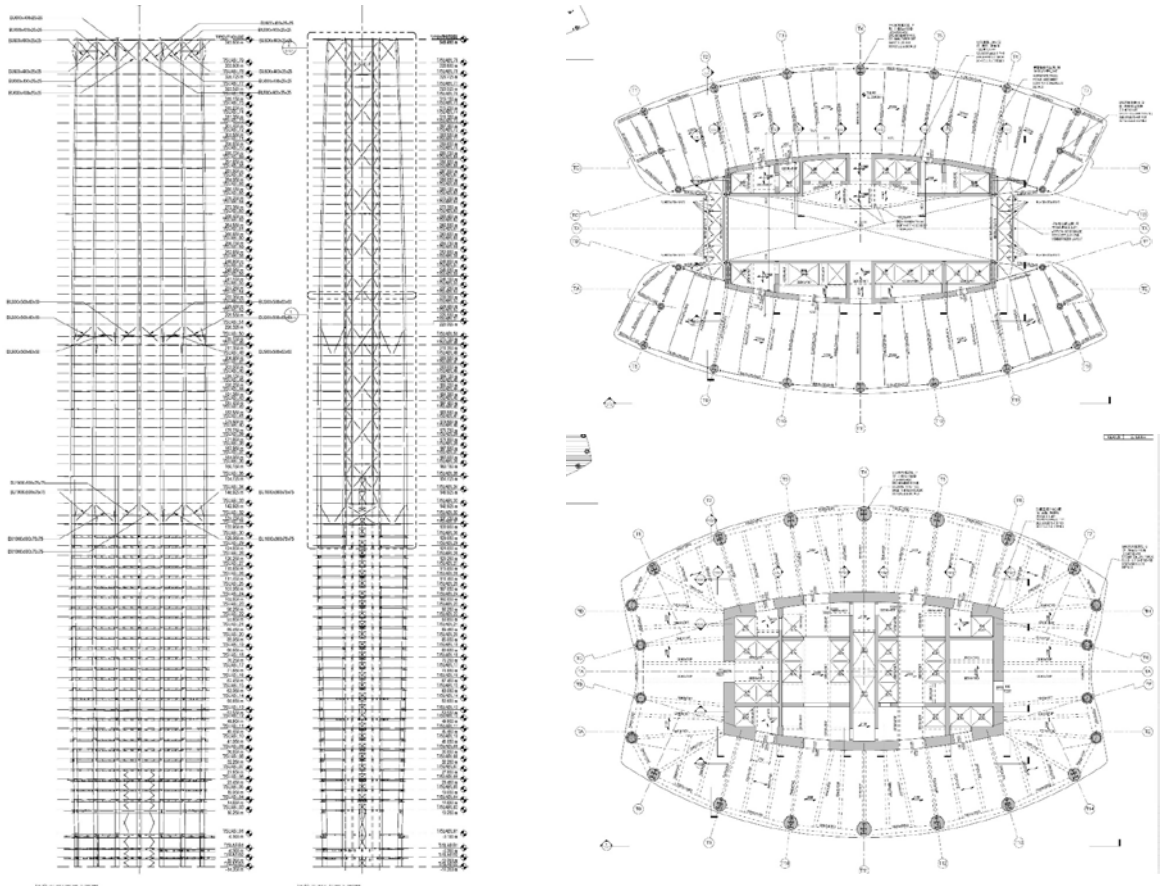


Figure 03 - Building Elevations (Left); Hotel Level framing plan (Top Right); Typical lower level framing plan (Bottom Right)

Elastic Analysis

ETABS was used as the elastic analysis software, with modeling assumptions and loadings defined per the requirements of the Chinese codes. During the initial design process the columns and walls are sized to meet the axial stress ratio limits as defined in the Chinese code. The steel bracing members at the coupled core, outriggers and belt truss members were sized using in-

house optimization program that proportions structures such that internal work is done with a minimum volume structure with the target of achieving maximum material efficiency without exceeding a drift limit of H/500 under wind tunnel loads.

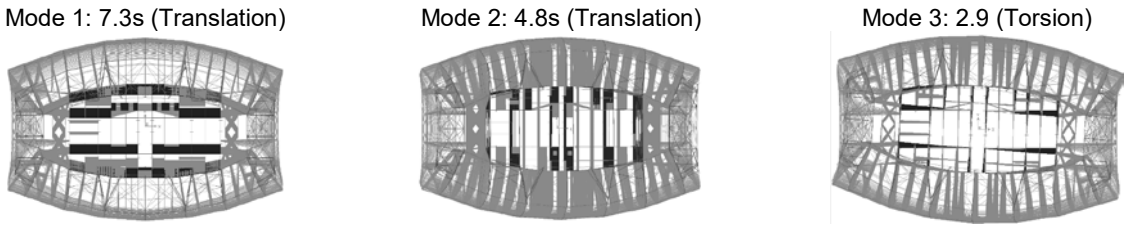


Figure 04 - Dynamic properties of building

Seismic Engineering

PERFORM 3D was used as the nonlinear time history analysis software. Seven sets of site specific time histories very provided by the local seismic consultant. The analysis is performed to meet performance targets set by the Chinese code as well as by the expert panel. The connecting braces were required to remain non yielding under rare earthquake. Hence, the inelastic energy dissipation is achieved by yielding of core link beams and perimeter moment frame beams (see figure 05). The drifts under rare earthquake time histories were within the code limit.

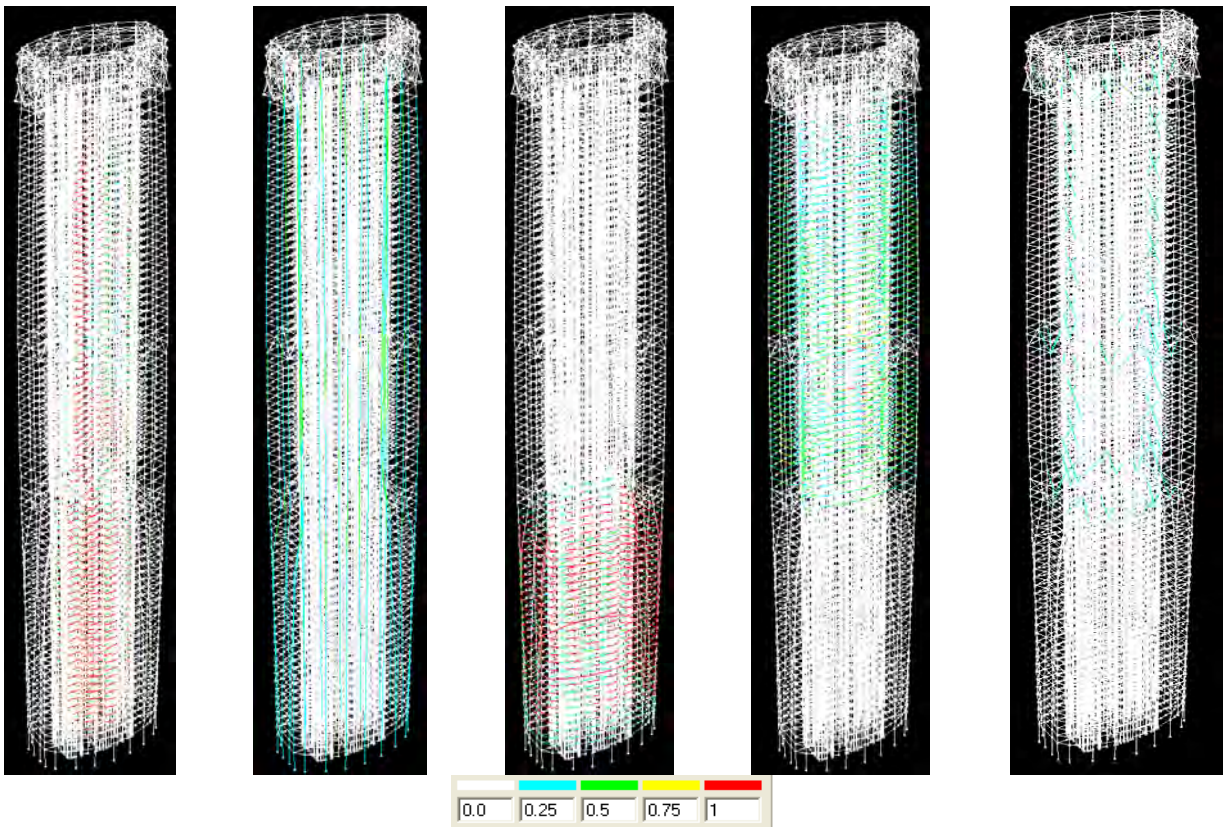


Figure 05: Elements ratios as multiples of yielding limit state under rare earthquake time histories; R/C link beams; Composite Moment Frame columns; R/C Moment Frame beams; Steel Moment Frame Beams; Steel Diagonals at coupled core and outrigger/ belt truss levels. (from left to right)

Connection Analysis and Design

The coupled-core wall lateral system consists of cross-brace members that join into an embedded truss inside the core wall. In addition to the cross-braces, the members embedded in the core wall are divided into four types: primary embedded verticals, secondary embedded verticals, primary embedded braces and secondary embedded braces (see figure 06). The preliminary sizing of embedded members was based on maintaining steel-to-steel load path at the connections. The primary embedded braces continue the same section as the diagonal braces. These braces transfer the vertical component of the forces along the diagonals to the primary embedded verticals. For embedded verticals under net compressive forces, gradually increasing contribution from composite action is assumed as studs are introduced along the member length. The secondary embedded members are sized for the resultant forces due to the slight kink between the cross-brace and the embedded primary brace.

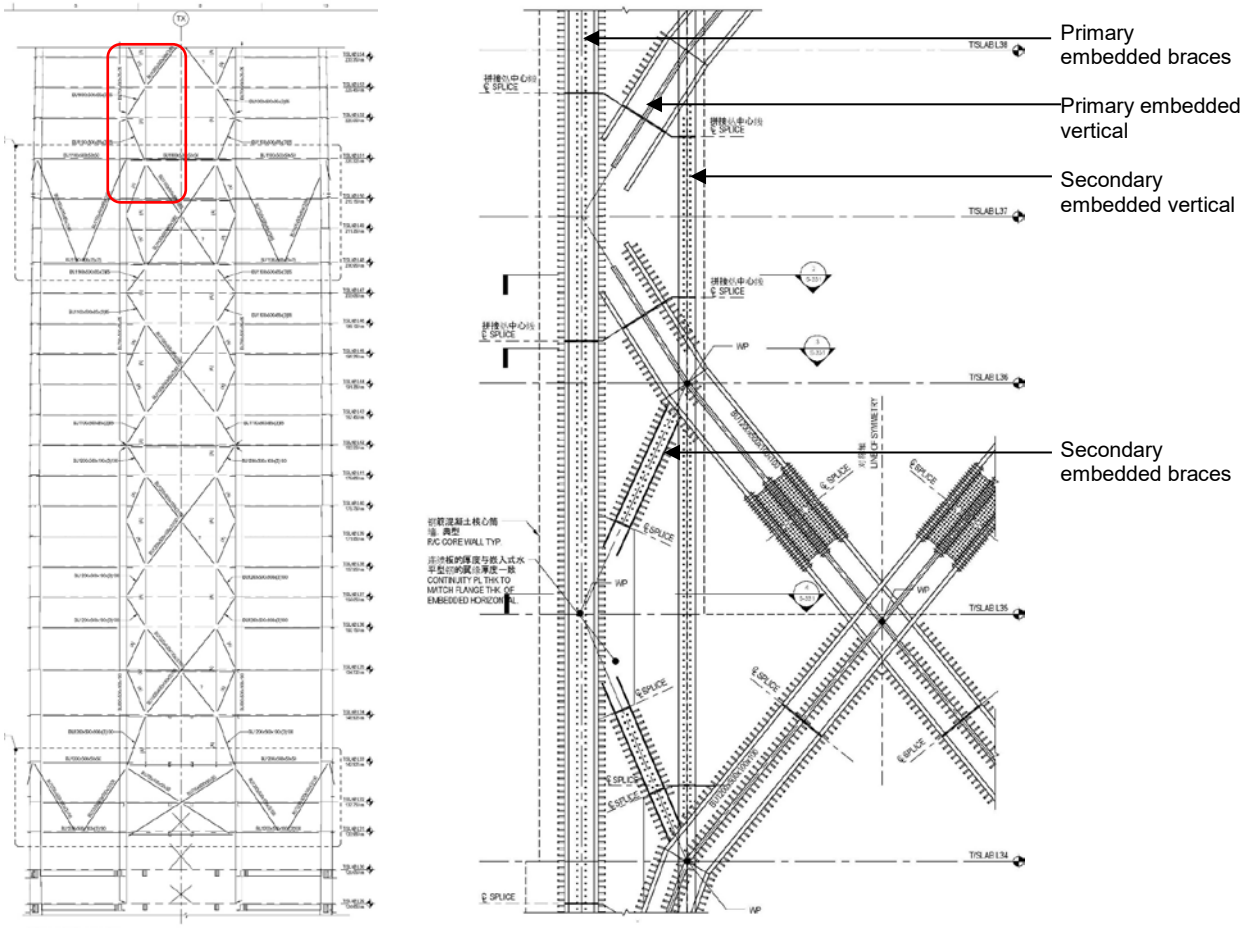


Figure 06 - Embedded truss at the split core levels

Additionally, the connection was analyzed using general purpose finite element software Strand 7, to verify that the stresses in the steel do not exceed the design limits of Q345GJ steel and that the stress level in concrete would not exceed the design capacity of C60 concrete in tension or compression. The target performance for the connection is to remain elastic under moderate earthquake forces. The forces were based on the elastic ETABS model. Based on the results of the analysis, it was found that concrete cracks under moderate earthquake forces but the

embedded steel members and the longitudinal reinforcement have enough reserve capacity to transfer the load (see figure 07). Since the embedded steel is designed to resist all the tension forces by itself, the connection has enough capacity to resist earthquake forces.

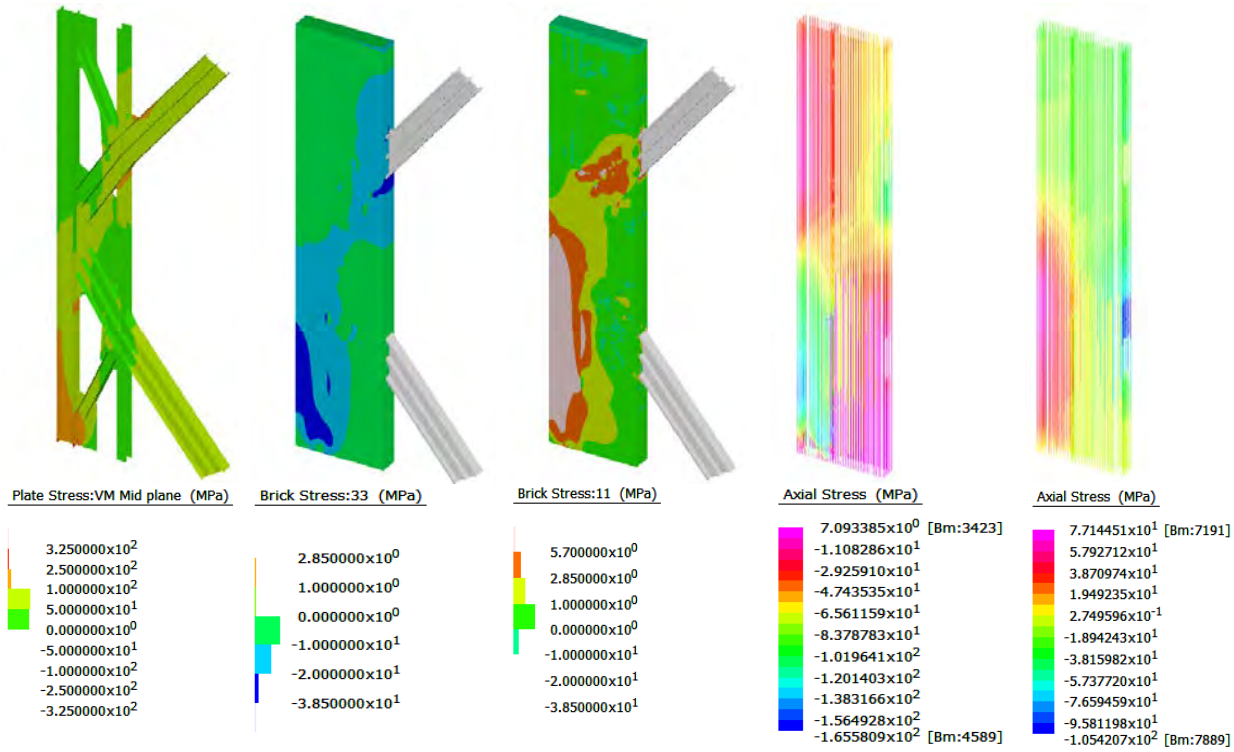


Figure 07: Finite element modeling of core bracing connection; stresses in embedded steel, concrete compression/ tension and reinforcement compression/tension (from left to right)

Resistance to Racking Motion

Resistance to racking between individual building halves is provided by having full diaphragm connectivity at levels 77-79 and level 51 as well as from link bridges at all upper levels. A horizontal axial spring connecting diagonally opposite corners of the split core walls is used to measure the racking motion in the analysis model. If there is no connection between the split core, there is a net 108mm spring deformation under moderate earthquake time histories. Once the split cores are tied together with vertical cross-bracing this measured displacement reduces to 89mm. If the diaphragm connectivity at levels 77-79 and Level 51 is considered the maximum displacement reduces considerably to 6.4mm. Alternatively if connectivity at all the link bridges is considered, the maximum displacement reduces to 3mm. In the building as designed with cross braces, discrete diaphragm connectivity and link bridges the maximum displacement due to racking motion is 2mm

COUPLED BUILDINGS

After connecting two distinct building cores within a single building for enhanced performance, a logical development of the thought would be to study the connection of building cores in two adjacent buildings. As high rise towers become increasingly slender, the structural efficiency is greatly reduced and the construction cost increases exponentially. This raises the possibility of it being more cost effective to construct two slender towers that are structurally connected together, rather than being conventional independent towers. The logic being that when combined, the effective slenderness of the coupled towers would be lower as it would be based on the plan dimension of the combined structural system. This idea was developed further in SOM's competition entry for the Zhengzhou Greenland Towers project (see figure 08).

The competition brief called for a twin tower configuration on the site of new district planned on the outskirts of Zhengzhou, China. After developing multiple twin tower forms, the architectural design team challenged the structural design team to explore how the decision to build twin towers could enhance the structural performance and thus yield a more efficient design solution. These explorations yielded two concepts that shaped the final building form.



Figure 08: Architectural rendering

Firstly, by connecting the cores of two slender buildings together with a structural steel truss, the towers could mutually stiffen each other, with the core of building B acting as an outrigger column to the core of building A, and vice versa. This allowed each of the towers to be more slender than cost effective for an individual tower. It also informed the plan configuration of each tower. As the outrigger behavior between the two towers would only work when one tower was moving in the direction towards or away from the other tower, this mutual stiffening was only advantageous in one direction of movement for each of the towers. Consequently, the towers would each need to have sufficient stiffness acting alone when deflecting perpendicular to its neighboring tower, but would be supplemented by the outrigger effect when displacing towards or away from its neighbor. This resulted in a need for a rectangular plan and core, with the long axis of each building running parallel to each other.

Secondly it was recognized that the connected towers approach allowed the use of an offset core plan configuration, that would normally not be satisfactory for towers of this height. For twin tower configurations, there is generally an architectural concern about view blockage, where one tower blocks the views from one face of the other tower and vice versa. Consequently, for twin tower

configurations there is typically a low value side of the floor plate. It is therefore logical to design the plan configuration of the tower such that the majority of rentable floor area is biased towards the preferred views. This can be achieved through the use of an offset core configuration. The building core components are relocated from their more typical location at the center of the floor plate and are instead offset to the side of the building with the least beneficial views. As well as improving the quality of views, this configuration also yields a clean rectangular office floor plan, rather than the more typical ring configuration resulting from the use of a central core. This plan configuration was most famously employed at the Inland Steel Building, completed in Chicago, IL in 1958 (see fig. 09), and has remained a desirable yet uncommon configuration since that time.

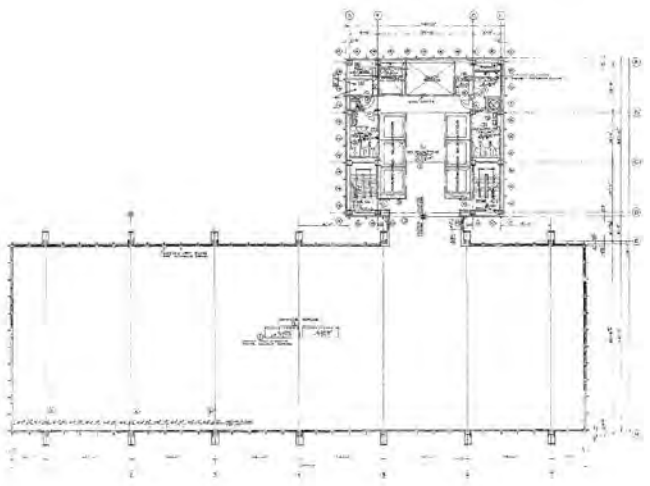


Figure 09 - Inland steel building – Typical floor plan with offset core configuration

While the offset core configuration offers many architectural benefits, this layout complicates the structural engineering design as the offset core introduces a significant torsional irregularity to the structure, which results in a torsional building response when the building is subjected to lateral wind or seismic loads. A significant eccentricity is introduced between the midpoint (for wind) and center of mass (for seismic) of the floor plate which are closer to the center of the office floor plate, and the center of stiffness of the lateral force resisting systems which is closer to the center of the building core. The torsional response that this creates can increase motion perception in the tower, complicate the detailing of the exterior wall, and increase the cost of the structural system to control these issues. For these reasons this plan configuration has typically seen limited use in office buildings up to approximately 20 stories tall. Here too the connected twin towers concept offers significant benefit. As well making a flexural connection between the two offset cores, allowing each building core to act as an outrigger to the other, there is the potential to make a diaphragm connection between the two towers also. When connected together by a stiff diaphragm, each tower can no longer twist independently about its own center of stiffness and the torsional response is restricted to the combined building twisting around the center point between the two towers, significantly increasing the torsional stiffness. In addition to the stiffness increase, as the towers can now be thought of as one combined building structure, the torsional eccentricity is eliminated as the center of mass, center of geometry and center of stiffness are all now located at the center point between the towers.

Zhengzhou Greenland Structural System

Zhengzhou is located in a region of high seismicity, and moderate wind. In the stronger east-west direction, the lateral system of the towers consists of a reinforced concrete core and a perimeter moment frame with 9m column spacing. In the transverse direction, the lateral system consists of the reinforced concrete shear wall core, and a perimeter moment frame with closely spaced columns. At the top of the office zone where the hotel floor is set back, the transfer trusses also work as outrigger trusses connecting the core and perimeter columns. The hotel amenity bridge floors at the top of the building connect the cores of the two towers, and the amenity floor slabs provide diaphragm connectivity between the two towers (see figure 10).

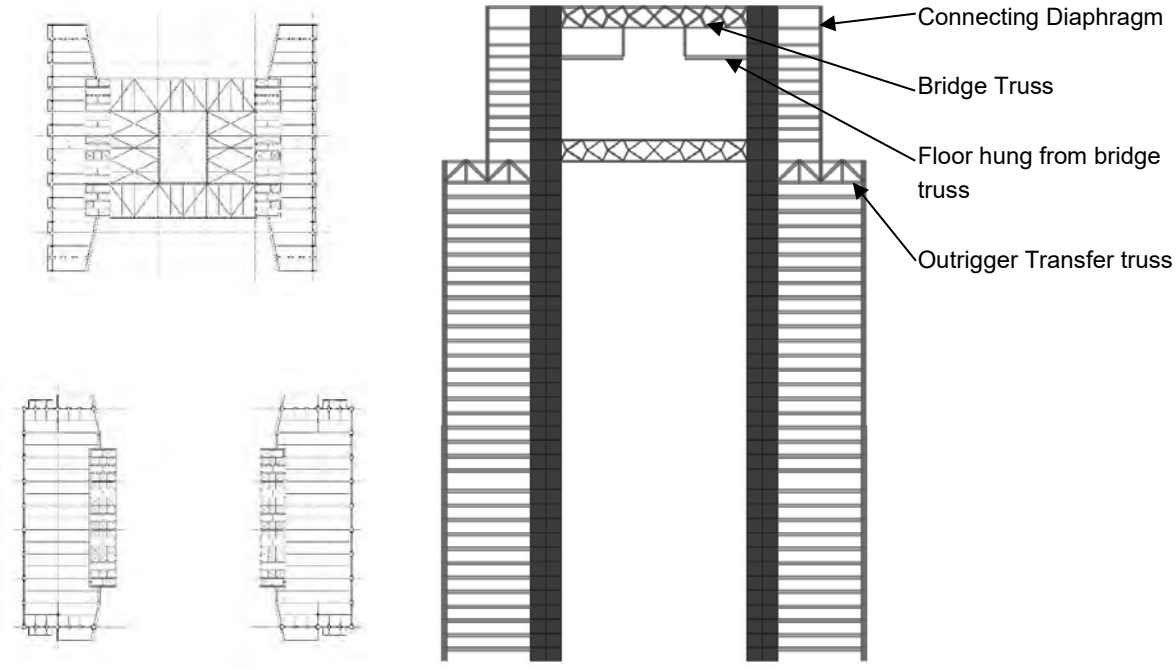


Figure 10 - Connected level plan (top left); Typical plan with two offset core floor plates (bottom left); weak axis structural system diagram (right)

Unconnected, each tower is relatively slender and has a low torsional stiffness. Due to the offset core configuration, the buildings have a significant torsional response when subjected to lateral loads. By tying together, the twin towers at the top with two floor diaphragms, the displacement of each tower is constrained to the other, and the overall torsional stiffness is significantly improved. This results in the torsional period being reduced by 18% (see figure 11). Additionally, by connecting the two towers together, overall building drift under lateral loading is reduced by 10%.



Torsional mode without bridge truss T=4.0 s

Torsional mode with bridge truss T=3.3s

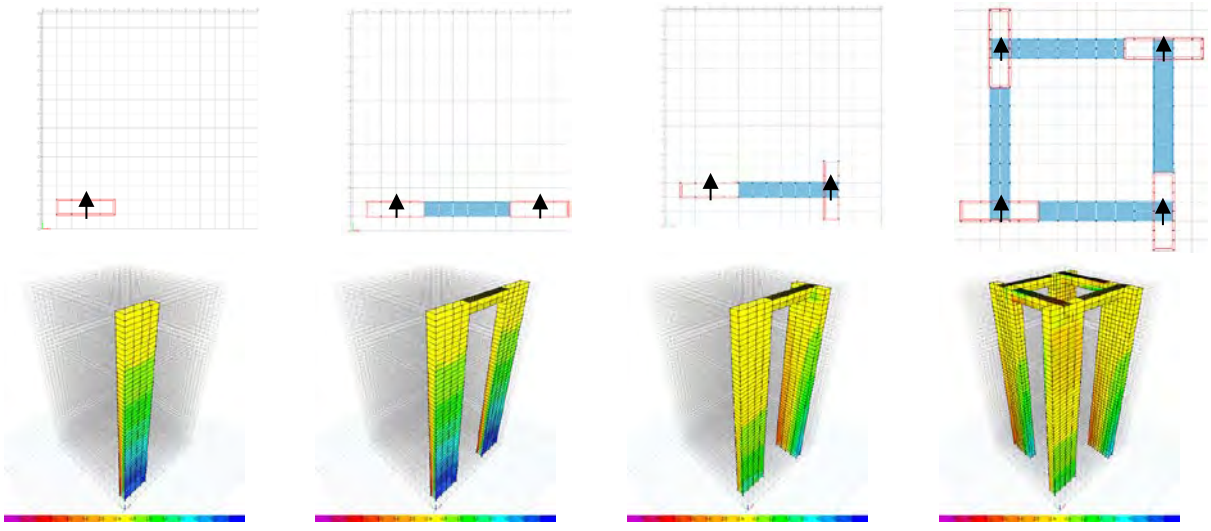
Figure 11: Enhanced torsional performance with connected bridge trusses

BUILDING CLUSTERS

This connected towers concept was further developed in the design of a competition entry for a multi tower mixed use development in Sudirman City, Indonesia. An architectural design idea was developed to interconnect the residential and hotel towers with pedestrian bridges, allowing all the residential occupancies to share a common amenity space. Given the programmatic desire to interconnect the buildings, a series of studies were undertaken to determine the most beneficial configurations to allow the four connected towers to mutually support each other and maximize the structural efficiency of the cluster of buildings as a whole. For residential towers, where floor area in proximity with the façade is at a premium, the optimal architectural design solution often results in elongated towers with a pronounced 'narrow' dimension and 'wide' dimension. While enhancing views this configuration makes the structural engineering design of the towers difficult, as additional material is required to provide sufficient structural strength and stiffness in the narrow, weak direction. The structural concept behind the connected bridges was to tie the weak direction movements of one building to the strong axis of another building. Through this approach, the strong axis of a building where excess strength and stiffness is available, is used to strengthen the weak axis of the supported building.

Pinwheel Configuration

Below is a study comparing weak axis core stresses and dynamic behavior of rectangular cores with a plan aspect ratio of 1:4 tied together in various configurations. Connecting two rectangular bars oriented in the same direction results in no improvement in core stresses and makes the torsional behavior worse than that of an individual building. Connecting two rectangular buildings orthogonal to each allows one building to assist the other. However, connecting the buildings in a pinwheel configuration allows each building to provide support and be supported.



Mode 1 – 7.0s Translation
Mode 2 – 2.3 s Translation
Mode 3 – 0.95s Torison

Mode 1 – 7.1s Translation
Mode 2 – 2.7s Translation
Mode 3 – 2.2s Torison

.
Mode 1 – 4.0s Translation
Mode 2 – 3.1 s Translation
Mode 3 – 1.9 s Torison

Mode 1 – 3.1s Translation
Mode 2 – 3.1s Translation
Mode 3 – 2.4s Torison

Figure 12: Connecting multiple buildings study

Sudirman City Structural System

Similar idea as discussed above was used for the lateral system for the Sudirman city competition. Instead of four buildings as shown in figure 12, there buildings were interconnected with skybridges to control the building drift. For the tallest residential building, building drift exceeds the drift limit when designed for gravity loads alone. However, it was found that the building drift can be controlled by interconnecting to other towers with sky bridges as shown in figure 13.

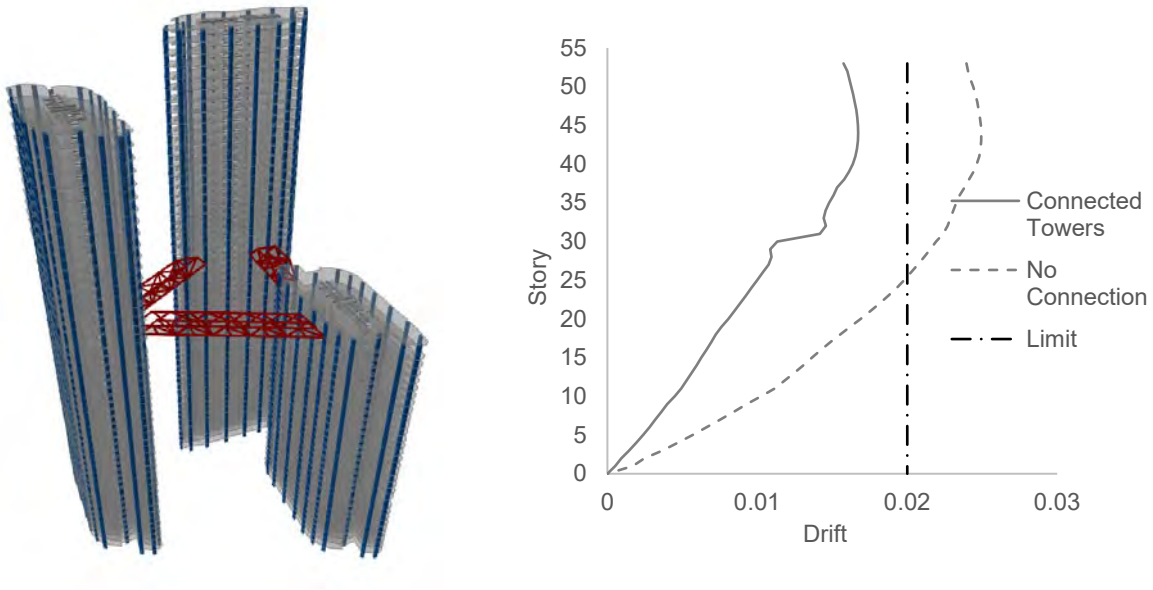


Figure 13 –3D analysis model of the connected towers (left); Drift along weak axis of the tallest tower (right)

CONCLUSIONS

Composite construction offers many possibilities for new efficient building configurations when considered in the context of building scale and multi-building scale composite systems. The use of different structural materials within a building structure based on the suitability of a material for the specific structural function is well established. Reinforced concrete is commonly used for axially loaded elements such as building cores and perimeter columns, while structural steel is commonly used for flexural elements such as floor framing, and certain special connecting elements such as outrigger and belt trusses. These conventional approaches at the building scale can be also applied to the multi-building scale for further efficiency gains, when the building geometries and configurations can be established to leverage these potential benefits.

TOWARDS THE USE OF HIGH STRENGTH STEEL AND CONCRETE IN HIGH-RISE CONSTRUCTION

J Y Richard Liew
Department of Civil & Environmental Engineering, National University of Singapore
ceeljy@nus.edu.sg

Yan-Bo Wang
Department of Civil & Environmental Engineering, National University of Singapore
ceewyb@nus.edu.sg

Yong Du
College of Civil Engineering, Nanjing University of Technology, Nanjing, China
yongdu_mail@njtech.edu.cn

ABSTRACT

Concrete filled steel tubular column comprising a hollow steel tube infilled with concrete has been used widely in high rise buildings. Although modern design codes provide guides on concrete filled steel tubular members, they do not cover their applications involving high strength concrete and high tensile steel. To fill this research gap, new tests have been conducted on concrete filled steel tubular members with ultra-high strength concrete (f_{ck} up to 190N/mm^2) and high tensile steel (f_y up to 780N/mm^2). In this paper, a design guide has been proposed for concrete filled steel tubular members based on an extension of Eurocode 4 method for concrete compressive strength up to 190N/mm^2 and high tensile steel with yield strength up to 550N/mm^2. More than 2030 test data on concrete filled steel tubes with normal and high strength materials have been analysed to formulate this design guide.

1 INTRODUCTION

High strength construction materials are now attractive owing to their economic and architectural advantages. For columns at the lower floors and basements of a high-rise building, the use of high strength materials has an advantage of reducing the members' cross-sectional size. This helps to increase the usable floor space and reduce the overall cost of investment in high-rise building. However, material brittleness could be one of the problems for high strength concrete and local buckling may be a problem for structural members with high tensile steel. To overcome these problems, one solution is to use composite structural members, especially concrete filled steel tubes as columns [1-3], where the ductility and strength of the concrete core can be enhanced by the confinement effect from the steel tubes while the local buckling of the steel tube can be delayed or even prevented by the concrete core. However, modern design codes do not cover their applications involving high strength concrete (HSC) and high tensile steel (HTS).

The material strength limitation of various design codes for composite columns are compared in Table 1. EC 4 [4] is applicable to composite columns with normal weight concrete of strength classes C20/25 to C50/60 and steel grades S235 to S460. AISC 360-10 [5] only applies to composite columns with normal weight concrete cylinder strength from 21 N/mm^2 to 70 N/mm^2 and steel yield strength up to 525 N/mm^2. The Chinese Code [6] only applies to composite columns with concrete cylinder strength from 25 N/mm^2 to 67 N/mm^2 and steel yield strength from 235 N/mm^2 to 420 N/mm^2. The Japanese Code [7] allows the use of high strength concrete with f_{ck} up to 90 N/mm^2. Composite structural members generally exhibit better ductility and higher buckling resistance compared with steel or reinforced concrete members.

However, EC 4 [4] gives a narrower range of material strength for steel and concrete compared with EC 2 [8] and EC 3 [9, 10] for concrete and steel structural design, respectively.

Table 1. Limitation on characteristic strength (N/mm^2) in modern design codes

Codes	Steel yield strength (N/mm^2)	Concrete cylinder strength (N/mm^2)
ANSI/AISC 360-10:2010	≤ 525	21 ~ 70
GB 50936:2014	235 ~ 420	25 ~ 67
AIJ, 1997	235 ~ 440	18 ~ 90
EN 1992-1-1:2004	N.A.	12 ~ 90
EN 1993-1-1:2005 EN 1993-1-12:2005	235 ~ 700	N.A.
EN 1994-1-1:2004	235 ~ 460	20 ~ 50

This highlights the dearth of a new design guide to fill the gap by allowing the design of CFST columns with concrete cylinder strength up to 90 N/mm^2 and steel of yield strength up to 550 N/mm^2. In this paper, a design guide has been proposed for concrete filled steel tubular members based on an extension of Eurocode 4 method EC 4 [4, 12] with special considerations for the high strength concrete and the high tensile steel. The design method was calibrated against the test data collected worldwide.

2 NEW TESTS AND COLLECTED TEST DATA

A total of 45 new tests, including short column (Figure 1) and beam-column (Figure 2) have been conducted to provide additional data of concrete filled steel tubular members with ultra-high strength concrete (UHSC, f_{ck} up to 190N/mm^2) and high tensile steel (f_y up to 780N/mm^2).

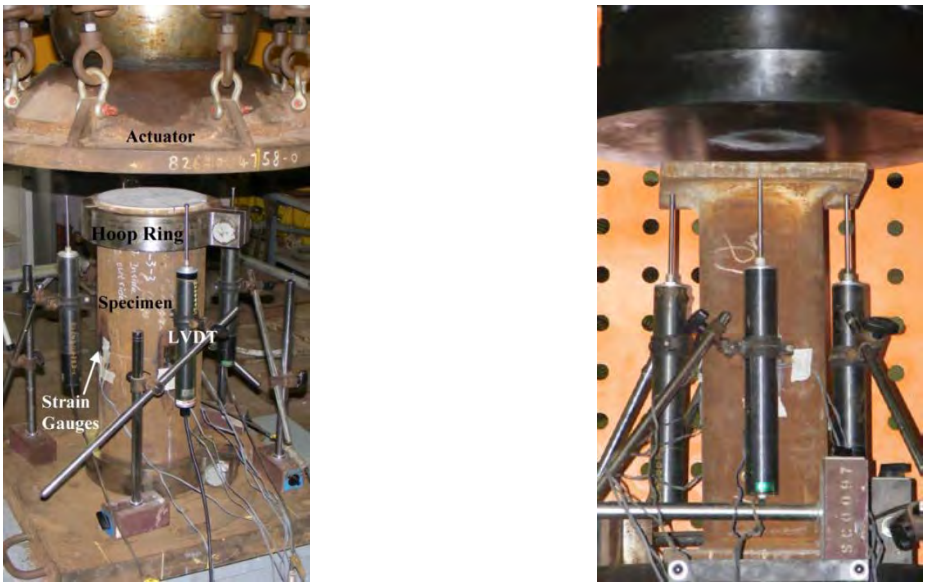
For short column, tests have been carried out on three series of specimens under concentric compression. For Series 1 tests, 11 small scale specimens were prepared with trial tests on UHSC infilled in S275 and S355 steel tubes under different loading conditions. For Series 2 tests, 8 larger specimens were tested for further verification with both of UHSC and normal strength concrete (NSC). For Series 3 tests, 17 specimens were tested to evaluate the performance of CFST columns in which 12 specimens used the UHSC and S700 steel tubes and 5 specimens employed the UHSC and mild steel. The CFST column specimens in Series 1, 2 and 3 tests are shown in Table 2 where λ is the relative slenderness, δ is the steel contribution ratio as in EC 4 and $N_{test,u}$ is the testing values of the ultimate resistance.

Table 2. Configuration details and test results for short CFST specimens

Series	No.	L (mm)	Steel sections	f_y (MPa)	f_{ck} (MPa)	λ	δ	$N_{test,u}$ (kN)
Series 1	S1-1-1(a)	250	CHS114.3×3.6	403	-	0.088	-	486
	S1-1-2(a)	250	CHS114.3×6.3	428	-	0.094	-	1039
	S1-1-2(b)	250	CHS114.3×6.3	428	-	0.094	-	990
	S1-2-1(a)	210*	CHS114.3×6.3	428	173.5	0.110	0.493	2866
	S1-2-1(b)	210*	CHS114.3×6.3	428	173.5	0.110	0.493	2595
	S1-3-1(a)	250	CHS114.3×3.6	403	173.5	0.142	0.326	2422
	S1-3-1(b)	250	CHS114.3×3.6	403	173.5	0.142	0.326	2340
	S1-3-2(a)	250	CHS114.3×3.6	403	184.2	0.145	0.313	2497
	S1-3-2(b)	250	CHS114.3×3.6	403	184.2	0.145	0.313	2314
	S1-3-3(a)	250	CHS114.3×6.3	428	173.5	0.131	0.493	2610
	S1-3-3(b)	250	CHS114.3×6.3	428	173.5	0.131	0.493	2633
Series 2	S2-1-1	600	CHS219.1×5	380	-	0.109	-	1190
	S2-1-2	600	CHS219.1×5	380	51.6	0.142	0.520	3118

	S2-1-3	600	CHS219.1×5	380	185.1	0.191	0.232	7837
	S2-1-4	600	CHS219.1×5	380	193.3	0.193	0.224	8664
	S2-2-1	600	CHS219.1×10	381	-	0.109	-	3050
	S2-2-2	600	CHS219.1×10	381	51.6	0.130	0.700	5241
	S2-2-3	600	CHS219.1×10	381	185.1	0.168	0.394	9085
	S2-2-4	600	CHS219.1×10	381	193.3	0.170	0.384	9187
Series 3	S3-1-1	450	SHS150×8	779	152.3	0.173	0.688	6536
	S3-1-2	450	SHS150×8	779	157.2	0.175	0.682	6715
	S3-1-3	450	SHS150×8	779	147.0	0.174	0.696	6616
	S3-1-4	450	SHS150×8	779	164.1	0.177	0.672	7276
	S3-1-5	450	SHS150×8	779	148.0	0.174	0.695	6974
	S3-1-6	450	SHS150×8	779	-	0.150	-	3695
	S3-2-1	450	SHS150×12	756	152.3	0.171	0.777	8585
	S3-2-2	450	SHS150×12	756	157.2	0.173	0.771	8452
	S3-2-3	450	SHS150×12	756	147.0	0.172	0.783	8687
	S3-2-4	450	SHS150×12	756	164.1	0.174	0.764	8730
	S3-2-5	450	SHS150×12	756	148.0	0.172	0.782	8912
	S3-2-6	450	SHS150×12	756	-	0.154	-	6456
	S3-3-1	450	SHS150×12.5	446	152.3	0.149	0.655	5953
	S3-3-2	450	SHS150×12.5	446	157.2	0.151	0.648	5911
	S3-3-3	450	SHS150×12.5	446	147.0	0.150	0.663	6039
	S3-3-4	450	SHS150×12.5	446	164.1	0.153	0.638	6409
	S3-3-5	450	SHS150×12.5	446	148.0	0.150	0.662	6285

* Loaded only on the concrete core which was 210mm in height.



(a) Circular specimen (b) Square specimen

Fig.1 Test set-up of short column

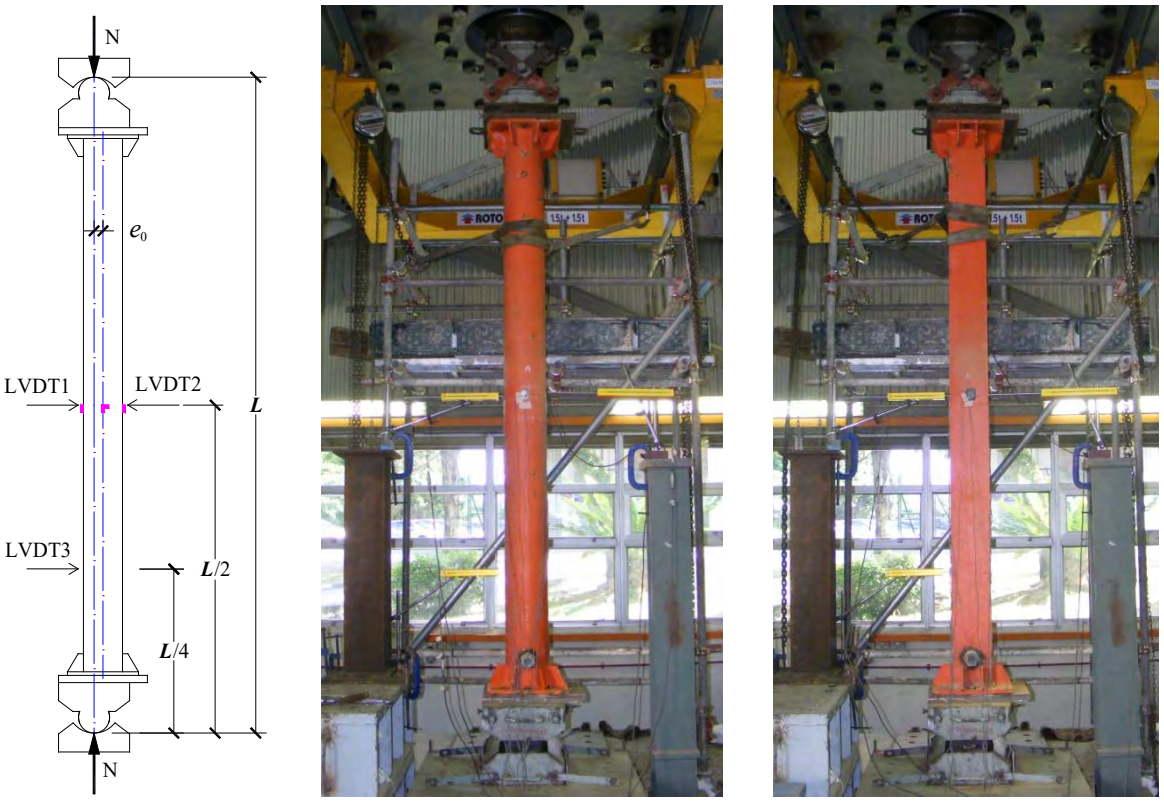
On the other hand, there were 9 slender CFST beam-column specimens of which 6 were circular sections (CS) and 3 were square sections (SS). The steel sections include 6 hot finished circular hollow mild steel sections, one hot finished square hollow mild steel section, and two welded square hollow HTS sections. All the sections are Class 1 sections according to EC 3. The column details and test results are shown in Table 3, where e_0 is the load

eccentricity to apply an end moment, Ne_o, to the column, and L is the effective length between the centres of the end roller supports, as shown in Figure 2.

Table 3. Configuration details and test results for CFST beam-column specimens

No.	Steel section(s)	f_y (MPa)	f_u (MPa)	E_a (GPa)	f_{ck} (MPa)	E_{cm} (GPa)	e_0 (mm)	L (mm)	$N_{test,u}$ (kN)
CS-1	CHS219.1×16	374	551	202	186	68	0	4195	6324
CS-2	CHS219.1×16	374	551	202	181	68	20	3640	4389
CS-3	CHS219.1×16	374	551	202	176	68	50	3640	3246
CS-4	CHS273×10	412	521	204	180	68	0	4195	8592
CS-5	CHS273×10	412	521	204	184	68	50	4450	5083
CS-6	CHS273×16	401	522	203	180	68	50	4450	5284
SS-1	SHS200×12.5	465	559	206	183	68	20	3640	5187
SS-2	SHS200×12*	756	825	199	176	68	20	3640	7136
SS-3	SHS200×12*	756	825	199	177	68	50	3640	4997

* For 6mm-thick mild steel backing strip used in welded sections, f_y = 325MPa, f_u = 467MPa, and E_a =201GPa



(a) Instrumentaion (b) Circular specimen (c) Square specimen

Fig.2 Test set-up of beam-column

In addition, the test database expands the work of Goode [13] to include 2033 test results on CFST columns with additional test data on CFST columns with ultra-high strength concrete reported above and elsewhere. The new test data includes steel tubes infilled with ultra-high strength concrete with cylinder compressive strength greater than 90N/mm^2. Test specimens involving short and long CFST members subjected to compression, uniaxial bending, and bi-axial bending, are categorized for comparison with EC 4 predictions. Tests on encased columns, columns with stainless steel and aluminium steel sections are excluded. Tests involving preload effect, sustained loading for creep and shrinkage studies and dynamic loadings are not included. CFST columns with Class 4 slender sections, in which the d/t ratio

exceeds the class 3 limit stipulated in EC 4, are also excluded although they were included originally in Goode's database [13]. In this database, the concrete compressive cylinder strength is in the range between 8.5N/mm^2 to 243N/mm^2, and the steel yield strength ranges from 178N/mm^2 to 853N/mm^2. The ratio of column height over section smaller dimension is between 0.67 and 60, and the relative slenderness $\bar{\lambda}$ ranges from 0.02 to 1.30.

3 INFLUENCE OF CONCRETE STRENGTH

The average test/prediction ratios against concrete cylinder strength are shown in Table 5. The ratios are categorized into three groups based on concrete strength. By studying the values which are not bracketed, the average test/EC 4 value for each type of CFST specimens is greater than unity indicating a conservative average prediction by EC 4, both for normal and high strength concretes.

Table 5 also provides the percentage of conservative prediction (i.e., test/EC 4 prediction ≥ 1.0) which reflects the reliability of the prediction by EC 4. For high strength concrete (50N/mm^2 < f_{ck} ≤ 90N/mm^2), the percentages of all circular columns and the axially loaded rectangular cross sections are lower than those of their counterparts with normal strength concrete (f_{ck} ≤ 50N/mm^2). For ultra-high strength concrete (f_{ck} > 90N/mm^2), the percentages of all columns are lower than those of their counterparts with normal strength concrete. This reflects the increasing complexity and severity as the concrete strength increases. To allow for this in design, the effective compressive strength of concrete is adopted in accordance with EC 2 [8] for high strength concrete and ultra-high strength concrete. The effective strength is determined by multiplying a reduction factor η with the concrete strength given as:

$$\eta = \begin{cases} 1.0 - \left(f_{ck} - 50\right)/200 & 50\ \text{N/mm}^2 < f_{ck} \le 90\ \text{N/mm}^2 \\ 0.8 & f_{ck} > 90\ \text{N/mm}^2 \end{cases} \tag{1}$$

For ultra-high strength concrete with f_{ck} > 90N/mm^2, it is recommended that η = 0.8 should be adopted and the increase of concrete strength due to confinement effect from steel tube should be ignored. With the introduction of reduction factor η, the effective compressive strengths are given in Table 4 for various high strength concrete classes. Accordingly, the secant modulus for high and ultra-high strength concrete should be modified based on the effective strength as

$$E_{\mathrm{cm}} = 22[(\eta \cdot f_{\mathrm{ck}} + 8)/10]^{0.3} \tag{2}$$

The percentage of reduction in the secant modulus for high strength concrete is less as compared to the compressive strength as shown in Table 4.

Table 4. Effective compressive strength and modified secant modulus of HSC

Strength classes	**C55/67**	**C60/75**	**C70/85**	**C80/95**	**C90/105**
Effective compressive strength (N/mm^2)	54	57	63	68	72
Reduction ratio	2.5%	5.0%	10.0%	15.0%	20.0%
Modified secant modulus (N/mm^2)	38.0	38.6	39.6	40.4	41.1
Reduction ratio	0.7%	1.3%	2.8%	4.3%	5.9%

Table 5. Influence of concrete strength on test/EC 4 prediction ratios for CFST columns

Type of column		**Compressive cylinder strength of concrete**		
		≤50 N/mm^2	**≤90 N/mm^2**	**>90 N/mm^2**
	Nos.	295	130	44

Axially loaded circular cross section	Test/EC4 ≥ 1	66.8% (99.3%)	59.2% [66.9%]{97.7%}	47.7% <100%>|100%|
	Av.	1.068 (1.355)	1.023 [1.062]{1.383}	1.016 <1.298>|1.646|
	St. Dev.	0.136 (0.169)	0.111 [0.132]{0.190}	0.104 <0.139>|0.153|
Axially loaded circular column	Nos.	383	60	22
	Test/EC4 ≥ 1	85.9% (97.4%)	68.3% [83.3%]{98.3}	81.8% <100%>|100%|
	Av.	1.186 (1.388)	1.039 [1.075]{1.339}	1.085 <1.195>|1.512|
	St. Dev.	0.246 (0.267)	0.110 [0.121]{0.162}	0.095 <0.093>|0.157|
Circular beam-column	Nos.	240	66	46
	Test/EC4 ≥ 1	82.1% (98.8%)	71.2% [81.8%]{98.5%}	69.6% <78.3%>|91.3%|
	Av.	1.192 (1.352)	1.086 [1.136]{1.356}	1.008 <1.121>|1.378|
	St. Dev.	0.217 (0.237)	0.182 [0.189]{0.216}	0.172 <0.205>|0.266|
Axially loaded rectangular cross section	Nos.	282	63	39
	Test/EC4 ≥ 1	80.1% (99.6%)	68.3% [90.5%]{96.8%}	56.4% <89.7%]|100%|
	Av.	1.122 (1.287)	1.068 [1.118]{1.330}	1.032 <1.136>|1.321|
	St. Dev.	0.150 (0.196)	0.123 [0.117]{0.168}	0.093 <0.099>|0.132|
Axially loaded rectangular column	Nos.	101	40	12
	Test/EC4 ≥ 1	62.4% (94.1%)	70.0% [77.5%]{95.0%}	58.3% <91.7%>|100%|
	Av.	1.059 (1.220)	1.057 [1.099]{1.321}	1.095 <1.212>|1.458|
	St. Dev.	0.140 (0.172)	0.134 [0.140]{0.177}	0.206 <0.193>|0.233|
Rectangular beam-column	Nos.	160	23	27
	Test/EC4 ≥ 1	73.1% (98.1%)	87.0% [87.0%]{100%}	70.4% <85.2%>|100%|
	Av.	1.107 (1.338)	1.099 [1.128]{1.461}	1.044 <1.089>|1.314|
	St. Dev.	0.279 (0.341)	0.112 [0.102]{0.148}	0.115 <0.117>|0.124|
All test data	Nos.	1461	382	190
	Test/EC4 ≥ 1	77.3% (98.3%)	67.0% [78.3%]{97.6%}	62.6% <90.0%>|97.9%|
	Av.	1.133 (1.339)	1.052 [1.094]{1.361}	1.034 <1.175>|1.440|
	St. Dev.	0.210 (0.240)	0.132 [0.141]{0.186}	0.132 <0.165>|0.224|

Notes:

1) For the value1, (value2), [value3], {value4}, <value5> and |value6| in the table, value1 is based on the characteristic strengths of steel and concrete; (value2) is based on design strengths; [value3] is based on characteristic strengths with reduction factor η for concrete; {value4} is based on design strengths with reduction factor η for concrete.

<value5> is based on characteristic strengths with reduction factor η and neglect of confinement for concrete; |value6| is based on design strengths with reduction factor η and neglect of confinement for concrete.
2) The design partial factor is 1.5 and 1.0 for concrete and steel, respectively.
3) This table does NOT include test specimens with class 4 section as in EC4.
4) Av.=Average value; St.Dev.=Standard Deviation.

The predictions of CFST members using EC4 based on the effective strength and modified secant modulus are given in
Table 5 where values are in the brackets [ ] and < >. It is found that the percentages of all columns with high strength and ultra-high strength concretes are comparable with those of their counterparts with normal strength concrete. The comparable reliability with normal strength concrete has been achieved for high strength concrete and ultra-high strength concrete with the introduction of concrete strength reduction factor η in Eq. (1) and by neglecting the confinement effect for ultra-high strength concrete. Hence, the modified EC4 method can be extended to CFST columns with higher concrete strength.

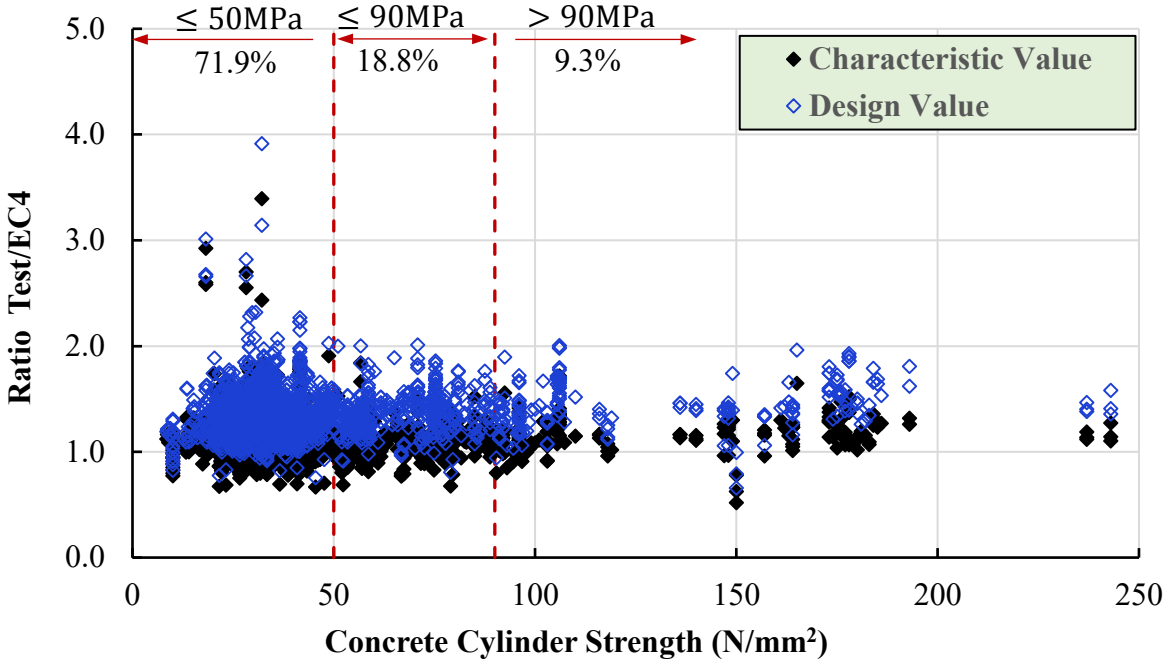


Fig.3 Comparison of test/EC4 prediction ratio against concrete strength

Table 5 gives the percentages for all the test data in terms of concrete strength. Overall, the percentage decreases with increasing concrete strength (refer to values not in the brackets). Considering the reduction factor η and ignoring the concrete confinement effect, the percentages of Test/EC4 prediction ≥ 1.0 of high strength concrete and ultra-high strength concrete are higher than those of their counterparts with normal strength concrete. The design values (refer to values in ( ), { } and | |) are also provided in
Table 5 with the introduction of partial factors of 1.5 and 1.0 for concrete and steel, respectively. When the codes specified design values are compared with the test results, the percentages of under-prediction (i.e., test/EC4 prediction < 1.0) are less than 3%.
The Test/EC4 ratios are plotted in Figure 3, with the effective strength and modified modulus of elasticity applied for concrete with compressive strength higher than 50N/mm^2. Most data lies close to unity, except one data showing a rather high test/EC4 value (=3.39, characteristic value). This data was taken from tests by Assis et al.[14]. The test/prediction ratio was given as 1.98 in Ref.[14], implying there might be problem in this test. There is also difference between the authors' prediction and the prediction in Ref.[14], but it remains unknown. Figure

3 shows that, in order to further extend the EC4 scope to include the ultra-high strength concrete, more test data could be done for CFST columns with concrete compressive strength between 120 N/mm^2 to 150 N/mm^2. Alternatively, the use of ultra-high strength concrete for CFST column is made possible if a condition on the strain compatibility between steel and concrete material is observed as described in Section 5.

4 INFLUENCE OF STEEL STRENGTH

The average test/prediction ratios against steel yield strength are shown in Table 6. All the values are based on the reduction factor η in Eq. (1) and they neglect the confinement for ultra-high strength concrete. The ratios are categorized into three groups based on steel strength. It is observed that the average ratio of test/EC4 prediction for each type of column with mild steel ($f_y \leq 460$N/mm^2) is greater than unity. However, this is not true for columns with high tensile steel ($f_y > 460$N/mm^2). This might be due to the lack of consideration of the strain compatibility between steel and concrete. Thus, for CFST columns with steel strength $f_y >$ 460N/mm^2, the reliability of the proposed method needs to be further investigated.
Table 6 also gives the percent of test/EC4 prediction > 1.0 and the average prediction of all test data in terms of steel yield strength. The ratios between test and design prediction are also provided. The average test/EC4 prediction ratio for CFST with high tensile steel is higher than those with mild steel, but the standard deviation is higher indicating that wide scattering of results is observed for specimens with high tensile steel. When the codes' design values are compared with the test results, the percentage of under-prediction (i.e., test/EC4 prediction < 1.0) is less than 5%, although the average ratio is higher than those with mild steel.

Table 6. Influence of steel strength on test/EC4 prediction ratios for CFST columns

Types of column		**Yield strength of steel**		
		≤460N/mm^2	**≤550N/mm^2**	**>550N/mm^2**
Axially loaded circular cross section	Nos.	450	5	14
	Test/EC4 ≥ 1	71.6% (99.6%)	40.0% (40.0%)	28.6% (100%)
	Av.	1.093 (1.399)	0.922 (1.133)	0.975 (1.180)
	St. Dev.	0.150 (0.189)	0.200 (0.215)	0.068 (0.081)
Axially loaded circular column	Nos.	414	38	13
	Test/EC4 ≥ 1	85.7% (97.6%)	89.5% (100%)	92.3% (92.3%)
	Av.	1.152 (1.378)	1.399 (1.532)	1.160 (1.270)
	St. Dev.	0.167 (0.210)	0.544 (0.526)	0.112 (0.122)
Circular beam-column	Nos.	346	6	-
	Test/EC4 ≥ 1	82.4% (98.0%)	33.3% (83.3%)	-
	Av.	1.175 (1.356)	1.032 (1.367)	-
	St. Dev.	0.211 (0.236)	0.213 (0.268)	-
Axially loaded rectangular cross section	Nos.	308	21	55
	Test/EC4 ≥ 1	84.7% (99.0%)	100% (100%)	65.5% (100%)
	Av.	1.135 (1.324)	1.132 (1.310)	1.048 (1.146)
	St. Dev.	0.147 (0.189)	0.071 (0.096)	0.089 (0.117)
Axially loaded rectangular column	Nos.	145	8	-
	Test/EC4 ≥ 1	67.6% (95.2%)	87.5% (87.5%)	-
	Av.	1.078 (1.262)	1.152 (1.328)	-
	St. Dev.	0.141 (0.181)	0.267 (0.331)	-
Rectangular beam-column	Nos.	187	8	15

	Test/EC4 ≥ 1	73.8% (98.4%)	87.5% (100%)	100% (100%)
	Av.	1.099 (1.338)	1.061 (1.385)	1.221 (1.459)
	St. Dev.	0.255 (0.319)	0.071 (0.119)	0.219 (0.168)
All test data	Nos.	1850	86	97
	Test/EC4 ≥ 1	78.9% (98.3%)	84.9% (94.2%)	69.1% (99.0%)
	Av.	1.128 (1.357)	1.226 (1.410)	1.079 (1.216)
	St. Dev.	0.181 (0.222)	0.409 (0.395)	0.141 (0.165)

The Test/EC4 ratios are also plotted in Figure 4. It is observed that more than 90% test data are from CFST columns with mild steels. The test data is insufficient to establish the validity of using the high tensile steels according to EC 4. The following section provides additional guideline to limit the use of high tensile steel by selecting matching grades of steel and concrete materials for composite construction.

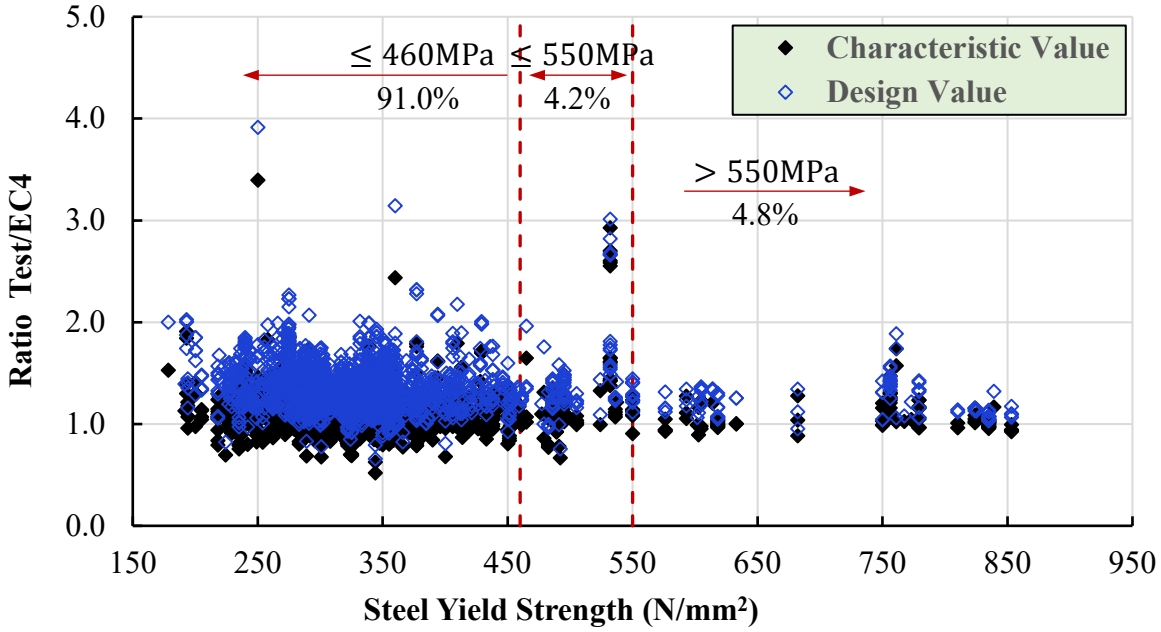


Fig.4 Comparison of test/EC4 prediction ratio against steel strength

5 STRAIN COMPATIBILITY BETWEEN STEEL AND CONCRETE

For high strength concrete filled steel tubular columns subjected to compression, it is necessary to ensure that yielding of the steel section occurs before the concrete core reaches its maximum stress. Otherwise, the full plastic resistance of the composite section cannot be achieved due to brittle failure of high strength concrete after reaching the maximum stress. Hence, the selections of steel grade and concrete class have to ensure that the yield strain of steel is smaller than the compressive strain of concrete at the peak stress. The yield strain of steel and the strain of concrete at peak stress may be calculated as [8&9]:

Steel yield strain: $$\varepsilon_y = f_y / E_a \quad (3)$$

Concrete strain at peak stress (‰): $$\varepsilon_{c1} = 0.7 f_{cm}^{0.31} \quad (4)$$

where $f_{\mathrm{cm}} = f_{\mathrm{ck}} + 8$ is the mean compressive strength of concrete at 28 days, in N/mm^2. E_a = 210000 N/mm^2 is the elastic modulus of steel tube. It is noted that the calculation for the strain of concrete at peak stress ignores the confinement effect from the steel tubes. Steel

with yield strength greater than 550N/mm^2 may be used provided that a more accurate assessment on the concrete strain at peak stress, considering the tri-axial confinement effect from the steel tube, is carried out.

Table 7. Compatibility between steel and concrete materials for CFST columns

	S235	S275	S355	S420	S460	S500	S550
C25/30	√	√	√	√	×	×	×
C30/37	√	√	√	√	×	×	×
C35/45	√	√	√	√	√	×	×
C40/50	√	√	√	√	√	×	×
C45/55	√	√	√	√	√	√	×
C50/60	√	√	√	√	√	√	×
C55/67	√	√	√	√	√	√	×
C60/75	√	√	√	√	√	√	×
C70/85	√	√	√	√	√	√	√
C80/95	√	√	√	√	√	√	√
C90/105	√	√	√	√	√	√	√
C110/-	√	√	√	√	√	√	√
C130/-	√	√	√	√	√	√	√
C150/-	√	√	√	√	√	√	√
C170/-	√	√	√	√	√	√	√
C190/-	√	√	√	√	√	√	√
Notes: "√" indicates compatible materials and "×" is not recommended.							

Table 7 gives the recommendation on the matching grades of steel and concrete suitable for use in CFST columns. This is based on the condition $\varepsilon_y < \varepsilon_{cl}$ and the experimental observations on the new test data presented in [1-2]. It is recommended that the steel tubular sections up to Grade S550 may be used with concrete class up to C190, although test evidence by Liew et al. [3] shows that the strain of the confined concrete at peak stress of CFST is much higher than the concrete without any lateral confinement. Alternatively, the maximum steel strength can be determined according to the concrete characteristic strength with strength class up to C190 using the following expression:

$$f_y = \min\left(0.7E_a\left(f_{ck}+8\right)^{0.31},\ 550\right) \tag{5}$$

6 CASE STUDY

The M-N interaction curves for a CFST column with section shown in Figure 5 are determined according to the proposed design method given in above.

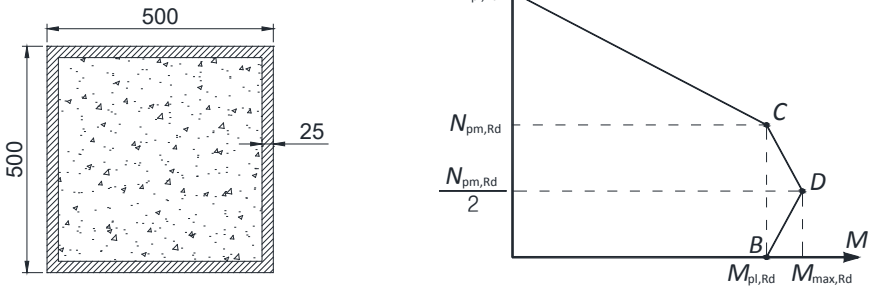
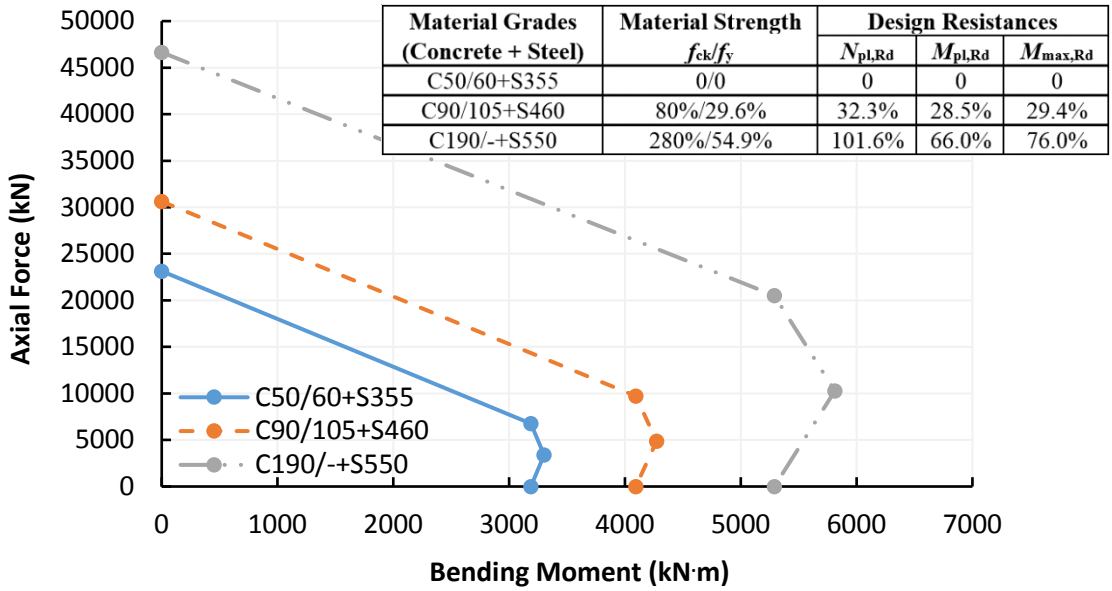


Fig.5 CFST column for case study and illustration for M-N interaction curve

For the CFST columns used in high-rise buildings, they are usually subject to combined effects of high compression force and bending moment. These effects could be effectively resisted by increasing the concrete and steel strengths as shown in Figure 6. The combined use of C190 concrete and S550 steel shows superior performance on improving the overall resistance and thus it is more economical in terms of reducing steel and concrete materials, using less weld consumable, reducing the cost of fire protection and fabrication, reducing construction time and increasing usable floor area.



Material Grades (Concrete + Steel)	Material Strength f_{ck}/f_y	Design Resistances		
		$N_{pl,Rd}$	$M_{pl,Rd}$	$M_{max,Rd}$
C50/60+S355	0/0	0	0	0
C90/105+S460	80%/29.6%	32.3%	28.5%	29.4%
C190/-+S550	280%/54.9%	101.6%	66.0%	76.0%

Fig.6 Comparison between CFSTs with varying both concrete and steel strengths

7 CONCLUSIONS

Based on calibration with 2033 test data, the current EC 4 method can be safely extended to the design of concrete filled steel tubular (CFST) members with steel strength up to 550N/mm^2 and concrete compressive cylinder strength up to 190N/mm^2, with the following modifications and restrictions:

- This design guide is meant for CFTS members with at least Class 3 steel section. Class 4 steel section should not be used.
- Matching grades of steel and concrete materials should be used. Table 7 provides a guide to select the grade of steel and class of concrete for the design of CFST members to avoid the crushing of the core concrete before yielding of steel section.
- A strength reduction factor should be applied for high strength concrete with cylinder strength greater than 50N/mm^2 but less than 90N/mm^2. Accordingly, the secant modulus of concrete should also be modified.
- For ultra-high strength concrete with compressive cylinder strength higher than 90N/mm^2 but less than 190N/mm^2, a conservative approach is to adopt the concrete strength reduction factor of 0.8 and further ignore the concrete confinement effect. Steel with yield strength greater than 550N/mm^2 may be used with ultra-high strength concrete provided that a more accurate assessment on the concrete strain at peak stress, considering the tri-axial confinement effect from the steel tube, is carried out.
- The key parameters for numerical analysis of ultra-high strength concrete under lateral confinements were obtained from tests on UHSC under various confinement pressure. These parameters were recommended so that proper analysis and design can be carried on steel tubular members infilled with UHSC for them to be used economically in high-rise buildings.

The design recommendations proposed in this paper will endow structural engineers with the confidence to use high strength materials in a safe and economic manner to design high-rise buildings. The authors aware that there is a size effect needs to be investigated in view of the smaller size specimens tested in the laboratory relative to those use in practice. Although the size effect has been partially accounted for in the partial factors in design codes, more tests on larger size columns are needed to gain confident in designing composite columns with high strength materials.

REFERENCES

[1] Liew J.Y.R., Xiong D.X. (2012). Ultra-high strength concrete filled composite columns for multi-storey building construction. *Advances in Structural Engineering*, 15(9), 1487-1503.

[2] Liew J.Y.R., Xiong M.X., Xiong D.X. (2014). Design of high strength concrete filled tubular columns for tall buildings. *Journal of high-rise buildings*, 3(3), 1-7.

[3] Liew, J.Y.R. (2004). Buildable design of multi-storey and large span steel structures, *Journal of Steel Structures*, 4(2). 53-70.

[4] EN 1994-1-1 (2004). *Eurocode 4: Design of composite steel and concrete structures – Part 1-1: General rules and rules for buildings*.

[5] AISC 360-10 (2010). *Specification for structural steel buildings*. American Institute of Steel Construction (AISC), Chicago, USA.

[6] GB 50936 (2014). *Technical code for concrete-filled steel tubular structures*. Ministry of Housing and Urban-Rural Development of the People's Republic of China, in Chinese. 6

[7] AIJ (1997). *Recommendations for design and construction of concrete filled steel tubular structures*, Architectural Institute of Japan, Japan.

[8] EN 1992-1-1 (2004). *Eurocode 2: Design of concrete structures – Part 1-1: General rules and rules for buildings*.

[9] EN 1993-1-1 (2005). *Eurocode 3 - Design of steel structures – Part 1-1: General rules and rules for buildings.*

[10] EN 1993-1-12 (2007). *Eurocode 3 – Design of steel structures – Part 1-12: Additional rules for the extension of EN 1993 up to steel grades S700*.

[11] Liew J.Y.R., Xiong M.X. (2015). *Design guide for concrete filled tubular members with high strength materials – An extension of Eurocode 4 method to C90/105 concrete and S550 steel*. Research Publishing Singapore.

[12] EN 1994-1-2 (2005). *Eurocode 4: Design of composite steel and concrete structures – Part 1-2: General rules – Structural fire design*.

[13] Goode C.D. (2008). Composite columns – 1819 tests concrete filled steel tube columns compared with Eurocode 4. The Structural Engineer, 86(16), 19 August.

[14] Assi I.M., Qudeimat E.M., Hunaiti Y.M. (2003) Ultimate moment capacity of formed and lightweight aggregate concrete filled steel tubes. *Steel and Composite Structures*, 3(3):199-212.

DEVELOPMENT OF A NEW PUSH TEST FOR EUROCODE 4

Stephen J. Hicks
General Manager Structural Systems
Heavy Engineering Research Association
Auckland, New Zealand
stephen.hicks@hera.org.nz

Adrian Ciutina
Professor, Politehnica University Timişoara
Department of Overland Communication Ways, Foundation and Cadastral Survey
Timişoara, România
adrian.ciutina@upt.ro

Christoph Odenbreit
ArcelorMittal Chair of Steel and Façade Engineering
University of Luxembourg, Laboratory of Steel and Composite Structure
Luxembourg-Kirchberg, Luxembourg
christoph.odenbreit@uni.lu

ABSTRACT

The standard push test specimen in the current version of Eurocode 4 does not provide any information on what modifications should be made when profiled steel sheeting is introduced. Whilst the lack of information was intended to encourage innovation, this has sometimes lead to test results implying that stud connectors possess a lower resistance and ductility than assumed in current Standards. From full-scale beam and companion push tests in Europe, it has been shown that modifying the push test through the introduction of a normal force to the face of the test slabs provides comparable load-slip performance to that encountered within a beam. Within the work programme for developing the second generation of Eurocodes, this paper presents part of the background to Sub-task 1 of SC4.T3, whose aim is to develop an improved push test for Eurocode 4 when stud connectors are welded within profiled steel sheeting.

INTRODUCTION

STANDARD PUSH TEST

The forces that occur in the concrete flange of a composite beam are shown schematically in Fig. 1(a). Should a distributed load q be introduced, the vertical shear forces are affected such that $\Delta V = V_l - V_r = q \times \Delta_l$. If the distributed load q acts on the concrete flange, as well as the longitudinal shear force F_ℓ, a compression force $q \times \Delta_l$ exists at the interface between the concrete and the top flange of the steel beam.

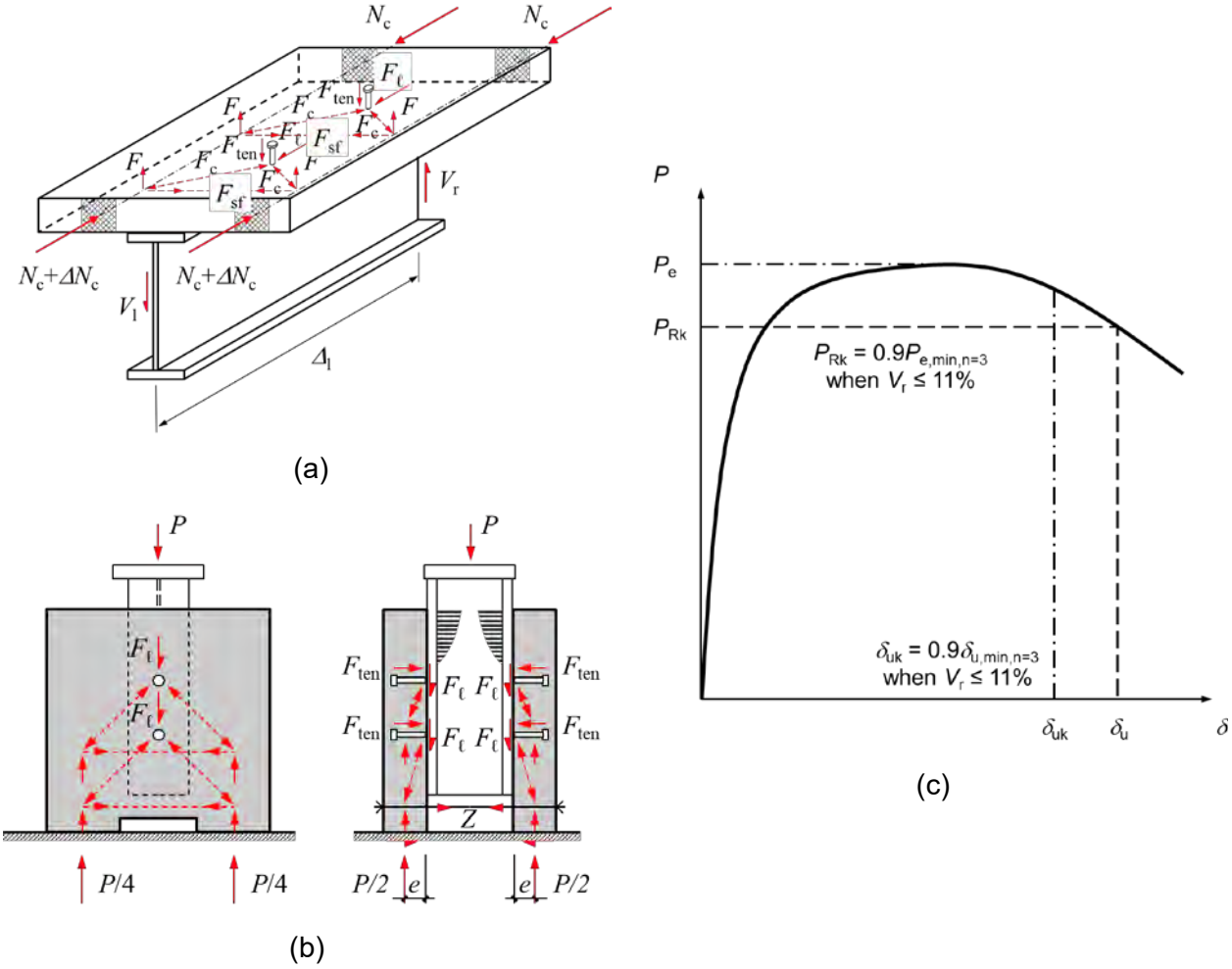


Fig. 1 - (a) Internal forces within: a composite beam; (b) a push test (Roik and Hanswille, 1987); and (c) determination of characteristic resistance and slip capacity from push test load-slip curve according to Eurocode 4.

The load-slip performance of shear connectors has been historically established from small-scale push specimens of the type shown in Fig. 1(b). By applying a load to the top end of the steel-section, the load-slip behaviour of the connectors can be determined. This type of specimen is known as a 'push test specimen' in Eurocode 4 (EN 1994-1-1, 2004) and, apart from slight variations in its geometry, has hardly changed since its inception in the early 1930's (Roš, 1934). The internal forces in the push specimen are shown in Fig. 1(b) to enable direct comparisons to be made with those in a composite beam. The forces F_ℓ are transferred through

the concrete in a similar way as a composite beam (N.B. the recess at the bottom of the slab is optional in the standard test in Eurocode 4). The moment $P \times e$, resulting from the eccentric load introduction, causes tension in the studs and compression at the interface between the concrete and the flange of the steel section. In the Eurocode 4 standard test, the magnitude of the tension forces in the studs F_{ten} is therefore affected by frictional forces developing at the interface between the test slabs and the strong floor $\mu \times P$ (where μ is the friction coefficient); if these frictional forces are eliminated, F_{ten} increases, which has been shown to reduce the shear resistance of the studs by approximately 30% (Hicks and McConnel, 1997).

EVALUATION OF THE RESULTS FROM PUSH TESTS

Characteristic resistance P_{Rk}

According to current requirements of Eurocode 4, if 3 nominally identical push tests are carried out, and the deviation of any individual result from the mean value does not exceed 10%, the characteristic resistance of a shear connector P_{Rk} is defined as 0.9 times the minimum failure load per stud (see Fig. 1(c)). Letting $P_{e,m}$ be the mean measured resistance per connector from three nominally identical push tests, and $P_{e,min,n=3}$ be the lowest of the three measured resistances per connector, this requirement can be written as follows:

$$P_{Rk} = 0.9P_{e,\min,n=3} \text{ provided that } \left|P_{e,e} - P_{e,m}\right| \le 0.1P_{e,m} \quad (1)$$

where $P_{e,e}$ is each extreme (maximum or minimum) measured resistance.

If the scatter of results exceeds the 10% limit (i.e. $\left|P_{e,e} - P_{e,m}\right| > 0.1P_{e,m}$), the test evaluation should be carried out according to EN 1990, Annex D (2005).

Equation (1) is effectively based on the EN 1990 provisions for the evaluation of a characteristic value from a small number of test results, when the coefficient of variation V_r is known from a significant number of previous tests (i.e. 'V_X known'). Although there may be some debate on the exact value for the coefficient of variation from historical push tests, it can be deduced from EN 1990 that, for a set of three results with extreme measured resistances $P_{e,e}$ less than 10% of the mean value $P_{e,m}$, the method in Eurocode 4 implies that V_r = 11% (Johnson, 2012).

It would be unwise to assume that V_r = 11% is always satisfied since, from a recent investigation undertaken in the UK (Smith and Couchman, 2010), 3 of the 9 groups of nominally identical push tests did not satisfy the 10% limit for the scatter of results. Furthermore, if three nominally identical tests are not undertaken, it would be impossible to verify the Eurocode 4 requirement for the scatter of the results. Therefore, hypothetically, if only one push test was undertaken, the characteristic resistance could be at least 20% lower than expected.

Characteristic slip capacity δ_{uk}

The ductility of a shear connector is measured by the slip capacity δ_u, which is defined in Eurocode 4, B.2.5 as the slip corresponding to the point where the characteristic resistance of the connector intersects the falling branch of the load-slip curve (see Fig. 1(c)). The characteristic slip capacity δ_{uk} is taken as 0.9 times the minimum test value of $\delta_{u,min}$, such that $\delta_{uk} = 0.9\delta_{u,\min,n=3}$. Alternatively, the characteristic properties of a shear connector can be determined by a statistical evaluation of all of the results according to EN 1990. It is therefore implied by Eurocode 4, that the coefficient of variation for the slip capacity is V_r = 11% when $\delta_{uk} = 0.9\delta_{u\,\min,n=3}$, but no information is given to the designer on when it is appropriate to use EN 1990.

PUSH TESTS ON HEADED STUDS WELDED WITHIN TRAPEZOIDAL PROFILED STEEL SHEETING TRANSVERSE TO A BEAM

Questions have arisen on the appropriateness of using the reduction factors contained within Eurocode 4, owing to the fact that the failure mechanisms of studs in trapezoidal profiled steel sheeting are quite different to those experienced in solid slabs. For example, when push tests are conducted on studs welded favourably or centrally within the ribs of a sheet (see Fig. 2), a typical failure mode known as concrete cone pull-out occurs (Hawkins and Mitchell,1984; Lloyd and Wright, 1990). In this case, the whole cone together with stud rotates and is pulled out of the slab, carrying with it a wedged-shaped pyramidal portion of concrete (see Fig. 2(d)); in these cases the axial tension in the stud can be significant, which has been measured in some special test specimens to be in the order of 30% of the longitudinal shear resistance (van der Sanden, 1996). Due to the tension and rotation of the stud, the concrete slab can separate from the profiled steel sheeting relatively early in push tests, which brings into question whether it is entirely appropriate to neglect the compression at the interface between the concrete and the steel section that would occur in a composite beam subjected to a uniformly distributed load together with its self-weight (see Fig. 1(a)).

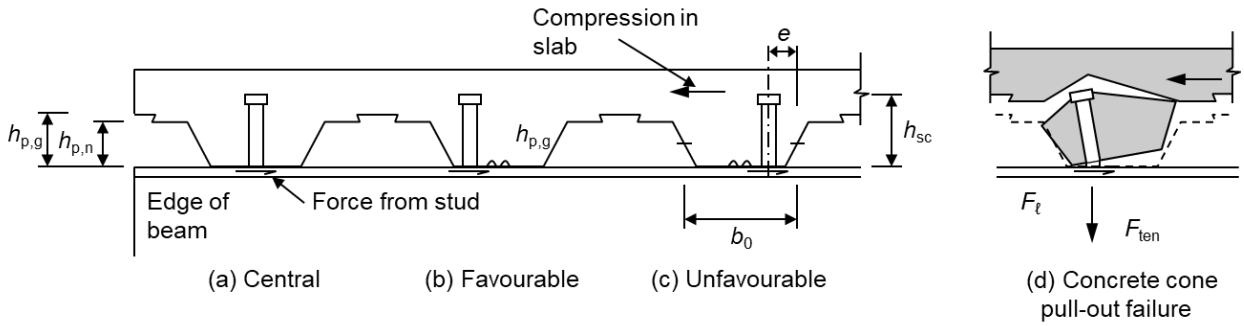


Fig. 2 - Dimensions of profiled steel sheeting and studs in the (a) Central (b) Favourable (c) Unfavourable position

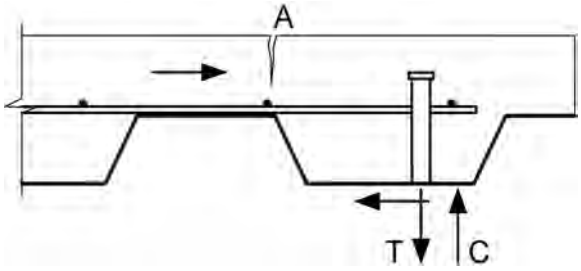
The Eurocode 4 rules for partial shear connection are based on two independent studies (Johnson and Molenstra, 1991; Aribert, 1990). These studies assumed that, in solid concrete slabs and composite slabs using profiled steel sheets prevalent in the 1980's, the characteristic slip capacity of 19 mm diameter studs was approximately δ_{uk} = 6 mm (see Fig. 1(c)). The rules for partial shear connection in Eurocode 4 were limited to situations where the required slip did not exceed 6 mm. Studs were deemed to be 'ductile' in those situations.

Push tests in Australia (Patrick, 2004) suggested that studs welded within the ribs of modern trapezoidal profiled steel sheeting possess lower resistance and ductility than assumed in Eurocode 4. To investigate whether the claims were affected by the thinner (0.75 mm), high strength steel decking (550 MPa) that is common in Australasia, 24 push tests with trapezoidal decking were undertaken at Imperial College London in 2003 (Hicks, 2007a). Each test slab had three concrete ribs with studs through-deck welded in the two ribs to the top of the specimens. However, it was found that the specimens with two studs per rib in the favourable position (n_r = 2F) gave consistently lower resistances than those with one stud per rib (n_r = 1F), irrespective of the stud layout. From an inspection of the specimens it was clear that the results had been affected by an artificial 'back-breaking' failure mode, which was characterised by the last studded rib at the top of the specimen rotating, causing a horizontal crack to appear across the full width of the test slab (see Fig. 3(a)). It was believed that this failure was caused by the couple of internal forces in the last studded rib at the top of the specimen (see Fig. 3(b)). To

remedy this situation, it appeared that the provision of an unstudded rib at the top of specimen eliminated this artificial back-breaking failure mode.



(a)



(b)

Fig. 3 - (a) Back-breaking failure experienced in Imperial College London tests (b) Internal forces causing rotation of the last studded rib at the top of the specimen

An obvious question regarding stud connectors in push specimens is whether their behaviour is comparable to that which would occur in a full-scale beam. In an attempt to address this question, tests on a 10.0, 5.0 and 11.4 m span composite beam, together with 12 companion push tests were undertaken in the UK between 2004 and 2008 (Hicks, 2007b; Hicks and Smith, 2014). To enable the internal forces to be evaluated, the steel beams were instrumented with strain gauges on the top and bottom flange at cross-sections corresponding to the shear connector positions. As well as determining the build-up of axial force, the internal bending moments were evaluated to check the reliability of the strain gauge readings. The slip distribution at the shear connection was established from horizontally mounted transducers, which monitored the relative displacement between bars cast in the concrete behind the shear connector positions and the top flange of the beam. The internal load–slip curves for the shear connectors were therefore evaluated by plotting the change in axial force at each cross-section against the corresponding slip.

The load-slip curves for studs with the lowest failure load in the beam tests are compared to their companion push tests in Fig. 4. As can be seen from these plots, there is no similarity in performance of studs for these two types of specimen. In Fig. 4, the slips measured in the push tests are well below the levels achieved in the beam and, if considered in isolation, would suggest that the studs should not be taken to be ‘ductile’ (which has adverse implications for partial shear connection design). Furthermore, the tests showed that the resistance per stud for n_r = 3F was no better than n_r = 2F, thereby indicating that the design equations in BS 5950-3.1 (1990) and ANSI/AISC 360-16 (2016) were unconservative by up to 45%. As a direct result of this work, an amendment was made to BS 5950-3.1 (2010).

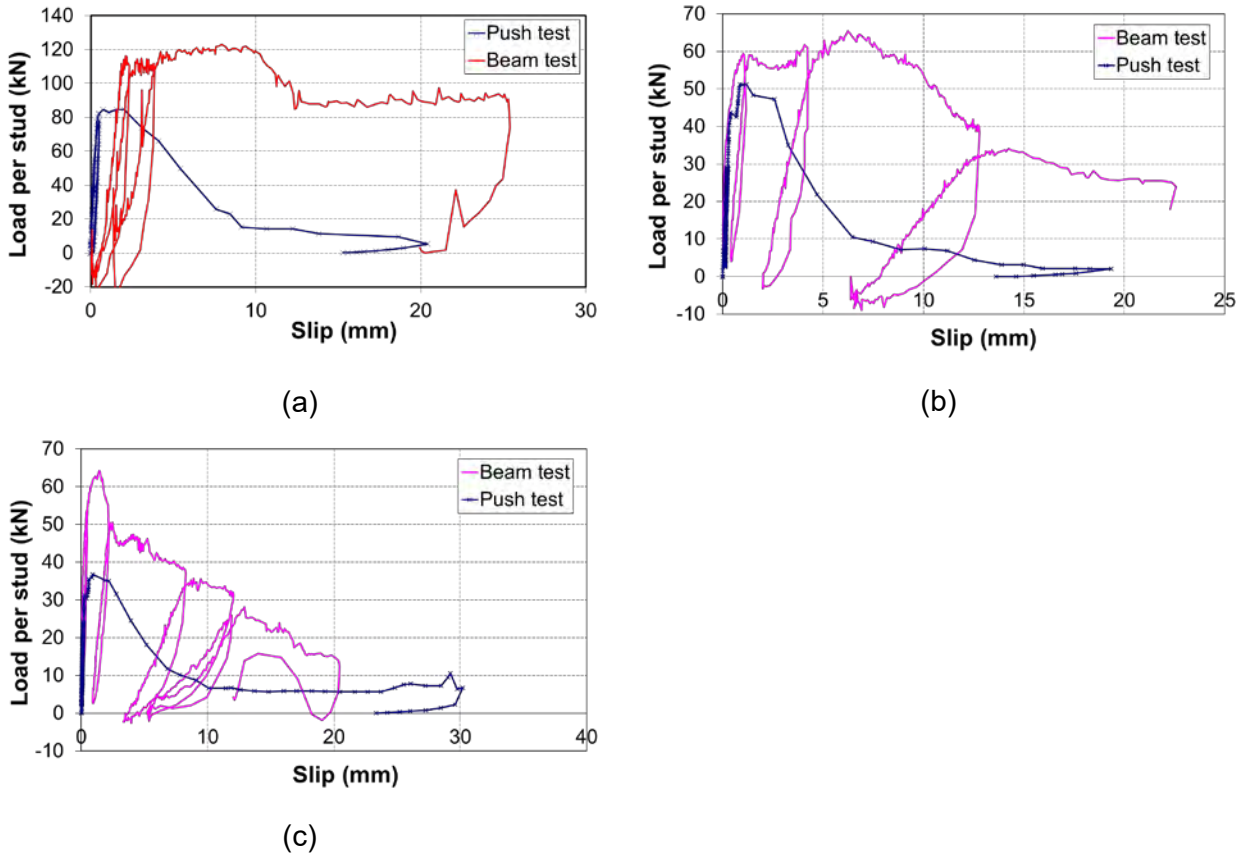


Fig. 4 – Load-slip curve for through-deck welded studs in beam test compared to standard push test for: (a) one stud per rib n_r = 1F; (b) two studs per rib n_r = 2F; and (c) n_r = 3F three studs per rib in the favourable position, respectively.

DEVELOPMENT OF AN IMPROVED PUSH TEST FOR HEADED STUDS WELDED WITHIN TRAPEZOIDAL PROFILED SHEETING

NORTH AMERICAN INVESTIGATIONS

It was considered that the reason for the poor performance of studs welded within trapezoidal sheeting in push tests was due to the absence of the compression force at the interface between the concrete and the flange of the steel section, which exists in real composite beams from the floor loading (see Fig. 1(a)). Easterling *et al.* (1993) can be credited for attempting to remedy the problem of poor load-slip performance by modifying the standard push test through the introduction of a normal force to the face of the test slabs. In these North American investigations normal forces equivalent to between 0 and 20% of the vertical load, were applied directly over the centre-line of the steel section. In total, 234 push tests and 4 full-scale composite beam tests were undertaken. It was concluded that “only a 5% normal load in the push test causes a lot of variability in stud strength” (Rambo-Roddenberry, 1994). It was also deemed that the results from push tests with a normal force equivalent to 10% of the vertical load compared favourably with the performance of the four 9.0 m span companion beam tests.

AUSTRALIAN INVESTIGATIONS

Bradford *et al.* (2006) found that the standard push test shown in Fig. 1(b) was inappropriate for composite slabs using trapezoidal decking. It was found that the specimen tended to twist (similar to the 'back-breaking failure' shown in Fig. 3), and fail in a brittle and premature way. The standard push test was modified to a single-sided arrangement and tested in the horizontal position. A total of 10 push specimens were tested, where normal forces equivalent to between 0 and 10% of the longitudinal load was applied along the edges of the specimen at an eccentricity of 600 mm, thereby applying a hogging moment over the centre-line of the steel section. The eccentric loading was chosen to introduce the beneficial effect on the stud connector resistance from the presence of this hogging moment (from a compression force being applied to the base of the stud), and to reflect the loading conditions on two 8.05 m span companion composite beam tests (Ranzi *et al*., 2009).

EUROPEAN INVESTIGATIONS

Taking inspiration from the earlier North American and Australian modifications a new test was devised in the UK, which was thought to better reflect the conditions that exist in a real beam. As good quality *in situ* load-slip data existed from three full-scale composite beam tests, the new test could be calibrated against this performance (Hicks, 2007b; Hicks and Smith, 2014). Also, rather than developing a completely new specimen, it was proposed to modify the standard specimen given in Eurocode 4, in the interests of developing a relationship with historical push test resistances. Due to the possibility of different friction coefficients at the base of the test slabs affecting the repeatability of the tests, it was decided to develop a self-contained rig that could be disassembled and erected in different locations without the need of a strong floor.

The improved push rig is shown in Fig. 5(a). The loading system consists of vertical jacks applying the longitudinal shear force, accompanied with horizontal jacks applying a uniform normal force to the face of the test slabs. From testing a total of 14 nominally identical specimens that had been constructed from a single concrete mix using the same details that had been provided in the companion beam tests (with n_r = 1F and n_r = 2F), the following levels of normal force were applied (taken as a proportion of the longitudinal force): 0; 4%; 8%; 12%; and 16%. The load-slip curves for these tests are presented in Fig. 5(b) and Fig. 5(c), which are compared with those measured in the beam tests. It was considered that the results with a 12% lateral load provided the closest match with the load-slip behaviour from the beam tests.

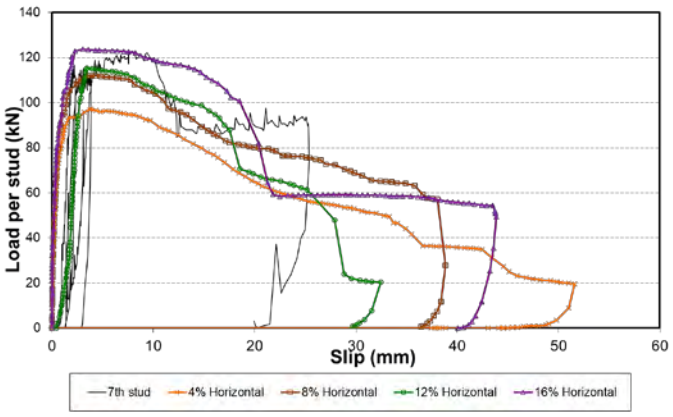
A further two tests with a lateral load of 12% were conducted to evaluate the characteristic values for n_r = 1F and n_r = 2F. By employing the test evaluation procedure given in Eurocode 4, the improved push rig delivered characteristic resistance and slip capacity values that were comparable to those achieved in the companion the beam tests (Hicks and Smith, 2014). The improved push rig was subsequently used to investigate the effect of a number of key variables on the load-slip arrangement of headed stud connectors by Smith and Couchman (2010) whom undertook 27 push tests.

The development work described above was extended through the major RFCS DISCCO research project (Aggelopoulos *et al*., 2016), which included both beam and push tests. A total of 64 push specimens were tested, where normal forces equivalent to between 0 and 16% of the longitudinal load were applied directly over the steel beam (concentrically) or through the slab at different eccentricities to the steel beam. The eccentric loading was chosen to introduce the beneficial effect on the headed stud connector resistance from the presence of this hogging moment and to reflect the loading conditions in composite floors. Also, as well as considering that the normal force increased in proportion to the applied longitudinal shear force (as would

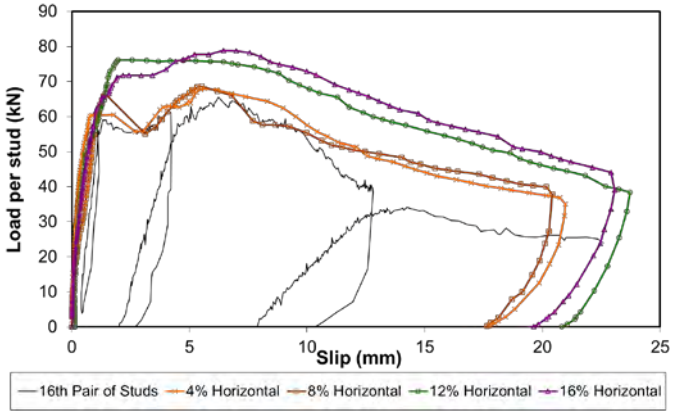
occur in a beam), the maximum required normal force was established and fixed before the longitudinal shear force was applied (i.e. a constant normal force).



(a)



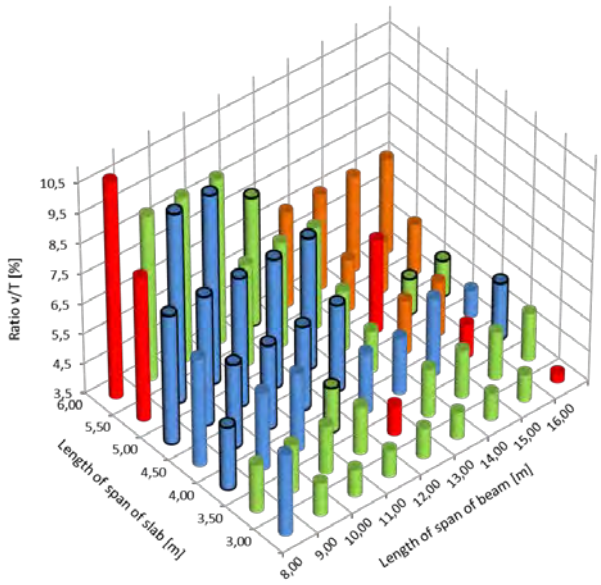
(b)



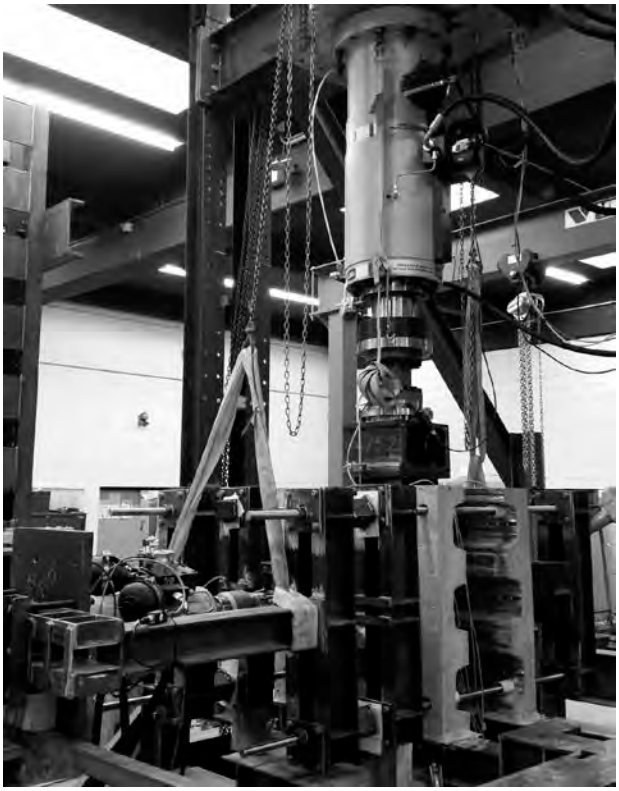
(c)

Fig. 5 - (a) Improved push test rig developed in the UK; Comparison of load-slip behaviour for the new improved test with that measured in beam tests for: (b) n_r = 1F; and (c) n_r = 2F)

In order to define reasonable values for the normal force, a typical floor bay within a building was considered (Nellinger *et al.*, 2017), which consisted of an internal simply-supported composite beam which, in turn, supported a double-span composite slab. To reflect current practice, steel grades of S235 and S355 were considered, together with a concrete grade of C30/37. Furthermore, two different composite slabs with a deck height of 58 and 80 mm were considered in the study. An imposed load of q_k= 3,5 kN/m² was considered in all cases. Using the current Eurocode 4 design provisions (i.e. rigid-plastic material was considered), the spans of the beams and slab were varied to determine the range of normal forces v versus longitudinal shear forces T that would be expected in practice. The results from this study are presented graphically in Fig. 6(a), which showed that the degree of transverse loading v/T ranged from 5 to 10%.



(a)



(b)

Fig. 6 - (a) Degree of transverse loading v/T (b) Improved push test developed within the RFCS DISCCO project

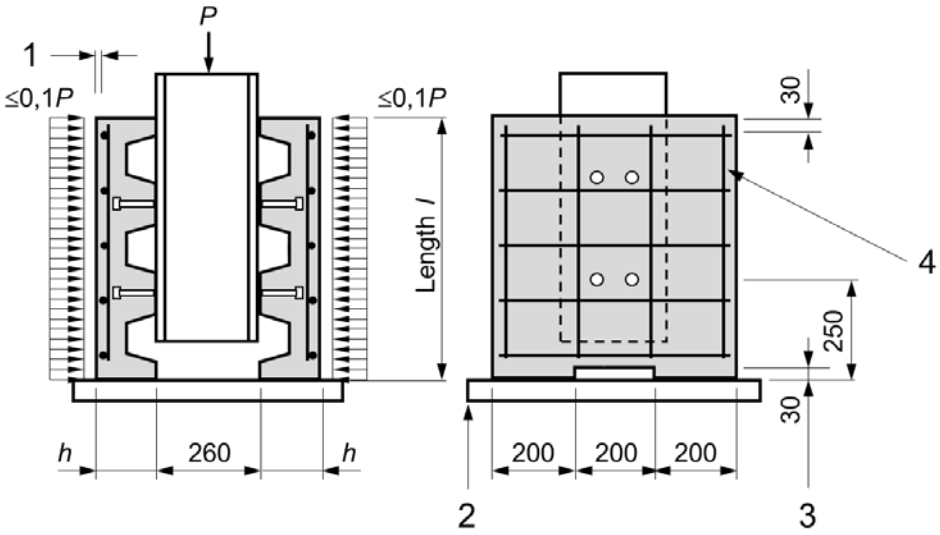
In some of the subsequent push tests where no normal force was applied to the face of the test slabs, a 'torsional failure mode' was reported which was characterised by the last studded rib at the top of the specimen rotating, causing a horizontal crack to appear across the full width of the test slab (see Fig. 3). In subsequent push tests that were carried out in the DISCCO project, it was considered important to include a normal force in the push tests, in order to suppress this artificial failure mode.

Through the comprehensive test programme within the DISCCO project, similar findings to that reported in the earlier investigations were made, in that the resistance and ductility of stud connectors welded within the ribs of trapezoidal profiled steel sheeting were strongly affected by the magnitude of the normal force applied to the face of the test slabs (Nellinger *et al*., 2017). The improved push test arrangement that was developed by the University of Luxembourg within this RFCS project is shown in Fig. 6(b).

DEVELOPMENT OF A NEW STANDARD PUSH TEST FOR THE SECOND GENERATION OF EUROCODE 4

Due to the favourable comparisons with full-scale composite beam tests, as well as similar levels of lateral force being found to be appropriate in the earlier North American and Australian research programmes, it is recommended that besides the standard push test procedure for shear connectors, a distinct push test should be used for stud connectors welded within the ribs

of trapezoidal profiled steel sheeting to ensure that this popular form of construction is supported by Eurocode 4. The proposed test arrangement that is currently being considered is presented in Fig. 7.



1 cover 15 mm

2 bedded in mortar, gypsum or similar

3 recess optional

4 reinforcement:
ribbed bars with $450 \leq f_{sk} \leq 550$ MPa

steel section: HE 260 B or 254 x 254 x 89 kg. UC

Fig. 7 – Proposed test specimen for headed stud connectors welded within trapezoidal profiled sheeting

To avoid the premature back-breaking failure mode observed previously (see Fig. 3), and provide comparable load-slip performance of shear connectors in full-scale beams, it is proposed to provide a lateral force normal to the face of the test slabs. From the above review of previous international push tests, the value of the lateral force has ranged between 5 to 12% of the longitudinal shear force. As a compromise, it is currently proposed that a normal force not greater than 10% of the longitudinal shear force should be applied in the improved push test. This upper value is consistent with that used in the North American test programme whose results were used to form the basis of the design rules for stud connectors in the AISC Specification (ANSI/AISC 360-16, 2016).

CONCLUSIONS

From the considerable variations that have been observed in the behaviour of stud connectors in terms of resistance and ductility, it would appear that a clear case exists for the need to standardize the push specimen test regime when trapezoidal profiled steel sheeting is employed. From a review of international experiments (comprising 12 full-scale composite beams and 361 push tests), it was found that the application of a normal force to the face of the slabs in push specimens eliminated an unrealistic premature back-breaking failure mode. Moreover, the application of a normal force also provided comparable characteristic resistances and slip capacities to that achieved in companion full-scale beams. From a consideration of this wealth of international data, a push test specimen for headed stud connectors welded within

trapezoidal profiled sheeting is proposed for the second generation of Eurocode 4. Given that the value of the maximum normal force proposed is similar to that used to form the basis for the provisions in the 2016 AISC Specification, it is hoped that the new Eurocode 4 test will encourage international harmonization for push tests, which will lead to more consistent experimental data and improved design equations in the future.

ACKNOWLEDGMENTS

Whilst the present authors are members of the Eurocode 4 Project Team SC4.T3 'Revised rules for shear connection in the presence of modern forms of profiled sheeting', any views expressed in this paper do not necessarily reflect those of the entire Project Team. The draft revisions to Eurocode 4 are still at a draft stage and may be subject to change. Any views expressed in this paper may not necessarily reflect those of sub-committee responsible for Eurocode 4 (CEN/TC250/SC4).

REFERENCES

Aggelopoulos E.S., Lawson, R.M, Kuhlmann, U., Eggert, F., Odenbreit, C., Nellinger, S., Lam, D., Dai, X, Sheehan, T. and Obiala, R. (2016). "Development of Improved Shear Connection Rules in Composite Beams (DISCCo)", Draft Final Report, RFSR CT 2012-00030.

ANSI/AISC 360-16. (2016) Specification for Structural Steel Buildings. American Institute of Steel Construction, Chicago, IL.

Aribert J-M. (1990). "Dimensionnement de poutres mixtes en connection partielle". Mixed Structures Including New Materials. IABSE Symposium, Brussels, International Association for Bridge and Structural Engineering. 60. pp. 215–220

Bradford, M.A., Filonov, A., Hogan, T.J., Ranzi, G. and Uy, B. (2006). "Strength and ductility of shear connection in composite T-beams". 8th International Conference on Steel, Space & Composite Structures, Kuala Lumpar, Malaysia, 15-17 May, pp. 15-26

BS 5950-3.1 (1990). Structural use of steelwork in buildings: Part 3: Section 3.1: Code of practice for design of simple and continuous composite beams, British Standards Institution, London.

BS 5950-3.1+A1 (2010) Structural use of steelwork in buildings: Part 3: Section 3.1: Code of practice for design of simple and continuous composite beams, British Standards Institution, London.

Smith, A.L. and Couchman, G.H. (2010). "Strength and ductility of headed stud connectors in profiled steel sheeting". Journal of Constructional Steel Research, 66. pp. 748-754

Easterling, W.S., Gibbings, D.R. and Murray, T.M. (1993). "Strength of Shear Studs in Steel Deck on Composite Beams and Joists" Engineering Journal, American Institute of Steel Construction, Second Quarter. pp. 44-55

EN 1990 (2005). Eurocode: Basis of structural design. European Committee for Standardization, Brussels

EN 1994-1-1 (2004). Eurocode 4: Design of composite steel and concrete structures - Part 1-1: General rules and rules for buildings, European Committee for Standardization, Brussels.

Hawkins, N. M. and Mitchell, D. (1984). “Seismic response of composite shear connections”. J. Struct. Eng. 110, 9. pp. 2120–2136.

Hicks, S.J. and McConnel, R.E. (1997) “The shear resistance of headed studs used with profiled steel sheeting”. In Composite Construction in Steel and Concrete III, Buckner, C.D., Shahrooz, B.M, ASCE: New York. pp. 325-338

Hicks S. (2007a) “Resistance and ductility of shear connection: full-scale beam and push tests”. Sixth International Conference on Steel and Aluminium Structures (ICSAS ‘07), Beale, RG (ed). Oxford Brookes University, UK, pp. 613-620

Hicks, S. (2007b) “Strength and ductility of headed stud connectors welded in modern profiled steel sheeting”. Structural Engineer. 85(10). pp. 32-38.

Hicks, S.J. and Smith, A.L. (2014). “Stud Shear Connectors in Composite Beams that Support Slabs with Profiled Steel Sheeting”. Structural Engineering International. 24(2). pp. 246-253

Johnson, R.P. (2012). Designers’ Guide to Eurocode 4: Design of Composite Steel and Concrete Structures EN 1994-1-1 (Second Edition), London, Thomas Telford.

Johnson, R.P. and Molenstra N. (1991) “Partial shear connection in composite beams for buildings”. Proc. Inst. Civ. Eng. 91(Part 2). pp. 679–704.

Lloyd, R. M. and Wright, H. D. (1990). “Shear connection between composite slabs and steel beams”. Journal of Constructional Steel Research. 15. pp. 255–285.

Nellinger, S., Odenbreit, C., Renata Obiala, R. and Lawson, R.M. (2017). “Influence of transverse loading onto push-out tests with deep steel decking”, Journal of Constructional Steel Research, 128. pp. 335-353

Patrick, M. (2004). Composite beam shear connection design and detailing practices for Australian steel decks, University of Western Sydney, Report CCTR-CBSC-001-04, Sydney.

Rambo-Roddenberry, M. (1994). “Behavior and Strength of Welded Stud Shear Connectors”, PhD Dissertation, Virginia Polytechnic Institute and State University, Blacksburg, VA.

Ranzi, G, Bradford, M.A., Ansouriana, P., Filonov, A., Rasmussen, K.J.R., Hogan, T.J., Uy, B. (2009). “Full-scale tests on composite steel–concrete beams with steel trapezoidal decking”. Journal of Constructional Steel Research, 65(7). pp. 1490-1506

Roik, K. and Hanswille, G. (1987) “Zur Dauerfestigkeit von Kopfbolzendübeln bei Verbundträgern”. Der Bauingenieur. 62. pp. 273–285.

Roš, M. (1934) “Les constructions acier-béton système «Alpha»”. L’Ossature Métallique. 3(4). pp. 195-208

Smith, A.L. and Couchman, G.H. (2010). “Strength and ductility of headed stud connectors in profiled steel sheeting”. Journal of Constructional Steel Research. 66. pp. 748-754.

van der Sanden, P.G.F.J. (1996). The behaviour of a headed stud connection in a ‘new’ push test including a ribbed slab, Tests: Main report. BKO Report 95-15, Eindhoven.

DEVELOPMENT OF EUROPEAN DESIGN GUIDANCE FOR STEEL-CONCRETE (SC) STRUCTURES IN NUCLEAR POWER PLANT

Bassam A. Burgan
Director
The Steel Construction Institute (SCI)
Ascot, UK
b.burgan@steel-sci.com

Eleftherios S. Aggelopoulos
Senior Engineer
The Steel Construction Institute (SCI)
Ascot, UK
e.aggelopoulos@steel-sci.com

ABSTRACT

New European design guidance for SC structures has been developed following completion of a major research project. The project conducted full and large scale tests on structural members, connections, members subjected to thermal conditions representative of loss of coolant accident (LOCA) and members in fire. It also addressed design issues relating to the non-composite construction stage.

The results of the tests have been used in the validation of numerical models. Extensive finite element parametric studies were also performed to study configurations beyond those tested and a large database of test results from international sources has been assimilated.

The project led to the development of European design guidance for SC structures following the principles of the Eurocodes. This paper discusses the guidance developed for the structural design of SC members in ambient conditions.

NOTATION

A_a total area of the two steel plates ($A_{pc} + A_{pt}$);
A_c area of the concrete;
A_{pc} area of the compression steel plate ($A_{pc} = t_{pc} b_w$);
A_{pt} area of the tension steel plate ($A_{pt} = t_{pt} b_w$);
A_{sw} total cross-sectional area of the shear reinforcement
b_w width of the cross-section;
d effective depth of SC section ($h - t_{pt}/2 - t_{pc}$)
E_a Young's modulus of steel;
E_{cm} elastic modulus of concrete;
f_{ck} characteristic compressive cylinder strength of concrete at 28 days;
f_y yield strength of the steel plates;
f_{ywk} characteristic yield strength of the shear reinforcement
G shear modulus of elasticity of steel
h total depth of SC section
I second moment of area of the SC member;

I_a second moment of area of the steel plates;
I_c second moment of area of the uncracked concrete section;
P_{Rd} shear resistance of a single stud calculated from EN 1994-1-1, clause 6.6.3.1(1);
$s_{l.tie}$ longitudinal spacing of the shear reinforcement;
t_c concrete infill thickness;
t_{pt} thickness of the tension steel plate;
t_{pc} thickness of the compression steel plate;
t_p thickness of the steel plate where both plates are of equal thickness (i.e. $t_{pt} = t_{pc}$);
V_{Rd} out-of-plane shear resistance of the SC member;
$V_{i,Rd}$ in-plane shear resistance of the SC member;
ε_y yield strain of the compression steel plate
φ compression plate slenderness $= s/t_{pc}$;
χ reduction factor given in EN 1993-1-1, clause 6.3.1.2 as a function of the relative slenderness, $\bar{\lambda}$;
γ_C partial factor for concrete, given in EN 1992-1-1;
γ_M^* partial factor for member resistance;
γ_{M0} partial factor for cross-section resistance of steel, given in EN 1993-1-1.

INTRODUCTION

SC is the name for a generic steel-concrete composite construction system comprising two steel plates connected by a grid of tie bars with structural concrete between the plates. The plates act as load bearing formwork during the placement of the concrete and hence no additional formwork is required. In the completed condition the plates act as reinforcement to the concrete. The tie bars, apart from holding the two plates together during construction, provide transverse shear reinforcement. Composite action between the steel plates and the concrete core is achieved through the use of headed shear studs welded to the steel plates. The construction form is shown in Figure 1.

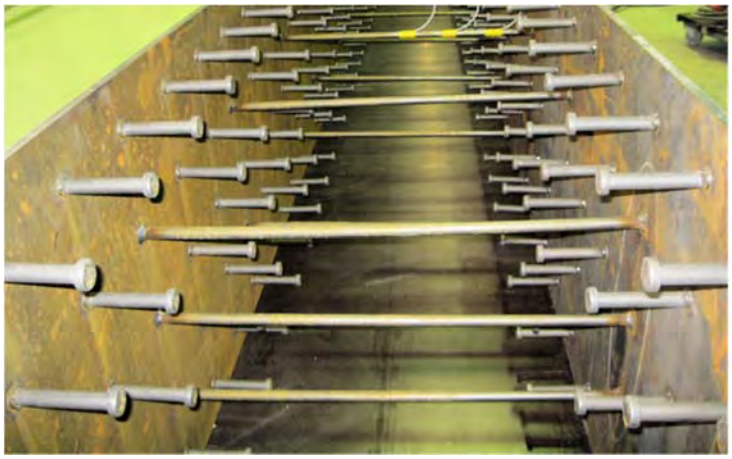


Fig. 1 – Typical SC member prior to concreting

A European funded four year project investigating the behaviour of SC structures was recently completed (SCIENCE, 2017). Structural member tests were conducted to study bending and out-of-plane shear failure. Connection tests studied wall-to-wall, floor-to-wall and foundation-to-wall behaviour. LOCA tests were performed at small scale with highly controlled boundary conditions under thermal loading and at large scale (including comparative reinforced concrete specimen tests) under combinations of thermal and mechanical loading.

Fire tests were conducted on floor, floor-to-wall and wall large scale specimens. This was supported by FE parametric studies. Design guidance following the format of the Eurocodes was developed using the results from this project and other studies available in the literature. A reliability analysis to Annex D of EN 1990 (2002) was performed to derive partial safety factors. The guidance has been trialled by applying it to the design of the "Diesel Ultime Secours (DUS)" building (Diesel Generator Building), which is being used as a post Fukushima safety measure on all EDF nuclear reactor sites in France. This paper focuses on the ultimate limit state design of SC members.

MEMBERS IN TENSION

The resistance of an SC member in tension is conservatively taken as the resistance of the steel plates without any contribution from the concrete. The latter is determined in accordance with EN 1993-1-1 (2005). This assumption is reasonable since the tensile resistance of the concrete is negligible.

MEMBERS IN COMPRESSION

Cross-section resistance to compression

The compression resistance of SC members is given (in accordance with EN 1994-1-1:2004) by:

$$N_{pl,Rd} = \frac{A_a f_y}{\gamma_{M0}} + \frac{0.85 A_c f_{ck}}{\gamma_C} \quad (1)$$

The factor of 0.85 applied to the concrete contribution is used in EN 1994-1-1 for concrete encased or partially concrete encased steel sections. The factor may be taken as 1.0 for concrete filled steel sections. The case of a SC member would justify a higher factor than 0.85 due to the better containment of the concrete compared with an encased section. However, in the absence of specific data, 0.85 is conservatively retained.

Local plate buckling

Equation 1 does not account for local (plate) buckling and global (member) buckling. Plate buckling may be ignored provided that the plate slenderness given by $\varphi = s/t_{pc,}$ is within the limits shown in Table 1.

Table 1: Limits to stud spacing

Steel Grade	S235	S275	S355	S460
φ	37	34	30	26

The limits in Table 1 are based on a large number of test results (Akiyama et al., 1991; Usami et al., 1995; Miyauchi et al., 1996; Choi and Han, 2009) as shown in Figure 2. The critical buckling strain (normalised by the yield strain) is plotted as a function of the plate slenderness parameter ($\varphi\sqrt{(f_y/E_a)}$). The Euler buckling curve is also shown for a partially fixed ended strut (with effective length factor $K = 0.7$) and provides a good fit to the experimental results as previously observed (Zhang et al., 2014).

The limits in Table 1 correspond to a plate slenderness parameter limit of 1.25. This ensures ductile behaviour following plate buckling with no sudden reduction in the member resistance and a gradual redistribution of the force from the compression plate to the concrete. Such behaviour has been demonstrated. For example, in one test (Choi and Han, 2009), although both plates buckled at around 60% of the yield strain, the specimen was able to resist at least

20% more load than that which caused plate buckling. The plate slenderness limits in Table 1 are also consistent with the limits in JEAC 4618 (2009).

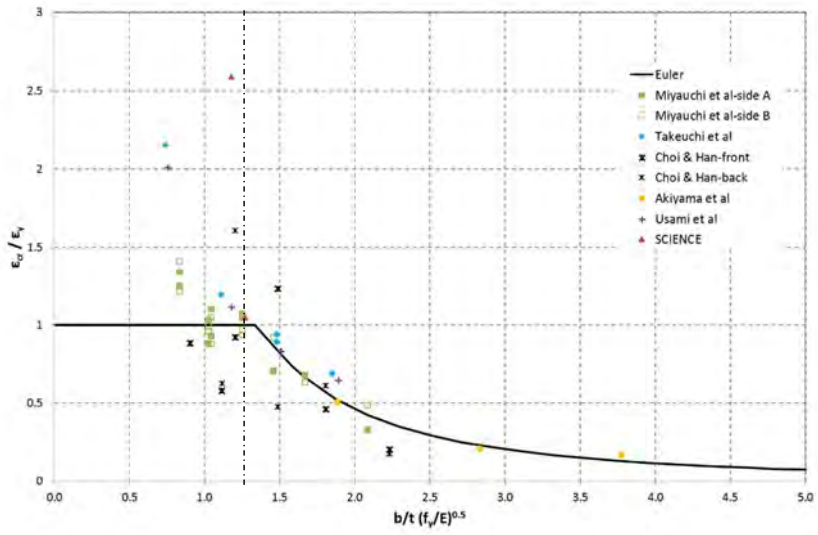


Fig. 2 - Plate buckling strain as a function of plate slenderness parameter

Member resistance to compression

A member in compression should also satisfy the following relationship to prevent global buckling:

(2) $$\frac{N_{Ed}}{\chi N_{pl,Rk}/\gamma_M^*} \leq 1.0$$

where

N_{Ed} is the design value of the compression force;

$N_{pl,Rk}$ is the characteristic value of the plastic resistance to compression given by Equation 1 with the partial factors set to unity;

χ is the buckling reduction factor which depends on member slenderness

γ_M^* is the partial factor, taken as 1.15 for global buckling.

The relative slenderness is given by:

(3) $$\bar{\lambda} = \sqrt{\frac{N_{pl,Rk}}{N_{cr}}}$$

N_{cr} is the elastic critical normal force. To calculate N_{cr}, EN 1994-1-1 stipulates the use of an effective flexural stiffness, $(EI)_{eff}$ given by:

(4) $$(EI)_{eff} = E_a I_a + K_e E_{cm} I_c$$

Where K_e is a correction factor accounting for the reduced stiffness of cracked concrete and should be taken as 0.6. A method for calculating the flexural stiffness allowing for the effect of partial shear connection (slip between the plates and the concrete) was also considered, as was the effect of setting $K_e = 1.0$ in Equation 4. The sensitivity of the flexural reduction factor, χ, to the three methods of calculating the flexural stiffness is shown in Figure 3 to be low, with

Equation 4 leading to conservative results. In this Figure, s1 and s2 are spacing of shear studs in the direction of the compression force and orthogonally to it and are used to achieve different levels of shear connection. Based on this comparison, Equation 4 obtained from EN 1994-1-1 is recommended.

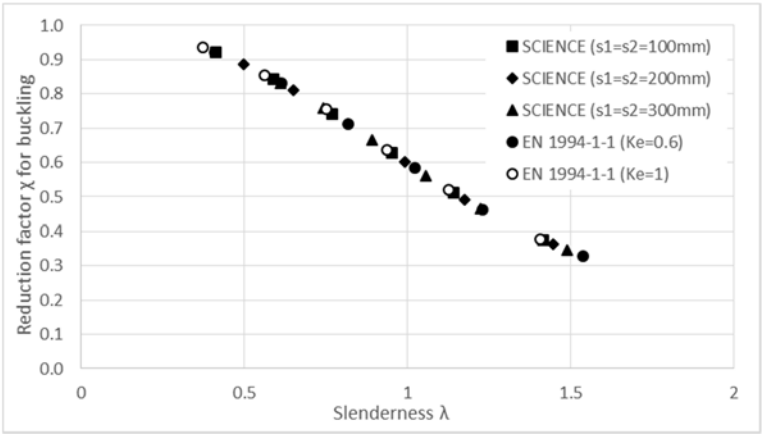


Fig. 3 – Buckling reduction factor, χ, calculated using different methods of estimating the flexural stiffness

OUT-OF-PLANE BENDING

The resistance to out-of-plane bending is calculated from stress block analysis neglecting the tensile strength of concrete (see Figure 4).

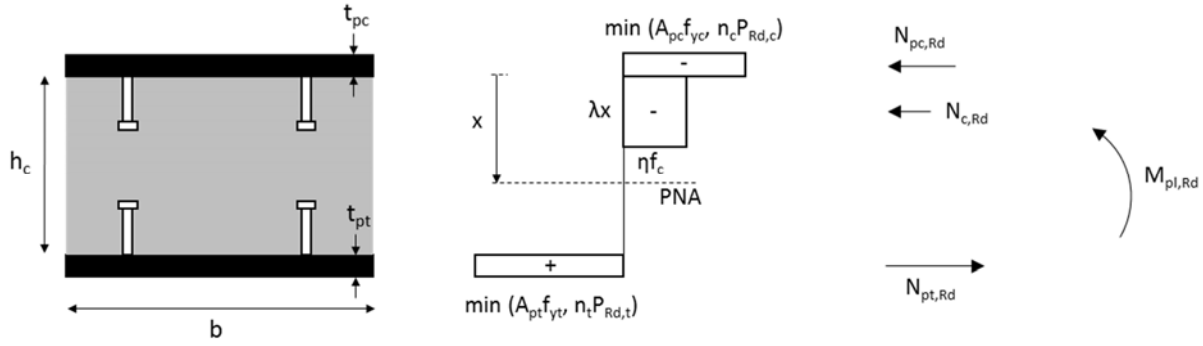


Fig. 4 – Assumed plastic stress distribution in SC members in bending

The design plastic moment resistance is given by:

(5) $$M_{pl,Rd} = \left[N_{pc,Rd}\left(x + \frac{t_{pc}}{2}\right) + N_{c,Rd}\left(1 - \frac{\lambda}{2}\right)x + N_{pt,Rd}\left(h_c - x + \frac{t_{pt}}{2}\right)\right]/\gamma_M{}^*$$

where

$N_{pc,Rd}$ is the axial resistance of the compression plate = min $(A_{pc}f_{yc}, n_cP_{Rd})$;

$N_{pt,Rd}$ is the axial resistance of the tension plate = min $(A_{pt}f_{yt}, 0.8n_tP_{Rd})$;

$N_{c,Rd}$ is the resistance of the concrete in compression = $\eta f_c b(\lambda x)$;

λ is a factor defining the effective height of the compression zone $= 0.8$ for $f_{ck} \leq 50$ MPa;

η is a factor to account for the idealisation of the concrete stress distribution = 1.0 for $f_{ck} \leq 50$ MPa;

f_c is the concrete strength = $\alpha_{cc} f_{ck}$, where α_{cc} can be taken as 0.85 for bending;

x is the depth to the neutral axis from the top of the concrete;

n_c is the number of studs on the compression plate between the point of maximum moment and the nearest point of contraflexure;

n_t is the number of studs on the tension plate between the point of maximum moment and the nearest point of contraflexure;

$\gamma_M{}^*$ is the partial factor for bending to be taken as 1.24.

For SC members with nominally identical steel plates, x is zero and the design plastic moment resistance is:

(6) $$M_{pl,Rd} = N_{p,Rd}(h_c + t_p)/\gamma_M{}^*$$

For SC members in bending with slender compression plates that fall outside the limits of Table 1, the bending resistance can be calculated using Equation 5, ignoring any contribution from the compression plate.

Figure 5 shows a comparison of bending resistance from experiments with values obtained using Equation 5. The Figure shows test results from published sources (Takeuchi et al., 1999 and Sener and Varma, 2014, also presented in Sener et al., 2015). It also shows two results from bending tests carried out in SCIENCE project, one of which was a 'hybrid' specimen (austenitic stainless steel compression plate and carbon steel tension plate). The bending resistance was under-predicted by 9.1% for the carbon steel specimen and by 9.4% for the hybrid specimen.

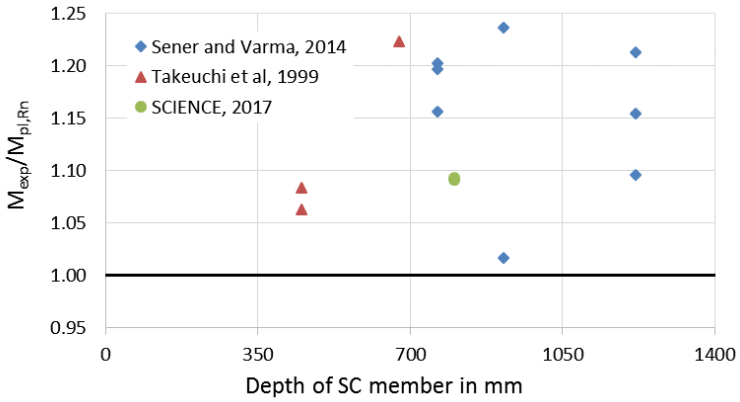


Fig. 5 - Comparison of experimental and predicted nominal values of plastic moment resistance

OUT-OF-PLANE SHEAR

The design models of EN 1992-1-1 are adopted for out-of-plane shear. Although out-of-plane shear reinforcement is always present in SC members (in the form of tie bars), the resistance is calculated for members with and without out-of-plane shear reinforcement in accordance with EN 1992-1-1. This is because, in certain cases (e.g. widely spaced tie bars), the equation for unreinforced members may govern. The spacing of tie bars in SC members should not exceed d, the effective depth of the member.

Members without shear reinforcement

The shear strength of members without shear reinforcement is governed by the concrete strength, the tensile reinforcement ratio provided by the bottom steel plate (which is taken as the smaller of the actual ratio or 2%) and the section depth. For members with no shear reinforcement, the design shear resistance is given by:

(7) $$V_{Rd,c} = [C_{Rd,c}k(100\rho_t f_{ck})^{\frac{1}{3}} + k_1\sigma_{cp}]b_w d/\gamma_M^*$$

The minimum value of $V_{Rd,c}$ is given by:

(8) $$V_{Rd,c} = (v_{min} + k_1\sigma_{cp})b_w d$$

where

k $= 1 + \sqrt{200/d} \leq 2.0$

ρ_t is the tensile reinforcement ratio ($= A_{st}/(b_w d) \leq 0.02$)

σ_{cp} $= N_{Ed}/A_c < 0.2 f_{cd}$

N_{Ed} is the axial force in the cross-section due to external loading ($N_{Ed} > 0$ for compression)

f_{cd} $= f_{ck}/\gamma_c$

$C_{Rd,c}$ $= 0.18$

v_{min} $= 0.035\sqrt{k^3 f_{ck}}$

k_1 $= 0.15$

In Equations 7 and 8, all dimensions are in [mm], areas in [mm^2], forces in [N] and strengths and stresses in [MPa]. The partial factor, $\gamma_M{}^*$, for out-of-plane shear for members with no shear reinforcement is taken as 1.28.

Figure 6 shows a comparison of values calculated using Equation 7 (with $\gamma_M{}^*$ set to unity) and experimental results (from Sener et al., 2016, Takeuchi et al., 1999 and from SCIENCE, 2017). The ratio of experimental to predicted values, V_{exp}/V_{EC2}), are ploted as a function of the ratio of the bending moment to shear force divided by the depth of the section (M/Vd) at the critical section. The design model underestimates the shear resistance particularly for smaller values of (M/Vd). This is partly because Equation 7 ignores arching action.

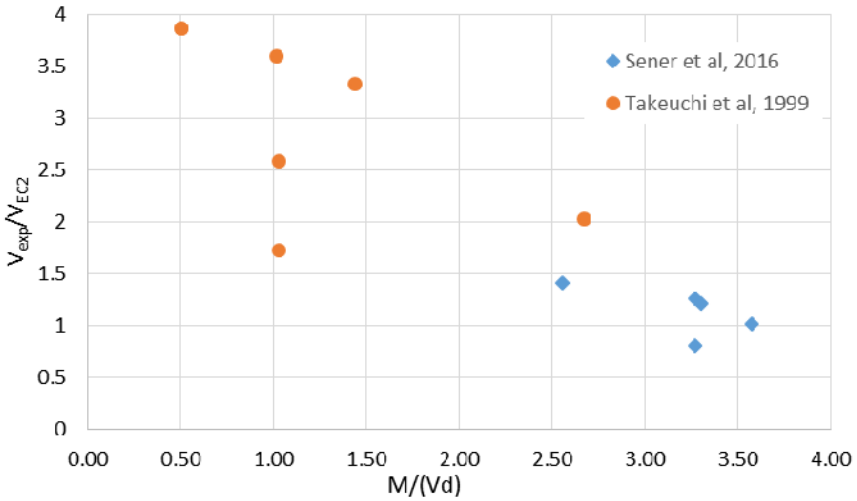


Fig. 6 - Predicted nominal shear resistance against experimental results for specimens without shear reinforcement

Members with shear reinforcement

For members with shear reinforcement, the design shear resistance is given by the smaller of:

(9) $$V_{Rd,s} = \frac{A_{sw}}{s_{l.tie}} z f_{ywk} \cot\theta / \gamma_M{}^*$$

and

(10) $$V_{Rd,max} = b_w z v_1 f_{cd} / (\cot\theta + \tan\theta)$$

where

z is the lever arm. If there is no axial force, a value of $z = 0.9d$ may be used [mm]

θ is the angle between the concrete compression strut and the member axis perpendicular to the shear force, limited to $1 \leq \cot\theta \leq 2.5$ (i.e. 21.8 to 45°)

v_1 $= 0.6[1 - f_{ck}/250]$, where f_{ck} is in MPa as provided in EN 1992-1-1, clause 6.2.3(3). EN 1992-1-1 allows the use of a higher value of v_1 if the design stress in the shear reinforcement is less than $0.8 f_{ywk}$

$s_{l.tie}$ is the longitudinal spacing of shear reinforcement. $s_{l.tie}$ should not exceed $0.75d$.

In equations 9 and 10, all dimensions are in [mm], areas in [mm^2] and strength in [MPa]. $\gamma_M{}^*$ is the partial factor for out-of-plane shear (members with shear reinforcement), taken as 1.44.

Comparison of tests (from Hong et al., 2009, Takeuchi et al., 1998 and from SCIENCE, 2017) against predictions using Equation 9 and 10 is presented in Figure 7. In all cases, the calculations were performed for a strut inclination angle of 21.8°. The comparisons are for specimens with shear reinforcement in the form of tie bars. Predictions using the simplified modified compression field theory (MCFT) by Bentz et al. (2006) are also plotted. Equation 9 is generally conservative. In the case of the test performed by Hong et al. (2009) with M/Vd=3.65, failure occurred due to shear and bending interaction (rather than pure shear failure).

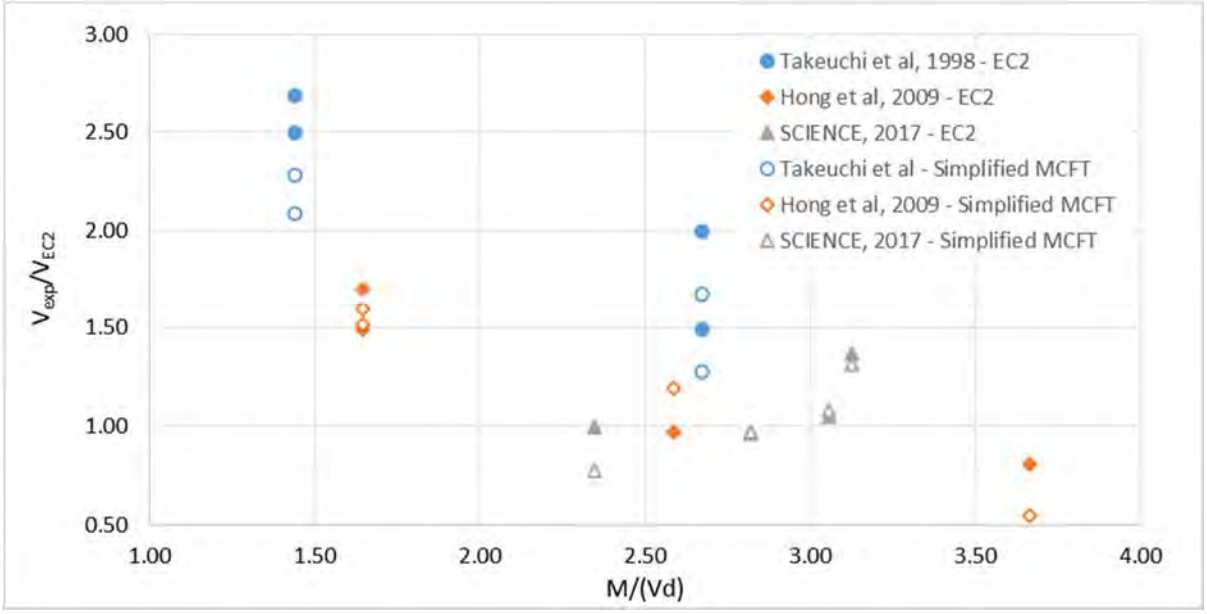


Fig. 7 - Predicted nominal shear resistance against experimental results for specimens with shear reinforcement

IN-PLANE SHEAR

The resistance to in-plane shear is calculated in accordance with the relationship originally developed by Ozaki et al. (2004):

(11)
$$V_{i,Rd} = \frac{1}{\gamma_M{}^*} \frac{K_s + K_{sc}}{\sqrt{3K_s^2 + K_{sc}^2}} (2t_p f_y)$$

$$K_s = 2t_p G$$

$$K_{sc} = \frac{1}{\frac{4}{0.7E_{cm}t_c} + \frac{2(1-v)}{2t_p E}}$$

In Equation 11, all dimensions are in [mm] and strengths and moduli in [MPa]. $\gamma_M{}^*$ is the partial factor for in-plane shear, taken as 1.32.

The results from using Equation 11 (with γ_M^* set to unity) are compared against experimental results in the literature in Figure 8. In almost all cases, Equation 11 is conservative and reasonably accurate. The experimental results in Figure 8 are taken at the point where the steel plate yields in the test. This is consistent with the basis of Equation 11. Therefore, in most cases, the conservatism is in part due to the fact that members can sustain higher loads in the post-yield stage (as demonstrated in the tests) until concrete failure occurs. However, further research is required to allow exploitation of this additional strength.

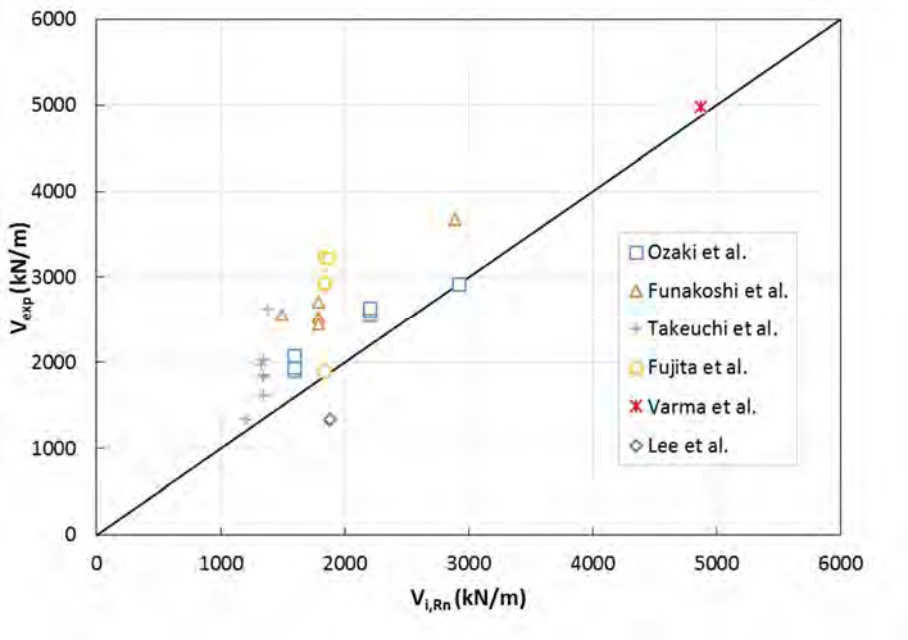


Fig. 8 - Comparison between experimental in-plane shear results (Seo et al., 2016) and the nominal in-plane shear resistance predicted by Equation 11

SHEAR CONNECTION REQUIREMENTS

A limit on the minimum degree of shear connection is necessary so as not to adversely affect the strength and stiffness of SC members. This is achieved by using a maximum stud spacing given by:

(12a) $$s \leq \sqrt{\frac{P_{Rd} b_w}{V_{L,Ed}}}$$ for the tension plate

(12b) $$s \leq \sqrt{\frac{0.8 P_{Rd} b_w}{V_{L,Ed}}}$$ for the compression plate

where

$V_{L,Ed}$ is the longitudinal shear force per unit length of member, given by:

(13) $$V_{L,Ed} = \frac{V_{Rd} A_{pt} \bar{y}}{I} \; or \; \frac{V_{Rd} A_{pc} \bar{y}}{I}$$

where

$\bar{y}$ is the distance of the centroid of the plate from the neutral axis;

The above requirement is based on the methodology used in EN 1994-2 (2005) for distributing studs along the length of a bridge beam, as well as similar requirements in the Bi-Steel Manual (2003), KEPIC SNG (2009) and AISC N690 (2015). It offers a practical way of choosing the spacing with a sensible level of conservatism.

CONCLUSIONS

Guidance for the design of SC structures that follows the Eurocode format has been developed using the findings from a recently completed research project and other published data. Partial factors which can be used with the nominal design values of the resistance have been calculated for the new design equations and comparisons made with test results.

ACKNOWLEDGMENT

This work was funded by the European Union's Research Fund for Coal and Steel (RFCS) under grant agreement no. RFSR-CT-2013-00017 and Electricité De France (EDF). The technical work was performed by The Steel Construction Institute (UK), University of Surrey (UK), Teknologian tutkimuskeskus VTT (Finland), VTT Expert Services Ltd (Finland), Karlsruhe Institute of Technology (Germany), SMP Ingenieure im Bauwesen GmbH (Germany), EGIS Industries SA (France), Electricité De France (France), Ecole Normale Superieure de Cachan (France), Ecole Speciale des Travaux Publics (France), Centre Technique Industriel de la Construction Métallique (France), Efectis (France).

REFERENCES

AISC N690-12 + N690s1-15 (2015). Specification for Safety-Related Steel Structures for Nuclear Facilities (including supplement No. 1), American Institute of Steel Construction (AISC).

Akiyama, H., Sekimoto, H., Fukihara, M., Nakanishi, K. and Hara, K. (1991). A compression and shear loading test of a concrete filled steel bearing wall. *11th International Conference on Structural Mechanics in Reactor Technology (SMiRT 11),* Vol. H, Tokyo.

Bentz, E.C., Vecchio, F.J. and Collins, M.P. (2006). Simplified modified compression field theory for calculating shear strength of reinforced concrete elements. *ACI Structural Journal*, July-August 2006, 614-624.

Choi, B.J. and Han, H.S. (2009). An experiment on compressive profile of the unstiffened steel plate-concrete structures under compression loading. *Steel and Composite Structures*, *9*(6), 439-454.

Corus (2003). *Bi-Steel Design and Construction Guide* (2nd ed.). Corus UK Ltd.

EN 1990:2002. Eurocode: Basis of structural design.

EN 1992-1-1:2004. Eurocode 2: Design of concrete structures - Part 1-1: General rules and rules for Buildings.

EN 1993-1-1:2005. Eurocode 3: Design of steel structures — Part 1-1: General rules and rules for buildings.

EN 1994-1-1:2004. Eurocode 4: Design of composite steel and concrete structures — Part 1-1: General rules and rules for buildings.

EN 1994-1-2:2005. Eurocode 4. Design of composite steel and concrete structures. General rules. Structural fire design.

EN 1994-2:2005. Eurocode 4. Design of composite steel and concrete structures. General rules and rules for bridges.

Hong, S.-G., Lee, K.-J., Park, D.-S., Ham, K.-W. and Lee, H.-W. (2009). Out-of-plane shear strength of steel plate concrete walls dependent on bond behaviour. *20th International Conference on Structural Mechanics in Reactor Technology (SMiRT 20)*, Espoo, Finland, August 9-14, 2009.

JEAC 4618 (2009). Japan Electric Association: Technical Code for Aseismic Design of Steel Plate Reinforced Concrete Structures. Translated into English in January 2012 by the Obayashi Corporation.

KEPIC-SNG (2009). Specification for Safety-Related Steel Plate Concrete Structures for Nuclear Facilities.

Miyauchi, Y. et al. (1996). Experimental study on a concrete filled steel structure. Summaries of Technical Papers of Annual Meeting, Vol. 3, Architectural Institute of Japan.

Ozaki, M., Akita, S., Osuga, H., Nakayama, T. and Adachi, N. (2004). Study on steel plate reinforced concrete panels subjected to cyclic in-plane shear. *Nuclear Engineering and Design*, *228*, 225-244.

SCIENCE (2017). SC for Industrial, Energy and Nuclear Construction Efficiency. *Research Fund for Coal and Steel (RFCS)*, RFSR-CT-2013-00017.

Sener, K.C. and Varma, A.H. (2014). Steel-plate composite walls: Experimental database and design for out-of-plane shear. *Journal of Constructional Steel Research*, *100*, 197-210.

Sener, K.C., Varma, A.H. and Ayhan, D. (2015). Steel plate composite (SC) walls: Out-of-plane flexural behaviour, database and design. *Journal of Constructional Steel Research*, *108*, 46-59.

Sener, K.C., Varma, A.H. and Seo, J. (2016). Experimental and numerical investigation of the shear behavior of steel-plate composite (SC) beams without shear reinforcement. *Engineering Structures*, *127*, 495-509.

Seo, J., Varma, A., Sener, K. and Ayhan, D. (2016). Steel-plate composite (SC) walls: In-plane shear behaviour, database and design. *Journal of Constructional Steel Research*, *119*, 202-215.

Takeuchi, M., Fujita, F., Funakoshi, A., Shohara, R., Akira, S., and Matsumoto, R. (1999). Experimental Study on Steel Plate Reinforced Concrete Structure, Part 28 Response of SC Members Subjected to Out-of-Plane Load (Outline of the Experimental Program and the Results). *Proceedings of the Annual Conference of Architectural Institute of Japan*, (in Japanese), 1037- 1038.

Takeuchi, M., Narikawa, M., Matsuo, I., Hara, K. and Usami, S. (1998). Study on a concrete filled structure for nuclear power plants. *Nuclear Engineering and Design*, *179*(2), 209-223.

Usami, S., Akiyama, H., Narikawa, M., Hara, K., Takeuchi, M. and Sasaki, N. (1995). Study on a concrete filled steel structure for nuclear power plants (part 2). Compressive loading tests on wall members. *13th International Conference on Structural Mechanics in Reactor Technology (SMiRT 13)*, Porto Alegre, Brazil, August 13-18, 1995.

Varma, A., Zhang, K., Chi, H., Booth, P. and Baker, T. (2011). In-plane shear behaviour of SC composite walls: Theory vs. experiment. *21st International Conference on Structural Mechanics in Reactor Technology (SMiRT 21)*, New Delhi, India, November 2011.

Zhang, K., Varma, A.H., Malushte, S.R. and Gallocher, S. (2014). Effect of shear connectors on local buckling and composite action in steel concrete composite walls. *Nuclear Engineering and Design*, *269*, 231-239.

THE NEW AUSTRALIA/NEW ZEALAND STANDARD ON COMPOSITE STEEL-CONCRETE BUILDINGS, ASNZS2327

Brian Uy
School of Civil Engineering, The University of Sydney
New South Wales, Australia
brian.uy@sydney.edu.au

Stephen J. Hicks
Heavy Engineering Research Association
Auckland, New Zealand
stephen.hicks@hera.org.nz

Won-Hee Kang
Centre for Infrastructure Engineering, Western Sydney University
New South Wales, Australia
w.kang@westernsydney.edu.au

Huu-Tai Thai
School of Engineering and Mathematical Sciences, La Trobe University
Victoria, Australia
tai.thai@latrobe.edu.au

Farhad Aslani
School of Civil, Environmental and Mining Engineering, The University of Western Australia
Western Australia, Australia
farhad.aslani@uwa.edu.au

ABSTRACT

This paper will provide a summary of the new Australia-New Zealand Standard on the design of composite steel-concrete buildings ASNZS2327 which is due for release in 2017. This standard which has included over five years of development has harmonized design provisions across the Tasman Sea, in steel, concrete and composite structures. This project was carried out in parallel with the standard for bridge structures (ASNZS 5100.6) and thus there was significant commonality and cross-over. ASNZS2327 covers the design of structural elements such as slabs, beams, columns and joints, as well as addressing the system behaviour for serviceability and fire which are highly pertinent for the design of steel and composite structures. Methods for the design for earthquake have also been included. The standard allows for the increase in concrete compressive strength up to 100 MPa and steel strengths up to 690 MPa. In addition, the standard has involved significant amounts of structural reliability studies to be carried out. This paper will provide a summary of some of the salient issues as well as highlighting future areas of interest which may be considered for future revisions.

INTRODUCTION

The concept of steel-concrete composite construction generally produces structural behaviour where the overall response is greater than the sum of the parts. This concept holds true for composite beam behaviour where the introduction of longitudinal shear connection can provide flexural stiffness and strength of a member which is greater than the constituent parts, namely the structural steel section and the reinforced concrete slab. Throughout the latter half of the twentieth century this concept has been further applied to composite steel-concrete columns to produce column stiffnesses and strengths which are greater than the sum of the parts of the steel section and the reinforced concrete elements. These benefits have been further exploited by taking advantage of the confinement effects that steel tubes can provide to interior concrete infill and the subsequent benefits provided by the concrete infill on delaying local buckling of the steel shell. This concept is now so widespread that in the last calendar year, more than 50 % of all tall buildings constructed worldwide, utilized composite frames, typically incorporating concrete filled steel columns (Council of Tall Buildings and Urban Habitat, 2016).

In Australia, builders of the recently completed Perth Tower (the tallest tower in Perth), chose to adopt composite construction throughout the entire structure and a concrete filled steel column solution. In order to secure this type of solution the builder pre-ordered and stored all spirally welded steel tubes in the columns (see Figure 1) to ensure steel cost fluctuations were minimized and construction costs were able to be controlled (Australian Steel Institute, 2010). The emphasis in Australia has been mainly focussed on construction economy when it relates to steel and steel-concrete composite structures.



(a) Completed building (b) Building during construction

Fig. 1 - BHP Billiton Tower, Perth, Australia

In New Zealand the emphasis in steel and steel-concrete composite construction whilst also concerned with construction economy, is heavily influenced by seismic behaviour and performance. The new 14-storey 20 Customhouse Quay in Wellington (see Figure 2) is due to be completed in 2017 to replace the earthquake damaged BP House on Wellington's waterfront. This building was designed post Christchurch earthquake and utilizes base isolators (Schouten, 2015), resulting in an estimated seismic resilience of up to 180% of code. The building incorporates many steel-concrete composite components, including a steel diagrid external frame and long span composite cellular beams.



Fig. 2 – 20 Customhouse Quay, Wellington, New Zealand

DRAFT BUILDING STANDARD FOR COMPOSITE STEEL-CONCRETE, ASNZS 2327

The Australian Standard for composite steel-concrete structures in buildings, AS2327.1 only ever covered the design of simply supported composite beams (Standards Australia, 2003). A major initiative some 5 years ago involved ensuring that all forms of composite systems, including beams, slabs, columns and joints would be covered for design and has resulted in the Australia/New Zealand harmonisation of the standard, ASNZS2327 (Standards Australia/Standards New Zealand 2017a). The standard table of contents is shown below and salient features of the standard will described herein

SECTION 1 GENERAL

SECTION 2 DESIGN OF COMPOSITE SLABS

SECTION 3 DESIGN OF COMPOSITE BEAMS

SECTION 4 DESIGN OF COMPOSITE COLUMNS

SECTION 5 DESIGN OF COMPOSITE JOINTS

SECTION 6 DESIGN OF COMPOSITE FLOOR SYSTEMS

SECTION 7 SYSTEM DESIGN FOR FIRE RESISTANCE

SECTION 8 DESIGN FOR EARTHQUAKE

APPENDICES

DESIGN OF COMPOSITE SLABS

Section 2 of ASNZS2327 covers the comprehensive design of composite slabs, (see Figure 3). The intent of this section is to cover the strength and serviceability design of composite slabs utilising metal decking. Issues including flexural strength, longitudinal shear and vertical shear provisions are covered in this section. Concepts of partial interaction are also considered and this section also links quite closely to that being proposed for testing in the Appendices of the standard. Furthermore, post-tensioned concrete construction is also extremely prominent in Australian buildings and recent innovations into post-tensioning concrete slabs with metal decking have been carried out (see Figure 4). One of the major issues is the changes that need to be introduced to deal with the presence of the metal decking for serviceability and strength provisions and these will be considered as part of this section, namely the concepts of non-uniform shrinkage (Al Deen et al., 2015).

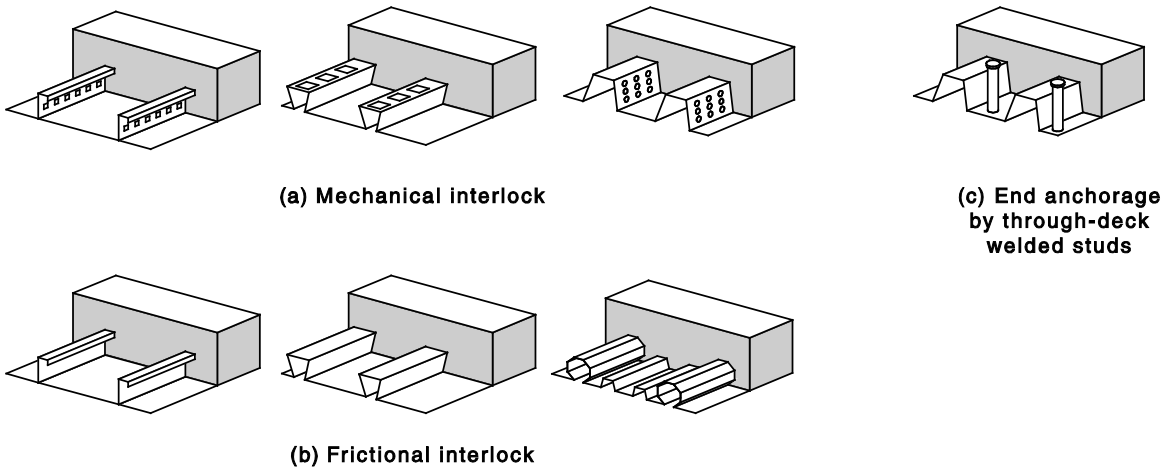


Fig. 3 – Types of interlock for composite slabs

(Standards Australia/Standards New Zealand 2017a)



Fig. 4 – Post-tensioned composite slabs

DESIGN OF COMPOSITE BEAMS

Section 3 of ASNZS2327 covers the comprehensive design of composite steel-concrete beams. This section covers the design of composite beams, considering flexural strength, shear strength and combined actions as well as serviceability provisions. Partial shear connection approaches are also highlighted for the design of simply supported and continuous beams. This section also considers the design of composite beams using hollow core slabs as illustrated in Figure 5, (Uy and Bradford, 2007).



Fig. 5 – Precast hollowcore units

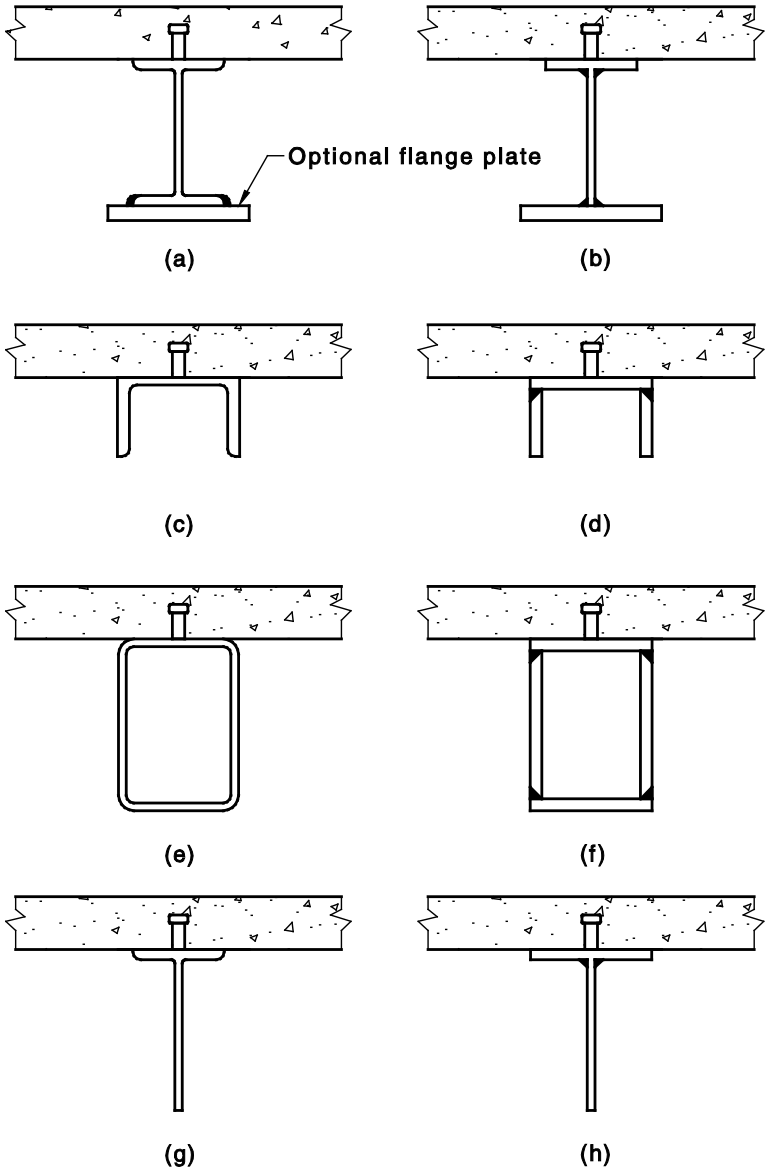


Fig. 6 – Alternative steel beam types (Standards Australia/Standards New Zealand 2017a)

DESIGN OF COMPOSITE COLUMNS

This section covers the design of composite columns and closely follows the approach in the AS/NZS 5100 Part 6 (Standards Australia/Standards New Zealand, 2017b). The design of composite columns for strength, stability incorporating axial force, uniaxial and biaxial bending is considered. In particular, the important effects of confinement are covered by this section. Furthermore, the capacity factor for concrete in compression is proposed to be 0.65 based on reliability analyses using the design assisted by testing method provided in EN 1990 Annex D.8 (European Committee for Standardization, 2002). The reliability analyses were carried out for 1583 CFST columns included in Tao et al.'s database (Tao et al., 2008). Figure 7 shows the analysis results along the squash load ratio of steel, where the average capacity factors for concrete are above 0.65. If a practical range of squash load ratio such as 0.1~0.6 is considered, the average capacity factor will increase even further.

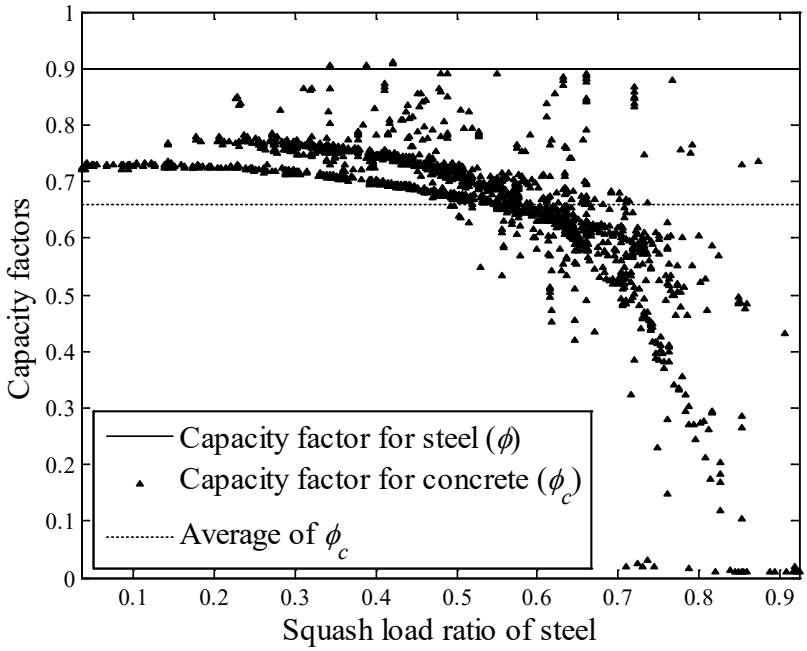


Fig. 7 – Calibrated capacity factors for concrete in compression when the capacity factor steel is fixed to be 0.9

One major area of innovation which this section will cover includes the use of high strength concrete (cylinder strengths up to 100 MPa) and high strength steel (nominal yield strengths up to 690 MPa) (Aslani et al., 2015a, b). In addition the standard has involved calibration and has been extended to permit spiral welded tubes to be used in design (Aslani et al., 2015c and Aslani et al., 2017).



Fig. 8 – Spiral welded composite columns, Aslani et al. (2017)

DESIGN OF COMPOSITE JOINTS

This standard has also involved in the development of a section for strength and serviceability design of semi-rigid joints including beam-to-beam and beam-to-column joints as shown in Figure 9. For beam-to-column joints, the column could be either open sections with/without stiffeners or hollow sections with/without infilled concrete. The design of joints to hollow section columns is based on the stiffness model of Thai and Uy (2016) which was calibrated with experimental results of 44 available tests on bolted endplate beam-to-CFST column joints.

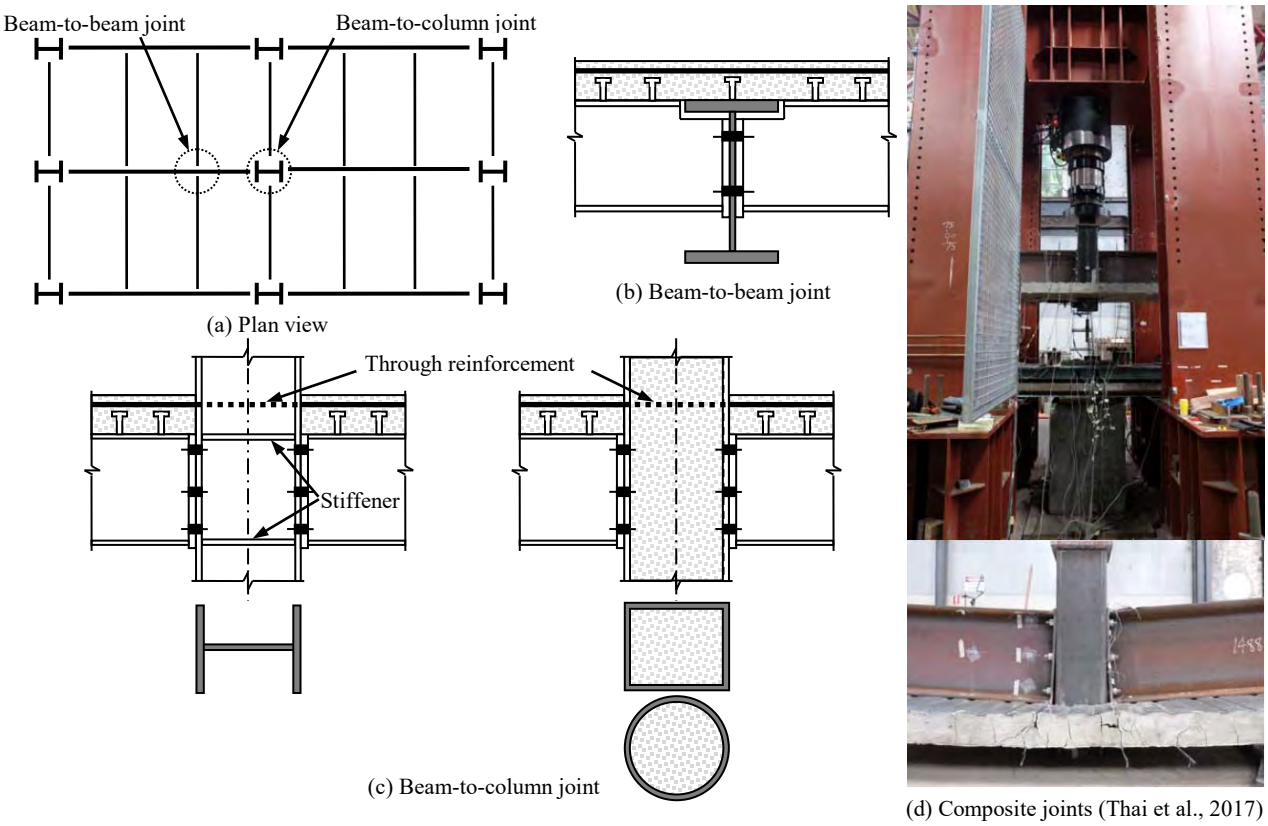


Fig. 9 - Composite steel-concrete beam and slab systems, Australia

(Standards Australia/Standards New Zealand 2017a)

DESIGN OF COMPOSITE FLOOR SYSTEMS

The intent of this section is to address system behaviour particularly for deflections and vibrations for panels. This will then give designers the ability to take into account the beneficial effects of system behaviour in addressing these important serviceability provisions which sometimes penalize steel frame structures from a design perspective (Steel Construction Institute, 2012).

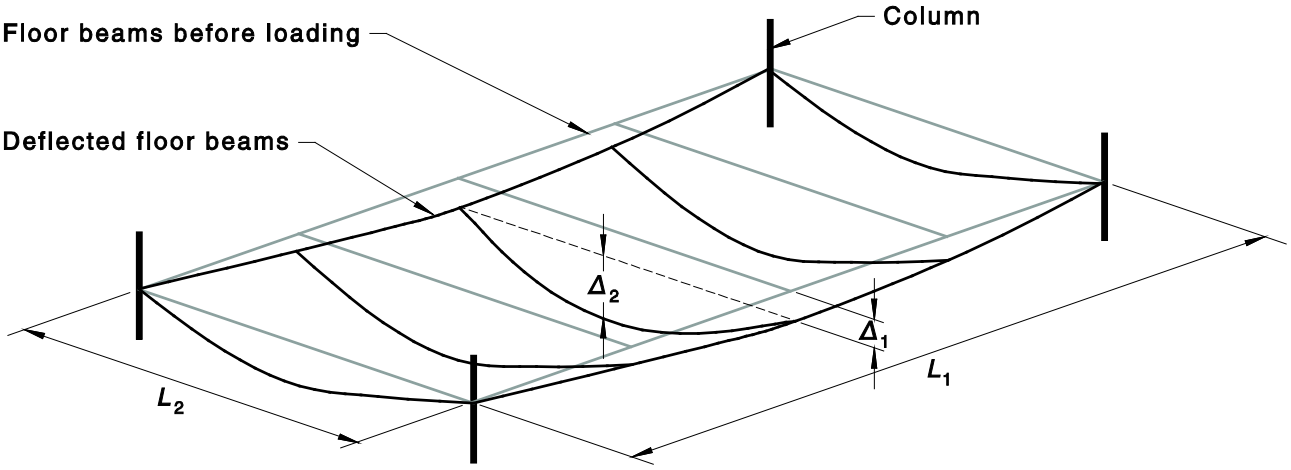


Fig. 10 – Deflection requirements for composite floor systems

(Standards Australia/Standards New Zealand 2017a)

SYSTEM DESIGN FOR FIRE RESISTANCE

This section is also intended to give guidance on design for fire using a system based approach, which acknowledges that for indeterminate systems there is a significant degree of redundancy that provides additional structural capacity within a fire that is unable to be addressed considering single elements within a building. State of the art approaches for dealing with this will be provided herein (Steel Construction Institution, 2006 and Abu et al., 2011).

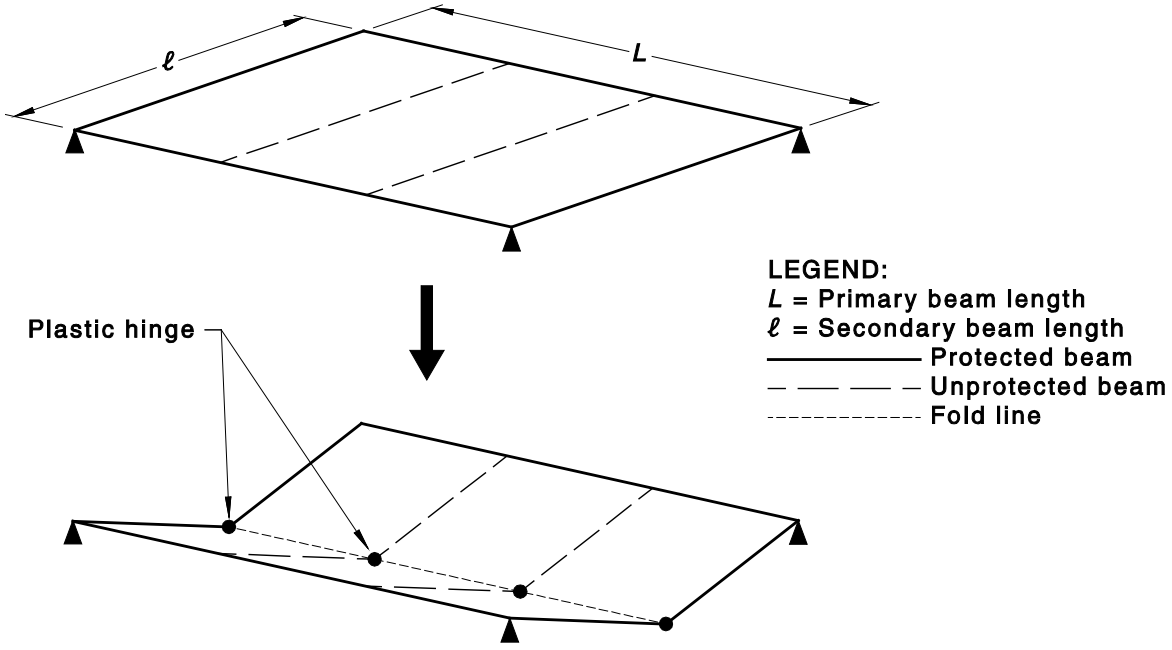


Fig. 11 – Collapse mechanism for an isolated panel

(Standards Australia/Standards New Zealand 2017a)

DESIGN FOR EARTHQUAKE

This section covers the design for earthquake of composite frame systems. One of the major elements of the section is the specific guidance provided to Australian and New Zealand designers in accordance with AS1170.4 and NZS1170.5 (Standards Australia 2004 and Standards New Zealand 2007).

APPENDICES

This section of the proposed standard is meant to provide standard test methods for a number of specific issues which are covered. Push test methods for establishing the strength, stiffness and ductility of shear connectors will be outlined in this section as will test methods for establishing the strength characteristics of composite slabs incorporating profiled steel sheeting. In addition, provisions for evaluating design resistance from tests will also be presented. Finally, ASNZS 2327 will be one of the first international composite design standards to present provisions for beams with both regular and isolated web-openings, thereby supporting the use of long-span cellular beams (Steel Construction Institution, 2011).

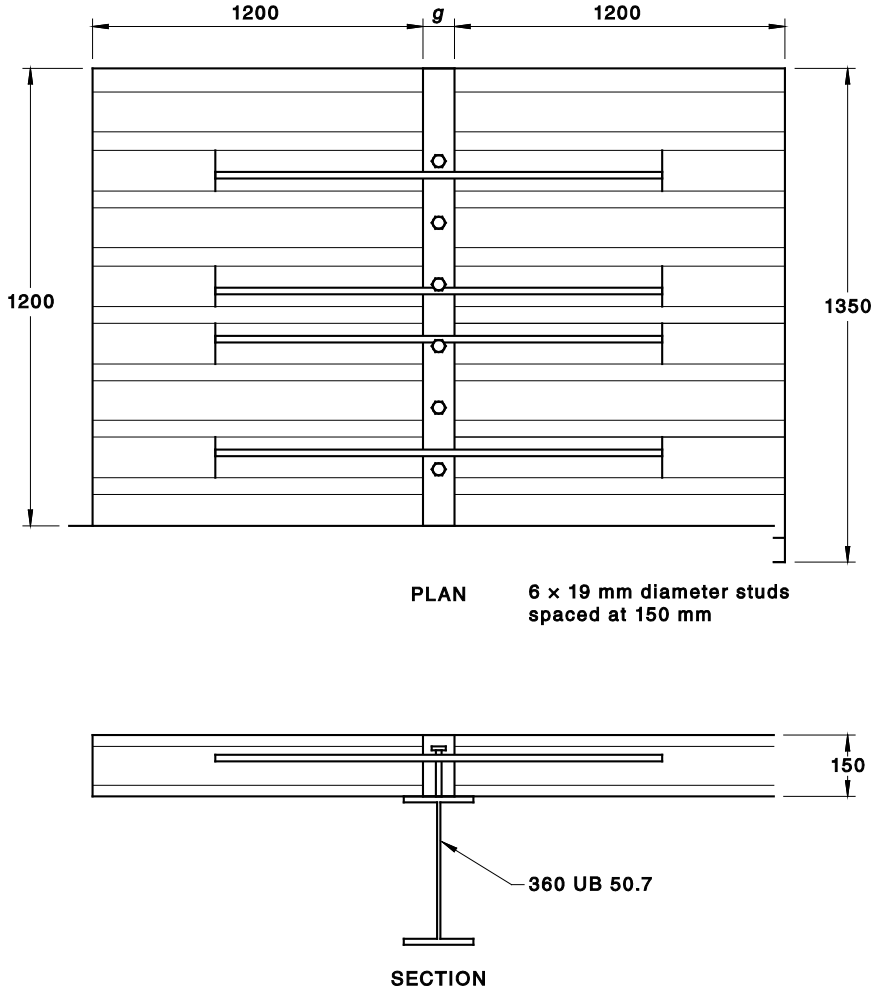


Fig. 12 – Method for determining the longitudinal shear capacity of headed shear studs in voided concrete slabs made composite with steel
(Standards Australia/Standards New Zealand 2017a)

CONCLUSIONS AND FURTHER RESEARCH

Whilst there is ongoing research into structural steel and some of the technical issues associated with materials and systems, it is felt that further research will be punctuated by approaches that provide paradigm shifts in the design of steel and steel-concrete composite building structures. Some of the more prominent issues that will promote these paradigm shifts include precast and prefabricated construction, deconstructability and new and higher performance materials.

In particular steel and steel-concrete composite framed buildings have the ability to be designed and constructed with deconstruction in mind. Advanced economies around the world are now looking toward reuse as a potential for addressing the issue of shortages in natural resources in future. Composite action has the ability to reduce steel usage and deconstruction has the ability to provide reuse options. Reduce and reuse strategies are far superior to recycling options and have the ability to provide much greater benefits to society from the perspectives of sustainability.

ACKNOWLEDGEMENTS

The authors would like to thank the members of the BD-32 Committee for all their hard work to date; in particular, the Standards Australia Project Manager, Declan Robinson. As members of the BD-32 Committee, the present authors have prepared this paper according to what they consider to be the significant changes to the existing AS 2327.1. However, the standard is still being prepared for public comment and, as a consequence of this, may be subject to change. Any views expressed in this paper may not necessarily reflect those of the other members of the Committee, nor those of Standards Australia and Standards New Zealand

REFERENCES

Abu A.K., Ramanitrarivo V., Burgess I.W., (2011) Collapse Mechanisms of Composite Slab Panels in Fire, *Journal of Structural Fire Engineering*, 2 (3), 205-216.

Al-Deen, S., Ranzi, G., Uy, B. (2015) Non-uniform shrinkage in simply-supported composite steel-concrete slabs. *Steel and Composite Structures*, 18(2), 375-394.

Aslani, F., Uy, B., Tao, Z., Mashiri, F., (2015a) Behaviour and design of composite columns incorporating compact high-strength steel plates, *Journal of Constructional Steel Research*, 107, 94-110.

Aslani, F., Uy, B., Tao, Z., Mashiri, F., (2015b) Predicting the axial load capacity of high-strength concrete filled steel tubular columns, *Steel and Composite Structures*, 19, 967-993.

Aslani, F., Uy, B., Hicks, S., Kang, W.H., (2015c) Spiral welded tubes – imperfections, residual stresses, and buckling characteristics, The Eighth International Conference on Advances in Steel Structures, July 21–24, Lisbon, Portugal.

Aslani F., Uy B., Hur J. and Carino P., (2017) Behaviour and design of hollow and concrete-filled spiral welded steel tube columns subjected to axial compression, *Journal of Constructional Steel Research*, 128, 261-288.

Australian Steel Institute (2010) Perth tower agape to grand views, *Steel Australia*, 34 (6), 18-20.

Council on Tall Buildings and Urban Habitat (2016) *The Skyscraper Surge Continues in 2015, "The Year of 100 Supertalls"*. CTBUH Year in Review: Tall Trends of 2015, and Forecasts for 2016, http://www.skyscrapercenter.com/research/CTBUH_ResearchReport_2015YearInReview.pdf accessed 15/05/2017.

European Committee for Standardization (2002) EN 1990:2002 Eurocode: Basis of structural design, Brussels, 2002.

Schouten, H. (2015) $80m hi-tech tower to replace Wellington's Perth House, http://www.stuff.co.nz/business/67536882/80m-hi-tech-tower-to-replace-Wellingtons-BP-House, accessed 15/05/2017.

Standards Australia (2003) *Composite structures, Part 1: Simple supported beams*, AS 2327.1:2003, New South Wales, Australia.

Standards Australia (2007) *Australian Standard, AS 1170.4—2007* Structural design actions Part 4: Earthquake actions in Australia.

Standards Australia/Standards New Zealand (2017a) *Composite Structures*, *AS/NZS 2327-2017*, Sydney, Australia.

Standards Australia/Standards New Zealand (2017b), *AS/NZS 5100.6: 2017, Bridge Design, Part 6: Steel and composite construction*, Sydney/Wellington, Australia/New Zealand.

Standards New Zealand (2004) *New Zealand Standard, NZS 1170.5—2004* Structural design actions Part 5: Earthquake actions in New Zealand.

Steel Construction Institute (2006) *Fire Safe Design: A New Approach to Multi-Storey Steel-Framed Buildings*, SCI P288, United Kingdom.

Steel Construction Institute (2011) *Design of composite beams with large web openings*, SCI P355, United Kingdom.

Steel Construction Institute (2012) *Design of floors for vibration: a new approach*, SCI P354, United Kingdom.

Tao Z., Uy B., Han L.H., He S.H., (2008) Design of concrete-filled steel tubular members according to the Australian Standard AS 5100 model and calibration, *Australian Journal of Structural Engineering*, 8 (3), 197-214.

Thai H.T., Uy B., (2016) Rotational stiffness and moment resistance of bolted endplate joints with hollow or CFST columns, *Journal of Constructional Steel Research*, 126, 139-152.

Thai H.T., Uy B., Yamesri, Aslani F., (2017) Behaviour of bolted endplate composite joints to square and circular CFST columns, *Journal of Constructional Steel Research*, 131, 68-82.

Uy B. and Bradford M.A., (2007) Composite action of structural steel beams and precast concrete slabs for the flexural strength limit state, *Australian Journal of Structural Engineering*, 7, 123-133.

THE NEW JOINT AUSTRALIAN AND NEW ZEALAND DESIGN STANDARD FOR STEEL AND COMPOSITE BRIDGES AS/NZS 5100.6 - PART 6: STEEL AND COMPOSITE CONSTRUCTION

Stephen J. Hicks
General Manager Structural Systems
Heavy Engineering Research Association
Auckland, New Zealand
stephen.hicks@hera.org.nz

Brian Uy
Professor and Head of School
School of Civil Engineering, The University of Sydney
New South Wales, Australia
brian.uy@sydney.edu.au

Won-Hee Kang
Senior Lecturer in Structural Reliability
Centre for Infrastructure Engineering, Western Sydney University
New South Wales, Australia
W.Kang@westernsydney.edu.au

ABSTRACT

This paper presents some of the innovations that are included within the new Bridge Design Standard for Steel and Composite Construction AS/NZS 5100.6, which will be the first harmonized standard between Australia and New Zealand for the design of bridges. As Chairs of the Committees responsible for AS/NZS 5100.6 and AS/NZS 2327, the authors of this paper present the challenges faced from the introduction concrete compressive strengths up to 100 MPa and quenched and tempered steels with a yield strength up to 690 MPa. Perhaps one of the most innovative aspects of this standard is the introduction of an appendix that provides design rules for steel products that are not manufactured to Australia and New Zealand standards. This appendix is underpinned by rigorous structural reliability analyses undertaken by Australian and New Zealand researchers, which included the present authors of this paper.

INTRODUCTION

This paper provides an overview of the new Australasian Bridge Design Standard for Steel and Composite Construction AS/NZS 5100.6 (2017). Building on earlier steel design standard harmonisation initiatives, such as the cold-formed steel structures standard AS/NZS 4600 (2005), AS/NZS 5100.6 is the first joint Australian and New Zealand design standard for bridges. It has been a catalyst for further harmonization activities in design standards for steel construction, such as the development of the new standard for steel and concrete composite buildings DR AS/NZS 2327 (2016). In the future, it is hoped that this work may lead to a harmonization of the existing AS 4100 (1998) and NZS 3404 (1997) into a joint Australian and New Zealand steel structures standard. The structure of the current Australasian structural steel standards follows that of many other international standards and is presented in Fig. 1.

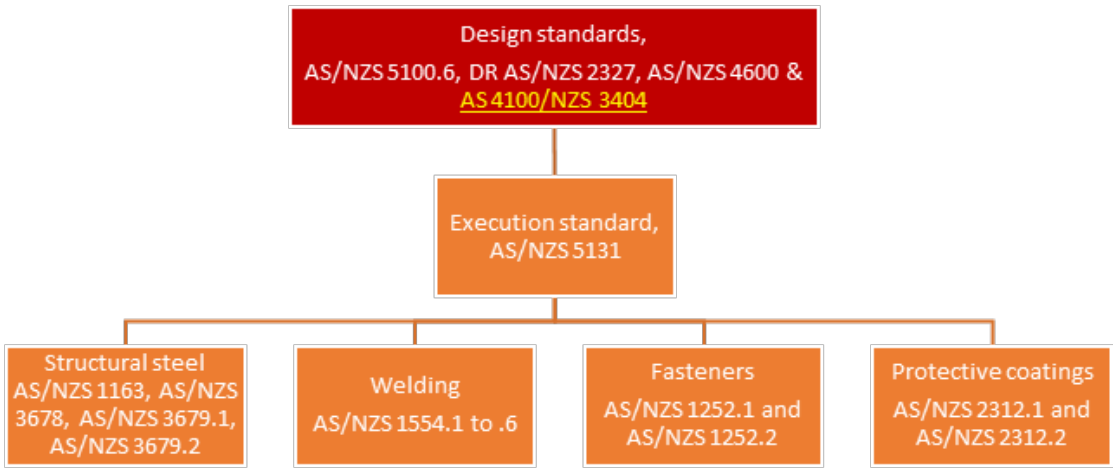


Fig. 1 - Current structure of Australasian structural steel standards.

Steel bridges have historically been used in both Australia and New Zealand. Two of the most iconic bridges in these countries are the Sydney Harbour Bridge (see Fig. 2(a)) and the Auckland Harbour Bridge: both of which used imported steel from Dorman Long, UK. Due to its limited domestic steel supply, New Zealand continues to use imported steel in many of its bridges such as the Te Rewa Rewa Bridge in New Plymouth shown in Fig. 2(b) (Mulqueen, 2011). The success of using imported structural steel in New Zealand is reflected in a market share of 50% for steel in construction, rising to 80% in Christchurch.



(a) (b)

Fig. 2 - (a) Sydney Harbour Bridge, Australia (b) Te Rewa Rewa Bridge, New Zealand.

A number of technical and political challenges were presented in the development of AS/NZS 5100.6. On the technical side, the introduction of higher strength steel and concrete meant that many of the existing composite design provisions given in AS 5100.6 (2004) had to be reconsidered. In both technical and political terms, the requirement by New Zealand bridge designers to include steels manufactured to overseas standards resulted in reliability analyses being undertaken to demonstrate that the same margins of safety for designs using steels manufactured to AS and AS/NZS standards were maintained. Many of the other changes that will be presented in this paper drew on work that underpin the design provisions given in the structural Eurocodes (EN 1994-2 (2005) and EN 1993-1-9 (2005)) as well as AISC 360-16 (2016).

AS/NZS 5100.6 consists of 15 Sections and several Appendices. The structure is presented below in the following subheadings. Where significant changes have been made compared to the existing AS 5100.6, these are highlighted and an overview of the background work given

SECTION 1, 2 & 3 - SCOPE AND GENERAL, MATERIALS & GENERAL DESIGN REQUIREMENTS

AS/NZS 5100.6 is concerned with the design of structural steelwork in bridges together with steel-concrete composite members, including composite beams and composite columns. In addition, for consistency with the concrete bridges design standard AS 5100.5 (2017), concrete compressive cylinder strengths f'_c of up to 100 MPa are permitted. The standard applies to the design of other steel components of bridges including steel piers, steel railings and sign structures. The scope does not, however, include bridges with orthotropic plate decks, cold-formed steel members other than structural hollow sections, steel elements less than 3 mm thick nor steel members where the value of yield stress f_y > 690MPa. In a similar way as its predecessor, the structural steel product standards recognized are AS/NZS 1163 (2016), AS/NZS 1594 (2002), AS/NZS 3678 (2016), AS/NZS 3679.1 (2016) and AS/NZS 3679.2 (2016). However, the new addition is quenched and tempered steel plate produced according to AS 3597 (2008).

A design life of 100-years is assumed in the AS(/NZS) 5100: 2017 suite of standards. In a similar manner to North American practice, a global factor approach is adopted, where the design resistance is calculated by multiplying the nominal (characteristic) resistance by a capacity reduction factor ϕ (cf. partial factor approach, where $\phi = 1/\gamma_M$). Whilst this approach is simple to apply in structural steel and reinforced concrete design, it can prove problematical to apply in composite design as the equations for nominal capacity can consist of up to four different materials. As a consequence of this, the existing AS 5100.6 adopts a hybrid approach, where the capacity factors in composite columns are applied to the individual material components with ϕ = 0.9 for structural steel together with reinforcing steel and ϕ_c = 0.6 for concrete; this hybrid approach is maintained in AS/NZS 5100.6.

ALTERNATIVE STEEL PRODUCTS

According to AS/NZS 1170.0 (2002), it is based on the philosophy and principles set out in ISO 2394 (1998) (AS 5104 (2005) identical). In probability-based design, the probability of failure P_f is the basic reliability measure that is used. An alternative measure is the reliability index β and is related to the probability of failure P_f by:

$$P_f = \Phi(-\beta) \tag{1}$$

where Φ is the cumulative distribution function of the standardised normal distribution

The target reliability index is related to the expected social and economic consequences from a design failure. According to ISO 2394 and AS 5104, the suggested reliability index for ultimate limit state design is β = 3.8, which corresponds to the case when the consequence of failure is great (the highest level) and the relative costs of safety measures are moderate. Design values of resistances R_d are defined such that the probability of having a more unfavourable value is as follows:

$$P(R \le R_d) = \Phi(-\alpha_R \beta) \tag{2}$$

where α_R is the First Order Reliability Method (FORM) sensitivity factor for resistance.

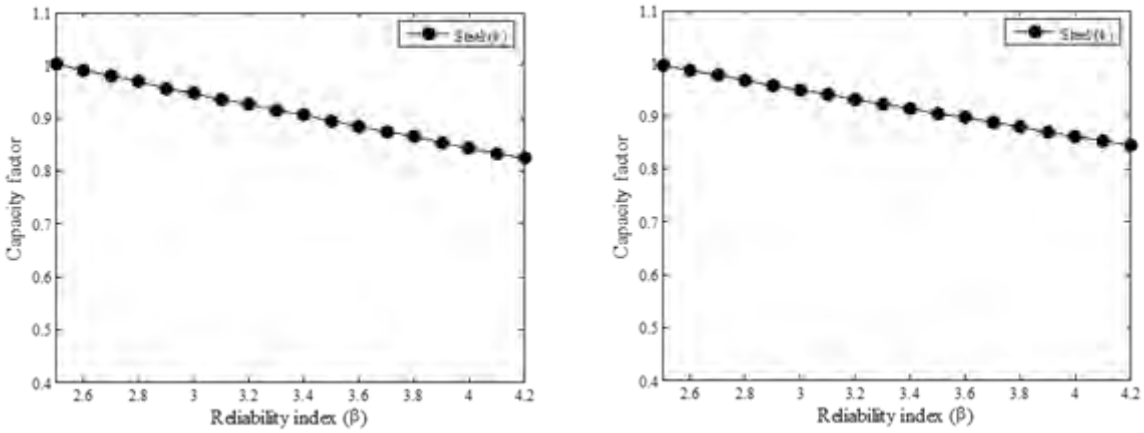
For a dominating resistance parameter, ISO 2394 and AS 5104 recommend α_R = 0.8. Therefore, the design value for resistance corresponds to the product $\alpha_R\beta$ = 0.8 × 3.8 = 3.04 (equivalent to a probability of the actual resistance falling below the design resistance of 1 in 845 = 0.0012). The remaining safety is achieved in the specification of actions.

In the interests of closer economic relations, the New Zealand Steel Bridge Group together with other key-stakeholders confirmed the wish to revise the Steel and composite bridge design standard AS 5100.6 as a joint AS/NZS document in 2012. Due to the long history of successfully using overseas structural steels with the design standard NZS 3404, it was required by New Zealand designers that steel products conforming to EN 10025 (2004), JIS G 3106 (2004) and JIS G 3136 (2005) should be supported by the resulting AS/NZS 5100.6. In response to concerns that the use of overseas steels might cause an erosion to the safety margins required by AS/NZS 1170.0, a structural reliability investigation was undertaken by Kang *et al.* (2015a), which considered both the material variability and geometric manufacturing tolerances.

Some typical results from the reliability analyses are presented in Fig. 3, which shows the relationship between the capacity factor ϕ and the reliability index β. As can be seen, for the target reliability index β = 3.04, the calibration results are almost identical within rounding errors, *viz.* the capacity reduction factor ϕ = 0.94, irrespective of the different manufacturing tolerances; this finding was confirmed in further structural reliability work on columns, composite

columns and composite beams, and was later shown by Uy *et al*. (2015) that it could also be safely extended to a wider range of steel products manufactured to Korean (KS), Chinese (GB) and American (ASTM) standards, which are currently recognized for design in Singapore by the Building and Construction Authority (BC1, 2012). Therefore, the existing capacity factor of ϕ = 0.90 given in AS 5100.6 for beams in bending is on the conservative side for steel sections complying with BS EN 10025, JIS G 3106 and JIS G 3136. This finding led to a proposed normative appendix to AS/NZS 5100.6 together with design rules for these alternative steel materials.

Unfortunately, on comparing the differences between the traceability and conformity requirements in the 2016 edition of the product standards (AS/NZS 1163, AS/NZS 3678, AS/NZS 3679.1 and AS/NZS 3679.2), the committee agreed that further work would need to be undertaken in the future to resolve these differences. Therefore, the rules for alternative steel materials are currently provided within a New Zealand-only appendix.



(a) ϕ=0.94 at β = 3.04 (b) ϕ=0.95 at β = 3.04

Fig. 3 - Capacity factor versus reliability index for compact sections using products complying with manufacturing tolerances given in (a) EN 10034 (1993) and (b) JIS G 3192 (2005)

SECTION 4 & 5 - METHODS OF STRUCTURAL ANALYSIS & STEEL BEAMS

Owing to the fact that finite element methods of analysis are now available in most engineering software packages, bridges are often being designed using these tools. However, there is a general paucity of information at a standards level on how different structures should be modelled. To remedy this situation, provisions are given in AS/NZS 5100.6 on modelling material behaviour in different types of analyses, together with required geometric imperfections.

One potential buckling mode that may occur when intermediate restraints are flexible is now recognized in AS/NZS 5100.6. The mode of buckling features one or two half wavelengths over the span, with the restraint positions in each half wavelength being displaced by the buckling. This mode occurs in multi-girder and ladder deck bridges during construction when there is no plan bracing; the only bracing is in planes (triangulated bracing or stiff cross-girders) between beam pairs. These planes offer torsional restraint to the main beams, by virtue of the vertical stiffness of the main beams themselves. The mode of buckling with torsional restraints is shown in Fig. 4, for a single half wave in a simply supported span (whilst the mode is illustrated with

stiff cross-girders, it can equally apply to beams with triangulated bracing). Once the deck slab has been cast, the cross-girders effectively form inverted U-frames and these may be used to provide some restraint to the bottom flanges adjacent to intermediate supports

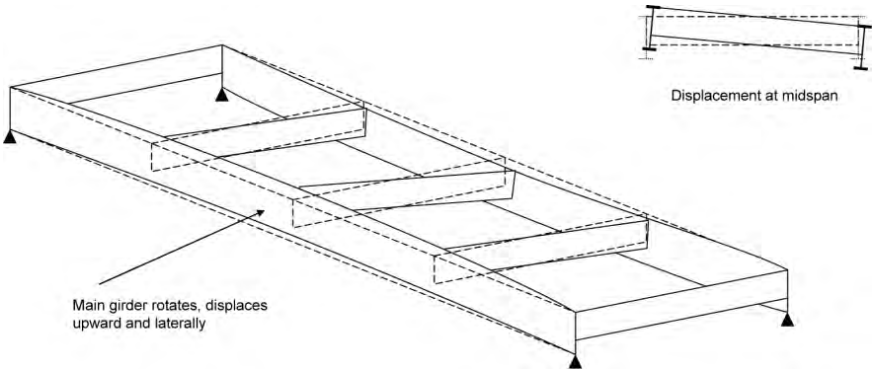


Fig. 4 - Buckling mode with intermediate torsional restraints

SECTION 6 & 7 - COMPOSITE BEAMS & COMPOSITE BOX GIRDERS

The most common form of shear connector in composite construction is the headed stud. A structural reliability study was undertaken specifically for AS/NZS 5100.6 (Hicks and Jones, 2013), which considered the results from 113 push tests. This work demonstrated that the following equations for the design shear capacity f_{ds} can be used for stud connectors embedded in solid concrete slabs and encasements:

$$f_{ds} = \phi 0.70 d_{bs}^2 f_{uc} \tag{3}$$

or

$$f_{ds} = \phi 0.29 d_{bs}^2 \sqrt{f'_{cy} E_c} \tag{4}$$

whichever is smaller.

where ϕ is the capacity reduction factor, which may be taken as ϕ = 0.8 (previously given as ϕ = 0.85 in AS 5100.6), d_{bs} is the nominal diameter of the shank of a stud connector, but 16 mm ≤ d_{bs} ≤ 25 mm; f_{uc} is the ultimate tensile strength of the stud material, but not greater than 500 MPa; f'_{cy} is the characteristic strength of the concrete at the age considered, but 16 MPa ≤ f'_{cy} ≤ 100 MPa; E_c is the modulus of elasticity of concrete at the age being considered, which may be taken as: $E_c = \rho^{1.2}\left(0.043\sqrt{f_{cmi}}\right)$ for f_{cmi} ≤ 40 MPa; or $E_c = \rho^{1.2}\left(0.024\sqrt{f_{cmi}} + 0.12\right)$ for f_{cmi} > 40 MPa, ρ is the density of concrete (kg/m³) and f_{cmi} is the mean value of the in situ compressive strength.

In AS/NZS 5100.6, Equation (3) has been extended to include high strength structural bolts as shear connectors. In these circumstances, the constant of 0.70 is replaced with 0.50.

From reliability analyses of 84 push tests using channel shear connectors, it was found that many of the international rules were on the unconservative side (Hicks *et al.*, 2016; CSA S16-09, 2009; AISC 360-16, 2016). To remedy this situation, the following equation for the design shear capacity f_{ds} was developed

$$f_{ds} = \phi 33.1\left(t_f + 0.5 t_w\right) L_{sc} \sqrt{f'_{cy}} \tag{5}$$

where t_f, t_w and L_{sc} is the flange thickness, web thickness and length of the channel shear connector in millimetres, respectively.

SECTION 8 & 9 – TRANSVERSE MEMBERS AND RESTRAINTS & MEMBERS SUBJECT TO AXIAL TENSION

Section 8 brings together the requirements for transverse members and restraints, and their design requirements, which are based on AS 4100 and NZS 3404. The Section also covers the requirements of AS 4100 and NZS 3404 for restraints to compression members.

Section 9 covers the design of members subject to axial tension forces that are statically loaded. Members subject to fatigue loading should also be assessed in accordance with Section 13 of AS/NZS 5100.6 (see below).

SECTION 10 & 11 - MEMBERS SUBJECT TO AXIAL COMPRESSION & MEMBERS SUBJECT TO COMBINED ACTIONS

In Eurocode 4, composite columns are limited to steel with a nominal yield strength of 235 MPa ≤ f_y ≤ 460 MPa and a concrete characteristic compressive strength of 20 MPa ≤ f'_{cy} ≤ 50 MPa. Through structural reliability work that considered an extensive database of 1583 test results by Kang *et al.* (2015b), it was found that the existing capacity factors of ϕ = 0.9 for the steel and ϕ_c = 0.65 for the concrete were justified for the design equations given in the existing AS 5100.6. However, it was also shown that the provisions for composite columns can be extended in AS/NZS 5100.6 to permit f_y values of up to 690 MPa and f'_{cy} values of up to 100 MPa.

SECTION 12 & 13 – CONNECTIONS & FATIGUE

According to Taplin *et al.* (2013), the design truck loading originally used in Australia was derived from the AASHTO H20-S16 combination, where the loading was increased by approximately 35% and the drive and trailer axles were replaced by tandem axle sets. Subsequent weigh-in-motion (WIM) data suggested that the average extreme daily events exceeded the load effects given by this design truck loading (Heywood, 1995). To remedy this situation, the SM1600 loading model was developed to ensure new bridges would possess sufficient resilience to future productivity enhancements in road transport. The SM1600 loading model represents the W80, A160, M1600 and S1600 traffic design loads in AS 5100.2 (2017). The A160 axle load and M1600 moving traffic load are presented in Fig. 5 (the S1600 static traffic load is similar to the latter, except that the UDL is increased to 24 kN/m and the 4 × 360 kN tri-axle set is reduced to 4 × 240 kN).

The fatigue loading provisions in AS 5100.2 (2017) are equivalent to the damage-tolerant method given in EN 1993-1-9 and the International Institute of Welding (Hobbacher, 2016) in that, although a 100-year design life is considered in the design of the bridge, the fatigue life is based on 75-years because of the following assumptions (AS 5100.2 Supp 1, 2007): the belief that bridges will be inspected regularly and that intervention will occur when fatigue damage is detected; and the uncertainty associated with the prediction of the fatigue life.

For road bridges, the current fatigue design traffic load effects are determined from 70% of the effects of a single A160 axle load (Fig. 5(a)), or 70% of the M1600 moving traffic load excluding the UDL (Fig. 5(b)), whichever is more severe. In both cases, a load factor of 1.0 is used and the load effects are increased by the dynamic load allowance α. The loads shown in Fig. 5 should be placed within any design traffic lane to maximize the fatigue effects for the component under consideration. When multiple traffic lanes are used, the current design approach is to undertake a Palmgren-Miner summation.

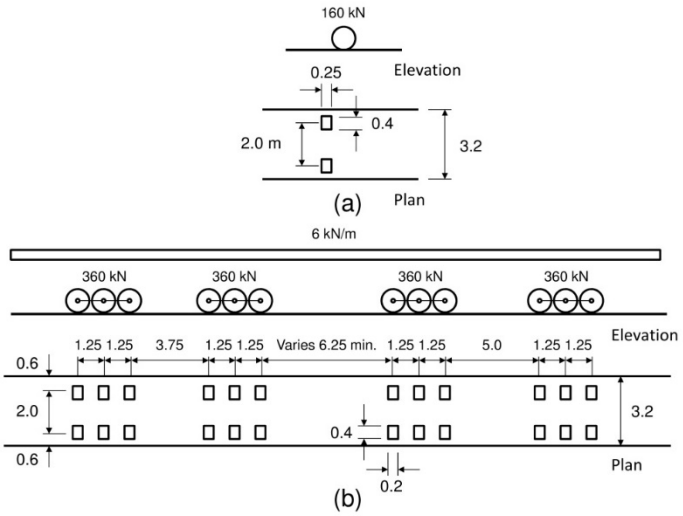


Fig. 5 - Road traffic loads according to AS 5100.2 (a) A160 axle load (b) M1600 moving traffic load (all dimensions in metres)

To provide greater alignment with international practice, AS/NZS 5100.6 has adopted the IIW provisions for fatigue design. In addition, to simplify bridge design, the damage equivalent approach from EN 1993-1-9 has been specifically developed for the loading given in AS 5100.2 (Hobbacher *et al.*, 2016), which has led to the following simple equation for fatigue verification of road bridges:

$$\gamma_{Ff}\Delta\sigma_{E,2} = \gamma_{Ff}\left[(1+\alpha)\lambda\Delta\sigma_{\max}\right] \le \phi_{Mf}\Delta\sigma_c \tag{6}$$

where γ_{Ff} is the load factor for equivalent constant amplitude stress ranges (taken as γ_{Ff} = 1.0), $\Delta\sigma_{E,2}$ is the characteristic value of equivalent nominal stress range for 2 million cycles, α is a dynamic load allowance from AS 5100.2, λ is the damage equivalent factor (see Equation (6) below), $\Delta\sigma_{max}$ is the maximum stress range caused by the fatigue loads specified in AS 5100.2, ϕ_{Mf} is the capacity reduction factor (for high consequence of failure taken as: 0.85 for the 'damage tolerant' method, where there will be regular inspection; or 0.75 for the 'safe life' method, where there will be little/no inspection over the design life of the structure) and $\Delta\sigma_c$ is the fatigue resistance of the detail at 2 million cycles (the detail category).

The damage equivalent factor for road bridges is given by:

$$\lambda = \lambda_c\lambda_L\lambda_R\lambda_Y\lambda_M \tag{7}$$

where λ_c is for vehicles per day, λ_L is for consideration of span, λ_R is the route factor, λ_Y is the service life and λ_M is the effect of multiple lanes (if not yet covered in load assumptions).

A similar expression as Equation (7) is given for rail bridges and, for ease of use, the various damage equivalent factors are given in tabular form. For cases when the designer wishes to squeeze out the very last remaining capacity from a design or assess existing bridges, the Palmgren-Miner summation is supported within an appendix to AS/NZS 5100.6.

SECTION 12 & 13 – BRITTLE FRACTURE & TESTING OF STRUCTURES OR ELEMENTS

Given the introduction of quench and tempered steel plate, the steel types for brittle fracture have been extended to include AS 3597 products. Also, to remedy the unsatisfactory situation that the permissible service temperatures according to steel type and thickness are only appropriate for steels currently made in Australia or New Zealand, rules for evaluating the notch toughness of non-domestic steel products are given. It is hoped that these rules will be incorporated within AS/NZS 1163, AS/NZS 1594, AS/NZS 3678 and AS/NZS 3679.1 in due course.

CONCLUSIONS

Bridge design – Part 6: Steel and composite construction, is the only part of the AS 5100 suite of standards that has been revised as a joint AS/NZS standard. Overseas steels that have historically been used in New Zealand bridge design for the last 24 years are to be included in an appendix. Following the international trend of using less natural resources, design rules for higher strength steel and concrete are given. The new design rules within the proposed AS/NZS 5100.6 provide greater alignment with international best practice and, in some cases, significant improvements are given.

ACKNOWLEDGEMENTS

The authors would like to thank the members of the BD-090-06 Committee for all their hard work to date; in particular, the Standards Australia Project Manager, June Chen, responsible for Part 6 and the complete AS 5100 suite of standards. As members of the BD-090-06 Committee, the present authors have prepared this paper according to what they consider to be the significant changes to the existing AS 5100.6. However, the standard is still being prepared for public comment and, as a consequence of this, may be subject to change. Any views expressed in this paper may not necessarily reflect those of the other members of the Committee, nor those of Standards Australia and Standards New Zealand.

REFERENCES

ANSI/AISC 360-16. (2016). Specification for Structural Steel Buildings. American Institute of Steel Construction, Chicago, IL.

AS 3597 (2008). Structural and pressure vessel steel - Quenched and tempered plate, Standards Australia, Sydney, Australia.

AS 4100 (1998). Steel structures, Standards Australia, Sydney, Australia.

AS 5100.2 (2017). Bridge design, Part 2: Design loads, Standards Australia, Sydney, Australia.

AS 5100.2 Supp 1 (2007). Bridge design – Design loads – Commentary (Supplement to AS 5100.2 - 2004), Standards Australia, Sydney, Australia.

AS 5100.5 (2017). Bridge Design, Part 5: Concrete, Standards Australia, Sydney, Australia.

AS 5100.6 (2004). Bridge Design, Part 6: Steel and composite construction, Standards Australia, Sydney, Australia.

AS 5104 (2005). General principles on reliability for structures, Standards Australia, Sydney, Australia.

AS/NZS 1163 (2016). Cold-formed structural steel hollow sections, Standards Australia/Standards New Zealand, Sydney/Wellington, Australia/New Zealand.

AS/NZS 1170.0 (2002). Structural Design Actions, Standards Australia/Standards New Zealand, Sydney/Wellington, Australia/New Zealand.

AS/NZS 1594 (2002). Hot-rolled steel flat products, Standards Australia/Standards New Zealand, Sydney/Wellington, Australia/New Zealand.

AS/NZS 3678: 2016, Structural steel - Hot-rolled plates, floorplates and slabs, Standards Australia/Standards New Zealand, Sydney/Wellington, Australia/New Zealand.

AS/NZS 3679.1 (2016) Structural steel – Part 1: Hot-rolled bars and sections, Standards Australia/Standards New Zealand, Sydney/Wellington, Australia/New Zealand.

AS/NZS 3679.2 (2016). Structural steel – Part 2: Welded I sections, Standards Australia/Standards New Zealand, Sydney/Wellington, Australia/New Zealand.

AS/NZS 4600 (2005). Cold-formed steel structures, Standards Australia/Standards New Zealand, Sydney/Wellington, Australia/New Zealand.

AS/NZS 5100.6 (2017). Bridge Design, Part 6: Steel and composite construction, Standards Australia/Standards New Zealand, Sydney/Wellington, Australia/New Zealand.

BC1 (2012). Design guide on use of alternative structural steel to BS 5950 and Eurocode 3, Building and Construction Authority, Singapore, See http://www.bca.gov.sg (accessed 30/01/14)

CSA S16-09 (2009). Design of steel structures. Canadian Standards Association, Ontario.

DR AS/NZS 2327 (2016). Composite steel-concrete construction for buildings, Standards Australia/Standards New Zealand, Sydney/Wellington, Australia/New Zealand.

EN 1993-1-9 (2005). Eurocode 3: Design of steel structures – Part 1-9: Fatigue, European Committee for Standardization, Brussels, Belgium.

EN 1994-2 (2005). Eurocode 4: Design of composite steel and concrete structures – Part 2: General rules and rules for bridges, European Committee for Standardization, Brussels, Belgium.

EN 10025-1 *et seq*. (2004). Hot rolled products of structural steels, General technical delivery conditions, CEN, Brussels, Belgium.

EN 10034 (1993). Structural steel I- and H-sections – Tolerances on shape and dimensions, CEN, Brussels, Belgium.

Heywood, R (1995) Live loads on Australian bridges – statistical models from weigh-in-motion data. Australian Civil Engineering Transactions CE37(2), pp. 107–116

Hicks, S., Cao, J., McKenzie, C., Chowdhury, M. and Kaufusi, R. (2016). “Evaluation of shear connectors in composite bridges”, Research Report 602, NZ Transport Agency, Wellington, https://www.nzta.govt.nz/resources/research/reports/602/

Hicks, S. and Jones, A. (2013). “Statistical Evaluation of the Design Resistance of Headed Stud Connectors Embedded in Solid Concrete Slabs”. Structural Engineering International. 23(3), pp. 269-277.

Hobbacher, A. (2016). Recommendations for Fatigue Design of Welded Joints and Components, IIW Collection, Springer International, Switzerland.

Hobbacher, A.F., Hicks, S.J., Karpenko, M., Thole, F. and Uy, B. (2016). “Transfer of Australasian bridge design to fatigue verification system of Eurocode 3”. Journal of Constructional Steel Research, 122. pp. 532–542.

ISO 2394 (1998). General principles on reliability for structures, International Organization for Standardization, Geneva, Switzerland.

JIS G 3106 (2004). Rolled steels for welded structure, Japanese Standards Association, Tokyo, Japan.

JIS G 3136 (2005). Rolled steels for building structure, Japanese Standards Association, Tokyo, Japan.

JIS G 3192 (2005). Dimensions, mass and permissible variations of hot rolled steel sections, Japanese Standards Association, Tokyo, Japan.

Kang, W-H, Hicks, S, and Uy, B. (2015a). “Safety factors for the resistance of steel sections”. Australian Journal of Structural Engineering. 16(2). pp. 116-128.

Kang, W-H., Uy, B., Tao, Z. and Hicks, S. (2015b). “Design strength of concrete-filled steel columns”. Advanced Steel Construction. 11(2), pp. 165-184.

Mulqueen, P.C. (2011). “Creating the Te Rewa Rewa Bridge, New Zealand”, Structural Engineering International, 21(4). pp. 486-491.

NZS 3404.1 (1997). Steel structures standard, Standards New Zealand, Wellington, New Zealand.

Taplin, G., Deery, M., van Geldermalsen, T., Gilbert, J., Grace, R. (2013) “A new vehicle loading standard for road bridges in New Zealand”, Research Report 539, NZ Transport Agency, Wellington.

Uy, B., Hicks S. and Kang, W-H. (2015). “Australasian advances in steel & composite structures to enhance cross-border practice”. 17th ASEP International Convention (17AIC), Pasig City, Philippines.

SHEAR CONNECTIONS BY HEADED STUDS CLOSE TO THE CONCRETE EDGE

Prof. Dr.-Ing. Ulrike Kuhlmann
University Stuttgart, Germany
sekretariat@ke.uni-stuttgart.de

Dr.-Ing. Jochen Raichle
Consultancy Prof. Dr. -Ing. Kuhlmann, Ostfildern-Nellingen, Germany
Raichle@ing-nellingen.de

Dr.-Ing. Ana M. Pascual
University Stuttgart, Germany
ana.pascual@ke.uni-stuttgart.de

ABSTRACT

Headed studs arranged close to the concrete edge present a limited carrying capacity because of the splitting forces induced in the concrete. In the past years several investigations have been carried out at the Institute of Structural Design of the University of Stuttgart on the shear behavior of the headed studs close to the concrete edge (originally called horizontally lying shear studs) under static and cyclic loading, considering shear in longitudinal and vertical direction. As a result, the equations for the design resistance of the headed studs and the fatigue strength have been provided and included in EN 1994-2 in the Annex C.

Meanwhile, further studies of the behavior have led to possible improvements and enhancements of the existing rules and these investigations and results are reported in this paper. New researches have especially dealt with the behavior of the connection under cyclic loading in order to assess the fatigue strength under vertical shear and the influence of the edge distance. As a consequence, the design equations for the headed stud close to the concrete edge or close to the concrete surface have been redefined and a proposal has been developed to be included in the future version of EN 1994.

1. INTRODUCTION

Independently, if the stud is in vertical or horizontal position, there may be a reduction of the connection capacity due to the splitting forces (Fig. 1) that appear when the center of the stud is close to the edge of the concrete. The failure mode depends directly on the edge distance a_r (see Fig. 2). On the other hand, this type of connection allows interesting forms of construction, such as building edge beams in car park construction or slim-floor beams, see (Lam, Dai, Kuhlmann, Raichle, & Braun, 2015).



Fig. 1 Concrete splitting under longitudinal shear

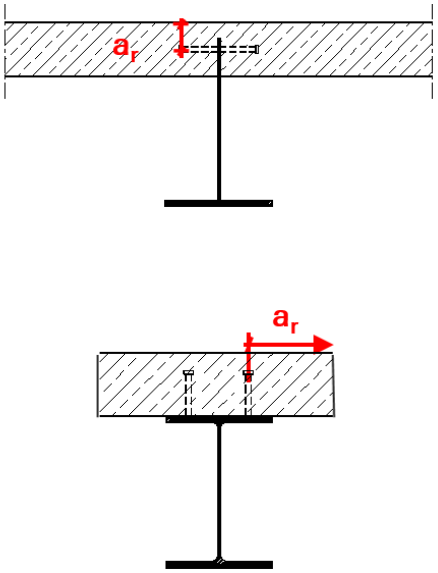


Fig. 2 Headed studs close to the concrete edge

In bridge construction, the horizontal studs may serve to longitudinally connect the steel girder to the concrete slab, as for instance in an arch bridge. Similarly, an arrangement of horizontal studs represents the basis of an innovative composite bridge girder, where the upper flange of the girder has been replaced by two layers of horizontally lying studs (Fig. 3 and Fig. 4), the lower is embedded into a prefabricated concrete slab and the upper is in concrete in-situ, therefore a reduction in the steel consumption is achieved together with the constructional advantages of prefabrication. Additionally, this section can be enhanced by using a corrugated steel web for the girder, which improves the transversal bending capacity and the longitudinal connection.



Fig. 3 Prefabricated composite bridge girder with horizontally lying studs

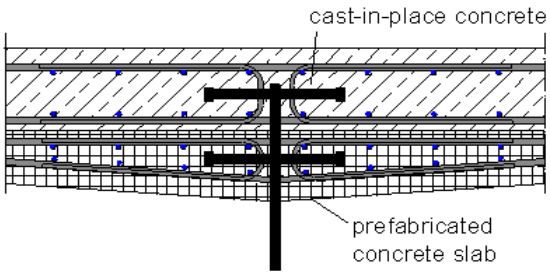


Fig. 4 New section with two layers of horizontally lying studs

The study of the particular behavior of the headed studs close to the concrete edge has been the objective of several researches, see (Breuninger & Kuhlmann, 2001) (Breuninger, 2000) (Kuhlmann & Breuninger, 2000) as well as (Kürschner, 2003) (Kürschner & Kuhlmann, 2004) (Kürschner & Kuhlmann, 2005) under static longitudinal and vertical shear and the combination of both. Furthermore, also the fatigue strength has been under analyses. The results of these works are included in Annex C of (EN 1994-2), so they can be used in practice.

Nonetheless, there are still some aspects that require a further development, this is the case of the fatigue strength of the connection under vertical shear, as it occurs under the fatigue loading derived from wheel loads, see Fig. 5. In this framework, this paper presents the proposal of enhancement of the Annex C based on the works from (Raichle & Kuhlmann, 2016) (Raichle, 2015). Regarding the fatigue strength under vertical shear, the experimental program developed and the evaluation of the results is described.

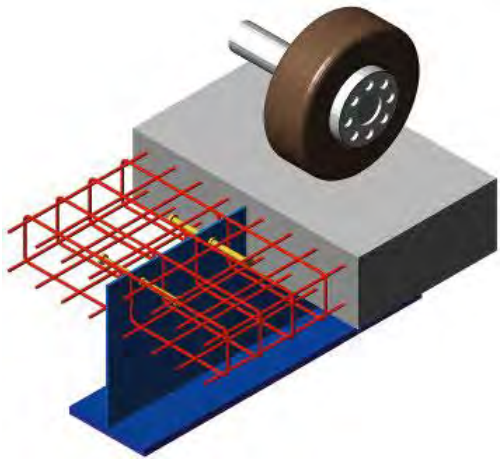


Fig. 5 Fatigue loading under transverse shear

2. STATE OF THE ART AND ENHANCEMENT

There are different geometrical parameters that affect the behavior of the stud connection, but the most important one is the effective edge distance a_r', which is the distance between the bolt axis and the axis of the reinforcement (Fig. 6). Additionally, it is necessary to distinguish between middle and edge position, since the edge position is more unfavorable due to the tensional forces on the studs, not balanced as in the middle position.

The research on the existing rules for headed studs that cause splitting forces in the direction of the slab thickness in (EN 1994-2) Annex C leads to some technical corrections in order to provide more appropriate values of strength for common applications and to extend the application scope.

According to the investigations from (Breuninger, 2000) to prevent the pull-out of the headed studs for the case of an edge position, a length v of the headed studs is required (Fig. 6). These geometrical conditions for the edge position are also included in the Annex C, (EN 1994-2) in clause C1 (2). Nonetheless, they are currently under revision because they lead to extremely long studs, and a further research is being carried to introduce alternatively the application of the fastening technology, (EN 1992-4) in order to verify the pull-out forces.

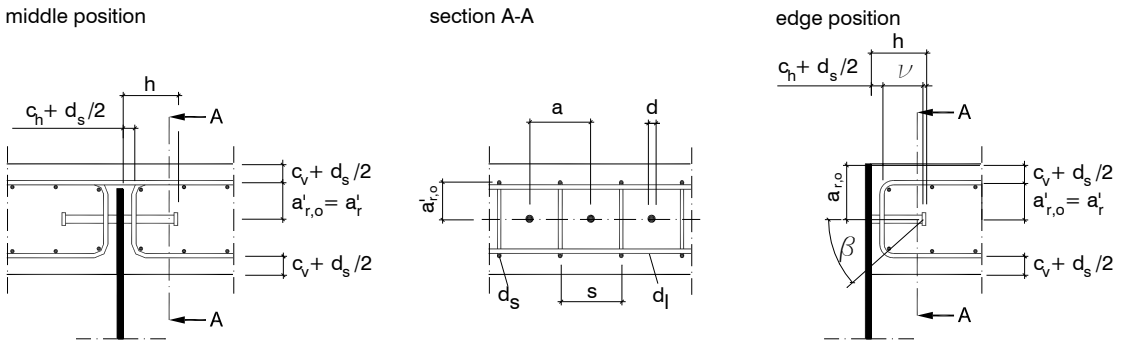


Fig. 6 Geometrical parameters in headed studs close to the concrete edge

The design shear resistance of the headed studs in longitudinal and vertical direction can be determined according to the equation (C.1) and equation (C.4) of (EN 1994-2) Annex C respectively. In both cases the coefficient k_v considers whether the arrangement of studs is at edge or middle position. For simplification, this factor is the same for headed studs in case of longitudinal and vertical shear. However, (Kürschner & Kuhlmann, 2004) recommends 1.25 for k_v to calculate the shear resistance under vertical shear in middle position. This position and loading in the connection are quite common in practice and the simplified normative regulation (k_v=1.14) is too conservative and does not lead to economic results, so 1.25 may be used instead.

(Kürschner & Kuhlmann, 2004) studied also the influence of a multi-row array of shear studs under vertical shear load. The results proved that the vertical shear strength of each row of studs may be calculated individually. However, the numerical investigations in (Kürschner & Kuhlmann, 2004) verified that for a distance a_v between the rows of studs smaller than 200 mm, the total capacity is reduced, and the factor η has to be considered, as it is given in eq. (1).

$$0.7 \leq \eta = a_v / 200 \text{ mm} \leq 1.0 \text{ with } a_v \geq 100 \text{ mm} \quad (1)$$

Moreover, the existing rules in Annex C EN 1994-2 section C.1 (3) allow the dimensioning of the stirrup reinforcement for the splitting forces induced longitudinal shear. Nonetheless, the stirrups are also required for vertical shear, as it was determined by (Kürschner & Kuhlmann, 2004). Currently, the tensile force in the stirrups T_d according to eq. (C.2) in section C.1 (3) should be improved according to eq. (2) with $F_{d,L}$ and $F_{d,V}$ being the stud shear forces in longitudinal and vertical direction.

$$T_d = 0.3\, F_{d,L} + F_{d,V} \quad (2)$$

Related to the fatigue strength of the headed studs under longitudinal loading according to (Raichle, 2015), the equation (C.5) is derived from (Breuninger & Kuhlmann, 2001) (Kürschner, 2003) (Kürschner & Kuhlmann, 2004) for normal weight concrete:

$$(\Delta P_R)^m N = (\Delta P_{L,c})^m N_c \quad (3)$$

With

ΔP_R	Fatigue strength based on difference of longitudinal shear force per stud
$\Delta P_{L,c}$	Reference fatigue strength at $N_c = 2 \times 10^6$ according to Table C.1 in (EN 1994-2)
m	Slope of the fatigue strength curve with m = 8
N	Number of force range cycles

In Table C.1 the maximum fatigue strength for longitudinal shear without edge influence $\Delta P_{L,c}$ is 35.6 kN per stud. This value for a stud of diameter 22 mm leads to a fatigue strength $\Delta\tau_R$ of 95 MPa. However, the current standard EN 1994-1-1, section 6.8.3 (3) provides a maximum fatigue strength for longitudinal shear $\Delta\tau_c$ not higher than 90 MPa, that means 34.2 kN / stud. The maximum fatigue strength should be therefore adjusted in Table C.1 to 34.2 kN to be consistent.

On the other hand, the equation (C.5) only makes reference to the longitudinal shear, but it is assumed that the splitting forces due to fatigue appear similarly under vertical loading. In this paper the study of the fatigue behavior of the headed studs close to the concrete edge under vertical shear is presented and also an interaction equation of fatigue strength under the longitudinal and vertical shear, see (Raichle, 2015). The research results also indicate that a fatigue analysis under shear stress is required for the stirrups.

3. EXPERIMENTAL INVESTIGATIONS

The test specimens correspond to the specimens from the static tests with headed studs at the edge position under vertical shear from (Kürschner & Kuhlmann, 2004). The most important parameter on the connection behavior according to previous investigations is the effective edge distance $a_{r,o}$´ (definition, see Fig. 6). This parameter also in this case was analyzed and served to define the two test series: (QE1) with an edge distance of 100 mm and (QE2) with an edge distance of 50 mm, see Fig. 7. An edge position was adopted on the safe side, because it is more unfavorable than the middle position. For each series a specimen was tested under static loads. For the series (QE1), with the distance of 100 mm, 10 specimens were tested, and for the edge distance of 50 mm, 6 test specimens. The headed studs were of a length of 150 mm and had a diameter of 22 mm. The concrete compressive strength was individually measured and varied between 30 and 35 MPa (cylinder strength). Sinusoidal load cycles at similar maximum load level and different load ranges were applied.

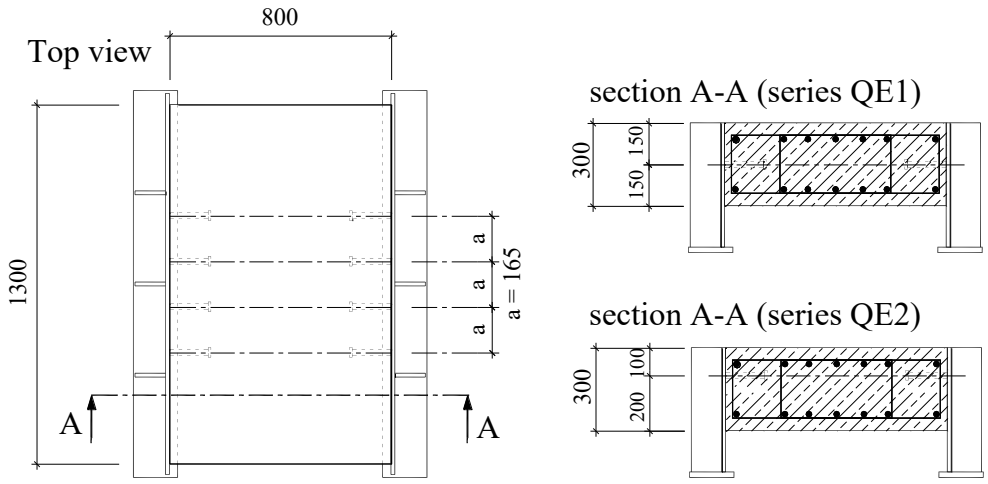


Fig. 7 Geometrical parameters in headed studs close to the edge

The cyclic loading was introduced by pressure applied with a girder on the slab in order that the load was distributed through the slab and all the studs were equally loaded (Fig. 8).

The typical failure of headed studs without edge influence appears due to the fatigue fracture at the collar of the headed studs. The fatigue crack increases as long as the residual cross section is no longer able to bear the load. Later on, the failure of the rest of the headed studs occurs and there is a sudden shearing-off of the studs. This type of failure was also observed in the specimens tested here, with the studs close to the concrete edge and vertically loaded, see Fig. 9. In all the specimens, cracks appeared in the concrete between the headed studs. Additionally, cracks also occurred at the surface of the concrete.



Fig. 8 Test rig of fatigue tests under transverse shear



Fig. 9 Headed studs shearing-off as failure mode. a) View on test specimen, b) View on facture surface

The second type of failure observed was the concrete breakout on the top (Fig. 10). Outgoing from the steel part two cracks grew in the concrete that finally joined in a common crack. From the reinforcement, specifically from the stirrups, in spite of separation cracks compression struts appeared, which allowed to continue the cyclic loading for a while. A strut-and-tie model illustrates the tension stresses transferred by the reinforcement that are in balance with the compression struts transmitted by the concrete. The load taken by the reinforcement prevents the crack formation between the dowels and a sudden failure.

So, together with the shearing-off of the headed studs and the concrete breakout, there was a third failure mode that took place in two of the tested specimens, the fatigue fracture of the reinforcement, see Fig. 11. In both cases, the fatigue fracture was in the upper bending. The failure of the reinforcement illustrates the necessity to consider in the connection design the verification of its strength together with the appropriate definition of the mandrel diameter.

In summary, under longitudinal and vertical shear load when the headed studs are close to the concrete edge a concrete crushing takes place that results on the reduction of the stiffness. Directly above the stud collar local compressive stresses appear in the concrete, which lead to the concrete failure. The increasing flexibility in the area of the stud base generates not only the shear stress but also an unfavorable bending stress at this point, so that, a fatigue crack in the base of the stud appears. The progressive cracking in the concrete and in the headed studs eventually leads to the failure either by shearing-off of the stud or concrete break-out.





Fig. 11 Fatigue failure of a stirrup

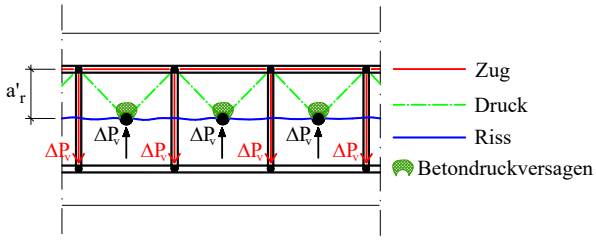


Fig. 10 Concrete breakout failure mode, a) view on test specimen b) belonging strut-and-tie model

4. FATIGUE STRENGTH UNDER VERTICAL SHEAR

Based on these test results a statistical evaluation has defined an S-N curve, see (Kuhlmann & Raichle, 2007) (Raichle, 2015) (Raichle & Kuhlmann, 2016). The equation follows in principle eq. (3) for longitudinal cyclic loading except for the reference value.

$$(\Delta P_R)^m \, N = (\Delta P_{V,\,c})^m \, N_c \qquad (4)$$

With

ΔP_R	Fatigue strength based on difference of vertical shear force per stud
$\Delta P_{V,c}$	Reference fatigue strength at $N_c = 2 \times 10^6$ according to Table 1
m	Slope of the fatigue strength curve with m = 8
N	Number of force range cycles

The fatigue strength curves of horizontally lying headed studs under longitudinal and vertical shear for the two edge distances ($a_{r,}´ = 50$ mm and $a_{r,}´ = 100$ mm) and without edge influence are shown in Fig. 12. For horizontally lying headed studs under longitudinal and vertical shear and an effective edge distance $a_{r,o}´$ of 100 mm the fatigue strength is lower than for studs without an edge influence. Therefore, there has to be a reduction also for an effective edge distance greater than

100 mm. For $a_{r,o}'$ of 125 mm the fatigue strength of headed studs without edge influence is reached which therefore give the upper limit.

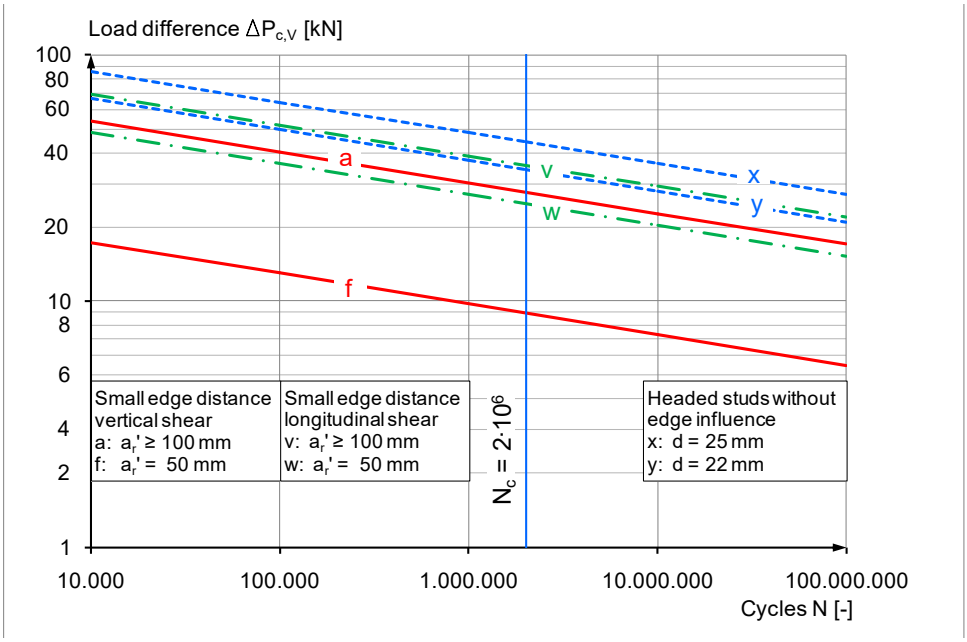


Fig. 12 Fatigue strength S-N curves

Based on the test results (Kuhlmann & Raichle, 2007) (Raichle, 2015) (Raichle & Kuhlmann, 2016) and the experiences on the fatigue behavior of horizontally lying headed studs under longitudinal loading as well as headed studs without an edge influence the fatigue strength for headed studs with edge influence under transverse loading has been derive. As a result, the Table C1 of the Annex C (EN 1994-2) should include the values of $\Delta P_{V,c}$ for the fatigue strength under vertical shear force, Table 1 is proposed to replace it.

Table 1. – Fatigue strength ΔP_R for headed studs close to the concrete edge.

	Longitudinal shear	Vertical shear
a_r' (mm)	$\Delta P_{L,c}$ (kN)	$\Delta P_{V,c}$ (kN)
50	24.9	8.9*
100	34.2(~~35.6~~)	27.7*
≥ 125	34.2~~(35.6)~~	34.2
NOTE Intermediate values should be determined by linear interpolation *In case of cracked concrete slab due to tension a reduction with k = 0.5 is necessary.		

The parametric studies in (Kuhlmann & Raichle, 2008), (Raichle & Kuhlmann, 2016) show that for concrete strength f_{ck}<30 MPa and stud diameter of 19 mm some changes of the data in Table C.1 (EN 1994-2) are required. These changes could be included in the table adding the following text:

In case of concrete strength f_{ck}<30 MPa the fatigue strength ΔP_c should be reduced with $f_{ck}/30$. The values in Table C.1 are valid for stud diameter ≥22 mm. In case of stud diameter of 19 mm the fatigue strength should be reduced to 75% of the values on Table C.1.

In case of cracked concrete slab due to tension a reduction with k=0.5 is necessary (Kuhlmann & et al., 2013) (Kuhlmann & Maier, 2012)In the experiments, see Fig. 11 also fatigue cracking of the stirrups was observed. These cracks occurred in the mandrel region. Therefore, besides the verification of the strength capacity of the stirrups by using the eq. (2), it is necessary to check their fatigue capacity with (EN 1992-1-1) Section 6.8.4 taking into account the mandrel diameter.

4. INTERACTION OF LONGITUDINAL AND VERTICAL SHEAR

For some constructions, for example composite beams without upper steel flange, longitudinal and transverse loading can occur simultaneously. The longitudinal shear loading may be introduce by global bending, whereas the local load introduction by the wheel load may induce vertical shear loading. Static experiments of (Kürschner & Kuhlmann, 2004) under the combined action of both showed that in the edge position the interaction should be taken into account.

Since no additional fatigue tests have been carried out for this case of combined loading, a design recommendation, which is on the safe side, is given at this point. A typical equation for the interaction proof is the following expression eq. (5):

$$\left(\frac{\gamma_{Ff}\,\Delta P_{L,E2}}{\Delta P_{L,c}/\gamma_{Mf,S}}\right)^{0,75} + \left(\frac{\gamma_{Ff}\,\Delta P_{V,E2}}{\Delta P_{V,c}/\gamma_{Mf,S}}\right)^{0,75} \leq 1 \qquad (5)$$

$\Delta P_{L,E2}$ and $\Delta P_{V,E2}$ can be determined according to clause 6.8.6.2 (EN 1994-2).

The value 0.75 for the exponent in the equation (5) is chosen conservatively in absence of an extensive test program. Similarly, as for the static resistance an interaction should only be observed for the edge position and not for the middle position (Kürschner & Kuhlmann, 2004) this is also assumed to be the case for fatigue.

For the stirrups a fatigue design as given in (EN 1992-1-1) clause 6.8.4 is necessary. The mandrel diameter should be considered.

5. CONCLUSIONS

The ultimate resistance as well as the fatigue strength of horizontally lying studs or better headed studs close to the concrete edge are strongly influenced by the effective edge distance a_r' (see Fig. 2) because the shear forces may cause splitting forces, which lead to an earlier failure as for headed studs positioned without any edge influence. Therefore, not the horizontal or vertical arrangement of the shear studs is of importance but the distance to the concrete edges. So the title of this chapter, which is at the moment named “Headed studs that cause splitting forces in the direction of the slab thickness” should be changed accordingly when taken over in a new version of Eurocode 4. For the moment it is also planned to transfer this content of the existing Annex C of EN 1994-2 to the future EN 1994-1-1, as the rules are of course not only valid for bridges but

also for buildings and it is more due to the history of development that it is placed in the bridge part Eurocode 4.

This paper summarizes some of the improvements which have been suggested for the conversion of this Annex to the new version of Eurocode 4 which is under development at the moment. Some of the improvements are simply clarifications, some are also real enhancements due to research which has been realized in the meantime. This especially concerns the fatigue behavior under transverse shear loading for which design rules are introduced similar to what has been included for longitudinal shear.

Some open questions are still left. This concerns the interaction of longitudinal and vertical shear but also the geometric restrictions given so far in order to prevent pull-out failure for horizontally lying studs in edge position. For the latter research has started to consider also the experience from the fastening technique, meanwhile given in EN 1992-4.

These new developments now allow a design for both static and fatigue loading in longitudinal and vertical direction and the development and application of interesting new composite sections.

REFERENCES

Breuninger, U. (2000). Zum Tragverhalten liegender Kopfbolzen unter Längsschub-beanspruchung. *Dissertation, Institute of Structural Design, University of Stuttgart, Issue No. 2000-1, ISSN 1439-3751.*

Breuninger, U., & Kuhlmann, U. (2001). Tragverhalten und Tragfähigkeit liegender Kopfbolzendübel unter Längsschubbeanspruchung. *In: Stahlbau, Volume 70 , Issue 11, Berlin: Ernst & Sohn.*, S. 835–845.

EN 1992-1-1. (2004). Eurocode 2. Design of concrete structures – Part 1-1: General rules and rules for buildings. Brussels, Belgium: Comité Européen de Normalisation.

EN 1992-4. (2015). Eurocode 2, draft. Design of concrete structures – Part 4: Design of fastenings for use in concrete, prEN1992-4. Brussels, Belgium: Comité Européen de Normalisation.

EN 1994-2. (2005). Eurocode 4. Design of composite steel and concrete structures. Part 2: General rules and rules for bridges. Brussels, Belgium: Comité Européen de Normalisation.

Kuhlmann, U., & Breuninger, U. (2000). Behaviour of Horizontally Lying Studs with Longitudinal Shear Force. *Hajjer, J. et al. (Ed.): Proceedings of Composite Constructions in Steel and Concrete IV, May 28 to June 2, Banff, Alberta, Canada. pp. 438-449*.

Kuhlmann, U., & et al. (2013). Sustainable Steel-Composite Bridges in Built Environment (SBRI), Final Report, RFSR-CT-2009-00020, RFCS-Publication, EUR 26322 EN EUROPEAN COMMISSION. *Directorate-General for Research and Innovation Directorate G — Industrial Technologies Unit G.5 — Research Fund for Coal and Steel, RTD-PUBLICATIONS@ec.europa.eu*.

Kuhlmann, U., & Kürschner, K. (2004). Structural Behaviour of Horizontally Lying Shear Studs. *Leon, R. and Lange, J. (Ed.): Proceedings of Composite Constructions in Steel and Concrete V, July 18t to 23, Kruger National Park, South Africa. pp. 534-543.*

Kuhlmann, U., & Maier, P. e. (2012). Optimizing bridge design by improved deterioration models through fatigue tests. *Frangopol, D. and Biondini, F. (Ed.): Proceedings of 6th International Conference on Bridge Maintenance, Safety and Management (IABMAS), Stresa, Lake Maggiore, Italy. pp. 1816-1821.*

Kuhlmann, U., & Raichle, J. (2007). Fatigue Behaviour of Horizontally Lying Shear Studs. *In: Eligehausen, R. (Ed.), Connections between Steel and Concrete. Proceedings of the 2nd International Symposium 4th to 7th September, Stuttgart, Germany, Vol. 2, pp. 1359-1368*.

Kuhlmann, U., & Raichle, J. (2008). Ermüdungsverhalten liegender Kopfbolzen infolge Querschub. *Institute of Structural Design, University of Stuttgart. Research report, research project FE 15.0407/2004/CRB for Bundesanstalt für Straßenwesen (bast), Issue 99, Publisher: Bremerhaven: Wirtschaftsverlag NW, Verlag für Neue Wissenschaft. ISBN 978-3-8650*.

Kuhlmann, U., & Raichle, J. (2008). Headed Studs Close to the Concrete Surface - Fatigue Behaviour and Application. *Leon, R. (Ed.): Proceedings of Composite Constructions in Steel and Concrete VI, July 20.-24., Colorado, USA. pp. 26-38.*

Kürschner, K. (2003). Trag- und Ermüdungsverhalten liegender Kopfbolzen im Verbundbau. *Dissertation, Institute of Structural Design, University of Stuttgart, Issue No. 2003-4, ISSN 1439-3751.*

Kürschner, K., & Kuhlmann, U. (2004). Trag- und Ermüdungsverhalten liegender Kopfbolzendübel unter Quer- und Längsschub. *In: Stahlbau, Volume 73, Issue 7, pp. 505–516, Berlin: Ernst & Sohn.*

Kürschner, K., & Kuhlmann, U. (2005). Mechanische Verbundmittel für Verbundträger aus Stahl und Beton. *In: Stahlbaukalender 2005, Editor: U. Kuhlmann, pp. 455–534, Berlin: Ernst & Sohn.*

Lam, D., Dai, X., Kuhlmann, U., Raichle, J., & Braun, M. (2015). Slim-floor construction - design for ultimate limit state. *In: Steel Construction, Volume 8, Issue 2, p. 79-84 DOI: 10.1002/stco.201510019, Berlin: Ernst & Sohn. – ISSN 1867-0539*.

Raichle, J. (2015). Randnahe Kopfbolzen im Brückenbau. *Dissertation, Institute of Structural Design, University of Stuttgart, Issue No. 2015-2, ISSN 1439-3751.*

Raichle, J., & Kuhlmann, U. (2016). Randnahe Kopfbolzen – Ermüdungsverhalten unter Querschub. *In: Stahlbau, Volume 85, Issue 2, pp. 153–160, Berlin: Ernst & Sohn.*

CONSIDERATION ON COMPOSITE BEAM CONNECTION DUE TO PLASTIC DEFORMATION CAPACITY AND STRENGTH RATIO

Yuko Shimada
Faculty of Engineering, Chiba University
Chiba, Japan
yshimada@faculty.chiba-u.jp

Satoshi Yamada
FIRST, Tokyo Tech
Yokohama, Japan
yamada.s.aa@m.titech.ac.jp

ABSTRACT

This paper is a fundamental study of quantitatively relationship between plastic deformation capacity and strength in composite beam. First, analytical method of composite beam based on the previous experiment results is shown. Specifically, there are three steps in the analysis; invalid area of beam web near scallop is set according to previous experiment results, stress balance between tension and compression in the section is kept under monotonic loading, and deformation of a section is calculated assuming Bernoulli-Euler theory. Secondly, the relationship between plastic deformation of composite beam and geometric condition of beam-to-column connection or material characteristics by parametrical study. In this paper, the effect of steel strength and width-to-thickness ratio of column is focused. All composite beam in this paper is presupposed fracture of lower beam flange. Thus, the strain near scallop at lower flange is used as an index that shows progression of plastic deformation.

1. INTRODUCTION

In seismic design, the detail of beam-to-column connections should prevent early fracture to retain seismic performance of buildings. In order to guarantee sufficient strength of connection for the strength that it makes plastic hinge at beam edge, the maximum strength of connection is designed by connection coefficient α such as Eq.(1). The formula is stated in Technical criteria references on structure of buildings in Japan [1], and it should be generally used in steel structure for designing safety building against earthquake.

$$ {}_{j}M_{u} \geq \alpha \, {}_{b}M_{p} \qquad (1) $$

here, ${}_jM_u$ is the maximum strength of connection, α is connection coefficient, and ${}_bM_p$ is full-plastic moment of beam.

Generally, beams of building are postulated as bare steel on the calculation of strength in the present seismic design, and composite effect by concrete slab on steel beam is neglected. In previous studies, it has been already known that the strength of composite beam is greater than bare steel beam by moving the neutral axis from center of web to near concrete slab [2]-[6]. Moreover, the plastic deformation of composite beam which presupposed fracture of lower beam flange is smaller than bare steel beam, however, it is not clear that composite beam-to-column connection can keep enough energy absorption capacity as bare steel beams. In order to judge whether composite beam-to-column connection have enough energy absorption capacity or not, it should evaluate not only the growth of strength by composite effect but also the deference of the plastic deformation capacity between composite beam and bare steel beam.

The authors have been considered the relationships between strength and deformation capacity of composite beam recently. In [7], the plastic strength was defined as a strength when the plastic hinge is made at the composite beam end, and in [8], connection coefficient of composite beam was defined as a ratio of the maximum strength of composite beam connection to the plastic strength of composite beam.

The connection coefficient of composite beam is defined according to the definition of the connection coefficient of bare steel beam. The recommended value of connection coefficient of bare steel beam in seismic design is decided by considering the relationships between plastic deformation capacity and steel grade, strain hardening, connection detail. However, the connection coefficient of composite beam is not used in seismic design. This reason is that it has not been examined the relationships between connection coefficient and plastic deformation capacity of composite beam yet. It should be clarify the effects of above elements and other elements such as concrete strength and slab thickness for the connection coefficient of composite beam to understand the recommended value for seismic design.

This paper presents an algorithm of composite beam, which has RHS column, H-shaped beam, and slab with deck plate to achieve preliminary trend of plastic deformation capacity. To validate the performance of our algorithm, experimental results in [8] is used. The composite effect of slab to the plastic deformation capacity of composite beam is examined based on the algorithm.

2. Algorithm of composite beam under one-way positive bending

The algorithm in this paper is based on the analysis method shown in [9]. Assuming Bernoulli-Euler theory, a moment and a curvature in a section are obtained according to calculation of stress balance in the section. The relationship between bending moment and rotation angle at beam end are calculated by integrating these moments and curvatures in each section from beam-to-column connection to beam end. There are two differences between this algorithm and previous analysis method; existence of concrete slab and representation of moment transmission efficiency of beam web.

Under random loading as similar as earthquake, the plastic deformation capacity of steel beam is affected by loading protocol. In this paper, the aims are grasping basic trends between plastic deformation capacity of composite beam and sizes of steel members, material characteristics of steel beam. Therefore, load is one-way positive moment.

In the positive-moment region of a composite beam, the effective width of concrete slab is changing according to the location of beam section, however, the effective width in this paper is determined as same as column width as shown Figure 1, regardless the location of section.

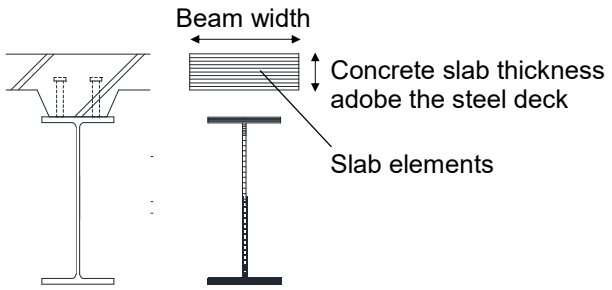
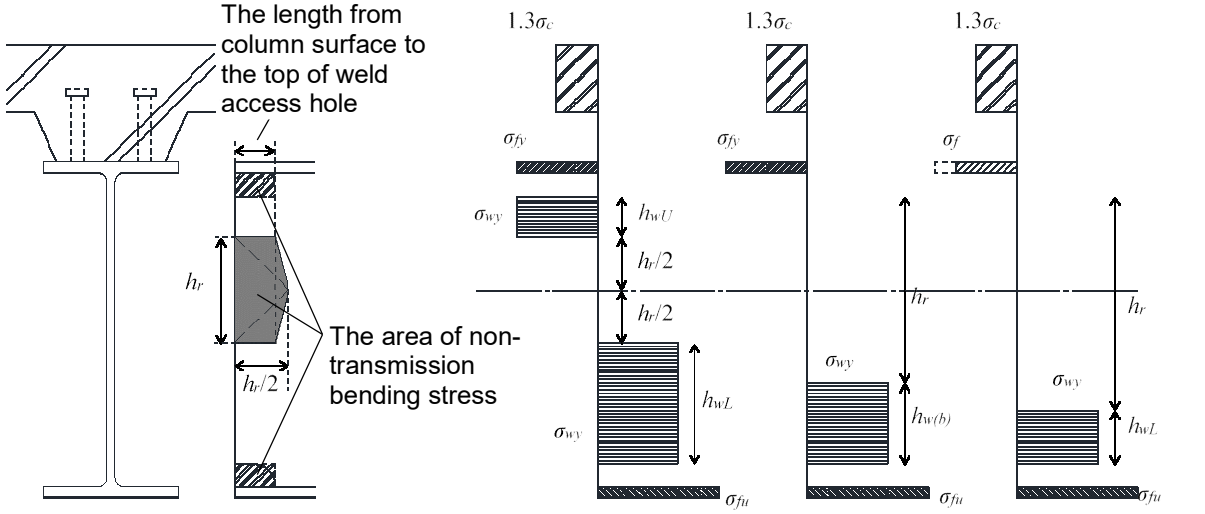


Fig. 1 – Concrete slab setting

Previous studies pointed out that moment transmission efficiency of beam web decreased at the beam end when the partial loss of beam section to the weld access hole and local out-of-plane deformation of RHS column flange are occurred. These are represented in our algorithm as shown in Figure 2. If the beam end is welded to the enough thick column flange, the maximum bending moment of composite beam connection is obtained as ${}_{cj}M_u$ [6]. While there is local out-of-plane deformation, the area of the beam web near beam end is not transferred stress. The height of this area (h_r) is calculated by the balance of each stress block as shown in Figure 2. In the calculation of moment in the connection, it is assumed that the lower beam flange reach to ultimate stress, and the upper beam flange beam web reach to yield stress. If the moment in case that the all of the compression side of beam web is not transferred stress is larger than ${}_{cj}M_u$, the stress balance is re-set according that stress of upper beam flange decreases than yield stress. Here, ${}_{cj}M_u$ is originally not considered weld access hole, therefore, ${}_{cj}M_u$ in this paper is modified for existence of weld access hole.

Steel hysteresis model is based on the results of coupon test. That is, the tension side of steel is used the relationship between nominal stress and nominal strain obtained by each coupon test of beam flange and beam web. While, the compression side of steel is used the following equipment; this is obtained by replacing from the tension side value. When the nominal strain is larger than the uniform elongation, the calculation is continued as the strain progress during the stiffness of the tension side is zero.

Concrete hysteresis model is shown in Figure 3. In the compression side of concrete, the maximum strain is assumed 0.3%, the maximum stress is assumed 1.3 σ_c. When the compression strain is smaller than the maximum strain, the hysteresis model is used the formula modified from the relationship between stress and strain shown in [10]. While, the compression strain is larger than the maximum strain, the strain progress during the stiffness of the tension side is zero. In the tension side of concrete, the calculation is continued as the strain also progress during the stiffness of the tension side is zero.



(a) Case ${}_bM<{}_{cj}M_u$ (b) Case ${}_bM={}_{cj}M_u$ (c) Case ${}_bM>{}_{cj}M_u$

$$h_{w(b)} = \frac{C + N_{fy} - N_{fu}}{N_{wy}}$$

$$M_{(b)} = N_{fu}\left(d_j + t_{bf}\right) + C\left(t_{bf}/2 + t_{dp} + t_s/2\right) + N_{wy}h_{w(b)}\left(t_{bf}/2 + d_j - S_r - h_{w(b)}/2\right)$$

In case of ${}_bM<{}_{cj}M_u$ or ${}_bM={}_{cj}M_u$

$$h_{wU} = \frac{1}{2}\left\{\left(d_j - 2S_r - h_{w(b)}\right) \pm \sqrt{\left(d_j - 2S_r - h_{w(b)}\right)^2 - \frac{4\left({}_{cj}M_u - M_{(b)}\right)}{N_{wy}}}\right\}$$

$$h_{wL} = h_{wU} + h_{w(b)}$$

$$h_r = d_j - 2S_r - h_{wU} - h_{wL}$$

In case of ${}_bM>{}_{cj}M_u$

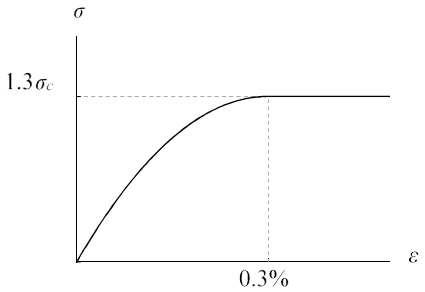
$$h_{wL} = \left(t_{bf}/2 + d_j - S_r\right) \pm \sqrt{\left(t_{bf}/2 + d_j - S_r\right)^2 - 2\left\{h_{w(b)}\left(t_{bf}/2 + d_j - S_r - h_{w(b)}/2\right) - \frac{M_{(b)} - {}_{cj}M_u}{N_{wy}}\right\}}$$

$$h_r = d_j - 2S_r - h_{wL}$$

${}_bM$: Beam bending moment
σ_{fu}: Tension strength of beam flange
σ_{fy}: Yield strength of beam flange
σ_{bw}: Yield strength of beam web
σ_c: Compression strength of concrete slab
H_b: Beam height
B_b: Beam width
t_{bf}: Beam flange thickness
t_{bw}: Beam web thickness
S_r: Weld access hole height
t_s: Concrete slab thickness adobe the deck
t_{db}: Steel deck height
B_c: Column width

$C=1.3\sigma_c\ t_s\ B_c$: Concrete strength
$N_{fu}=\sigma_{fu}\ t_{sf}\ B_b$: Beam flange ultimate strength
$N_{fy}=\sigma_{fy}\ t_{sf}\ B_b$: Beam flange yield strength
$N_{wy}=\sigma_{wy}\ t_{bw}$: Beam web yield strength
$d_j = H_b - 2t_{bf}$: Beam inner height between both flanges

Fig. 2 – Setting & condition of moment transmission efficiency



$$[0 \le \varepsilon < 0.3\%]$$

$$\sigma = 1.3f_c \times \frac{\varepsilon}{0.003} \times \left(2 - \frac{\varepsilon}{0.003}\right)$$

$$[0.3\% \le \varepsilon]$$

$$\sigma = 1.3f_c$$

Fig. 3 – Concrete hysteresis model

3. The comparison between test results and analysis results

In order to examine the validation of the algorism, the analysis results are compared to test results. The test results including specimen number are based on the database for completely composite beam under cyclic loading tests [8]. According that the skeleton curve under cyclic loading test results is equivalent to the relationship between moment and rotation angle under monotonic loading, the comparisons are conducted. The skeleton curve is obtained by relationship between moment and rotation angle in test results [11], [12].

Figure 5 shows the comparisons of relationship between moment and rotation angle. The specimen name is based on the database of composite beam [8]. The analysis results are generally smaller than test results. According to the results, the beam height has little effect on the elastic stiffness and the moment. From Ex01 to Ex03 results, the effect of moment transmission efficiency is little. Also, the ratio of section area of web to flange has also little effect on the moment. In Figure 5, the comparisons of strain progress of the lower beam flange

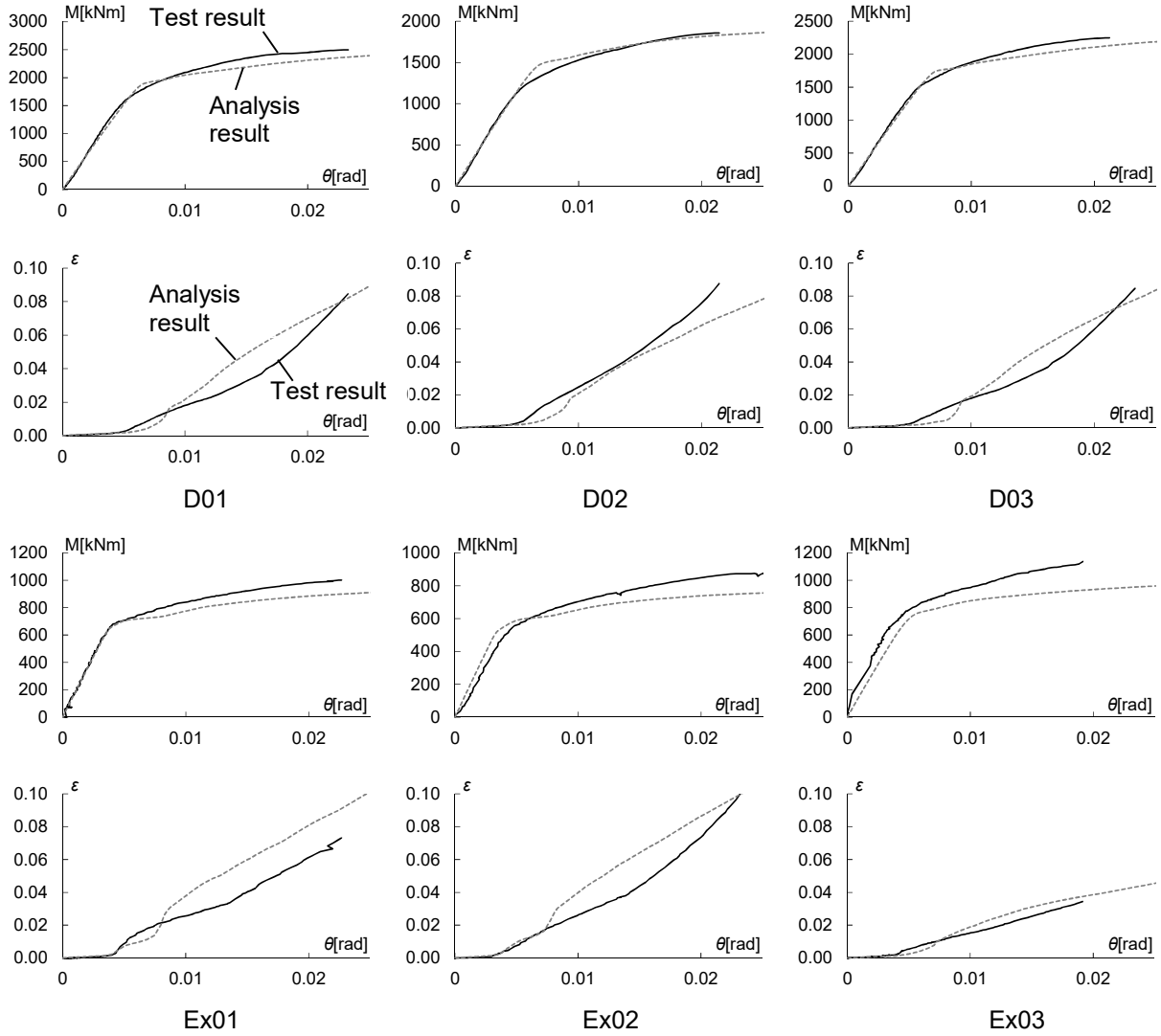


Fig. 5 – The comparison between the analysis results and test results

at the smallest section of web are also shown. Generally the analysis results are corresponded to test results. According to these progresses, the effects of beam height and the moment transmission efficiency are also little.

4. Parametric studies

4.1 Procedure of the studies

In order to clarify the effect of steel strength and the size of columns and beams to plastic deformation capacity of composite beam, parametric studies was conducted. The common parameters are steel kinds (beams are SN400B and columns are BCR295), the beam length (2,350mm), steel yield stress, and detail of concrete slab. The steel yield stresses are used the average values based on the survey of the steel stresses [13], that is, the yield stress of column is 392N/mm^2, the yield stress of beam is 305N/mm^2. The concrete slabs are designed with similar deck to previous test [7], that is, deck height is 75mm and slab thickness on the deck is 100mm. The tension strength of concrete is designed 21N/mm^2.

There are three parameters in this examination; the combination of the column and beam sizes, the existence of concrete slab, and the yield ratio of beam material. The beams in this study are set RH-400x200x8x13 and RH-600x200x11x17 according to the general beam size of middle-and-low rise buildings. The columns are set basically □350x350x12 or □350x350x19 in both beam. In case that the beam is RH-400x200x8x13, □300x300x16 and □300x300x19 are also added. This is because that these beam and column combinations have almost 1.3 on the connection coefficient of bare steel beam, however, the value of connection coefficient of composite beam are valid. The purpose of changing the combinations subcomponents is considered to the moment transmission efficiency. Also, the deference of slab effect is considered according to two size of beam and concrete slab with constant thickness. The yield ratio of beam material are set two case; 71.6% and 67.4%, which are corresponded to the sum or difference to the average value and the standard deviation of yield ratio [13].

Table 1 – Parameter List & energy dissipation capacity

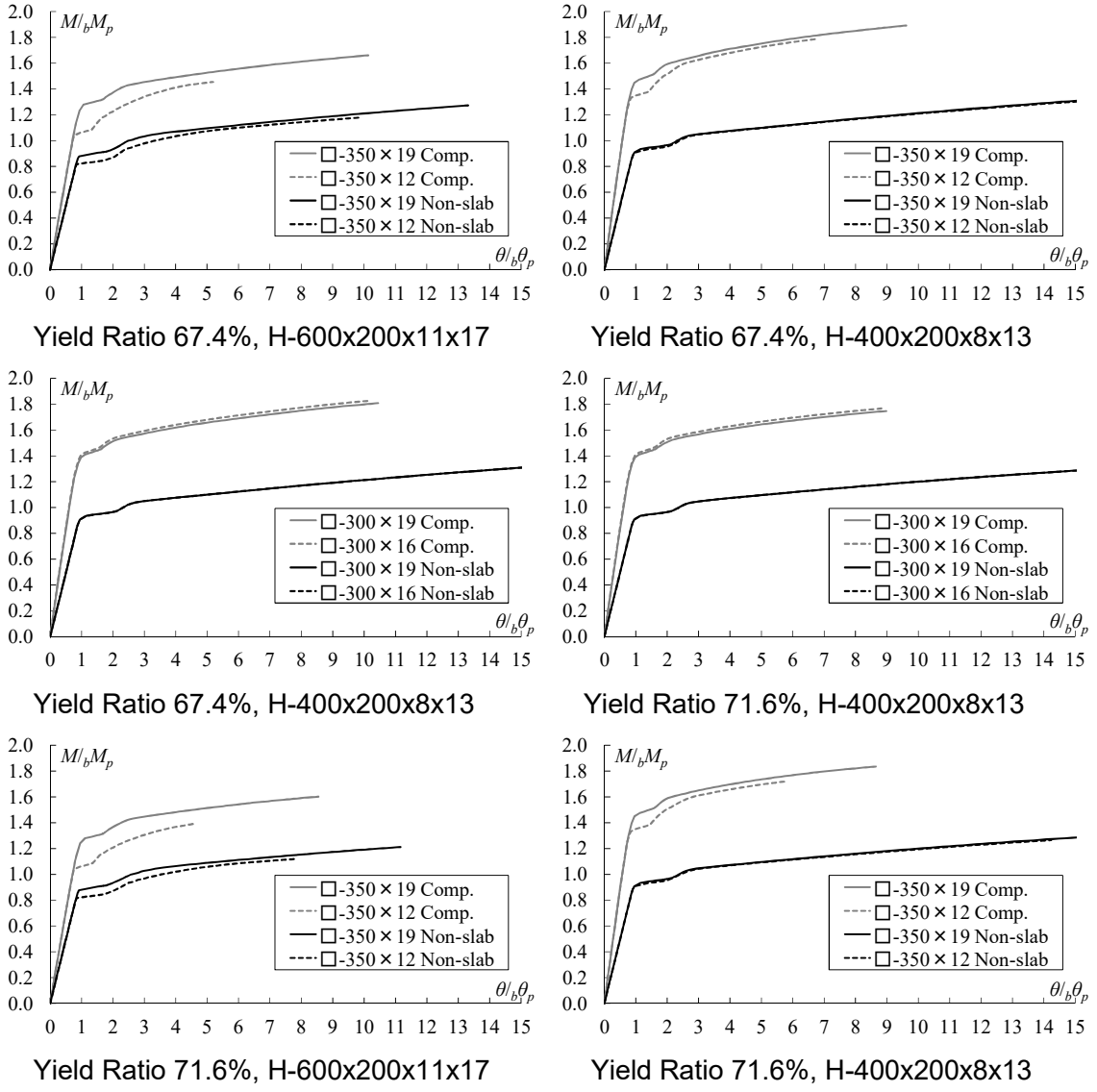
Beam [mm]	Column [mm]	Yield Ratio (σ_y/σ_u)	${}_s\alpha$	${}_c\alpha$	Wp Strain 2%		Wp Strain 5%		Wp Strain 10%	
					Bare steel	Composite	Bare steel	Composite	Bare steel	Composite
H-400×200×8×13	□-300×300×16	67.4%	1.31	1.29	3.0	2.9	21.2	14.9	61.8	43.4
		71.6%	1.24	1.24	3.0	3.0	18.2	13.2	53.1	36.2
	□-300×300×19	67.4%	1.31	1.33	3.0	3.0	21.2	14.7	61.8	44.0
		71.6%	1.24	1.28	3.0	3.0	18.2	13.0	53.0	36.5
	□-350×350×12	67.4%	1.30	1.20	2.7	2.5	16.1	6.6	50.0	26.8
		71.6%	1.23	1.15	2.7	2.5	12.9	6.3	41.7	21.6
	□-350×350×19	67.4%	1.31	1.32	3.0	3.0	21.2	15.3	61.8	42.1
		71.6%	1.24	1.27	3.0	3.1	18.2	13.2	53.1	36.8
H-600×200×11×17	□-350×350×12	67.4%	1.15	1.06	3.0	2.7	11.2	8.2	41.5	24.8
		71.6%	1.09	1.01	3.0	2.7	9.9	7.9	31.1	20.6
	□-350×350×19	67.4%	1.22	1.17	3.7	4.3	17.1	16.4	62.3	62.5
		71.6%	1.16	1.14	3.6	4.4	12.9	13.6	49.8	50.4

*'strain -%' shows the strain value of the lower beam flange

4.2 The relationships between moment and rotation angle

Figure 6 shows the relationships between moment and rotation angle in bare steel beam and composite beam obtained by the algorism as showed at chapter 2. Here, every rotation angle is

divided by ${}_b\theta_p$ (the idealized rotation angle of bare steel beam to elastic-theory deformations when the moment is the full-plastic moment). Generally, the moment of composite beam is 1.5 times larger than the moment of bare steel beam, although rotation angle of composite beam is smaller than the value of bare steel beam. When the beam height is 600mm and skin-plate is relatively thin, both moments of composite beam and bare steel beam are smaller than the moment with thick skin-plate. Moreover, deformation capacity of composite beam is affected by beam height.



Yield Ratio 67.4%, H-600x200x11x17

Yield Ratio 67.4%, H-400x200x8x13

Yield Ratio 67.4%, H-400x200x8x13

Yield Ratio 71.6%, H-400x200x8x13

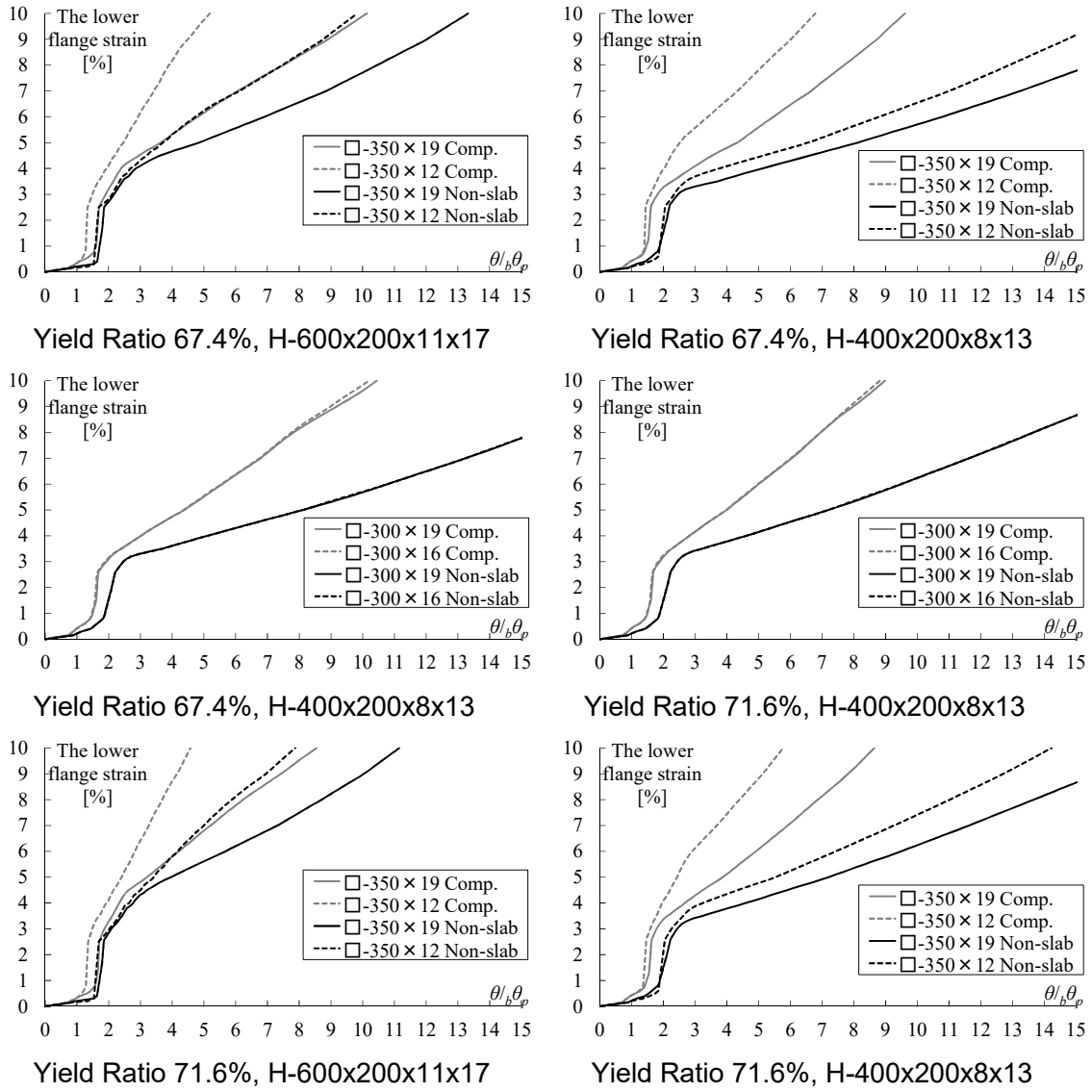
Yield Ratio 71.6%, H-600x200x11x17

Yield Ratio 71.6%, H-400x200x8x13

Fig. 6 – The relationships between moment and rotation angle

Figure 7 shows the comparisons of strain progress of the lower beam flange at the smallest section of web. The horizontal axis is dimensionless rotation angle $\theta/{}_b\theta_p$ as same value in Figure 6. When $\theta/{}_b\theta_p$ is under 2.0, the strain of each model are similar regardless the existence of concrete slab, beam height, and moment transmission efficiency. After that, the strain of

composite beam are increased immediately than bare steel beam through $\theta/_b\theta_p$ is small. This trend is remarkable in case the beam height is 400mm, or skin-plate is relatively thin. On the other hand, yield ratio is little affected to the relation of strain and rotation angle. One of the effective reasons that plastic deformation capacity of composite beam is smaller than the value of bare steel beam is rise of the plastic neutral axis of beam [7]. In composite beam, the plastic neutral axis moves to near the upper beam flange. Therefore, plastic deformation capacity of composite beam decreases according to plastic area of composite beam is smaller than bare steel beam accompany with strain hardening.



Yield Ratio 67.4%, H-600x200x11x17

Yield Ratio 67.4%, H-400x200x8x13

Yield Ratio 67.4%, H-400x200x8x13

Yield Ratio 71.6%, H-400x200x8x13

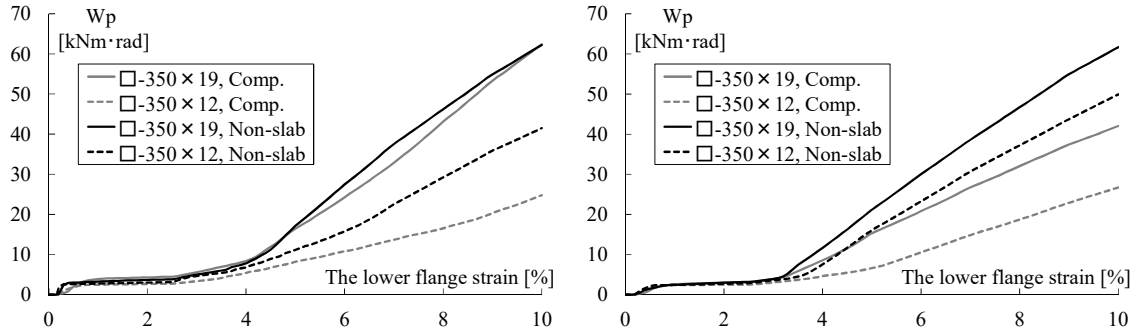
Yield Ratio 71.6%, H-600x200x11x17

Yield Ratio 71.6%, H-400x200x8x13

Fig. 7 – The relationships between strain and rotation angle

4.3 Plastic energy dissipation capacity and damage of beam

The plastic deformation capacity of beams is deeply corresponded to the strain of the lower beam flange at the smallest section of web as shown above. The strength of composite beam is generally smaller than the value of bare steel beam, therefore, plastic energy dissipation capacity of composite beam and bare steel beam are focused in this section. According to integrate the moment at the beam end and rotation angle, plastic energy dissipation capacity W_p is obtained. W_p in composite beam or bare steel beam have almost linear relationship to the strain of the lower beam flange after these beams are yield as shown in Figure 8. W_p in composite beam is smaller than the value of bare steel beam after the strain of the lower beam flange is 5%, this trend is remarkable when the beam height is relatively small and moment transmission efficiency of web is small according to column flange is thin. Plastic energy dissipation capacity in composite beam ${}_cW_p$ and plastic energy dissipation capacity in bare steel beam ${}_bW_p$ of each parametric model are also shown in Table 1.



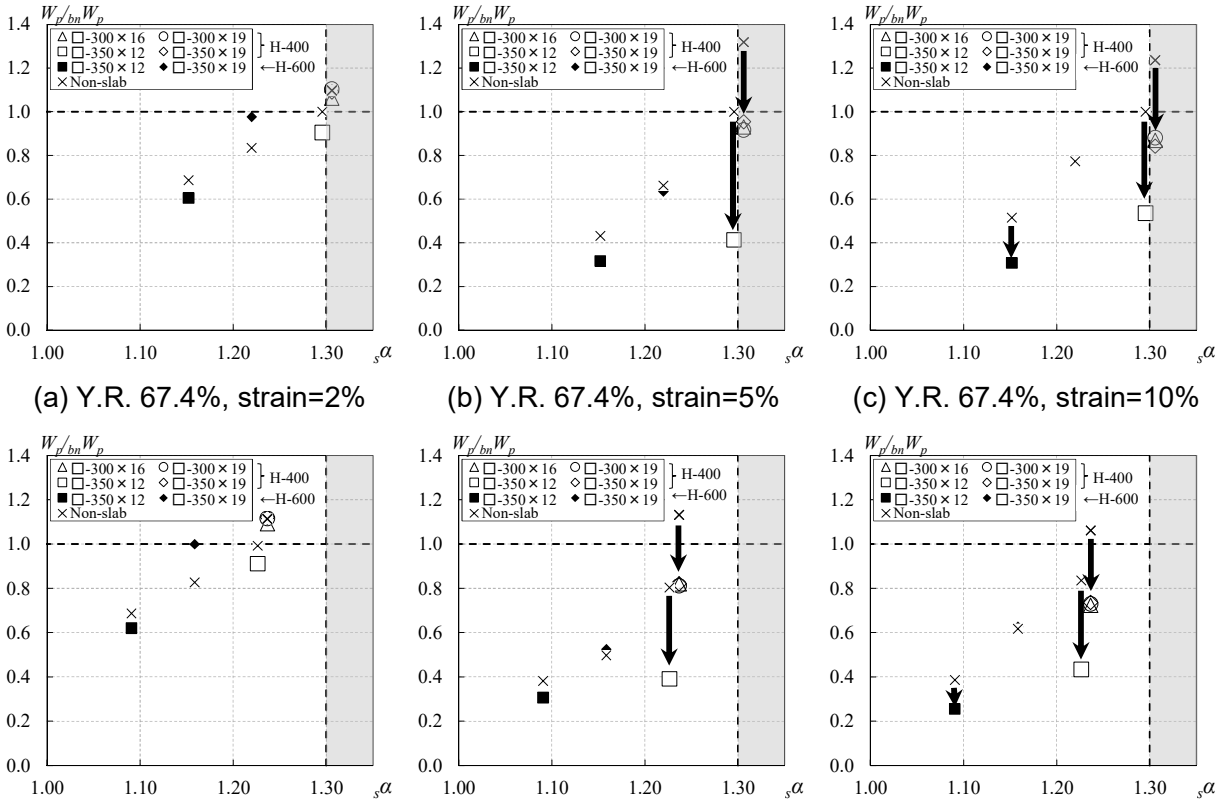
Yield Ratio 67.4%, H-600x200x11x17 Yield Ratio 67.4%, H-400x200x8x13

Fig. 8 – Plastic energy dissipation capacity and strain at the lower beam flange relationships

In order to show the effect of slab and member size, plastic energy dissipation ratio ${}_{bn}W_p/W_p$ is decided. The numerator is plastic energy dissipation capacity in each parametric model W_p. The denominator is the plastic energy dissipation capacity in the bare steel beam (${}_{bn}W_p$) which have RH-400x200x8x13 as beam, □350x350x12 as column, and 67.4% as member yield ratio. The reason that the model is selected as the denominator of the ratio is its connection coefficient as bare steel beam is 1.3. As shown chapter 1, in seismic design in Japan, the connection coefficient of bare steel beam is very important and it is recommended to over 1.3 in steel beam. Therefore, using the plastic energy dissipation capacity in bare steel beam which connection coefficient is 1.3 as the denominator, the plastic energy dissipation ratio means the structural margin of plastic deformation capacity in composite beam or bare steel beam against demand value of bare steel beam in seismic design.

In this section, three timings are focused as the example of plastic deformation; the strain of the lower beam flange is 2%, 5%, and 10%. According to the stress and strain relation of the lower beam flange, 2% strain is showed when it is just after yield, 5% strain is showed when strain hardening is progressed, and 10% strain is showed when it is just before fracture occurred. Figure 9 shows plastic energy dissipation ratio ${}_{bn}W_p/W_p$ in these three timings. When the strain of the lower beam flange is 2% as shown Figure 9 (a) & (d), ${}_{bn}W_p/W_p$ in composite beam have little deference to ${}_{bn}W_p/W_p$ in bare steel beam. However, the strain of the lower beam flange is 5% and 10%, ${}_{bn}W_p/W_p$ in composite beam decreased 30-50% than ${}_{bn}W_p/W_p$ in bare steel beam.

The decreasing of $W_p/_{bn}W_p$ in composite beam is remarkable when column flange thickness is 12mm, that is, moment transmission efficiency is small. In case of beam height is 600mm which the connection coefficient in bare steel beam is originally small, the differences of $W_p/_{bn}W_p$ between composite beam and bare steel beam is little. As shown in Figure 9 (d)-(f), high yield ratio is affected to the connection coefficient in bare steel beam is small, however, the decreasing of $W_p/_{bn}W_p$ in composite beam is small. Moreover, if beam and column combinations have sufficient plastic deformation capacity as bare steel beam as shown gray area in Figure 9 (a)-(c), concrete slab make plastic deformation capacity of the beam small.



(a) Y.R. 67.4%, strain=2% (b) Y.R. 67.4%, strain=5% (c) Y.R. 67.4%, strain=10%

(d) Y.R. 71.6%, strain=2% (e) Y.R. 71.6%, strain=5% (f) Y.R. 71.6%, strain=10%

*'strain -%' shows the strain value of the lower beam flange

Fig. 9 – Plastic energy dissipation ratio & connection coefficient in bare steel beam relationships

5. Conclusion

Based on previous cyclic loading test of wholly composite beam, the algorithm of composite beam with RHS column, deck-plate typed concrete slab is shown. In order to achieve preliminary trend of plastic deformation capacity of composite, parametric studies was conducted. Focused on the energy dissipation ratio as comparing to the plastic deformation capacity between composite beam and bare steel beam, obtained results shows that energy dissipation capacity in composite beam are almost similar to bare steel beam just after beams have been yield. However, energy dissipation capacity in composite beam are decreased after plastic deformation of beams have been increased. The trend is remarkable in case that both

beam height and moment transmission efficiency are small. Moreover, if beam and column combinations have sufficient plastic deformation capacity as bare steel beam, concrete slab make plastic deformation capacity of the beam small.

REFERENCES

[1] Editorial committee of technical criteria references on structure of buildings (2007). Technical criteria references on structure of buildings Ver. 2007.

[2] Igarashi S, Inoue K, Kim SE, & Tada M (1983). Experimental studies on the Elastic-plastic hysteretic behavior of fully composite beams subjected to earthquake type of loading. *Journal of Structural and Construction Engineering, AIJ, 333*, 63-72, JAPAN

[3] Tateyama E, Inoue K, Sugimoto S, & Matsumura H (1988). Study on ultimate bending strength and deformation capacity of H-shaped beam connected to RHS column with through diaphragms. *Journal of Structural and Construction Engineering, AIJ*, 389, 109-121, JAPAN.

[4] Okada K, Oh SH, & Yamada S (2003). Effect of joint efficiency at beam-to-column connection on ductility capacity of composite beams. *Journal of Structural and Construction Engineering, AIJ*, 573, 185-192, JAPAN.

[5] Ishii T, & Morita K (2001). Experimental Study on Fracture Behavior of Composite Beam-to-SHS Column Connection. *JSSC Journal of Constructional Steel, JSSC, 8(31)*, 65-79, JAPAN.

[6] Tanaka T, Suita K, Asakura N, Tsukada T, Uozumi N, & Takatsuka K (2015). Influence of floor slab on deformation capacity - Deformation capacity of welded beam-to-column connection subjected to repeated plastic strain Part 5 -. *Journal of Structural and Construction Engineering, AIJ, 707*, 127-136, JAPAN.

[7] Yamada S, Kishiki S, & Shimada Y (2010): Strength Evaluation of Fully Composite beam under positive bending. *Proceedings of JSSC (18), JSSC*, 93-98, JAPAN.

[8] Shimada Y, Yamada S & Yasuda B (2016). Calculation Method of Connection Coefficient of Composite Beam. *Journal of Structural and Construction Engineering, AIJ, 724*, 1005-1014, JAPAN.

[9] Yamada S, Jiao Y & Kishiki S (2015). Evaluation Method of Plastic Deformation Capacity of Steel Beam governed by Ductile Fracture at the Toe of the Weld Access Hole. *Journal of Structural and Construction Engineering, AIJ, 711*, 767-777, JAPAN.

[10] Japan Concrete Institute (1996). *Concrete Handbook the Second Edition*, 240, JAPAN.

[11] Kato B & Akiyama H (1968). The Ultimate Strength of the Steel Beam-Column (Part 4), *Journal of Structural and Construction Engineering, AIJ, 151*, 15-20, JAPAN.

[12] Akiyama H & Takahashi M (1990). Influence of Bauchinger Effect on Seismic Resistance of Steel Structures, *Journal of Structural and Construction Engineering, AIJ, 418*, 49-57, JAPAN.

[13] Fujisawa K, Ichinose Y, Sugimoto M, & Sonoda M (2013). Statistical Study on Mechanical Properties and Chemical Compositions of SN Steels. *Summaries of Technical Papers of Annual Meeting of AIJ, AIJ, stru.-3*, 699-700, JAPAN.

BEHAVIOR OF COMPOSITE DOWELS POSITIONED CLOSE TO THE SURFACE OF CONCRETE SLABS

Prof. Dr.-Ing. Wolfgang Kurz
Yannick Broschart, M.Sc.
Institute of Steel Structures, University of Kaiserslautern,
Paul-Ehrlich-Straße 14, 67663 Kaiserslautern, Germany
wolfgang.kurz@bauing.uni-kl.de
yannick.broschart@bauing.uni-kl.de

Dipl.-Ing. Joanna Gajda
BORAPA Ingenieurgesellschaft mbH,
Luxemburger Straße 1, 67657 Kaiserslautern, Germany
gajda@borapa.de

ABSTRACT

Composite dowels are efficient shear connectors that become more and more common in use for composite beams. They can be used as an economic alternative to headed studs with various advantages.

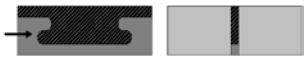
Modern concrete slabs are dimensioned increasingly thinner and often include several additional functions, for example air conditioning or thermal activation of the concrete. For those applications composite dowels can be positioned horizontally in the concrete slab (Fig. 1). Existing investigations on composite dowels describe different failure modes such as splitting of the concrete, local compression of the concrete, prying-out of a concrete cone or plasticizing of the steel.

At *University of Kaiserslautern* composite dowels with positions close to the free surface of the concrete slab were investigated experimentally by push-out-tests and on the basis of numerical simulations. In addition, the positive influence of a spiral reinforcement in the dowels was analyzed. Further primary and secondary failure mechanisms were observed for this specific position of the composite dowels. These investigations and a design approach will be presented within the paper.

INTRODUCTION

In composite slabs longitudinal shear forces have to be transferred between the concrete section and the steel profiles. This shear connection is conventionally realized by headed studs. As an alternative, composite dowels can be installed. Existing investigations and regulations on composite dowels include various failure modes of the structure. These are summarized and illustrated schematically within Table 1 in compliance with [Berthellemy 2011] and [Heinemeyer 2011].

Table 1 – Compilation of observed failure modes of composite dowels

Symbol	Failure mode	Failure pattern longitudinal section / cross section
P_{sp}	splitting	
P_{lc}	local compression of the concrete	
P_{sh}	shearing of the composite dowel	
P_{po}	pry-out of the concrete	
P_{pl}	plasticizing of the steel	
P_{edge}	edge failure	
P_{spo}	semi-pry-out of the concrete	

Specifically, if the position of the composite dowels is close to the free concrete surface, as to be seen in Fig. 1, an additional failure mode can occur in which the concrete cover at the edge of the concrete slab spalls. This failure mode was called ‘edge failure’. At *University of Kaiserslautern* push-out-tests with puzzle-shaped composite dowels positioned close to the free surface were performed in the context of a research project aiming to respect these effects within the design approaches. Furthermore, the experimental test results were compared to the outputs of numerical simulations.

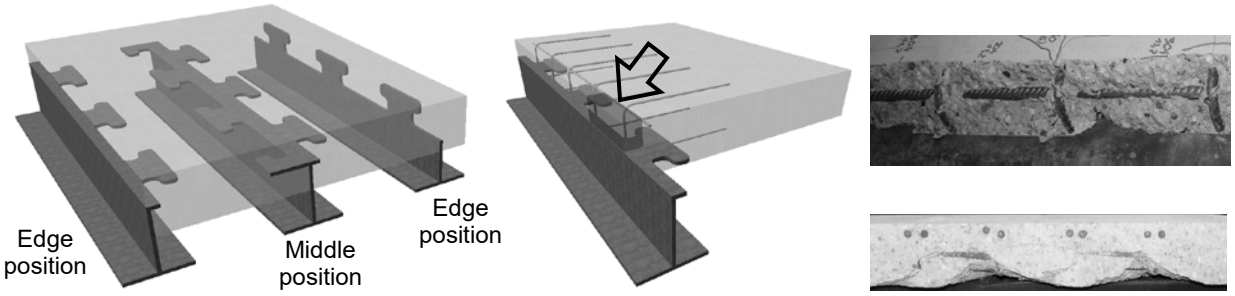


Fig. 1 – Possible positions of puzzle-shaped composite dowels close to the free surface (left), affected concrete cuboid (center), fracture area after the spalling (top right) and semi-pry-out of half concrete cones (bottom right)

EXPERIMENTAL INVESTIGATIONS

The behavior of composite dowels close to the free surface of concrete slabs was investigated experimentally with the help of push-out-tests. In total, 46 push-out-tests were performed with varying constructive and geometric parameters as well as with different material properties. Table 2 summarizes the investigated parameters. Two types of push-out specimens were realized: PO, representing the edge position of the composite dowels, and PO A, representing the middle

position, as to be seen in Fig. 3 and Fig. 4. The PO A specimens were produced by bending the steel teeth alternately to the left and to the right.

Table 2 – Overview of the varied parameters and material properties

Parameter	Range of variation
Composite dowel geometry	P – Puzzle shape (r)*
	K – Clothoid shape
Composite dowel thickness t_w	4 mm (r)
	6 mm
	8 mm
Steel grade	S 235 JR (r)
	S 355 JR
Concrete strength class	C 25/30 (r)
	C 30/37
	C 35/45
Concrete slab thickness d_c	100 mm (r)
	150 mm
Concrete slab width b_c	200 mm
	300 mm (r)
Embedment depth of the composite dowel h_e	25 mm (r)
	50 mm
Reinforcement per composite dowel A_B	non-existent
	1Ø8
	2Ø6
	3Ø6
	2Ø8 (r)
Spiral reinforcement per composite dowel A_w	non-existent (r)
	ø 50 mm, d_s=5 mm, s_w=25 mm
	ø 60 mm, d_s=5 mm, s_w=25 mm

* (r) reference test

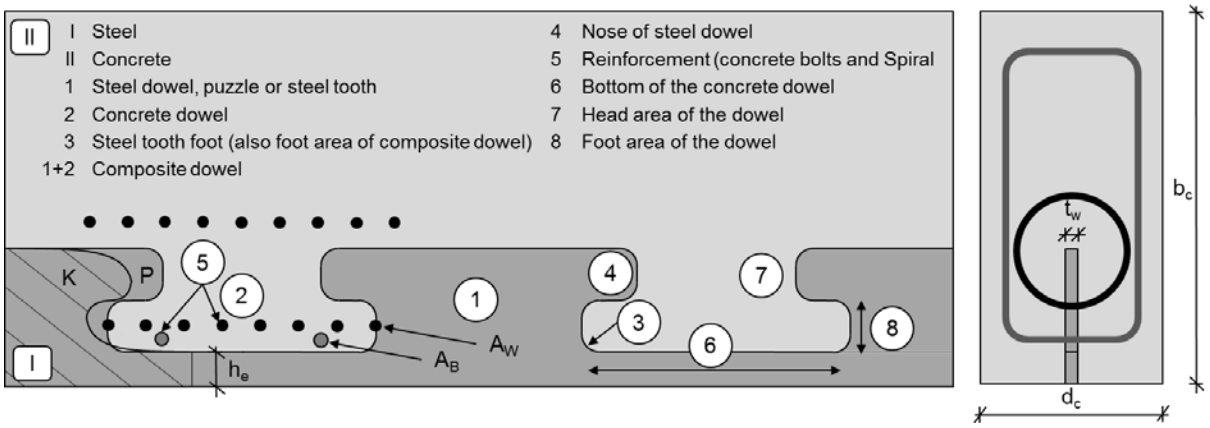


Fig. 2 – Designation of the different parts of the composite dowel

The first series consisted of first trial tests to define the dimensions of the subsequent specimens. As a consequence, the thickness of the concrete slab was set to 100 mm, comparable to slim sandwich constructions. Further dimensions of the specimens can be seen within Fig. 4. The width of the supports as well as the relation between the height and the width of the specimen were chosen with regard to receiving concrete compression struts with an angle of approximately 45°.

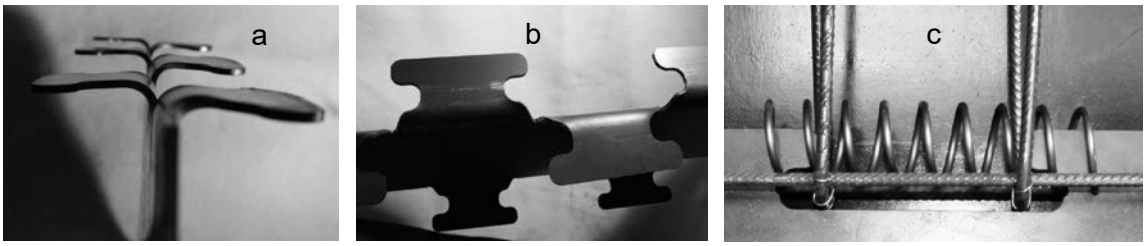


Fig. 3 – Puzzle geometry after bending (a, b), spiral and stirrup reinforcement (c)

The reference type of reinforcement consisted of two stirrups per concrete dowel placed 12,5 cm apart from each other with diameters of 8 mm. Furthermore, a spiral reinforcement was installed in some specimens to improve the hydrostatic compression stress area in front of the steel teeth by a confinement of the concrete. Underneath the lowest half steel teeth in test specimen, polystyrene cuboids were installed (Fig. 4) to avoid the contact between steel and concrete in this area, because this would have fuged the measurement of the resistance of the full composite dowels. At the bottom of the concrete slabs, a tension rod was applied to avoid drifting apart.

The load on the specimen was increased up to 100 kN with a speed of 4 mm/min and afterwards decreased to 20 kN. This cycle was repeated for 25 times, in order to set aside the adhesive friction, before the load was raised to the failure of the specimen with a speed of 0,25 to 0,5 mm/min. The load increase was paused at load level steps of 50 kN to determine the quasi-static load-displacement diagram.

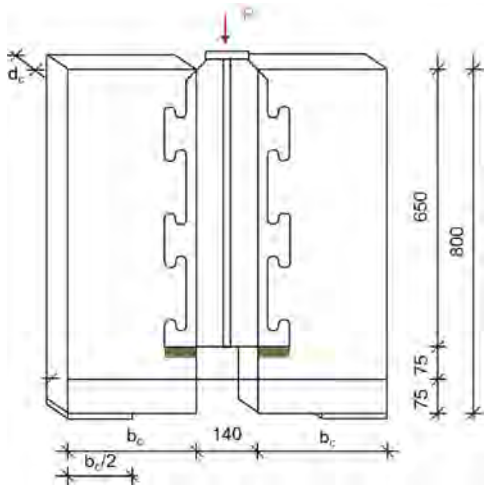
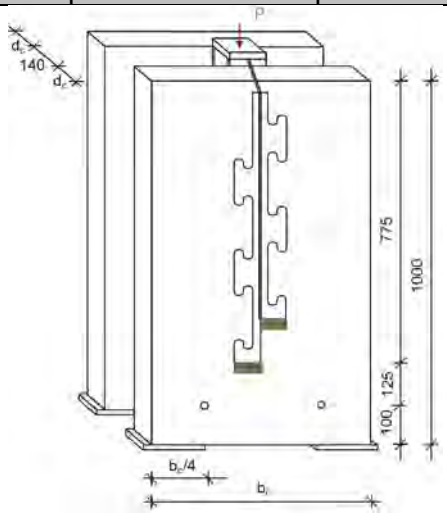
Experimental setup of the push-out-tests	
PO push-out-tests Edge position of the composite dowel	**PO A push-out-tests** Middle position of the composite dowel
	

Fig. 4 – Experimental setup of the two types of push-out-tests

During the experimental procedure, the load was measured as well as the slip δ, which describes the relative displacement between the steel profile and the concrete section in direction of the x-axis. Additionally, the relative displacement Δ of the two concrete slabs to one another in direction of the z-axis was registered with the help of inductive displacement transducers as well as the thickness variation of the concrete slabs in direction of the y-axis (Fig. 5).

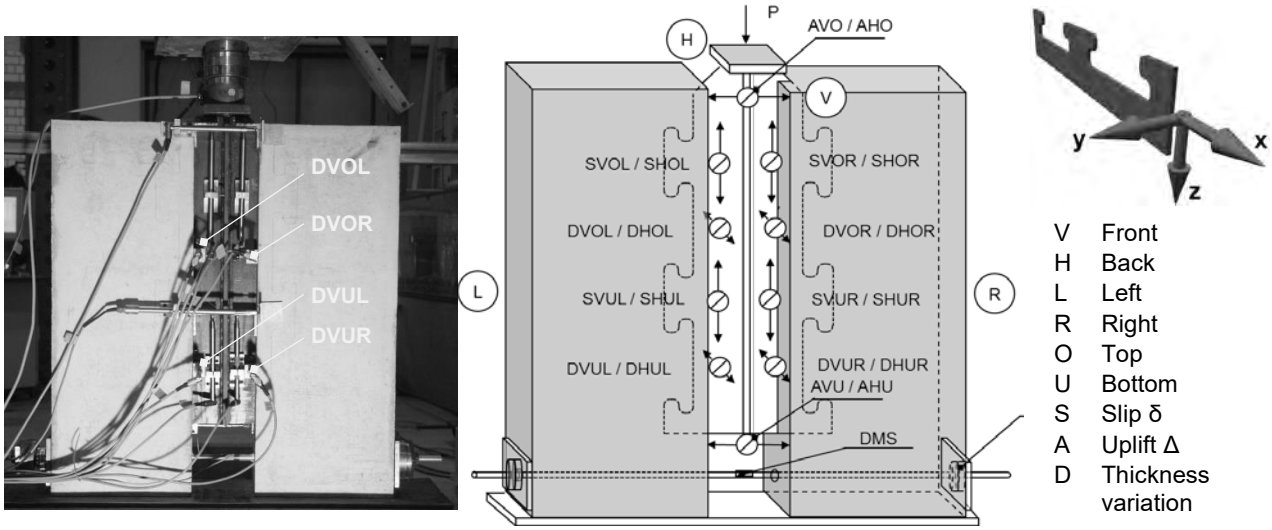


Fig. 5 – Geometric assumptions for the design approach in xz-view (left) and yz-view (right)

The following table shows the varied properties of seven push-out-specimens (PO) without a spiral reinforcement: the thickness of the concrete slab b_c, the depth of the embedding of the steel web into the concrete slab h_e, the tensile strength of the concrete f_{ctm} and the yield strength of the steel f_y.

Table 2 – Properties of the tested specimens without spiral reinforcement

Without spiral reinforcement			**PO 34**	**PO 36**	**PO 38**	**PO 40**	**PO 42**	**PO 44**	**PO 46**
Thickness of the concrete slab	b_c	[mm]	100	100	150	100	100	150	150
Depth of the embedding	h_e	[mm]	25	25	25	25	50	25	50
Tensile strength of the concrete	f_{ctm}	[MPa]	2,2	2,2	2,2	2,9	2,9	2,9	2,9
Yield strength of the steel	f_y	[MPa]	362	296	296	296	296	296	296

The typical crack pattern of the PO specimens is shown within Fig. 6. The splitting of the concrete slabs within the xz-plane could not be seen at the surface. The first surface cracks appeared as splitting cracks underneath the steel teeth in direction of the z-axis and successively grew towards the centre of the concrete slabs with an increasing incline towards the supports. The final surface cracks initiated the spalling of the concrete cover and the edge failure, starting at the upper end of the concrete slab and growing downwards in direction of the x-axis immediately.

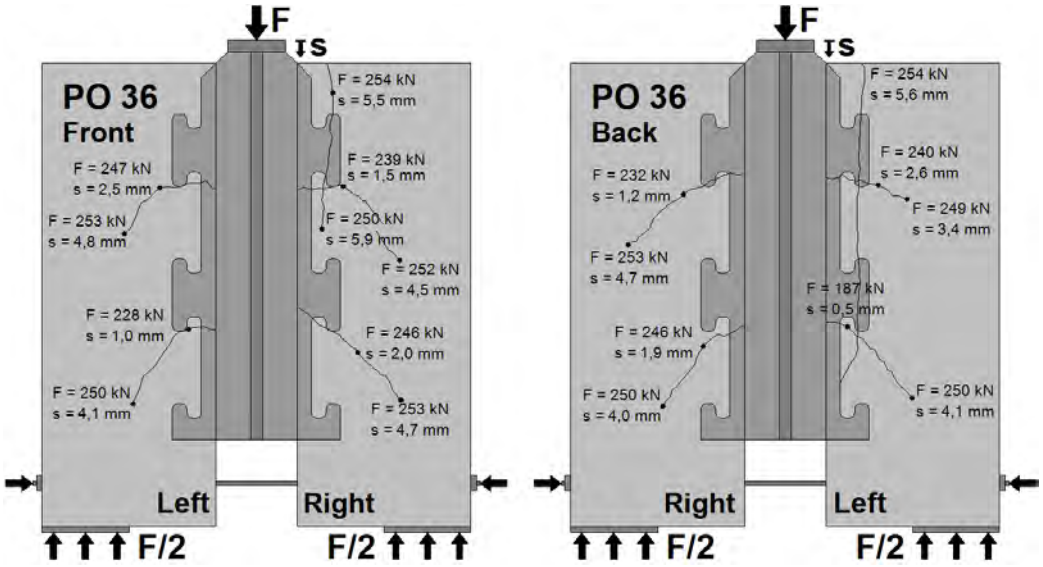


Fig. 6 – Typical crack pattern after the failure of the specimen using the example of PO 36

The load-slip-diagram in Fig. 7 shows the testing machine load as a function of the slip of the composite dowels in direction of the x-axis. The final failure mode of the specimens is edge failure. In spite of the slim structure elements, a distinctly ductile behavior could be observed.

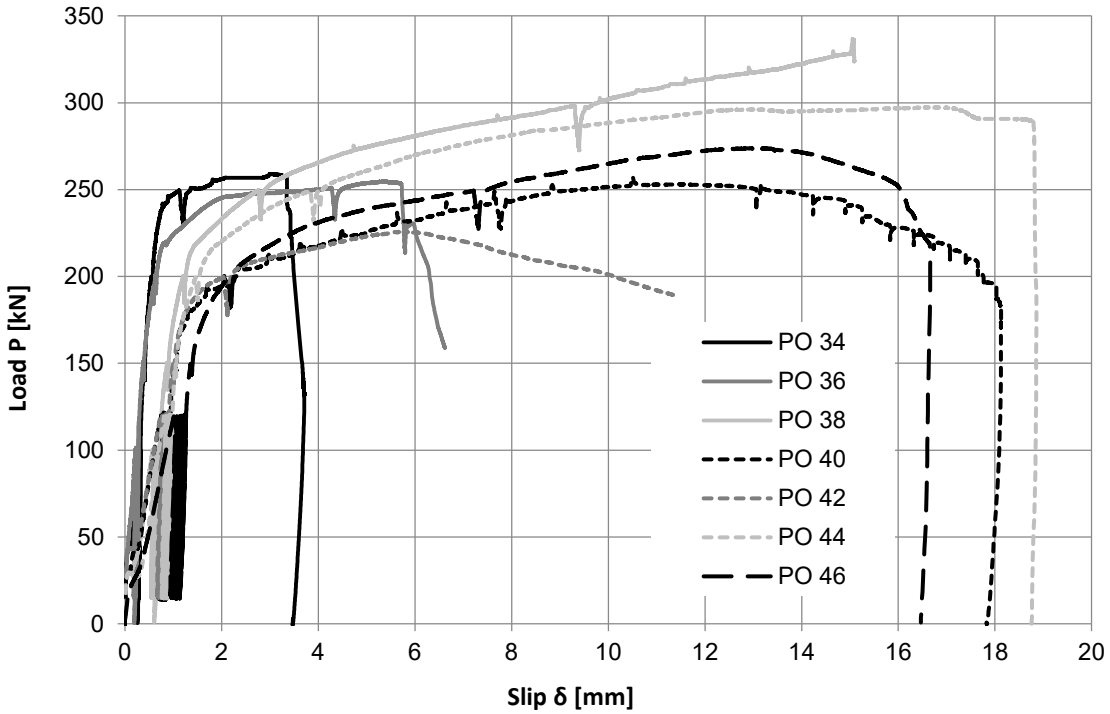


Fig. 7 – Load-slip-diagram of the PO specimens

NUMERICAL SIMULATIONS

The experimental tests were numerically simulated with the FE software ABAQUS 6.14-2 from Simulia. The software does not only consider geometric non-linearity but also material non-linearity. As a matter of fact the modelling of the concrete's tension and compression stress behavior decisively influences the simulation results and should be represented as realistically as possible. The so-called 'Concrete Damage Plasticity Model' (CDP) was most appropriate to simulate the experimental results and to show a realistic failure pattern. The approximation of the concrete's material properties is schematically presented in Fig. 8.

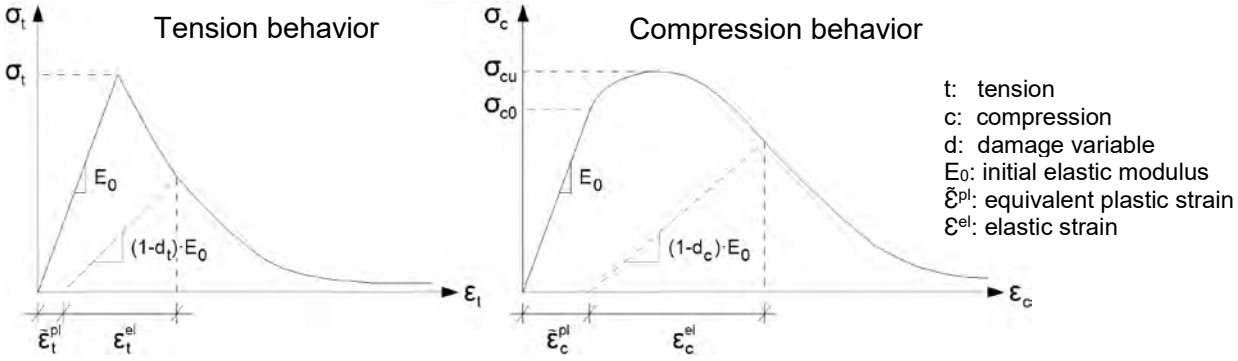


Fig. 8 – Uniaxial tension and compression stress behavior of the concrete [Simulia 2014]

The following figures (Fig. 9 and Fig 10) show the load-slip-curves of the simulations in comparison to those of the experiments. Up to a certain point, there is a high conformity. But the decrease of the resistance of the composite dowels cannot be sufficiently simulated due to the underlying model of tension behavior. In reality, if concrete reaches its tensile fracture strain, a crack occurs and the transferable stress declines immediately, while in the simulation's material model some load bearing capacity has to remain for numerical reasons.

Additionally, the tensile-damage-rate of the concrete is illustrated (Fig. 9, right). The visible pattern is similar to surface cracks in direction of the x-axis which initiated the edge failure (Fig. 6).

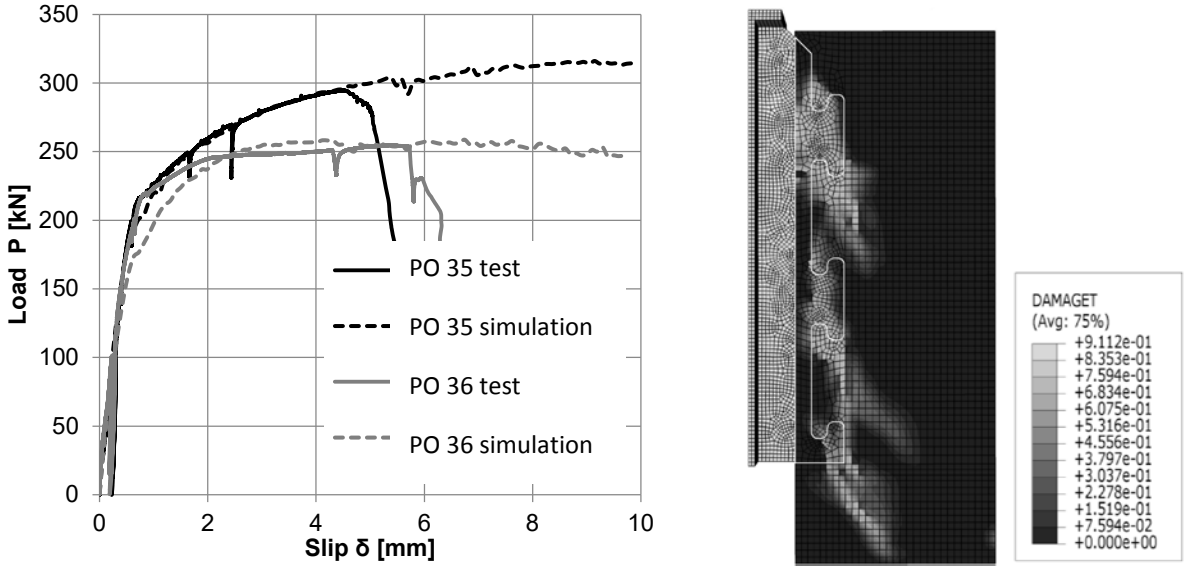


Fig. 9 – Comparison of the tested and the numerically simulated load-slip-curves of PO specimens (left) and tensile-damage-rate of the concrete (right)

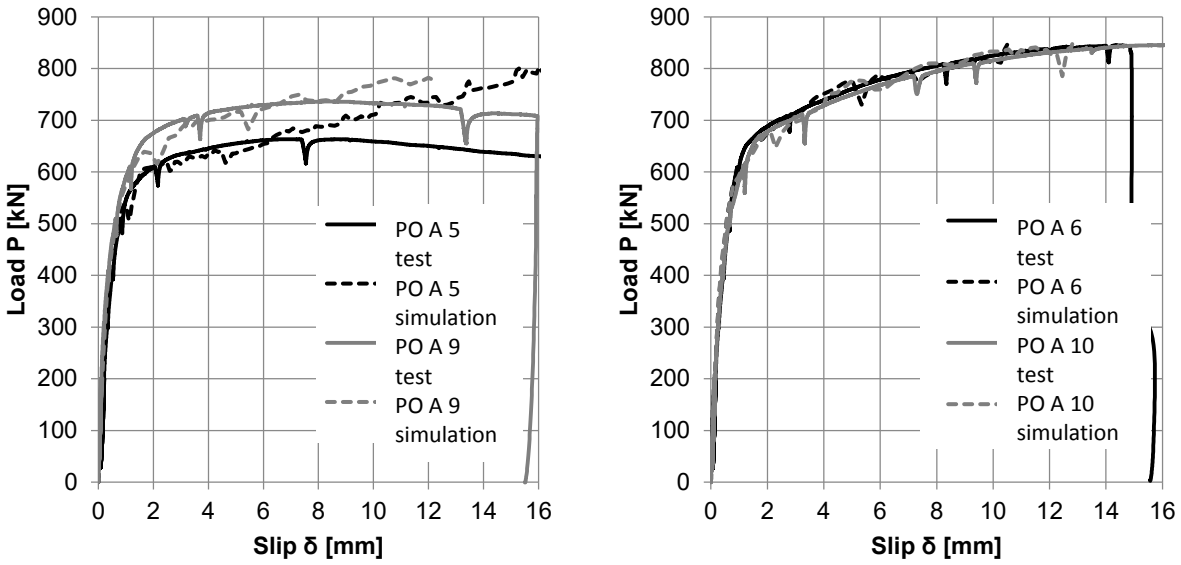


Fig. 10 – Comparison of the experimentally tested and the numerically simulated load-slip-curves of PO A specimens

CONSIDERATIONS ON THE LOAD TRANSFER MECHANISMS

On the basis of the measurement results and the numerical simulations, load transfer mechanisms were modelled and are illustrated three-dimensionally at the bottom of Fig. 11 in a simplified way. The load-slip-diagram of PO 36 can be partitioned into five sections. The successive decline of the specimen's stiffness is an indicator for the transition of the load transfer mechanism. The first decline of the stiffness (Fig. 11-A) is considered to occur because of the detaching of the adhesive friction. Independently of this effect, in sections I and II (Fig. 11) the concrete struts were considered to start at the hydrostatic compression stress area in front of the steel tooth. At their other end the cone-shaped struts are supported by the concrete slab. To obtain the state of equilibrium, the compression struts have to be connected by circularly arranged tension struts. This tension ring is interrupted by the steel plate of the composite dowel. As a matter of fact and corresponding to the measurement of the stirrup's strain and the thickness variation of the concrete slab in direction of the y-axis, the first crack area seems to appear inside of the concrete slab parallel to the xz-plane (Fig. 11-B). This crack area cannot be seen as a surface crack. In sections III and VI (Fig. 11) further tension struts occur behind the hydrostatic stress area because of the connection of the concrete in front of the steel tooth to the concrete area behind the steel tooth. Point C (Fig. 11) can be interpreted as the plasticizing of the steel teeth. The second crack area appears in the yz-plane, as a consequence of the previously mentioned tension struts reaching the tensile strength of the concrete, and is visible at the specimen's surface (Fig. 11-D). Immediately after the occurrence of the first crack area, the compression struts transform with regard to the newly shaped concrete cuboids and form two elliptical compression cones. To design the schematic illustration more clearly, these two elliptical compression cones were not shown right after their occurrence but only afterwards in Fig. 11-V. Finally, the concrete tension in direction of the z-axis reaches the concrete tensile strength and the third crack area appears in xy-plane, initiating the edge failure (Fig. 11-E).

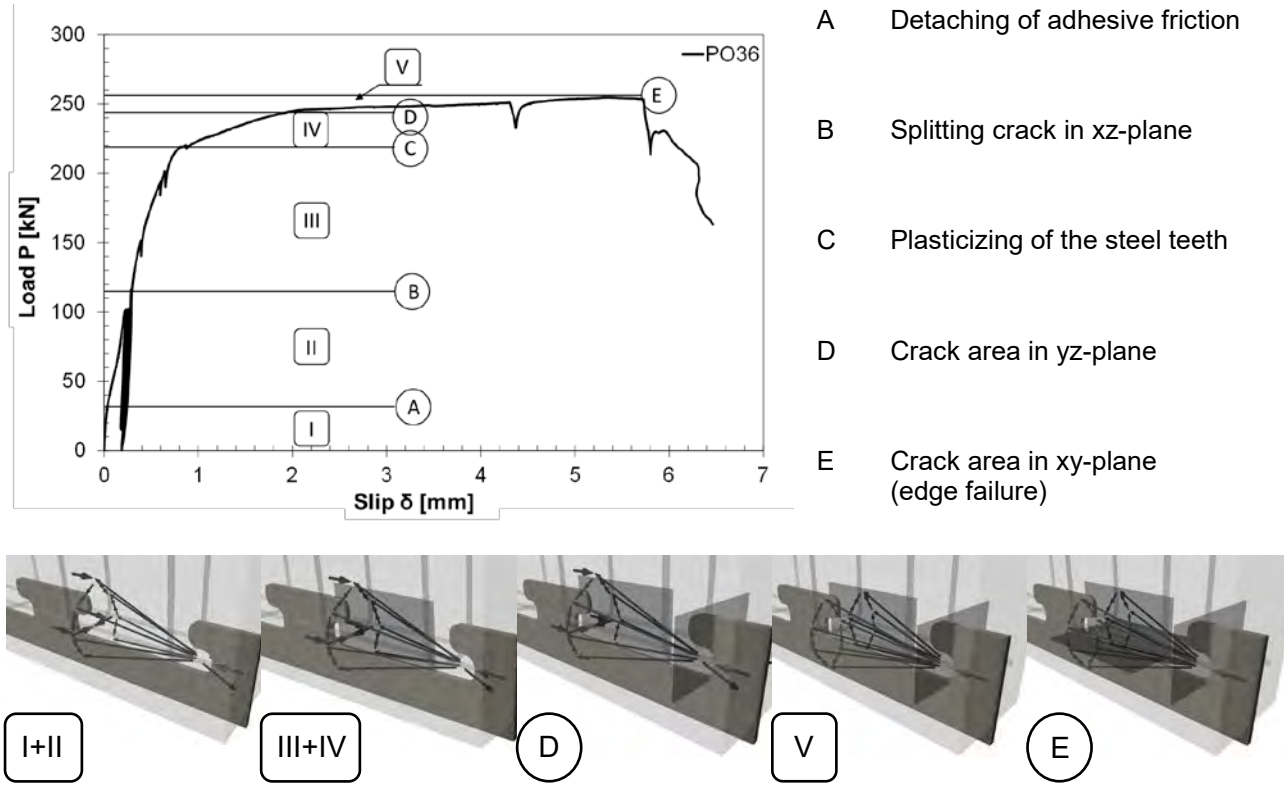


Fig. 11 – Load transfer mechanisms and resulting crack areas

DEVELOPMENT OF A CALCULATION MODEL

On the basis of the previously presented considerations on the load transfer mechanisms, a design approach was developed for the failure mode edge failure. Therefore, geometric assumptions were made, which are illustrated within Fig. 12 for one half of the concrete slab at one side of the composite dowel. Into this concrete area half the steel tooth force ½·P spreads out. Unavoidably, a part of this force spreads out in z-direction into the concrete cover because of its stiffness. The resulting force flow can be idealized by a strut-and-tie model. As a first assumption the present force ½·P was split into one half entering the upper concrete slab and one half entering the concrete cover. This force component consequently has an amount of ¼·P. A more reasonable apportionment of this force will subsequently be taken into account by the calibration factor η. Corresponding to this model, the resulting vertical component F_z depends on the height of the concrete cover c_z and on the distance between the steel tooth and the reinforcement stirrup s_x. Definitively, the vertical component F_z has to be transferred into the stirrup reinforcement by concrete tension. The model assumes a load diffusion angle α. As a result, an operational crack area $A_{cr,op}$ can be imagined on the level of the stirrup reinforcement. This area is not equivalent to the true crack area. It only serves as an operational value to calculate the resistance against edge failure, which is assumed to occur as soon as the present stress within $A_{cr,op}$ reaches the concrete's tensile strength f_{ct}. Furthermore, there is a horizontal force component F_y because of the offset of the steel tooth force relative to the concrete cuboid in direction of the y-axis, which causes a bending of the concrete cuboid around the x-axis and leads to additional bending stresses within $A_{cr,op}$. The superposition of these stress distributions is schematically shown within Fig. 12, too. The exceedance of f_{ct} also initiates the longitudinal crack formation in direction of the x-axis which is specific for this failure mode.

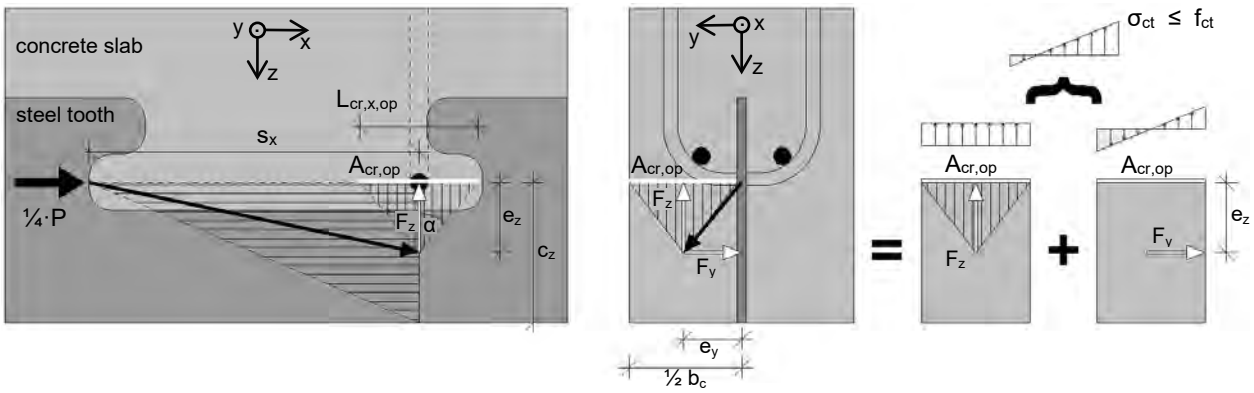


Fig. 12 – Geometric assumptions for the design approach in xz-view (left) and yz-view (right)

Corresponding to these assumptions, a design approach was derived. The value of the crack area $A_{cr,op}$ can be quantified as follows. All quantities are shown within Fig. 12.

$$A_{cr,op} = L_{cr,x,op} \cdot \frac{b_c}{2} = c_z \cdot \tan(\alpha) \cdot \frac{b_c}{2} \tag{1}$$

Consequently, the section modulus around the x-axis $W_{x,op}$ of the concrete cuboid underneath $A_{cr,op}$ can be characterized by:

$$W_{x,op} = \frac{L_{cr,x,op} \cdot \left(\frac{b_c}{2}\right)^2}{6} = \frac{c_z \cdot \tan(\alpha) \cdot {b_c}^2}{24} \tag{2}$$

The vertical force component affecting $A_{cr,op}$ has the value:

$$F_z = \frac{P}{4} \cdot \frac{e_z}{s_x} = \frac{P}{8} \cdot \frac{c_z}{s_x} \tag{3}$$

The bending moment to the concrete cuboid is:

$$M_x = F_y \cdot e_z = \frac{P}{4} \cdot \frac{e_y}{s_x} \cdot e_z = \frac{P}{32} \cdot \frac{b_c}{s_x} \cdot c_z \tag{4}$$

On the basis of these values, the resulting stress within $A_{cr,op}$ can be calculated. The failure mode ‘edge failure’ was assumed to occur as soon as this stress reaches the tensile strength of the concrete f_{ctm}:

$$\sigma_{ct} = \eta \cdot \left[\frac{F_z}{A_{cr,op}} + \frac{M_x}{W_{x,op}}\right] = \eta \cdot \frac{1}{tan(\alpha)} \cdot \frac{P}{b_c \cdot s_x} \leq f_{ctm} \tag{5}$$

With the help of this design approach, the experimentally obtained resistances were recalculated using the following formula. With an assumed load diffusion angle of 40°, which seemed appropriate due to numerical simulations, the calibration factor was set to $\eta = 1{,}67$ to achieve plausible values for the theoretically calculated resistance per steel tooth.

$$P_{theo} = \frac{tan(\alpha)}{\eta} \cdot b_c \cdot s_x \cdot f_{ctm} = 1{,}4 \cdot b_c \cdot s_x \cdot f_{ctm} \tag{6}$$

With the calibration factor η the apportionment of the force component ½·P into the upper concrete slab and into the concrete cover can be respected as well as the linear deviation between the theoretical assumptions of the model and the true experimental conditions. For instance, the load transfer mechanisms are based on strut-and-tie models while in reality, the load spreads out

three-dimensionally into the concrete cuboid. Additionally, the integration of non-linear factors is possible. Therefore, further experimental investigations would be necessary to define these parameters in a statistically reliable way.
A comparison between the experimental results and the theoretically calculated resistances is shown in Table 3. The deviation lies between -16% and +15%.

Table 3 – Recalculation of the experimentally tested resistances per composite dowel

Without spiral reinforcement			**PO34**	**PO36**	**PO38**	**PO40**	**PO42**	**PO44**	**PO46**
Experimental resistance	P_{exp}	[kN]	64,3	63,3	85,8	55,0	50,0	72,5	60,3
Theoretical resistance	P_{theo}	[kN]	60,9	60,9	91,3	46,2	46,2	69,3	69,3
Deviation from P_{exp} to P_{theo}			-5%	-4%	+7%	-16%	-8%	-4%	+15%

With respect to the specimens with an installed spiral reinforcement (Fig. 3c), a linear magnification factor $\lambda_{spiral} = 1,4$ was inserted additionally as a first proposal. This leads to a deviation between the experimentally tested and the theoretically calculated resistances of specimens with a spiral reinforcement of -15% to +24%.
After a statistical evaluation and an evaluation on safety factor γ_c, the complete proposed calculation of the design value of the resistance against edge failure of composite dowels positioned close to the concrete surface in consideration of the integration into the safety concept of the Eurocodes results in:

$$P_{edge,Rd} = \frac{1}{\gamma_V} \cdot P_{edge,Rk} = \frac{1}{1,25} \cdot 0,80 \cdot 1,4 \cdot b_c \cdot s_x \cdot f_{ctm} = 0,90 \cdot b_c \cdot s_x \cdot f_{ctm} \quad (7)$$

OUTLOOK

In general, the decisive failure mode is influenced by various parameters. Not all of them have been investigated sufficiently and taken into account within the design approach yet. Furthermore, a greater amount of data is necessary to allow statistically reliable propositions. Therefore, the investigations will be continued in the context of a subsequent research project, which has started in April 2017. The project is performed by *University of Kaiserslautern* in cooperation with *RWTH Aachen University* and is aimed at developing a consistent design approach for composite dowels. It includes further experimental investigations on composite dowels positioned close to the free surface of the concrete slabs as well as corresponding numerical simulations. The long-term goal is to integrate a consistent design approach for composite dowels into the Eurocode as an alternative to headed studs.

ACKNOWLEDGEMENTS

The presented test results were achieved by the financial support of the state Rheinland-Pfalz during the pilot project InnoProm with funds of MBWWK and EFRE. The project's promotion number was 964-52708-1/81029978.

REFERENCES

Berthellemy, J.; et al. (2011). *Zum Tragverhalten von Verbunddübeln – Teil 1: Tragverhalten unter statischer Belastung*. Stahlbau 80, Heft 3, Ernst & Sohn Verlag, Berlin, Germany.

Broschart, Y. (2016). *Development of a design approach for the failure mode 'edge failure' of composite dowels positioned close to the surface of concrete slabs*. MSc thesis, University of Kaiserslautern, Germany.

Broschart, Y.; Gajda, J.; Kurz, W. (2018). *Untersuchungen zum Tragverhalten randnaher Verbunddübelleisten*. Stahlbau 87, Heft 5, Ernst & Sohn Verlag, Berlin, Germany.

DIBt Deutsches Institut für Bautechnik (2013). *Allgemeine bauaufsichtliche Zulassung: Verbunddübelleisten*. Approval number Z-26.1-23, Berlin, Germany.

European Committee for Standardization (2002). *Eurocode: Basis of structural design.* EN 1990:2002 + A1:2005 + A1:2005/AC:2010. Brussels, Belgium.

European Committee for Standardization (2004). *Eurocode 4: Design of composite steel and concrete structures - Part 1-1: General rules and rules for buildings.* EN 1994-1-1:2004 + AC:2009. Brussels, Belgium.

Gajda, J. (2019): *Loadbearing effect of concrete dowels close to the concrete surface*. PhD thesis (not published yet), Technische Universität Kaiserslautern, Germany.

Gajda, J.; Kurz, W. (2013). *Tragverhalten randnaher Betondübel unter Längsschub-beanspruchung*. Stahlbau 82, Heft 9, Ernst & Sohn Verlag, Berlin, Germany.

Gajda, J.; Kurz, W. (2013). *Analysis of near to free surface located concrete dowels in composite structures*. Composite Construction in Steel and Concrete VII, ASCE American Society of Civil Engineering, North Queensland, Australia.

Heinemeyer, S. (2011). *Zum Trag- und Verformungsverhalten von Verbundträgern aus ultrahochfestem Beton mit Verbundleisten*. PhD thesis, Aachen, Germany.

Kopp, M.; Wolters, K.; et al. (2018) *Composite dowels as shear connectors for composite beams – Background to the design concept for static loading*. Journal of Constructional Steel Research, Amsterdam, Netherlands.

Simulia (2014). *Abaqus 6.14 Analysis User's Guide – 23.6.3 Concrete damaged plasticity.* Dassault Sytèmes Simulia Corp., Providence, USA.

PIN SHEAR CONNECTORS FOR STEEL-CONCRETE COMPOSITE CONSTRUCTIONS

Maik Kopp
RWTH Aachen University, Division 10.2 - Construction Management
Aachen, Germany
maik.kopp@zhv.rwth-aachen.de

Kevin Wolters
RWTH Aachen University, Institute of Steel Construction
Aachen, Germany
k.wolters@stb.rwth-aachen.de

Markus Feldmann
RWTH Aachen University, Institute of Steel Construction
Aachen, Germany
feldmann@stb.rwth-aachen.de

Martin Claßen
RWTH Aachen University, Institute of Structural Concrete
Aachen, Germany
mclassen@imb.rwth-aachen.de

Johannes Schäfer
RWTH Aachen University, Laserline GmbH
Mülheim-Kärlich, Germany
johannes.schaefer@laserline.com

ABSTRACT

The use of high-strength steel as well as ultra-high-performance concrete (UHPC) in composite constructions enable slender, wide spanning and highly sustainable composite elements in architecturally sophisticated structures. Compared to normal-strength materials, high-strength concrete and steel allow a significant reduction of the dimensions of load-bearing elements. Thus, for certain fields of application the theoretical thicknesses of concrete chords can be reduced to a few millimeters. However, for such slender composite structures and concrete chords the applicability of conventional shear connectors like headed studs is no longer given. The systematic connection of the composite cross sections requires novel, small-scaled shear connectors transmitting anchorage and shear forces through the composite joint.

This paper deals with the load-bearing and slip capacity of the novel small-scaled pin shear connectors due to static forces. The experimental and numerical results as well as the resulting design equations are presented.

INTRODUCTION

Steel-concrete composites combine the favorable material properties of structural steel and concrete in an optimal way. Concrete is arranged in the compression area and steel in the tensile zone. To ensure the composite between both materials, effective connectors are necessary, which have a high load as well as a sufficient deformation capacity (Hanswille, Schäfer & Bergmann, 2010).

The usage of high-strength materials (e.g. high-strength steel and UHPC) increases the load capacity of the composite structure significantly and allows smaller dimensions of the load-bearing elements respectively (Feldmann, Hegger, Hechler & Rauscher, 2007) (Heinemeyer, Gallwoszus & Hegger, 2012) (Feldmann et al., 2014). In certain applications the theoretical thicknesses of concrete chords can be reduced to less than 30 mm, so that shear connectors like headed studs (EN 1994-1-1, 2010) or composite dowels (Feldmann, Kopp & Pak, 2016) are non-executable. Therefore novel small-scale shear connectors are developed.

In a national research project the pin-structures (Figure 1) were investigated with regard to the static load-bearing capacity and slip capacity (Claßen, Gallwoszus, Kopp & Schäfer, 2015) (Schäfer et al., 2015) (Claßen et al., 2015) (Kopp et al., 2016). By means of push-out tests the local resistance was determined. The global load-bearing behavior was investigated in composite beam and plate tests. Numerical simulations supported the experimental test series. Based on the experimental and numerical results, engineering models were derived to describe the load-bearing mechanisms (concrete and steel failure). Finally, design equations for composite construction with pin structures as shear connectors were determined.

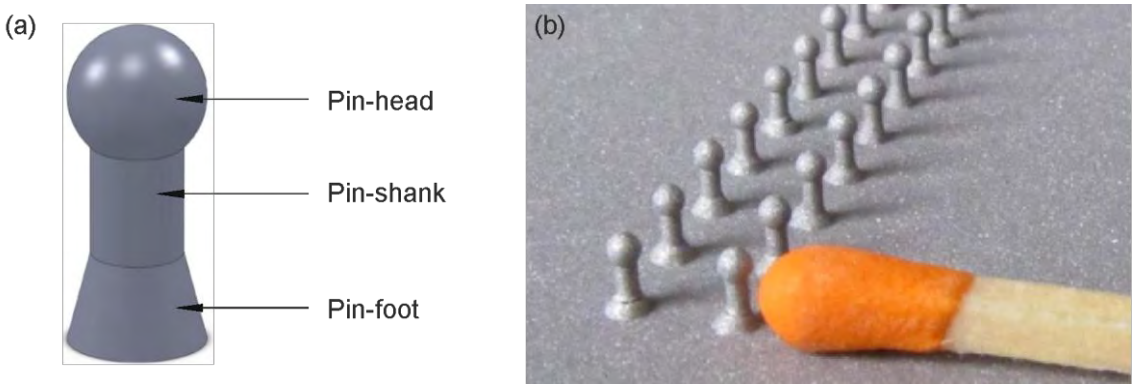


Fig. 1 - (a) Terms of the pin structures and (b) example of group arrangement

PRODUCTION AND MATERIALS

Pin-welding process

The pin-connectors are produced directly from the welding wire using a novel welding process, based on the so called Cold Metal Transfer (CMT) procedure. In this process the wire is moved towards the base material until it is welded on due to a short circuit (Figure 2 a, b). Subsequently the wire is pulled backwards without any electricity supply (Figure 2 c). At a coordinated point a renewed electricity supply cuts and melts the wire. The material is formed to a sphere due to surface tension (Figure 2 d-f).

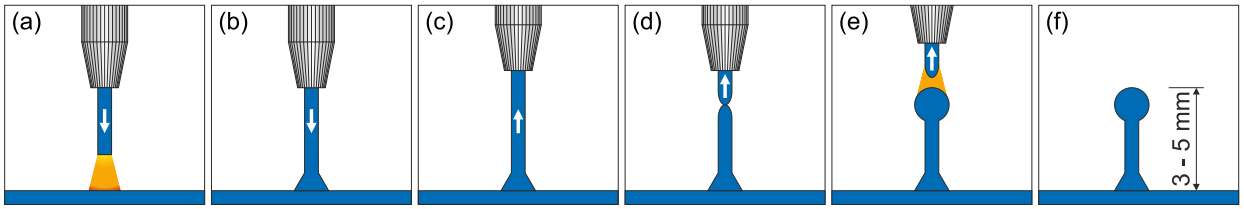


Fig. 2 - (a) Terms of the pin structures and (b) example of group arrangement

Current pins can be reliably produced up to a height of about 5 mm depending on the wire material and diameter. Several pin-geometries, including varying height and diameters of the pins, are considered in the investigations.

Materials

In order to take advantage of the multiple benefits of the innovative welding process for applications in steel-concrete composites, the combination of small-scale pins with high-strength and ultra-high-performance concrete is effective. Subsequently, the material properties of the used pins, steel and the concrete are assembled.

During the experimental investigations two different welding wires with 0.8 mm and 1.2 mm are tested. First, austenitic welding wires ER308LSi are combined with an austenitic steel sheets (AISI 304) with a thickness t = 3.0 mm. The nominal tensile strength of ER308LSi is about 590 N/mm². Furthermore, welding wires out of low-alloy steel (ER70S-6) are used for tests with steel sheets ASTM A633 (t = 3.0 mm).

In order to achieve a completely form-locked and force-locked embedding of small-scale pin connectors in the concrete microstructure, a small grain size and high fluidity of the concrete are desirable from the perspective of concrete technology. These requirements are fulfilled in a fine-grained concrete mixture, which was developed for applications with textile-reinforced concrete (Brockmann, 2006). Therefore, in the experimental tests, this fine-grained concrete is combined with both welding wires. The used fine-grained concrete has a maximum grain diameter of 0.6 mm and a compressive strength of about 70 N/mm². Due to its high binder content and the small fraction of coarse aggregates, the fine concrete has a smaller elastic modulus and greater ductility compared to normal concretes of the same strength.

Furthermore, the combination of pin shear connectors with ultra-high-performance concrete (UHPC) is analyzed in the context of the current research project (Claßen et al., 2015). Due to the combination of optimized mixture designs with steel fibers UHPC is a dense structured concrete. This concrete has an extremely high characteristic compressive strength (>180 N/mm²), bending tensile strength (>40N/mm²) and elastic modulus (>50,000 N/mm²).The addition of steel fibers influences the ductility and strength affirmatively. A sufficient ductility and a crack bridging effect can only be guaranteed with high tensile strength and with high elongation at rupture of the fibers (Leutbecher, 2008).

EXPERIMENTAL INVESTIGATIONS

Local load-bearing behavior of pin-connectors due to shear loading (push-out tests)

Several test series were performed to determine the load-bearing and slip capacity of pin-connectors (Kopp et al., 2016). The shear capacity of a single pin was investigated by push-out tests (cp. Figure 3) based on the standard push-out test for headed studs of EN 1994-1-1,

Annex B (EN 1994-1-1, 2010). Overall 24 test series, each with ten push-out specimen, were performed with regard to shear capacity, initial stiffness and deformability.

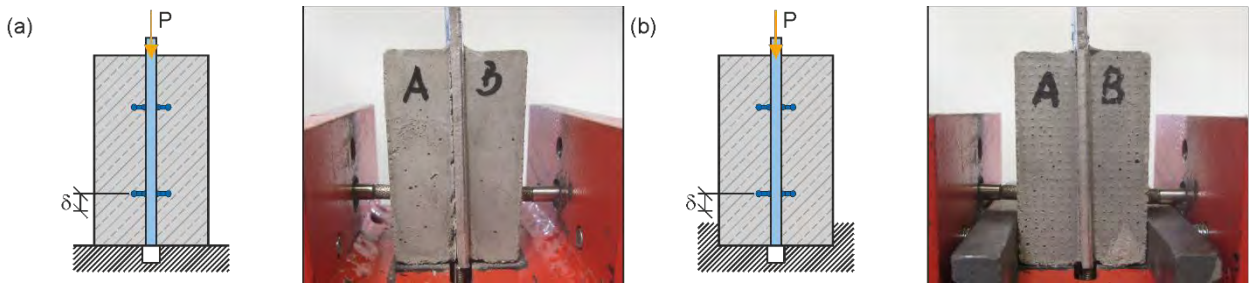


Fig. 3 - Push-out test (a) without and (b) with horizontal bearing

The first test of each series was performed path-controlled until failure. Based on the maximum force all other test samples were preloaded with 25 force-controlled load cycles (between 5 and 40% maximum load) to loosen the adhesion bond and subsequently loaded path-controlled until failure. During the experiments, the slip in the composite joint was measured with inductive displacement transducers.

The influence of the horizontal bearing of the concrete slabs was also examined. The experiments show a clear dependence of the failure mode to the horizontal bearing. If a horizontal gaping of the composite joint is prevented by a bracing of the concrete slabs mainly steel failure (pin shearing) occurs. If the horizontal bracing of concrete slabs is omitted, the usual failure is prying-out of a concrete cone around the pin. Thus, the ultimate loads of experiments without horizontal bracing are on average 25 % below the fracture loads of experiments with horizontal bearing. This effect can be explained by the simultaneous interaction of shearing and tensile forces in the composite joint.

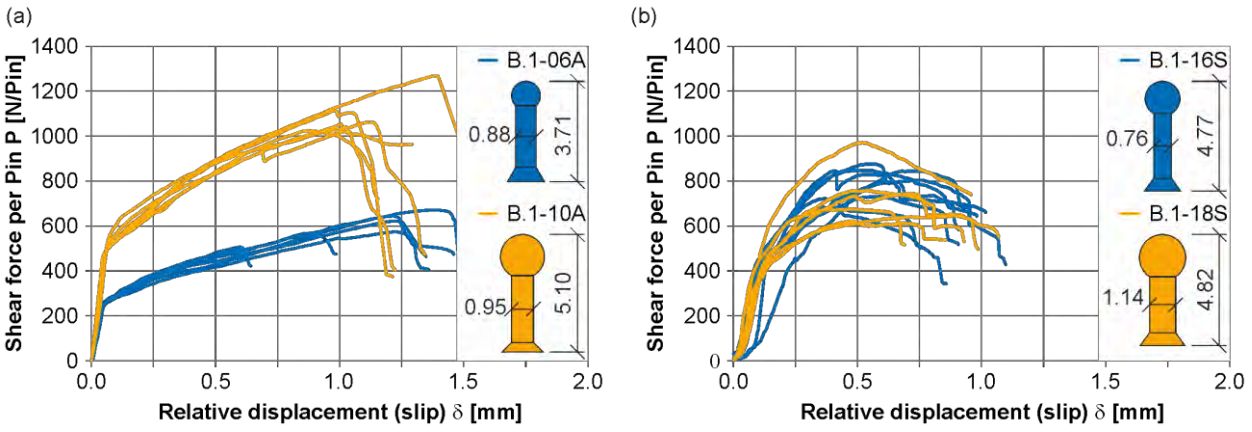


Fig. 4 - Force-slip curve of (a) austenitic steel and (b) construction steel

Exemplarily the test curves of austenitic and structural steel combined with high-strength concrete (HSC) are plotted in Fig. 5. Load-bearing capacity increases significantly when using thicker and higher pins (Figure 4 a, B.1-06 compared to B.1-10, austenitic steel). The results of

the tests using structural steel are characterized by a higher scatter and lower ultimate loads (Figure 4 b). This might be caused by a better thermal conductivity of structural steel compared to austenitic steel and therefore a worse connection between pin and base material. In consequence, pin shearing often occurs in the heat-affected zone underneath the pin-foot.

Table 1 shows selected results of the currently greatest possible pin-heights. The usage of UHPC increases the load-bearing and decreases the deformation capacity δ_{uk} compared to HSC.

Table 1 - Test results series B.1 (push-out tests, maximum pin-heights)

Series	Steel plate / wire	Concrete	$Ø_{wire}$ [mm]	h_{pin} [mm]	$C_{ini,m}$ [N/mm]	P_{max} [N/Pin]	P_{Rk} [N/Pin]	δ_{uk} [mm]
B.1-06A	AISI 304 / ER308LSi	HSC	0.8	4.35	5980	670.9	454.8	0.63
B.1-10A	AISI 304 / ER308LSi	HSC	1.2	5.10	6852	1268.0	918.7	1.07
B.1-11AU	AISI 304 / ER308LSi	UHPC	0.8	4.35	8912	971.1	459.0	0.44
B.1.12AU	AISI 304 / ER308LSi	UHPC	1.2	5.10	12 611	1601.5	571.8	0.62
B.1-16S	ASTM A633 / ER70S-6	HSC	0.8	4.77	5825	874.8	616.1	0.81
B.1.18S	ASTM A633 / ER70S-6	HSC	1.2	4.82	5850	970.1	558.0	1.28
B.1-19SU	ASTM A633 / ER70S-6	UHPC	0.8	4.77	7051	1027.5	647.2	0.36
B.1-20SU	ASTM A633 / ER70S-6	UHPC	1.2	4.82	11 469	1471.5	853.5	0.37

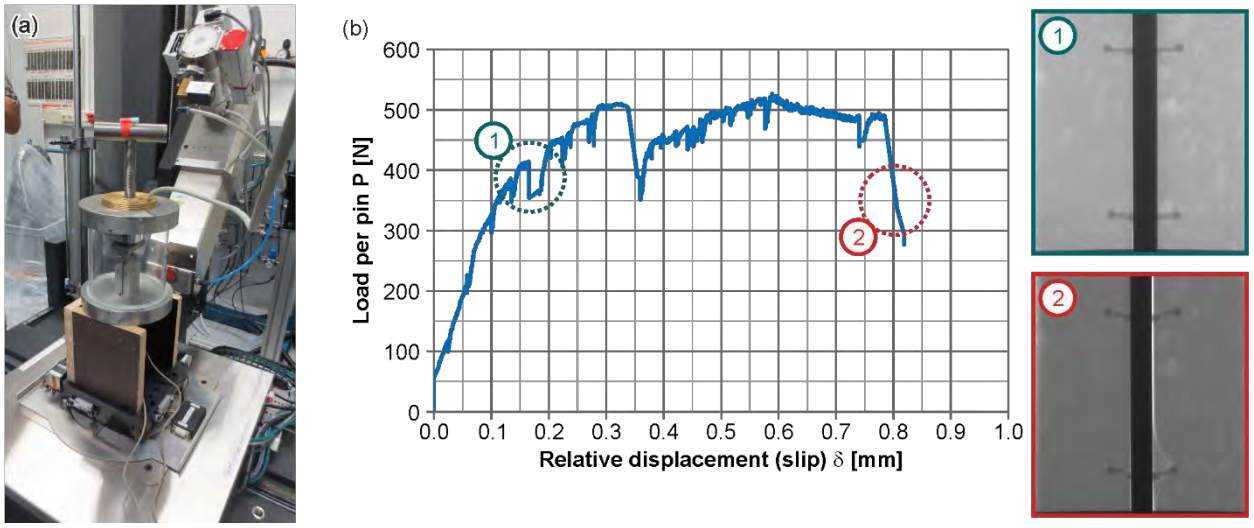


Fig. 5 - (a) Computer tomography (CT) system with specimen and (b) Load-slip-curve of a push-out test with CT images

During the experimental tests, push-out tests with the aid of computer tomography (CT) were performed. Hereby, it was possible to look into the composite specimens during some load levels. Figure 5 (a) shows the CT system with the developed load introduction. The load introduction consists of an acrylic glass pipe and two round steel plates. The upper steel plate has an opening to position the specimen within the acrylic glass. The glass enabled 3D CT

images without interferences due to density difference. Figure 5 (b) exemplifies a load-slip-curve of a push-out tests with two CT images at different times. The upper image (1, green frame) shows the first steel crack in the lower left pin, which resulted in a load drop (green dotted circle in the diagram). In the lower CT image (2, red frame) both the steel cracks (lower left and upper right pin) as well as a concrete pry-out cone (lower right pin) are visible at the end of the test. These combined failures resulted in the total collapse of the specimen.

Global load-bearing behavior (beam tests)

To research the global load-bearing characteristics of pin-structures in composite construction, bending tests of composite beam (Series C.1) and composite slabs (Series C.2) are performed to detect the required slip capacity of the pin shear connectors. Furthermore, it is supposed to verify the transferability of the local mechanisms on the global load-bearing and deformation behavior. The beam test program included six tests with positive (sagging) bending stress and two tests with negative (hogging) bending stress. In Series C.2 four composite slab tests are performed to investigate the behavior of the pin-structures in cracked concrete.

Table 2 - Test results series C.1 (beams)

Series	Steel wire	Concrete	$Ø_{wire}$ [mm]	h_{pin} [mm]	η [%]	L [m]	M_{max} [kNm]	δ_{max} [mm]
C.1-01A	ER308LSi	HSC	1.2	5.10	100	2.60	17.6	0.11
C.1-02A	ER308LSi	HSC	1.2	5.10	50	2.60	14.8	1.11
C.1-03A	ER308LSi	HSC	1.2	5.10	100	3.75	15.1	0.11
C.1-04A	ER308LSi	HSC	1.2	5.10	50	3.75	10.9	0.63
C.1-05SU	ER70S-6	UHPC	1.2	4.82	100	3.15	43.7	0.05
C.1-06SU	ER70S-6	UHPC	1.2	4.82	50	3.15	25.3	0.04
C.1-07SN	ER70S-6	HSC	1.2	4.82	100	3.00	-15.4	0.05
C.1-08SN	ER70S-6	HSC	1.2	4.82	50	3.00	-7.2	0.01

The design of the composite beams under sagging moment ensures the plastic neutral axis to be located in the composite joint in order to reach an optimum use (concrete in compression area, steel in tension zone). The individual beams differ regarding span length, materials and degree of shear connection η. Parameters and results of series C.1 are shown in Table 2 and Figure 6.

For all beam tests 4-point bending test setup is chosen. It is obvious that a higher degree of shear connection leads to a higher load-bearing capacity and lower vertical deflection respectively less slip in the composite joint. By the use of UHPC the load-bearing capacity increases at the expense of a lower deformability. In case of a full shear connection, the load can be increased until a failure of the compressive zone occurs, while there is shear failure of the pins in case of 50 percent degree of shear connection.

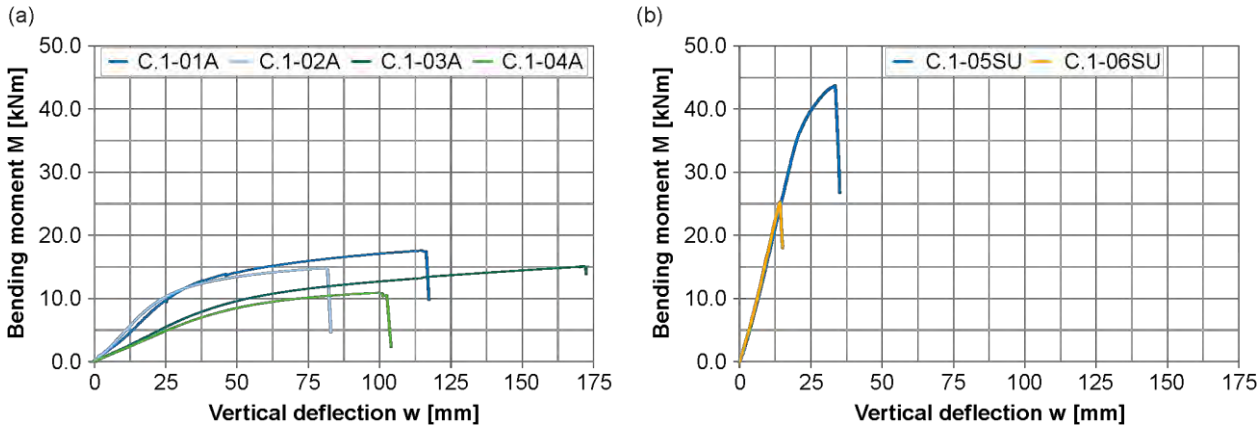


Fig. 6 - Force-deflection curves of composite beam tests with (a) austenitic steel combined with HSC and (b) structural steel with UHPC

NUMERICAL INVESTIGATION

Structure of FE-model and material characteristics

To examine the influences of pin-geometry (dimensions of pin-head, pin-shank and pin-foot), pin-distance, bonding depth (pin-height) and strength of steel and concrete on the shear behavior of the pin-structures, parametric studies were performed using the finite-element software ABAQUS. The push-out test is modelled with C3D8R volume elements with non-linear material characteristics (Figure 7). Double symmetry is exploited to reduce computing time. The model was validated by the experimental results (Claßen et al., 2016).

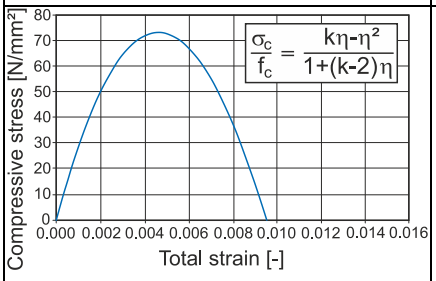
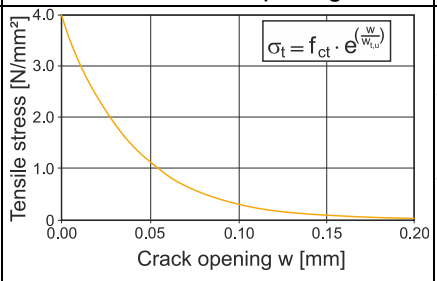
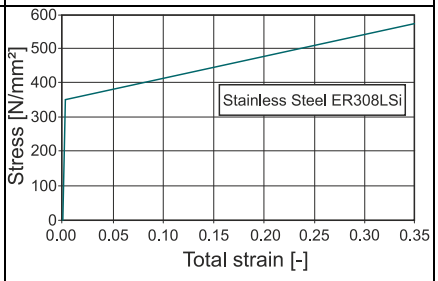
Material models		
HSC		**Welding wire ER308LSi**
Compression	**Tension**	**Compression and tension**
Stress-strain	Stress-crack opening	Stress-strain
		
Concrete Damage Plasticity (CDP)		**Elastic-plastic (strain-hardening)**
Material parameters	CDP-Parameters	Material parameters
Comp. strength f_{cm} = 73.0 N/mm² Tensile strength f_{ct} = 4.0 N/mm² Young's modulus E_{cm} = 31 200 N/mm² Poisson's ratio v = 0.2 Sargin parameter D = 0 Plastic strain ε_{c1} = 0.0046 Crack energy G_f = 42.0 N/mm²	Dilation Angle Ψ = 35° Eccentricity ε = 0.3 Strength ratio f_{b0}/f_{c0} = 1.16 Damage parameter K = 0.667	Yield strength f_y = 350 N/mm² Tensile strength f_u = 570 N/mm² Young's modulus E = 170 000 N/mm² Poisson's ratio v = 0.3

Fig. 7 - Exemplary material characteristics and parameters in the numeric model

The plastic concrete behavior is modelled using the Concrete Damage Plasticity (CDP) theory (Kueres, Stark, Herbrand & Claßen, 2015). An elastic-plastic material behavior including strain hardening after the yielding point is allocated to the steel components. Contact definitions are introduced to prevent penetration between steel and concrete. While the tangential behavior is characterized by friction (μ=0.2), there is a “hard-contact” in normal direction.

Influence of pin-distance and number of pins in a group

To examine the influence of pin-distance to the load-bearing capacity, a group of four pins was modelled and the distance was varied systematically. Thereby, a ratio of $a/h_{pin} < 2.25$ decreases the shear capacity. Higher ratios cannot increase the capacity because a concrete compression failure occurs (Figure 8 a). A pin-distance $a > 2.3\ h_{pin}$ is recommended. In case the distance lies beneath this limit (e.g. a = 7.5 mm) the shear capacity decreases with a greater number of pins in a group (Figure 8 b).

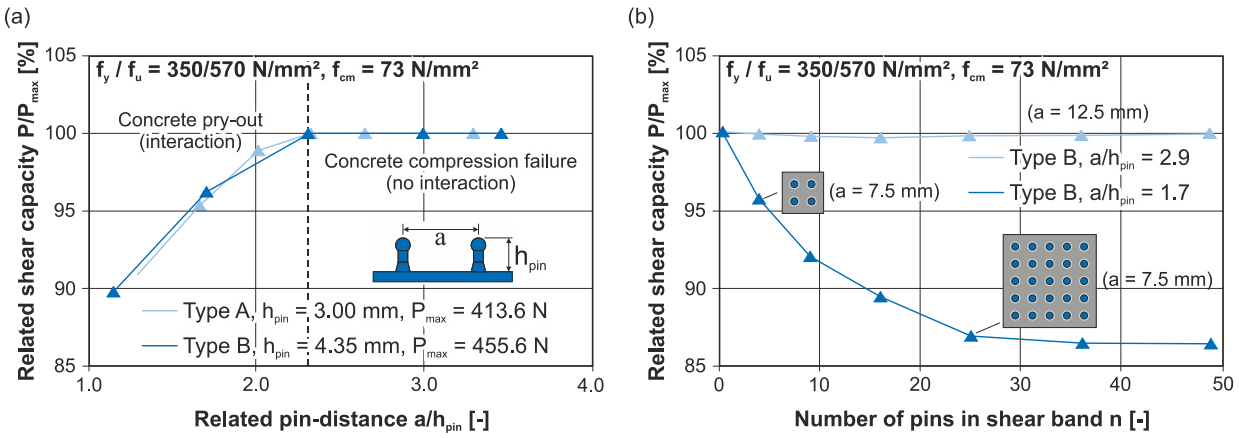


Fig. 8 - (a) Related shear capacity P/P_{max} subject to the pin-distance ratio a/h_{pin}; (b) related shear capacity P/P_{max} as a function of the number of pins in a group

Influence of pin-geometry (head, shank, foot)

Besides pin-geometries A to C several pin-diameters are executable. Figure 9 (a) shows the influence of the shank-diameter on the shear capacity, which increases nearly quadratic. This correlation is similar to headed studs. Also the ratio between d_{head} to d_{shank} respectively d_{foot} to d_{shank} influences the shear capacity as far as the ratio lies beneath 1.4 (Figure 9 b). A greater head-diameter ensures the necessary anchorage against a pull-out failure of the connection.

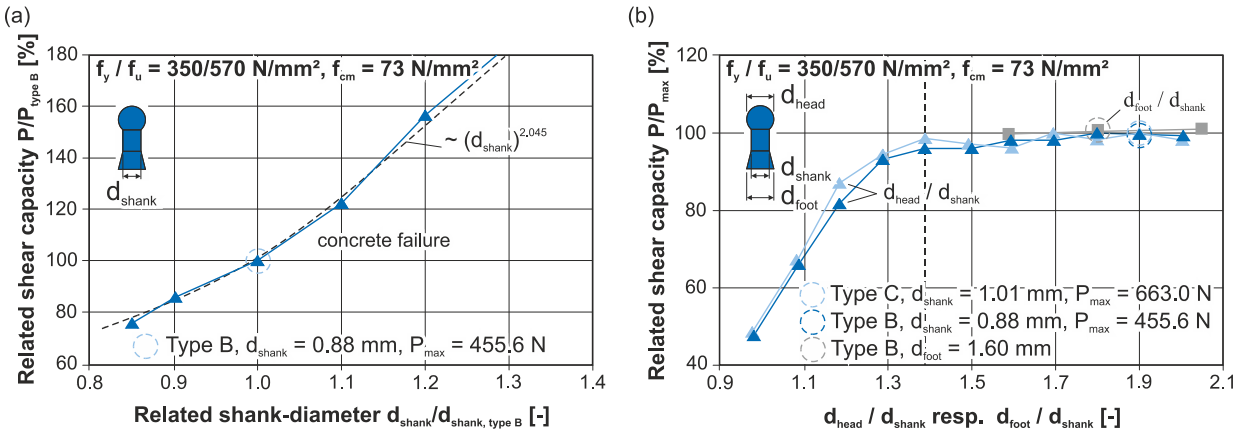


Fig. 9 - (a) Influence of pin-shaft diameter on shear capacity related to the standard pin type B; (b) influence of different pin-head and pin-foot ratios

Influence of bonding depth

The simulations with varying bonding depths show a bad influence on shear capacity for ratios h_{pin}/d_{shank} beneath 4, the effect is almost linear (Figure 10 a). There is no increasing capacity for higher ratios because of a limited height of the zone which is activated for a support of the concrete compression strut $h_z = 4\ d_{shank} - d_{head}$ (Figure 10 b). For lower ratios the compression strut cannot be built up completely.

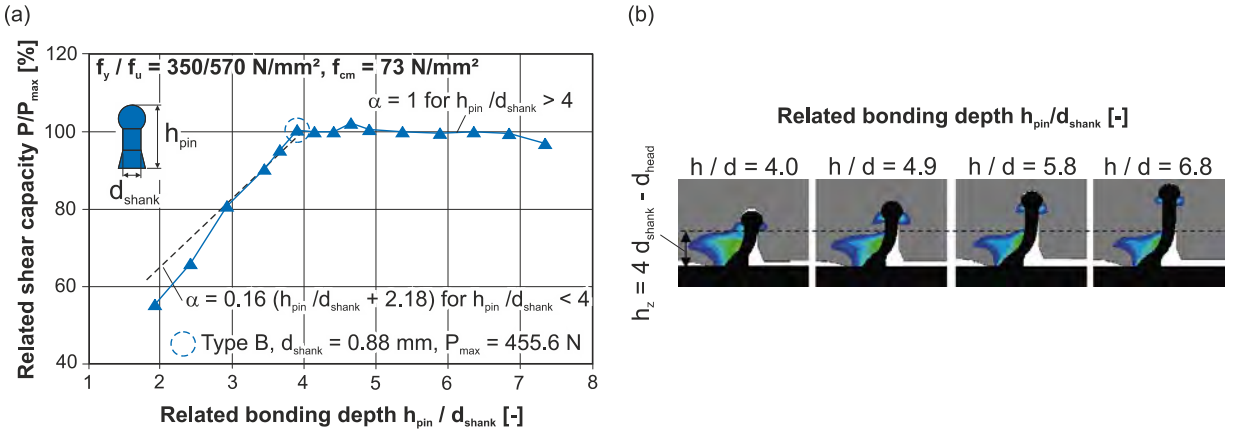


Fig. 10 - (a) Influence of the bonding depth on shear capacity related to the standard pin type B; (b) development of concrete pressure at the pin-foot for different bonding depths

Influence of concrete and steel strength

Furthermore the effect of varying concrete compressive strengths on shear capacity is investigated. The shear capacity increases affine to the square root of the product of compressive strength and modulus of elasticity until steel failure occurs (Figure 11 a). Finally a parametrical study, where steel failure is enforced by high-performance concrete, examines the

influences of steel strength and shank-diameter. The shear capacity increases proportional to ultimate strength and to the square of the shaft-diameter (Figure 11 b).

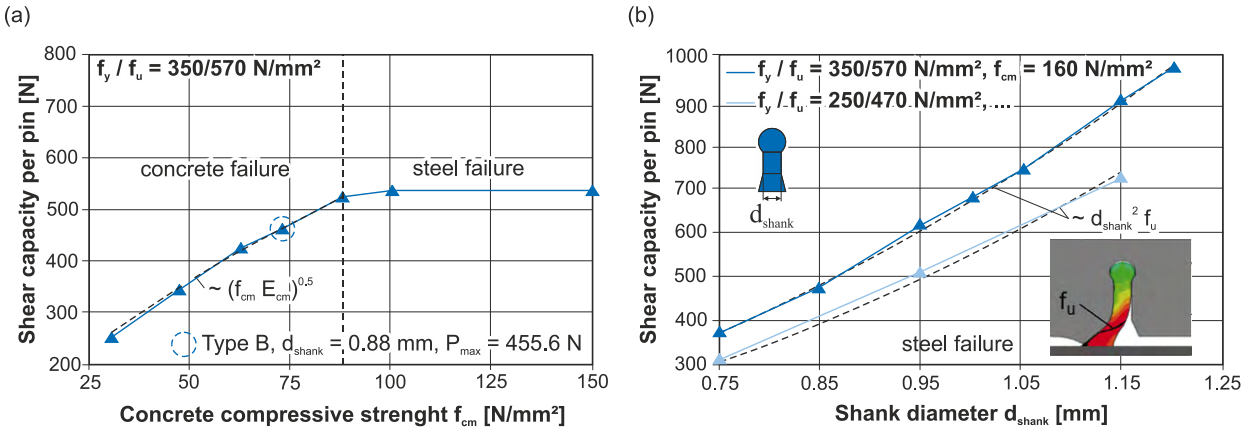


Fig. 11 - (a) Influence of the concrete compressive strength on shear capacity; (b) influence of shank diameter and steel strength

DESIGN OF PIN SHEAR CONNECTORS

Based on the findings in the previous chapters an approach was developed for the design of composite joints using small-scaled pin-connectors. As some phenomenological parallels exist between pin-structures and headed studs, the approach of the latter connecters according (EN 1994-1-1, 2010) can be transferred.

The shear capacity limited by concrete failure modes is influenced by the shank-diameter, the ratio h_{pin}/d_{shank} as well as the concrete compressive strength. Considering an empirical factor 0.4, the maximum shear capacity can be expressed as

$$P_{Rm,Concrete} = 0.4 \cdot \alpha \cdot d_{Shank}^{2.045} \cdot \sqrt{f_{cm} \cdot E_{cm}}$$

where: $\alpha = 0.16 \cdot \left(\frac{h_{Pin}}{d_{Shank}}\right) + 2.18$ for $2.5 \leq \frac{h_{Pin}}{d_{Shank}} \leq 4.0$

$\alpha = 1.0$ for $4.0 < \frac{h_{Pin}}{d_{Shank}}$

In case of a steel failure the shear capacity is proportional to the square of the shank-diameter and the ultimate steel strength. Considering the cross-sectional area and an empirical factor of 1.5 the maximum shear capacity limited by steel properties is

$$P_{Rm,Steel} = 1.5 \cdot \frac{\pi \cdot d_{Shank}^{2.045}}{4} \cdot f_u$$

The maximum shear capacity can be determined by the minimum of both limits:

$$P_{Rm} = min \begin{cases} 0.4 \cdot \alpha \cdot d_{Shank}^{2.045} \cdot \sqrt{f_{cm} \cdot E_{cm}} \\ 1.5 \cdot \frac{\pi \cdot d_{Shank}^{2.045}}{4} \cdot f_u \end{cases}$$

These rules are valid for the two constructive provisions:

$$1.4 \leq \frac{d_{head}}{d_{shank}}$$

$$2.3 \leq \frac{a}{h_{Pin}}$$

CONCLUSIONS AND OUTLOOK

The local static load-bearing and slip capacity due to shear forces of the pin-structures as shear connectors in steel-concrete-composite structures was investigated in experimental tests and numerical simulations. The experimental investigations show that pin-structures are able to transfer the inner forces between the steel and concrete cross sections. Hence, the pin-structures are usable in composite constructions with thin concrete slabs alternative to headed studs. On the other hand, the deformability is not sufficient. In most of the component tests the plastic load-bearing capacity is reached, but afterwards the tests show brittle failure. This is caused by a current pin-height h_{pin} = 5.1 mm and the brittle shear failure of pin-structures consisting of structural steel.

In a numerical parametric study the effects of pin-geometry (dimensions of pin-head, pin-foot, pin-shank), pin-distance, bonding depth and material strengths on the longitudinal shear resistance were investigated systematically. The determined relations were transferred in an engineering model, which is based on the Eurocode 4. The engineering model includes the design equations to determine the longitudinal shear resistance and constructive provisions like pin-distance. This enables the design of filigree composite structures for potential applications (Figure 12).

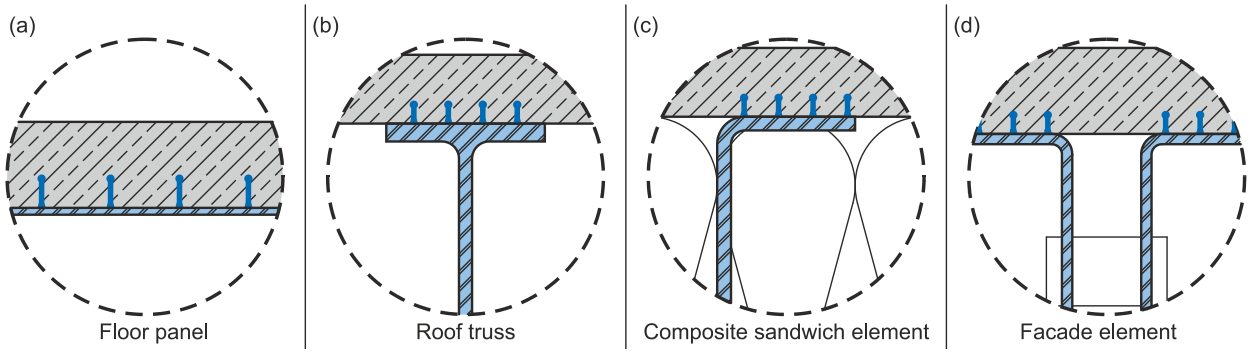


Fig. 12 - Application examples for small-scaled pin connector

ACKNOWLEDGMENT

This research work has been funded by the German research foundation (DFG) and is part of the research project FE 459/5-1 “Untersuchung der Tragmechanismen neuartiger, kleinskaliger Pin-Verbundmittel zwischen Stahl und Beton”. The researchers would like to express their thanks for the support.

REFERENCES

Brockmann, T. (2006). *Mechanical and fracture mechanical properties of fine grained concrete for textile reinforced composites* (Doctoral dissertation). RWTH Aachen University, Aachen, Germany.

Claßen, M., Gallwoszus J., Kopp, M. & Schäfer J. (2015). Kleinskalige Pin-Verbundmittel für den Stahl-Beton-Verbundbau, *Bauingenieur, 90*(3), 200-208.

Claßen, M., Hegger, J., Kopp, M., Feldmann, M., Schäfer, J. & Reisgen, U. (2015). Verbundträger mit kleinskaligen Pin-Verbundmitteln – Experimentelle Untersuchungen und Finite-Elemente-Simulation. *Stahlbau, 84*(10), 771-779.

Claßen, M. & Herbrand, M. (2016). Mindestverdübelung von Verbundträgern mit kleinskaligen Verbundmitteln – Herleitung des Mindestverdübelungsgrades durch systematischen Einsatz nicht-linearer Finite-Elemente-Berechnungen. *Bauingenier, 91*(4), 140-151.

Claßen, M., Felber, L., Herbrand, M., Kueres, D. & Hegger, J. (2016). Längsschubtragfähigkeit von kleinskaligen Pin-Verbundmitteln – Numerische Analyse und Handrechenmodell. *Beton- und Stahlbetonbau, 111*(6), 366-376.

EN 1994-1-1 (2010). *Eurocode 4: Design of composite steel and concrete structures – Part 1-1: General rules and rules for buildings*. Berlin: Beuth.

Feldmann, M., Hegger, J., Hechler, O. & Rauscher, S. (2007). *Forschung für die Praxis: P621 - Untersuchungen zum Trag- und Verformungsverhalten von Verbundmitteln unter ruhender und nichtruhender Belastung bei Verwendung hochfester Werkstoffe*. Düsseldorf: FOSTA - Forschungsvereinigung Stahlanwendung e. V.

Feldmann, M., Gündel, M., Kopp, M., Hegger, J., Gallwoszus, J., Heinemeyer, S., Seidl, G. & Hoyer, O. (2014). *Forschung für die Praxis: P804 - Neue Systeme für Stahlverbundbrücken – Verbundfertigteilträger aus hochfesten Werkstoffen und innovativen Verbundmitteln*. Düsseldorf: FOSTA - Forschungsvereinigung Stahlanwendung e. V.

Feldmann, M., Kopp, M. & Pak, D. (2016). Composite dowels as shear connectors for composite beams – background to the German technical approval. *Steel Construction, 9*(2), 80-88.

Hanswille, G., Schäfer M. & Bergmann M. (2010). *Stahlbau-Kalender 2010: Verbundtragwerke aus Stahl und Beton - Bemessung und Konstruktion. Kommentar zu DIN V 18800-5*. Berlin: Ernst & Sohn.

Heinemeyer, S., Gallwoszus, J. & Hegger, J. (2012). Verbundträger mit Puzzleleisten und hochfesten Werkstoffen. *Stahlbau, 81*(8), 595-603.

Kopp, M., Feldmann, M., Claßen, M., Hegger, J., Schäfer, J. & Reisgen, U. (2016). Untersuchungen zur statischen Schubtragfähigkeit kleinskaliger Pin-Verbundmittel. *Stahlbau, 85*(3), 200-206.

Kueres, D., Stark, A., Herbrand, M. & Claßen, M. (2015). Numerische Abbildung von Beton mit einem plastischen Schädigungsmodell – Grundlegende Untersuchungen zu Normalbeton und UHPC. *Bauingenieur, 90*(6), 252-264.

Leutbecher, T. (2008). *Rissbildung und Zugtragverhalten von mit Stabstahl und Fasern bewehrtem Ultrahochfesten Beton (UHPC)* (Doctoral dissertation). University of Kassel, Kassel, Germany.

Schäfer, J., Willms, K., Reisgen, U., Claßen, M., Hegger, J., Kopp, M. & Feldmman, M. (2015). Small-scale pin-structures: Requirement for a multi material joint. *CWA Journal, 11*(5), 52-61.

BEHAVIOR OF A NEW TYPE OF SHEAR CONNECTORS FOR U-SHAPED STEEL-CONCRETE HYBRID BEAMS

Pisey KEO
LGCGM/Structural Engineering Research Group, INSA de Rennes, 20 avenue des Buttes de Coësmes, CS 70839, F-35708 Rennes Cedex 7, France
pisey.keo@insa-rennes.fr

Clémence LEPOURRY
INGENOVA, Civil Engineering Office, 5 Rue Louis Jacques Daguerre, 35136 Saint-Jacques-de-la-Lande, France
clemence.lepourry@bet-ingenova.fr

Hugues SOMJA
LGCGM/Structural Engineering Research Group, INSA de Rennes, 20 avenue des Buttes de Coësmes, CS 70839, F-35708 Rennes Cedex 7, France
hugues.somja@insa-rennes.fr

Frank PALAS
INGENOVA, Civil Engineering Office, 5 Rue Louis Jacques Daguerre, 35136 Saint-Jacques-de-la-Lande, France
franck.palas@bet-ingenova.fr

ABSTRACT

This paper presents an investigation of the behavior of a new type of shear connectors for U-shaped steel-concrete hybrid beams. Besides the role in transferring the force between concrete and steel material, this new type of shear connectors, welded on the upper flange of the U-section, serves to maintain the shape of the steel cross-section during concrete encasement. Several forms of shear connectors can be used such as L-shaped or square cross-sections. The experimental investigation of the behavior of these shear connectors through asymmetrical push-out tests is presented in this paper. A finite element model has been developed in order to identify the stress behavior of the connectors and the surrounding concrete. The FE model is validated by comparing its results against experimental data. Based on the FEA results, an analytical formula for calculating the force transfer capacity of the connector is proposed.

INTRODUCTION

In composite construction, profiled steel sheets have been successfully used as permanent and integral formworks for the underneath of reinforced concrete slab (Wright, Evans, & Harding, 1987). Profiled steel sheets serve not only as the form for the concrete during construction but also as the principal tensile reinforcement for the bottom fibers of the composite slab, offering

economic design solutions over plywood formwork. Acting compositely with a reinforced concrete slab, profiled steel sheets produce a considerably stiffer and stronger floor system than many others. Lately, the profiled steel sheet was introduced as permanent formwork and integral shuttering for the sides of reinforced concrete beams (Oehlers, Wright, & Burnet, 1994). The collaboration of the profiled steel sheet and RC beams was ensured by bond strength (Oehlers, Wright, & Burnet, 1994) which can be broken under severe loading. For classical composite beams, the shear connection between the two materials is usually ensured by mechanical devices such as headed studs. The behavior of headed stud shear connectors has been investigated by numerous researchers worldwide by conducting push-out experimental tests (Viest, 1956) (Chinn, 1965) (Valente & Cruz, 2009). Although the common type of shear connectors is the headed stud, over the last decade some older generations of shear connectors such as channel, angle or square bar shear connectors have been increasingly interested by many researchers (Abe & Hosaka, 2002) (Maleki & Bagheri, 2008) (Shariati, et al., 2013). The installation of these older generations is not expensive since the installation procedure is similar to the one used for steel beam stiffeners or steel connection components, where a specific welding equipment with high voltage is not required. Recently, angles connectors have been used in steel-concrete composite beams with U-shaped steel girders (Liu, Guo, Qu, & Zhang, 2017). However, no analytical models were readily available for calculating the shear force transfer capacity of the angle shear connector used in this new composite beam configuration as yet.

In this paper, the behavior of a new type of shear connectors used in U-shaped steel-concrete hybrid beams (USCB) is investigated. Besides the role in transferring the force between the two materials, this new type of shear connectors, welded on the upper flange of the U-section, serves to maintain the shape of the steel cross-section during concrete encasement. Several forms of the connector cross-section can be used such as L-shaped or square cross-sections. The L-shaped shear connectors, in the absence of top flange, could be cheaper and more economical in comparison to the channel ones. In general, for classical composite beams a hoop reinforcement should be provided for the L-shaped shear connector to prevent uplift of the concrete (ENV, 1994). However, it is not the case for L-shaped shear connector used in USCB, see Figure 1, in consideration of the connector part fully embedded in the concrete. This new type of shear connection is not covered in present norms of composite structures and it requires an investigation on its behavior and on force transfer mechanism. This paper presents the experimental investigation of the behavior of these shear connectors through asymmetrical push-out tests. Two different types of the shear connector cross-section are considered in the experimental test: square and L-shaped section. To get a further insight into force transfer mechanisms while using L-shaped shear connectors as connector devices in USCB, a finite element model has been developed. The later has been validated by comparing its results against four experimental data tests. Based on the FEA results, an analytical formula for calculating the force transfer capacity of the connector is proposed.

EXPERIMENTAL PROGRAM

An experimental program is developed to quantify the strength and deformation capacities of shear connectors as well as to gain an insight into force transfer mechanisms in the USCB. A modification of the typical push-out test setup proposed by Eurocode 4, which is usually adopted for classic shear stud connectors, is made to represent the real situation on the USCB. The experimental test setup is presented in the following section.

Test specimens

The specimen, Figure 1, consists of a U-shaped steel beam, two precast-slab, a reinforced concrete beam encased in U-shaped steel beam and several shear connectors. The internal surfaces of U-shaped steel beam were greased before concrete encasement to ensure that the force transfer between the two materials is done only through shear connectors. The geometry of the specimen is the following. U-shaped steel beam is 500 mm high, 300 mm wide and 6 mm thick. The precast slabs with 70 mm thick and 450 mm wide are posed on each steel flange. The connectors are welded on the flanges of the steel beam. Five specimens with different types of connector are evaluated. The first specimen denoted “PO-S20”, Figure 2.b), has 4 shear connectors with square-shaped section of 20×20 mm. The second specimen denoted “PO-L40”, Figure 2.a), has 3 shear connectors with L-shaped section of 40×40×4 mm. The third to fifth specimen denoted respectively “PO-L50a”, “PO-L50b” and “PO-L50c” have 3 shear connectors with L-shaped section of 50×50×5 mm. The spacing between each connector for all specimens is 300 mm.

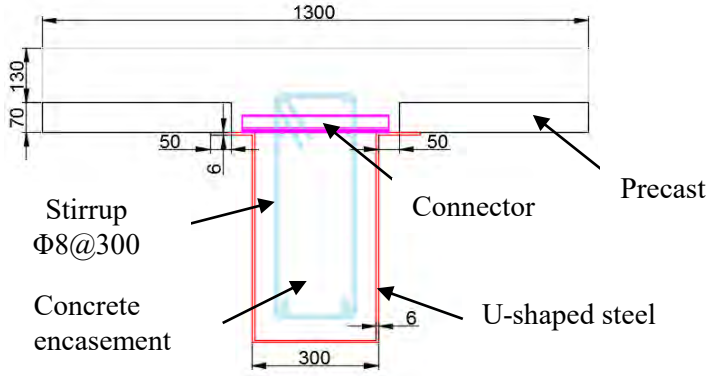
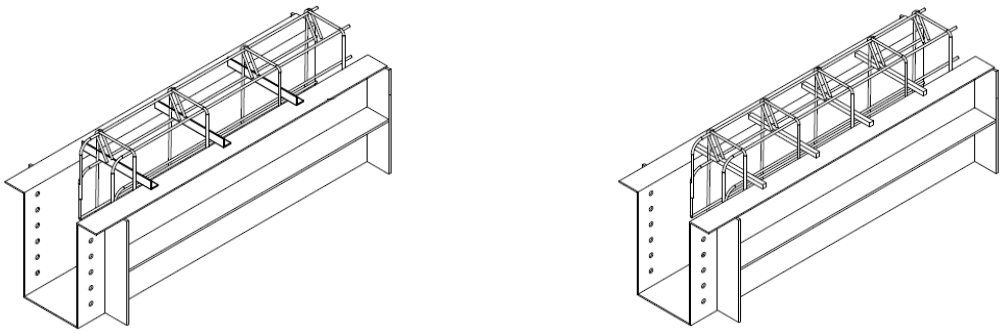


Fig. 1 – Specimen cross-section.



a) PB-POL40/L50 b) PB-POS20

Fig. 2 – Test specimens without concrete encasement.

Materials

The concrete for RC beam-floor has a strength class of C25/30. The concrete characteristics at the day of test were determined on cylinder samples with dimensions of 11×22 cm. Due to the different usage of concrete in precast slab and RC beam-floor, the concrete characteristics of precast slab were measured separately. The steel grades of U-shaped steel beam, of L-shaped steel profile and of square section steel profile are S355, S235 and S235, respectively. Coupon samples were taken from the steel sheet and from the shear connector used in the push-out specimens. Results of material characteristic tests are summarized in Table 1. It is worth

mentioning that PO-L50a,b,c specimens have been tested at an early age of the concrete in order to have a concrete strength at the day of test equal to 70% of concrete characteristic strength as prescribed in Eurocode 4 (EC4-1-1, 2005).

Table 1 – Mean material properties.

Specimen	Concrete	Precast	U-shaped		Connectors	
	f_{cm} (MPa)	f_{cm} (MPa)	f_y (MPa)	f_u (MPa)	f_y (MPa)	f_u (MPa)
S20	27.75	42.29			555	693
L40	26.97	43.29			430	550
L50a	20.27	38.15	491	553		
L50b	21.29	38.79			325	445
L50c	22.71	38.04				

Loading and test procedure

The specimens were tested under monotonic loading. The compressive load was applied horizontally and monotonically on the specimen via a hydraulic jack with a capacity of 1500 kN. The actuator was attached to a 40 mm-thick steel plate that serves as a platform for push-out test specimens. The 40 mm thick steel plate was welded to two 6 mm-thick gussets, which are connected to the webs of steel beam at one end via twelve 20 mm-diameter high-strength bolts, see Figure 3 and 4. At the other end of the specimen, the back side surface of the concrete floor was put in contact with a rigid steel beam. The specimen was positioned horizontally on 2 vertical supporting short steel columns where at the top surface of their end-plate (with slotted holes), two greased PTFE plates were placed, allowing the horizontal displacement of the steel beam to occur.

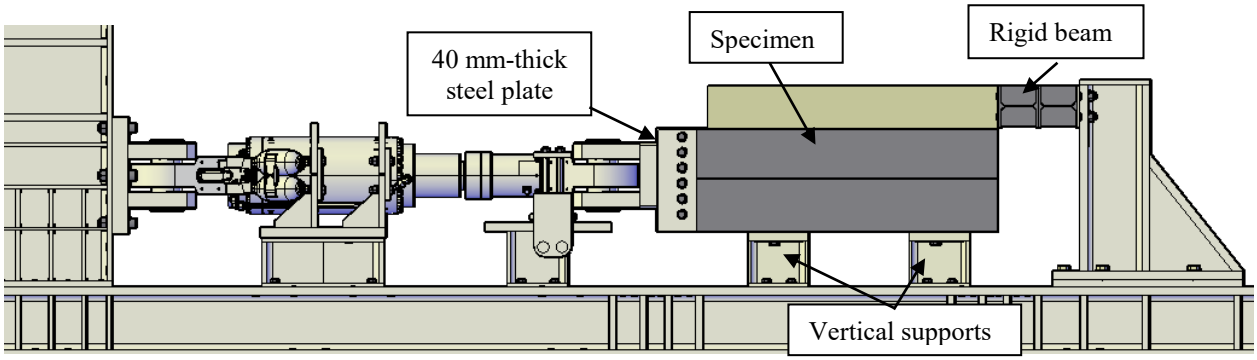


Fig. 3 – Schematic of pushout test setup.

To measure the relative horizontal displacement (slip) between the concrete and the steel beam, 6 LVDT displacement sensors were installed at both sides of the beam (3 for each side), the location where the connectors were placed. The measurement of the vertical separation between the reinforced concrete and the steel beam (uplift) was done through 4 LVDT displacement sensors (2 for each size of the beam), see Figure 5 where the sensors with odd numbering are on the other side of the specimen, not presented in figure. The sensors C_1 to C_6 and C_9 to C_{12} correspond to slip and uplift measurements, respectively. The force and displacement readings were recorded by the universal machine and through a data acquisition system connected to the displacement transducers, respectively.



Fig. 4 – View of pushout test setup.

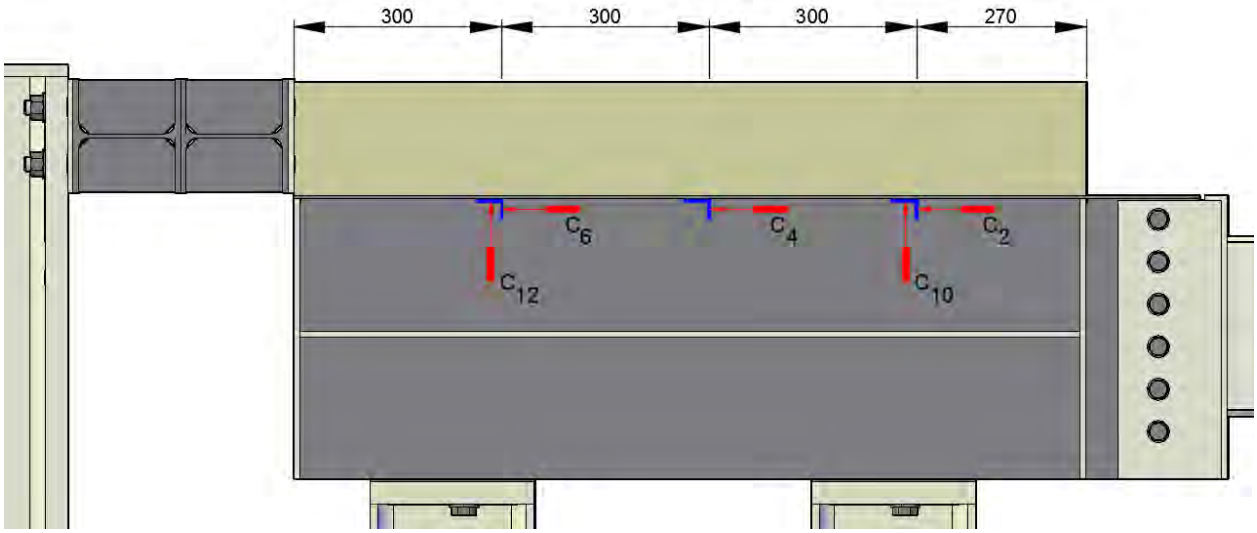


Fig. 5 – Sensors position on the specimen.

Test results

The relation between the push-out load and the mean slip and uplift between the concrete beam-floor and the steel beam is illustrated in Figure 6. One can observe that the specimens with L-shaped shear connectors present a ductile behavior while the one with square bar shear connectors, PB-S20, exhibits a less ductile behavior. Besides, it can be seen that at 80% of ultimate load after peak for each specimen, the vertical separation between concrete and steel beam is less than half of the longitudinal slip. The ultimate load and corresponding slip of each specimen are presented in Table 2.

Table 2 – Ultimate load and corresponding slip.

Specimen	**PO-S20**	**PO-L40**	**PO-L50a**	**PO-L50b**	**PO-L50c**
P_{max} (kN)	748.6	637.1	932.1	916.5	975.9
δ_{max} (mm)	2.743	5.054	5.081	3.032	3.341

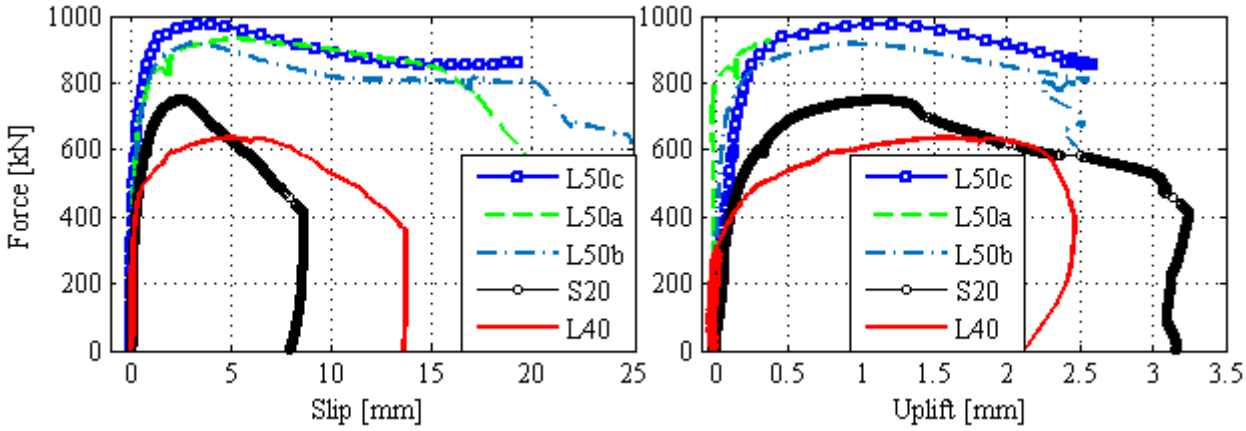


Fig. 6 – Load-mean slip and uplift response.

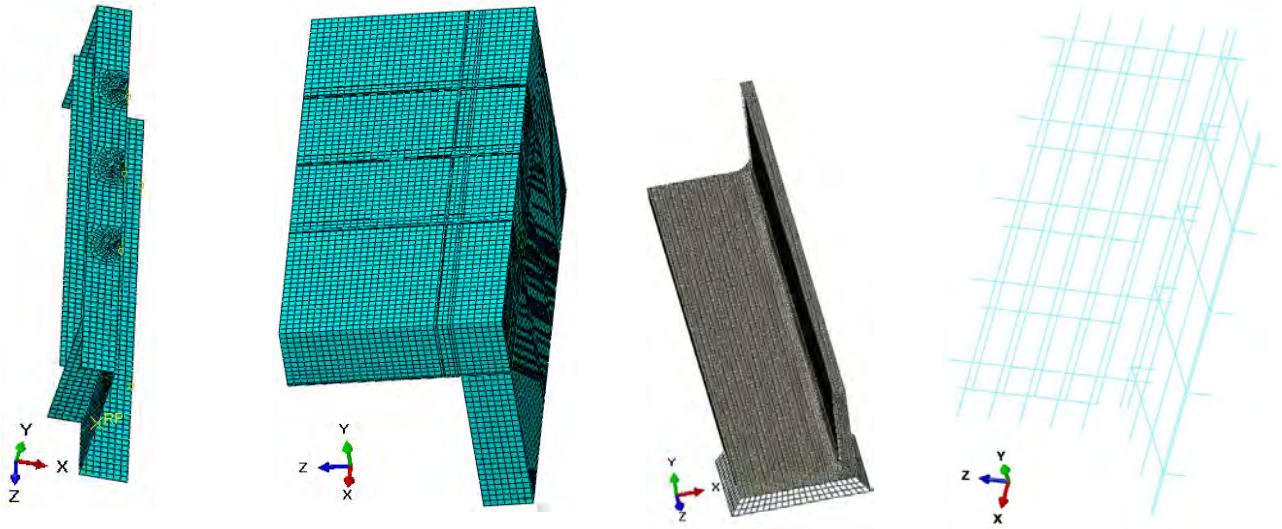
For PB-S20 and PB-L40 specimens, no concrete cracking was observed during the test. The failure of PB-S20 was due to the local concrete crushing. Due to the lack of ductility, which is required in design codes for partial shear connection design, PB-S20 solution is withdrawn and no further discussed in this paper. For specimens with L-shaped shear connectors, the concrete was removed to examine the connectors after testing. The failure of these specimen was associated with the plastic deformation due to shear of L-shaped shear connector, near the fillet between the angles of the cross-section and at the leg angle welded on the flange of steel beam. This mode of failure leaded to a large ductility in the force-slip response. The end of the plastic yielding was due to the rupture of the connector and the welds, see Figure 7.



Fig. 7 – Fracture of L-shaped shear connector.

FINITE ELEMENT SIMULATIONS

In order to get further information, a numerical simulation has been performed on ABAQUS/Explicit. Since the use of square bar shear connectors is not a solution for partial shear connection design in U-shaped steel-concrete hybrid beam, FEA was performed only for specimens with L-shaped shear connectors. All main components that may affect the behavior of shear connection were considered in the model. By taking the advantage of symmetry, only a half of the specimen was simulated.



a) Steel beam (S4R) b) Concrete beam-floor (C3D8R & C3D6R) c) Connectors & welds (C3D8R) d) Rebars (B31)

Fig. 8 – FE model.

Finite element type and mesh

The components were modeled in separate parts as presented in Figure 8. The concrete component was meshed with combine solid element C3D8R and C3D6R available in ABAQUS library. The former element type is an 8-node brick element and the latter is 6-node linear triangular prism element. Each node has three translational degrees of freedom. C3D8R element was also used for meshing shear connectors and welds. The steel beam was meshed with 4-node shell element (S4R) while the reinforcement bars were meshed with beam element (B31). An overall mesh size of the concrete component, steel beam, shear connectors, welds and of the rebars are 20 mm, 20 mm, 1 mm, 2 mm and 20 mm, respectively. For concrete and steel beam component, a fine mesh was used at zones in contact with shear connectors.

Constraints and contact interactions

Once all parts of the model were positioned together into an assembly, appropriate constraints were used to describe the interaction between components. The surfaces in contact between shear connectors and welds were tied together. The bottom surfaces of the latter were tied to the surface of the beam flange. This is equivalent to the actual push-out specimen where shear connectors remained tied to the steel beam flange via welding. For rebars which were placed inside the concrete beam-floor, the embedded constraint was applied. In this constraint, the translational DOF of the nodes on the rebar elements were constrained to the interpolated values of the corresponding DOF of the concrete element. The slip and debond of the rebar was ignored. Contact interactions were applied for the remaining contact surfaces. The interaction properties of the contact interactions used in the model were defined by the tangential and normal behavior to the surfaces. Since the interior surfaces of the U-shaped steel beam were greased, the frictionless for tangential behavior was used at the contact surfaces between steel beam and other components. The penalty friction formulation was used for tangential behavior of the contact surfaces between shear connectors/welds and concrete

with a coefficient of friction equal to 0.2. The default normal behavior (hard contact) was assumed for all contact surfaces. The latter allows a minimum penetration of the slave surface into the master surface. For all contact pairs, the penalty contact formulation was used.

Material models

Cap plasticity model available in ABAQUS (Systemes, 2012) was adopted to model the concrete material. The cap parameters used for each specimen (RC-L40 and Precast-L40 for PO-L40, and RC-L50 and Precast-L50 for PO-L50a,b,c) are listed in Table 3 in which the envelop curve of the cap model was matched with Mohr-Coulomb surface using simple tensile and compressive strength.

Table 3 – Concrete cap plasticity parameters.

	Cohesion (MPa)	Angle of friction	Cap eccentricity parameter	Initial cap yield surface position	Transition surface radius	Flow stress ratio
RC-L40	3.9548	68.66	0.65	0	0.01	1
RC-L50	3.1405	68.66				
Precast-L40	6.0074	68.84				
Precast-L50	5.4222	68.78				

Table 4 shows the true stress-strain data for the L-shaped shear connectors as input in ABAQUS. The elastic-perfectly plastic model was adopted for steel beam. The modulus of elasticity and the Poisson's ratio of steel used in the model were 210 GPa and 0.3, respectively.

Table 4 – Steel connector properties.

L40×40×4		**L50×50×5**	
Yield stress (MPa)	Plastic strain	Yield stress (MPa)	Plastic strain
430.88	0.0000	325.50	0.0000
438.80	0.0182	330.03	0.1320
660.00	0.1792	534.00	0.1798

Validation of finite element model

Push-out tests presented in previous section were used to verify the developed finite element models. The shear connection capacity obtained from the tests and finite element analysis as well as the load-slip and load-uplift behavior of the shear connector, including its failure modes, have been investigated. Figure 9 and 10 show the comparison of load-slip and load-uplift obtained from FEA against the experimental results. Due to the same properties of materials used in PO-L50a,b,c specimens, only one FE simulation was performed for those specimens. It can be seen that there is a good agreement between the pairs. For PO-L40 specimen, FEA produced a quite similar load-slip curve up to ultimate load. When the shear connector fully yields and the fracture begins to occur, the two curves diverge. After the ultimate load, the experimental load descends progressively while the numerical one drops insignificantly.

The stress pattern in the components is illustrated in Figure 11 and 12 for PO-L50 specimen. One can observe that there are two plastification plans due to shear in the L-shaped shear connector and that there is local pressure effect in the concrete block.

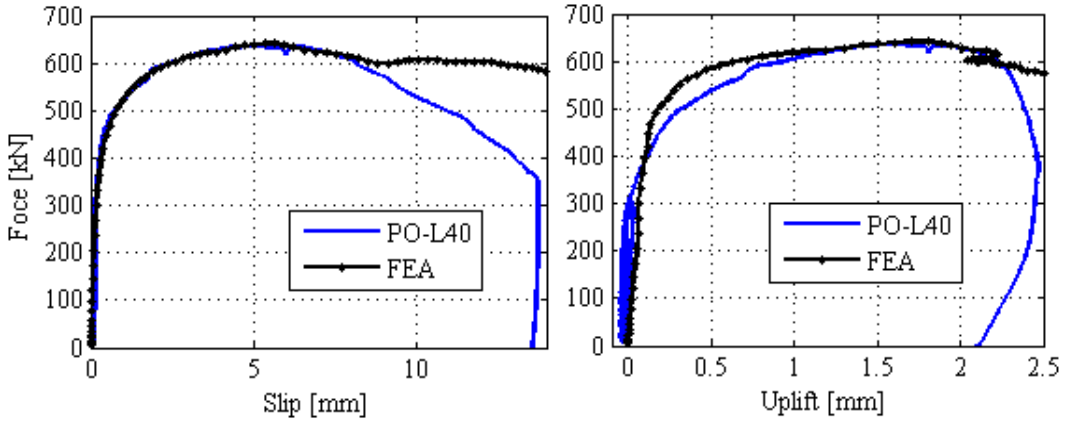


Fig. 9 – Comparison of FEA results against experimental test for PO-L40 specimen.

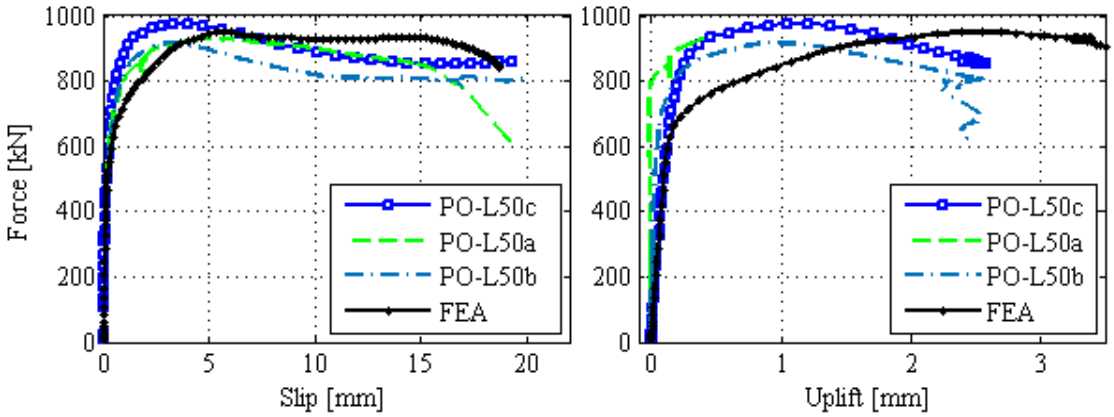


Fig. 10 – Comparison of FEA results against experimental test for PO-L50a,b,c specimen.

FORMULATION OF A NEW DESIGN EQUATION

A new design equation was developed to predict the strength of the L-shaped shear connector used in USCB. This equation was derived based on the observation on deformation of shear connectors and the stress pattern obtained from FEA. It showed that the shear connector resistance may be divided into two parts: concrete contribution and shear resistance of the connector. Herein, it is assumed that the concrete block in front of shear connector is idealized by a rectangular stress block. The new design equation for one shear connector is then given by:

$$P_u = 2\left(A_{s1} + A_{s2}\right) \times \frac{f_u}{\sqrt{3}} + 2K_c \times A_c \times f_c$$

where A_{s1}, A_{s2} and A_c are defined in Figure 13 in which L_c is the welded length of shear connector to the steel beam flange; f_u is the ultimate strength of shear connector; f_c is compressive strength of concrete; and K_c is a calibrated factor on concrete strength due to local pressure effect. The latter is defined by the following expression obtained from a regression analysis of a parametric study, which is not presented in this paper:

$$K_c = 2.229\sqrt{\frac{f_u}{f_c}} - 3.565\frac{L_c}{h_a}$$

in which h_a is the height of the L-shaped cross-section. Table 5 shows the comparison between the ultimate loads given by proposed design equation against experimental results. P_s and P_c represent the contribution of L-shaped shear connector and concrete, respectively, to the shear capacity of the connectors.

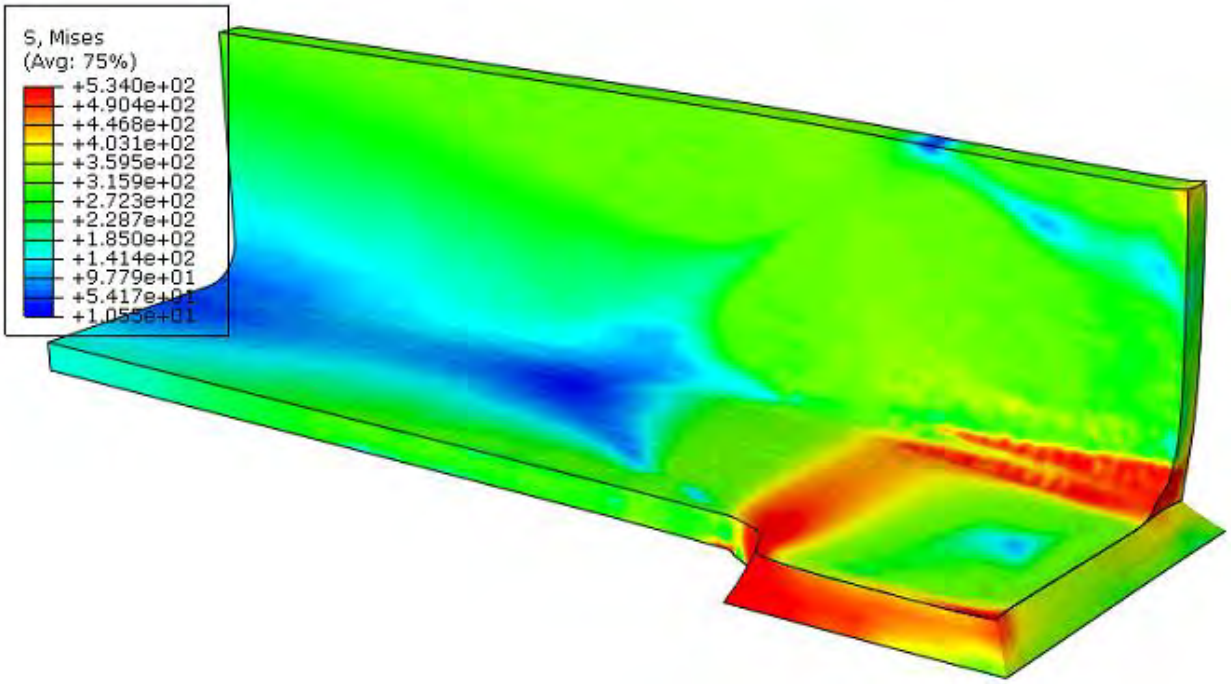


Fig. 11 – Stress pattern of shear connectors at ultimate load for PO-L50a,b,c specimen.

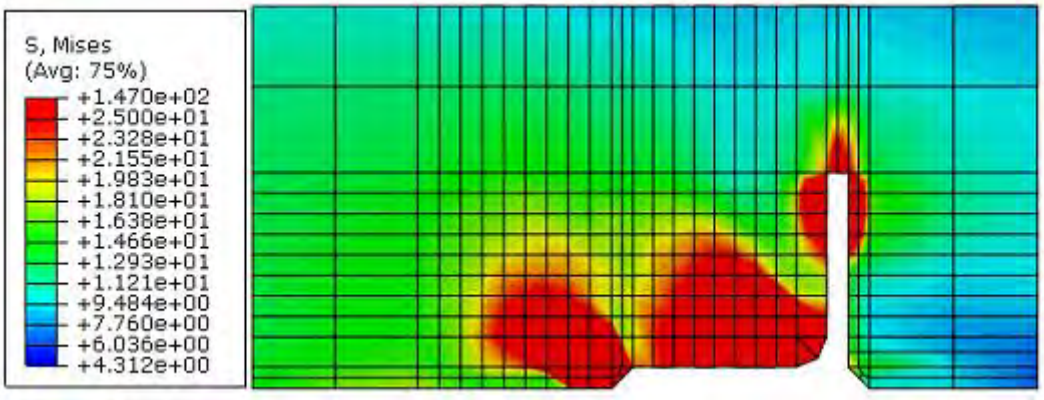


Fig. 12 – Stress pattern of surrounding concrete at ultimate load for PO-L50a,b,c specimen.

In the proposed equation, the width of the concrete block was assumed to be equal to the length of shear connector welded to the steel flange which is extensively larger than what is observed in numerical results.

Table 5 – Comparison of the ultimate loads given by proposed design equation against experimental results.

	f_u (MPa)	f_c (MPa)	L_c (mm)	h_a (mm)	K_c	P_s (kN)	P_c (kN)	$P_{u,th}$ (kN)	$P_{u,exp}$ (kN)	$P_{u,th}/P_{u,exp}$
L50a	445	20.27	40	50	7.59	763.8	184.7	948.52	932.1	1.02
L50b	445	21.29	40	50	7.34	763.8	187.5	951.34	916.5	1.04
L50c	445	22.71	40	50	7.01	763.8	191.2	955.02	975.9	0.98
L40	550	26.97	20	40	8.28	517.7	107.2	624.94	637.1	0.98

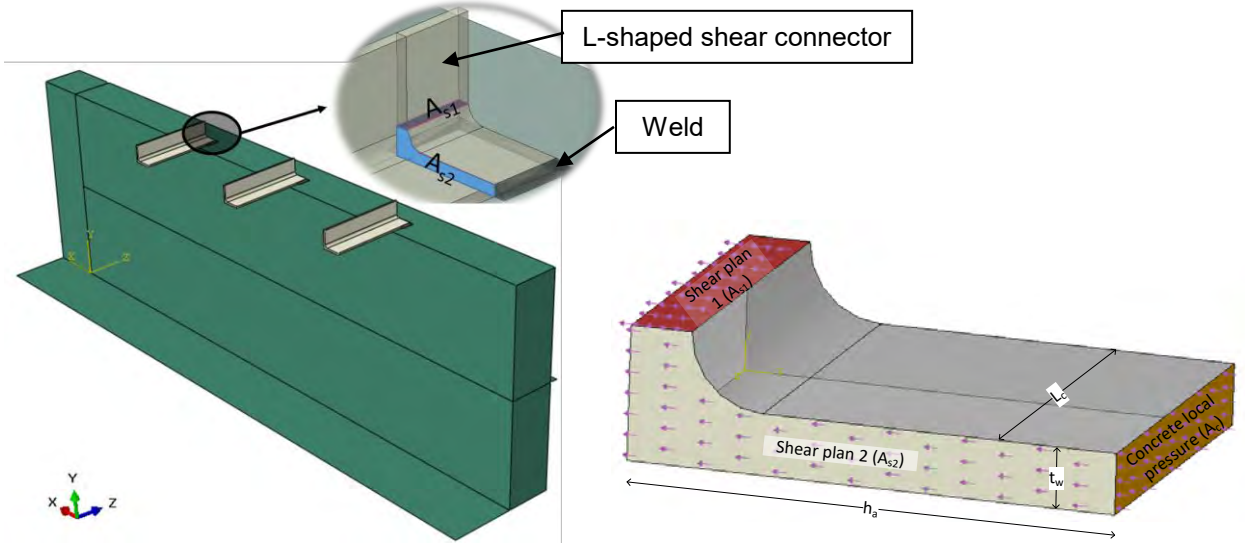


Fig. 13 – Shear failure plans and concrete local pressure zones.

CONCLUSION

Push-out tests of U-shaped steel-concrete hybrid beams with two different shapes of shear connectors were conducted. It was shown that the beam with L-shaped shear connector exhibited a ductile behavior while the beam with square bar shear connector presented less ductility. For that reason, the later solution was withdrawn. Identification of the stress behavior of the shear connector and the surrounding concrete was performed using FE model. It gave the key features in developing the new design equation for L-shaped shear connectors used in U-shaped steel-concrete hybrid beams. It showed that the shear connector resistance may be divided into two parts: concrete contribution and shear resistance of the connector. The former was due to the local pressure effect in the concrete block. To take into account this effect, a calibration factor obtained from a regression analysis has been introduced in the proposed design equation for the ultimate load of the shear connectors. It showed that the estimated ultimate loads are in good agreement with experimental results.

ACKNOWLEDGMENTS

The authors gratefully acknowledge financial support by the ANR (Agence Nationale de la Recherche, France) through the project LabCom ANR B-HYBRID.

REFERENCES

Abe, H., & Hosaka, T. (2002). Flexible shear connectors for railway composite girder bridges. *Composite construction in steel and concrete IV*, 71--80.

Chinn, J. (1965). Pushout Tests on Lightweight Composite Slabs. *AISC Engineering Journal 2*, 129-134.

EC4-1-1. (2005). *Calcul des structures mixtes acier-béton. Règles générales et règles pour les bâtiments.*

ENV. (1994). *Eurocode 4: design of composite steel and concrete structures—Part 1.1: General rules and rules for buildings.* Brussels: European Committee for Standardization.

Liu, Y., Guo, L., Qu, B., & Zhang, S. (2017). Experimental investigation on the flexural behavior of steel-concrete composite beams with U-shaped steel girders and angle connectors. *Engineering Structures*, 492-502.

Maleki, S., & Bagheri, S. (2008). Behavior of channel shear connectors, Part I: Experimental study. *Journal of Constructional Steel Research*, 1333--1340.

Oehlers, D. J., Wright, H. D., & Burnet, M. J. (1994). Flexural strength of profiled beams. *Journal of Structural Engineering*, 378--393.

Shariati, M., Sulong, N. R., Suhatril, M., Shariati, A., Khanouki, M. A., & Sinaei, H. (2013). Comparison of behaviour between channel and angle shear connectors under monotonic and fully reversed cyclic loading. *Construction and Building Materials*, 582--593.

Systemes, D. (2012). ABAQUS 6.12 Theory manual. *Dassault Systemes Simulia Corp., Providence, Rhode Island*.

Valente, I. B., & Cruz, P. J. (2009). Experimental analysis of shear connection between steel and lightweight concrete. *Journal of Constructional Steel Research 65*, 1954-1963.

Viest, I. M. (1956). Investigation of stud shear connectors for composite concrete-steel T-beams. *Journal of the american concrete institute*, 875-891.

Wright, H., Evans, H., & Harding, P. (1987). The use of profiled steel sheeting in floor construction. *Journal of Constructional Steel Research*, 279--295.

SHEAR PERFORMANCE OF NONPARALLEL TYPE TWIN PERFOBOND STEEL PLATE SHEAR CONNECTORS: FEM ANALYSIS AND EXPERIMENTAL VERIFICATION

Hai Chen
Ph.D. Candidate of Structural Engineering, College of Civil Engineering, Huaqiao University
Xiamen, China
E-mail: 1300222006@hqu.edu.cn

Yang Liu (corresponding author)
Associated Professor of Structural Engineering, College of Civil Engineering, Huaqiao University
Xiamen, China
E-mail: lyliuyang@hqu.edu.cn

Zixiong Guo
Professor of Structural Engineering, College of Civil Engineering, Huaqiao University
Xiamen, China
E-mail: guozxcy@hqu.edu.cn

Yong Ye
Lecturer of Structural Engineering, College of Civil Engineering, Huaqiao University
Xiamen, China
E-mail: qzyeyong@126.com

Bahram M. Shahrooz
[a] Professor of Structural Engineering, Dept. of Civil and Architectural Engineering
Construction Management, Univ. of Cincinnati, Cincinnati, U.S.
[b] Distinguished Professor, College of Civil Engineering, Huaqiao University
Xiamen, China
E-mail: Bahram.shahrooz@uc.edu

ABSTRACT

This paper describes a new type of shear connector, which consists of two pieces of nonparallel perfobond plate ribs (NPP). Using three-dimensional finite element models, calibrated against experimental data, were used to conducted parametric studies on the influence of different parameters such as, rib arrangement and thickness of rib on the shear capacity of the NPP connectors. A total of 81 push-out specimens were analyzed with different angles and gaps between the ribs, rib thickness, and concrete strengths. The numerical results show that increases in the rib thickness and concrete strength enhance the shear capacity of NPP connectors. The shear strength of NPP connectors is reduced with an increase in the angles between the ribs. The gap between the ribs does not have a significant influence on the shear-slip relationships. The NPP connectors are a viable alternative to conventional shear connectors. Different strength and stiffness requirements can be met by adjusting rib configuration.

INTRODUCTION

The many benefits of steel and concrete structures rely on sufficient bond transfer between these two materials to prevent separation of steel and concrete at their interface. This goal is

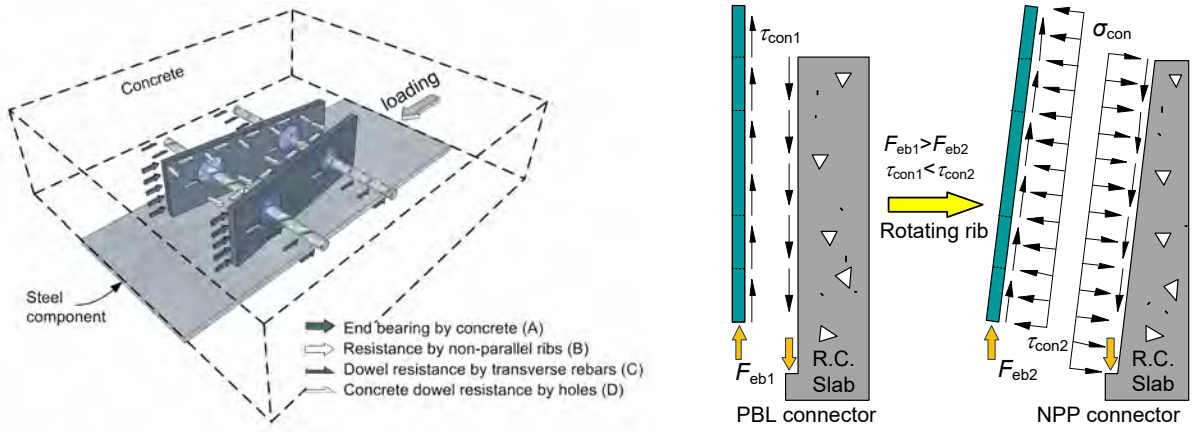
achieved through the use of shear connectors. Headed studs are the industry standard developed based on many past studies [e.g., Oehlers and Coughlan 1986]. Another emerging type is perfobond connectors. These connectors consist of perforated steel plates welded to steel at the concrete-steel interface. Variations of perfobond connectors have studied, e.g., perfobond ribs [Leonhardt et al. 1987], T-perfobond ribs [Vianna et al. 2008], long-hole perfobond ribs [Zheng et al. 2016], or Y-type perfobond ribs [Kim et al. 2017]. Compared with the headed stud connector, perfobond connectors have higher shear stiffness and improved fatigue performance.

A number of previous experimental and numerical simulation studies have examined the shear capacity and behavior of perfobond connectors [e.g., Medberry and Shahrooz 2002; Valente and Cruz 2004; Ahn et al. 2010; Oguejiofor and Hosain 2011]. However, previous studies were limited to single perfobond connectors and the behavior of twin perfobond connectors have not been evaluated, in particular the influence of the angle between the ribs.

The main objective of this paper is to present a new type of shear connector, which is composed of two pieces of nonparallel perfobond plate ribs (NPP). The impacts of the rib arrangement, the rib thickness and rib angle, the concrete strength, and the gap between the ribs on the shear resistance were investigated. Three-dimensional finite element models were developed and calibrated using experimental data, and were employed to conduct parametric studies.

SHEAR RESISTANCE CHARACTERISTICS OF NPP CONNECTOR

Figure 1 illustrates the load carrying mechanism of the NPP connector under in-plane shear. Four components contribute towards the shear resistance: (A) end bearing resistance of the steel plate; (B) the resistance of the non-parallel ribs; (C) the dowel resistance of transverse reinforcing bars, if present; and (D) dowel resistance of concrete studs in the steel plate holes.



(a) Shear resistance mechanism of NPP connector (b) Conventional PBL and NPP connectors

Fig.1 - Mechanical behavior of a NPP connector

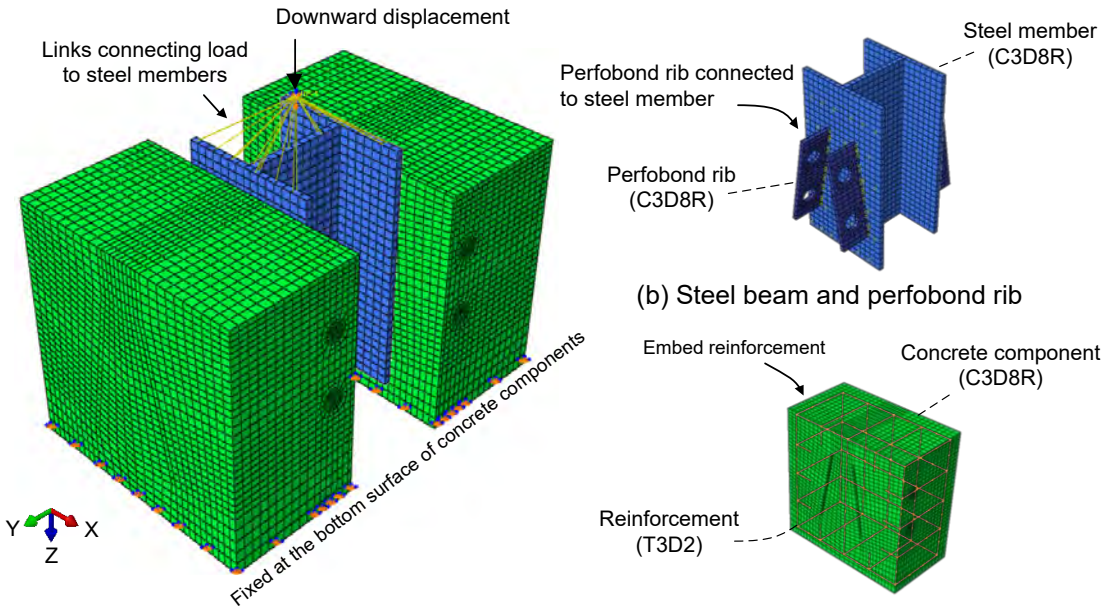
The differences between shear resistance mechanism between conventional perfobond shear connector (Perfobond Leisten, abbreviated as PBL) and NPP connector are shown in Figure 1(b). For the orientation of perfobond rib shown, the end bearing resistance F_{eb} of NPP is smaller than that of PBL connector. However, the normal stress (σ_{con}) in NPP increases the frictional resistance and the interfacial shear (τ_{con}) is larger than that in PBL, i.e., $\tau_{con2} > \tau_{con1}$. The angle between the ribs is a crucial factor that affects the shear strength of NPP connectors.

FINITE ELEMENT MODEL

To investigate the influence of different parameters three-dimensional finite element models simulating a typical push-out experiment were developed using finite element pre-processor ABAQUS/CAE [Hibbit, K. 2014]. Suitable contact interactions, constraints, boundary conditions, and material models were specified to estimate the shear performance of NPP connectors.

FINITE ELEMENT TYPE AND MESH

A push-out specimen consists of four parts: (A) two concrete components, (B) a structural steel member, (C) two perfobond ribs, and (D) reinforcing bars, if present. A three-dimensional finite element modeling of such specimen is shown in Figure 2. Three-dimensional eight-node reduced integration element (C3D8R) was used to model the perfobond rib, concrete components, and structural steel member. The reinforcing bars were modelled by three-dimensional two-node truss elements (T3D2). A fine mesh was used for the concrete dowels and the regions around the holes in the perfobond rib, to more accurately capture the high stress levels in these regions. The coarse mesh size was 20 mm and the fine size was about 3 mm.



(a) Push-out model

(b) Steel beam and perfobond rib

(c) Concrete slab and reinforcement rebar

Fig.2 - Finite element model

INTERACTION AND BOUNDARY CONDITIONS

The various components were assembled in accordance with the actual configuration of a typical push-out specimen. The perfobond ribs were tied to the flanges of the structural steel members to prevent relative slip, simulating welds that would not fail prior to fully developing the capacity of the perfobond connection. The contact pair algorithm available in ABAQUS was used to define the perfobond-flange interface as well as the contact between the perfobond rib and the surrounding concrete. The default normal behavior was assumed to be a 'hard' contact pressure-overclosure relationship. The penalty frictional formulation was adopted, and the coefficient of friction between perfobond rib and concrete was taken as 0.4 based on the results of a sensitivity study. The other contact interactions were assumed to be frictionless. Anchorage

of reinforcing bar was simulated by embedded constraints.

As illustrated in Figure 2(a), the bottom surfaces of the concrete segments were assigned fully fixed. The downward displacement (i.e., in the Z direction) was applied to a reference that was linked to the top of the structural steel members. To ensure a quasi-static solution from the explicit dynamic procedure, the inertia effects were minimized by using a smooth amplitude function to increase the downward displaced at a rate of 24 mm/min.

CONCRETE MATERIAL MODEL

The concrete damage plasticity model (CDP) was implemented in the reported research. CDP model needs to be defined in terms of plastic, compressive, and tensile properties. To define the plastic property, five parameters need to be specified: (A) dilation angle ψ=30°, (B) flow potential eccentricity ϵ=0.1, (C) ratio of biaxial to uniaxial compressive strength σ_{b0}/σ_{c0}=1.16, (D) ratio of second stress invariant on the tensile meridian to that on the compressive meridian K=2/3, and (E) viscosity parameter μ=0 [Hibbit K. 2014].

The nonlinear behavior of plain concrete material in uniaxial compression was presented by a uniaxial compressive stress-strain curve shown in Figure 3(a). The stress-strain relationships (i.e., $\sigma_c - \varepsilon_c$) were determined from Eq. (1), as suggested in FIB [FIB MC 2010].

$$\frac{\sigma_c}{f_c} = \begin{cases} 0.4 \cdot \dfrac{\varepsilon_c}{\varepsilon_{ce}} & \left(0 < \varepsilon_c \le \varepsilon_{ce}\right) \\ \dfrac{\kappa \cdot \eta - \eta^2}{1 + (\kappa - 2) \cdot \eta} & \left(\varepsilon_{ce} < \varepsilon_c \le \varepsilon_{cp}\right) \\ 1 - 0.15 \cdot \dfrac{\varepsilon_c - \varepsilon_{cp}}{\varepsilon_{cu} - \varepsilon_{cp}} & \left(\varepsilon_{cp} < \varepsilon_c \le \varepsilon_{cu}\right) \end{cases} \tag{1}$$

where f_c is the cylinder compressive strength of concrete (MPa). The plasticity factor $\kappa = E_c \cdot \varepsilon_{cp}/f_c$; $\eta = \varepsilon_c/\varepsilon_{cp}$; and ε_{ce}, ε_{cp}, ε_{cu} are the elastic strain, peak strain, and ultimate strain, respectively with the following values: $\varepsilon_{ce} = 0.4 f_c/E_c$, $\varepsilon_{cp} = 2.3\times10^{-3}$, 2.4×10^{-3} and 2.5×10^{-3} for C30, C40, C50 concrete respective, and $\varepsilon_{cu} = \alpha \cdot \varepsilon_{cp}$. The coefficient α=13.6 was iteratively calibrated to match push-out test results from a previous study [Zheng et al. 2016]. The initial Young's modulus (E_c) was calculated by Eq. (2), according to FIB [FIB MC 2010].

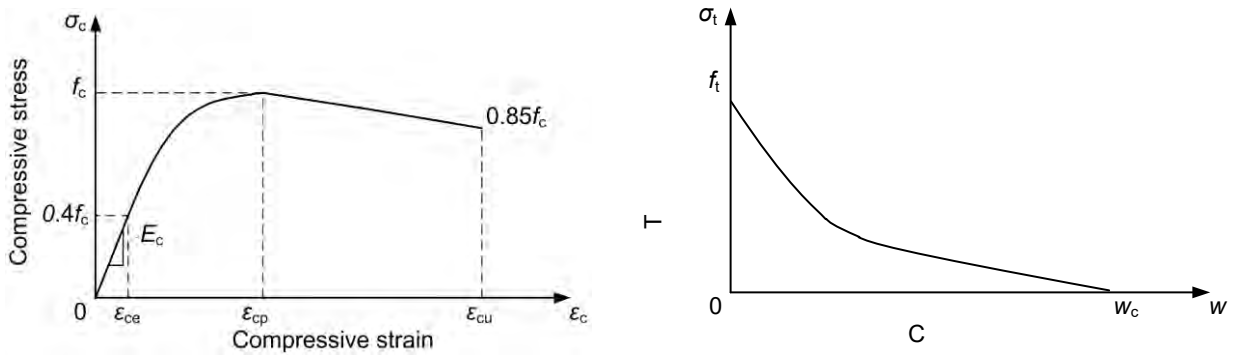
$$E_c = E_{c0} \cdot \alpha_E \cdot \left(f_c / 10\right)^{1/3} \tag{2}$$

where $E_{c0} = 21.5\times10^3$ MPa and α_E=1.0 for quartzite aggregates.

As shown in Figure 3(b), tension plasticity curve was defined as a function of the tensile stress and crack width, obtained from Eq. (3) [Birtel and Mark 2006].

$$\frac{\sigma_t}{f_t} = \left[1 + \left(\frac{c_1 \cdot w}{w_c}\right)^3\right] \cdot \exp\left(-\frac{c \quad w}{w_c}\right) - \frac{w}{w_c} \cdot \left(1 + c_1^3\right) \cdot \exp\left(-c_2\right) \tag{3}$$

where σ_t is the tensile stress of concrete (MPa); f_t is the tensile strength (MPa); w is the crack width (mm); w_c is the crack width (mm) at the complete loss of tensile strength taken, $w_c = 5.14\, G_F/f_t$ in which G_F is the fracture energy (N/mm) required to create a unit area of stress-free crack, $G_F = 0.073 f_c^{0.18}$; and the constants are c_1=3, and c_2 =6.93 according to [Zheng et al. 2016].



(a) Compression (b) Tension

Fig.3 - Material constitution of concrete

MATERIAL MODEL FOR STRUCTURAL STEEL AND REINFORCEMENT

The stress-strain relationship of structural steel and reinforcement was modeled by a tri-linear curve, as shown in Figure 4 [Zheng et al. 2016]. The material behavior is initially elastic followed by strain yielding and then hardening. The tensile yield strength f_y and the ultimate tensile strength f_u were selected based on material test data. For structural steel and reinforcement steel, the Young's modulus E_s was taken as 206GPa and 200GPa, respectively. As shown in Figure 4, E_{sp} set equal to $0.01E_s$.

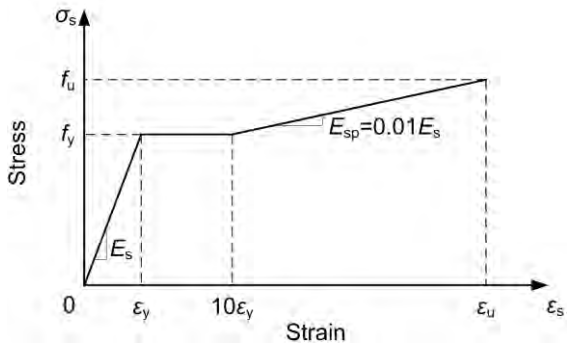


Fig.4 - Stress-strain relationship for structural and reinforcement steel

VERIFICATION OF FINITE ELEMENT MODEL

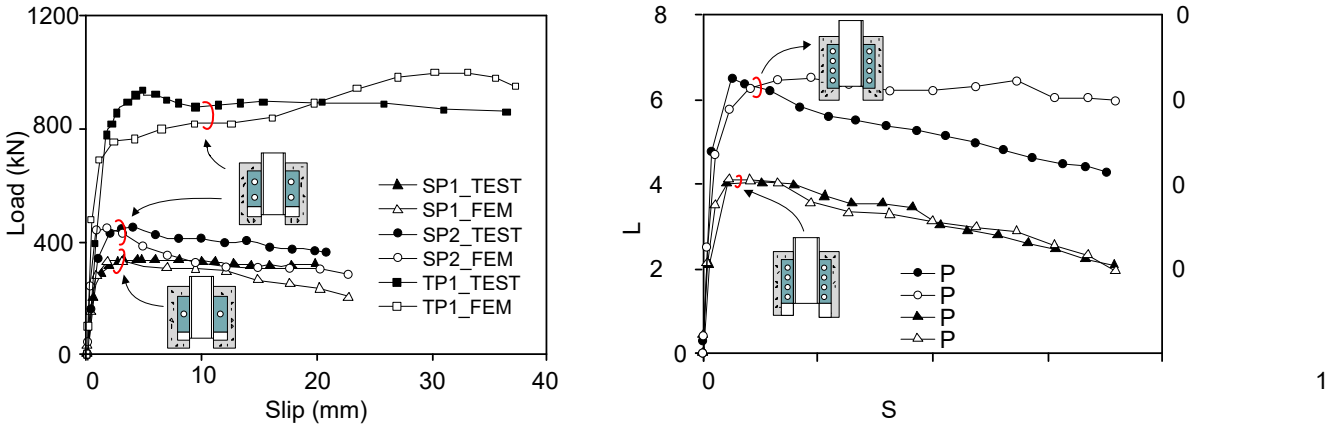
The finite element model was verified against previous data from a number of tested push-out specimens [H. Chen 2016; Ahn et al. 2008; Cândido et al. 2010]. These test specimens (A) had single or twin perfobond connectors, (B) were with and without end bearing, (C) used various concrete strengths, (D) had thin to relatively thick plates as perfobond ribs, and (E) utilized a different number of holes in the perfobond connectors.

As evident from Table 1, the results obtained from finite element analysis accurately replicate the experimental capacities. The mean value of the finite element results over the experimental ones is 0.98 with a coefficient of variation of 0.038. Moreover, Figure 5 shows a good agreement between the experimental and numerically generated load–slip curves. Having demonstrated the accuracy of the finite element modeling (FEM) procedure presented herein, a similar FEM method was used to perform a series of parametric studies.

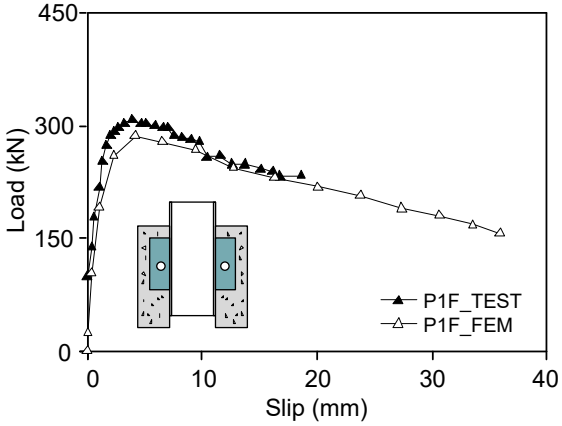
Table 1 - Comparison of shear connector capacity obtained from experiments and finite element analysis

Specimen	f_c (MPa)	D (mm)	t (mm)	n (mm)	P_{test} (kN)	P_{FE} (kN)	P_{test}/P_{FE}	Reference
SP1	26	50	12	1	336.1	331.0	1.02	
SP2	26	50	12	2	452.4	449.6	1.01	[H. Chen, 2016]
TP1	26	50	12	2	940.9	1005.1	0.94	
PF-S-A2	28	55	6	4	628.3	650.4	0.97	[Ahn et al. 2010]
PF-S-B2	28	55	6	4	410.0	410.1	1.00	
P1F	31	30	15	1	309.4	331.5	0.93	[Cândido-Martins et al. 2010]

f_c is measured concrete strength; D is Holed diameter; t is thickness of perfobond rib; n is number of holes in perfobond; P_{test} is measured capacity; P_{FEM} is calculated capacity from FEM



(a) [H. Chen, 2016] (b) [Ahn et al. 2010]



(c) [Cândido-Martins et al. 2010]

Fig.5 - Comparison of experimental and numerical load–slip behavior of push-out test

PARAMETRIC STUDY

A parametric study was conducted to study the influence of the following parameters on the shear performance of NPP connector: (A) the rib gaps (L), (B) the angle between ribs (α), (C) the thickness of the rib (t), and (D) the concrete strength. A total of 81 push-out simulations were conducted. The cases were divided into 27 groups, each group having identical parameters but with different concrete strengths: 30, 40 and 50 MPa (designated as NO.1, NO.2, and NO.3, respectively). The details of the cases are shown in Figure 6.

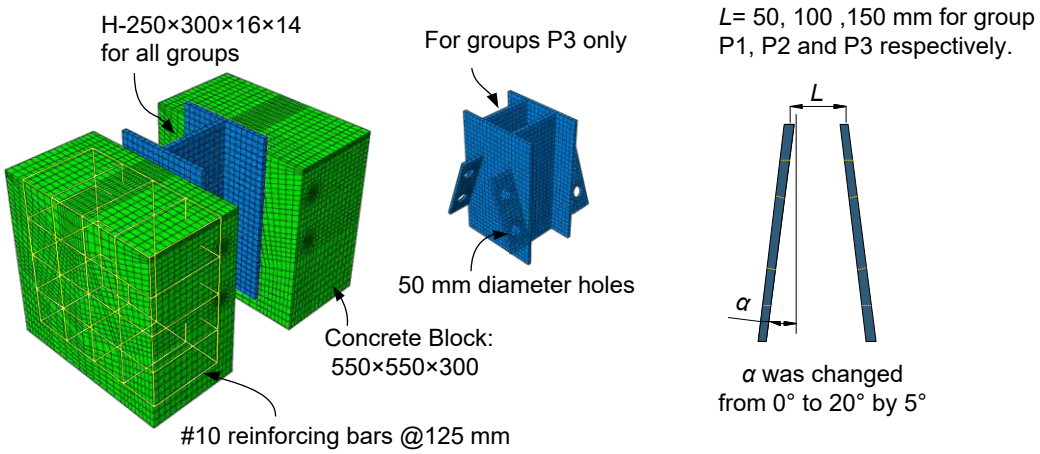


Fig.6-Details of finite element model in parametric study

The shear strength of the 81 push-out specimens obtained from the finite element analysis are summarized in Table 2. As expected, the ultimate load capacity becomes larger as the concrete strength is increased. The effects of the other variables will be discussed after presenting and discussing the load-slip relationships.

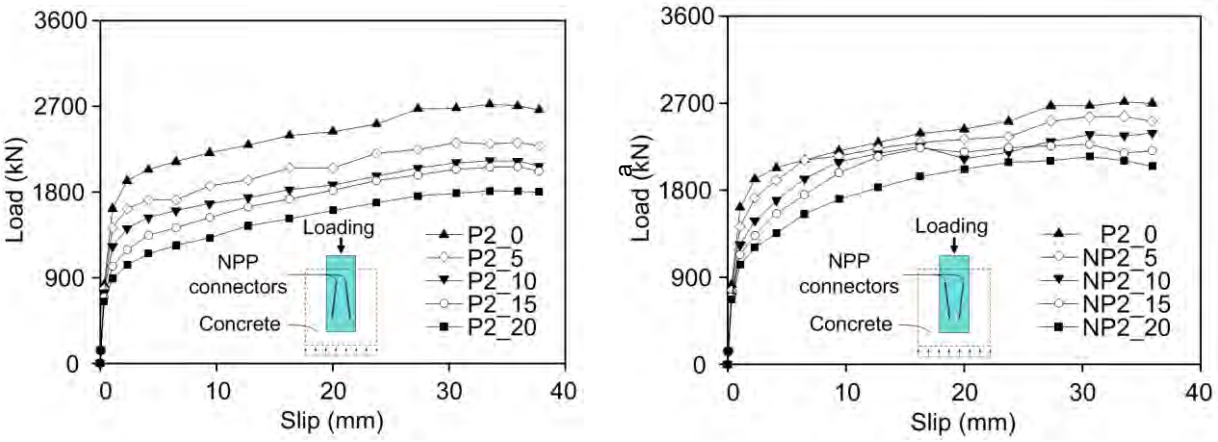
Figure 7 illustrates the load versus slip curves for specimens in group P2 with a 100mm gap. The trend of load-slip curves do not change as a function of ribs angle α although the maximum load becomes larger when the rib angles have negative angles. These curves can be divided into three stages: (A) elastic, (B) elastoplastic, and (C) plastic. These stages are described with reference to the load-slip relationship for specimen P2_15 in Figure 7(c). The elastic stage starts from the origin to Point A. The curve at this stage is almost linear with a very small slip(<0.5mm). The applied shear load is resisted by the concrete studs in the hole of the rib, as evident by the inset in Figure 7(c). The peak average stress is concentrated in the vicinity of the concrete studs, while the average stress in other regions is much smaller than the maximum concrete stress. The elastoplastic stage starts at Point A and ends at Point B, at which the displacement is several times larger than that for Point A. A gradual loss of stiffness is evident. The areas subjected to high stress spread beyond the concrete studs, suggesting good interaction between the ribs and the surrounding concrete. The contribution to the shear resistance of end bearing becomes more important. Beyond Point B, the slope of the curve gradually increases up to a very large displacement, labeled as plastic stage (Point C). A similar trend may be observed for the other cases. The results indicate that NPP connectors have sufficient ductility and may be used in composite members where fully plastic rotation is needed.

Table 2 – Calculated capcities

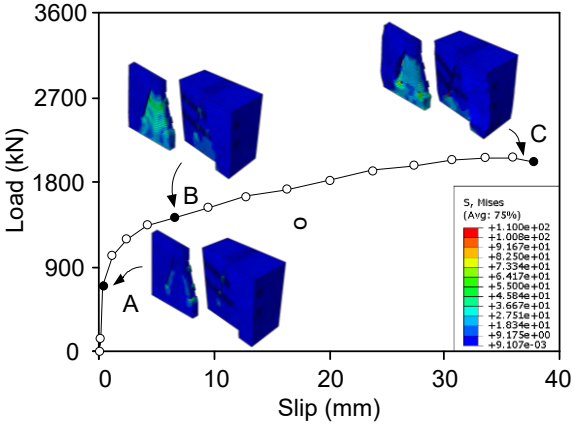
Group	L	α	t	concrete cylinder strength (MPa)			Ultimate load (kN)		
	(mm)	(°) [a]	(mm)	NO.1	NO.2	NO.3	P_1	P_2	P_3
P1_0		0	12	30	40	50	2740	3295	3570
P1_5		5	12	30	40	50	2674	3164	3392
P1_10	50	10	12	30	40	50	2379	2859	3177
P1_15		15	12	30	40	50	2152	2677	2984
P1_20		20	12	30	40	50	2128	2611	2863
P2_0		0	12	30	40	50	2714	3090	3284
P2_5		5	12	30	40	50	2311	2792	3000
P2_10		10	12	30	40	50	2123	2597	2758
P2_15		15	12	30	40	50	2061	2437	2668
P2_20		20	12	30	40	50	1806	2238	2443
P2_N20		-20	12	30	40	50	2149	2366	2585
P2_N15		-15	12	30	40	50	2273	2660	2883
P2_N10		-10	12	30	40	50	2388	2805	2927
P2_N5	100	-5	12	30	40	50	2559	2955	3140
P2_5A		5	6	30	40	50	1687	1990	2147
P2_10A		10	6	30	40	50	1502	1934	2137
P2_15A		15	6	30	40	50	1530	1960	2135
P2_20A		20	6	30	40	50	1315	1751	1873
P2_5B		5	18	30	40	50	2923	3454	3627
P2_10B		10	18	30	40	50	2630	3090	3314
P2_15B		15	18	30	40	50	2599	3069	3264
P2_20B		20	18	30	40	50	2286	2825	3046
P3_0		0	12	30	40	50	2963	3456	3674
P3_5		5	12	30	40	50	2588	3036	3330
P3_10	150	10	12	30	40	50	2218	2744	3060
P3_15		15	12	30	40	50	2173	2648	2883
P3_20		20	12	30	40	50	2046	2511	2781

[a] Negative angle indicates reversed load – see the inset in Figure 7(b)

To understand the influence of the rib angle *α*, the shear capacity is plotted in Figure 8 versus *α* for different concrete strength and rib gaps *L*. In this figure, N indicates a negative angle of the NPP connectors, i.e., the load enters the connectors from their wider gap, refer to the inset in Figure 8(a). The loading direction only affects the shear strength of NPP connectors, with a higher strength in the negative direction than that in the positive direction. The strength is increased by 20.8% when *α* changed from -20° to 0° and reduced by 33.5% when *α* is changed from 0° to 20° for concrete with compressive strength of 30MPa. Figure 8 clearly demonstrates a similar trend for the other concrete strengths and rib gaps. However, as discussed previously (see Figures 7(a) and 7(b)), the angle does not have an obvious difference on the load-slip relationships between both directions and the ductility is not adversely affected by the orientation of rib connectors relative to the loading direction.

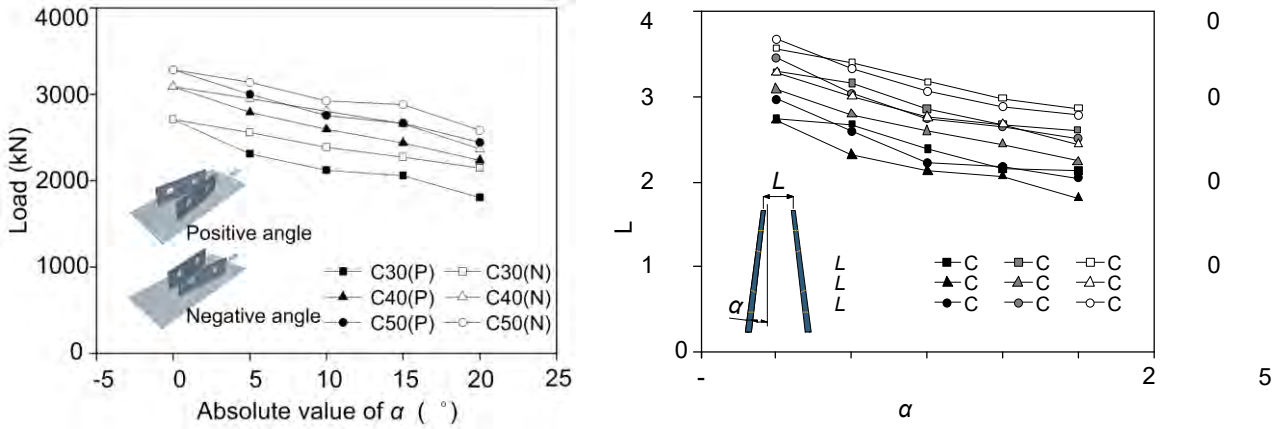


(a) Positive angle (b) Negative angle



(c) Specimens P2_15

Fig.7 – Load versus slip curves for specimens of group P2



(a) Rib gaps of 100 mm (b) Rib gaps of 50, 100 and 150 mm

Fig.8 - Load versus ribs angle curve for specimens with different rib gaps

The load versus rib thickness (*t*) for group P2 is shown in Figure 9. The shear strength is increased almost linearly. The increases for *t*=18 mm in comparison to *t*=6mm are summarized in Table 3.

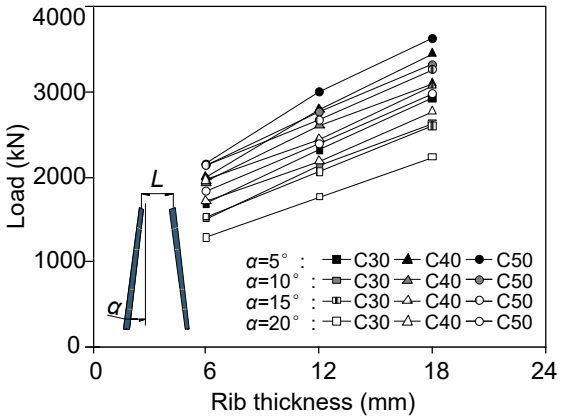


Fig.9- Load versus rib thickness for group P2 specimens with different rib angles (α)

Table 3 - Influence of rib thickness on strength (18mm vs. 6mm)

α (°)	f_c (MPa)	% increase
5	30	73.2%
	40	73.6%
	50	69.0%
10	30	75.2%
	40	59.2%
	50	55.1%
15	30	69.9%
	40	56.6%
	50	52.9%
20	30	73.9%
	40	61.3%
	50	62.6%

The load versus the gap between the ribs (L) is plotted in Figure 10. Increasing the gap from 50 to 100mm is seen to reduce the capacity. This reduction is deemed to be because of the out of plane bending deformation of the flange of the structural steel member onto which the NPP connectors are welded. This deformation depends on the stiffness of flange extending beyond the web. The gap between the ribs affects the stiffness. The out-of-plane flange stiffness is larger for L=50mm than that for L=100mm; hence, the shear capacity is larger for the small gap. In the case of L=150mm, the capacity is nearly the same as that for L=50mm because two webs were used. It should be noted that the "span" over which the flange can bend out of plane is nearly equal for L=50mm with one web and L=150mm with two webs. The results suggest that the shear capacity of NPP depends not only on the properties of the connector but it also depends on the stiffness of the flanges onto which they are welded. Additional studies are needed to quantify the flange stiffness in calculation of shear capacity of NPP connectors.

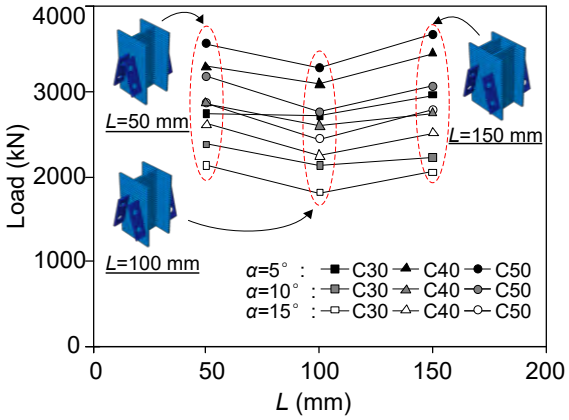


Fig.10 - Load versus rib gaps curves for different concrete strengths

SUMMARY AND CONCLUSIONS

Refined three-dimensional nonlinear finite element analyses were conducted to investigate the shear capacity of non-parallel type twin perfobond plate(NPP) connectors. The focus of the analyses was on modeling of push-out specimens that have been used in past experimental studies. The models accounted for nonlinear material properties of concrete, structural steel member, steel reinforcement, and steel ribs; and contact surfaces between steel beam flanges, steel rib surfaces, and concrete. The shear capacity and load-slip curves of conventional perfobond shear connector (PBL) from a number of past experimental programs could successfully be predicted. After validating the nonlinear finite element model, an extensive parametric study of 81 cases was conducted to examine the influence of various parameters was. The following conclusions can be drawn based on the reported results:

1) The proposed NPP connector has adequate shear capacity and exhibits excellent ductility. This type of connector can be used as a practical alternative to meet different connector performance requirements in composite structures.
2) The load-slip relationships of NPP connectors have three distinct stages: elastic, elastoplastic, and plastic. The large plastic characteristics of NPP connectors make them a good choice for composite members where fully plastic rotation is needed.
3) The loading direction relative to the orientation of the ribs in NPP connector affects the shear strength of NPP connectors, with a higher strength in the negative direction (the load enters the connector on its wider gap) than that in the positive direction. The load-slip relationships are, however, not affected. In other words, the ductility of NPP connectors is not affected by the loading direction.
4) The angle between ribs is a key parameter influencing the shear strength The strength decreases with an increase in the angle irrespective of the loading direction being positive or negative.
5) The gap between the ribs has no obvious infect on shear strength.
6) The shear strength becomes higher with an increase in the concrete strength and rib thickness.

ACKNOWLEDGMENTS

Dr. S. Zheng from Huaqiao University provided significant assistance with the FEM analyses. The authors sincerely appreciate his help. The research presented in this paper was funded by the Key Program of Natural Science Foundation for Young Scholar in University of Fujian Province, China (Grant No. JZ160410) and the Natural Science Foundation of Fujian Province, China (Grant No. 2014J05061), both of which are greatly acknowledged.

REFERENCES

Oehlers, D. J., & Coughlan, C. G. (1986). The shear stiffness of stud shear connections in composite beams. Journal of Constructional Steel Research, 6(4), 273–284.

Leonhardt, F., Andrä, W., Andrä, H. P., & Harre, W. (1987). Neues, vorteilhaftes verbundmittel für stahlverbund-tragwerke mit hoher dauerfestigkeit. Beton- und Stahlbetonbau, 82(12), 325-331.

Vianna, J. D. C., Costa-Neves, L. F., Vellasco, P. C. G. D. S., & Andrade, S. A. L. D. (2008). Structural behaviour of T-perfobond shear connectors in composite girders: an experimental approach. Engineering Structures, 30, 2381-2391.

Zheng, S., Liu, Y., Yoda, T., & Lin, W. (2016). Parametric study on shear capacity of circular-hole and long-hole perfobond shear connector. Journal of Constructional Steel Research, 117, 64-80

Kim, S. H., Park, S., Kim, K. S., & Jung, C. Y. (2017). Generalized formulation for shear resistance on y-type perfobond rib shear connectors. Journal of Constructional Steel Research, 128, 245-260.

Medberry, S. B., & Shahrooz, B. M. (2002). Perfobond shear connector for composite construction. Engineering Journal, 39, 2-12.

Valente, I., & Cruz, P. J. S. (2004). Experimental analysis of perfobond shear connection between steel and lightweight concrete. Journal of Constructional Steel Research, 60, 465-479.

Ahn, J. H., Lee, C. G., Won, J. H., & Kim, S. H. (2010). Shear resistance of the perfobond-rib shear connector depending on concrete strength and rib arrangement. Journal of Constructional Steel Research, 66, 1295-1307.

Oguejiofor, E. C., & Hosain, M. U. (2011). Behavior of perfobond rib shear connectors in composite beams: full-sized test. Canadian Journal of Civil Engineering, 19(2), 224-235.

Ahn, J. H., Jeong, Y. J., & Kim, S. H. (2008). Shear behaviour of perfobond rib shear connector under static and cyclic loadings. Magazine of Concrete Research, 60(5), 347-357.

FIB, Model Code 2010 — Final Draft, vol. 1, 2010 (Lausanne).

Birtel, V., & Mark, P. (2006). Parameterised finite element modelling of RC beam shear failure. 2006 ABAQUS Users' Conference, 95-106.

Nguyen, H. T., & Kim, S. E. (2009). Finite element modeling of push-out tests for large stud shear connectors. Journal of Constructional Steel Research, 65, 1909-1920.

Hibbit, K. (2014). ABAQUS documentation, Version 6.14.

Cândido-Martins, J. P. S., Costa-Neves, L. F., & Vellasco, P. C. G. D. S. (2010). Experimental evaluation of the structural response of perfobond shear connectors. Engineering Structures, 32, 1976-1985.

Hai Chen (2016). Experimental and Analytical study on A Novel Perfobond Strip Connector. Master's dissertation, Huaqiao University.

EXPERIMENTAL STUDIES OF COMPOSITE SLIM FLOOR BEAMS

Therese Sheehan
University of Bradford
Bradford, United Kingdom
t.sheehan@bradford.ac.uk

Dennis Lam
University of Bradford
Bradford, United Kingdom
d.lam1@bradford.ac.uk

Xianghe Dai
University of Bradford
Bradford, United Kingdom
x.dai@bradford.ac.uk

ABSTRACT

Composite slim floor beam is characterized by incorporating the steel section into the depth of the floor which leads to the reduction of the overall depth of the composite beam. Although Eurocode 4 does not exclude slim floor beams from its scope, no specific requirement or guidance is given for this form of construction. A series of shear beam tests incorporated dowel reinforcement as shear connectors had been tested to evaluate the shear connector capacity and composite action of these beams. The objective of these tests is focused on the degree of shear connection on the plastic resistance of the composite beam, as well as the effects of clamping due to eccentric loading. This paper presents the test arrangement and the initial results obtained from the shear beam tests. Findings from this research will provide fundamental understanding to the behaviour of this form of composite construction.

INTRODUCTION

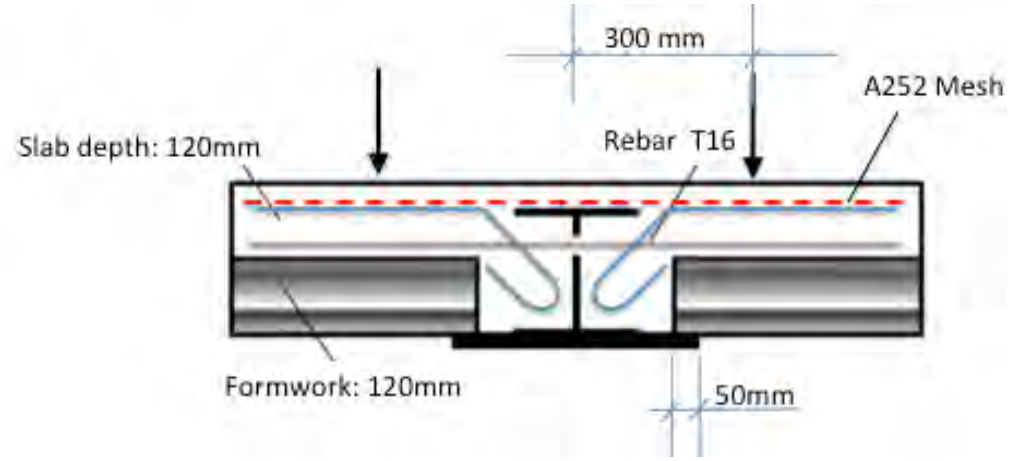
Composite beams are widely used in multi-storey buildings and for large, unsupported spans. Considerable research has been carried out in recent years on conventional types of composite beams, which consist of a concrete slab on top of a steel section and detailed design guidelines are provided in Eurocode 4. Slim floor beams are a variant of this type of structure in which the steel section is embedded in the concrete slab. This set-up offers the advantage of reducing the depth, but the design rules for conventional beams cannot be applied to slim floor beams, since the position of the plastic neutral axis in slim floor beams tends to be lower in the section. Thus, the concrete may fail under large strains before the steel beam has reached its plastic resistance. Furthermore, Eurocode 4 outlines a minimum degree of shear connection of 40% which is not economic for slim floor solutions [1-3]. Slim floor systems are also susceptible to punching shear near inner supports [4], excessive deflection and vibration owing to the shallow construction depth [5-7].

To date, no one has systematically examined the different mechanisms that contribute to the shear connection between steel and concrete in this type of configuration, such as shear studs, friction effects, clamping effects and the effect of holes in the beam web and transverse reinforcement bars. This paper presents the initial findings of an experimental campaign

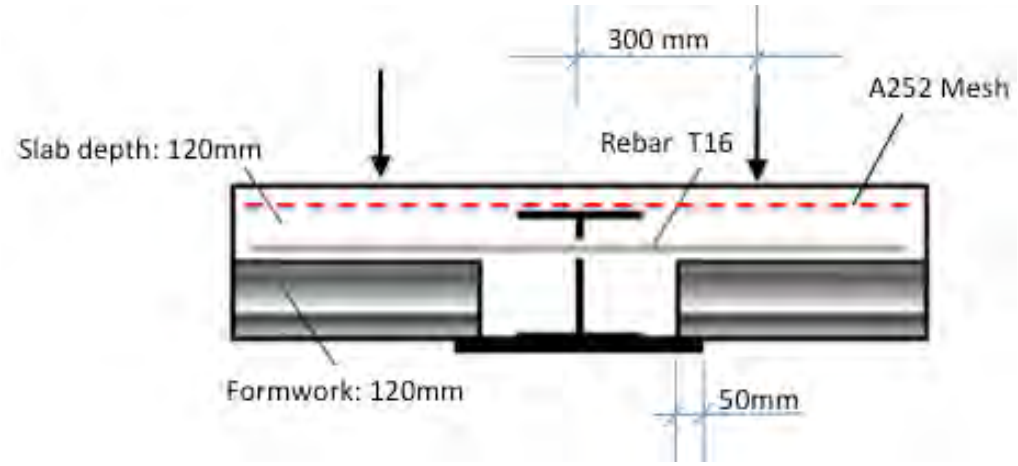
comprising 8 shear beam tests conducted in the University of Bradford. This paper reports the results of the first 5 shear beam tests, which explored different arrangements of reinforcement and shear connectors. Specimen details are provided in the following sections

TEST SPECIMENS

All test specimens included in this paper employed a HEB200 steel section positioned upon a 400 mm × 15 mm bottom steel plate, encased in a 240 mm deep concrete slab, which the topping depth was 120 mm. A252 reinforcing mesh was placed 40 mm below the top of the slab and T16 reinforcement bars were placed transverse to the beam length to provide shear connection, passing through 40 mm diameter holes in the steel beam web at 400 mm spacings. All specimens were 4300 mm long (4000 mm span between supports). C25/30 concrete was used for each of the test specimens. Some specimens were loaded concentrically along the middle of the cross-section and some were loaded at an eccentricity of 300 mm from the centre to investigate the clamping and friction effect. Cross-sectional and side views of typical specimens under eccentric loading are shown in Figures 1 and 2. A summary of test specimens is provided in Table 1. All specimens were designed to have 40% composite action except for SBT3.



(a)



(b)

Fig. 1 – Cross-section view of test specimens: (a) SBT1a (with stirrups); (b) SBT1b

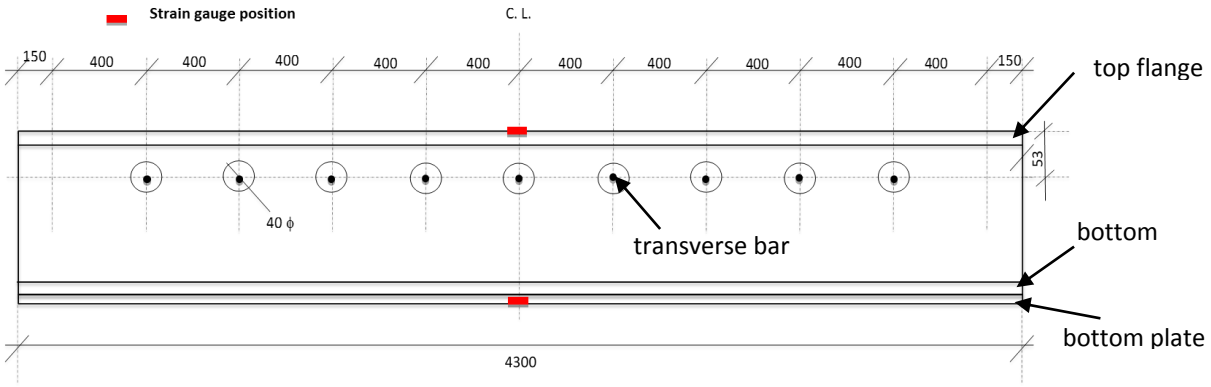


Fig. 2 – Side elevation view of steel beam and bottom plate

Table 1 – Test specimen details

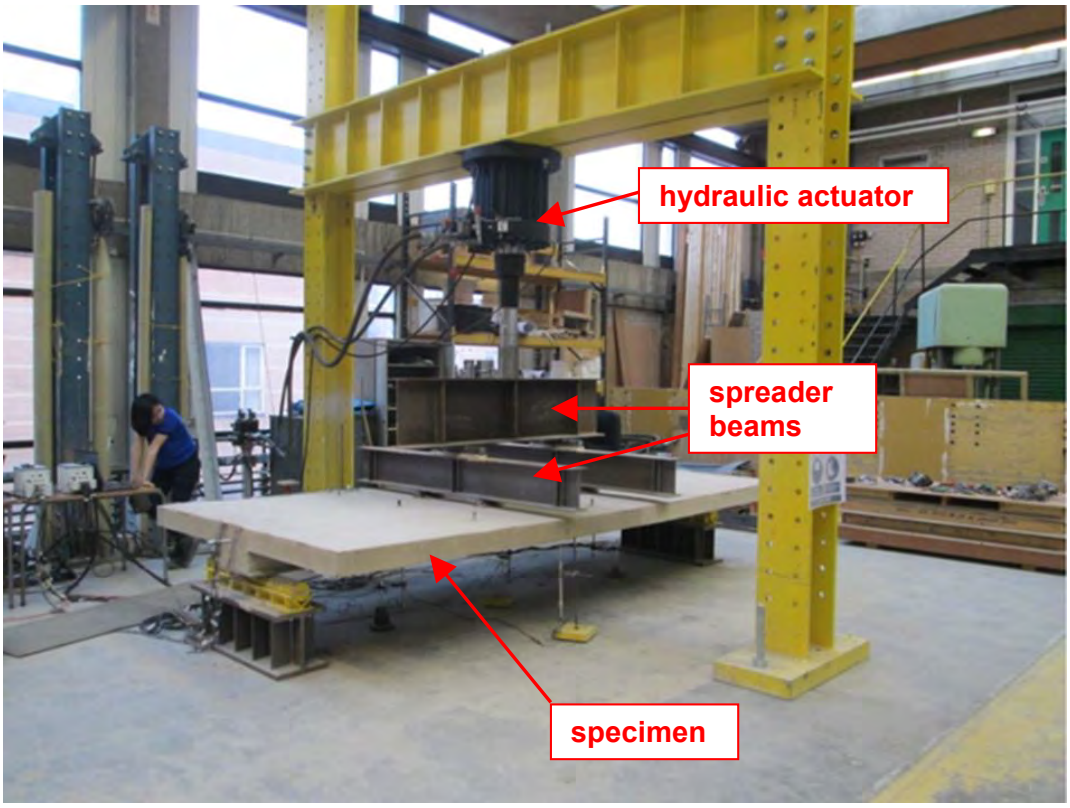
Specimen	Loading	Other comments
SBT1a	eccentric	reinforcing stirrups
SBT1b	eccentric	
SBT2	concentric	
SBT3	eccentric	no transverse bars
SBT5	concentric	cellular beam with 80mm holes

SBT1a and SBT1b were identical except for the fact that SBT1a contained extra reinforcement in the form of stirrups, running from the slab topping into the lower part of the slab. SBT1a, SBT1b and SBT3 were loaded at an eccentricity of 300 mm from the centre of the cross section, as shown in Figure 1. SBT3 contained no shear connectors, i.e., no transverse reinforcement bars or holes in the beam web, and was used to investigate the clamping action as the edges of the concrete slab were bent downwards under the eccentric loading. SBT2 utilised the same cross-section and reinforcement as SBT1b but was loaded at the centre of the cross-section. SBT5 was loaded concentrically and contained larger holes in the beam web (80 mm diameter) than the other specimens.

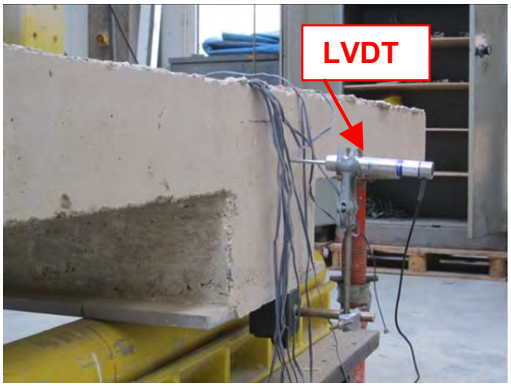
TESTING PROCEDURE

The specimens were positioned in the test rig shown in Figure 3. Load was applied at two locations along the specimen length, 500 mm from the mid-span (applied through either two or four points in total, depending on whether the loading was concentric or eccentric). Two LVDTs were used to measure the relative slip between the concrete slab and bottom plate, one placed at each end of the beam. 9 LVDTS were placed underneath the beam to measure the vertical deflection – 3 of these were positioned in a line running longitudinally under the centre of the cross-section whilst the remaining 6 LVDTs were used to measure the vertical deflections of the edges of the beam. Strain gauges were placed on the top flange of the steel section and the bottom of the steel plate to measure longitudinal strains at the mid-span. Strain gauges were also placed on top of the concrete slab at the mid-span for specimens. Strains were monitored in the reinforcement bars in order to check whether these were activated during the experiment. For the first test (SBT1a) 20 strain gauges were placed on the bars: 4 at the bars closest to each end and 3 on the second and third bars from each end. A comparison of strains at different locations along a single bar, at distances of 50 mm, 300 mm and 600 mm from the centre, is shown in Figure 4(a) and strains on the first, second and third bar from the end are shown in Figure 4(b).

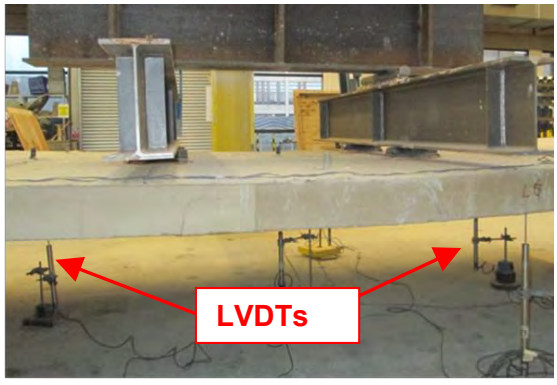
Most of the measured strains in the first test were below the yield strength of the material. Lower strains occurred in the bars close to the end than the second/third bars. Larger strains were measured towards the centres of the bars than at the other locations, which was to be expected, as the bars were bent as the beam deformed. Upon examining the data after the first test, it was decided to reduce the number of strain gauges to be used in subsequent tests, and focus more on areas of interest on the bars where larger strains were likely to occur and so for the remaining tests, two strain gauges were placed on each bar: one at the centre and the second 50 mm from the centre.



(a)

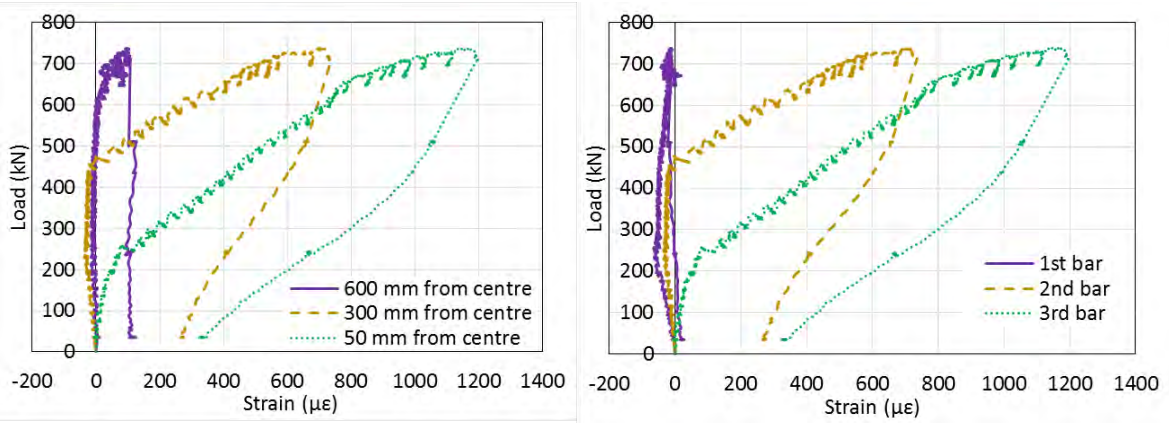


(b)



(c)

Fig 3 – Photos of test setup for SBT1a: (a) full specimen view; (b) LVDT at end to measure slip; (c) LVDTs underneath to measure vertical deflection



(a) (b)

Fig 4 - Comparison on strains in shear connector bars for SBTa: (a) at different locations along a single bar; (b) on adjacent bars

RESULTS

The tests continued until the specimens could resist no further loading. All tests exhibited similar load-displacement behaviour, with an initially stiff response. When the first concrete cracks and initial slippage occurred, the stiffess was suddenly reduced to approximately half of the initial value, and stayed fairly constant for most of the specimens until the final stage of the test, when the steel began to yield and the concrete cracks what initiated around the steel section web and outer edge of the slab, grew deeper and longer and propogated through the underside of the slab. The concrete cracks during the early and late stages of the test, the end-slip and deformed shape for typcial specimens, in addition to the load-deflection response for all specimens, are presented in Figures 5 and 6. . Vertical shear cracks as shown in Figure 5 (a) became visible early in the test, after initial yielding of the specimen. These cracks grew in size as the test progressed and extended along the underside of the slab as shown in Figure 5 (b). In the later stages of the test, the end-slip (Figure 5(c)) also increased significantly. For specimen SBT1a, one of the loading plates punched through the slab at the end of the test. However, it was evident from the load deflection relationship that the specimen had already reached/was close to a maximum load and this was further evidenced by the presence of visible, deep cracks in the concrete slab and yielding of the steel. A larger loading plate was employed in subsequent tests to mitigate punching shear.



(a)

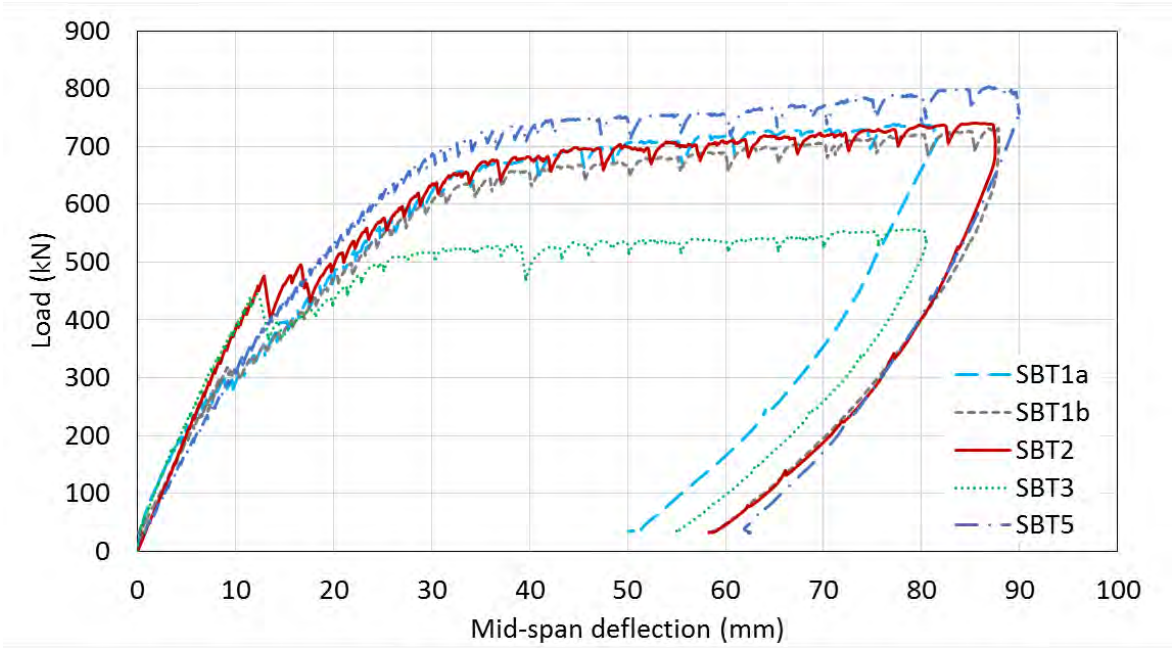


(b)



(c)

Fig 5 – Specimens during test: (a) vertical shear cracks in side of slab and beam for SBT1a; (b) deep cracks on underside of slab for SBT3; (c) visible end-slip between steel section and concrete for SBT3



(a)



(b)

Fig 6 – Deflection of beam during test: (a) Relationship between load and mid-span deflection; (b) Photo of specimen SBT5 undergoing vertical deflection during test

The maximum loads resisted by SBT1a, SBT1b and SBT2 were 738 kN (corresponding to a shear force of 39 kN and a bending moment of 554 kNm), 732 kN and 741 kN, showing that the use of reinforcing stirrups or concentric loading did not significantly affect the load capacity. The shapes of the load-deflection curves for these specimens presented in Figure 6 were also very similar, apart from the load at which the initial slippage occurred, but this was similar to that of SBT3 and was therefore attributed to the concrete properties, since SBT2 and SBT3 had been cast with the same concrete mix. Specimen SBT3 reached a maximum load of 559 kN. Comparing this load with SBT1b, it is evident that the presence of the shear connectors contributed over 170 kN to the load resistance. Specimen SBT5 reached a maximum load of 804 kN. The larger concrete dowel (80 mm diameter) contributed an extra 60 kN to the total load.

All specimens exhibited reasonably large end-slips prior to the end of the test. SBT1 had maximum end-slips of 11.7 mm and 13.4 mm recorded during the test. These values were considerably larger than the minimum slip of 6 mm specified by Clause 6.6.1.1 in Eurocode 4 for ductile shear connector behaviour. The failure of SBT1b was not symmetric along the length, and the maximum end-slips were 7.2 mm and 14.1 mm at each end. However, this was not caused by the presence of the stirrups (which were symmetrical). The end-slips were 9.6 and 11.3 mm respectively for SBT2, 18.6 mm and 1.6 mm for SBT3 and 10.4 mm and 11.7 mm for SBT5.

The maximum strain measured in the bottom steel plate for SBT1a at the mid-span was 2637με and the top steel flange was -9148 με (positive strains were tensile and negative strains were compressive), where the estimated yield strains for these were 2167 με and 2038 με respectively. Only one of the reinforcement bars exceeded the yield strain. Similar strains were measured in the top flange and bottom plate for SBT1b and SBT2, indicating that the steel had exceeded the yield strain by the end of the test. In SBT2, most of the reinforcement bars exceeded the yield strain before the end of the test, In SBT3, the maximum strain in the bottom plate at the mid-span was 1297 με, less than that associated with yielding, and the strain in the top plate was only -3003 με, but larger strains were observed further from the mid-span, with values of -7511 μ and 3484 μ at 500 mm from the mid-span in the top and bottom steel respectively. As mentioned in the previous paragraph, the end-slips for SBT3 varied significantly between each end, suggesting that failure did not propogate from the mid-span. In SBT5, the top flange only reached a maximum strain of -391 με, while the bottom plate reached 2195 με, demonstrating that the use of larger concrete dowels (SBT5), affected the strain distribution through the cross-section.

All specimens were very ductile, exceeding a maximum mid-span deflection of 80 mm (span/50). In each of the five tests, the maximum compressive strain measured on the concrete top surface at the mid-span was less than that associated with failure of the concrete. A summary of the maximum load N_{max}, maximum mid-span deflection δ_{max}, end-slip δ_u, top steel strain $\varepsilon_{s,top}$, bottom steel strain $\varepsilon_{s,bot}$, concrete strain ε_c and initial stiffness k (applied load/mid-span deflection) for each specimen is presented in Table 2. Some variation was observed between specimens with regard to the initial stiffness with specimen SBT5 having a slightly lower stiffness than the other specimens owing to the enlarged holes in the steel beam web, whereas SBT2, which was subjected to concentric loading exhibited a slightly higher stiffness than the other specimens.

Table 2 Summary of results

Specimen	N_{max} (kN)	δ_{max} (mm)	δ_u (mm)	$\varepsilon_{s,top}$ (με)	$\varepsilon_{s,bot}$ (με)	ε_c (με)	k (kN/mm)
SBT1a	738	81.5	13.4	-9148	2637	-	32.4
SBT1b	732	87.8	14.1	-8780	2214	-1205	33.5
SBT2	741	87.5	11.3	-9790	2142	-1290	39.2
SBT3	559	80.5	18.6	-3003	1297	-1708	35.1
SBT5	804	89.9	11.7	-391	2195	-1276	28.1

ANALYSIS

For the bare steel section, as shown in Figure 7, the distance of the plastic neutral axis, y, from the top of the steel section, can be calculated as follows

.

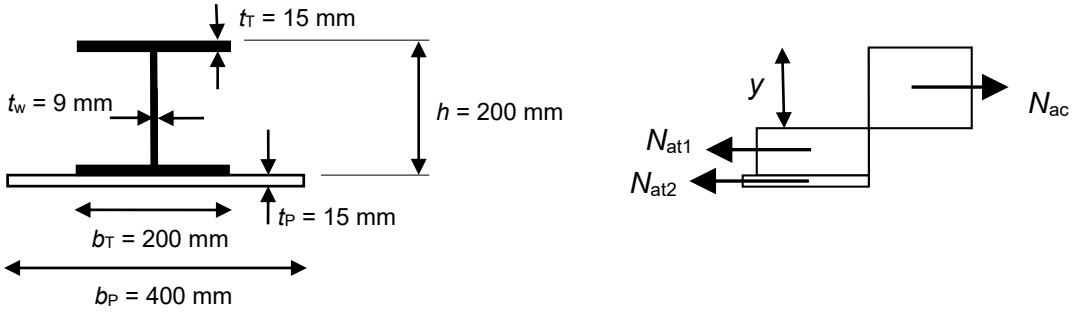


Fig 7 – Moment capacity of bare steel section

Assuming neutral axis is in bottom flange of HEB

$b_T \times t_T + t_w \times (h-2t_T) + b_T(y - (h-t_T) = b_T \times (h - y) + b_P \times t_P$ (1)

$200 \times 15 + 9 \times (200-30) + 200 \times (y-(200-15)) = 200 \times (200-y) + 400 \times 15$

y = 196.18 mm

Moment capacity = $A_s f_{y,HEB} \times (h/2 - y) + b_p \times t_p \times f_{y,p} (t_p/2 + 200-y)$ (2)

= $7810 \times 428 \times (200/2 - 196.18) + 400 \times 15 \times 455 (15/2 + 200-196.18)$

= 352 kNm

b_T is the width of the top flange of the HEB section, h is the depth of the HEB section, A_s is the area of the HEB section, b_p and t_p are the width and thickness of the bottom plate respectively, t_w is the thickness of the web, and $f_{y,HEB}$ and $f_{y,p}$ refer to the yield strengths of the HEB section and bottom plate respectively.

352 kNm equates to a shear force of 352/1.5 = 234.7 kN and an applied load of 234.7×2 = 469 kN. The maximum load for specimen SBT3 was 559 kN, which is 19% higher, suggesting that despite the lack of shear connectors, clamping and friction contribute towards the cross-section resistance. However, overall, the applied load in SBT3 was mostly resisted by the steel section.

Using measured yield strengths of 428 N/mm^2 for the HEB section, 455 N/mm^2 for the bottom steel plate and a concrete cube strength of 41.3 N/mm^2,and assuming plastic behaviour of the cross-section, the neutral position and bending moment capacity, $M_{pl,Rd}$ can be calculated using the stress-blocks shown in Figure 8, where y_c is the depth of the plastic neutral axis below the top of the slab

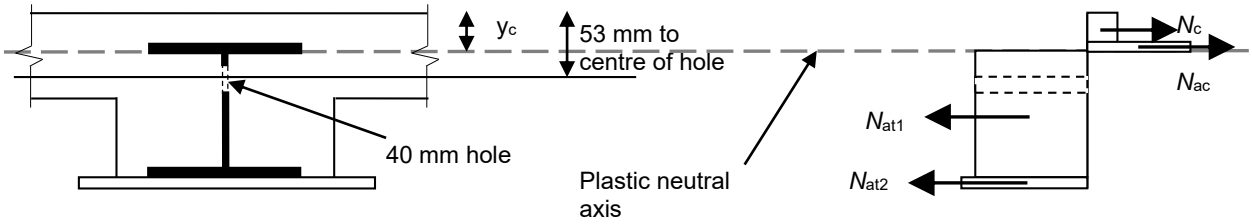


Fig 8 – Stress-blocks for calculating moment capacity

There is a 40 mm hole in the HEB section web, and hence the cross-sectional area A_s is reduced from 7810 mm^2 to 7810 – 40×9 = 7450 mm^2 ($A_{s,red}$). If the section has 100% composite action, assuming that the neutral axis is located in the HEB upper flange, the depth y_c can be calculated using force equilibrium

$$N_c + N_{ac} = N_{at1} + N_{at2} \quad (3)$$

where N_c is the compressive force in the concrete, N_{ac} is the compressive force in the HEB section above the neutral axis, N_{at1} is the tensile force in the HEB section and N_{at2} is the tensile force in the bottom plate. These forces can be calculated using Equation 2, where b_{eff} is the effective width of the slab, f_{ck} is the concrete strength, y_c is the depth of the neutral axis.

$$0.85\times b_{eff}\times f_{ck}\times y_c + (y_c-40)\times b_T\times f_{y,HEB} = (A_{s,red}-((y_c-40)\times b_T)\times f_{y,HEB} + b_p\times t_p\times f_{y,p} \quad (4)$$

Substituting in the values gives:
$0.85\times2000\times41.3\times y_c + (y_c-40)\times200\times428 = (7450-((y_c-40)\times200)\times428 + 400\times15\times455$
y_c = 52.88 mm

Taking moments about line of action of concrete force, $M_{pl,Rd}$, is calculated to be:
$M_{pl,Rd} = N_{at2}\times (240 + t_p/2 - y_c) + (N_{at1} - N_{ac}) \times(140-y_c) = 726.4$kNm (5)

This corresponds to an applied failure load of 726.4/1.5 ×2 = 968.57 kN

For 40% composite action, the maximum bending moment capacity is 564 kNm, corresponding to an applied load of 752 kN, which is close to the test results.

The area of each concrete dowel in SBT5 (80 mm hole, with 16 mm bar) is equal to $\pi\times80^2/4 - \pi\times16^2/4$ = 4825 mm^2 per hole. The area of each concrete dowel in SBT2 (40 mm hole with 16 mm bar) is equal to $\pi\times40^2/4 - \pi\times16^2/4$ = 1056 mm^2 per hole. If the shear strength of the concrete is taken as the limit of $0.8\sqrt{f_{cu}} = 0.8\sqrt{(41.3)} = 5.14$ MPa (Clause 3.4.5.2 in BS 8110) and the dowel is in double shear, the concrete in each activated connector in SBT5 can resist 4825×2×5.14 = 49.6 kN in shear and each connector in SBT2 can resist 10.9 kN in shear. The strain gauge data for SBT5 indicated that only 3 of the reinforcement bars exceeded the yield strain whereas for SBT2, 7 bars reached yield. Considering the active bars in each case, the expected concrete contribution in SBT2 can be estimated to be 10.9×7 = 76.3 kN and the concrete contribution for

SBT5 is 49.6×3 = 148.8 kN. The expected difference in load is 148.8 – 76.3 = 72.5 kN, which exceeds the measured difference (63 kN) by 15%.

The neutral axis position was estimated for different specimens using the strains measured in the top flange and bottom plate. The strains (μ) and neutral axis depth are illustrated for Specimen SBT1a at four different stages of the test in Fig 9, and the four stages are marked on the load-displacement curve.

Table 3 summarises the estimated neutral axis positions for the other specimens at similar stages of their respective tests, based on the strain gauge data. The first point for each specimen is taken at a low load, when the specimen is in the elastic range. The second point is taken at the stage when the stiffness first decreases. The third point is taken at the beginning of the final plateau and the fourth point is taken further on in the plateau (up to half-way between the previous point and the maximum load. It was not possible to take reliable strain readings during the later stages of the test in many cases as the strain gauges had become damaged or strained beyond their working limit. In all of the specimens except for SBT5, a consistent trend can be found in the strain gauge data, with the neutral axis position appearing to move downwards as the test progressed and the behaviour became increasingly plastic. The neutral axis position during Stage 4 of the test is close to that calculated previously for the bare steel section, which can be expected as a significant degree of slippage had occurred between the steel and concrete components at this stage.

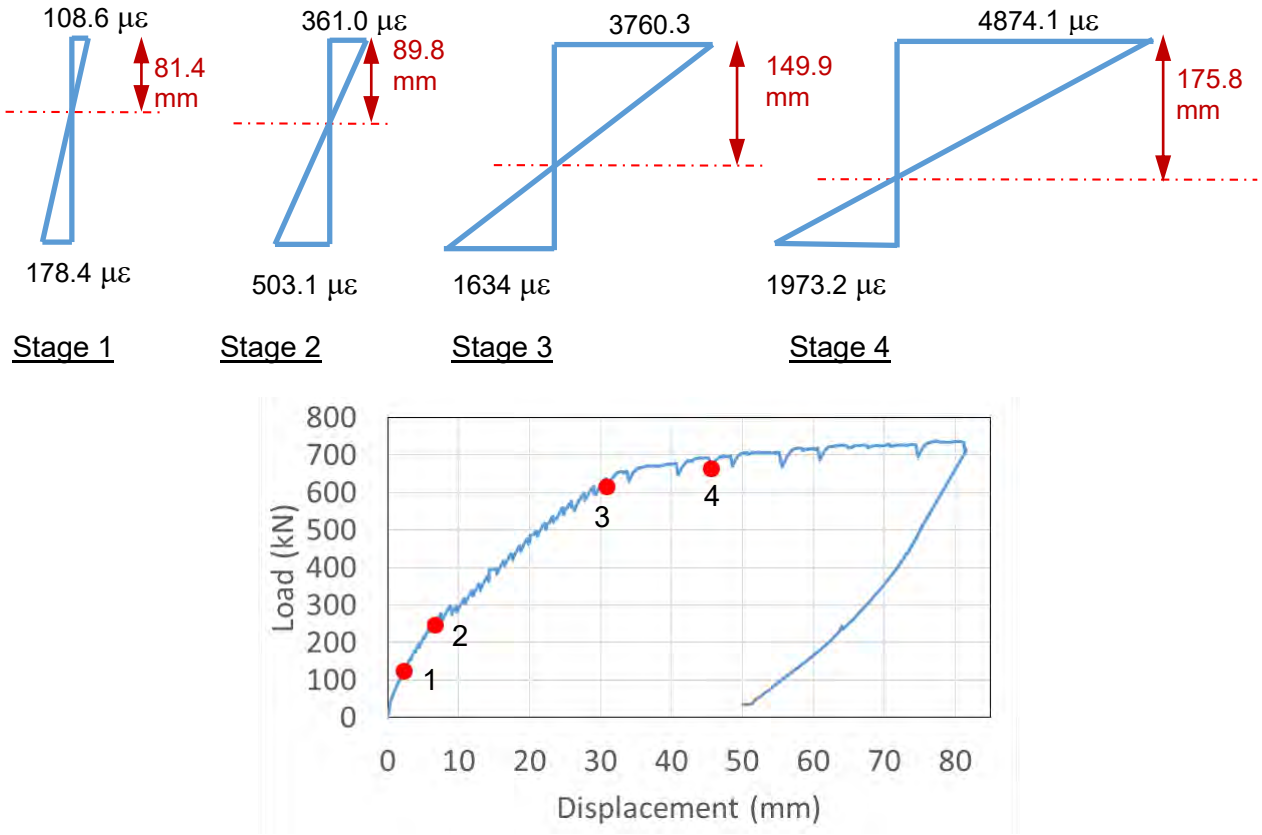


Fig 9 - Neutral axis position at different stages of test for SBT1a

Table 3 – Estimated positions of neutral axis (distance below top steel flange) from strain gauge data

Specimen	Point no.	Average $\varepsilon_{s,top}$ (με)	Average $\varepsilon_{s,bot}$ (με)	Neutral axis depth (mm)
SBT1b	1	-80	168	69.3
	2	-209	462	67.0
	3	-3311	1449	149.6
	4	-8586	1782	178.0
SBT2	1	-165	429	59.8
	2	-375	839	66.4
	3	-1782	1355	122.1
	4	-6028	1704	167.6
SBT3	1	-228	420	75.7
	2	-456	763	80.5
	3	-1309	948	124.7
	4	-2305	1189	141.8
SBT5	1	-49.6	377	25.0
	2	-83.6	771	21.0
	3	-153.2	1510	19.8
	4	-201.3	1793	21.7

CONCLUSIONS

The initial test results demonstrate the contributions of different components within a slim floor system. Some initial conclusions can be drawn from these tests:

1. Reinforcing stirrups do not make a significant contribution to the beam performance.
2. The beams exhibited a very ductile response, undergoing a mid-span deflection exceeding span/50 prior to failure. This was despite being designed for a low degree of shear connection (40%).
3. The application of eccentric load did not significantly alter the beam behaviour in comparison with applying the load concentrically.
4. The steel shear connectors have a significant effect on the beam performance. Specimen SBT3 without shear connectors achieved a maximum load over 20% lower than equivalent specimens with 40% composite action, and was closer to the response of a steel section acting alone.
5. The size of the concrete dowel impacts the performance. By increasing the size of the holes in the steel web by a factor of 2, the load capacity was increased by 8%.

Further tests will be conducted in future, including a specimen without concrete cover to the top reinforcement, a steel beam with horizontal shear studs on the beam web.

ACKNOWLEDGEMENT

The authors gratefully acknowledge the funding received from the European Community Research Fund for Coal and Steel under grant agreement number RFSR-CT-2015-00020.

REFERENCES

[1] Årskog, V., Fosssal, S. and Gjørv, O. Methodology and data for calculation of LCE (Life Cycle Ecology) in repair planning, Lifecon deliverable D 5.3, VTT Building and Transport, Finland, 2003.

[2] Aribert, J. M. Analysis and practical solutions for the influence of steel grade on the minimum degree of shear connection of a composite beam, Construction Metallique, 40-55, 1997.

[3] Bernuzzi, C., Zandonini, R. Joint action in non-sway frames with steel-concrete composite slim floor systems, Journal of Singapore Structural Steel Society, 1995, Vol. 6, No. 1, 75-85.

[4] Kuhlmann, U., Hauf, G. Querkrafttragfähigkeit von Slim-Floor Trägem, AiF research project no. 15639, Institute of Structural Design, University of Stuttgart, Stuttgart, 2011.

[5] Bernuzzi, C., Gadotti, F., Zandonini, R. Semi-continuity in slim floor steel-concrete composite systems, Proceedings of Eurosteel 95 ed. Kounadis, A. N.; Athens, Greece, 1995, 287-294.

[6] Feldmann, M., Heinmeyer, C., Butz, C., Caetano, E., Cunha, A., Galanti, F., Goldack, A., Hechler, O, Hicks, S., Keil, A., Lukic, M, Obiala, R., Schlaich, M., Sedlacek, G., Smith, A, Waarts, P. Design of floor structures for human induced vibrations, JRC-ECCS, Eds. G. Sedlacek, Ch. Heinemeyer, Chr, Butz, 2009.

[7] Ranzi, G., Leoni, G., Zandonini, R.. State of the art on the time-dependent behaviour of composite steel-concrete structures, Journal of Constructional Steel Research, 80, 252-263, 2013.

SLIM-FLOOR CONSTRUCTION
DEFORMATION AND LOAD CARRYING BEHAVIOUR

Johannes Schorr, M.Sc.
University of Stuttgart
Institute of Structural Design
Stuttgart, Germany
johannes.schorr@ke.uni-stuttgart.de

Prof. Dr.-Ing. Ulrike Kuhlmann
University of Stuttgart
Institute of Structural Design
Stuttgart, Germany
ulrike.kuhlmann@ke.uni-stuttgart.de

Prof. Dr.-Ing. Gunter Hauf
DHBW Mosbach
Mosbach, Germany
gunter.hauf@mosbach.dhbw.de

Abstract

For realistic predictions of beam deformations, a good knowledge of the beam´s load carrying behavior is necessary. For slim-floor constructions in difference to normal height composite beams, the bending behavior of the concrete slab brings a substantial contribution to the load carrying behavior. However, the concrete slab of slim-floor constructions cracks under bending moments already at the serviceability stage. The analytical models presented here allow to make use of the concrete slabs contribution despite of cracking.

The aim of an ongoing European project (SlimAPP), involving a huge amount of various testing, is to develop a holistic approach by considering all aspects of efficient design of slim-floor constructions for implementation in Eurocode 4. Particular attention lies on the composite shear connection between the steel beam and the concrete floor slab. Push-out tests, beam tests, and long-term tests are carried out, testing among others the innovative CoSFB connection system.

INTRODUCTION

Composite beams may be differentiated due to their height into three main types: composite beams of normal height, composite beams of reduced height and slim-floor beams (see Figure 1). In slim-floor constructions a steel beam is embedded into the concrete slab.

Due to high degree of prefabrication, buildings with slim-floor constructions can be erected very fast and economically. In combination with profiled sheeting, as shown in Figure 2, the production of the slim-floor can furthermore be achieved by hand and so independently from cranes.

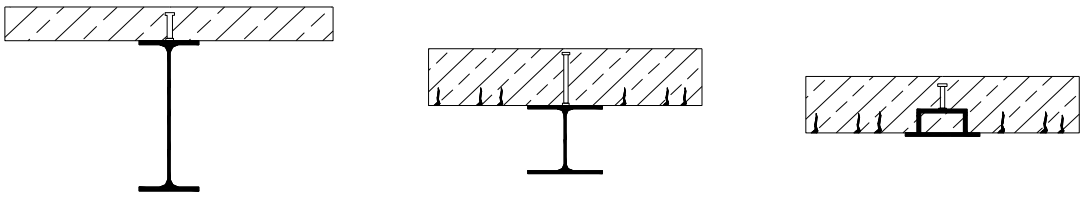


Fig. 1: Composite beam of normal height, composite beam of reduced height, slim-floor beam (Hauf G. , 2010)

The integration of the steel profile into the floor and the accordingly missing joists enable to lay building technology easily at the bottom side of the floor without horizontal breaches.

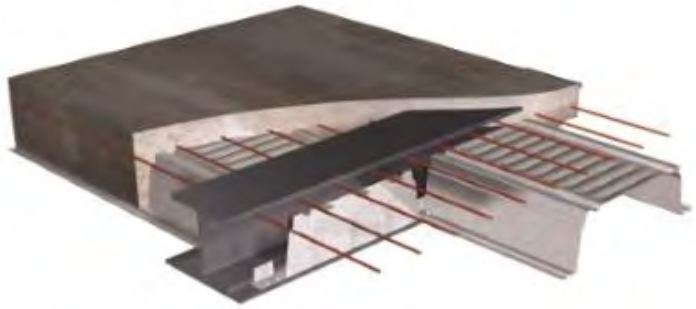


Fig. 2: Slim-floor system in combination with profiled sheeting

Whereas a neglection of the bending capacity of the concrete slab M_c of normal height composite beams leads to sufficiently good results in the calculation of realistic deformations, the influence on the deformation behavior of slim-floor constructions is much higher and not negligible. The approximation of the neutral axes of the concrete slab and the overall slim-floor beam results into cracking at the tensile side of the girder under bending. This may occur already in the serviceability state.

Figure 3 shows the strain distribution and the cracking at the bottom of a slim-floor beam under positive bending.

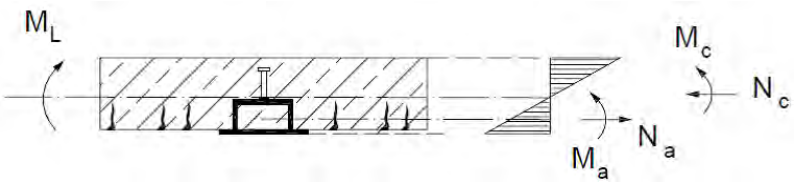


Fig. 3: Strain distribution of a slim-floor beam (Hauf G. , 2010)

For a realistic calculation of the deformation of slim-floor construction the bending capacity of the concrete slab and consequently the cracking has to be taken into account. Eurocode 4 (EN 1994-1-1, 2009) is not providing rules or recommendations for consideration of the concrete slabs bending capacity and cracking. This leads to an overestimation of the deformation behavior of slim-floor construction. As the deflection criterion is decisive in many cases for slim-floors, an overestimation leads to uneconomically designed constructions.

Within several research projects regarding slim-floor solutions of the Institute of Structural Design at the University of Stuttgart, Germany, the deformation behavior was investigated. To take all parameters into account, an analytical model was developed verifying an effective width referring to deformation. Based on this approach a quasi-elastic calculation method was developed for single span and two span slim-floor girders.

ANALYTICAL MODELS FOR DEFORMATION CALCULATION OF SLIM-FLOOR CONSTRUCTIONS

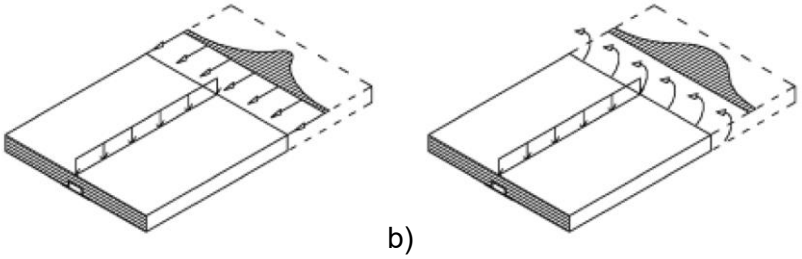
Introduction

Deformation calculations need to represent reality as close as possible. As a consequence the bending of the concrete slab in slim-floor constructions has to be taken into account in contrary to the present practice. Otherwise, the deformations may be overestimated leading to uneconomically designed slim-floor constructions. Among others, the bending capacity M_c of slim-floor constructions depends on cracking of the concrete. Starting from a nonlinear analytical model, an approach with a deformation based effective width and further on a quasi-elastic model have been developed. The models are outlined in the following. For a more detailed description please refer to (Hauf G. , 2010) and results on underlying testing are also given in (Kuhlmann & Hauf, 2008).

Effective width

Two different states for the concrete slab may generally be differentiated (Figure 4). In membrane state, it is assumed that the concrete obtains only compression forces N_c. The slab works as a shear panel (Figure 4a). $b_{m,S}$ is the corresponding effective width.

In the bending state, it is assumed that the concrete slab has no shear stiffness, but a bending stiffness I_c. This results in a bending moment M_c in the concrete (Figure 4b)). Calculating the deformation of normal height composite girders this state can easily be neglected without major effects. Calculating realistic deformations on slim-floor constructions the bending capacity has to be considered by an appropriate effective width $b_{m,B}$ (Hauf & Kuhlmann, 2015).



a) b)

Fig. 4: Membrane state a) and bending state b) of the concrete slab (Hauf & Kuhlmann, 2015)

In combination, the above membrane and the bending state lead to an overall stiffness of the slim-floor girder as indicated in equation (1).

$$I_{i,0} = I_a + I_{c,0} + S_{i,0} \cdot a_{st} = I_a + \frac{b_{m,B} \cdot h_c^3}{12 \cdot n_0} + \frac{\frac{b_{m,S} \cdot h_c}{n_0} \cdot A_a}{\frac{b_{m,S} \cdot h_c}{n_0} + A_a} \cdot a_{st}^2 \quad (1)$$

Where:

A_a	Cross sectional area of the steel profile
I_a	Inertia of the steel profile
h_c	Height of the concrete
a_{st}	Distance between centroid concrete and steel section
$n_0 = E_a/E_{cm}$	Number of reduction (E_a = young modulus of steel, E_{cm} = young modulus of concrete)

This overall stiffness $I_{i,0}$ forms the basis for a nonlinear analytical model that is presented in the following section.

Nonlinear Analytical Model

Based on the assumption made on the effective width and in consideration of cracking an analytical model was developed to calculate the deflection of slim-floor girders (Hauf G. , 2010)

For determination of the slim-floor beam deflection cracking has to be considered. This is achieved by dividing the slim-floor girder into a number of elements (Figure 5). Each element is assigned by an effective width for the membrane state $b_{m,S}$ and by an effective width for the bending state $b_{m,B}$.

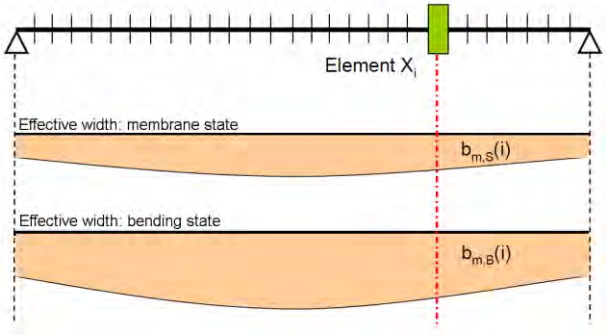


Fig. 5: Discretization and distribution of membrane and bending state for a one span girder

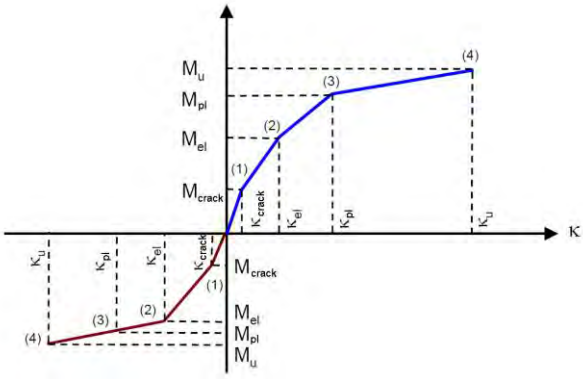


Fig. 6: M-κ-curve for positive and negative bending

A simplified M-κ curve (Figure 6) under positive bending is defined by four characteristic points:

1. Development of first cracks M_{crack}, κ_{crack}

   Until first cracks develop on the bottom of the slim-floor beam an elastic calculation is possible. This includes also a consideration of the tensional concrete strength f_{ct} (Figure 7). After M_{crack} is reached, a linear-elastic calculation is no longer possible for this element.

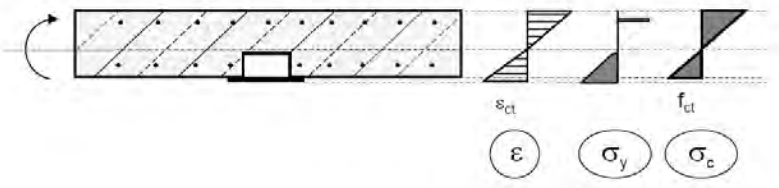


Fig. 7: Stress-strain relationship – cracking moment (index: “crack”)

2. First yield of the steel profile M_{el}, κ_{el} (bottom)

   This point of the M-κ curve (Figure 6) is reached when the steel profile begins to yield at the bottom (Figure 8). Therefore a nonlinear material model has to be implemented.

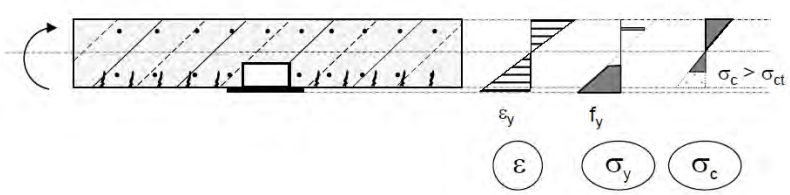


Fig. 8: Stress-strain relationship – yield moment (Index: “el”)

3. Steel profile fully plasticized M_{pl}, κ_{pl}

   Concrete reaches its maximum stresses f_c at a concrete strain of 2 ‰. Furthermore, the steel profile is fully plasticized and is not able to carry any more loading (Figure 9).

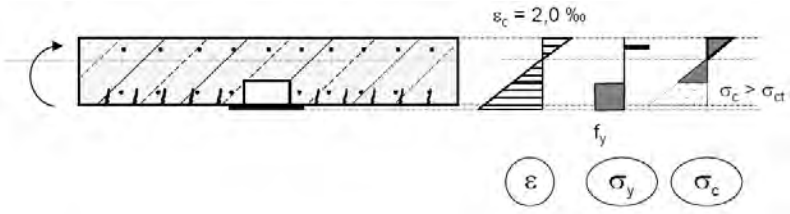


Fig. 9: Stress-strain relationship – plastic moment (Index: “pl”)

4. Concrete reached maximum strains M_u, κ_u

   If the load is inducing a concrete strain over 3.5 ‰, the ultimate moment is reached and the slim-floor is going to fail (Figure 10).

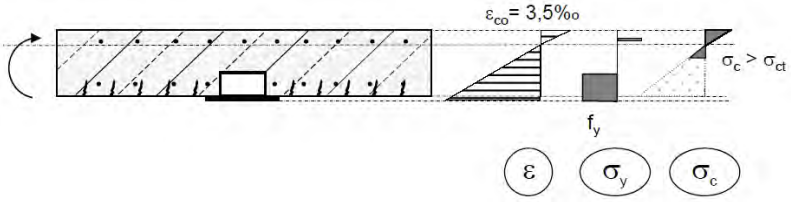


Fig. 10: Stress-strain relationship – ultimate moment (index: “u”)

For statically determinate systems direct computation of the internal forces (moments) is possible. The bending can be determined for each element by using the M-κ relationship (Figure 6) and consequently the deflection of the slim-floor beam.

Due to their cracking, statically indeterminate systems, like two span beams (Figure 11) result in midspan and on the support in a more complex calculation. A corresponding model is presented in (Hauf G. , 2010).

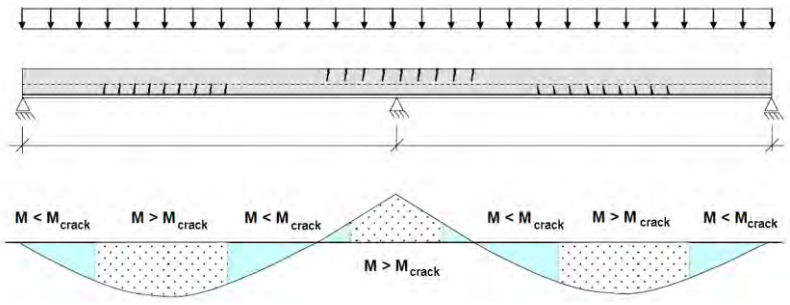


Fig. 11: Crack development on statically indeterminate two span slim-floor beam

The above developed analytical model showed a good conformity with test series performed in (Kuhlmann, Hauf, & Rieg, 2006), (Kuhlmann & Fries, 2001) and (Kuhlmann, Konrad, & Hauf, 2010). Parameter studies were performed to determine the influences on the deflection of:

Material parameter:	concrete tensional strength f_{ct}, concrete compressive strength f_c, young modulus of concrete E_c, young modulus of steel E_a, yield strength of the steel f_y
Geometrical parameter:	height of the concrete slab h_c, cross sectional area of the steel profile A_a, reinforcement content $a_{s,u}$ & $a_{s,o}$, geometrical ratio between concrete slab width and length of the beam b/L

In general, those parameters are reducing the deflection of the beam, which are increasing the stiffness of the beam. For example: height of the concrete slab or the used steel profile.

Deformation based effective width

The deformation based effective width comprises for single span slim-floor girders the effective width of the membrane state $b_{m,S}$ and an elastic value of the deformation based effective width $b_{m,V,0}$. The cracking is taken into account by a reduction of the difference between $b_{m,V,0}$ and $b_{m,S}$ with factor $\beta_{m,V}$, see equation (2).

$$b_{m,V} = b_{m,S} + \left(b_{m,V,0} - b_{m,S}\right) \cdot \beta_{m,V} \tag{2}$$

The reduction factor $\beta_{m,V}$ was determined by comparing deformations derived from calculations with the nonlinear analytical model with deformation derived from calculations with an introduced constant effective width over the length of the beam. The value for the constant effective width was adapted so that equilibrium of the deformations for both approaches was reached (Hauf G. , 2010). For single span slim-floor girders the calculation of the reduction factor $\beta_{m,V}$ is also given in (Hauf & Kuhlmann, 2015). In (Hauf G. , 2010) an additional formula is provide for $\beta_{m,V}$ in two span slim-floor girders.

Quasi-elastic calculation method

A more simple approach has been developed for slim-floor girders with I- or hat-profiles as a quasi-elastic calculation method. Accordingly, an effective moment of inertia $I_{i,eff}$ was introduced in equation (3).

$$I_{i,eff} = I_a + \alpha_c \cdot \left(I_{c,0} + S_{i,0} \cdot a_{st}\right) \tag{3}$$

The adjustment factor α_c takes cracking of the concrete into account by introducing a loss of stiffness that is originally provided by the concrete slab. At load beginning, when concrete is uncracked, a linear elastic deflection behavior is considered: $\alpha_c = 1.0$ and the effective stiffness is equal to the stiffness of composite beams with normal height. When $\alpha_c = 0$ no stiffness is provided by the fully cracked concrete slab. The effective stiffness of the slim-floor girder is equal to the stiffness of the steel profile. $0 < \alpha_c < 1$ means the concrete is cracked, but still contributing to the stiffness of the beam.

Adjustment factor α_c itself takes material and geometrical influences into account (see equation (4)). It depends on a factor α_V (equation (5)), material factor α_{Mat} (equation (6)), factor for the influences of the cross sectional area α_{QS} (equation (7)) and loading factor α_M (equation (8)).

$$\alpha_c = \alpha_V \cdot \alpha_{Mat} \cdot \alpha_{QS} \cdot \alpha_M \tag{4}$$

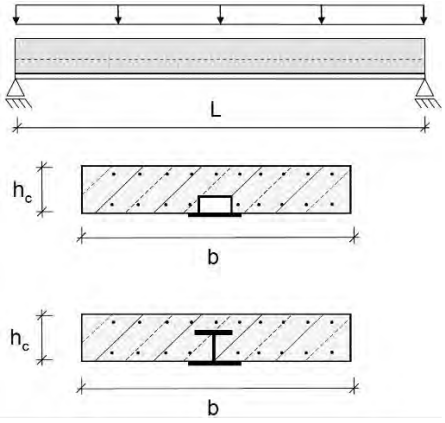
(5) $$\alpha_{\mathrm{V}} = 0.4 \qquad \text{for I-Profiles}$$

(6) $$\alpha_{\mathrm{Mat=}} = \left(\frac{f_{\mathrm{ct}}}{f_{\mathrm{ct,0}}}\right)^{-0.26} \cdot \left(\frac{f_{\mathrm{c}}}{f_{\mathrm{c,0}}}\right)^{0,46} \cdot \left(\frac{f_{\mathrm{y}}}{f_{\mathrm{y,0}}}\right)^{0,29}$$

(7) $$\alpha_{\mathrm{QS=}} = \left(\frac{A_{\mathrm{s,u}}+A_{\mathrm{a}}}{A_{\mathrm{ci,0}}}\right)^{0,17} \cdot \left(\frac{I_{\mathrm{c,0}}}{I_{\mathrm{i,0}}}\right)^{3,18} \cdot \left(\frac{a_{\mathrm{st}}}{h_{\mathrm{c}}}\right)^{-1,27} \cdot \left(\frac{b}{t}\right)^{-0,56} \text{ for I-Profiles}$$

(8) $$\alpha_{\mathrm{M}} = \left(\frac{M_{\mathrm{crack}}}{M_{\mathrm{Ed}}}\right)^{1,22}$$

The exponential factors in equations (6) to (8) are determined by a parametric study varying geometrical parameters as well as material parameters. Therefore the here presented exponents are only valid in range of the varied parameters as indicated in Figure 12 (Hauf G. , 2010).



Span L:	4.0 – 9.0 m
Concrete slab thickness h_c:	16 – 34 cm
Concrete slab width b:	2.0 – 8.0 m
Steel-Profile:	UPE-, IFB-, SFB-profiles
Concrete compressive strength f_c:	20 – 50 N/mm²
Concrete tensional strength f_{ct}:	1.0 – 5.5 N/mm²
Steel yield strength f_y:	235 – 460 N/mm²
Reinforcement top $a_{s,o}$:	0 – 18 cm²/m
Reinforcement bottom $a_{s,u}$:	0 – 18 cm²/m

Fig. 12: Range of varied parameters for determination of exponential factors in equations (6) to (8) (Hauf G. , 2010)

The effective stiffness $I_{i,eff}$ allows to assess the deformation of slim-floor constructions with small effort taking all geometrical and material parameters into account.

RFCS-PROJECT SLIMAPP

Introduction

The RFCS-Project “Slim-Floor Beams – Preparation of application rules in view of improved safety, functionality and LCA” (RFCS-SLIMAPP, 2015) is a European project coordinated by the University of Stuttgart in partnership with the Universities of Bradford (UK) and Trento (Italy), the Steel Construction Institute (SCI, UK) as well as industrial partners ArcelorMittal Belval & Differdange and LINDAB/Astron (both from Luxembourg).

The aim is to develop a holistic approach considering the design for safety and functionality as well as a lifecycle assessment. The rules and guidelines, which will be developed should fill the lack of design rules for slim-floor constructions in Eurocode 4 (EN 1994-1-1, 2009). To achieve this aim a comprehensive testing program is realized that is expected to widen the knowledge on the load carrying behavior of slim-floor constructions. Furthermore an inventory of the already available constructions on the main European markets is made. This forms the basis for the lifecycle assessment (LCA) and the basis for a comparison with pure concrete constructions, where slim-floor constructions are mainly competing with.

Experimental program

Overview

Push-out tests, beam tests and long term tests are part of the project. The cross sections of all tests have a strong interrelation. Dimensions of the specimens, material parameters and shear connection devices are kept the same. This ensures a transferability between all tests. The focus within the testing is on the innovative shear-connection system CoSFB, presented hereafter.

Composite Slim-Floor Beam

The Composite Slim-Floor Beam (CoSFB) consist of a commercially available H-profile. Holes are introduced into the web under the upper flange of the profile by drilling or flame cutting. For proper shear connection, reinforcement bars are conducted through the web holes (Figure 13).



Fig. 13: CoSFB-System: H-profile with holes in the web and reinforcement bars through the holes (before concreting)

The load capacity of the shear connection is dependent on the load capacities of the pure concrete dowel, the reinforcement bar and on friction. The ratio between the shear force of the reinforcement bar and the load capacity that the concrete can develop locally influences the overall load bearing capacity of the shear connection. Concrete with low strength is damaged locally and allows the reinforcement to bend and activate tensional forces in the bar as indicated in Figure 14 a). High strength concrete may lead to shearing of the reinforcement bar Figure 14 b) (Braun, Hechler, & Obiala, 2014).

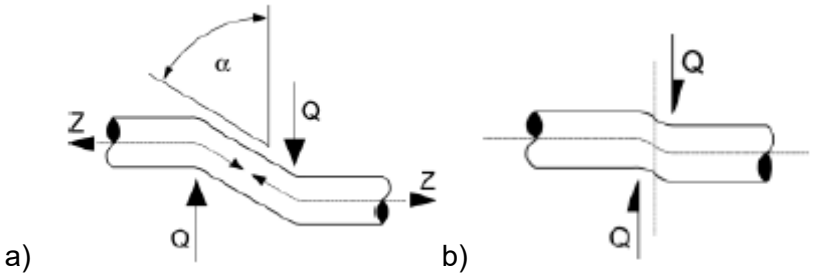


Fig. 14: a) Bending and activation of tensional forces in the reinforcement bar, b) pure shearing of the reinforcement bar

The embedment of the shear connector in the concrete slab allows reducing the height of the construction in comparison with other construction as e.g. headed studs placed on top of the profile, mostly used for normal composite girders (Figure 15). For a German national approval of the CoSFB-system (DIBT, 2014) various test series were conducted at the University of Stuttgart. Within the presented project the already investigated range of parameters is extended.

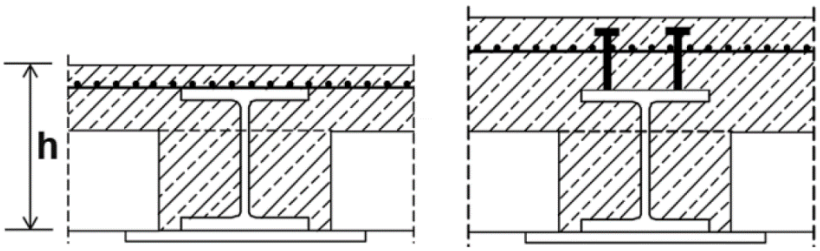


Fig. 15: Comparison of overall height with identical profiles and different shear connector systems (Braun, Hechler, & Obiala, 2014)

Basic test configuration

For assurance of good transferability between all test setups (push-out tests, beam tests and long term beam tests) a basic test configuration has been chosen. The basic test configuration for all tests consists of:

- HEB 200 with steel grade S355, all profiles are supplied from one batch
- Holes in the web Ø40 mm
- Reinforcement bars Ø16 mm (B500B), supplied from one batch
- Concrete grade C25/30 (f_{ck} = 30 N/mm²)

The above described basic test configuration is also indicated in a push-out test setup in Figure 16. The supply of the reinforcement bars as well as HEB 200 profiles from one batch for all tests ensures a good comparability between all test setups and test series.

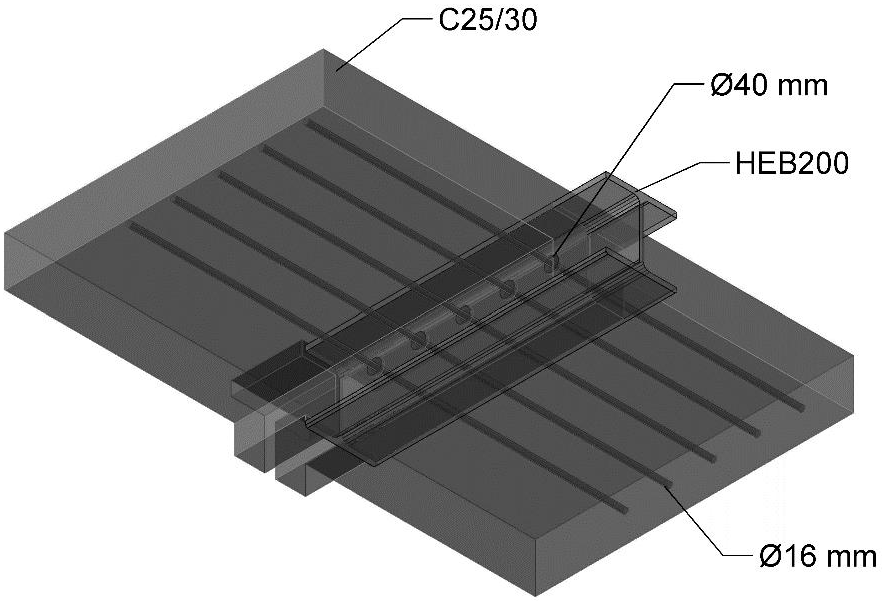


Fig. 16: Basic push-out test configuration (HEB200 (S355), Ø40 mm of the holes in the profile web and Ø16 mm reinforcement)

Push-out tests

For determination of the longitudinal shear connection behavior 21 push-out tests in seven test series were conducted (POT1 – POT6) at the University of Stuttgart. In Figure 16 the basic test configuration is shown for the push-out test (test specimen half). Aim of the tests is to verify the influence of the following parameters on the shear connection:

- Diameter of the reinforcement (Ø12 mm, Ø16 mm and Ø20 mm)
- Concrete grade (C25/30 and C60/70)
- Diameter of the hole in the web (Ø40 mm and Ø80 mm)

Each push-out test series differs only in one varied parameter from the other test series. Along with push-out test series conducted in earlier projects (Braun, Obiala, & Odenbreit, 2015) and (Braun M. , et al., 2014) the presented testing program widens the knowledge on the longitudinal shear connection behaviour of the Composite Slim-Floor Beam system.

Table 1 gives an overview on the varied parameters of the push-out tests compared to the basic test configuration.

Tab. 1: Overview of push-out test series

Push out test no	Parameter	Remarks
POT1	Basic push test	Basic test configuration
POT2	Reinforcement Ø 12	Influence of bar diameter on longitudinal shear force
POT3a	Reinforcement Ø 20	Depending on the modification of the shape
POT3b	Reinforcement Ø 20 / Concrete grade C50/60	Influence of bar diameter on longitudinal shear force
POT4	Large circular openings, no rebar	Behavior of pure concrete dowel
POT5	Large circular openings Eccentricity of the rebars	Behavior of “concrete dowel” (different diameter)
POT6	Concrete grade C50/60	C50/60, Influence of bar diameter on longitudinal shear force

Results

In Table 2 the maximum load per shear connector for each test specimen is presented. For each test series the lowest value for the shear connection was obtained in the test number one (except for POT4). In these tests strain gauges were applied on the reinforcement bars. The correct application of the strain gauges could only be realized by milling down the specific location, what led to a reduction of the reinforcement diameter.

Tab. 2: Maximum load per shear connector [kN/shear connector]

Number	POT1	POT2	POT3a	POT3b	POT4	POT5	POT6
1	201	201	344	360	93	261	255
2	237	214	356	411	92	279	267
3	245	206	355	403	86	279	261

The lowest value for the shear connection was obtained for POT4 due to missing reinforcement bars. The highest value was observed for POT3b as here the higher concrete grade C50/60 was combined with the biggest used reinforcement diameter within all test series (Ø 20).

During the push-out tests two main failure modes were obtained. The failure of the shear connector (reinforcement bar) was the desired failure mode. It was observed when the higher concrete grade (C50/60) was used and when the basic concrete grade was combined with a small reinforcement diameter (POT2).

The second obtained failure mode was a premature crumbling of the concrete at the support of the test specimens before the connection itself did fail; see in Figure 17 for POT1-1. This failure mode was observed when concrete grade C25/30 was combined with Ø ≥ 16 mm reinforcement bars.



Fig. 17: Failure of the concrete support of POT1-1

Beam tests and Long-term Beam tests

Within the scope of the SlimAPP project, also beam tests are carried out at the University of Bradford, UK for the investigation of the load carrying behavior of slim-floor constructions under shear and under bending. At the University of Trento, Italy the long term behavior like creep and shrinkage of slim-floor constructions is investigated.

CONCLUSION

Deformation calculations as part of serviceability checks should represent the reality as good as possible. In difference to normal height composite beams the bending capacity of the slim-floors concrete slab has to be considered for realistic predictions of the deformations. Otherwise, an overestimation of the deformation may lead to uneconomically designed slim-floor girders. Slim-floors are due to their shallow geometry subjected to nonlinear effects of cracking, already in the serviceability state.

Within several projects at the Institute of Structural Design at the University of Stuttgart, Germany an analytical model was developed and verified. This model allows taking bending capacity of the concrete slab and consequently the nonlinear cracking into account by an implemented M-κ curve. In a second model an effective width was introduced, that can be assumed constantly over the length of the girder. A third model, which was oriented for practical application, introduces an effective stiffness for calculating the deformations. All three models are verified by various tests conducted within several projects at the Institute of Structural Design at the University of Stuttgart.

Within the ongoing European project SlimAPP (RFCS-SLIMAPP, 2015) the development of a holistic approach for slim-floor constructions is planned, comprising existing rules and construction systems as well as lifecycle assessments. During the project four test setups including push-out tests, shear beam tests, beam tests and long term beam tests are planned. All test series are

correlating to achieve consistent and plausible results. The load capacities of the shear connectors obtained during the push-out tests conducted at the University of Stuttgart are presented.

REFERENCES

Braun, M., Hechler, O., & Obiala, R. (2014). Untersuchungen zur Verbundwirkung von Betondübeln. *In: Stahlbau 83, issue 5*, S. pp. 303-308.

Braun, M., Hechler, O., Obiala, R., Kuhlmann, U., Eggert, F., Hauf, G., & Konrad, M. (2014). Experimentelle Untersuchungen von Slim-Floor-Trägern in Verbundbauweise. *Stahlbau 83, Issue 10, pp. 741-749*.

Braun, M., Obiala, R., & Odenbreit, C. (2015). Analyses of the loadbearing behaviour of deep-embedded concrete dowels, CoSFB. *IN: Steel Construction, Volume 8, Issue 3, pp. 167-173*.

DIBT. (2014). Z-26.4-59: Allgemeine bauaufsichtliche Zulassung: CoSFB-Betondübel.

EN 1994-1-1. (December 2009). Eurocode 4: Design of composite steel and concrete structures - Part 1-1: General rules and rules for buildings; EN 1994-1-1:2004 + AC:2009. CEN (European Commitee for Standardization).

Hauf, G. (2010). *Trag- und Verformungsverhalten von Slim-Floor-Trägern unter Biegebeanspruchungen, Dissertation.* Stuttgart: University of Stuttgart, Mitteilung des Instituts für Konstruktion und Entwurf No. 2010-2.

Hauf, G., & Kuhlmann, U. (2015). Deformation calculation methods for slim floors. *In: Steel Construction, Volume 8, Issue 2, pp. 96-101*.

Kuhlmann, U., & Fries, J. (2001). *Optimierung der Bemessung von deckengleichen Verbundträgern in Hutform.* Institute of Structural Design, University of Stuttgart: Schlussberich, AiF-Forschungsvorhaben 12017 N.

Kuhlmann, U., & Hauf, G. (2008). Efficient design for the calculation of the deflection and the shear capacity of slim-floor girder. *Proceedings of Composite Constructions in Steel and Concrete VI, July 20.-24., Colorado, USA*.

Kuhlmann, U., Hauf, G., & Rieg, A. (2006). *Effiziente Dimensionierung niedriger Verbundträger.* research project No. 668, funded by Stiftung Industrieforschung, No. 2006-22X, Institute of Structural Design, Unviersity of Stuttgart.

Kuhlmann, U., Konrad, M., & Hauf, G. (2010). *Slim Floor girder with COFRADAL200 deck elements.* Institute of Structural Design, University of Stuttgart: Technical report for ARCELORMITTAL Belval & Differdange S.A., No. 2010-2X.

RFCS-SLIMAPP. (2015). Grant Agreement RFSR-CT-2015-00020 - Slim-Floor Beams - Preparation of Application rules in view of improved safety, functionality and LCA. Coordinator: University of Stuttgart, Partners: Steel Construction Institute, Università degli Studi Trento, University of Bradford, ArcelorMittal, Lindab Buildings, (running project).

ACKNOWLEDGEMENTS

The authors gratefully acknowledge the financial support of the research project SlimAPP “Slim-Floor Beams – Preparation of Application rules in view of improved safety, functionality and LCA” by the Research Fund for Coal and Steel (RFCS). They also thank the project partners for their good cooperation and the Material testing Institute at the University of Stuttgart (MPA) for their help with the realization of the test.

EXPERIMENTAL AND NUMERICAL STUDY ON MECHANICAL BEHAVIOUR OF COMPOSITE SLABS WITH CLOSED PROFILED SHEETING

Guochang Li
School of Civil Engineering, Shenyang Jianzhu
University Shenyang, China
liguochang0604@sina.com

Xiao Zhang
School of Civil Engineering, Shenyang Jianzhu
University Shenyang, China
syzx024@sina.com

Zhijian Yang
School of Civil Engineering, Shenyang Jianzhu
University Shenyang, China
faemail@163.com

Fengwei Guo
School of Civil Engineering, Shenyang Jianzhu
University Shenyang, China
807876272@qq.com

ABSTRACT

In this paper, the mechanical behavior of composite slabs with closed profiled steel sheeting was studied through test and finite element analysis (FEA). Eleven full-scale specimens were tested under static loading to examine the ultimate capacity of this composite slab. The test results showed that the failure modes of composite slabs can be divided into three types, which are longitudinal shear failure, bending-shear failure and flexural failure. The relationship between load and displacement, development of cross-sectional strain and distribution regularity of slip were obtained through test, respectively. Based on experimental study, FEA was conducted with ABAQUS and the accuracy of finite element model (FEM) is also verified through comparing with test result. With the consideration of different failure modes, a parameter analysis of ultimate bearing capacity of the slab is carried and the effect of each design parameter on the ultimate bearing capacity is given.

INTRODUCTION

Composite slab with profiled steel sheeting is one of new steel-concrete composite members in which profiled steel sheeting and concrete are integrated by using construction measures to

take advantage of the respective properties. Nowadays, the bond behavior between profiled steel sheeting and concrete has been paid more attention to ensure the effective of composite action. A good bond behavior in composite slab is the foundation of cooperative work between two different materials, which can also affect failure mode and ultimate bearing capacity of this kind of composite slab.

Hicks *et al*.[1] presented an experiment of static load on composite slabs with profiled steel sheeting using high-strength steel. The result showed that longitudinal shear behaviour of composite slab with high-strength steel decreased significantly compared with that of using plain steel. Meanwhile, an amendment to revise the rules given in Eurocode 4, Annex B.3.1 was proposed. Rehman *et al*. [2] conducted 12 full-scale push-off tests, which showed that the demountable shear connector in composite slab has similar shear capacity and behaviour with welded shear studs and it also fulfills the requirement of ductility in Eurocode 4. Tremlay *et. al* [3] carried out a total of 26 two-point bending slab tests and 50 pullout tests to evaluate the effect of steel thickness, surface coating, deck position, curing age of the concrete, and the presence of electrical conduits in the slab on the performance of composite floor deck systems. The results of the test showed that an increase in the thickness of the steel deck generally results in a higher overall capacity of the composite slab. Degtyarev [4] presented the results of parametric studies on steel-deck-reinforced composite slabs with end anchorages provided by welded shear stud connectors. Effects of the number of studs, longitudinal shear strength, deck height, steel thickness, deck yield strength, concrete cover depth, concrete compressive strength, and deck span conditions on strength of the composite slabs and the stud strength mobilization were investigated. Rana *et. al* [5] carried out a series of tests on both solid and profiled composite slabs to investigate the effect of end anchorage on the ultimate load carrying capacities and failure modes. The test results showed that end anchorage has a positive effect on the ultimate strength of composite slabs, and the effect of concrete strength and sheeting thickness on the load-deflection behaviour is significant. Shi et al. and Wu, et. al. [6-7] conducted series of tests on full scale composite slabs with closed galvanized sheeting plate. The effects of shear span, sheeting thickness, shear connecting piece on the bond – slip behavior were analyzed. Wang, *et al.* [8] investigated the shear bond behavior, failure mode, deflection, end-slip, and longitudinal shear resistance of the flat-type composite deck slab Econdek 65-675. The test results showed that the all of the specimens presented significant end-slip and occurred longitudinal shear failure. Li *et a*l. [9] presented an experimental investigation of opened profiled steel sheeting and concrete composite slabs, and considered the influence of design parameters on bond property between profiled steel sheeting and concrete. Hedaoo *et al*. [10] did a test study on 18 composite slabs with profiled steel decking. The comparison of experimental and analytical results of ultimate bearing capacity of composite slabs revealed that both m-k and PSC methods agreed with test well, and m-k method was proved to be more conservative than PSC method. Zhang *et al*. [11] proved that ductility and ultimate bearing capacity of composite slab with closed profiled steel sheeting is better than others by conducting the test of composite slabs on static loading. Abdullah *et al*. [12] studied the mechanical behavior of steel deck-concrete composite slabs, a new method for modeling the horizontal shear bond was proposed. Hao *et al*. [13] reported the test and analysis results of composite slab with closed profiled steel sheeting, the equation of relationship between shear bond stress and relative slip was conducted. Crisinel *et al*. [14] proposed a new design approach for the prediction of composite slab behaviour by test. Wendel *et al*. [15] presented a nonlinear finite element analysis of steel-concrete composite structure, the result showed that deformation performance and mechanical behavior of composite slabs were simulated well by considering the crack of concrete. Patrick *et al*. [16] presented an experiment of composite slabs under uniform load and concentrated load respectively, the calculation methods of shear capacity considering two different load forms was proposed and an amendment of partial shear

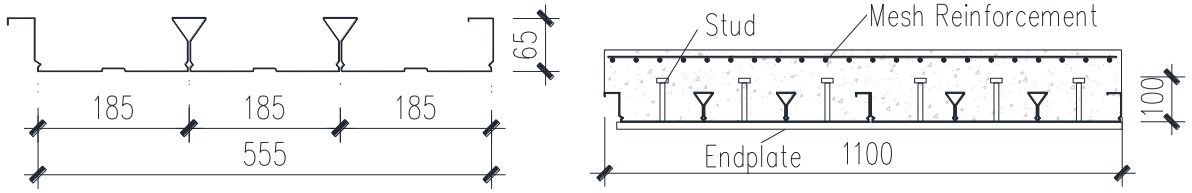
connection design of composite slabs was also given.

The requirement of long-span composite slabs increases with rapid development of large-span spatial structures at present. Due to their advantages, more and more researches have been focusing on the mechanical behaviour of composite slabs with closed profiled steel sheeting, thus the study about this kind of composite slab in this paper is very meaningful.

2. EXPERIMENTAL INVESTIGATION

2.1 Test design

A total of 11 simply supported composite slab specimens were designed, which decked with closed profiled steel sheeting, as shown in Figure 1. The parameters of span, depth of the composite slab and configuration of the end-anchorage stud were considered, the details of specimens are listed in in Table 1. For all the specimens, two steel plates with size 1110 × 150 × 10 mm were welded at both ends.



(a) Cross-section of the steel sheets (b) End anchorage details of the specimens

Fig.1 Details of test specimens

Table 1 Details of the composite slabs with profiled steel sheeting

No.	Specimen	$B\times t\times L$ (mm×mm×mm)	Studs	f_y (MPa)	f_{cu} (MPa)	Failure mode
1	VBI-1	1110×180×2000	D19	348	33.1	Bending-shear
2	VBI-2	1110×180×2000	D19	348	33.1	Bending-shear
3	VBI-3	1110×180×2000	None	348	33.1	Longitudinal shear failure
4	VBII-1	1110×150×3400	D19	348	33.1	Flexural failure
5	VBII-2	1110×150×3400	D19	348	33.1	Flexural failure
6	VBIII-1	1110×160×4800	D19	348	33.1	Flexural failure
7	VBIII-2	1110×200×4800	D19	348	33.1	Flexural failure
8	VBIII-3	1110×160×4800	None	348	33.1	Flexural failure
9	VBIV-1	1110×200×6000	D19	348	33.1	Flexural failure
10	VBIV-2	1110×250×4800	D19	348	33.1	Flexural failure
11	VBIV-3	1110×200×4800	None	348	33.1	Flexural failure

Note: B is the width of the slab. t is the slab thickness. L is the span. D19 means studs' diameter is 19mm. f_y is steel yield strength. f_{cu} is the actual measured 28-day concrete. cube strength.

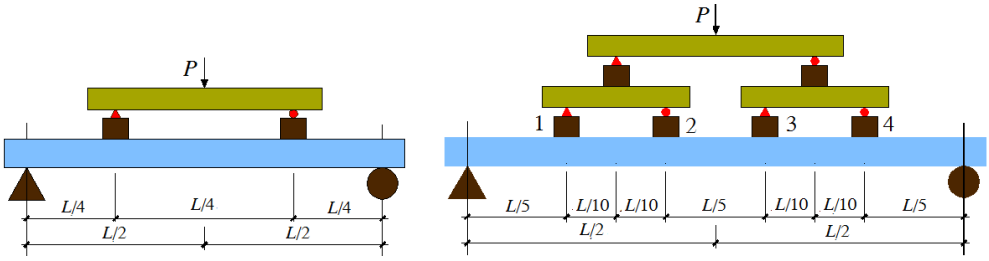
2.2 Experimental scheme and layout of measurement points

Two different types of loading devices were used according to the different spans of the specimens. A four-point loading device was used for specimens with a span 2.0 m, with two equal point loads applied by a load-distribution beam, as illustrated in Figure 2(a). A six-point loading device was used for the specimens with spans of 3.4, 4.8, and 6.0 m, with four equal point loads applied by two levels of load-distribution beams, as displayed in Figure 2(b). The vertical load was applied by a 500 kN hydraulic jack with load sensor and collected by an automatic data collection system IMP.

The vertical load was applied with a step increase, which is 10% of theoretical ultimate bearing

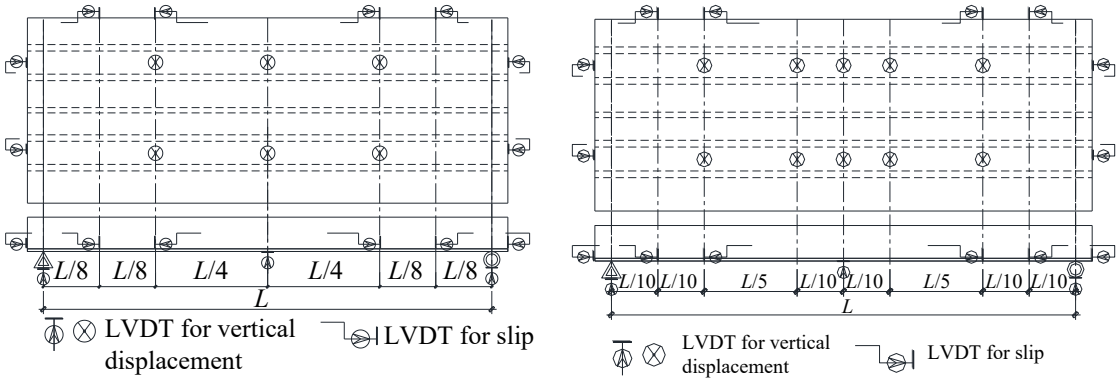
capacity of the specimen. At each load level, the vertical load held for 5 min. After the specimen yielded, the load level was reduced to 1/15 of the theoretical ultimate bearing capacity. As the deflection of midspan was more than 1/50 of the span, the test was terminated.

The strains of profiled steel sheet and concrete were measured by strain gauges. The displacement and slip between the steel sheet–concrete were measured using linear variable differential transformer (LVDT) sensors. Figure 3 shows the configuration of the LVDT sensors.



(a) Four-point bending test (b) Six-point bending test

Fig. 2 Test setup



(a) Four-point bending test (b) Six-point bending test

Fig. 3 Arrangement of the LVTDs

2.3 Test results and discussions

2.3.1 Failure mode

The failure modes of test specimens could be divided into three types according to experimental phenomena, as shown in Figure 4.

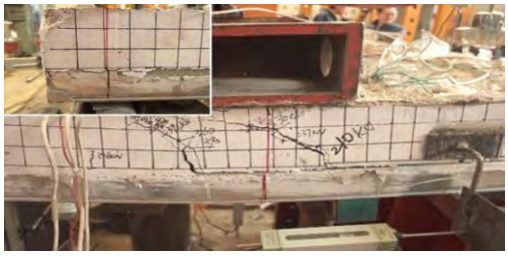
The failure mode of specimen VBI-3 is longitudinal shear failure. First vertical crack appeared near the load point, and then the crack extended through the slab. As the longitudinal crack appeared, the vertical separation between profiled steel sheeting and concrete occurred significantly with the increase of load. At the end of test, composite action of specimen lost and the end slip was 5.13mm.

The failure mode of specimen VBI-1 and VBI-2 is bending-shear failure. First vertical crack appeared near load point, and became the main crack during failure stage. Longitudinal crack occurred in shear span, and developed through the slab suddenly when the end studs were broken. Then, the vertical separation appeared between profiled steel sheeting and concrete. At the end of failure stage, the composite action of specimen was destroyed and the end slip increased quickly. The bottom of profiled steel sheeting of mid-span was ruptured when approaching its ultimate bearing capacity.

The failure mode of specimen VBII, VBIII and VBIV is flexural failure. First vertical crack appeared near the mid-span, and many small cracks emerged at the begining of failure stage. Longitudinal crack occurred in shear span but not throughout the slab. The strain of mid-span section increased rapidly when approaching failure load. Large slip did not happen and composite action of slab still existed as the specimen failed.



(a) Longitudinal shear failure



(b) Bending-shear failure

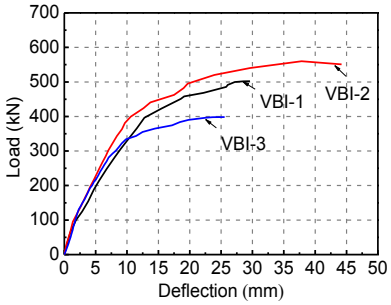


(c) Flexural failure

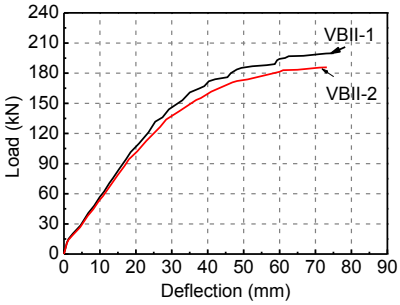
Fig. 4 Failure mode of typical specimen

2.3.2 Analysis of the load - deflection curves

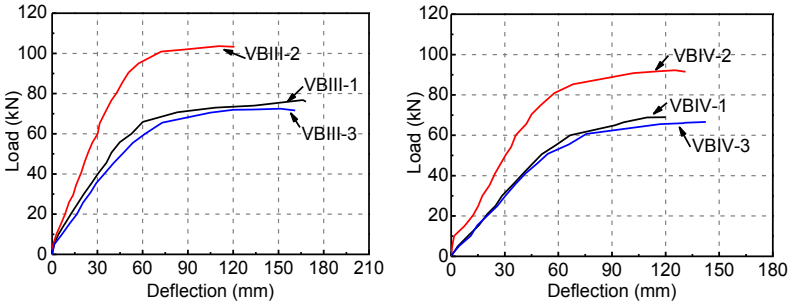
The load - deflection curves of mid-span are showed in Figure 5. It can be seen that the load - deflection curves are similar but the stiffness is quite different. Due to good performance of co-working between profiled steel sheeting and concrete, specimens show good ductility and rigidity. The end stud has a great effect on increasing the ultimate bearing capacity of 2.0m specimen.



(a) 2.0m specimen



(b) 3.4m specimen



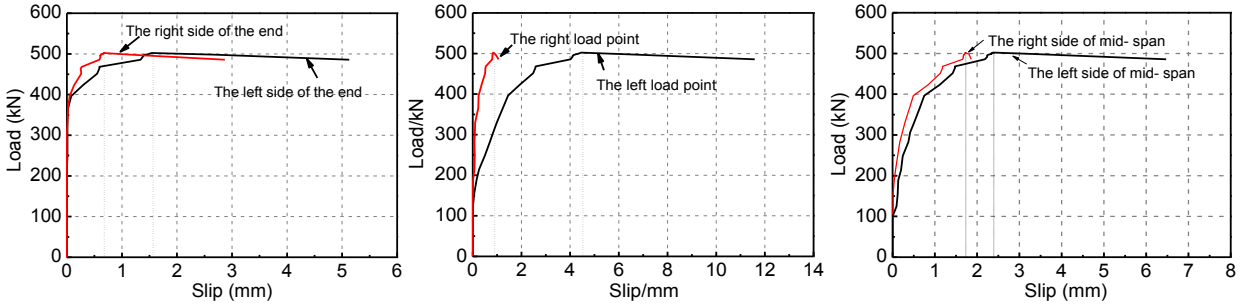
(c) 4.8m specimen (d) 6.0m specimen

Fig. 5 The load-deflection curve of specimens

2.3.3 Analysis of the load - slip curves

The slip between profiled steel sheeting and concrete of 2.0m specimen is larger than other specimens. The measured points of slip are placed at the end of slab, load point, mid of span. The load-slip curve of specimen VBI-1 in different parts is showed in Figure 6. The development of slip in ends is asymmetry during loading. And sequence of slip appearance: first in mid of shear span, next in load point and last in end of slab. When reaching failure load, the maximum slippage is in load point and the minimum slippage is in end of slab.

The load-slip curve of specimen VBI-3 in different parts is showed in Figure 7. The sequence of slip appearance is the same with that of specimen VBI-1 but the final slippage in three different parts is quite different. It indicates that end studs have a great effect on restraint of end slip but there is no stud in specimen VBI-3.



(a) End (b) Load point (c) Shear span

Fig. 6 The load-slip curve of specimen VBI-1

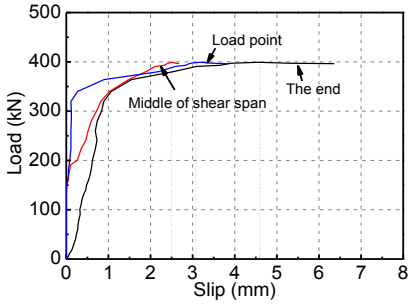


Fig. 7 Load-slip curve of specimen VBI-3

2.3.4 Analysis of the strain-load curve

The load – strain curves of mid-span are showed in Figure 7. As the bottom and web of profiled steel sheeting yielded, the strain decreases rapidly. The strain at the top of profiled steel

sheeting increases with the increase of span under same loading.

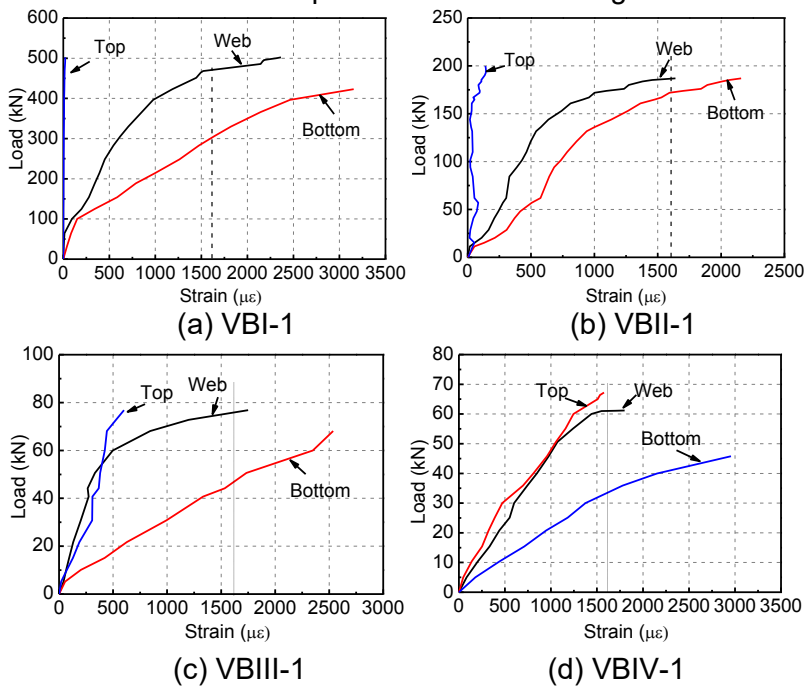


Fig. 8 Load-strain curve of profiled steel sheeting in mid span

2.3.5 Strain distribution of mid-span section

Strain distribution of mid-span section is showed in Figure 9. It can be seen that the neutral axis of specimen VBI-1 moves upward slightly with the increase of load. For specimen VBI-3, the strain presents nonlinear due to the earlier appearance of slip without end studs, the change of its neutral axis is similar to that of specimen VBI-1. For specimen VBII-1, large slip and vertical separation did not appear between profiled steel sheeting and concrete, and the neutral axis has little changes. The span of VBII-1 is larger than VBI-1 and VBI-3, therefore the neutral axis is lower at last.

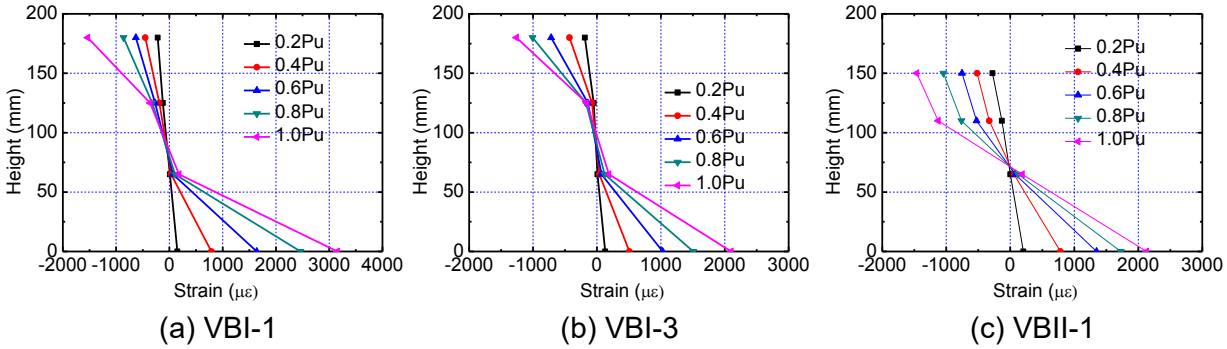


Fig. 9 The strain distribution of mid-span section

3. FINITE ELEMENT ANALYSIS

3.1 Establishment of FEM

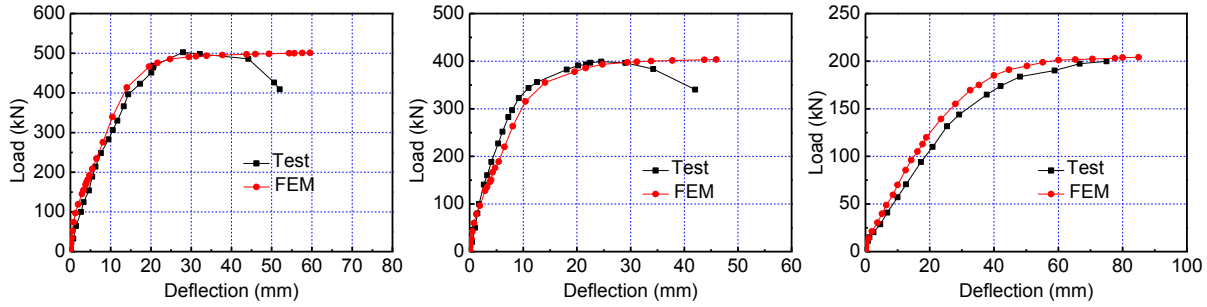
The plastic damage model and the constitutive relation of the Code for design of concrete structures (GB50010-2010) [17] were used for concrete. Bilinear constitutive model was adopted for steel, which included elastic stage and hardening stage, the module is E_s and $0.01E_s$ respectively. Three-dimensional eight-node solid element (C3D8R) was used to simulate

concrete. Profiled steel sheeting was simulated by the four-node reduced integrated shell element (S4R). Three-dimensional two-node truss element (T3D2) and beam element (B31) were selected to simulate reinforcement and end studs respectively.

The surface-to-surface contact was used to simulate the interaction between concrete and profiled steel sheeting, which considered the friction in tangent direction. The friction coefficient was defined as 0.65 obtained by push-out test. Meanwhile, normal constraint was defined by "Hard Contact" which allows the appearance of vertical separation between concrete and steel. Reinforcement was embedded into concrete.

3.2 Comparison between FEA and test results

The comparison between simulation results and the test is shown in Fig. 9. The load – deflection curve of simulation agreed well with the test. The ultimate bearing capacity of the simulation results was defined as deflection of mid-span reached L/50. The error of ultimate bearing capacity between the simulation and test is less than 5%, so the FEM can effectively simulate the mechanical behaviour of the composite slab.



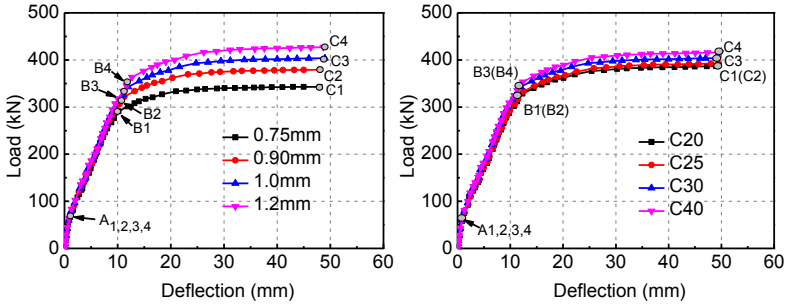
(a) VBI-1 (b) VBI-3 (c) VBII-1

Fig.9 Comparison of load-deflection curve between test and FEM

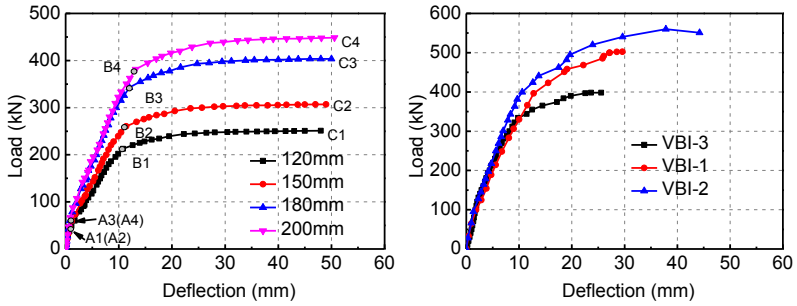
4. PARAMETERS ANALYSIS

4.1 Longitudinal shear-bond bearing capacity

Parameters analysis is made by control variable method and using specimen (VBI-3) as example. The effect of different parameters on shear-bond bearing capacity is showed in Fig. 10, where point A, B, C are crack of concrete, yield of the steel, the ultimate bearing capacity of specimen.



(a) Effect of profiled sheeting thickness (b) Effect of concrete strength



(c) Effect of slab thickness (d) Effect of end studs

Fig.10 Parameters analysis of longitudinal shear-bond bearing capacity

From Figure 10(a), it can observed that point A1 to point A4 is quite close, the thickness of profiled steel sheeting has little effect on the cracking load but has great impact on the yielding load (point B) and ultimate bearing load (point C). The yielding load increases with the increase of thickness. As the thickness increases from 0.75mm to 1.00mm and 1.2mm, the shear-bond bearing capacity increases by 18.2% and 24.5, respectively. It shows that the bearing capacity can be improved effectively by increasing the thickness of profiled steel sheeting.

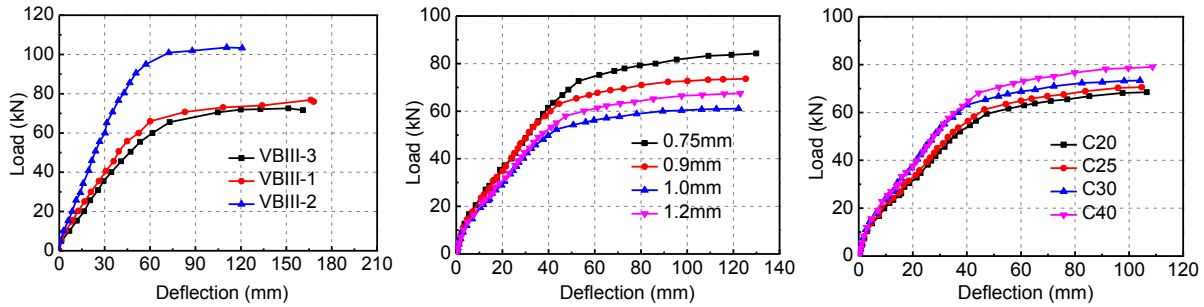
It can be seen from Figure 10(b) that concrete strength has little effect on the ultimate bearing capacity of the slab. The bearing capacity increases by 7.51% as the concrete strength increases from C20 to C40. The increasing of concrete strength has impact on the chemical bond between concrete and profiled steel sheeting, but it is a small part of bond force.

It can be seen from Figure 10(c) that the bearing capacity increases 22.3%, 60.6%, 78.5% as the thickness of slab increases from 120mm to, 150mm, 180mm, 200mm. It indicates that the bearing capacity of composite slab can be increased effectively by increasing slab thickness. However, once shear strength exceeds maximum bond strength between concrete and profiled steel sheeting, the influence of slab thickness is inexistence.

Figure 10(d) indicates that the bearing capacity of specimen VBI-1 with end studs is 25% bigger than specimen VBI-3. The end stud has great effect on restraining the development of slip and improving ductility.

4.2 Parameters analysis of flexural bearing capacity

Specimen VBIII-3 is selected as example to make parameters analysis on flexural bearing capacity. The effect of different parameters on flexural bearing capacity is showed in Fig. 11.



(a) Slab thickness (b) Profiled sheeting thickness (c) Concrete strength

Fig.11 Parameters analysis of flexural bearing capacity

It can be seen from Fig. 11(a) that the flexural bearing capacity increases 35% and the rigidity of slab enhances effectively as the slab thickness increase from 160mm to 200mm. The

bearing capacity of specimen VBIII-1 is 6% bigger than specimen VBIII-3. Thus the end stud has little effect on long- span composite slabs, because the capacity of the long-span specimen is influenced by its bending performance. As flexural failure occurs, bonding performance still keep in good condition and there is no slip in the end, so the end stud can't be fully used.

It is observed that Figure 11(b) that flexural rigidity and bearing capacity of specimens improves obviously with the increase of profiled steel sheeting thickness. When the thickness increases form 0.7mm to 0.9mm, 1.0mm, 1.2mm, the capacity improves 9.8%, 19.7%, 37.7%, respectively.

Mechanical principle of long-span composite slab is similar with reinforced concrete beam, on the basis of the equation $M=f_yA_sZ$ (Z is arm of internal force), the resistance moment of slab can improve with the increase of profiled steel sheeting thickness effectively.

Figure 11(c) shows that the bearing capacity increases 2.9%, 4.9 %, 13%, respectively as the concrete strength increases from C20 to C25, C30, C40. The increase of concrete strength has little impact on the flexural bearing capacity.

5. CONCLUSIONS

Based on the analysis and discussion on the test and FEA results, the following conclusions can be drawn:

(1) The composite slab with closed profiled steel sheeting under static load has a good ductility and its bearing capacity is influenced by failure mode.

(2) In the test, there are three different failure modes, which are longitudinal shear failure, bending- shear failure and flexural failure. In each failure modes, the effect of end studs has different impact on improving the bearing capacity, only in longitudinal shear failure, they work well.

(3) The FEA result shows that thickness of slab and profiled steel sheeting has good effect on the bearing capacity in longitudinal shear failure and flexural failure but the influence of concrete strength is little.

(4) The failure mode of this kind of composite slabs varies with the change of span. Although longitudinal shear failure is the main failure mode, the capacity of long-span specimens depends on their flexural behaviour.

ACKNOWLEDGEMENTS

This project was supported by the Twelfth Five-year National Key Technology Support Program of China (2011BAJ09B0402), Innovative Research Team of Higher Education in Liaoning Province (LT2014012), Shenyang Engineering and Techno-logical Research Center for Civil Steel Construction Industrialization (F16-076-8-00).

REFERENCES

[1] Hicks, S., Jones, A., & Pennington, A. (2013) Performance of Composite Slabs with Profiled Sheeting Using High-Strength Steel. Proceedings of the 2013 International Conference on Composite Construction in Steel and Concrete, 744-753.

[2] Rehman, N., Lam, D., Dai, X., & Ashour, A. F. (2016). Experimental study on demountable shear connectors in composite slabs with profiled decking. Journal of Constructional Steel Research, 12(2), 178-189. doi: 10.1016/j.jcsr.2016.03.021.

[3] Tremlay. R., Gignac, P., Degrange G, et al. (2002). Variables affecting the shear-bond resistance of composite floor deck systems. International Specialty Conference on Cold-Formed Steel Structures, 663-676.

[4] Degtyarev, V. V. (2014). Strength of composite slabs with end anchorages. Part II: Parametric studies. Journal of Constructional Steel Research, 94, 163-175. doi: 10.1016/j.jcsr.2013.10.004.
[5] Rana, M. M., Uy, B., Mirza O. (2015). Experimental and numerical study of end anchorage in composite slabs. Journal of Constructional Steel Research, 115: 372-386. doi.org/10.1016/j.jcsr.2015.08.039.
[6] Shi Q X., Hao J H., Zhang, X H. (2007). Experiments on shear – bond – slip behavior of steel deck and concrete composite slabs. Journal of Harbin Institute of Technology, 39(S2), 487-490.
[7] Wu, L., Shi, Q. X., Wei, X. (2008). Experimental study on shear-bearing capacity of composite floor slab with closed profiled steel sheet-concrete. Journal of Water Resources and Architectural Engineering, 6(4), 137-138.
[8] Wang Y. Q., Cheng, Z. T., Shi, Y. J. (2010). Experimental analysis on the longitudinal shear resistance of flat-type composite slab. Journal of Civil, Architectural &Environmental Engineering, 32(6), 1-6.
[9] Li, G. C., Wang, Y. K., Yang, Z. J., & Xu, W. (2015). Study on bond property between opened profiled steel sheet and concrete composite slabs. Journal of Building Structures, S1, 100-106. doi: 10.14006/j.jzjgxb.2015.S1.016.
[10] Hedaoo, N. A., Gupta, L. M, & Ronghe, G. N. (2012). Design of composite slabs with profiled steel decking: a comparison between experimental and analytical studies. International Journal of Advanced Structural Engineering (IJASE), 4(1), 1-15.
[11] Zhang, J., & Liu, Z. H. (2013). Experimental study on longitudinal bond behaviors of closed profiled steel sheet-concrete composite slabs. Structural Engineers, 1(13), 124-129.
[12] Abdullah, R., Easterling, W. S. (2009). New evaluation and modeling procedure for horizontal shear bond in composite slabs. Journal of Constructional Steel Research, 65(4), 891-899. doi: 10.1016/j.jcsr.2008.10.009.
[13] Hao, J. H. (2007). Experimental study on shear bond-slip behavior of profiled sheeting concrete composite slabs. Xi'an University of Architecture and Technology, Master's Thesis.
[14] Crisinel, M., & Marimon, F. (2004). A new simplified method for the design of composite slabs. Journal of Constructional Steel Research, 60(3), 481-491. doi: 10.1016/S0143-974X(03)00125-1.
[15] Wendel, M., & McConnell, J. (2001). Nonlinear finite element analysis of steel-concrete composite structures. Journal of Structural Engineering, 126(6), 662-674.
[16] Patrick, M., & Bridge, R. Q. (1994). Partial shear connection design of composite slabs[J]. Engineering Structures, 16(5), 348-362. doi: 10.1016/0141-0296(94)90028-0
[17] Standards China. (2010). Code for design of concrete structures (GB 50010-2010). Beijing: China Architecture & Building Press

ROLE OF THE FLOOR SYSTEM IN THE CYCLIC RESPONSE OF COMPOSITE STEEL GRAVITY FRAMING

Sean Donahue, Michael Engelhardt, Patricia Clayton, Eric Williamson, Todd Helwig
University of Texas at Austin, Austin, TX, USA
Contact: sdonahue@utexas.edu

ABSTRACT

In typical U.S. design practice for steel buildings, lateral loads are assumed to be resisted by a small number of lateral-force-resisting frames, while the rest of the structure consists of gravity framing, assumed to have no flexural resistance. It has long been recognized that the simple shear connections used in gravity framing do possess some flexural strength; however, there is little experimental data on the cyclic response of these connections, particularly double-angle connections. This paper details ongoing experimental research into the response of such connections. Full-scale cruciform composite beam-column subassemblies were tested cyclically under large inter-story drifts. These tests have shown that simple shear connections can exhibit significant flexural resistance under large drifts, largely due to the large tensile capacity of the metal decking in the floor system. Given the large number of shear connections in most structures, this capacity could significantly enhance the seismic collapse resistance of a structure.

Keywords: seismic behavior; composite connections; steel buildings; cyclic loads; gravity framing.

1 INTRODUCTION

Seismic resistance is typically provided in steel structures by a small number of moment frames, braced frames, or shear walls. The remainder of the structure is composed of gravity framing (beams framing into columns with “simple shear” connections, topped by a composite slab). These simple shear connections are typically designed as perfect pins, assumed for design purposes to have no flexural strength or stiffness. This assumption implies that these connections cannot contribute to the seismic resistance of a structure. In reality, these connections do provide non-negligible flexural strength, particularly when they act compositely with the floor slab. While this strength may be relatively small, the large number of gravity frames present in a typical steel structure means their overall contribution can be significant.

After the 1994 Northridge earthquake, many steel structures experienced significant fractures in the moment-resisting connections of their lateral frames, yet none of those structures exhibited full collapse [1]. During the investigations that followed that event, analytical studies suggested that the gravity framing can play a key role in the survival of steel buildings in earthquakes, in some cases being the difference between survival and collapse [2,3]. Though these studies suggest that gravity framing can play a significant role in the seismic response of steel buildings, their behavior is not yet fully understood. Current models of shear connection behavior are based on a limited number of experimental studies, primarily testing of shear tab connections done by Liu and Astaneh [4], but also tests of other semi-rigid connection details conducted by Leon [5], Azizinamini and Radziminski [6], and others. While those studies have shown that simple shear connections can exhibit significant flexural capacity, especially in the presence of a composite floor slab, the strength, stiffness and ductility of those connections can vary significantly depending on connection and floor system details. Given the large number of different details and configurations used in gravity framing systems, research is necessary to better characterize the seismic behavior of the wide range

of such systems. This paper details large-scale experimental research intended to improve our understanding of the behavior of simple shear connections, particularly the behavior of double-angle shear connections with a variety of different floor slab details.

2 TEST SETUP

The experimental study includes testing of full-scale cruciform beam-column subassemblies subjected to large cyclic column rotations. The sub-assemblies were designed as components of a prototype building, with W12x96 columns at 8.99 m (29.5 ft.) spacing and with W 14x22 floor beams framing in to W21x55 girders at 2.21 m (7.25 ft.) spacing. The prototype structure was assumed to have 3.51 m (11.5 ft.) floor heights.

The cruciform subassemblies and boundary conditions of the test set-up shown in Figure 1 were designed to be representative of a section of the prototype building, cut out at mid span of the girders and mid height of the column. The floor slab was constructed with an assumed tributary width of one-fourth the girder span (i.e., the slab was 2.21 m (7.25 ft.) wide). Through the use of a series of hydraulic actuators, concentrated forces and moments were applied to the test girders to simulate the gravity loads recommended by ASCE for a seismic load scenario (1.2 times dead load and 0.5 times live load) over the full length of the specimen, which was maintained throughout the test. Once the gravity load was applied, horizontal actuators at the top and bottom of the column applied equal and opposite displacements, rotating the column to simulate the inter-story drifts expected during a seismic event. Drifts were applied according to the SAC load protocol [7].

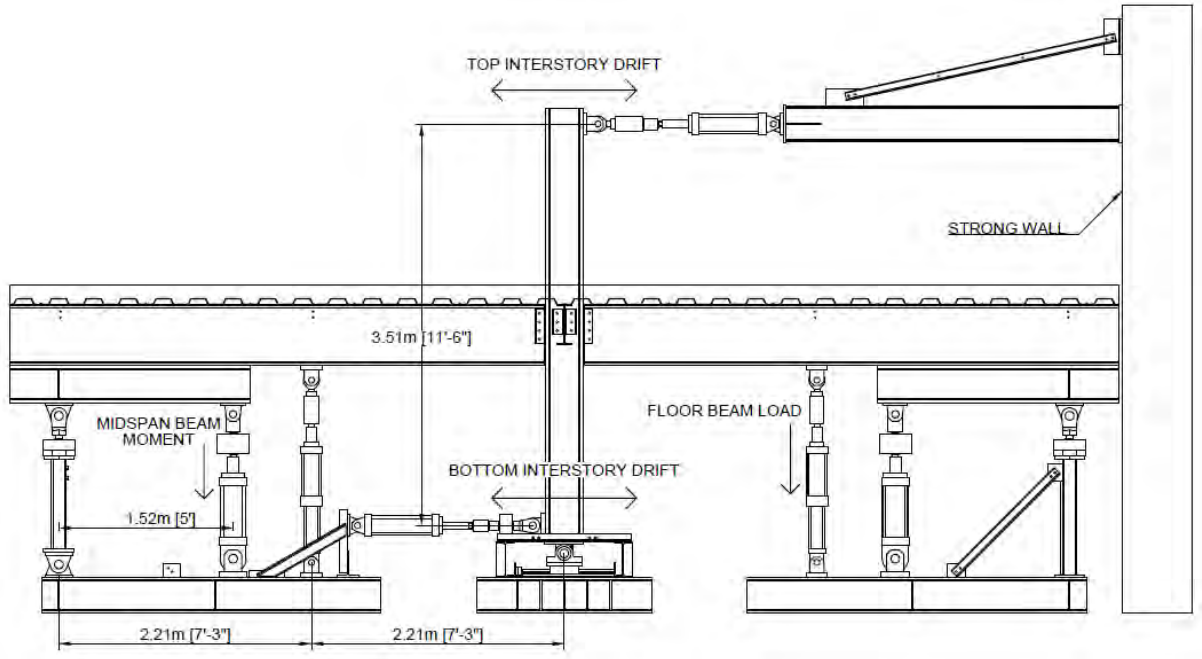


Figure 1-Test setup (plan view)

The double-angle shear connections used in all the test specimens consisted of 2L4x4x1/4 angles (also called web cleats), each with four 19mm (3/4”) A325 bolts connected to both the column and girder. The floor system consisted of a 165mm (6-1/2”) thick normal-weight concrete slab on 51mm (2”) tall, 1mm thick (20GA) corrugated metal decking. Welded wire reinforcement (WWR 6x6x2.9) was placed in the slab for shrinkage control, and 19 mm (3/4”) shear studs were welded through the decking to the girder to achieve approximately 25% composite action with the slab as shown in the connection detail in Figure 2.

This paper will discuss five test specimens completed as part of this research to date, though more tests are planned. The first specimen (designated 1B) consisted of only the bare steel beam-column subassembly, with no composite slab system included. The next two specimens

consisted of an identical double-angle connection, with the composite concrete slab included. The second specimen (designated 1W) had the ribs of the corrugated decking running perpendicular to the girders (referred to as “weak axis” decking in this document), while the third specimen (designated 1S) had the ribs running parallel to the girders (referred to as “strong axis” decking in this document). The fourth specimen (designated 2W) was similar to specimen 1W, however, additional 1.52 m (5’) lengths of reinforcement were placed over the secondary beam (Figure 3). The fifth specimen (designated 2S) was similar to specimen 1S, with the addition of a transverse seam in the decking at the column location, instead of a continuous sheet. One end of the metal decking was attached to the secondary beam with 5/8” puddle welds at each low rib, while the other end was attached through the weld in the shear stud, also at each low rib (Figure 4).

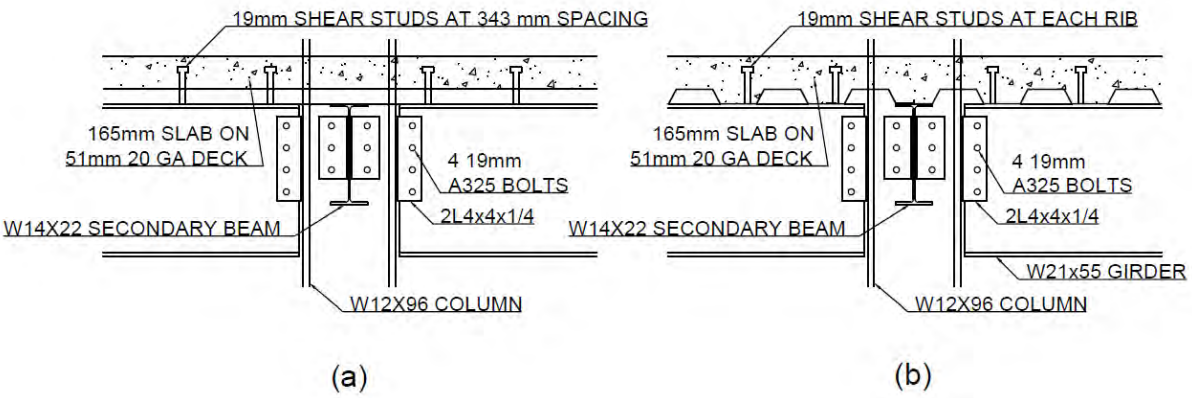


Figure 2-Connection detail (a) specimen 1S (b) specimen 1W

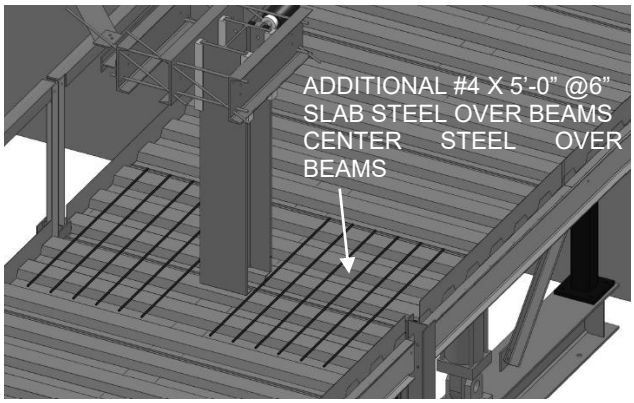


Figure 3-Additional reinforcement in specimen 2W

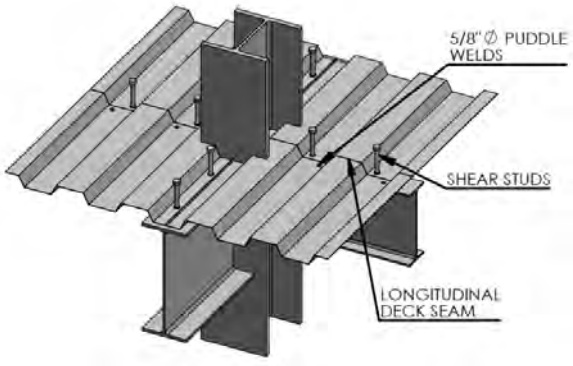


Figure 4-Deck connection at longitudinal seam in specimen 2S

3 TEST RESULTS

The presence of a floor slab is known to significantly increase the flexural capacity of simple shear connections under seismic loading [4,5]; however, this increase in strength is highly dependent on the detailing of the composite floor system. Additionally, the response of the connection is very different under positive and negative moment. Thus, although the test specimens each consist of two shear connections, the discussions below will examine the connections independently, to highlight the different mechanisms of the connection's positive and negative moment behavior. Similarly, the moment-rotation response plots shown below represent the response of one connection, rather than the response of the full, two-connection system. The flexural response of the single connections was obtained from consideration of the specimen free-body diagram and actuator load cells, and the rotation response was obtained from string potentiometers located at the top and bottom of the test column. Full details of the data analysis can be found in [10].

3.1 Response of Bare Steel Connection (Specimen 1B)

The flexural capacity of the bare steel double-angle connection was very small relative to the flexural capacity of the beam. At small inter-story drifts, the flexibility of the angles prevented them from generating significant moment resistance as they pried away from the column. This observation is relatively consistent with the perfect pin assumption typically used in design. At approximately 3.5% drift, however, the bottom flange of the girder began to bear on the flange of the column, creating a force couple between the beam bottom flange and the angles, significantly increasing the flexural stiffness and negative moment capacity of the connection (Figure 5). At approximately 5% drift, tearing at the top of the angles resulted in a rapid degradation in negative moment capacity of the connections, with the capacity peaking at approximately 10% of the plastic moment capacity of the girder (Figure 6). While the flexural strength of the connection was relatively small, the shear strength of the connection was maintained up to very high drift levels. Despite the tears in the angles propagating nearly the entire length of the angles (as shown in Figure 7), the angles continued to carry the full gravity load of the girder up to 10% drift, the maximum rotation that could be accommodated by the test setup.

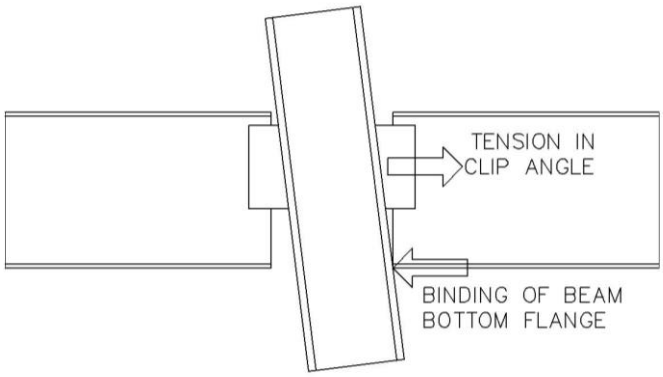


Figure 5-Response of specimen 1B at high drifts

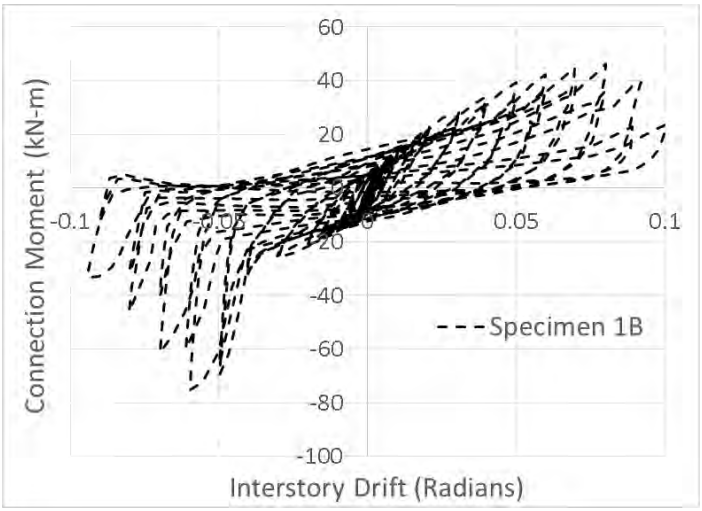


Figure 6-Moment-rotation response of connection (specimen 1B)

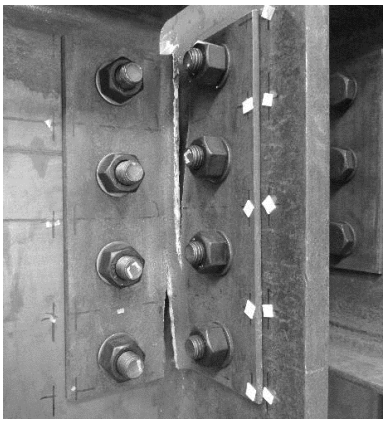


Figure 7-Fracture in bare steel double-angle connection

3.2 Response of Connection with Perpendicular Deck Ribs (Specimen 1W)

The inclusion of a floor slab significantly increased the positive moment capacity of the connection, as suggested by previous researchers [8]. As the column rotated, the concrete floor slab bore on the column flange. This compression in the slab was opposed by tension in the angle as the column pulled away from the girder as shown schematically in Figure 8. This force couple produced a positive moment in the connection that reached approximately 20% of the plastic moment capacity of the girder. This capacity began to drop off quickly after 5% drift, as tearing initiated at the bottom of the angles and quickly grew as shown in Figure 9.

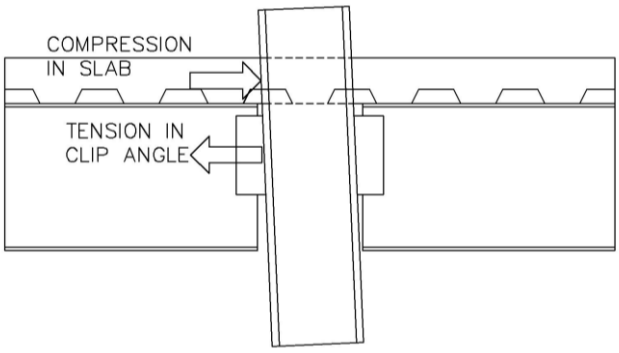


Figure 8-Response of specimen 1W at low drifts

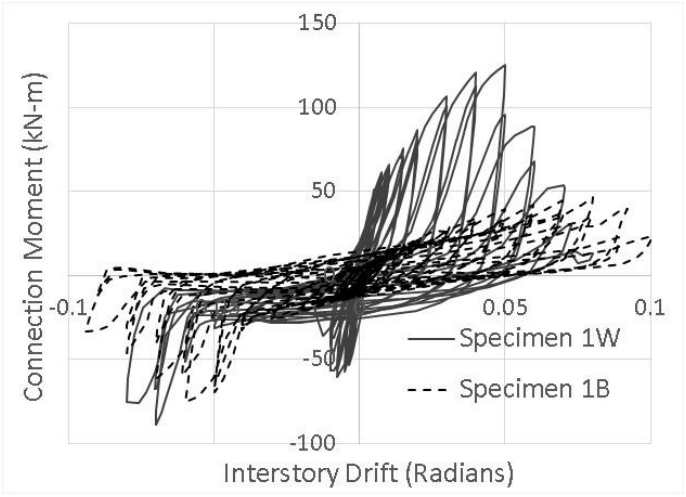


Figure 9-Moment rotation response of connection (specimen 1W vs. 1B)

When the column rotated in the opposite direction, causing the column flange to pull away from the slab, the negative moment connection capacity was limited. Due to the cracking in the concrete and fracture of the slab welded wire reinforcement, the floor slab had minimal tensile capacity, and the connection's negative moment capacity was limited to the moment capacity of the clip angle itself, similar to what was observed in Specimen 1B. This negative moment-resisting mechanism also had limited robustness, reaching its peak strength at 1.5% drift, and decaying significantly thereafter.

Due to the much greater stiffness of the compressive elements of the connection (primarily bearing of the concrete slab on the column face) compared to the tensile elements (prying in the angles) and due to the roller support at the end of one of the girders, a phenomenon known as frame expansion was evident over the course of the test, with the girders pulling further away from the column as drift demands increased. This frame expansion delayed the onset of flange binding, which occurred at 5.5% drift, rather than at 3.5% drift as in specimen 1B (Figure 10). As tearing in the angles had already begun by this point, the increase in flexural capacity associated with bottom flange binding was limited, reaching approximately 12% of the girder's plastic moment capacity before degrading almost immediately.

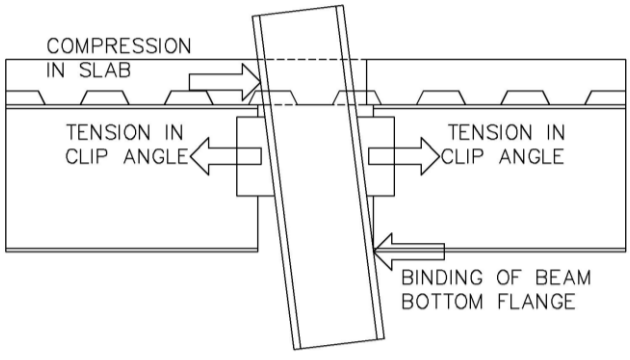


Figure 10-Response of specimen 1W at high drifts

Additionally, due to the greater tensile demand placed on the angles when opposing the compression in the concrete slab, tearing initiated at a smaller drift demand compared to the bare steel specimen (tearing was first observed in Specimen 1W at 5% drift, rather than 6%

in Specimen 1B) and occurred only at the bottom of the angles, rather than the top and bottom. These increased tensile demands caused the tears to propagate through the entire depth of the angle, leading to loss of gravity load-carrying capacity of the connection at 8% drift (Figure 11). These finding suggest that the inclusion of a composite concrete slab can reduce the overall rotational capacity of the double-angle connection.

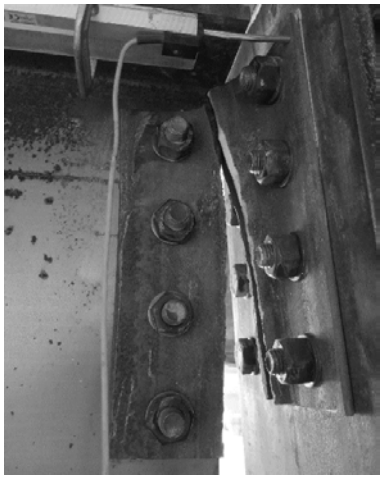


Figure 11-Complete tearing of connection in specimen 1W at end of testing

3.3 Response of Connection with Parallel Deck Ribs (Specimen 1S)

The positive moment response of specimen 1S was similar to the response of specimen 1W. A force couple formed between the compressive force from the concrete slab bearing on the column, and tension in the angles; however, the “strong axis” orientation increased the tensile stiffness and strength of the metal decking, increasing the positive moment capacity of the connection to approximately 25% of the plastic moment capacity of the girder. This increase in strength also altered the failure mode of the connection, with the positive moment response governed by concrete crushing rather than tearing in the angles. This concrete crushing behavior reduced the strength of the connection at larger drifts (compared to specimen 1W), with the positive moment capacity peaking at 3% drift, and degrading significantly afterwards as shown in Figure 12.

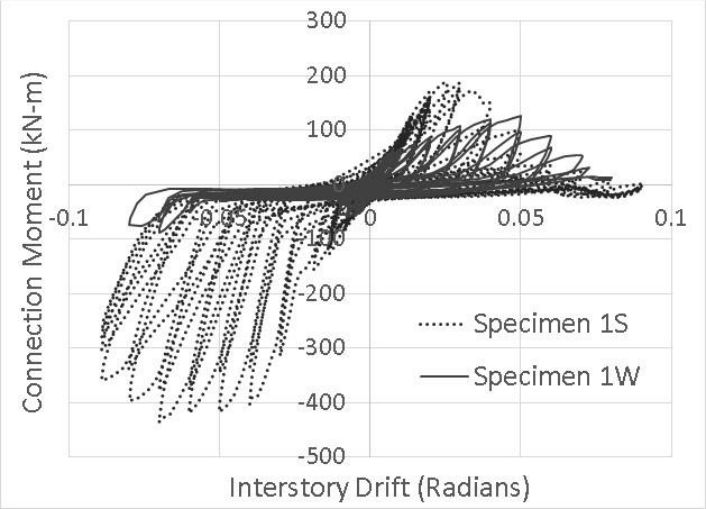


Figure 12-Moment-rotation response of connection (specimen 1S vs. 1W)

The presence of a tensile component in the slab (i.e. the decking oriented in its “strong axis”) had a much greater effect on the negative moment capacity of the connection. At small drifts, a force couple was formed between the tension in the metal decking and compression in the clip angle, significantly increasing the negative moment capacity compared to specimen 1W,

reaching approximately 20% of the girder's plastic moment capacity (Figure 13). Additionally, because the strong-axis orientation of the metal decking increased the resistance to frame expansion, the bottom flange of the beam began to bind on the column at approximately 2.5% drift, creating a new force couple between the tension in the metal decking and this bearing force (Figure 14). This new force transfer mechanism in the bottom beam flange significantly increased the stiffness and strength of the connection, reaching moments in excess of 50% of the girder's plastic moment capacity by 4% drift.

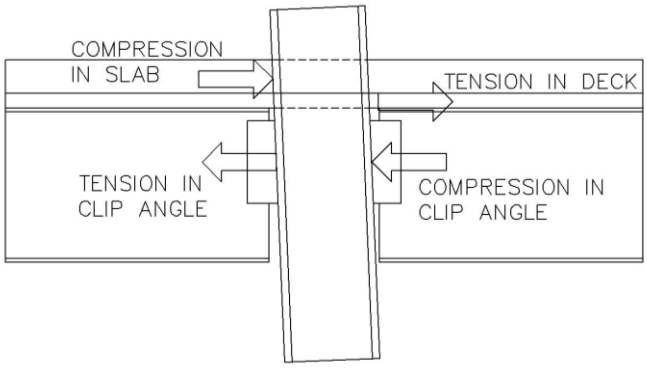


Figure 13-Response of specimen 1S at low drifts

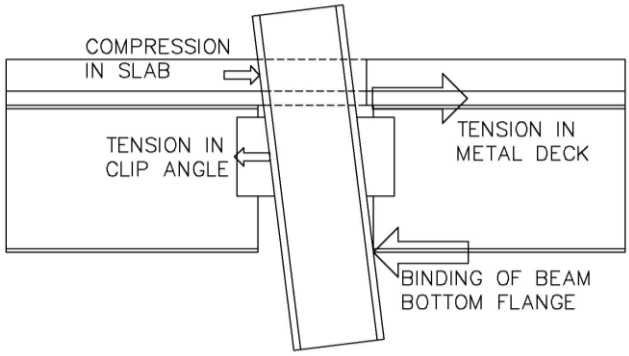


Figure 14-Response of specimen 1S at high drifts

The flexural resistance developed by beam bottom flange binding and tension in the metal decking showed little degradation up to very large drift demands. Even after multiple cycles of 9% inter-story drift (the largest drift accommodated by the test setup for composite specimens), the connection still possessed a negative moment capacity of approximately 33% of the plastic moment capacity of the girder, unlike the previous tests, which exhibited negligible moment capacity at similar drifts. The additional tensile resistance in the metal deck also may have limited the tension demands on the angles, delaying the onset of tearing in the angles compared to specimen 1W. As in the bare steel case, despite nearly full depth tearing in the angles, the connection continued to support the full gravity load even at the maximum drift accommodated by the test setup. Although the connection does retain its strength at high drifts, there is significant pinching of the hysteretic loops, as the force couple between the flange binding and metal decking only demonstrates significant flexural resistance after closing any gaps formed by plastic deformation of the connection in previous cycles of loading.

3.4 Response of Connection with Additional Reinforcement (Specimen 2W)

The tensile capacity in the floor system in specimen 1S, where the metal decking was oriented in its "strong axis" direction, significantly increased the overall strength of the connection compared to comparable specimens with metal decking oriented in the "weak axis" direction. In current building practice, short lengths of rebar are often placed over flexural members perpendicular to the weak axis of the steel decking to limit cracking in the floor slab during

service. It was hypothesized that this additional crack control reinforcement might provide additional tensile resistance to increase the flexural capacity of composite connections with metal decking in the “weak axis” orientation. To test this hypothesis, a specimen with metal decking oriented in its “weak axis” was tested with this crack control reinforcement included. As the amount of crack control reinforcement in a typical building can vary significantly, the reinforcement in this specimen was designed to have approximately the same cross-sectional area of steel as the metal decking oriented in its strong axis.

The presence of reinforcement in the floor slab did result in moderate tensile forces developing in the composite floor slab system, producing a significant increase in the negative moment capacity of the connection under low drifts compared to specimen 1W, reaching approximately 20% of the girder’s plastic moment capacity (Figure 15). By 1% drift, however, cracks developed in the floor slab at the ends of the reinforcement. These cracks grew quickly, leading to a complete shear failure in the slab at 3% drift as shown in Figure *16*. This slab failure severely limited the ability of the reinforcement to carry tensile load, and the connection’s negative moment capacity quickly degraded. The reinforcement was still able to develop small tensile forces through the few shear studs connecting the undamaged portion of the slab and the girder, resulting in a slight increase in negative moment strength upon the onset of flange binding, but the connection never regains its initial peak strength.

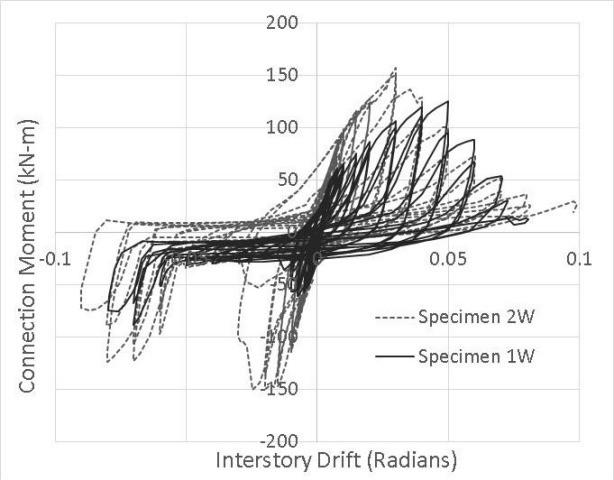


Figure 15-Moment-rotation response of connection (specimen 2W vs. 1W)

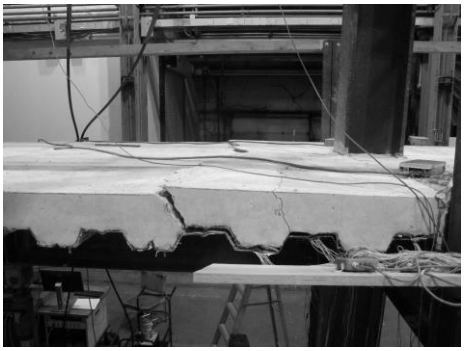


Figure 16-Fracture in slab at end of supplementary reinforcement

3.5 Response of Connection with Transverse Deck Seam (Specimen 2S)

While the metal decking used in composite construction has the potential to generate significant tensile forces, particularly if oriented in its “strong axis,” this capacity is not considered in typical design. Thus, the connections between decking elements are intended only for construction purposes, and typically can only develop a fraction of the deck’s tensile capacity [9]. If the metal decking is discontinuous at the connection (i.e. if there is a seam

between decking sheets), the ability of the floor system to generate tensile capacity (and form a force couple with the flange binding), will be limited by these weak, brittle connections.

Despite the low capacity of the deck-to-beam puddle welds in specimen 2S, there was some development of tensile resistance in the composite floor system at low drifts, resulting in a slight increase in negative moment capacity compared to specimen 1W (Figure 17). However, at approximately 2.5% drift, the puddle welds began to fracture, causing a significant loss in the deck's tensile capacity, and a corresponding drop in negative moment capacity of the connection. By 5% drift, the connection's negative moment capacity was approximately equal to that of specimen 1W, implying a near complete loss in the floor system's tensile capacity, similar to that of metal decking oriented in its "weak axis." The connection did also experience an increase in positive moment capacity compared to specimen 1W, but this is believed to primarily be due to an unexpectedly high concrete strength in the specimen, and not a virtue of the connection detailing.

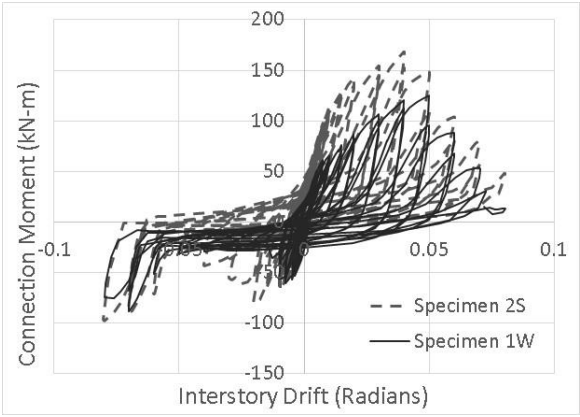


Figure 17-Moment-rotation response of connection (specimen 2S vs. 1W)

4 DISCUSSION AND CONCLUSIONS

This paper discussed preliminary results from a series of ongoing tests on the response of double-angle shear connections with and without a composite floor slab under cyclic loading. These results indicate that the inclusion of the composite floor slab significantly alters the response mechanism of such connections, increasing their stiffness and strength. If the floor system possesses significant tensile capacity, as in the case with continuous metal decking with ribbing oriented parallel to the direction of lateral drift (i.e., "strong axis" orientation), this increase in strength can be very large, resulting in negative moment capacities greater than 50% of the girder's plastic moment capacity, approximately four times the capacity of a comparable connection with decking oriented in the orthogonal direction. However, as the composite slab and decking system is not explicitly designed to carry tension, such configurations may be rare in many structures.

There are inherent limitations in examining the response of a subassembly specimen rather than a full structure. While every effort was made to match the boundary conditions present in a full building, practical limitations and uncertainty about the response of a real structure meant some aspects of the test setup may not adequately represent the conditions in an actual building. For example, in specimen 1S, our testing suggests that the metal decking developed significant tensile force along the entire width of our test specimen. In a full structure, with a much greater width of decking present, it is possible a greater tensile force could develop, increasing the flexural capacity of the connection. The increased width could also serve to delay the shear cracking seen in specimen 2W; the additional puddle welds in a wider deck could also improve the ability of the deck to transmit tension across a seam, improving the capacity of both details.

Additionally, in a full structure, the presence of neighboring bays of gravity framing would provide some degree of restraint to the type of frame expansion observed in these tests that

were free to expand due to the pin-roller support conditions at the ends of the specimen. Accurately simulating this restraint to frame expansion in a subassembly test is difficult and was not attempted in this test program or in other cruciform subassembly test programs. In specimen 1S, the tensile resistance of the decking provided significant restraint against expansion of the system, and thus the lack of external restraint to frame expansion is believed to have had less impact. In the other specimens, however, as the compressive elements of the connection (the bearing of the concrete slab on the column face and the binding of the bottom girder flange on the column) had much greater stiffness and strength than the tensile ones (primarily the angles), significant frame expansion occurred, with the girders pulling further away from the column as the test progressed. In a full structure, the neighboring bays would likely limit this frame expansion, potentially improving the flexural capacity of the connection. The effect of adding such restraint to the connection will be examined in future tests.

5 ACKNOWLEDGEMENTS

Funding for this test program was provided by the National Science Foundation (Award #CMMI 1344592) through the Network for Earthquake Engineering Simulation. Any opinions, findings, conclusions, and recommendations presented in this paper are those of the authors and do not necessarily reflect the views of the sponsors.

6 REFERENCES

[1] Anderson, J.C. et al. (1995) *Case Studies of Steel Moment Frame Performance in the Northridge Earthquake of January 17th, 1994. Report No. SAC 95-07.* SAC Joint Venture.

[2] Foutch, D.A. and Yun, S.Y. (2002). “Modeling of steel moment frames for seismic loads,” *Journal of Constructional Steel Research*, Vol. 58, pp. 529-564.

[3] Ji, X., Kato, M., Wang, T., Hitaka, T., Nakashima, M. (2009). “Effect of gravity columns on mitigation of drift concentration for braced frames,” *Journal of Constructional Steel Research*, Vol. 65, pp. 2148-2156.

[4] Liu, J. and Astaneh-Asl, A. (2000). “Cyclic Testing of Simple Connections Including Effects of Slab.” *Journal of Structural Engineering,* Vol. 126, No. 1, pp. 32-39.

[5] Leon, R. T. (1990). “Semi-rigid Composite Construction.” *Journal of Constructional Steel Research*, Vol. 15, No. 1-2, pp. 99-120.

[6] Azizinamini, A and Radziminski, J. (1989). “Static and Cyclic Performance of Semirigid Steel Beam-to-Column Connections,” *Journal of Structural Engineering*, Vol. 115, No. 12, pp. 2979-2999.

[7] Clark, P., Frank, K. Krawinkler, H., and Shaw, R., 1997. “Protocol for Fabrication, Inspection, Testing and Documentation of Beam-Column Connection Tests and Other Experimental Specimens,” *SAC Steel Project Background Document*. October, Report No. SAC/BD-97/02

[8] Liu, J. and Astaneh-Asl, A. “Moment-Rotation Parameters for Composite Shear Tab Connections,” *Journal of Structural Engineering*, Vol. 130, No. 9, pp. 1371-1380.

[9] Rogers, C. A., and Tremblay, R. (2003). “Inelastic Seismic Response of Frame Fasteners for Steel Roof Deck Diaphragms.” *Journal of Structural Engineering*, Vol. 129, No. 12 pp. 1647-57.

[10] Donahue, S., Engelhardt, M., Helwig, T., Clayton, P., Williamson, E. (2018) “NEES Planning–Role of Gravity Framing in Seismic Performance of Steel Buildings,” DesignSafe-CI [publisher], Dataset, doi:10.17603/DS2M38H.

A DESIGN APPROACH FOR THE SERVICEABILITY LIMIT STATE OF COMPOSITE STEEL-CONCRETE SLABS

Gianluca Ranzi
School of Civil Engineering
The University of Sydney
Sydney, Australia
gianluca.ranzi@sydney.edu.au

ABSTRACT

Composite floors are a well-established cost-efficient and effective form of construction. These flooring systems include thin-walled profiled steel sheeting, concrete and steel reinforcement. This paper presents a design model for the evaluation of the service deflections of composite floor slabs that account for the deformations induced by instantaneous loads, creep and shrinkage effects. In the latter case, the model considers the occurrence of a non-uniform shrinkage profile that develops through the slab thickness due to the inability of the concrete to dry from its underside because of the presence of the profiled sheeting. The proposed approach is validated against experimental measurements available in the literature for full-scale long-term tests of composite slab samples.

INTRODUCTION

Composite steel-concrete slabs are widely used for building floors and include thin-walled profiled steel sheeting, concrete and steel reinforcement (Figure 1). Their design is usually governed by serviceability limit state requirements associated with deflections (Ranzi et al, 2013a). At present, available design codes provide different design recommendations for this limit state condition and, in some cases, deflection checks can be omitted if the slabs fall within specific requirements, such as specified span-to-depth ratios (e.g. EN 1994-1-1, 2004). Usually, engineers have accounted for the time-dependent behavior of the composite slabs based on design guidelines available for concrete floors, e.g. (EN 1992-1-1, 2004; AS3600, 2009). In the latter case, the shrinkage strain to be used in design is determined assuming a hypothetical thickness t_h equal to about twice the slab thickness to account for the sealing action provided by the presence of the profiled sheeting (i.e. equal to $t_h = 2A_g/u$, where A_g represents the gross area of the concrete component and u depicts the exposed perimeter) and the calculated shrinkage is then assumed to remain constant over the slab thickness for the service analysis and calculations.

In this context, this paper presents a design model for the serviceability limit state of composite steel-concrete slabs that has been included in the final draft of the Australian composite steel-

concrete standard expected to come out in 2017 (AS2327, 2017). The model builds on recent experimental observations that observed a non-uniform shrinkage profile to occur through the thickness of a composite slab due to the sealing action provided by the presence of the profiled steel sheeting that prevents moisture egress from the slab underside. The first part of the paper provides an overview of the time-dependent behavior of concrete relevant to composite floor systems and it is followed by a presentation of the key features of the design model. The design approach is then validated against the experimental measurements performed on the long-term tests of composite steel-concrete slabs reported in (Gholamhoseini et al 2014, Gholamhoseini 2014).

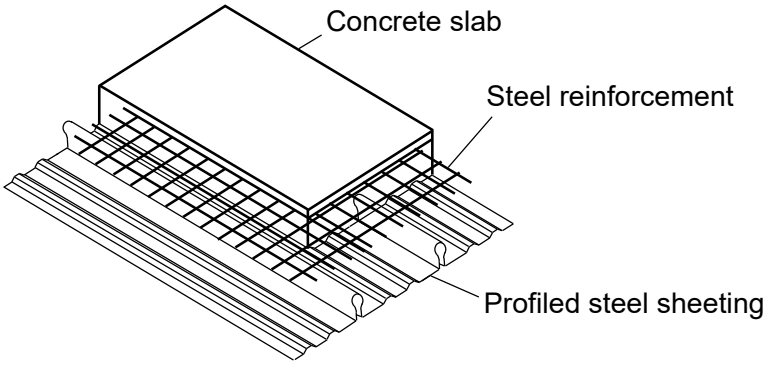


Fig. 1 – Typical composite steel-concrete slab

TIME-DEPENDENT BEHAVIOUR OF THE CONCRETE

The time-dependent behaviour of concrete, such as creep and shrinkage, produces variations in deformations and stresses over time. In particular, when concrete is subjected to a sustained stress it undergoes deformations which increase with time. There are two limit conditions which are usually referred to when dealing with this behaviour, namely the creep and relaxation problems. The former relates to the case in which a concrete member is loaded with a constant sustained load and, being unreinforced and unrestrained, is free to deform with time. The consequent time-dependent deformations are accompanied by no changes in stress. The relaxation problem defines the condition in which a concrete component is subjected over time to a constant deformation (i.e. constant strain) and, due to creep, reduces its time-dependent stress state over time. Shrinkage is a stress-independent effect and leads to significant volume changes which, if restrained, can induce the development of internal stresses and possible occurrence of cracking (CEB, 1984; Gilbert and Ranzi, 2011). It is usually convenient to express the total deformation exhibited in an uncracked uniaxially loaded concrete element at an instant in time t as the sum of an instantaneous strain component $\varepsilon_e(t_0)$, which depicts the elastic strain occurred at the time of loading t_0, a creep strain $\varepsilon_{cr}(t,t_0)$ and a shrinkage strain $\varepsilon_{sh}(t)$. Based on this, the concrete strain developed in a point of a structure at constant temperature can be calculated using:

$$\varepsilon(t) = \varepsilon_e(t_0) + \varepsilon_{cr}(t,t_0) + \varepsilon_{sh}(t) \quad (1)$$

in which it is assumed that these strain contributions can be conveniently treated independently from each other, even if this might not be strictly the case in reality.

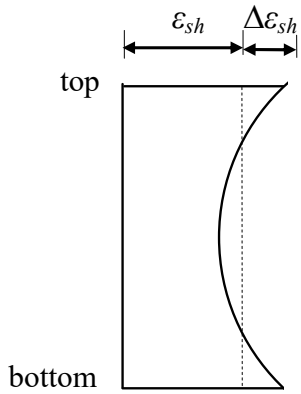
The extent of the time-dependent behaviour of concrete depends on its mix design, dimensions and geometry of the component considered, as well as the environmental conditions. A convenient parameter used to capture the tendency of concrete to creep is referred to as the creep coefficient and is defined as the ratio between the creep and instantaneous strains induced by a sustained stress at time t first applied at time t_0:

$$\varphi(t,t_0)=\frac{\varepsilon_{cr}(t,t_0)}{\varepsilon_e(t_0)} \tag{2}$$

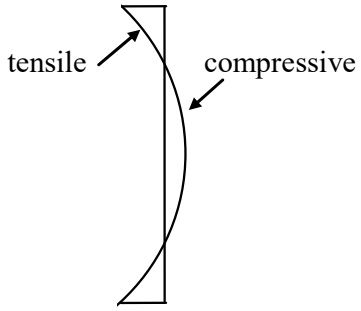
For compressive stress levels smaller than half of the compressive concrete strength, creep deformations are approximately proportional to the stress and this representation is commonly referred to as linear creep. For higher stress levels creep increases at a faster rate and becomes nonlinear with respect to stress (CEB, 1984; Gilbert and Ranzi, 2011).

There are different components that contribute to shrinkage effects, such as plastic shrinkage, autogenous shrinkage, thermal shrinkage and drying shrinkage. Among these, the drying component is of particular interest to composite floor behaviour considered in this paper and it represents the reduction in volume caused principally by the loss of water during the drying process. Figure 2a shows the shrinkage strains through the thickness of an unloaded and unrestrained plain concrete slab that is drying on both its top and bottom surfaces. The mean shrinkage strain ε_{sh} represents the average contraction. The strain marked $\Delta\varepsilon_{sh}$ is the portion of the shrinkage strain that causes the internal stresses required to restore strain compatibility (Figure 2b). These self-equilibrating internal stresses occur in all concrete structures and are tensile near the drying surface and compressive in the interior of the member. Because the shrinkage-induced internal stresses develop gradually with time, they are relieved by creep. Nevertheless, soon after the commencement of drying, the tensile stresses near the drying surfaces may overcome the tensile strength of the concrete and result in surface cracking. The total strain distribution, obtained by summing the elastic, creep and shrinkage components, is linear, as shown in Figure 2c (e.g. Gilbert and Ranzi, 2011).

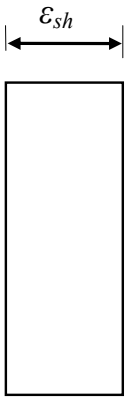
Recent work carried out on composite floor systems has highlighted the occurrence of a shrinkage gradient through the depth of the slab. In particular, this behavior has been first noted in long-term experiments performed on composite steel-concrete beams prepared with a composite slab (Al-Deen et al 2011). Subsequent work has dealt with the service behaviour of composite floor slabs and post-tensioned composite slabs, e.g. (Shayan et al 2010, Ranzi et al 2013b, Al-deen et al 2015, Gholamhoseini et al 2014). Modelling work in this area has also been reported in the literature and focused on the inclusion of shrinkage gradients in the service representation of the composite floors, e.g. (Ranzi and Vrcelj 2009, Bradford 2010, Ranzi et al 2013b, Gilbert et al 2012, Al-Deen and Ranzi 2015).



(a) Shrinkage strain of an unreinforced, unloaded and unrestrained concrete sample



(b) Elastic and creep strain caused by internal stresses

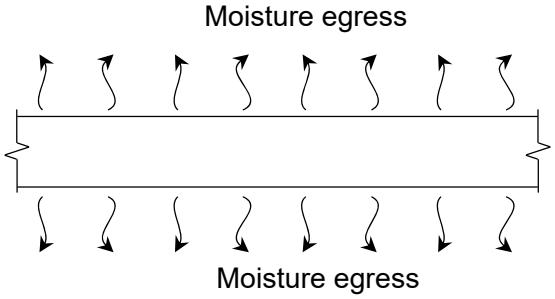


(c) Total strain caused by shrinkage.

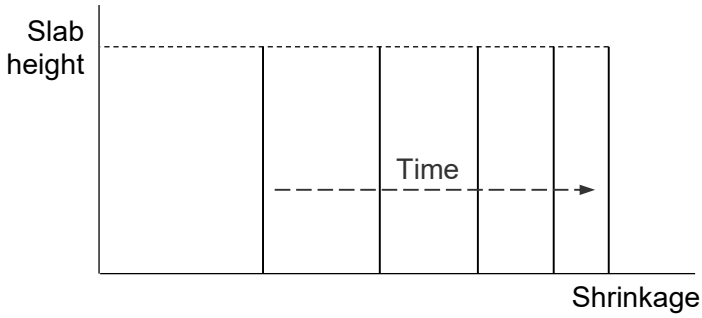
Fig. 2 – Development of shrinkage through slab thickness.

The experimental characterization of the non-uniform shrinkage profile has been carried out by monitoring the total deformations that take place over time in isolated unreinforced concrete samples thought the thickness of the slab, e.g. (Al-Deen et al 2011, Gilbert et al 2012, Ranzi et al 2013b). In this work, companion samples with different exposure conditions have been prepared and monitored, i.e. with one exposure condition allowing the concrete to dry from both sides of the slab sample (Figure 3a) and a second exposure condition exposing only one side for drying and sealing the opposite slab surface (Figure 4a). Qualitative representations of the total deformations recorded during these tests for the two exposure conditions are outlined in Figures 3b and 4b. In particular, Figure 3b depicts constant deformations taking place through a slab exposed on both sides and varying over time. Under the simplifying assumptions of linear shrinkage profiles (commonly adopted for reinforced concrete design), the total deformations depicted in Figure 3b can be assumed to represent the shrinkage deformations. In reality, the shrinkage distribution is non-uniform and produces self-equilibrating stresses, e.g. (Gilbert and Ranzi 2011). In the case of a slab exposed on one side only (Figure 4), a strain gradient develops through the cross-section over time. Relying on the simplifying assumption of linear shrinkage distributions (acceptable for design purposes), it is possible to assume that the measured total deformations correspond to the shrinkage profile. Also in this case, the real

shrinkage distribution is more complex. Obviously, higher order polynomials, or other functions, could be considered for refined service calculations while it is assumed that a linear shrinkage distribution is sufficient for routine design purposes.



(a) Drying conditions of typical concrete slab exposed on both sides.



(b) Qualitative shrinkage distribution of typical concrete slab exposed on both sides (plotted assuming a linear shrinkage profile)

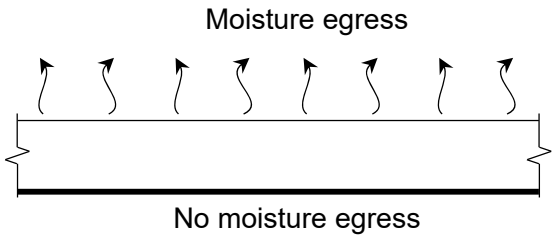
Fig. 3 – Typical concrete slab exposed on both sides.

DESIGN MODEL

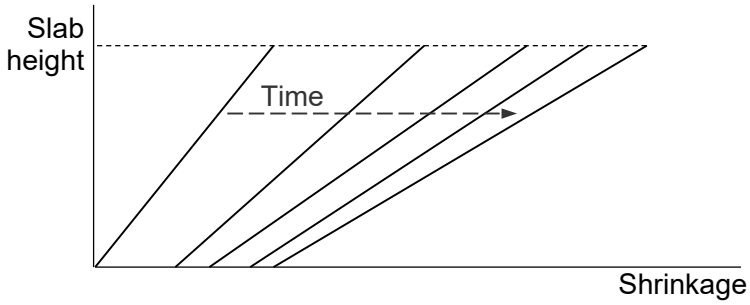
The main features of the model proposed for the serviceability limit state design of composite slabs associated with the deflection requirements is outlined in this section and further details can be found in references (AS2327, 2017; Ranzi, 2017). The proposed procedure is suitable for composite floors whose service behavior is not affected by the partial interaction between the profiled steel sheeting and the concrete slab.

The total deflection of a composite slab δ can be by combining the contributions of the components associated with the instantaneous deflection δ_0 and the deflections associated with creep (δ_{cc}) and shrinkage (δ_{cs}) effects:

$$\delta = \delta_0 + \delta_{cc} + \delta_{cs} \tag{3}$$



(a) Drying conditions of typical concrete slab exposed on one side only.



(b) Qualitative shrinkage distribution of typical concrete slab exposed on one side only (plotted assuming a linear shrinkage profile)

Fig. 4 – Typical concrete slab exposed on one side only.

The instantaneous deflection δ_0 is calculated considering an effective flexural rigidity $E_c\ I_{ef}$, in which E_c depicts the modulus of elasticity of the concrete and I_{ef} represents the effective second moment of area usually available in concrete design standards. For the purpose of this paper, the following expressions is provided: (AS2327, 2017; Ranzi, 2017)

$$I_{ef} = I_{cr} + \left(I_{uncr} - I_{cr}\right)\left(\frac{M_{cr}}{M_s}\right)^3 \leq I_{ef.\max} \tag{4}$$

where I_{uncr} and I_{cr} are the second moment of area of the uncracked and cracked composite slab sections, respectively, with the steel reinforcement and steel sheeting transformed to an equivalent area of concrete, M_s is the maximum in-service moment resisted by the cross-section, $I_{ef.max}$ represents the maximum effective second moment of area corresponding to the uncracked properties, and M_{cr} denotes the cracking moment and is determined as:

$$M_{cr} = Z\left(f'_{ct.f} - \sigma_{cs}\right) \geq 0 \tag{5}$$

where $f'_{ct.f}$ defines the characteristic flexural tensile strength of concrete, Z is the section modulus of the uncracked section referred to the extreme tensile fibre, and σ_{cs} is the maximum shrinkage-induced tensile stress at the extreme fibre of the uncracked section.

The creep deflection component δ_{cc} is determined based on the effective modulus method, e.g. (Gilbert and Ranzi 2011), and is calculated considering the creep deformations produced by the sustained part of the service load. For this purpose, the instantaneous deflection produced by the sustained service load is denoted as $\delta_{0.sus}$ and the creep deflection δ_{cc} can then be determined as follows:

$$\delta_{cc} = \delta_{0.sus}\alpha_{cc} \tag{6}$$

and

$$\alpha_{cc} = \frac{E_{\mathrm{c}} I_{\mathrm{ef}}}{E_{\mathrm{ef.cc}} I_{\mathrm{ef.cc}}} - 1 \tag{7}$$

where $E_{ef.cc}$ equals E_c / (1+φ_{cc}), $I_{ef.cc}$ represents the effective second moment of area (calculated using the format of Equation 4 with the concrete effective modulus $E_{ef.cc}$) and φ_{cc} is the concrete creep coefficient.

The deflection component due to shrinkage δ_{cs} is evaluated considering the effects of the following shrinkage-induced curvature κ_{cs} on the overall member response:

$$\kappa_{cs} = (1-\gamma_{cs})\kappa_{cs,cr} + \gamma_{cs}\kappa_{cs,uncr} \tag{8}$$

and

$$\gamma_{cs} = \left(\frac{M_{cr}}{M_s}\right)^2 \leq 1 \tag{9}$$

where $\kappa_{cs.uncr}$ is the shrinkage-induced curvature over an uncracked section, and $\kappa_{cs.cr}$ depicts the shrinkage-induced curvature over a cracked section. The cross-sectional properties used for the calculation of Equation 8 are based on an effective modulus for the concrete $E_{ef.cs}$ (= E_c / (1+0.55φ_{cc})).

For design purposes, the shrinkage gradient to be used for routine design can be expressed (under the simplifying assumptions of a linear shrinkage profile as discussed in the previous section) as a function of a reference shrinkage ε_{sh} calculated in accordance with reinforced concrete guidelines, e.g. (EN 1992-1-1, 2004; AS3600, 2009), considering a hypothetical thickness equal to the thickness of the composite slab and assuming both sides of the slab to

be exposed. The shrinkage gradient is then assumed, for the purpose of the design model, to vary from a value of 0.2 ε_{sh} at the base of the slab to 1.2 ε_{sh} at the top surface of the slab. The selection of the reference strain ε_{sh} is a consequence of the fact that the top and bottom values of the non-uniform shrinkage profile have been calibrated experimentally against those exhibited by companion concrete slab samples exposed on both sides with same thickness as the composite specimens, e.g. (Al-deen et al 2011, Al-deen and Ranzi 2015). The adopted shrinkage distribution is a simplification of the real shrinkage behaviour that takes place in the slab over time. More refined representations could be implemented to describe the shrinkage distribution.

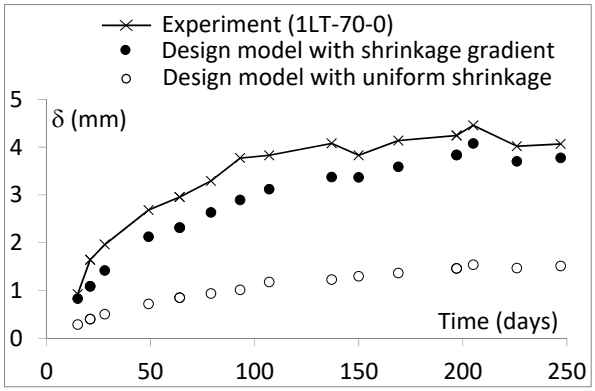
VALIDATION

The model described in this paper is validated in the following against the experimental long-term tests on composite slabs reported in (Gholamhoseini et al 2014, Gholamhoseini 2014). For this purpose, five representative test results have been considered in the following of which two samples (referred to in the following as 1LT-70-0 and 1LT-70-6) were cast on KF70 trapezoidal profiled steel sheeting (Fielders 2008) with a trough height of about 70 mm and the remaining three specimens (denoted as 6LT-40-0, 9LT-40-6 and 10LT-40-6) were prepared using KF40 trapezoidal profiled steel sheeting (Fielders 2008) with a 40 mm trough height. These samples were subjected to different loading histories. In particular, specimen 1LT-70-0 was placed in a simply-supported configuration at 7 days from casting and maintained unloaded for the entire duration of the long-term test (i.e. 247 days), as shown in Figure 5a. Sample 4LT-70-6 followed the same loading history of specimen 1LT-70-0 till 64 days, after which it was subjected to an external load of 6.1 kPa and increased to 7.9 kPa at 197 days from casting (Figure 5b). Specimen 6LT-40-0 was kept unloaded for the entire duration of the long-term experiment (i.e. 223 days) as depicted in Figure 6a. Samples 6LT-40-9 and 6LT-40-9 were loaded at 28 days from casting with an external sustained load of 6.4 kPa as shown in Figure 6b.

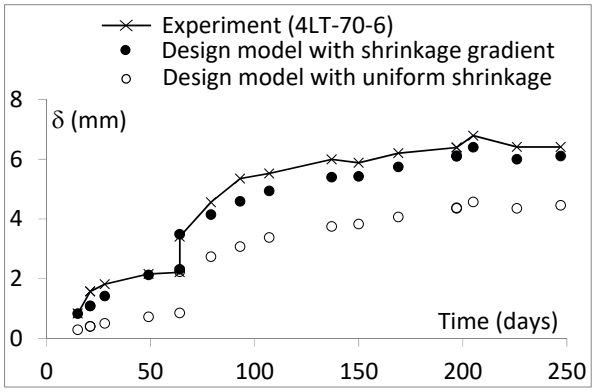
Figures 5 and 6 illustrate the comparisons carried out between the measured deflections and the values calculated with the proposed approach. In all comparisons, good predictions have been observed when considering the numerical values obtained based on the non-uniform shrinkage profile while the use of the uniform shrinkage underestimated the experimental deflections.

CONCLUSIONS

This paper presented a model for the serviceability limit state design of composite steel-concrete slabs associated with the deflection calculations. The proposed approach builds on recent experimental observations that identified the occurrence of a shrinkage gradient through the thickness of composite slabs due to the inability of the slab to dry from its underside because of the presence of the profiled steel sheeting. The main features of the design model have been presented placing particular attention at the occurrence shrinkage effects. The proposed approach has then been validated against representative long-term measurements reported in the literature on composite steel-concrete slabs. The comparisons presented between experimental deflections and numerical values highlighted the need to account for the non-uniform shrinkage profile for a good representation of the long-term response, while the use of the constant shrinkage profile underestimated the experimental results.



(a) Sample 1LT-70-0

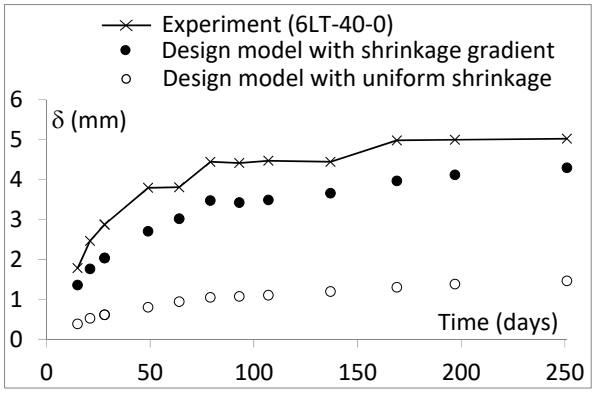


(b) Sample 4LT-70-6

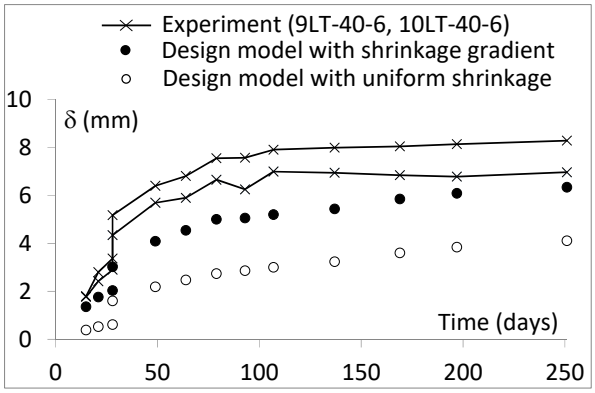
Figure 5. Comparisons between experimental measurements and calculated values.

ACKNOWLEDGEMENTS

The contribution of the work reported in this paper was supported by the Australian Research Council through its Future Fellowship scheme (FT140100130). Support from the University of Sydney (Materials & Structures Research Cluster) is also gratefully acknowledged.



(a) Sample 6LT-40-0



(b) Samples 9LT-40-6 and 10LT-40-6

Figure 6. Comparisons between experimental measurements and calculated values.

REFERENCES

Al-Deen S and Ranzi G (2015) Effects of non-uniform shrinkage on the long-term behaviour of composite steel-concrete slabs. *International Journal of Steel Structures* 15(2): 415-432.

Al-Deen S, Ranzi G and Uy B (2015) Non-uniform shrinkage in simply-supported composite steel-concrete slabs, *Steel and Composite Structures* 18(2): 375-394.

Al-deen S, Ranzi G and Vrcelj Z (2011) Full-scale long-term and ultimate experiments of simply-supported composite beams with steel deck. *Journal of Constructional Steel Research* 67(10): 1658-1676.

AS2327 (2017) *Australian Standard for Composite Structures AS32327-2017*. Final draft. Standards Australia.

AS3600 (2009) *Australian Standard for Concrete Structures AS3600-2009*. Standards Australia.

Bradford MA (2010) Generic modelling of composite steel-concrete slabs subjected to shrinkage, creep and initial thermal strains including partial interaction. *Engineering Structures* 32: 1459-1465.

CEB (Comité Euro-International du Béton) (1984) CEB Design manual on structural effects of time-dependent behaviour of concrete. Edited by Chiorino MA, Napoli P, Mola F, Koprna M. Georgi Publishing.

EN 1992-1-1 (2004) *Eurocode 2: Design of concrete structures - Part 1-1: General rules and rules for buildings*, European Committee for Standardization.

EN 1994-1-1 (2004) *Eurocode 4: Design of composite steel and concrete structures – Part 1.1: General rules and rules for buildings*, European Committee for Standardization.

Gholamhoseini A (2014) *Time-dependent behaviour of composite concrete slabs*. PhD Thesis, The University of New South Wales, Australia.

Gholamhoseini A, Gilbert RI, Bradford MA and Chang ZT (2014) Time-dependent deflection of composite concrete slabs. *ACI Structural Journal* 111(4): 765-776.

Gilbert RI, Bradford MA, Gholamhoseini A and Chang Z-T (2012) Effects of Shrinkage on the Long-Term Stresses and Deformations of Composite Concrete Slabs. *Engineering Structures* 40: 9-19.

Gilbert RI, Ranzi G. (2011) Time-dependent behaviour of concrete structures. Spon Press.

Ranzi G (2017) Service design approach for composite steel-concrete floors. *Proceedings of the Institution of Civil Engineers, Structures and Buildings,* http://dx.doi.org/10/1680/jstbu.16.00196.

Ranzi G, Leoni G and Zandonini R (2013a) State of the art on the time-dependent behaviour of composite steel-concrete structures. *Journal of Constructional Steel Research* 80: 252-263.

Ranzi G, Al-Deen S, Ambrogi L and Uy B (2013b) Long-term behaviour of simply-supported post-tensioned composite slabs. *Journal of Constructional Steel Research* 88: 172-180.

Ranzi G and Vrcelj Z (2009) Closed form solutions for the long-term analysis of composite steel-concrete members subjected to non-uniform shrinkage distributions. *Proceedings of the 5th International Conference on Advances in Steel Structures (ICASS'09), Hong Kong 16-18 December 2009*.

Shayan S, Al-Deen S, Ranzi G and Vrcelj Z (2010) Long-term behaviour of composite concrete slabs: an experimental study. *Proceedings of the 4th International Conference on Steel & Composite Structures (ICSCS'10) Sydney 21-23 July 2010.*

Fielders Australia (2008) *Specifying Fielders – Kingflor – Composite steel formwork system design manual*, Fielders Australia Pty Ltd.

LONGITUDINAL SHEAR RESISTANCE OF COMFLOR 210

Roland Abspoel
Delft University of Technology, Faculty of Civil Engineering and Geosciences
Delft, The Netherlands
r.abspoel@tudelft.nl

Jan Stark
Delft University of Technology, Faculty of Civil Engineering and Geosciences
Delft, The Netherlands
janstark@planet.nl

ABSTRACT

The longitudinal shear resistance of steel-concrete floors can only be determined with full scale experiments since no theoretical model is available. The properties of the steel decking may vary over time due to wear and maintenance of the rollers. Retesting of the composite slabs is therefore necessary at regular intervals.

The longitudinal shear resistance can be determined by using two methods, namely the *m-k* method and the $\tau_{u.Rd}$ method. Although the deep deck ComFlor 210 is not within the scope of EN1994-1-1 the test procedure in Annex B is used. Two series of three specimens were tested. Three additional tests were performed to get information about the effective cross-sectional area of the sheeting, the influence of the rib reinforcement and the influence of end anchorage.
The results of laboratory tests by O'Leary and Duffy (1992), the Salford experiments, are re-evaluated in line with the Delft Experiments to compare both results.

INTRODUCTION

Full scale tests to investigate longitudinal shear resistance of ComFlor 210 were conducted in the nineties of the twentieth century. Because of the large time lap and because of possible variations of the rolling equipment the manufacturer, Tata Steel UK, wanted to confirm the design information. Therefore new tests were conducted in the Stevin II laboratory of the Delft University of Technology.

In EN1994 a subdivision of composite slabs is given based on the spacing of the webs. EN1994 covers only narrow spaced webs which are defined by the ratio b_r / b_s, where b_r is the width of the upper flange and b_s is the distance between centers of adjacent ribs. The recommended value for the upper limit of this ratio is b_r / $b_s \leq 0.6$. ComFlor 210 has a ratio b_r / $b_s = 0.71 > 0.6$ and is consequently not covered in EN1994. Although ComFlor 210 is not within the scope of EN1994-1-1 the test procedure in Annex B of EN1994-1-1 is used as far as possible. In Figure 1 the ComFlor 210 decking system is shown.

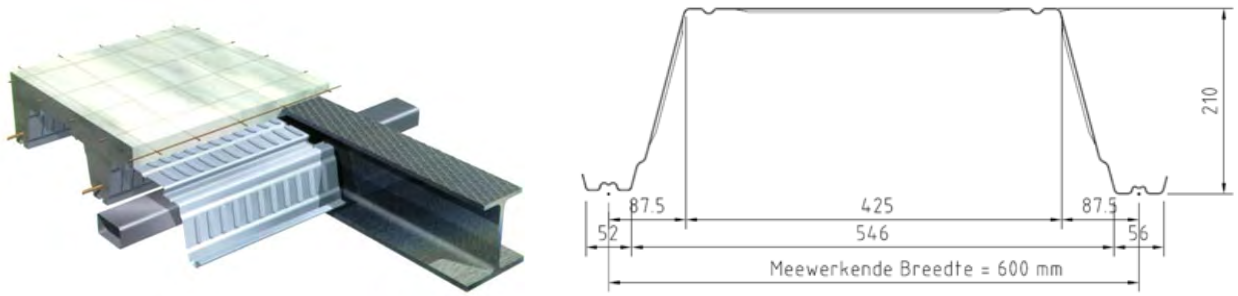


Fig. 1 – ComFlor 210

According EN1994-1-1 (Eurocode 4) the longitudinal shear resistance can be defined by using one of two different methods, the *m-k* method, developed in the USA, and the $\tau_{u.Rd}$ method, developed in Europe. The $\tau_{u.Rd}$ method is only suitable for slabs with ductile connection. The *m-k* method can be used for slabs with either ductile or non-ductile connections. The $\tau_{u.Rd}$ method can take into account both end anchorage and rib reinforcement. Two series of three tests with a different span were performed, series A with a nominal span of 3.60 m and Series B with a span of 5.4 m.

The methods result in properties of the longitudinal shear for the specific tested slabs, but also for slabs consisting of the same steel sheet, but with higher material properties or larger dimensions. The longitudinal shear is based on interconnection of the steel sheeting and the concrete topping, so without reinforcement in the ribs. Both methods are covered in EN1994 and each method has advantages and disadvantages. The largest advantage of the $\tau_{u.Rd}$ method is that it is designed to take into account the influence of end-anchorage and rib reinforcement. A minimum of six test specimens are required for the *m-k* method, subdivided into two groups of three specimens with different lengths, and for the $\tau_{u.Rd}$ method a limited number of four specimens is required and so these tests are combined.

Three additional test specimens were tested to verify the influence of the rib reinforcement and the effect of end-anchorage on the longitudinal shear resistance. ComFlor 210 in practice is always with rib reinforcement. This paper shows the test specimens, the test rig and the test results of the nine test specimens. Particular attention is given to the evaluation procedure for the *m-k* method in case of rib reinforcement and the influence of large areas of embossments and indentations. In this paper the results are presented of a test program carried out in the Stevin II laboratory of the Delft University of Technology for the re-evaluation of the longitudinal shear resistance of ComFlor 210 deep decking profile.

TEST SETUP

The test set-up was designed according to Annex B of EN1994-1-1. Two line loads, located at L/4 and 3L/4 on the span, were applied to the specimen by using a spreader beam. Load cells were used for every support of the three ribs instead of the line support according Annex B.

The test loading procedure consisted of an initial cyclic test and a subsequent deformation controlled loading test in accordance with EN1994-1-1, Annex B clause B.3.4.

TEST SPECIMENS

To determine the *m* and *k* values at least 6 tests have to be performed and for the $\tau_{u.Rd}$ a minimum of 4 tests are necessary. In the Delft experiments, the 6 tests were used for the evaluation of both methods. With the 3 additional specimens a total of 9 specimens were prepared and tested, see Figure 2:

- 6 for the determination of the *m* and the *k* values and the $\tau_{u.Rd}$ values
  - 3 specimens with L = 3.6 m
  - 3 specimens with L = 5.4 m
- 3 additional specimens
  - 1 specimen with L = 7.2 m intended to determine the sagging moment resistance.
  - 2 specimens with L = 3.6 m
    - 1 with a practical support detail consisting of concrete end beams at both supports of the specimen
    - 1 without rib reinforcement



Fig. 2 - Test rig including test specimen during testing

It was expected that specimen 7 with a span of 7.2 m and specimen 8 with the concrete beams as supports would fail in flexure, while the other test specimens would fail in longitudinal shear.

All test specimens have a width of 1.80 m with 3 profile ribs, so consisting of 3 steel sheets of 600 mm width. One of the sheets is cut half and both halves are used for the longitudinal edges. Load introducers are used at the places of load introduction, so the shear length is well defined.

The nominal thickness of the sheet is 0.96 mm without a zinc layer on both sides. The average actual thickness measured is 0.954 mm. The sheeting has transverse embossments in the top flange and the webs (see figure 1). The total length of the embossments per sheet is 577 mm. According to EN1994-1-1 clause 9.7.2 the length of the embossments perpendicular to the rib should be completely neglected for the effective cross-sectional area. Using this rule the effective cross-sectional area is 403.54 mm^2/rib or 672.57mm^2/m.
The strains were measured during testing by 21 strain gauges onto one profiled sheet of specimens 1 and 9 (without rib reinforcement) of the Delft experiments with a span of 3.6 m and 7 strain gauges for specimen 7 with a span of 7.2 m. Based on the measurements of the sheets

with 21 strain gauges, Van Erp (2016) concluded that the effective area is close to 560 mm^2/rib or 933 mm^2/m.

The mesh reinforcement is #8-150 for all specimens and the rib reinforcement is Ø12 for all specimens, except specimen 9, which is tested without rib reinforcement. The test specimens were assembled in Zoeterwoude and after hardening of the concrete, transported to the Stevin II laboratory in Delft. The geometry of the specimens and the instrumentation are presented in Figure 3.

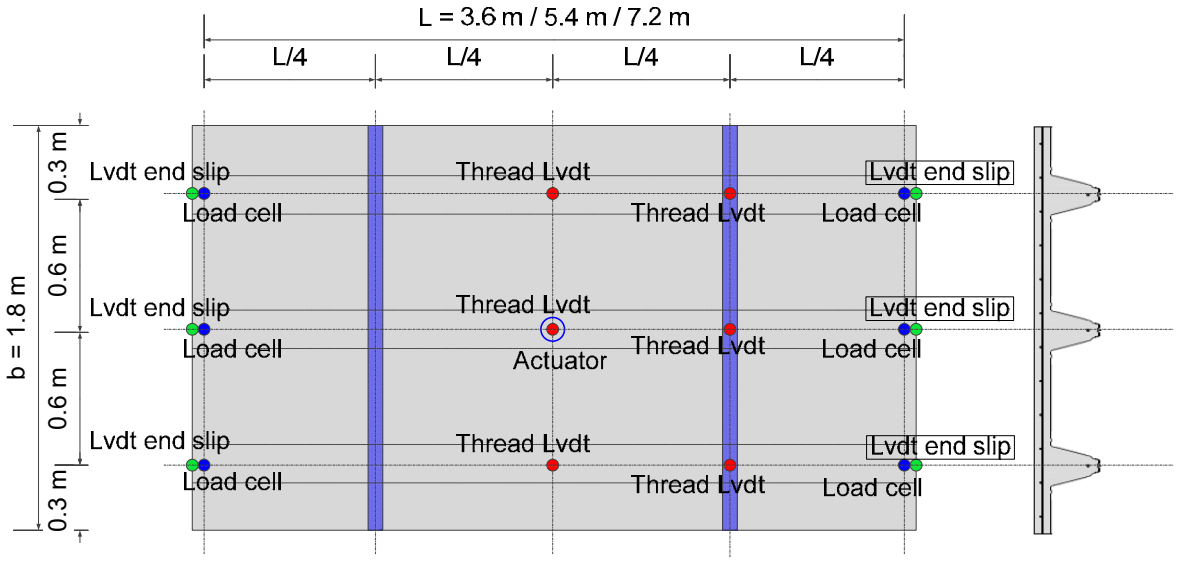


Fig. 3 - Plan and cross-section of the test specimens, including the instrumentation

To determine the actual material properties coupon tests were carried out for the profiled sheeting, the mesh reinforcement and the reinforcement bars in the ribs. The sheeting is roll formed from one coil material and 7 coupons were tested. The coupons were cut from the effective areas of the sheeting. The average lower yield stress is $f_{y.p}$ = 407.10 MPa and the average ultimate stress $f_{u.p}$ = 471.21 MPa. The average thickness of the test specimens is $t = 0.954\ mm$ without taken into account both zinc layers. The mesh reinforcement in the concrete topping has a diameter of #8-150 with an average yield stress $f_{y.r8}$ = 606.69 MPa and an average ultimate stress $f_{u.r8}$ = 612.41 MPa. The rib reinforcement is Ø12-600 with an average yield stress $f_{y.r12}$ = 564.32 MPa and an average ultimate strength $f_{u.r12}$ = 600.21 MPa. The average diameter is 11.85 mm. The concrete properties were determined by testing 3 or 4 cubes of a total of 40 at the day the slabs were tested. The average strength of these 3 a 4 cubes tested are shown in Table 1.

RESULTS OF THE DELFT EXPERIMENTS

The test specimens were tested according to the requirements in Annex B of EN1994-1-4. Table 1 shows the specimens and their average dimensions, the span L, the width b and the height h_{av}. Next to this the average concrete strength and the measured reaction forces, respectively the total reaction force under loading R_{tot}, the total self-weight including, $R_{sw.tot}$, and R_{sw} excluding the weight of the spreader beam used in all tests.

Table 1 – Test results of the Delft experiments specimens 1 to 9

Test	L [mm]	b [mm]	h_{av} [mm]	f_c [MPa]	R_{tot} [kN]	$R_{sw.tot}$ [kN]	R_{sw} [kN]
1	3600	1831	274.0	26.42	263.05	30.81	20.13
2	3614	1827	269.0	24.41	256.91	27.94	17.26
3	3603	1831	266.5	23.44	260.07	28.44	17.76
4	5390	1836	269.3	27.92	182.81	37.39	26.71
5	5388	1829	267.5	28.61	178.21	37.59	26.91
6	5394	1826	267.5	31.05	185.03	36.44	25.76
7	7183	1838	271.0	31.75	136.80	46.60	35.92
8	3597	1815	280.0	31.35	306.18	30.86	20.18
9	3599	1824	271.0	29.97	157.61	29.04	18.36

LONGITUDINAL SHEAR RESISTANCE

The longitudinal shear resistance of a composite slab is based on the composite behavior of a part of the concrete and the steel sheeting. The influence of the rib reinforcement is not taken into account and so this influence during testing has to be deduced from the results. For the ratio $\frac{V_t}{b \cdot d_p}$ as used in this *m-k* method, the lever arm z_p is not used, but instead the height measure d_p, see Figure 4, the measure distance of the centroid of the steel sheets and the extreme fiber of the composite slab in compression.

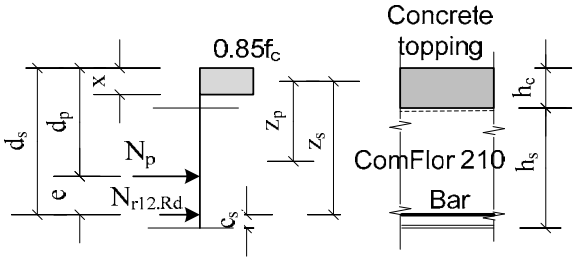


Fig. 4 - Stress distribution composite slab

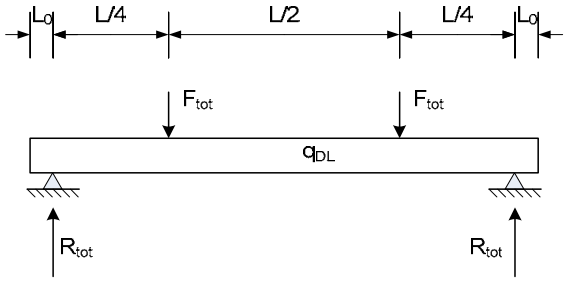


Fig. 5 - Loading scheme of the slab

It seems obviously to deduce the influence of the rib reinforcement on the reaction force V_t by using the measure d_s, the distance of the centroid of the rib reinforcement and the extreme fiber of the composite slab in compression. The contribution of the rib reinforcement bar with a diameter of 12 mm to the bending moment resistance is in this case:

$$(1) \qquad M_{r12} = N_{r12} \cdot d_s$$

The force in the rib reinforcement bars is N_{r12} = 186.35 kN, based on an average actual diameter of 11.85 mm and an average yield strength of 564.32 MPa. The reaction force V_t per support can to be determined as follows:

$$(2) \qquad V_t = \frac{R_{tot}}{2} - \frac{M_{r12}}{L/4}$$

For the partial shear interaction method it is necessary to determine the longitudinal shear N_c, but this force is not measured during the experiments. Nevertheless, the reduced bending moment resistance of the slab, based on partial longitudinal shear, but without the influence of the rib reinforcement, is based on:

$$(3) \qquad M_{u.Rd} = N_c \cdot z + 1.25 \cdot M_{pl.se} \cdot \left(1 - \frac{N_c}{A_{pe} \cdot f_{y.p}}\right)$$

This reduced bending moment resistance $M_{u.Rd}$ is also determined by the measured total reaction force R_{tot} times the distance L_s from the support to the load introduction minus the moment by the dead load of the slab, see Figure 5, in which L_0 = 50 mm for all specimens:

$$(4) \qquad M_{u.Rd} = \frac{R_{tot}}{2} \cdot L_s - \frac{1}{2} \cdot q_{DL} \cdot \left(L_s + L_0\right)^2$$

With q_{DL} the dead load of the slab, based on the reaction force of the total self-weight $R_{sw.tot}$ minus the weight of the spreader beam $R_{sw.sb}$:

$$(5) \qquad q_{DL} = \frac{R_{sw}}{L + 2 \cdot L_0}$$

The lever arm z between the effective height of the concrete and the centroid of the longitudinal shear force is based on EN1994-1-1:

$$(6) \qquad z = h - \frac{x}{2} - e_p + \left(e_p - e\right) \cdot \frac{N_c}{A_{pe} \cdot f_{y.p}}$$

With e the centroid of the steel sheeting, e_p the plastic neutral axis of the effective cross-sectional area A_{pe} and the centroid of the effective height x of the concrete. This formula is a simplification, because the lever arm will be in between the centroid e and the plastic neutral axis e_p. Many researchers calculated the effective height of the concrete x based on the reinforcement force, but this has to be based on the longitudinal shear N_c and the force N_{r12} in the reinforcement with nominal diameter 12 mm:

$$(7) \qquad x = \frac{N_c + N_{r12}}{b \cdot 0.85 \cdot f_c}$$

The plastic bending moment resistance of the effective areas of the steel sheeting is:

$$(8) \qquad M_{pl.pe.Rd} = W_{y.pe.pl} \cdot f_{y.p}$$

Based on above equations the longitudinal shear force N_c has to be determined, in this case by using a solver in the Excel spreadsheet program. For the nominal span of 3.6 m, the longitudinal shear force N_c is solved for the effective area $A_{pe} = 1210.63\ mm^2$ over the width of 1.8 m or

maybe better, for the three ribs used. The plastic section modulus is $W_{pl.pe} = 94663\ mm^3$ over the width of the slab or $W_{pl.pe} = 31554\ mm^3$ per rib.

The plastic bending moment resistance of the composite slab without reinforcement is based on yielding of the effective cross-sectional area of the sheeting by taken into account the nominal effective cross-sectional area A_{pe} = 406.08 mm^2 per rib, so:

$$(9) \qquad N_c = A_{pe} \cdot f_{yp} = 406.08 \cdot 407.1 \cdot 10^{-3} = 165.32\ kN$$

The effective height x of the concrete is based on only axial resistance N_c and by taken into account the average strength $f_{c.av}$ of the concrete:

$$(10) \qquad x = \frac{N_c}{b \cdot 0.85 \cdot f_c} = \frac{165.32 \cdot 10^3}{600 \cdot 0.85 \cdot 27.0} = 12.0\ mm$$

The lever arm z_s is calculated as follows:

$$(11) \qquad z_s = h - \frac{x}{2} - e_p + \left(e_p - e\right) \cdot \frac{N_c}{A_{pe} \cdot f_{yp}} = 270 - \frac{12.0}{2} - 95 = 169\ mm$$

And so:

$$(12) \qquad M_{pl.Rd} = N_c \cdot z_s = 165.32 \cdot 0.169 = 27.94\ kNm \text{ per rib}$$

In contradiction to the *m-k* method in which the gross cross-sectional area A_p is taken into account, in this partial shear resistance the effective cross-sectional area A_{pe} is used. EN1994-1-1 requires to neglect the areas with the embossments. This means that the effective cross-sectional area for this deep deck ComFlor 210 with relative large embossments is rather small, compared with the gross cross-sectional area. In shallow deck profiles other types of embossments are commonly used and so their effective area is rather large, when compared to their gross cross-sectional area.

DETERMINATION OF THE *m*- AND *k*-VALUES

DELFT EXPERIMENTS

Based on the results of the laboratory tests the value of *m* and *k* have to be determined. The vertical shear as effect of the load is checked to the requirement as given in EN1994-1-1:

$$(13) \qquad V_{Ed} \le V_{t.Rd} = \frac{b \cdot d_p}{\gamma_{vs}} \cdot \left(\frac{m \cdot A_p}{b \cdot L_s} + k \right)$$

The characteristic *m*- and *k*-values are determined from two parameters, $\frac{A_p}{b \cdot L_s}$ which relates the gross cross-sectional area A_p of the sheeting to the dimensions of the test specimens and $\frac{V_t}{b \cdot d_p}$ which relates the reaction force V_t to the dimensions of the test specimen. The *m*- and *k*-values are based on the regression line through 90% of the minimum values of the two series of test specimens for the scenarios that the deviation from the average value is less than 10%. The specimens of series A have a nominal span of 3.6 m and the specimens of series B have a

nominal span of 5.4 m. For the six mentioned specimens of the Delft experiments these results of the calculations are summarized in Table 2.

Table 2 – Results for the *m-k* method of the Delft experiments of specimens 1 to 6

Test	d_s [mm]	M_{r12} [kNm]	d_p [mm]	V_t [kN]	$\frac{A_p}{b \cdot L_s}$ [-]	$\frac{V_t}{b \cdot d_p}$ [MPa]
1	219.0	40.88	179.0	86.10	<u>0.00174</u>	<u>0.263</u>
2	214.0	39.95	174.0	84.24	0.00174	0.265
3	211.5	39.48	171.5	86.21	0.00175	0.275
4	214.3	40.00	174.3	61.72	0.00116	0.193
5	212.5	39.67	172.5	59.66	<u>0.00117</u>	<u>0.189</u>
6	212.5	39.67	172.5	63.10	0.00117	0.200

Based on these results the value for *m* and *k* are determined, using the smallest values of the first series of three test specimens, series A, and the second series of three test specimens, series B, are used as underlined in the table:

$$(14) \qquad m = \frac{\Delta\left(0.9 \cdot \frac{V_t}{b \cdot d_p}\right)}{\Delta\left(\frac{A_p}{b \cdot L_s}\right)} = \frac{0.9 \cdot (0.263 - 0.189)}{0.00174 - 0.00117} = 116.71\ MPa$$

The value *k* is determine by using the value *m* in Equation (14) in Equation (15):

$$(15) \qquad k = 0.9 \cdot \left(\frac{V_t}{b \cdot d_p}\right) - m \cdot \left(\frac{A_p}{b \cdot L_s}\right) = 0.9 \cdot (0.263) - 116.71 \cdot (0.00174) = 0.0337\ MPa$$

For the special test specimens 7 to 9 the results are shown in Table 3.

Table 3 - Results for the *m-k* method of the Delft experiments of specimens 7 to 9

Test	d_s [mm]	M_{r12} [kNm]	d_p [mm]	V_t [kN]	$\frac{A_p}{b \cdot L_s}$ [-]	$\frac{V_t}{b \cdot d_p}$ [MPa]
7	216.0	40.32	176.0	45.95	0.00088	0.143
8	225.0	42.00	185.0	106.4	0.00125	0.315
9	-	-	176.0	78.81	0.00175	0.245

SALFORD EXPERIMENTS

O'Leary and Duffy (1992) conducted similar tests on ComFlor 210 at Salford University. Series A have a span of 5.0 m, total height 310 mm and reinforcement bar in the ribs of Ø12-600 and series B have a span of 7.5 m, total height 300 mm and reinforcement bar in the ribs of Ø20-600. Both reinforcement bars used are located at 70 mm from the bottom of the sheeting. The width of all test specimens were 1.20 m. Figure 6 shows the geometry of the specimens.

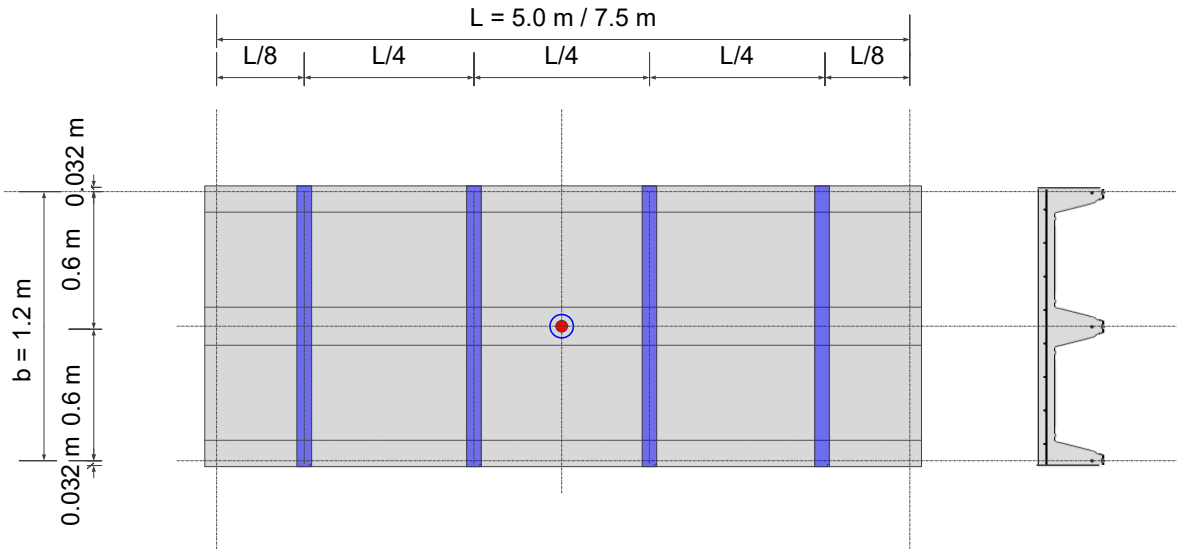


Fig. 6 - Plan and cross-section of the Salford test specimens

The test specimens are loaded according to BS 5950, which means that the load is applied with four line loads and two spreader beams. According O'Leary and Duffy (1992), the shear length is *L*/4, but this has to be changed into 3L/8, the location with the largest bending moment. The values for *m* and *k* are determined similarly to previous calculations for the Delft experiments.

$$(16) \qquad m = \frac{\Delta\left(0.9 \cdot \frac{V_t}{b \cdot d_p}\right)}{\Delta\left(\frac{A_p}{b \cdot L_s}\right)} = \frac{0.9 \cdot (0.108 - 0.063)}{0.00085 - 0.00057} = 128.3 \; MPa$$

$$(17) \qquad k = 0.9 \cdot \left(\frac{V_t}{b \cdot d_p}\right) - m \cdot \left(\frac{A_p}{b \cdot L_s}\right) = 0.9 \cdot (0.108) - 128.3 \cdot (0.00085) = -0.0167$$

The value for *m* according to the Delft and Salford experiments are very similar, see Figure 7.

PARTIAL SHEAR METHOD

DELFT EXPERIMENTS

The second method given in EN1994-1-1 to determine the longitudinal shear is the partial shear method, the $\tau_{u.Rd}$ method. For this method, the minimum number of specimens required is four.

One test specimen with a relative small span and three specimens with a relative large span. The first test is to check that the slab behaves ductile and the three others are used to determine $\tau_{u.Rd}$ according to EN1994:

$$\tau_u = \frac{\eta \cdot N_{c.f}}{b \cdot (L_s + L_0)} \quad (18)$$

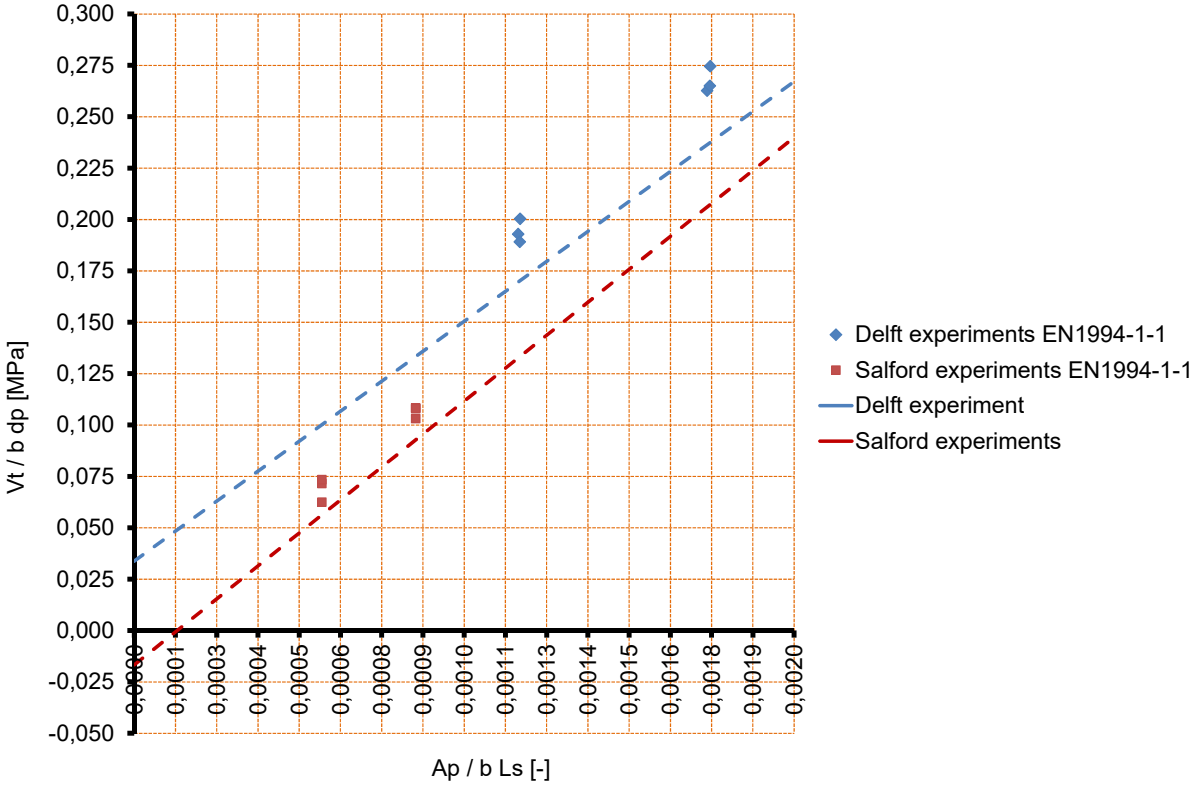


Fig. 7 - Results of the Delft and Salford experiments for the *m-k* method

EN1994-1-1 gives also the possibility to take into account the friction in longitudinal direction due to the reaction force V_t:

$$\tau_{u.\mu} = \frac{\eta \cdot N_{c.f} - \mu \cdot V_t}{b \cdot (L_s + L_0)} \quad (19)$$

This shear stress $\tau_{u.\mu}$ according to Equation (19) will be smaller than τ_u according to Equation (18). For the friction coefficient $\mu = 0.5$ is used. The characteristic value for $\tau_{u.Rk}$ is determined according to EN1994-1-1 which refers to EN1990 Annex D:

$$\tau_{u.Rk} = \tau_{u.Rm} \cdot (1 - k_n \cdot V_\tau) \quad (20)$$

With $\tau_{u.Rk}$, the characteristic value of the longitudinal shear, $\tau_{u.Rm}$ the average longitudinal shear related on the laboratory tests, k_n is the coefficient that relates the average value to

characteristic based on the number of tests performed (with n = 3 is $k_n = 3.37$) and V_τ is the coefficient of variation for the longitudinal shear. The results for the partial shear resistance is shown in Table 4. The design value for the longitudinal shear is determined with:

$$\tau_{u.Rd} = \frac{\tau_{u.Rk}}{\gamma_v} \quad (21)$$

Table 4 - Results for the partial shear method of the Delft experiments of specimens 1 to 6

Sp	q_{DL} [kN/m]	M_{tot} [kNm]	N_c [kN]	x [mm]	z_s [mm]	M_{r12} [kNm]	z_p [mm]	M_u [kNm]	τ_u [MPa]	$\tau_{u.\mu}$ [MPa]
1	5.44	115.9	291.7	11.6	213.2	39.80	193.0	76.1	0.168	0.143
2	4.65	114.0	303.8	12.9	207.5	38.74	186.1	75.2	0.174	0.150
3	4.80	113.3	318.5	13.9	204.6	38.19	181.8	75.1	0.183	0.158
4	4.87	118.4	389.0	13.2	207.7	38.77	178.0	79.6	0.152	0.140
5	4.90	115.2	334.9	11.7	206.6	38.57	182.2	76.7	0.131	0.119
6	4.69	120.2	481.6	13.9	205.6	38.37	167.0	81.8	0.189	0.176

Additional to the above 6 test specimens as used for the *m-k* method, 3 more specimens are tested, namely specimen 7 with a span of 7.2 m, specimen 8 with a concrete beam at the supports as commonly used in practice and specimen 9 without rib reinforcement. The results of these tests are shown in Table 5.

Table 5 - Results for the partial shear method of the Delft experiments of specimens 7 to 9

Sp	q_{DL} [kN/m]	M_{tot} [kNm]	N_c [kN]	x [mm]	z_s [mm]	M_{r12} [kNm]	z_p [mm]	M_u [kNm]	τ_u [MPa]	$\tau_{u.\mu}$ [MPa]
7	4.93	114.4	283.3	9.5	211.2	39.43	191.8	75.0	0.084	0.077
8	5.46	135.2	496.0	14.0	218.0	40.70	178.0	94.5	0.286	0.254
9	4.96	68.7	197.9	8.3	-	-	200.7	68.7	0.114	0.091

The ultimate moment M_u of specimen 7 is of the same magnitude of this moment of specimens 1 to 6. This means that the contribution of the sheeting on the resistance is rather high, which is, related to the height of the sheeting, expected.

Specimen 8, the one with concrete beams at the ends, an end anchorages of the deck, shows that M_u is larger than the plastic bending moment resistance as determined in Equation (12), based on nominal values. This means that the effective area A_{pe} of the sheet has to be larger than the effective area as defined in EN1994-1-1. Assuming that M_u = 94.5 kNm for specimen 8 is the plastic bending moment resistance, an effective cross-sectional area can be determined, namely A_{pe} = 436.05 mm^2 per rib. Although the effective cross-sectional area increases less than 10%, the longitudinal force N_c decreases much more than this 10% and so the shear stress reduces as well. Table 6 shows the adapted longitudinal force N_c and the both shear stresses.

The characteristic shear stress is based on an average shear stress $\tau_{u.Rm} = 0.127\ MPa$ of specimens 4 to 6, and a variation coefficient of $V_\tau = 0.015\ MPa$ and $k_n = 3.37$:

$$\tau_{u.Rk} = \tau_{u.Rm} \cdot (1 - k_n \cdot V_\tau) = 0.127 \cdot (1 - 3.37 \cdot 0.015) = 0.121\ MPa \quad (22)$$

Table 6 - Adapted results of the Delft experiments specimens 1 to 9

Sp	N_c [kN]	τ_u [MPa]	$\tau_{u,\mu}$ [MPa]		Sp	N_c [kN]	τ_u [MPa]	$\tau_{u,\mu}$ [MPa]
1	258.5	0.149	0.124		6	365.6	0.143	0.131
2	264.8	0.152	0.128		7	251.5	0.075	0.068
3	273.7	0.157	0.132		8	532.6	0.307	0.277
4	323.7	0.126	0.114		9	180.9	0.104	0.082
5	287.4	0.112	0.101					

SALFORD EXPERIMENTS

To compare the partial shear resistance of the Delft and Salford experiments, the differences in especially the yield stress, but also the concrete strength is too big.

CONCLUSIONS

The following can be concluded:

- The rather high difference in especially *m* in different researches is caused by using an effective cross-sectional area A_{pe} instead of the required gross cross-sectional area A_p
- For shallow decks the ratio A_{pe} / A_p is much closer to 1 than for a deep deck like the ComFlor 210, which means that by using A_{pe} instead of A_p the difference in *m* is much larger for those deep decks than for shallow decks
- The influence of the rib reinforcement on the bending moment has to be reduced on the bending moment by using the distance d_s and not by using the effective height *x* of the concrete based on only the resistance of this rib bar
- The effective cross-sectional area A_{pe} of the sheeting is larger than the cross-sectional area without the areas of the embossments

REFERENCES

Van Erp (2016). *The horizontal shear resistance of ComFlor 210.*

O'Leary, D. and Duffy, C. (1993). *The Behaviour of ComFlor 210 Long-Span Composite Floor Slabs*.

NEN-EN 1994-1-1 (2004). *Eurocode 4: Design of composite steel and concrete structures – Part 1-1: General rules and rules for buildings.*

SCI Steel Knowledge (2010). *Assessment of CF225 Composite Decking Profile*. Berkshire, United Kingdom: Smith, A.

Behavior of a sustainable composite floor system with deconstructable clamping connectors

Lizhong Wang
Department of Civil and Environmental Engineering, Northeastern University
Boston, MA, USA
wang.l@husky.neu.edu

Mark D. Webster
Simpson Gumpertz & Heger Inc.
Waltham, MA, USA
MDWebster@sgh.com

Jerome F.Hajjar
Department of Civil and Environmental Engineering, Northeastern University
Boston, MA, USA
JF.Hajjar@northeastern.edu

ABSTRACT

This paper presents the behavior of a sustainable composite steel/concrete floor system under gravity and seismic loading. In this system, precast concrete planks are attached to steel beams using deconstructable clamping connectors, enabling reuse of the structural components and reducing the energy consumption related to material fabrication and waste disposal. The results of several composite beam tests are presented along with the companion pushout tests. In the pushout tests, both monotonic and cyclic load-slip curves were established for the clamping connectors. Full-scale composite beams were then designed and tested to investigate the flexural behavior of the system under gravity loading.

INTRODUCTION

In 2012, buildings are responsible for approximately 47.6% of the energy consumption and 44.6% of the CO2 emission in the U.S. (Energy Information Administration 2012; Architecture 2030, 2013). To preserve the natural environment, the building industry has to be transformed from the major contributor to the solution to climate changes and global warming. In addition to exploiting renewable energy, reduction of energy consumption and emission of greenhouse gases is most effectively achieved by implementing sustainable design strategies, such as selecting materials and products with lower embodied energy, utilizing energy efficient operating systems, adopting deconstructable structural systems to maximize material reuse, etc. Great progress has been made to optimize material and energy use, for example, replacing cement in concrete with fly ash (Bilodeau et al. 2000), designing green roofs to reduce the solar radiation reaching the structures below (Castleton et al. 2010), etc. However, limited research is focused on new structural systems

to facilitate design for deconstruction, particularly for composite construction (Lam et al. 2013; Lee et al. 2013).

As the most ubiquitous type of structural steel framing for commercial and institutional buildings, steel-concrete composite floor systems make efficient use of the two materials, with concrete being subjected to compression and steel resisting tension. However, the integration of steel beams and concrete slabs via shear studs inhibits the separation of the two materials, making impossible the deconstruction of the composite flooring systems and reuse of the structural components. Steel beams and shear studs can be recycled after being extracted from demolition debris, while concrete slabs are crushed for fill or making aggregates for new concrete. Conventional composite floor systems are therefore not the best choice for reducing the long-term environmental impacts of building materials.

In this paper, a sustainable composite floor system is presented. Deconstructable clamping connectors are utilized to attach the precast concrete planks to the steel beams, and the planks are connected in-plane with post-tensioned rods. To investigate the behavior of the floor system under gravity and seismic loading, both pushout tests and composite beam tests were conducted. In the pushout tests, both monotonic and cyclic load-slip curves were established for the clamping connectors. Full-scale beam tests were then performed to study the strength, stiffness, and ductility of the composite beam specimens.

DECONSTRUCTABLE COMPOSITE FLOOR SYSTEM

The deconstructable composite prototype is illustrated in Figure 1; this concept was first introduced in Webster et al. (2007).This system is designed to maintain the benefits of steel-concrete composite construction, such as enhanced flexural strength and stiffness, reduced steel beam size and weight, and ease of construction, and to enable sustainable design of composite floor systems in steel building structures, components disassembly and reuse of the structural components.

In this system, high-strength T-bolts, which are inserted into the cast-in channels embedded in precast concrete planks, are pretensioned to firmly clamp the top flanges of the steel beams with the underside of the concrete planks. Composite action is thus achieved by utilizing the friction generated at the steel-concrete interface and the steel-clamp interface. In addition to deconstructability, the proposed system also offers adaptability and flexibility in that no predrilled holes are required, and the embedded channels allow for beams with different flange widths.

Grouting precast concrete panels and placing a cast-in-place topping are common in conventional precast concrete construction, but they may impede the deconstruction of the system and are thus not recommended. Therefore, load transfer under gravity loading is achieved with tongue and groove joints that also facilitate alignment during construction. Shown in Figure 2, unbonded threaded rods are post-tensioned to clamp adjacent concrete planks, and the resulting friction resists plank joint sliding under shear and plank joint opening under flexure during earthquakes. The planks are staggered to assist diaphragm load transfer in the perpendicular direction and to enhance reuse flexibility. After the end-of-life of the structural system, the precast concrete planks and steel beams can be easily disassembled and reconfigured in future projects by loosening the bolts and rods.

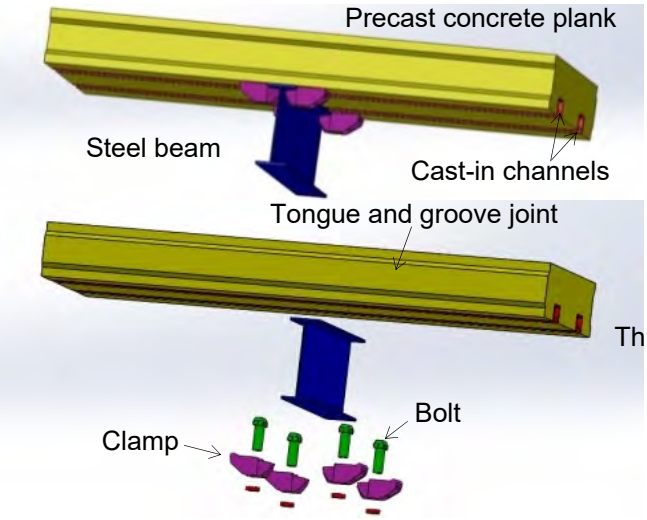


Fig. 1 - Deconstructable composite beam prototype

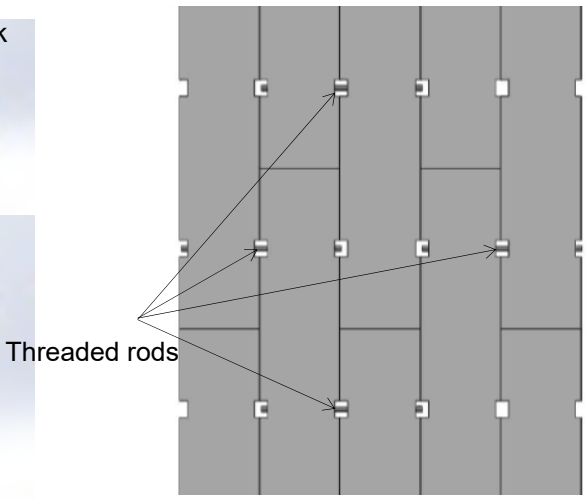


Fig. 2 - Precast concrete plank connections

PUSHOUT TESTS

Pushout tests were conducted under both monotonic and cyclic loading to establish the behavior of the clamping connections for both gravity applications and for use as fasteners to accomplish load transfer between diaphragms and lateral load-resisting systems in seismic applications.

Pretension tests

For the T-bolt connections, as the nut is turned, both the T-bolt heads and the channel lips deform. Consequently, the nut rotation calibrated for regular bolted connections, which is given in Table 8.2 in RCSC Specification (2009), does not apply to the pretensioning of the T-bolts. Pretension tests were thus performed to decide the number of turns of nut. The pretension test configuration is given in Figure 3. Three bolts were snug-tightened to restrain the movement of the beam, whereas the tested bolt was first snug-tightened and then torqued until fracture.

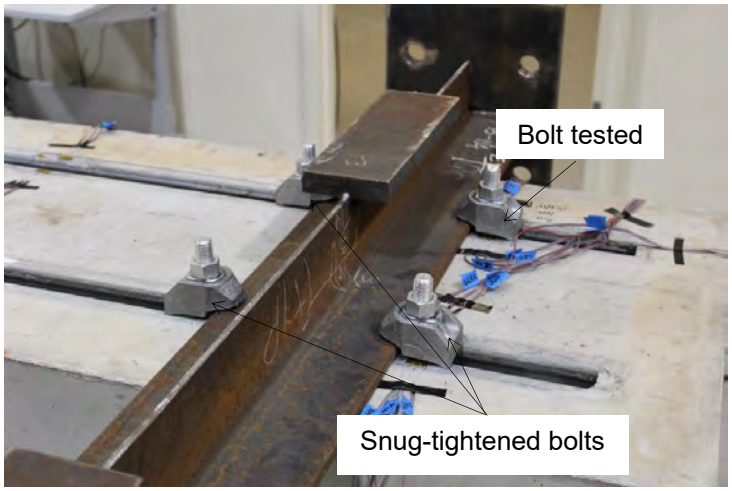


Fig. 3 – Pretension test setup



M24 bolts



M20 bolts

Fig. 4 – Fractured bolts

As shown in Figure 4, three M24 and M20 bolts were tested, and the axial strain variation was tracked for each bolt throughout the test using uniaxial strain gages attached on the bolt shank.

The bolt axial stress was then converted from the strain measurements utilizing the stress-strain curves obtained from tensile testing of round coupons machined from the bolts. Because bolt yielding is clearly shown in the plots in Figure 5, 2.0 turns and 1.5 turns after a snug-tight condition are recommended for pretensioning the M24 and M20 bolts, respectively.

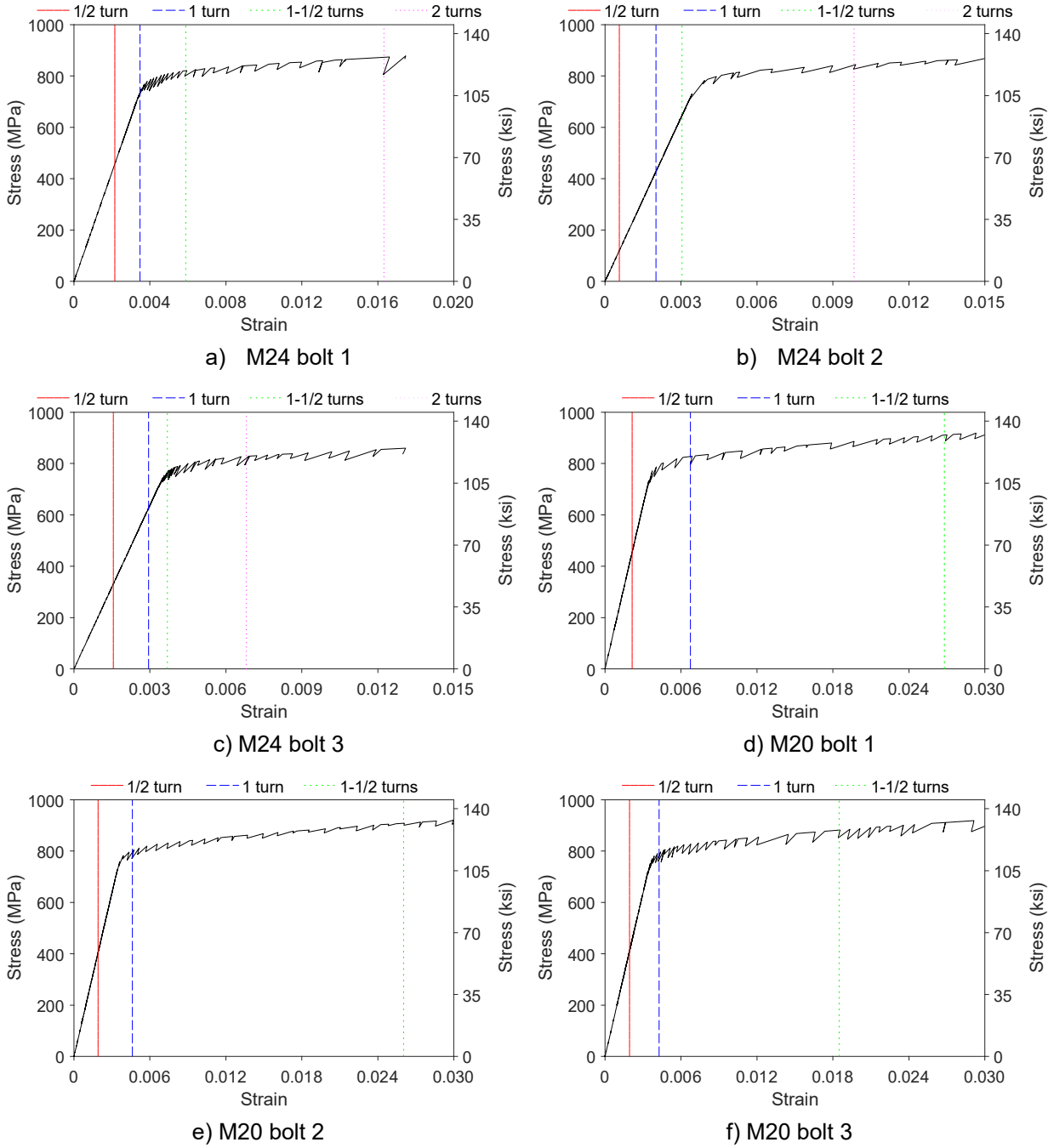
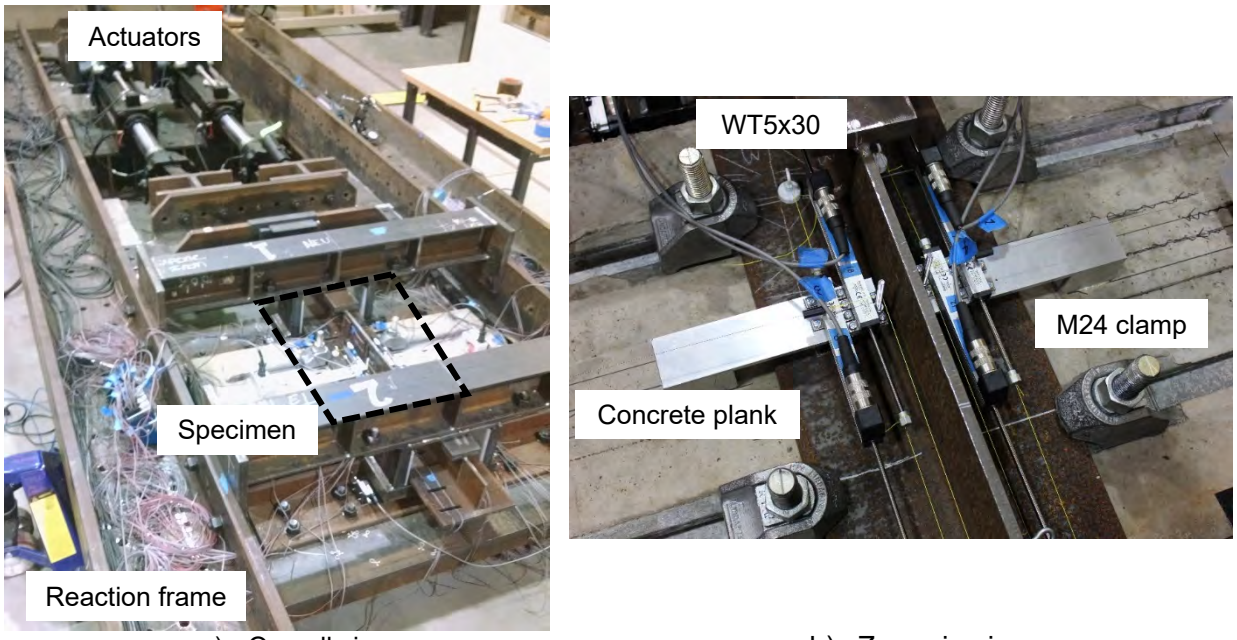


Fig. 5 – Bolt axial stress and strain variation in pretension tests

Pushout tests

As shown in Figure 6, each pushout specimen consisted of a 4 ft. x 2 ft. x 6 in. (1219 mm x 610 mm x 152 mm) concrete plank connected with a WT5x30 or WT4x15.5 section using either M24

or M20 clamps. The specimen was mounted upside down to view the motion of the clamps and steel beam. The pushout test matrix is given in Table 1. The light reinforcement configuration was designed only for gravity loading, while additional supplementary reinforcement was placed around the channel anchors to prevent anchor-related concrete failure modes. Since the flanges of the WT4x15.5 sections were very thin, testing of the WT4x15.5 sections with the M24 clamps required shims placed between the clamps and the steel beam flanges. The specimen naming convention is explained using Specimen 3-M24-T4-RH-S, with M describing monotonic loading, 24 describing M24 bolts, T4 describing two-channel specimens, RH describing heavy reinforcement configuration, and S describing shims. More details about the test configuration and test matrix can be found in Wang et al. (2015).



a) Overall view b) Zoom-in view

Fig. 6 – Typical pushout test specimen

Table 1 - Pushout test matrix

Series	Specimen	Test parameters				Number of turns
		Bolt diameter	Number of T bolts	Reinforcement configuration	Shim	
M	2-M24-T4-RH	M24	4	Heavy	No	3 turns
M	3-M24-T4-RH-S	M24	4	Heavy	Yes	3 turns
M	4-M24-T6-RH	M24	6	Heavy	No	2 turns
M	5-M20-T4-RH	M20	4	Heavy	No	1.5 turns
C	6-C24-T4-RH	M24	4	Heavy	No	2 turns
C	7-C24-T4-RL	M24	4	Light	No	2 turns
C	8-C24-T4-RH-S	M24	4	Heavy	Yes	2 turns
C	9-C24-T6-RH	M24	6	Heavy	No	2 turns
C	10-C20-T4-RH	M20	4	Heavy	No	1.5 turns

The pushout test results are illustrated in Figure 7 and Figure 8. The load-slip curves of Specimens 2-M24-T4-RH and 4-M24-T6-RH exhibit ductile behavior and excellent slip capacity. Provided the limit state is fracture in the stud shank, the peak shear strength of a 19 mm (3/4 in.) diameter shear stud embedded in a solid concrete slab is 95.6 kN (21.5 kips), close to 98.3 kN (22.1 kips) which is the average shear strength of an M24 clamp. Both specimens retained almost 80% of their peak strengths at a slip of 127 mm (5 in.). In contrast, according to the statistical analysis conducted by Oehlers and Coughlan (1986), the mean ultimate slip of shear studs is 7.4 mm (0.29 in.). Initially, three complete turns of nut were applied to the bolts in the first two tests (Tests 2 and 3) before it was determined in subsequent pushout tests to use 2.0 turns of nut for the M24 clamps, as discussed above. The head of one of these bolts fractured in Test 3-M24-T4-RH-S because of the excessive rotation, as is demonstrated by the sharp strength drop at a slip around 25.4 mm (1 in.). Shortly after the fracture, load oscillation occurred, which could be attributed to a stick-slip mechanism exaggerated by the shims. The stick-slip behavior was also confirmed in prior research by Grigorian et al. (1994) on the cyclic behavior of clamped bolted connections with steel-steel sliding surfaces. Compared to the M24 clamps, the post-peak strength of the M20 clamps degraded more quickly because the M20 clamps were smaller and they were prone to rotate when significant displacements occurred along the steel beam, as shown in Figure 9. This was due to the channel lips (which were the same size for all tests) not being adequately large to support the M20 clamps as fully as the M24 clamps were supported, or due to the contact of the clamp teeth with the steel flange having too small an area compared to the M24 clamp. Consequently, the bolt pretension decreased as the clamps rotated. It might be advised that the M20 clamping connections be redesigned to delay rotation, e.g., a design where the embedded channel restrains the rotation of the clamp using an interlocking connection, in which case it is anticipated that the behavior of the clamps will be comparable to the M24 clamps in this work.

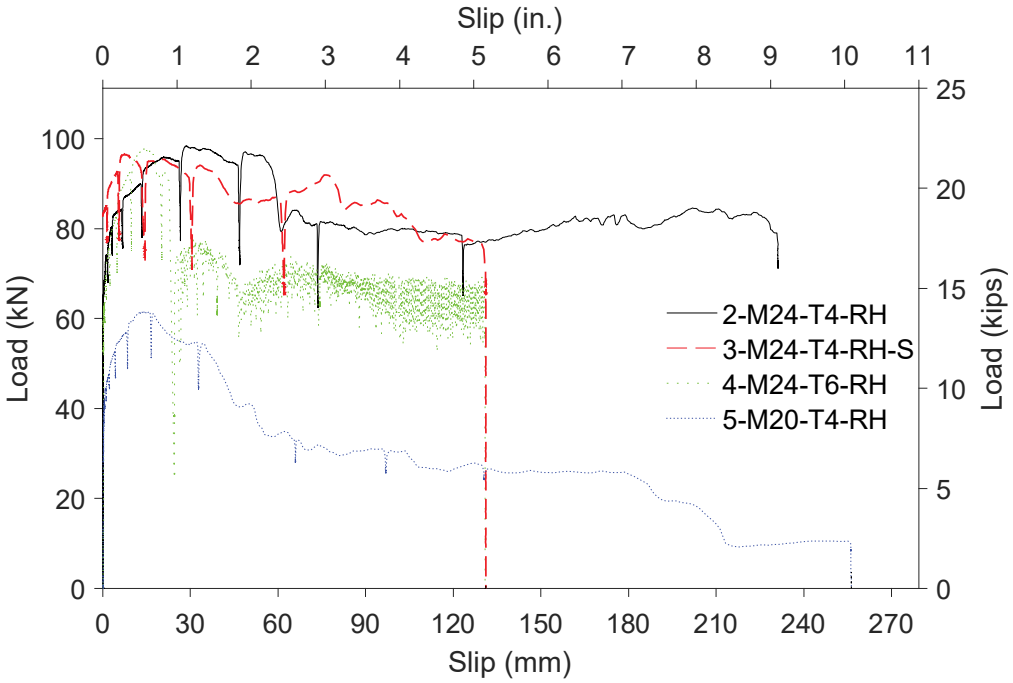
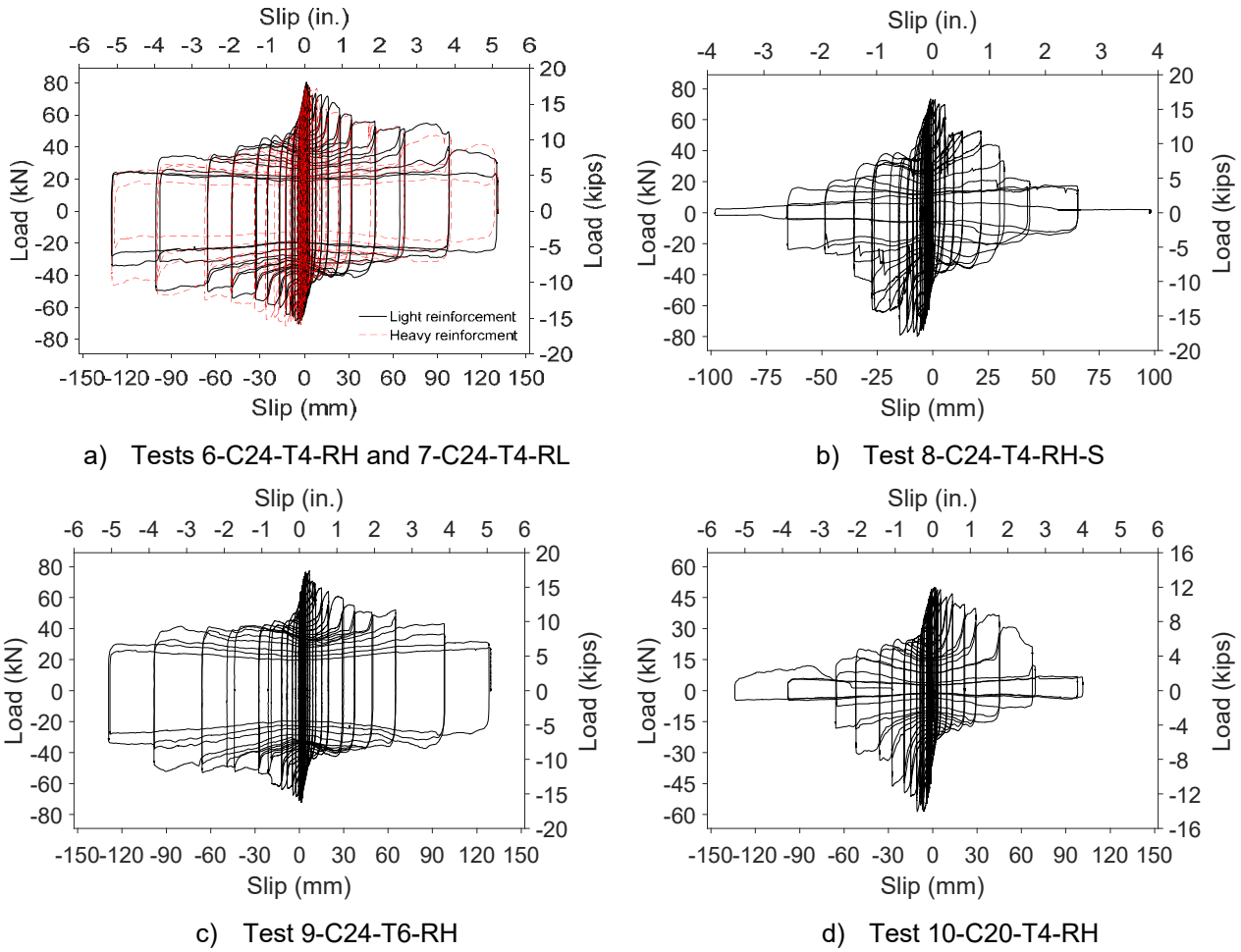


Fig. 7 – Load-slip curves of monotonic specimens (per connector)

Similar to the strength reduction seen in shear studs under cyclic loading (Pallarés et al 2009), the cyclic load-slip curves of the clamping connectors also exhibit decreasing shear strength as the cyclic behavior continues. In the clamping system, the abrasion between the concrete plank and the steel beam and between the clamp and the steel beam smoothed the contact surfaces and damaged the clamp teeth and the steel flanges, lowering the frictional coefficients and releasing the bolt pretension, as shown in Figure 10. This strength reduction can be accounted for in design, thus enabling the clamping connectors to be designed reliably to connect composite diaphragms and lateral load-resisting systems due to the excellent energy dissipation. The lightly reinforced concrete plank did not display any anchor-related concrete failure modes, and the comparison in Figure 8 also indicates that the light reinforcement configuration had negligible effects on the strength of Specimen 7-C24-T4-RL. Also, as seen when comparing monotonic specimens 2-M24-T4-RH and 3-M24-T4-RH-S, and cyclic specimens 6-C24-T4-RH and 8-C24-T4-RH-S, adding a shim between the clamp and steel flange produced oscillations due to stick-slip behavior and may not be recommended for design.

All the tests were terminated when the stroke of the linear potentiometers was reached or when all the clamps detached from the steel beam. No other specific limit states were observed.



a) Tests 6-C24-T4-RH and 7-C24-T4-RL

b) Test 8-C24-T4-RH-S

c) Test 9-C24-T6-RH

d) Test 10-C20-T4-RH

Fig. 8 – Load-slip curves of cyclic specimens (per connector)



Fig. 9 – Large rotation of M20 clamp

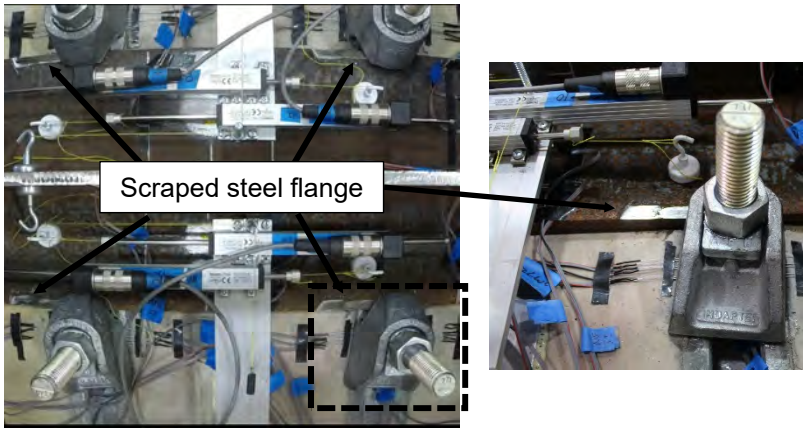


Fig. 10 – Damage of the steel flange in Test 6 at 1.28 in. (32.5 mm) slip

COMPOSITE BEAM TESTS

After completing the pushout tests, four full-scale composite beams were designed and tested. As shown in Figure 11, each beam specimen consisted of a 30-foot (9144 mm) long beam attached with fifteen 2-ft.-wide (609.6 mm) planks using clamping connectors. The actuator loads were spread using spreader beams at four points along the length (six-point bending) to mimic a secondary beam under approximately uniform loading. A pin support and a roller support were placed at the ends of the beams to permit horizontal movement as well as end rotation. Braces were utilized to prevent lateral deformation of the system due to accidental eccentricity existing in the test setup and load application. To simplify specimen construction, tongue and groove joints at the plank edges shown in Figure 1 were eliminated. Grade A36 5/8 in. (16 mm) diameter fully threaded rods were utilized to connect adjacent concrete planks to resist in-plane diaphragm forces. One full turn of nut from the snug-tight position was determined for pretensioning the rods after performing calibration tests in which rods passing through two planks were torqued until fracture. The concrete planks were 8 ft. (2438 mm) wide, which is sufficient to avoid any premature concrete failure in narrow slabs (Grant et al. 1977). The composite beam test matrix is given in Table 2. The naming convention of the specimens is explained using Test 2-M24-1C-RL, with M24 describing M24 bolts, 1C describing one channel embedded in each concrete plank, RL describing light reinforcement pattern. The heavy reinforcement pattern contained not only bars required to resist negative bending of the planks under concentrated loads but also supplementary rebar placed around channel anchors.



Fig. 11 – Composite beam test setup

Table 2 – Composite beam test matrix

Composite beam #	Bolt size	Beam size	Reinforcement configuration	# of clamps	Degree of composite action
1-M24-2C-RH	M24	W14x38	Heavy	56	82.7%
2-M24-1C-RL	M24	W14x38	Light	30	45.1%
3-M20-3C-RL	M20	W14x26	Light	90	137.8%
4-M20-1C-RL	M20	W14x26	Light	30	43.8%

The specimens were loaded to 40% of their expected flexural strength and then reloaded three times. Two more cycles were then undertaken, with one cycle at 60% and the other one at 80% of the estimated flexural strength. These cycles were intended to mimic serviceability conditions. After completing the loading/unloading cycles, the beams were then loaded until the deflections were excessive, surpassing *L*/25, where *L* is the beam span. All the beams were shored during construction, and the load-deflection curves plotted in Figure 12 are shifted from the origins to account for the bending moment and deflection under the self-weight of the composite beam and loading structures. All the beams demonstrated ductile behavior. Major events are identified on the curves, including slip of the clamps, yielding of the steel beam, concrete crushing, and first bang heard during the test. Slip is identified when the maximum relative movement between the steel beam and the concrete planks is larger than 0.02 in. Bangs were heard when abrupt slips occurred between the steel beam and the concrete planks. All the tests were terminated because of excessive deflection.

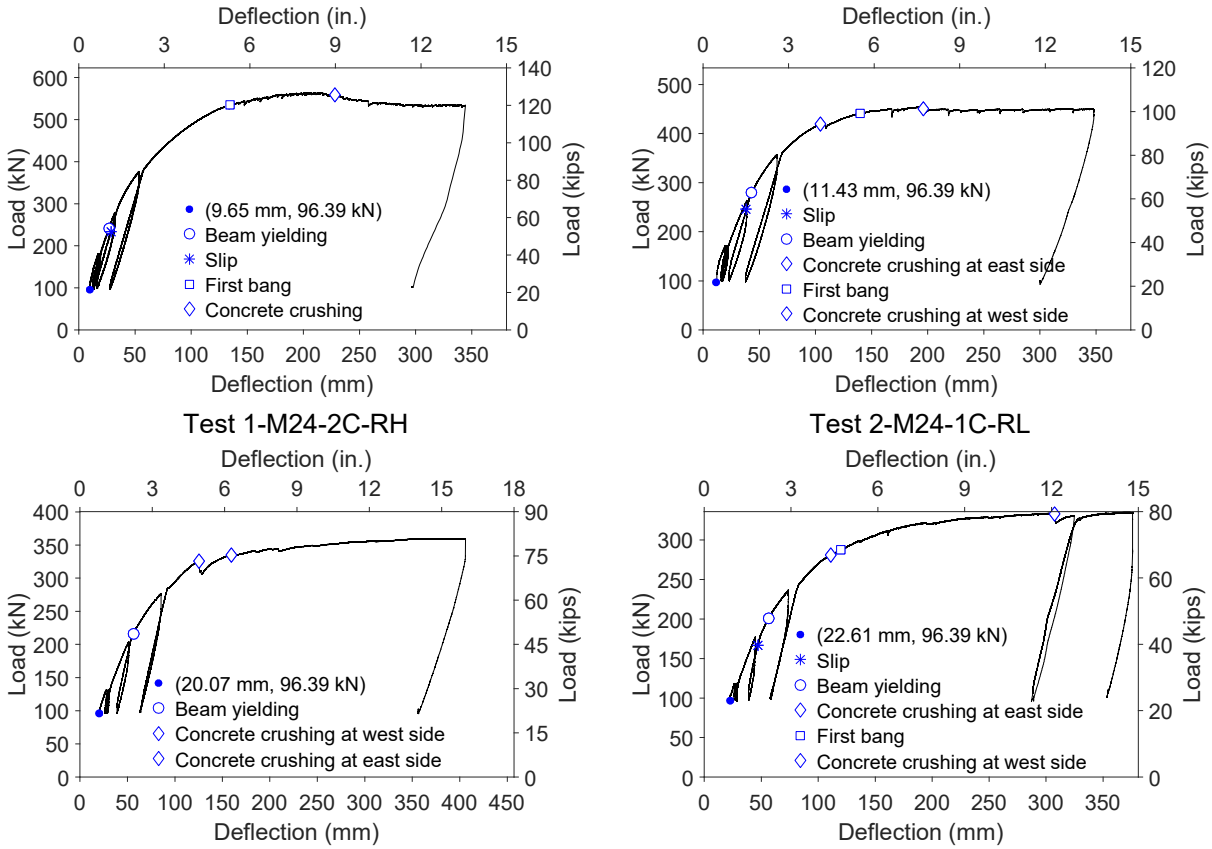


Fig. 12 – Load-deflection curves of composite beam specimens

The key results are summarized in Table 3 for all the specimens. For the specimens using the same steel section, the stiffness increases as the percentage of composite action of the beam increases. The stiffness calculated using a lower bound moment of inertia [I_{LB} from AISC (2016)] is below the tested stiffness of the deconstructable composite beam specimens and establishes that I_{LB} remains an appropriate lower bound estimate for these composite beams. The reason could be the different mechanisms of achieving composite action for the two types of shear connectors, with clamping connectors relying on the friction between the structural components and shear studs bearing against concrete slabs. The ultimate flexural strengths of the beams are also predicted using AISC design equations (AISC 2016), and the tested strengths are close to the predictions. It is seen that the degree of shear connection is proportional to the degree of composite action, with the maximum and minimum amount of slip occurring in beams with the smallest and largest degree of composite action, respectively. In the composite beam tests, the maximum slip demand on the clamping connectors was much smaller than the clamp slip demand during the pushout tests. After completing the tests, the composite beams were disassembled and a deconstructed steel beam is shown in Figure 14. The beam is intact except for the impressions on the top flange under the clamp teeth. In typical applications where a beam would not be subjected to ultimate loads, it is anticipated the steel beam would be in its elastic state when deconstructed.

Table 3 – Composite beam test results

Specimen #	Stiffness			Moment			Max slip mm (in.)	
	Test	AISC	Test/AISC	Test	AISC	Test/AISC		
	kN/mm (kips/in.)			kN-m (ft-kips)			West end	East end
1-M24-2C-RH	9.24 (52.8)	8.67 (49.5)	1.07	777 (571)	767 (566)	1.01	5.94 (0.234)	6.43 (0.253)
2-M24-1C-RL	7.76 (44.3)	6.81 (38.9)	1.14	634 (469)	632 (466)	1.00	8.18 (0.322)	6.45 (0.254)
3-M20-3C-RL	6.46 (36.9)	5.99 (34.2)	1.08	494 (364)	510 (376)	0.97	0.46 (0.018)	0.23 (0.009)
4-M20-1C-RL	6.08 (34.7)	4.43 (25.3)	1.37	476 (351)	400 (295)	1.19	8.79 (0.346)	8.08 (0.318)



Fig. 13 – Concrete crushing between planks



Fig. 14 – Deconstructed steel beam

CONCLUSIONS

A new deconstructable composite floor system is proposed to promote sustainable design of composite floor systems within bolted steel building construction through comprehensive reuse of all key structural components.

Based on the pretension tests, 2.0 turns and 1.5 turns after a snug-tight condition were recommended for pretensioning the M24 and M20 bolts in the deconstructable composite floor system. Under monotonic loading, the pushout specimens using M24 clamps were ductile, with almost 80% of their peak strengths retained at a slip of 127 mm (5 in.). In contrast, the post-peak strength of the M20 clamps declined more quickly because the clamps were prone to rotate as the beam moved. Nonetheless, the slip at which the curve started to descend was much larger than the slip demand on shear connectors in composite beams. If the rotation were restrained or an interlocking component design were developed, the M20 clamps would behave similarly as the M24 clamps. Because of the abrasion between the steel flange and the concrete plank and between the steel flange and the clamps, the strengths of the cyclic pushout specimens were lower than the strengths of the corresponding monotonic specimens; this reduction should be accounted for in design. Adding a shim between the clamp and steel flange produced oscillations due to stick-slip behavior and may not be recommended for design. The hysteresis load-slip loops demonstrate the potential of the clamping connectors to transfer in-plane diaphragm forces.

Four composite beams of different levels of composite action were designed and deflected to about L/25. Although some localized concrete crushing occurred along the top edges of the precast planks at large deflections, all the beams behaved in a ductile manner with little or no strength degradation. Compared to the stiffness calculated using a lower bound moment of inertia, the actual stiffness of the deconstructable composite beam specimens was slightly larger. The tested flexural strengths of the beams were close to those predicted by the AISC (2016) design equations. The specimens were readily deconstructed after the testing was completed.

The channel, T-bolt, and clamp are commercially available components. The components are not designed to work together in the proposed configuration, which resulted in certain behavior limitations that could be addressed by the development of modified components tailored to this particular application.

ACKNOWLEDGMENTS

This material is based upon work supported by the National Science Foundation under Grant No. CMMI-1200820 and Grant No. IIS-1328816, the American Institute of Steel Construction, Northeastern University, and Simpson Gumpertz and Heger. In-kind support is provided by Benevento Companies, Capone Iron Corporation, Fastenal, Halfen, Lehigh Cement Company, Lindapter, Meadow Burke, S&F Concrete, and Souza Concrete. This support is gratefully acknowledged. The authors would like to thank Kyle Coleman, Michael McNeil, Kurt Braun, Corinne Bowers, Edward Myers, Majed Alnaji, Madeline Augustine, Ian Carver, Morgan Foster, Michael Bangert-Drowns, Kara Peterman, Angelina Jay, Justin Kordas, David Padilla-Llano, and Yujie Yan for their assistance with the experiments. Any opinions, findings, and conclusions expressed in this material are those of the authors and do not necessarily reflect the views of the National Science Foundation or other sponsors.

REFERENCES

AISC (2016). *Specification for Structural Steel Buildings*, American Institute of Steel Construction, Chicago, Illinois.

Architecture 2030 (2013). Available at: http://architecture2030.org/buildings_problem_why/ (accessed April 2017).

Bilodeau, A. and Malhotra, V. M. (2000). “High-Volume Fly Ash System: Concrete Solution for Sustainable Development,” *ACI Materials Journal*, Vol. 97, No. 1, pp. 41-50.

Castleton, H. F., Stovin, V., Beck, S. B., and Davison, J. B. (2010). “Green roofs; building energy savings and the potential for retrofit”. *Energy and buildings*, Vol. 42, No. 10, pp. 1582-1591.

Energy Information Administration (2012), *Annual Energy Review*, U.S. Energy Information Administration, Washingtong, D.C.

Grant, J. A., Fisher, J. W., and Slutter, R. G. (1977). “Composite beams with formed steel deck,” *Engineering Journal*, Vol. 14, No.1, pp. 24-43.

Grigorian, C. E., and Popov, E. P. (1994), "Energy Dissipation with Slotted Bolted Connections,” Report UCB/EERC-94/02, Earthquake Engineering Research Center, College of Engineering, University of California at Berkeley, Berkeley, California.

Lam, D., Dai, X., and Saveri, E. (2013), "Behavior of Demountable Shear Connectors in Steel-Concrete Composite Beams," *Composite Construction in Steel and Concrete VII*, American Society of Civil Engineers, July 2013, Queensland, Australia, pp. 618-631.

Lee, S. S. M., and Bradford, M. A. (2013), “Sustainable composite beam behavior with deconstructable bolted shear connectors,” *Composite Construction in Steel and Concrete VII*, American Society of Civil Engineers, July 2013, Queensland, Australia, pp. 445-455.

Oehlers, D. J., and Coughlan, C. G. (1986). "The shear stiffness of stud shear connections in composite beams," *Journal of Constructional Steel Research*, Vol. 6, No. 4, pp. 273-284.

Pallarés, L. and Hajjar, J. F. (2009). “Headed Steel Stud Anchors in Composite Structures: Part I. Shear,” Report No. NSEL-013, Newmark Structural Laboratory Report Series (ISSN 1940-9826), Department of Civil and Environmental Engineering, University of Illinois at Urbana-Champaign, Urbana, Illinois, April.

RCSC (2009). *Specification for Structural Joints Using High-Strength Bolts*, Research Council on Structural Connections, Chicago, Illinois.

Wang, L., Webster, M. D., and Hajjar, J. F. (2015). “Behavior of Deconstructable Steel-Concrete Shear Connections in Composite Beams,” Proceedings of the 2015 SEI Structures Congress, Portland, Oregon, April 23-25, 2015, ASCE, Reston, Virginia.

Webster, M., Kestner, D., Parker, J., Johnson, M. (2007) “Deconstructable and Reusable Composite Slab,” Winners in the Building Category: Component – Professional Unbuilt, Lifecycle Building Challenge http://www.lifecyclebuilding.org/2007.php

Preliminary Assessment of a Composite Flooring System for Reuse

Martin Nijgh
Delft University of Technology
Delft, The Netherlands
M.P.Nijgh@tudelft.nl

Mareike von Arnim
Karlsruhe Institute of Technology
Karlsruhe, Germany

Marko Pavlović
Delft University of Technology
Delft, The Netherlands

Milan Veljković
Delft University of Technology
Delft, The Netherlands

ABSTRACT

Composite flooring systems consisting of concrete slabs and steel beams are used extensively, mainly because of competitive design of the cross-section. Shear interaction is often achieved by welded shear studs, which inherently prohibit demountability of the connection and reusability of the individual components. Demountability of composite structures can be achieved by using bolted shear connectors embedded in the concrete. The goal of this paper is to show how such demountable shear connections can be implemented, which allows for easy execution and the reuse of all structural components. A key element in the suggested longitudinal shear device is injection bolts, used to fill the hole clearance with epoxy resin, increasing stiffness and ductility compared to traditional demountable composite structures. Push-out tests and beam tests are planned and pre-analysis is made for these tests using extensive Finite Element modelling. Based on current experience, recommendations for design and execution are made.

INTRODUCTION

Composite flooring systems consisting of a concrete slab and steel beams are used extensively in structures, mainly because of the reduced material demand to achieve a certain strength and

stiffness. In composite flooring systems, the different elements are loaded in their most favourable way (i.e. concrete in compression, steel in tension) and interaction is often achieved by welded shear studs, which prohibit the demountability of the connection and reusability of the individual structural components. An alternative to welded shear studs are bolted shear connectors. Depending on the way such bolted shear connectors are used, demountability of the connection and reusability of the structural members is possible. The goal of this paper is to show how to achieve demountable shear connections with appropriate stiffness and ductility, allowing for the fast execution and accompanying requirements for the reuse of a composite structure.

This paper focuses on the pre-analysis of dry flooring systems, which have a new type of shear connector embedded in the concrete slab. Common solution of the embedded bolted shear connector is that the bolt sticks out from the concrete deck. The possibility of damaging one of the bolts during transporation, execution and demounting is very realistic and will cause that the deck segment is not suitable for (re)use. In order to avoid such problems, an embedded coupler is used (Figure 1). The goal of the coupler is to separate the internal (embedded) part of the shear connector from the externally in-situ assembled bolt.

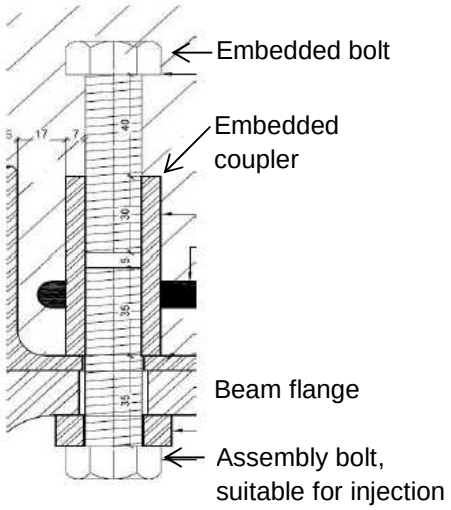


Figure 1 - Embedded coupler including embedded bolt and assembly bolt (suitable for injection) (Kozma & Odenbreit, 2017)

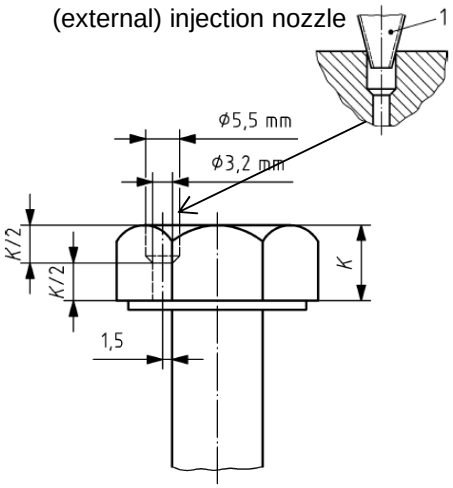


Figure 2 - Geometry of an injection bolt, showing a distinct injection channel through its head (EN 1090-2)

Fabrication tolerances and the requirement for easy demounting influence the needs for the hole clearances in the beam's top flange. Within the EU-research project REDUCE (Reuse and Demountability using Steel Structures and the Circular Economy), the magnitude of the hole clearance is investigated. Preliminary results from ABAQUS simulation indicate that a 6 mm hole clearance (3 mm bolt-to-hole gap) would be sufficient for a typical span of 16 m consisting of large prefabricated concrete decks of 8.00 x 2.60 metres, since no bearing occurs due to self-

load. Excessive hole clearances (i.e. hole clearances that are not closed by the self-weight of the concrete slabs) increase the speed of erection and accomplish the demountability of the structure. However, if excessive hole clearances are used, the bending stiffness of the composite floor decreases as a result of initial slip between both members.

In order to overcome the reduction in stiffness, the clearance between the bolt and hole may be injected with an epoxy resin, which mitigates the slip between slab and beam as well as the vertical displacement of composite deck. Injecting the hole clearance with epoxy resin can be done using bolts with a small hole through the bolt head, which is known as an injection bolt (Figure 2). Such injection bolts have been used since the 1970s in The Netherlands, initially for refurbishment of railway bridges (Gresnigt & Stark, 1995) (Gresnigt et al., 2000). According to the resin (RenGel SW 404 + HY 2404) manufacturer, the resin is fully cured after 24 hours, but earlier investigations for this resin at TU Delft have shown that there is no significant increase in strength and stiffness after 6 hours of curing. In order to prevent the resin from escaping through the beam-slab interface during injection, the injection bolt must be slightly preloaded in order to close any gaps in this interface (e.g. as a result of welding, shrinkage, etc.). Since the small preload is only to facilitate the injection procedure and is not of any structural importance, it is not a problem that this preload is lost in time as a result of (through-thickness) concrete creep. A recent TU Delft innovation in the field of injection bolts is the strengthening by (steel) shot prior to injection of the resin (Nijgh, 2017). This way, a stiff load bearing skeleton of steel particles is obtained, and the resin functions as a binder rather than a load bearer.

Although epoxy resins are generally highly adhesive, the adhesion of the epoxy to the steel and concrete substrate can be prevented by the use of a wax-based release agent, which allows for demountability of the shear connection (Figure 3). Nijgh (2017) has proven that all common release agents (wax-, silicon- and PVA-based) work, but that a wax-based release agent has the preference given that it provides a non-porous resin structure and is not known to degrade the epoxy material properties.



Figure 3 - Prevention of adhesion between steel and epoxy resin using wax-based release agent. (a): steel plate with resin infill after removal of the bolt, and (b): resin infill pressed out of the steel plate (Nijgh, 2017)

Previous research by Pavlović (2013) has shown that bolted shear connectors may not provide enough ductility (e.g. minimum of 6 mm of slip demanded by EN 1994-1-1) to allow for a plastic design of a composite structure. The use of injection bolts may provide additional ductility compared to non-injected connections by deformation of this epoxy layer. The largest contribution to the ductility is mostly observed when the connection is close to its ultimate resistance, because of plastic deformation (e.g. in the steel section) the confinement of the epoxy resin is significantly reduced and crushing occurs (Figure 4). The ultimate resistance of shear connector is independent of the injection material; after failure of the resin in compression the behaviour is defined by the bolted shear connector resistance.



Figure 4 - Crushing of the resin resulting from plastic plate deformation approaching the failure load of the plate (bearing failure) (Nijgh, 2017)

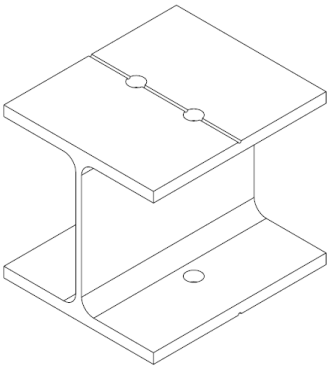


Figure 5 - HE260B beam used in push-out tests, featuring a special groove (Ø 5mm) which indicates successful injection if resin exits at side of flange

DEMOUNTABLE SHEAR CONNECTOR

The (demountable) bolted shear connector system under consideration in the push-out tests is shown in Figure 6. The edge angle, 70 mm bolt and coupler are embedded within the concrete slab with $h_c = 150\ \mathrm{mm}$. On the assembly site, the concrete slab is placed on the steel beam and connected using an injection bolt. The allowable deviation between the centre of the coupler and the centre of the injection bolt is 3 mm. After installation of the injection bolt, all clearances are filled using epoxy resin (RenGel SW 404 + HY 2404) and adhesion is prevented by applying a wax-layer to all components a priori. An air vent is foreseen in the beam flange in order to allow air to escape during injection and to confirm that the injection procedure is successful (Figure 5). The geometry of the push-out tests is not conform EN 1994-1-1, but has (1) larger shear connector spacing (300 vs 250 mm) and (2) more reinforcement to more closely resemble the final application.

The potential of injection bolts in composite structures is assessed based on numerical analysis and laboratory experiments. The numerical analysis is largely based on the work of Pavlović (2013) (including damage models for concrete and steel) and combined with the results from

Nijgh (2017) to include resin behaviour. Experiments will be carried out at the University of Luxembourg (push-out tests) and Delft University of Technology (additional push-out tests and feasibility test of the composite floor system).

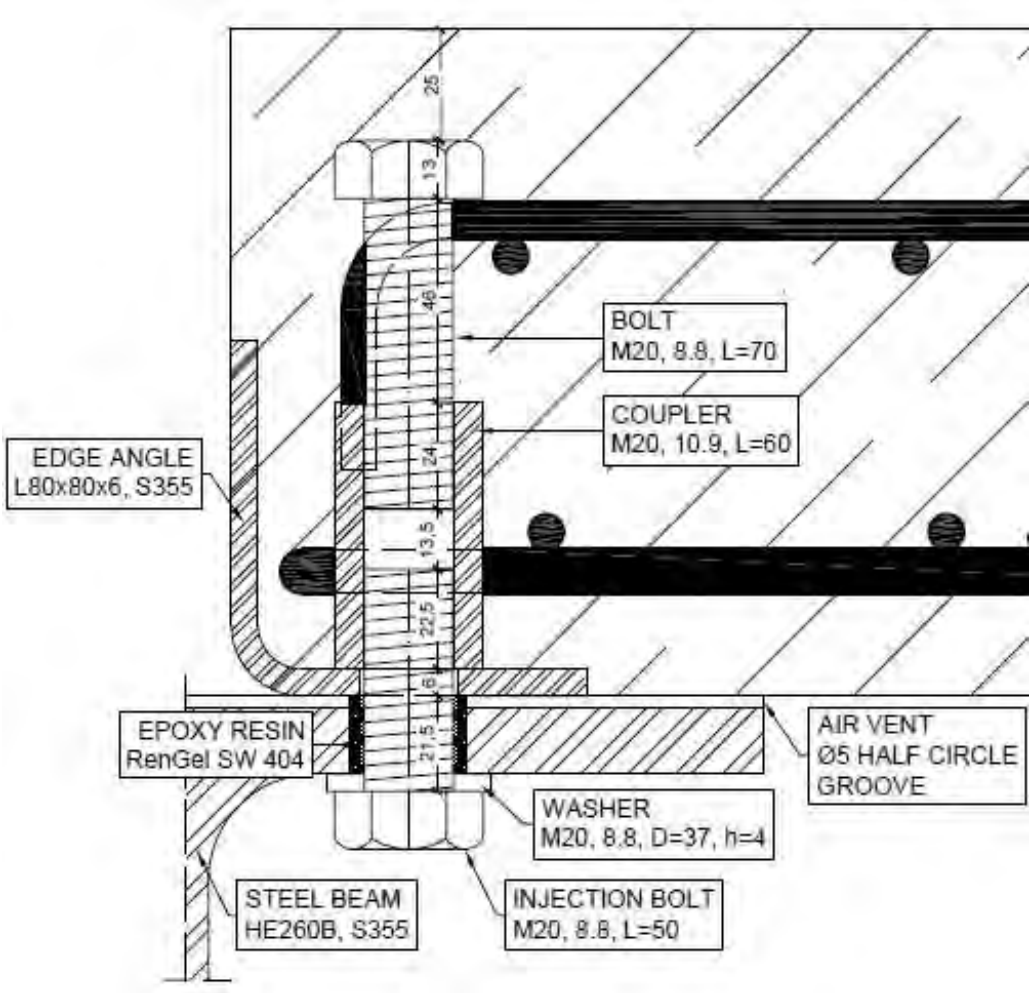


Figure 6 - Bolted shear connector system, dimensions in mm (Kozma & Odenbreit, 2017)

CASE STUDY: COMPOSITE STRUCTURE WITH DEMOUNTABLE FLOORING SYSTEM

The results of the push-out tests on the system described above are used to predict the behaviour of a composite flooring system, as in Figure 8, with the same bolted shear connector. Beams with a 16 meter span and a 2.60 m centre-to-centre distance are assumed. The beam (grade S355, modelled elastic-plastic), is assumed to be tapered, with height 590 mm at the supports and 740 mm at midspan. The web is 4.5 mm thick with a stiffener is foreseen at midspan. The flanges are 300 mm wide, with thickness 10 and 12 mm for the bottom and top flange, respectively. The concrete slab is assumed to be grade C35/45 with thickness $h_c = 120\ \mathrm{mm}$ (modelled elastic, $E = 34000\ \mathrm{MPa}$). According to hand calculation, 44 shear connectors

on each flange-side are required which are uniformly distributed in *Reference Spacing,* as illustrated in Figure 7. Since shear force reduces towards the middle of the girder, a decreased number of couplers (32) with wider spacing only in the middle of the girders is examined as well (*Spacing 1*). Moreover, influence of partly injected structure for both spacing arrangements is considered where only outer ten bolts on each beam-side are injected with resin while middle shear connectors have blank bolt-to-hole clearance. Fewer shear connectors and less injection bolts reduce overall costs of structure since less material, and more important, fewer workers are required. The shear connectors are assumed to be centrically in all their respective bolt holes. Loads on the floor are adopted as: self-weight of concrete elements (2.83 kN/m^2), additional flooring load (0,5 kN/m^2) and live load (2.5 kN/m^2). During installation of concrete decks, only self-load in the amount of 2.83 kN/m^2 is applied. After completed installation imposed design load on structure is $1.35 \times 0.5 + 1.5 \times 2.5 = 4.43\ \mathrm{kN/m^2}$. Hence, total load on structure is $(2.83 + 4.43) \times 2.6 \times 8 \times 4 = 604\ \mathrm{kN}$.

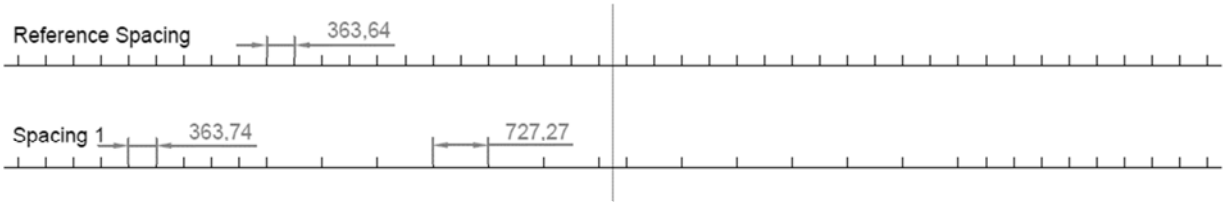


Figure 7 - Spacing arrangements of shear connectors (mm)

FE PREDICTION OF PUSH-OUT TEST AND BEAM TEST EXPERIMENTS

The ABAQUS/Explicit finite element models of Pavlović (2013), including material and damage models for concrete (C35/45) and steel (grade 8.8), have been used as a basis to model the push-out tests and obtain an indication on the initial stiffness of the demountable shear connector system. The finite element model is shown in Figure 9. Based on earlier numerical work by Nijgh (2017), a Young's Modulus of 4250 MPa and Poisson's ratio of 0,3 are assumed for the resin. No damage or plasticity models are available yet for this specific resin meaning that only until a certain load level (90 kN for this case) the results are reliable. Under the same conditions, also resin reinforced with steel shot is modelled ($E = 9500\ \mathrm{MPa}$) as sensitivity study. The connection elements causing most of the slip are identified by assuming one connection element to be infinitely stiff per analysis. A friction coefficient of 0,14 is assumed for all tangential interactions, whereas for the normal contact the 'hard contact' formulation is used.

The results obtained from the numerical analysis of the push-out tests are used to predict the behaviour of the composite floor tests. Finite element analysis was made using ABAQUS/Standard to examine the behaviour during and after installation of concrete slabs on the tapered steel beam. Therefore, a model with three steel girders was made where four concrete decks are put in place step by step, as Figure 8 shows, before loading the structure. Results indicate that the installation-order of concrete decks has small influence (5%) on deflection. The work is further extended by investigating what the effects are if only part of the total amount of bolted shear connectors is injected.

Spring elements with non-linear behaviour in longitudinal direction represent bolted shear connectors between concrete decks (solid elements) and steel girders (shell elements) in ABAQUS model. To prevent twisting of girders during step by step installation of concrete slabs L-shaped diagonals (beam elements) are used to stiffen the structure. They are fixed crosswise at bottom flange of steel beams. Furthermore, concrete decks are connected with “Tie constraint” in longitudinal direction while they do not interact in transversal direction. As well as in finite element model of push-out test friction coefficient of 0.14 is assumed for tangential interaction and hard contact for normal interaction.

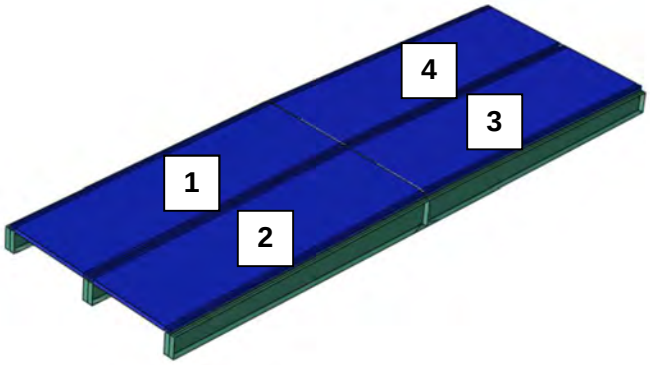


Figure 8 - Model for beam test with installation order of concrete decks, order of installation is most unfavourable for deflection

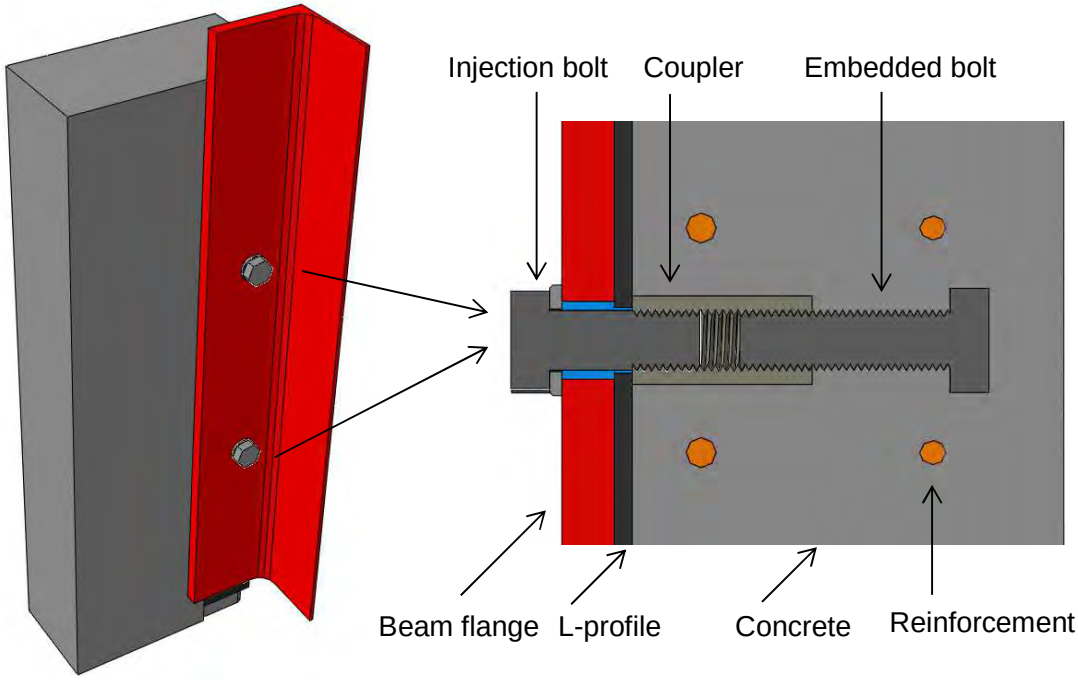


Figure 9 - Finite element model of push-out test. Double symmetry is used to reduce computational cost.

RESULTS OF PRELIMINARY INVESTIGATIONS

The load-slip relationship derived for the bolted shear connector is shown in Figure 10 for resin, reinforced resin (as developed by Nijgh, 2017) and steel infill in the 6 mm bolt-to-hole clearance (M20 bolt centrically in Ø26 mm hole). The preliminary investigation focuses on the execution process and behaviour at the Serviceability Limit State. Based on the FE-analysis it is predicted that the failure load per shear connector is approximately 140 kN. The resin reduces the initial shear connector stiffness by 30% compared to a connection injected with steel. The reinforced resin expects to reduce the stiffness by 20%.

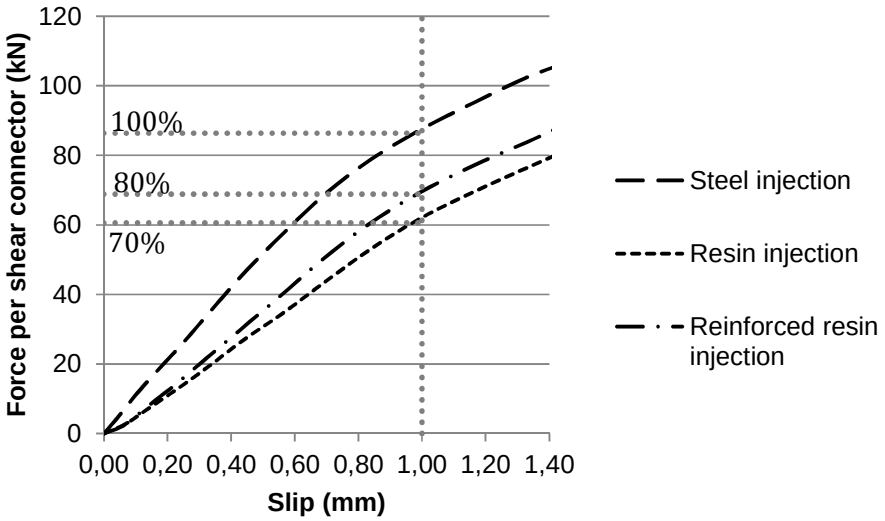


Figure 10 – Load-slip diagram derived using FE model for connections injected with steel, resin and a combination of resin and shot. Above 90 kN the resin starts to crush (not included in model) meaning the prediction is less accurate.

Figure 11 illustrates the increase of the initial connection stiffness (i.e. until 1 mm of slip) depending on which element is modelled infinitely stiff. The connection elements responsible for most of the slip are the resin, injection bolt and concrete, whereas the coupler and embedded bolt do not provide a significant contribution to the total deformation.

The effects of the decrease in bolted shear connector stiffness on the bending stiffness of the composite floor are shown through Figure 12. The effect of the rather deformable resin on the deflection at midspan is rather small: only a 5% increase of deflection is expected based on the SLS load level compared to the situation in which the bolt is directly bearing to the beam flange. In Figure 12 the horizontal line at 235 kN shows completed installation of concrete decks on steel beams. Deflection curves become steeper during installation-process of concrete decks since stiffness of structure increases with further installed decks. Difference in deflection with imposed design load (604 kN) between both spacing arrangements is rather small with 5%. Injecting only outer ten bolts with resin results in increased deflection of 8% for *Reference Spacing* and 6% for *Spacing 1*. In this respect, reducing shear connectors and injecting less bolt-to-hole gaps are considerations to decrease costs at the expanse of slightly increased deflection under imposed design load.

In all illustrated cases deflection at design load level is less than serviceability limit state of l/250 = 16000/250 = 64 mm; hence at SLS load level the deformation limit is also not exceeded.

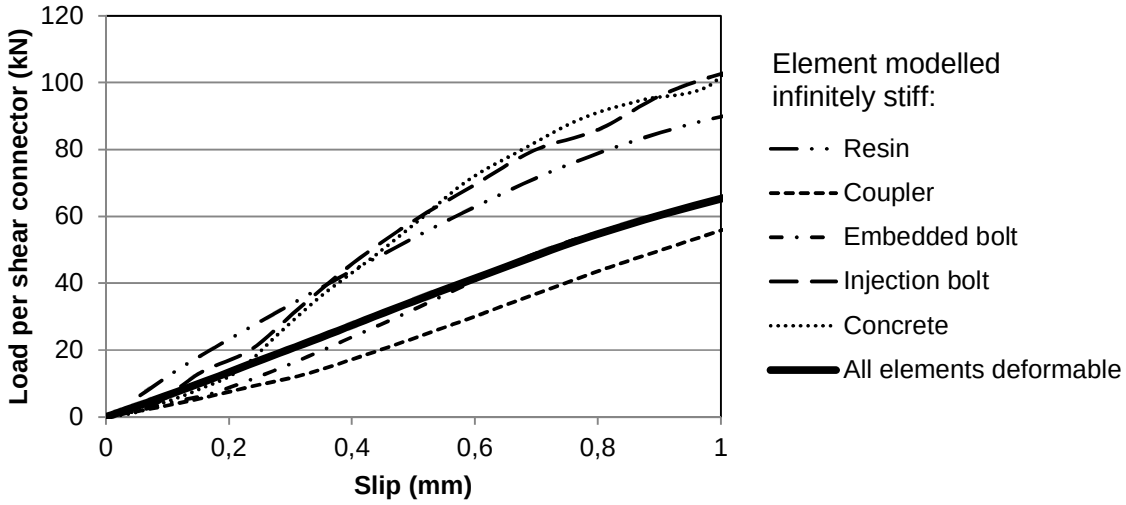


Figure 11 - Load-slip diagram in initial phase in case one of the elements is modelled infinitely stiff. A large increase of stiffness with respect to the case in which all elements are deformable indicates a large slip contribution

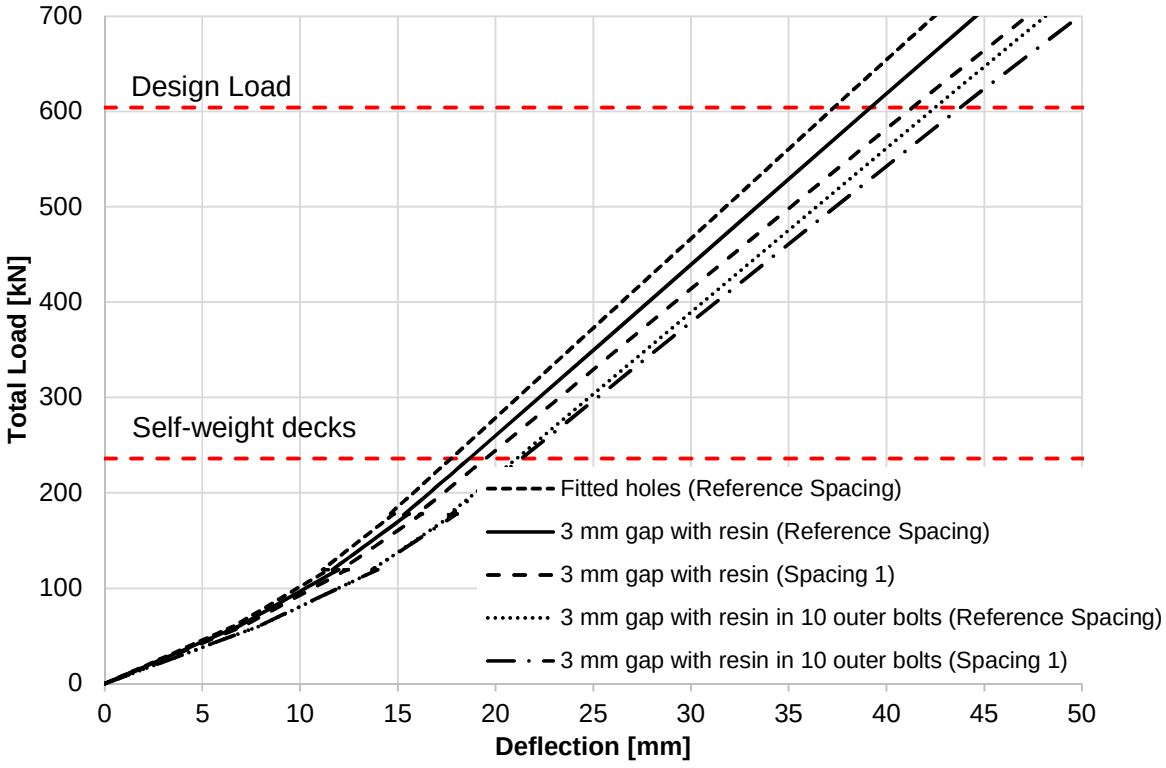


Figure 12 - Deflection of tapered beam as a function of injection material and shear connector spacing

EXECUTION OF A COMPOSITE FLOOR

The results show that the use of injection bolts in combination with oversize holes in the beam flange does not significantly affect the bending stiffness of the composite floor. It must be noted that the results are preliminary, given that (1) no effect of epoxy creep is taken into account and (2) the (reinforced) resin is modelled as elastic. The beam flange thickness is small compared to the diameter of the bolt, meaning the entire flange thickness can be assumed to be effective in load transfer, as also suggested in the European Recommendations for Bolted Connections with Injection Bolts (1994).

CONCLUSION

The pre-study demonstrates that a demountable composite dry flooring system with sufficient hole clearance to aid both execution and demounting can be achieved using injection bolts. The following conclusions are made based on the preliminary calculations:

1. Initial composite floor bending stiffness is largely unaffected (increased deflection of 5% at midspan) in case of 3 mm injected gap around the bolts for the considered case study of the composite flooring system.
2. The injected epoxy resin has the potential to increase ductility of the shear connector system by (plastic) deformation of the injected resin. A 30% increase in ductility is observed in the FE analysis compared to direct bolt-to-hole interaction in the linear branch of the load-slip relationship (slip < 1 mm).
3. The effect of epoxy creep leads to a time-dependent reduction in bending stiffness of the flooring system, and will be experimentally investigated in the ongoing project.
4. Compared to r*eference spacing*, partial interaction of the composite structure and wider spacing between shear connections result in larger deflection (up to 10%). Partial interaction in the considered composite structure leads to saving of in-situ labour.

Quality of FE prediction of the push-out test behaviour will be evaluated after results from the experiments are obtained.

ACKNOWLEDGEMENT

The authors acknowledge financial support of the Research Fund for Coal and Steel (RFCS) for funding the research project ”Reuse and Demountability using Steel Structures and the Circular Economy” REDUCE (RFCS-02-2015). Cooperation of the project partners (SCI, University of Luxembourg, University of Bradford, Lindab A/S, Tata Steel, Bouwen met Staal and AEC3) is gratefully acknowledged.

REFERENCES

European Convention for Constructional Steelwork. (1994). *European Recommendations for Bolted Connections with Injection Bolts.* ECCS.

Gresnigt, A. M., & Stark, J. W. (1995). Design of Bolted Connections with Injection Bolts. *Proceedings of the Third International Workshop on Connections in Steel Structures* (pp. 77-87). Trento: Elsevier.

Gresnigt, A. M., Sedlacek, G., & Paschen, M. (2000). Injection bolts to repair old bridges. *Proceedings of the Fourth International Workshop on Connections in Steel Structures.* Roanoke, VA, USA: Delft University of Technology.

Inter-Composite. (n.d.). *Gelcoat Resin - Araldite (R) SW 404 Resin with HY 2404 Hardener.* Retrieved from Inter-Composite: http://inter-composite.com/wp-content/uploads/2012/12/Araldite-SW-404-a-HY-2404.pdf

Kozma, A., & Odenbreit, C. (2017). Cross-section of demountable bolted shear connector system. *Background document of REDUCE project*. University of Luxembourg.

Nederlands Normalisatie-Instituut. (2011). *Eurocode 3: Design of steel structures - Part 1-8: Design of joints.* Delft: Nederlands Normalisatie-Insituut.

Nijgh, M. P. (2017). *New Materials for Injected Bolted Connections (MSc. thesis).* TU Delft.

Pavlovic, M. S. (2013). *Resistance of Bolted Shear Connectors in Prefabricated Steel-Concrete Composite Decks (PhD thesis).* University of Belgrade.

Seismic Collectors in Composite Steel Deck Diaphragms

Robert B. Fleischman
University of Arizona
Tucson, U.S.A.
rfleisch@email.arizona.edu

Anshul Agarwal, Haitham Ayyad
University of Arizona
Tucson, U.S.A.
anshul@email.arizona.edu, haithamayyad@email.arizona.edu

Richard Sause, James Ricles
Lehigh University
Bethlehem, U.S.A.
rs0c@lehigh.edu, jmr5@lehigh.edu

Chi-Ming Uang
University of California, San Diego
San Diego, U.S.A.
cmu@ucsd.edu

ABSTRACT

Seismic collectors are elements that bring inertial forces to the Seismic Force Resisting System elements. In steel composite structures, collectors are typically part of the underlying frame, modified to carry collector forces as needed. Due to the reversing nature of earthquake loads, collectors are designed both for tension (with a focus on connections) and compression (beam-columns). The actual seismic demands on the collector elements are poorly defined. The steel composite deck floor system is a complicated indeterminate assemblage that must maintain gravity load resistance while transferring the collector forces. An analytical research program is presented to study of the seismic performance of collectors in composite steel deck diaphragms, including load paths, characteristics under compression and tension, and the impact of the composite slab in load participation and bracing. Design recommendations are sought for appropriate strength and details of steel composite collectors.

1. INTRODUCTION

Seismic collectors are key elements of a building's Seismic Force Resisting System (SFRS). Current design code provisions for collectors recognize their critical role through special load combinations (ASCE 7, 2010) that include the System Overstrength Factor Ω_o (varying from 2.0 to 3.0), resulting in large design forces for collectors. This stringent prescriptive design approach is an attempt to ensure that critical collector elements remain elastic. Loss of collector elements can be catastrophic, as has been shown by failures of concrete structures, including the collapse of the CTV building in the 2011 Christchurch earthquake, in which 115 lives were lost (Royal Commission, 2012), or in the collapse of the Northridge Fashion Center parking structure (EERI, 1994) in which the shear walls were undamaged while the floor system detached and collapsed.

Collector behavior remains one of the less defined aspects of building response. In an earthquake, inertial forces must be carried through the floor or roof diaphragm to the primary elements of the SFRS. The collector path involves complicated indeterminate assemblages of different materials and geometries, acting at different elevations, and connected by elements

which may not be intended for collector action. Complex load paths develop in the floor system as a result not only of collector action, but also interaction with lateral load and the gravity load resisting system (GLRS). Due to the building's nonlinear dynamic response, peak inertial force magnitudes during an earthquake may significantly exceed the levels anticipated in past codes. With new larger inertial forces reflected in upcoming design codes, it is crucial to better understand how the collectors carry these forces to permit efficient and economical designs.

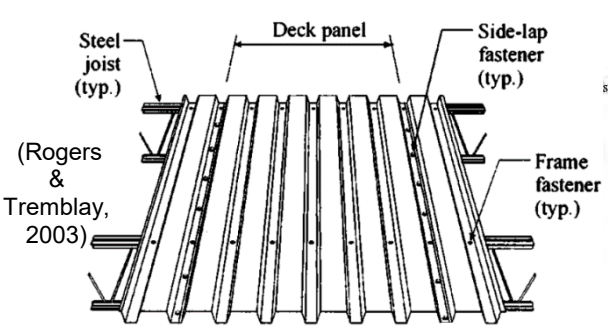
This paper presents the details of an ongoing analytical study aimed at examining collector paths in steel floor systems for the purposes of better describing these systems. The analytical study is based on models constructed and calibrated using previous testing of steel composite deck components and bays. Two-dimensional (2D, horizontal and vertical plane) have been developed to: (1) Characterize collector load paths within composite steel deck floor systems; (2) Quantify properties and performance of steel collectors; and (3) Examine capacity-based design solutions for steel collectors. In the future, 3D models will be used to investigate collector seismic demands.

2. SEISMIC COLLECTORS IN STEEL STRUCTURES

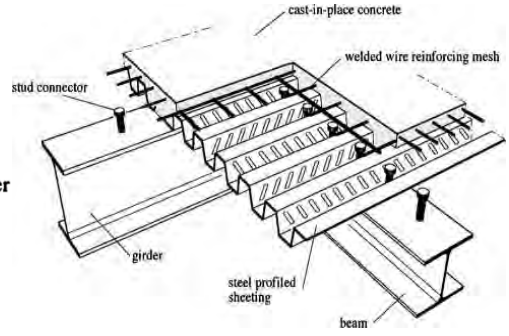
The SRFS of a steel structure has three primary components, which, acting in series, provide a complete load path between the seismic mass and the foundation: (1) the composite floor diaphragms, in which inertial forces from the floor mass and attached elements are transferred through the in-plane shear stiffness of the floor deck/slab system; (2) the vertical-plane elements that provide a laterally stiff vertical load path for these forces to the foundation; and (3) the seismic collectors, which serve as the critical link between these other two components.

2.1 STEEL COMPOSITE FLOOR SYSTEMS

Steel composite deck is the typical construction for floor systems in steel building structures. In this floor system, a concrete-filled metal deck is placed on top of the underlying steel gravity framing: girders span the columns; floor beams span the girders; and the metal deck (thin-gage cold-formed corrugated sheets attached by fasteners) spans the floor beams (See Figure 1a). The concrete floor slab is cast-in-place using the deck as formwork, and may be reinforced with bars or welded wire fabric. In composite floor systems, steel shear studs are welded to the underlying framing and project into the slab (See Figure 1b). Composite action is attained in floor systems through a combination of chemical bond between the slab and deck, mechanical interlock by embossments in the deck profile, and the shear studs.



(Rogers & Tremblay, 2003)



(Hedaoo, et al., 2012).

Fig. 1. Steel Deck Diaphragms: (a) Bare Metal-Deck; (b) Composite Steel Deck.

2.2 STEEL COLLECTOR DESIGN

Seismic collectors bring the inertial forces that develop in the floor system during earthquakes to the vertical plane SFRS elements, e.g. braced frames (See Figure 2a). Collector demands

depend on seismic hazard (ASCE 7, 2010) and collector length. In modern structures, SFRS elements have become isolated within the floor plan, resulting in significant collector runs.

Due to the reversing nature of earthquake loads, collectors must be designed both as tension and compression members. Tension member design focuses on the collector connections (Astaneh-Asl, 2005), e.g. TFW etc. (See Figure 2b). In compression, the collector is considered a beam-column, since the member is under combined flexure (due to gravity load) and compression (due to collector action). Collector design involves the special seismic load combination (ASCE 7, 2010) using the System Overstrength Factor Ω_o, resulting in amplified design forces.

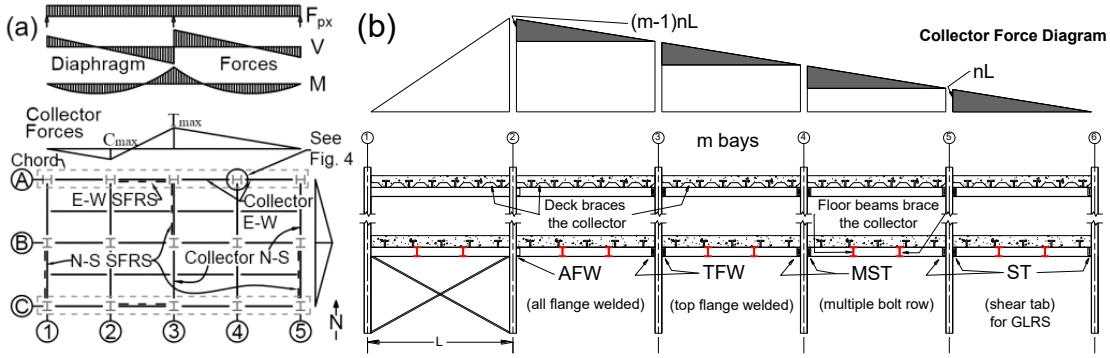


Fig. 2. Steel Collector Design Forces (AISC, 2010): (a) Plan View; (b) Collector Profile.

Under low seismic demands, collector forces are often sufficiently small that existing floor system elements serving as part of the GLRS can also counted as collectors, e.g. shear tabs (ST) with slip-critical bolted connections (AISC, 2010). In cases for wind or more modest seismic loads, the collector may be provided by reinforcing bars placed within the concrete slab (AISC, 2010). For moderate seismic demand, gravity system details may be modified to carry the loads, e.g. adding extra rows of bolts, MST (Figure 3a). For high seismic collector demands, however, the outcome of current code provisions is that expensive special elements must be introduced into the floor system specifically to carry the amplified forces. Members significantly larger than the surrounding gravity system elements are required to prevent instability under compressive collector forces; expensive full-penetration welded connections are often required for tension transfer, applied to only the top flange (TFW) if possible (Figure 3b) to minimize moment, but also to both flanges (AFW) when necessary. Due to the way collector forces build up (Figure 2b), different collector connection types may be used along a single collector run. Depending on the gravity framing layout, collectors in one direction might act through the column weak axis (e.g. Figure 3a).

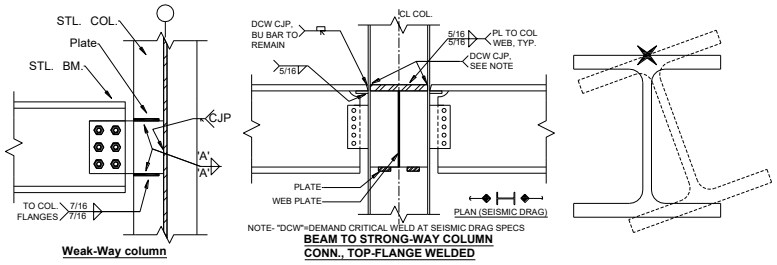


Fig. 3. Collector Details: (a) MST; (b) TFW; (c) Constrained Flange FTB (AISC, 2011)

Limit states in compression include flexural, torsional, flexural torsional, and lateral torsional buckling (AISC, 2011). The lateral and torsional bracing inherent in the floor framing and deck is an important consideration in design. Deck orientation (both are shown in Figure 2b), level of composite action, and the presence of openings all can have a significant effect (AISC, 2011). In

general, lateral bracing is ignored for parallel deck ribs. Torsional bracing, often ignored for a bare steel deck, is considered continuous for a composite steel deck (AISC, 2011). The unique boundary conditions for collectors, in comparison to most beam-column situations, leads to a constrained-flange flexural torsional buckling (FTB) mode about the top flange, where shear studs anchor the member (See Figure 3c). Designers are permitted to follow approximate methods based on design equations for other conditions (Helwig & Yura, 1999), as modified using simplified assumptions (AISC, 2011). Collectors are treated in several technical documents (Sabelli, et al., 2011) including for new construction (FEMA, 2009) and retrofit (ASCE, 2013).

New diaphragm seismic design forces are being adopted in the code (BSSC, 2014) in recognition of large peak inertial forces that can develop during a seismic event. These forces can be substantially larger than the prescribed current code (ASCE 7, 2010) equivalent lateral forces (ELF). Figure 4b compares the current and newly proposed ASCE 7 diaphragm design forces, indicating an impact on collector design. Collector overstrength factors are also treated differently.

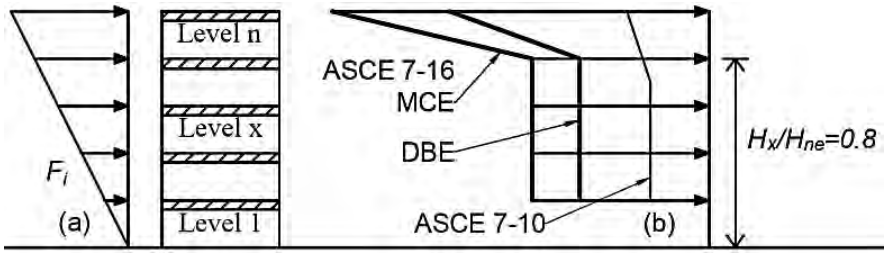


Fig. 4. Seismic design forces: (a) ELF; (b) F_{px} Comparison.

2.3 DISCUSSION: SEISMIC COLLECTOR ACTION IN COMPOSITE STEEL FLOORS

Seismic collectors must be able to transfer the seismic forces as axial load into the SFRS through a dependable, stiff load path. The collector forces are accumulated through shear studs on the elements, or to a lesser extent transverse framing members. Cowie, et. al. (2013) emphasize the need for sufficient shear strength in the composite slab along a collector to ensure inertial force transfer. MacRae & Clifton (2015) point to the influence of pre-existing shrinkage/temperature cracks on collector transfer strength. Codes do not formally address these conditions, with exceptions, e.g. shear strength design equations in (NZS 3404, 2007) based on rib orientation.

Collector compression forces may be strongly carried through the concrete slab (See Figure 5a). Little evidence exists to distinguish strut action (Bull, 1997) in the composite slab relative to the transfer of the underlying frame. Tension collector action depends on relative stiffness of the steel frame, deck and slab, the fixity of collector connections, and deck orientation (Cowie, et al., 2013). Experiments with composite steel decks show the slab contributing to frame action (Kasai & Matsuda, 2016) and laterally bracing members, except when early cracking of concrete ribs occurs (Zhang & Ricles, 2006). Large-scale tests of MRFs with composite slabs found collector forces influenced by the level of composite action (Herrera, et al., 2008). Easterling & Porter (1994) identified controlling limit states in composite decks, including slab X-cracking and longitudinal cracking in thin slabs; with higher strength for loading perpendicular to ribs. A compression collector reverses and becomes a tension collector with each earthquake oscillation. Relative stiffness changes during the seismic event as elements soften, yield, slip, crack, or crush.

The floor system profile also involves significant vertical eccentricity (See Figure 5b). The concrete slab detail at columns affects collector force developing due to floor slab inertial effects (Chaudhari, et al., 2014). Force transfer between the slab and column face can occur through bearing or strut and tie mechanisms (Braconi, et al., 2010). Moment in a collector due to the eccentricity of the slab inertial force transfer is assumed to be completely compensated by vertical

end shear force, and is ignored in design (Cowie, et al., 2013). The same elements providing collector action also provide gravity load resistance (Sabelli, et al., 2011). These interactions are typically ignored (Cowie, et al., 2013) as is gravity load interaction on shear studs (Burmeister & Jacobs, 2008). MacRae & Clifton (2015) suggest studs added to non-composite gravity beams for collector action may be overstressed unwittingly due to unavoidable gravity action.

Shear studs have a significant effect on cyclic stiffness (Zhang & Ricles, 2006). Tests on the shear stud-concrete interface found localized splitting behavior at low loads (Lowe, et al., 2014) and low-cycle fatigue failures (Bursi & Gramola, 1999). Adhesion between the slab and deck (Souici, et al., 2013) was the key transfer mechanism in non-composite decks (Majdi, et al., 2014). Tests on deck provide shear stiffness (Davies, 1986) and orthotropic properties (Wennberg, et al., 2011)

The collector load path must cross gravity columns. Collector connections at the columns are often detailed to minimize moment (e.g., Figure 3b). Nonetheless, these connections have partial fixity, especially when slab contributions are considered, unless special articulating details are introduced (MacRae, et al., 2010). At the building perimeter, gravity load transfer induces torsion into the collector, requiring proper spandrel beam slab reinforcement (Clifton & El Sarraf, 2005). Ubiquitous slab openings (e.g. Figure 5a), can create torsion and an unbraced collector condition.

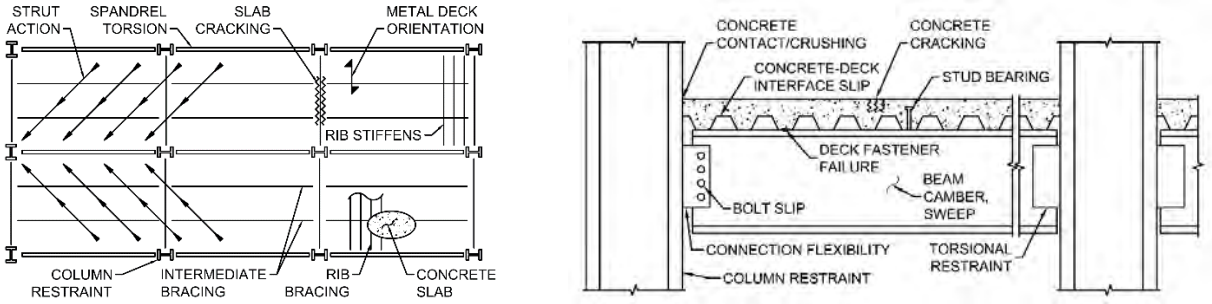


Figure 5. Composite Diaphragms Load Paths: (a) Horizontal-Plane; (b) Vertical Profile.

3 ANALYTICAL RESEARCH PROGRAM

The analytical research program involves three phases (See Table 1):

(1) Evaluation of isolated floor systems to determine collector force paths in composite steel deck diaphragms, including: (a) the horizontal-plane spatial distribution of collector forces; (b) the relative participation of the slab, deck, and underlying framing in the collector force transfer; and (c) the limit-state sequence of elements within the collector load path. This phase is achieved through 2D (horizontal plane) nonlinear pushover (NP) analyses of isolated floor diaphragms

(2) Evaluation of isolated collector frames to determine the properties (strength, stiffness and ductility) of the collector system in composite steel deck diaphragms for different: (a) Collector connections; (b) deck orientation; and (c) floor slab details. Strength and stability limit states are considered. This phase is achieved through vertical plane models of the collector frame with: 2D elements for strength (tension) limit states and 3D elements for stability (compression) limit states.

(3) Evaluation of seismic demands acting on collectors in composite steel deck diaphragms for different design approaches. This phase will be achieved through nonlinear time history analyses (NTHA) of full building structures under design and maximum considered earthquakes. This phase is future work and will not be considered further in the paper.

Three specific design approaches will be evaluated: (1) current code designs (ASCE 7, 2010) based on overstrength, $\Omega_0 F_{px}$; (2) collectors designed using emerging code provisions (BSSC, 2014); and, (3) new design concepts in which the collector overstrength requirement is relaxed, and instead different relative capacities of the collector and collector connections are considered.

Table 1. Analytical Research Phases.

Phase	Objective	Structure	Analytical Model	Elements	Loading	Analysis
1	Collector Force Path	Isolated Floor	2D (Horizontal Plane)	1D (Truss)	Body Force	NP
2	Collector Properties	Collector Frame	2D (Vertical Plane)	2D (Strength) 3D (Stability)	Body Force	NP
3	Collector Demands	Building	Whole Structure	1D	Earthquake	NTHA

3.1 EVALUATION STRUCTURE

An evaluation structure, a 4-story office building representing typical construction, has been designed for the study (See Figure 6a). The building footprint is 54.9m x 36.6m (See Figure 6b). The SFRS is a Special Concentric Braced Frame (SCBF). A baseline design is performed for current code (ASCE 7, 2010) SDC E (R=6, C_d=5, Ω_o=2.0) and typical live loads (LL = 2.4kN/m^2). Other designs used in the study are modified from this design (See Table 2).

Table 2. ELF Design Forces: Recent vs. New Code.

Level	Floor	h_i (m)	W_i (kN)	C_{vi}	V_i (kN)	M_i (kN-m)	ASCE 7-10 F_{px} (kN)	ASCE 7-16F_{px} (kN)
4	Roof	16.9	3132	0.261	1696	6979	1671	2626
3	4	12.8	9757	0.465	1061	19427	3574	5357
2	3	8.7	9757	0.214	1375	25158	2634	5308
1	2	4.6	9757	0.059	1461	29718	2602	5259

The floor gravity system framing is designed as composite members: 9.1m x 9.1m bays with floor beams at 3m on center (o.c.). The composite floor deck is a 63.5mm (2.5") concrete 20MPa (3ksi) slab over 50mm (2") LOK 18 gage steel deck with single 19mm (¾") diameter shear studs at 300mm o.c. All members are A992; detail material is A36.

The 2nd floor baseline design is presented in this paper and described here: The collector is shown in Figure 6b; collector connection schematics are shown in the inset and described in Table 3. Note that the braced frame on the east end of the floor system is removed to create a significant collector condition. The collector is designed as non-composite member as per current code guidelines (AISC, 2010). The floor beams are assumed to brace the collector (ribs parallel). Shear studs along the collector are in pairs at 280mm o.c. Gravity framing connections are standard shear tabs with 19mm (¾") diameter A-325 bolts (See Table 4).

Table 3. 2nd Floor Collector Baseline Design (without East End Braced Frame).

Column Line	B	C	C	D	D	E	E	F	F	G
Axial Force N_u (kN)	2169		1735		1301		867		434	
$\Omega_o N_u$ (kN)	4337		3470		2602		1735		867	
Shear V_u (kN)	262		262		262		262		262	
Moment M_u (kN-m)	761		761		761		761		761	
Collector	W24x131		W21x122		W21x111		W21x111		W21x101	
Collector Connection	AFW	TFW	TFW	TFW	TFW	MST	MST	ST	ST	ST

Table 4. Connection Design.

Connection Type	Collector				Gravity	
Location on Plan (Figure 6b)	A	B	C	D	E	F
Plate Thickness (mm)	22.2	19.05	31.75	22.2	9.5	12.7
# of bolts* per row / # of rows	21 / 3	14 / 2	14 / 2	7 / 1	3 / 1	4 / 1
Connection Detail	AFW	TFW	MST	ST	ST	ST
* 1" (25.4mm) Dia A490 bolts are used for collector connections; ¾" (19 mm) Dia A325 bolts for gravity connections.						

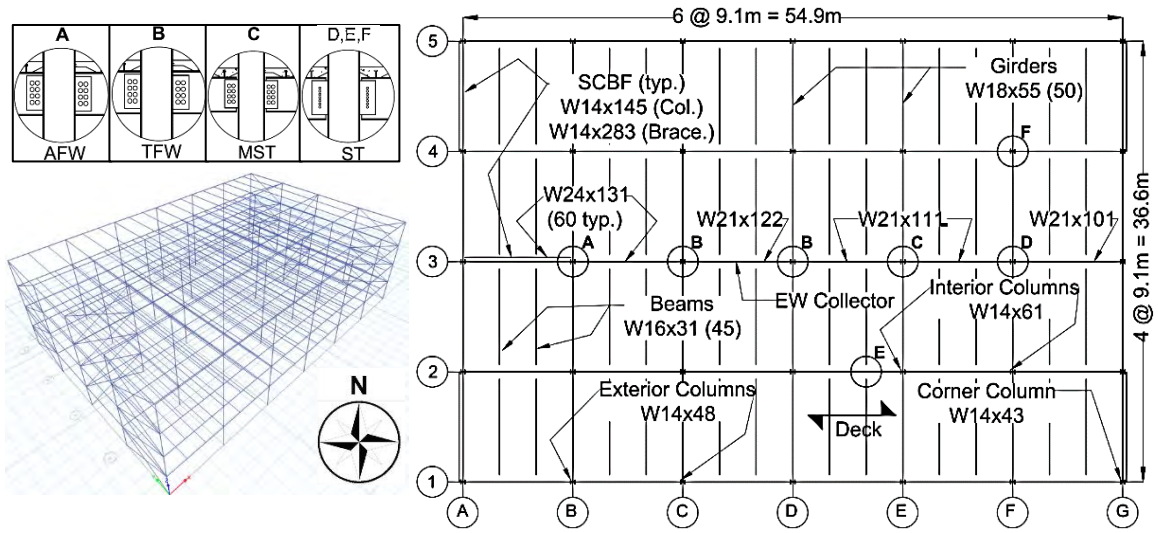


Fig. 6. Evaluation Structure: (a) collector connections; (b) 2nd Floor plan (baseline design).

3.2 ANALYTICAL MODELING

The analytical models are created using the general purpose finite element program ANSYS[1]. The models are constructed using existing data from tests of components within the composite floor system. The models are calibrated using results from past subassemblage testing of composite frames and bays. The models used in each phase are described in detail here:

(1) Isolated Floor System Models: The isolated floor system models encompass one floor and associated vertical elements (gravity columns, SCBFs) of the evaluation structure (See Figure 7a). The floor system was initially modeled in the horizontal plane (with slab and framing at the same elevation), and was subsequently extended to account for the vertical offset of the slab (See Figure 7b). The models are subjected to NP (body force) analyses creating collector tension or compression, as well as cyclic load protocols. It is noted that reduced degree-of-freedom versions of this model, calibrated by the results of Phase 2, are needed for the 3D NTHA structure models. The model consists of nonlinear 1D beam elements for framing members (including collectors); non-linear degrading spring elements for collector and gravity connections (Main & Sadek, 2012), and shear studs (Hwang & Kwak, 2013); 2D nonlinear orthotropic shell elements for the metal deck, and a nonlinear 2D truss model for the concrete slab (See Figure 7c). Concrete bearing is modeled with contact elements; slab-to-deck slip is modeled using interface elements as needed.

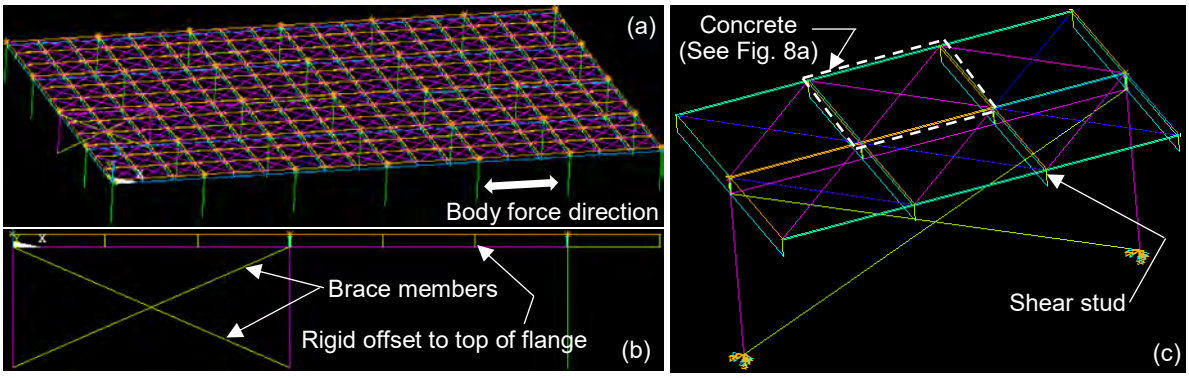


Fig. 7: Isolated Floor models: (a) Isometric View; (b) Elevation View; (c) Close-up at SFRS.

[1] ANSYS Inc., Canonsburg, PA.

Collector yielding is captured in the beam elements; yielding, degradation and failure of connections and shear studs are included directly in the nonlinear springs. The 2D truss model used for the concrete slab is shown schematically in Figure 8a. The model, based on (Lu & Panagiotou, 2014) (Scarry, 2014) is capable of capturing cracking and crushing of the concrete. The model was calibrated vs. test results (Easterling & Porter, 1994) as shown in Figure 8b.

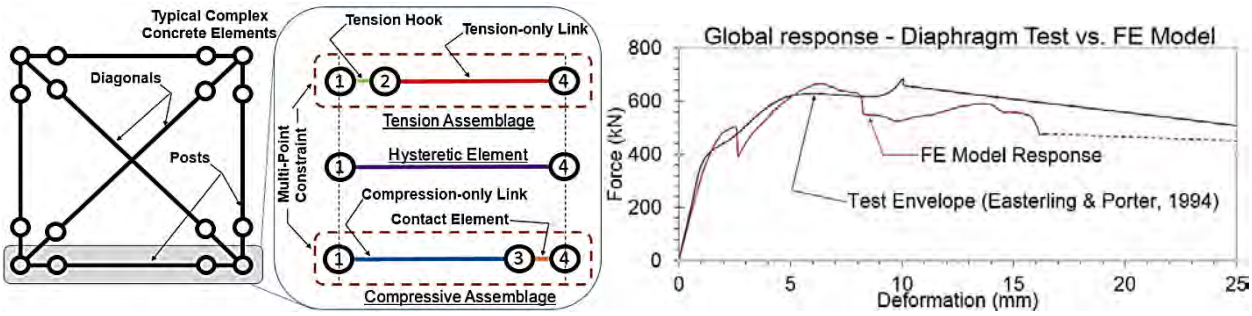


Fig.8. Concrete Truss model: (a) Schematic; (b) Calibration using test data.

(2) Collector Frame Models: The evaluation structure composite collector frame (collector, connections, deck, slab, studs and columns) is modeled using a vertical plane 2D model. Different models are used to investigate tension and compression limit states.

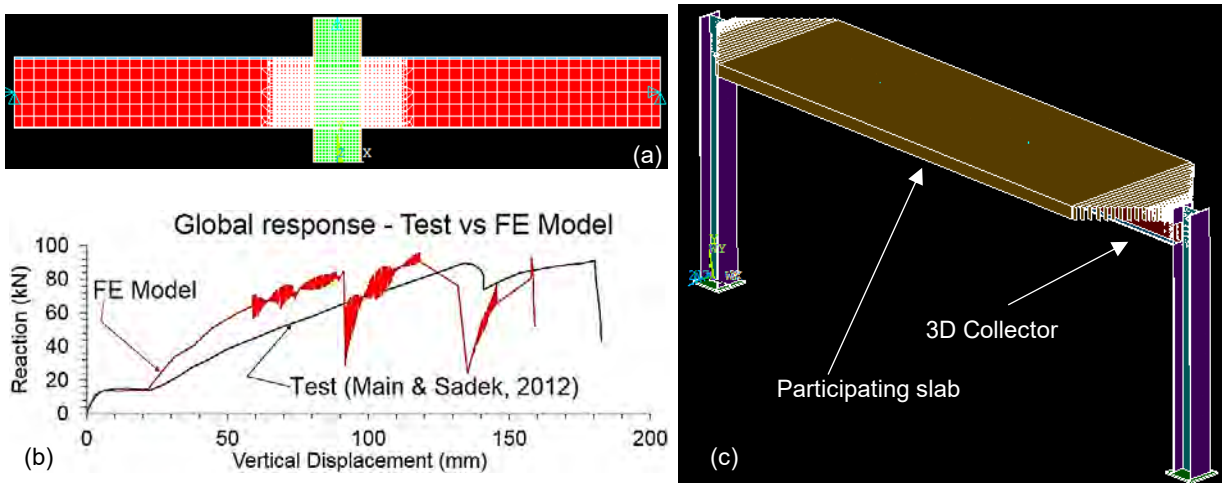


Fig. 9. Collector Frame Model: (a) 2D Elements; (b) Test Calibration; (c) 3D Elements.

For tension (strength), 2D plane stress elements are used (See Figure 9a). The model is calibrated (Figure 9b) using test results of shear tabs with (Liu & Astaneh-Asl, 2000) and without (Main & Sadek, 2012) the composite slab. For compression (stability), the frame is represented in the vertical plane by 3D elements with nonlinear geometry capabilities (Figure 9c). The collector frame models are subjected to monotonic NP and cyclic body force analyses. The results from this phase provides information on the collector characteristics for different connection and slab bracing details, and will be used to update the isolated floor models.

3.3 ANALYTICAL STUDY MATRIX

The analytical research first focuses on existing structures with collector systems based on the current/recent design codes. The Phase 1 and 2 models will be used to investigate: (1) axial force distribution along the collector; (2) the limit-state sequence as the floor-system reaches the capacity; (3) relative strength and ductility of the collector elements in comparison to other elements in the floor system; (4) the difference in tension and compression load paths as the

collector response reverses; (5) slab effects; (6) collector stability limit states, and; (7) the evolution of the collector load path as the collector and surrounding region takes on damage. The parameters varied in this step will include: (1) Collector connection details; (2) Slab thickness; (3) Deck depth and orientation; and (4) Shear stud layout. The evaluation structure will be considered for other live load conditions (e.g. heavy manufacturing) to examine the sensitivity of collector response to gravity load design. Bounding cases (top story, new code, etc.) will be evaluated.

The analytical research will then focus on the relative strength of the collector elements. The design overstrength factors applied to the collectors (Ω_{coll}) and collector connections (Ω_{conn}) will be reduced from current levels (See Table 5). The goal of the (Phase 1 and 2) analyses will be to examine inelastic deformation demands in these intentionally "weaker" systems to determine optimum relative strengths for the collector with respect to collector connections. The need for special details in the collector system or slab (e.g. seismic joints) will be assessed through deformation compatibility. In Phase 3, seismic demand reduction vs. collector inelastic demands will be assessed for different building heights to determine optimum strength relative to the SFRS.

Table 5. Analytical Study Matrix: Collector Design Overstrength.

Case	Ω_{Coll}	Ω_{Conn}	Objective	Case	Ω_{Coll}	Ω_{Conn}	Objective
Strong Collector	2.0	2.0	Current Code Design	Weak Collector	1.0	1.0	No Overstrength Design
		1.5	Concentrated inelastic deformation at collector connections		0.7	2.0	Distributed Inelastic Deformation demand along collector elements
		1.0				1.5	
		0.7	Fuse in connections			1.0	
						0.7	Weak collector system

4 ANALYTICAL RESULTS

Preliminary analysis results are briefly summarized here for the baseline collector design shown in Figure 6b. Figure 10a shows the pushover curve for total diaphragm force vs. collector drift as the inertial force increases creating compression in the collector. The loads transferred to the SFRS by key components of the system (collector, slab frame) are shown in the figure. Individual limit state occurrences are indicated as markers on the global response curve (offset for clarity), providing the limit state sequence (stability is not considered for now). Diaphragm response is seen to remain essentially linear to the design strength ($\Omega_o N_u/\phi$ = 4800kN), though local cracking of concrete, and some yielding of shear studs and gravity system connections (in the vicinity of the SFRS) is observed. The concrete transfers over half of the collector forces in this range; this mechanism is essentially lost after reaching the strength limit, primarily due to shear stud failure, followed by concrete crushing. Figure 10b shows the axial force profile in collector along the run at the design force (Point A) and at maximum collector force (Point B). Also shown is the typical internal force profile assumed in design. As seen, the axial force profile in collector is not linear at design force level (prior to slab damage), contrary to design assumptions, but matches at ultimate.

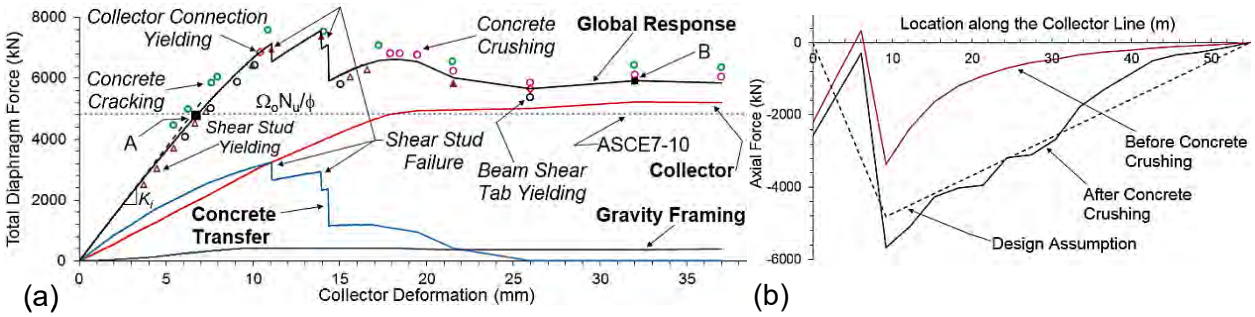


Fig. 10. Compression NP Results: (a) Global response; (b) Collector axial force profile.

The nonlinear profile shown in Figure 10b leads to overstressing of the shear studs near the SFRS, which causes the shear stud failures indicated in Figure 10a. Note that slab strength and collector strength are developed at different deformation demands, meaning that their strengths are not additive. Figure 11 shows contour plots of concrete total strain for the compression body force. Compression struts are shown in (a,b); tension struts in (c,d). Result before and after damage (Points A,B) are shown in both cases. "Hotter" colors (and thicker lines) indicate crushing/cracking. Both pairs of contours show the domination of strut actions in the linear response range, and the concentration of demands in the slab at the SFRS in the nonlinear range.

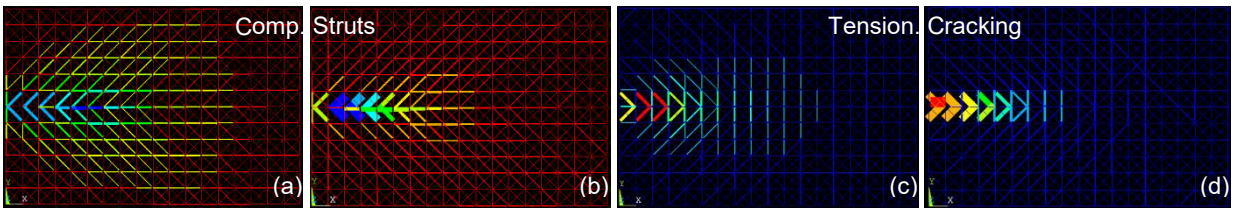


Fig. 11. Comp. NP Strain Contours: (a,b) before, after crushing; (c,d) before, after cracking.

Figure 12a shows the corresponding pushover curve for inertial force creating tension in the collector. The initial stiffness of the collector, K_i, is essentially the same in tension as it is in compression. However, as seen the global stiffness decreases noticeably during the early stages of response due to cracking of concrete (adjacent to the SFRS). The collector deformation at the design force is approximately 45% larger in tension than in compression. The collector connection yields next to the SFRS at 11mm collector deformation. The collector limit state sequence under tension is also indicated in Figure 12a. Initially, the concrete cracks. Forces redistribute to the frame, which acts as a tie; leading to some force transfer through forwardly-inclined compression struts (shown subsequently in Figure 13a,b), causing yielding of shear studs on SFRS and the adjacent collector. Shear stud failure does not occur from reduction in demands due to concrete cracking. Since the collector element is designed for stability, the collector connection yields first.

As seen in Figure 12b, the axial force profile in the collector before the concrete cracks is similar to the profile in compression. The profile is nonlinear, with the collector element adjacent to the SFRS transferring more force. The gradient of the profile near the SFRS explains why the shear studs on the collector adjacent to the LFRS yielded early in the response. As seen in Figure 12b, the axial force profile in the collector after concrete cracking remains nonlinear.

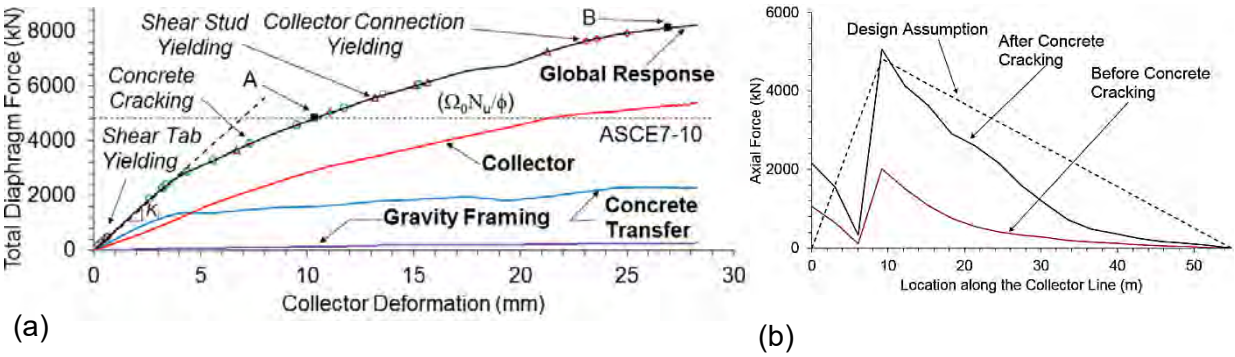


Fig. 12. Tension NP Results: (a) Global response; (b) Collector axial force profile.

Figures 13a,b show the compression strut action in the concrete slab; Figures 13c,d show the tension action. The first plot of each pair is prior to concrete cracking; the second plot of each

pair is after concrete cracking. As seen, after cracking, forces redistribute to the frame which acts as a tie; leading to some force transfer through forwardly-inclined compression struts.

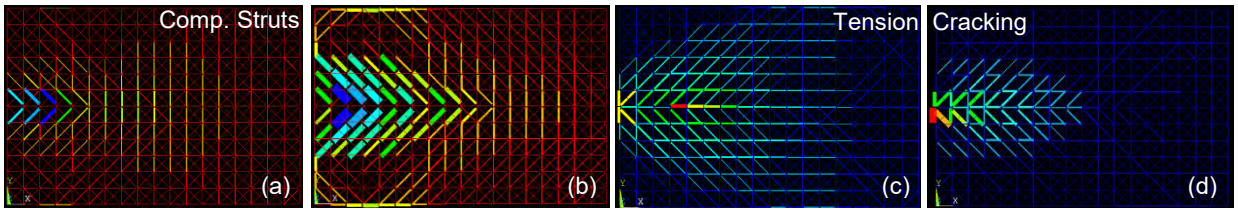


Fig. 13. Tension NP Strain Contours: (a,b) compression; (c,d) tension (before, after cracking).

5 CONCLUSIONS AND FUTURE WORK

Nonlinear models of steel composite deck collector systems have been developed. These models include isolated floor models (2D horizontal plane) and collector frame models (2D vertical plane). The isolated floor models are being used to examine collector force paths in tension and compression as various limit states are reached for different slab conditions. The collector frame models with 2D plane stress elements are being used to determine collector strength limit states and inelastic deformation demands for different collector connection details. Collector frame models with 3D nonlinear geometric elements are being used to examine collector stability states for different bracing schemes and deck orientations. The calibrated model will be used to create reduced degree of freedom full structure models for earthquake simulations to examine collector seismic demands. Recommendations will be made on appropriate design force patterns, levels and details for steel composite deck collectors and their connections.

6 REFERENCES

AISC. (2010). Seismic Design Manual 2nd Edition. American Institute of Steel Construction.

AISC. (2011). Steel Construction Manual 14th edition.

ASCE. (2013). Seismic Evaluation and Retrofit of Existing Buildings (ASCE/SEI 41-13).

ASCE 7. (2010). Minimum Design Loads for Buildings and Other Structures (ASCE/SEI 7-10).

Astaneh-Asl, A. (2005).Steel Tips: Design of Shear Tab Connections for Gravity & Seismic Loads.

Braconi, A., Elamary, A., &Salvatore, W. (2010). Seismic Behavior of beam-to-column partial-strength joints for steel-concrete composite frames. Jrnl. of Const. Steel Research, 65, 1431-44.

BSSC. (2014). Diaphragm Design Force Level. Proposal IT06-001 - Revise ASCE/DEI 7-10 Chapters 11&12. Building Seismic Safety Council, Committee IT6.

Bull, D. (1997). "Diaphragms", Seismic Design of Reinforced Concrete Structures. Technical report No 20, New Zealand Concrete Society.

Burmeister, S., & Jacobs, W. P. (2008, December). Horizontal floor diaphragm load effects on composite beam design. Modern Steel Construction.

Bursi, O., & Gramola, G. (1999). Behaviour of headed stud shear connectors under low-cycle high amplitude displacements. Materials and Structures, 32, 290-297.

Chaudhari,T.,MacRae, G.,Bull, D.,Chase,G.,Hobbs,M.,Clifton,C.,& Hicks,S. (2014). Composite slab effects on beam-column subassemblies: Further development. 2014 NZSEE Conference.

Clifton, G., & El Sarraf, R. (2005). Composite Floor Construction Handbook. Namukau City, New Zealand: HERA Report R4-107. N.Z. HERA.

Cowie,K., Hicks,S., MacRae,G., Clifton,G., & Fussell,A. (2013).Seismic Design of Composite Metal Deck & Concrete-filled Diaphragms-a discussion paper. Steel Innovation Conference 2013.

Davies, J. (1986). A General Solution for the Shear Flexibility of Profiled Sheets II: Application of the Method. Thin-Walled Structures, 4, 151-161.

Easterling, W., & Porter, M. (1994). Steel Deck Reinforced Concrete Diaphragms I. Journal of Structural Engineering, 120(2), 560-576.

EERI. (1994). Preliminary Report Northridge, California, Earthquake of January 17, 1994. www.eeri.org/products/reconnaissance-reports/preliniary-report-northridge-eq-of-jan-17-1994-2/.

FEMA. (2009). NEHRP Recommended Seismic Provisions for New Buildings & Other Structures.

Hedaoo, N.A., Gupta, L.M. & Ronghe, G.N. (2012). Design of composite slabs with profiled steel decking: A comparison between experimental & analytical studies. Int. Jrnl. of Adv. Str. Eng.

Helwig, T., & Yura, J. (1999). Torsional Bracing of Columns. ASCE STJ., 125(5), 547-555.

Herrera, R., Ricles, J., & Sause, R. (2008). Seismic Performance Evaluation of a Large-Scale Composite MRF using Pseudo-Dynamic Testing. ASCE STJ., 134(2), 279-288.

Hwang, J.-W., & Kwak, H.-G. (2013). Improved FE model to simulate interfacial bond-slip behavior in composite beams under cyclic loading. Computers and Structures, 164-176.

Kasai,K., & Matsuda,Y.(2016). Cyclic Behavior of Comp. Beam, Column, & Gusset Pl. Connection under Multiple Loads from Frame & Damper Actions. AISC Connections Workshop VIII. Boston.

Liu, J., & Astaneh-Asl, A. (2000). Cyclic Testing of Simple Connections Including Effects of Slab. Journal of Structural Engineering, 32-39.

Lowe,D., Das,R., & Clifton,C. (2014). Characterization of the Splitting Behavior of Steel-Concrete Composite Beams with Shear Stud Connection. Procedia Material Science, 3, 2174-2179.

Lu, Y., & Panagiotou, M. (2014). Three-Dimensional Cyclic Beam-Truss Model for Nonplanar Reinforced Concrete Walls. Journal of Structural Engineering.

MacRae, G., & Clifton, G. (2015). Research on Seismic Performance of Steel Structures. Steel Innovations 2015 Conference. Auckland, NZ.

MacRae,G., Clifton,G., Mackinven,H., Mago,N., Butterworth,J.,& Pampanin,S. (2010).The Sliding Hinge Joint Moment Connection. Bulletin of New Zealand Society for EQ Eng., 43(3), 202-212.

Maffei, J. (2008). Floor diaphragms, collectors, and podium and backstay effects in tall buildings. http://peer.berkeley.edu/tbi/wp-content/ /2010/09/Maffei_LATBSDC_9may08_without_extra-.pdf

Main, J. A., & Sadek, F. (2012). Robustness of Steel Gravity Frame Systems with Single-Plate Shear Connections. U.S. Dept. of Commerce. National Institute of Standards and Technology.

Majdi, Y., Hsu, C.-T. T., & Punurai, S. (2014). Local bond-slip behavior between cold-formed metal and concrete. Engineering Structures, 69, 271-284.

Royal Commission. (2012), Canterbury Earthquakes Royal Commission, Christchurch NZ. http://canterbury.royalcommission.govt.nz/Final-Report---Volumes-1-2-and-3

NZS 3404. (2007). Steel Structures Standard, Standards New Zealand. Wellington, New Zealand.

Rogers, C. A., & Tremblay, R. (2003). Inelastic Seismic Response of Side Lap Fasteners for Steel Roof Deck Diaphragms. Journal of Structural Engineering, 129(12), 1637-46.

Sabelli, R., Sabol, T. A., & Easterling, W. (2011). Seismic Design of Composite Steel Deck & Concrete-filled Diaphragms. National Institute of Standards and Technology.

Scarry, J. (2014). Floor diaphragms– Seismic bulwark or Achilles' heel. 2014 NZSEE Conference.

Souici, A., Berthet, J., Li, A., & Rahal, N. (2013). Behavior of both mechanically connected and bonded steel-concrete composite beams. Engineering Structures, 49, 11-23.

Wennberg, D., Wennhage, P., & Stichel, S. (2011). Orthotropic Models of Corrugated Sheets in Finite Element Analysis. International Scholarly Research Network, 2011.

Zhang, X., & Ricles, J. (2006). Experimental Evaluation of Reduced Beam Section Connections to Deep-Columns. Journal of Structural Engineering, 132(3), 346-357.

EVALUATION OF STRENGTH AND STIFFNESS PREDICTIONS FOR STEEL DECK DIAPHRAGMS WITH STRUCTURAL CONCRETE FILL

Patrick O'Brien
Virginia Tech, M.S. Student
Blacksburg, VA, USA
pato91@vt.edu

W. Samuel Easterling
Virginia Tech, Montague-Betts Professor of Structural Steel Design and Department Head
Blacksburg, VA, USA
seaster@vt.edu

Matthew R. Eatherton
Virginia Tech, Associate Professor
Blacksburg, VA, USA
meather@vt.edu

ABSTRACT

Steel deck floor and roof systems, common to steel framed buildings, distribute lateral forces to vertical frames through diaphragm action. Floor diaphragms offer significant shear resistance, primarily due to the concrete fill placed on the steel deck. Current diaphragm design documents (AISI, 2013a; Luttrell et al., 2015) offer shear strength and stiffness expressions for steel deck diaphragms with structural concrete fill, hereby referred to as SDDCFs. In this paper, a shear strength expression, as proposed in Porter and Easterling (1988), and an alternative shear stiffness equation are compared to current design procedures and test results from the extensive Iowa State University experimental program on SDDCFs (Porter and Greimann, 1980; Porter and Easterling, 1988; Easterling and Porter, 1994a, 1994b). A resistance factor is also recommended based on available test data. It is shown that the proposed equations result in a 46% and 52% improvement in predicting experimental strength and stiffness, respectively.

INTRODUCTION

Steel deck is used for its many advantages, including light weight, low cost, and ease of installation, among others. In addition to a chemical bond, embossments rolled into composite steel deck improve the mechanical bond with the concrete placed on top, thus creating a composite system. In this case, steel deck acts as the flexural reinforcement for gravity loads, negating need for flexural reinforcing bars. Steel headed stud anchors used for composite beams also promote composite action. When properly constructed, these systems exhibit significant strength and stiffness when loaded in-plane. A schematic for a typical SDDCF in a steel framed building is shown in Figure 1. Adjacent steel sheets are attached to each other at panel edges

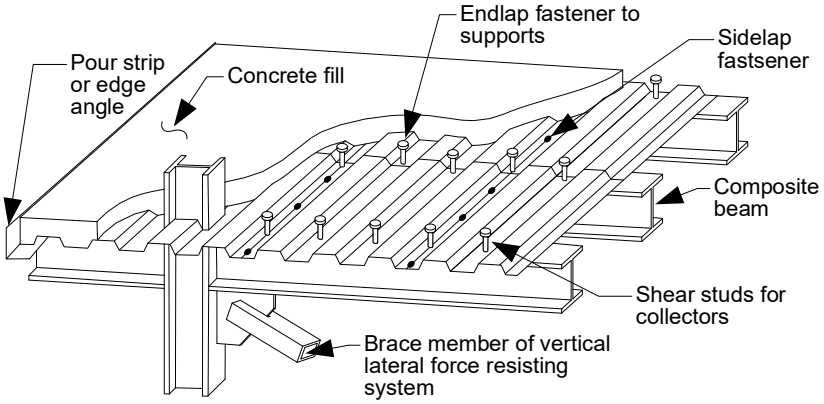


Figure 1 – Concrete filled diaphragm components

through sidelap connections. Panels are usually butted at their ends creating an 'endlap' condition, and fastened to the supporting frame with deck-to-support fasteners, hereby referred to as structural fasteners, ensuring there is no gap below for the concrete to fall through when placed. Steel headed stud anchors, hereby referred to as shear studs, are fastened through the deck directly to underlying composite beams. Temperature and shrinkage steel (e.g. welded wire fabric) for the concrete slab may also be added.

Research initially focused on this system's ability to resist gravity loads before examining in-plane resistance. Due to the proprietary nature of many diaphragm testing programs, and the extensive cost and time needed for construction, concrete curing, and disassembly, only a very limited amount of experimental research is available on SDDCFs.

A series of eleven monotonic cantilever tests, nine with insulating concrete fill utilizing welded structural fasteners, was carried out by Luttrell (1971). Concrete compressive strengths (f'_c) ranged from 0.7 MPa to 1.2 MPa. Ultimate experimental shear strengths ranged from 8 – 35 kN/m with shear stiffness values ranging from 6 – 185 kN/mm for the nine specimens with concrete fill. Davies and Fisher (1979) tested four full scale cantilever SDDCF specimens with nominal f'_c = 25 MPa. Three of four specimens incorporated re-entrant profile steel deck types (uncharacteristic of North American SDDCF construction), with the final specimen using the more traditional trapezoidal steel deck profile. Ultimate diaphragm shear strengths, predominantly limited by failure of the structural fasteners, which were screws, ranged from 15 to 29 kN/m.

A series of fourteen diaphragm tests were performed by ABK (1981), with only one specimen including structural concrete fill (nominal f'_c = 20.7 MPa). The specimen was tested in a three span, simply supported condition with welded structural fasteners and subjected to displacement histories at a dynamic rate. The specimen, however, was not loaded to failure; the maximum recorded shear strength was 41.6 kN/m. In combination with the Iowa State University experimental research program on SDDCFs, as discussed in detail in the following section, this test represents the only other SDDCF specimen subject to reversed-cyclic loading, which is a more representative loading protocol to simulate seismic demands. Fukuda et al. (1991) also tested similar composite-type specimens in reversed cyclic loading, but included geometric irregularities, thus dismissing experimental results from consideration in this paper. A substantial amount of private, proprietary testing on SDDCFS was also performed in the 1960s through 1980s by S.B. Barnes and Associates, as identified by Porter and Easterling (1988).

The findings of these research programs and proprietary testing data led to the development of SDDCF design equations provided in the Steel Deck Institute's Diaphragm Design Manual, 4th

edition (Luttrell et al., 2015), widely considered as the principal document for diaphragm design in North America and hereby referred to as DDM04. The Seismic Design for Buildings Manual, commonly referred to as the Tri-Services Manual, is a less utilized design guide that also incorporates findings from earlier experimental research (Army, Navy and Air Force, 1982). The American Iron and Steel Institute (AISI) produced a consensus document summarizing these design guides into AISI S310-13, North American Standard for the Design of Profiled Steel Diaphragm Panels (AISI, 2013a), hereby referred to as AISI S310.

This paper evaluates current strength and stiffness equations available in AISI S310 and DDM04, and recommends alternative strength and stiffness equations that better represent the mechanics of shear resistance in a SDDCF. Strength and stiffness predictions are calculated for the SDDCF specimens tested in the Iowa State University experimental program (Porter and Greimann, 1980; Porter and Easterling 1988). Furthermore, resistance factors per AISI S310 are also calculated for the recommended shear strength prediction equation.

IOWA STATE UNIVERSITY EXPERIMENTAL PROGRAM

A series of 32 full scale SDDCF specimens were tested at Iowa State University's (ISU) Structural Engineering Research Laboratory in two phases. The first phase tested specimens 1 – 9, reported by Porter and Greimann (1980), and identified a need for further testing. The second phase included specimens 10 – 32 and are reported in Porter and Easterling (1988). Six of these specimens included a combination of in-plane and vertical loads, as examined by Neilson (1984). Figure 2 shows a schematic of the diaphragm test frame setup. Table 1 gives general information about each test specimen setup. All specimens were cantilever tested and subjected to a reversed cyclic loading protocol applied at a quasistatic rate. Plan dimensions of specimens 1 - 21 were 4.57 m x 4.57 m. Specimens 22 – 32 plan dimensions were 3.66 m x 4.57 m. The 3.66 m dimension was the span dimension, oriented perpendicular to the applied load. A concrete reaction block, post tensioned with anchor rods, comprised the fixed depth dimension (parallel to applied load) of the cantilevered diaphragm test setup. In order to fasten the steel deck to the test frame, a steel plate was embedded in the concrete reaction block. Shored construction negated the need for intermediate support test frame members. All specimens used arc spot welds, shear

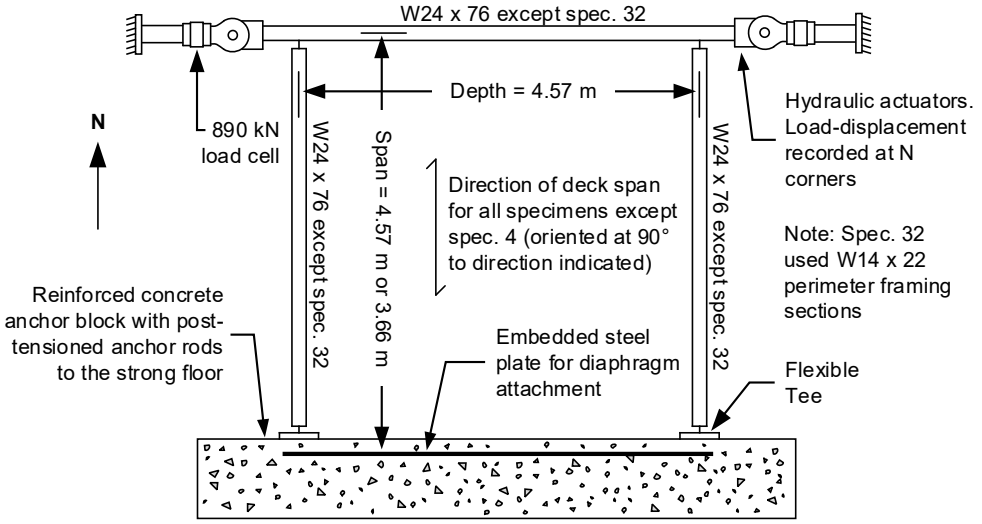


Figure 2 – Test frame for Iowa State University SDDCF program

Table 1 – ISU Test Setup Variables

Spec. ID	Measured Steel Deck Properties			Measured Conc. Properties		Connections per side
	Thickness (mm)	F_y (MPa)	F_u (MPa)	Thickness[a] (mm)	f'_c (MPa)	
1	0.86	288	368	137	38.8	30 studs
2	0.86	288	368	140	36.2	30 studs
3	0.86	288	368	144	28.0	60 welds
4	0.86	288	368	134	26.5	60 welds
5	1.57	332	419	90	20.5	30 welds
6	1.57	332	419	189	31.4	60 welds
7	1.47	343	421	137	37.5	60 welds
8	0.89	288	368	139	23.1	4 studs (N,S) 6 studs (E,W)
9[b]	1.47/1.45	357/361	436/447	139	37.3	60 welds
10	1.57	279	367	140	22.8	60 welds
11	1.19	619	646	145	24.3	60 welds
12[c]	1.57	279	367	142	23.5	60 welds
13[b,c]	1.47/1.45	357/361	436/447	140	42.7	60 welds
14[c]	1.57	279	367	208	25.5	60 welds
15	1.19	619	646	107	19.6	60 welds
16[c]	1.19	619	646	106	20.4	60 welds
17[c]	1.57	317	375	189	29.4	60 welds
18[c]	1.57	279	367	141	21.0	60 welds
19	1.57	341	383	146	18.5	60 welds
20	0.94	335	388	141	27.4	40 welds
21	1.57	279	367	144	25.1	15 welds
22	1.57	279	367	144	22.8	60 welds (N,S) 48 welds (E,W)
23	0.94	335	388	146	24.1	40 welds (N,S) 34 welds (E,W)
24	1.57	341	383	143	27.9	48 welds
25	1.57	279	367	145	32.2	16 studs (N,S) 8 studs (E,W)
26	0.91	640	645	120	23.9	8 studs 15 welds (N,S) 7 studs (W) 11 studs (E)
27	0.94	335	388	144	19.9	8 studs 15 welds (N,S) 9 welds (E,W)
28	0.94	335	388	142	24.9	8 studs 15 welds (N,S) 6 studs (E,W)
29	0.89	599	619	141	19.9	16 studs (N,S) 11 studs (E,W)
30	0.89	599	619	144	24.6	12 studs 4 welds (N,S) 7 studs (E,W)
31	0.89	599	619	146	23.0	23 welds (N,S) 13 welds (E,W)
32	0.89	599	619	144	16.9	30 welds (N,S) 23 welds (E,W)

[a] = *thickness measured from top of concrete fill to bottom of steel deck panel*
[b] = *cellular deck; steel deck properties reported as flat sheet/corrugated sheet*
[c] = *combination of gravity and in-plane loads*

studs, or a combination of both as structural fasteners. Normal weight structural concrete fill was placed on top of steel deck for all specimens except specimen 26, which used lightweight concrete. Steel deck profile dimension details for the different deck types can be found in Easterling and Porter (1988).

The reversed cyclic loading protocol specified increasing displacement steps after a minimum of three cycles. Due to cyclic strength degradation, loads at a specific displacement step dropped during successive cycles. A second criteria for progressing to the next displacement step was for the peak load of a cycle to stabilize within a 5% difference from the previous cycle.

FAILURE MODES

The restraining effects that concrete imposes on steel deck dismisses several bare deck diaphragm limit states (i.e. steel deck warping, plate-like shear buckling and out-of-plane movements are no longer of concern). Three major limit states were identified during the ISU research program for SDDCFs, only two of which are deemed practical to typical construction.

Shear transfer failure is the least probable of the three limit states, as a set of unusual construction conditions must apply. Shear transfer failure describes the failure of a SDDCF due to separation of the concrete from steel deck. To create strong composite action, embossments are rolled into the steel deck. Additionally, shear studs are the standard fasteners used in this system, and allow for a direct load path between the structural frame and concrete, promoting composite behavior at composite beam locations. Aside from these mechanical bonds, the chemical bond between the concrete and deck allows for additional shear transfer strength.

For this failure mode to occur, an unusually large amount of structural fasteners must be used without any shear studs, or other structural fasteners that allow for a direct mechanical connection between steel frame and concrete fill (e.g. standoff screws). This ensures a strong connection between deck and frame, but a weaker connection between deck and concrete. Test setup configurations likely to exhibit this failure mode included specimens with 13 welds/m. Specimens also subjected to gravity loads were less likely to fail in this fashion, due to normal loads imposing additional shear resistance from increased deck-concrete friction (Neilsen, 1984). Although this failure mode was investigated in the ISU program, it does not represent practical construction and is excluded from the limit state equations of a SDDCF further examined in this paper.

Perimeter fastener failure occurs when there is a fracture of structural fasteners that transfer forces between the structural frame and the deck-concrete system. This failure results in relative motion between the steel deck-concrete and the supporting steel beams. Steel deck sidelap connection strength is of little importance since the majority of the shear is transferred through the concrete and the deck-concrete bond prevents slip at sidelaps. The ISU program identifies a diaphragm ‘edge zone’ over which shear forces are transferred to and from the steel frame (Porter and Easterling, 1988). Structural fasteners to intermediate beams oriented perpendicular to collectors can lie within this edge zone and contribute to the collector’s perimeter fastener shear strength. The effects of connector force distributions at SDDCF perimeters are further analyzed in Widjaja (1993). For the ISU program, which did not employ intermediate supports, perimeter fastener limit shear strength is calculated by summing the total strength of the structural fasteners in both the depth and span dimension of the SDDCF, with the lesser value controlling.

Diagonal tension failure of a SDDCF occurs when the concrete placed on the steel deck behaves as a deep concrete beam and fails through shear cracking. Adequate concrete cover must also be provided to eliminate possible longitudinal cracks. Fire ratings typically govern the minimum depth of the concrete and provide enough concrete cover to alleviate this concern. Failure of the concrete will occur at a 45° angle to the diaphragm edge, initiating a diagonal crack. This behavior is analogous to shear failure of concrete beams. Although steel reinforcement (e.g. welded wire fabric for shrinkage and thermal effects) in the slab may impact shear strength, it is not explicitly considered in strength predictions for SDDCFs.

CURRENT STRENGTH EQUATION

AISI S310 and DDM04 provide a strength equation for SDDCFs, as shown in eq. (1). The diaphragm shear strength, S_n, is the summation of a steel deck connector contribution and concrete fill contribution. The concrete fill contribution (second term of summation in eq. (1)) is the product of four variables. The product of unit width, b (1000 mm), and concrete cover (between

top of steel deck and top of concrete fill), d_c (mm), represents the concrete cross sectional shear area per unit width, with specified concrete compressive strength, f'_c (MPa) The structural concrete strength factor, k, as shown in eq. (4), is dependent on the concrete mix unit weight, w_2.

The steel deck contribution to a SDDCF's shear strength (first term of summation in eq. (1)) is a statics based expression that considers the shear strength and location of each fastener along a panel. The term β is a fastener distribution factor that when multiplied by the fastener shear strength, P_{nf}, and divided by the panel's length, L, gives a shear strength per unit length for the steel deck's contribution towards a SDDCF's diaphragm strength. Figure 3 shows a free body diagram of a steel panel restrained to in-plane deformations only. The deck contribution is limited to 25% of total shear strength of SDDCF. This rational limit, as described in AISI S310 commentary, is to ensure that strength contribution from the panels for thicker decks and heavier fastener configurations is not overstated. Note that P_{nf} for shear studs is specified to be calculated as an arc spot weld for application in eq. (1). Conversely, AISC 360 equations for shear studs is to be used when checking diaphragm strength limited by perimeter fastener. DDM04 specifies the perimeter fastener strength be checked to ensure development of S_n, as given in eq. (1).

The fastener distribution factor, β (see eq. (2)), considers the location of fasteners along a panel, and effectively reduces the diaphragm strength contribution of a fastener dependent on its location with respect to the panel width centerline. DDM04 acknowledges that yielding can first occur at the edge-most fasteners. The progression of yielding, assuming adequate ductility, can allow for the fasteners towards the panel centerline to approach their capacity. However, brittle behavior is assumed and capacities for fasteners towards the panel centerline are scaled down

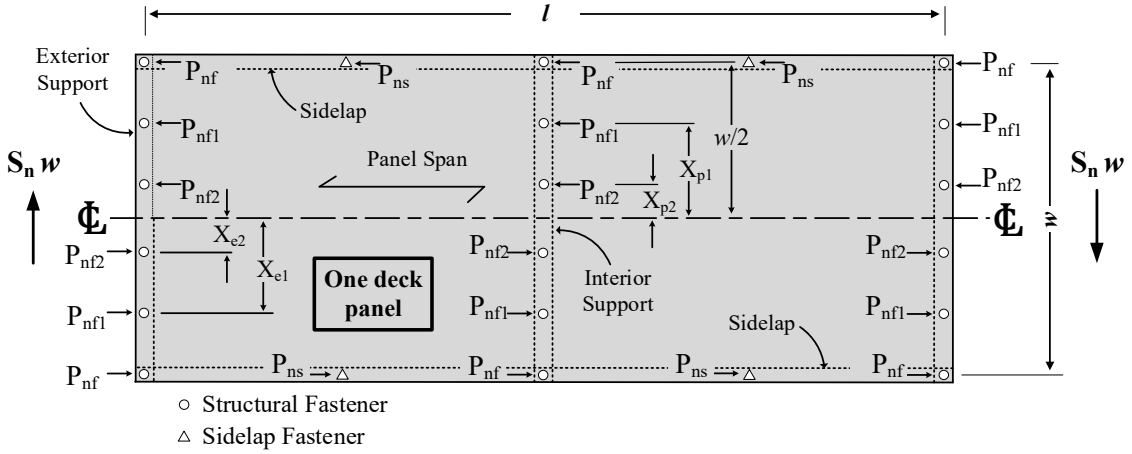


Figure 3 – Shear forces on a steel deck panel without concrete fill

(1) $$S_n = \frac{\beta P_{nf}}{L} + kbd_c\sqrt{f'_c}$$

(2) $$\beta = n_s\alpha_s + 2n_p{\alpha_2}^2 + 4{\alpha_1}^2$$

(3) $$\alpha_1 = \frac{\sum x_e}{w}\,,\ \alpha_2 = \frac{\sum x_p}{w}$$

(4) $$k = \frac{{w_2}^{1.5}}{452(10^3)}\ ,\ w_2 \text{ in } (\text{kg/m}^3)$$

proportional to the distance between the fastener and the panel centerline (i.e. $P_{nf1} = P_{nf}[X_{e1}/(w/2)]$ in Figure 3). The term n_s in eq. (2) gives the amount of sidelap fasteners along a single panel edge (n_s = 2 for Figure 3); α_s is the sidelap shear strength, P_{ns}, divided by structural fastener shear

strength, P_{nf}. Expressions for sidelap and structural fastener shear strengths are available in AISI S310 and DDM04. The number of intermediate supports is represented by n_p (n_p = 1 in Figure 3). The term α_1 and α_2 in eq. (3) are structural fastener distribution factors (x_e, x_p, and w are further defined in Figure 3).

PROPOSED STRENGTH EQUATION

The method described in the previous section uses the same approach to calculate diaphragm strength for SDDCFs as bare deck diaphragms. However, this implies assumptions that don't accurately represent the mechanics of shear load resistance in a SDDCF. The strength contribution from the deck for a SDDCF is dependent on the deck thickness and interfacial deck-concrete bond, and is not dependent on fastener strength. Thus, fastener strengths need only to be calculated when checking the perimeter fastener failure mode. The concrete strength contribution in eq. (1) characterizes the shear strength of the concrete placed *above* the top flute. However, diagonal tensions cracks can pass through the concrete in the flutes therefore contributing towards diaphragm strength, especially when deeper panels with gradual changes in panel profile dimensions between top and bottom flutes are used.

To address these issues, a method for predicting SDDCF strength limited by diagonal tension failure, as proposed in Porter and Easterling (1988), is recommended here. ACI 318 (Section 22.5.5.1) defines a range of concrete shear strengths for beams without axial force, as shown in eq. (5) (ACI, 2014). The product of beam width, b_w (mm), and depth, d (mm), in eq. (5) represents the beam shear area, with λ serving as a lightweight concrete factor (f'_c is as previously defined). Porter and Easterling (1988) take a similar approach by idealizing a SDDCF as a deep, horizontal beam and calculating an equivalent cross sectional shear area.

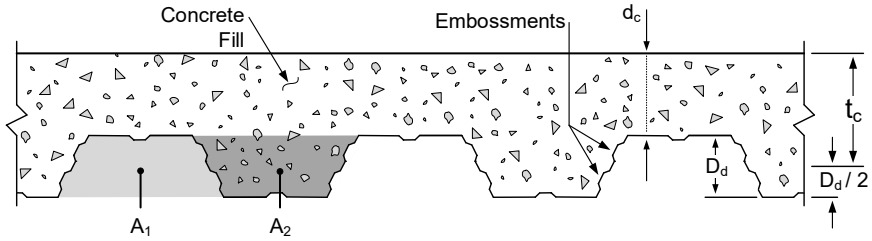


Figure 4 – SDDCF profile dimensions

Equation (6) is the SDDCF shear strength equation recommended by this work as reported by Porter and Easterling (1988). A value of 0.26 is given for the concrete strength factor, k. Concrete compressive strength, f'_c, is as previously defined. The product of the average concrete thickness,

(5) $$V_n = k\lambda b_w d\sqrt{f'_c}\ ,\ k = 0.17 \text{ to } 0.29 \text{ per ACI-318}$$

(6) $$S_{n_p} = k t_e b\sqrt{f'_c}\ ,\ k = 0.26$$

(7) $$t_e = t_c + n_{sc} t_{cd} \frac{d}{s}$$

t_e (mm) and diaphragm width, b (mm), represent the cross sectional shear area of the SDDCF, as defined in the following. Note that using a unit width, b, will result in SDDCF shear strength per unit length. Equation 7 gives an equivalent average concrete thickness, t_e, defined as the summation of the average depth of concrete, t_c (as shown in Figure 4), and an equivalent transformed concrete thickness for the steel deck. The steel deck's shear strength contribution is accounted for by converting the steel deck thickness, t_{cd}, into an equivalent concrete thickness

through a shear modular ratio, n_{sc}. The d / s term is a ratio that reduces the shear strength of a panel the more its profile geometry diverges from its equivalent flat plate-like condition, with d equal to a panel corrugation's pitch and s equivalent to a developed flute width. DDM04 contains calculation procedures for s. Note that the recommended eq. (6) is independent of fastener strengths.

Table 2 compares test and predicted strength values for the ISU SDDCF specimens that failed in diagonal tensions cracking using the DDM04 equation and Easterling (1988) equation. Test to predicted ratios are calculated by dividing the maximum experimental shear strength by the predicted strength. Test to predicted ratios using DDM04 predictions (eq. (5)) and the recommended prediction equation (eq. (6)) are also given in Table 2. Specimens are grouped by whether studs were included. Average values are given for both groups individually, and a total average for all specimens, regardless of fastener type, is presented at the bottom of Table 2. DDM04 prediction equations can give overly conservative values, as shown by an average test to predicted ratio for of 1.54 for all specimens. This ratio reduces to a more accurate value of 1.08 when using eq. (6), marking a 46% improvement over the DDM04 prediction methods.

It is also worth noting that the variability in predicted strengths using eq. (6) reduces in comparison to DDM04 values, as shown by a standard deviation of 0.10 for eq. (6) vs. 0.20 for DDM04. When using eq. (6), the test / predicted ratios closer to unity in combination with lower standard deviations indicate a more reliable prediction method than DDM04's procedure. It is important to note that these expressions are calibrated to the ISU experimental data, with a specific range of measured compressive strengths ranging from 16.9 - 42.7 MPa. Table 2 and Figure 5 compare test vs. predicted values for strength and stiffness. Strength is only reported for diagonal tension failure (DT). For the remaining specimens, the failure mode S refers to shear transfer failure mode and P refers to the perimeter fastener failure mode. Specimens listed with multiple failure modes indicates specimens where a clear distinction between the failure modes was not possible (Porter and Easterling, 1988).

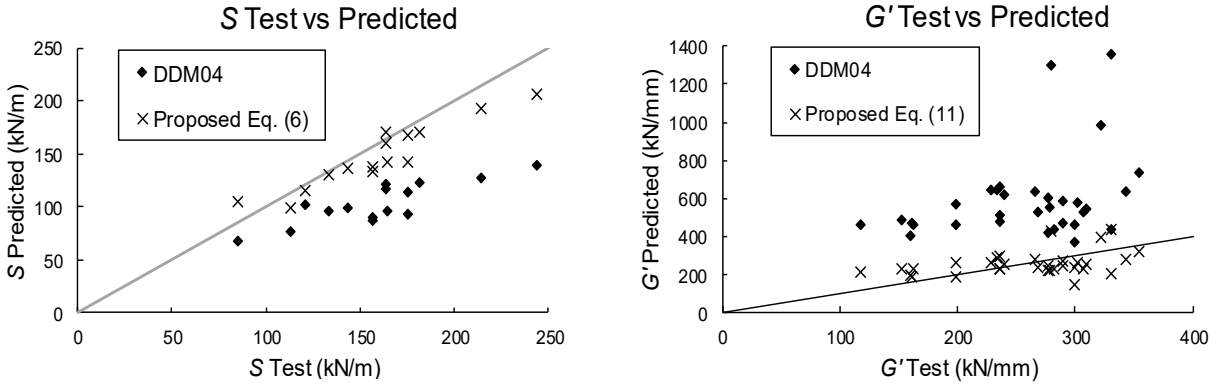


Figure 5 – Strength and stiffness: test to predicted comparison

RESISITANCE AND SAFETY FACTORS

The current resistance factor specified in AISI S310 for all steel deck diaphragms utilizing structural or insulating concrete fill, regardless of the structural fastener type used, is $\Phi = 0.5$ (for LRFD). If the DDM04 strength equation is coupled with this resistance factor, design strengths for SDDCFs are dramatically reduced in comparison to their experimental strengths. This relationship is indicated by an average test/predicted ratio of 3.02 for all specimens failing in diagonal tension when using the DDM04 equation with $\Phi = 0.5$. Considering the accuracy and low variability in test

to predicted ratios for eq. (6), a need to calculate a new Φ factor was identified. AISI S310 uses eq. (8) to calculate resistance factors for a rational analytical model when corresponding large-scale diaphragm tests are available.

Table 2 – Strength and stiffness test to predicted comparisons for ISU specimens

Spec. ID	S_n Test[a] (kN/m)	Test / Predicted		G' Test (kN/mm)	Test / Predicted	
		DDM04	Eq. (6)		DDM04	Eq. (11)
Welded						
3	S			198	0.34	0.75
4	S			236	0.49	1.00
5	113	1.46	1.15	299	0.80	1.95
6	S			331	0.24	0.75
7	S			234	0.36	0.80
9	214	1.68	1.11	236	0.35	0.79
10	157	1.75	1.14	282	0.64	1.20
11	S			310	0.57	1.21
12	175	1.88	1.24	300	0.65	1.24
13	243	1.75	1.18	354	0.48	1.10
14	S			322	0.33	0.81
15	S and DT			198	0.42	1.04
16	121	1.19	1.05	161	0.34	0.84
17	S			279	0.21	0.65
18	157	1.81	1.17	277	0.65	1.22
19	143	1.44	1.05	163	0.35	0.70
20	S and P			228	0.35	0.86
21	S and P			152	0.31	0.65
22	164	1.73	1.15	290	0.61	1.17
23	S and P			240	0.38	0.93
24	163	1.40	1.02	290	0.49	1.07
31	S and P			236	0.46	1.00
32	S and P			161	0.39	0.80
Average	165	1.61	1.13	251	0.45	0.98
Std. dev	37.3	0.21	0.06	57.8	0.15	0.28
Including Shear Studs						
1	163	1.35	0.96	266	0.42	0.94
2	181	1.48	1.07	343	0.54	1.22
8	P			118	0.25	0.54
25	175	1.54	1.05	302	0.52	1.13
26[b]	84.6	1.26	0.81	279	0.50	1.27
27	P			307	0.57	1.34
28	P			277	0.45	1.10
29	133	1.40	1.03	330	0.75	1.57
30	P			269	0.51	1.12
Avg.	147	1.41	0.98	277	0.50	1.14
Std. Dev.	35.5	0.10	0.09	61.7	0.13	0.27
Avg. Total	159	1.54	1.08	258	0.46	1.02
Std. Dev. Total	37.6	0.20	0.10	60.0	0.14	0.29

[b] *DT = diagonal tension failure, P = perimeter fasteners failure, S = shear transfer failure*
[a] *Using eq. (6) with lightweight concrete reduction factor of λ = 0.75*

Equation (8) utilizes calibration methods and probability analysis concepts considering several sources of variability. Calibrations factors consider construction variability (F_m, V_f), material variability (M_m, V_m), test data scatter (P_m, V_p), load effects (C_Φ, V_Q) and more. AISI S310 further defines the variables in eq. (8). Using prescribed AISI S310 calibration factors, as given in Table 3, results in a calculated resistance factor (using eq. (8)) of Φ = 0.58 with ASD safety factor, Ω =

2.74. Because calibration factors considered for SDDCFs are limited by both the fasteners and the concrete slab, a worst case target reliability index, β_0 = 3.5, is assigned to the current resistance factor in AISI S310. However, for the proposed shear strength equation constrained to the diagonal tension failure mode, concrete failure will be the limiting condition. Therefore, the conservative β_0 = 3.5 may no longer be appropriate. Instead, diagonal tension failure is treated as a member limit state rather than a connection limit state. As such, AISI specifies β_0 = 2.5 and an 'adapted' resistance factor of Φ = 0.79 (Ω = 2.74) is calculated as shown in Table 3. Further reliability studies are recommended to evaluate whether calibration factors as given by AISI S310 are appropriate, before conclusively proposing a resistance.

$$\emptyset = C_\phi (M_m F_m P_m) e^{-\beta_0 \sqrt{V_M^2 + V_F^2 + C_P V_P^2 + V_Q^2}} \quad (8)$$

Table 3 – Calibration factors and calculated resistance factors for diagonal tension limit state

Calibration Method	C_Φ	V_Q	M_m	V_M	F_m	V_F	V_P[a]	n[a]	C_P[a]	P_m[a]	β_0	Φ
AISI S310	1.6	0.25	1.10	0.10	0.90	0.10	0.095	15	1.24	1.08	3.5	0.58
Adapted											2.5	0.79

[a]*Calculated using ISU test data*

CURRENT STIFFNESS EQUATION

Equation (9) is AISI S310's shear stiffness equation, *G'* (kN/mm), for SDDCFs. Like the strength equation, eq. (9) is the summation of a steel deck term and concrete term. The steel deck term is equivalent to DDM04's *G'* equation for steel deck diaphragms without concrete, with the only modification being that a warping term is no longer applicable, due to the restraining effects of the concrete fill on the steel deck. The first term in the denominator of Eq. (9) is a mechanics based expression that accounts for the stiffness of the panel in pure shear (Poisson's ratio for steel of *u* = 0.3) with an applied factor of *s* / *d* (as previously discussed) effectively decreasing *G'* for corrugated sheets. The second term in the denominator, *C*, is a fastener slip term that accounts for movement of a steel deck panel with width, *w*, due to both structural and sidelap fastener flexibility, as shown in eq. (10). AISI S310 provides expressions for structural fastener (S_f) and sidelap fastener (S_s) flexibility. However, no expression is available for shear studs. Instead, shear stud flexibility is calculated as an arc spot weld. Equations (9) and (10) *E* and *t* terms correspond to the steel deck's elastic modulus (MPa) and thickness (mm), respectively. Equation (10) uses a concrete cover thickness, d_c, as shown in Figure 4. The concrete term follows classical mechanics stiffness derivations for concrete material in shear and is a semi-empirical expression adjusted to fit test data, hence the 0.7 exponent and 0.786 coefficient (Mattingly, 2017).

$$G' = \frac{Et}{2(1+\upsilon)\frac{s}{d} + C} + 0.786 d_c (f'_c)^{0.7} \quad (9)$$

$$C = \left(\frac{Et}{w}\right)\left(\frac{2L}{2\alpha_1 + n_p \alpha_2 + 2n_s \frac{S_f}{S_s}}\right) S_f \quad (10)$$

PROPOSED STIFFNESS

A few modifications to the current *G'* equation are proposed here. There are several sources of flexibility that may contribute to an SDDCF's shear stiffness. First, flexural stiffness of the beams parallel to the diaphragm's span may contribute to G', but the effects are often considered negligible. In experiments, support movement of the test frame may also contribute to flexibility, but published load-deformation data is often corrected to account for these movements. The most

significant contribution to *G'* is due to the composite deck/concrete system. There is also the potential for slip between the deck and the supporting steel frame due to the structural fasteners' flexibility, as captured in the fastener slip term, *C*, in eq. (10). This effect may be more prevalent for SDDCFs utilizing a light structural fastening configuration. The sidelap fastener flexibility, however, will not contribute due to the deck-concrete bond and its restraining effects on the deck. As such, a minor modification to *C* to exclude sidelap flexibility term is suggested, as shown in eq. (12).

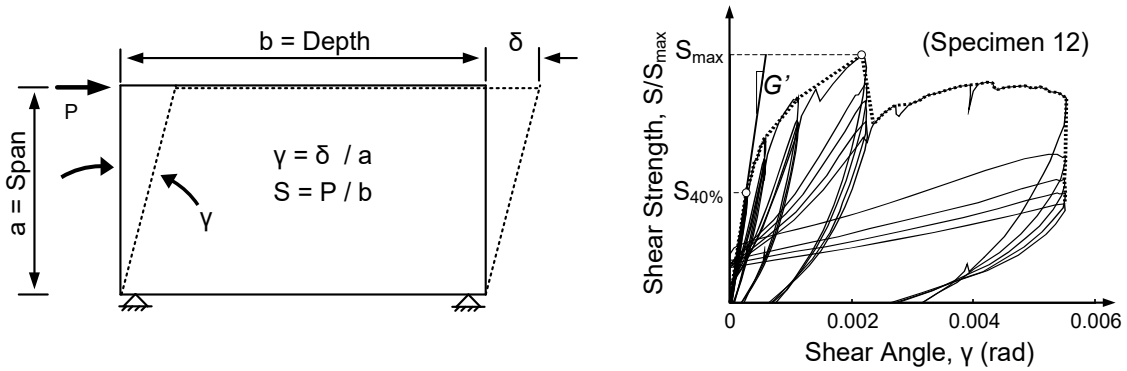
A less usual source of flexibility may occur from the deck-concrete interface de-bonding at a diaphragm's 'edge zone'. This behavior is only observed for diaphragms with an unusually large amount of structural fasteners, but no shear studs which is atypical for SDDCFs, and is therefore not considered further. The concrete term in eq. (9) only considers the concrete cover, d_c. Instead, an average concrete thickness, t_e, as previously defined and used in the proposed eq. (6) is recommended to account for the stiffness contributions of the concrete in the steel deck flutes and the steel deck itself. The coefficient and exponent in the concrete term was calibrated to give best fit predictions to experimental results, as shown in Table 2, by an average test/predicted ratio of 1.02 for all 32 specimens, in comparison to DDM04's average value of 0.46, giving a 52% more accurate prediction. Prediction values are compared to experimentally obtained G' calculated as a secant stiffness at 40% S_{max}, in keeping with AISI specified test standards and as shown in Figure 6 (AISI, 2013b).

(11) $$G' = \frac{Et}{C_2} + 0.40 t_e \sqrt{f'_c}$$

(12) $$C_2 = \left(\frac{Et}{w}\right)\left(\frac{2L}{2\alpha_1 + n_p \alpha_2}\right) S_f$$

CONCLUSIONS

SDDCF strength and stiffness predictions were evaluated and compared to experimental results currently available from the ISU testing program. Current methods for predicting strength were found not to accurately represent the mechanics of a SDDCF subjected to shear. Alternative equations to predict SDDCF strength and stiffness were proposed. The resulting expressions give average test to predicted ratios of 1.08 and 1.02 for strength and stiffness, respectively. This marks 46% and 52% improvements when compared to DDM04 strength and stiffness methods, respectively. Reduced variability when using the recommended prediction equations is also noted. A resistance factor of Φ = 0.58 (LRFD) for the proposed strength equation is calculated using prescribed calibration factors given in AISI S310. Furthermore, an 'adapted' resistance



a.) Cantilever test schematic b.) 1st quadrant of load-deformation data

Figure 6 – Determination of *G'* from ISU experimental data

factor of Φ = 0.79 (LRFD) is calculated when using a target reliability index β_0 = 3.5, appropriate for member limit states as applicable to diagonal tension failure investigated in this paper.

ACKNOWLEDGEMENTS

This work was part of the Steel Diaphragm Innovation Initiative (SDII) which is funded by AISI, AISC, SDI, SJI, and MBMA. Input from Ben Schafer and Jerry Hajjar was instrumental. This material is based upon work supported by the National Science Foundation under Grant No. (CMMI-1562669). Any opinions, findings, and conclusions or recommendations expressed in this material are those of the authors and do not necessarily reflect the views of the National Science Foundation or other sponsors.

REFERENCES

ACI Committee 318. (2014) *Building code requirements for structural concrete: (ACI 318-14).* Farmington Hills, Michigan.

ABK, A Joint Venture. (1981). *Methodology for mitigation of seismic hazards in existing unreinforced masonry buildings: diaphragm testing*. El Segundo, California.

AISC 360 (2010). *Specification for structural steel buildings*. American Institute of Steel Construction.

AISI (2013a). *North American standard for the design of profiled steel diaphragm panels, AISI S310-13*. American Iron and Steel Institute.

AISI (2013b). *Test Standard for Cantilever Test Method for Cold-Formed Steel Diaphragms, AISI S907-13.* American Iron and Steel Institute.

Davies, J., & Fisher, J. (1979). *The diaphragm action of composite slabs.* Proceedings of the Institution of Civil Engineers. DOI: http://dx.doi.org/10.1680/iicep.1979.2780

Departments of Army, Navy and Air Force. (1982). *Seismic design for buildings (Tri-services manual)*. Government Printing Office.

Easterling, W. S., and Porter, M. (1994a, 1994b). Steel□deck□reinforced concrete diaphragms. I and II. *Journal of Structural Engineering*, 120(2), pp. 560–576, and 577-596.

Luttrell, L. (1971). *Shear Diaphragms with lightweight concrete fill*. Paper presented at the 1st International Specialty Conference on Cold-Formed Steel Structures. Paper 2.

Luttrell, L., Mattingly, J., Schultz, W., & Sputo, T. (2015). *Diaphragm design manual, fourth edition*. Steel Deck Institute.

Mattingly, J. (2016), Personal communication, August 29, 2016.

Neilsen, M. (1984). *Effects of gravity load on composite floor diaphragm behavior* (Master's thesis). Iowa State University, Ames, Iowa.

Porter, M., & Easterling, W. (1988). *Behavior, analysis, and design of steel-deck-reinforced concrete diaphragms* (Report no. 88305). Iowa State University, Ames, Iowa.

Porter, M., & Greimann, L. (1980). *Seismic resistance of composite floor diaphragms* (Report no. 800133). Iowa State University, Ames, Iowa.

Widjaja, B. (1993). *Analytical investigation of composite floor diaphragms strength and behavior* (Master's thesis). Virginia Tech, Blacksburg, Virginia.

Review of plastic moment resistance for composite beams
Development of second generation of Eurocode 4

Univ.-Doz. Dr.-Ing. Markus Schäfer
University of Luxemburg
Luxemburg
markus.schaefer@uni.lu

ABSTRACT

For composite cross-sections of classes 1 and 2 the moment resistance can be determined by plastic design methods according to Eurocode 4. Thereby it is still assumed, that each cross-sectional fibre can plastify without any limitation of strains. For normal composite beams in case of sagging moments and a high-lying plastic neutral axis, the real moment resistance is quite greater than the plastic design. This is based on the large strains at the bottom side of the section, so that the lower steel flange reaches the solidification range. In case of sections with a large compression zone height x_{pl}, a concrete failure in the compression zone can happen, before reaching the plastic moment resistance $M_{pl,Rd}$. EN 1994-1-1 provides only for sections with steel grades S420 and S460 a limitation of plastic design. Hence, the plastic design can lead to unsafe results.

Analyses of plastic and strain limited moment resistance for different composite cross sections underline the requirement of additional design rules for plastic bending design.

1 Composite beam sections and classification in cross-sections classes

While classic composite beams are often characterized by a double-symmetrical steel profile with an upper concrete chord; today even slimmer, more compact and more individual beam systems become important. The trend in the last years often shows sections which are integrated into the concrete slab (shallow-floor or slim-floor), partially encased composite beams as well as composite beams with a low construction height.

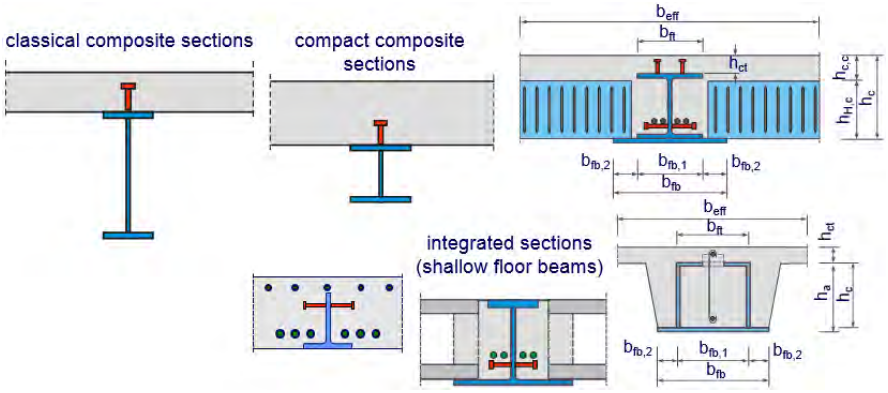


Fig. 1 - Forms of composite beam sections

Especially in case of welded slim-floor profiles, it has to be differentiated between open-sections and box-sections. These sections are used in combination with solid concrete slabs, pre-cast elements or composite slabs constructed by ribbed metal sheets with in-situ concrete. Depending on the slab-system, the upper concrete flange can increase the moment resistance

if it is connected by shear connectors to the steel section (Fig. 1). The thickness h_{ct} of the upper concrete above the steel flange has to be greater than 1/6 of the steel flange width b_{ft}, but in each case more than 50 mm. This regulation is defined according to the requirements of composite columns, consisting of fully encased steel profiles [1]. The effective width b_{eff} is also assigned by EN 1994-1-1. Based on the b/t-ratio of the flanges and web a differentiation in four cross-section classes is possible. This indirectly reflects the rotation capacity and provides local buckling effects. For the one-side attached bottom flange ($b_{fb,2}$) the identification follows the requirements for flanges of partially-encased steel sections [1]. The middle part of the bottom flange ($b_{fb,1}$) of a concrete filled box-section can be classified based on the criterions for concrete-filled rectangular hollow steel sections. For full encased sections there is no local stability threat to the encased web plates, a steel web of class 3 encased in concrete, is represented by an effective web of the same cross-section of class 2 [1]. If a classification into the classes 1 and 2 is possible, the plastic moment resistance can be taken into account.

In case of a large cross-section rotation, there is a risk of losing the stabilizing effect by the concrete due to exceeding the concrete limit strains. Thereby the rotation capability is limited. Actually, there is not sufficient experimental experience to ensure the application of plastic methods for the calculation of action effects for partial or fully encased cross-sections. So that the action effects are to be determined by the theory of elasticity, also in case of class 1 sections. Nerveless it needs to be pointed out, that the rotation capacity depends not only on the limits due to buckling of the steel parts, but also on the effects of the concrete part due to the limitation of strains in the external section fibres. Especially for composite beams with a massive concrete chord, partially encased sections with a high degree of reinforcement, slim-floor sections and systems whose effective width in the concrete chord is limited due openings or using precast elements, the strain limit design becomes often decisive, because of the reduced rotation capacity. For such sections, the plastic design can lead to an overestimation of moment resistance. Therefore, further verifications are necessary.

2 Review of plastic bending design for composite beam sections

2.1 Confusion in the approach of bending design of composite sections according to EC 4

In Eurocode 2 [2] the concrete compression strength is defined as $f_{cd} = \alpha_{cc} f_{ck}/\gamma_c$. Where the coefficient α_{cc} takes into account long-term effects on the concrete compressive strength and unfavorable effects resulting from the way the load is applied to the test specimen. This reduction factor considers mainly the difference of the concrete compressive strength under long-term loading and short-term resistance. EN 1992-1-1 suggests a coefficient α_{cc} between 0.8 and 1.0, often defined as 0.85.

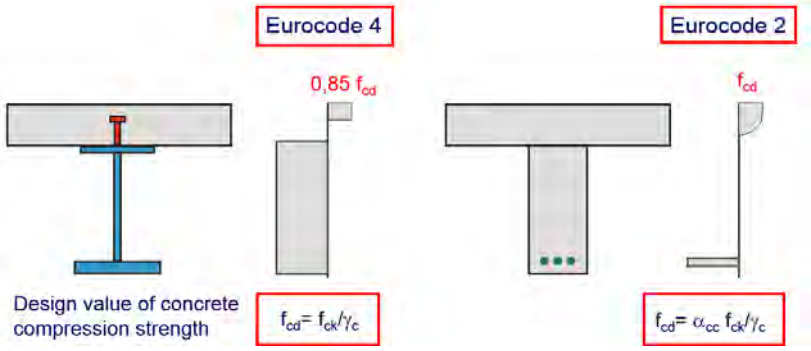


Fig. 2 - Difference in designation of design approaches in Eurocode 2 and Eurocode 4

The plastic design of composite sections according to Eurocode 4 is based on concrete stress block, whereby the concrete compression strength is defined as $f_{cd} = f_{ck}/\gamma_c$. While simultaneously the concrete compressive stresses over the total stress block x_{pl} needs to be reduced by a constant factor 0.85.

Currently, there are several discussions, whether the reduction of the design value of concrete strength in EN 1994 by the coefficient 0.85 results either from a rectangular compression block over the total height of its compression zone [4], or if it is reducible to long-term effects (α_{cc}) of concrete. In order to explore this, the historical development of Eurocodes has to be considered. In the previous version ENV 1992-1-1:1992 [3] the concrete compression strength was still defined as $f_{cd} = f_{ck}/\gamma_c$ and the coefficient α taking into account the long-term effects on the compression strength and other unfavorable effects was added to the stress-strain curve (αf_{cd}). So that the stress ordinate of the idealized stress-strain diagram was defined by the characteristic value of the concrete compression strength f_{ck} multiplied with the factor α/γ_c. Only in later versions of EN 1992 the definition of f_{cd} was changed to $f_{cd} = \alpha_{cc}\ f_{ck}/\gamma_c$, used until now. However, EN 1994 has been developed in the same time and today it is not comprehensible, if the change from ENV- to EN-Version of concrete code was also followed for the design of composite structures. Based on the background information it appears reasonable, that the added coefficient 0.85 (*Fig. 2*) for the design of composite beams corresponds to α_{cc}. Therefore, the design level seems to be the same. In parallel, the comment to EN 1994 in [4] underlines the relevance of the approximation made by the shape of the concrete stress-block, leading to an overestimation of the moment resistance. Though, the illumination in [7] leads to the result that for beam sections the plastic design based on rectangular stress block does not need any reduction, because of the high rotation capacity of composite beams. But concurrently, an additional reduction factor of 0.8 is claimed for the concrete stress $\alpha\ f_{ck}/\gamma_c$ when using the rectangular concrete stress bloc for the design of composite slabs. Assuming, the consideration of the long-term effects by factor $\alpha = 0.85$, results in a design value of concrete compression stress about $0.68\ f_{ck}/\gamma_c$. The following chapter will clarify the significance of rotation capacity and the impact off stress block onto plastic bending for composite beams, considering also new forms of composite beam sections, representing often a structural element between classical beam and slab.

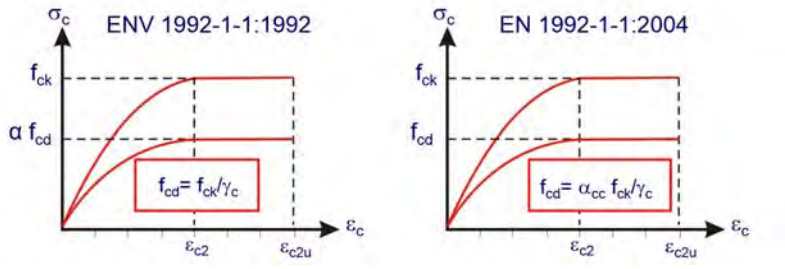


Fig. 3 - Stress-strain diagram and design value of concrete compression strength according to ENV 1992-1-1: 1992 [3] and EN 1992-1-1:2004 [1]

2.2 Comparison of parabola-rectangular and rectangular shape of concrete stresses

Of course, there is an impact of the stress block's shape on the bending design. According to EN 1992 mainly curved shapes are used for the stress-strain curves. Therefore, the approach of a simplified rectangular stress-block for the structural use of concrete can lead to an overestimation of the concrete compression force in the concrete chord if the height of the

compression stress block is defined by the strain distribution. Therefore, in case of a strain-limited design, the height of the stress-block has to be reduced by factor λ (EN 1992-1-1, section 3.1.7). However, also in this case there remains a divergence in the position of the resulting compression force with its impact on the bending resistance. The concrete compression force N_{cd} results by integration of the parabola-rectangular stress-strain function over its surface, respectively above the compression zone height x(z), *Fig. 5*.

To compare the parabola curve with a rectangular equivalent stress block, a dimensionless coefficient can be derived by dividing N_{cd} by the compression force $b \cdot x \cdot f_{cd}$ resulting from a rectangular stress block. This coefficient describes the solidity ratio αr of the surface of parabola curve.

$$\alpha_r = \frac{b \int_0^x \sigma_c(x)\, dx}{b \cdot x \cdot f_{cd}} \qquad (1)$$

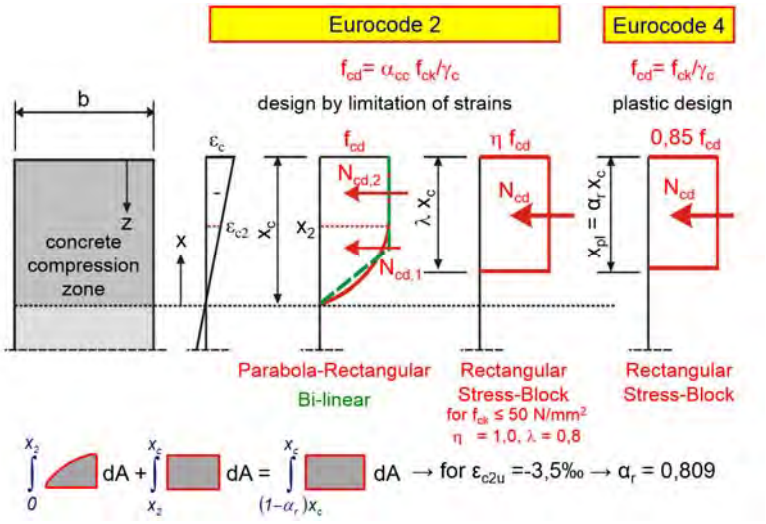


Fig. 4 - Shapes of stress-strain curves used in EN 1992 and comparison to rectangular stress-block according to EN 1994

The solidity ratio α_r depends on the concrete strains at the top fibre of the concrete compression zone. For the pure parabola shape with a strain limitation of ε_c equal -2‰ the solidity ration results to 2/3, which represents the area of a parabola compared to a rectangle. Assuming a concrete strain at the top fibre of -3.5‰, which will be reached for ductile concrete or composite sections with sufficient rotation capacity, the solidity range arises to a value of 0.809. Consequently, a rectangular stress block with the same resulting concrete compression force N_{cd} has always a height of 0.809 times the height of a parabola rectangular shaped stress curve. Therefore, only in case of strain limited design and use of a simplified rectangular stress block according to EN 1992, the height of concrete compression zone has to be reduced by factor λ compared to the strain zero-point.

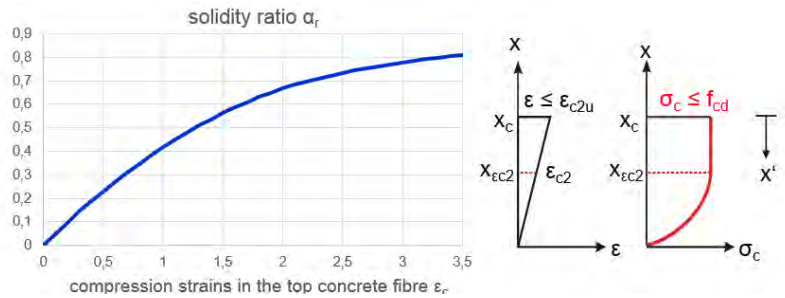


Fig. 5 - Comparison of shape form for parable-rectangular stress-strain curve and rectangular stress block

However, in case of plastic design the height of the plastic neutral axis is not determined by the strain distribution over the section! In this case, the compression force is defined by the equilibrium of the internal normal forces ($\sum N_i = 0$: $N_{pl.a.Rd} + N_{cd} = 0$). This means, the compression force N_c in the concrete chord corresponds to the tension force N_a in steel section. Finally, for common composite beam sections the height of the plastic concrete compression block in the chord is 19.1% (1-0.809) lower in contrast to a parabola-rectangular stress block, based on the hypothesis that the full plastic internal normal force $N_{pl.a.Rd}$ of the steel section is achieved. An additional reduction coefficient established by the scale of the resulting compression force is not necessary in case of plastic design. Hence, the assumption that in EN 1994 the reduction factor 0.85 for the concrete stresses in plastic design results from the approach of the stress block over the total compression zone height is invalidated. This is only valid for a strain-limited design in combination with a pure rectangular stress block; note the reference of application of factor λ in EN 1992!

Even if there is no impact on the magnitude of the resulting concrete compressive force of the concrete slab, there remains a difference in the position of this force compared to parable-rectangular shape form. The centre of the stress-shape of a parable-rectangular relation results by equation (2):

$$x_s = \frac{\int_0^{x_c} \sigma_{c(x)} \cdot x \, dA}{\int_0^{x_c} \sigma_{c(x)} \, dA} = \frac{b \int_0^{x_c} \sigma_{c(x)} \cdot x \, dx}{b \int_0^{x_c} \sigma_{c(x)} \, dx} \qquad (2)$$

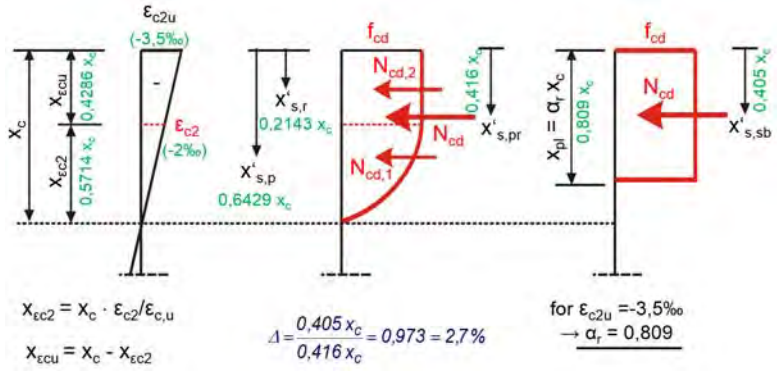


Fig. 6 - Difference Δ related to position of resulting concrete compression force

Fig. 6 shows the deviation of the position of the resulting concrete compression force relative to its compression zone height x_c based on the hypothesis of reaching ε_{c2u} for normal weight concrete of -3.5‰ at the outer section fibre. The difference of the position of resulting compression force N_{cd} is about 2.7%. For sections with non-ductile behaviour where e.g. the strains are limited by the ductility of reinforcement in tension zone, lower strains are reached in the outer section fibre. Of course, in this case the difference in position of the resulting force N_{cd} becomes more important. This is also valid for composite columns where in case of N-M-interaction the edge strains are between -2.0‰ and -3.5‰. *Fig. 7* illustrates the increasing difference in the position of resulting compression force by decreasing of concrete strains. Indeed, comparison in *Fig. 7* presents only ductile composite beam sections of cross-section classes 1 and 2 with plastic neutral axis in the concrete chord. The graphic demonstrates an impact of the divergences in position of resulting compression forces for the two mentioned design methods up to 3% on the resulting bending moment for common composite beam sections. It should be pointed out, that the importance increases with the height of concrete compression zone and with decrease of the lever arm for the internal forces. For composite slabs the discrepancy for the design based on a stress block will be more important than for composite beam sections [7]. At least, for classical composite beam sections with a high rotation capacity the difference between parabola-rectangular and rectangular stress block can normally be neglected. For slabs, shallow-floor beams and composite beams with a low height further investigation needs to be provided.

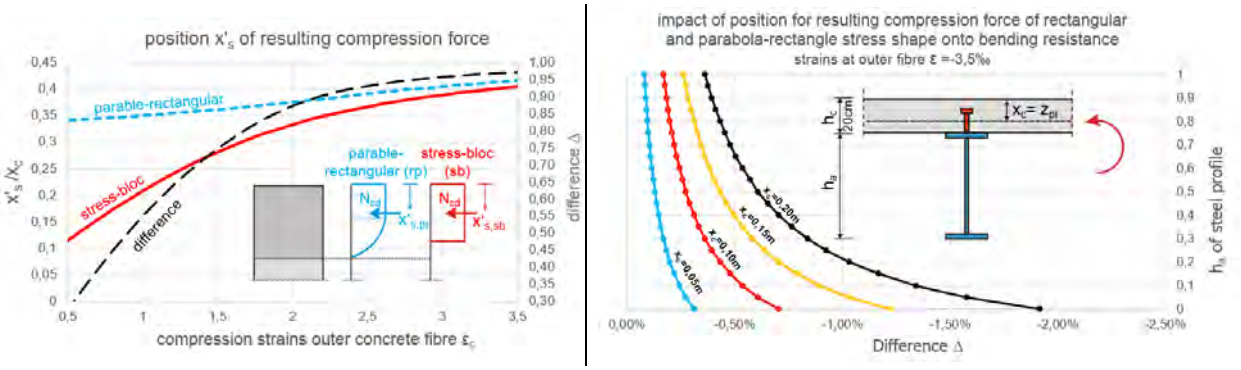


Fig. 7 - Difference in position of resulting concrete compression force and for bending resistance

2.3 Comparison of strain limited and plastic design

Furthermore, the question is whether the steel part of the section reaches its plastic strain level with its full plastic stress bloc! If not, there will be a significant difference between plastic and strain limited design. *Fig. 8* demonstrates the design methods for an IPE 500-S355 with its difference between both stress shapes. On one hand a strain limited calculation according to EN 1992-1-1 (Fig. B, M_{Rd} = 1554 kNm) without activation of strain hardening range for steel, on the other hand plastic design according to EN 1994-1-1 (Fig. C, $M_{pl.Rd}$ = 1557 kNm). To ensure a comparable result, the concrete compression strength in all cases is defined according to EN 1992 considering the long-term effects (α_{cc} = 0.85). The result shows clearly, a difference between compression zone height of B and C by factor 0.809 and nearly the same moment resistance. The strain distribution in A considers the strain hardening range of steel stress-strain relationship.

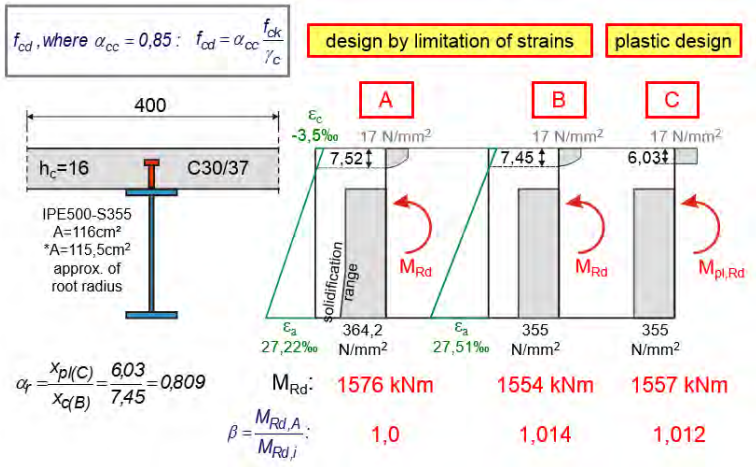


Fig. 8 - Comparison of plastic and strain limited of bending resistance for common composite beam-section

This example, presenting a typical composite beam, e.g. for car parks, shows that the bending moment resistance M_{Rd} (Fig. A) due to a strain limited design is at least higher than the full plastic moment resistance $M_{pl.Rd}$. (Fig. C). Changing the steel grade to S235, would result in a strain limited moment resistance 7% higher than the plastic resistance. In comparison, the impact of reducing the stress block by an additional factor 0.85 would be negligible (< 2%). This points out, that a general reduction of the stress block in case of plastic design is not justifiable, even though the impact on this kind of sections is very low.

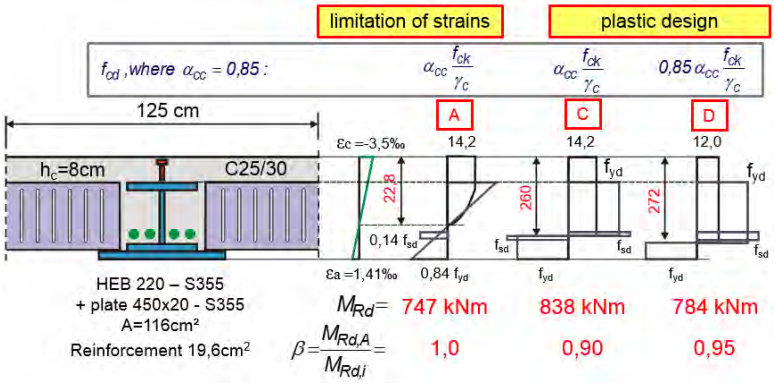


Fig. 9 - Comparison of strain-limited and plastic bending resistance for a slim-floor section

The approach of reducing the plastic moment resistance becomes more relevant in case of composite sections with a small depth and inner lever arm z or for composite slabs. Especially for slim-floor sections this phenomenon is also exposed in [9] - [11]. The example of a slim-floor section with a small effective width in *Fig. 9* demonstrates this effect. It results in a high value of 0.81 for the relationship $\xi_{pl} = x_{pl}/h$. The moment resistance based on strain-limited design (A) becomes decisive; it represents only 90% of the plastic moment resistance (C). Even the approach of an additional reduction coefficient of 0.85 for the concrete stress block overestimates the moment resistance, *Fig. 9* (D).

If the stresses in the section are limited by the strains, the plastic bending design can lead to an overestimated bending resistance. This occurs, if the rotation capacity of the cross section is limited.

3 Development of additional design rules for plastic bending resistance

3.1 Impact of concrete part on rotation capacity

In case of classical composite beams a classification in four cross-section classes based on the b/t-ratio of the flanges and web is possible. For partially or fully encased sections the rotation capacity depends not only on the limits due to buckling of the steel parts, but also the effects of the concrete part influence the limitation of strains in the external section fibres. Especially for composite beams with a massive concrete chord, partially encased sections with a high degree of reinforcement, slim-floor sections and systems whose effective width in the concrete chord is limited due to openings or using precast elements, the strain limited design becomes often decisive, because of the reduced rotation capacity.

For the plastic design of the moment resistance it is still assumed, that each cross-sectional fibre can plastify without any limitation of the strains. For normal composite beams in case of sagging moments and a high-lying plastic neutral axis, the real moment resistance is considerably greater than the plastic design moment. This is based on the large strains at the bottom side of the section, so that for the lower steel flange strain hardening can be taken into account.

In case of sections with a large compression zone height x_{pl}, a concrete failure in the compression zone can happen before reaching the plastic moment resistance $M_{pl,Rd}$. Therefore, the plastic moment resistance has to be reduced. Nevertheless, this is not only a question of the shape of the concrete stresses, moreover a combination of rotation capacity, stress-strain curve and maximum strains in the external fibre of cross-section. A general reduction of the concrete stresses or the plastic moment due to these effects is not appropriate for the design.

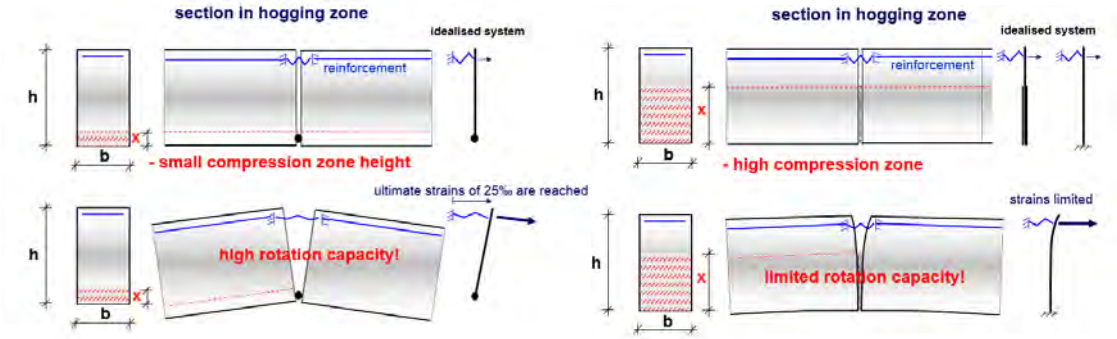


Fig. 10 - Rotation capacity of a concrete section

The reduction of full plastic moment resistance depends among others on the relation of the concrete compression zone height to the total section height. This indirectly reflects the limitation of rotation capacity for the section. *Fig. 10* illustrates the principle for rotation capacity of concrete sections in hogging zone, depending on the compression zone height. EN 1992-1-1, section 5.5 allows for the moment redistribution a simplified estimation of rotation capacity through the relationship x/d. For a limited rotation capacity, also the strains in the steel sections will be reduced and therefore the full plastic force $N_{pl.a.Rd}$ cannot be reached. The comparison of plastic and strain limited moment resistances for a multiplicity of cross-sections will lead to an adequate reduction factor, chapter 3.2. EN 1994-1-1 still provides a limitation of plastic design only for sections with steel grades S420 and S460. Thereby the plastic ultimate moment resistance, according to section 6.2.1.2 (2), is limited by the coefficient β, taking into account that for large compression zones the design moment capacity is restricted by attaining the

ultimate strain in the concrete chord [8]. The verification of the coefficient β for S420 and S460 is based on analysis in [12].

3.2 Implementation of a reduction factor for plastic moment resistance

The in Eurocode 4 currently used design value for concrete compression strength in combination with the coefficient 0.85 at the plastic concrete compression block displays an inadmissible mixing of two different phenomena. On one hand there is the reduction due to long-term effects; on the other hand, this non-variable coefficient for the reduction of the stress block (*Fig. 2*). The problem of the strain limitation should not be mixed with the long-term coefficient according to Eurocode 2! It would be more correct to introduce a correction coefficient for the moment design resistance in composite cross sections and to consider the long-term effects according to EN 1992. Therefore, the concrete compressive strength in Eurocode 4 should be defined by reference to Eurocode 2. This will lead to consistence in design and harmonization of Eurocode 4 and Eurocode 2. Actually, the evaluation of Eurocode 2 should be attained. Anyway, the long-term effect has to be considered in design of composite structures.

To respect the effects of a limited rotation capacity for sections with an important compression zone height due to strain limitation, an additional reduction coefficient β for the plastic moment resistance is to be introduced. This correction coefficient would capture the difference between a strain limited design and a full plastic design. Furthermore it would consider, through the relationship x_{pl}/h the rotation capacity considering the concrete part. Eurocode 4 provides this already for high strength steels. This correction coefficient will always be 1.0 for typical composite cross sections. Additionally, it could take better into account untypical cross-sections, where the plastic zero line lies very deep.

$$M_{Rd} = \beta \cdot M_{pl,Rd} \qquad (3)$$

The deviation of the reduction functions of the plastic moment resistance for different steel grades are based on extensive comparisons of plastic and strain limited design in [9], [13] and [14]. About 35.000 combinations of different cross sections and materials have been considered. The results of different analysis are consolidated in [15], to reach a general design approach.

The analyses are based on stress-strain relationship for concrete according to EN 1992-1-1, whereby the parabola-rectangular shape was used. *Fig. 11* visualizes the used stress-strain relationship for concrete.

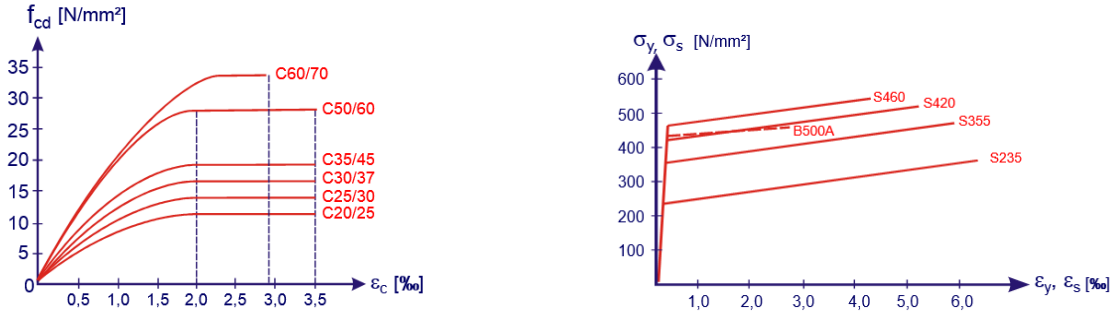


Fig. 11 - Stress-strain relationship for concrete, structural steel and reinforcement

For structural, steel the stress-strain relationship according EN 1993-1-5, Annex C6, with strain hardening of tan-1(E/10000) was applied. Only for the analysis of slim-floor section in [9] a horizontal plateau for yielding was considered. Reinforcement steel follows the rules of EN 1992-1-1, also for this steel the strain hardening was applied behind the elastic strains.

Fig. 12 to *Fig. 14* show the comparison and analysis of strain limited moment resistance and plastic moment resistance for concrete class up to C50/60. Thereby it needs to be pointed point out, that with a relationship of x_{pl}/h about 0.15 a reduction of plastic moment resistance becomes important for steel grades S420 and S460. For grades of S355 the plastic moment resistance is to be reduced if the relationship x_{pl}/h is more than 0.20 and for steel grade S235 if the relationship is more than 0.3. The definition of these limits prevent an inefficient reduction of plastic moment resistance for common composite sections with a high lying plastic neutral axis. Concrete strength of C60/70 and higher are not considered in these figures. Because for this concrete strengths, the variety is very high.

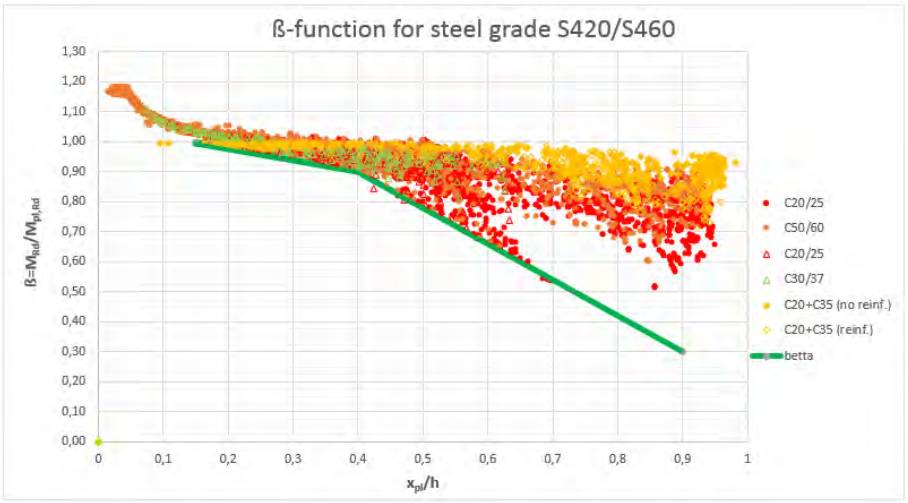


Fig. 12 - Reduction coefficient β for concrete C20/25 to C50/60 and steel grades S420/S460

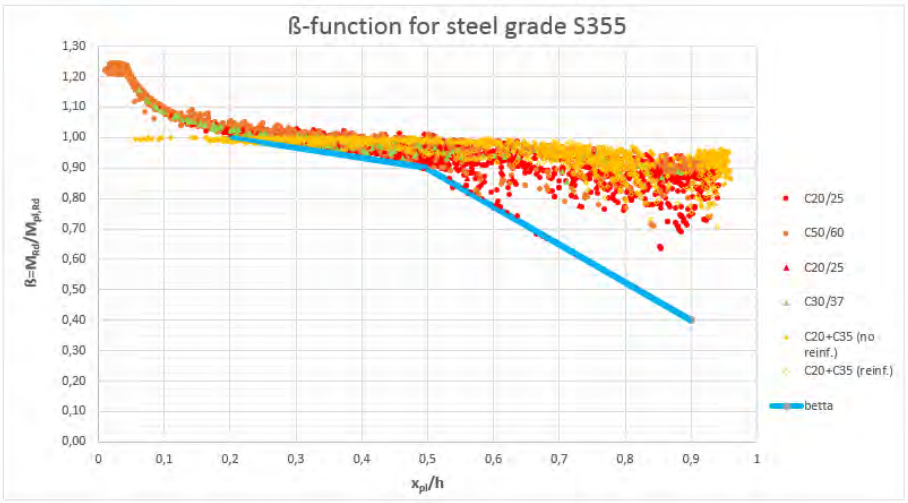


Fig. 13 - Reduction coefficient β for concrete C20/25 to C50/60 and steel grades S355

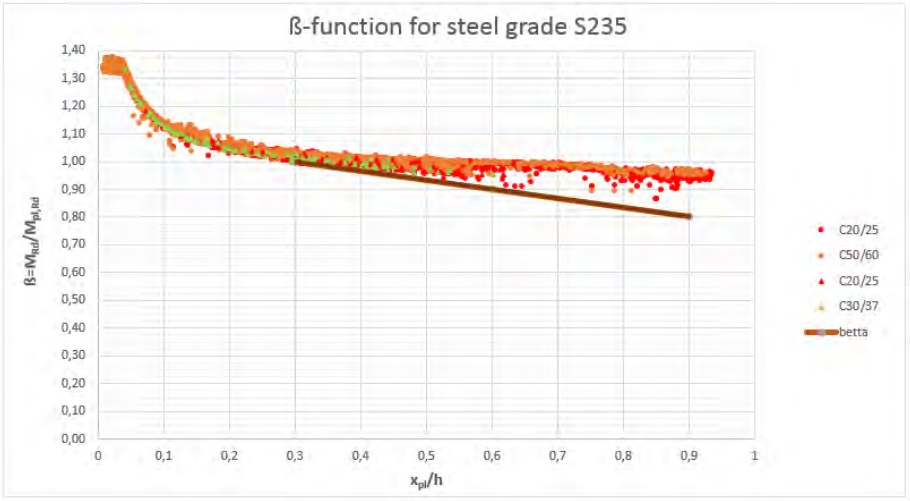


Fig. 14 - Reduction coefficient β for concrete C20/25 to C50/60 and steel grades S235

4 Summary

The analysis of plastic moment resistance points out, that the plastic design can lead to an overestimation of the bending resistance, if the rotation capacity is limited due to the ultimate strains of concrete. In the current version of Eurocode 4 for the design of composite structures in steel and concrete, the impact of concrete part due to rotation capacity is not considered. If no more exact design method will be applied, the introduction of an additional reduction factor for the plastic moment resistance, based on the relationship x_{pl}/h, leads to a reliable design level. For classic composite beams with a double-symmetrical steel profile with an upper concrete chord and a slight compression zone height, there will be no impact on the bending design by the reduction factor β. However, the risk in case of compact and encased sections will be covered. Actually, this design approach is proposed for the development of the second generation of Eurocode 4.

5 References

[1]	DIN EN 1994-1-1: Eurocode 4: Design of composite steel and concrete structures - Part 1-1: General rules and rules for buildings; German version EN 1994-1-1:2004 + AC:2009
[2]	DIN EN 1992-1-1:2011-01: Eurocode 2: Design of concrete structures - Part 1-1: General rules and rules for buildings; German version EN 1992-1-1:2004 + AC:2010
[3]	ENV 1992-1-1: EuroCode 2: Design of concrete structures, Part 1. General rules for buildings (1992)
[4]	Johnson, R., P., Anderson, D.: Designers' Guide to EN 1994-1-1, Eurocode 4: Design of composite steel and concrete structures: Part 1.1: General Rules

	and Rules for Buildings, Thomas Telford (2004)
[5]	Rüsch, H.: Researches Toward a General Flexural Theory for Structural Concrete, In: ACI Journal 57, (1960)
[6]	Rüsch, H., Sell, R., Rasch C., Grasser, E., Hummel, A., Wesche, K., Flatten, H.: Festigkeit und Verformung von unbewehrtem Beton unter konstanter Dauerlast. DAfStb-Heft, Ernst & Sohn, Berlin, (1968)
[7]	Bode, H.: Euro-Verbundbau, 2nd Edition, Werner Verlag (1998)
[8]	Hanswille G., Schäfer M., Bergmann M.: Verbundtragwerke aus Stahl und Beton, Bemessung und Konstruktion - Kommentar zu DIN 18800-5 Ausgabe März 2007, Stahlbau-Kalender 2010, Ernst & Sohn Verlag für Architektur und technische Wissenschaften GmbH, Berlin (2010)
[9]	Schäfer M. „Zum Tragverhalten von Flachdecken mit integrierten hohlkastenförmigen Stahlprofilen“, Dissertation, Institut für Konstruktiven Ingenieurbau, Heft 8, Bergische Universität Wuppertal, 2007
[10]	Schäfer, M.: Design rules for slim-floor girders considering the composite behaviour, Nordic Steel Construction Conference 2015, Tampere, Finland (2015)
[11]	Schäfer, M.: Zur Biegebemessung von Flachdecken in Verbundbauweise; Stahlbau, 84. Jahrgang, Heft 4, Ernst & Sohn Verlag, Berlin (2015)
[12]	Hanswille, G., Sedlacek, G., Anderson, D.: The Use of Steel Grades S460 and S420 in Composite Structures, ECCS-Eurofer, Improvements by TC 11 to Eurocode 4, University of Wuppertal, RWTH Aachen, Ernst & Sohn Verlag, Berlin (1996)
[13]	Banfi, M.: The next generation of Eurocode 4, EUROSTEEL conference, September 13–15, 2017, Copenhagen, Denmark
[14]	Bahovic, A.: Comparison of strain limited an plastic design for composite beam sections, bachelor thesis supervised by M. Schäfer, University of Luxemburg, in progress
[15]	Schäfer, M., Banfi, M.: Plastic moment resistance of composite beams - harmonization of Eurocode 4 with Eurocode 2, Background Report to EN 1994, Development of Second generation of Eurocode 4, European Committee for Standardization CEN, Project Team CEN/TC250/SC4.T1, Luxemburg/London (2017)

INFLUENCE OF THE COMPOSITE ACTION ON THE LOAD BEARING AND DEFORMATION BEHAVIOR OF COMPOSITE BEAMS WITH PROFILED STEEL SHEETING

Dr.-Ing. Florian Eggert
PERI GmbH
Weißenhorn, Germany
florian.eggert@peri.de
Former: University of Stuttgart, Institute of Structural Design

Prof. Dr.-Ing. Ulrike Kuhlmann
University of Stuttgart
Institute of Structural Design
Stuttgart, Germany
ulrike.kuhlmann@ke.uni-stuttgart.de

ABSTRACT

In the frame of the European research project DISCCO (Aggelopoulos et al., 2016), composite beams with additional profiled steel decking were investigated. Under certain conditions, current Eurocode 4 (EN 1994-1-1, 2004) leads to inefficient dimensions of composite beams especially in view of the minimum degree of shear connection, above all when using modern profiled steel decking. Furthermore, the rib distance of the steel decking profiles limits the connection of steel beam and concrete slab. To investigate the realistic behavior of composite beams with low degrees of shear connection, a comprehensive study on push-out specimens and short composite beams was carried out. New findings gained by these tests lead to new rules for the minimum degree of shear connection and for the load-bearing capacity of headed studs in combination with additional profiled steel decking.

1 GENERAL

The usage of composite beams with composite slabs in modern building applications has a lot of advantages. However, the existing rules for the minimum degree of shear connection, in some cases, make the design of composite beams impossible, particularly with the use of modern deck profiles with high, narrow but widely spaced ribs and hence with widely spaced shear connectors.

Recent research (Konrad, 2011; Nellinger, 2015) showed that shear connector resistances according to Eurocode 4 (EN 1994-1-1, 2004) insufficiently predict the observed concrete failure modes and resistances in the presence of modern forms of steel decking. New approaches to the shear connector resistance (Konrad, 2011; Nellinger, 2015) lead to more accurate predictions of the shear resistance of headed studs.

This paper presents the transfer and the influence of these results to composite beams. The results of a parametric study on eight short-span composite beam tests with small degrees of shear connection between 16% and 38% are presented. The beam tests were conducted using composite slabs with a modern form of profiled steel sheeting. Important parameters of the shear connection, such as stud diameter, number of studs per rib, reinforcement pattern, welding procedure

and concrete strength, were varied. All the test configurations were selected in accordance with a previously conducted study on the behavior of shear connectors in corresponding push-out specimens. A comparison of the bending resistance of the beam tests and the calculated plastic bending resistance is presented.

1 SHEAR RESISTANCE OF HEADED STUDS

1.1 PROCEDURE OF EN 1994-1-1

The currently used Eurocode 4 (EN 1994-1-1, 2004) uses empirically derived formulae to determine the shear connector resistance in solid slabs. The mean shear connector resistance (Roik et al., 1988) is calculated as the minimum of Equations (1) and (2). To consider the influence of the deck profiles, a reduction factor according to Equation (3) is applied.

Steel failure: $$P_{t1} = k_t \cdot 1.00 \cdot f_u \cdot \pi \cdot d^2/4 \quad (1)$$

Concrete failure: $$P_{t2} = k_t \cdot 0.374 \cdot \alpha \cdot d^2 \sqrt{f_{cm} \cdot E_{cm}} \quad (2)$$

Reduction: $$k_t = \frac{0.7}{\sqrt{n_r}} \cdot \frac{b_m}{h_p} \cdot \left(\frac{h_{sc}}{h_p} - 1\right) \leq k_{t,max} \quad (3)$$

With
- d: Diameter of the shear stud [mm]
- f_u: Tensile strength of the stud [N/mm²]
- α: = 1 for $h_{sc}/d > 4$, d and h_{sc} in [mm]
- f_{cm}: Concrete compressive strength [N/mm²]
- E_{cm}: Modulus of elasticity of concrete, using $E_{cm} = 9500 \cdot f_c^{1/3}$ [N/mm²]
- n_r: Number of studs per rib (max. $n_r = 2$)

1.2 NEW DESIGN APPROACHES

Evaluations by (Kuhlmann and Raichle, 2005) already showed that the current formulae of Eurocode 4 (EN 1994-1-1, 2004) overestimate shear stud resistances when using modern decking. This is due to the value $k_{t,max}$, cf. Equation (3), that is decisive in most of the cases. This means that important geometrical parameters of the deck profiles as well as the position of the stud are not considered for the determination the reduction factor.

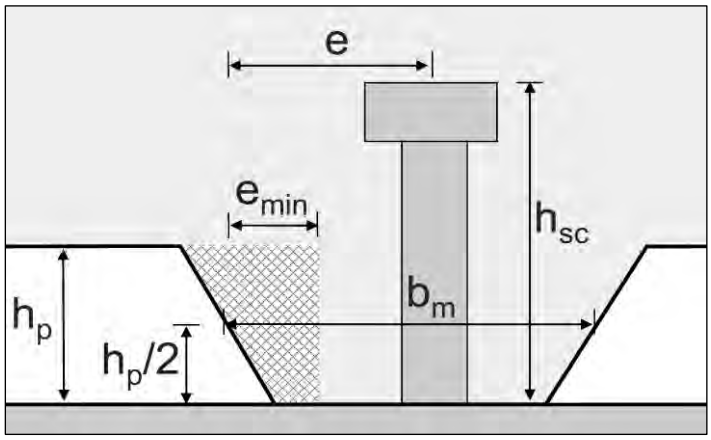


Fig. 1 – Geometrical parameters of the profiled decking

Recent tests and investigations (Konrad, 2011; Kuhlmann and Konrad, 2009; Kuhlmann and Konrad, 2010; Rambo-Roddenberry, 2002; Nellinger, 2015) consider the position of the headed stud as well as the geometry of the decking. It could be shown (Konrad, 2011) that a shear connector is in so-called “unfavourable position” if the distance *e* between the web of the rib and the shear stud is less than 55 mm. In the now performed tests this distance

was clearly smaller than 55 mm. New developed formulae (Konrad, 2011) determine the failure load of a shear stud as the minimum of Equations (4) and (5) in combination with the reduction factors given by Equation (6) for open sheeting geometry ⌒⌣⌒.

According to (Konrad, 2011), the reduction factor is controlled by the distance e between the web of the rib and the shear stud. Formally, the procedure is the same as in Eurocode 4 (EN 1994-1-1, 2004): the shear connector resistance in a solid slab is reduced by a reduction factor. However, the dimension of the reduction depends on the position of the stud in the rib, see Equation (6):

- e > 100 mm: favourable position
- 55 mm < e ≤ 100 mm: mid position
- e ≤ 55 mm: unfavourable position

Steel failure:
$$P_{m,s} = k_t \cdot 39.85 \cdot A_{Wulst,eff} \cdot f_{c,cyl}^{\frac{2}{3}} + 0.59 \cdot f_u \cdot d^2 \quad (4)$$

Concrete failure:
$$P_{m,c} = k_t \cdot 39.85 \cdot A_{Wulst,eff} \cdot f_{c,cyl}^{\frac{2}{3}} + 3.75 \cdot d^2 \cdot f_{c,cyl}^{1/3} \cdot f_u^{1/2} \quad (5)$$

Reduction:
$$k_t = k_n \cdot \left(0.084 \cdot \left(\frac{b_m}{h_p}\right) + 0.663\right) \leq 1.00 \text{ („favourable position“)}$$
$$k_t = k_n \cdot \left(0.042 \cdot \left(\frac{b_m}{h_p}\right) + 0.663\right) \leq 1.00 \text{ („mid position“)} \quad (6)$$
$$k_t = k_n \cdot \left(0.317 \cdot \left(\frac{b_m}{h_p}\right) + 0.060\right) \leq 0.80 \text{ („unfavourable position“)}$$

With
- d: Diameter of the shear stud [mm]
- $f_{c,cyl}$: Concrete compressive strength [N/mm²]
- n_r: Number of studs per rib (max. n_r = 2)
- f_u: Tensile strength of the stud [N/mm²]
- $A_{Wulst,eff}$: Bead weld area of the shear stud [mm²]; cf. Table 1
- k_n: 1 if n_r = 1, 0.80 if n_r = 2

Table 1 – Bead weld area of the shear stud of eq. (4) and (5) according to (Konrad, 2011)

Diameter of the stud [mm]	Bead weld area $A_{Wulst,eff}$ [mm²]
16	47.3
19	63.0
22	87.0
25	140.0

1.3 PUSH-OUT TEST RESULTS

Several reports (Aggelopoulos et al., 2016; Kuhlmann, Eggert et al., 2014) present results of numerous push-out tests performed within the DISCCO project. Most tests used ArcelorMittal Cofraplus60 decking representing the open decking geometry. Figures 2a and 2b show exemplarily a push-out specimen at the end of the test as well as its typical failure modes. Beside the delamination of the sheeting, concrete pull-out failure could be observed (top half of Figure 2b). Larger deflections led to an additional rib punch-through failure (bottom half of Figure 2b).

Figure 3 shows the comparison of the push-out test results and the calculated values according to Eurocode 4 (EN 1994-1-1, 2004; Roik et al., 1988) and (Konrad, 2011). The results prove that there is a wide difference between the two calculation approaches when using modern deck profiles with a narrow rib. (Konrad, 2011) slightly underestimates the test results which is safe and conservative. On the other hand, the recalculation using Eurocode 4 (EN 1994-1-1, 2004) overestimates the test results considerably. None of the performed tests is conservative for this comparison, but some tests are extremely unconservative nearly by factor 2 which means that the calculated stud capacity is nearly twice as high as the measured value.

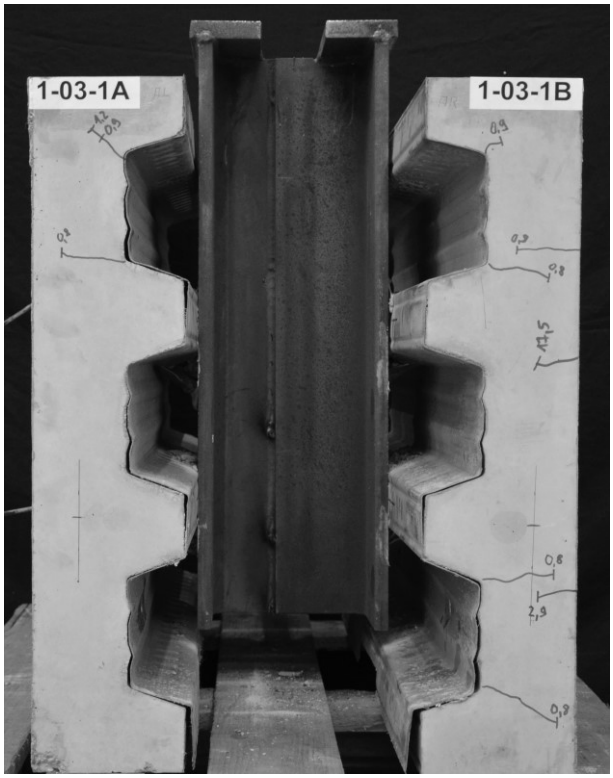


Fig. 2a – Push-out specimen 1-03 after testing (Kuhlmann, Eggert et al., 2014)

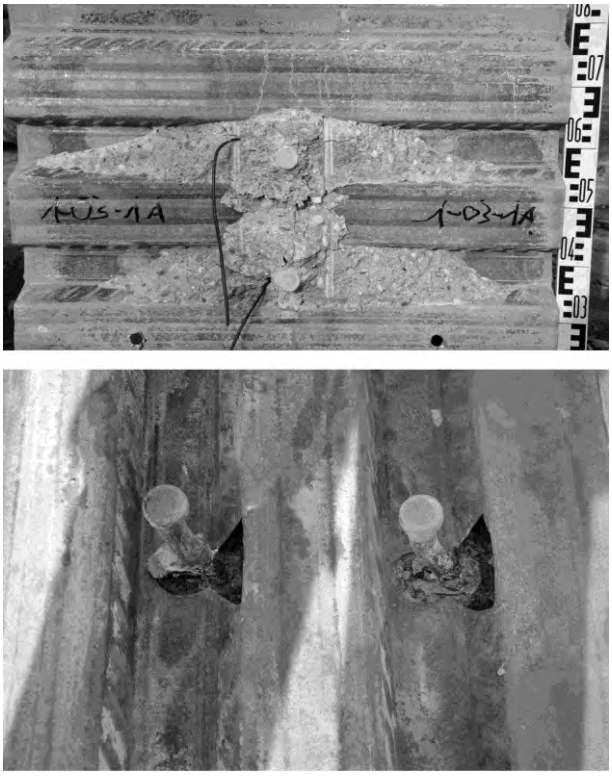


Fig. 2b – Typical push-out failure modes (top: concrete pull-out; bottom: rib punch-through) (Kuhlmann, Eggert et al., 2014)

The currently used approach of Eurocode 4 (EN 1994-1-1, 2004) for the reduction factor k_t was mainly calibrated using undercut decking profiles or open profiles with a wide rib. Therefore, special effects of open decking profiles with narrow ribs – like a reduced bearing capacity caused by a missing concrete strut at the weld bead – are not considered – although the Cofraplus60 decking profile complies with the geometrical specifications of Eurocode 4 (EN 1994-1-1, 2004). Considering these new findings, the authors propose to revise the respecting rules in a future edition of Eurocode 4.

1.3 INFLUENCE OF SPECIAL PARAMETERS ON THE STUD BEARING CAPACITY

1.3.1 WELDING METHOD

According to Eurocode 4 (EN 1994-1-1, 2004), through-deck welding of the studs leads to an increase of the stud bearing capacity of about 13% in contrast to composite slabs using prepunched decking. (Konrad, 2011) estimates an increase of about 11% based on a numerical

parametric study. The performed tests showed an increase of about 22% when studs were through-deck welded compared with stud welded directly on the flange of the steel beam.

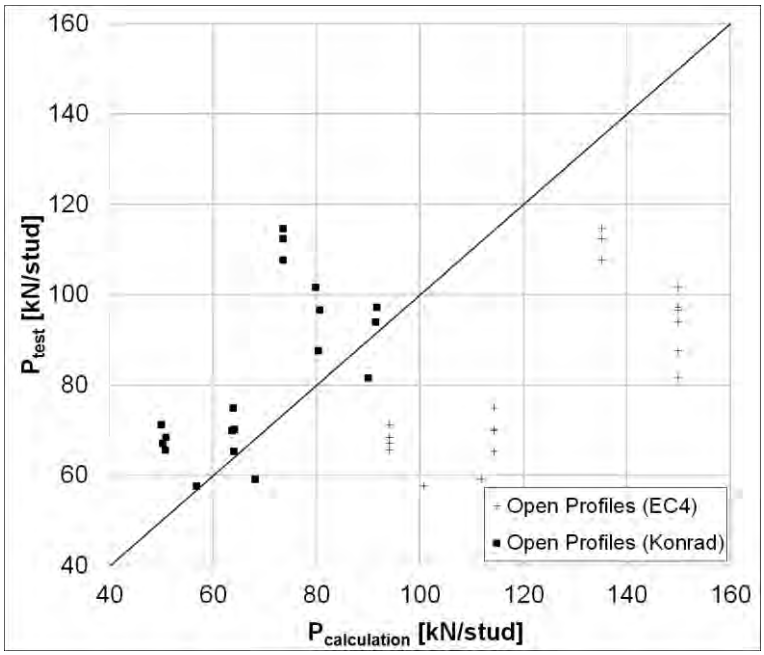


Fig. 3 – Comparison of the push-out test results to different calculation approaches

1.3.1 NUMBER OF STUDS PER RIB

If shear studs are placed too close together, the influencing concrete zones might overlap which may lead to a decrease of the load bearing capacity. Therefore, Eurocode 4 reduces the capacity per stud by the factor $1/\sqrt{n_r} = 1/\sqrt{2} = 0.71$ (cf. Equation (3)) for a minimum stud distance of 4*d. (Konrad, 2011) improved this factor to 0.80 – based on numerical studies. The now performed tests with 5*d showed, that the reduction per stud was only about 2.5%. This proves, that the improved reduction factor of Konrad is more realistic for open decking geometries.

1.3.2 STUD DIAMETER

Both Eurocode 4 (EN 1994-1-1, 2004) and (Konrad, 2011) assume that the load bearing capacity of a stud is proportional to the square of its diameter. This would lead to an increase of about 34% when using a diameter 22 mm stud instead of a 19 mm one. Although the tests were performed with narrow ribs, an increase of about 65% could be observed. Therefore, the rules of (EN 1994-1-1, 2004) as well as (Konrad, 2011) are conservative and on the safe side for narrow open decking geometries.

1.3.3 POSITION OF REINFORCEMENT LAYERS

Current standards do not provide any information about the influence of the reinforcement on the ductility behavior of composite beams. Therefore, some push-out tests were carried out only with a single reinforcement layer on top of the slab and some with an addition layer positioned directly at the top of the metal deck sheeting as required in (EN 1994-1-1, 2004). The load slip curves

showed that two layers of reinforcement increase the ductility behavior nearly by factor 2 but do not influence the bearing capacity itself significantly.

1.3.4 CONCRETE QUALITY

According to Eurocode 4 (EN 1994-1-1, 2004), the load bearing capacity is in proportion to the square root of the concrete compressive strength. Numerical investigations of (Konrad, 2011) showed a depending on $\sqrt{f_c^{2/3}}$. Applied on the actual measured concrete compressive strengths 40 N/mm² and 46 N/mm², Eurocode 4 predicts an increase of 7%; Konrad's equations led to an increase of 11% which fits very well with the measured increase of about 11%.

1.3.5 INFLUENCE OF CONCRETE RELAXATION

Although push-out tests are performed quasi-static, the influence of the loading speed (0.01 mm/s) on concrete relaxation behavior shouldn't be neglected. Numerous relaxation load drops were provoked by keeping the deflection constant for 5 minutes. During this time, the concrete relaxed and the load decreased. The German National Annex of Eurocode 4 (DIN EN 1994-1-1/NA, 2010) considers this effect by increasing the partial factor γ_v for Equation (2) from 1.25 to 1.50 which implies a reduction of the failure load of about 16%. The now determined relaxation was in the range of 10%.

2 BEAM TESTS

2.1 TEST SETUP

Within the European research project DISCCO (Aggelopoulos et al., 2016) 8 beam tests (ST 1 – ST 8) were performed using open Cofraplus60 decking. The beam design was derived from corresponding push-out tests. The beams had a length of 5 m and the tests were performed as four-point bending tests. Therefore, the shear studs of the outer – 1.80 m long – areas were predicted to take shear force at the same level (cf. Figure 4). The rib distance of the decking limited the number of shear studs. 8 (single positioning) or 16 (pairwise positioning) shear studs per shear stressed area led to very low degrees of shear connection. In addition, the beams were designed to fail first by shear failure in the composite joint before bending failure occurred. To connect directly to the push-out tests, the same parameters were investigated in the beam tests, see Chapter 1.3.

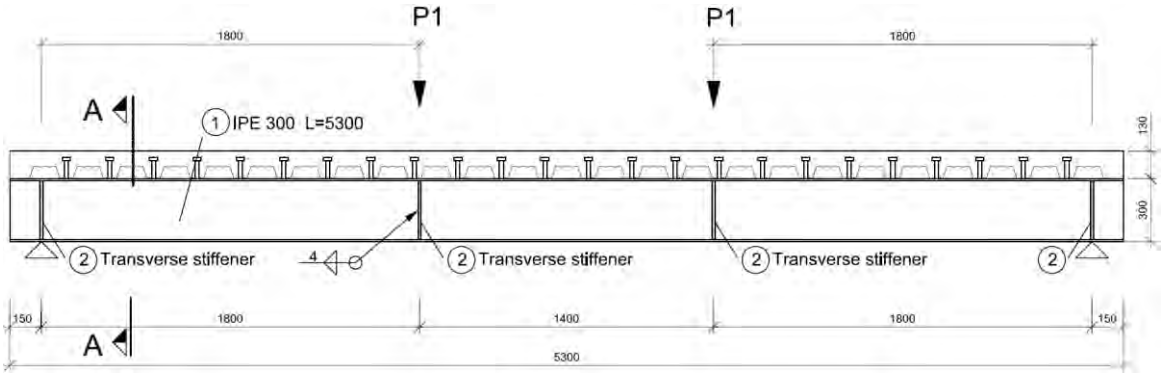


Fig. 4 – Structural system of the DISCCO composite beam tests (Aggelopoulos et al., 2016)

2.2 TEST PROCEDURE

The beam tests were performed following the Eurocode 4 (EN 1994-1-1, 2004) guidelines for push-out tests. Especially, 25 load cycles were carried out, before the actual test started, to eliminate influences of friction as best as possible. All tests were performed deflection-controlled running 1 mm/min. In addition, the tests were stopped in intervals of about 5 mm vertical deflection to capture the influence of concrete relaxation. Beside the vertical deflection, the development of slip was measured as well as strains of concrete and steel beam. Figure 5 exemplarily shows the load-deflection graph of beam test ST 1. The pre-loading cycles can be identified as well as the load drops caused by concrete relaxation. The influence of concrete relaxation was determined to 4-6% in average. After having reached the maximum load, the load of all beams decreased very slowly which shows the very ductile behavior of the investigated beams. Figure 6 exemplarily shows beam test ST 1 during testing.

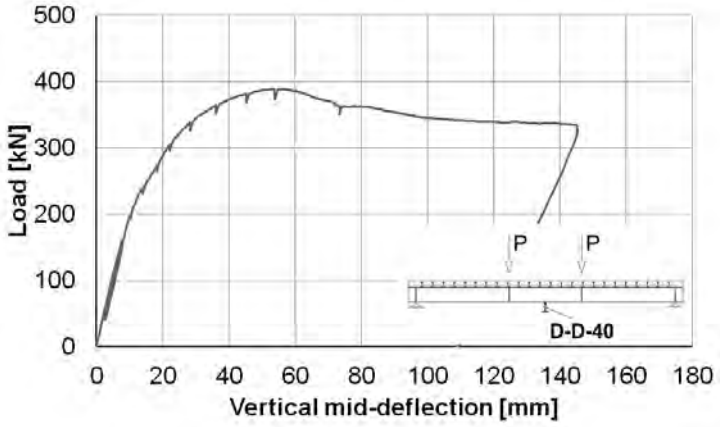


Fig. 5 – Load-deflection graph of the beam test, exemplarily shown for test ST 1 (Eggert and Kuhlmann, 2016)



Fig. 6 – Composite beam ST 1 during test realization (Aggelopoulos et al., 2016)

2.3 TEST RESULTS AND TEST EVALUATION

Shear studs need to be sufficiently ductile to resist the occurring shear forces when performing a plastic analysis of a composite beam. According to Eurocode 4, clause 6.6.1.2 (EN 1994-1-1, 2004), shear studs can be regarded as ductile if the degree of shear connection satisfies Equation (7). It is known that shear studs within a rib have a larger deformation capacity as studs in solid slabs. In this case, shear studs can also be regarded as ductile, if Equation (8) can be satisfied which is a bit more optimistic. As a lower limit, Eurocode 4 (EN 1994-1-1, 2004) gives a minimum degree of shear connection of 40%.

Using Equation (8) is only possible in compliance with the following criteria of Eurocode 4 (EN 1994-1-1, 2010):

- the studs have an overall length after welding not less than 76 mm, and a shank of nominal diameter of 19 mm,
- the steel section is a rolled or welded I or H with equal flanges,

- the concrete slab is composite with profiled steel sheeting that spans perpendicular to the beam and the concrete ribs are continuous across it,
- there is one stud per rib of sheeting, placed either centrally within the rib or alternately on the left side and on the right side of the trough throughout the length of the span,
- for the sheeting b_m / h_p ≥ 2 and h_p ≤ 60 mm (see Figure 1),
- the force N_c is calculated in accordance with the simplified method of Eurocode 4.

$$\eta \geq 1 - \left(\frac{355}{f_y}\right)(0.75 - 0.03L_e) \text{ and } \eta \geq 0.4 \quad (7)$$

$$\eta \geq 1 - \left(\frac{355}{f_y}\right)(1.00 - 0.04L_e) \text{ and } \eta \geq 0.4 \quad (8)$$

With: L_e = Equivalent span [m] and f_y = Yield strength of structural steel [N/mm²]

Using Cofraplus60 decking it was not possible to satisfy the geometrical criterion, because the ratio b_m / h_p is only 1.4 and therefore clearly below the given limit. In addition, some of the tests used pairs of shear connectors per rib or studs with a diameter of 22 mm.

Because of this according to Eurocode 4, Equation (7) should be used instead of Equation (8). According to Equation (7), the minimum degree of shear connection is 44.4%. Equation (8) leads to a minimum degree of shear connection of only 25.8%. But Equation (8) is also limited to a minimum degree of shear connection of 0.4 = 40%.

The degree of shear connection of the beam tests were determined to 16% up to 37.9%. Thereby, all tests showed a degree of shear connection below the Eurocode 4 (EN 1994-1-1, 2010) limit. All performed tests didn't satisfy the Eurocode 4 rules and therefore, none of the tests may be calculated using the plastic analysis including partial interaction, as described in Eurocode 4 (EN 1994-1-1, 2004).

Although the beams didn't satisfy the guidelines, all beam tests were recalculated using Eurocode 4 plastic analysis method for partial interaction. The stud bearing capacity is one of the most influencing parameters of this method. Therefore, this parameter was considered in three versions:

- stud capacities of own corresponding push-out tests ("WP1"),
- according to Equations (1) – (3) of Eurocode 4 (EN 1994-1-1, 2004)
- according to Equations (4) – (6) of (Konrad, 2011).

Table 2 – Results of the recalculation of the beam tests: $M_{test}/M_{calculation}$ and belonging degrees of shear connection in [%]

	ST 1	**ST 2**	**ST 3**	**ST 4**	**ST 5**	**ST 6**	**ST 7**	**ST 8**	**Average**
„WP 1"	0.96 (23.4)	1.02 (19.4)	*0.83 (46.2)*	0.98 (41.1)	0.92 (32.6)	0.96 (31.2)	0.94 (38.1)	1.06 (19.7)	0.98
Konrad	0.94 (25.9)	0.95 (25.7)	*0.85 (41.5)*	0.98 (41.1)	0.91 (33.6)	0.95 (33.6)	0.93 (40.2)	0.96 (29.7)	0.95
Roik / EC4	0.85 (41.3)	0.86 (41.3)	*0.78 (58.5)*	0.90 (58.5)	0.82 (55.4)	0.85 (55.4)	0.87 (55.4)	0.90 (41.3)	0.86

Table 2 shows the results of the determined moment bearing capacities related to the calculated values $M_{test}/M_{calculation}$ as well as the belonging degrees of shear connection. M_{test} means the plastic bending moment considering the partial interaction including measured material strengths. Figure 7 compares the results in a graphical presentation. Values directly on the bisecting line would mean a full accordance of test result and calculation.

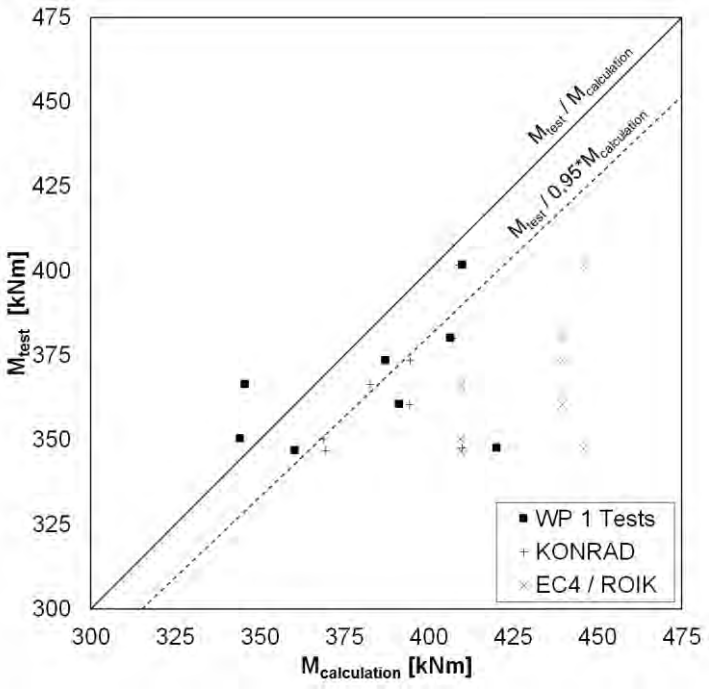


Fig. 7 – Graphical comparison of the results of the recalculation of the beam tests (Eggert and Kuhlmann, 2016)

The mean values of Table 2 are determined neglecting the results of beam test ST 3. This composite beam used pairwise through-deck welded shear studs. Because of a bad quality of the welding the shear studs couldn't achieve their full load-bearing capacity. It should be noted that the quality of through-deck welding is very sensitive to several influencing factors – especially if studs are not welded centric on the beam – as it is the case for pairs of studs that are placed eccentric on the flange of the beam. The eccentric welding position and incomplete contact of decking and steel beam may cause an incorrect magnetic field, which may lead to imperfections of the welding and therefore reduced stud capacities.

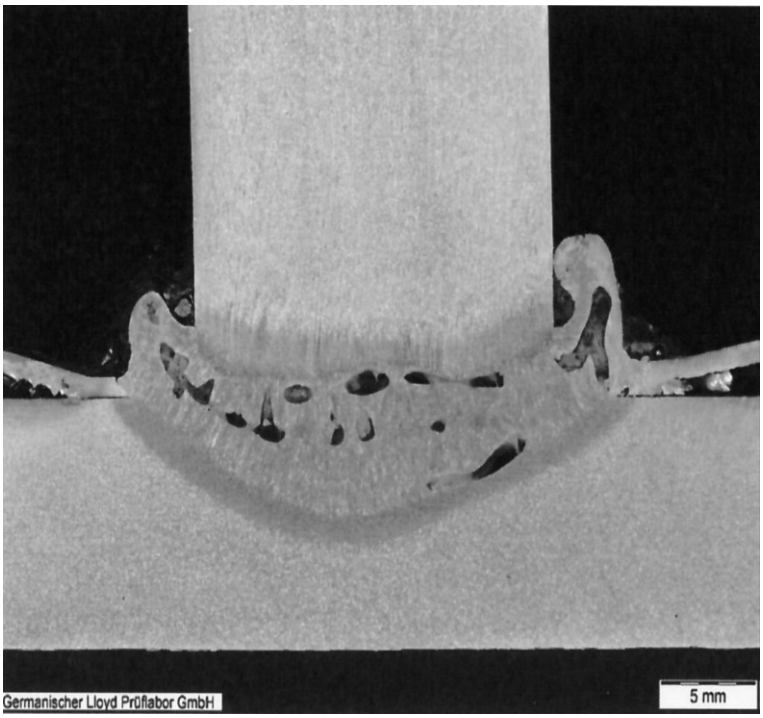


Fig. 8 – Welding imperfections of eccentric positioned through-deck welded studs (Aggelopoulos et al., 2016)

Comparisons using "WP1" stud capacities lead to mean value of $M_{test}/M_{calculation} = 0.98$. Using equations of (Konrad, 2011) leads to a mean value of 0.95. This means a very good accordance of test and calculation. As 100% of the calculated plastic moment bearing capacity comes along with very high strains in the concrete, it is hard to reach this in a test. Therefore, $M_{test}/M_{calculation} = 0.95$ is considered sufficient for the assessment of M_{pl}. The results of the recalculation (cf. Figure 7 and Table 2) clearly show that the "95%-criterion" is reached or even exceeded. However, predictions using

stud capacities of Eurocode 4 on the mean level (Roik et al., 1988) clearly overestimate the test results. None of the tests reaches the “95%-criterion”. Therefore, this calculation approach should be improved, though of course, the comparison is not made with design values. It may be assumed that the safety margin, included in the existing statistical evaluation of (Roik et al., 1988), is not satisfying for the presented problems.

2.4 FURTHER INVESTIGATIONS

Based on the test results, a numerical model was created using SOFiSTiK finite element software (SOFISTIK, 2014) to investigate further parameters and especially have a look at the development of slip depending on several parameters.

One of the main results of this study describes the relation of slip and vertical mid-deflection of the beam. The lower the degree of shear connection the larger is the vertical deflection of the beam. Therefore, in most of the cases the design of the beam is controlled by SLS and not ULS.

The parametric study on single span composite beams (Eggert, 2019; Mahler, 2016) showed that the development of slip can be divided into three main parts. First, all elements of the composite beam behave elastically. Then, the outermost studs close to the support of the beam reach their bearing capacity which leads to a “kink” in the load-slip diagram (cf. Figure 9). When all studs have reached their maximum load, the steel beam starts to yield and the concrete reaches the compression strength which finally leads to the failure (plastic hinge) of the composite beam.

The current Eurocode 4 (EN 1994-1-1, 2004) gives no precise deflection limit for composite beams. Eurocode 2 (EN 1992-1-1, 2004) and a pre-standard of Eurocode 3 (ENV 1993-1-1, 1992) limit the deflection of slabs and beams to l/250. Most of the available shear connectors (e.g. headed studs, Hilti X-HVB shear connectors, Arcelor Mittal COSFB concrete dowels) have a deformation capacity of at least 6 mm.

To understand better the load-slip development of a composite beam, several parameters were identified that have a large influence on the development of slip. Based on previous work of (Johnson and Molenstra, 1991), the length to depth ratio was identified as one of the most influencing parameters on the load-slip behavior. Figure 9 exemplarily shows an excerpt of the parametric study showing the results of several composite beam configurations having a length/depth ratio of 18 and a degree of shear connection of 30%, which is significantly below the restrictions of Eurocode 4.

The results of this partial result of the study clearly shows that the deflection criterion l/250 is reached at an end slip of only 2.5 mm. So, there is no danger of a premature shear connector failure when designing the composite beam in compliance with the deflection criterion. Even the steel beam is still in an elastic state at this point which is the same for most of the investigated cases.

3 CONCLUSIONS

Within the European research project DISCCO (Aggelopoulos et al., 2016) the realistic behavior of some versions of modern composite beams with profiled sheeting was investigated. The results of the conducted beam tests showed that in some cases the failure load was clearly lower than expected by the equations given in Eurocode 4 (EN 1994-1-1, 2004). Although the minimum degree of shear connection in Eurocode 4 (EN 1994-1-1, 2004) is defined as a limit of the occurring slip, it could be shown that going below this limit is possible using sufficiently ductile shear connectors.

The exact knowledge of the stud bearing capacity is a basic requirement for a good quality of the prediction of the moment bearing capacity of composite beams with partial interaction. The current approach of Eurocode 4 (EN 1994-1-1, 2004) is not a satisfying solution because of an incorrect reduction factor k_t when using the new generation of open decking. New design approaches or the use of stud capacities gained from corresponding push-out tests lead to very good results.

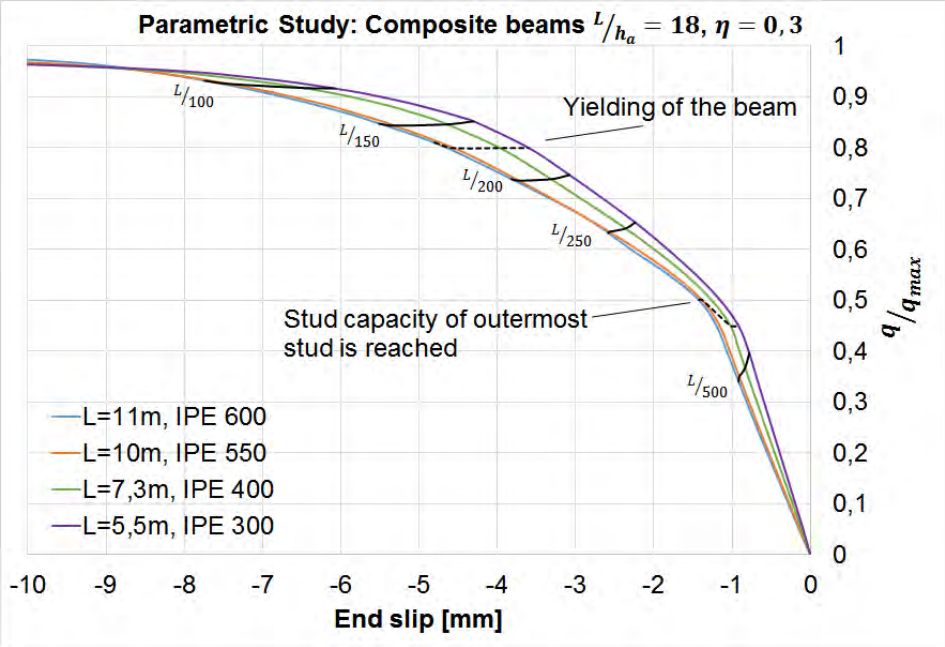


Fig. 9 – Numerical parametric study: Load ratio q/q_{max} vs. end slip (Eggert, 2019)

Furthermore, it could be shown that a plastic analysis of composite beams with low degrees of shear connection is possible, although the requirements of the code concerning the minimum degree of shear connection were not satisfied. The evaluation of the tests showed that the current restrictions – concerning decking geometry as well as the limit of the minimum degree of shear connection – are very conservative which makes it hard to realize composite structures in an economical way, although a sufficient beam capacity could be proved by the tests. Further investigations regarding the occurring slip are used in (Eggert, 2019) to show new design approaches.

4 ACKNOWLEDGEMENTS

The research leading to these results was part of a common project of the Steel Construction Institute, University of Stuttgart, University of Luxembourg, University of Bradford, and ArcelorMittal. We thank all involved colleagues for the good cooperation and the professional exchange. The project received funding from the European Community's Research Fund for Coal and Steel (RFCS) under grant agreement RFSR-CT-2012-00030.

5 REFERENCES

Aggelopoulos, E. S., Lawson, R. M., Kuhlmann, U., Eggert, F., Odenbreit, C., Nellinger, S., Lam, D., Dai, X., Sheehan, T. and Obiala, R. (2016). *Development of Improved Shear Connection Rules in Composite Beams (DISCCO)*, Final Report, RFCS Project No. RFSR CT 2012-00030.

Eggert, F. (2019): *Influence of the composite action on the load-bearing and deflection behavior of composite beams with and without additional steel sheeting*, PhD Thesis; Institute of Structural Design, University of Stuttgart, Issue 2019-1, ISSN 1439-3751.

Eggert, F., Kuhlmann, U. (2016). *Influence of the degree of shear connection on the load-bearing behavior of composite beams with additional profiled steel decking*. In: Stahlbau, 85, 7. pp. 459–465 (2016).

DIN EN 1994-1-1/NA (2010). *National Annex – Eurocode 4: Design of composite steel and concrete structures – Part 1-1: General rules and rules for buildings.*

EN 1992-1-1 (2004). *Eurocode 2: Design of concrete structures – Part 1-1: General rules and rules for buildings*; German version: DIN EN 1992-1-1:2004 + AC:2010.

ENV 1993-1-1 (1992). *Eurocode 3: Design of steel structures; Part 1.1 – General rules and rules for buildings*; German version: DIN ENV 1993-1-1:1993.

EN 1994-1-1 (2004). *Eurocode 4: Design of composite steel and concrete structures – Part 1-1: General rules and rules for buildings*; German version DIN EN 1994-1-1:2004 + AC:2009.

Johnson, R. P., Molenstra, N. (1991). *Partial shear connection in composite beams for buildings*. In: Proceedings of the Institution of Civil Engineers - Structures and Buildings, Part 2, Bd. 91. pp. 679–704 (1991).

Konrad, M. (2011). *Load-bearing behavior of headed studs in combination with composite slabs with additional steel sheeting spanning transverse to the supporting*, PhD Thesis; Institute of Structural Design, University of Stuttgart, Issue 2011-1, ISSN 1439-3751.

Kuhlmann, U., Eggert, F., Odenbreit, C., Nellinger, S. (2014): *Push-out tests with modern deck sheeting to evaluate shear connector resistances*. In: Eurosteel 2014, 7th European Conference on Steel and Composite Structures, Naples, Italy, pp. 519–520.

Kuhlmann, U., Konrad, M. (2009). *Bearing capacity of headed studs when using profiled sheeting*. University of Stuttgart, Institute of Structural Design, No. 2009-1X, DIBt research project ZP 52-5-17.20-1260/07, Fraunhofer IRB-Verlag.

Kuhlmann, U., Konrad, M. (2010). *Guarantee of sufficient load-bearing capacity of headed studs when using profiled sheeting*. University of Stuttgart, Institute of Structural Design, No. 2010-3, DIBt research project ZP 52-5-17.20-1287/08, Fraunhofer IRB-Verlag.

Kuhlmann, U., Raichle, J. (2006). *Shear strength of composite beams when using additional steel sheeting according to Eurocode 4, Part 1.1*, Research report; University of Stuttgart, Institute of Structural Design, No. 2006-9X.

Mahler, F. (2016). *Numerical investigations on the load-slip behavior of composite beams with low degree of shear connection*, Master Thesis; University of Stuttgart, Institute of Structural Design, No. 2016-44X.

Nellinger, S. (2015). *On the Behavior of Shear Stud Connections in Composite Beams with Deep Decking*, Dissertation; The Faculty of Sciences, Technology and Communication, Université du Luxembourg.

Rambo-Roddenberry, M.D. (2002). *Behavior and strength of welded shear stud connectors.* Virginia, Virginia Polytechnic Institute and State University, PhD Thesis.

Roik, K., Hanswille, G., Cunze, A., Lanna, O. (1988). *Background document on Eurocode 4 - Clause 6.3.2: Stud connectors*, Ruhr-University Bochum. Research report.

SOFiSTiK AG: *SOFiSTiK Version 2014, Finite Element Software.*

EFFECT OF POST-WELDING RESIDUAL STRESSES ON DISTORTIONAL BUCKLING OF COMPOSITE BEAMS

Marian A. Gizejowski
Warsaw University of Technology, Faculty of Civil Engineering, Warsaw, Poland
m.gizejowski@il.pw.edu.pl

Radoslaw Szczerba
r.szczerba@il.pw.edu.pl

Marcin Gajewski
m.gajewski@il.pw.edu.pl

Wioleta Barcewicz
w.barcewicz@il.pw.edu.pl

ABSTRACT

Welded steel-concrete composite beams with large openings are nowadays more frequently used for commercial applications in multi-storey buildings. The openings may be placed in a regular spacing along the beam length or only at certain locations leaving the full webbed sections in zones where they are not requested from the structural or functional purposes (for services passing through the beam depth). With regard to the optimum integration of load bearing structures and services, continuous or semi-continuous composite web perforated beams may be used. Such beams demonstrate at the hogging moment much weaker behavior against distortional buckling in comparison with their plain-webbed counterparts. This paper discusses different techniques for finite element modeling of the effect of post-welding residual stresses on distortional buckling resistance of steel-concrete composite beams in reference to a different arrangement of web openings. The results of verification and validation exercise of proposed modeling technique are also summarized hereafter.

INTRODUCTION

Thin-walled I-section steel-concrete composite beams are in hogging bending zones susceptible to lateral, lateral-torsional or torsional distortional buckling of the structural steel section flange that is not restrained by the reinforced slab. The buckling resistance of I-section rolled plain-webbed composite beams subjected to hogging bending had been well researched so that corresponding design procedures were proposed and codified (Eurocode 4, 2004). However, in modern applications of composite beams, they are made of welded thin-walled I-sections with larger openings than those in castellated beams made out of steel rolled sections. Welded thin-walled sections inherit material and geometric imperfections as a result of their fabrication process. The effect of such imperfections on the distortional buckling of composite beams may be modeled with use of the finite element method and available commercial software. In research carried out at the Warsaw University of Technology, the effect of residual stresses was

considered implicitly by using a single parametric equivalent constitutive model of post-welded steel (Gizejowski, Salah and Barcewicz, 2008c). The shape of adopted equivalent curvilinear relationship σ-ε is dependent upon the model parameter n [cf. eqn. (1) in this paper]. Its value may be approximated by using the inverse modeling technique, either by fitting the experimental equilibrium path of the welded full scale specimen or by fitting the experimental results from the stub test of the short length plate girder of the same welded section size as the full scale specimen, depending upon the problem being under consideration. This model was successfully applied for the numerical evaluation of buckling resistance of composite beams (Gizejowski and Salah, 2008a). Geometric imperfections were considered independently adopting their profile to be the lowest buckling mode from LBA with the amplitude scaled to conform with the maximum web bulging deflection of fabricated steel section. Reinforced concrete was modeled using smeared crack model adopted in ABAQUS software (ABAQUS, 2011a and 2011b). The developed finite element model of the composite beam behavior was validated with use of results of experimental investigations on long- and short-length composite beams (Gizejowski and Salah, 2008b). The parameter of steel equivalent constitutive model was calibrated in such a way that the validated finite element model represented the most accurately the equilibrium paths of experimentally tested beams. The entire investigations considering the other aspects of the composite beam behavior were then presented as a Ph.D. thesis (Salah, 2009).

There are several ways of modeling the contributing effects of post-welding residual stresses as well as the reinforced concrete slab stiffness degradation and inelastic stress redistribution processes on the buckling resistance of composite beams. In this paper, an alternative finite element modeling technique to that of (Salah, 2009) is proposed in which geometric imperfections are introduced first and then the residual stresses are superimposed and modeled through a direct application of the residual stress block to a geometrically imperfect beam model. The shape of stress block is predefined and based on the experimental evidence. The goal of above mentioned two stages of analysis is to identify the initial self-equilibrated state of the structural steel product in order to determine its initial configuration prior to assembling it for a full-scale composite beam to be analyzed for the mechanical response to applied loads. Finite element analysis deals with the response of two specimens of composite beams tested experimentally (Gizejowski and Salah, 2008b) and (Salah, 2009). Investigations were concerned with distortional buckling and post-buckling behavior of specimens consisting of the plain-webbed span and the overhanging part with a different number of circular openings. The created numerical models are then validated using the results recorded in experiments. Different ways of modeling the effect of residual stresses on the beam response are discussed. As the reference, the other four specimens were analyzed, two with plain webbed girder and two girders with openings in both the span and the overhang. The summary of predicted buckling strength is presented and conclusions for engineering practice are drawn.

SCOPE OF INVESTIGATIONS

Figure 1 shows the composite beams tested experimentally, C2S355 and C4S355, that are considered hereafter for numerical investigations and validation of the proposed finite element modeling technique. Beam specimens consisted of steel welded girders that were compositely connected to the reinforced concrete slab with a use of commercial steel studs welded to the beam upper flange. The steel girders were assembled in one product by MAG automatic welding of three plates, the prefabricated web plate of 4 mm in thickness the openings of which had been made by laser cutting and two flange plates of 6 mm in thickness. Prior to welding, the maximum geometric out-of-flatness imperfections of the perforated web plate were measured by the manufacturer and used in numerical modeling for scaling the amplitude of geometric imperfection profile. The beam section was reinforced in the three locations corresponding to

the points of concentrated load transfer, i.e. at the load application and support points. The welded steel girder was then equipped with shear studs M12 and the reinforced slab of a constant width as shown in Figure 1a). The side view of specimens is also shown in Figure 1, for the short span specimen in Figure 1b) and the long span one in Figure 1c). The steel grades applied were S 355 for the structural steel, A-III (A400) for the rebars, S 520 for the studs, their measured average mechanical properties are given in Table 1. Concrete strength class C35/45 was used for the composite beam slab the actual compressive and tensile strength properties of which were derived from standard material tests. The average concrete properties are given in Table 2. The Young modulus for steel and concrete are taken hereafter at their nominal values.

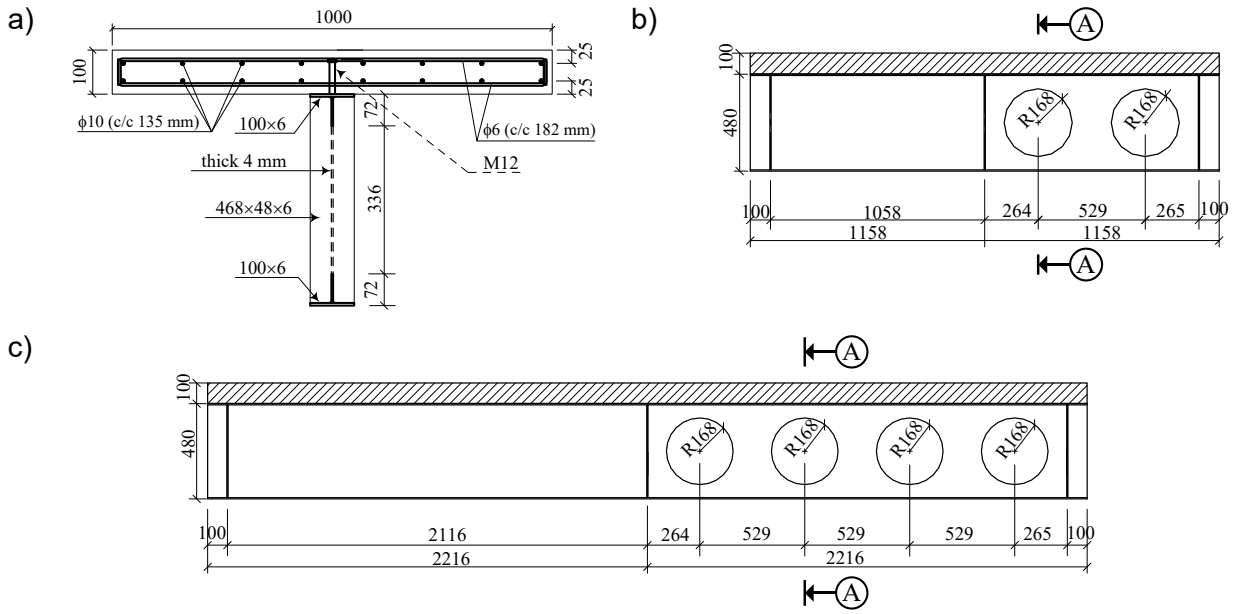


Fig.1 – Composite beams tested experimentally, a) cross section, b) short span beam, c) long span beams

Table 1 - Measured steel average properties of composite beam

Steel for	Yield stress f_y *)	Ultimate strength f_u *)	Hardening strain ε_{har} *)	Ultimate strain ε_u *)
Beam plates	391.4	506.8	1.42	16.0
Shear studs	611.3	662.5	-	-
Main rebars	459.6	608.0	0.22	15.7
*) in N/mm^2, **) in %				

Table 2 - Measured concrete average properties of composite beam slab

Concrete for	Age on the test day	Cube compression strength*)	Tension strength*)
Long span beam	46	56.5	4.7
Short span beam	40	46.6	3.8
*) in N/mm^2			

The sketch of specimen placement in the test stand is shown in Figure 2. The load is distributed over an area of the slab and the slab is additionally reinforced there in order to avoid the local concrete failure. The support closer to the applied load ensures a linear contact between the beam bottom flange and the roller. The support placed away from the applied load was uplifted so that an additional frame-to-floor resisting structure had been designed that elastically supported the specimen in order to transfer the resultant uplifting reactive force. In numerical modeling, the translational springs in the direction of gravity force are applied covering the area of contact between the upper flange and the rafter of the frame-to-floor resisting structure.

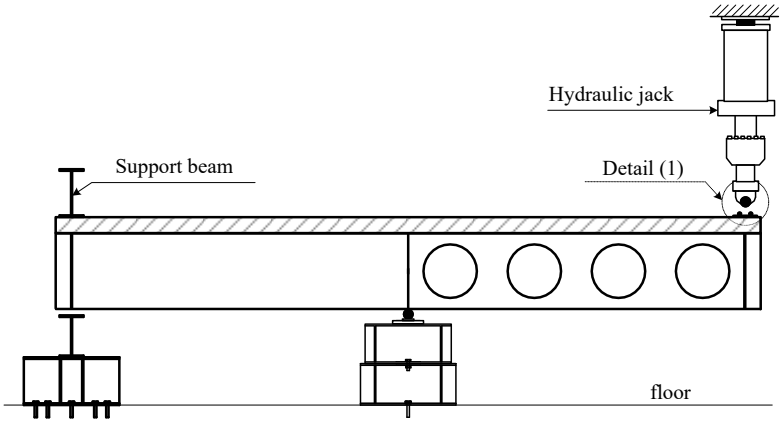


Fig. 2 – Arrangement of testing stand and beam specimen

NUMERICAL MODEL

Structural steel, rebars and studs

Typical multi-linear uniaxial stress-strain relationships for the girder steel grade of S 355 are given in Figure 3, IEP with nominal values and EXP with actual values of mechanical properties. IEP model is used also for rebars and studs.

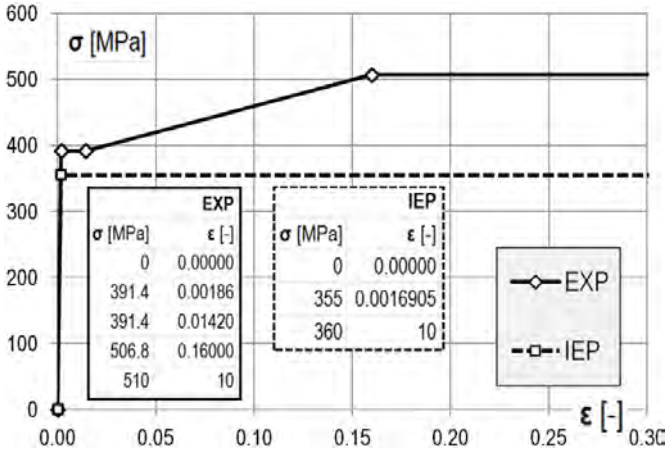


Fig. 3 – Standard stress-strain relationships for parent steel

The constitutive model of steel in the beam girder is dependent upon the modeling technique of the effect of residual stresses. In the case of implicit residual stress modeling, the concept of

equivalent isotropic hardening constitutive model (CUR) of post-welded steel used in (Gizejowski and Salah, 2008a) and (Salah, 2009) is followed hereafter. The parametric stress-strain relationship for such a model is given by:

(1) $$\sigma = \left[\left(\frac{1}{E\varepsilon} \right)^n + \left(\frac{1}{f_{y,red} + E_{st}\varepsilon} \right)^n \right]^{-1/n}$$

where:

(2a,b) $$f_{y,red} = f_y - E_{st}\varepsilon_{st} \qquad , \qquad E_{st} = \frac{f_u - f_y}{\varepsilon_u - \varepsilon_{st}}$$

Figure 4 presents the graphical representation of eqn. (1) for different values of n parameter. The parameter n is to be calibrated in order to represent the experimental equilibrium path in numerical simulations as close as possible. The simulations presented in (Salah, 2009) were conducted using such a model together with the smeared crack model available in ABAQUS. The values of n between 2 to 4 were shown for representing the best fit of numerical equilibrium paths to those obtained from experimental investigations.

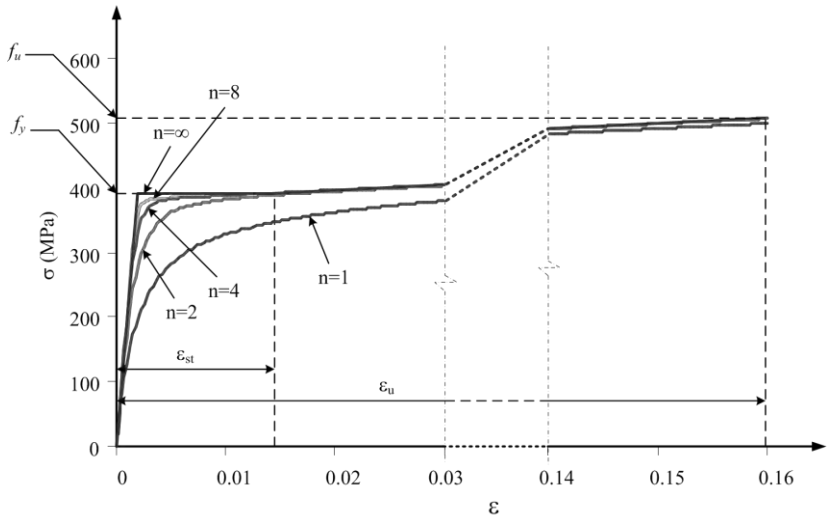


Fig. 4 – Equivalent isotropic hardening constitutive model

The other modeling of the residual stress effect on the structural behavior of composite beams is based on the explicit modeling of residual stress distribution. A number of investigations have been conducted for welded sections in order to come up with a standard section residual stress distribution diagram for plain webbed steel girders (Gizejowski, Szczerba and Gajewski, 2017). Such a parametric residual stress block being dependent upon the type of welding process through the parameter c_w is given in Figure 5. Tensile residual stresses are taken as equal to the nominal yield stress of parent steel while the compressive residual stresses are equal to the factored yield stress in which the flange and web factors are given by:

(3) $$\psi_1 = \frac{2\,c_2}{b - 2\,c_2}, \qquad \psi_2 = \frac{2 \cdot \left(c_{fw} + 0.5\,t_f \right)}{h_w + t_f - 2 \cdot \left(c_{fw} + 0.5\,t_f \right)}$$

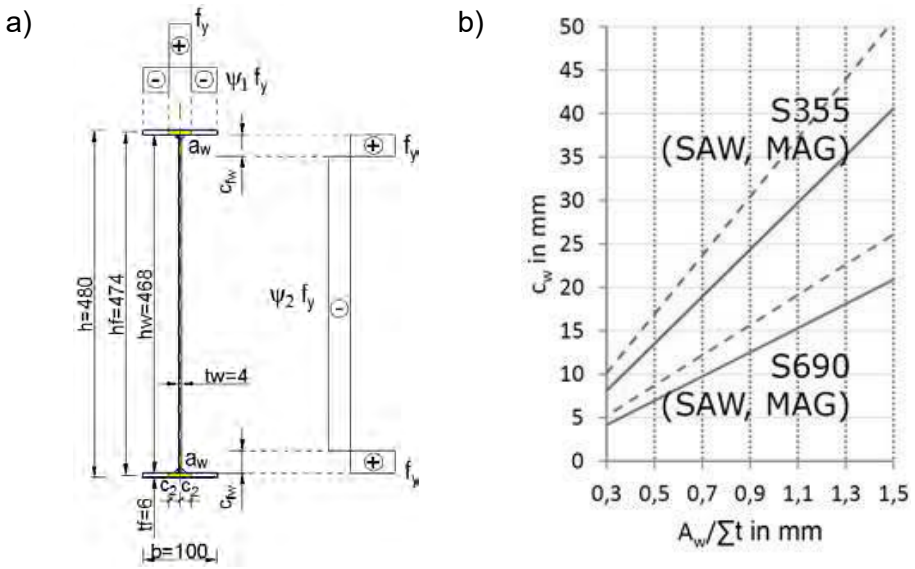


Fig. 5 – Standard residual stress distribution, a) parametric stress block, b) diagram for c_w

For the weld thickness a_w=3.5 mm, there are $\frac{A_w}{\sum t} \approx 0.8\,\text{mm}$, $c_w = \frac{12000 \cdot p}{f_y} \cdot \frac{A_w}{\sum t}$ (p = 0.8 for MAG) and $c_{fw} = c_w$, $c_2 = c_w + 0.5\,t_w$. The stress block geometric parameters calculated are $c_{fw}+0.5t_f$=23.6 mm, c_2=22.7 mm, ψ_1=0.83 and ψ_2=0.11. The application of residual stresses applied together with the tri-linear parent steel constitutive model given in Figure 3 implies dealing with the material anisotropy.

Concrete

Numerical models of reinforced concrete using ABAQUS software are usually based on the models of Concrete Smeared Crack (CSC) or the Concrete Damage Plasticity (CDP). The former one was used in (Gizejowski and Salah, 2008b) and (Salah, 2009). Smeared Crack model represents cracked concrete as an elastic orthotropic material with reduced elastic modulus in the direction normal to the crack plane. With this continuum approach, the local displacement discontinuities at cracks are distributed over some tributary area within the finite element and the behavior of cracked concrete can be represented by average stress-strain relations. In contrast to the discrete crack model, the continuity of the displacement field remains intact in CSC model. Adopting such an approximation of discrete nature of concrete cracking, some model parameters need to be calibrated as not having the physical meaning in order to get a better reproduction of the experimental equilibrium path of composite beams with openings (Salah, 2009). The CDP model is therefore claimed nowadays of being more practically related since its major parameters may be directly derived from material testing while the secondary parameters may be taken as default values for certain concrete classes (Kaminska and Szwed, 2015). The CDP constitutive model is described in ABAQUS manuals (ABAQUS, 2011a and 2011b) and discussed in many papers. The most crucial point for CDP is the parameter determination, cf. (Jankowiak and Lodygowski, 2005) and (Szczecina and Winnicki, 2015). Here some of the data is assumed on the basis of the tests conducted on concrete samples like compression test and Brazilian test (see Table 2), while the rest is evaluated on the literature basis.

In Table 3, the parameters assumed for concrete in case of the tested long span beam are fully presented. The physical data is always extended for abnormally large strains to provide convergence in case of local strain concentrations. It is worth to underline here that the convergence of full composite beam models is dependent mainly upon the concrete behavior. The concrete slab is locally heavily loaded through the studs what causes the stress and strain concentrations and activates the yield condition just from the beginning of the load incrementation.

Table 3 - Assumed parameters of CDP (long span beam), cf. (Kaminska and Szwed, 2015) and (Jankowiak and Lodygowski, 2005)

Material's parameters	Concrete	Yield condition shape	
		m	0.1
Elasticity		β	31^{o}
E [GPa]	36.0	f_{b0} / f_c	1.16
ν	0.167	γ	0.66
Compression hardening		Compression damage	
Stress [MPa]	Crushing strain [-]	d_c [-]	Crushing strain [-]
55.0	0.00	0.00	0.00
56.5	0.001	0.70	0.01
40.0	0.01	0.95	10.0
20.0	0.1		
5.0	10.0		
Tension stiffening		Tension damage	
Stress [MPa]	Cracking strain [-]	d_t [-]	Cracking strain [-]
4.7	0.00	0.00	0.00
3.9	0.01	0.70	0.01
1.7	0.1	0.80	0.1
0.1	10.0	0.95	10.0

Finite elements, discretization and mesh size

Numerical models of tested composite beams are constructed with the use of ABAQUS commercial software. In order to get the simplest representation of the tested composite beam specimens, numerical models developed hereafter do not involve the brick elements and the discrete representation of the crack and reinforcement bond effects. The reinforced slab and wall elements of the structural steel section are modeled with use of shell elements S4R. The shear studs are modeled with use of one beam element B31 per stud that connects the mid-surfaces of the slab and the upper flange of structural steel welded section by using the ABAQUS *_Tie_* option. Rebars are modeled with use of *_Rebar Layer_* option placed at the slab mid-surface.

The boundary and loading conditions refer to the physical conditions of tested specimens. The uplifted support is modeled through directional u_z springs of the stiffness k_z= 100 N/mm, applied at each node of the contact surface, using the ABAQUS *_Spring_* option. Such a modeling

reproduces the actual behavior of the frame-to-floor resisting structure (u_x allowed while u_y=0). At the pressed down support, the beam web is reinforced in the out-plane direction by the stiffener and the flange is constrained along the stiffener width (u_x=0, u_y=0, u_z=0). In slab modeling at the load application, the edge node translations are constrained in the direction perpendicular to the specimen axis (u_y=0). All the nodes on the intersection line of the web and flanges are constrained against translations in the y-direction and against twist rotation about the specimen axis (u_y=0, R_x=0). The load is distributed over the contact area of 150x200 mm^2.

For short span beams, the mesh at which the slab and beam section are modeled consisting of 7030 shell elements of dimensions close to 23x23 mm on average. In the case of long span beams, there are as much as 13298 elements of the similar in-plane dimensions. The fact that the reinforced concrete slab is modeled as a shell 2D object, the studs are modeled by beam elements joining the nodes of steel beam and reinforced concrete slab mid-surface.

Modeling of material imperfections

Imperfections for the prediction of the composite beam initial configuration are modeled using two approaches. Approach 1 conforms with that of (Salah, 2009) where the post-welded steel is represented by an equivalent constitutive model (see Figure 4) and the geometric imperfection profile corresponds to the lowest buckling mode from LBA. The amplitude of 4 mm web out of flatness is used. Approach 2 developed in this paper requires evaluating of geometric imperfection profile as in the Approach 1 and then superimposing the residual stress state. Predefined numerical model of the imperfect welded steel product is then linked compositely with the reinforced concrete slab model in such a way that stud elements connect vertically the respective nodes of the top flange of welded section and the reinforced concrete slab.

Method of analysis

The multistep analysis is carried out for the evaluation of composite imperfect beam response. In the case of Approach 1 three steps of analysis carried out with the use of ABAQUS software are required:
1. Analysis of LBA type using **Buckle* option in order to get the eigenmodes the combination of which are used for the representation of imperfection profile.
2. Analysis using **Static General* option in order to find the stress state and beam configuration of the initially imperfect beam due to self-weigh acting prior to the load application.
3. Incremental analysis of GMNIA type using **Nlgeom* option and Riks algorithm for the evaluation of pre-limit branch, limit point and post-limit branch of the equilibrium path.

In the case of Approach 2 four steps of analysis are required. The first one is identical to that of Approach 1. In the second step, the material imperfections are introduced using the standard residual stress block of Figure 5a) and **Predefined Field, Mechanical, Stress* ABAQUS option. This step is followed by steps 3 and 4 identical to 2 and 3 of Approach 1. Figure 6 shows the magnified residual deformation state of the C4S355 beam as a result of the welding imperfections.

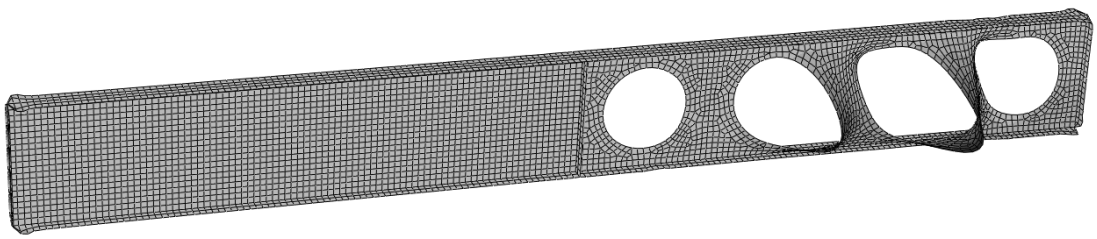
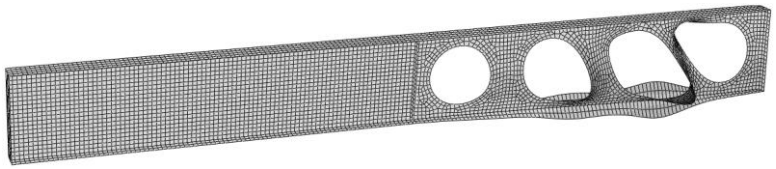
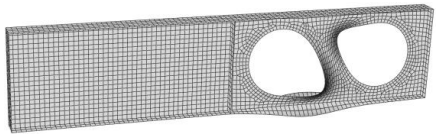


Fig. 6 – Magnified post-welding initial deformation profile of steel girder
(deformation scale factor: 1500)

VALIDATION OF NUMERICAL MODEL

Table 4 presents the results from LBA as to the lowest eigenmode and eigenvalue. Comparing the eigenmodes and the eigenvalues from the present simulation in comparison of those in (Salah, 2009) (given in round brackets), one may conclude that the eigenmode profiles seem to be identical while slight differences may be seen for eigenvalues.

Table 4 – Lowest eigenmodes and eigenvalues

Beam	Lowest eigenmode	Eigenvalue [kN]
C4S355		63.4 (62.7)
C2S355		76.1 (76.0)

Figures 7 presents the results of numerical equilibrium path response carried out for C4S355 composite beam using Approach 1 (with the implicit residual stress modeling by using an equivalent constitutive relationship with the parameter n=2) and Approach 2 (with the explicit residual stress modeling developed in this study). The numerical results are validated with use of experimental equilibrium path presented in (Gizejowski and Salah, 2008a) and (Salah, 2009).

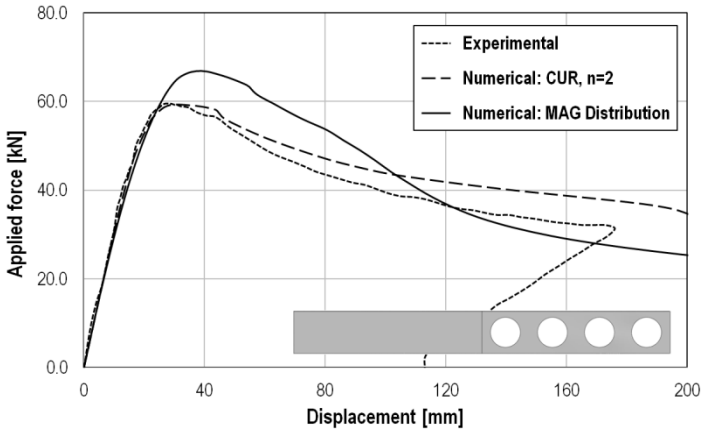


Fig. 7 – Equilibrium path response for C4S355 composite beam

Approach 1 is able to reproduce the experimental equilibrium path quite accurately in the pre-limit range and as to the evaluation of limit point. The post-limit range of the behavior is however traced less accurately. Approach 2 gives in this case less accurate results and only in the range of advanced post-limiting displacements allows for a safe estimation of the equilibrium path.

Figure 8 presents the similar comparison for the C2S355 composite beam. One can draw similar conclusions to those derived from the validation of the C4S355 beam numerical results.

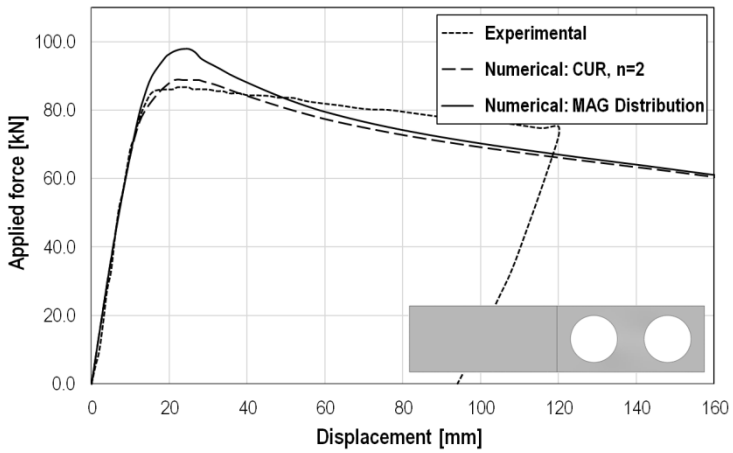
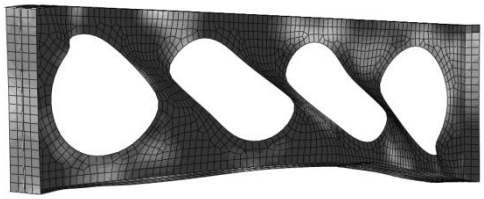
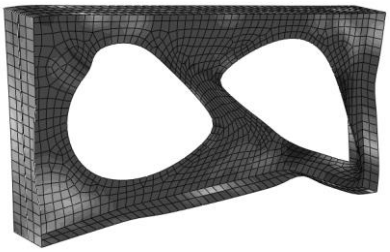
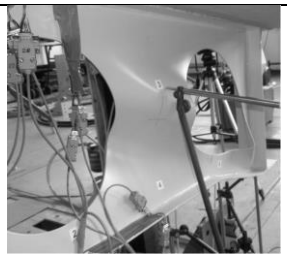


Fig. 8 - Equilibrium path response for C2S355 composite beam

Table 5 shows the validation of deformed shapes of considered beams obtained from numerical simulations EXP,MAG-355 against those recorded during experimental investigations.

Table 5 – Deflected profiles of composite beams

Beam	Numerical	Experimental
C4S355		
C2S355		

NUMERICAL RESULTS FOR REFERENCE COMPOSITE BEAMS

The numerical model developed in the previous section is used hereafter for the evaluation of beam response of composite full plain webbed girders (LPS355 and SPS355) and girders with circular openings along the full specimen length (LFS355 and SFS355) that correspond to the analyzed earlier beams C4S355 and C2S355, respectively.

Figures 9 presents the numerical equilibrium path responses of the LPS355 beam in Figure 9a) and the SPS355 beam in Figure 9b). The results are compared with the experimental curves for C4S355 and C2S355, respectively. Figure 10 shows the similar comparison but for the LFS355 beam in Figure 10a) and the SFS355 beam in Figure 10b).

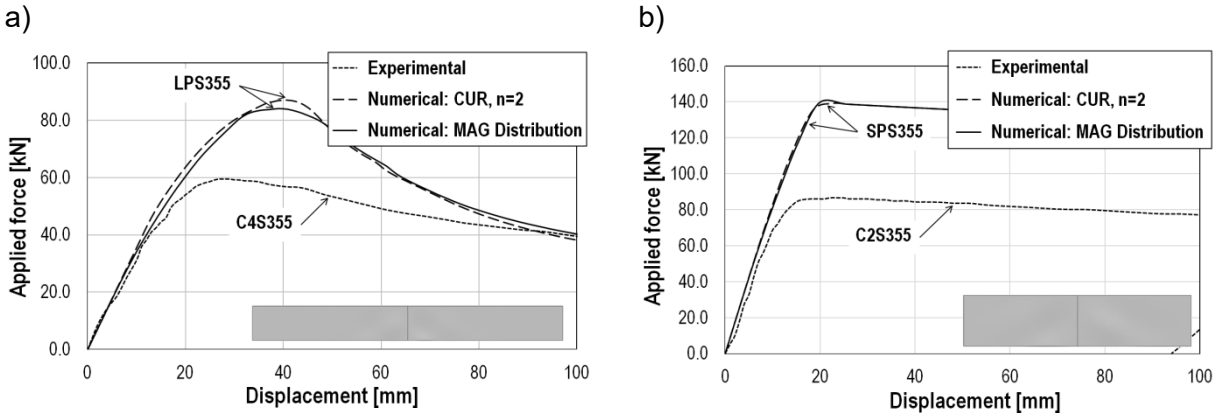


Fig. 9 - Equilibrium path response of plain webbed composite beams

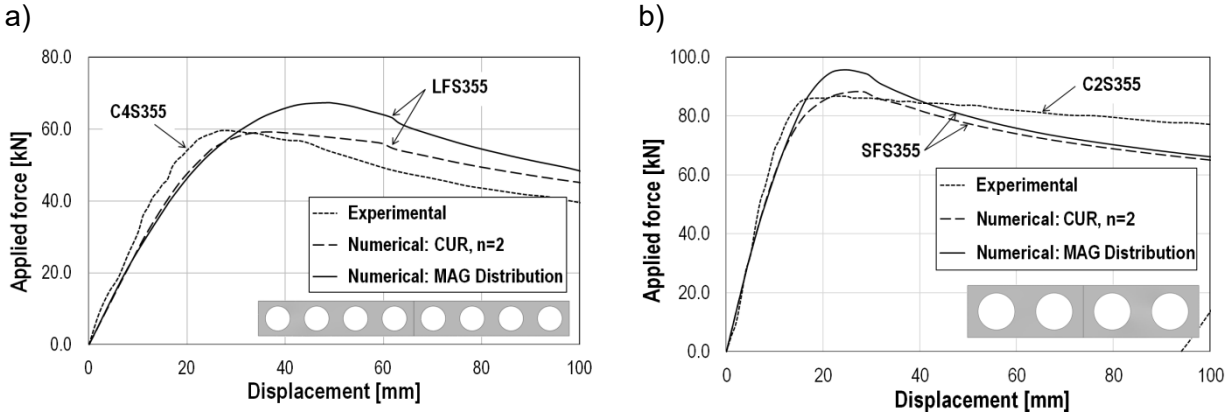


Fig. 10 - Equilibrium path response of composite beams with openings along the full length

From the observation of results presented in Figures 9 and 10 one may come up with the conclusion that composite beams with large openings are much more prone to distortional buckling than their plain webbed counterparts. The differences between the beams with openings are however meaningless for composite beams with openings only on one side of the internal support and with openings arranged symmetrically on both sides of the internal support.

COCLUDING REMARKS

Aspects of two approaches to the residual stress modeling and its effect on the equilibrium path response using finite element numerical simulations were the primary objectives of the present study. Numerical models were developed using the implicit and explicit modeling of the section residual stress distribution. Both approaches were validated with use of experimental results for the beams with the overhang having openings. The validation exercise allows for the following conclusions to be drawn:

1. Approach 1 of implicit residual stress modeling with the equivalent constitutive relationship and model parameter n=2 allows for more accurate estimation of the experimental equilibrium paths for both long span and short span composite beams taking account for both the beam stiffness in the pre-limit range and the limit point at the beam ultimate state.

2. Approach 2 is less accurate and predicting safely the beam stiffness in the pre-limit range but overestimating the limit point at the beam ultimate state.
3. The distortional failure modes are predicted accurately in numerical simulations with regard to both imperfection modeling approaches. The distortional failure load is very sensitive to the number of openings in the regions of the hogging moment.
4. Numerical simulations of the reference composite beams, plain webbed and with the openings along the full length, clearly show that the openings weaken the distortional buckling resistance. It is however proven that the distortional buckling resistance for the beams having the openings only on one side of the internal support is practically at the same level as for the beams having the openings on both sides of the internal support. Taking the resistance of the full webbed composite beams as 100%, the resistance reduction of the perforated beams is as follows:
- by approx. 1/3 for the long span beams,
- by approx. 2/5 for the short span beams,
regardless whether the openings are arranged only on one side of the internal support or on both sides.

REFERENCES

ABAQUS. (2011a). *Theory manual* (Version 6.11). Dassault Systèmes.

ABAQUS (2011b). *Standard User's manual* (Version 6.11). Dassault Systèmes.

Eurocode 4. (2004). *Design of Composite Steel and Concrete Structures. Part 1-1: General rules and rules for buildings*. Brussels: CEN.

Gizejowski, M., & Salah, W. (2008a). Experimental investigation of the stability behaviour of slender section steel-concrete composite beams with web openings. In J. Obrebski (Ed.), *XIV Lightweight Structures in Civil Engineering – Contemporary Problems*: *Proceedings of Polish IASS Chapter Seminar*, *Warszawa, 2008* (68-75). Warszawa: Micro-Publisher.

Gizejowski, M., & Salah, W. (2008b). Numerical finite element modelling of the stability behaviour of slender section steel-concrete composite beams with web openings. In J. Obrebski (Ed.), *XIV Lightweight Structures in Civil Engineering – Contemporary Problems*: *Proceedings of Polish IASS Chapter Seminar*, *Warszawa, 2008* (76-86). Warszawa: Micro-Publisher.

Gizejowski, M., Salah, W., & Barcewicz, W. (2008c). Finite element modeling of the behaviour of steel end-plate beam-to-column joints. *Archives of Civil Engineering*, LIV(4), 693-733.

Gizejowski, M., Szczerba, R., & Gajewski, M. (2017). Resistance of mono-axially bent beams of welded I-sections. In: *Proceedings of the 8th European Conference on Steel and Composite Structures, Copenhagen, 2017* (submitted).

Jankowiak, T., & Lodygowski, T. (2005). Identification of parameters of concrete damage plasticity constitutive model. *Foundation of Civil and Engineering*, (6), 53-69.

Kaminska, I., & Szwed, A. (2015). Calibration of concrete constitutive model and experimental tests used for it. In E. Szmigiera, P. Łukowski & S. Jemioło (Eds.), *Concrete and concrete structures – experimental tests* (pp. 93-110), Warsaw: Warsaw University of Technology Printing House (in Polish).

Salah, W. (2009). *Modelling of Instability Behaviour in Hogging Moment Regions of Steel-Concrete Composite Beams*. Ph.D. thesis, Warsaw University of Technology.

Szczecina, M. & Winnicki, A. (2015). Calibration of the CDP model parameters in Abaqus. In: *Proceedings of the 2015 World Congress on Advances in Structural Engineering and Mechanics (ASEM15), Incheon, Korea, 2015*.

STRENGTH OF LATERAL–TORSIONAL BUCKLING OF A COMPOSITE STEEL BEAM SUBJECTED TO REVERSE CURVATURE BENDING

Satoshi KITAOKA
Nippon Steel Corporation
Futtsu, Japan
kitaoka.7pn.satoshi@jp. nipponsteel.com

Ryoichi KANNO
Nippon Steel Corporation
Futtsu, Japan
kanno.kx4.ryoichi@ jp.nipponsteel.com

Satoru HIROSHIMA
Nippon Steel Corporation
Futtsu, Japan
hiroshima.kp9.satoru@jp. nipponsteel.com

Koji HANYA
Nippon Steel Corporation
Futtsu, Japan
hanya.rs9.koji@jp. nipponsteel.com

Keiichi TAKADA
Retired from Nippon Steel Corporation
Tokyo, Japan
n1000835kt@feel.ocn.ne.jp

Fumihisa YOSHIDA
Daiwa House Industry Co., Ltd.
Nara, Japan
fumihisa@daiwahouse.jp

ABSTRACT

Design guidelines for lateral–torsional buckling of I-shaped steel beams have been well established, but those of a composite beam consisting of an I-shaped beam and a floor slab have not been sufficiently understood. It is especially true for a beam subjected to reverse curvature bending, where the top flange is continuously restrained with a slab but the bottom flange may still buckle laterally. Although several strength formulae have been derived, as far as the authors know, the restraining effect is not widely considered as a common practice, partly due to lack of behavioral data available. Therefore, in this study, three sub-assemblage specimens consisting of two box steel columns, an I-shaped beam, and a composite floor slab were tested to clarify the behavior. Then a closed-form buckling strength formula was derived for the beam based on an energy method, and the results were compared with those of finite element analyses and the test results. Overall, the restraining effects were clearly observed, and the proposed formula was found to provide reasonable strength estimates.

INTRODUCTION

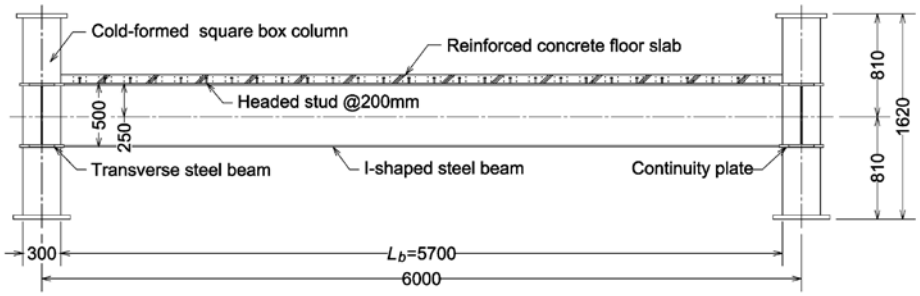
There has been a substantial amount of research work on lateral–torsional buckling (called LTB hereafter) of I-shaped steel beams in steel building frames (Ziemian, 2010). Design guidelines for the strength evaluation and its bracing have been well established. However, the strength evaluation for a composite beam consisting of an I-shaped beam and a floor slab is not well understood yet. It is especially true for a composite beam subjected to reverse curvature bending, where the top flange is continuously restrained with a floor slab but the bottom flange may still buckle laterally due to the compression stress. There would be an obvious benefit especially in seismic design for eliminating bracing members when such a restraining effect of the floor is considered in design. As a result, some strength evaluation formulae have been

proposed, such as those by Wakabayashi and Nakamura (1973), Bradford and Gao (1992), Yura (1995), and Kimura and Yoshino (2011).

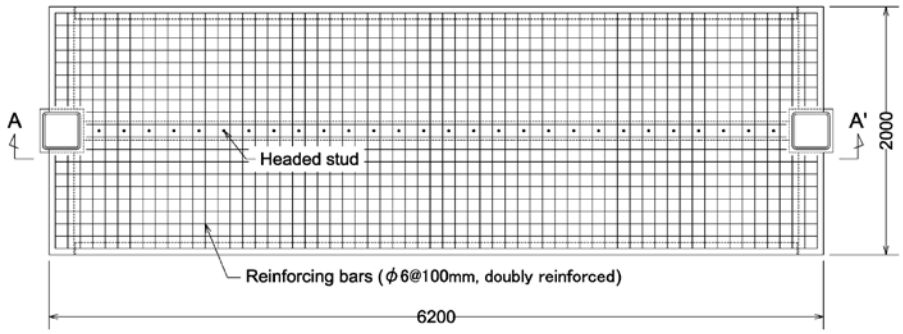
However, as far as the authors know, the restraining effect by the floor slab is not widely considered as a common practice in design. This is partly because of the fact that enough behavioral data on the interaction between the I-shaped beam and the floor slab are not available, resulting in insufficient resources on the strength formulae. From this background, in this study, three sub-assemblage specimens consisting of two box steel columns, an I-shaped beam, and a reinforced concrete floor slab were first tested under horizontal loading applied to the columns. Such a loading condition is typically seen in seismic design. Then, a formula for closed-form elastic buckling strength for the restrained I-shaped steel beam under various moment gradients was developed based on an energy method using newly proposed displacement functions. Comparisons of results of elastic finite element buckling analyses, the proposed formula, and a typical existing formula were made, and finally, the accuracy of the proposed formula was examined with the experimental data.

OUTLINE OF EXPERIMENTS

Sub-assemblage specimens shown in Figure 1 were fabricated and tested under a horizontal loading condition typically encountered in strong seismic and/or wind regions. The specimens were designed as a part of a moment-resisting frame seen in Japan, consisting of two square box columns, an I-shaped beam, and a reinforced concrete floor slab. The box columns were made of cold-formed (roll-formed) steel and have a length of 1620 mm and a square section with 300 mm width and 16 mm thickness. An I-shaped beam with a length of 5700 mm was welded rigidly to the columns at both its ends. At the beam–column connections, reinforcement was made with continuity plates between the beam flanges and the columns so that rigid connection can be realized. The floor slab above the beam was of reinforced concrete with 70



(a) Side view (A-A' section)



(b) Plan view

Fig. 1 – Specimen overview

mm thickness and 2000 mm width. A flat-type form deck was set beneath the floor for concrete casting. Headed steel studs with 10 mm in diameter and 50 mm in length were welded at the middle of the top flange. Following Japanese practice, the studs were arranged with a spacing of 200 mm in a row along the entire steel beam, which provides about one-half of the full composite action required by the AISC specification. From strong restraints by the continuity plates, columns and floor slab, it can be assumed that both twisting and warping were substantially restrained at the beam ends.

Table 1 – Specimens and their beam sizes

Specimen no.	Depth (mm)	Width (mm)	Web thickness (mm)	Flange thickness (mm)
No.1	500	150	9	12
No.2	500	116	9	12
No.3	500	65	9	12

There were three specimens (Specimens No. 1 through No. 3). The experimental variable was straightforward and was only the width of the beam that significantly affects the LTB behavior. The width changed from 65 mm to 150 mm, while the height, flange thickness, and web thickness remained constant in all specimens. Geometry information for the specimens is shown in Table 1. As understood from information in the table, all the sections were categorized into a compact section. The beams were built-up sections, and the yield strengths of the steel plates used for the flange and web were 360 N/mm^2 and 382 N/mm^2, respectively. Based on a widely used Japanese design standard, strength estimates of the steel beams without the floor slab were $0.64M_p$, $0.41M_p$, and $0.17M_p$ for Specimens No. 1 through No. 3, respectively, where M_p is the plastic moment. As seen, no specimens would reach M_p if the slab restraining effect was not taken into account.

The test set-up is shown in Figure 2. The top and bottom parts of the two columns were pin-supported and two horizontal actuators were located at the top of the columns, which gave an equal displacement in the same direction. The loading provided by the actuators was controlled by displacement and the following protocol was applied: two cycles of loading at 0.5% drift angle and then monotonically increasing loading until an obvious buckling was observed.

EXPERIMENTAL RESULTS AND OBSERVATIONS

Load and displacement relationships are shown in Figure 3. The load is represented by bending moment M that acts at the ends of the beam, and the displacement is represented by the story drift angle θ, which is defined by an inclination between the upper and lower pin-supports of the columns. Since composite beams behaved differently in positive and negative bending, both

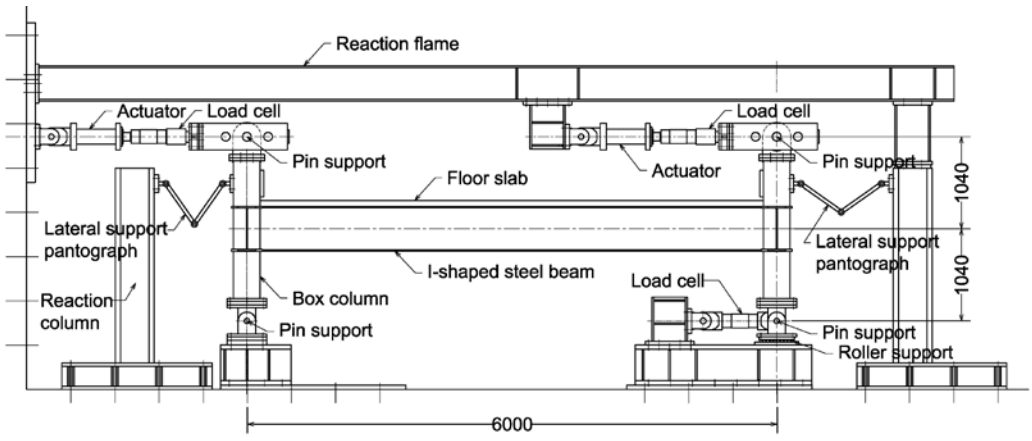
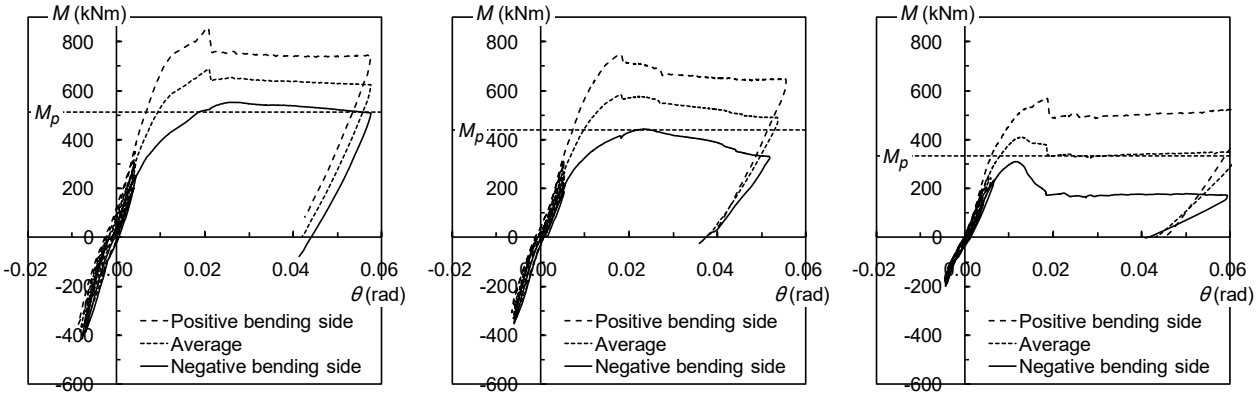


Fig. 2 – Test set-up and loading condition

relationships at positive and negative sides are shown in Figure 3. The average relationships are also indicated in the same figures with finer broken lines. From the average relationships, it can be said that the specimens were quite ductile and relatively similar to each other. They started with elastic behavior, reached the maximum strength, and then showed yielding without much strength deterioration. The figure also indicates that both stiffness and strength were apparently larger in positive bending side than in negative side because of the composite action. In the three specimens, no buckling and cracking were observed in the slabs at the cyclic loading of 0.5% drift angle.



(a) Specimen No. 1 (b) Specimen No. 2 (c) Specimen No. 3

Fig. 3 – Load–displacement relationships



(a) Specimen No. 1 (b) Specimen No. 2 (c) Specimen No. 3

Fig. 4 –Buckling deformation observed at the negative bending side

Each specimen's behavior is described as follows: Specimen No. 1 having the widest flange showed an obvious load drop at a drift angle of around 1.9% due to concrete crushing of the slab around the column face at the positive side. Subsequently, flange local buckling occurred at a drift angle of about 2.5% as seen in Figure 4 (a), but little strength deterioration was observed until the loading was terminated. LTB did not occur in this case, instead, local flange buckling was identified as in Figure 4 (a). Specimen No. 2 showed a similar load–displacement relationship to that of Specimen No. 1. After concrete crushing was observed, buckling occurred at a drift angle of around 2.4% with LTB and slight flange local buckling as shown in Figure 4 (b). The last specimen, Specimen No. 3 also showed concrete crushing at the positive bending side and a clear LTB at a smaller drift angle of around 1.9% than those of the previous two specimens. Although concrete crushing of the floor slabs was observed in all the specimens, obvious damage was not identified around the stud connections, as seen in Figure 5.

Through the behaviors of the three specimens shown in Figure 4, it is clear that the top flange of the steel beam was completely restrained at least laterally. This demonstrated that the floor slabs had enough capability to restrain the lateral movement of the steel beams, even though the beams were not fully composite. Plastic moment strengths M_p are shown with horizontal broken lines in Figure 3, indicating that for all the specimens, the maximum strengths of the beams in the negative bending side were found around their plastic moment strengths. The strengths were $1.06M_p$, $1.00M_p$, and $0.91M_p$ for Specimens No. 1 through No. 3, respectively. Compared with the previously indicated strength estimates for those without a floor slab, substantial strength increases were found especially in Specimens No. 2. and No. 3. These observations indicate that floor slabs possess considerably strong restraining effects on the LTB of the I-shaped steel beams.



(a) Concrete crushing around the columns (b) Appearance around the studs

Fig. 5 – Damage and appearance observed in and around reinforced concrete slab

EXISTING STRENGTH FORMULA

Various design formulae for LTB of I-shaped beams have been proposed. All the formulae are established primarily as a function of plastic moment strength M_p and elastic bucking strength M_{cr}. For the cases where the top flange is continuously restrained with a floor slab, as seen in the previous experiments, several LTB formulae have been proposed; for example by Wakabayashi and Nakamura (1973), Bradford and Gao (1992), Yura (1995), and Kimura and Yoshino (2011). Most of the formulae are developed based on governing differential equations or the equivalent energy equation, but their derivation is so complex that the closed-from solution is rarely possible. Therefore, existing formulae are rather approximate, established based on numerical analysis.

Among the formulae, widely recognized is the one adopted in the AISC specification (AISC, 2010), which is originally proposed by Yura (Yura, 1995). It provides the following elastic buckling strength M_{cr}:

$$M_{cr} = C_b M_{cr0} \tag{1}$$

where M_{cr0} is the elastic buckling strength for uniform bending moment, and C_b is the LTB modification factor for non-uniform moment including reverse curvature bending:

$$C_b = 3.0 - \frac{2}{3}\left(\frac{M_1}{M_o}\right) - \frac{8}{3}\left[\frac{M_{CL}}{(M_o + M_1)^*}\right] \tag{2}$$

where M_o is the moment at the end of the unbraced length, which gives the largest compressive stress in the bottom flange, M_1 is the moment at the other end of the length, and M_{CL} is the moment at the middle of the length. Note that in Eqn. (2) that $(M_o + M_1)^* = M_o$, if M_1 is positive.

To obtain the design strength M_n , the elastic buckling strength M_{cr} is applied to design equations given in the AISC specification.

PROPOSED CLOSED FORM STRENGTH FORMULA

Since the existing formulae for the buckling are approximate, there might be some errors in the strength estimation. As far as the authors know, no closed-form solution is currently available for the elastic LTB strength of an I-shaped steel beam restrained by a floor slab. This is because the equation becomes so complex that only numerical solutions can solve the problem.

A closed-form solution is derived in this study based on an energy method (Rayleigh-Ritz method) by assuming rather untraditional displacement functions. Figure 6 shows a stability problem of simply supported doubly symmetric I-shaped beam whose top flange is continuously restrained laterally (a sign "X" means the lateral restraint). The beam is subjected to arbitrary end moments, where β is introduced as a parameter to express various moment gradients. At the middle of the top flange, the lateral displacement is continuously restrained, while the twist rotation is free to move. Two types of end restraint conditions are considered: torsional simple support and fixed support conditions. Composite action with floor slab is neglected.

Note on this model in Figure 6 that Bradford and Gao (1992) assumed a laterally and torsionally fixed condition at the top flange, resulting in what they called "lateral-distortional buckling." Since it is still uncertain from a practical viewpoint whether the torsionally fixed condition is assumed, this study employs only a laterally fixed condition, which is considered conservative for strength evaluation.

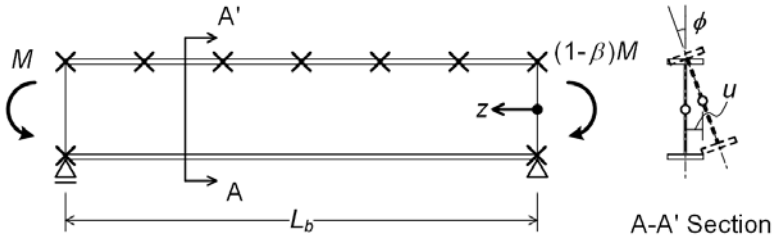


Fig. 6 – Restrained I-shaped beam with end moments

Back to the formulation, the total potential energy is described as follows (Trahair, 1993):

$$\Pi = \frac{1}{2}\int_0^{L_b} EI_y u''^2 dz + \frac{1}{2}\int_0^{L_b} GJ\phi'^2 dz + \frac{1}{2}\int_0^{L_b} EC_w \phi''^2 dz + \int_0^{L_b} M_z \phi u'' dz \qquad (3)$$

where E is Young's modulus, G is the shear modulus, I_y is the moment of inertia about the weak axes, J is the torsional constant, C_w is the warping constant, L_b is the unbraced length as shown in Figure 6, M_z is the bending moment along the beam, and u and ϕ are the horizontal displacement and twist rotation at the centroid of the beam, respectively. Neglecting the sectional distortion of the beam, the following relationship can be assumed:

$$u = \frac{d_b}{2}\phi \qquad (4)$$

where d_b is the distance between the centers of the flanges. Referring to Figure 6, M_z can be expressed at a location of z as follows:

$$M_z = \left(1 - \beta + \beta\frac{z}{L_b}\right)M \qquad (5)$$

Substituting Eqns. (4) and (5) into Eqn. (3), the total potential energy becomes as follows:

$$\Pi = \frac{1}{2}\frac{d_b}{L_b}\left[\frac{2\pi^2 E I_{yf} d_b}{L_b^2}B + A\frac{GJ}{d_b} - M\{(1-\beta)A + \beta\ C\}\right] \qquad (6)$$

where I_{yf} is the moment of inertia for one flange. Note that an approximate relationship of $I_y = 2\,I_{yf}$ is used in the derivation from Eqn. (3). A, B and C in Eqn. (6) are functionals of ϕ shown as follows:

$$A = L_b \int_0^{L_b} \phi'^2 dy\,, \qquad B = \frac{L_b^3}{2\pi^2} \int_0^{L_b} \phi''^2 dy\,, \qquad C = \int_0^{L_b} z\phi'^2 dy \tag{7), (8), (9}$$

As seen in Figure 6, ϕ is the only variable to describe the buckled displacement field. Here, ϕ is expressed with the following finite series such that the given boundary conditions are satisfied:

$$\phi = a_0 + \sum_{n=1}^{n} a_n\, \phi_n \tag{10}$$

where a_0 and a_n are arbitrary constants, ϕ_n is the base function, and n is the number of series. Generally, the Fourier series have been applied to Eqn. (10), but in this study, rather special functions are applied to make the closed-form solutions possible. The functions were found through try and error, and are shown for two end restraint conditions against LTB as follows:

$$\phi_n = \sin\left\{\pi \left(\frac{z}{L_b}\right)^n\right\} \qquad \text{for torsional simple support (no twist, free to warp)} \tag{11}$$

$$\phi_n = \cos\left\{2\pi \left(\frac{z}{L_b}\right)^n\right\} \qquad \text{for torsional fixed support (no twist and no warping)} \tag{12}$$

With the above functions, enough accuracy can be obtained using only three series, i.e., $n = 3$, whereas the number of series is considerably larger with traditional Fourier series, especially for the cases with various moment gradients. This large number of series has made the closed-form solutions quite difficult. The proposed displacement functions can describe the buckled shape more efficiently. Substituting Eqn. (10) into Eqn. (6) and applying a stationary condition in terms of a_n to Eqn. (6), a cubic equation in terms of M can be obtained as an eigenvalue problem. By solving the equation, the following closed-form elastic buckling strength M_{cr}^* can be found:

$$M_{cr}^* = \min\left\{M^0,\, M^1,\, M^2\right\} \tag{13}$$

where

$$M^k = \omega_k \sqrt[3]{-\frac{q}{2} + \sqrt{\left(\frac{q}{2}\right)^2 + \left(\frac{p}{3}\right)^3}} + \omega_{3-k} \sqrt[3]{-\frac{q}{2} - \sqrt{\left(\frac{q}{2}\right)^2 + \left(\frac{p}{3}\right)^3}} - \frac{A_2}{3}\,, \quad k = 0, 1, 2 \tag{14}$$

$$\omega_0 = \omega_3 = 1\,, \quad \omega_1 = \frac{-1 + \sqrt{3}\,i}{2}\,, \quad \omega_2 = \frac{-1 - \sqrt{3}\,i}{2} \tag{15), (16), (17}$$

$$p = A_1 - \frac{1}{3}A_2^2\,, \quad q = A_0 - \frac{1}{3}A_1 A_2 + \frac{2}{27}A_2^2\,, \quad A_j = \frac{\alpha_j}{\alpha_3} \tag{18), (19), (20}$$

$$\alpha_0 = \begin{vmatrix} h_{11} & h_{12} & h_{13} \\ h_{21} & h_{22} & h_{23} \\ h_{31} & h_{32} & h_{33} \end{vmatrix} \tag{21}$$

$$\alpha_1 = \begin{vmatrix} g_{11} & g_{12} & g_{13} \\ h_{21} & h_{22} & h_{23} \\ h_{31} & h_{32} & h_{33} \end{vmatrix} + \begin{vmatrix} h_{11} & h_{12} & h_{13} \\ g_{21} & g_{22} & g_{23} \\ h_{31} & h_{32} & h_{33} \end{vmatrix} + \begin{vmatrix} h_{11} & h_{12} & h_{13} \\ h_{21} & h_{22} & h_{23} \\ g_{31} & g_{32} & g_{33} \end{vmatrix} \tag{22}$$

$$\alpha_2 = \begin{vmatrix} h_{11} & h_{12} & h_{13} \\ g_{21} & g_{22} & g_{23} \\ g_{31} & g_{32} & g_{33} \end{vmatrix} + \begin{vmatrix} g_{11} & g_{12} & g_{13} \\ h_{21} & h_{22} & h_{23} \\ g_{31} & g_{32} & g_{33} \end{vmatrix} + \begin{vmatrix} g_{11} & g_{12} & g_{13} \\ g_{21} & g_{22} & g_{23} \\ h_{31} & h_{32} & h_{33} \end{vmatrix} \tag{23}$$

$$\alpha_3 = \begin{vmatrix} g_{11} & g_{12} & g_{13} \\ g_{21} & g_{22} & g_{23} \\ g_{31} & g_{32} & g_{33} \end{vmatrix} \tag{24}$$

$$g_{nm} = (1-\beta) L_{nm} + \beta\, N_{nm} \tag{25}$$

$$h_{nm} = -\, M_{nm} \frac{2\pi^2\, E\, I_{yf}}{{L_b}^2} d_b - L_{nm}\, \frac{G\, J}{d_b} \tag{26}$$

$$L_{nm} = L_b \int_0^{L_b} \phi_n' \, \phi_m' \, dz\,, \qquad M_{nm} = \frac{{L_b}^3}{2\pi^2} \int_0^{L_b} \phi_n'' \, \phi_m'' \, dz \tag{27), (28}$$

$$N_{nm} = \int_0^{L_b} z\, \phi_n' \, \phi_m' \, dz \tag{29}$$

Applying the displacement functions in Eqns. (11) and (12), L_{nm}, M_{nm}, and N_{nm} become constants by utilizing partial integration technique and numerical integration. Tables 2 and 3 show the values of L_{nm}, M_{nm}, and N_{nm} for simple support case and fixed support case, respectively.

Table 2 – Values of L_{nm}, M_{nm}, and N_{nm} for torsional simple support

	n =1, m=1	*n=2, m=2*	*n=3, m=3*	*n=1, m=2*	*n=1, m=3*	*n=2, m=3*
L_{nm}	4.935	6.310	8.589	3.799	2.750	6.667
M_{nm}	2.467	9.329	26.33	1.899	1.375	13.49
N_{nm}	2.467	4.935	7.402	2.802	2.489	5.604

Table 3 – Values of L_{nm}, M_{nm}, and N_{nm} for torsional fixed support

	n=1, m=1	*n=2, m=2*	*n=3, m=3*	*n=1, m=2*	*n=1, m=3*	*n=2, m=3*
L_{nm}	19.74	26.75	35.96	9.224	-0.2315	23.93
M_{nm}	39.48	128.8	362.8	18.45	-0.4629	165.7
N_{nm}	9.870	19.74	29.61	6.763	1.077	19.21

Eqn. (14) is known as Cardano's formula, which provides three roots. They may take real numbers and/or complex numbers, depending on the value of the discriminant $D = (q/2)^2 + (p/3)^3$. Since the real roots are meaningful, their minimum value becomes the solution for Eqn. (13), which is the buckling strength M_{cr}^*. Although the solution is expressed in a closed-form, rather bothersome calculation work is needed.

ACCURACY OF PROPOSED FORMULA

The accuracies of the proposed strength formula and Yura's formula were examined by comparing elastic finite element buckling analysis (i.e., eigenvalue analysis). Note that the comparisons made here is on elastic buckling strength, and the inelastic strength will be discussed later in this paper. Figure 7 shows a finite element (FE) model of simply supported I-shaped beam with end moments and shearing forces with the top flange continuously restrained horizontally at the middle of the flange. Variables considered in the analyses included the beam end support condition for LTB, beam size, beam length L_b , and moment gradient defined by β . There were two end restraint conditions: one is torsional simple support (only sway is restrained) and another is torsional fixed support (both sway and warping are prevented). These end restraint conditions were made possible by discrete restraints given at the centroids of the sections and rigid-bar addition along the sections at the beam ends. Note that as mentioned previously, the fixed support case may correspond to the experiments conducted in this study. The beam sizes considered here is shown in Table 4. Three types of beams with different widths and depths were taken into consideration. The beam length L_b was varied such that L_b / H (H is the beam depth) changes from 6 to 100 at an interval of 2. Four types of moment gradients were also considered by taking β equal to 0, 1, 2, and 3. In these moment gradients, β = 2 corresponds to an equal end moment and a double curvature bending case that is typically seen in seismic design. By combining all the variables, more than 500 cases of buckling analyses were carried out to obtain a database for the critical buckling strengths M_{FEM} .

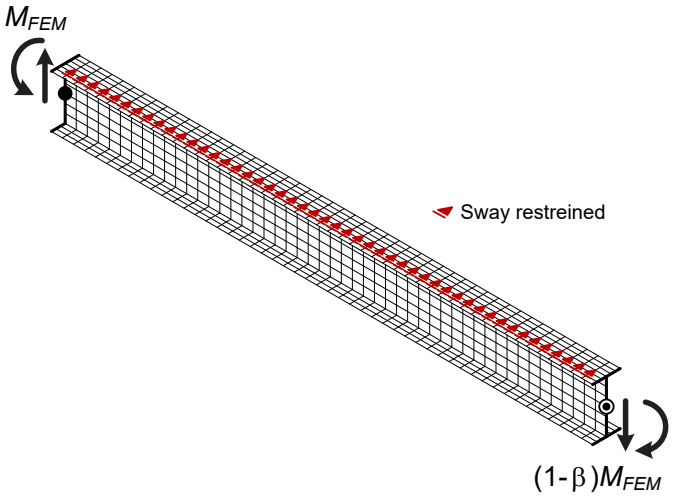
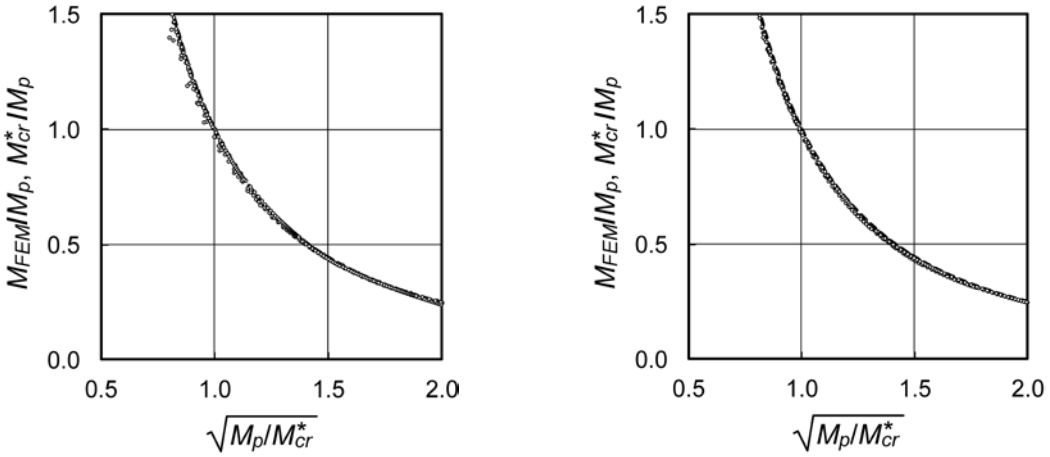


Fig. 7 – Finite element analysis model

Table 4 – Beam sizes considered in the analyses

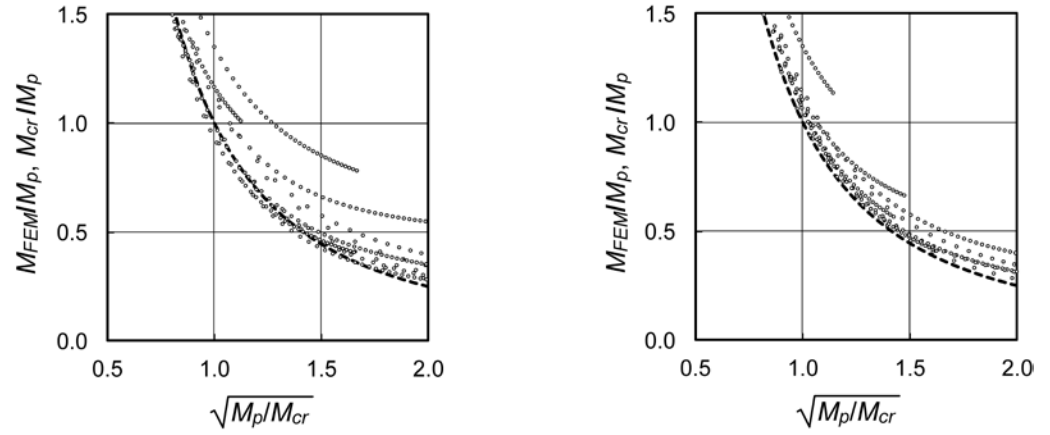
Beam type	Depth (mm)	Width (mm)	Web thickness (mm)	Flange thickness (mm)
Case 1	400	400	13	21
Case 2	588	300	12	20
Case 3	600	200	11	17

Figure 8 shows comparisons between the FE analyses and the proposed formula given by Eqn. (13). Both simple and fixed cases are shown in Figure 8 (a) and (b), respectively. In the figure, the horizontal axis represents the non-dimensional slenderness ratio defined by $\sqrt{M_p / M_{cr}^*}$, where M_p is the plastic moment strength and M_{cr}^* is the calculated buckling strength given by Eqn. (13). Yield strength of the steel beams was assumed to be $F_y = 325$ N/mm^2. On one hand, the vertical axis shows the ratio of calculated strength to plastic moment strength for the FE analysis and the proposed formula. The ratios for the FE results and the proposed formula are expressed as M_{FEM} / M_p and M_{cr}^* / M_p and are shown in the graphs with a small circles and a broken line, respectively. When both circles and line are closely situated, it indicates that the proposed formula has good accuracy. Keeping in mind this basis for evaluation, the proposed formula provides good overall strength estimates. Note that in Figure 8 (a), there is some scatter in the smaller $\sqrt{M_p / M_{cr}^*}$ region. This is possibly caused by LTB and web shear buckling interaction, which was not directly considered in the proposed formula.



(a) Torsional simple support (b) Torsional fixed support

Fig. 8 – Comparisons between proposed formula and FE analyses



(a) Torsional simple support (b) Torsional fixed support

Fig. 9 – Comparison between AISC formula (Yura's formula) and FE analyses

On the other hand, regarding the AISC formula (Yura's formula) given in Eqn. (1), comparisons with the FE analyses are made in Figure 9. Note that Yura's formula was provided primarily for torsional simple support condition, but in this comparison, an effective length factor of 0.5 was applied as an attempt to the torsional fixed support case. Overall, Yura's formula provided conservative strength estimates, but relatively wider scatter was observed for some cases. Although relatively good approximation was provided for uniform bending moment cases, larger scatter was found especially in the cases where the moment gradient was larger (i.e., β was larger), the depth of the steel beam became smaller, and the length of the beam was longer. It is interesting to note that smaller depth and larger length conditions corresponded to the cases where uniform torsion resistant became dominant in comparison with warping torsion resistance. The larger scatter might be caused by the fact that Yura's formula was approximate based on limited numerical solutions. It should be noted that Yura's formula slightly overestimated the cases with β = 3, the largest moment gradient in the calculations. Overall, Figures 8 and 9 show that the proposed formula provided better accuracy than Yura's formula.

COMPARISON BETWEEN PROPOSED FORMULA AND EXPERIMENTAL RESULTS

Since the proposed LTB formula only provided elastic strength, design equations (mapping functions) were needed to consider the effects of inelastic behavior and initial imperfections. Generally, such equations are described as functions of plastic moment, elastic buckling strength and slenderness ratio. In the AISC specification, which is the most widely recognized formula, the unbraced length L_b was used to represent the slenderness ratio. In the proposed buckling formula, however, one might notice that the elastic buckling strength M_{cr}^* was not explicitly expressed as a function of L_b. Therefore, the AISC design equations cannot directly be used for the proposed formula. Based on a Japanese design standard, the following equations were proposed as functions of non-dimensional slenderness ratio $\lambda_b = \sqrt{M_p / M_{cr}^*}$:

(a) When $\lambda_b \leq \lambda_p$:

$$M_n^* = M_p \tag{30}$$

(b) When $\lambda_p < \lambda_b \leq \lambda_e$:

$$M_n^* = \left(1 - 0.4\frac{\lambda_b - \lambda_p}{\lambda_e - \lambda_p}\right) M_p \tag{31}$$

where

$$\lambda_b = \sqrt{M_p / M_{cr}^*}, \quad \lambda_e = \sqrt{1/0.6}, \quad \lambda_p = 0.6 \tag{32), (33), (34}$$

(c) When $\lambda_b > \lambda_e$:

$$M_n^* = M_{cr}^* \tag{35}$$

In the above equations, M_n^* is the design buckling strength considering the inelastic behavior of the beam. λ_p is the slenderness ratio where M_n^* reaches M_p, and λ_e is the ratio of a transition point between elastic and inelastic buckling. The value of 0.6 for λ_p was assumed on the basis of material and geometrical non-linear buckling analyses separately conducted.

Figure 10 shows a comparison between the experimental data and the design equations given in Eqns. (30) through (35). The horizontal axis represents the non-dimensional slenderness ratio, where M_{cr}^* is given by the proposed formula of Eqn. (13). The vertical axis represents the strength normalized by plastic moment, where the strength is given by the experiments or the above equations. In Figure 10, elastic buckling strength shown in Eqn. (13) is also indicated as a reference. In calculating M_{cr}^*, the fixed support condition was applied by using Table 3 and the moment gradient parameter β was assumed to be 2, corresponding to a double curvature and an equal end moment condition. Note that setting an appropriate β is relatively difficult because of the beam composite action seen in positive bending. Based on the calculated stresses of the bottom flanges at both ends of the composite beam, $\beta = 2$ was approximately assumed for a comparison with the experiments.

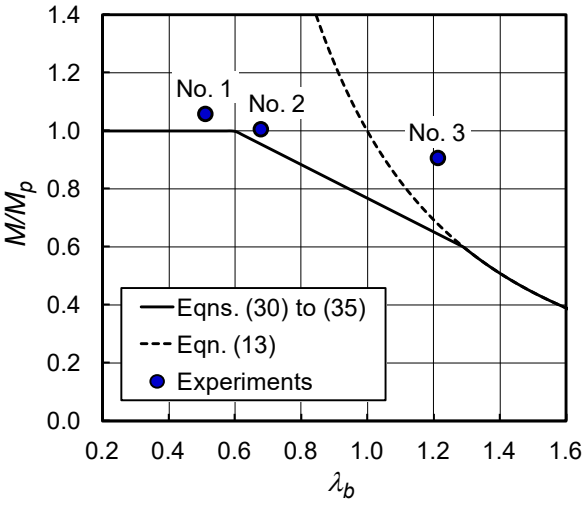


Fig. 10 – Accuracy of the proposed formula

As seen in the figure, the design equations are on the safe side against the experimental results, providing with relatively good estimates for

Specimens No. 1 and No. 2, and with a conservative estimate for Specimen No. 3. This conservative estimate may be explained possibly by the following two reasons: One is an additional effect from the rotational restraint at the top of the flange. As seen in Figure 6, the rotational restraint was conservatively neglected in the model. The other is the moment gradient definition for a composite beam. As stated previously, β = 2 was assumed in calculating M_{cr}^{*}, but the actual gradient subjected to the steel beam might become larger, resulting in some strength increase. Note that the AISC (Yura's) formula is not shown together in Figure 10, because the torsional fixed support condition seemed to be out of scope for the AISC design equations. Therefore, a comparison of elastic buckling strength with the same end condition and moment gradient as those in Figure 10 was made in Table 5 between Yura's and the proposed formulae. Yura's formula provided conservative elastic strength estimates.

Table 5 – Accuracy of Yura's formula

Specimen no.	Yura's M_{cr}/M_p	Proposed M^{*}_{cr}/M_p
No.1	3.26	3.84
No.2	1.89	2.18
No.3	0.63	0.68

CONCLUSIONS

This study aimed to clarify the behavior and design of LTB of an I-shaped steel beam with the top flange continuously restrained laterally using a reinforced concrete floor slab and headed studs. Three sub-assemblage specimens having different flange widths were first tested under horizontal loading applied to the columns. The loading condition was reverse curvature and equal end moment, which is typically seen in seismic design. Through the experiments, it was shown that the floor slab effectively restrained the flexural-torsional buckling for all the cases. An elastic buckling strength formula was then derived for the restrained steel beam based on an energy approach. New displacement functions were introduced so that a closed-form formula was made possible. In comparison with finite element analyses, the accuracy of the proposed formula together with that of the existing AISC formula (Yura's formula) was examined. The comparisons indicated that the proposed formula provided good accuracy while the existing AISC formula had a relatively large scatter for some cases. Finally, the proposed formula was compared with experimental results. In doing so, new design equations to consider the inelastic effect were proposed. The comparison showed that the proposed equations provided reasonably accurate and conservative strength estimates to the experimental results.

REFERENCES

American Institute of Steel Construction (AISC). (2010). *Specification for structural steel buildings*. Chicago, IL: AISC Committee on Specifications.

Bradford M.A. & Gao, Z. (1992). Distortional buckling solutions for continuous composite beams. *Journal of Structural Engineering* (ASCE). 118 (1). 73-89.

Kimura Y. & Yoshino Y. (2016). Effect of lateral-torsional restraint of continuous braces on lateral buckling strength for H-shaped beams with flexural moment gradient. *Journal of Structural and Construction Engineering*. 81 (726). 1309-1319 (in Japanese).

Trahair, N. S. (1993). *Flexural-torsional buckling of structures*. Bosa Roca, FL: CRC Press.

Wakabayashi, M. & Nakamura, T. (1973). Numerical analysis of Lateral buckling strength of H-shaped steel beams subjected to end moments and uniformly distributed load. *Transactions of the Architectural Institute of Japan*. 208. 7-13 (in Japanese).

Yura, J. A. (1995). Bracing for stability - State-of-the-Art. *Proceedings of the ASCE Structures Congress XIII*. (pp. 88–103). New York, NY: American Society of Civil Engineers (ASCE).

Ziemian, R. D. (Ed.). (2010). *Guide to stability design criteria for metal structures*, 6th Edition. Hoboken, NJ: John Wiley & Sons.

Deformation-based reliability concept for composite beams

Prof. Dr.-Ing. Wolfgang Kurz
Dipl.-Ing. Natali Kostadinova Kostadinova
Institute of Steel Structures, University of Kaiserslautern (TU),
Paul-Ehrlich-Straße 14, 67663 Kaiserslautern, Germany
wolfgang.kurz@bauing.uni-kl.de
natali.kostadinova@bauing.uni-kl.de

Prof. Dr.-Ing. Karsten Geißler
Gregor Korpas M. Sc.
Institute of Design and Steel Construction, University of Berlin (TU),
Gustav-Meyer-Allee 25, 13355 Berlin, Germany
ek-stahlbau@tu-berlin.de
wojciech.g.korpas@tu-berlin.de

Abstract

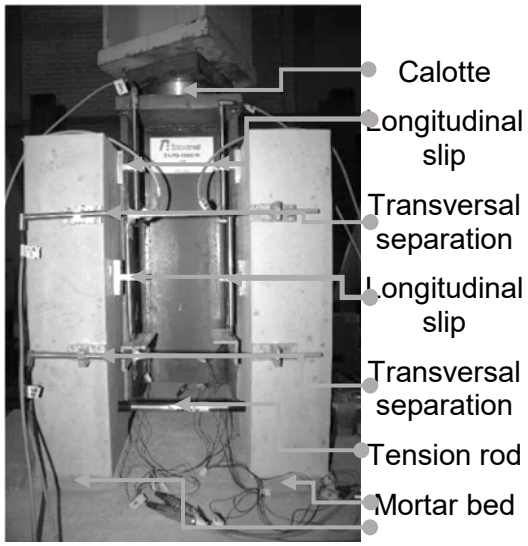
The safety concept of Eurocodes is based on design values for actions and material or member resistance. The resistance of materials and members is defined by their strength, not by their deformation capacity. However deformation capacity of material, members and joints is needed to realize the performance of structural elements. This is of specific evidence for composite beams where slip in the joint between steel and concrete is commonly used to create efficient and economic structures. An analytical model that is based on the differential equation for elastic composite action was developed to describe slip and strain distribution in composite beams. The deformability and the distribution of deformations represent an ultimate limit state for the composite beam. With scattering parameters for the materials and the composite joint, a Monte Carlo Simulation was used to define the reliability of the whole composite beam as well as the weighting for the constituent material parameters. This method provides the possibility to evaluate the behavior of the members during the whole loading process up to the ultimate limit state.

INTRODUCTION AND PUSH-OUT TESTS AT THE UNIVERSITY OF KAISERSLAUTERN

In the 1920s composite beams were tested with regard to their load bearing capacity. The type of connection played a major role in the bearing and deformation behavior of the composite structure. Today, the headed studs are the most widely used connectors. In the course of intensive research activities in the 1960s, international standardization of the test methods for screening tests was developed.

On the basis of [Eurocode 4 2010], twelve Push-out tests were performed to determine the deformation capacity parallel to (longitudinal slip) and perpendicular to the force direction of headed studs in solid concrete slab and to extend the existing test data. The test results show that the theoretical load-bearing capacity is in good agreement with the shear test value. In addition, the stiffness of the headed studs in the concrete is taken into account. The maximum capacities of the Tests are summarized in Table 1 and Figure 1.

Table 1 – Specimen of Push-out (left) and test results of Push-out (right)



Specimen details					
Speciment at the University of Kaiserslautern	Variation of stud connectors	Number	Cubic concrete compressive strength	Arithmetic average of maximal loads	Arithmetic average of measured slip
	Ø/lengh [mm]		$f_{ck,cube}$ [N/mm²]	P_u [kN]	$\delta_u(P_u)$ [mm]
S1	16/100	3	69,17	126,54	5,99
S2	22/100	3	69,17	205,97	7,16
S3	16/100	3	46,06	115,51	7,46
S4	22/100	3	46,06	173,31	7,26

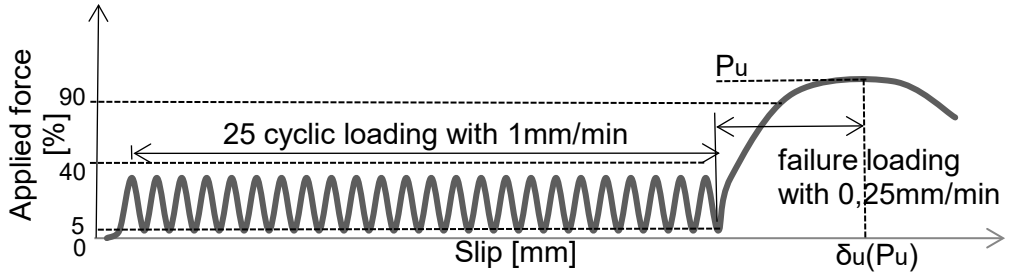


Fig. 1 – Push-out during test realization

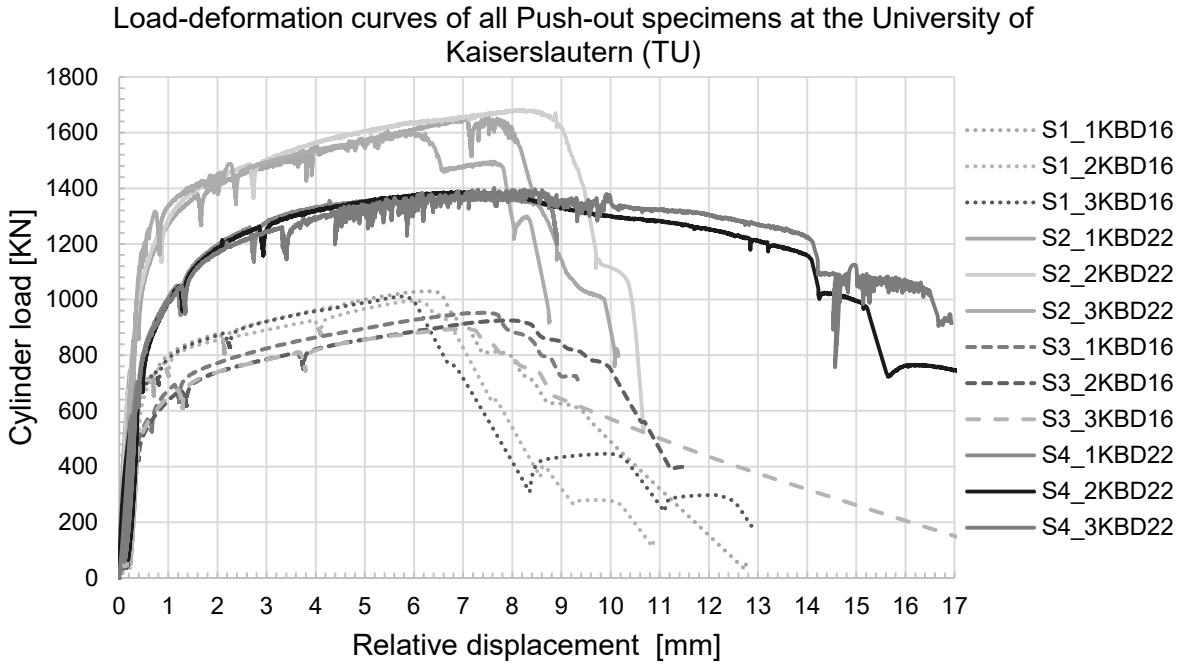


Fig. 2 – Load-deformation curves of Push-out test

As a summary, it was confirmed that the headed studs rigidity increases with increasing stud diameter in case of constant concrete strength. The composite joint uplifted at the top and bottom with increasing slippage, the uplift in the joint at the upper row of headed studs being proportionally faster than the uplift at the lower row of headed studs. As a consequence of the support of the Push-out tests, compressive forces are generated in the upper region of the specimen perpendicular to longitudinal shear. Because of the eccentric load transmission, a bending moment appears as well as a tensile force in the lower region of the specimen to obtain the state of equilibrium. This compressive force leads to relieving friction forces within the joint. Cracks began to from at the recesses and grew in the direction of compressive struts from the lower row of headed studs towards the support. These splitting tensile stresses were transferred by the transverse reinforcement in the test specimen. In addition, cracks grew from the headed studs to the bearing and, at the same time, a horizontal crack formed below the upper headed bolt ridges, resulting from bending in the concrete slabs. Figure 3 presents typical crack patterns and the headed studs shearing-off as failure mode.



a) b) c) d)

Fig. 3 – Push-out specimens after testing: a) S2 – PO-1KBD22 b) S1 – PO-3KBD16 c) Rotation of concrete slaps by S1 – PO-3KBD16 d) Failure by S1 – PO-1KBD16

TESTS ON FRICTION

Friction is a part of the transmission of longitudinal shear force. In addition to the existing test results, further 31 tests (V1 - V31) were performed in the laboratory for structural engineering at the University of Kaiserslautern to determine the coefficient of friction between concrete and steel. For these experiments a direct proportionality between sliding friction and compressive force of the specimens was assumed. During the test, both sides of the steel plate were pressed with a perpendicular load. For this reason, the following relation could be used to determine the coefficient of friction:

$$\mu = \frac{P}{2 \cdot C} \tag{1}$$

with: P pulling force and C compressive force of perpendicular hydraulic press systems

Four test variants of different coatings of steel surfaces were tested. Table 2 presents the summary of results obtained of both coated and uncoated surfaces.

Table 2 – Conclusions of mean values of friction tests (left) and test procedure (right)

Specimen	contact surface		arith. mean of friction μ [-]
	concrete	**uncoated steel**	
V1 to V10	unoiled	unoiled	0,46
V11 to V12	unoiled	oiled	0,37
V13 to V19	oiled	oiled	0,22
	concrete	**steel coated with epoxy**	
V20 to V25	unoiled	unoiled	0,17
V26 to V31	oiled	oiled	0,19



TESTS ON COMPOSITE BEAMS AT THE UNIVERSITY OF KAISERSLAUTERN

In the laboratory for structural engineering at University of Kaiserslautern, six tests on composite beams with concrete slabs were performed. The specimens were loaded in a 4-point bending test up to the ultimate limit state. The deflection, the uplift, the slip between concrete slab and steel beam, the concrete compression and the steel strains were measured. Table 3 presents the parameters and results of the slab tests. A schematic illustration and the measuring techniques used can be found in Figure 4.

Table 3 – Specimen details

Specimens at the University of Kaiserlslautern	Dimensions					Headed Stud Connectors		Materials			**Maximal cylinder load**	**Deflection**
	Steel beam	Length of composite beam	Width of concrete plate	Thickness of concrete slab	Section load	Diameter / Height	Number	Concrete properties on the day of the experiment		Steel		
								Cubic conpressive strenght	Young`s Modul	Strengt		
								$f_{ck,cube}$	E_{cm}	f_{yk}		
		[mm]	[mm]	[mm]	[mm]	[mm]	-	[N/mm²]	[N/mm²]	[N/mm²]	[kN]	[mm]
T1	IPE 400	8000	1500	140	1600	16 / 100	61	62,51	29565	434	683,14	290,6
T2							39	67,88	30473	335	489,62	189,3
T3							89	61,88	27657	335	634,56	311,2
T4							59	47,37	31667	349	556,67	222,8
T5							35	45,19	32016	349	444,5	129,3
T6							18	44,87	30812	349	356,34	67,04

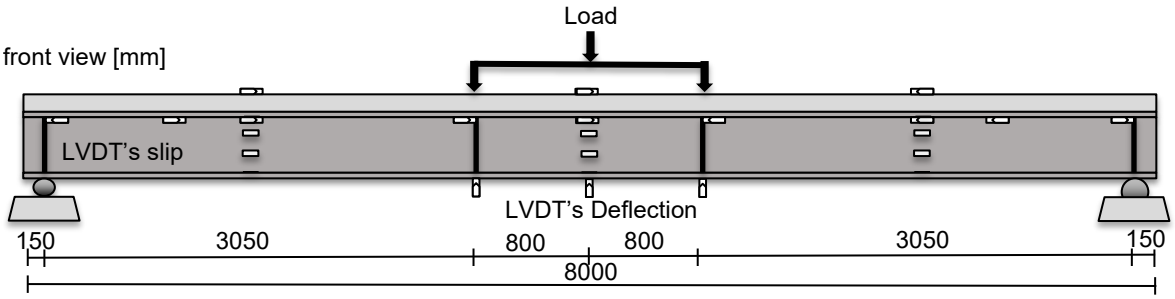


Fig. 4 – Experimental setup of the composite beam

The composite beams were subjected to a test load which was increased with a constant cylinder speed of 0.25 mm / min until failure. In several steps, the loading was paused for the crack formation to be investigated, as well as for the relaxation of materials to be observed. As a result of the large deformation of the composite beam and large slip of shear connection, the connecting studs suddenly failed. In the case of 5 tested composite beams, the failure of the thrust joint occurred over the entire half of the beam. In composite beams with a higher degree of shear connection rearrangements of the dowel forces were observed.

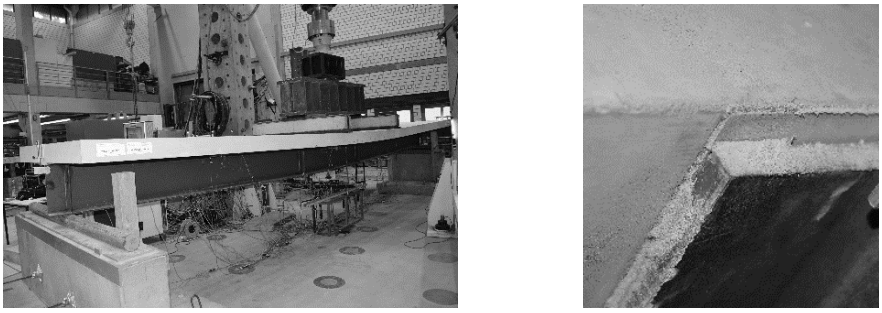


Fig. 5 – Composite beam during test procedure (left) and shear failure of T5 (right)

ANALYTICAL DERIVATION AND CALCULATION METHOD FOR HYBRID CONSTRUCTIONS WITH ELASTIC COMPOSITES

In the past, numerous experimental investigations were carried out on composite structures with regard to the influence of deformations, e.g. slip on the load bearing behavior. Also several analytic approaches taking account of rigidity of load bearing components (concrete, shear connectors and steel beams), internal static indeterminacy and cross-section geometry were developed to describe the elastic load-bearing behavior of composite beams.
The determination of the stress resultants in the different parts of a composite beam leads to the solution of limit value problem by inhomogeneous differential equations. The derived basic equation for determining the deformation of a simple supported beam was considered by many researchers. [Zhou 2014] provided a closed solution for the differential equation of a 4-point bending test of composite beams with elastic composite action. This solution is illustrated in Figure 7 and Figure 8. The sum of the partial bending moments in concrete slab and steel beam results from the difference between total bending moment and a “composite moment” of axial forces in both partial sections. The relation between curvature w`` and bending moment is shown in Figure 6.

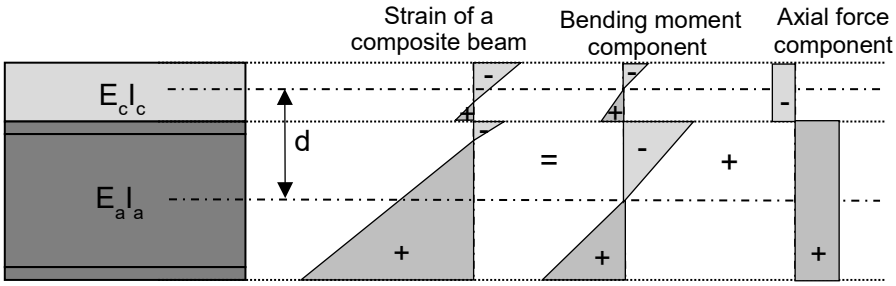
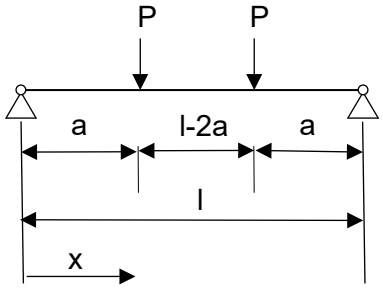


Fig. 6 – Strain distribution of a composite beam

$$w``(E_cI_c+E_aI_a) = -(M - N \cdot d) \tag{2}$$

The deflection is determined by the double integral of the curvature.

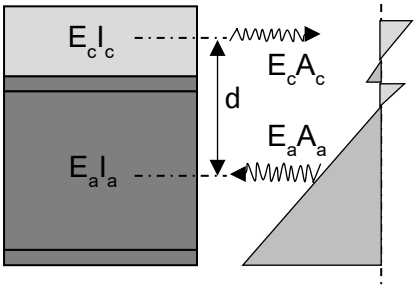


$$(a \le x \le l\text{-}a),\ M = P{\cdot}a \tag{3}$$

$$N = \gamma M - \frac{P\gamma \sinh(\omega a)\left(\sinh(\omega x)+\sinh\left(\omega(l\text{-}x)\right)\right)}{\omega \sinh(\omega l)} \tag{4}$$

$$w = -\frac{1}{6}\frac{P\left(3x^2+a^2-3lx\right)}{EI_{eff}(1+\beta_{eff})} + \frac{\gamma dPa}{\omega^2 EI_{eff}} - \frac{P\gamma d \sinh(\omega a)\left(\sinh(\omega x)+\sinh\left(\omega(l\text{-}x)\right)\right)}{\omega^3 \sinh(\omega l) EI_{eff} I} \tag{5}$$

Fig. 7 – Structural System of 4 point bending test (left) and theoretical formula (right)



$$EI = E_cI_c + E_aI_a \tag{6}$$

$$EA_{eff} = \left(\frac{K_cK_FK_a}{K_cK_F + K_FK_a + K_cK_a}\right)l \tag{7}$$

$$EI_{eff} = EI(1+\beta_{eff}) \text{ whit } \beta_{eff} = \frac{EA_{eff}d^2}{EI} \tag{8}$$

$$\gamma = \frac{\beta_{eff}}{(1+\beta_{eff})\cdot d} \text{ and } \omega = \sqrt{\frac{K_F}{EA_{eff}} \cdot (1+\beta_{eff})}$$

$$K_c = \frac{E_cA_c}{l},\ K_a = \frac{E_aA_a}{l},\ K_F = \frac{1}{\pi^2}nk$$

k = Spring stiffness of connectors, n = Number of connectors

Fig. 8 – Model of springs for a composite beam

Stresses and deformations are basic information for the description of material stiffness. The internal forces can be calculated on the basis of the integrals of the stress distribution. The deformation is a result of geometry and strains changes. With the equations according to [Zhou 2014], the fundamental equations for the stresses can be calculated over the height of the partial cross section.

Based on this method a new analytic approach to elastic-plastic behavior was developed. Therefore the cross-section was divided into lamellae. Material behavior of steel and concrete was described by bi-linear approximations. In case that stresses in a lamella leave the elastic sector, Young`s modulus for this lamella is assumed to be zero and stresses remain fixed on yield strength or compressive strength. In longitudinal direction the beam is divided into sections. By that method the differential equation established for elastic theory can be used to calculate beams with non-elastic materials on a segment-by-segment base. Figure 9 presented the cross-section

of beam portioned into lamellae. Fig. 9 shows at the top illustration a Segment were the whole cross section shows elastic behavior. In the lower illustration the bottom steel flange in the segment is yielding. Transition conditions between adjoining segments have to be formulated to use the elastic analytical approach as a finite solution for elastic-plastic beams.

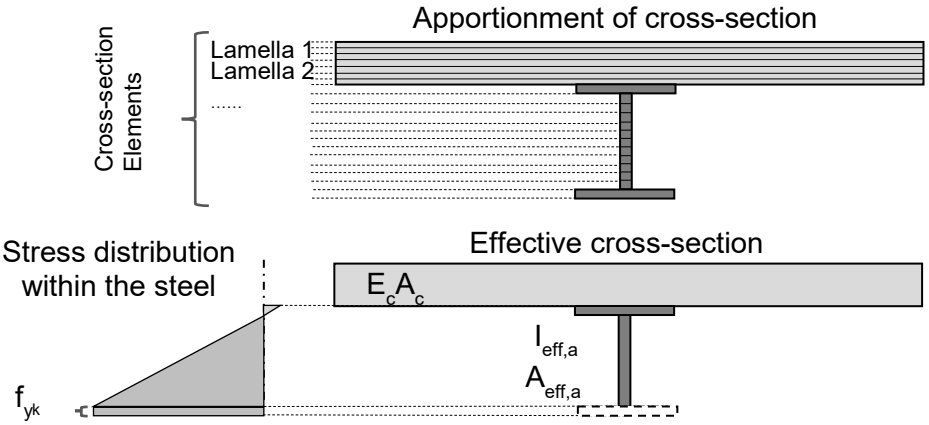


Fig. 9 – Schematic illustration of analytical procedures for the first Step

In the following Figure 10, the results of analytical evaluations are compared to the results of 4-point bending tests of the composite beam.

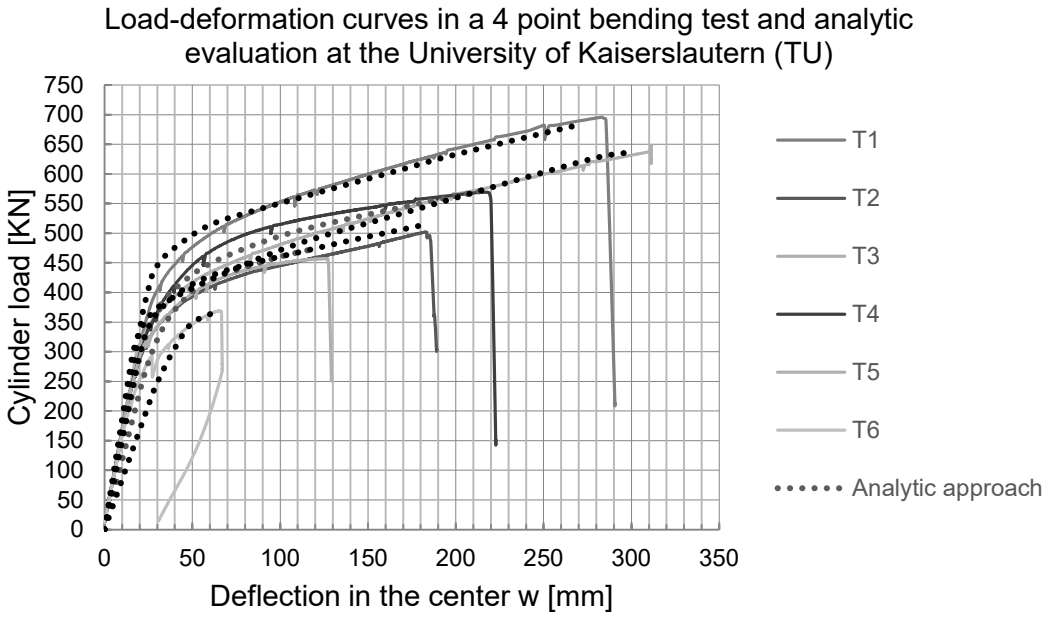


Fig. 10 – Load-deformation curves for test from T1 to T6 compared to analytical approaches

COMPOSITE BEAM TESTS AT TU BERLIN

The six composite beam tests at the Technical University of Berlin were separated into two series with three beams in each. They were planned as three point bending tests. Set one included a span of the composite beam of 6 m with a HEB 400 steel girder (S235) and a concrete plate (C30/37) with the height of 14 cm and width of 150 cm. At the second set the span of the composite beams was 10 m and the steel girder was an IPE 400 (S235) with a concrete plate (C30/37) with the height of 14 cm height and width of 150 cm. In Figure 11 the load deformation curves (LDC) of the component tests are shown. The dashed line represents the calculations. The beam with the minimal degree of partial shear-connection of the second set showed a stud fracture at a load of 270 kN. After that the load was elevated further up to 276 kN with a huge increase in deformation. The failure of the other beams was characterized through concrete compressive fracture.

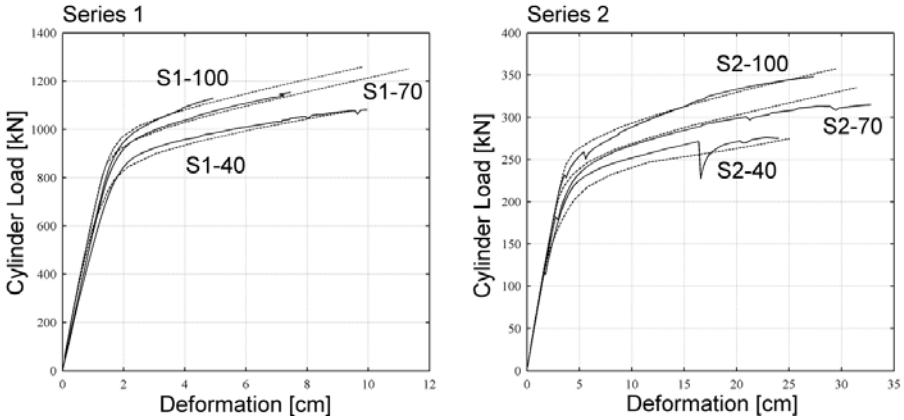


Fig. 11 – Comparison of the load deformation curve at testing and simulation (TU Berlin)

Table 4 – Results of the tests

Set 1				
	Elastic limit		Ultimate limit state	
partial degree of shear connection	Deformation [cm]	Cylinder load [kN]	Deformation [cm]	Cylinder load [kN]
η = 100% S1-100	1,31	750	4,93	1128
η = 70% S1-70	1,29	720	7,45	1152
η = 40% S1-40	1,32	660	9,96	1077
Set 2				
η = 100% S2-100	3,25	220	27,30	348
η = 70% S2-70	3,18	190	32,74	315
η = 40% S2-40	3,18	185	16,38 / 22,84	270 / 276

PROBABILISTIC CALCULATIONS

The reliability of buildings and their components is important for its safety and economy. The reliability could be described by probability of failure p_f or reliability index β. Both are directly linked to each other.

Table 5 – Reliability elements

	Reference period			
	50 years		1 year	
Limit state	Reliability index β	Failure probability p_f	Reliability index β	Failure probability p_f
Sustainability	3,85	$7{,}5 \cdot 10^{-5}$	4,7	$1{,}3 \cdot 10^{-6}$
Serviceability	1,5	$6{,}68 \cdot 10^{-2}$	3,0	$1{,}34 \cdot 10^{-3}$

If the influence factors α_i and the reliability index β are known, it is possible to calculate the design values for instance for each material property. For lognormal distributed variables, which are usually used for modeling the resistance properties, the following equation can used.

$$r_{di} = m_{Ri} \cdot \exp(-\tilde{\alpha}_R \cdot \alpha_{Ri} \cdot \beta \cdot V_{Ri} - 0{,}5 \cdot V_{Ri}^2) \quad (9)$$

The characteristic value is structural independent. In civil engineering it refers to the 5% fractile (k=1,645).

$$r_{ki} = m_{Ri} \cdot \exp(k_{Ri} \cdot V_{Ri} - 0{,}5 \cdot V_{Ri}^2) \quad (10)$$

With the calculation algorithm developed at this research project, the range of resistance with scattering material values is going to be rated. In contrast to previous investigations, not only the strength of the materials is considered but also the strain is variated and its influence is evaluated. For this purpose, the significant points at the stress-strain diagram have been varied as shown principle in Figure 12. The correlations of the material parameters were considered. For the characteristics of the shear connection (load capacity and description of deflection along the length) distributions resulting for instance from push out- and friction- tests by TU Kaiserslautern were used.

The number of resulting random material parameter combinations is huge, including the characteristics of the composite joint. For each random combination a simulation (with increasing the load) has been taken through and the load-deformation curve was calculated.

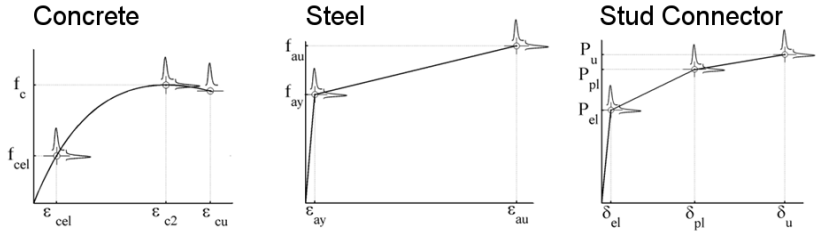


Fig. 12 – Variation of the stress-strain-relationships

In Figure 13 the load deformation relationship of the composite beam test (set 2, test with the minimal degree of 40 % for shear connection) is superposed with the probabilistic calculation based on the same beam characteristics. The simulation results were plotted in form of a point cloud for achievement the ultimate limit state and - the smaller point cloud at the left side of the diagram – an elastic material limit value.

Every point represents one simulation with a random material combination according to the distributions for the material properties. The results show a high median and a wide variance with regard to the possible deflection achieving the limit state of load capacity, is a typical characteristic

for composite beams. The high deflection is caused by the materials (especially the mild steel) and the flexible composite joint too.

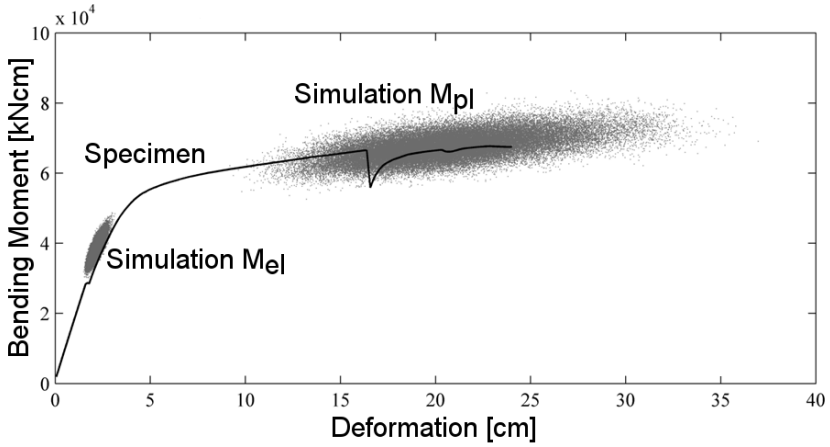


Fig. 13 – Comparison of LDC - test and probabilistic simulation

LIMIT STATE OF LOAD CAPACITY - DESIGN VALUES

Both, stress and resistance, are distributed variables. The calculation of the resistance density function is performed with random scattering material value combinations. To define the structural safety, these two variables are assembled into a two dimensional density function. It represents the event-space with a volume of 1,0 under the function respectively 100 % probability of occurrence. The space is being separated into failure and survival area by the limit state function, which encompasses the point in which the resistance and the stress are equal. The structure is safe when the failure area is smaller than the required failure probability.

The calculations were performed using a limited number of material combinations N = 50.000. To increase this number and improve the accuracy of the statistical statement, a field around the design point is created, which extends by 1 % around the design point (figure 15). Afterwards the material combinations were sorted according the common probability. The combination with the highest common probability is the design combination.

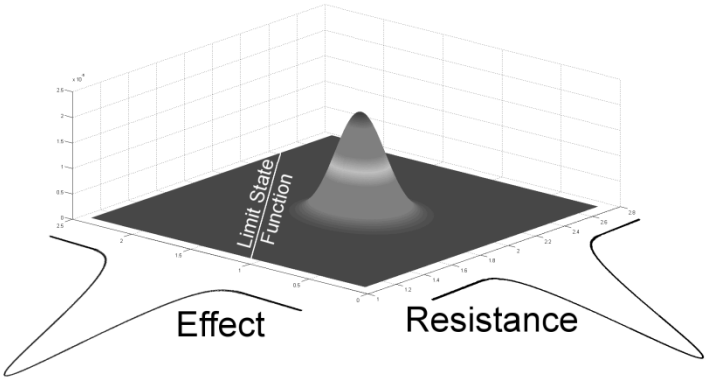


Fig. 14 – Event-space

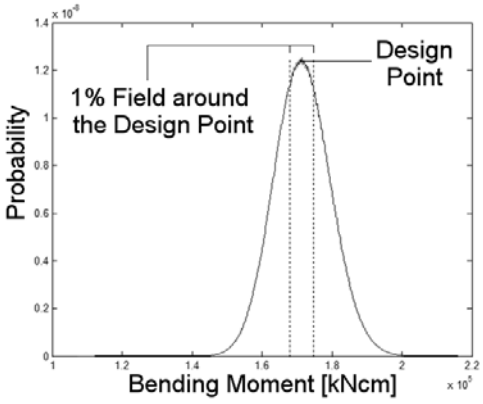


Fig. 15 – Two dimensional density function

LIMIT STATE OF SERVICE LIFE

The serviceability of a structural component could be achieved either by limiting the component strains with the aim, that no plasticity occurs, through limiting the width of cracks (for concrete members) or through limiting the component deformation for instance by a criteria depending from the span like L/300.

Probabilistic simulation were conducted for an exemplary beam that generate a huge number of load deformation curves (N = 30.000), each for one possible material combination. In figure 16 the 5%, 50% (mean) and 95% fractile curves of the LDC are presented. In addition to that, two lines were included, which represent the occurrence of plastic strains within the components. For each load step the design deformation with a probability of failure $6{,}68 \cdot 10^{-2}$, respectively β= 1,5, was determined. By a smaller degree of shear connection the plastic deformations within the composite joint begin at lower load steps, this influences the distribution of the deformation.

Of course it's possible to analyse the results of the probabilistic calculations in different directions. For instance in figures 17 and 18 a number of deformation criteria for each load step in the LDC were examined. One result is the reliability index for a deformation at a certain load. At the figures is to recognize, that the beam with the full shear connection could develop plastic strains and is still safe with regard to the deformation criteria. In contrast to that, at the beam with the minimal degree of shear connection some deformation criteria occur at lower loads (and before plasticity begin).

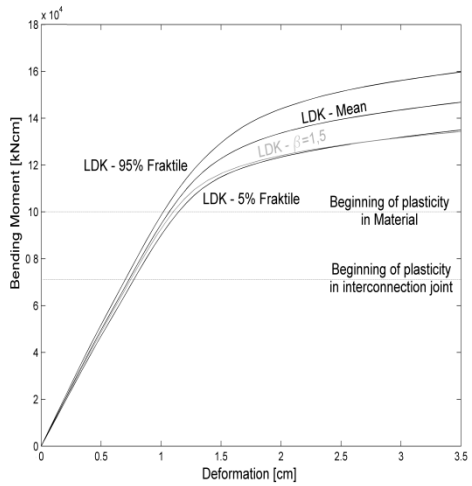


Fig. 16 – Probabilistic - LDC

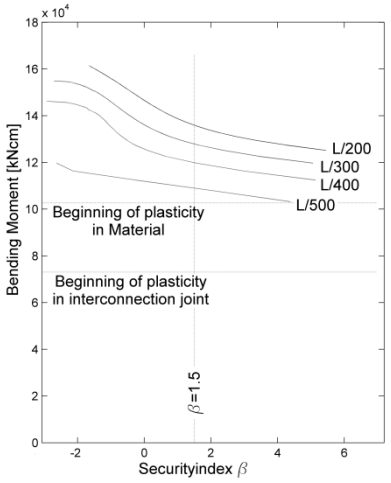


Fig. 17 – Reliability index, η=100%

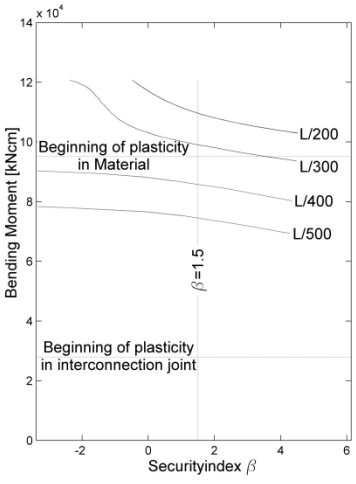


Fig. 18 – Reliability index, η=40%

OUTLOOK

The basic principles of this safety concept were first developed for the well known single span composite beam. Until now the deformation behavior of the composite joint was idealized and not exactly considered. New quotas for the description of composite joints are developed.
The main target of the actual research is to develop deformation based criteria to design the composite beam (in analogy to the steel concrete beam) and to quantify the ductility. Further all

hybrid beams, with a flexible composite joint too, should be calculated with a design concept on the same basics.

ACKNOWLEDGEMENTS

The presented results were financed by the support of the DFG research project "Probabilistic method for deflection - based design of composite beams". The project's numbers are KU 2571/2-1 / 602657 and GE 2011/4-1 / 10041685. The authors would like to thank Nelson Bolzenschweißtechnik GmbH & Co.KG and the steel construction company C&P Freiberg for their support.

REFERENCES

DIN EN 1994-1-1 (2010). *Eurocode 4: Design of composite steel and concrete structures – Part 1-1: General rules and rules for buildings*. Beuth-Verlag, Berlin, Germany.

Vlascici, Milivoi-R. (2016). *Bestimmung der Reibkoeffizienten zwischen Stahl und Beton*. Bachelor thesis, University of Kaiserslautern, Germany.

Kludka, M.; Kurz, W. (2015) *Schlussbericht zu dem IGF-Vorhaben Klebstoff als dauerhaftes Verbundmittel bei Stahlverbundträgern.* Final Report IGF 17458 N, Joint Research Center University of Kaiserslautern, Germany

Korpas, G., Geißler, K. (2016). *Zuverlässigkeitstheoretisches Konzept für die verformungsorientierte Bemessung von Verbundträgern*, 20. DASt- Forschungskolloquium Essen, Germany.

Zhou, D.; Pahn, M.; Kurz, W. (2014). *Beitrag zur Berechnung von Verbundträgern mit elastischem Verbund*. Stahlbau 83, Heft 4, Ernst & Sohn Verlag, Berlin, Germany.

EFFECTS OF COMPOSITE SLAB ON SHEAR STRENGTH OF STEEL PLATE GIRDERS

Peter Y. Wang
Princeton University
Princeton, NJ
pywang@princeton.edu

Maria E. Moreyra Garlock
Princeton University
Princeton, NJ
mgarlock@princeton.edu

ABSTRACT

Steel plate girder bridges are often vulnerable to shear buckling at elevated fire temperatures due to their slender webs. A composite slab could be effective in increasing the shear capacity in fire, but a measure of this slab effectiveness has not been done to-date. Using nonlinear finite element models, this paper evaluates the amount of additional shear strength that a composite slab can provide to a steel plate girder under fire. The elastic shear buckling load (V_{cr}), (ultimate) shear post-buckling load (V_u), and stiffness are evaluated for 16 models with varying parameters: composite slab (or not), web slenderness ratio, and stiffener spacing. The steel girders are subject to a temperature of 700°C. Results show that the composite slab increases V_{cr} on the order of 10% and V_u on the order of 30% compared to the non-composite models. The slab is most effective at increasing V_{cr} and V_u for larger stiffener spacings.

1. INTRODUCTION:

Fire in bridges are not uncommon and have serious economic consequences. Fires underneath or adjacent to highway bridges can directly expose bridge girders to elevated temperatures. The effect of fire on bridges has ranged from extensive deformation to complete collapse, often requiring costly demolition, replacement and detours. Shear buckling is a prominent failure mode for steel plate girder bridges under fire due to the high slenderness ratios found in plate girder webs as well as the reduction in mechanical properties of steel at elevated temperatures. While there have been some studies related to this subject, there have been very few that discuss how a composite slab affects the shear strength.

Shear buckling was identified as the mode of failure for both the MacArthur Maze bridge fire in Oakland, California and the bridge fire in Birmingham, Alabama [1] as observed by the typical diagonal out-of-plane web deformation that characterizes this type of buckling. Following *elastic shear buckling*, the thin plates are capable of significantly more strength, referred to as (ultimate) *post-buckling* shear strength. While analytical solutions exist for the elastic shear buckling load of plates [2], the shear post-buckling behavior is more difficult to characterize analytically. This is true for ambient temperature and elevated temperatures caused by fires. Glassman et al. [3] have proposed a means of measuring this post-buckling shear strength of a non-composite steel girder under fire; however, the elastic and post-buckling capacities of plate girders are more difficult to predict when a composite slab is present.

To the authors' knowledge, there have been two studies of web shear buckling that consider the composite slab on a steel girder: Aziz et al. [4] performed an experimental study, while Glassman et al. [1] performed a comparative analysis using finite element modeling and experimental results. These two papers reference other publications related to web shear buckling for non-composite steel girders. Especially relevant are [5], [6], [7] and [8], the last of which discusses a compression-based shear buckling model and empirical equations for post-buckling shear strength prediction for plate girders.

Study [1] found that modeling the composite slab added significant shear strength to the steel girder and matched well with experimental values, while neglecting the slab resulted in post-buckling shear capacities of about half of the experimental values. Modeling thermal gradients were not found to be significantly more accurate than modeling a uniform average temperature. For optimizing efficiency and accuracy, the authors recommended using a uniform temperature in the steel girder equal to the average temperature of the cross section and to include the slab in the model if it is a composite section.

The current study builds upon previous studies [1,4]. The objective of this paper is to evaluate the amount of additional shear strength that a composite slab can provide to a steel plate girder under fire. The influence of web slenderness and vertical stiffener spacing on the slab effectiveness for increasing shear strength is evaluated. To this end, 16 finite element models were analyzed, where each model had a different combination of the following parameters: composite slab vs. no slab; web plate slenderness (D/t_w); and vertical stiffener spacing (a/D).

2. BACKGROUND:

Case study

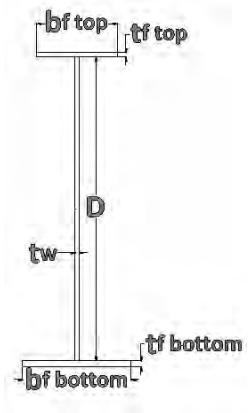
On May 9, 2013, a tanker truck near Harrisburg, PA crashed on a highway ramp leading from I-81 Northbound to Route 322 Eastbound. The truck was carrying 7,500 gallons of fuel and ignited upon collision, directly exposing the bridge girders of Route 322 to fire for a duration of 45 minutes (see Figure 1). While the exposed Span 2 of Route 322 Eastbound did not collapse, extensive out-of-plane web deformation and waving were observed in the steel plate girder webs, prompting demolition by PennDOT. This highway bridge girder was used as the prototype for the current study.



Fig. 1 – Bridge fire near Harrisburg, PA in 2013

The slenderness ratio of a web is defined as the web depth (D) divided by the web thickness (t_w). While typical bridge plate girders from the Federal Highway Administration's 1982 *Standard Plans* have web slenderness ratios ranging from 128 to 270 [9], the Harrisburg bridge girder had a stockier web, with a slenderness ratio of 80. The dimensions of the original Harrisburg girder are given in Table 1. Note that this girder did not have vertical stiffeners (as will be discussed later).

Table 1 - Dimensions of Girder from the Harrisburg Bridge Fire

	Dimension	**Description**	**Cross-Section View (without slab)**
A	N/A (no stiffeners)	transverse stiffener spacing	
D	1.143 m	web depth	
T_w	0.0143 m	web thickness	
D/t_w	80	web slenderness ratio	
a/D	N/A (no stiffeners)	panel aspect ratio	
L	39.2 m	span between supports	
$b_{f\ top}$	0.3048 m	top flange width	
$t_{f\ top}$	0.0159 m	top flange thickness	
$b_{f\ bottom}$	0.4064 m	bottom flange width	
$t_{f\ bottom}$	0.0222 m	bottom flange thickness	

Elastic Shear Buckling

Equation 1 presents the elastic shear buckling load, V_{cr} [2]. In this equation, *E* is the modulus of elasticity, υ is the Poisson's ratio, and *D* and t_w were defined above.

(1) $$V_{cr} = k * \frac{\pi^2 E}{12*(1-\upsilon^2)*\left(\frac{D}{t_w}\right)^2} * D t_w$$

The coefficient for elastic shear buckling, *k,* depends on the *a/D* ratio, also referred to as the panel aspect ratio. The parameter *a* is the transverse (vertical) stiffener spacing. Smaller *a/D* ratios result in larger *k* and therefore greater resistance to elastic shear buckling. Equations 2(a) and 2(b) describe how to calculate *k* for a panel that represents flanges as simply supported and fixed, respectively [2]. Equation 2(c) represents the flange stiffness by considering the flange t_f and web thickness t_w.

(2a) $$k_{ss} = 5.34 + \frac{4.00}{\left(\frac{a}{D}\right)^2} \quad \text{for } a/D \geq 1$$

(2b) $$k_{sf} = 8.98 + \frac{5.61}{\left(\frac{a}{D}\right)^2} - \frac{1.99}{\left(\frac{a}{D}\right)^3} \quad \text{for } a/D \geq 1$$

(2c) $$k = k_{ss} + \frac{4}{5}\left(k_{sf} - k_{ss}\right)\left[1 - \frac{2}{3}\left(2 - \frac{t_f}{t_w}\right)\right] \quad \text{for } \frac{1}{2} < \frac{t_f}{t_w} < 2$$

3. FINITE ELEMENT MODELS

Parameters

In the finite element study, three modeling parameters were addressed: composite slab vs. no slab, web slenderness ratios (D/t_w), and panel aspect ratios (a/D). Sixteen different models were developed based on varying these three parameters for the Harrisburg bridge girder case study defined earlier. The different models of the parametric study are listed in Table 2. The naming convention is as follows: *C* signifies a composite slab and *N* signifies no slab (thus essentially assuming a non-composite section); the first number refers to the *a/D* ratio of the panel; and the number following the hyphen refers to the web slenderness ratio. For example, C2-80 signifies a model with a composite slab, an *a/D* ratio of 2 (panel length *a* equal to *2*D*), and a web slenderness ratio of 80.

Table 2 – Modeled specimens for finite element parametric study

Model name	Slab modeling	*a/D*	D/t_w	t_w (m)	a (m)
N1-80	No slab	1	80	0.0143	1.143
N1-120		1	120	0.0095	1.143
N1-160		1	160	0.0071	1.143
N1-200		1	200	0.0057	1.143
N2-80	No slab	2	80	0.0143	2.286
N2-120		2	120	0.0095	2.286
N2-160		2	160	0.0071	2.286
N2-200		2	200	0.0057	2.286
C1-80	Composite slab	1	80	0.0143	1.143
C1-120		1	120	0.0095	1.143
C1-160		1	160	0.0071	1.143
C1-200		1	200	0.0057	1.143
C2-80	Composite slab	2	80	0.0143	2.286
C2-120		2	120	0.0095	2.286
C2-160		2	160	0.0071	2.286
C2-200		2	200	0.0057	2.286

The dimensions of the modeled slab are based on the tributary width of the Harrisburg case study: 2.34 m wide and 0.23 m deep. The same concrete slab was modeled for all specimens.

Because the Harrisburg bridge girder was not considered “slender” (D/t_w = 80), no transverse stiffeners were present along the 39.2 m span of the girders. In this study, however, we will assume *a/D* equal to 1.0 and 2.0 as shown in Figure 2. The authors realize that for the given *D*, the combinations of *a/D* and D/t_w might not be used in design (e.g. D/t_w = 80 would not use stiffeners); however the study is nevertheless effective in giving us insights on the contributions that a composite slab has on the shear strength of a steel girder in fire.

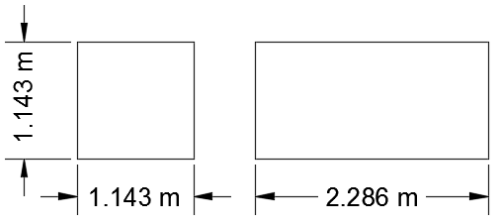


Fig. 2 - Web panel aspect ratios; left *a/D* = 1.0, right *a/D* = 2.0

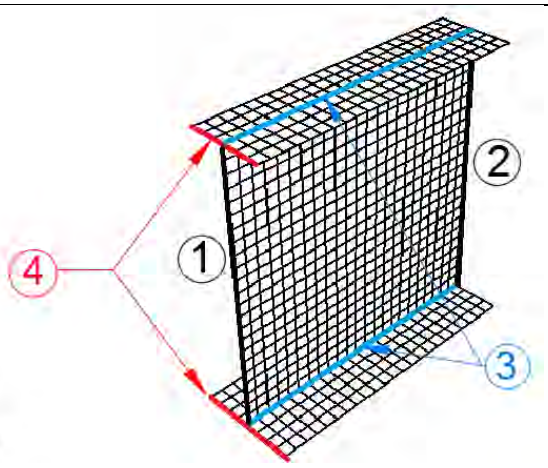
A range of web slenderness ratios was achieved by varying the thickness of the girder web; web depth was kept constant at the *D* value of 1.143 m from the Harrisburg case study (Table 1). The slenderness ratios tested were D/t_w = 80, 120, 160 and 200, where D/t_w = 80 corresponds to the original Harrisburg bridge girder dimensions. Flange dimensions were held constant for all specimens based on the Harrisburg cross section in Table 1. Note that the thickness of the web also plays a role in the amount of restraint afforded by the flanges (Equation 2(c)).

Finite Element Properties and Restraints

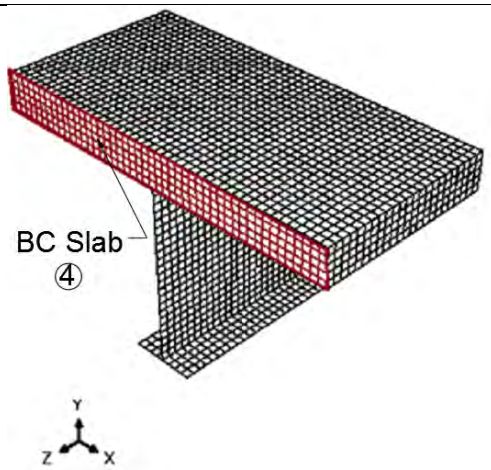
The steel was modeled as ASTM A572 Gr. 50 (345 MPa). The modulus of elasticity at ambient temperatures was taken as 200 GPa, while the Poisson's ratio was taken as 0.3. Stress-strain curves for the steel at elevated temperatures were given by Eurocode 3 Part 1.2 [10]. Concrete was modeled with a strength of f'_c = 27.6 MPa (4 ksi). The stress-strain curve for concrete was based on EC2 Part 1.2 [11].

The steel girder is modeled with deformable S4 shell elements with five integration points through the thickness. The concrete slab is modeled with 3D deformable solid elements (C3D8R hex elements). The finite element models and mesh are shown in Figure 3. The mesh size was validated by comparison to the elastic shear buckling, where values lay within 5% of the theoretical value based on Equation 1. Because the theoretical solution assumed a symmetric section, and the Harrisburg bridge girder had different top and bottom flanges, the average thickness of the flanges was used for determining the *k* (Eqn. 2c) for the theoretical solution [2, 12]. The concrete slab mesh was chosen to match the mesh size of the steel shell elements. Although an optimization study could also have been conducted for the concrete mesh, the size used in this study is reasonable compared to [1], where the model was validated against experimental results.

A tie constraint was imposed between the bottom surface of the concrete slab and the top surface of the top flange in order to achieve composite action, where the top flange surface was selected as the master surface [13]. In addition, the shear studs were not modeled and thus 100% composite action is assumed in the fire condition. Such an assumption is not unreasonable given the experimental and numerical conclusions of [1, 4], which indicate that the slab adds about 50% more shear capacity compared to a member without a slab. Such results imply that the slab has some composite action in a fire although it cannot be quantified how much. Other boundary conditions are shown in Figure 3.



(a) Steel Plate Girder Boundary Conditions



(b) Slab Boundary Conditions

	Translation			Rotation		
	UX	UY	UZ	URX	URY	URZ
①	X	X	X	X		X
②	X		X	X		X
③	X		X			
④		X				

(c) Boundary conditions defined

Fig. 3 – Finite element model boundary conditions shown for *a/D* = 1 (*a/D* = 2 is the same).

Analysis Method and Temperature

An eigenvalue extraction analysis was employed to find the elastic shear buckling load V_{cr}. The first positive eigenmode was chosen as the initial imperfection, which was scaled to a factor of D/10,000. This imperfection magnitude was validated by previous authors as discussed in [1, 12].

A nonlinear solver employing Newton's method was used to determine the post-buckling shear strength, V_u, and behavior (load-displacement) of each girder specimen. The post-buckling strength was taken as the maximum load value on the load displacement curve. The web was loaded on side "2" of Figure 3. To meet the paper objectives, a pure shear scenario is modeled using the boundary conditions of Figure 3.

Real fire temperatures change with time and create thermal gradients in the girders. It was observed by Glassman et al. [1] that modeling the thermal gradients created did not increase the accuracy of V_u significantly more than modeling the whole girder at a uniform temperature equal to the average section temperature. Thus, the steel girders were modeled at a steady state uniform temperature of 700°C, which represents a temperature close to the maximum average based on experiments [1, 4] and CFD modeling [7]. Aziz et al [4] indicates that when the average temperature is about 700°C, the average slab temperature is about 100°C. Therefore a constant slab temperature of 100°C was used in the models.

At 700°C, steel has a modulus of elasticity, proportional limit, and yield stress equal to 0.23, 0.075, 0.13, respectively, times the ambient temperature values. It therefore represents a state in the fire event where the material has weakened but it is less than the temperature causing a

phase change to austenite [7, 14]. V_{cr} is proportional to the modulus of elasticity (as seen in Equation 1), while shear yield, V_y , is proportional to the yield stress of steel. Since the modulus of elasticity has a greater reduction factor than the yield stress at 700°C, girder sections that would be governed by shear yield at ambient temperatures may be governed by shear buckling at fire temperatures.

4. PARAMETRIC STUDY RESULTS

The results of the parametric finite element study are shown in Table 3, which summarizes the elastic shear buckling load (V_{cr}) and post-buckling shear capacities (V_u) of each girder specimen modeled. V_{cr} / V_{crN} describes the ratio of the elastic shear buckling load of the specimen to that of the same specimen with no slab modeled (e.g. C1-80/N1-80, C2-120/N2-120, etc). Similarly, V_u / V_{uN} describes the ratio of the post-buckling shear strength of the specimen to that of the same specimen with no slab modeled. Also included in the Table is the value of shear when the proportional limit is reached, V_p, represented by:

$$V_p = \frac{k_p \sigma_y}{\sqrt{3}} D t_w \quad (3)$$

where σ_y is the yield stress at ambient temperature (345 MPa) and k_p is the proportional limit reduction factor (0.075 for 700°C) [10]. Note in Table 3 that there are only four values of V_p that repeat for each set since only t_w varies in Eqn. (3).

Table 3 –Finite Element Parametric Study Results

Model name	V_{cr} (kN)	V_u (kN)	V_p (kN)	V_{cr}/V_{crN}	V_u/V_{uN}
N1-80	696	653	245	1	1
N1-120	219	396	163	1	1
N1-160	93	278	122	1	1
N1-200	48	213	98	1	1
N2-80	503	550	245	1	1
N2-120	164	328	163	1	1
N2-160	72	226	122	1	1
N2-200	37	169	98	1	1
C1-80	764	809	245	1.10	1.24
C1-120	237	507	163	1.08	1.28
C1-160	102	365	122	1.10	1.31
C1-200	53	285	98	1.10	1.34
C2-80	592	743	245	1.18	1.35
C2-120	186	447	163	1.13	1.36
C2-160	81	311	122	1.12	1.37
C2-200	42	234	98	1.13	1.38

From Table 3, the following is observed:

- V_p is reached before V_{cr} for all models with D/t_w equal to 80 and 120. Therefore, for stockier webs, a stiffness change should occur before elastic buckling (stiffness is discussed later).
- The presence of a slab increases V_{cr} as noticed by the V_{cr} / V_{crN} ratios for the C1 and C2 models. On average V_{cr} increases by 12%.
- The presence of a slab increases V_u as noticed by the V_u / V_{uN} ratios for the C1 and C2 models. On average V_u increases by 33%.
- The V_{cr} / V_{crN} ratios are similar for the C1-80 through C1-200 specimens, as well as the C2-80 through C2-200 models. The slab's effectiveness in increasing V_{cr} does not appear to be affected by plate slenderness for a/D ratios = 1.0 and 2.0.
- The V_u / V_{uN} ratios increase with increasing slenderness ratios for both C1 and C2 models. The relationship between this ratio and slenderness is plotted in Figure 4, where it is seen that the relationship is nearly linear.
- The presence of a slab increases V_{cr} and V_u more for a/D = 2.0 than a/D = 1.0. Such is observed by the larger V_{cr} / V_{crN} *and* V_u / V_{uN} ratios for C2 models compared to C1 models.

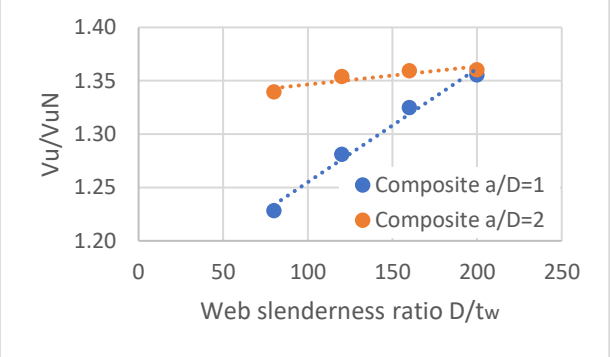
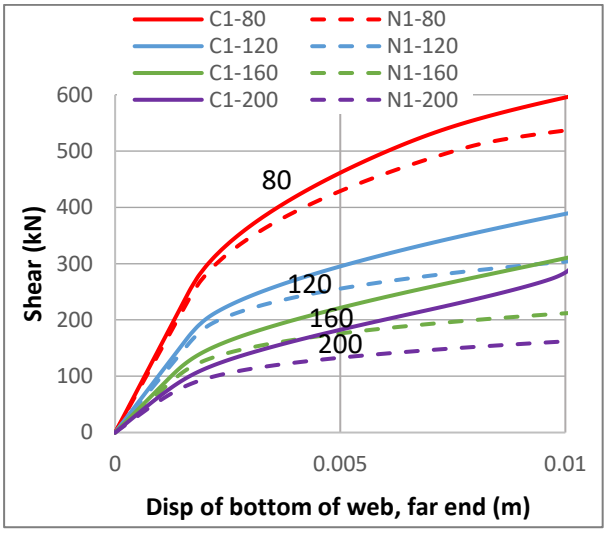


Fig. 4: Ratio of post-buckling strength of composite specimen over that of no-slab specimen vs. slenderness ratio

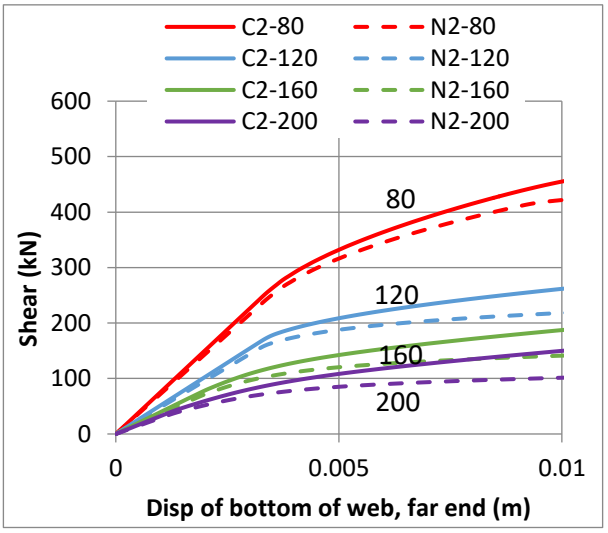
Figure 5 plots the shear load versus vertical deformation (of the lower corner) of the plate. Only the initial stages of loading are shown to highlight the stiffness of each model. These curves peak at V_u shear values listed in Table 3, which is intended to document strength (whereas in Figure 5 stiffness is documented). Each of the three plots of Figure 5 keeps one variable constant, as labeled in the figure caption. The following is observed:

- The models with 80 and 120 slenderness show a clear change in stiffness at values close to the V_p values listed in Table 3. At this point, the paths of the composite vs. no slab models show clear divergence, where the composite model has more stiffness. Therefore, the slab appears to be most effective in providing shear stiffness only after reaching the proportional limit of steel.
- The models with 160 and 200 slenderness change stiffness more gradually; however, a bifurcation of the composite vs. no slab models is seen at values less than V_p. Since V_{cr} is less than V_p in these cases, the slab will begin to contribute more strength (and stiffness) after V_{cr} is reached.

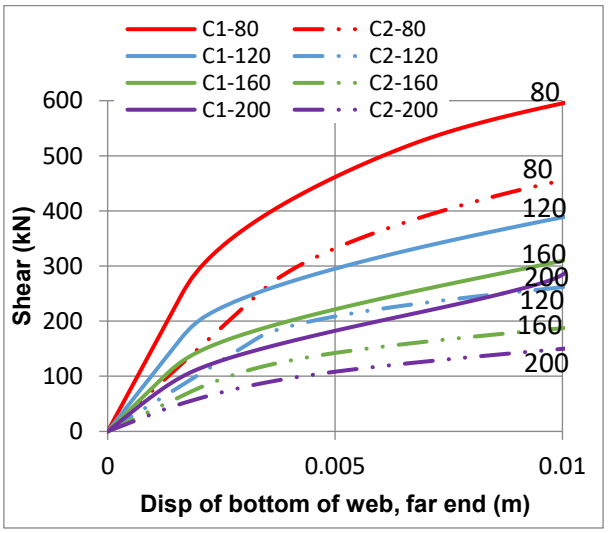
- A larger D/t_w corresponds to a lower stiffness. This is expected and observed for all combination of parameters.
- The a/D = 1.0 models show that the slab has a greater effect on stiffness than the a/D = 2.0 models (Figure 5(a) vs.5(b))
- Models with a/D = 1.0 have significantly higher stiffness than a/D = 2.0 (Figure 5(c)).
- The slab is most effective in increasing the girder stiffness when D/t_w is large. Note, for example, in Figure 5(a), how the solid lines (representing composite models) rise further above the similarly colored dashed lines (representing the non-composite models) for larger D/t_w.



(a) constant variable: a/D = 1.0



(b) constant variable: a/D = 2.0



(c) constant variable: *composite slab*

Figure 5 – Load-deflection curves of specimens

5. SUMMARY AND CONCLUSIONS

The objective of this paper was to evaluate the amount of additional shear strength that a composite slab can provide to a steel plate girder under fire. Using finite element analysis, 16 plate girder specimens were modeled using the following parameters: with and without a composite slab, two stiffener spacing (*a/D)* ratios, and four slenderness (D/t_w) ratios. The elastic shear buckling load (V_{cr}), the (ultimate) shear post-buckling load (V_u), and the stiffness are evaluated. The following conclusions are based on the study:

- The effect of the composite slab on V_{cr} and V_u was not negligible. The presence of a composite slab increased V_{cr} and V_u by 12 and 33 percent, respectively, on average, for the parameters studied.
- Regarding *a/D*, the presence of a composite slab increases V_{cr} and V_u more for *a/D* = 2.0 than *a/D* = 1.0. Conversely, the composite slab has a greater effect on stiffness for *a/D* = 1.0 compared to *a/D* = 2.0.
- Regarding D/t_w, the composite slab is most effective in increasing the girder stiffness when D/t_w is large. The slab's effectiveness in increasing V_{cr} does not appear to be affected by D/t_w.

These conclusions are limited to the parameters and assumptions described throughout. More research is needed before general conclusions that apply to all steel girders in fire can be made. For example, larger *a/D* and D/t_w are needed for validation of the proposed relationships. Experimental studies to verify the predicted post-buckling shear strengths would also benefit the study. Further, a closer examination of the effectiveness of the shear studs in providing composite action in areas of high shear and elevated temperature are also needed. Nevertheless, this paper provides good insight to understand the additional shear strength that a composite slab can provide to a steel plate girder under fire.

ACKNOWLEDGMENTS

The authors would like to acknowledge Spencer Quiel, José Alos-Moya, and Jonathan Glassman for their contributions to this work.

REFERENCES

[1] Glassman, J. D., Garlock, M. E. M., Aziz, E. M., and Kodur, V. K. (2016). Modeling parameters for predicting the postbuckling shear strength of steel plate girders. *Journal of Constructional Steel Research*, *121*, 136-143.

[2] Timoshenko, S. P. and Gere, J. M. (1961). *Theory of Elastic Stability*, *Second Edition*. New York: McGraw-Hill Book Company, Inc.

[3] Glassman, J., and Garlock, M. (2017). A compression model for ultimate postbuckling shear strength at elevated temperatures. *Journal of Structural Engineering*, *143*(6).

[4] Aziz, E. M., Kodur, V. K., Glassman, J. D. and Garlock, M. E. M. (2015). Behavior of steel bridge girders under fire conditions. *Journal of Constructional Steel Research, 106*, 11-22.

[5] Vimonsatit, V., Tan, K.-H, and Ting, S.-K. (2007). Shear strength of plate girder web panel at elevated temperature. *Journal of Constructional Steel Research, 63*, 1442-1451.

[6] Vimonsatit, V., Tan, K.-H., and Qian, Z.-H. (2007). Testing of Plate Girder Web Panel Loaded in Shear at Elevated Temperature. *Journal of Structural Engineering, 133*(6), 815-824.

[7] Alos-Moya, J., Paya-Zaforteza, I., Garlock, M.E.M., Loma-Ossorio, E., Schiffner, D., & Hospitaler, A. (2014). Analysis of a bridge failure due to fire using computational fluid dynamics and finite element models. *Engineering Structures*, 68, 96-110.

[8] Glassman, J., and Garlock, M. E. M. (2016). "A Compression Model for Ultimate Postbuckling Shear Strength." *Thin-Walled Structures*, vol. 102, pp. 258-272.

[9] *Standard plans for highway bridges*. (1982). Washington, D.C.: U.S. Dept. of Transportation, Federal Highway Administration (FHWA).

[10] *Eurocode 3: Design of steel structures: Part 1.2 General rules - Structural fire design (together with United Kingdom National Application Document)*. (2001). London: BSI.

[11] *Eurocode 2: Design of concrete structures: Part 1.2 General rules - Structural fire design (together with United Kingdom National Application Document) / British Standards Institution).* (2000). London: BSI.

[12] Garlock, M. E. M., Glassman, J.D. (2014). Elevated temperature evaluation of an existing analytical model for steel web shear buckling, *J. Constr. Steel Res. 101*, 395–406.

[13] Dassault Systemes. (2010). ABAQUS Analysis User's Manual (6.10).

[14] Payá-Zaforteza, I., & Garlock, M. E. M. (2012). A numerical investigation on the fire response of a steel girder bridge. *Journal of Constructional Steel Research,75*, 93-103.

STRUCTURAL RELIABILITY OF STEEL-CONCRETE COMPOSITE COLUMNS AND FRAMES

Mark D. Denavit
University of Tennessee, Knoxville
Knoxville, Tennessee, USA
mdenavit@utk.edu

ABSTRACT

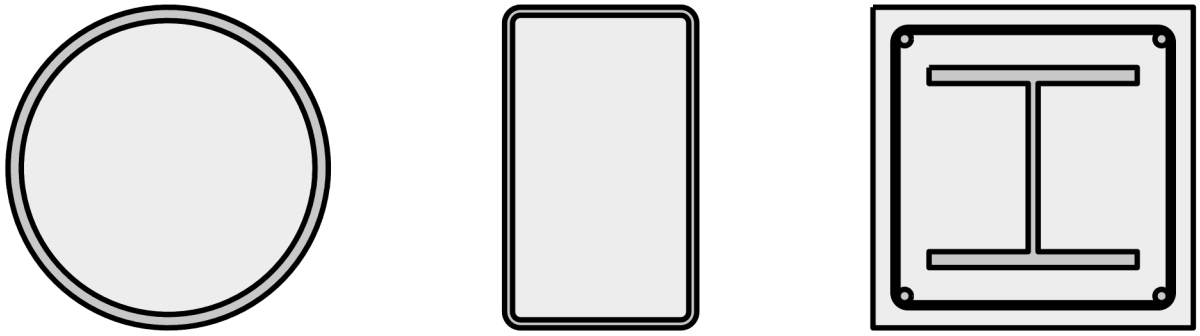
The design provisions for steel-concrete composite columns in the AISC *Specification for Structural Steel Buildings* have evolved significantly in recent editions. The changes have made the provisions more accurate, direct, and broadly applicable. These developments have been justified through comparisons to prior provisions and analyses that indirectly address reliability. Thus, a full accounting of the structural safety of the current provisions in the AISC *Specification* for the strength of composite members has not been performed. This work represents the first steps of such an assessment. Reliability analyses are performed using Monte Carlo simulations and specifically focusing on two aspects. First, the resistance factor for compressive strength of highly steel dominant members. Second, the transition between the relatively lower resistance factor for compressive strength to the relatively higher resistance factor for flexural strength for members subjected to combined load.

INTRODUCTION

Steel-concrete composite columns are a viable alternative to traditional structural steel or reinforced concrete columns for use within building framing systems. Advantages of composite columns include high strength, stiffness, and ductility. Advantages can also be realized during construction. For concrete-filled steel tubes (CFT), whether they be circular (CCFT, Figure 1a) or rectangular (RCFT, Figure 1b) in shape, the steel tube takes the place and eliminates the need for temporary formwork. For steel-reinforced concrete (SRC, Figure 1c) columns within taller buildings, the steel columns can be erected several stories above of the placement of concrete. In this cost-effective construction process, the steel can support the construction loads and the different trades can work with minimal interference.

One disadvantage of composite framing systems is that the development of their design provisions has often lagged behind that of the traditional systems. This has resulted in

provisions that do not consistently reflect the advantages that composite columns and framing systems can provide. When composite columns were first introduced to the AISC *Specification* in the 1986 edition (AISC 1986), the strength of a composite column was based on that of an equivalent steel column. More mechanistic strength provisions were introduced as part of a major restructuring of the composite provisions for the 2005 edition (AISC 2005). Further changes were made for the 2010 edition (AISC 2010) mainly addressing the use of noncompact or slender tubes in CFT members. In the recently released 2016 edition (AISC 2016), the provisions for the compressive strength of composite columns have been revised and new frame stability provisions have been added which were specifically calibrated for composite systems (Denavit et al. 2016).



(a) CCFT (b) RCFT (c) SRC

Figure 1 – Composite cross sections

Over the same time period, several investigations of the reliability and structural safety of composite columns were conducted. Kogut and Chou (2004) investigated the possibility of the use partial resistance factors within the AISC *Specification*. Mirza and Skrabek (1991, 1992) investigated the safety of SRC columns designed with ACI *Code* provisions. Kvedaras and Kudzys (2006) investigated the safety of CFT columns with an internal void designed with European provisions. Beck et al. (2009) investigated the safety of CCFT columns designed with several design codes. Aslani et al. (2016) investigated the reliability of flexural stiffness provisions, focusing on serviceability limit states. However, a rigorous and complete reliability analysis of the composite column provisions within the AISC *Specification* (AISC 2016) has not been performed since the member strength was based on that of an equivalent steel section (Lundberg and Galambos 1996). The structural safety of the changes to the design provisions have been justified based on comparisons to previous provisions or through analyses that indirectly address reliability.

In this work, the structural safety of steel-concrete composite columns designed by the provisions of the 2016 AISC *Specification* (AISC 2016) is evaluated. The focus of this work is on the compressive strength of composite columns and the strength of short composite columns subjected to combined axial compression and bending moment.

CURRENT DESIGN PROVISIONS

For practice in the United States, design provisions for composite columns currently exist in both the AISC *Specification* (AISC 2016) and the ACI *Code* (ACI 2014). As noted in the introduction, the provisions for composite columns within the AISC *Specification* have been the subject of significant development over the past several editions. The provisions within the ACI

Code, on the other hand, have been relatively unchanged and have been considered for removal in future editions.

The axial compressive strength of a composite column per the AISC *Specification* (AISC 2016) is given by Equations (1) through (6) noting that CFT members with internal reinforcing or not classified as compact are excluded in this work.

$$P_n = \begin{cases} P_{no}\left[0.658^{P_{no}/P_e}\right] & \text{when} \quad P_{no}/P_e \le 2.25 \\ 0.877P_e & \text{when} \quad P_{no}/P_e > 2.25 \end{cases} \tag{1}$$

$$P_e = \frac{\pi^2 EI_{eff}}{L_c^{\,2}} \tag{2}$$

$$P_{no} = \begin{cases} F_y A_s + F_{ysr} A_{sr} + 0.85 f_c' A_c & \text{for} \quad \text{SRC} \\ F_y A_s + C_2 f_c' A_c & \text{for} \quad \text{CFT} \end{cases} \tag{3}$$

$$EI_{eff} = \begin{cases} E_s I_s + E_s I_{sr} + C_1 E_c I_c & \text{for} \quad \text{SRC} \\ E_s I_s + C_3 E_c I_c & \text{for} \quad \text{CFT} \end{cases} \tag{4}$$

$$C_1 = 0.25 + 3\left(\frac{A_s + A_{sr}}{A_g}\right) \le 0.7 \tag{5}$$

$$C_3 = 0.45 + 3\left(\frac{A_s}{A_g}\right) \le 0.9 \tag{6}$$

where, P_n = axial compressive strength, P_{no} = axial compressive strength without length effects, P_e = elastic critical buckling load, EI_{eff} = effective flexural rigidity, L_c = column effective length, F_y = steel yield stress, A_s = area of steel, F_{ysr} = reinforcing yield stress, A_{sr} = area of reinforcing, f'_c = concrete compressive strength, A_c = area of concrete, E_s = modulus of elasticity of steel, I_s = moment of inertia of steel, I_{sr} = moment of inertia of reinforcing, E_c = modulus of elasticity of concrete, I_c = moment of inertia of concrete, A_g = gross cross-sectional area, and C_2 = 0.85 for RCFT and 0.95 for CCFT.

Using these equations, the nominal compressive strength of a composite member, P_n, is always greater than that of the bare steel component, $P_{n,steel}$ (which is also calculated with Equation (1), but using $P_{no} = A_s F_y$ and $EI_{eff} = E_s I_s$). However, since the resistance factors are different (ϕ = 0.75 for composite, ϕ = 0.9 for steel), it is possible for the design compressive strength of a highly steel dominant composite column, ϕP_n, to be less than the design compressive strength of the bare steel component, $\phi P_{n,steel}$. Recognizing this possibility, there is a provision within the AISC *Specification* (AISC 2016) that ϕP_n need not be taken as less than $\phi P_{n,steel}$. This provision is logical and ensures that the addition of concrete never results in a reduction of compressive strength, but it is unclear how this provision could be applied to the determination of strength under axial compression and bending moment. A potentially more consistent approach could include a resistance factor for composite columns that increases with the steel ratio for highly steel dominant members. However, such a recommendation would require strong justification.

There are several methods defined within the AISC *Specification* (AISC 2016) for determining the interaction strength of composite cross sections under combined axial compression and bending moment. The most widely cited and widely used method is the plastic stress distribution (PSD) method. In this method, the steel components are assumed to have reached the yield

stress, F_y, in either tension or compression and the concrete components are assumed to have reached a stress of $0.85f'_c$ in compression (a higher stress, $0.95f'_c$, is permitted for CCFT to account for confinement). The strength can be computed for a continuum of points in the interaction diagram based on different locations of the neutral axis. Such an interaction diagram is shown for the case of a RCFT cross section in Figure 2a. For this cross section, the outside dimensions of the steel tube are $H = B = 304.8$ mm and thickness is $t_n = 7.94$ mm, which corresponds to a steel ratio, $\rho_{sn} = A_{sn}/A_g = 0.10$. Material strengths were selected as $F_{yn} = 344.7$ MPa and $f'_{cn} = 55.16$ MPa. The subscript "n" indicates that these values are nominal (or, for the case of t_n, the nominal design thickness of the steel tube).

Closed-form solutions based on the PSD method are published for five specific anchor points in the interaction diagram (AISC 2013). These five points, labeled "A", "E", "C", "D", and "B", when connected by straight lines (Figure 2b) form a approximation of the continuous curve. The interaction diagram for the cross section constructed using the strain compatibility method defined within the ACI *Code* (ACI 2014) is shown in Figure 2c.

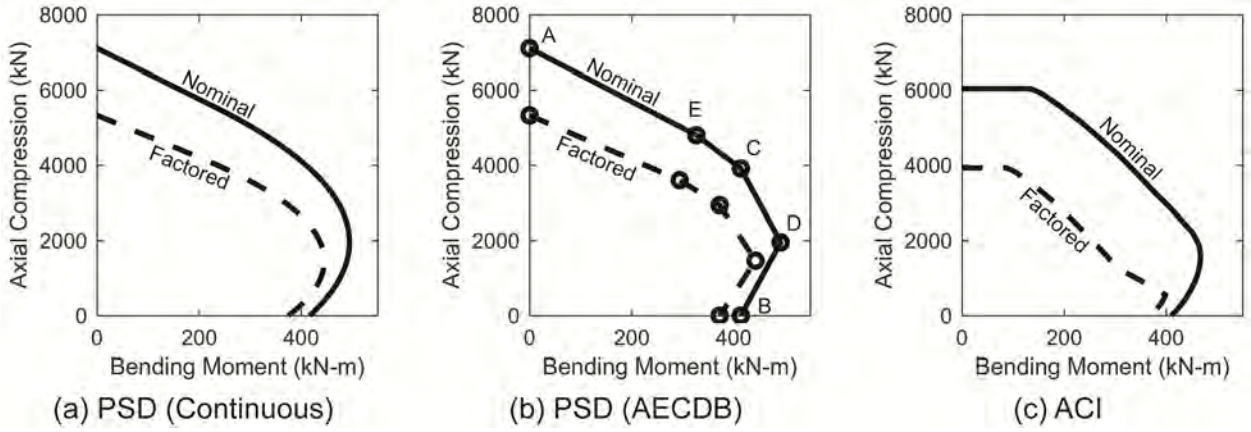


Figure 2 – Axial compression and bending moment interaction diagrams

The AISC *Specification* (AISC 2016), does not specifically state how to apply the resistance factor for strength under combined axial compression and bending moment, only that $\phi = 0.75$ for axial compressive strength and $\phi = 0.9$ for flexural strength. The commentary to the AISC *Specification* provides an approximate method for applying these resistance factors whereby the ordinate of each calculated point within the interaction diagram is multiplied by $\phi = 0.75$ and the abscissa is multiplied by $\phi = 0.9$. This method can lead to potentially unconservative situations where an insufficient reduction is applied to the "bulge" region near point "D". Note that in Figure 2b point "D" within the factored interaction diagram is near the line between points "D" and "B" of the nominal interaction diagram. The potential unconservative nature of this approximate method of applying the resistance factor is part of the reason it is recommended within the commentary to use only points "A", "C", and "B" when constructing interaction diagrams for the design of composite columns.

A potentially more consistent approach, and one which would not restrict the number of points that could be used in an interaction diagram, would be to apply the resistance factor in a similar manner to the method given within the ACI *Code* (ACI 2014). Within the ACI *Code*, the resistance factor for combined axial load and bending moment is given as a function of the extreme tensile strain in the steel and computed for each point on the interaction diagram. Thus, each point has only one resistance factor, effectively moving the point inward to the origin, as opposed to down and to the left as in the approach defined within the commentary to the AISC *Specification* (AISC 2016). This method cannot be directly applied to the AISC *Specification* since infinite curvature and thus infinite strain are assumed within the PSD method. However,

this method can be used if the resistance factor is reformulated as a function of the ratio of the location of the neutral axis to the depth of the section (*c*/*d*) as in Equation (7). Such a formulation would be compatible with the provisions of the AISC *Specification* and thus an resistance factor similar to Equation (7) represents a promising alternative to the current approximate approach given in the commentary to the AISC *Specification* (AISC 2016).

$$\phi = \begin{cases} 0.75 & \text{for} \quad c/d \geq 0.6 \\ 0.75 + 0.15\left(d/c - 5/3\right) & \text{for} \quad 0.375 \leq c/d < 0.6 \\ 0.9 & \text{for} \quad c/d < 0.375 \end{cases} \tag{7}$$

RELIABILITY ANALYSIS

The resistance factor used in the evaluation of a strength limit state can be calculated using Equation (8) (ASCE 2010).

$$\phi = \frac{\mu_R}{R_n} e^{-\alpha\beta V_R} \tag{8}$$

where, α is a linearization coefficient, β is the desired reliability index, V_R is the coefficient of variation (CV) of the resistance, μ_R is the mean value of the resistance, and R_n is the nominal resistance.

In this work, the linearization coefficient is taken as α = 0.70 (ASCE 2010) and the desired reliability index is taken as β = 2.6, a value appropriate for member strength (AISC 2016). When examining column behavior, the resistance is the axial compressive strength and when examining short beam-columns it is the radial distance along a line from the origin to a point on the interaction curve. In both cases, the mean value and CV of the resistance are determined, in part, through Monte Carlo simulations.

Variations in resistance come from a variety of sources. The sources can generally be categorized as relating to either material, fabrication, or professional factors (Ravindra and Galambos 1978). Material variations arise because of the variability in the mechanical properties of the steel and concrete. Fabrication variations arise because of the variability in geometric dimensions. Professional variations arise because of the uncertainty in the underlying theory and design provisions. In this work, material and fabrication variations will be accounted through Monte Carlo simulations. Each parameter with significant variability will be identified and assigned a probability distribution. Then for any selected nominal case, a number of simulations are performed by sampling each probability distribution and using the resulting parameters to compute the strength. This process is represented by the generic function in Equation (9) [i.e., *f*(…)]. The resistance is assumed to be the product of the computed strength and a random variable representing the uncertainty within the selected model, X_{model}, which accounts for the professional variations. Following this assumption, the mean value and CV of the resistance (μ_R and V_R) can be computed per Equations (10) and (11), where μ_{model} and V_{model} are the mean value and CV of X_{model} and $\mu_{f(\ldots)}$ and $V_{f(\ldots)}$ are the mean value and CV of the strengths computed from the Monte Carlo simulations.

$$R = X_{\text{model}} f\left(X_{F_y}, X_{E_s}, X_{f'_c}, \ldots\right) \tag{9}$$

$$\mu_R = \mu_{\text{model}} \mu_{f(\ldots)} \tag{10}$$

$$V_R = \sqrt{V_{\text{model}}^2 + V_{f(\ldots)}^2} \tag{11}$$

In this work, the strength of each simulated case is computed using current code provisions (AISC 2016) (e.g., Equations (1) through (6) for axial compressive strength). The statistical properties of random variables were identified from the literature and listed in Table 1. For the steel yield strength, steel modulus of elasticity, and steel tube thickness, the statistical properties are given for random variables normalized by the nominal value. For the concrete compressive strength and concrete modulus of elasticity, the statistical properties are not normalized and are only applicable for concrete with a nominal compressive strength of 55.16 MPa. These values were obtained following the recommendations of Mirza et al. (1979) which account for variations between in-situ strength and control cylinder strength as well as speed of loading. Outside dimensions of the steel tube and the length of the columns were taken as deterministic.

Table 1 – Statistics of random variables

Parameter	Mean	CV
Steel yield strength, F_y/F_{yn} (Bartlett et al. 2003)	1.10	0.06
Steel modulus of elasticity, E_s/E_{sn} (Bartlett et al. 2003)	0.993	0.034
Steel tube thickness, t/t_n [approximates statistical properties recommended for A_s (e.g., Lundberg and Galambos 1996)]	1.00	0.05
Concrete compressive strength, f'_c (Mirza et al. 1979)	40.71 MPa	0.136
Concrete modulus of elasticity, E_c (Mirza et al. 1979)	27740 MPa	0.105

EXPERIMENTAL DATABASE

A database of experimental results was developed and analyzed to define the random variable X_{model}. The database is based on similar, previously developed, databases (Goode 2008; Kim 2005) but is limited to columns specimens subjected to concentric axial compression and short proportionally loaded beam-column specimens with a length to depth ratio, $L_c/d \leq 5$. The database was further specialized by removing CFT specimens not classified as compact and specimens with outside dimensions less than 76.2 mm.

A total of 410 CCFT, 150 RCFT, and 88 SRC column specimens were included in the database. For each of these specimens, a test-to-predicted ratio was obtained by taking the ratio of the experimentally determined strength to the strength computed per Equation (1). Plotting the test-to-predicted ratio versus length, as in Figure 3 for CCFT, reveals key regions of behavior. For short columns, there is high variation and high test-to-predicted ratios this is likely due to the high levels of concrete confinement which can be present in CFT columns but is only partially accounted for in the design equations. For intermediate length columns, the variation is less and the test-to-predicted ratios center at about unity. For long columns, the test-to-predicted ratios begin to rise indicating there again may be bias in the design equations that result in underprediction of strength. Plotting the test-to-predicted ratio versus other key parameters, such as steel ratio (Figure 3), does not reveal such definitive trends. Statistical data for the test-to-predicted ratio for various subsets of the database are presented in Table 2.

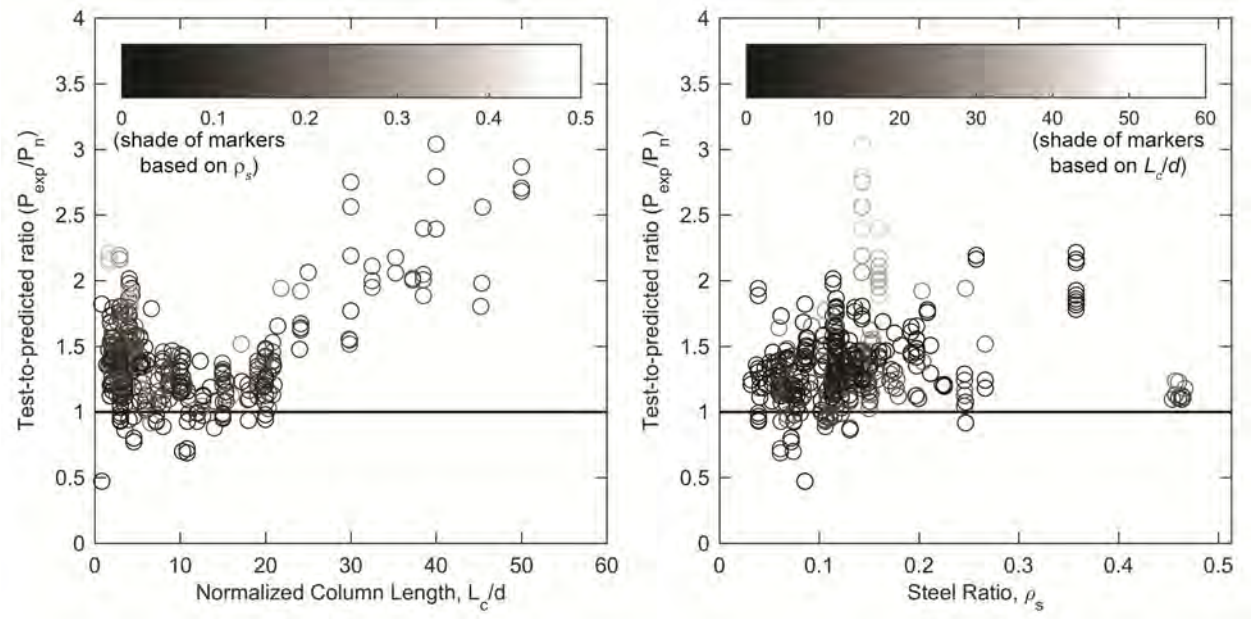


Figure 3 – Database results for CCFT column specimens

Table 2 – Test-to-predicted ratio statistics for column specimens

Member Type	Case	Number of Specimens	Mean	Standard Deviation	CV
CCFT	All	410	1.384	0.348	0.251
	$L_c/d \le 6$	225	1.399	0.266	0.190
	$6 < L_c/d \le 20$	131	1.180	0.170	0.144
	$20 < L_c/d$	54	1.815	0.521	0.287
RCFT	All	150	1.165	0.219	0.188
	$L_c/d \le 6$	104	1.140	0.193	0.169
	$6 < L_c/d \le 20$	25	1.080	0.088	0.081
	$20 < L_c/d$	21	1.393	0.300	0.215
SRC	All	88	1.484	0.849	0.572
	$L_c/d \le 16$	60	1.158	0.146	0.126
	$16 < L_c/d$	28	2.184	1.236	0.566

A total of 252 CCFT, 117 RCFT, and 17 SRC short beam-column specimens were included in the database. A majority of these specimens were subjected to axial load only. Again, for each of these specimens, a test-to-predicted ratio was obtained. An interaction diagram was constructed for each specimen using measured material and geometric properties. The test-to-predicted ratio was taken as the ratio between the distance along a radial line from the origin to the experimentally determined strength to the distance along the same line from the origin to the intersection with the interaction diagram. These test-to-predicted ratio results are plotted with respect to eccentricity and steel ratio in Figure 4 for CCFT beam-columns. The mean value and variation is significantly higher for the specimens with zero eccentricity and again, no definitive trends are identified with respect to the steel ratio. Statistical data for the test-to-predicted ratio for various subsets of the database are presented in Table 3.

A more detailed analysis of these results is warranted to better understand the variations in the test-to-predicted ratio. For the analyses in the following sections, the statistical data for X_{model} is taken as $\mu_{model} = 1.00$ and $V_{model} = 0.08$ for both RCFT columns and short beam-columns.

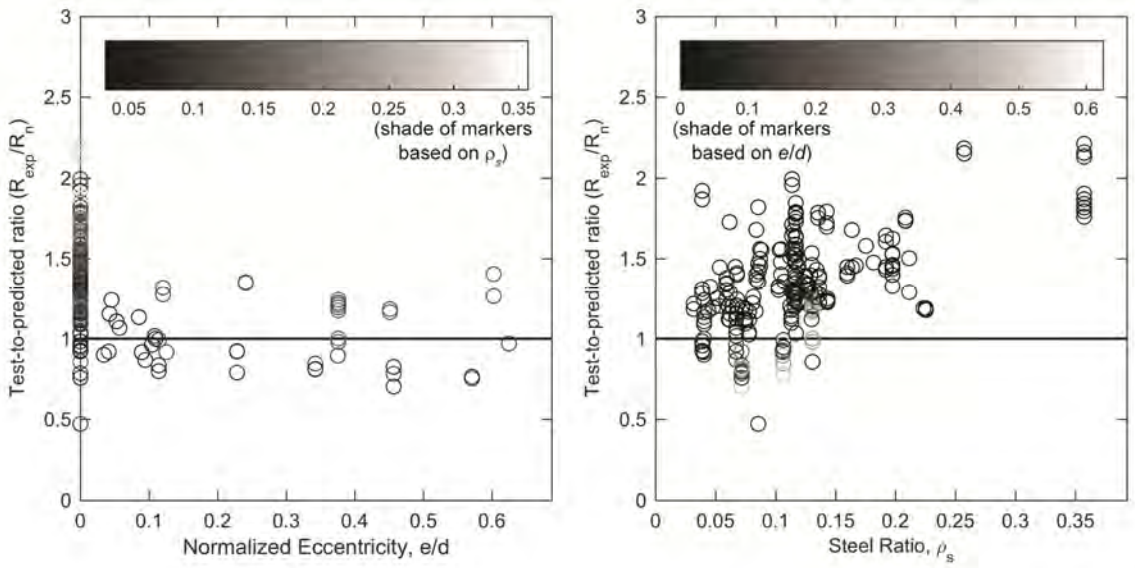


Figure 4 – Database results for CCFT short ($L_c/d \leq 5$) beam-column specimens

Table 3 – Test-to-predicted ratio statistics for short ($L_c/d \leq 5$) beam-column specimens

Member Type	Case	Number of Specimens	Mean	Standard Deviation	CV
CCFT	All	252	1.328	0.296	0.227
	$e = 0$	206	1.396	0.272	0.195
	$e > 0$	46	1.026	0.191	0.186
RCFT	All	117	1.077	0.138	0.128
	$e = 0$	91	1.094	0.148	0.135
	$e > 0$	26	1.019	0.076	0.074
SRC	All	17	1.279	0.181	0.142
	$e = 0$	9	1.246	0.157	0.126
	$e > 0$	8	1.315	0.210	0.159

COLUMNS

The results of a Monte Carlo simulation of a RCFT column are presented in Figure 5. These results are for the cross section described previously for the interaction diagrams of Figure 2. Monte Carlo simulations were run, obtaining 500 instances of the cross section following the statistical data given in Table 1. For each cross section, the compressive strength was computed using Equation (1) for column lengths ranging from 0 to 50H. At each length, the minimum, 5th percentile, median, 95th percentile, and maximum strengths were identified and plotted along with the strength using nominal properties. Histograms of the strength are shown for L_c/H = 0, 20 and, 40. Note that in this figure, the strength is normalized by the compressive strength without length effects, P_{no}, calculated with nominal properties. The variation in the material and geometric properties is shown in Figure 5. The variation due to uncertainty in the model (i.e., the professional factor) is not included in Figure 5.

In Figure 5, the nominal strength coincides most closely with the 95th percentile. The primary reason for this is the mean concrete compressive strength is about 74% of the nominal strength (Table 1). The value for the mean concrete compressive strength was obtained following the recommendations of Mirza et al. (1979) which account for variations between in-situ strength

and control cylinder strength as well as speed of loading. Other, more recent, references may provide different values.

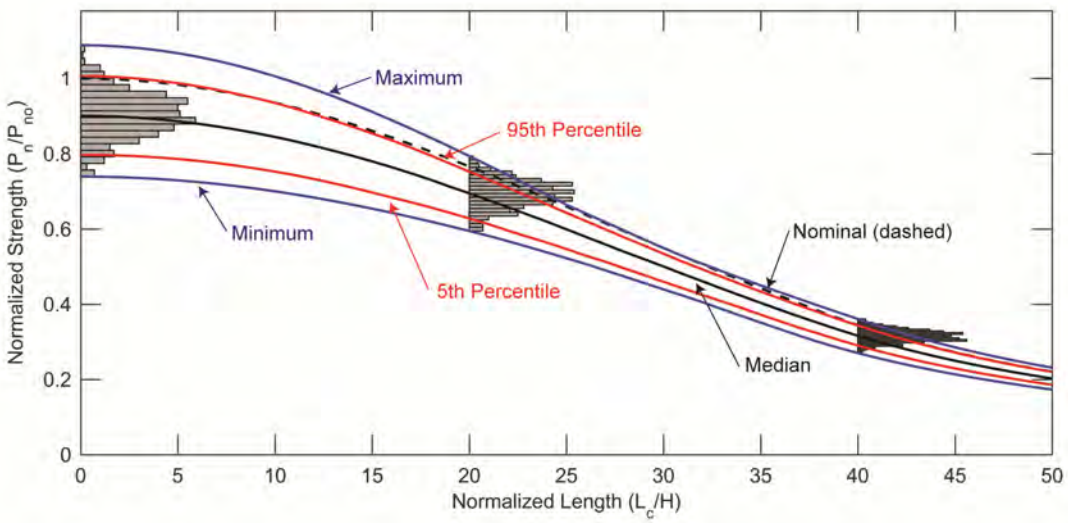


Figure 5 – Column Monte Carlo simulation results

The resistance factor is obtained using Equation (8) and combining the Monte Carlo simulation results (Figure 5) with the statistical data of the model in accordance with Equations (10) and (11). The computed resistance factor as a function of length is shown in Figure 6 for the RCFT cross section as well as variations of the cross section with different steel ratios. The smallest selected steel ratio is $\rho_s = 0.07$, which results in a tube slenderness near the limit for compact shapes. The largest selected steel ratio is $\rho_s = 0.50$, which is an extreme value, but could be obtained using built up steel shapes. The selected steel ratios are listed in Table 4 including the ratio of bare steel to composite design strength. Note that for the highest steel ratios, the design strength of the bare steel exceeds that of the composite member. As seen in Figure 6, there is a definite trend of the increasing steel ratio resulting in increased computed resistance factor, in some cases approaching the resistance factor for steel. Nonetheless, the current value (ϕ = 0.75) remains a reasonable average value, especially given that the minimum permitted steel ratio is $\rho_s = 0.01$.

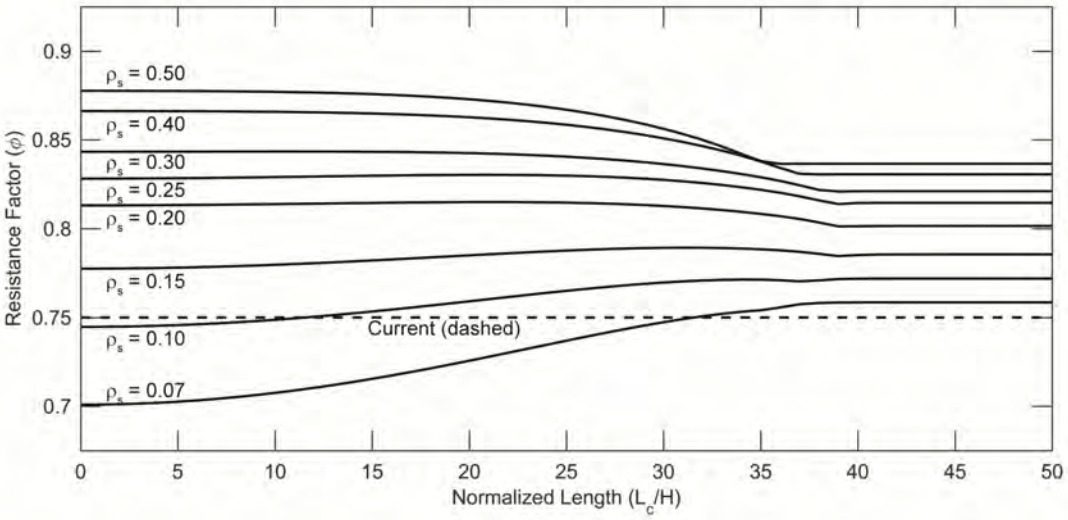


Figure 6 – Column resistance factor results

Table 4 – Steel ratio case data

Steel Ratio, ρ_{sn}	Tube Thickness, t_n	H/t_n	$\phi P_{n,steel}/\phi P_n$		
			$L_c/H = 0$	$L_c/H = 20$	$L_c/H = 40$
0.07	5.49 mm	55.5	0.426	0.476	0.658
0.10	7.94 mm	38.4	0.536	0.581	0.737
0.15	12.17 mm	25.1	0.671	0.706	0.821
0.20	16.57 mm	18.4	0.767	0.801	0.912
0.25	21.15 mm	14.4	0.838	0.871	0.978
0.30	25.91 mm	11.8	0.892	0.923	1.029
0.40	36.01 mm	8.5	0.965	0.997	1.097
0.50	46.84 mm	6.5	1.010	1.044	1.137

SHORT BEAM-COLUMNS

The results of a Monte Carlo simulation of a short RCFT beam-column are presented in Figure 7. These results are also for the cross section described previously for the interaction diagrams of Figure 2. Monte Carlo simulations were run, obtaining 500 instances of the cross section following the statistical data given in Table 1. For each cross section, the strength interaction diagram for combined axial compression and bending moment was computed using the PSD method for enough points to effectively approximate the continuous curve. At various eccentricities (i.e., angles from the origin), the minimum, 5th percentile, median, 95th percentile, and maximum strengths were identified and plotted along with the strength using nominal properties. Histograms of the strength are shown for e/H = 0, 0.2, and infinity (pure bending). Again, the variability shown in Figure 7 is representative of the variation in the material and geometric properties only, variation due to uncertainty in the model (i.e., the professional factor) is additional.

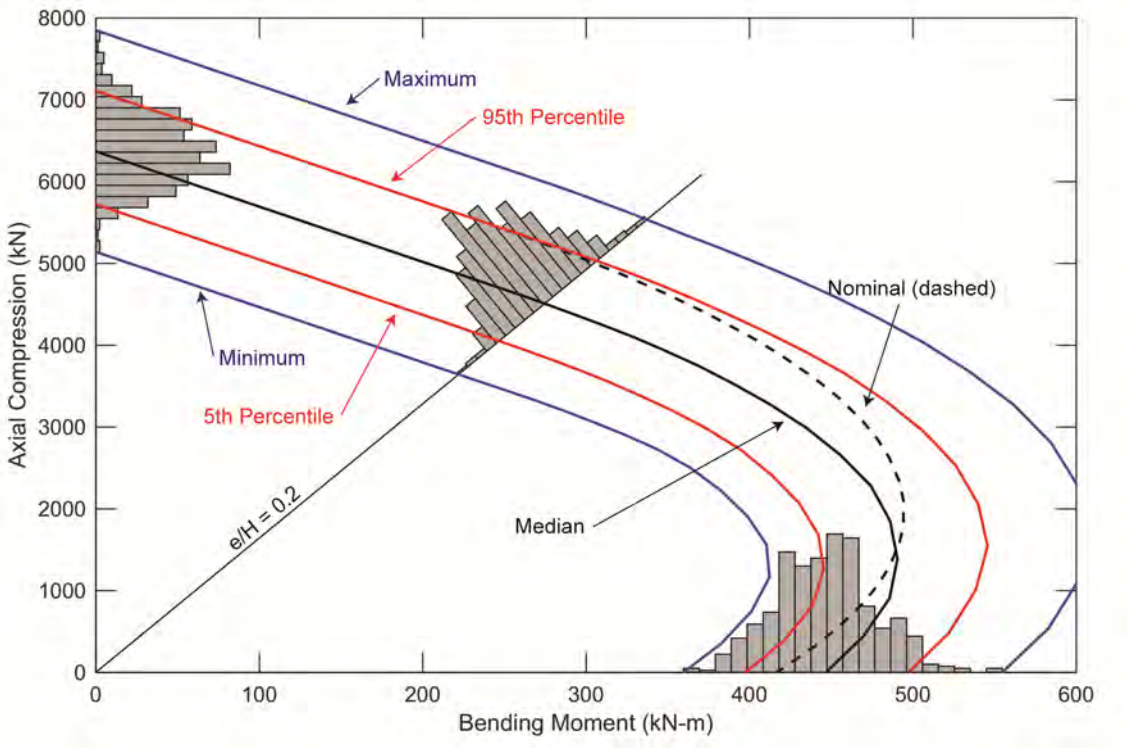


Figure 7 – Short beam-column Monte Carlo simulation results

The resistance factor is obtained using Equation (8) and combining the Monte Carlo simulation results (Figure 7) with the statistical data of the model in accordance with Equations (10) and (11). The computed resistance factor, as a function of eccentricity, is shown in Figure 8. Also shown in Figure 8 are the current resistance factor and one defined by Equation (7). To obtain the current resistance factor, the nominal interaction diagram was computed and a factored interaction diagram was obtained following the recommendations in the commentary to the AISC *Specification* (AISC 2016), these diagrams are shown in Figure 2a. The resistance factor as a function of eccentricity was computed as the ratio of the radial distance from the origin to the factored curve to the radial distance from the origin to the nominal curve. Note the range of eccentricities where the current resistance factor exceeds 0.9, these are within the "bulge" region of the interaction diagram where potential unconservative results were noted previously. To obtain the resistance factor per Equation (7), the location of the neutral axis was recorded during the computation of each point on the nominal interaction diagram. With Equation (7), a monotonic transition between the resistance factor for compression (ϕ = 0.75) and the resistance factor for flexure (ϕ = 0.9) is obtained. This more closely matches the calculated resistance factor, further indicating it may provide a better solution than the current recommendations.

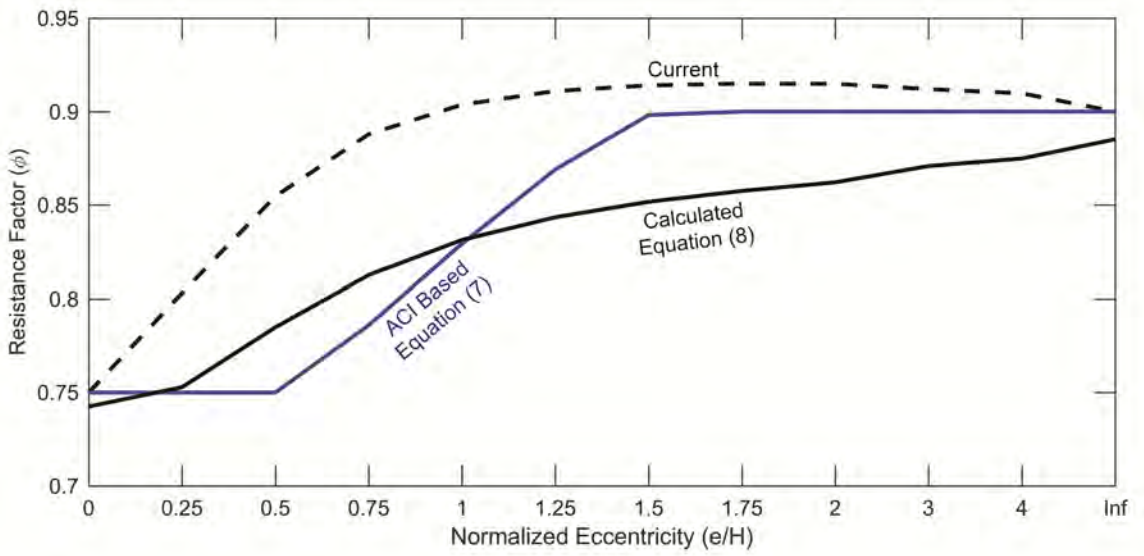


Figure 8 – Short beam-column resistance factor results

CONCLUSIONS

In this paper, the reliability of steel-concrete composite columns and their provisions within the AISC *Specification* (AISC 2016) was examined. Variations due to uncertainty in the material and geometric properties were accounted for through Monte Carlo simulations. Variations due to uncertainty in the prediction of strength was approximated through evaluation of an experimental database. A RCFT cross section was selected for detailed examination and the resistance factor was computed for axial compressive strength for a variety of steel ratios and for short beam-columns. The following conclusions were noted. There remains some inconsistency in the provisions for the resistance factor for composite columns, notably for highly steel dominant columns and for the application of the resistance factor to strength under combined axial compression and bending moment. A sizable portion of the uncertainty originates in the modeling capability (i.e., the "professional factor"), and further research would be useful to better understand and reduce the variation. The computed resistance factor is

dependent on cross-sectional properties, including steel ratio, as well as, column length, and eccentricity. The potential for a more accurate and more consistent method of applying resistance factors to interaction diagrams based on provisions within the ACI *Code* (ACI 2014) was identified, however, further research is required too fully calibrate such an approach.

REFERENCES

ACI. (2014). *Building Code Requirements for Structural Concrete and Commentary*. American Concrete Institute, Farmington Hills, MI.

AISC. (1986). *Load and Resistance Factor Design Specification for Structural Steel Buildings*. American Institute of Steel Construction, Chicago, Illinois.

AISC. (2005). *Specification for Structural Steel Buildings*. American Institute of Steel Construction, Chicago, Illinois.

AISC. (2010). *Specification for Structural Steel Buildings*. American Institute of Steel Construction, Chicago, Illinois.

AISC. (2013). *Seismic Design Manual, 2nd Ed.* American Institute of Steel Construction, Chicago, Illinois.

AISC. (2016). *Specification for Structural Steel Buildings*. American Institute of Steel Construction, Chicago, Illinois.

ASCE. (2010). *Minimum Design Loads for Buildings and Other Structures*. American Society of Civil Engineers, Reston, Virginia.

Aslani, F., Lloyd, R., Uy, B., Kang, W.-H., and Hicks, S. (2016). "Statistical calibration of safety factors for flexural stiffness of composite columns." *Steel and Composite Structures*, 20(1), 127–145.

Bartlett, F. M., Dexter, R. J., Graeser, M. D., Jelinek, J. J., Schmidt, B. J., and Galambos, T. V. (2003). "Updating Standard Shape Material Properties Database for Design and Reliability." *AISC Engineering Journal*, (1), 2–14.

Beck, A. T., de Oliveira, W. L. A., De Nardim, S., and ElDebs, A. L. H. C. (2009). "Reliability-based evaluation of design code provisions for circular concrete-filled steel columns." *Engineering Structures*, 31(10), 2299–2308.

Denavit, M. D., Hajjar, J. F., Perea, T., and Leon, R. T. (2016). "Stability Analysis and Design of Composite Structures." *Journal of Structural Engineering*, ASCE, 142(3), 04015157.

Goode, C. D. (2008). "Composite Columns - 1819 Tests on Concrete-Filled Steel Tube Columns Compared with Eurocode 4." *The Structural Engineer*, 86(16), 33–38.

Kim, D. K. (2005). "A Database for Composite Columns." M.S. Thesis, School of Civil and Environmental Engineering, Georgia Institute of Technology, Atlanta, Georgia.

Kogut, G. F., and Chou, K. C. (2004). "Partial resistance factor design on steel–concrete beam-columns." *Engineering Structures*, 26(7), 857–866.

Kvedaras, A. K., and Kudzys, A. (2006). "The structural safety of hollow concrete-filled circular steel members." *Journal of Constructional Steel Research*, 62(11), 1116–1122.

Lundberg, J. E., and Galambos, T. V. (1996). "Load and Resistance Factor Design of Composite Columns." *Structural Safety*, 18(2–3), 169–177.

Mirza, S. A., Hatzinikolas, M., and MacGregor, J. G. (1979). "Statistical Descriptions of Strength of Concrete." *Journal of the Structural Division*, ASCE, 105(6), 1021–1037.

Mirza, S. A., and Skrabek, B. W. (1991). "Reliability of Short Composite Beam-Column Strength Interaction." *Journal of Structural Engineering*, ASCE, 117(8), 2320–2339.

Mirza, S. A., and Skrabek, B. W. (1992). "Statistical Analysis of Slender Composite Beam-Column Strength." *Journal of Structural Engineering*, ASCE, 118(5), 1312–1332.

Ravindra, M. K., and Galambos, T. V. (1978). "Load and Resistance Factor Design for Steel." *Journal of the Structural Division*, ASCE, 104(9), 1337–1353.

CALIBRATION OF THE ELASTIC FLEXURAL RIGIDITY FROM AMBIENT VIBRATION MEASUREMENTS FOR A BUILDING WITH ENCASED COMPOSITE COLUMNS

Tiziano Perea
Universidad Autónoma Metropolitana, Azcapotzalco
Mexico City, Mexico.
tperea@azc.uam.mx

Miguel A. Garcia
Kiewit Energy de Mexico
Mexico City, Mexico.
miguel.garcia@kiewit.com

Manuel E. Ruiz-Sandoval
Universidad Autónoma Metropolitana, Azcapotzalco
Mexico City, Mexico.
mrh@azc.uam.mx

Roberto T. Leon
Virginia Polytechnic Institute and State University
Blacksburg, Virginia, USA.
rleon@vt.edu

Mark D. Denavit
University of Tennessee, Knoxville
Knoxville, Tennessee, USA.
mdenavit@utk.edu

Jerome F. Hajjar
Northeastern University
Boston, Massachusetts, USA.
JF.Hajjar@northeastern.edu

ABSTRACT

Calibrated results of the elastic flexural rigidity ($EI_{elastic}$) for the determination of the fundamental period of a building with encased composite columns, also known as Steel Reinforced Concrete (SRC) columns, are discussed in this paper. This calibration is carried out from the natural frequencies measured from an ambient vibration test and from modal analyses using available semi-empirical equations proposed by researchers and adopted in some codes. The twenty-five-story building evaluated in this study is an ordinary composite moment frame system (C-OMF) in the longitudinal direction, with two ordinary X braced frames (C-OBF) in the transversal direction, and with SRC composite columns integrated by an H built-up steel section encased with a reinforced concrete section. Vibration periods obtained from the ambient vibration test show that the use of the effective flexural stiffness for encased composite columns in the previous AISC Specification were too conservative for the period prediction in modal analysis. The lowest errors for the evaluated building are those given in Eurocode, ACI, and the one proposed by Denavit *et al*. that was recently adopted in the latest AISC Specification.

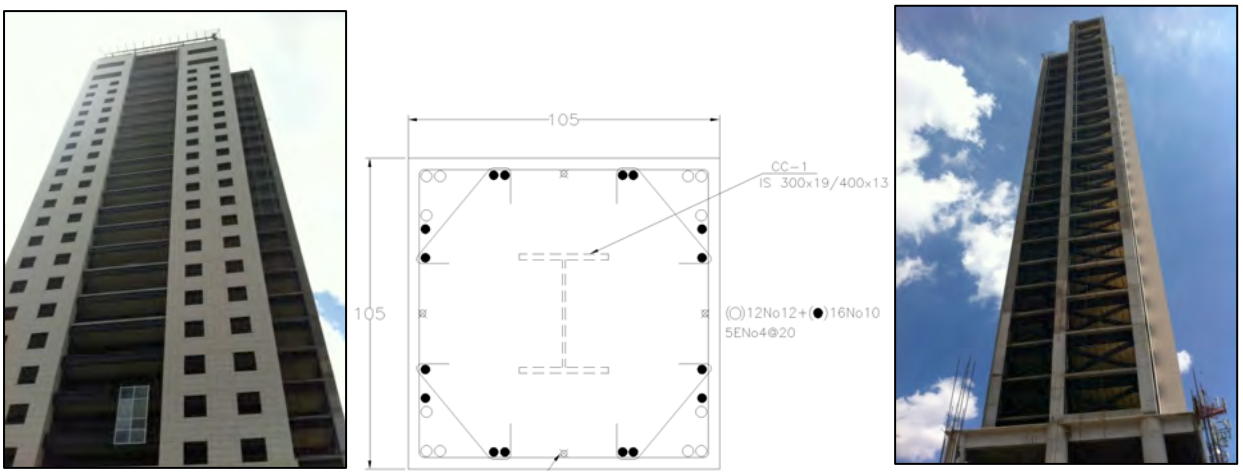
INTRODUCTION

Structural systems based on steel-concrete composite construction have developed a growing popularity in past few decades because of their many structural and constructional advantages. However, the increasing construction of composite structural systems in high seismic risk zones around the world has shown that existing specifications are not capable of providing the robust parameters needed to check all critical strength and service limit states. Particularly, the lack of clear guidelines on the flexural stiffness that must be used in the elastic analysis of structural systems with composite columns is a significant unresolved issue, making difficult the determination of the dynamic properties and thus the seismic forces for these systems. The common practice of only using either the concrete or the steel stiffness generally tends to be significantly conservative. Other efforts have considered a weighted superposition of each material stiffness, but some of them have not been fully validated for all the limit states, such as those regarding the strength, stability, and serviceability, as well as for the determination of the vibration frequencies or periods, and the lateral interstory drifts. In this paper, unique ambient vibration tests on a large structure incorporating steel concrete reinforced (SRC or encased) columns are used to attempt to validate several proposed approaches to determining column stiffness elastic properties.

AMBIENT VIBRATION TESTS

Description of the building

The evaluated structure in this study is shown in Figure 1. It is a 25-story building with a height of 98.2 m. intended for commercial and office use, with four basement levels supported on concrete piles. As shown in Figures 1(a) and 1(c), the structural system is a composite ordinary moment frames (C-OMF) in the longitudinal direction, and two ordinary composite X braced frames (C-OBF) in the transversal direction. A typical plan view of the building is shown in Figure 2. All the columns have encased or SRC composite cross-section as illustrated in figure 1(b), consisting of a steel built-up I-shape encased by a square reinforced concrete section with 105 cm. sides. The steel section is built-up by plates (ASTM A-572 Gr. 50) of 300x19 mm. for the flanges, and 400x13 mm. for the web. The concrete has a compression strength of f_c' =24.5 MPa (3.6 ksi), reinforced with 12#38 bars (12#12) and 16#32 bars (#10), and confined by double #13 (#4) ties spaced at 200 mm as shown in Figure 1(b). The floor system consists of a precast slab supported by the principal steel beams in non-composite action.



(a) North side (b) SRC cross-section (c) West side

Figure 1 – Composite building studied

Ambient vibration measurements

Shortly after most of the structure had been completed, an ambient vibration test was conducted on the structure. In these types of measurements, the quality of the data depends on the correct horizontal and vertical distribution of the sensors, as well as the sensitivity and precision of the instruments.

The equipment used for recording the ambient vibration consisted of a data acquisition (DAQ) system (Siglab 20-42), with a 20-bit analog-digital converter (A/D), and an anti-alias filter of 90 dB. Also, four seismic sensors (PCB, model 393B31) were used, as well as a laptop to command the DAQ system and store the vibration data.

Four sensors were used to measure the ambient vibrations for 15 minutes. Figure 4 illustrates the sensor layout placed on the building roof, with two sensors located at the centroid oriented in both the longitudinal and transverse directions, and two additional sensors placed at the roof ends with the aim of evaluating twisting.

It should be noted that, when this test was performed, the building was under construction, presenting a progress of 100% for the structural members (i.e. beams, columns, braces), but with no presence of contents or non-structural elements (e.g. facade, partitions, collateral loads). Thus, the only mass source during the testing was the self-weight of the structural members and the sources of lateral stiffness could be easily identified.

With the aim to determine dynamic properties of the soil, vibrations were also measured in the ground using two sensors, one oriented in the north direction and the other in the vertical direction.

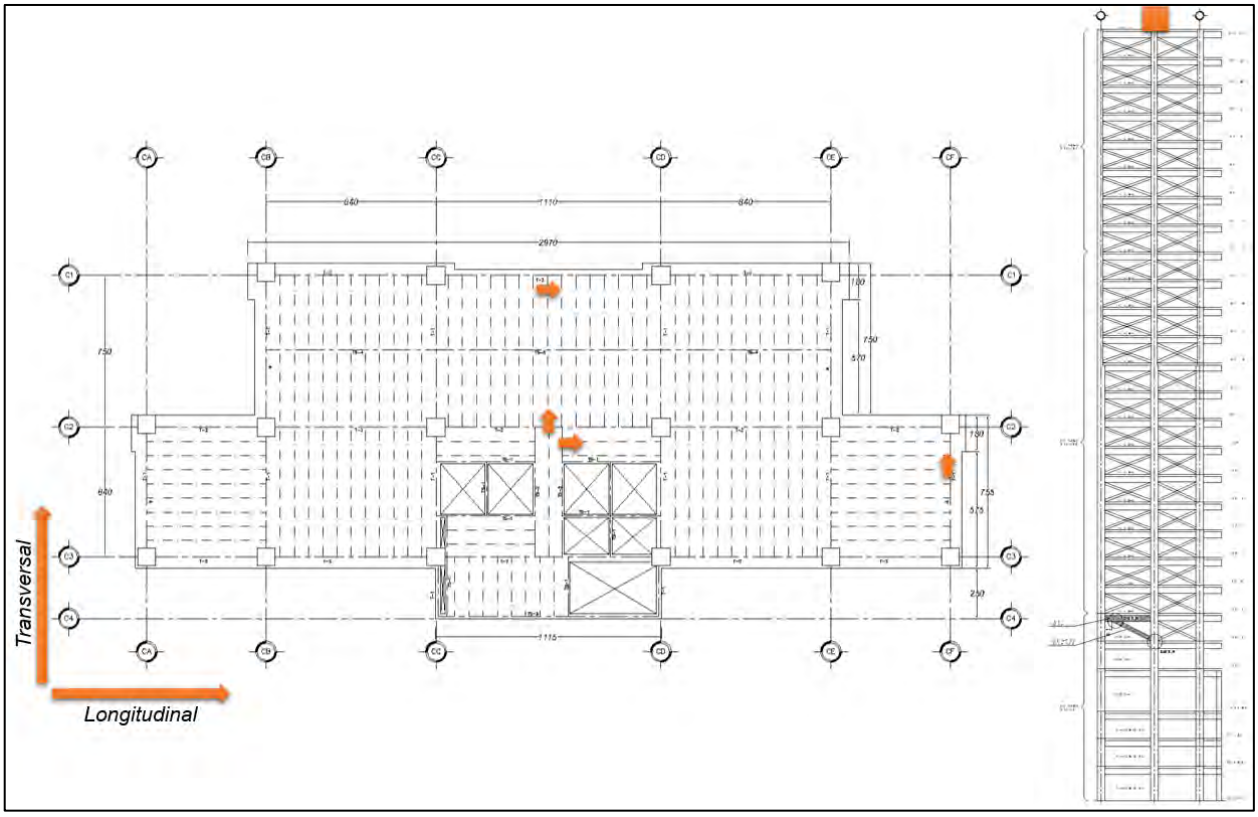


Figure 2 – Plan view and frontal view of the building showing the location of sensors

Data processing

The process to determine the dynamic properties is divided into two stages. The first consists in recording the vibrations captured by sensors in the central unit. The second is data processing, including a baseline correction, signal filtering, and finally transforming the vibration data from time domain to frequency domain. The technique used to make the switch domain is the fast Fourier transform (Bendat and Piersol, 1989). The Fourier transform can be defined by the following equation:

$$\ddot{X}(f) = \int_0^T \ddot{x}(t) e^{-i \cdot 2\pi f \times dt} \tag{1}$$

which can be written as:

$$\ddot{X}(f) = \int_0^T \ddot{x}(t) \cos(2\pi f \times t) dt - i \int_0^T \ddot{x}(t) sen(2\pi f \times t) dt \tag{2}$$

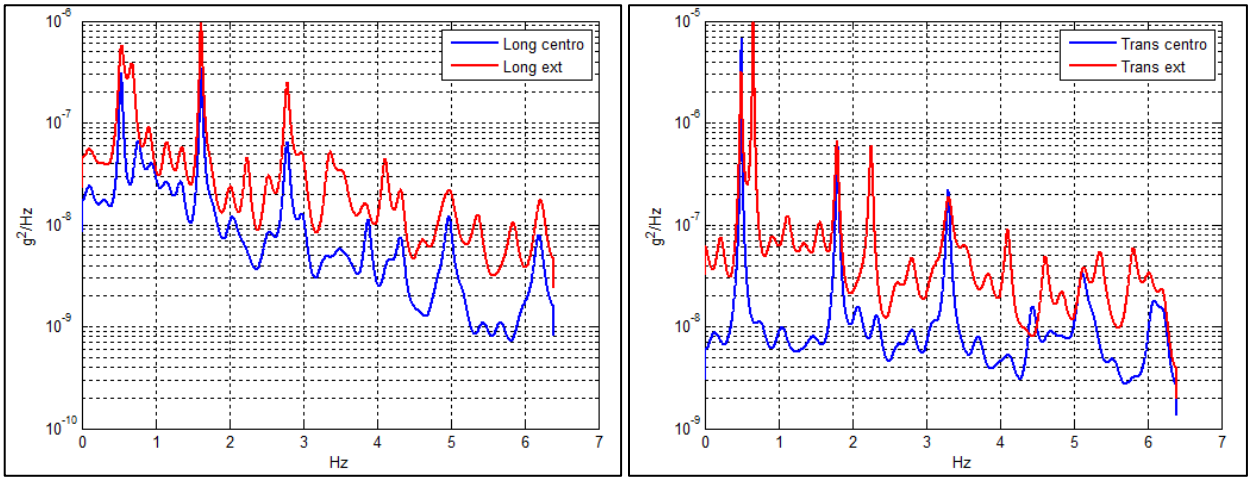
Fourier amplitudes $\ddot{X}(f)$ are made up of a real part $\ddot{X}_R(f)$ and an imaginary $\ddot{X}_I(f)$.

$$\left|\ddot{X}(f)\right| = \sqrt{\ddot{X}_R(f)^2 + \ddot{X}_I(f)^2} \tag{3}$$

The power spectral density of the signals is calculated per the following equation:

$$S_{xx}(f) = \ddot{X}(f) \times \ddot{X}(f) \tag{4}$$

The natural frequencies of the system will produce peaks in the power spectral density, indicating that they have greater participation in the frequency content of the recorded signals. These peaks can easily identify the natural frequencies for the principal modes, as shown in Figures 3(a) and 3(b). The reciprocals of these frequencies correspond to the vibration periods.



(a) Longitudinal or X direction (b) Transversal or Y direction

Figure 3 – Power spectra obtained from the vibration recordings

Table 1 shows the estimated periods for the first three vibration modes corresponding to the longitudinal, transversal, and torsional directions. Environmental vibrations were also measured in the field adjacent to the building to determine the site period. After applying the Nakamura´s technique (1989), the ground period resulted with a value of 0.79 seconds.

Table 1 – Natural vibration periods measured of the building

Mode	Period (s)		
	Longitudinal (X)	Transversal (Y)	Torsional
1	2.030	1.890	1.509
2	0.555	0.617	0.443
3	0.302	0.359	0.244

EQUATIONS FOR THE FLEXURAL STIFFNESS OF ENCASED COMPOSITE COLUMNS

One of the main issues related to the design of composite systems regards the determination of the appropriate stiffness for composite members to be used in the different analysis and calculations required, including periods, stability and displacements.

Some current design codes include equations for the determination of the effective flexural stiffness for composite members; however, the values determined with these equations vary significantly from each other, creating uncertainty about which is the closest to the real performance value.

Table 2 shows some expressions to calculate the effective flexural stiffness (EI_{eff}) for encased or SRC composite columns. This table includes both equations contained in design codes and those proposed by researches. The one proposed by Denavit *et al*. (2014, 2016) was recently adopted in the latest AISC Specification (AISC 2016). Eurocode (CEN 2004) has two equations of the effective flexural stiffness, one for the slenderness calculation in buckling analysis, and a second one (which is used in this work) for internal forces calculation in second-order analysis.

Table 2 – Available equations of the effective flexural stiffness for encased composite columns

Code / Author	Equation	X direction	Y direction
Tikka and Mirza (2006)	$EI_{eff} = \frac{\alpha_c E_c \left(I_g + I_s\right)}{\left(1-\beta_d\right)} + 0.8\left(I_s + I_{sr}\right)$	$EI_{eff} = 0.537E_cI_g$ $EI_{eff} = 14.404E_sI_s$ $EI_{eff} = 0.563E_cI_c$	$EI_{eff} = 0.514E_cI_g$ $EI_{eff} = 72.304E_sI_s$ $EI_{eff} = 0.539E_cI_c$
Denavit *et al*. (2014) AISC (2016)	$EI_{eff} = E_sI_s + E_sI_{sr} + C_1E_cI_c$ $C_1 = 0.25 + 3\left(\frac{A_s + A_{sr}}{A_g}\right) \le 0.70$	$EI_{eff} = 0.72E_cI_g$ $EI_{eff} = 19.335E_sI_s$ $EI_{eff} = 0.756E_cI_c$	$EI_{eff} = 0.69E_cI_g$ $EI_{eff} = 97.224E_sI_s$ $EI_{eff} = 0.724E_cI_c$
AISC (2010)	$EI_{eff} = E_sI_s + 0.5E_sI_{sr} + C_1E_cI_c$ $C_1 = 0.10 + 2\left(\frac{A_s}{A_s + A_c}\right) \le 0.30$	$EI_{eff} = 0.328E_cI_g$ $EI_{eff} = 8.792E_sI_s$ $EI_{eff} = 0.344E_cI_c$	$EI_{eff} = 0.297E_cI_g$ $EI_{eff} = 41.893E_cI_g$ $EI_{eff} = 0.312E_cI_c$
ACI (2014)	$EI_{eff} = 0.7E_cI_g$	$EI_{eff} = 0.7E_cI_g$ $EI_{eff} = 18.786E_sI_s$ $EI_{eff} = 0.734E_cI_c$	$EI_{eff} = 0.7E_cI_g$ $EI_{eff} = 98.592E_sI_s$ $EI_{eff} = 0.734E_cI_c$
Eurocode (2004)	$EI_{eff} = 0.9\left(E_sI_s + E_sI_{sr} + 0.5E_cI_c\right)$	$EI_{eff} = 0.764E_cI_g$ $EI_{eff} = 20.499E_sI_s$ $EI_{eff} = 0.801E_cI_c$	$EI_{eff} = 0.737E_cI_g$ $EI_{eff} = 107.577E_sI_s$ $EI_{eff} = 0.764E_cI_g$
Gross flexural stiffness	$EI_{gross} = E_sI_s + E_sI_{sr} + E_cI_c$	$EI_{gross} = 1.325E_cI_g$ $EI_{gross} = 35.57E_sI_s$ $EI_{gross} = 1.39E_cI_c$	$EI_{gross} = 1.295E_cI_g$ $EI_{gross} = 182.426E_sI_s$ $EI_{gross} = 1.358E_cI_g$

Table 2 also includes the calculated values for each effective flexural stiffness equation, and for each direction, using the material and geometric information of the encased composite column (Figure 1(b)) for the building under study (Figures 1 and 2). These values are normalized with the concrete Young´s modulus and the gross moment of Inertia (E_cI_g), the flexural stiffness of the steel stiffness (E_sI_s), and the flexural stiffness of the concrete section (E_cI_c). The gross flexural stiffness (E_cI_g) is defined as the superposition of the steel, reinforcement and concrete flexural stiffness using a value of E_s = E_{sr} = 210 GPa (29,000 ksi) for the steel and E_c = 21.7 GPa (3,150 ksi) for the concrete as determined from the local concrete code.

MODAL ANALYSIS

This section shows the results of the modal analysis for the composite building previously described, in which the different values of effective stiffness of composite columns that were presented in Table 2 are used. Figure 6 shows the first three vibration modes of the building. The structural model of the building includes the concrete walls already built when the vibration test was performed.

Note that the prediction of the masses in the structure correspond to the best estimate at the time when the vibrations were measured. Since the building was under construction (and thus an absence of non-structural members or contents), the main source of masses in the building correspond to the self-mass of the structural members and the construction loads, which allowed to reduce the expected dispersion at frequencies of vibration due to uncertainties in the masses of the system. Therefore, the rigidity of the structure, which mainly depends on the elastic flexural stiffness ($EI_{elastic}$) of the composite columns, is the target variable to calibrate for the accurate determination of the natural vibration periods in composite moment frames.

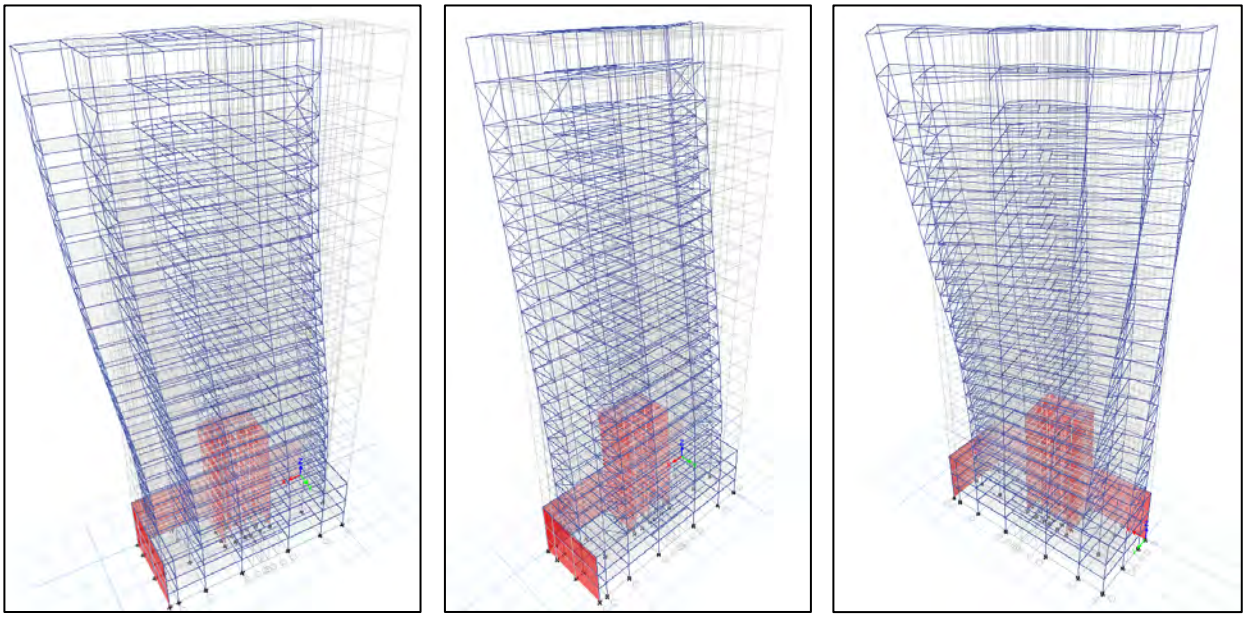


Figure 4 – Analytical models of the studied building

Table 3 shows the results of the modal analysis for the evaluated building. Although higher modes and periods were calculated from modal analysis, this table shows only the fundamental

period for each direction. For the beams, the flexural stiffness of the steel was used since they are in non-composite action with the concrete precast slab. For the encased composite columns, the effective flexural stiffness enlisted in table 3 were used in the modal analysis.

Table 3 – Fundamental vibration periods obtained from modal analysis

Code / Author	Equation	Fundamental vibration period (s)		
		Longitudinal	Transversal	Torsional
Tikka and Mirza (2006)	$EI_{eff} = \frac{\alpha_c E_c \left(I_g + I_s\right)}{\left(1-\beta_d\right)} + 0.8\left(I_s + I_{sr}\right)$	2.282	2.237	1.740
Denavit *et al*. (2014) AISC (2016)	$EI_{eff} = E_s I_s + E_s I_{sr} + C_1 E_c I_c$ $C_1 = 0.25 + 3\left(\frac{A_s + A_{sr}}{A_g}\right) \le 0.70$	2.211	2.075	1.643
AISC (2010)	$EI_{eff} = E_s I_s + 0.5E_s I_{sr} + C_1 E_c I_c$ $C_1 = 0.10 + 2\left(\frac{A_s}{A_s + A_c}\right) \le 0.30$	2.637	2.446	1.966
ACI (2014)	$EI_{eff} = 0.7E_c I_g$	2.218	2.089	1.591
Eurocode (2004)	$EI_{eff} = 0.9\left(E_s I_s + E_s I_{sr} + 0.5E_c I_c\right)$	2.198	2.045	1.613
Gross flexural stiffness	$EI_{gross} = E_s I_s + E_s I_{sr} + E_c I_c$	2.087	1.799	1.431

EXPECTED DIFFERENCES WITH FORCED AND SEISMIC VIBRATIONS

Studies reveal that, for different levels of vibrations, such as those generated by an earthquake, the natural frequencies or periods may change depending on the excitation amplitudes that affects the structure (Trifunac 1972, Lamarche 2002, Murià 2007, among others). The increase in the vibration intensity causes a decrease in the fundamental frequency (or an increase in the period) of the structure relative to the corresponding one that would be obtained with lower intensities such as those generated by ambient vibrations. This is due to changes in the structure rigidity and damping, particularly when the system is at the non-linear range. Therefore, it is expected that the periods obtained from ambient vibrations will be relatively lower compared to those measured from forced vibrations and seismic vibrations. To illustrate the possible dispersion, Table 4 shows some ratios reported in the literature of periods obtained from forced vibrations over periods obtained from ambient vibrations. Although this table does not report all the available studies on the subject, this reflects that the expected discrepancy between ambient and forced vibrations is about 1% to 5%. Due to possible changes in the structure rigidity during strong ground motions, higher values and more dispersion are expected between periods obtained from seismic vibration and those obtained from ambient vibration measurements (Rodríguez 2001, Murià 2000, 2001, 2007).

Table 4 – Ratios of forced vibration periods to ambient vibration periods

Reference	Ratios			Structural system
	Longitudinal	Transversal	Torsional	
Trifunac (1972a)	1.038	1.047	1.035	22-story steel building
Trifunac (1972b)	1.017	1.033	1.011	9-story concrete building
Lamarche (2002)	1.019	1.017	1.017	2-story concrete frame system

Since the vibration periods in a modal analysis are determined from the elastic stiffness of the system, it is expected that the periods obtained with ambient vibrations are the best estimators of analytical periods under the actual conditions of mass and stiffness (as assumed in this study). However, slight errors between analytical and measured periods are possible due to some uncertainties (e.g. real elastic modulus of the component materials, potential soil-structure interaction, differences between estimated and actual mass, among others).

Also, note that the reported periods in this paper correspond to the conditions when the building was measured (which was under construction as described earlier). However, the system periods will change when the construction is completed and the building is under full operation (i.e. when the building is under the ultimate conditions of stiffness and mass).

COMPARISON OF RESULTS

This section presents and discusses the obtained periods (for the first vibration mode at each direction) extracted from the ambient vibration testing (reported in Table 1), and those calculated from the modal analysis (reported in Table 3) assuming the different effective stiffness equations of the composite columns (reported in Table 2).

The error values between the periods calculated from the modal analysis and those measured from ambient vibration testing are listed in Table 5. These errors are also plotted in Figure 7.

Table 5 – Errors between ambient vibrations calculated and measured periods

Code / Author	Equation	Longitudinal	Transversal	Torsional
Tikka and Mirza (2006)	$EI_{eff} = \frac{\alpha_c E_c \left(I_g + I_s\right)}{\left(1-\beta_d\right)} + 0.8\left(I_s + I_{sr}\right)$	12.4%	18.4%	15.3%
Denavit *et al*. (2014) AISC (2016)	$EI_{eff} = E_s I_s + E_s I_{sr} + C_1 E_c I_c$ $C_1 = 0.25 + 3\left(\frac{A_s + A_{sr}}{A_g}\right) \le 0.70$	8.9%	9.8%	8.9%
AISC (2010)	$EI_{eff} = E_s I_s + 0.5 E_s I_{sr} + C_1 E_c I_c$ $C_1 = 0.10 + 2\left(\frac{A_s}{A_s + A_c}\right) \le 0.30$	29.9%	29.4%	30.3%
ACI (2014)	$EI_{eff} = 0.7 E_c I_g$	9.3%	10.5%	5.4%
Eurocode (2004)	$EI_{eff} = 0.9\left(E_s I_s + E_s I_{sr} + 0.5 E_c I_c\right)$	8.3%	8.2%	6.9%
Gross flexural stiffness	$EI_{gross} = E_s I_s + E_s I_{sr} + E_c I_c$	2.8%	-4.8%	-5.2%

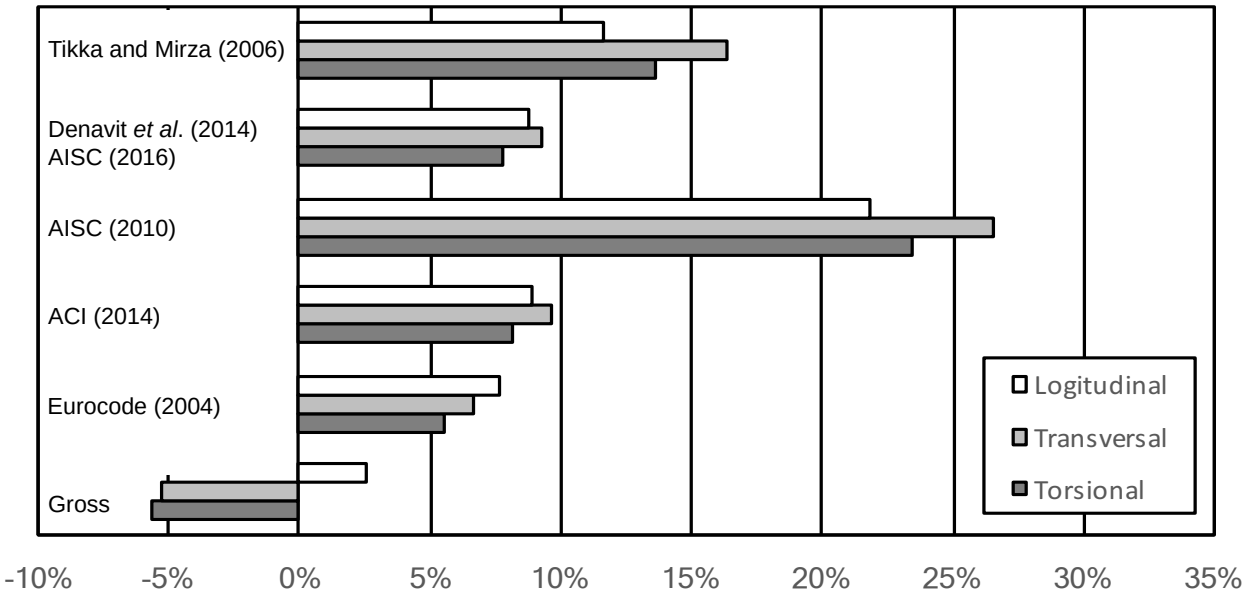


Figure 7 – Errors between periods calculated from the modal analysis and those measured from ambient vibration testing

As seen by comparing the results and the corresponding errors, the gross flexural stiffness provides the smaller absolute errors. However, for both the transversal and torsional direction, these are negative errors, which means that the assumed stiffness is greater than the one developed by the system (presumed as the one obtained from the ambient vibration test), and thus resulting in an inconsistency. Consequently, the gross flexural stiffness is likely too high for general use within an elastic analysis.

Somewhat larger errors (between 5% to 10%) were obtained when the effective flexural stiffness for the encased composite columns were determined by the equation in Eurocode (2004), ACI (2014), and Denavit *et al*. (2014). Note that, for the encased composite columns in this building, the effective flexural stiffness is near $0.7E_cI_g$ with these three equations as shown in Table 2. For different encased cross-sections, the ACI equation will retain the value of $0.7E_cI_g$, while the equations by Denavit *et al*. (2014) and Eurocode (2004) may vary due to the different participation coefficients within these two equations.

The highest errors were obtained from the equations proposed by Tikka and Mirza (2008), with an average error about 15%, and from the equation of the AISC Specification (AISC 2010), with an average error around 30%. It is worth mention that these two equations were originally calibrated for the slenderness and the axial compressive strength of the available experimental data of encased composite columns and thus were intended for stability-type calculations.

Thus, these results suggest that the equations proposed by Eurocode (2004), ACI (2014) and Denavit *et al*. (2014) provide an adequate estimate of the expected fundamental periods, and so an adequate estimation of the seismic design forces.

CONCLUSIONS

A calibration study of the effective flexural stiffness for encased SRC composite columns in moment frames is performed utilizing unique data from an ambient vibration test and modal analysis. The results of the ambient vibration test demonstrate that this approach is relatively simple and very efficient to determine some dynamic structural properties such as vibration frequencies or periods.

Vibration frequencies and periods obtained from the ambient vibration test show that previous AISC Specification (AISC 2010) was too conservative for use in modal analysis. On the other hand, the gross flexural stiffness of the composite cross-section overestimate the actual stiffness, and thus underestimates the periods. The effective stiffness equation that provided results with the lowest errors for the evaluated building are those in Eurocode (2004), ACI (2014), and the one proposed by Denavit *et al*. (2014) that was recently adopted in the latest AISC Specification (AISC 2016).

The calibration of the elastic flexural stiffness, as presented in this article along with other methodologies, will allow to understand the evolution and degradation of the effective flexural stiffness and determine the different responses of structural systems with encased or SRC composite columns.

NOTATION

$EI_{elastic}$	Elastic flexural stiffness of the composite section.
EI_{eff}	Effective flexural stiffness of the composite section.
EI_{gross}	Gross flexural stiffness of the composite section.
E_s	Elasticity modulus of the structural steel shape.
I_s	Moment of inertia of the structural steel shape.
E_{sr}	Elasticity modulus of the reinforcement steel.
I_{sr}	Moment of inertia of the reinforcement steel.
E_c	Elasticity modulus of the concrete.
I_c	Moment of Inertia of the concrete section.
I_g	Moment of Inertia of the gross composite section (superposition of the steel, reinforcement and concrete sections).
C_1	Coefficient of the concrete stiffness in the effective stiffness of the composite column.
β_d	Relationship between the sustained axial force and the maximum required axial force.
α_c	Ratio of the axial load eccentricity and the element length.

REFERENCES

ACI. (2014). Building Code Requirements for Structural Concrete and Commentary. American Concrete Institute, Farmington Hills, MI.

AISC. (2010). Specification for Structural Steel Buildings. American Institute of Steel Construction, Chicago, Illinois.

AISC. (2016). Specification for Structural Steel Buildings. American Institute of Steel Construction, Chicago, Illinois.

Bendat J.S., Piersol A.G. (1986). “Random data, analysis and measurement procedures”. John Wiley and Sons.

CEN. (2004). Eurocode 4: Design of composite steel and concrete structures – Part 1-1: General rules and rules for buildings. European Committee for Standardization, Brussels, Belgium.

Denavit M.D., Hajjar J.F., Leon R.T., Perea. T. (2014). “Analysis and Design of Steel-Concrete Composite Frame Systems”. Structures Congress 2014, pp. 2605–2616.

Denavit, M. D., Hajjar, J. F., Perea, T., and Leon, R. T. (2016). “Stability Analysis and Design of Composite Structures.” Journal of Structural Engineering, ASCE, 142(3), 4015157.

Lamarche C.P., Mousseau S., Paultre P., Proulx J. (2002). “A comparison of ambient and forced-vibration testing of a full scale concrete structure”. Université de Sherbrooke, Sherbrooke, QC, Canada.

Murià D. (2007). “Experiencia mexicana sobre la respuesta sísmica de edificios instrumentados”. Instituto de Ingeniería UNAM. México. In Spanish.

Murià D., Fuentes L., González R. (2000). "Incertidumbres en la estimación de las frecuencias naturales de vibración de edificios". Información Tecnológica, Vol. 11, No. 3, pp. 177-184. Chile. In Spanish.

Murià D., Rodríguez G. (2001). “Análisis de los registros sísmicos obtenidos de 1993 a 1998 en el edificio Jalisco”. Instituto de Ingeniería UNAM. Colección: Serie Azul No. 628. México. In Spanish.

Nakamura Y. (1989). “A method for dynamic characteristics estimation of surface using microtremors on the ground surface”. QR of RTRI. Vol. 30, No.1, pp. 25-33.

Rodríguez G., Macías M., Murià D., Palacios C. (2001). “Respuesta sísmica de un edificio instrumentado en un periodo de 10 años”. XIII Congreso Nacional de Ingeniería Sísmica, Guadalajara, Jalisco, México. In Spanish.

Trifunac M.D. (1972). “Comparisons between ambient and forced vibration experiments”. Earthquake Engineering and Structural Dynamics, Vol. 1, pp. 133-150. John Wiley & Sons. USA.

Pushing the Envelope of Composite Column Design Using High-Strength Materials

Amit H. Varma
Professor, Lyles School of Civil Engineering, Purdue University
West Lafayette, IN, USA
ahvarma@purdue.edu

Zhichao Lai
Postdoctoral Research Associate, Lyles School of Civil Engineering, Purdue University
West Lafayette, IN, USA
laizhichao@gmail.com

ABSTRACT

AISC 360-16 prevents the use of high-strength materials (F_y ≥ 525 MPa and f'_c ≥70 MPa) for CFT columns due to lack of adequate research and comprehensive design equations. This paper addresses this gap using a three-step method. The first step consists of compiling the experimental database of high-strength rectangular CFT column tests in the literature and evaluating the possibility of extending the current AISC 360-16 design equations for estimating the strength of high-strength rectangular CFT short columns. The second step consists of conducting parametric studies using benchmarked finite element (FEM) models to: (i) address gaps in the database and (ii) develop effective stress-strain relationships for modeling the high-strength steel tube and high-strength concrete infill of rectangular CFT members. The third step consists of proposing new design equations that accurately predict the behavior and strength of high-strength rectangular CFT short columns.

INTRODUCTION

Concrete-filled steel tube (CFT) members are usually comprised of rectangular or circular steel tubes filled with concrete. CFT members can have more efficient behavior than reinforced concrete or structural steel members due to the interaction between the steel tube and concrete infill. The steel tube provides confinement to the concrete infill, while the concrete infill delays the local buckling of the steel tube (Lai et al. 2014, Lai and Varma 2015, and Lai et al. 2016). As an innovative structural component, CFT members have been used widely around the world in various structures. For example, they have been used as: (i) chords in composite arch bridges (Huang et al. 2017), (ii) mega columns in high-rise buildings (Lai et al., 2016), (iii) piles in floodwall structures (Lai and Varma, 2017), and (iv) bridge piers (Chen et al., 2017).

The current AISC Specification (AISC 360-16, 2016) prevents the use of high-strength materials for CFT columns. According to AISC 360-16 (2016), the steel yield stress (F_y) should not exceed 525 MPa, and the concrete compressive strength (f'_c) should not exceed 70 MPa. CFT members are classified as high-strength if either F_y or f'_c exceeds the specified limits. CFT members are classified as conventional-strength if both F_y and f'_c are less than or equal to the limits.

Significant experimental studies have been conducted to evaluate the behavior of conventional-strength CFT members as columns, beams, and beam-columns. For example, experimental tests on CFT columns have been conducted by researchers such as Furlong (1967), Janss and Anslijn (1974), Lin (1988), Fujimoto et al. (1995), Schneider (1998), and Han et al. (2001) among others. Experimental tests on CFT beams have been conducted by researchers such as Ichinohe et al. (1991), Elchalakani et al. (2001), Wheeler and Bridge (2004), Lennie et al. (2008), and Jiang et al. (2013) among others. Experimental tests on CFT beam-columns have been conducted by researchers such as Ichinohe et al. (1991), Prion and Boehme (1994), Nakahara and Sakino (2000), Uy (2001), and Mursi and Uy (2004) among others.

These studies have been summarized independently by researchers such as Nishiyama et al. (2002), Kim (2005), Hajjar et al. (2013), Lai et al. (2014), and Lai and Varma (2015) among others. Additional discussions of these tests and database can be found in Lai (2014). These experimental tests indicate that the behavior and strength of conventional-strength CFT members depend on parameters such as the concrete compressive strength (f'_c), steel yield stress (F_y), tube width-to-thickness ratio (b/t) or diameter-to-thickness ratio (D/t), and member length (L).

Based on the findings from these prior experimental investigations, AISC 360-16 (2016) provides design provisions for conventional-strength CFT members, which include: (i) steel tube slenderness limits (i.e., tube width-to-thickness limits) to categorize CFT members into compact, noncompact, and slender; and (ii) design equations for estimating the compressive, flexural and beam-column strength of CFT members. The authors have presented the basis (development and verification) of these design provisions elsewhere in Lai et al. (2014), Lai and Varma (2015), and Lai et al. (2016).

According to AISC 360-16 (2016), a conventional-strength rectangular CFT column is classified as compact if the governing tube slenderness ratio (λ) ≤ λ_p ($\lambda_p = 2.26\sqrt{E_s/F_y}$); if $\lambda_p < \lambda \le \lambda_r$ ($\lambda_r = 3.0\sqrt{E_s/F_y}$), the column is classified as noncompact; if $\lambda_r < \lambda \le \lambda_{limit}$ ($\lambda_{limit} = 5.0\sqrt{E_s/F_y}$), the column is classified as slender.

AISC 360-16 (2016) also provides the design equations (Eqs. 1-5) for estimating the cross-sectional strength of conventional-strength rectangular CFT columns (P_{no}). The cross-sectional strength (P_{no}) depends on the classification of the section as compact, noncompact or slender as per AISC 360-16 (2016), Section I1.4. Eq. (1) is for compact sections; Eqs. (2) and (3) are for noncompact sections; and Eqs. (4) and (5) are for slender sections.

For compact sections: $$P_{no} = P_p = A_s F_y + 0.85 f'_c A_c \quad (1)$$

For noncompact sections: $$P_{no} = P_{nc} = P_p - \frac{P_p - P_y}{(\lambda_r - \lambda_p)^2}(\lambda - \lambda_p)^2 \quad (2)$$

where, $$P_y = A_s F_y + 0.70 f'_c A_c \quad (3)$$

For slender sections: $$P_{no} = P_{cr} = A_s F_{cr} + 0.70 f'_c A_c \quad (4)$$

where, $$F_{cr} = \frac{9E_s}{(b/t)^2} \quad (5)$$

Several researchers have experimentally investigated the behavior of high-strength rectangular CFT columns, including Cederwall et al. (1990), Varma (2000), Uy (2001), Liu et al. (2003), Mursi and Uy (2004), Sakino et al. (2004), Liu and Gho (2005), Lue et al. (2007), Aslani et al. (2015), and Xiong et al. (2017) among others. These prior studies have provided valuable insights into the fundamental behavior of high-strength rectangular CFT columns. However,

there is a lack of comprehensive design equations based on the compilation of these studies. Consequently, AISC 360-16 (2016) prevents the use of high-strength rectangular CFT columns.

This paper makes a contribution towards addressing this gap, and proposes effective stress-strain relationships and new design equations for high-strength rectangular CFT members using a three-step method. The first step consists of compiling an experimental database of high-strength rectangular CFT column tests and evaluating the possibility of extending the current AISC 360-16 design equations for estimating the strength of high-strength rectangular CFT short columns. The second step consists of developing and benchmarking detailed 3D nonlinear finite element models for predicting the behavior of high-strength CFT columns from the database. The benchmarked models were then used to perform parametric studies to (i) address gaps in the database and (ii) develop effective stress-strain relationships for high-strength steel tube and high-strength concrete infill of rectangular CFT members. The third step consists of using the effective stress-strain relationships and the enhanced database and to propose new design equations that more reliably predict the behavior and strength of high-strength rectangular CFT short columns.

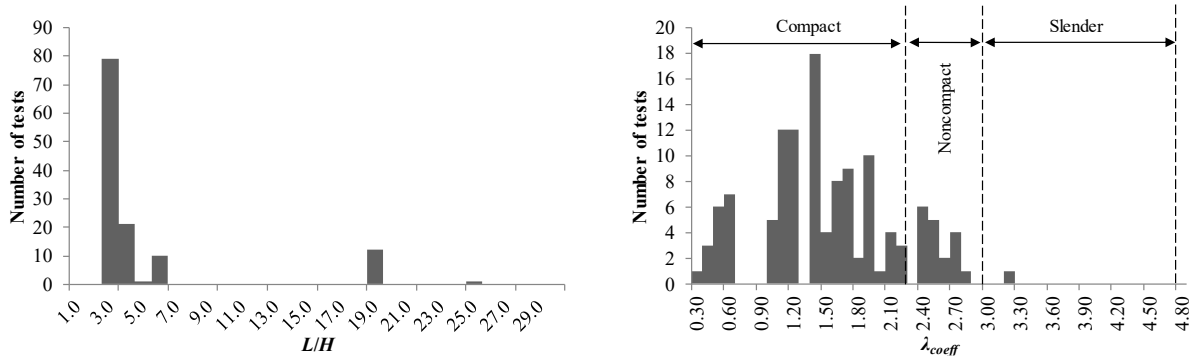
EXPERIMENTAL DATABASE

As discussed in the previous section, several experimental tests have been conducted to evaluate the behavior and strength of high-strength rectangular CFT columns. This section compiles an experimental database by reviewing these tests. A total of 124 tests on high-strength CFT columns were included in the database. The experimental database covers a broad range of material and geometric parameters. The column length (L) varies from 300 to 3000 mm (length-to-depth ratio varies from 3.0 to 25.0), the width (B) varies from 100.3 to 324.0 mm, the depth (H) varies from 80.0 to 324.0 mm, the flange thickness (t_f) and web thickness (t_w) varies from 4.0 to 12.5 mm, the tube slenderness ratio (b/t_f and h/t_w) varies from 13.0 to 72.0, the slenderness coefficient (λ_{coeff}) varies from 0.47 to 3.21, the concrete compressive strength (f'_c) varies from 20.0 to 164.1 MPa, and the steel yield stress (F_y) varies from 259.0 to 835.0 MPa. Details of the database have been presented elsewhere by the authors (Lai and Varma, 2017) and are not repeated here for brevity.

Figure 1(a) shows the distribution of test data with respect to the length-to-depth ratio (L/H). As shown, most tests (111 out of 124) were conducted on short (stub) columns ($L/H \leq 6.0$), while there are only 13 data points for relatively long columns ($L/H > 6.0$). This paper focuses on stub (short) columns, i.e., the cross-sectional strength. The corresponding investigations of long columns are currently being investigated by the authors and will be part of a future paper. Figure 1(b) shows the distribution of the test data with respect to λ_{coeff}. As shown, most tests were conducted on columns with compact (105 out of 124) and noncompact (18 out of 124) sections, while there is only one test data for columns with slender sections.

Figure 2 compares the strengths calculated using the AISC design equation (P_{no}) with those obtained from the experiments (P_{exp}) for the 111 short column specimens. The data points showing these comparisons are identified as “EXP” in the figure. Figure 2 indicates that the AISC design equations can reasonably estimate the cross-sectional strength of high-strength rectangular CFT columns. The mean P_{exp}/P_{no} ratio is 1.07, and the corresponding coefficient of variation is 0.09. These comparisons also indicate that the AISC design equations are conservative for columns with compact sections and slightly unconservative for columns with noncompact sections. There is only one comparison for columns with slender sections due to lack of test data. Therefore, no conclusions can be made regarding the conservatism of the AISC 360-16 equations for designing high-strength rectangular CFT columns with slender

sections, and additional data points are required. This will be addressed later by conducting finite element analysis.



(a) (b)

Fig. 1 - Distributions of test data for high-strength rectangular CFT columns with respect to: (a) length-to-depth ratio (L/H) and (b) slenderness coefficient (λ_{coeff})

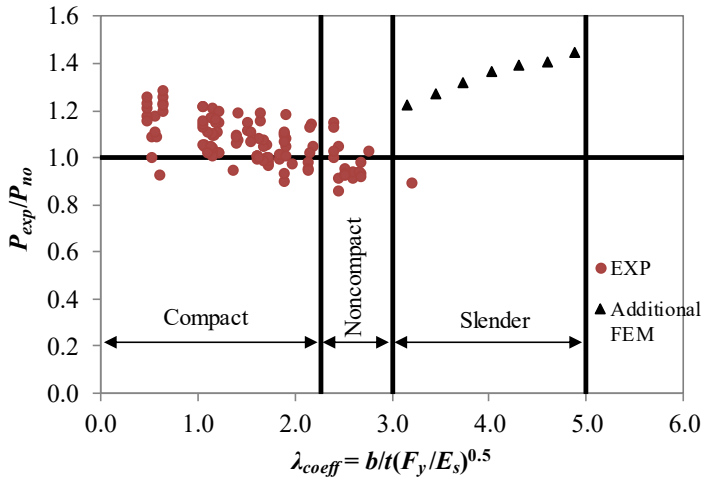


Fig. 2 - Comparisons of the axial compressive strengths calculated using the AISC 360-16 design equations with the corresponding experimental and analysis results

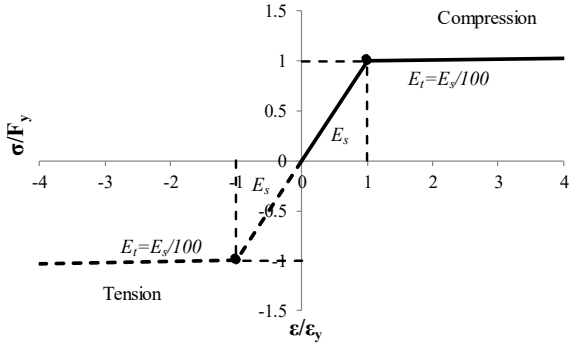
FINITE ELEMENT MODELS

This section develops and benchmarks detailed 3D nonlinear FEM models for high-strength rectangular CFT short columns. The FEM models were developed using ABAQUS (2016). Details of the FEM models include: (i) element types, (ii) contact interaction, (iii) steel and concrete material models, (iv) geometric imperfections, (v) boundary conditions, and (vi) analysis method. Most of these details are the same as those presented by the authors in a prior research (Zhichao Lai et al., 2014) for conventional-strength rectangular CFT members. For example, an idealized bilinear curve was used to specify the steel uniaxial stress-strain behavior in both compression and tension (see Figure 3a). The only exceptions are the parameters used to define the concrete material model. This is explained as follows.

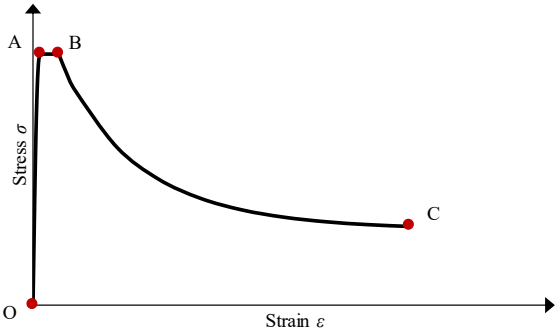
This paper used the CDP model to model the material multiaxial behavior of concrete for high-strength rectangular CFT columns. The default value in ABAQUS was used for eccentricity (ϵ = 0.1). The dilation angle (ψ), concrete biaxial-to-uniaxial compressive strength ratio f'_{bc}/f'_c, and the ratio of compressive to tensile meridians of the yield surface in Π space (K_c) were determined based on the recommendations by Tao et al. (2013), i.e., ψ = 40°, f'_{bc}/f'_c defined by Eq. (6), and K_c defined by Eq. (7). Also, the Tao et al. (2013) stress-strain relationship (see Figure 3b) was used to specify the concrete uniaxial behavior in compression. Similar to Lai et al. (2014), the concrete tensile stress-crack opening displacement behavior was specified using the empirical model developed by CEB-FIP (2010), as shown in Figure 3(c).

$$\frac{f'_{bc}}{f'_c} = 1.5(f'_c)^{-0.075} \tag{6}$$

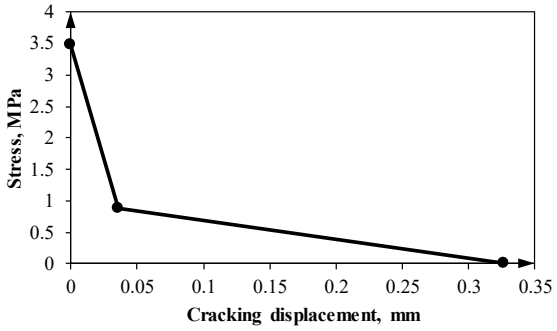
$$K_c = \frac{5.5}{5 + 2(f'_c)^{-0.075}} \tag{7}$$



(a) Steel uniaxial stress-strain curve



(b) Compressive stress-strain relationships for concrete



(c) Tensile stress-crack opening displacement curve for concrete (f'_c = 110 MPa)

Fig. 3 - Steel and concrete uniaxial stress-strain behavior used in the FEM analysis

The developed FEM models were benchmarked by using them to predict the behavior and strengths of the 111 high-strength stub CFT columns in the experimental database. Figure 4 compares the strengths obtained from FEM analyses (P_{FEM}) with those obtained from corresponding tests (P_{exp}). As shown, the mean experimental-to-predicted strength ratio (P_{exp}/P_{FEM}) ratio is 1.03, and the corresponding coefficient of variation is 0.07. Figure 5 shows representative comparisons of the axial force-displacement responses. Figures 4 and 5 indicate that the FEM models can reasonably predict the behavior and strengths of high-strength

rectangular CFT columns. It should be noted that, for some specimens, there are some discrepancies between the measured and predicted stiffness (especially before the peak load). However, the reason for this is unclear.

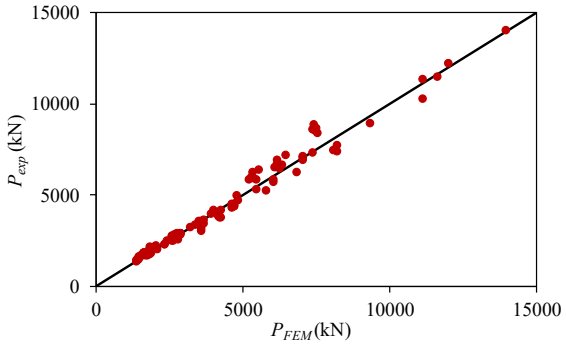
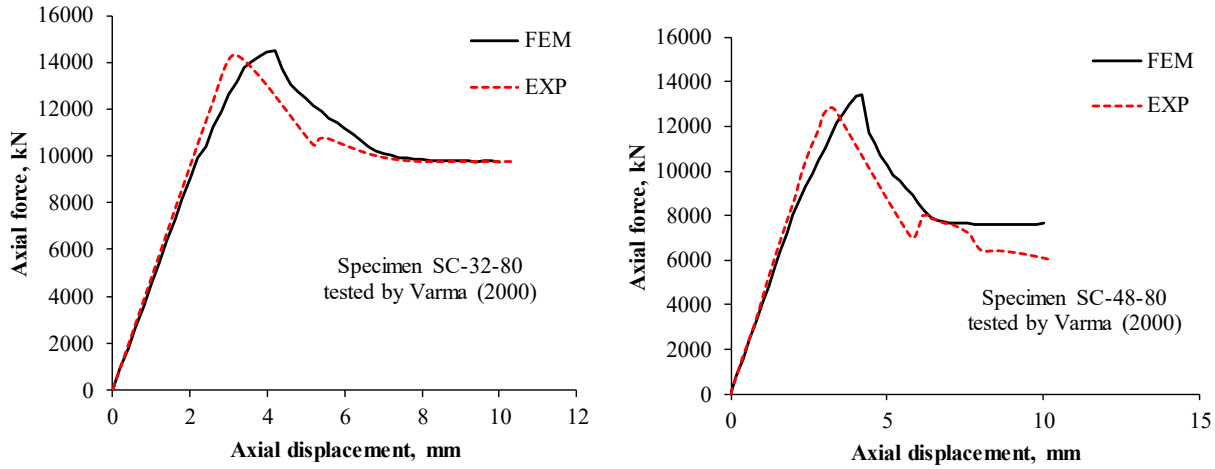
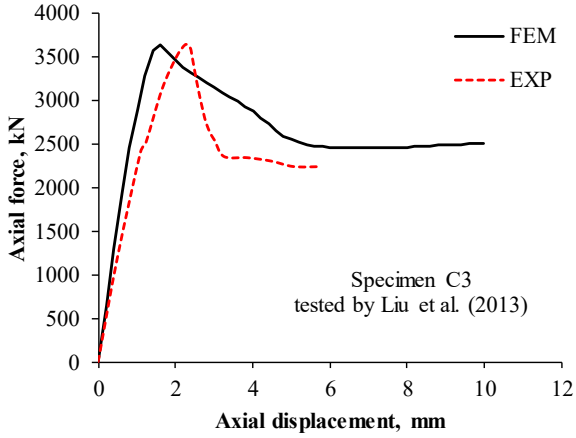


Fig. 4 - Comparisons of the strengths obtained from the finite element analyses and corresponding tests

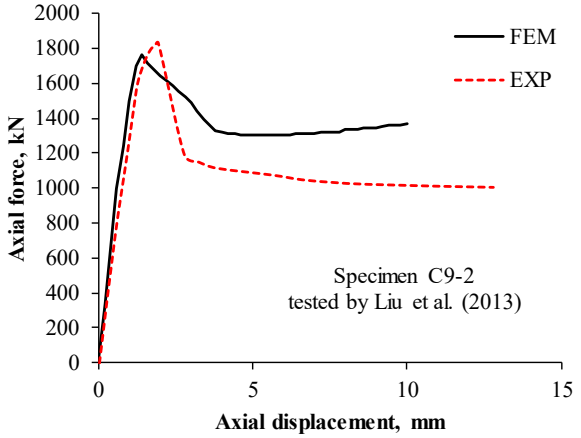


(a) Specimen SC-32-80

(b) Specimen SC-48-80



(c) Specimen C3



(d) Specimen C9-2

Fig. 5 - Representative comparisons of the axial force-displacement responses

FURTHER EVALUATION OF AISC DESIGN EQUATIONS

To address gaps in the experimental database, additional FEM analyses were conducted using the FEM models developed and benchmarked in the previous section. Specimen SC-48-80 tested by Varma (2000) was selected as the prototype member. Seven additional FEM analyses were conducted using the benchmarked FEM model of this specimen by changing the tube wall thickness while keeping the tube width constant at 400 mm. Figure 2 compares the strengths obtained from the additional FEM analyses with those calculated using AISC 360-16 (2016). The data points showing these comparisons are identified as "Additional FEM" in the figure. These comparisons indicate that the AISC 360-16 design equations are over conservative in estimating the cross-sectional strength of high-strength rectangular CFT columns with slender sections. This is because AISC 360-16 (2016) underestimates (i) the critical buckling stress for steel tube and (ii) the strength contribution from concrete. These two reasons will be explained in detail later.

EFFECTIVE STRESS-STRAIN RELATIONSHIPS

The FEM models benchmarked previously in this paper were used to conduct 40 analyses on stub CFT columns with: (i) five steel tube wall slenderness ratios (b/t = 20, 40, 60, 80, and 100), (ii) three steel yield stress values (F_y = 317 MPa, 525 MPa, and 827 MPa), and (iii) three concrete compressive strength values (f'_c = 21 MPa, 70 MPa and 110 MPa). Results from the finite element analysis of each stub column model included: (i) complex state of multiaxial stresses and strains of finite elements modeling the steel tube and the concrete infill, and (ii) overall axial load-displacement (P-Δ) response. These results were post-processed to obtain average stress-strain relationships for the steel tube and concrete infill and develop the effective stress-strain relationships. In a previous research (Lai and Varma, 2017), the authors have presented the details regarding the development and validation of these effective stress-strain relationships; therefore, they are not repeated here for brevity.

Figure 6(a) shows the resulting effective σ-ε relationship developed for the steel tube. As shown, only two anchor points (ε_p, σ_p and ε_5, σ_2) are required to define this σ-ε relationship: σ_p is the peak stress (i.e., steel critical buckling stress), ε_p is the peak strain, σ_5 is the post-buckling stress at $5\varepsilon_y$, and ε_y is the steel yield strain estimated as F_y divided by E_s. The peak strain (ε_p) can be calculated using Eq. (8).

$$\varepsilon_p = \frac{\sigma_p}{E_s} \tag{8}$$

Eq. (9) defines σ_p and σ_5. This equation was obtained from regression analysis, as shown in detail by the authors in (Lai and Varma, 2017). In this equation, t is the thickness of the steel tube wall.

$$\frac{F_{cr}}{F_y} = 0.99 - 0.07\lambda_{coefl} \tag{9-1}$$

$$\frac{\sigma_{5.0}}{F_y} = 0.9 - 0.1\left(11\frac{f'_c}{F_y} + \lambda_{coeff}\right) \tag{9-2}$$

$$\lambda_{coeff} = \frac{b/t}{\sqrt{E_s/F_y}} \tag{9-3}$$

Figure 6(b) shows the effective σ-ε relationship developed for the concrete infill. As shown, this σ-ε relationship consists of the ascending branch (OA), descending branch (AB), and residual strength branch (BC). The ascending branch (OA) is defined by Eq. (10), where parameters A and B determine the shape, ε_c is the strain at peak stress, and the concrete elastic modulus (E_c) is determined as per ACI 318-14 (2014). The descending branch BC is defined by point B ($5\varepsilon_c$, σ_{5c}), where σ_{5c} is the stress at $5\varepsilon_c$ and can be defined by Eq. (11).

$$\frac{\sigma}{f'_c} = \frac{A \cdot X + B \cdot X^2}{1 + (A-2)X + (B+1)X^2} \tag{10-1}$$

$$X = \frac{\varepsilon}{\varepsilon_c} \tag{10-2}$$

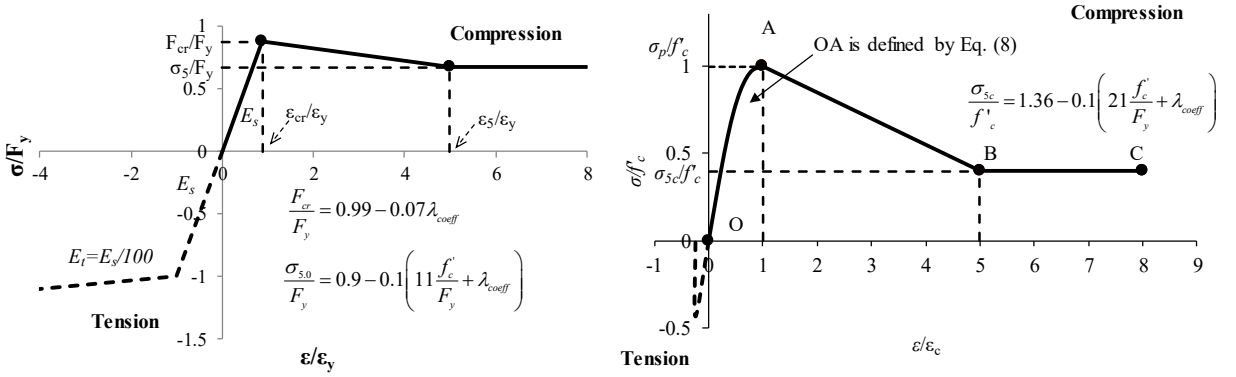
$$A = \frac{E_c \varepsilon_c}{f'_c} \tag{10-3}$$

$$B = \frac{(A-1)^2}{0.55} - 1 \tag{10-4}$$

$$\varepsilon_c = 0.00076 + \sqrt{(0.626 f'_c - 4.33) \times 10^{-7}} \tag{10-5}$$

$$E_c = 4700\sqrt{f'_c} \tag{10-6}$$

$$\frac{\sigma_{5c}}{f'_c} = 1.36 - 0.1\left(21\frac{f'_c}{F_y} + \lambda_{coeff}\right) \tag{11}$$



(a) (b)

Fig. 6 - Idealized effective stress-strain relationships for high-strength rectangular CFT columns: (a) steel tube and (b) concrete infill

DESIGN EQUATIONS

As discussed earlier in the paper, the AISC 360-16 (2016) design equations can reasonably estimate the cross-sectional strengths of compact high-strength rectangular CFT columns. However, they are slightly unconservative for those with noncompact sections, and over conservative for those with slender sections. To explain this, the critical buckling stresses (F_{cr}) calculated using AISC 360-16 (Eq. 5) was compared to those calculated by Eq. (9-1). Figure 7 shows representative comparisons for Specimen SC-48-80 tested by Varma (2000). This figure indicates that F_{cr} calculated using AISC 360-16 (2016) is conservative when the slenderness coefficient (λ_{coeff}) is greater than a certain limit (e.g., 3.4 for Specimen SC-48-80). The degree of conservatism increases as the member cross-section becomes more slender (thinner). For

example, F_{cr} calculated using AISC 360-16 (2016) is only 56.3% of that calculated by Eq. (9-1) when λ_{coeff} = 5.0. When λ_{coeff} is less than the limit, F_{cr} calculated using AISC 360-16 (2016) is unconservative. AISC 360-16 (2016) assumes that conventional-strength CFT columns with compact and noncompact sections ($\lambda_{coeff} \leq 3.0$) can develop yield stress in the steel tube. However, as shown in Figure 7, this is inaccurate for high-strength rectangular CFT columns because: (i) for noncompact sections, local buckling instead of yielding of the steel tube governs, and (ii) compact sections develop yielding in the steel tube; however, hoop stresses (resulting from the interaction with concrete infill) lead to the reducing of the longitudinal stress capacity required to cause yield of the steel tube in compression (Lai and Varma, 2016). The AISC design equations also assume that CFT columns with noncompact and slender sections can develop only 0.70 f'_c in the concrete infill. However, as shown in Figure 6(b) (the first quadrant), this is also inaccurate for high-strength rectangular CFT columns.

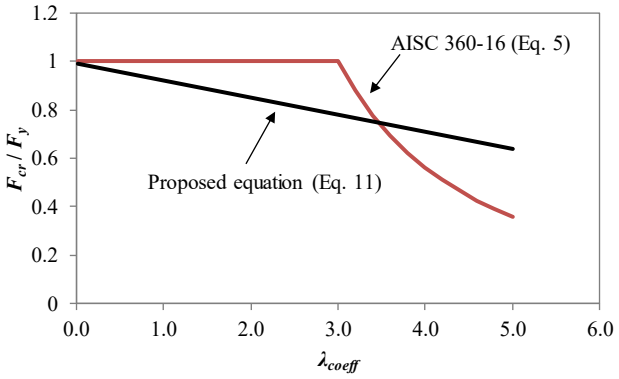


Fig. 7 - Typical comparisons of the critical buckling stress (F_{cr}) calculated by AISC 360-16 and the proposed equation (Eq. 9-1).

In order to more accurately represent the behavior of high-strength rectangular CFT columns and to better estimate their cross-sectional strengths, the following equation was proposed:

$$P_c = A_s F_{cr} + 0.85 f'_c A_c \tag{12}$$

Eq. (12) assumes that high-strength rectangular CFT columns can develop F_{cr} in the steel tube. The concrete compressive stress was limited to $0.85f'_c$ to account for accidental load eccentricity and difference of field-cured and standard-cured concrete. In this equation, F_{cr} is calculated using Eq. (9-1). Eq. (12) implies that, for high-strength rectangular CFT columns, the AISC 360-16 (2016) steel tube slenderness limits (that are used to categorize CFT section) can be removed. The cross-section local stability is addressed directly by Eq. (9-1).

Figure 8 shows comparisons of the cross-sectional strengths estimated using Eq. (12) with those obtained from (i) experimental investigations of the 111 stub columns in the database, and (ii) seven additional FEM analyses that addressed gaps in the database. In this figure, the ordinate represents the experimental (or FEM)-to-calculated strength ratio (P_{exp}/P_c). As shown, the mean P_{exp}/P_c ratio is 1.14, and the coefficient of variation is 0.07. These comparisons indicate that the proposed design equations can reasonably estimate the cross-sectional strength of high-strength rectangular CFT columns (all three types). It should be noted that Eq. (12) applies to high-strength rectangular short CFT columns with: (i) steel yield stress $F_y \leq 827$ MPa, (ii) concrete compressive strength $f'_c \leq 110$ MPa, (iii) tube width-to-thickness ratio $b/t \leq 100$, and (iv) length-to-depth ratio $L/H \leq 6.0$. The applicability of Eq. (12) to other cases need to be further evaluated.

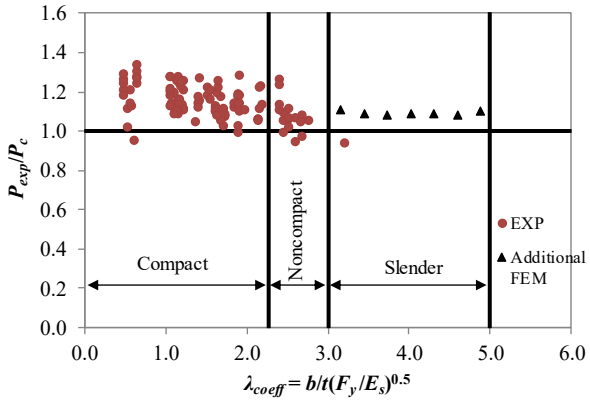


Fig. 8 - Comparisons of the axial compressive strengths calculated using the proposed equations with the corresponding experimental and analysis results.

SUMMARY AND CONCLUSIONS

This paper presented the results of a three-step method that was used to address gaps in AISC 360-16 (2016) for designing high-strength rectangular CFT short columns, and to propose effective stress-strain relationships and new design equations for these members. In the first step, an experimental database consisting of 124 high-strength rectangular CFT column tests was compiled. Test results from the database were used to evaluate the possibility of extending the AISC 360-16 design equations for estimating the strength of high-strength rectangular CFT short columns. The evaluations indicated that AISC design equations reasonably estimated the strength of high-strength rectangular CFT short columns with compact sections. However, they were slightly unconservative for those with noncompact sections.

In the second step, detailed 3D nonlinear FEM models for high-strength CFT columns were developed and benchmarked. The benchmarked models were used to perform parametric studies to (i) address gaps in the database and (ii) develop effective stress-strain relationships for modeling the high-strength steel tube and high-strength concrete infill of rectangular CFT members, accounting for the effects of confinement and local buckling. Figure 6 together with Eqs. (9) - (11) defined these relationships. Further evaluations of the AISC 360-16 design equations with the enhanced (gaps addressed) database indicated that these equations were over-conservative for estimating the strengths of high-strength rectangular CFT short columns with slender sections.

In the third step, the effective stress-strain relationships together with the enhanced database were used to propose new design equations (Eqs. 9-1 and 12) for estimating the strength of high-strength rectangular CFT short columns. The conservatism of these proposed design equations was confirmed by using them to predict the strengths of CFT columns from the enhanced database.

REFERENCES

ABAQUS. (2016). *ABAQUS Version 6.16 Analysis User's Manuals*. Providence, RI, USA: Dassault Systemes Simulia Corporation.

ACI 318-14. (2014). *Building code requirements for structural concrete*. Farmington Hills, MI, USA: ACI.

AISC 360-16. (2016). *Specification for structural Steel buildings*. Chicago, IL, USA: AISC.

Aslani, F., Uy, B., Tao, Z., & Mashiri, F. (2015). Behaviour and design of composite columns

incorporating compact high-strength steel plates. *Journal of Constructional Steel Research*, *107*, 94–110.
CEB-FIP (Euro-International Committee for Concrete (CEB)-International Federation for Prestressing (FIP).). (2010). *Model Code for concrete structures. (CEB-FIP MC 2010)*. London, U.K.: Thomas Telford.
Cederwall, K., Engstrom, B., & Grauers, M. (1990). High-strength concrete used in composite columns. In T. T. Hester (Ed.), *Proceedings of the 2nd International Symposium on Utilization of High Strength Concrete* (pp. 195–214). Berkeley, CA, USA.
Chen, B., Lai, Z., Yan, Q., Varma, A. H., & Yu, X. (2017). Experimental behavior and design of CFT-RC short columns subjected to concentric axial loading. *Journal of Structural Engineering*.
Elchalakani, M., Zhao, X. L., & Grzebieta, R. H. (2001). Concrete-filled circular steel tubes subjected to pure bending. *Journal of Constructional Steel Research*, *57*, 1141–1168.
Fujimoto, T., Nishiyama, I., Mukai, A., & Baba, T. (1995). Test results of eccentrically loaded short columns -- square CFT columns. In *Proceedings of the Second Joint Technical Coordinating Committee Meeting, U.S.-Japan Cooperative Research Program, Phase 5: Composite and Hybrid Structures*. Honolulu: National Science Foundation.
Furlong, R. W. (1967). Strength of steel-encased concrete beam Columns. *Journal of the Structural Division, ASCE*, *93*(ST5), 113–124.
Gonzalez, Lennie, A. R., Kowalsky, Mervyn, J., Nau, J., & Hassan, T. (2008). *Reversal cyclic testing of full scale pipe piles, Technical Report No. IS-08-13, Constructed Facilities Laboratory, North Carolina State University*. North Carolina State University, Raleigh, NC, USA.
Hajjar, J. F., Gourley, B. C., Tort, C., Denavit, M. D., & Schiller, P. H. (2013). *Steel-concrete composite structural systems, http://www.northeastern.edu/compositesystems*. *Department of Civil and Environmental Engineering, Northeastern University*. Northeastern University. Retrieved from http://www.northeastern.edu/compositesystems
Han, L.-H., Zhao, X., & Tao, Z. (2001). Tests and mechanics model of concrete-filled SHS stub columns, columns and beam–columns. *Steel and Composite Structures*, *1*(1), 51–74.
Huang, W., Lai, Z., Chen, B., Xie, Z., & Varma, A. H. (2017). Concrete-filled steel tube (CFT) truss girders: experimental tests, analysis, and design. *Engineering Structures*.
Ichinohe, Y., Matsutani, T., Nakajima, M., Ueda, H., & Takada, K. (1991). Elasto-plastic behavior of concrete filled steel circular columns. In M. Wakabayashi (Ed.), *Proceedings of 3rd International conference on steel-concrete composite structures* (pp. 131–136). Fukuoka, Japan: Association for International Cooperation and Research in Steel-Concrete Composite Structures.
Janss, J., & Anslijn, R. (1974). Le Calcul des Charges Ultimes des Colonnes Métalliques Enrobés de Béton. *Rapport CRIF, MT*, *89*, (Bélgica).
Jiang, A., Chen, J., & Jin, W. (2013). Experimental investigation and design of thin-walled concrete-filled steel tubes subject to bending. *Thin-Walled Structures*, *63*, 44–50.
Kim, D. K. (2005). *A database for composite columns [Thesis]*. Georgia Institute of Technology.
Lai, Z. (2014). *Experimental database, analysis and design of noncompact and slender concrete-filled steel tube (CFT) members [Dissertation]*. Purdue University.
Lai, Z., Huang, Z., & Varma, A. H. (2016). Seismic analysis and performance of high strength composite special moment frames (C-SMFs). *Structures*, *9*, 165–178.
Lai, Z., & Varma, A. H. (2015). Noncompact and slender circular CFT members: experimental database, analysis, and design. *Journal of Constructional Steel Research*, *106*(3), 220–233.
Lai, Z., & Varma, A. H. (2016). Effective stress-strain relationships for noncompact and slender CFT members. *Engineering Structures*, *124*, 457–472.
Lai, Z., & Varma, A. H. (2017). High-strength rectangular CFT members: database, modeling, and design of short columns. *Journal of Structural Engineering*.

Lai, Z., & Varma, A. H. (2017). Seismic behavior and modeling of circular concrete partially filled spirally welded pipes (CPFSWP). *Thin-Walled Structures*, *113*, 240–252.

Lai, Z., Varma, A. H., & Griffis, L. G. (2016). Analysis and design of noncompact and slender CFT beam-columns. *Journal of Structural Engineering*, *142*(1).

Lai, Z., Varma, A. H., & Zhang, K. (2014). Noncompact and slender rectangular CFT members: experimental database, analysis, and design. *Journal of Constructional Steel Research*, *101*(10), 455–468.

Lin, C. Y. (1988). Axial capacity of concrete infilled cold-formed steel columns. In W.-W. Yu & H. S. Joseph (Eds.), *Ninth International Specialty Conference on Cold-Formed Steel Structures* (pp. 443–457). St. Louis: University of Missouri - Rolla.

Liu, D., & Gho, W.-M. (2005). Axial load behaviour of high-strength rectangular concrete-filled steel tubular stub columns. *Thin-Walled Structures*, *43*(8), 1131–1142.

Liu, D., Gho, W. M., & Yuan, J. (2003). Ultimate capacity of high-strength rectangular concrete-filled steel hollow section stub columns. *Journal of Constructional Steel Research*, *59*(12), 1499–1515.

Lue, D. M., Liu, J.-L., & Yen, T. (2007). Experimental study on rectangular CFT columns with high-strength concrete. *Journal of Constructional Steel Research*, *63*(1), 37–44.

Mursi, M., & Uy, B. (2004). Strength of slender concrete filled high strength steel box columns. *Journal of Constructional Steel Research*, *60*(12), 1825–1848.

Nakahara, H., & Sakino, K. (2000). Flexural behavior of concrete filled square steel tubular beam-columns. In *Proceedings of the 12th World Conference on Earthquake Engineering* (pp. 441–448). Upper Hutt, New Zealand: New Zealand Society for Earthquake Engineering.

Nishiyama, I., Morino, S., Sakino, K., Nakahara, H., Fujimoto, T., Mukai, A., … Hayashi, Y. (2002). *Summary of research on concrete-filled structural steel tube column system carried out under the U.S.-Japan cooperative research on composite and hybrid structures*. Ibaraki Prefecture, Japan.

Prion, H. G. L., & Boehme, J. (1994). Beam-column behaviour of steel tubes filled with high strength concrete. *Canadian Journal of Civil Engineering*, *21*, 207–213.

Sakino, K., Nakahara, H., Morino, S., & Nishiyama, A. (2004). Behavior of centrally loaded concrete-filled steel-tube short columns. *Journal of Structural Engineering*, *130*(2), 180–188.

Schneider, S. P. (1998). Axially loaded concrete-filled steel tubes. *Journal of Structural Engineering*, *124*(October), 1125–1138.

Tao, Z., Han, L. H., & Wang, Z. Bin. (2005). Experimental behaviour of stiffened concrete-filled thin-walled hollow steel structural (HSS) stub columns. *Journal of Constructional Steel Research*, *61*(7), 962–983.

Uy, B. (2001). Strength of short concrete filled high strength steel box columns. *Journal of Constructional Steel Research*, *57*(2), 113–134.

Varma, A. H. (2000). *Seismic behavior, analysis and design of high strength square concrete filled steel tube (CFT) columns [Dissertation]*. Lehigh University.

Wheeler, A., & Bridge, R. Q. (2004). The behavior of circular concrete-filled thin-walled steel tubes in flexure. In R. T. Leon & J. Lange (Eds.), *Proceedings of the fifth international conference on Composite Construction in Steel and Concrete* (pp. 412–423). Kruger National Park, Berg-en-Dal, Mpumalanga, South Africa: American Society of Civil Engineers.

Xiong, M.-X., Xiong, D.-X., & Liew, J. Y. R. (2017). Axial performance of short concrete filled steel tubes with high- and ultra-high- strength materials. *Engineering Structures*, *136*, 494–510.

Strength of CFT Columns with Various Material Strengths and Sectional Slenderness

Ho-Jun Lee
Dept. of Architecture and Architectural Engineering, Seoul National Univ.
Seoul, Korea
hojun1032@gmail.com

Hong-Gun Park
Dept. of Architecture and Architectural Engineering, Seoul National Univ.
Seoul, Korea
parkhg@snu.ac.kr

ABSTRACT

To enhance the structural performance of concrete-filled steel tubular (CFT) columns, there is an increasing interest in utilizing high-strength materials. Nevertheless, current international standards have limitations pertaining to material grades in composite constructions. The present research focuses on assessing the load-carrying capacities of rectangular CFT columns and beam-columns, incorporating broad ranges of the sectional slenderness as well as material strengths. Concentric and eccentric axial load tests were conducted to investigate the effects of steel yield strength and width-to-thickness ratio. Extensive sets of test specimens were further collected from previous studies to investigate the applicability of current design codes and verify fiber model analysis. Based on parametric studies, a simplified strength model for the composite section was developed.

INTRODUCTION

From the viewpoints of enhancing structural performance and saving resources, high-strength materials are gaining popularity in building constructions. The use of such high-strength concrete and steel in composite structures is also expected to improve the economy and constructability. Recently, high-strength materials (concrete compressive strength up to 150 MPa, steel tensile strength up to 780 MPa) have been applied to concrete-filled tube (CFT) columns mainly for high-rise buildings (Aoki et al., 2012; Endo et al., 2011; Matsumoto et al., 2012).

However, as observed in Table 1, the available material strengths for composite structures are limited in current design codes (AIJ, 2008; AISC, 2016; CEN, 2004). Generally, high-strength concrete is not recommended owing to its brittle behavior. In case of high-strength steel, the restriction mainly comes from the incompatibility between yield strain of the steel and crushing strain of the concrete: early crushing of the concrete may occur prior to development of plasticity

in the steel components. Meanwhile, recent studies have been focusing more on adopting high-strength materials (Aslani et al., 2015; Lee et al., 2016; Liew et al., 2016; Wang et al., 2017).

Test results for high-strength rectangular CFT (RCFT) members are available in latest literatures. According to the experimental studies, by using high-strength materials, the structural performance of RCFT columns was definitely improved in terms of strength and stiffness, while many test results also revealed that the ultimate strengths were generally overestimated by current specifications. However, as most studies were limited to individual test results, the effects of material strengths should be further clarified based on comprehensive databases.

This study focuses on assessing the load-carrying capacities of RCFT columns and beam-columns, incorporating broad ranges of the sectional slenderness as well as material strengths. First, concentric and eccentric axial load tests were conducted to examine the effects of steel yield strength and width-to-thickness ratio. Applicability of current design codes are further examined based on extensive databases from previous studies. For the use of high-strength materials and large sectional slenderness, a simplified model to construct *P-M* interaction curve was developed.

REVIEW OF CURRENT DESIGN CODES

In ANSI/AISC 360, the sectional class of the steel tube is classified into compact ($b/t \le \lambda_p$), non-compact ($\lambda_p < b/t \le \lambda_r$), and slender ($b/t > \lambda_r$) sections (Table 1). For non-compact and slender sections, the theoretical elastic buckling stress F_{cr} is used in design. In Eurocode 4, only compact section is allowed. In the recommendations of the Architectural Institute of Japan (AIJ, 2008), a strength degradation factor γ_s is used to account for the local buckling.

Table 1 – Structural provisions for RCFT columns

Provisions	Eurocode 4[a]	AIJ (CFT recommendations)	ANSI/AISC 360-16
Material strengths (MPa)	$235 \le F_y \le 460$ $20 \le f'_c \le 50$	$235 \le F_y \le 440$ $18 \le f'_c \le 90$	$F_y \le 525$ $21 \le f'_c \le 69$
Width-to-thickness ratio	$B/t \le 1.78\sqrt{E_s/F_y}$	$B/t \le 2.44\sqrt{E_s/F_y}$	Compact: $b/t \le 2.26\sqrt{E_s/F_y} = \lambda_p$ Non-compact: $b/t \le 3.00\sqrt{E_s/F_y} = \lambda_r$ Slender: $b/t \le 5.00\sqrt{E_s/F_y}$
Effective material strengths	Concrete: $1.0f'_c$ Steel: F_y	Concrete: $\gamma_c f'_c$ Steel: $\gamma_s F_y$	Concrete: $0.85f'_c$ (compact) $0.7f'_c$ (slender) Steel: F_y (compact) F_{cr} (slender)
Stress block	Rectangle	Rectangle	Rectangle (compact) Triangle (slender)

[a]Intended for use with hollow structural steel sections (i.e., rounded corners)

Effective material strengths and stress distribution assumed in the cross-section design are also summarized in Table 1. Figure 1 illustrates typical rigid-plastic analysis for cross-sectional design of compact RCFTs. Although the definition for the compact section is not identical among the various international standards, all design codes allow the use of yield strength F_y. Strength factor γ only for infill concrete is different. The AISC code uses γ = 0.85 for ordinary reinforced concrete columns, while the Eurocode 4 uses γ = 1.0 addressing the lateral confinement effect. In Eurocode, the slenderness limit for the compact section is stricter than in AISC code. In the AIJ recommendations, a reduction factor γ_c addressing the scale effect (Sakino et al., 2004) is used. These factors are generally consistent in the design of axial strength and combined axial-flexural strength.

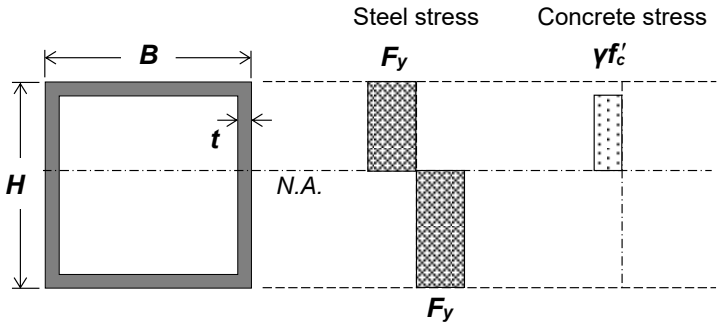


Fig. 1 – Typical stress distribution in rigid-plastic analysis

For slender sections in AISC specifications, a strength reduction factor for the infill concrete is defined as 0.7, addressing the poor lateral confinement. The steel compressive stress is replaced with F_{cr}. Also, instead of uniform stress block, triangular stress distribution is assumed for conservative design. In the case of noncompact sections, the nominal strength is calculated by interpolating the strengths for compact and slender sections. For construction of *P-M* interaction relationships, a bilinear model connecting the nominal axial and flexural strengths is recommended.

In the axial-flexural design of AIJ recommendations, the effective strength and depth of the concrete stress block, are reduced when either high-strength concrete ($f_c' > 60$ MPa) or large width-to-thickness ratio ($B/t > 2.4\sqrt{E_s/F_y}$) is used (Nakahara & Sakino, 2003). Such provision accounts for the brittle behavior of the high-strength concrete or poor confinement of slender tube section.

EXPERIMENTAL PROGRAM

To investigate the structural performance of RCFT columns with high-strength steel thin plates, concentric and eccentric axial load testing was performed (Lee et al., 2017; Lee et al., 2019). Major test parameters were eccentricity (eccentricity ratio = e/H), steel yield strength, and the use of stiffeners (Figure 2 and Table 2). With the same width-to-thickness ratio, a tube section with mild steel (yield strength = 301 MPa) was classified as compact section while a tube section with high-strength steel (yield strength = 746 MPa) was classified as slender section (AISC, 2016). Since a stiffener was located at the center of the tube wall, the width-to-thickness

ratio of the subpanel was decreased from 58.0 to 29.0, satisfying the requirement for compact section. Higher concrete strength was used in rectangular sections to maintain the similar axial-load contribution of steel and concrete as in square sections.

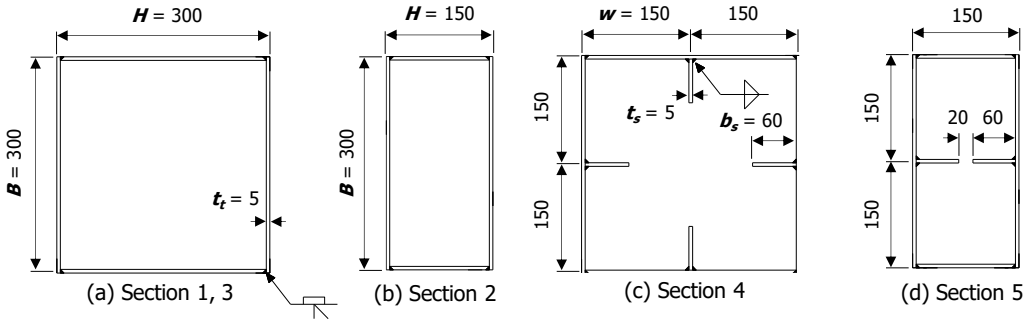


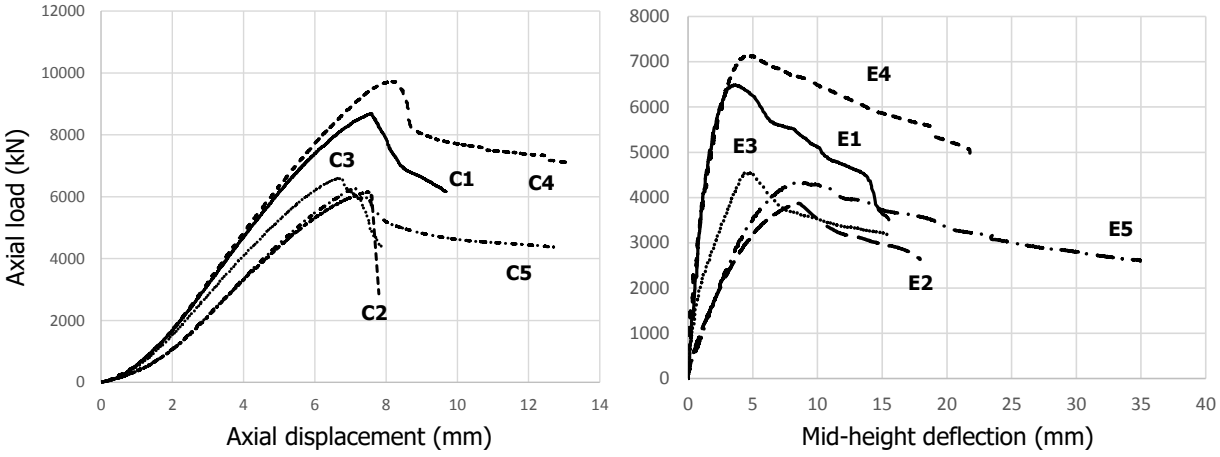
Fig. 2 – Cross sections of test specimens

Table 2 – Test parameters and results of specimens

Specimen	B (mm)	H (mm)	t_t (mm)	$F_{y,t}$ (MPa)	f'_c (MPa)	e (mm)	P_{test} (kN)	Note
C1	300	300	5	746	70.5	-	8,686	-
C2	300	150	5	746	83.6	-	6,152	-
C3	300	300	5	301	70.5	-	6,602	-
C4	300	300	5	746	70.5	-	9,726	Stiffened
C5	300	150	5	746	83.6	-	6,253	Stiffened
E1	300	300	5	746	70.5	40	6,491	-
E2	300	150	5	746	83.6	20	3,873	-
E3	300	300	5	301	70.5	40	4,553	-
E4	300	300	5	746	70.5	40	7,131	Stiffened
E5	300	150	5	746	83.6	20	4,322	Stiffened

Figure 3 shows load-displacement relationships of test specimens. Effects of sectional and material properties were consistent in two series of testing, regardless of axial-load eccentricity. In specimens with square sections 1, 3, and 4, the peak strength was the greatest in section 4 (high-strength steel plus stiffeners) and the lowest in section 3 (mild steel). In specimens with rectangular sections 2 and 5, the load-carrying capacity of section 5 (high-strength steel plus stiffeners) was greater than that of section 2 (high-strength steel). The test result indicates that the stiffeners enhanced the strength by restraining the tube local buckling, satisfying the

predictions for compact section. Also, although early local buckling took place in sections 1 and 2 without stiffeners, the load-carrying capacity continued to increase without significant stiffness degradation.



(a) Concentric axial loading (b) Eccentric axial loading

Fig. 3 – Load-displacement relationships of test specimens

APPLICABILITY OF CURRENT DESIGN CODES

In the present study, to extend the applicability of current design codes for RCFT columns covering wide ranges of material strengths [f_c' > 70 MPa, F_y > 525 MPa, AISC (2016)] and sectional slenderness, relevant test results were extensively collected. The constructed database is categorized into two parts: 1) short columns for axial capacity and 2) beam and beam-columns for flexural and combined axial-flexural capacity. The properties of existing test specimens are summarized in Table 3.

Table 3 – Parameter ranges of existing test specimens

	Stub-columns	Beam-columns
No. of specimens	195	210
B	180 ~ 500 mm	149 ~ 600 mm
H	135 ~ 500 mm	150 ~ 600 mm
b/t	10.4 ~ 131.7	13.6 ~106.7
F_y	211 ~ 835 MPa	211 ~ 913 MPa
$(b/t)\sqrt{F_y/E_s}$	0.47 ~ 4.94	0.65 ~ 4.46
f_c'	20.0 ~ 202.0 MPa	20.0 ~ 183.0 MPa

In selecting test specimens, careful attention was paid to obtain reasonable results: 1) wide ranges of material strengths and sectional slenderness were included, 2) exceptionally small

specimens were excluded, and 3) the compressive strength of concrete was modified considering the shape and size of the material test specimens. Small-scale specimens with $B \times H < 180^2$ mm^2 were excluded to minimize the size effect (Nakahara et al., 1998).The concrete compressive strength f_c' was defined as the strength of an equivalent concrete cylinder with a 100 mm diameter (Yi et al., 2006). In this study, concrete strength greater than 70 MPa was regarded as high strength.

Figure 4 shows the comparison between test strengths and predictions for stub-columns. Generally, the AISC code shows unsafe predictions for noncompact specimens with high-strength materials. Thus, in the AISC code, the use of high-strength materials is restricted. On the other hand, the conservative nature of the AISC predictions significantly increases as the slenderness ratio increases.

While the AIJ predictions accurately estimated the capacity of specimens with high-strength steel by considering the local buckling, the capacity of specimens with high-strength concrete was generally overestimated. This is partly because the reduction factor addressing the concrete size effect does not adequately reflect the early failure of the high-strength concrete. Eurocode 4 was only applicable for test specimens with specified material strengths ($F_y \leq 460$ and $f_c' \leq 50$ MPa) and sectional slenderness ($B/t \leq 1.78\sqrt{E_s/F_y}$).

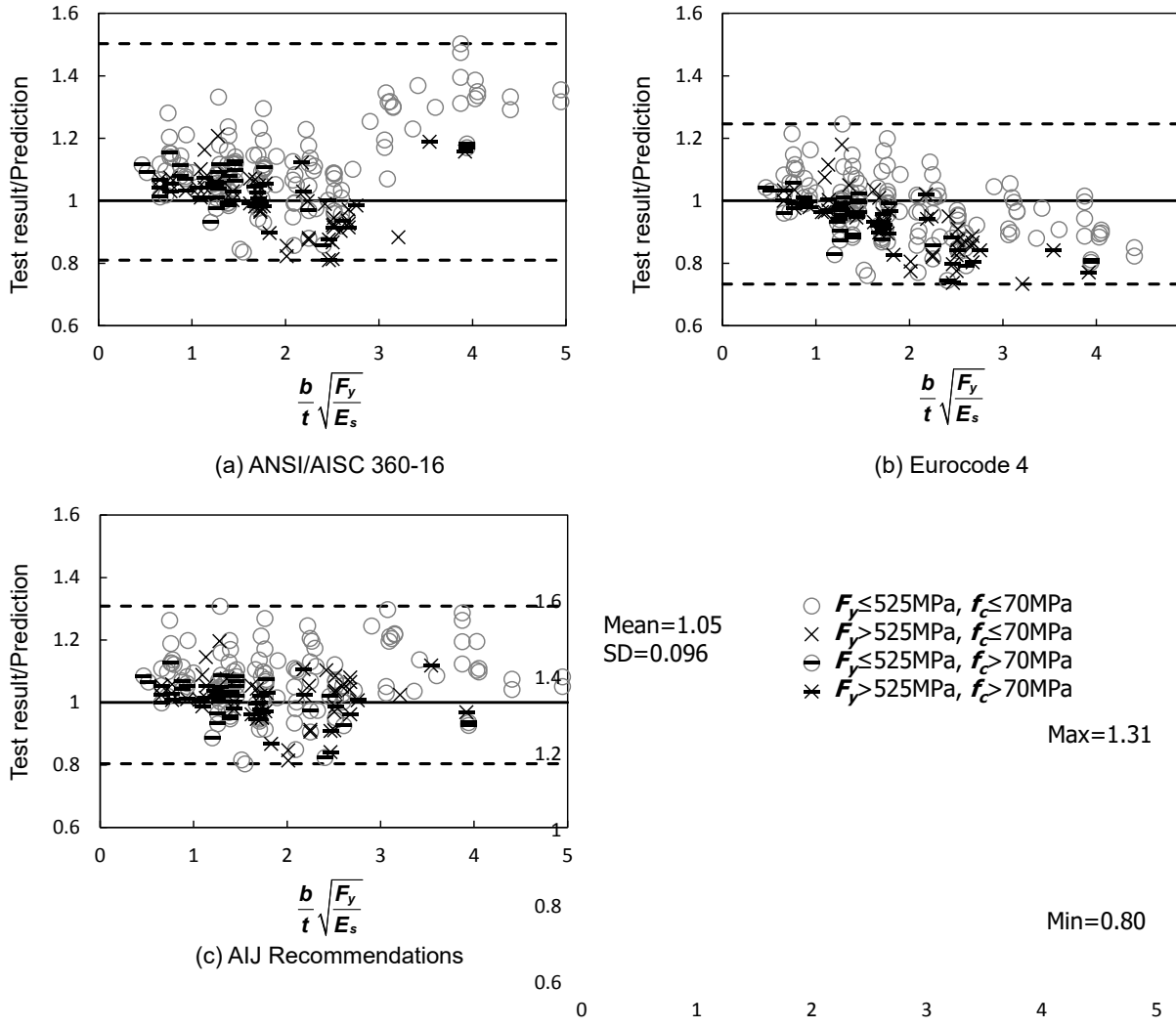


Fig. 4 – Strength evaluation of short columns based on current design codes

Figure 5 shows the comparison between test strengths and predictions for beam-columns. The test strength was defined as the measured one at the critical section, considering additional moment due to the axial force (i.e., second-order effect). It is also noted that test results obtained from experimental set-ups, which may be affected by base confinement, were omitted in strength evaluation (AIJ, 2008). The results showed similar tendency as in the case of stub-column specimens.

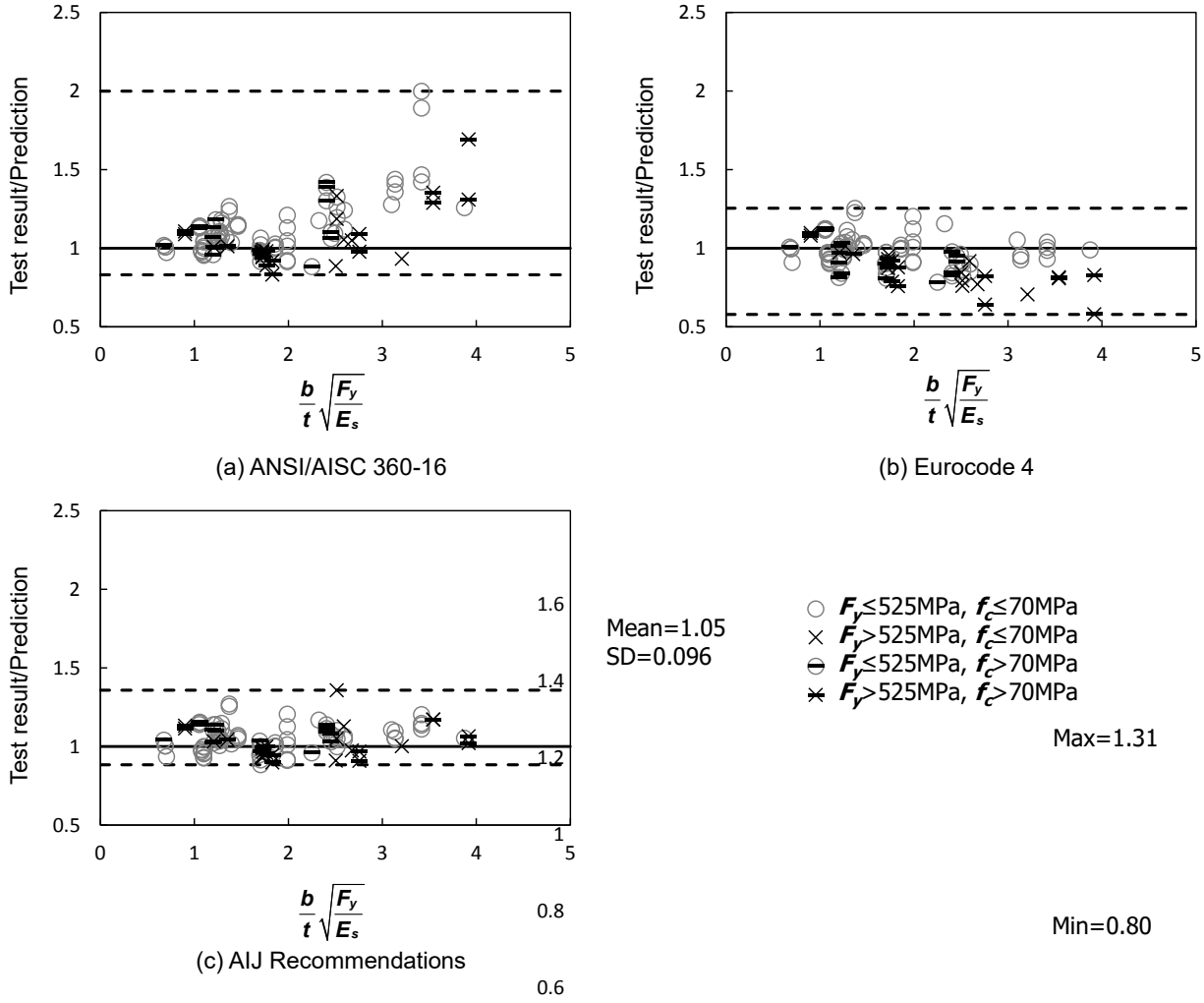


Fig. 5 – Strength evaluation of beam-columns based on current design codes

STRENGTH MODEL FOR RCFT BEAM-COLUMNS

For the use of high-strength materials and large sectional slenderness, methods to construct simplified *P-M* interaction curve were investigated. First, to check strain compatibility between steel and concrete, section analysis using fiber models was performed and verified with existing test results. Uniaxial constitutive laws proposed by Sakino et al. (2004) were modified to obtain better agreement with the database (Lee et al., 2019). Particularly, strength reduction factor was

not applied to the infill concrete. Figure 6 and Figure 7 show comparisons with the test results and analytical results. Except for high-strength concrete, the predictions agreed with the test strengths. This indicates that, in the case of high-strength concrete, the ultimate capacity of composite section is affected by premature failure of the concrete rather than strain compatibility based on material tests. Therefore, reasonable reduction factors are required for high-strength concrete (Liew et al., 2016), which is not a scope of this paper.

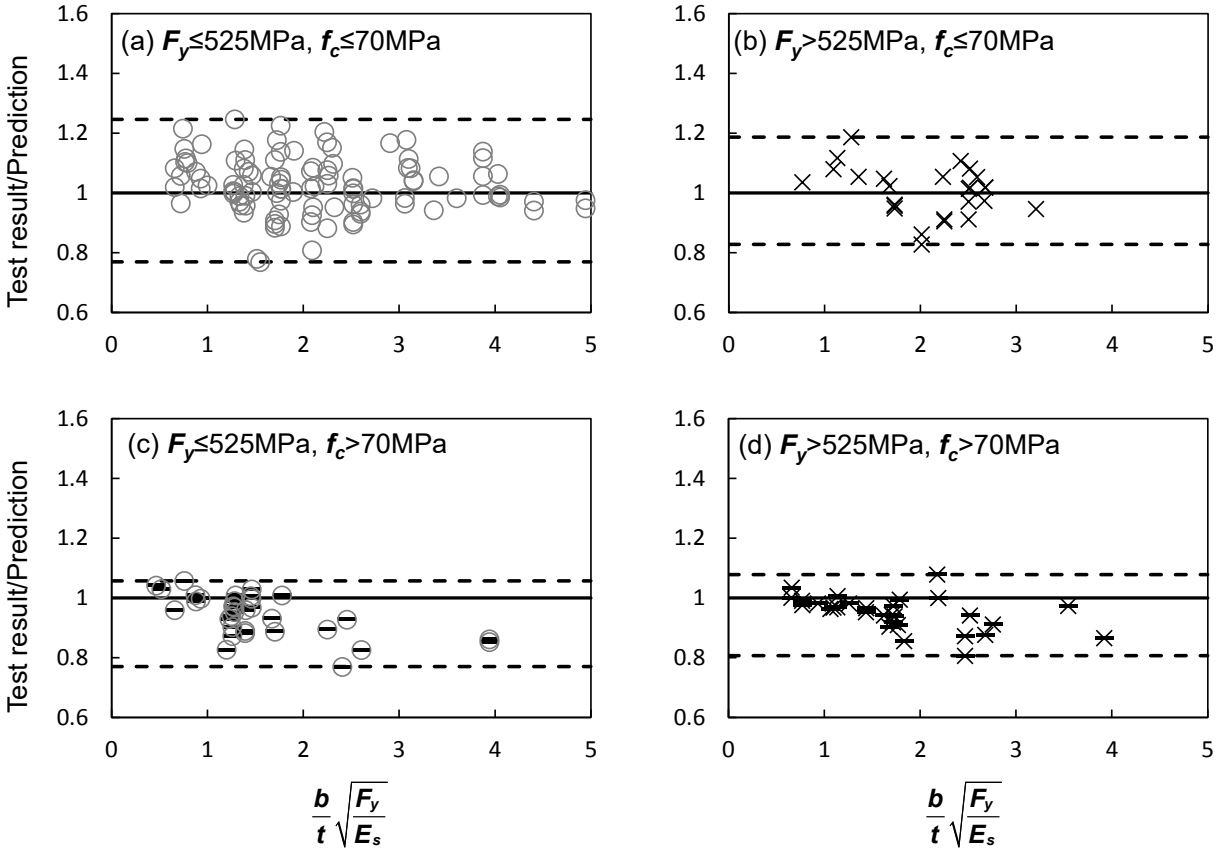


Fig. 6 – Comparison between test results and analytical results for stub-columns

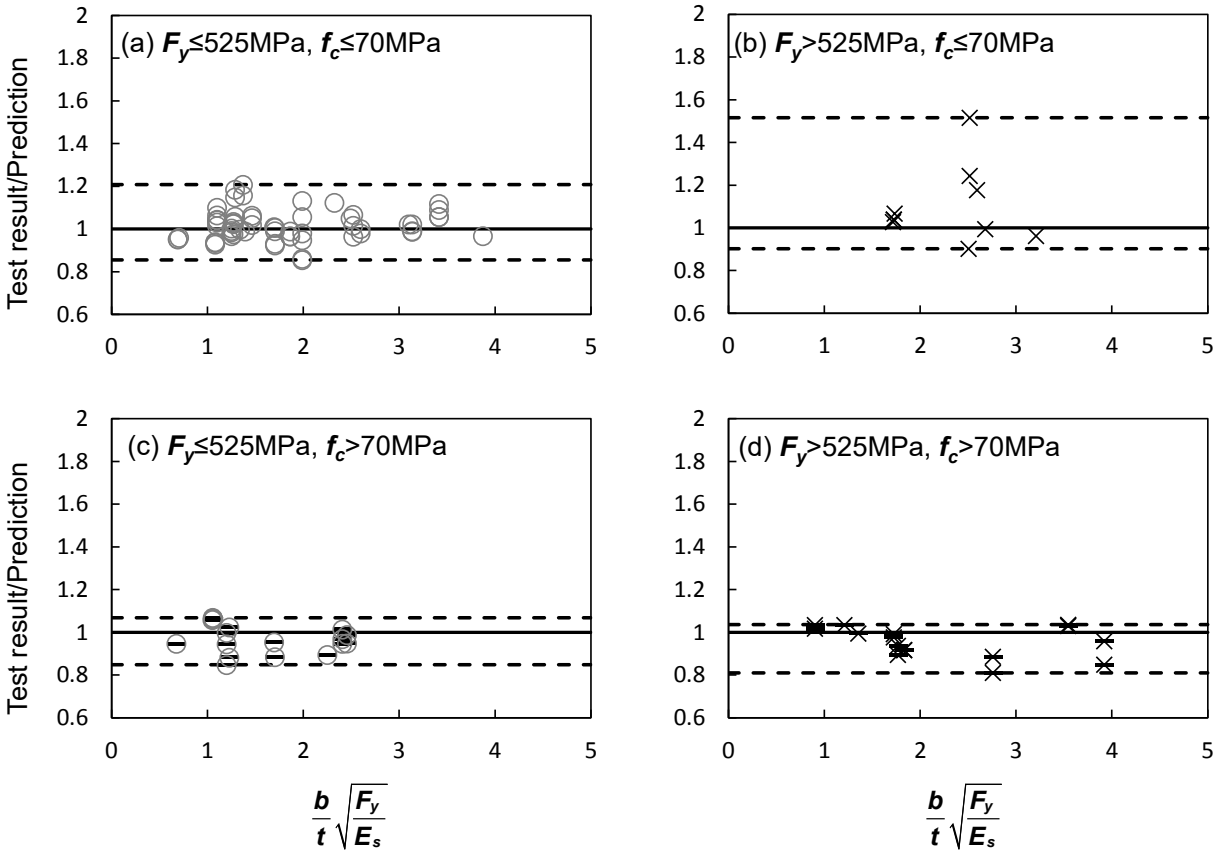


Fig. 7 – Comparison between test results and analytical results for beam-columns

For construction of *P-M* relationships, it is essential to define reasonable performance points for pure compression and pure flexure (points A and B in Figure 8). Based on parametric study using fiber model analysis (b/t = 15 ~ 80, f_c' = 20 ~ 150 MPa, F_y = 200 ~ 900 MPa), simplified equations for points A and B were suggested.

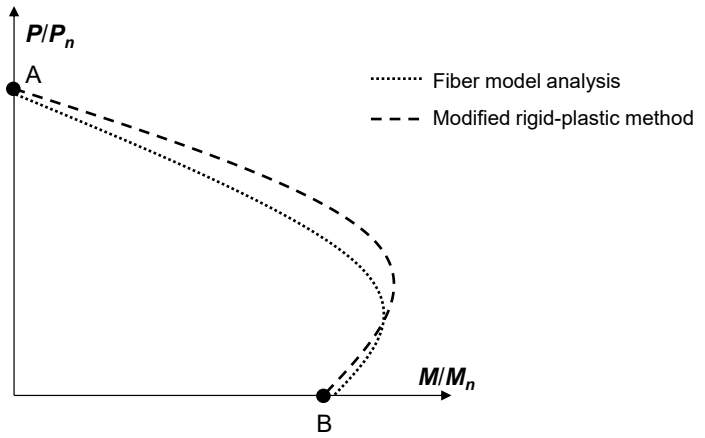


Fig. 8 – Comparison between fiber model analysis and modified rigid-plastic analysis

The pure compressive capacity P_n of composite section is calculated as follows.

$$P_n = A_c\left(\alpha f_c'\right) + A_s\left(\beta F_y\right) \tag{1}$$

Where α and β are strength reduction factors for the high-strength concrete and slender tube section, respectively. In the case of $f_c' \leq 70$ MPa, $\alpha = 1.0$. For $f_c' > 70$ MPa, further test results are needed to determine appropriate α. The peak stress of steel βF_y was calculated based on an existing post-buckling model (Guo et al., 2007), which was also adopted in the fiber model. The strain incompatibility of peak stresses between steel and concrete may be significant when high-strength steel or conventional steel slender section is used. According to the results of section analysis, in the case of high-strength steel, the peak load of composite section was generally governed by the failure of steel component. In the case of conventional steel slender section, the peak load was governed by the failure of infill concrete. In both cases, the effect of strain incompatibility on the pure compression of composite section was marginal [the difference between analytical result and Equation (1) was less than 2%]. Consequently, Equation (1) still gives conservative predictions.

For pure flexure, it is consistent to assess the nominal capacity M_n using the same effective stresses $1.0f_c'$ and βF_y defined for pure compression. For convenience, a conventional rigid-plastic approach (Figure 1) was modified with the compressive stresses $1.0f_c'$ and βF_y. In such case, depth of the neutral axis is expressed as follows.

$$a = \frac{2F_y H t_w + f_c' b t_f + \left(1-\beta\right)F_y b t_f}{2F_y t_w + f_c' b + 2\beta F_y t_w} \tag{2}$$

According to the parametric study, when normal-strength materials are used, the modified rigid-plastic method yields M_n comparable or smaller than the value calculated by the fiber model analysis, which is conservative for practical uses. On the other hand, when high-strength steel thin plates are used, predictions of the modified approach tend to be greater than those of the analytical model. Since the overestimation is greater than 5% when steel yield strength is greater than 800 MPa and concrete compressive strength is less than 30 MPa, the modified method is not recommended for such combination.

In the range of medium axial-load ratio (Figure 8), the prediction of modified rigid-plastic method (with effective stresses $1.0f_c'$ and βF_y) generally overestimates the analytical result which is assumed as actual capacity. Thus, the method is not applicable for determining the entire curve. Instead, it is recommended to use effective concrete stress of $0.85f_c'$ in axial-flexural design of the composite section with normal-strength materials. In the case of high-strength steel, since relative strength contribution of the steel component is dominant, it is conservative to use an equivalent steel-column method (Method 1 of the AISC specifications).

CONCLUSIONS

Concentric and eccentric axial load tests were conducted to examine the effects of steel yield strength and width-to-thickness ratio on the strength of RCFT columns and beam-columns.

Applicability of current design codes were further examined based on extensive databases from previous studies, incorporating broad ranges of the sectional slenderness as well as material strengths. The major findings of this study are summarized as follows.

1) In the specimens with high-strength steel thin plates, despite early local buckling, the load-carrying capacity continued to increase without significant reduction of the stiffness. In the stiffened specimens, the load-carrying capacity reached the plastic strength of composite section owing to restrained local buckling.

2) It was confirmed that the current design codes (ANSI/AISC 360-16, Eurocode 4, AIJ recommendations) safely predict the test strengths of RCFT columns and beam-columns with conventional material strengths and width-to-thickness ratios. In particular, the test specimens with normal-strength materials and large sectional slenderness significantly outperformed the nominal strengths by the AISC specifications, attaining the plastic capacity of composite section.

3) For application of high-strength materials and large width-to-thickness ratio, strength models were developed for the composite section subjected to pure compression and flexure. When constructing the *P-M* interaction curve for the high-strength steel, it is recommended to use the method for equivalent steel column.

REFERENCES

AIJ. (2008). Recommendations for design and construction of concrete filled steel tubular structures. Tokyo: AIJ (Architectural Institute of Japan).

AISC. (2016). Specification for structural steel buildings *ANSI/AISC 360-16*. Chicago: AISC (American Institute of Steel Construction).

Aoki, Y., Iwashimizu, T., Yamada, Y., & Nagano, K. (2012). Construction of the ultra-high-strength concrete CFT pillar of design strength 150 N/mm^2 : 'ABENO HARUKAS' 300 meters super-high-rise compound building. *Concrete Journal, 50*(8), 683-688.

Aslani, F., Uy, B., Tao, Z., & Mashiri, F. (2015). Predicting the axial load capacity of high-strength concrete filled steel tubular columns. *Steel and Composite Structures, 19*(4), 967-993.

CEN. (2004). Design of composite steel and concrete structures, Part 1-1: general rules and rules for buildings *Eurocode 4*. Brussels: CEN (European Committee for Standardization).

Endo, F., Yamanaka, M., Watanabe, T., Kageyama, M., Yoshida, O., Katsumata, H., & Sano, T. (2011). Advanced technologies applied at the new “Techno Station” building in Tokyo, Japan. *Structural Engineering International, 21*(4), 508-513.

Guo, L., Zhang, S., Kim, W.-J., & Ranzi, G. (2007). Behavior of square hollow steel tubes and steel tubes filled with concrete. *Thin-Walled Structures, 45*(12), 961-973.

Lee, C.-H., Kang, T. H.-K., Kim, S.-Y., & Kang, K. (2016). Strain compatibility method for the design of short rectangular concrete-filled tube columns under eccentric axial loads. *Construction and Building Materials, 121*, 143-153.

Lee, H.-J., Choi, I.-R., & Park, H.-G. (2017). Eccentric compression strength of rectangular concrete-filled tubular columns using high-strength steel thin plates. *Journal of Structural Engineering*, *143*(5), 04016228.

Lee, H.-J., Park, H.-G., & Choi, I.-R. (2019). Compression loading test for concrete-filled tubular columns with high-strength steel slender section. *Journal of Constructional Steel Research*, *159*, 507-520.

Liew, J. R., Xiong, M., & Xiong, D. (2016). Design of concrete filled tubular beam-columns with high strength steel and concrete. *Structures, 8*, 213-226.

Matsumoto, S., Komuro, T., Narihara, H., Kawamoto, S., Hosozawa, O., & Morita, K. (2012). *Structural design of an ultra high-rise building using concrete filled tubular column with ultra high strength materials.* Paper presented at the 15th World Conference on Earthquake Engineering, Lisbon, Portugal.

Nakahara, H., Inai, E., & Sakino, K. (1998). Axial compressive load capacities of square steel tubular columns. *Journal of structural engineering. B, 44*, 167-174.

Nakahara, H., & Sakino, K. (2003). Flexural behavior of concrete filled square steel tubular columns using high strength materials. *Journal of Structural and Construction Engineering*(567), 181-188.

Sakino, K., Nakahara, H., Morino, S., & Nishiyama, I. (2004). Behavior of centrally loaded concrete-filled steel-tube short columns. *Journal of Structural Engineering, 130*(2), 180-188.

Wang, Z.-B., Tao, Z., Han, L.-H., Uy, B., Lam, D., & Kang, W.-H. (2017). Strength, stiffness and ductility of concrete-filled steel columns under axial compression. *Engineering Structures, 135*, 209-221.

Yi, S.-T., Yang, E.-I., & Choi, J.-C. (2006). Effect of specimen sizes, specimen shapes, and placement directions on compressive strength of concrete. *Nuclear Engineering and Design, 236*(2), 115-127.

BUCKLING RESISTANCE OF HYBRID STEEL-CONCRETE COLUMNS

Pisey KEO
LGCGM/Structural Engineering Research Group, INSA de Rennes, 20 avenue des Buttes de Coësmes, CS 70839, F-35708 Rennes Cedex 7, France
pisey.keo@insa-rennes.fr

Hugues SOMJA
LGCGM/Structural Engineering Research Group, INSA de Rennes, 20 avenue des Buttes de Coësmes, CS 70839, F-35708 Rennes Cedex 7, France
hugues.somja@insa-rennes.fr

Quang Huy NGUYEN
LGCGM/Structural Engineering Research Group, INSA de Rennes, 20 avenue des Buttes de Coësmes, CS 70839, F-35708 Rennes Cedex 7, France
quang-huy.nguyen@insa-rennes.fr

Mohammed HJIAJ
LGCGM/Structural Engineering Research Group, INSA de Rennes, 20 avenue des Buttes de Coësmes, CS 70839, F-35708 Rennes Cedex 7, France
mohammed.hjiaj@insa-rennes.fr

ABSTRACT

This paper presents an assessment of the application of simplified design methods proposed in EC2 and EC4 for the design of slender hybrid columns with several embedded steel profiles. It relies on an extensive numerical parametric study on the ultimate load of hybrid columns subjected to combined axial load and bending moment. To accurately estimate the ultimate load, a nonlinear beam element which accounts for slip has been developed. The predictions of ultimate loads by the numerical model are compared against the results given by both EC2 and EC4 simplified methods. This comparison shows that the effective stiffness proposed by EC2 and EC4 are not appropriate for hybrid column design. A new expression of the effective stiffness is then proposed, which provides an accurate estimation of the ultimate load of hybrid column subjected to combined axial load and uniaxial bending moment while compared to the predictions obtained by FE analysis.

INTRODUCTION

Over nearly a century, Steel Reinforced Construction (SRC) consisting of steel structural framing partially or totally encased in concrete has been adopted by engineers. The advantages of SRC over reinforced concrete construction are: greater ductility, more compact cross-section, reduced

creep deformation, and faster concrete casting (Morino S. , 1998). Those over steel construction are: multiple roles of concrete as structural, fireproofing and buckling-restraining elements, higher stiffness, and greater damping. Modern SRC members (hybrid members) commonly have extensive transverse and longitudinal reinforcement, and some use shear connectors between steel section and the surrounding concrete (Roeder, 1998).

In high-rise reinforced concrete buildings, columns or concrete walls containing multiple embedded steel profiles are often used, because the loads are such that standard reinforcement with rebars is not sufficient. Those composite elements belong to structures defined as “hybrid”, which means that they are neither reinforced concrete structures in the sense of EC2 (EC2-1-1, 2005), nor composite steel concrete structures in the sense of EC4 (EC4-1-1, 2005). It is unclear whether these hybrid elements behave as reinforced concrete elements or as composite ones. For columns being sensitive to instability, both EC2 and EC4 propose simplified design methods based on moment magnification approach where the second order bending moment is equal to the first order bending moment multiplied by a magnification factor k. Different expressions of factor k have been proposed; the most common formula is $k = \beta/(1-N_{Ed}/N_{cr})$ where N_{Ed} is the applied normal force. The accuracy of moment magnification method strongly depends on two factors. The first one is the equivalence factor to uniform moment diagram β. The second one is, as included in N_{cr}, the effective flexural stiffness (EI) which depends on, among other factors, the nonlinearity of the concrete stress-strain curve, the creep and the cracking along the column length. The formulation of the effective flexural stiffness (EI) used to design reinforced concrete and composite columns has been studied for decades and there is a vast amount of its formulations in the literature, see among others (Westerberg, 2002) (Tikka & Mirza, 2008) and (Bonet, Romero, & Miguel, 2011).

This paper aims to present an evaluation of the simplified methods (bending moment magnification method) proposed in EC2 and EC4 when applied for hybrid columns. To do so, a FE model has been developed in which the geometrical/material nonlinearities as well as the partial interaction effect between steel profiles and concrete are taken into account. Since there is no data available in the literature for buckling experimental tests of hybrid columns, the FE model is validated by comparing its predictions against experimental results of standard composite columns. This validation was performed in (Keo, Somja, Nguyen, & Hjiaj, 2015).The FE model then serves as reference for an extensive parametric study in which the simplified methods proposed in EC2 and EC4 are evaluated in case of hybrid columns. The comparison between the results obtained with Eurocode simplified methods and with FEA shows that simplified method of EC2 and EC4 leads somehow to unsafe results when applied for hybrid columns. It means that the proposed effective flexural stiffness (EI) of EC2 and EC4 are not appropriate for slender hybrid column design. As a result, in this paper, a new expression of (EI) for slender hybrid columns is proposed.

FINITE ELEMENT MODEL

In order to analyze the behavior of slender hybrid columns, a two-dimensional beam-column finite element formulation was developed based on Euler-Bernoulli kinematics and fiber cross-section model. The co-rotational approach was adopted. In this context, the element displacements are separated into rigid-body and deformational degrees of freedom. The element rigid-body motion is handled separately within the mapping from the co-rotational to global element frames. The developed FE model is capable to consider the following aspects: a cross-section with more than one steel section in partial interaction; geometrical and material nonlinearities; initial imperfection; residual stresses; and confinement of concrete. The detail of FE formulation in co-rotational frame for hybrid beam-column element can be found in (Keo, Nguyen, Somja, & Hjiaj, 2015). In the following, we highlight only the degrees of freedom and beam kinematic of hybrid beam-column

with two encased steel profiles in local and global coordinate system. All variables subscripted with "s_k" belong to the embedded steel element and those with "c" belong to the surrounding concrete component. The quantities in local frame are denoted with the overline variables.

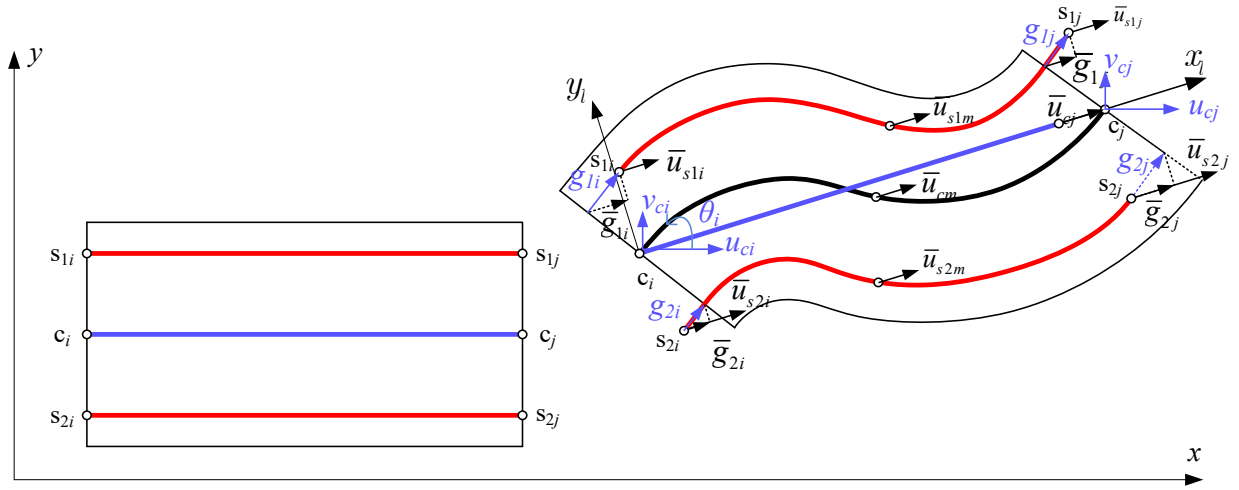


Fig. 1- Degrees of freedom and kinematic of the element

In global co-rotational frame, the element has 10 degrees of freedom: global displacements and rotation of the node (c_i and c_j) and slips (g_{ki}, g_{kj}) between the steel node (s_{ki}, s_{kj}) and concrete node (c_i, c_j) with k=1, 2, see Figure 1. It is here assumed that the slips (g_{ki}, g_{kj}) are perpendicular to the end of cross-sections. The vector of global nodal displacements is defined by

(1) $$p_g = \left[u_{ci}\ v_{ci}\ \theta_i\ g_{1i}\ g_{2i}\ u_{cj}\ v_{cj}\ \theta_j\ g_{1j}\ g_{2j} \right]^T$$

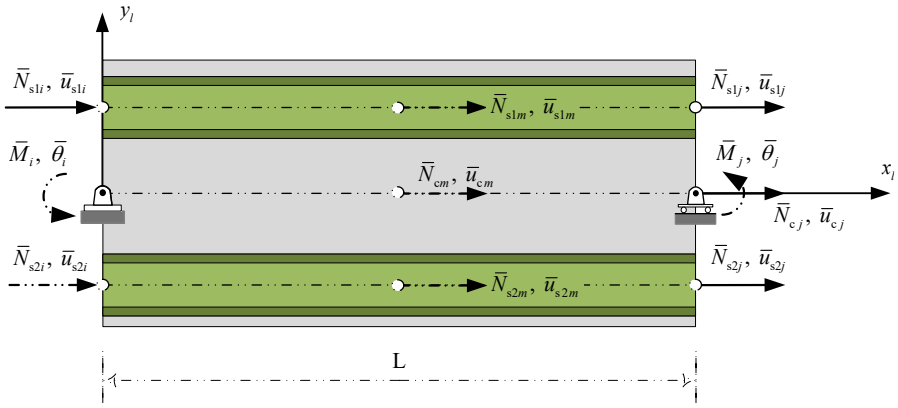
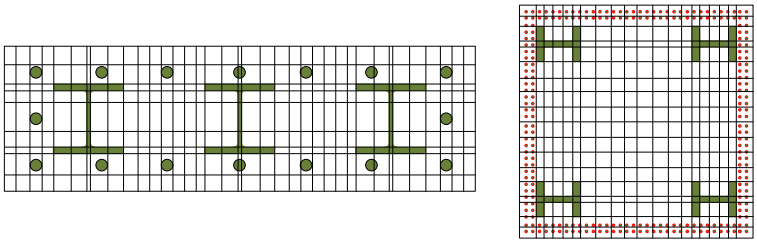


Fig. 2- Degree of freedoms of local linear element with two encased steel profiles

In local frame, the local element has 10 degrees of freedom (see Figure 2). The transverse displacement $\bar{v}$ is approximated using cubic Hermite interpolations. In order to avoid the curvature locking, three internal nodes are added in order to use quadratic shape function for axial displacement interpolation. However, for saving the calculation time, three degrees of freedom corresponding to the internal nodes will be statically condensed out thereafter to obtain the local displacement vector containing only the degrees of freedom at the element ends. The material

non-linearity is taken into account by adopting the distributed plasticity model with fiber section discretization (see Figure 3).



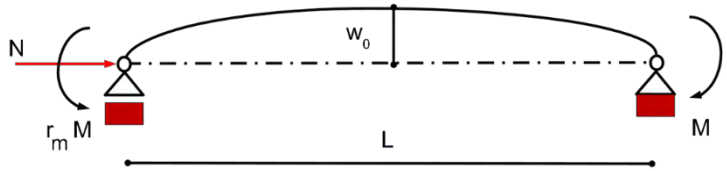
(a) Hybrid column with 3 embedded steel profiles

(b) Mega column with 4 embedded steel profiles

Fig. 3- Fiber discretization of sections

EUROCODE DESIGN METHODS FOR SLENDER COLUMNS

For a design of columns against instability, both EC2 and EC4 permit using a geometrically and materially nonlinear analysis, so-called a general method. However, this method is difficult to implement. Both Eurocodes propose a simplified method, called “moment magnification method”, in which the first-order bending moment M_{Ed} is modified by a magnification factor k to obtain the second-order one. The factor k largely depends on the flexural stiffness and equivalent moment distribution. Hence, two steps are needed in this method. The first one is to compute the effective stiffness (EI) and the second one is to estimate the first-order moment magnification factor following the shape of bending moment diagram. In general, not only the factors mentioned previously influence the flexural stiffness of the columns but also the column slenderness, the eccentricity, the normal force and the reinforcement ratio. The mathematical formulations of EC2 and EC4 simplified method applied for hybrid columns are summarized in Figure 4.



Second order bending moment: $M_{Ed,2} = k\, M_{Ed,1}$

Effective flexural stiffness: $EI = K_c E_{cd} I_c + K_s E_s I_s + K_a E_a I_a$

EC2

$$k = 1 + \frac{\beta}{\frac{N_{cr}}{N_{Ed}} - 1} \geq 1,\ \beta = \frac{\pi^2}{c_0};$$

$$N_{cr} = \frac{\pi^2}{L^2} EI; k_1 = \sqrt{\frac{f_{ck}}{20}}; k_2 = n \times \frac{\lambda}{170} \leq 0,2;$$

$$n = \frac{N_{Ed}}{A_c f_{cd}}; K_c = \frac{k_1 k_2}{1 + \varphi_{ef}}; K_s = K_a = 1;$$

$$w_0 = L / 400$$

EC4

$$k = \frac{\beta}{1 - \frac{N_{Ed}}{N_{cr,eff}}} \geq 1,$$

$$\beta = 0,66 + 0,44 r_m \geq 0,44$$

$$N_{cr,eff} = \frac{\pi^2}{L^2} EI;$$

$$K_c = 0,45 \times 1,2\ ;\ K_s = K_a = 0,9;$$

w_0 : according to steel shape

Fig. 4- Moment magnification method of EC2 and EC4

ASSEMEMENT OF SIMPLIFIED METHODS OF EC2 AND EC4

The developed FE model which was successfully validated above is used to conduct an extensive parametric study in order to assess the validity of simplified methods of EC2 and EC4 for the hybrid columns. To do so, slender hybrid columns with different types of cross-sections (HSSRC1-5, see Figure 5) are modeled using the present FE model and calculated using Eurocode simplified methods. The obtained results is compared to highlight the applicability of Eurocode simplified methods to hybrid columns. For all cases, the limit of elasticity for steel profile is 355 MPa and for reinforcement rebar is 500 MPa. Three classes of concrete strength C35, C60 and C90 are considered. The parametrical study (totally 1140 data sets) is summarized in Table 2.

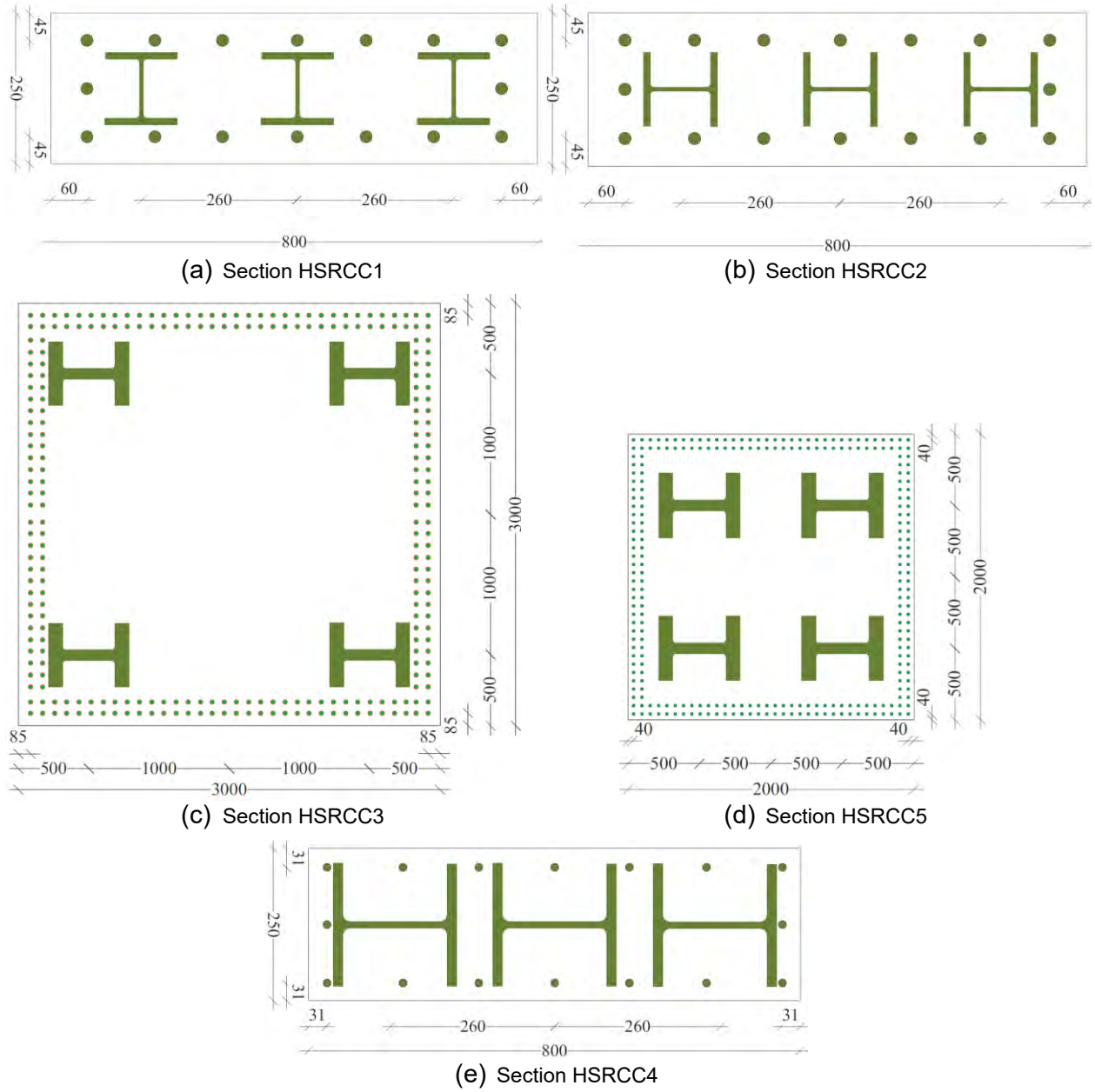


Fig. 5-. Cross-sections considered in parametric study

Table 1- Summary of case-studies.

Section	HSRCC1–5
Concrete	C35/45; C60/75; C90/105
f_{yk}	500 MPa
f_a	355 MPa
λ	25–180
e/h	0.0–3.0
δ	0.2–0.62
φ_{ef}	0; 1.5

In order to evaluate the accuracy of the safety level when applying the simplified design methods proposed in EC2 and EC4 for hybrid column design, nonlinear material models as well as the safety format have to be properly described. The comparison of the results provided by simplified method of EC2 against FE analysis is readily achieved by using the stress-strain relationship based on the design values of the constitutive model parameters as it is clearly defined in EN 1992-1-1: 5.8.6. Regarding the safety format for nonlinear FE analysis, the Eurocode for composite structures recommends to use the stress-strain relationships defined in EC2 and EC3 as stated in EN 1994-1-1: 6.7.2(8). Therefore, the material constitutive laws and the partial factors recommended by EC2 and EC3 are adopted (Figure 6).

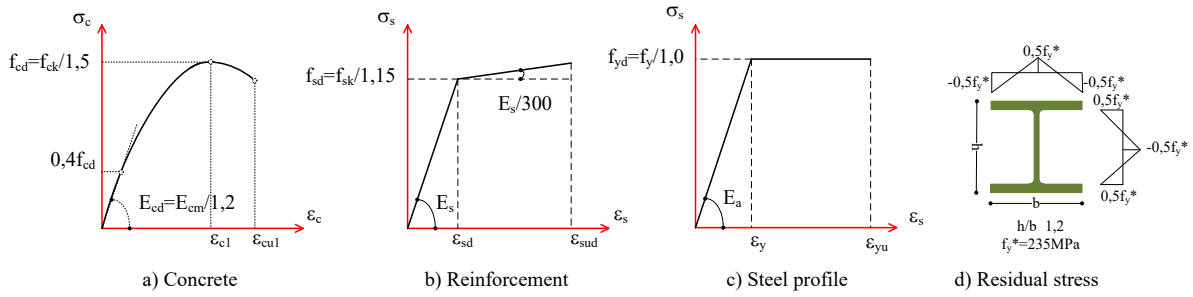


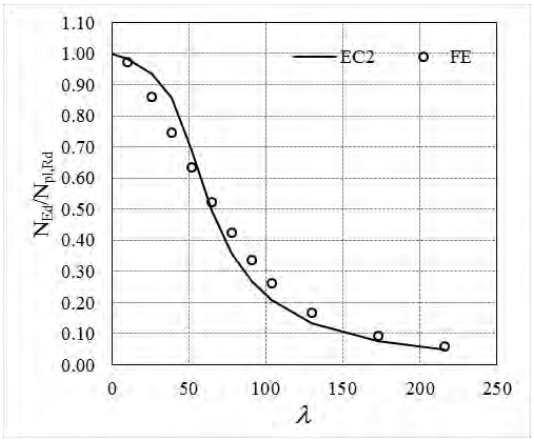
Fig. 6- Material constitutive laws and residual stress distribution used for FE analysis

The numerical model takes into account the residual stresses existing in the steel profiles (Figure 6-d)), as well as a sinusoidal geometric imperfection. The recommendations for the amplitude of the latter are different in each standard. For steel members, a value of $l_0/1000$ is proposed by EC3, while EC2 proposes a value of $l_0/400$ for concrete columns. Since the construction of hybrid columns is being alike to reinforced concrete columns where the uncertainty regarding to the geometry is significant, we adopt an initial imperfection w_0 equal to $l_0/400$ combined with an explicit representation of the residual stress distribution in order to ensure the best accuracy of the results. Besides, following the recommendations of Eurocode 4, a complete shear connection is imposed in FE model.

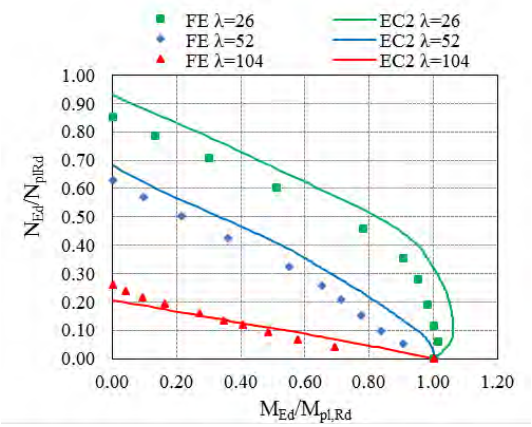
Before presenting the general conclusion of the comparison of FEA to simplified methods, the results obtained for different slenderness and loading cases for the HSRCC1 section are shown in Figure 7 and 8. The concrete used is C60 and the effective creep coefficient is taken equal to 1.5. In the case of pure compression (Figure 7a), it appears that the method is not safe for low slenderness. In the case of columns subjected to single curvature bending (Figure 7b and c), Eurocode 2 again gives non-conservative results for low to moderate slenderness. Similar results

are observed in the case of double curvature bending, except for very high load eccentricities (close to pure bending). (Figure 7d), for which the EC2 method gives good results.

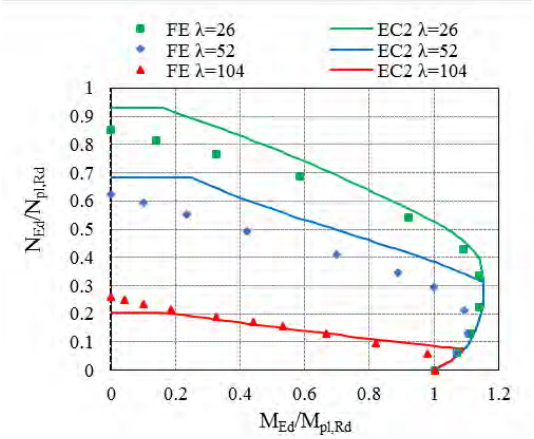
The same comparison is made for the simplified method of Eurocode 4 (Figure 8). Quite surprisingly, the latter seems to perform less well. Under pure compression (Figure 8a), the simplified method of EC4 gives safe results regardless of column slenderness. For a small eccentricity, the ultimate load given by EC4 formulation is safe regardless of column slenderness (see Fig. 10b to d). For a moderate load eccentricity, EC4 method always overestimates the ultimate load.



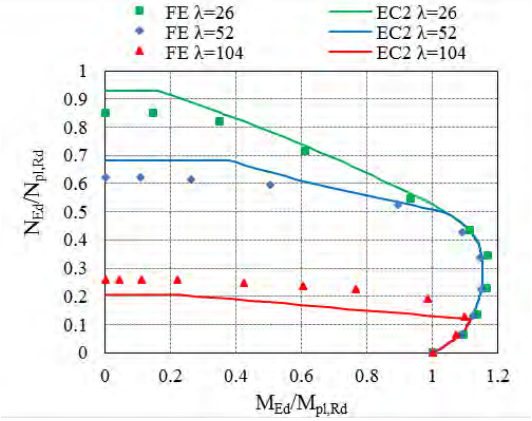
a) Buckling curve



b) Symmetrical single curvature bending (r_m = 1)



c) Single curvature bending (r_m = 0)



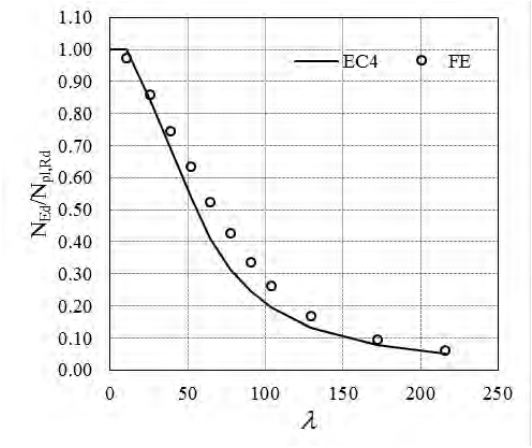
d) Double symmetrical curvature bending (r_m = −1)

Fig. 7- Comparison of simplified method of EC2 against FE analysis results

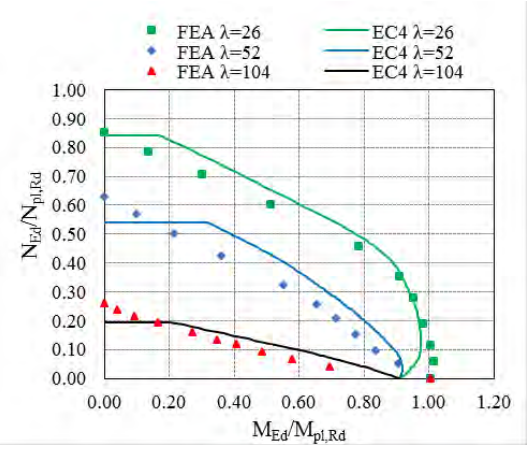
To generally evaluate the EC2 and EC4 simplified methods, the ratio of the numerical failure load R_{FE} to the corresponding resistance given by simplified method R_{SM} is selected in our investigation.

(2)
$$R = \frac{R_{FE}}{R_{SM}}$$

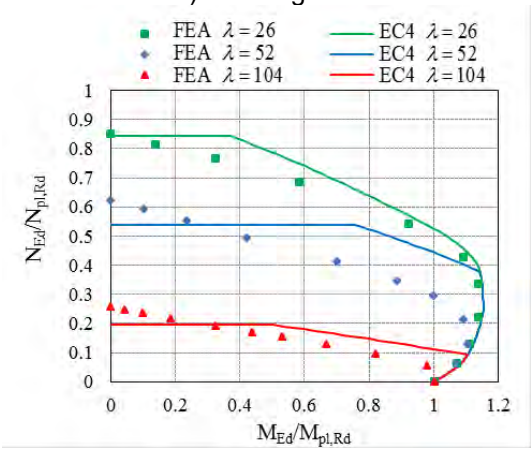
with $R_{FE} = \sqrt{\left(\frac{N_{FE}}{N_{pl,Rd}}\right)^2 + \left(\frac{M_{FE}}{M_{pl,Rd}}\right)^2}$ and $R_{SM} = \sqrt{\left(\frac{N_{SM}}{N_{pl,Rd}}\right)^2 + \left(\frac{M_{SM}}{M_{pl,Rd}}\right)^2}$.



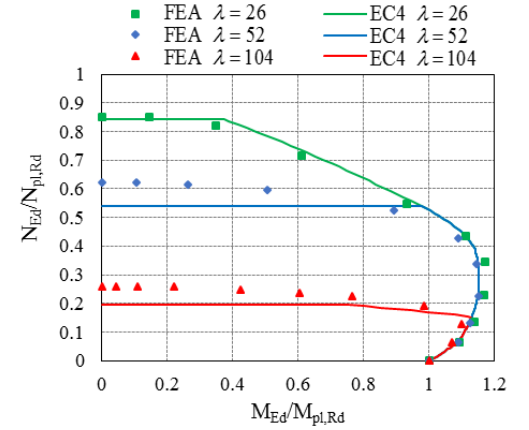
a) Buckling curve



b) Symmetrical single curvature bending (r_m = 1)



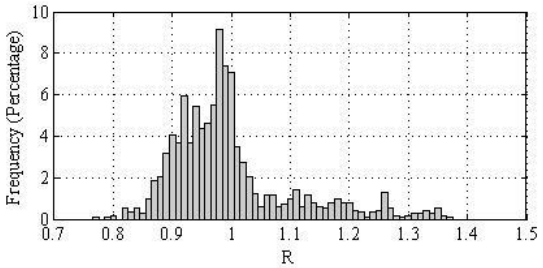
c) Single curvature bending (r_m = 0)



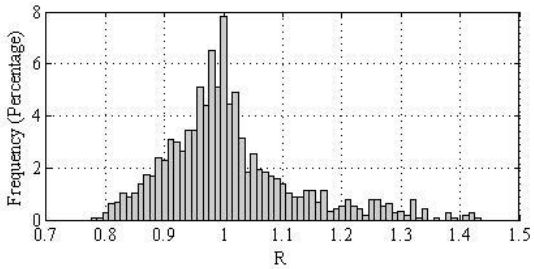
d) Double symmetrical curvature bending (r_m = −1)

Fig. 8- Comparison of simplified method of EC4 against FE analysis results

The histogram of ratio R obtained with both simplified methods is illustrated in Figure 9. It was found that the mean value “r” and the standard deviation “s” of the resistance ratio are respectively equal to 0.996 and 0.104 for EC2 simplified method, and 1.010 and 0.112 for EC4 simplified method. The percentage of R below 0.97 is 41.84% and 34.86% for EC2 and EC4 simplified method, respectively. As a general conclusion, it can be pointed out that mean estimations of both design codes seem to be correct but that their shortcomings lead to a large scatter of the results.



(a) Eurocode 2



(b) Eurocode 4

Fig. 9- Histogram of ratio R for simplified method of Eurocode 2 et 4

PROPOSAL OF A MOMENT MAGNIFICATION DESIGN METHOD FOR HYBRID COLUMN

Before suggesting new expressions for correction factors involved in the moment magnification method for hybrid column design, some effects are analyzed to get further insight into the physical behavior of hybrid column. Remarkably, the analysis of the results show that the residual stresses have a marginal effect on the behavior of hybrid columns and they can be ignored. It is worth to mention that the steel profiles, being placed eccentrically from the center of gravity of RC section, are summited to a large normal force. The latter reduces the effect of residual stresses. Therefore, it can be presumed that the structural steels behave as large rebars in lieu of structural steels under bending. Considering the above comments, it can be concluded that the new method for hybrid columns should be based on the EC2 variant rather than from the EC4 version.

On the other hand, the effect of concrete creep is investigated. The analysis of the results show that, due to compressive creep strains of concrete, longitudinal steel compressive strains can exceed the yield strain. This implies that the steel modulus that collaborates in the effective stiffness EI of the hybrid column could not be the elastic modulus but should rather be the secant modulus which varies with concrete creep. Moreover, for slender columns, plastification in the compression zone of the steel section may not develop before instability. Hence, the secant modulus of steel should be a function of the creep coefficient φ_{ef} and the geometric slenderness λ. For higher values of the creep coefficient, the value of the secant modulus of the steel section will be rather lower. However, for higher values of slenderness this modulus will be higher. Therefore, in addition to the previous cases already analyzed, we need to investigate the effect of the steel yield stress on the ultimate load of hybrid columns. The parametric study with 1140 data sets presented previously is then extended to 2960 including different yield stress of steel section (S235 and S460 added).

New expressions for β and the correction factors (K_s, K_a, K_c) involved in the definition of the effective flexural stiffness EI are proposed. The proposed simplified method based on moment magnification approach is summarized in the following.

The second-order bending moment, which has to be compared with the plastic bending moment $M_{pl,N,Rd}$ corresponding to the applied normal force N_{Ed}, is obtained by multiplying the first-order bending moment by a factor:

$$k = \frac{\beta}{1 - \frac{N_{Ed}}{N_{cr}}} \tag{3}$$

where $\beta = 0.6 r_m + 0.4 \geq 0.4$, and N_{cr} is the critical buckling load of the column calculated using the expression of effective flexural stiffness as follow:

$$EI = K_c E_{cd} I_c + K_s E_s I_s + K_a E_a I_a \tag{4}$$

Two versions of the correction factors has been proposed. The first version was proposed by the same authors in (Keo, Somja, Nguyen, & Hjiaj, 2015) where the factors used in Eurocode 2 were adopted for the concrete and the steel rebars expressed as follow:

$$K_c = k_1 k_2 / (1 + \varphi_{ef}); \qquad K_s = 1$$

$$k_1 = \sqrt{\frac{f_{ck}}{20}}; \; k_2 = n \frac{\lambda}{170} \leq 0.2; \; n = \frac{N_{Ed}}{N_{pl,Rd}}$$

The calibration factor for steel profiles in the first version is:

$$K_a = \frac{0,76\left(\frac{f_y}{f_{ck}}\right)^{0,0124}}{1+105\varphi_{ef}\exp(-0,078\lambda)} \leq 1$$

This first version of K_a is calibrated by adopting K_c and K_s of Eurocode 2 to give a good accuracy in estimating the ultimate load of the hybrid columns. However, it does not give a mechanical sense when considering the stiffness contribution of steel shape sections. Comparing to rebars contribution with the factor K_s equal to 1, steel shape sections provide less contribution to the flexural stiffness since the factor K_a is inferior to 1. For that reason, the second version of correction factors is proposed in this paper.

Since the behavior of rebars and steel profile used in hybrid columns is similar, they should share the same contribution. Thus, the same correction factor for steel profile and rebars is proposed in the second version as follow:

$$K_c = k_1 k_2 / (1+\varphi_{ef}); \qquad K_s = K_a = K_{sa} = \frac{0.450\lambda^{0.147}}{1+1.433\varphi_{ef}\exp(-0.027\lambda)} \leq 1$$

$$k_1 = \sqrt{\frac{f_{ck}}{20}};\ k_2 = n\frac{\lambda}{170} \leq 0.2;\ n = \frac{N_{Ed}}{N_{pl,Rd}}$$

To give a global view of the accuracy of the proposed second version of formulations, the frequency histogram shown in Figure 10 was constructed.

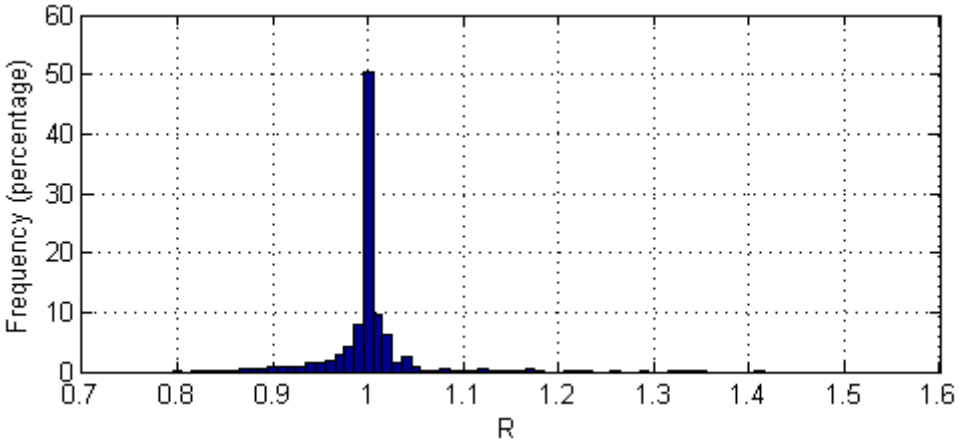


Fig. 10- Histogram of frequency of proposed formulations

Mean value of the distribution “r” and standard deviation “s” are 0.9988 and 0.0445, respectively. The percentage of R below 0.97 is 11.69%. Its overall variability gives a good estimation of the mean value of the ultimate load with relatively small deviation. The mean value “r” and the standard deviation “s” provided by the proposed second version of simplified methods are respectively equal to 0.9988 and 0.0445 which is as accurate as the first version of formulations.

CONCLUSION

The assessment of the bending moment magnification method proposed in EC2 and EC4 when applied to hybrid columns subjected to combined axial load and uniaxial bending moment have been performed. To do so, a FE model has been developed in which the geometrical/material nonlinearities as well as the partial interaction effect between the steel profiles and the

surrounding concrete are taken into account. The FE model has been validated by comparing its predictions against experimental results for standard composite columns. To thoroughly analyze the applicability of EC2 and EC4 variants of the moment magnification method to hybrid columns, an extensive parametric study with 1140 data sets (cross-sections, column slenderness and creep coefficient) has been carried out. The comparison between the results obtained with Eurocode simplified methods and with FE analyzes shows that simplified method of EC2 and EC4 leads to a wide scatter where half of case-studies are unsafe. It means that the proposed effective flexural stiffness (EI) of EC2 and EC4, which involves in determining the magnification factor, are not appropriate for hybrid column design. It was observed that the secant modulus of compressed part of the steel section varies as a function of the creep coefficient φ_{ef} and the geometric slenderness λ. Therefore, in addition to the previous cases already analyzed to evaluate EC2 and EC4 simplified method, a further investigation of the effect of the steel yield stress on the ultimate load of hybrid columns has been carried out. This later investigation leaded to an extensive numerical parametric study with 2960 data sets that serves as a database for developing a simplified method for hybrid column design. New expressions for the correction factors (for the determination of effective flexural stiffness (EI)) were proposed in order to take into account the creep effect and the effect of plastification of the steel profiles. Two versions of the correction factor K_a for steel shape sections has been proposed. The first version of K_a is calibrated by adopting K_c and K_s of Eurocode 2 to give a good accuracy in estimating the ultimate load of the hybrid columns. However, it does not give a mechanical sense when considering the stiffness contribution of steel shape sections. Comparing to rebars contribution with the factor K_s equal to 1, steel shape sections provide less contribution to the flexural stiffness of the column since the factor K_a is inferior to 1. For that reason, the second version of correction factors is proposed in this paper. The same correction factor for steel profile and rebars is proposed in the second version. The comparisons between the proposed second version of formulations and FE analyzes show that the developed method provides the ultimate load for typical slender hybrid columns with adequate accuracy.

ACKNOWLEDGMENTS

The authors gratefully acknowledge financial support by the European Commission (Research Fund for Coal and Steel) through the project SMARTCOCO (SMART COmposite COmponents: concrete structures reinforced by steel profiles) under grant agreement RFSRCT-2012-00039.

NOTATIONS

$M_{Ed,1}$	design first-order bending moment
$M_{Ed,2}$	design second-order bending moment
N_{Ed}	design axial load
$N_{pl,Rd}$	design value of the plastic resistance of the cross-section to compressive normal force
$M_{pl,N,Rd}$	design value of the plastic resistance moment of the cross-section taking into account the compressive normal force
N_{cr}	elastic critical normal force
l_0	effective column length
β	equivalent moment factor
k	moment magnification factor
EI	flexural stiffness of the compression member
E_c	elastic modulus of concrete
E_a	elastic modulus of structural steel
E_s	elastic modulus of reinforcement
I_c	moment of inertia of concrete cross section
I_a	moment of inertia of structural steel about the axis through the center of hybrid section

I_s moment of inertia of longitudinal reinforcing bars about the axis through the center of hybrid section
E_{cd} design modulus of elasticity of concrete: $E_{cd} = E_{cm}/\gamma_{cE}$
λ geometric slenderness ratio
ρ geometrical reinforcement ratio

REFERENCES

Al-Shahari, A., Hunaiti, Y., & Ghazaleh, B. (2003). Behavior of lightweight aggregate concrete-encased composite columns. *Steel and Composite Structures*, 97–110.

Bonet, J., Romero, M., & Miguel, P. (2011). Effective flexural stiffness of slender reinforced concrete columns under axial forces and biaxial bending. *Engineering Structures*, 881-893.

Chen, C., & Yeh, S. (1996). Ultimate strength of concrete encased steel composite columns. *Proceedings of the third national conference on structural engineering*, 2197-2206.

EC2-1-1. (2005). *Calcul des structures en béton. Règles générales et règles pour les bâtiments.*

EC4-1-1. (2005). *Calcul des structures mixtes acier-béton. Règles générales et règles pour les bâtiments.*

Kent, D. C., & Park, R. (1971). Flexural members with confined concrete. *Journal of the Structural Division*, 1969-1990.

Keo, P., Nguyen, Q.-H., Somja, H., & Hjiaj, M. (2015). Geometrically nonlinear analysis of hybrid beam-column with several encased steel profiles in partial interaction. *Engineering Structures*, 66-78.

Keo, P., Somja, H., Nguyen, Q.-H., & Hjiaj, M. (2015). Simplified design method for slender hybrid columns. *Journal of Constructional Steel Research*, 101-120.

Morino, S. (1998). Recent developments in hybrid structures in Japan-research, design and construction. *Engineering structures*, 336-346.

Morino, S., Matsui, C., & Watanabe, H. (1985). Strength of biaxially loaded SRC columns. *Composite and Mixed Construction, Proceedings of the U. S. /Japan Joint Seminar, ASCE*, 185-194.

Roeder, C. W. (1998). Overview of hybrid and composite systems for seismic design in the United States. *Engineering structures*, 355-363.

Tikka, T. K., & Mirza, S. A. (2008). Effective flexural stiffness of slender structural concrete columns. *Canadian Journal of Civil Engineering*, 384-399.

Westerberg, B. (2002). *Slender column with uniaxial bending, International Federation for Structural Concrete (fib).* Technical report, bulletin 16. Design examples for 1996 FIP recommendations practical design of structural concrete.

The seismic stability and ductility of steel columns interacting with concrete footings

Hiroyuki Inamasu
Doctoral Assistant, Swiss Federal Institute of Technology (EPFL)
Lausanne, Switzerland
hiroyuki.inamasu@epfl.ch

Amit Kanvinde
Professor, University of California at Davis
Davis, United States of America
kanvinde@ucdavis.edu

Dimitrios Lignos
Associate Professor, Swiss Federal Institute of Technology (EPFL)
Lausanne, Switzerland
dimitrios.lignos@epfl.ch

ABSTRACT

First-story columns in steel moment resisting frames are subjected to various forms of geometric instabilities during earthquakes. These instabilities have the potential to seriously compromise structural performance, and expedite structural collapse. In turn, these instabilities are influenced by the interactions of the column boundary conditions. Of specific concern are base connections that involve embedding the column into a concrete footing. These connections are nominally assumed to be fixed, although recent experimental data suggests that they could be significantly flexible. A finite element parametric study examining the effect of connection flexibility on interior column seismic performance is presented. Several key variables, including column base flexibility, cross-section, axial load, and column length are interrogated. Results of the finite element study are presented in support of developing quantitative relationships between column base conditions and deformation capacity of the columns. Incorporation of these relationships into modeling frameworks is discussed.

1. Introduction

A number of recent experimental and numerical studies investigated the hysteretic response of wide flange steel columns in moment resisting frames (MRFs) under multi-axial cyclic loading

(Newell and Uang 2008; Suzuki and Lignos 2015; Uang et al. 2015; Elkady and Lignos 2015, 2016; Fogarty and El-Tawil 2016). In the studies by Elkady and Lignos (2016), the influence of the column end boundary conditions on the member hysteretic response was highlighted. Local and global geometric instabilities resulted into severe flexural strength deterioration and column axial shortening. In all cases the column was fixed at its base, which is a common assumption for columns embedded in a concrete footing.

Past experiments on embedded column base connections (Grilli et al. 2017) revealed that they have an appreciable flexibility due to the elastic deformation of the concrete subject to bearing stress, the base plate and the column embedment length. Notably, findings from reconnaissance reports from past earthquakes (Clifton et al. 2011; MacRae et al. 2015) as well as system-level numerical studies (Lignos et al. 2013) suggest that a flexible column base that may be partially damaged could enhance the seismic behavior of steel MRFs.

Although the influence of the column base flexibility on the structural behavior has only been investigated through nonlinear response history analyses (Zareian and Kanvinde 2013), its influence on the column member hysteretic response has never been examined.

This paper investigates the effect of the embedded column base connection flexibility on the column hysteretic behavior through rigorous nonlinear finite element (FE) simulations. A continuum FE model is first developed and validated with recent full-scale column tests. The steel columns utilize a variety of boundary conditions and cross-sectional characteristics. The FE model is then extended such that the column base flexibility can be considered. This flexibility is inferred on the basis of available full-scale tests on steel columns embedded on concrete footings. A parametric study is then conducted in which several key variables, including the column base flexibility, cross-section, axial load, and column length are interrogated. The influence of these variables on the column hysteretic behavior is highlighted through a number of illustrative examples.

2. Review of experimental data on wide flange steel columns and embedded columns in concrete footings

2-1. Recent experiments on wide-flange steel columns

Uang et al. (2015) tested twenty-five deep columns subjected to inelastic cyclic loading coupled with a constant compressive axial load and fixed end boundaries. They found that global and local slenderness ratios as well as the compressive axial load influence the observed failure modes that can vary from local to lateral torsional buckling.

Suzuki and Lignos (2015) examined the influence of the loading history on the seismic performance of cantilever wide-flange columns. Tests on nominally identical columns subjected to symmetric loading histories were complemented with monotonic and ‘collapse consistent’ loading histories that characterize the ratcheting behavior (Ibarra and Krawinkler 2005) a structure experiences prior to earthquake-induced collapse. They found that routinely used symmetric cyclic loading histories provide insufficient information regarding the deterioration characteristics of steel columns that primarily control structural collapse.

More recently, Elkady and Lignos (2016, 2017a) investigated the influence of boundary conditions on the seismic performance of interior wide flange steel columns with fixed-flexible boundary conditions. Referring to Figure 1a, columns with a flexible top boundary exhibit larger plastic deformation capacity compared to fixed end columns. The response of the latter is controlled by column axial shortening as shown in Figure 1b.

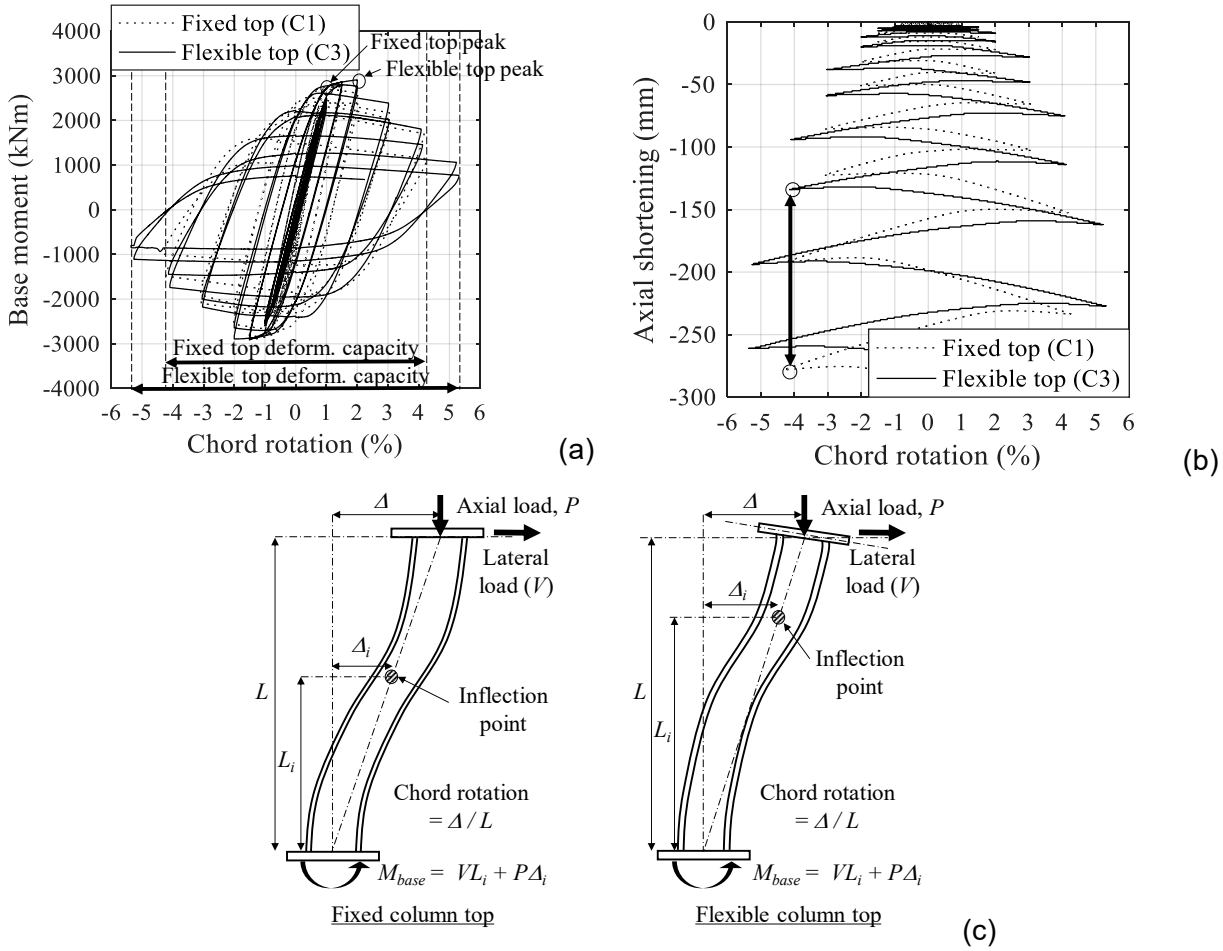


Figure 1 – Typical steel column hysteretic response and boundary conditions: (a) Moment-rotation relation; (b) axial shortening-rotation, and (c) deformed shapes (data from Elkady and Lignos 2016, 2017a).

2-2. Recent experiments on embedded column base connections

Grilli et al. (2017) recently investigated the seismic performance of embedded column base connections subjected to axial load, P, and lateral drift demands. Columns were designed to be elastic such that the observed failures were concentrated at the column base connection. Table 1 summarizes the main test parameters including the embedment depth, d_{embed}, and the applied axial load. The same table summarizes the measured maximum flexural strength, M_{max} and stiffness, β of the embedded column base connection (after subtracting the elastic contribution of the column). All the columns were tested in a cantilever fashion. Figure 2 illustrates the hysteretic response of a typical embedded column base connection. Table 1 as well as Figure 2 suggest that an embedded column base connection has an appreciable column base flexibility. The reported β values correspond to about 0.4 - 0.8% rotation under the design base moment.

It should also be noted that regardless of the column base flexibility, the specimens exhibited a considerable plastic deformation capacity without any strength loss.

Table 1 – Summary of embedded column base connection test data (Grilli et al. 2017)

Specimen ID	Column cross-section	Column length (m)	P (kN)	d_{embed} (mm)	M_{max} (kNm)	β (10^5kNm/rad)
#1	W14x370	2.84	445	508	2613	3.23
#2	W18x311	2.84	445	508	2324	3.84
#3	W14x370	3.10	0	762	3741	3.07
#4	W14x370	3.10	445	762	4124	3.38
#5	W14x370	3.10	-667*	762	3800	3.25

* minus sign indicates tension

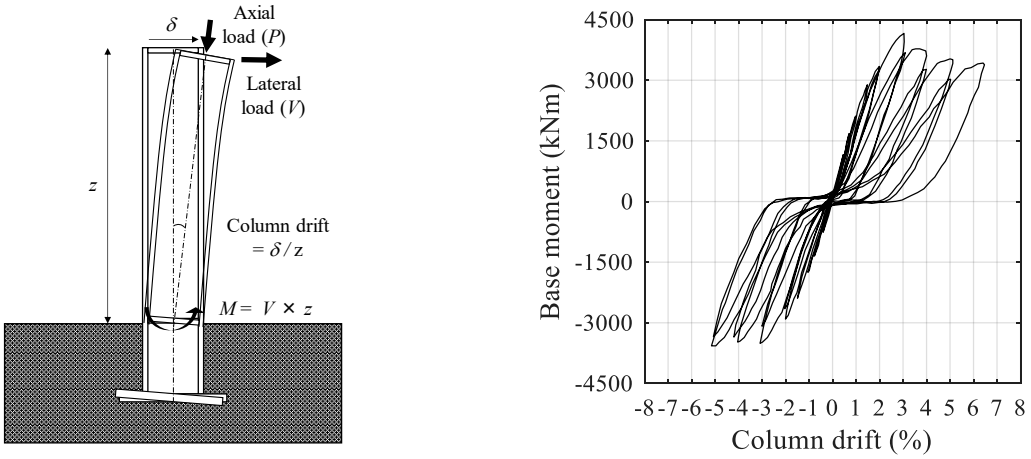


Figure 2 – Representative hysteretic response of embedded column base connection (Grilli et al. 2017)

3. Finite element model development and verification

In order to investigate the hysteretic response of steel columns embedded on column footings a FE model should be developed. This is done in two steps. In the first step, the FE model is validated with column specimens tested by Elkady and Lignos (2016, 2017a) that their base boundary was nominally fixed. Table 2 summarizes key features of the employed test specimens including the applied constant compressive axial load ratios (P is the applied axial load; $P_y = f_y A$; f_y is the expected yield stress; A is the column cross-section area) and the corresponding member slenderness, L_b/r_y (L_b and r_y are the unbraced length and the radius of gyration about weak-axis of the cross-section, respectively). Both fixed end and fix-flexible column specimens are considered. The FE model is developed in the commercial finite element analysis software ABAQUS (version 6.14-1) (ABAQUS 2014). Wide flange columns are modelled with shell elements based on the modeling approach discussed in Elkady and Lignos (2015, 2017a, 2017b). The material nonlinearity is considered with a combined isotropic/kinematic material hardening law (Lemaitre and Chaboche 1994) and residual stresses due to hot-rolling. Local and member geometric instabilities are triggered by assigning local and out-of-straightness geometric imperfections within the ASTM (2003) and AISC (2010b) limits.

Figures 3 illustrates comparisons of the column base moment, M_{base}, – chord rotation, θ, relations obtained from FE simulations and test results. The column base moment, M_{base}, is the reaction moment at the column bottom surface. The second order moment demand has been subtracted in all cases. The chord rotation, θ, is defined as the horizontal displacement at the top divided by

the actual column height, L by considering the corresponding column axial shortening if any. The comparisons suggest that the developed FE model simulates relatively well the test results throughout the entire loading history regardless of the employed cross-section and member end boundary conditions. Therefore, the FE model is deemed to be reliable and is further extended to assess the influence of the column base flexibility on the column hysteretic response.

Table 2 – Selected column specimens for the FE model development and verification (Elkady and Lignos 2016, 2017a)

Specimen ID	Cross -section	Slenderness ratio, L_b/r_y	Axial load ratio, P/P_y	Boundary conditions (Top-Bottom)	EI/L^{*1} (10^5 kNm/rad)
C1	W24x146	79	20%	Fixed – Fixed	0.923
C2	W24x146	79	50%	Fixed - Fixed	0.923
C3	W24x146	79	20%	Flexible - Fixed	0.923
C7	W24x84	51	20%	Flexible - Fixed	0.488

*[1] E: Young's modulus of steel, and I: the second moment of inertia about strong axis

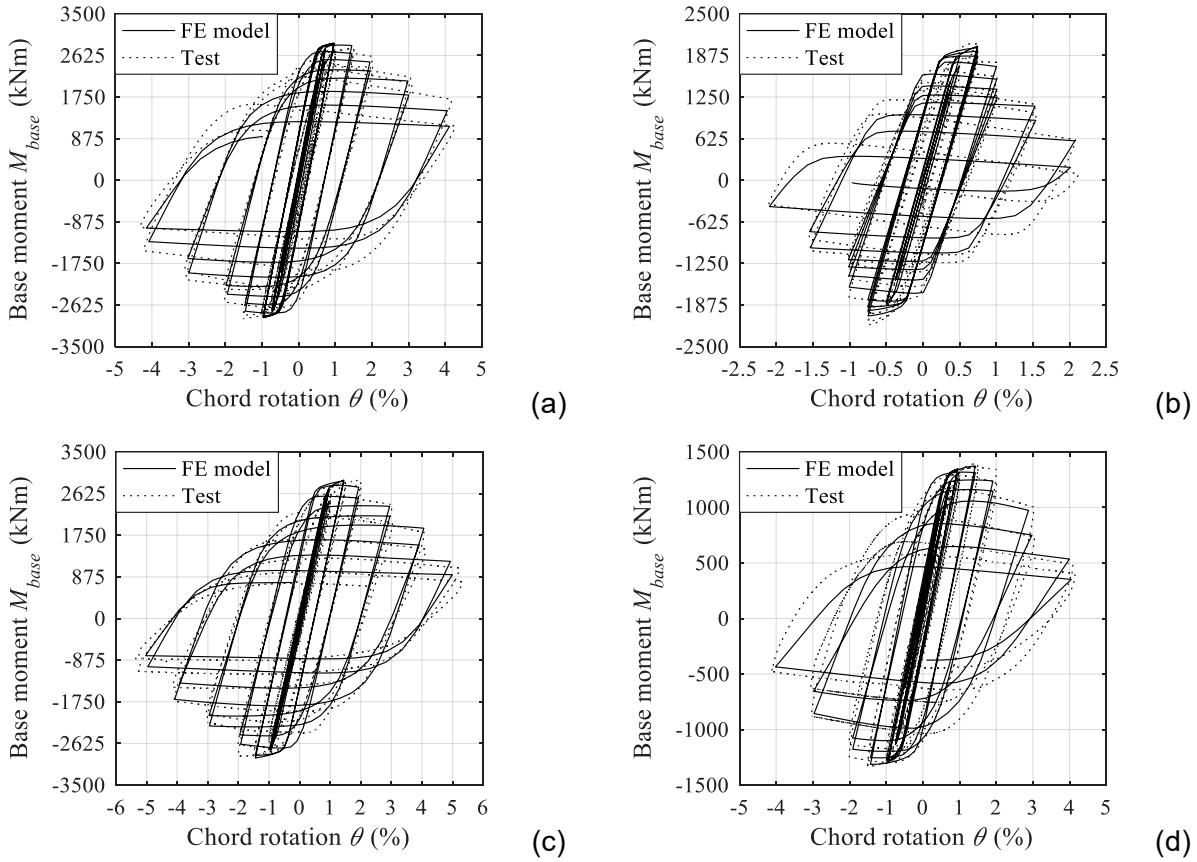


Figure 3 – Comparison between tests and FE simulations: (a) C1; (b) C2; (c) C3; and (d) C7. (data from Elkady and Lignos 2016, 2017a)

4. Refinement of finite element model boundary conditions

Figure 4 shows schematically the boundary conditions of a typical interior steel MRF column. In order to simulate the corresponding rotational stiffness attributed to the embedded column base connection, a rotational spring is assigned at the column base. The elastic stiffness, β of this spring is inferred based on the corresponding values of Table 1 (Grilli et al. 2017) by considering notional column sizes corresponding to the assumed column base connection strength.

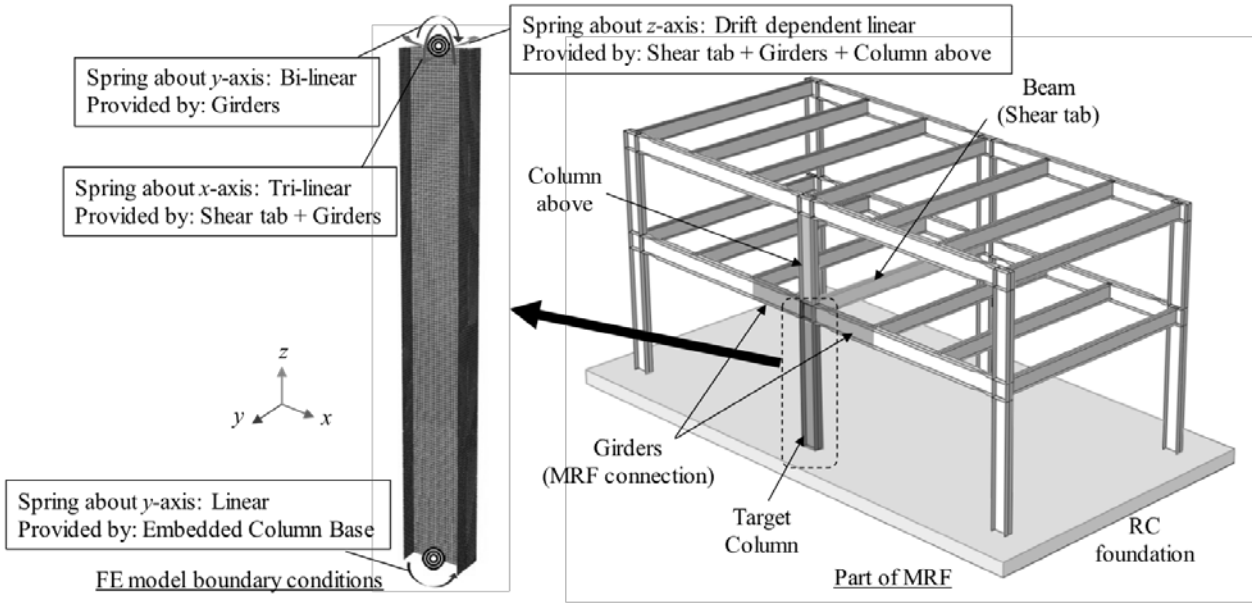


Figure 4 – Schematic representation of column end boundary conditions

Referring to Figure 4, three rotational springs are assigned at the column top to represent its member top end boundary conditions. The spring assigned with respect to the y-axis characterizes the in-plane rotational stiffness of the girders intersecting the column. A bilinear hysteretic response is assigned to this spring to consider the inelastic behavior of the steel girders. The rotational spring assigned with respect to the x-axis, represents the out-of-plane flexibility due to the shear tab beam-to-column connection (Liu and Astaneh-Asl 2000, 2004) and the torsional resistance of the girders. This spring is characterized by a tri-linear hysteretic behavior. A third spring is assigned at the column top end with respect to the z-axis that represents the torsional resistance due to bending of the shear tab plate, the torsional resistance of the 2nd story column and the weak-axis bending resistance of the girders. The contributions of these three components are lumped in a drift-dependent linear behavior that is idealized based on experimental findings summarized in Zhang and Ricles (2006). The authors plan to conduct further physical testing to characterize this relationship.

Prior experiments on beam-to-column connections that utilized deep columns and typical beams with reduced beam sections (RBS) (Chi and Uang 2002; Zhang and Ricles 2006) indicated that deep columns experience additional torque demands after the onset of severe local buckling within the RBS region. These demands are considered in the present study. In particular, the corresponding torque force – lateral drift relation is established on the basis of mechanics-based equations and experimental observations (Chi and Uang 2002; Zhang and Ricles 2006; Lignos et al. 2010; Lignos and Krawinkler 2012).

5. Parametric study to assess the effect of column base flexibility

A parametric study is conducted to evaluate the influence of the column base flexibility on the column performance based on the refined FE model discussed in Section 4. In all cases it is assumed that the concrete footing strength is sufficiently large such that the structural damage always occurs in the steel column. Table 3 and Figure 5 provides a summary of the investigated cases. Most of the employed cross-sections are highly ductile as per AISC-341-10 (AISC 2010a). Note that the rotational stiffness, β corresponding to the one deduced from experiments is referred as 'real' (Grilli et al. 2017). The AISC symmetric cyclic lateral loading protocol is employed in the context of this study.

Table 3 – Variables in the parametric study

Column base rotational stiffness, β	Length L	Axial load ratio P/P_y	Cross-section
5 cases (Fixed, Real, 75%Real, 50%Real, Pin)	3 cases (3.0, 4.5, 6.0m)	4 cases (5, 20, 35, 50%)	18 cases (see Figure 5)

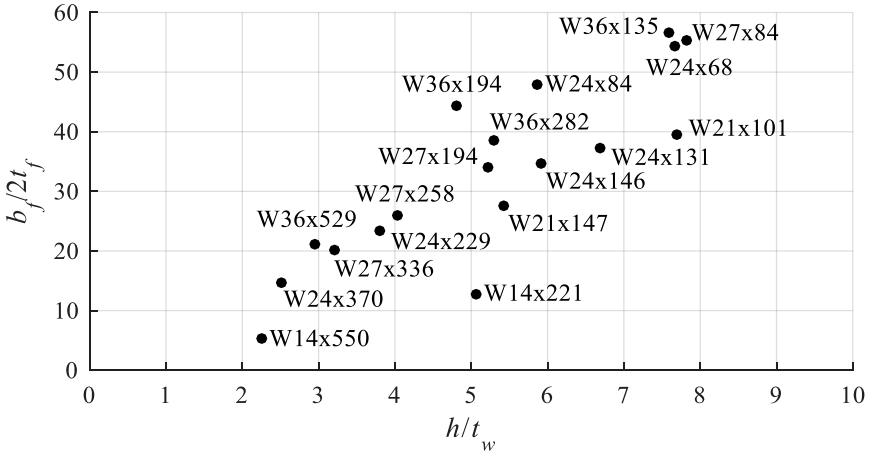


Figure 5 – Selected steel column cross-sections for the parametric study

6. Results and Discussion

6-1. Qualitative assessment of representative cases

Figure 6 shows the FE analysis results obtained from representative cases examined (i.e., W24x146-L4.5m-P/P_y=20%) with different column base flexibilities. Figure 6(a) shows a typical column base moment - chord rotation relation. The emphasis on this paper is on the maximum base moment, M_{max}*, corresponding to the capping rotation, θ_{max}*, and the post-capping plastic rotation θ_{pc}* that characterizes the post-buckling behavior of a member. These parameters are commonly used in component deterioration models employed in nonlinear frame analysis (PEER/ATC 2010).

Figure 6(b) shows the influence of the assumed column base flexibility on the first-cycle envelope curve of a steel column. From this figure, while the column base flexibility increases, the onset of local buckling is delayed. Therefore, θ_{max}* increases while the column base stiffness decreases. Referring to Figure 6b, the rate of flexural strength deterioration, which is related to the local

buckling progression seems to be more or less the same regardless of the employed column base stiffness. This is to be expected because the concrete footing is assumed to remain elastic in the context of the present study. The maximum column base moment was found to be almost the same regardless of the column base flexibility. Note that the torque force demand applied at the column top did not practically influence the hysteretic response of the column for the considered lateral loading protocol. This is attributed to the fact that the column strength mostly deteriorated due to local buckling rather than lateral torsional buckling. FE simulations with asymmetric lateral loading histories indicate that lateral torsional buckling is strongly influenced by the torque force demand.

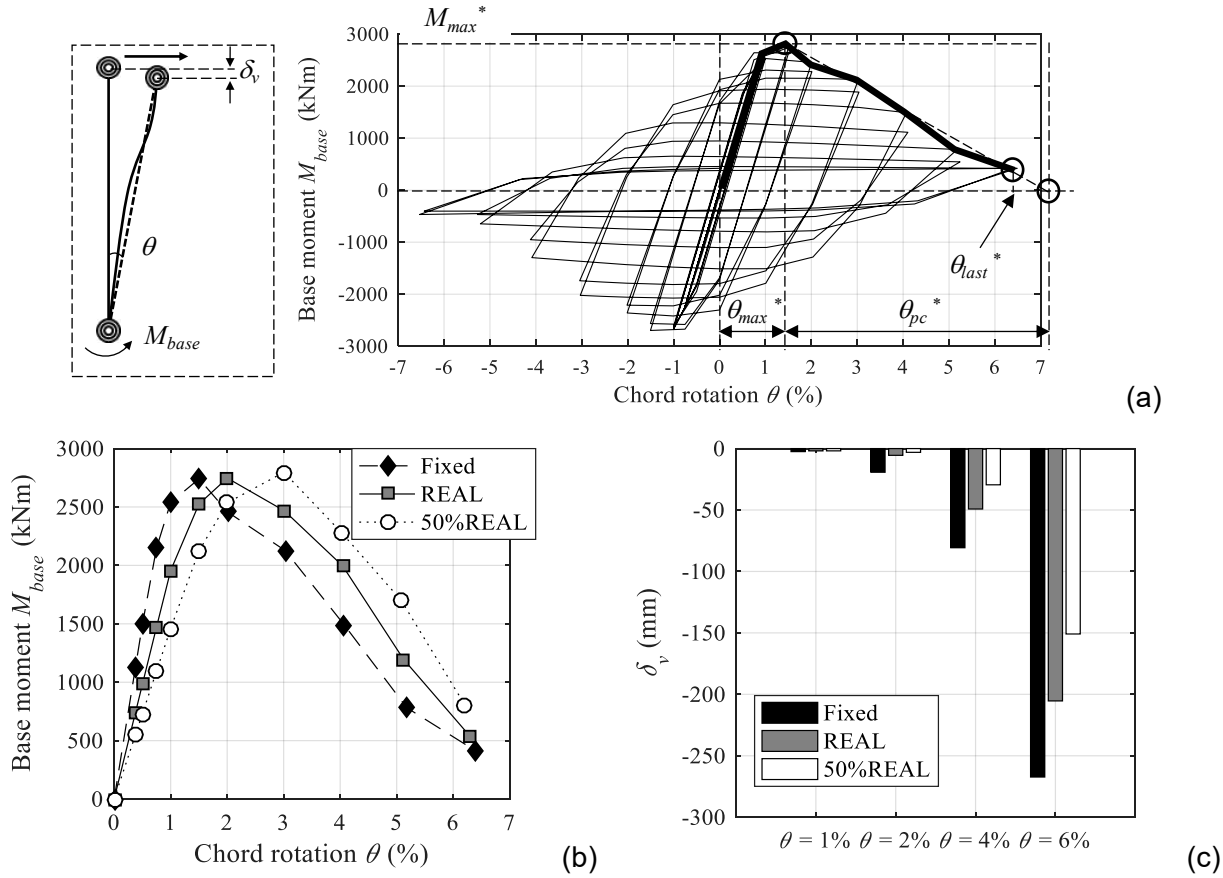


Figure 6 – FE analysis results of representative specimens (W24x146-*L*4.5m-P/P_y=20%): (a) Typical moment-rotation relation, (b) first-cycle envelope, and (c) vertical displacement of the column top

Figure 6(c) shows the influence of the column base flexibility on the vertical displacement of the column top, δ_v (see Figure 6(a)), which is strongly related to the observed axial shortening once local buckling occurs. δ_v is distinguished from axial shortening since the value of δ_v depends on the column dimensions. The figure suggests that the vertical displacement in a 'real' case is smaller than the nominally "fixed" column base case. For instance, at a reference chord rotation of 2% radians representative of design basis seismic events, the column axial shortening reduction is more than 50% compared to the "fixed" case. This is attributed to the fact that the cumulative plastic rotation in flexible column bases is smaller than that of a fixed base case at a given drift.

6-2. Capping rotation, θ_{max}*

Figure 6(b) suggests that the capping rotation, θ_{max}* increases while the elastic concrete footing stiffness decreases. Prior research (Elkady and Lignos 2015) suggests that the pre-peak plastic rotation, θ_p* (i.e., θ_p* = θ_{max}* - θ_y) increases exponentially while the local and/or global slenderness and/or the column axial load ratio decrease. Same observations hold true in the present study.

Figure 7 shows the θ_{max}* versus h/t_w relation for 4.5m long steel columns subjected to P/P_y = 20% with four different column base flexibilities. The FE simulations suggest that if the concrete footing stiffness decreases then θ_{max}* increases in most cases. This finding hold true regardless of the member length and the applied axial load ratio. For all practical purposes, the θ_{max}* increase compared to the ideally "fixed" condition may be approximated as 0.5% radians for the 'real' case and 1.0%rad for the '50% of real' case.

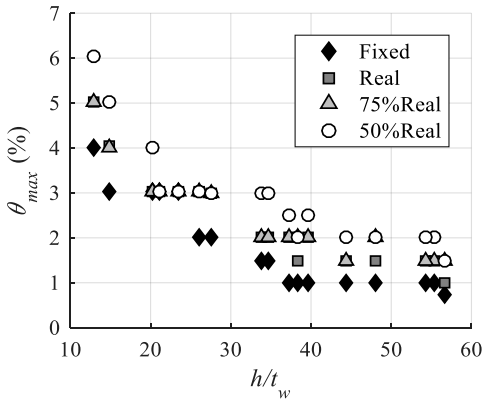


Figure 7 – Capping plastic rotation, θ_{max}* – web local slenderness ratio relation (L4.5m-P/P_y=20%)

6-3. Post-capping plastic rotation, θ_{pc}*

Figure 6(b) indicates that the post-capping plastic rotation, θ_{pc}* is practically not influenced by the column base flexibility given that the column base strength is assumed to be infinite (i.e., elastic concrete footing). Therefore, regardless of the employed column base flexibility, the predictive equations proposed by Hartloper and Lignos (2017) may be adopted. Note that the deduced θ_{pc}* values are in the range of 5-10% radians if P/P_y =20% and 20 < h/t_w < 45. At higher axial load ratios and/or higher h/t_w ratios, the θ_{pc}* values range between 2-5%radians.

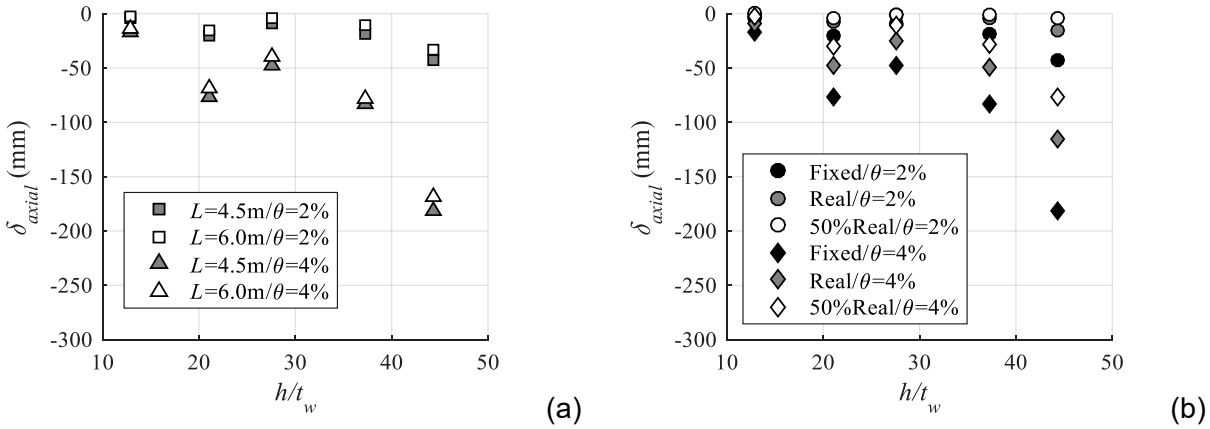
6-4. Column axial shortening, δ_{axial}

In order to assess the column axial shortening among models with different length, the vertical displacement at the column top of each model, δ_v, is subtracted by the vertical displacement of same model with pinned column base, $\delta_{v,pin}$. Therefore axial shortening, δ_{axial}* = δ_v - $\delta_{v,pin}$.

Figure 8 shows the δ_{axial}* - h/t_w relation for different column lengths and column base flexibilities. In general, the observed axial shortening at a given rotation is slightly smaller for longer columns because the yield rotation is larger due to the smaller column flexural stiffness. However, column axial shortening is almost the same regardless of the column length. The reason is that column

axial shortening mainly depends on the onset of local buckling, which in turn depends on the employed cross-sectional properties.

Referring to Figure 8(b) the column axial shortening is shown at characteristic drift demands. Notably, at a drift of 2% the column axial shortening is minor if the column base flexibility is considered. In that respect, the column-base 'fixed' assumption is fairly conservative. From the same figure, if a 50% reduction of the real column base flexibility is assumed, the corresponding axial shortening at a lateral drift of 2% is almost zero in most of the cases. Similarly, if a 50% reduction of the real column base flexibility is assumed, the corresponding axial shortening reduction is, 80% and 30% at a lateral drift of 2% and 4%, respectively.



(a) (b)

Figure 8 – Column axial shortening – web local slenderness ratio relation:(a) P/P_y=20% and β = Fixed and (b) P/P_y=20% and L = 4.5m

7. Summary and Conclusions

This paper investigated the influence of the column base flexibility on the hysteretic behavior of first story interior wide flange steel columns typically seen in moment-resisting frames (MRFs). This was achieved through a parametric study that was conducted with rigorous finite element (FE) simulations. The parameters that were investigated include the column base flexibility, the applied axial load ratio and the geometric properties of the employed cross-section. The developed FE model was validated with representative test results from full-scale steel column experiments. The boundary conditions of the FE model were further refined to reflect representative column base connection flexibilities inferred from recent full-scale embedded column base tests. The main findings are summarized as follows,

1. The corresponding capping rotation, θ_{max}* increases while the elastic stiffness of the column base foundation decreases. This increase is on average, 0.5% radians when the 'real' column base flexibility is considered relative to the nominally fixed-base case. The corresponding, θ_{max}* increases by 1.0%rad if the 'real' column base flexibility is reduced by 50%. It was also found that the influence of the column base flexibility on the post-capping rotation, θ_{pc}* was practically negligible.
2. The column axial shortening is overestimated if the embedded column base flexibility is neglected. In particular, the FE simulation results suggest that the column axial shortening reduction relative to the theoretically 'fixed' base can be more than 30% at a reference lateral drift demand of 4%.

References

ABAQUS. (2014). *ABAQUS analysis user's manual version 6.14-1.* Dassault Systems Simulia Corp., RI, USA.

AISC. (2010a). *Seismic Provisions for Structural Steel Buildings. ANSI/AISC-341-10.* American Institute of Steel Construction.

AISC. (2010b). *Specification for Structural Steel Buildings. ANSI/AISC 360-10.* American Institute of Steel Construction.

ASTM. (2003). Standard Specification for General Requirements for Rolled Structural Steel Bars, Plates, Shapes, and Sheet Piling. American Society for Testing and Materials.

Chi, B., and Uang, C. M. (2002). Cyclic Response and Design Recommendations of Reduced Beam Section Moment Connections with Deep Columns. *Journal of Structural Engineering*, *128*(4), 464–473.

Clifton, G. C., Bruneau, M., MacRae, G. A., Leon, R., and Fussell, A. (2011). Steel Structures Damage from the Christchurch Earthquake Series of 2010 and 2011. *Bulletin of the New Zealand Society for Earthqauke Engineering*, *44*(4), 297–318.

Elkady, A., and Lignos, D. G. (2015). Analytical investigation of the cyclic behavior and plastic hinge formation in deep wide-flange steel beam-columns. *Bulletin of Earthquake Engineering*, *13*(4), 1097–1118.

Elkady, A., and Lignos, D. G. (2016). Dynamic Stability of Deep and Slender Wide-Flange Steel Columns - Full Scale Experiments. *Proceedings of the Annual Stability Conference Structural Stability Research Council*.

Elkady, A., and Lignos, D. G. (2017a). Full-Scale Cyclic Testing of Deep Slender Wide-Flange Steel Beam-Columns under Unidirectional and Bidirectional Lateral Drift Demands. *16th World Conference on Earthquake Engineering (16WCEE), Santiago, Chile*, num. 944.

Elkady, A., and Lignos, D. G. (2017b). Stability Requirements of Deep Steel Wide-Flange Columns under Cyclic Loading. *Proceedings of the Annual Stability Conference Structural Stability Research Council, San Antonio, Texas*.

Fogarty, J., and El-Tawil, S. (2016). Collapse Resistance of Steel Columns under Combined Axial and Lateral Loading. *Journal of Structural Engineering*, *142*(1), 4015091.

Grilli, D. A., Jones, R., and Kanvinde, A. M. (2017). Seismic Performance of Embedded Column Base Connections Subjected to Axial and Lateral Loads. *Journal of Structural Engineering*.

Hartloper, A., and Lignos, D. G. (2017). Updates to the ASCE-41-13 Provisions for the Nonlinear Modeling of Steel Wide-Flange Columns for Performance-Based Earthquake Engineering. *EUROSTEEL 2017, Copenhagen, Denmark*.

Ibarra, L. F., and Krawinkler, H. (2005). *Global Collapse of Frame Structures under Seismic Excitations. John A. Blume Earthquake Engineering Center Technical Report 152. Stanford Digital Repository.* Available at http://purl.stanford.edu/dj885ym2486

Lemaitre, J., and Chaboche, J.-L. (1994). *Mechanics of solid materials*. Cambridge university press.

Lignos, D. G., Hikino, T., Matsuoka, Y., and Nakashima, M. (2013). Collapse Assessment of Steel Moment Frames Based on E-Defense Full-Scale Shake Table Collapse Tests. *Journal of Structural Engineering*, *139*(1), 120–132.

Lignos, D. G., Kolios, D., and Miranda, E. (2010). Fragility assessment of reduced beam section moment connections. *Journal of Structural Engineering*, *136*(9), 1140–1150.

Lignos, D. G., and Krawinkler, H. (2012). Development and utilization of structural component databases for performance-based earthquake engineering. *Journal of Structural Engineering*, *139*(8), 1382–1394.

Liu, J., and Astaneh-Asl, A. (2000). Cyclic Testing of Simple Connections Including Effects of Slab. *Journal of Structural Engineering*, *126*(1), 32–39.

Liu, J., and Astaneh-Asl, A. (2004). Moment–Rotation Parameters for Composite Shear Tab Connections. *Journal of Structural Engineering*, *130*(9), 1371–1380.

MacRae, G. A., Clifton, G. C., Bruneau, M., Kanvinde, A. M., and Gardiner, S. (2015). Lessons from Steel Structures in Christchurch Earthquakes. *Proceedings of the 8th International Conference on Behavior of Steel Structures in Seismic Areas (STESSA), Shanghai, China*.

Newell, J. D., and Uang, C.-M. (2008). Cyclic Behavior of Steel Wide-Flange Columns Subjected to Large Drift. *Journal of Structural Engineering*, *134*(8), 1334–1342.

PEER/ATC. (2010). Modeling and acceptance criteria for seismic design and analysis of tall buildings, PEER/ATC 72–1. Prepared for Pacific Earthquake Engineering Research Center (PEER) by Applied Technology Council (ATC), Redwood City, San Diego.

Suzuki, Y., and Lignos, D. G. (2015). Large Scale Collapse Experiments of Wide Flange Steel Beam-Columns. *Proceedings of the 8th International Conference on Behavior of Steel Structures in Seismic Areas (STESSA), Shanghai, China.*

Uang, C. M., Ozkula, G., and Harris, J. (2015). Observations from cyclic tests on deep, slender wide-flange structural. *Proceedings of the Annual Stability Conference Structural Stability Research Council, Tennessee, Nashville.*, 247–263.

Zareian, F., and Kanvinde, A. (2013). Effect of Column-Base Flexibility on the Seismic Response and Safety of Steel Moment-Resisting Frames. *Earthquake Spectra*, *29*(4), 1537–1559.

Zhang, X., and Ricles, J. M. (2006). Experimental Evaluation of Reduced Beam Section Connections to Deep Columns. *Journal of Structural Engineering*, *132*(3), 346–357.

Performance based evaluation of a multiple CFT bridge pier with buckling restrained braces

Chi-Ho Jeon

Chung-Ang University, Dept. of Civil and Env. Engineering

Seoul, Korea

chihobeer@cau.ac.kr

Dong-Wook Kim

Chung-Ang University, Dept. of Civil and Env. Engineering

Seoul, Korea

chihobeer@cau.ac.kr

Chang-Su Shim

Chung-Ang University, Dept. of Civil and Env. Engineering

Seoul, Korea

csshim@cau.ac.kr

ABSTRACT

In recent construction industry, accelerated bridge construction method has been risen as a main issue especially in urban construction. As an alternative of typical columns for accelerated bridge construction method, a pier of four concrete filled steel tube (CFT) columns with braces has been introduced. Experiments of the multiple CFT columns with buckling restrained braces (BRB) have been conducted using static and quasi-static load to investigate structural behavior. In this paper, fiber element analysis has been simulated to evaluate the performance of the CFT columns. The OpenSEES software is used for detailed modeling of piers and both of geometrical and material nonlinearities and behavior of connections are considered at them. A spring element in OpenSEES was used to express buckling restrained brace details. According to required performance criteria, design parameters of the CFT bridge pier with BRBs were determined.

1. INTRODUCTION

The CFT bridge pier was developed from the accelerated bridge concept. Unlike the typical RC substructures, this bridge pier consists of four CFT columns and braces, and it could be modularized and is designed with standardized commercial products as shown in Figure 1. In the previous research, Shim et at. (2014) found that low cycle fatigue failure was occurred

between brace and CFT column at the connection of small-scale test. The author, therefore, performed tests on four different brace connections, and proposed enhanced connection detail. Kim et al. (2016a) conducted full-scale test of CFT bridge pier with the enhanced connection detail and Buckling Restrained Brace (BRB). The author verified that the enhanced connection detail and BRB improved structural performance of the CFT bridge pier. Also, he suggested plastic-hinge analysis concept to the structure. Kim et al. (2016b) also conducted analytical study on the CFT bridge pier according to directivity of load. It was found that stress concentration at the bracing joint could be prevented by BRBs, and displacement ductility of the structure was satisfied.
In this paper, the CFT bridge pier was evaluated by performance based concept according to the brace details.

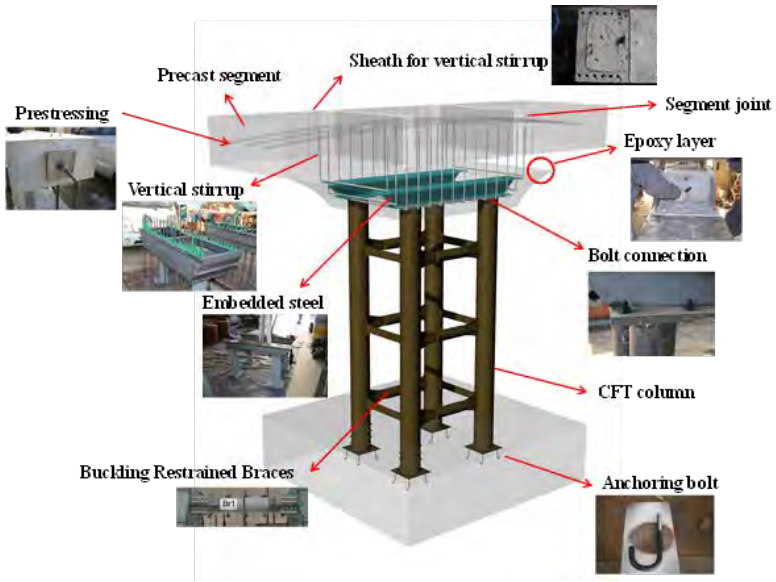


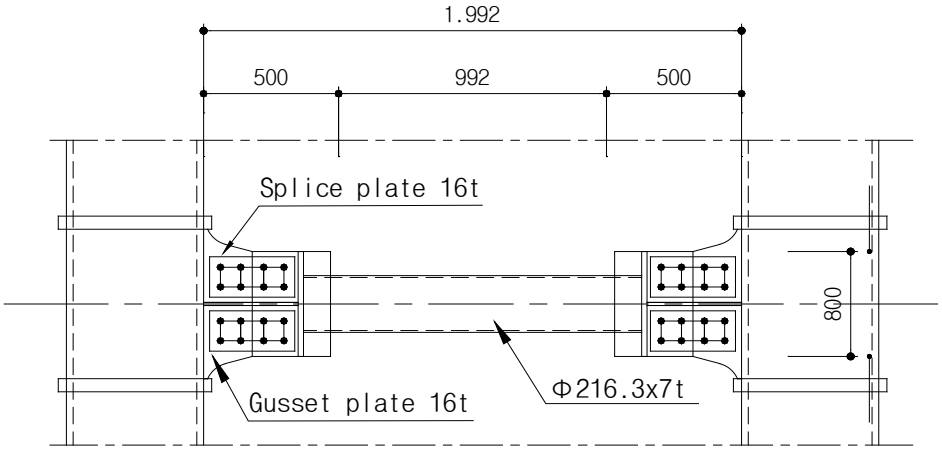
Fig. 1 Schematic of the CFT bridge pier

2. Experimental program

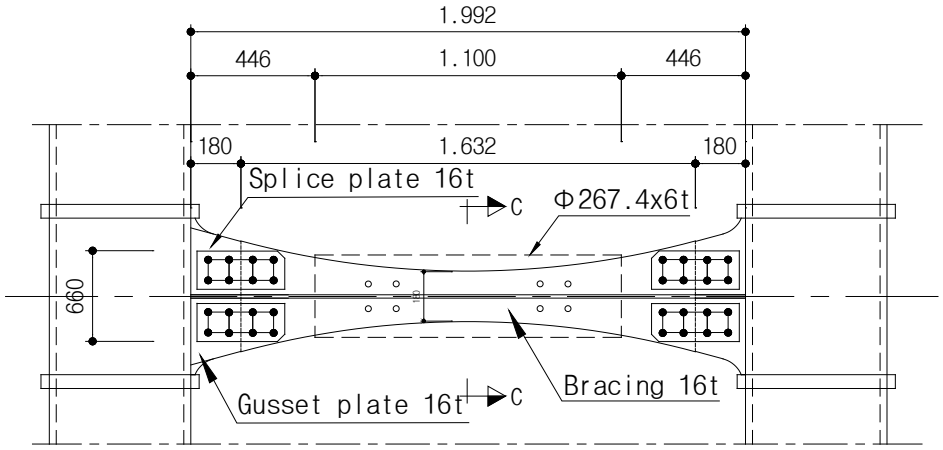
2.1 Test specimen

In the previous research (Kim et al, 2016a), a bridge pier with four CFT columns and braces was designed to investigate the performance under static and cyclic loading conditions. The height of specimen was 7,950 mm, and the four CFT columns had the dimension of Φ508 x 16 x 5,800 with distance of 2,500 mm and 2,000mm between columns in strong and weak axes, respectively. The dimension of pier cap was 5,000 mm x 3,000 mm x 1,900 mm. In the pier cap, 2-I407x428x20x35 beams were embedded on the top of columns in strong axis. The footing had the dimension of 4,800 mm x 4,200 mm x 1,200 mm and embedded length of columns in the footing was 1.5 times(770 mm) of diameter of the CFT section. The design compressive strength of concrete was 40 MPa, and measured strength on the day of experiment was 42 MPa. The yield and tensile strength of CFT columns and braces were 315 MPa and 490 MPa, respectively.
The experiments were planned to consider two types of braces (Figure 2), and both were used without CFT columns change in sequence; after the first test was conducted with circular hollow steel tube (CHST) braces under cyclic loading in elastic range, the second

test was conducted with buckling restrained brace (BRB) up to drift ratio of 2.76. The experiments followed loading program in the previous research (Kim et al, 2016a).



(a) Circular hollow steel tube brace for first test



(b) Buckling restrained brace for second test

Fig. 2 Brace details

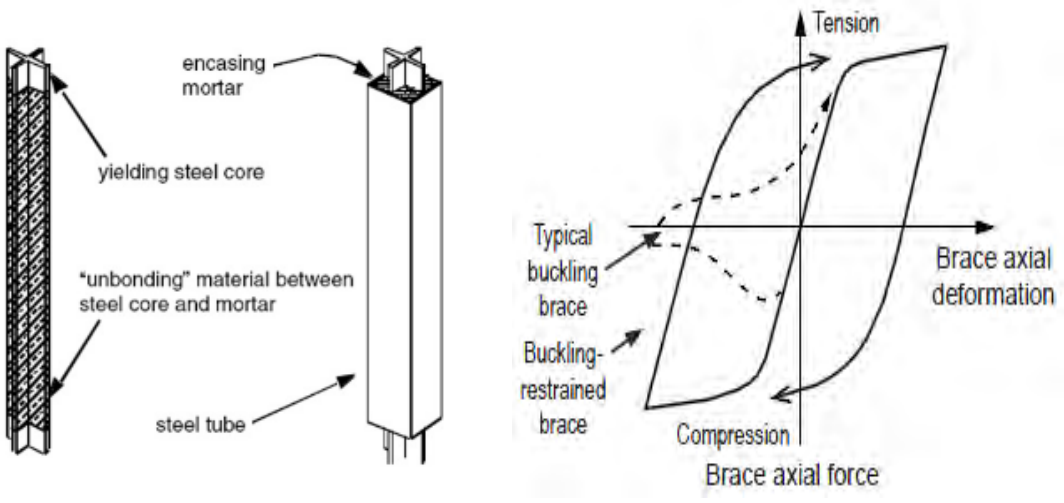
3. Buckling restrained brace

3.1 Introduction

In the extreme event limit state design, it is important to provide enough energy dissipation against to earthquake for the safety of structures. The buckling restrained braces (BRBs) were introduced for those objectives, initially used in frame structures (Roeder an Popov, 1977). The design concept that BRBs have a role of sacrificial members to dissipate the seismic energy, while other main components maintain their integrity is known as the structural fuse concept.

The typical BRBs consist of steel core-plate and surrounding steel tube casing filled with grout or concrete as shown in Figure 3(a) (Ei-Bahey and Bruneau, 2011). Other steel core

sections such as single plate or multiple plates could be used. Figure 3(b) shows the comparison of behavior in compression between typical buckling brace and BRB. Due to the buckling behavior, the core area of typical buckling brace is designed for seismic load based on the critical buckling stress of the section, while BRB section is sized by yield stress. This advantage is reflected in the larger response modification coefficient, R, assigned to BRBFs (R=8) by ASCE 2010. In contrast, R values for Ordinary Concentrically Braced Frame (OCBF) and Special Concentrically Braced Frames (SCBFs) are 3 1/4 and 6, respectively.



(a) (b)

Fig. 3 (a) Typical BRB assembly; (b) Buckling versus buckling restrained brace behavior (Ei-Bahey and Bruneau, 2011)

3.2 Research on bridge bents with BRBs

As the recent seismic design standard provides more strict provisions for important bridges, several existing bridges which followed old design standard can no longer guarantee seismic safety. Therefore, many researchers have tried to use BRBs to bridge bents, especially, in a retrofitting manner, because of its structural advantage and maintenance benefit. Bazaez and Dusicka (2015) introduced idealized response when BRBs are used to RC bent as shown in Figure 4. The BRB needs to be designed in such way to reduce the demands on the bare bent, therefore, the bare bent would respond elastically under the 500-year and 1000-year event. However, the increased forces in the bent system due to BRBs, sometimes, have the demands in the concrete elements exceed their capacity. For that reason, minor inelastic behavior is allowed to occur for the 1000-year event. Xiaone and Bruneau (2016) conducted case study on application of BRB to bridge bents. The author intended full elastic column response for conservative design objective by limiting demands in the columns to their yield flexural strength. This study showed at least 50% of drift reductions with increase in base shear demands no greater than 20%. Wang et al. (2016) conducted also a case study using a three-span RC box girder bridge. In the study, it was found that BRBs reduces column bent drift ratio up to 75% and prevents deck unseating. Also, the BRBs redistribute

the stiffness of bridge bents and abutments, which results in dissipation of shear demand from 6 to 15%. The authors conclude that BRBs prevent or delay the occurrence of column plastic hinge from an evidence of the concrete and reinforcement strains in the columns were reduced.

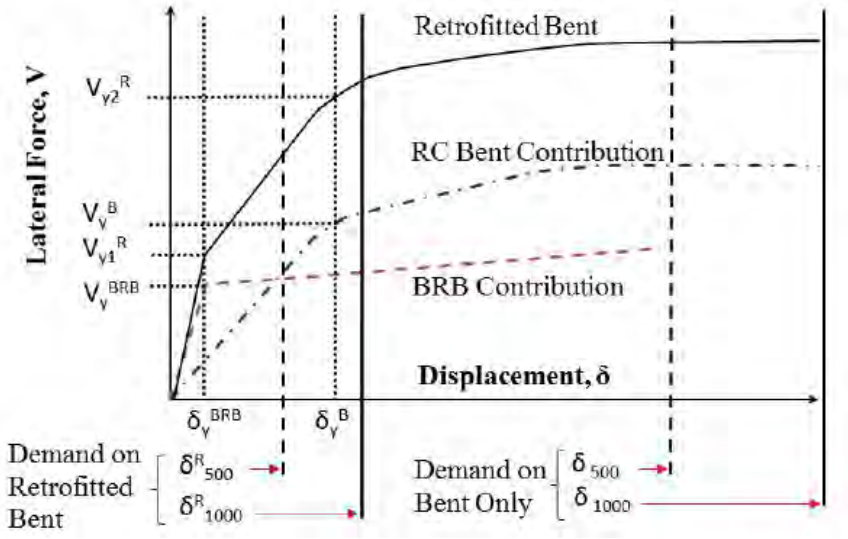


Fig. 4 Idealized pushover response (Bazaez and Dusicka 2015)

4. Performance based evaluation using analysis

4.1 Definition of performance level of CFT columns.

The researchers introduced above referred to the stress or strain condition of columns when BRBs were installed. However, they did not suggest the performance level for the columns with the BRBs. It is necessary to consider performance base design so that the columns give proper capacity to their signifiance. The performance based design has four performance levels; fully operational, delayed operational (which can be classified into immediate occupancy with short-term restoration and life safety and long-term restoration), and collapse prevention. The structural fuse concept is valid up to delayed operational level, however, the performance of the columns according to previous design process (AISC 2010) could be less safe level because section of BRBs are decided from the load acting on the BRBs and limited deformation.

In order to evaluate the CFT bridge pier according to the performance based design, the performance level of CFT columns should be defined. The definition of performance level of CFT columns is shown in Table 1. For the fully operational level, column should be in elastic range after seismic excitation, which can be expressed by $\varepsilon < \varepsilon_y$ (ε_y: yield strain of steel tube). For delayed operational level, it could be defined as the CFT columns are in status from yield to buckling of steel tube. The collapse prevention level, therefore, from strain at buckling to fracture strain. The behavior of CFT columns varies with not only aspect ratio (L/D) and material properties, which are similar to typical RC columns, but also axial load ratio (N/N_u) and diameter to thickness ratio (D/t). Thus, buckling behavior could not be defined by only strain of steel tube. SAISHO et al. (2004) conducted a research on local buckling behavior of CFT columns considering the factors above. Figure 5 plots one of the buckling behaviors of CFT column in the research under the condition of L/D = 10.0,

concrete compressive strength σ_c = 30 & 120 MPa, and steel tube tensile strength σ_u = 440 MPa. The considered value in this study was N/N_u = 0.3, σ_c = 30 MPa, which cause the value of Φ_{lb}/Φ_u = 9. In which, $N_u = \sigma_c A_c + \sigma_u A_s$, Φ_{lb} = deformation of CFT column when the steel tube buckled locally, Φ_u = upper bound of elastic deformation (M_e/K_0, M_e: elastic bending moment right before yielding, K_0: elastic bending stiffness)

Table 1 Qualitative and quantitative performance levels

CFT column performance level	Qualitative performance description	Quantitative Performance description
Fully operational	No cracks No inelastic deformation	$0 < \varepsilon < \varepsilon_y$
Delayed operational	Initiation of inelastic deformation No buckling	$\varepsilon_y < \varepsilon < \varepsilon_{lb}$
Collapse prevention	Occurrence of buckling No failure	$\varepsilon_{lb} < \varepsilon < \varepsilon_u$

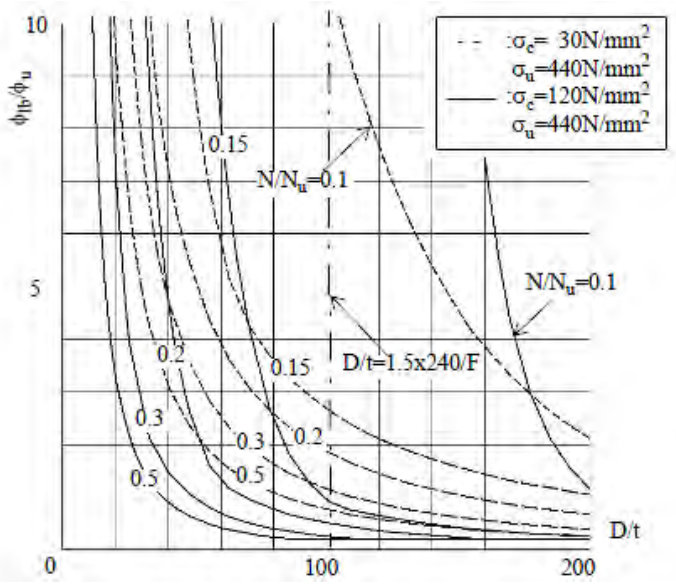
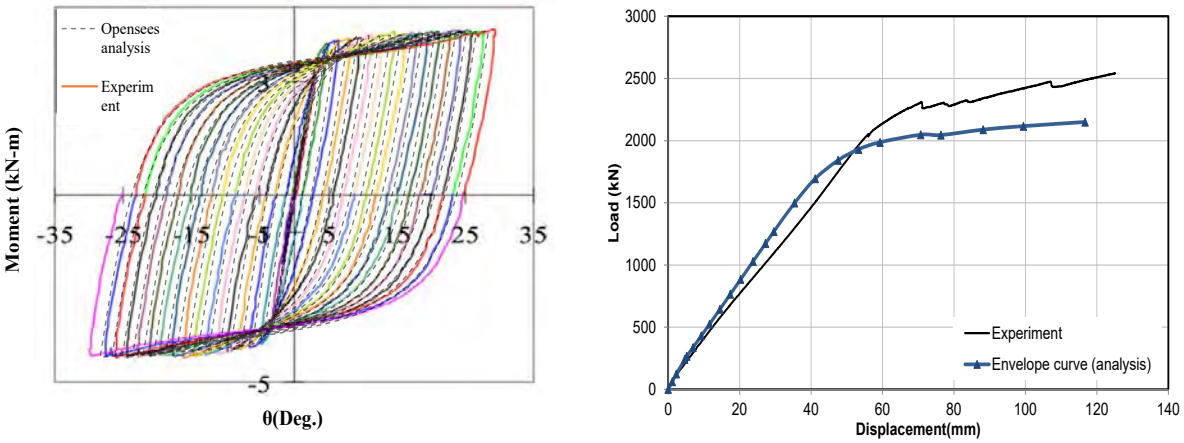


Fig. 5 Plastic deformation until CFT column buckles locally with aspect ratio L/D=10.0) (SAISHO et al., 2004)

4.2 Verification of analysis model

In the previous research (Jeon et al. 2015), the single CFT model was verified using OpenSEES analysis program as shown in Figure 6(a). The analysis model was compared with pure bending test specimen, and the simulated strength, initial stiffness, and reduction of stiffness were well corresponded with test result. Figure 6(b) shows comparison of push over test result from CFT bridge pier and cyclic analysis result modeled with verified CFT column model and BRB model. The difference was around 6 % in elastic range and an average of 12 % in inelastic range. The simulation of analysis model showed similar behavior to the full-scale test such as plastic hinge location and stress distribution



(a) (b)

Fig. 6 Verification of analysis model for (a) single CFT column and (b) CFT bridge pier

4.3 Analysis result

In order to clearly identify the behavior of the braces, analysis model was revised from test specimen as shown in Figure 7. The braces were inclined to behave effectively in lateral load, and two types of braces were compared; one is steel tube brace which has dimension of Φ216.3x4t, and another one is BRB with same dimension of the test.

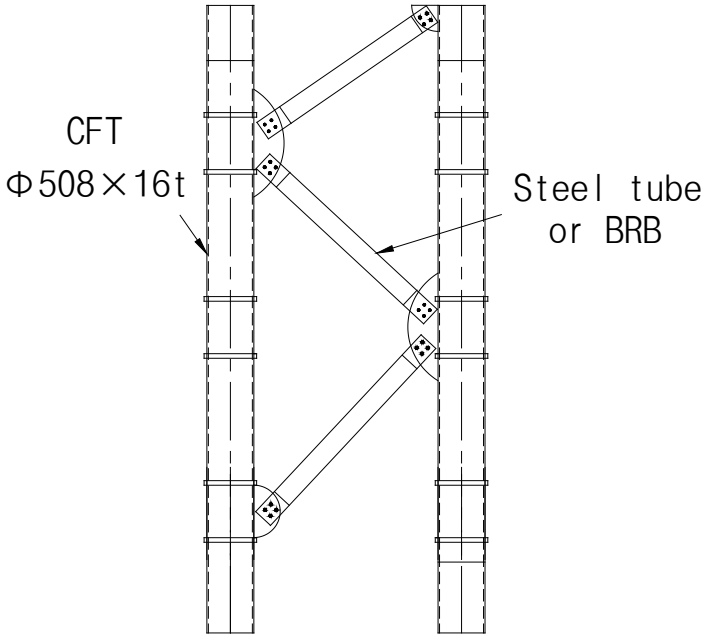
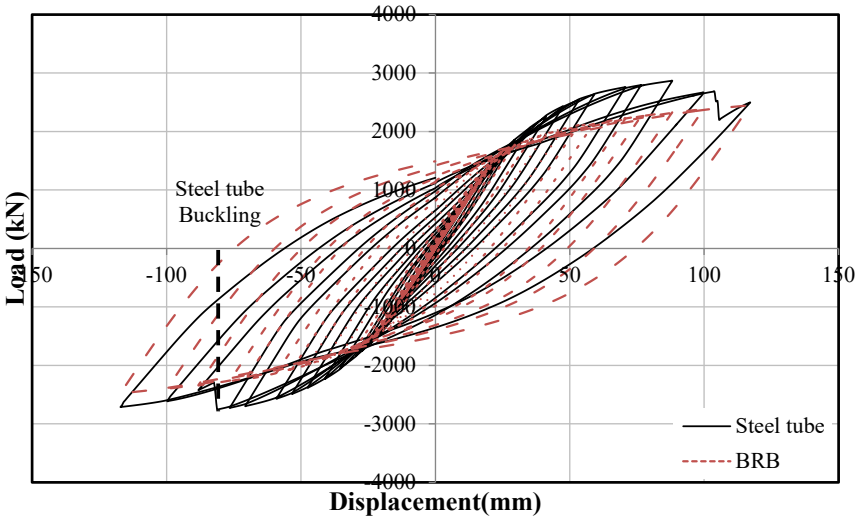


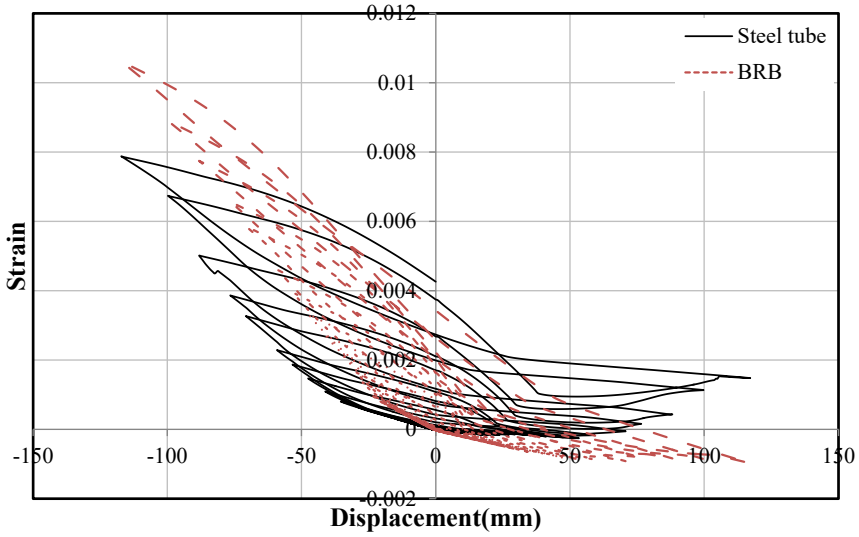
Fig. 7 The revised analysis model

The buckling behavior of steel tube braces was simulated using strength deterioration constitutive model (Yongtao BAI et al. 2012). According to the model, the buckling strain of steel tube (Φ216.3x4t) is ε_{lb} = 0.022 and CFT (Φ508x16t) is 0.021, respectively. Figure 8(a) shows comparison of load-displacement curves according to the brace types. At the drift

ratio of 1.4%, buckling of steel tube brace was occurred. The steel tube reached buckling strain. As shown in Figure 8(b), both analysis models could not show the buckling strain of CFT column because section of CFT was class 1, therefore, two models were judged to have fully operational performance level.



(a)



(b)

Fig. 8 Analysis result of (a) Load-displacement curve and (b) strain development of CFT at plastic hinge

For the further research, it is necessary to simulate different size of BRB and CFT columns up to higher drift ratio for application of performance based design because the analysis

model above showed the behavior up to 2.1 due to convergence problem. Also, it is expected that delayed operational performance level of CFT columns will be occurred in higher drift ratio according to the BRB section.

5. Conclusion

1) In the previous research, a multiple CFT bridge pier was tested under cyclic loading, and evaluated according to two brace types; steel tube and BRB
2) An analysis model was built in a previous research for the multiple bridge pier, and verification work have been done.
3) The performance based evaluation for the multiple CFT bridge pier was conducted using the analysis model based on performance level definition.
4) The analysis showed fully operational performance level of the multiple CFT bridge pier when BRB and steel tube braces were used.
5) For the performance based design of the multiple bridge pier, it is required to conduct up to higher drift ratio and to confirm strain level of CFT column whether it reaches buckling strain

6. References

AISC (2010). Seismic provisions for structural steel buildings, (ANSI/AISC 341-10), *American Institute of Steel Construction*, Chicago, IL.

Bazaez R, Dusicka P. (2015). Design implementation of buckling restrained braces for seismic retrofitting of reinforced concrete multi-column bridge bents. In: Structures congress. Portland, OR.

C. H. Jeon, D. W. Kim, and C. S. Shim (2015). Cyclic behavior of multiple modular bridge piers in terms of diagonal load analyzed by OpenSEES, *Proceedings of 11th International Conference on Advances in Steel and Concrete Composite Structures* (pp.775-781), Tsinghua University, Beijing, China.

Dongwook Kim, Chiho Jeon, and Changsu Shim (2016a), Cyclic and static behaviors of CFT modular bridge pier with enhanced bracings, *Steel and Composite Structures*, 20(6), 1221-1236, DOI: 10.12989/scs.2016.20.6.1221

Dongwook Kim, Chiho Jeon, and Changsu Shim (2016b), Analytical evaluation of a modular CFT bridge pier according to directivity, *Steel and Composite Structures*, 20(6), 1193-1203, DIO: 10.12989/scs.2016.20.6.1193

Kersting RA, Fahnestock LA, López WA. Seismic Design of Steel Buckling-Restrained Braced Frames. NIST GCR 15–917-342015.

Motoo SAISHO, Masahiro KATO, and Shuyun GAO (2004). LOCAL BUCKLING OF CFT-COLUMN UNDER SEISMIC LOAD, *Proceedings of 11th World Conference on Earthquake Engineering* (pp. 2614), B.C., Canada

S. El-Bahey, M. Bruneau. (2011) Buckling restrained braces as structural fuses for the seismic retrofit of reinforced concrete bridge bents. *Engineering Structures*, 33, 1052–1061

W. Xiaone, M. Bruneau. (2016) Case Study on Applications of Structural Fuses in Bridge Bents. *Journal of Bridge Engineering*, 21(7),

Yongtao BAI, Akihiko KAWANO, Keita ODAWARA, and Shintaro MATSUO (2012), CONSTITUTIVE MODELS FOR HOLLOW STEEL TUBES AND CONCRETE FILLED STEEL TUBES CONSIDERING THE STRENGTH DETERIIORATION, *J. Struct. Constr. Eng AIJ.*, 77(677), 1141-1150

Yuandong Wang, Luis Ibarra, Chris Pantelides. (2016). Seismic Retrofit of a Three-Span RC Bridge with Buckling-Restrained Braces. Journal of Bridge Engineering, 21(11).

Seismic Performance of an Innovative Composite Column with Replaceable Steel Slit Dampers: FEM Analysis and Design Method

Yang Liu (corresponding author)
Associated Professor of Structural Engineering, College of Civil Engineering, Huaqiao University
Xiamen, China
E-mail: lyliuyang@hqu.edu.cn

Yifan Liao
Postgraduate of Structural Engineering, College of Civil Engineering, Huaqiao University
Xiamen, China
E-mail: 1511304021@hqu.edu.cn

Zixiong Guo
Professor of Structural Engineering, College of Civil Engineering, Huaqiao University
Xiamen, China
E-mail: guozxcy@hqu.edu.cn

Yingting Lu
Ph.D. Candidate of Structural Engineering, College of Civil Engineering, Huaqiao University
Xiamen, China
E-mail: 1300204040@hqu.edu.cn

Xiaojuan Liu
Lecturer of Structural Engineering, College of Civil Engineering, Huaqiao University
Xiamen, China
E-mail: liuxjty@hqu.edu.cn

Bahram M. Shahrooz
[a] Professor of Structural Engineering, Dept. of Civil and Architectural Engineering
Construction Management, Univ. of Cincinnati, Cincinnati, U.S.
[b] Distinguished Professor, College of Civil Engineering, Huaqiao University
Xiamen, China
E-mail: shahrobm@ucmail.uc.edu

Abstract

Over the last few decades, industrialization of building construction and rapid restoration of functionality of structures after earthquakes have emerged as important issues facing the structural engineering profession. An innovative composite column with replaceable steel slit

dampers has been developed for prefabricated reinforced concrete (RC) frame structures and reinforced concrete-steel (RCS) hybrid frame structures. This new composite column, which can be prefabricated, consists of several steel slit dampers, connection plates, and high strength bolts. The column was designed based on “strong column-weak damper” philosophy. The influences of different parameters, such as axial compression ratio, height/depth ratio, and replaceable details, on the cyclic behavior of this new structural system were studied using FEM method. The results suggested very good cyclic behavior. Plastic deformation was found to be concentrated only in the steel slit dampers under large drift angles, while the other major components stayed nearly elastic. Hence, the columns could easily be repaired. Based on the numerical simulations, the seismic behavior of this new composite column was further investigated, and a method for computing its flexural capacity was proposed.

INTRODUCTION

The post-earthquake repair cost of a building and the interruption in the use of the building cause major economic losses. In order to minimize economic losses, more attention has been paid to rapid post-earthquake repair techniques, e.g., by concentrating all the inelastic deformations in replaceable components while keeping the other components in the elastic range. After earthquakes, damaged components can be replaced with an equivalent one in order to restore the building function. At present, a variety of replaceable components, such as replaceable coupling beams and replaceable beam ends, have been developed. An innovative “fuse” steel coupling beam developed at the University of Cincinnati [Fortney, et al. 2007] allows post-damage repair/replacement and minimizes the repairing expense. A bolted end-plate connection was recommended to permit post-damage repair without costly repair of the wall pier-coupling beam connections. The viability of this system was demonstrated experimentally, and was subsequently validated through additional tests [Farsi, et al. 2016]. An integrated analytical and large-scale experimental study was conducted at the University of Toronto to extend and validate the concept of replaceable links in steel braced frames [Shen, et al. 2011]. It was found that end-plate links exhibited greater energy dissipation capacity than bolted web links, although latter achieved significantly higher rotational capacity. Steel slit dampers were regarded as effective “fuse” elements. Research showed that steel slit dampers had a good energy dissipation capacity, and its mechanical properties could be predicted well [Saffari, et al. 2013. Climent, et al. 1998]. Recently, steel slit dampers have also been used in beam-column connections. A steel slit damper system was developed to prevent formation of damage in conventional columns and beams by dissipating lateral loads at the beam-column connections [Köken and Köroğlu 2015]. Experimental and analytical results showed that plastic deformations were concentrated in the damper, and damage to the beam and column was prevented.

During a high intensity earthquake, columns are expected to sustain significant damage at their base. Due to gravity axial force, post-earthquake repair of the column base is very difficult, costly, and could be impractical. A post-tensioned (PT) column base connection was designed

to eliminate structural damage due to seismic loads at column bases in self-centering moment resisting frames (SC-MRFs) [Chi and Liu 2012]. The softening behavior at the connection was provided by gap opening and elongation of PT bars rather than yielding in the column. Both experimental and analytical studies were carried out to investigate the cyclic response of PT column base connections.

Because of its low yield point, good energy dissipation, and stable performance, mild steel has been used in the development of effective replaceable components. In line with these research trends, an innovative composite column base with replaceable steel slit dampers was proposed and evaluated by the authors.

OVERVIEW OF THE REPLACEABLE COMPOSITE COLUMN BASE

A schematic configuration of the innovative composite column base is shown in Figure 1. On each side of the column base, two fuses made of mild steel plate with slits are placed between the rocking column base and a fixed T-shape steel plate (or a T stub) by connecting plate I and connecting plate II, respectively. Over a certain height from the base, the steel tube column is filled with concrete to prevent local buckling. In conventional construction, the column base is rigidly connected to the foundation. Therefore, the earthquake energy is dissipated mainly through plastic deformations near the column base. By contrast, the new composite column base is designed as a rocking element in which the flexural capacity is provided by steel slit dampers, designed according to the “strong column-weak damper” philosophy. Steel slit dampers introduced at locations are expected to experience inelastic deformations. The other components are then designed to remain elastic under the force corresponding to yielding of the damper. Because the inelastic deformation is concentrated within the damper, damaged links can be quickly inspected and replaced following a major earthquake.

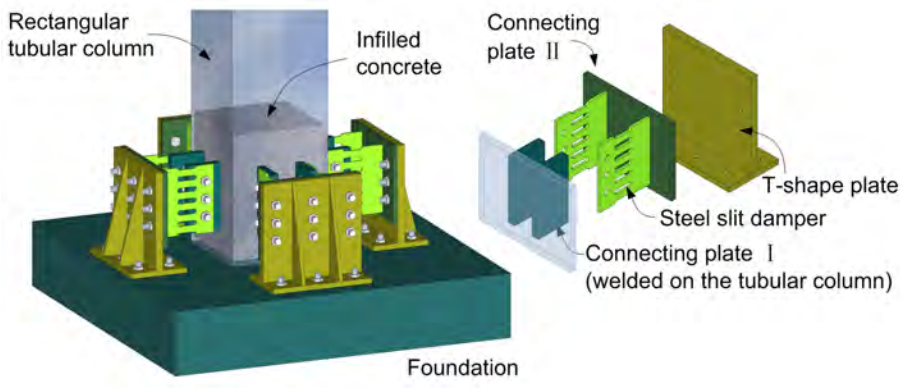


Fig. 1 - Construction details of the proposed composite column

In an effort to evaluate the behavior of the proposed replaceable composite column base, numerical analyses were conducted by using the finite element analysis program ABAQUS(Hibbit, K. 2014). The objectives of these analyses were to investigate (1) the

damage distribution, (2) the hysteretic behavior, and (c) the lateral loading capacity of the replaceable column base.

FE MODELS

The cross section of the column was a 400 mm square tubular with a wall thickness of 10 mm. The following parameters were considered in the analyses: (1) installation location of steel slit dampers: only parallel to the loading plane (represented with “S”), or both parallel and perpendicular to the loading plane (represented with “D”); (2) thickness of steel slit dampers (t = 15, 20, 30 mm); (3) column height-to-depth ratio (λ = 3, 5.5); and (4) ratio of the applied axial compressive load to design axial load capacity (n = 0.15, 0.4). For example, S20-3-0.15 represents a specimen with dampers installed only parallel to the loading plane, steel slit damper thickness of 20 mm, height/depth = 3, and applied axial compressive load = 0.15 times the design axial load capacity. All the replaceable steel slit dampers had identical dimensions and details (shown in Figure 2) but had different thicknesses (15, 20, 30 mm).

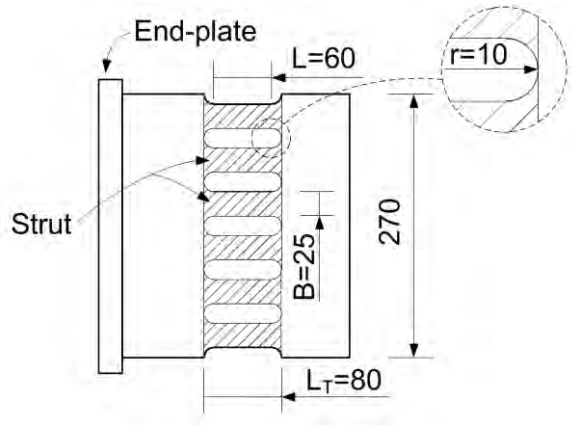


Fig. 2 - Dimension details of the replaceable link

The finite element model of the composite column was shown in Figure 3. Steel slit dampers were modeled using 20-node quadratic brick, reduced integration elements (C3D20R). The stiffeners welded to the T-shape plate were modeled with 10-node modified quadratic tetrahedron elements (C3D10M). The other components (the steel tube column, the infilled concrete, connecting plates, T-shape plate and the foundation) were modeled by 8-node linear brick, reduced integration, hourglass controlled elements (C3D8R).

Tie constraints simulating complete bond were applied to the interface between different components, ignoring the relative slip between two interfacial surfaces. The interaction between the bottom face of the steel tube column and the top surface of the reinforced concrete foundation was modeled with a “hard” contact, using a friction coefficient of 0.6 [Rabbat and Russell 1985]. The bottom face of the foundation was fixed. A constant axial compressive load and cyclic lateral displacement with increasing amplitudes were applied at the top of the column.

One cycle was performed at the following drift amplitudes: 1/500, 1/250, 1/150, 1/100, 1/75, 1/50, 1/25, and 1/20.

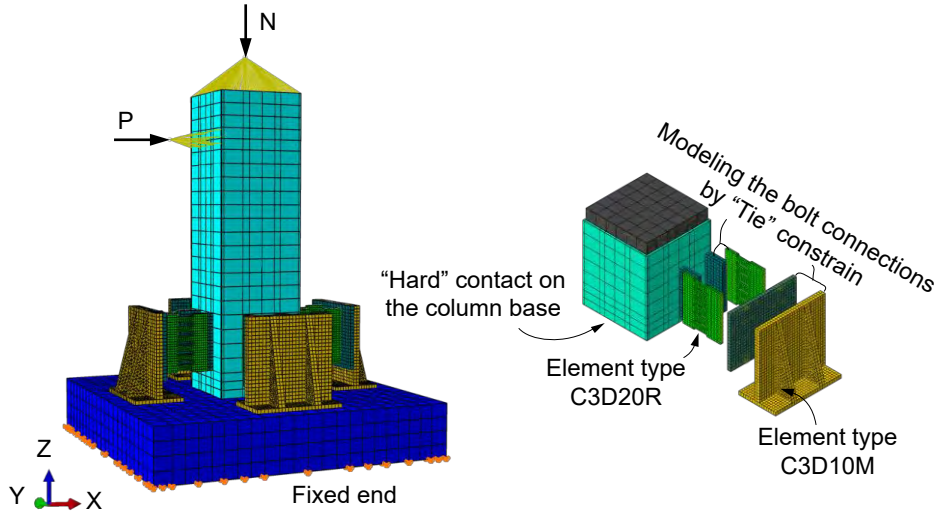
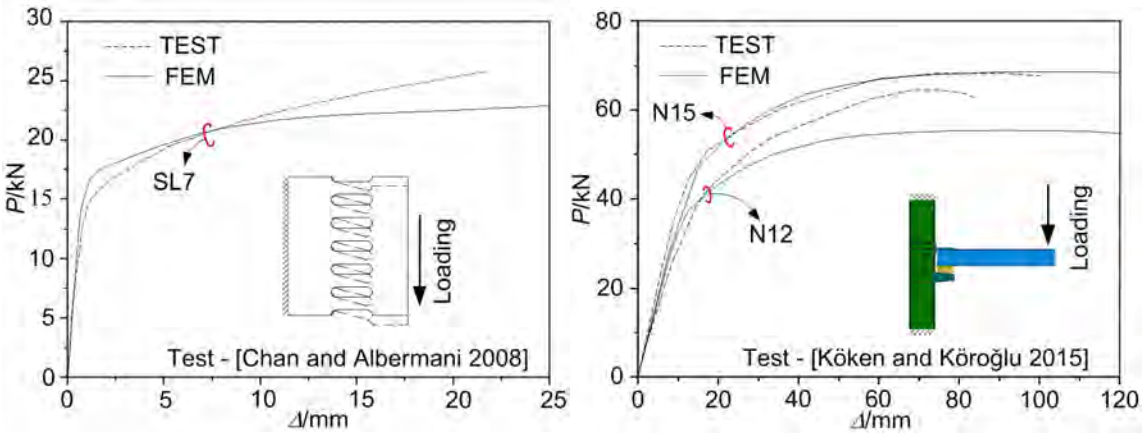


Fig. 3 - Finite element model

A concrete damage plasticity model with compressive constitutive relationship [Kent and Park 1971] was adopted for infilled concrete. Linear tensile stress-strain relationship was assumed for concrete [Nguyen and Kim 2009]. After reaching the peak tensile strength, concrete tensile stress declined linearly to 0 at the ultimate tensile strain 0.005. The compressive strength and peak tensile strength were taken as 26.8 MPa and 2.39 MPa, respectively. A value of 32,500 MPa was used as the concrete modulus of elasticity. The steel was assumed to exhibit elastic-perfectly plastic behavior. The elastic modulus of the steel was taken as 200000 MPa. The yield strengths of the steel slit damper and other steel components were 235 MPa and 345 MPa, respectively. The foundation was assumed to remain elastic with an elastic modulus of 32500 MPa.

VERIFICATION OF NUMERICAL MODEL

The results from a number of relevant past experimental studies were utilized to verify the aforementioned FE modeling technique. The studies examined steel slit dampers similar to that used in the reported research. One research program (Chan and Albermani, 2008) focused on the dampers only, and another study (Köken and Köroğlu, 2015) evaluated beam-column connections with dampers attached to the beam. The test results and numerical results were compared in Figure 4. Figure 4 (a) showed some differences between the calculated and measured curves. As seen from Figure 4 (b), the numerical result of specimen N15 agrees well with the experimental result, while the numerical curve of specimen N12, which had a thinner damper than specimen N15, shows a larger initial stiffness and a smaller maximum strength than the experimental result. Overall, the numerical simulations can reasonably replicate the test results.



(a) Steel slit damper (b) Beam-to-column connection

Fig. 4 - Comparison between test and numerical results

SIMULATION OF COMPOSITE COLUMNS: RESULTS AND DISCUSSION

The plastic strain contour of a typical specimen S15-3-0.15 at 1/20 drift ratio was shown in Figure 5. The plastic deformation was concentrated in the slit dampers while the other components remained nearly elastic.

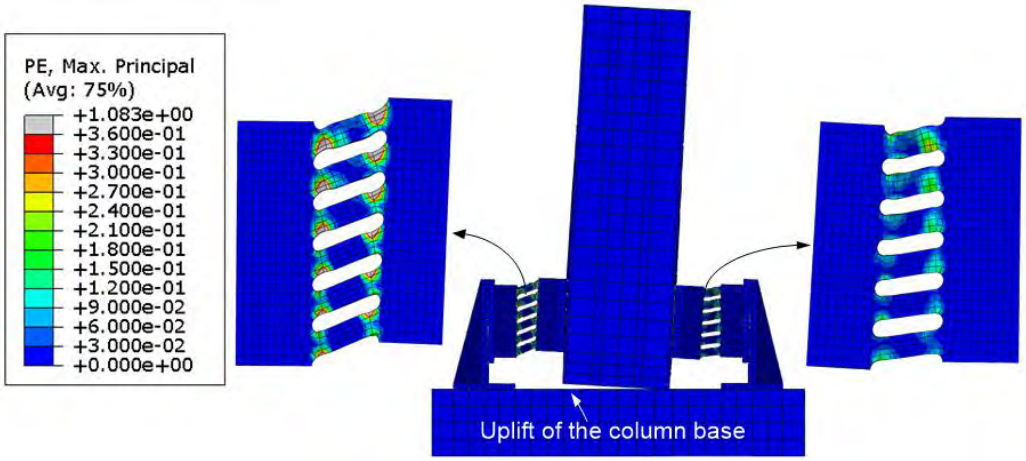


Fig. 5 - Plastic strain contour

Hysteretic curves and yield points of the replaceable composite columns were provided in Figure 6, which showed a similar trend for all the cases. The composite column base was characterized by gap opening and closing at the column-foundation interface. In the initial stage, the specimen remained elastic with a linear relationship between the horizontal load and horizontal displacement. When the moment capacity of the steel slit dampers and the counteracting moment from the applied axial load (which had an eccentricity with respect to the point at which the column rotated when it was uplifted) were exceeded, the column base decompressed and gap opening began to occur. Subsequently, struts in the slit dampers (see

Figure 2) began to yield. As the displacement was increased, more struts yielded before developing the maximum strength. In spite of significant pinching, the hysteretic loop was stable. Additional dampers (the “D” series) installed perpendicular to the loading plane improved the performance of the composite column but did not significantly affect the shape of hysteresis loop; appreciable pinching still occurred.

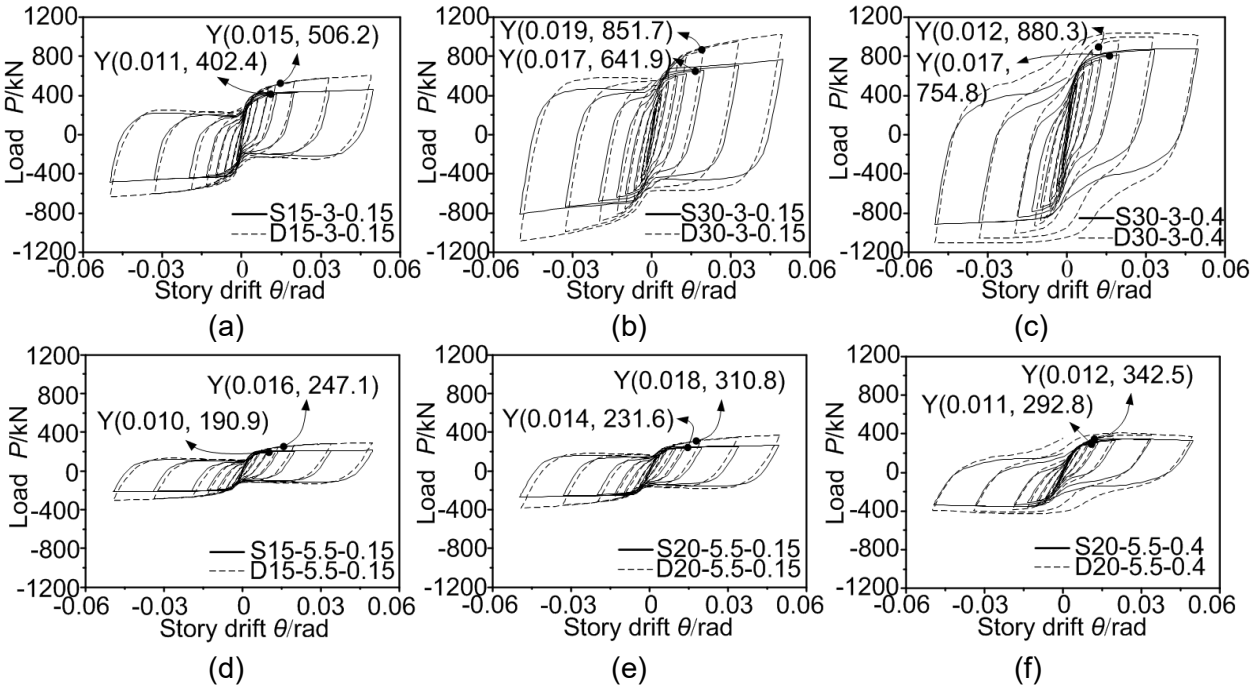


Fig. 6 - Hysteresis curves

The maximum strength versus damper thickness was plotted in Figure 7. Obviously, the maximum strength almost linearly increased as the damper thickness increased. It should be noted that the thickness needs to be limited to ensure the replaceable dampers are the energy dissipation mechanism. Larger axial compressive load suppressed the level of column uplift, which enhanced the lateral strength of the composite column. For specimens with identical column height/depth, the axial compressive load ratio had little influence on the slope of curves. As shown later (Eq. 6) the damper thickness and level of axial compressive load independently contributed towards the strength. As the aspect ratio increased, the lateral strength decreased significantly.

Skeleton curves were shown in Figure 8. Before gap opening, the horizontal displacement was mainly composed of the elastic deformation of the column. Therefore, the initial stiffness did not noticeably change as the damper thickness and axial compressive load were increased, but decreased as the column height/depth ratio became lager.

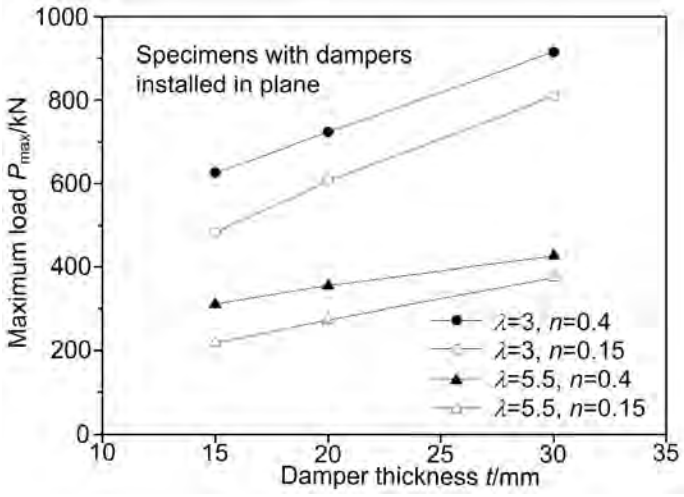


Fig. 7 - Maximum strength versus damper thickness relationship

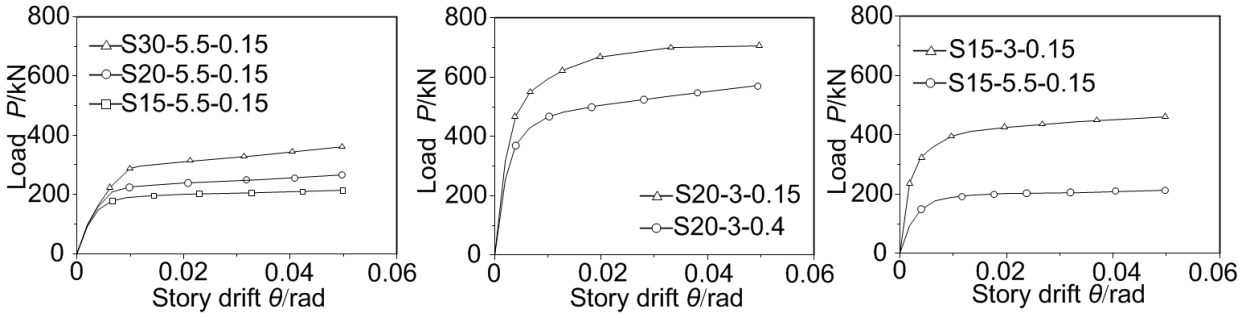


Fig. 8 - Skeleton curves

Steel slit dampers installed in the column base were subjected to combined cyclic tension and shear force, which is more severe than conventional steel plate dampers under pure shear. Numerical simulation of these two different loading conditions were conducted to a series of FEM analyses. The results indicated that the ultimate load carrying capacity was not influenced by the differences in the loading. However, Figure 9 clearly indicated that strength degradation of slit dampers in specimen S15-3-0.15 (solid line) was appreciably more severe than a comparable damper subjected to pure shear only (dashed line).

The shear yielding strength of steel slit dampers in the composite column base was computed based on Eqs. (1) and (2) [Oh, Kim, Ryu 2009]. The first term in Eq. (1) implies yielding is governed by flexure, whereas the second term is based on yielding in shear.

$$F_{q,s} = \min\left\{ k\frac{\sigma_y t B^2}{2L'}, k\frac{2\sigma_y t B}{3\sqrt{3}} \right\} \quad (1)$$

$$L' = L + 2r^2 / L_T \quad (2)$$

Where k is the number of struts; t is thickness of damper; σ_y is yield stress of steel; B is width of struts; L' is the equivalent height indicated by Eq. (2).

As evident from Figure 9, the capacity computed from Eqs. (1) and (2) is a reasonable conservative estimate of the values obtained from the FEM analysis. The FEM capacity is at most 1.24 times larger than the predicted capacity from Eqs. (1) and (2).

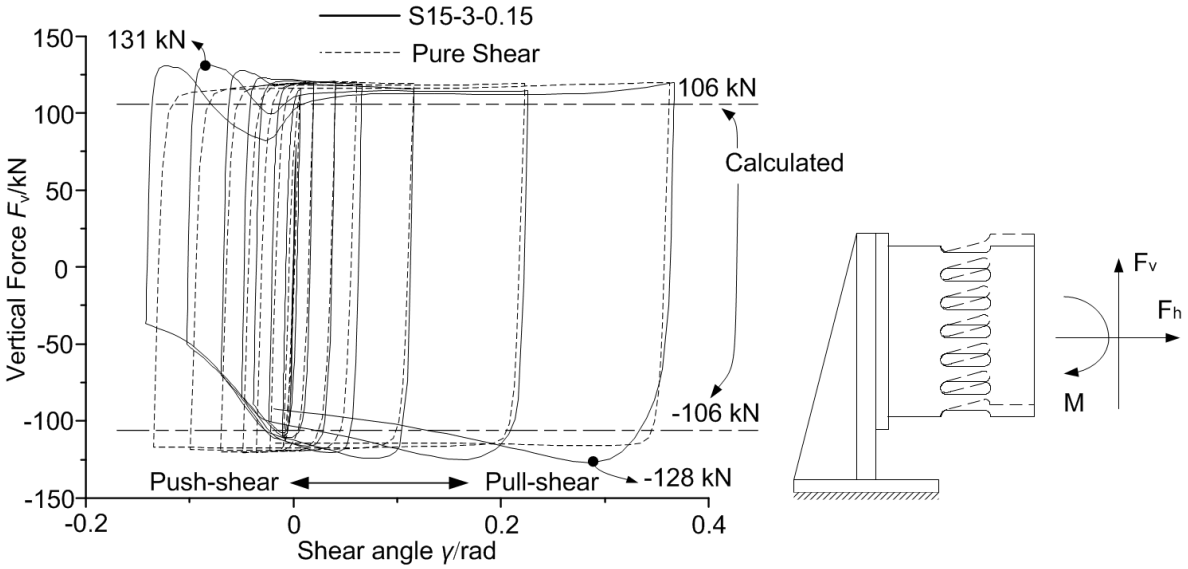


Fig. 9 - Vertical force versus shear angle relationship

DESIGN METHOD

With reference to Figure 10, a design methodology was developed. The nominal yield flexural strength M_y of specimen can be calculated based on Eq. (3).

$$M_{\mathrm{y}} = M_{\mathrm{d,\,v}} + M_{\mathrm{d,\,h}} \tag{3}$$

Where

$M_{\mathrm{d,v}}$ is the flexural strength provided by vertical shear forces of the steel slit dampers.

$M_{\mathrm{d,h}}$ is the flexural strength provided by horizontal tension and compression force of the struts of the dampers due to the rotational deformation of the column foot.

$M_{\mathrm{d,v}}$ is calculated from Eq. (4).

$$M_{\mathrm{d,\,v}} = \sum F_{\mathrm{q,\,s}} x_i \tag{4}$$

Where

x_i is the horizontal distance from the centroid of struts of the damper to the rotation point indicated in Figure 10.

$M_{\mathrm{d,h}}$ can be calculated based on Eq. (5).

$$M_{\mathrm{d,\,h}} = \sum_{j=1,2} \int n\sigma_{\mathrm{h},\,j} t y dy \tag{5}$$

Where

n is the number of dampers at one side of column. $\sigma_{h,j}$ is the normal stress of the steel slit dampers. The subscript j of $\sigma_{h,j}$ indicates each side of the column has a set of steel slit dampers. The integral variable y and the coordinate system were both shown in Figure 10. Determination of $\sigma_{h,j}$ needs to account for the elastic lateral stiffness of the T-shape plates, but it will complicate the calculation process. For design purposes, $M_{d,h}$ was ignored, leading to a conservative estimation of the flexural strength. Based on the rotational equilibrium of forces shown in Figure 10 with respect to the rotation point, we can figure out the design horizontal force of the composite column as follows:

$$P_{design} = \frac{N(h/2 - \Delta) + \sum F_{q,s} x_i}{H} \tag{6}$$

Where

Δ is the hypothetical horizontal yielding displacement which is approximately assumed to be $0.01H$, based on the results of FEM analyses.

H is the height of contra flexural point of the composite column.

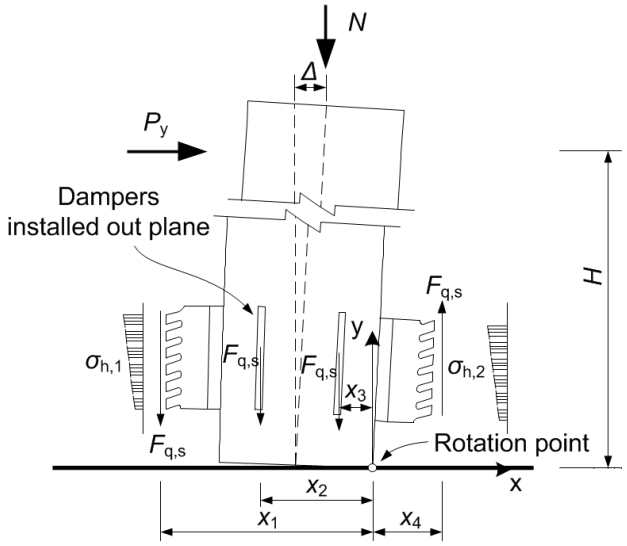


Fig. 10 – Design model

The horizontal yielding load calculated from Eq. (6) was compared against that from FEM analysis in Figure 11. The average value and coefficient of variation of P_{design}/P_{FEM} was 0.70 and 0.01, respectively. Therefore, Eq. (6) can conservative be used. Further studies are needed on the contribution of $M_{d,v}$.

CONCLUSIONS

This paper proposed an innovative composite column, which could be replaced in-situ after a major earthquake. The finite element model of the column was established, verified and used to

investigate the load transferring mechanism and seismic performance of the column. The following conclusions can be drawn based on this research:

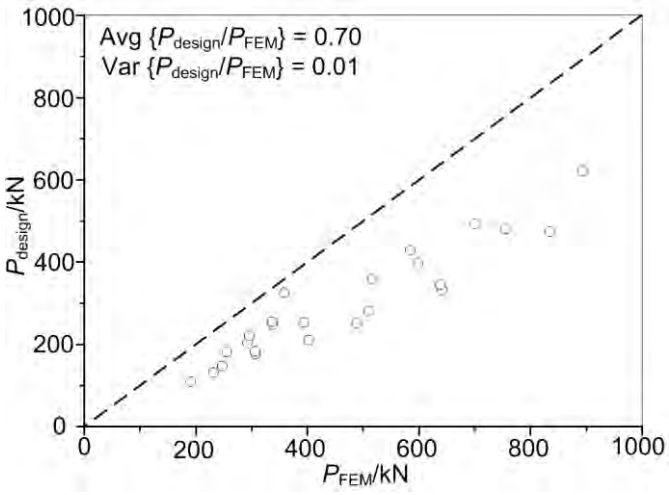


Fig. 11 - Comparison of calculate result with FEM

1) Designed based on “strong column-weak damper” philosophy, the innovative composite column showed stable hysteresis behavior.

2) Steel slit dampers were the main source of energy dissipation. Plastic deformation was found to be concentrated in the dampers; hence, the damaged components may easily be replaced after an earthquake.

3) The flexural strength of the composite column depends on the initial axial force and damper thickness. For the same height/depth ratio, the yield moment M_y increased as the initial axial force and damper thickness became larger.

4) A design method was developed to calculate the flexural strength of columns with replaceable steel slit dampers. Based on nonlinear FEM simulations, the method was found to produce a reasonable and conservative estimate of the strength.

ACKNOWLEDGMENTS

Ph.D. Candidate H. Chen from Huaqiao University gave a great help on the modification of the pictures in this paper. The author sincerely appreciates his help. The research was funded by the National Natural Science Foundation of China (Grant No. 51578254) and the National Natural Science Foundation of China (Grant No. 51378228), which is greatly acknowledged.

REFERENCE

Fortney, P. J., Shahrooz, B. M., Rassati, G. A. (2007). Large-scale testing of a replaceable “fuse” steel coupling beam. *Journal of Structural Engineering, 133*(12): 1801-1807.

Farsi, A., Keshavarzi, F., Pouladi, P., et al. (2016). Experimental study of a replaceable steel coupling beam with an end-plate connection. *Journal of Constructional Steel Research, 122*: 138-150.

Shen, Y., Christopoulos, C., Mansour, N., et al. (2011). Seismic design and performance of steel moment-resisting frames with nonlinear replaceable links. *Journal of Structural Engineering, 137*(10): 1107-1117.

Saffari, H., Hedayat, A. A., Nejad, M. P. (2013). Post-Northridge connections with slit dampers to enhance strength and ductility. *Journal of Constructional Steel Research, 80*(1): 138-152.

Climent, A. B., Oh, S. H., Akiyama, H. (1998). Ultimate energy absorption capacity of slit-type steel plates subjected to shear deformation. *Bull. math. statist, 28*: 115-126.

Köken, A., & Köroğlu, M. A. (2015). An experimental study on beam to column connections of steel frame structures with steel slit dampers. *Journal of Performance of Constructed Facilities, 29*.

Chi, H., & Liu, J. (2012). Seismic behavior of post-tensioned column base for steel self-centering moment resisting frame. *Journal of Constructional Steel Research, 78(*11): 117–130.

Hibbit, K. (2014). ABAQUS documentation, Version 6.14.

Guo, Z., Zhu, Q., Liu, Y., et al. (2012). Experimental study on seismic behavior of a new type of prefabricated RC column-steel beam frame connections. *Journal of Building Structures, 33*(7): 98-105. (in Chinese)

Liu, Y., Guo, Z., Dai, J., et al. (2013). Experimental study on seismic behavior of prefabricated RCS frame joints with different failure mechanisms. *China Civil Engineering Journal, 46*(3): 18-28. (in Chinese)

Rabbat, B. G., & Russell, H. G. (1985). Friction coefficient of steel on concrete or grout. *Journal of Structural Engineering, 111*(3): 505-515.

Kent, D. C., & Park, R. (1971). Flexural members with confined concrete. *Journal of the Structural Division, 97*: 1969-1990.

Nguyen, H. T., & Kim, S. E. (2009). Finite element modeling of push-out tests for large stud shear connectors. *Journal of Constructional Steel Research, 65*(10):1909-1920.

Chan, R. W. K., & Albermani, F. (2008). Experimental study of steel slit damper for passive energy dissipation. *Engineering Structures, 30*(4): 1058-1066.

Oh, S. H., Kim, Y. J., Ryu, H. S. (2009). Seismic performance of steel structures with steel dampers. *Engineer Structures, 31*(9): 1997-2008.

LIFE-CYCLE PERFORMANCE OF CONCRETE-FILLED STEEL TUBULAR COLUMN SUBJECTED TO CORROSION AND IMPACT

Lin-Hai Han
Department of Civil Engineering, Tsinghua University, Beijing, 100084 China
lhhan@tsinghua.edu.cn

Chuan-Chuan Hou
Department of Civil Engineering, Tsinghua University, Beijing, 100084 China
houcc@tsinghua.edu.cn

ABSTRACT

A finite element analysis (FEA) model was established to simulate the life-cycle performance of a concrete-filled steel tubular (CFST) column under the coupling effects of progressive and shock degradations. The imposed effects on the composite column covered a wide range of factors that may deteriorate its mechanical performance during the entire life-cycle, including construction issues (preload, residual stress, and imperfection), sustained load (axial load from upper structure), progressive degradation (chloride corrosion) and shock degradation (impact load). The numerical model was stage-by-stage verified with experimental results and showed good accuracy. It was then employed to analyze the performance of CFST column under the coupled degradations. Particularly, the effect of the coupled effects on the remaining capacity of the column was evaluated, which highlights the importance of the life-cycle design and assessment for the CFST columns.

INTRODUCTION

It is well known that life-cycle analysis (LCA) of structures, including design, performance assessment, management and maintenance, has been widely addressed in the past several decades (Biondini & Frangopol, 2016; Frangopol, 2011; Frangopol, Saydam, & Kim, 2012). One key aspect of the LCA is to assess the deterioration of structural capacity under various types of damage mechanisms, such as environmental aggressiveness, operating actions, and extreme hazards. These damage actions can be generally subdivided into two categories based on the relative length of their durations, namely progressive (continuous) degradation and shock (sudden extreme) degradation (Sanchez-Silva, Klutke, & Rosowsky, 2011).

The modeling of the structural degradation process is to provide the information of the time-variant remaining capacity of the structures. Lots of efforts have been devoted to the establishment of such models, some of which were reviewed in Frangopol, Saydam, & Kim (2012) and Sánchez-Silva & Klutke (2016). For instance, several researchers conducted LCA analysis of the seismic resilience of corroded RC structures. The effects of corrosion on the material properties of reinforcement and concrete were defined and the prediction of seismic resilience of corroded RC structures was carried out by some simplified single degree of freedom system (Akiyama, Frangopol, & Matsuzaki, 2011), beam element model with corrosion effect incorporated (Biondini, Camnasio, & Titi, 2015), or fiber-based model with OpenSees software package (Yuan, Guo, & Li, 2017).

In China, concrete-filled steel tubular (CFST) has been widely used as major structural components in large-scale structures in the past several decades, such as columns in high-rise buildings, subway stations, electricity pylons, and piers, arches and deck systems in bridges

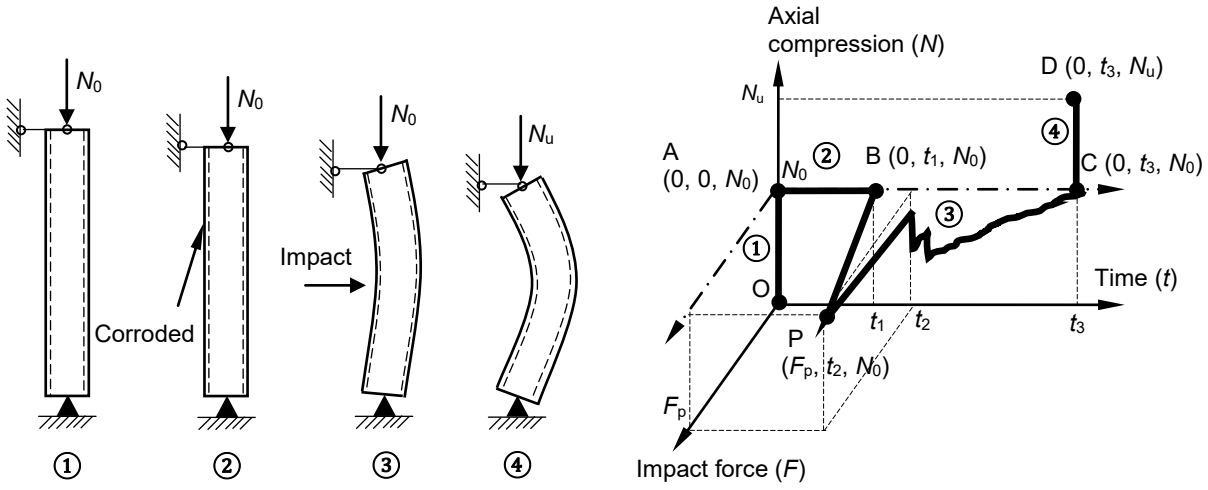
(Han, Li, & Bjorhovde, 2014c). Many of the constructions are located at relatively harsh environments with high level of humidity or chloride, such as the bridges across rivers and the Zhoushan electricity pylon near the East China Sea. These structures inevitably suffer from progressive degradation during their service life; on the other hand, the risk of extreme hazards like earthquake or impact from moving vehicles, vessels or floating ice cannot be ignored. The performance and design of CFST structures under these progressive and shock degradations have been separately addressed in the design codes as well as research works in the past (Han, Hou, & Wang, 2012; Hou, Han, & Zhao, 2013; Han, Hou, & Wang, 2014a; Hou, Han, Wang, & Hou, 2016; Bambach, Jama, Zhao, & Grzebieta, 2008; Deng, Tuan, & Xiao, 2012; Wang, Han, & Hou, 2013; Han, Hou, Zhao, & Rasmussen, 2014b). However, no significant attention has been paid to the life-cycle performance of CFST under the combination of such progressive and shock degradations.

This paper is thus an attempt to study the life-cycle performance of CFST subjected to progressive and shock degradations. A finite element analysis (FEA) model is established to simulate the structural behaviour with various types of actions incorporated. The FEA model was verified with experimental data and used to predict the capacity deterioration of the structure during its life-cycle. It was then employed to analyze the coupling effects of the progressive and shock degradations on the mechanical performance of the CFST structures, particularly the remaining capacity.

ESTABLISHMENT OF THE FEA MODEL

Example structure and loading path

A typical CFST column located in the corrosive environment is employed as the example structure for the life-cycle analysis, as shown in Figure 1(a), where N_0 and N_u standard for the axial sustained load and ultimate axial strength of the column. Due to the harsh environment, progressive corrosion occurs at the outside surface of the steel tube. At some time point during its life-cycle, the column might be impacted by a moving object, bringing permanent lateral deformation to the column. A detailed explanation of the loading path is presented below.



(a) Actions on the column (b) Loading path

Fig. 1 – A schematic view of the loading path for a CFST column

As illustrated in Figure 1(b), the lateral impact force (F), time (t) and axial compression (N) are used as (x, y, z) coordinates for the loading path. Figure 1(b) treats the corrosion procedure and impact procedure as time dependent parameters, while the short-term axial loading is seen as independent of time.

Stage① (O-A): the column is axially compressed to a certain level (N_0) to simulate the initial operation loading state;

Stage② (A-B): the column is then under sustained compression and corroded. During a period of t_1 (several years to decades), the outer steel tube of the column will be gradually corroded while the axial compression is kept constant;

Stage③ (B-P-C): the column is then impacted by a moving body, which can be described with an impact force curve. In Figure 1(b), the impact starts from point B and there is usually a peak point P in the curve. It then ends at point C and the impact duration is t_3-t_1, which is generally a very short period (of order 10^2 milliseconds);

Stage④ (C-D): it is assumed that the column does not collapse after the impact. To evaluate the residual strength of the column, it is axially compressed to failure in the final stage and the obtained axially compressive strength of the column is N_u.

Degradation condition assumptions

In the current analysis, only uniform corrosion of the steel tube is considered and it is assumed that uniform corrosion occurs over the full outside surface of the tube. Several models have been developed to predict the corrosion rate of steel (Biondini et al. 2016). In the current analysis, as uniform corrosion is assumed, the steel tube thickness loss Δt_s instead of the corrosion rate is directly used as the indicator of the corrosion severity. As a result, the corrosion rate and the time duration of the corrosion are not discussed in the analysis.

In real life collision incidents, the moving object that impacts the column generally undergoes plastic deformation and consumes part of the impact energy. For the simplification of the current analysis, the object is assumed to be a rigid mass body with a mass as m_0 and velocity as V_0.

General description

In the past studies, FEA models for CFST members under various types of static or dynamic loads have been developed. For example, Han et al. (2004) modeled the behavior of CFST columns under long-term sustained load; Wang et al. (2013) and Han et al. (2014b) modeled the behavior of CFST beams and columns under lateral impact; Han et al. (2014a) and Hou et al. (2013) developed FEA models for CFST stub columns and beams under sustained load and corrosion. In the above studies, the FEA models have been verified with experimental results and proven to be reasonable. The FEA model with the combined actions, as a result, can be established by assembling the above models with the different aforementioned actions considered. As long as the modeling in each loading stage is reliable, the FEA model is robust.

Material properties

The outer steel tube is modeled with a five-stage elastic-plastic model, as has been used by Han, Yao, & Tao (2007). During the impact process, the strain rate of the materials is relatively high and the strain rate effect of steel needs to be accounted. The Cowper-Symonds model (Abramowicz & Jones, 1984) is able to predict the dynamic yield strength of steel under dynamic loading. It has been proved to be suitable in the simulation of CFST under drop hammer impact by Wang et al. (2013) and Han et al. (2014b).

The core concrete is modeled with the uniaxial stress-strain model of core concrete presented in Han et al. (2007), which is able to consider the confinement effect of the outer steel tube on the core concrete. For circular CFST, the model is shown as follows:

$$y = \begin{cases} 2x - x^2 & x \le 1 \\ \dfrac{x}{\beta_0 (x-1)^2 + x} & x > 1 \end{cases} \tag{1}$$

where, $x=\varepsilon/\varepsilon_0$, $y=\sigma/\sigma_0$, $\sigma_0=f_c'$, $\varepsilon_0=\varepsilon_c+800\xi^{0.2}\times10^{-6}$, $\varepsilon_c=(1300+12.5f_c')\times10^{-6}$; f_c' is the cylinder strength of concrete (unit: MPa) and $\xi=(A_sf_y)/(A_cf_{ck})$ is the confinement factor; A_s and A_c are the sectional area of the circular steel tube and core concrete, respectively; f_y and f_{ck} are the yield strength of steel and characteristic strength of concrete, respectively. Coefficient β_0 can be calculated as:

$$\beta_0 = (2.36\times10^{-5})^{[0.25+(\xi-0.5)^2]}(f_c')^{0.5}\times0.5 \ge 0.12 \tag{2}$$

The long-term sustained load will influence the strain development of the core concrete due to shrinkage and creep, while the corrosion will change the confinement of steel tube on the core concrete. Both effects should be considered in the material model. The long-term effect of concrete is considered by modifying the strain development of the uniaxial stress-strain curve and the influence of corrosion is considered by using different confinement factors for concrete in the initial state and corroded state. More details can be found in Han et al. (2004). The tensile behavior of concrete is described with the model presented in Shen, Wang & Jiang (1993).

The strain rate effect of concrete should also be considered. After reviewing the various models for strain rate effects on concrete strength, Wang et al. (2003) and Han et al. (2014b) chose the model presented in Comite Euro-International du Beton (1993) for concrete under compression and the model developed by Malvar & Ross (1998) for concrete under tension, as follows:

$$f_{cd}'/f_c' = \begin{cases} (\dot{\varepsilon}_d/\dot{\varepsilon}_s)^{1.026\alpha} & \dot{\varepsilon}_d \le 30\mathrm{s}^{-1} \\ \gamma(\dot{\varepsilon}_d/\dot{\varepsilon}_s)^{1/3} & \dot{\varepsilon}_d > 30\mathrm{s}^{-1} \end{cases}, \qquad f_{td}/f_t = \begin{cases} (\dot{\varepsilon}_d/\dot{\varepsilon}_s)^{\delta} & \dot{\varepsilon}_d \le 1\mathrm{s}^{-1} \\ \beta(\dot{\varepsilon}_d/\dot{\varepsilon}_s)^{1/3} & \dot{\varepsilon}_d > 1\mathrm{s}^{-1} \end{cases} \tag{3}$$

where, f_c' is the static cylinder strength of concrete while f_{cd}' is the dynamic cylinder strength of concrete under strain rate $\dot{\varepsilon}_d$. $\dot{\varepsilon}_s$ is the strain rate of the static loading. The values for $\dot{\varepsilon}_s$, α and γ can be found in Comite Euro-International du Beton (1993); f_t and f_{td} are the tensile strength of concrete under static loading and dynamic loading with strain rate as $\dot{\varepsilon}_s$ and $\dot{\varepsilon}_d$, respectively. The values for $\dot{\varepsilon}_s$, β and δ can be found in Malvar & Ross (1998).

Pre-load and initial imperfections

One merit of CFST construction is that the steel tube could be first installed and used as formwork for the core concrete. So it is common that the steel tube bears pre-load from the upper structure before the concrete part gains strength and works together with the steel tube. The pre-load on the steel tube should be properly incorporated in the numerical model and can be achieved by applying pre-load on the steel tube and then establishing the contact and bond between the steel tube and core concrete (Li, Han, & Zhao, 2015).

Cold-forming and welding are common procedures for the fabrication of steel tubes. Residual stresses would be induced due to the weldment and cold-forming processes while the former might bring increase of yield strength to the corner area of the section. The distributions of residual stresses of the typical square and circular steel tubes can be defined with the models presented in Moen, Igusa, & Schafer (2008), Masubuchi (1980), and Gao, Usami, & Ge (1998).

Local geometrical imperfection of the steel tube is set to be the lowest buckling mode while bow imperfection with amplitude as L_0/1000 can be used to represent the global imperfection model (Gardner & Nethercot, 2004).

Modeling strategies

Different numerical algorithms should be used for different loading types. Implicit algorithms, such as the Newton method in Abaqus (Hibbitt, Karlsson & Sorensen Inc., 2005), are generally used for solving static problems. So for the simulation of the initial loading stage, corrosion stage, and the ultimate loading stage, the implicit algorithm is used, while for the simulation of impact process with large kinetic energy, short period and complex contact behavior, the explicit algorithm is a good choice.

As two different types of algorithms are used in the simulation and they are not compatible in the same model, the results need to be transferred between them. Abaqus provides the commands '*Restart' and '*Import' to transfer results between Standard and Explicit package in the analysis. Regarding the loading path in Figure 1(b), the initial loading stage and corrosion stage are simulated with Abaqus/Standard package. The analysis results are written to the restart file with '*Restart' command. Abaqus/Explicit package is then used to simulate the impact loading stage. The stress, strain and deformation information of the initial loading stage are imported into the current model with the command '*Import' prior to the dynamic simulation. When the impact analysis is over, the results are again written to a restart file, which is imported into the ultimate loading model to predict the residual axially compressive strength of the CFST column.

Contacts

The contact behavior between different geometrical parts in the FEA model should be well considered. For the interaction between the steel tube and the core concrete, hard contact is applied in the normal direction of the contact surfaces, which does not allow penetration through the contact surfaces. Coulomb friction model is used in the tangential direction and the friction coefficient is set to be 0.6. The bond strength between the steel tube and core concrete is considered with the model developed in Han et al. (2007).

Another contact is the collision between the column and impact body during the impact simulation. 'Hard contact' is applied in the normal direction of the contact surfaces and Coulomb friction model is used in the tangential direction. The friction coefficient is set to be 0. 'Surface to surface contact' algorithm is used in the implicit solution while 'general contact' algorithm is used in the explicit solution.

The corrosion of the outer steel tube is modeled with the '*Model change' command in the software. The corroded part of the steel tube is deactivated in the corrosion step with the 'Model change' command.

Elements and boundaries

8-node 3D solid elements with reduced integration are used to model both the outer steel tube and core concrete. The impact rigid body is modeled with 4-node 3D rigid element, as shown in Figure 2. Structural meshing technique is used to achieve uniformly distributed mesh style. Higher mesh density is used in the impact area of the column as there is very complex contact behavior and large deformation. Boundaries of the column are set to be simply supported.

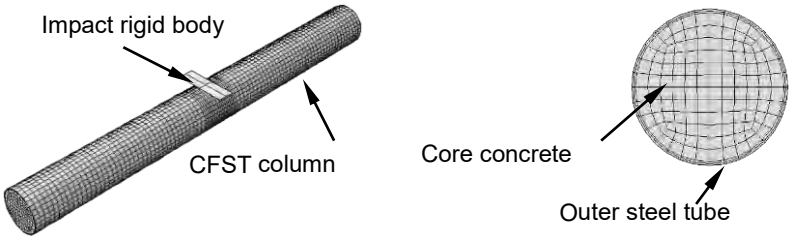
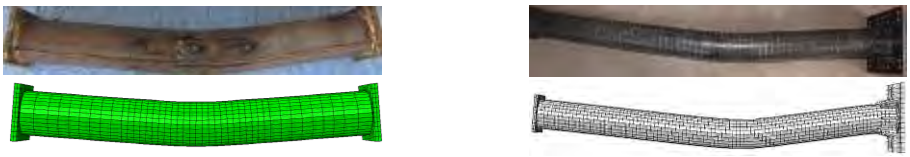


Fig. 2 – FEA model for impact simulation

VERIFICATION OF THE FEA MODEL

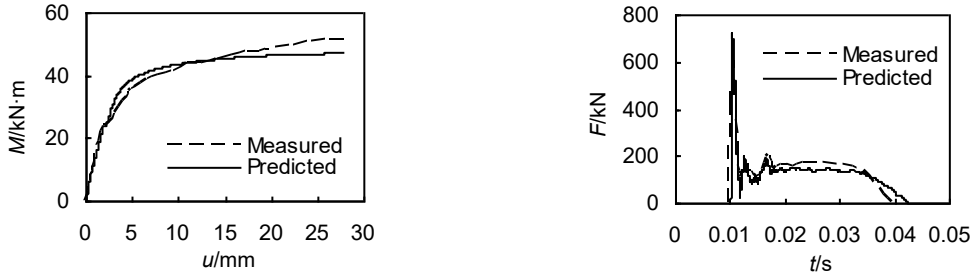
The FEA model should be verified against experimentally measured data to test its validity. Currently there are no experimental results with CFST columns that fully cover all the load stages in the aforementioned FEA model. Alternatively, test data for CFST columns under those separate loads or actions, such as long-term load, corrosion, and impact, are available. The verification of the FEA model, as a result, is carried out stage-by-stage with the available experimental results.

Hou et al. (2016) employed accelerated corrosion apparatus to carry out corrosion tests on circular CFST beams and recorded the failure modes and bending moment (*M*)-lateral deflection (*u*) curves for the specimens. Han et al. (2014b) carried out impact tests on CFST beams with drop hammer apparatus and obtained failure modes and impact force (*F*) history of the specimens. The experimental results in the aforementioned tests were used to stage-by-stage verify the accuracy of the FEA model and representative comparisons of the measured and predicted failure modes and force curves were presented in Figures 3 and 4, respectively.



(a) CFST beam under corrosion (b) CFST beam under impact

Fig. 3 – Comparison between the observed and predicted failure modes



(a) Bending moment (*M*) versus lateral displacement (*u*) (b) Impact force (*F*) curve

Fig. 4 – Comparison between experimental and numerical results

It shows that the FEA model is capable of accurately predicting the failure modes and force curves of the tested specimens. Evaluation of some other parameters, such as the ultimate strength of the corroded beams and the permanent deflection of the impacted beams also show good agreement between measurements and predictions. It shows that the established FEA model is sufficiently accurate for the prediction of the behaviour of CFST under the separate actions and can be reasonably assumed to be capable of predicting the effects of the coupled actions on CFST structures.

DESIGN OF NUMERICAL EXAMPLES AND ANALYSIS CASES

The established FEA model is used to do full-range analysis of circular CFST column under sustained load, corrosion and impact. First, numerical examples are designed to be used as representative cases for the analysis.

Basic parameters of the example

A CFST column example is used to shown the analytical procedure. The basic parameters of the FEA model for the example are set as follow: $D_0 \times t_s \times L_0 = 400 \times 9.3 \times 4000$ mm, where D_0 and t_s are the sectional diameter and thickness of the steel tube, and L_0 is the length of the column; the yield strength of steel (f_y) is set to be 345 MPa and the cubic strength of concrete is set as 60 MPa. Elastic modulus of steel (E_s) and concrete (E_c) are set as 201 GPa and 36.5 GPa, respectively.

The sustained axial compression N_0 is determined through the parameter axial loading ratio (n), which is defined as:

$$n = \frac{N_0}{N_{u0}} \tag{4}$$

where N_0 is the sustained axial compression, as shown in Figure 1(a) and N_{u0} is the ultimate axially compressive strength of the column under short-term static loading. The axial loading ratio depends on the design load level in the engineering structures. In the analysis, n is set as 0.4. For the simplification of analysis, it is assumed that the sustained load is applied on the whole CFST section, so the pre-load effect of steel tube needs not to be considered in the current example.

Han et al. (2004) showed that the long-term deformation of CFST will stabilize after about 100 days. As a result, the corrosion duration (t_1) is set to be 120 days. To better observe the influence of corrosion, a relatively large corrosion depth (Δt_s) as $0.25t_s$ is used in the simulations.

The impact energy is another important parameter to be designed. As has been studied in Wang et al. (2013) and Han et al. (2014b), impact will bring lateral deflection to the column, the value of which will increase with increasing impact energy. It is reasonable to conclude that the column will collapse due to the impact if the impact energy is large enough and there should be a critical impact energy for the axially compressed column, beyond which the column will be damaged under the impact. The calculation of the critical impact energy can be a future topic for the analysis. In the current research scope it is intended to analyze the influence of corrosion and impact on the full-range behavior as well as residual axially compressive strength of the CFST column. It is assumed that the composite column doesn't fail during the impact stage.

As a result, several trial-and-error calculations were taken out to find an impact energy which is under the critical energy for the current column. Finally, the mass of the impact rigid body (m_0) is

set as 1000kg and the initial velocity is set as 10m/s^2, resulting in an impact energy of 50kJ. The impact location is set at the mid-span of the column. It was found that the column still stands after the corrosion and impact stages.

Simulation cases

The above parameters are used in the modeling of the CFST column. To analyze the effect of different actions on the structure behaviour, several different simulation cases are considered, each with a different loading path:

Case 1: no sustained load, corrosion or impact load are considered. The column is statically loaded to failure;

Case 2: the effect of sustained load and impact are considered. The column is first loaded to N_0, and then impacted at mid-span;

Case 3: the effect of sustained load and corrosion are considered. The column is first loaded to N0, and then is corroded;

Case 4: the coupling effect of sustained load, corrosion and impact are considered. The column is first loaded to N_0, and then is corroded. After the corrosion stage, the column is impacted by the rigid body at mid-span.

Failure modes

The failure mode of the CFST column in Case 4 is analyzed. The deformed CFST column in each loading stage is presented in Figure 5, in which S33 stands for the longitudinal stress in the steel tube (in Pa). The corresponding loading stages can be found in Figure 1.

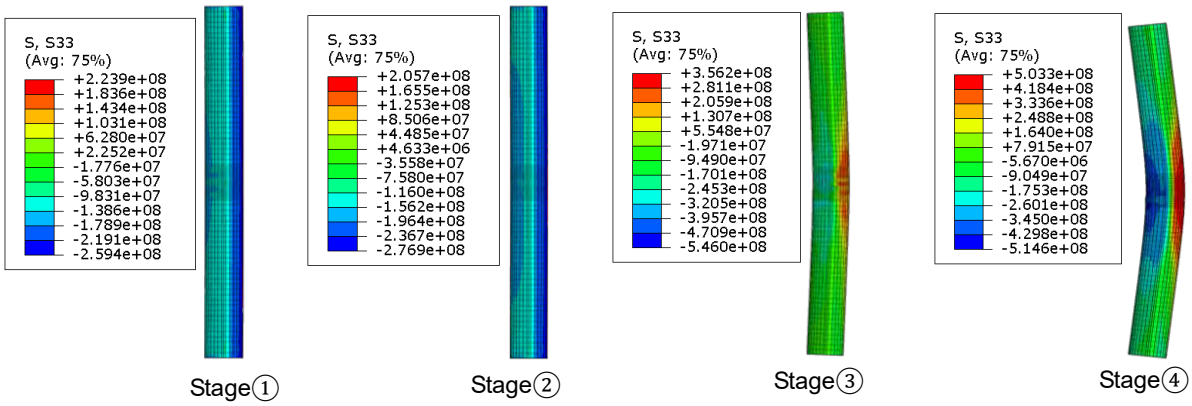


Fig. 5 – Deformed CFST at the end of each loading stage

It shows that the steel tube is under tension and compression in the initial loading stage①, which is due to the existence of tensile residual stress in the steel section. The compressive longitudinal stress then has a 10%-20% increment while the tensile stress has a decrease of the similar degree in the corrosion stage②. The reason is that 25% of the tube thickness is corroded and the load carried by the corroded part was gradually transferred to the remaining section, resulting in higher longitudinal stress.

The column is then impacted at mid-span from the left direction in stage③. It can be seen that there is obvious lateral deflection (u_0) in the column and the stress level is much higher at this stage, especially around the impact area. Another effect of impact is that very clear bending

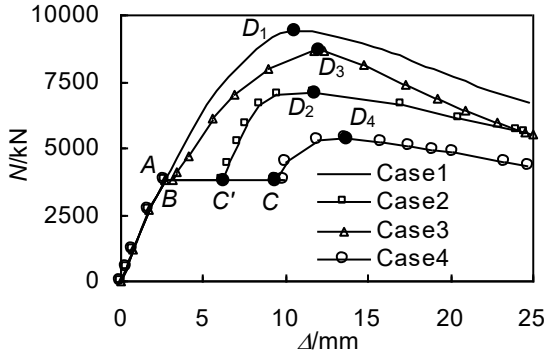
appears around the mid-span area. The left side of the section is under compression while the right side is under tension.

The bending moment obviously comes from the second order effect of the axial compression: as there is relatively large lateral deflection in the column, the axial compression will bring an extra bending moment at the mid-span of the column, which can be estimated as $M_0=N_0\times u_0$, where u_0 is the lateral deflection of the column brought by impact. This is the coupling effect between the axial compression and the lateral impact. The coupling of axial compression and bending brings much higher axial stress level in the column, as can be seen in the figure. It can be expected that if the axial compression or the impact energy is large enough so the moment brought by the second order effect (M_0) is high enough, the column might be damaged at this stage of loading. This second order effect will be further presented in the next section.

The column is axially loaded to failure in stage④ of the modeling. It shows that the lateral deflection of the beam kept increasing as it was axially compressed. The column is under compression and bending in the final state and the failure mode is global buckling.

Axial compression (N) versus displacement (Δ) curves

The axial compression (N) versus displacement (Δ) curves of the four simulation cases are illustrated in Figure 6. Note that the fluctuation of the axial compression in the impact stage due to the vibration of the column has been eliminated in the curves for clearer presentation of the results. The curves are calculated and analyzed stage-by-stage.



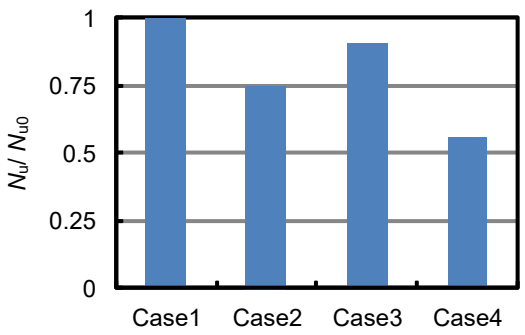


Fig. 6 – Axial compression (N) versus axial displacement (Δ) Fig. 7 – Ultimate strength ratios

The four curves shown in Figure 6 coincide with each other in the initial loading stage① (O-A), in which the columns are generally under elastic deformation. The curves then diverge dramatically in the following stages.

For the column under short-term loading (Case 1), it was kept loaded till failure. The curve goes from elastic stage to plastic and hardening stages, and then begins to descend after the peak point. The axially compressive strength of the column is obtained from point D_1 as 9484kN.

In the other three cases, the axial compression (N_0) was kept constant while corrosion and/or impact developed. It shows that the axial displacement values of the columns keep increasing while the axial compression is constant. For the column under corrosion (Case 3, range A-B), the development of Δ at this stage is 0.4mm, while for the column under impact (Case 2, range A-C′), the development is 3.6mm. It shows that increment of Δ under impact is much larger than

that under corrosion. The reason is that the axial displacement of the columns is caused by different mechanisms. For the corroded column (Case 3), the axial displacement is due to the axial strain development, which is the result of the axial stress increment, as shown in Figure 5. While for the impacted column (Case 2), the axial displacement increment is mainly attributed to the lateral deflection of the column brought by the impact, as can be understood from Figure 5.

For the column under corrosion and impact (Case 4, range A-B-C), the axial displacement increment is dramatically larger than that of the other cases. It is the result of the coupling effect of the sustained load, corrosion and impact. Han et al. (2014b) showed that the impact resistance of CFST will decrease with decreasing steel ratio (α=A_s/A_c). As corrosion reduced the steel ratio and thus reduced the impact resistance of the CFST column, the lateral deflection of the column will increase compared with the no-corrosion case. Simulation results showed that the lateral deflection brought by impact is 46.5mm for Case 2 while it is 64.0mm for Case 4. As the axial displacement of the column increases with increasing lateral deflection, a larger axial displacement is observed in the column of Case 4.

The ratios of the ultimate strength of the columns (N_u) to the ultimate strength of the column under short-term loading (N_{u0}) are presented in Figure 7. It shows that corrosion and impact cause different ratios of strength deterioration to the columns. Corrosion causes 9% reduction of the strength while impact causes 25% reduction. For the column under combined corrosion and impact, the strength reduction ratio is 44%, which is even larger than the summation of the other two cases (36%). The coupling of the two degradations causes higher deterioration to the column strength compared with the simple summation of deterioration ratios brought by the individual actions.

This phenomenon can be explained by the second order effect of the axial compression: the corrosion reduces the axial loading capacity as well as impact resistance of the column; the lateral deflection of the corroded column brought by impact will be larger under the same impact energy; larger lateral deflection means larger mid-span bending moment due to the second order effect. FEA results show that the impact on the corroded column (Case 4, Point C) brings a much larger bending moment than the impact on the no-corrosion column (Case 2, Point C). And the axially compressive strength of the column decreases with increasing bending moment level.

The above analysis shows that the coupling of sustained load, corrosion and lateral impact brings reduction to the ultimate axially compressive strength of the CFST column. It can be summarized as below:

(1) Corrosion will reduce the static as well as lateral impact resistance of the CFST column.

(2) As the impact resistance of the column is reduced, a larger lateral deflection occurs in the column compared with the no-corrosion situation under the same amount of impact energy.

(3) A higher bending moment will be generated at the impact location of the column due to the second order effect of the axial compression.

(4) The remaining axial strength of the column will be largely reduced due to the reduction of section steel ratio as well as the second order effect of the axial compression. The analysis shows that the reduction percentage of ultimate strength is higher than the summation of reduction percentages brought by the individual actions.

CONCLUDING REMARKS

This paper is an attempt to analyze the life-cycle performance of CFST columns under the coupled degradations of chloride corrosion and impact. FEA model was established to simulate the full-range behavior of circular CFST columns under the coupling of sustained load, corrosion and impact loading. In the model, the pre-load on steel tube, residual stresses and initial imperfection as well as the effects of several different types of actions were taken into account. Experimental data were employed to stage-by-stage verify the FEA model and reasonably good results were achieved. Subsequently, the models were used to do full-range analysis of circular CFST columns under the coupled actions. It shows that the coupling of sustained load, corrosion and impact brings notable deterioration to the remaining capacity of the circular CFST column. Meanwhile, the second order effect of the axial compression may intensify this deterioration. It demonstrates the significant influence of load history on the remaining capacity of deteriorated structures.

FEA modeling has been used in the present study to analyze the life-cycle performance CFST columns. In the next stage of the project, experimental study and further mechanical analysis, such as the quantitate relationship between the corrosion depth and the critical impact energy of corroded CFST columns, as well as simplified methods for the remaining life prediction of CFST structures, will be the future research interests.

ACKNOWLEDGEMENTS

The research reported in the paper is part of the Project 51378290 and supported by the National Natural Science Foundation of China (NSFC) and Suzhou-Tsinghua Initiative Program (2016SZ0212). The financial support is highly appreciated.

REFERENCES

Abramowicz, W., & Jones, N. (1984). Dynamic axial crushing of square tubes. *International Journal of Impact Engineering, 2*(2), 179-208. doi:http://dx.doi.org/10.1016/0734-743X(84)90005-8

Akiyama, M., Frangopol, D. M., & Matsuzaki, H. (2011). Life-cycle reliability of RC bridge piers under seismic and airborne chloride hazards. *Earthquake Engineering & Structural Dynamics, 40*(15), 1671-1687. doi:10.1002/eqe.1108

Bambach, M. R., Jama, H., Zhao, X. L., & Grzebieta, R. H. (2008). Hollow and concrete filled steel hollow sections under transverse impact loads. *Engineering Structures, 30*(10), 2859-2870. doi:https://doi.org/10.1016/j.engstruct.2008.04.003

Biondini, F., Camnasio, E., & Titi, A. (2015). Seismic resilience of concrete structures under corrosion. *Earthquake Engineering & Structural Dynamics, 44*(14), 2445-2466. doi:10.1002/eqe.2591

Biondini, F., & Frangopol, D. M. (2016). Life-cycle performance of deteriorating structural systems under uncertainty: review. *Journal of Structural Engineering-ASCE, 142*(9). doi:10.1061/(asce)st.1943-541x.0001544

Comite Euro-International du Beton. (1993). *CEB-FIP Model Code 1990: Design Code*: T. Telford.

Deng, Y., Tuan, C. Y., & Xiao, Y. (2012). Flexural behavior of concrete-filled circular steel tubes under high-strain rate impact loading. *Journal of Structural Engineering-ASCE, 138*(3), 449-456. doi:10.1061/(asce)st.1943-541x.0000464

Frangopol, D. M. (2011). Life-cycle performance, management, and optimisation of structural systems under uncertainty: accomplishments and challenges. *Structure and Infrastructure Engineering, 7*(6), 389-413. doi:10.1080/15732471003594427

Frangopol, D. M., Saydam, D., & Kim, S. (2012). Maintenance, management, life-cycle design and performance of structures and infrastructures: a brief review. *Structure and Infrastructure Engineering, 8*(1), 1-25. doi:10.1080/15732479.2011.628962

Gao, S. B., Usami, T., & Ge, H. B. (1998). Ductility of steel short cylinders in compression and bending. *Journal of Engineering Mechanics-ASCE, 124*(2), 176-183. doi:10.1061/(asce)0733-9399(1998)124:2(176)

Gardner, L., & Nethercot, D. A. (2004). Numerical modeling of stainless steel structural components - a consistent approach. *Journal of Structural Engineering-ASCE, 130*(10), 1586-1601. doi:10.1061/(asce)0733-9445(2004)130:10(1586)

Han, L. H., Hou, C., & Wang, Q. L. (2012). Square concrete filled steel tubular (CFST) members under loading and chloride corrosion: experiments. *Journal of Constructional Steel Research, 71*, 11-25. doi:10.1016/j.jcsr.2011.11.012

Han, L. H., Hou, C. C., & Wang, Q. L. (2014a). Behavior of circular CFST stub columns under sustained load and chloride corrosion. *Journal of Constructional Steel Research, 103*, 23-36. doi:10.1016/j.jcsr2014.07.021

Han, L. H., Hou, C. C., Zhao, X. L., & Rasmussen, K. J. R. (2014b). Behaviour of high-strength concrete filled steel tubes under transverse impact loading. *Journal of Constructional Steel Research, 92*, 25-39. doi:10.1016/j.jcsr.2013.09.003

Han, L. H., Li, W., & Bjorhovde, R. (2014c). Developments and advanced applications of concrete-filled steel tubular (CFST) structures: members. *Journal of Constructional Steel Research, 100*, 211-228. doi:10.1016/j.jcsr.2014.04.016

Han, L. H., Tao, Z., & Liu, W. (2004). Effects of sustained load on concrete-filled hollow structural steel columns. *Journal of Structural Engineering-ASCE, 130*(9), 1392-1404. doi:10.1061/(asce)0733-9445(2004)130:9(1392)

Han, L. H., Yao, G. H., & Tao, Z. (2007). Performance of concrete-filled thin-walled steel tubes under pure torsion. *Thin-Walled Structures, 45*(1), 24-36. doi:10.1016/j.tws.2007.01.008

Hibbitt, Karlsson & Sorensen Inc. (2005). *ABAQUS/Standard User's Manual (6.5.1 ed.):* New York: Rhode Island.

Hou, C., Han, L. H., & Zhao, X. L. (2013). Full-range analysis on square CFST stub columns and beams under loading and chloride corrosion. *Thin-Walled Structures, 68*, 50-64. doi:10.1016/j.tws.2013.03.003

Hou, C. C., Han, L. H., Wang, Q. L., & Hou, C. (2016). Flexural behavior of circular concrete filled steel tubes (CFST) under sustained load and chloride corrosion. *Thin-Walled Structures, 107*, 182-196.

Karren, K. W. (1967). Corner properties of cold-formed shapes. *Journal of the Structural Division, 93*(1), 401-433.

Li, W., Han, L. H., & Zhao, X. L. (2015). Behavior of CFDST stub columns under preload, sustained load and chloride corrosion. *Journal of Constructional Steel Research, 107*, 12-23. doi:10.1016/j.jcsr.2014.12.023

Malvar, L. J., & Ross, C. A. (1998). Review of strain rate effects for concrete in tension. *ACI Materials Journal, 95*(6), 735-739.

MaSubuchi, K. (1980). *Analysis of Welded Structures: Residual Stresses, Distortions and Their Consequences*: Pergamon, New York.

Moen, C. D., Igusa, T., & Schafer, B. W. (2008). Prediction of residual stresses and strains in cold-formed steel members. *Thin-Walled Structures, 46*(11), 1274-1289. doi:http://dx.doi.org/10.1016/j.tws.2008.02.002

Sánchez-Silva, M., & Klutke, G.-A. (2016). *Reliability and Life-Cycle Analysis of Deteriorating Systems*: Springer.

Sanchez-Silva, M., Klutke, G. A., & Rosowsky, D. V. (2011). Life-cycle performance of structures subject to multiple deterioration mechanisms. *Structural Safety, 33*(3), 206-217. doi:10.1016/j.strusafe.2011.03.003

Shen, J. M., Wang, C. Z., & Jiang, J. J. (1993). *Finite Element Analysis of Reinforced Concrete & Ultimate Analysis of Plate and Shell Structures*: Beijing, China (in Chinese).

Wang, R., Han, L. H., & Hou, C. C. (2013). Behavior of concrete filled steel tubular (CFST) members under lateral impact: Experiment and FEA model. *Journal of Constructional Steel Research, 80*, 188-201. doi:10.1016/j.jcsr.2012.09.003

Yuan, W., Guo, A., & Li, H. (2017). Seismic failure mode of coastal bridge piers considering the effects of corrosion-induced damage. *Soil Dynamics and Earthquake Engineering, 93*, 135-146. doi:10.1016/j.soildyn.2016.12.002

Research on deformation limits of SRC columns based on experiment data

Jing Ji
State Key Laboratory of Subtropical Building Science, South China University of Technology
School of Civil Engineering and Transportation, South China University of Technology
Guangzhou, China
cvjingji@scut.edu.cn

Lei Zhang
School of Civil Engineering and Transportation, South China University of Technology
City, Guangzhou, China
zhanglei.lk@qq.com

Xiaolei Han
State Key Laboratory of Subtropical Building Science, South China University of Technology
School of Civil Engineering and Transportation, South China University of Technology
City, Guangzhou, China
xlhan@scut.edu.cn

Tao You
School of Civil Engineering and Transportation, South China University of Technology
City, Guangzhou, China
asdf_7283@qq.com

Yuan Cao
School of Civil Engineering and Transportation, South China University of Technology
City, Guangzhou, China
137868396@qq.com

ABSTRACT

Based on the experimental results of 206 steel reinforced concrete (SRC) columns collected at home and abroad, the influence of five principal parameters that are shear span ratio, flexure shear ratio, axial load coefficient, transverse reinforcement ratio and shaped steel ratio on the failure modes of SRC columns was analyzed and subsequently a method was put forward using shear span ratio and flexure shear ratio to classify the failure modes. According to the current seismic design codes and the summary of phenomena related to different performance levels, the performances of SRC columns were divided into five levels, and limits of plastic rotations angle of these levels were obtained based on the feature points of the skeleton curves. It was found that axial load coefficient was the key parameter, and criteria of deformation limits corresponding to five performance levels were put forward via statistical analysis and verified via reliability analysis of 206 test specimens. Results show that the proposed criteria of failure modes can preferably predict the failure modes of SRC columns; the reliability of deformation limits of SRC columns derived from axial load coefficient stays within a reasonable range.

KEYWORDS: SRC column; experimental data collection; performance levels; deformation limits; regressive analysis

0. INTRODUCTION

The performance based design method (PBSD) has been known worldwide as an advanced theory of structural seismic design, in which the control of structural design switches from force to deformation. In the performance based design method, structures can be designed with the required performance targets and corresponding seismic details to satisfy the preference of owners and functions of structures. Recently, plenty of experiments have been conducted on the seismic performance of reinforced concrete (RC) members and steel reinforced concrete (SRC) members (Qi Yongle, 2012; Ji Jing, Xiao Qiyan, Huang Chao, Han Xiaolei, and Li Shoufang, 2010; Han Xiaolei, Cui Jidong, and Gong Huanjun, 2015; ASCE/SE 41-13, 2014). Meanwhile, performance criteria of RC beams, columns and walls that agree with the Chinese codes were proposed, which can be applied to estimate the seismic performance of building structures (Han Xiaolei, Xie Candong, and Cui Jidong, 2016). However, unlike RC members, performance criteria of SRC columns which are widely used in super high rise buildings has not been thoroughly studied.

In this study, experimental results of 206 SRC columns were collected at home and abroad. Based on the classification by failure modes and performance levels of SRC columns, critical parameters involved with the deformation limits of members have been analyzed, deformation limits corresponding to different performance levels for various failure modes were then obtained. Lastly, accuracy of the proposed deformation limits has been verified via reliability analysis.

1. CLASSIFICATIONS OF FAILURE MODES

1.1 COLLECTION OF EXPERIMENTAL RESULTS

Based on the analysis of failure modes of 206 collected SRC columns, it is found that shear span ratio λ, flexure shear ratio m, axial load coefficient n, transverse reinforcement ratio ρ_v and shape steel ratio ρ_s are the five critical parameters that determine the failure mode of SRC columns. As the difference in calculating these parameters of the collected data, calculations of the five parameters have been normalized according to the design codes *JGJ138-2012*, *GB50010-2010* and *GB50011-2010*, which eliminated the deviation of experiment results.

(1) The experimental axial load coefficient n is expressed as follows:

$$n = N / (f_c A_c + f_a A_a) \tag{1}$$

where N is the axial load force, f_c is the average value of axial compressive strength of concrete, f_a is the average yield strength of steel, and A_c and A_a are the section area of concrete and steel, respectively.

(2) The flexure shear ratio m is expressed as follows:

$$m = M_u / (V_u H) \tag{2}$$

where M_u and V_u are the ultimate flexural capacity and ultimate shear capacity calculated by section 6.2 in the code (JGJ138-2012), respectively. H is the height of inflection point.

Moreover, shape steel ratio ρ_s is defined by the design code *JGJ138-2012*. Shear span ratio λ and transverse reinforcement ratio ρ_v are calculated according to the code *GB50010-2010*. Table 1 gives the summary of normalized experiment results.

Table 1 – Experimental data of SRC column

Reference index	Number of specimen	λ	n	m	ρ_v/%	ρ_s/%	Column height/mm
[10]	3	3	0.3, 0.5	0.55~0.88	0, 1.49	5.16, 8.88	600
[11]	8	4.75, 6.13	0.12~0.25	0.4~0.58	0.34~1	0.9~2.8	1930, 2489
[12]	6	5.6	0.12	0.22~0.45	0.24	1.54~4.53	2075
[13]	20	1~2.5	0.2~0.33	0.73~1.37	0.8~1.6	6.11	220, 330, 440, 550
[14]	2	4	0.32, 0.48	0.38, 0.41	1.08	5.26, 8.85	1000
[15]	17	1.4~3.25	0.18~0.53	0.37~0.93	1.02~2.04	4.98	336, 444, 564, 780
[16]	12	3	0.12~0.35	0.73~0.87	0.8~1.4	4.6~6.8	630
[17]	13	1~3	0.22~0.66	0.47~1.06	0.82	5.6	240, 360, 480, 600, 720
[18]	10	1~3	0.22~0.66	0.47~1.06	0.82	5.6	240, 360, 480, 600, 720
[19]	8	3	0.4	0.44~0.51	1.27~2.41	7.22	900
[20]	2	1	0.34, 0.57	0.77, 1.03	1.05	1.38	333
[21]	2	3	0.4, 0.45	0.34, 0.35	2.71	2.88	750
[22]	6	2.75	0.15~0.45	0.39~0.7	0.78~1.19	4.53	825
[23]	5	3	0.31~0.44	0.42~0.57	1.01	1.23~4.88	750
[24]	9	4.23	0.31~0.48	0.32~0.51	0.95~2.05	6.15	1100
[25]	3	5	0.29	0.35~0.41	1.12~1.92	6.08	1000
[26]	4	3	0.29	0.63~0.81	0.89	3.98~8.42	600
[27]	4	5	0.32~0.34	0.45~0.57	0.89	3.98~7.26	1000
[28]	4	3	0.29	0.6~0.77	0.89~1.93	6.08	600
[29]	3	3	0.3	0.71~0.8	0.89~1.5	6.08	600
[30]	4	3	0.24~0.38	0.72~0.8	0.89	6.08	600
[31]	3	5	0.24~0.33	0.48~0.53	0.89	5.03	1000
[32]	6	2.2	0.43, 0.48	0.42~0.53	0.8, 1.6	5.6	440
[33]	12	1.75, 3	0.25~0.73	0.23~0.89	0.35, 0.7	3.01, 3.68	350, 600
[34]	32	1.5~2.5	0.32~0.56	0.47~1.12	0.8~2.2	4.52	300, 400, 500
[35]	5	1.88	0.32~0.57	0.51~1.07	0.6, 1.2	6.89	300
[36]	3	1.5	0.24~0.59	0.63~1.15	0.63	4.45	300

1.2 CLASSIFICATION OF FAILURE MODES

General failure modes of SRC columns contains four types of failure: shear-diagonal-compression failure, shear-bond failure, flexural-shear failure and flexural failure. To obtain the critical parameters that influence the failure mode, shear span ratio λ, flexure shear ratio m, axial load coefficient n, transverse reinforcement ratio ρ_v and shape steel ratio ρ_s are analyzed as illustrated in Figure 1~Figure 4.

It can be found from Figure 1~Figure 4 that axial load coefficient n, transverse reinforcement ratio ρ_v and shape steel ratio ρ_s have little effect on the failure modes. Thus, failure modes of SRC columns cannot be classified by these three parameters. On the other hand, shear span

ratio λ and flexure shear ratio m have a significant relevance with the failure modes. By considering above two factors, criteria of failure mode classification are obtained in Table 2.

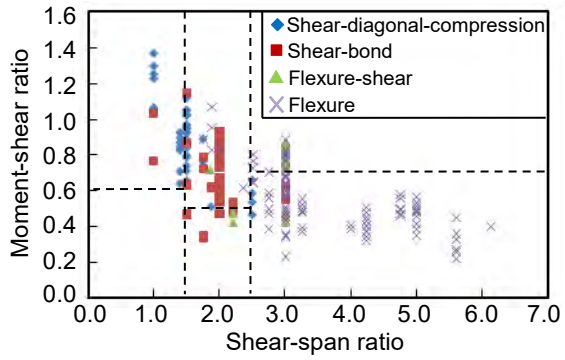


Fig. 1 –Failure modes influenced by shear-span ratio and flexure-shear ratio

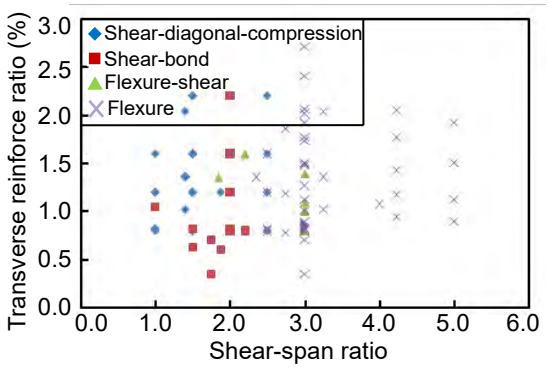


Fig. 2 –Failure modes influenced by shear-span ratio and transverse reinforce ratio

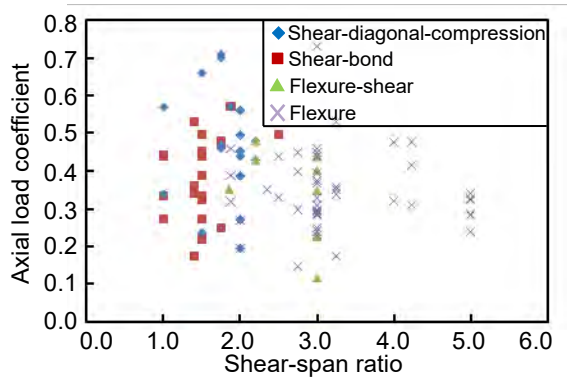


Fig. 3 –Failure modes influenced by shear-span ratio and axial load coefficient

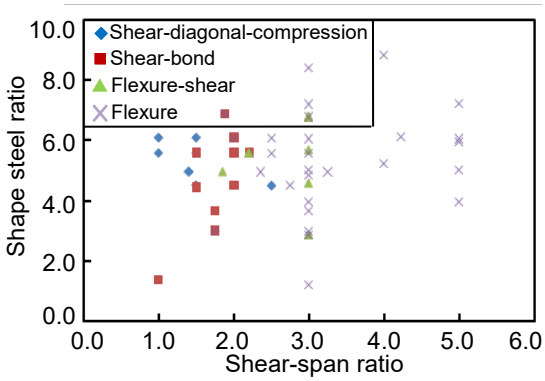


Fig. 4 –Failure modes influenced by shear-span ratio and steel ratio

Table 2 – Failure mode classification of SRC column

Failure mode	Criteria of classification
Shear-diagonal-compression failure	$\lambda \leq 1.5$, $m > 0.6$
Shear-bond failure	($1.5 < \lambda < 2.5$, $m > 0.5$) or ($\lambda \leq 1.5$, $m \leq 0.6$)
Flexural-shear failure	($1.5 < \lambda < 2.5$, $m \leq 0.5$) or ($\lambda \geq 2.5$, $m > 0.7$)
Flexural failure	$\lambda \geq 2.5$, $m \leq 0.7$

Based on the classification criteria of failure modes shown in Table 2, all the collected experimental results were re-classified and analyzed as presented in Table 3.

Table 3 – Accuracy of the classification of SRC column

Failure mode	Total Number of specimens	Number of accurate classification	Accuracy(%)
Shear-diagonal-compression failure	47	39	83
Shear-bond failure	39	29	74
Flexural -shear failure	15	11	73
Flexural failure	103	85	83
Total	204	164	80

As can be seen from Table 3, the accuracy of failure mode classification is 80% when using the two parameters, shear span ratio λ and flexure shear ratio m.

2. DEFORMATION LIMITS OF SRC COLUMNS

2.1 DIVISION OF PERFORMANCE LEVELS

Performance level of a structural member under earthquake with a given intensity refers to the maximum degree of damage that the structural member can resist. In this study, performance levels of a structural member have been divided into five phases, namely, intactness, slight damage, moderate damage, relatively severe damage and severe damage respectively. Failure phenomena of the five phases are given in Table 4.

Former study (Qi Yongle, 2012) shows that plastic rotation angle can preferably reflect the damage degree of structural members, and the plastic rotation angle was selected as the deformation index for structural members. Symbols θ_y, Δ_1, Δ_2, Δ_3 and Δ_4 were used to represent the total rotation angle limits corresponding to intactness, slight damage, moderate damage, relatively severe damage and severe damage level, respectively. Besides, symbols θ_1, θ_2, θ_3 and θ_4 represent the plastic rotation angle (with yield rotation angle θ_y subtracted from total rotation angle) corresponding to slight damage, moderate damage, relatively severe damage and severe damage level, respectively. On the other hand, rotation angle limits of each performance level were obtained from the skeleton curves of SRC columns. It was concluded from failure modes of 206 SRC columns that once the peak capacity is reached, the load-rotation angle curve decreases almost linearly and slowly. For this reason, rotation angle limits of moderate damage and relatively severe damage level were equally interpolated in the range between slight damage and severe damage level, which have been given in Table 4. Figure 5 illustrates the relationship between rotation angle limits corresponding to the five performance levels and loads on the skeleton curves, where P_y and P_{max} represent the yield load and peak capacity of SRC columns respectively.

According to the method given in Table 4, lateral displacements of SRC columns corresponding to intactness, slight damage and severe damage were extracted from the skeleton curve. The plastic rotation angle limit can be obtained by subtracting the yield rotation angle from the total rotation angle, which is the ratio of lateral displacement and the height of column, as given in Table 5.

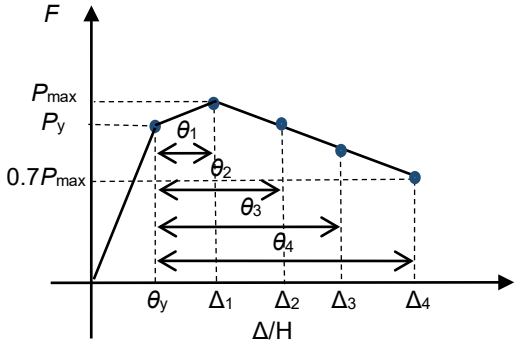


Fig. 5 –Rotation angles corresponding to 5 performance levels

Table 4 – Failure phenomena and rotation angle limits under 5 performance levels of SRC column

Performance level	Failure phenomena	Rotation angle limits
Intactness	No significant cracks occur in concrete, longitudinal bars have not been yield, no residual deformation after unload	R-park method, equivalent energy method, and general yield moment method
Slight damage	Fissure width<2mm, longitudinal bars are yield in tension, steel flange is yield in compression, concrete coverage spalling, load is close to the peak capacity	Rotation angle corresponding to the peak capacity, as the rotation angle of point C in Figure 5
Moderate damage	Fissure width≥2mm, stirrups are partially yield, steel flange is yield in tension, concrete coverage spalling further, decrease of capacity<10%	$\theta_2=\theta_1+1/3(\theta_4-\theta_1)$
Relatively severe damage	Most concrete coverage spalling, concrete starts to crashing, most stirrups are yield or slip out, the bottom of SRC column has a relatively severe damage, decrease of capacity>10%	$\theta_3=\theta_1+2/3(\theta_4-\theta_1)$
Severe damage	All the concrete coverage have spalled, most concrete have been crushed, fissures penetrate through the bottom of SRC columns, the bottom of SRC column has a severe damage, longitudinal bars and stirrups all bloat out, decrease of capacity>20%	θ_4 is the rotation angle when the capacity decrease to 70% of the peak value, as the rotation angle of point D in Figure 5

Table 5 – Rotation angle limits of SRC column

Reference index	Number of specimens	Yield displacement δ_y /mm	Displacement at peak load δ_1/mm	Ultimate displacement δ_4/mm	θ_y	θ_1	θ_4
[10]	3	6.25~7.32	11.6~17.41	18.15~84.76	0.01~0.012	0.009~0.017	0.020~0.13
[11]	8	25~46	39.37~72.47	201.91~245.3	0.013~0.018	0.006~0.025	0.063~0.114
[12]	6	28.49~48.41	56.95~70.08	148.27~312.11	0.014~0.023	0.009~0.019	0.057~0.127
[13]	20	1.36~3.74	2.41~7.99	4.76~21.46	0.005~0.009	0.003~0.01	0.015~0.041
[14]	2	4.01, 5.77	10.97, 11.19	26.36, 43.15	0.004, 0.006	0.005, 0.007	0.021, 0.039
[15]	17	3.69~5.97	6.98~15.18	10.39~41.83	0.005~0.014	0.004~0.016	0.013~0.051
[16]	12	3.12~3.93	7.78~10.57	14.65~29.08	0.005~0.006	0.007~0.011	0.018~0.04
[17]	13	3~6.15	4.65~12.21	12.49~35.18	0.006~0.013	0.003~0.008	0.011~0.07
[18]	10	2.71~4.68	3.88~5.58	9.82~22.62	0.006~0.012	0.001~0.004	0.021~0.039
[19]	8	5.18~6.49	11.21~17.23	29.32~38.84	0.006~0.007	0.006~0.012	0.026~0.036
[20]	2	0.94, 1.15	2.32, 2.87	7.19, 9.39	0.003	0.004, 0.006	0.019, 0.025
[21]	2	5.5, 5.9	9.9, 10.04	26.27, 32.82	0.007, 0.008	0.005, 0.006	0.027, 0.036
[22]	6	5.28~6.07	12.51~19.53	42.9~64.45	0.006~0.007	0.008~0.017	0.045~0.071
[23]	5	3.71~6.69	9.18~20.41	16.21~40.31	0.005~0.009	0.005~0.02	0.013~0.045
[24]	9	5.87~8.95	10.22~15.6	25.67~32.5	0.005~0.008	0.004~0.008	0.016~0.023
[25]	3	5.1~6.8	11.12~12.11	19.9~22.54	0.005~0.007	0.005~0.007	0.015~0.017
[26]	4	2.5~3	5.46~7.2	9.76~12.6	0.004~0.005	0.005~0.007	0.012~0.016

[27]	4	4.02~7.76	9.04~13.64	25.02~45.23	0.004~0.008	0.004~0.007	0.021~0.038
[28]	4	2.2~3.52	5.11~6.91	8.42~11.28	0.004~0.006	0.004~0.007	0.009~0.015
[29]	3	2.74~2.85	5.18~6.78	13.4~15.32	0.005	0.004~0.007	0.018~0.021
[30]	4	2.52~3.33	5.38~7.64	7.82~15.67	0.004~0.006	0.004~0.008	0.009~0.021
[31]	3	5.36~7.96	11.43~13.24	29.67~34.74	0.005~0.008	0.005~0.006	0.022~0.028
[32]	6	8.52~12.4	15.12~22.19	35.89~49.76	0.019~0.028	0.013~0.031	0.058~0.092
[33]	12	0.36~9.33	0.92~10.42	3.12~32.78	0.001~0.016	0.001~0.011	0.007~0.058
[34]	32	1.01~1.64	2.13~4.93	4.29~9.07	0.003~0.005	0.002~0.01	0.008~0.027
[35]	5	4.2~5.31	8.74~14.71	18.28~29.06	0.014~0.018	0.014~0.033	0.045~0.081
[36]	3	—	—	—	—	—	—

·2.2 VERTIFICATION OF DEFORMATION LIMITS FOR SRC COLUMNS

According to section 2.1, the way to obtain rotation angle limits is clear for the performance levels of intactness, slight damage and severe damage. However, for the performance levels of moderate damage and relatively severe damage, rotation angle limits were set up by the Equal Division Method. That is to say, rotation angle limits for performance levels of moderate damage and relatively severe damage are assumed to be at the points of trisection of rotation angle limits for performance levels of slight damage and severe damage, and be calculated as formulas presented in Table 4. In order to verify the accuracy of this method, 9 SRC columns with detail experiment records were collected and the analysis results are shown in Table 6. Meanings of the parameters in Table 6 are as follows:

δ_t: Displacement corresponding to the experiment phenomena in Table 4 during the loading process.

H: Height of the inflection point;

Experimental rotation angle θ_t: $$\theta_t = \delta_t / H \quad (3)$$

Mean divided value of rotation angle θ_d: rotation angle limits obtained from Table 4;

Errors: $$(|\theta_t - \theta_d|) / \theta_t \quad (4)$$

Table 6 – Error analysis of rotation angle by Equal Division Method

Specimens	H (mm)	Moderate damage				Relatively severe damage			
		δ_t (mm)	θ_t (rad)	θ_d (rad)	Errors (%)	δ_t (mm)	θ_t (rad)	θ_d (rad)	Errors (%)
SRHC-1	600	4.5	0.008	0.007	12.5	7.5	0.013	0.010	23
SRHC-2	600	5.5	0.009	0.009	0.0	8.3	0.014	0.011	21.4
SRHC-3	600	6	0.010	0.009	10.0	8.2	0.014	0.010	28.6
SRHC-4	600	6	0.010	0.010	0.0	8	0.013	0.013	0.0
SRC-1	825	24.75	0.030	0.035	16.7	41.25	0.050	0.053	6.0
SRC-2	825	24.75	0.030	0.025	16.7	33	0.040	0.041	2.5
SRC-3	825	16.5	0.020	0.022	10.0	24.75	0.030	0.035	16.7
SRC-4	825	24.75	0.030	0.025	16.7	33	0.040	0.040	0.0
SRC-5	825	24.75	0.030	0.030	0.0	41.25	0.050	0.048	4.0

According to Table 6, the errors of rotation angle limits for moderate damage level is less than 20% by the Equal Division Method. For relatively severe damage level, the errors is less than 30%, which is still in a reasonable range. It can be assumed that the rotation angle limits for moderate damage level and relatively severe damage level of SRC columns obtained by the Equal Division Method were reasonable.

3. ROTATION ANGLE LIMITS OF SRC COLUMNS

3.1 ROTATION ANGLE LIMITS OF DIFFERENT PERFORMANCE LEVEL

Correlation analysis has been carried out to study the relevance between rotation angle limits and 5 parameters in the study (Liu Han, 2016). It is found that the axial load coefficient that in a certain range is the most relevant parameter for rotation angle limits of different performance levels of different failure modes. Accordingly, the boundary values of axial load coefficient for different failure modes were presented in Table 7. Within the axial load boundary, the rotation angle limits were little changed, while the limits changed linearly when exceeding the boundary.

Table 7 – Boundary values of axial load coefficient for different failure modes

Failure mode	Axial load coefficient *n*
Shear-diagonal-compression failure	$n \le 0.3, n \ge 0.5$
Shear-bond failure	$n \le 0.3, n \ge 0.5$
Flexure-shear failure	$n \le 0.2, n \ge 0.4$
Flexure failure	$n \le 0.2, n \ge 0.4$

Table 8 – Rotation angle limits of Shear-diagonal-compression members with n≤0.3

Rotation angle limits	min	max	mean	standard deviation	Rotation angle limits
θ_y	0.006	0.013	0.009	0.002	0.007
θ_1	0.003	0.016	0.008	0.004	0.004
θ_2	0.014	0.035	0.022	0.007	0.015
θ_3	0.024	0.061	0.036	0.013	0.023
θ_4	0.033	0.088	0.050	0.018	0.032

Table 9 –Rotation angle limits of SRC columns (rad)

Failure mode	Performance level				
	Intactness	Light damage	Moderate damage	Relatively severe damage	Severe damage
Shear-diagonal-compression failure	$\lambda \le 1.5$，$m > 0.6$				
$n \le 0.3$	0.007	0.004	0.015	0.023	0.032
$n \ge 0.5$	0.003	0.004	0.008	0.012	0.016
Shear-bond failure	$1.5 < \lambda < 2.5$，$m > 0.5$				
$n \le 0.3$	0.007	0.006	0.014	0.021	0.029
$n \ge 0.5$	0.002	0.003	0.006	0.009	0.012
Flexure-shear failure	$1.5 < \lambda < 2.5$，$m \le 0.5$ or $\lambda \ge 2.5$，$m > 0.7$				
$n \le 0.2$	0.005	0.008	0.015	0.023	0.030
$n \ge 0.4$	0.005	0.006	0.012	0.018	0.024
Flexure failure	$\lambda \ge 2.5$，$m \le 0.7$				
$n \le 0.2$	0.009	0.008	0.026	0.042	0.056
$n \ge 0.4$	0.005	0.003	0.012	0.020	0.027

The value of limits was calculated as mean minus one time standard deviation using plastic rotation angles (total rotation angle minus elastic rotation angle).

The value of limits for shear-crush failure mode was calculated as shown in Table 8, and other cases were calculated the same way. Finally the limits criteria were summarized in Table 9 (Interpolation is permitted between these values).

3.2 GUARANTEED RATE OF ROTATION ANGLE LIMITS

Experimental data of different failure modes was collected. On this basis, rotation angle limits was verified by comparing the limits between Table 9 and experiments. This paper only validated the rotation angle limits for intactness, light damage and severe damage performance level, rotation angle limits for other performance levels were set up by means of Equal Division Method. The calculation method of guaranteed rate was based on ASCE/SEI 41.

Take shear-diagonal-compression failure as an example. 47 specimens with shear-diagonal-compression failure were collected, and the guaranteed rate of rotation angle in Table 9 is shown in Figure 6(a), (b), (c).

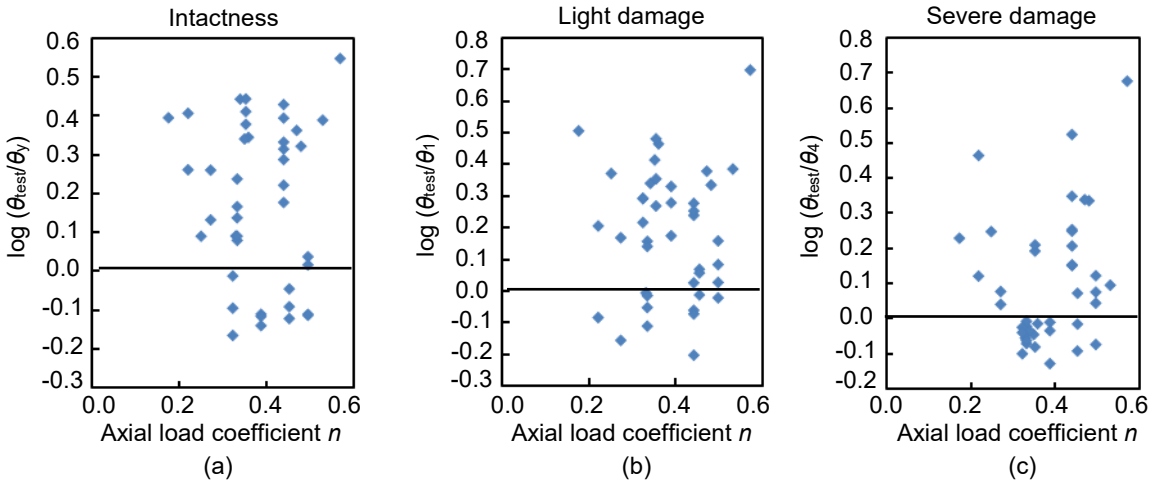


Fig. 6 – Success ratio of rotation angles correspongding to intactness, light damage and severe damage

Figure 6(a), (b), (c) shows the logarithmic distribution of the ratio between the experimental rotation angle and the limits in Table 9 for intactness, light damage and severe damage performance level. θ_{test} means the rotation angle limits obtained from experiments and θ_i (i=y,1,4) is obtained from Table 9. It can be assumed that θ_{test}/θ_i follows the lognormal distribution, the rotation angle limits in Table 9 is reasonable when $\log(\theta_{test} / \theta_i) \geq 0$, and the guaranteed rates of rotation angle limits for intactness, light damage and severe damage performance level are 80.6%, 81.6% and 71.1%, respectively.

Using the same method, the guaranteed rates of rotation angle limits of shear-bond failure, flexure-shear failure and flexure failure were calculated, and the rates for intactness, light damage and severe damage performance levels were shown in Table 10.

According to Table 10, the rotation angle limits for severe damage level have a low guaranteed rate of 71.1%. Mainly because there are many judgment conditions for severe damage failure

and the data are of high discreteness. Overall the guaranteed rates of proposed rotation angle limits range from 70% to 80%, which can meet the practical engineering need.

Table 10 – Success ratio of rotation angle under different performance levels(%)

Failure mode	Performance level		
	Intactness	Light damage	Severe damage
Shear-diagonal-compression failure	80.6	81.6	71.1
Shear-bond failure	81.7	83	72
Flexure-shear failure	79.8	79.9	69.6
Flexure failure	73	74.6	65

4. CONCLUSIONS

(1) Categorization criteria of failure modes of SRC columns based on shear-span ratio and moment-shear ratio were proposed and the accuracy reaches 80%.

(2) Five performance levels of SRC columns were put forward: intactness, light damage, moderate damage, relatively severe damage and severe damage. The standards of determining these states are also presented.

(3) Considering the influence of five parameters including shear-span ratio, axial load coefficient, moment-shear ratio, stirrup ratio and steel ratio on the rotation angle limits for different failure modes, the boundary value of axial load coefficient was determined, based on which the deformation limits criteria of SRC columns was summarized. Verifying the deformation limits in comparison with experiments, the guaranteed rate can be up to 70%, which can meet the practical demands in engineering.

REFERENCE

Qi Yongl (2015). *Research on Deformation Limits of RC Beams, Columns and Shear walls based on material strain*. Guangzhou, South China University of Technology.

Ji Jing, Xiao Qiyan, Huang Chao, Han Xiaolei, Li Shoufang (2010). Research on deformation limits of performance-based RC shear walls controlled by flexure. *Journal of Building Structures*, 31(9), 35-41.

Han Xiaolei, Cui Jidong, Gong Huanjun, et al (2015). Experimental study on seismic behavior of RC beams with different seismic grades. *Journal of Building Structure*s, 36(S2), 299-308

ASCE/SE 41-13 Seismic evaluation and retrofit of existing buildings (2014). Reston, VA, American Society of Civil Engineers.

Han Xiaolei, Xie Candong, Cui Jidong, et al (2016). Seismic performance evaluation of frame-supported shear wall structures based on component deformation. *J. Huazhong Univ. of Sci. & Tech.(Natural Science Edition)*, 44(07), 105-109+115.

Speicher M S, Harris J L (2016). Collapse Prevention seismic performance assessment of new eccentrically braced frames using ASCE 41. *Engineering Structures*, 117, 344-357

JGJ138-2012, Code for design of composite structure (2010). Beijing, China Architecture & Building Press.

GB 50010-2010, Code for design of concrete structures (2010). Beijing: China Architecture & Building Press, 2010

GB 50010-2010，Code for seismic design of buildings (2010). Beijing: China Architecture & Building Press, 2010

Gan D, et al (2011). Seismic behavior and moment strength of tubed steel reinforced-concrete (SRC) beam-columns. *Journal of Constructional Steel Research*. 67(10), 1516-1524

James M, Ricles S D P (1994). Seismic performance of steel-encased composite columns. *Journal of Structural Engineering*, 2474-2494

Hsu H L, Jan F J, Juang J L (2009). Performance of composite members subjected to axial load and bi-axial bending. *Journal of Constructional Steel Research*, 65(4), 869-878

Li Junhua (2005). *Study on the performance of steel reinforced high-strength concrete columns under low cyclic reversed loading*. Xi'an, Xi'an University of Architecture and Technology.

Wang Qiuwei (2013). Experimental study on seismic behavior of steel reinforced concrete columns with new-type cross sections. *Journal of Building Structures*, 11, 123-129.

Ma Hui (2013). *Research on seismic performance and design calculation methods of steel reinforced recycled concrete* columns. Xi'an, Xi'an University of Architecture and Technology.

Zheng Shansuo, Wang Bin, Hou Piji, et al (2011). Experimental study of the damage of SRHSHPC frame columns under low cycle reversed loading. *China Civil Engineering Journal*, 09, 1-10.

Ping Zhendong (2009). *Experimental Research on ductility of SRHSHPC frame columns*. Xi'an, Xi'an University of Architecture and Technology.

Peng Chunhua (2008). *Experimental Study and Theory Analysis on Limit Value of Axial Compression for SRHSHPC* columns. Xi'an, Xi'an University of Architecture and Technology.

Chen Xiaogang, Mou Zaigen, Zhang Jubing, et al (2009). Experimental study on the seismic behavior of steel reinforced concrete columns. *Journal of University of Science and Technology Beijing*, 31(12), 1516-1524.

Du Yongshan (2007). *An Experimental Study on Hysteretic Behavior of Reinforced Concrete Transnomal Short Columns and Steel Reinforced Concrete Transnomal Short Columns*. Harbin, Harbin Institute of Technology.

Xie Xiadi (2008). *Experiment Study on Seismic Design Details and Axial Compressive Performance of CSRC Columns*. Xiamen, HuaQiao University.

Zhang Zhiwei (2007). *Experiment Study on deformation performance and hysteretic characteristic of SRC columns*. Xiamen, Huaqiao University.
Liu Yang (2006). *Experiment Study on Seismic Behavior of Core Steel Reinforced Concrete Columns*. Xiamen, Huaqiao University.
Chen Caihua (2007). *Experiment Study and Numerical Analysis on Steel Reinforced Concrete Compression-bending Members*. Beijing, China Academy of Building Research.
Jiang Chuanxing (2007). *Study on Effect of Stirrup Ratio on Steel Reinforced High-strength Concrete when Shear-span Ratio is 5*. Chongqing, Chongqing University.
Chen Zijing (2007). *Experimental Study on Proper Ratio of Steel Skeleton of Steel Reinforced High-Strength Concrete Columns.* Chongqing, Chongqing University.
Yu Lei (2006). *Study on Reasonable Steel Contents of Steel High-Strength Reinforced Concrete Columns*. Chongqing, Chongqing University.
Yang Dingfeng (2007). *Experimental Research on the Effects of Loading Performance about SRHC Column with different stirrup ratio and λ=3 on the repeatedly horizontal load*. Chongqing: Chongqing University.
Ma Xiang (2009). *Experimental research on the effects of stirrup ratios on bearing performance of SRHC columns with studs*. Chongqing: Chongqing University.
Liu Wei (2007). *Study on Limited Value of Axial Compression Ratio of Steel Reinforced High Strength Concrete Column*. Chongqing, Chongqing University.
Shen Qinchuan. *Study on Limit Value of Axial Compression Ratio of Steel Reinforced High Strength Concrete Column*. Chongqing, Chongqing University
Sun Cangbai (2005). *The Study of seismic behavior on steel high-strength reinforced concrete columns*. Xi'an, Xi'an University of Architecture and Technology.
Jiang Donghong (2001). *Study on mechanical performance and seismic performance of steel reinforced high-strength concrete frame column*. Shenyang, Northeastern university.
Jia Jingqing (2000). *The research of SRHC short columns and high-strength concrete short columns on mechanics performance*. Dalian: Dalian University of Technology.
Li Xiangmin, Zhang Yu, Chen Zongliang (1999). The Limited Values of Steel Reinforced High Strength Concrete Column. *Journal of Building Structures*, 07, 10-13.
Zhang Sufang (1999). The Ductility of SRC Frame Short Column under Low Reversed Cyclic load. *Journal of Southwest JiaoTong University*, 02: 112-118.
Liu Han (2016). *Research on deformation limits of SRC beam and column based on experiment data*. Guangzhou: South China University of Technology.
Update to ASCE/SEI 41 Concrete Provisions (2007). US: Federal Emergency Management Agency.

Update of Design Provisions for Moment-Resisting Joints between Steel Beams and Reinforced Concrete Columns

Luis B. Fargier-Gabaldón
Director, Diseño y Construcciones Integrados,
Mérida, Venezuela
lfargier@dcintegrados.com

Paul Cordova
Senior Project Manager, Simpson Gumpertz & Heger
ppcordova@sgh.com

Gustavo J. Parra-Montesinos
C.K. Wang Professor of Structural Engineering. University of Wisconsin-Madison
gustavo.parra@wisc.edu

Gregory Deierlein
John A. Blume Professor. Stanford University
ggd@stanford.edu

Abstract

Composite moment frames consisting of steel beams continuous through reinforced concrete or concrete-encased steel composite columns offer an attractive alternative to concrete or steel special moment frames for buildings constructed in regions of high seismicity. The current state-of-practice to design connections between steel beams and concrete columns is based on the document "*Guidelines for design of joints between steel beams and reinforced concrete columns*", which was published in 1994 and does not incorporate subsequent research on the seismic performance of the connections. This paper summarizes an effort to update the 1994 Guidelines. Relevant test data on connection behavior are reviewed and summarized, including joint response under reversed cyclic loading of interior, exterior and roof-T connections, the use of high strength concrete, and connection details not included in the 1994 Guidelines, such as joints with steel band plates and transverse beams. Revised (updated) equations are presented to determine joint shear strength for various joint configurations, including validation against test data that demonstrates applicability to regions of high seismicity.

Introduction

Composite frames offer advantages over traditional reinforced concrete (RC) or steel structures with cost-savings and improved efficiency of construction, while exhibiting adequate performance under large displacement reversals. Continuous steel beams are more efficient than RC beams for long beam spans and the through-joint detail eliminates the risk of weld fractures at the beam-to-column flanges, as observed in steel-framed buildings that were damaged in the Kobe and Northridge earthquakes (Tremblay et al. 1996, FEMA-351). On the other hand, the RC columns can be significantly more cost-effective to resist axial forces than the heavy steel counterparts

(Griffis 1996). Composite frame construction can be faster than that of traditional RC or steel structures because the steel frame construction can advance as in a typical steel frame construction, but without the need of time consuming full penetration welds at beam-column joints. Light steel erection columns support the continuous steel beams and steel deck, which can be erected a few stories above the concrete operation related to assemblage of reinforcement cages and casting of the columns and slab. Alternatively, the composite frame can be constructed using precast concrete column – steel beam assemblies.

The design of moment connections between RC or concrete-encased columns and steel beams continuous through the joint was first addressed in the "*Guidelines for design of joints between steel beams and reinforced concrete columns*", published in 1994 by the ASCE Task Committee on Composite Structures. The document was based on the experimental work conducted at the University of Texas at Austin by Sheikh et al. (1989) and Deierlein el al. (1988). Since its publication, several experimental programs have been conducted in the US, including the work of Kanno (1993), Bugeja et al. (2000), Parra-Montesinos and Wight (2000), Liang and Parra-Montesinos (2004), Fargier-Gabaldón and Parra-Montesinos (2005); in Japan, Kuramoto and Noguchi, (1997), Nishiyama et al. (1998, 2000), Noguchi and Kim (1997, 1998), Baba and Nishimura (2000); and in Taiwan, Cordova et al. (2004), Chen et al. (2004). This paper presents a summary of the most relevant experimental research programs conducted over the past 30 years and an update of the design provisions for moment-resisting joints between through-joint steel beams and RC columns.

Research at the University of Texas at Austin

The work at the University Texas at Austin included the testing of seven specimens under monotonic loading and eight specimens under reversed cyclic loading (Sheikh et al. 1989 and Deierlein el al. 1989). All specimens featured a 200 mm deep built-up steel beam and a 510 mm square RC column. Joint details included the use of vertical stiffeners welded to the beam at the column faces, commonly referred to as face bearing plates, steel erection columns, and extended face bearing plates welded to the flanges of the steel beam to mobilize the concrete regions located outside the width of the beam.

Test results indicate that the web panel of the steel beam carries part of the joint shear, as in beam-column joints of steel frames (Figure 1a). Face bearing plates (Figure 1b) increased the connection strength by approximately 70% when compared to the steel web panel alone. The addition of extended face bearing plates increased the connection strength by 180%. Joints that featured face bearing plates in combination with steel columns experienced a nearly 130% increase in strength. Based on these observations, the joint shear strength was divided into three mechanisms: **(a)** the strength of the steel web panel (Figure 1a), **(b)** the contribution of an inner diagonal concrete strut that forms between flanges of the steel beam and the face bearing plate (Figure 1b), and **(c)** the contribution of a compression field or truss mechanism outside the width of the steel beam that is activated with the use of shear keys welded to the beam flanges and horizontal tie reinforcement above and below the beam (Figure 1c and 1d). Connections failing in shear exhibited ductile behavior and sustained its shear strength through large deformations (Figure 2a).

Test also showed localized concrete crushing above and below the top and bottom beam flanges, respectively, which led to rigid body rotations of the steel beam inside the joint (Figure 2b), pinched hysteresis, and reduced energy dissipation of the specimens. Vertical joint reinforcement welded to the top and bottom flanges of the steel beam near the column faces was found to be

effective in increasing joint bearing strength and preventing or postponing the occurrence of a bearing failure.

The results from the research conducted at the University of Texas at Austin led to the development of the "*Guidelines for design of joints between steel beams and reinforced concrete columns*" published by an ASCE Task Group on Composite Connection in 1994. Joint details covered in the Guidelines are shown in Figure 4, except for the steel band plates (Figure 3c) and cover plates (Figure 3f) which are addressed in the updated provisions.

Research at the Cornell University

Kanno and Deierlein (1993) conducted an extensive experimental program at Cornell University, which included the testing of nineteen specimens under reversed cyclic loading. One specimen was designed for beam yielding, two for a simultaneous joint shear failure and beam yielding, and the remaining ten and six to fail in shear and bearing, respectively. Three specimens featured 100 MPa strength concrete and the remaining used 40 MPa strength concrete. All specimens featured a 406 mm square RC column and face bearing plates. Other joint details included steel band plates wrapping around the column regions just above and below the steel beam, cover plates around the column faces within the beam depth, transverse steel beams, wide bearing plates, headed studs welded on the beam flanges, horizontal joint reinforcement in volumetric ratios ranging from 0.4 to 1.2%, and vertical joint reinforcement. An axial load corresponding to an average axial stress based on the gross concrete area of approximately $0.3f_c'$ was applied to five of the specimens.

Test results suggest that: **(a)** the axial load helps to mobilize the concrete regions located outside the flanges of the steel beam, **(b)** the use of high strength concrete increases the connection strength compared to the use of regular strength concrete, **(c)** vertical joint reinforcement is very effective in increasing the bearing strength of the joint, and **(d)** transverse beams enhance the participation of the concrete regions located outside the beam flanges to resist shear.

Kanno and Deierlein (1993) also studied the influence of confinement on the bearing strength of the concrete regions located just above and below the steel beam through tests of fifty small concrete blocks. It was found that heavily confined specimens failed at a stress of approximately 3.3 times larger than that corresponding to the 28-day concrete compressive strength. Given these findings, they concluded that the use of steel band plates above and below the steel beam significantly increases the bearing strength of the composite joint.

Research at the Texas A & M University

Bugeja et al. (1999) tested five interior and one exterior composite connections under reversed cyclic loading in two orthogonal directions. In all specimens, one steel beam ran continuous through the joint and the transverse steel beams were attached with a bolted moment connection to the continuous beam. Specimens were first tested in the continuous direction until a drop in the lateral load occurred, then they were rotated 90 degrees and tested to failure in the perpendicular direction. In one specimen, a reversed order was used and the specimen was tested to failure in the continuous beam direction.

The steel beams in all specimens were designed for composite action with a concrete slab over a metal deck in both directions. Joint details included face bearing plates, steel columns welded to the flanges of the steel beam, cover plates wrapping around the column faces within the beam

depth, and cover plates placed at 45 degrees with respect to the longitudinal axis of the beams, forming an octagon in a plan view, which encased the RC column region within the beam depth. The specimens featured a 380 mm square RC column and a W310 x 32.7 (W12 x 22) hot-rolled steel section as a beam in both orthogonal directions. All specimens showed a stable load versus displacement response and large energy dissipation capacity, significant beam yielding, and limited joint damage in the continuous direction. In the discontinuous direction, three of the six specimens experienced beam yielding with significant plastic rotation capacity. The failure of two specimens in the discontinuous direction was characterized by a relative rotation between beam segments located at either side of the joint, while the exterior joint exhibited a bearing failure. The test results showed that the effective flange width of the concrete slab correlated well to the recommendations given in the AISC Manual (1994), except for the cases of edge beams in positive bending for which the effective flange width can be taken as the column width. Steel beams exhibited full composite action throughout testing.

Research at the University of Michigan

Several researchers studied composite beam-column joint behavior at the University of Michigan between 1994 and 2005. Parra-Montesinos and Wight (2000) tested nine exterior connections under reversed cyclic loading. Joint details included face bearing plates, steel columns, steel band plates, transverse steel beams, and horizontal joint reinforcement in volumetric ratios ranging from 0.5 to 0.9%. Two specimens had the joints reinforced with discontinuous fiber reinforcement. All specimens featured a 400 mm square RC column. The beam-to-column depth ratio approached 0.6 for five of the specimens and 1.0 for the remaining four specimens. Results from this investigation showed: **(a)** all specimens exhibited a stable load versus displacement response with significant energy dissipation, **(b)** a hoop volumetric ratio of 0.9% was sufficient to confine the concrete in the joint region, **(c)** yielding of the steel web panel occurred over a width of approximately 0.8 times the column depth, and **(d)** steel band plates effectively activate an outer concrete strut through direct bearing on the concrete. A minimum beam depth-to-column longitudinal bar diameter ratio of 20 was recommended for use in design, except for the case of joints with steel band plates, in which a ratio of 16 was deemed appropriate.

Liang and Parra-Montesinos (2004) tested two interior and two exterior RC column-to-steel beam connections with a composite concrete slab over a metal deck under reversed cyclic loading. Joint details included face bearing plates and steel columns in all specimens in combination with either steel band plates and transverse steel beams or joint confinement reinforcement in a volumetric ratio of 1.1%. The column-to-beam flexural strength ratio was 2.2 and 1.3 for the exterior and interior connections, respectively. The specimens were designed for beam hinging, with the connections proportioned for a target joint shear deformation of 0.5% using a joint deformation model proposed by Parra-Montesinos and Wight (2001). All specimens were constructed with a 380 mm square RC column and W310x38.7 (W12x26) steel beam with a 90/50 mm steel deck. All specimens exhibited significant energy dissipation with full hysteresis loops and a response dominated by beam hinging and limited joint damage, as intended in the design. The load versus drift hysteretic response of Specimen 2 (interior connection) with steel band plates, transverse steel beams and without joint transverse reinforcement is shown in Figure 5. Concrete crushing of the slab at the column face occurred in all specimens during positive bending of the composite beam. Shear studs in the hinging zone showed no signs of damage at the end of the test. Maximum joint shear distortions of approximately 0.005 and 0.003 rad. and bearing deformations of approximately, 0.007 and 0.008 rad. were measured in the interior and exterior connections, respectively. Results from this investigation suggest that properly detailed composite connections

between RC columns and a composite continuous steel beam can be designed for beam hinging and limited joint damage during a major seismic event.

Fargier-Gabaldon and Parra-Montesinos (2006) tested two interior T joints under reversed cyclic loading to investigate joint details, including column longitudinal bar anchorage, that would allow adequate mobilization of joint concrete to resist shear. Specimens 1 and 2 featured a joint depth-to-bar diameter ratio of 12 and 20, respectively, and a 400 mm square RC column. Joint details used in Specimen 1 included face bearing plates, steel band plates and a steel column. No transverse reinforcement within the joint region was used in this specimen and the column longitudinal reinforcement was terminated above the top flange of the steel beam with heads to eliminate hooks and reduce reinforcement congestion. Joint horizontal reinforcement (0.5% volumetric ratio) was added to the joint region in Specimen 2 in combination with a hot-rolled steel channel running transversely above the top flange of the steel beam. The column longitudinal reinforcement ran through the channel and was anchored with headed bars that bear against the web of the steel section. Both specimens featured vertical joint reinforcement in the form of inverted U-shaped stirrups placed over the top flange of the steel beam. Specimen 1 was designed for joint failure and Specimen 2 was designed for column hinging with limited joint damage. Specimen 1 showed good energy dissipation capacity up to 3% drift. Beyond 3% drift, concrete crushing occurred underneath the heads of the longitudinal bars, which led to large beam rigid body rotations that accounted for nearly the totality of the applied drift at the end of the test. Specimen 2 exhibited large column plastic hinge rotations and limited joint damage, as intended in design, with beam rigid body rotations accounting for almost 30% of the applied drift throughout the test. Test results indicated that a joint depth-to-column bar diameter ratio of 20 is reasonable for composite T-connections, provided there is a sufficient bearing area at the end of the bars.

Fargier-Gabaldón and Parra-Montesinos (2005) tested two exterior column-to-steel beam connections to investigate effective outer panel width in connections where the concrete column is significantly wider than the steel beam. The two specimens featured a column-to-beam width ratio of 3.6, in which a 400 x 600 mm rectangular RC column was connected to a W360x57.8 (W14x38) hot-rolled steel beam. Both specimens featured face bearing plates and an embedded steel erection column. Additionally, Specimen 1 featured horizontal joint transverse reinforcement in a volumetric ratio of 0.7%, while Specimen 2 featured transverse steel beams and steel band plates. Except for the column width, Specimens 1 and 2 were nominally identical to Specimens 6 and 9, tested by Parra-Montesinos and Wight (2000), in which a 400 mm square RC column was used with a column-to-beam width ratio of 2.4. The hysteresis loops indicated that both specimens exhibited excellent energy dissipation and stiffness retention capacity. Extensive joint diagonal cracking was observed on the lateral faces of the RC column, which indicated that the entire column core was mobilized to transfer shear. Specimen 1 experienced a bearing failure, characterized by crushing of the concrete regions located just above and below the top and bottom flanges of the steel beam, with beam rigid body rotations accounting for most of the applied drift at the end of the test. Specimen 2, with steel band plates and transverse beams, showed an improved bearing response when compared to that observed in Specimen 1. The band plates effectively confined the concrete regions located above and below the connection, forcing a shear failure of the joint region while beam rigid body rotations were kept below 1.5% for drift cycles up to 4%. Shear distortions measured on the column lateral faces exceeded 1.5% in both beam-to-column connections. Specimens 1 and 2 experienced a 50% increase in the joint strength when compared to that measured in Specimens 6 and 9, respectively, tested by Parra-Montesinos and Wight (2000). Test results indicated that the use of steel columns and band plates was effective to mobilize the full core of the concrete column even in connections between wide concrete columns and steel beams.

Collaborative research program between the National Center for Earthquake Engineering, Taipei, Taiwan and Stanford University

A full-scale three-bay, three-story composite frame was tested at the National Center for Earthquake Engineering in Taipei, Taiwan (Deierlein et al. 2005, Cordova et al. 2004, Chen et al. 2004). The test frame included 650 mm square precast RC columns. The steel beams were 600, 500 and 396 mm deep at the first, second and third story, respectively. Welded shear studs over the steel beam length ensured composite action with the concrete slab over a metal deck. Joint details included face bearing plates, top and bottom steel band plates and transverse steel beams. Column longitudinal bars in the top level were tag-welded to a steel cap plate located on top end of the RC column. The frame was designed to meet the code requirements of a structure built in California and Taiwan and was subjected to four pseudo-dynamic tests scaled to represent seismic hazard levels with 50%, 10%, and 2% chance of exceedance in 50 years. Test results showed that these events correlated well with limited structural damage, repairable damage, and collapse prevention, respectively, and that the structure exhibited stable behavior through large deformations. A final push-over test was conducted up to an inter-story drift of approximately 10%. At this drift level, the lateral mechanism consisted of hinging concentrated at the base of the first story columns, top of the second story columns, and beam ends of the first story. Beyond 7% drift, bolted beam splices located at the third points of the beam span fractured, which led to a decrease in the lateral strength of the frame. Tests results showed that the behavior of the frame exceeded the performance expectations implied by modern design codes and was consistent, if not better, than that expected of conventional steel or RC moment frame buildings.

Update of design provisions for moment-resisting joints between steel beams and reinforced concrete columns

Based on the 1994 Guidelines and the results from experimental research conducted over the past 30 years, new design provisions for moment-resisting joints between steel beams and RC columns are currently under development. The design provisions broaden the scope of the 1994 Guidelines to consider the following: **(a)** explicit consideration of joint deformations, **(b)** high strength concrete within the joint region, **(c)** designs with steel band plates and transverse beams, and **(d)** design for high seismic regions (e.g., seismic design category D in ASCE 7). A comparison between the equations given in the Guidelines (1994) and those to appear in the updated design provisions can be found in Table 1. The detailing requirements given in Sections 4.3, 4.4 and 4.5 of the 1994 Guidelines, related to the thickness of face bearing plates, flanges of the steel beam, and extended face bearing plates, respectively, remain unchanged in the updated provisions.

The updated design provisions have significant advantages over the 1994 Guidelines in terms of computational effort: **(a)** the joint strength can be estimated without the need for iteration to determine the value of jh in equations 7 and 7a shown in Table 1, and **(b)** the calculation of the bearing strength is done in terms of the bearing forces acting on the inner panel (Fig. 4) and expressed in terms of horizontal shear (Equation 5' in Table 1). This allows for the use of a single equation to estimate the joint strength (Equation 7' in Table 1), as opposed to the procedure described in the Guidelines, in which the bearing strength and shear strength of the joint are checked independently (Equations 5 and 7 in Table 1, respectively). Note that a typical joint designed with the updated provisions requires the application of 10 to 12 compact equations, while the application of the 1994 Guidelines requires the use of 18 to 20 equations, some of which are lengthy, and in some cases requiring an iterative process.

The calculated-to-measured strength ratios of the updated design provisions for 29 composite connections are shown in Table 2. The average ratio is 0.88, with a standard deviation of 0.09 and a maximum and minimum of 1.09 and 0.70, respectively. The updated design provisions are expected to be released in 2017 with perhaps minor modifications to the equations presented in Table 1, after the feedback received during the review process before its publication.

Conclusions

Results from tests on composite joints conducted over the past 30 years between RC columns and continuous steel beams, as well as from the test of a full-scale three-story, three-bay composite frame under pseudo dynamic loading, validate the use of the composite frames in zones of high seismicity and provide substantial information to update the design procedure given in the 1994 Guidelines. The updated design provisions are calibrated using a database that contains reversed cyclic loading test results of interior and exterior connections with a variety of joint details, many of which are not included in the original guidelines. Details include face bearing plates, steel columns, steel cover plates, steel band plates, extended face bearing plates, and vertical joint reinforcement. The updated provisions allow the use of high strength concrete in the connection region, explicitly account for connection deformations, and require less computational effort than the 1994 Guidelines. The updated design provisions for composite connections presented herein can be used to proportion composite frame joints of buildings located in high seismic zones with a reasonable balance between the required computational effort and accuracy in the strength estimation, as confirmed by a calculated-to-measured strength ratio of 0.88 with a standard deviation of 0.09 for 29 subassembly connections tested to failure.

References:

ACI-ASCE Committee 352. (2010). *Recommendations for design of beam column joints in monolithic reinforced concrete structures. Report No. ACI 352R-10.* Farmington Hills, MI: American Concrete Institute.

AISC. (1994). *Manual of Steel Construction - Load and resistance factor design (LRFD).* Chicago: American Institute of Steel Construction.

ASCE Task Committee on Design Criteria for Composite Structures in Steel and Concrete. (1994). Guidelines for Design of Joints Between Steel Beams and Reinforced Concrete Columns. *Journal of Structural Engineering, 120*(8), 2330-2357.

ASCE 7 (2010). *Minimum Design Loads for Buildings and Other Structures, ASCE/SEI 7-10*, American Society of Civil Engineers.

Baba, N., & Nishimura, Y. (2000). Stress transfer on through beam type steel beam-reinforced concrete column joints. *Proceedings 6th ASCCS International Conference on Steel–Concrete Composite Structures*, 753-760.

Bugeja, M., Bracci, J. M., & Moore, W. P. (2000). Seismic behavior of composite RCS frame systems. *Journal of Structural Engineering, 126*(4), 429-436.

Chen, C. H., Cordova, P., Lai, W. C., Deierlein, G. G., & Tsai, K. C. (2004). Pseudo-dynamic test of full-scale RCS frame: Part 1 – Design, construction and testing. Paper No. 2178. *13th World Conference on Earthquake Engineering.* Vancouver, CA.

Cordova, P., Lai, W.C., Chen, C.H., & Tsai, K.C. (2004). Pseudo-dynamic test of full-scale RCS frame: Part 2 – Analyses and design implications. Paper No. 674. *13th World Conference on Earthquake Engineering.* Vancouver, CA.

Deierlein, G. G., Sheikh, T. M., Yura, J. A., & Jirsa, J. O. (1989). Beam–column moment connections for composite frames: Part 2. *Journal of Structural Engineering, 115(11),* 2877-2896

Deierlein, G. G., Cordova, P., Tsai, K. C., Chen, C. H., & Lai, W. C. (2005). Composite moment frames. *Concrete International, 27(05),* 39-44.

Fargier-Gabaldon, L. B., & Parra-Montesinos, G. J. (August 2005). *Seismic Behavior of RCS Connections with Special Configurations. Report No. UMCEE 05-11.* Ann Arbor, Michigan: Department of Civil and Environmental Engineering, University of Michigan.

Fargier-Gabaldon, L. B., & Parra-Montesinos, G. J. (2006). Behavior of Reinforced Concrete Column–Steel Beam Roof Level T-Connections under Displacement Reversals. *Journal Structural Engineering, ASCE, 132*(7), 1041-1051.

FEMA. (2000). *Recommended Seismic Evaluation and Upgrade Criteria for Existing Welded Steel Moment-Frame Buildings, prepared by the SAC Joint Venture for the Federal Emergency Management Agency-351.* Washington, DC: Federal Emergency Management Agency.

Griffis, L. (1986). Some design considerations for composite-frame structures. *AISC Engineering Journal, 23*(2), 59-64.

Kanno, R., & Deierlein, G. G. (1993). *Strength, deformation, seismic resistance of joints between steel beams and reinforced concrete columns. Report No. 93-6.* Ithaca, N.Y.z: Cornell University.

Kuramoto, H., & Noguchi, H. (1997). An overview of Japanese research on RCS systems. *Proceedings of ASCE Structures Congress XV* (pp. 716-720). Reston, Virginia: ASCE.

Liang, X., & Parra-Montesinos, G. J. (2004). Seismic behavior of reinforced concrete column-steel beam subassemblies and frame systems. *Journal Structural Engineering, 130*(2), 310-319.

Nishiyama, I., Itadani, H., & Sugihiro, K. (1998). Bi-Directional Seismic Response of Reinforced Concrete Column and Structural Steel Beam Subassemblies. Paper Ref. T177-2. *Proceedings of Structural Engineers World Congress* (p. 8). Reston, Virginia: ASCE.

Nishiyama, I., Kuramoto, H., Itadani, H., & Sugihiro, K. (2000). Bi-Directional Behavior of Interior-, Exterior, and Corner-Joints of RCS System. Paper No. 1911/6/A. *Proceedings 12th World Conference on Earthquake Engineering*, (p. 8).

Noguchi, H., & Kim, K. (1997). Analysis of beam–column joints in hybrid structures. *Proceedings ASCE Structures Congress XV* (pp. 726-730). Reston, Virginia: ASCE.

Noguchi, H., & Kim, K. (1998). Shear strength of beam-to-column connections in RCS system. Paper Ref. T177-3. *Proceedings Structural Engineers World Congress* (p. 7). Reston, Virginia: ASCE.

Parra-Montesinos, G., & Wight, J. K. (2000). *Seismic behavior, strength, and retrofit of exterior RC column-to-steel beam connections. UMCEE 00-09.* Michigan: Department of Civil and Environmental Engineering, University of Michigan.

Parra-Montesinos, G. J., & Wight, J. K. (2001). Modeling shear behavior of hybrid RCS beam-column connections. *Journal Structural Engineering, 127*(1), 3-11.

Sheikh, T. M., Deierlein, G. G., Yura, J. A., & Jirsa, J. O. (1989). Beam–column moment connections for composite frames: Part 1. *Journal Structural Engineering, 115*(11), 2858-2876.

Tremblay, R., Bruneau, M., Nakashima, M., Prion, H. G., Filiatrault, M., & DeVall, R. (1996). Seismic Design of Steel Buildings: Lessons from the 1995 Hyogo-ken Nanbu Earthquake. *Canadian Journal of Civil Engineering, 23*(3), 757-770.

Table - 1. Summary of design equations

	ASCE Guidelines (1994)	Updated provisions
Width of the inner panel	$b_i = \max(b_f, b_p)$	$b_i = b_f$
Width of the outer panel	Connections with steel columns, or extended face bearing plates: $b_o = C(b_m + b_i) < 2d_o$ [1] $b_m = \frac{(b_f + b)}{2} \le b_f + h \le 1.75 b_f \ \ldots C = \frac{x}{h}\frac{y}{b_f}$ [1a]	Connections with steel columns, or extended face bearing plates: $b_o = y + \frac{2}{3}x - b_f \ \le b - b_f$ [1′] Connections with steel band plates $b_o = 12 t_{bp} \le b - b_f$ [1′]
Nominal horizontal shear strength of the steel web (inner panel)	$V_{sn} = 0.6\, F_{ysp} t_{sp}\, jh$ [2] An iterative process is required to find jh (see Equation 7a)	$V_{spn} = 0.6\, F_{ysp}\, t_{sp}\, \alpha_{sp}\, h$ [2′] $\alpha_{sp} = 0.9$ interior joints, $\alpha_{sp} = 0.8$ exterior No iteration is required
Nominal horizontal shear strength of the concrete strut (inner panel)	$V_{csn} = 1.7\sqrt{f_c'} b_p h \le 0.5\, f_c'\, b_p d_w$ [3] Does not diferentiate between interior and exterior connections.	$V_{icn} = \alpha_{cs}\, 1.7\sqrt{f_c'}\, b_i\, h \ \le 0.5\, f_c'\, b_f\, d_j$ [3′] $\alpha_{cs} = 1.0$ interior joints, $\alpha_{cs} = 0.6$ exterior. Similar to the ACI 352 (2010) provision.
Nominal horizontal shear strength of the outer concrete panel	Strength given by a compression field mechanism: $V_{cfn} = \mathrm{V}_c' + \mathrm{V}_s' \le 1.7\sqrt{f_c'} b_o h$ [4] $\mathrm{V}_c' = 0.4\sqrt{f_c'}\, b_o h$ [4a] $\mathrm{V}_s' = \frac{A_{sh} F_{ysp} 0.9h}{s_h} \ldots$ [4b] $\ldots \frac{A_{sh}}{s_h} \ge 0.004\, b$ [4c] Does not differentiate between interior and exterior connections	Strength given by the contribution of a diagonal concrete strut (V_{on}) $V_{on} = \alpha_{cs} 1.25\sqrt{f_c'} b_o h$ [4′] $\alpha_{cs} = 1.0$ interior joints, $\alpha_{cs} = 0.6$ exterior Joints with steel band plates and transverse beams: no horizontal ties are required within the beam depth. Other cases: provide horizontal ties in a stirrup volume-to-joint volume of 0.01.
Bearing strength	Vertical bearing strength of the joint is considered appropriate if [5] is satisfied: $\sum M_c \le \phi[0.7 h C_{cn} + h_{vr}(T_{vrn} + C_{vrn})] - 0.35 h \Delta V_b$ [5] $C_{cn} = 2 f_c' b_j a_c$ [5a] $\ldots T_{vrn} + C_{vrn} \le C_{cn}/2$ [5b] $b_j = b_i + b_o$ [5c] $\ldots a_c = \frac{h}{2} - \sqrt{\frac{h^2}{4} - K} \le 0.3h$ [5d] $K = \frac{1}{\phi 2\, f_c' b_j}[\sum M_c + \Delta V_b\, h/2 - \phi(T_{vrn} + C_{vrn}) h_{vr}]$ [5e] $\phi = 0.7$	The vertical bearing strength of the inner panel in terms of horizontal shear is given by (Figure 4): $V_{ib} = \frac{(M_v - V_b\, h)}{d_j}$ [5′] $C_{cn} = \alpha_{cn}\, f_c'\, b_f\, (0.3\, h)$ [5a′] $T_{vrn} + C_{vrn} \le C_{cn}/2$ [5b′] $M_v = C_{cn}\, (0.7\, h) + h_{vr}(T_{vrn} + C_{vrn})$ $\alpha_{cn} = 2.5$ band plates, $\alpha_{cn} = 2.0$ other Joint bearing strength is checked with Equation [6′] Equation 5a' takes into account the beneficial effect of steel band plates in the joint bearing strength

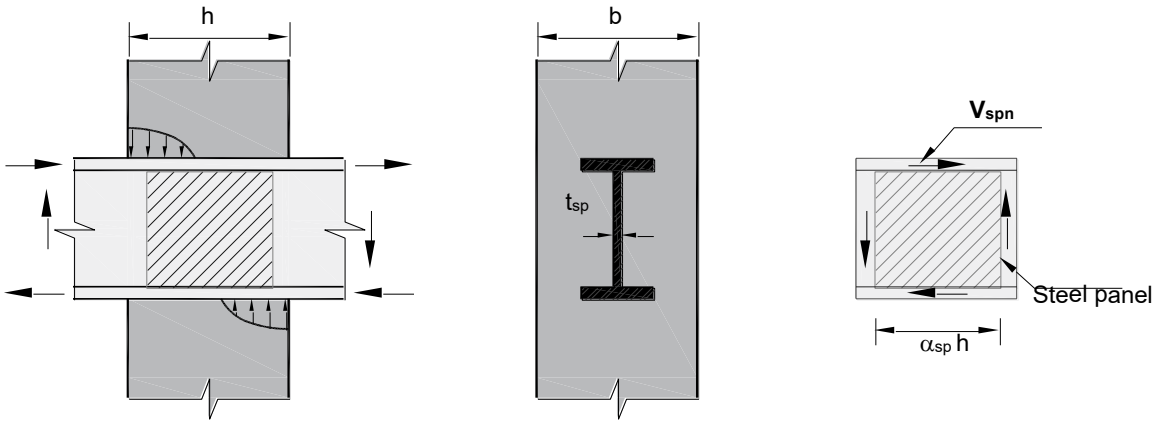
	ASCE Guidelines (1994)	Updated provisions
Nominal strength of the inner panel in terms of horizontal shear	$\phi\, V_i = \phi[V_{sn} + V_{csn}]$ [6] The strength of the inner panel given in [6] is independent of the connection bearing strength which is checked with Eq. (5) $\phi = 0.7$	$\phi\, V_i = \min[\ \phi_s(V_{sp} + V_{ic})\ ;\ \phi_b\, V_{ib}]$ [6′] $\phi_s = 0.85, \quad \phi_b = 0.75$ The strength of the inner panel is taken as the lesser of the horizontal shear strength of the inner panel $\phi_s\,(V_{sp} + V_{ic})$ and the vertical bearing strength of the inner panel in terms of horizontal shear $(\phi_b\, V_{ib})$ (Eq. 5')
Strength of the connection	The shear strength of the joint is checked with [7]: $\sum M_c - V_b jh \le \phi\big[V_{sn} d_f + 0.75 V_{csn} d_w + V_{cfn}(d + d_o)\big]$ [7] $jh = \dfrac{\sum M_c}{\phi(T_{vrn} + C_{vrn} + C_c) - {\Delta V_b}/{2}} \ge 0.7h$ [7a] An iterative process is required to find jh	The shear strength of the joint is checked with [7′]: $\dfrac{\Sigma\, M_b}{d_j} - V_c \le k\,[\phi V_{in} + \phi_s V_{on}]$ [7′] k = 1.0 where large joint deformations are allowed, and k = 0.85 where the intent is to limit joint deformations
Ties required above and below the steel beam	$A_t \ge \dfrac{V_{cfn}}{F_{yt}}$ [9]	$A_t \ge \dfrac{V_{on}}{F_{yt}}$ [9′]
Joint depth-to-bar diameter ratio	$\dfrac{(d + 2d_o)}{d_b} \ge 20$ [10]	$\dfrac{d_j\, 420}{d_b\, F_{yr}} \ge 20$ [10′]
Scope of the provisions	• Interior, exterior, top T and top corner (knee) joints. • Joint aspect ratio 3/4 ≤ h/d ≤ 2 • $f_c' \le 40\ MPa$ • Reinforcing steel $F_{yr} \le 410\ MPa$ • Structural steel $F_y \le 345\ MPa$ • Zones of low-to-moderate seismicity	• Interior, exterior, top T and top corner (knee) joints. • Joint aspect ratio 2/3 ≤ h/d ≤ 3/2 • $f_c' \le 100\ MPa$ • Reinforcing steel $F_{yr} \le 410\ MPa$ • Structural steel $F_y \le 345\ MPa$ • Zones of high seismicity • Applicable to control joint damage

Table - 2. Calculated-to-measured strength ratios
(updated design provisions)

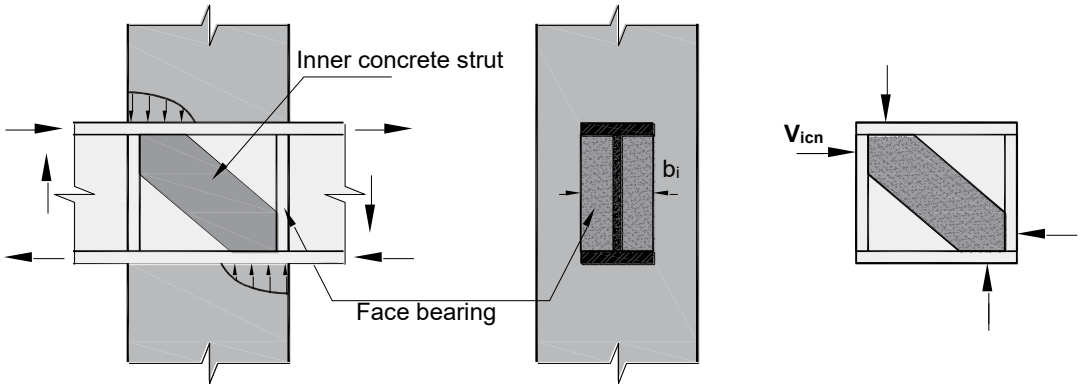
Research Program	Specimen	Joint Details	Calculated-to-measured strength ratio	Failure mode
Sheikh et al. (1989)	4	FBP	1.06	Shear
	5	Thick FBP	1.03	Shear
	6	Doubler plates	0.75	Shear
	7	Wide FBP (1.5 bf)	0.80	Shear
	8	Extended FBP	0.77	Shear
Deierlein et al. (1989)	10	FBP	1.08	Shear
	11	FBP	0.93	Bearing
	15	FBP+SC	0.91	Shear
	17	FBP+SC+VJR	1.09 (max)	Bearing
Kanno (1993)	OB1-1	FBP+EFBP	0.92	Shear
	OBJS1-1	FBP+EFBP	0.90	Shear
	OBJS2-0	FBP	0.83	Bearing
	OJS2-0	FBP+SC	1.02	Bearing
	OJS3-0	FBP+EFBP	0.88	Bearing
	OJS4-1	FBP+EFBP	0.85	Bearing
	OJS5-0	FBP+EFBP+BP	0.82	Bearing
	OJS6-0	FBP+EFBP	1.00	Bearing
	OJS7-0	FBP+EFBP	0.78	Bearing
	HJS1-0+	FBP+EFBP	0.92	Bearing
	HJS2-1+	FBP+EFBP	0.89	Bearing
	OJB-1	FBP+SC	0.85	Shear
	OJB4-0	FBP+SC	0.76	Shear
	OJB5-0	FBP+SC	0.85	Shear
	OJB6-1	FBP+SC	0.80	Shear
Parra-Montesinos and Wight (2001)	1	FBP+SC	1.03	Bearing
	6	FBP+SC	1.01	Shear
	9	FBP+SC+SBP	0.88	Bearing
Fargier-Gabaldón and Parra-Montesinos (2005)	1	FBP+SC+SBP	0.70 (min)	Shear
	2	FBP+SC+SBP	0.76	Bearing

FBP: Face bearing plates
EFBP: Extended FBP
SC: Steel column
SBP: Steel band plate
+ Featured 100 MPa concrete.

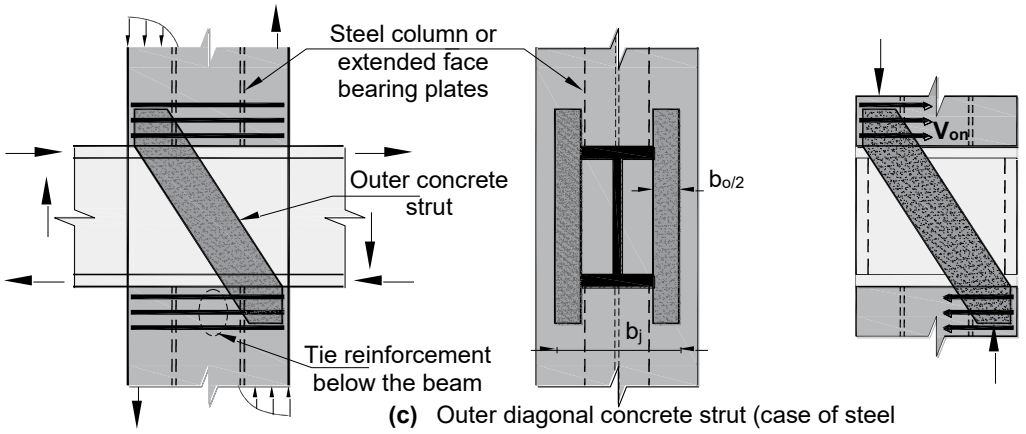
Average (μ) **0.88**
Std (σ) **0.09**



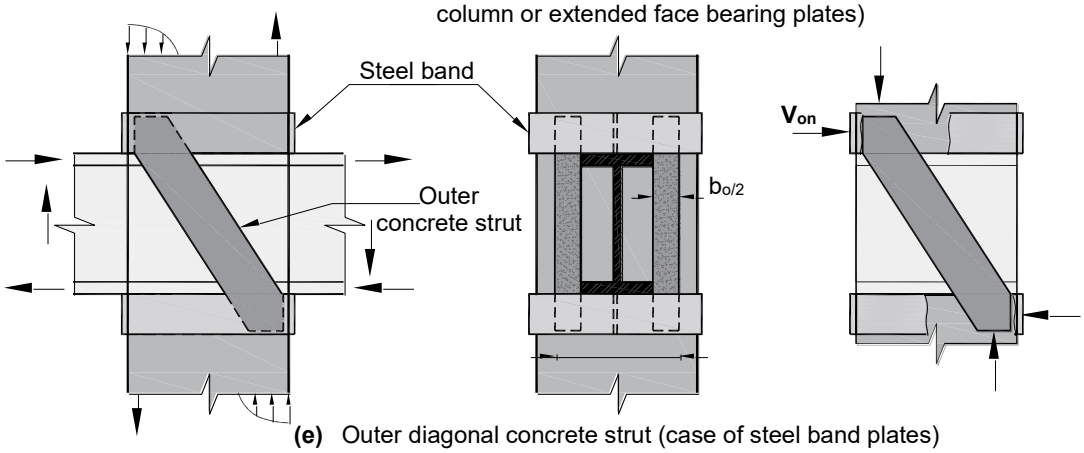
(a) Steel web panel



(b) Inner diagonal concrete



(c) Outer diagonal concrete strut (case of steel column or extended face bearing plates)



(e) Outer diagonal concrete strut (case of steel band plates)

Fig. - 1 Joint shear resisting mechanisms

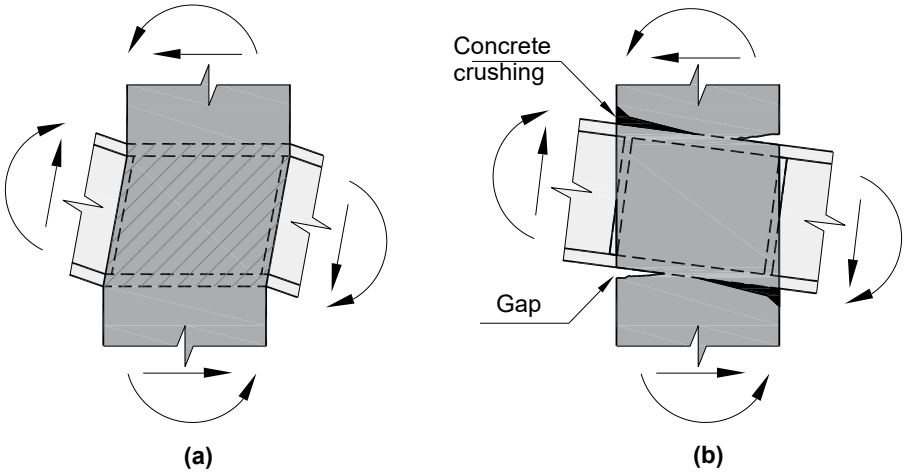


Fig. - 2 Joint failure modes: **(a)** Panel shear and **(b)** Vertical bearing

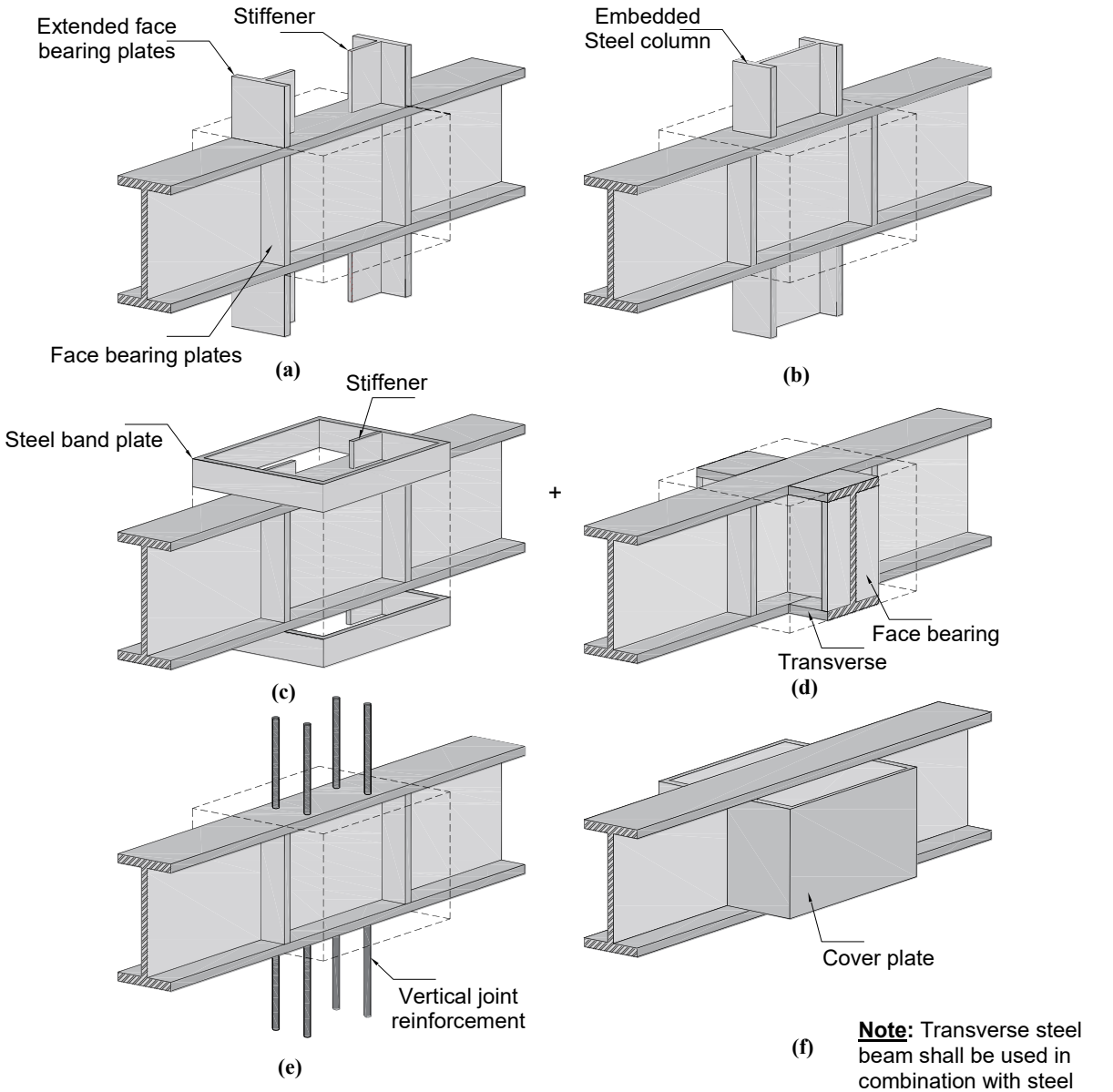


Fig. - 3 Joints details

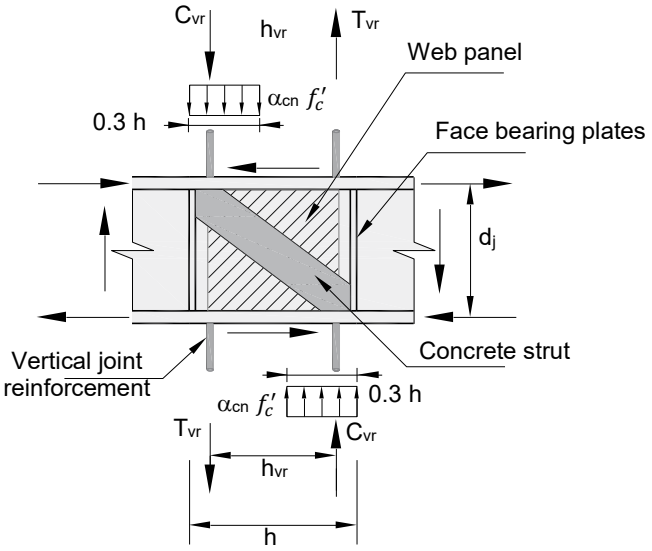


Fig. - 4 Bearing forces acting on the inner panel

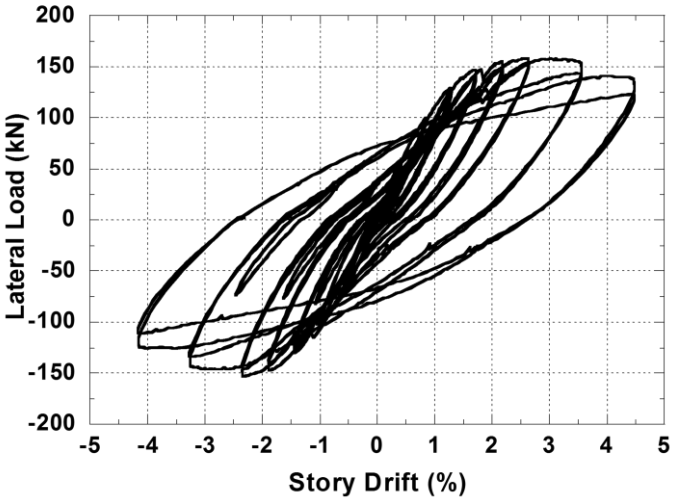


Fig. - 5 Hysteresis of Specimen 2 reported in Liang and Parra-Montesinos (2004)

Notation

A_t= minimum cross sectional area of ties or band plates located within a distance 0.4d above and below the beam;
A_{sh}= cross-sectional area of reinforcement parallel to beam (including cross ties) with spacing s_h;
a_c= length of concrete bearing zone;
b = width the concrete column measured perpendicular to the beam;
b_f = width of steel beam flanges;
b_i = width of inner concrete panel;
b_j = effective width of joint panel;
b_m= maximum effective width of joint region
b_o = width of outer concrete panel;
b_p = width of FBP;
b_p'= width of steel column or extended FBP;
C = mobilization coefficient;
C_c = compression force in concrete bearing zone;
C_{cn} = nominal compression strength of bearing zone;
C_{vr} = compression force in vertical reinforcement;
C_{vrn} = nominal compression strength of vertical reinforcement;
d = depth of steel beam measure parallel to de column axis;
d_b = diameter of column longitudinal bars;
d_{bp} = depth of steel band plate measured parallel to column;
d_c = steel column depth measured parallel to beam;
d_f = distance between beam flange centerlines;
d_j = effective joint depth = $d - t_w$;
d_w = distance between beam flanges (height of web);
F_y = specified yield strength of the structural steel;
F_{yr}= specified yield strength of the column longitudinal bars;
F_{ysp} = specified yield strength of steel web panel in the joint region;
f_c'= specified compression strength of concrete within the joint region;
h = depth of concrete column measured parallel to the beam axis;
h_{vr}=horizontal distance between vertical joint reinforcement;
jh = horizontal distance between bearing force resultant;
k = deformation-based strength reduction factor;
M_{vb} = bearing moment strength of joint;
s_h = center-to-center spacing of column ties;
T_{vr} = tension force in vertical joint reinforcement;
T_{vrn} = nominal tension strength of vertical joint reinforcement;
t_f = thickness of beam flanges;
t_{sp} = thickness of steel web panel;
V_b = beam shear;
$V_{cfn} = V_c' + V_s'$=nominal horizontal contribution of the compression field strength;
V_c = column shear;
V_{ib} = vertical bearing strength of the inner panel in terms of horizontal shear;
V_{in} = nominal horizontal shear strength of inner panel;
V_{icn} = horizontal shear strength of inner diagonal concrete strut;
V_s' = reinforcing steel contribution to nominal compression field strength;
V_c'= concrete contribution to nominal compression field strength;
V_n = nominal horizontal shear strength of the connection;
V_{on} = nominal horizontal shear strength of outer panel (same as the outer diagonal concrete strut);
V_j = horizontal joint shear;
V_{spn} = nominal horizontal shear strength of steel web panel;
V_{uj} = required connection strength in terms of horizontal joint shear;
x = h for the case of extended face bearing plates, h/2 + d_c/2 for the case of steel columns;
y = width of the steel column flange or extended face bearing plate;
ϕ = resistance (capacity reduction) factor;
ΔV_b = net vertical beam shear transferred into column;
ΔV_c = net horizontal column shear transferred into beam;
ρ_s = tie-to-joint volume ratio (volume of ties within the beam depth divided by the joint volume, (d_j h b);
$\sum M_c$= net column moments transferred through joint; $\sum M_b$ = net beam moments transferred through joint.

Innovative Slip-Critical Blind Bolts and Connections for Concrete-filled RHS Columns

Wei Wang[1,2], Mingxiao Li[1,2], Yiyi Chen[1,2] and
1 State Key Laboratory of Disaster Reduction in Civil Engineering,
Tongji University, Shanghai 200092, China;
2 Department of Structural Engineering, Tongji University, Shanghai 200092, China
weiwang@tongji.edu.cn

Xiaogang Jian[3]
3 School of Mechanical Engineering, Tongji University, Shanghai 200092, China
jianxgg@tongji.edu.cn

ABSTRACT. This paper presents an experimental investigation on beam-to-column blind bolted endplate connections using innovative slip-critical blind bolts (SCBB). Eight full-scale beam-to-column cruciform extended endplate connections using the SCBB were subsequently tested under cyclic loading. Three types of stiffening strategies were adopted for the RHS columns, i.e. inner diaphragms, thickened column wall, and filled concrete. For all the cases, the SCBB performed very well and exhibited almost identical behaviour to the traditional high strength slip-critical bolts. Two failure modes of the connections, namely, beam bucking (mode 1) and column damage (mode 2), were generally observed and were found to be influenced by the column stiffening strategies. The stiffening measures were also found to greatly influence the stiffness and strength of the connections. The test result generally showed that a properly design SCBB connection could exhibit very satisfactory cyclic performance, demonstrating a great potential of such concrete filled RHS column-to-beam connection for seismic applications.

1 INTRODUCTION

Concrete filled columns have become an attractive choice for steel and composite building construction, owing to several advantages over open sections. A square or rectangular hollow section (SHS or RHS) column is a typical kind of tubular column which presents the advantage of good bending and torsional resistance, due to its much larger flexural and torsional modulus than open sections. Besides, the column wall can provide constraints for filled concrete, a case which increases the compressive capacity of the concrete. Moreover, the surface painting becomes much easier for concrete filled tubular structures and the appearance is more elegant from an architectural point of view. Meanwhile, concrete filled RHS/SHS columns can be connected with H-beam more easily than circular hollow section (CHS) columns.

Despite the advantages described above, traditional bolting is not readily applicable to the connections between H-beams and concrete filled RHS/SHS columns due to the inaccessibility of the internal space of the tube. Nowadays, welding is still the main method employed for such

connections, where using interior diaphragms, through diaphragms, and external diaphragms are typical solutions. These kinds of connections usually have large initial stiffness, and thus they can be considered as rigid connections according to Eurocode 3 [1]. However, compared with the bolting solution, welding is more demanding in terms of construction effort and may cause quality issues, recalling that a large number of welded connections were severely damaged in the 1994 Northridge and 1995 Hyogoken-Nanbu earthquake. Alternatively, blind bolts, which can be installed and fastened from the outer side of the column, offer a convenient way for connecting H-beams to concrete filled tubular columns. Several types of blind bolts have been developed over the past several decades, including BOM, HSBB and Ultra-Twist from the US, Flowdrill technology from Netherland, Hollo-bolt, RMH and EHB from the UK and Ajax Oneside from Australia. However, it is found that almost none of them can achieve slip-critical bolted connections except Ajax-Oneside from Australia.

Mourad et al. [2] conducted experiments on connections using HSBB (High Strength Blind Bolt) under cyclic loading, but the sleeves were peeled off, leading to decreased preloading level of the bolts. Mourad et al. [3] proposed a design method for extended endplate connections using Ultra-Twist (a new blind bolt in the USA), and some constructional requirements were also given. Harada et al. [4] found that TCBB (Torque-control high-strength Blind Bolt, the same as Ultra-Twist) experienced unexpected pulling out failure of the blind bolt. Yeomans et al. [5] tested several endplate connections with hollo-bolts (published by the British Steel Tubes & Pipes [6]) and also found that the bolts were pulled out, which indicated low pre-tightening forces of the blind bolts. Elghazouli et al. [7] studied the monotonic and hysteretic behavior of hollo-bolt connections, and good ductility was exhibited. A theoretical model for the initial stiffness and bearing capacity of the hollo-bolt connections was proposed by Málaga-Chuquitaype [8]. Tizani et al. [9-10] reported an investigation into the cyclic behaviour of endplate connections to concrete filled tubular columns using the EHB. The results showed that the performance of the blind bolted connections was mainly influenced by the failure modes, and connections with relatively weak columns could exhibit higher energy dissipation and ductility. Lee et al. [11-12] reported an experimental program investigation on blind bolted connections to unfilled hollow section columns using Ajax Oneside [13] from Australia.

To further explore the potential of blind bolts for H-beam to concrete filled RHS/SHS columns, an innovative Slip-Critical Blind Bolt (SCBB) is proposed at Tongji University. The component parts, pre-tightening mechanism, installing procedures and the performances of SCBB are totally different with other blind bolts. A novel split-type spacer, allowing almost the same pre-tightening mechanism as traditional high strength bolt, was introduced into this blind bolt. This special detailing provides possibility for SCBB to possess sufficient pre-tightening force recommended by major codes and makes the blind bolt slip-critical. Experiments were conducted to investigate the connecting performances of the bolts and the hysteretic behaviour of the connections using SCBB with various types of stiffening measure, and the failure modes, strength capacity, ductility, initial stiffness, and energy dissipation are fully examined.

2 EXPERIMENTAL PROGRAM

2.1 Test specimens

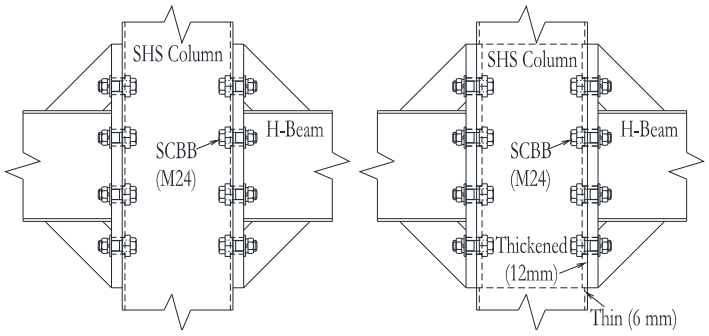
Eight full-scale beam-to-column cruciform extended endplate connections using the SCBB were tested under cyclic loading. The specimens are summarized in Table 1. For ease of identification, each specimen was assigned with a short name, which starts with the thickness of column wall, followed by the strengthening strategies, bolt types or other special characteristics. For example, C6DA5 represents the connection with 6mm column wall, inner diaphragms and axial load ratio 0.5 for the column. The nomenclature used for other specimens follows the same format, in which

CF stands for the concrete filled in the column, HB stands for hollo-bolt, and SB stands for strong beam. Three types of stiffening strategies, namely, inner diaphragms, thickened column wall and concrete filled columns, were adopted to strengthen the SHS columns, and the connection detailing is shown in Figure 1. The SHS columns used in the tests were all cold-formed, with the thickness (t_c) varying between 6 and 12 mm. The beams for specimens S1 through S7 were H-shaped (250×125×3.2×4.5) built-up sections and were fabricated by welding. A hot rolled H-shaped steel beam with a larger section (300×150×6×8 mm) was employed for specimen C6SB. Four rows of M24 SCBB (except C6HB) were used to connect the endplate (550×200×24 mm) to the column, and stiffeners were used between the beams and the extended parts of the endplates. For the parameter matrix among the eight specimens, specimen C6 did not have any stiffening measures. Inner diaphragms were added into the SHS columns of specimens C6D and C6DA5, with a column axial load ratio of 0.2 and 0.5, respectively. The local wall thickness (at the connection zone only) of the column of C12 was twice the thickness of C6, such that the stiffness of the column panel zone was increased. C6CF and C12CF were designed to study the influence of concrete filled columns, in comparison to C6 and C12, respectively. Hollo-bolt (designed by Lindapter, UK) was used in C6HB, designed to check the differences between the two types of blind bolts. Beams of larger sectional dimensions were adopted in C6SB, thus making C6SB a typical specimen of column failure.

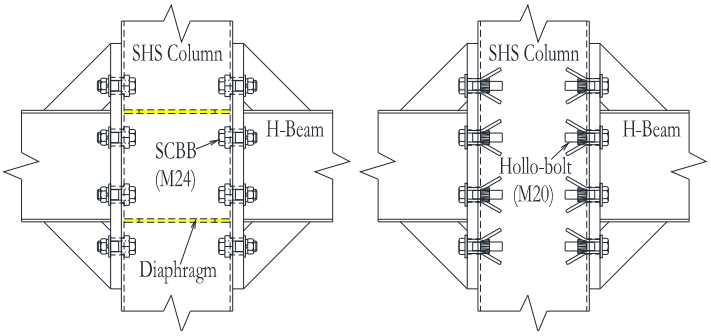
Table 1 – Overview of the eight specimens

No	Specimen	Column /mm	Beam /mm	Axial load ratio	Notes
S1	C6	250×6	250×125 ×3.2×4.5	0.2	No stiffening
S2	C6D	250×6			Diaphragm & axial load ratio 0.2
S3	C6DA5	250×6		0.5	Diaphragm & axial load ratio 0.5
S4	C12	250×6~12		0.2	Thickened column wall
S5	C6CF	250×6			Concrete filled
S6	C12CF	250×6~12			Thickened column wall & concrete filled
S7	C6HB	250×6			With hollo-bolt
S8	C6SB	250×6	300×150 ×6×8		Strong beam-to-weak column

The material properties of the specimens are shown in Table 2. Tensile coupon tests conforming to [14] were carried out to obtain the yield strength, ultimate strength and elongation at fracture of the varying parts of the steel specimens. The compressive strength of the 150 mm concrete cubes were tested soon after the experiment, with an average $f_{c,cube}$ value of 35MPa.



(a) C6, C6CF, C6SB (b) C12, C12CF



(c) C6D, C6DA5 (d) C6HB

Figure 1. – Configuration of the connections.

Table 2. – Material properties.

Steel type	f_y (MPa)	f_u (MPa)	Elongation at fracture
Thin column	313	461	35%
Thick column	411	568	23%
Beam (except C6SB)	350	466	33%
Beam (C6SB)	418	584	29%
Endplate	351	527	30%

2.2 Test set-up

The general test set-up is shown in Figure 2. The effective length of the column is 3180 mm, and the beam span is 1800 mm. Both far ends of the beams were pinned in plane, and spherical hinges were set at the top and bottom of the columns, respectively. To resist the horizontal reaction load, a bracing with a pipe section was placed between the top of the column and the reaction frame. Two actuators were vertically positioned at the east and west ends of the beams. Both beams were laterally supported by universal ball joints, avoiding out-of-plane stability problems. Besides, to study the influence of the axial load ratio, a constant axial load was applied to the column through a jack at the top.

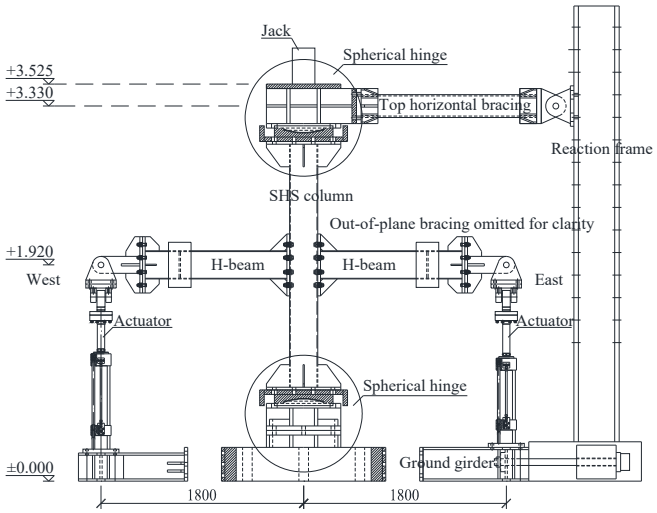


Figure 2. – Schematic of test set-up.

2.3 Loading procedure

Quasi-static cyclic loading procedure based on AISC 341-10 [15] was adopted, as illustrated in Figure 3, in which the whole procedure is displacement-controlled. The two actuators were connected to the same pump, and the loads at both beam ends were applied synchronously.

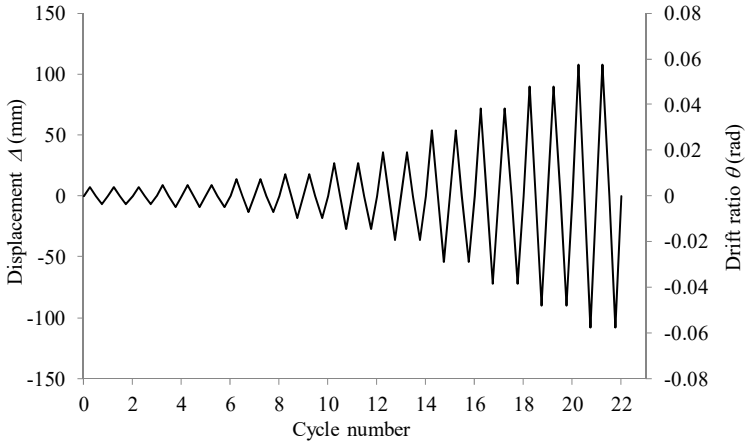


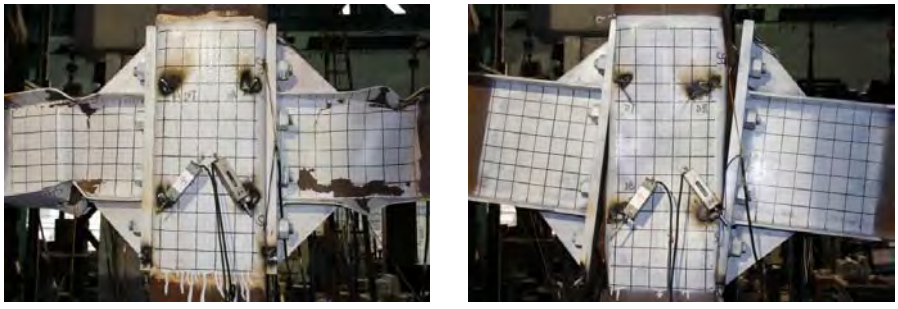
Figure 3. – Illustration of AISC cyclic loading procedure.

3 FAILURE MODES AND OBSERVATIONS

The end-plate was designed according to Chinese code CECS102-2002 [16], thus it is relatively strong in comparison to the H-beams and concrete filled SHS columns. Therefore, the failure modes were mainly influenced by the beams and columns, and the typical failure modes of the connections are shown in Figure 4. Two types of failure modes were generally identified which are described as follows:

Failure mode I: severe inelastic buckling of beam sections. The beams of this failure mode were relatively weaker than the column and the connection zone, thus buckling occurred to the beam sections after its initiation of section yielding. C12CF (shown in Figure 4(a)) is a typical specimen exhibiting failure mode I, where the column and the connection zone generally stayed elastic.

Failure mode II: excessive plastic deformation of column walls. The strength of the column wall was relatively small, and the column acted as the primary source of deformation. Due to the pulling-out tendency of the bolts, gaps were developed between the end-plates and the column walls, and were kept broadening with the increasing of the inter-story drift angle. Test C6SB is taken as representative of failure mode II, as shown in Figure 4.



(a) Connection with failure mode I (b) Connection with failure mode II

Figure 4. – Representative failure of the connections.

3.1 Specimens C6 & C6CF

For specimen C6, at the beginning of the loading process, the tensile action of the blind bolts caused local bending deformation of the column front walls accompanied by out-of-plane deformation of the column side walls. Soon afterwards, the column entered into the inelastic deformation stage. Due to the relatively thin column wall, a gap, with a maximum value of 22 mm, between the endplate and the column front wall was evidently formed. The steel beams experienced evident local buckling when the inter-story drift (θ) approached 7% and the load carrying capacity began to fall. Fractures occurred to the welds connecting the web and flange of the east beam (θ=9%), leading to a sharp drop (more than 50%) of the load carrying capacity.

The filled concrete in specimen C6CF restricted the concave deformation of the column wall, but the gap between the end-plate and the column front wall was still visible, although narrower than that of C6. The white wash applied over the panel showed that initial yielding started at 0.375% drift. Yielding of the beam was first recorded at 1.5% drift. The beams started to buckle at 3% drift and fractured at 6% drift, and afterwards the load carrying capacity started to decrease. For these two connections, failure mode II appeared first, but they finally failed by mode I (inelastic buckling of the beams).

3.2 Specimens C6D & C6DA5 with inner diaphragms

For specimen C6D, the diaphragm restricted the deformation of the column wall to some extent, thus reducing the aforementioned gap. At 1.5% drift, a gap developed between the endplate and the column at the height where the diaphragms located. The load reached its peak value at 4% drift, and then dropped very quickly upon buckling of the beam flanges and webs. It is recalled that the ductility of specimen C6D was lower than that of specimen C6. However, much higher initial stiffness was obtained in specimen C6D, and this phenomenon will be discussed in detail in section 4.2.

The observed failure mode of specimen C6DA5 (axial load ratio r=0.5) was similar to that of C6D. Due to the larger axial load ratio, the column in C6DA5 yielded earlier, and its initial stiffness was therefore slightly lower than C6D.

3.3 Specimens C12 & C12CF with thickened column wall

Due to the increased strength and stiffness of the panel zone, severe buckling occurred to the beams very early and led to a rapid fall of the load carrying capacity of specimens C12 and C12CF. Only a very small gap could be seen between the endplate and the column wall at 1.5% while the beam section experienced full yielding. The beams started to buckle at θ=2%, a drift level which is much smaller than that observed in the previously discussed specimens. The column of specimen C12 almost remained elastic and the gap at the endplate was very small. The initial stiffness was greatly improved due to the thickened column wall, but the ductility of the connection was lower than specimen C6 and this was attributed to the early buckling of the H-shaped beams.

The column of specimen C12CF was further strengthened by the presence of the filled concrete, and it almost stayed elastic during the entire test procedure. The load reached its peak value at only 1.5% drift and the plastic hinges were observed at the sections where the stiffeners and beams intersected. Beams buckled earlier compared with specimen C12.The loading capacity fell by 75% at 5% drift due to the fracture of the welding. White wash peeled off from the beam surface in a large area of the plastic hinge. The above test observations clearly indicate that the two specimens (C12 and C12CF) fail by failure mode I.

3.4 Specimen C6HB with hollo-bolts

Hollo-bolts were used in specimen C6HB to examine the influence of bolt types on the connection behavior. In a previous tensile test on hollo-bolts conducted by the authors, it was found that the

hollo-bolt is susceptible to shear failure of the sleeves, leading to decreased tensile capacity when compared with the traditional high strength bolt. This explains the large difference between specimen C6HB (hollo-bolt) and C6 (SCBB) which was that the column wall and the endplate in specimen C6HB became separate where the bolts located when encountering tensile forces, indicating low pre-tightening forces of the hollo-bolts. Some bolts even slacked at 8% drift with a tendency of being pulled out, after which the hollo-bolts almost quitted working. Beams remained elastic while the columns experienced excessive plasticity. This connection exhibited failure mode II accompanied with bolt failure.

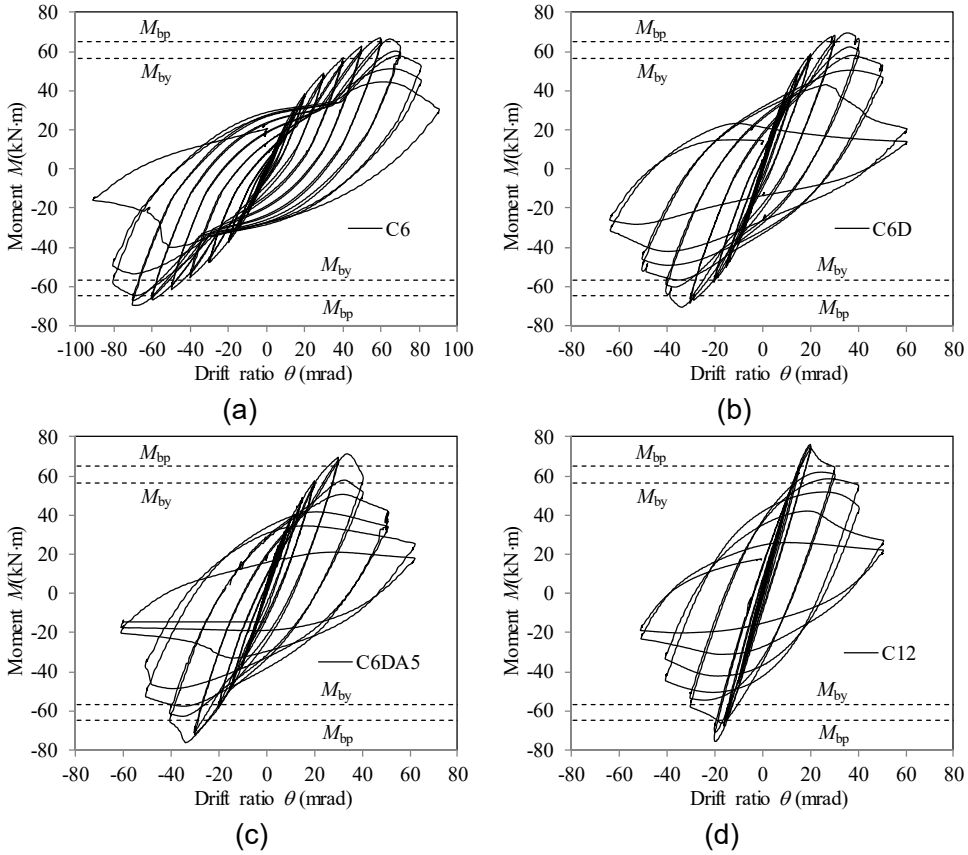
3.5 Specimen C6SB with stronger beams

The beams in specimen C6SB were relatively strong, leading to a 'strong beam, weak column' connection. The column demonstrated very large out-of-plane deformation and huge gaps were observed between the endplate and column wall. The load carrying capacity was higher than that of the other specimens because of the larger beam sections. Some of the bolt holes began to crack at 8% drift, resulting in relaxation of the SCBB. Severe concave deformation occurred to the column wall and the connection finally failed by mode II coupled with cracking of bolt holes.

4 MOMENT-ROTATION RESPONSES AND FURTHER DISCUSSIONS

4.1 Moment-rotation curves

The moment-rotation curves of the specimens are shown in Figure 5.



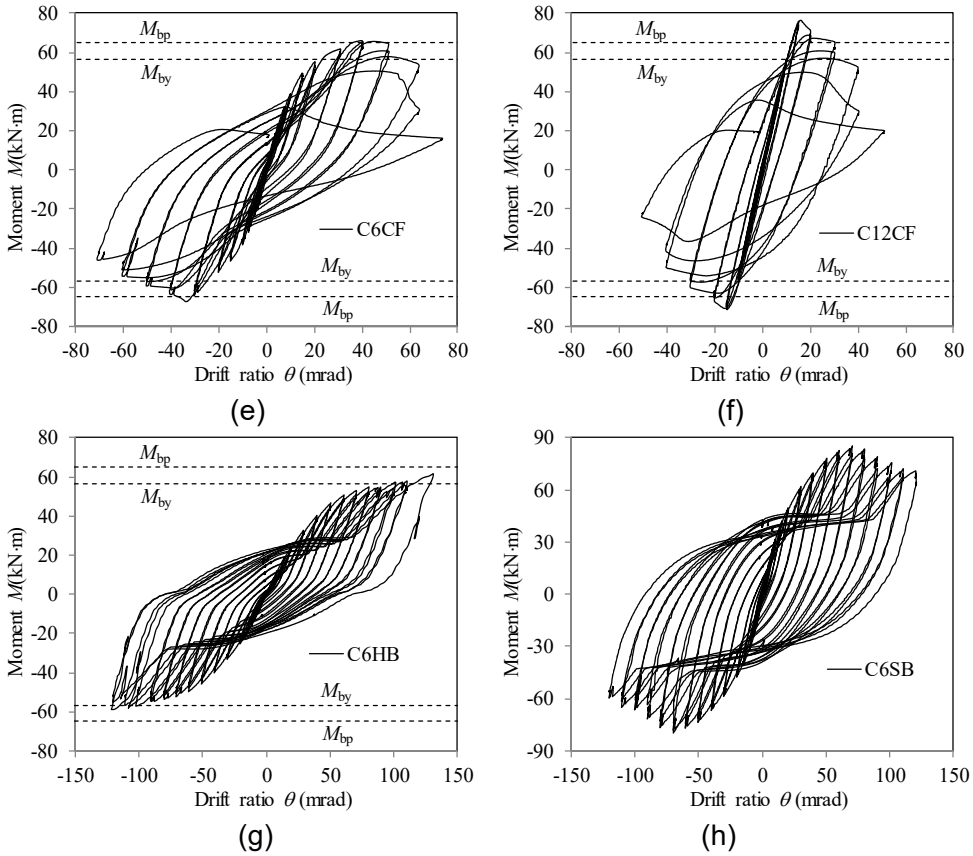


Figure 5. – Moment-rotation curves of each specimen.

Figure 5a and e show the hysteretic curves of specimens C6 and C6CF, both undergoing mode II but finally failed in mode I. The curves exhibited pinching effect at the beginning due to the excessive out-of-plane deformation of the column side walls and the gap between the column wall and the endplate. After the column experienced yielding, the stiffness of the column became much smaller, which led to the pinching hysteretic curves of the specimens. The curves experienced sharp drops when severe welding fracture occurred in the last two or three cycles, and some minor decrease of load took place due to beam buckling and micro-cracks of welds. The hysteretic curve of specimen C6CF demonstrated lower ultimate displacement due to the filled concrete which restricted the deformation of column and hence causing earlier buckling of the beams.

Figure 5b,c,d and f show the hysteretic curves of specimens C6D, C6DA5, C12 and C12CF that failed by mode I (inelastic buckling of beams). The hysteretic curves dropped very early compared with specimens C6 and C6CF due to the existence of inner diaphragms or thickened column walls, leading to early buckling of the beams.

Figure 5g and h show the hysteretic curves of specimens C6HB and C6SB that failed by mode II (column failure). These curves exhibited significant pinching effect and the beams did not buckle during the whole test. The load carrying capacity of C6SB fell slowly with the cracking of the bolt holes. The beams in specimen C6SB were stronger, and the ultimate load is significantly below the one causing yielding of the beam section.

4.2 Initial stiffness and connection classification

The connections can be classified by their initial stiffness (S_{ini}) and strength according to Eurocode 3 [1]. A connection may be classified as rigid when $S_{ini}$is no less than $k_b EI_b/L_b$ (k_b equals 8 and 25

for non-sway and sway frames, respectively; E and I_b are the elastic modulus and moment of inertia of the beam; L_b is the span of the beam, taken as 4 m in this paper), or nominally pinned when S_{ini} is no greater than $0.5EI_b/L_b$. A semi-rigid connection is that with S_{ini} between k_bEI_b/L_b and $0.5EI_b/L_b$. From a strength point of view, a connection may be classified as full-strength when its design moment resistance (M_{Rd}) is no less than either the design plastic moment of the beam ($M_{b,pl,Rd}$) or the column ($M_{c,pl,Rd}$), or nominally pinned when M_{Rd} is no greater than a quarter of the minimum value of $M_{b,pl,Rd}$ and $M_{c,pl,Rd}$, and again, a partial-strength connection is that with the moment resistance in between.

It should be noted that when calculating the connection stiffness, some sources of deformation, including beam elastic bending, column elastic bending and the rigid-body rotation of the column, should be excluded. The connection classification result is shown in Figure 6 and Table 3. Connection C6 without any stiffening measures is classified as semi-rigid with relatively low initial stiffness. Specimens S2 through S5 all have very large stiffness and can be classified as rigid (non-sway), which indicates that the inner diaphragms, the thickened column wall, or the filled concrete can greatly increase the initial stiffness of the connections. Specimen C12CF has a further increased stiffness due to the existences of both the thickened column wall and the filled concrete, and thus it can be classified as rigid in sway frames. The result above also reveals that the initial stiffness of the considered specimens is mainly influenced by the column panel zone. Larger stiffness can be obtained in the connections with stronger columns. Specimens S1 through S6 all failed in mode I finally, so they exhibited full-strength behavior. The remaining two connections which failed in column or blind bolt are partial-strength connections.

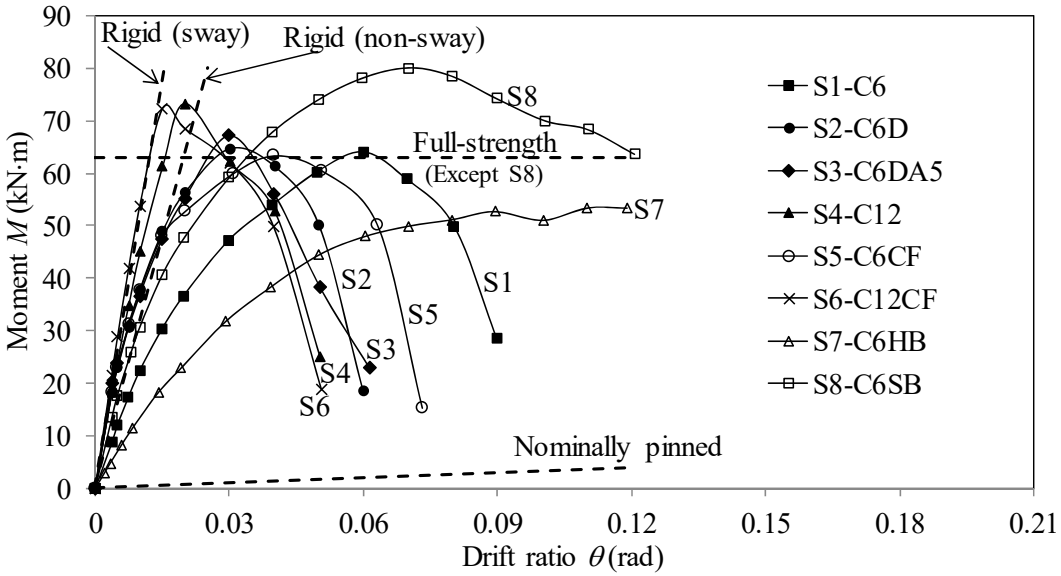


Figure 6. – Comparison of M-θ envelope curves.

Table 3. – Initial stiffness and connection classification.

Specimen	Features	S_{ini} (10^9N·mm/rad)	By stiffness	By strength
C6	Not stiffened	3.894	Semi-rigid	Full-strength
C6D	Inner diaphragms (r=0.2)	9.895	Rigid (non-sway)	
C6DA5	Inner diaphragms (r=0.5)	8.993		
C12	Double thickened column	13.974		
C6CF	With concrete filled	12.528		
C12CF	With concrete filled	33.414	Rigid(sway)	
C6HB	Hollo-bolt	1.650	Semi-rigid	Partial-strength
C6SB	Stronger beams	4.649		

5 SUMMARY AND CONCLUSIONS

Eight full-scale beam-to-column cruciform extended endplate connections using innovative slip-critical blind bolts have been tested under cyclic loading. Three types of stiffening strategies, namely, inner diaphragms, thickened column wall, and filled concrete, were adopted for the SHS columns. The load carrying capacity, ductility, initial stiffness, connection classification, stiffness degradation and energy dissipation of the specimens were discussed in this paper. Confidence was gained from the experimental study towards future application of the considered beam-to-concrete filled RHS column blind bolted connections against seismic action. The main conclusions can be summarized as follows:

(1) The SCBB performed very well and exhibited almost identical behavior to the traditional high strength slip-critical bolts. On the contrary, some hollo-bolts used in specimen C6HB experienced early relaxation prior to bolt hole damage, a phenomenon which indicated possible shear failure of the sleeves and its low pre-tightening forces.

(2) Two types of failure modes were observed, i.e. plastic beam buckling failure (mode I) and column failure (mode II). The connections with failure mode II exhibited pinching effect in their moment-rotation curves, and led to higher ductility but lower damping ratio compared with the specimens with failure mode I.

(3) The inner diaphragms, thickened column wall, or the concrete filled column can greatly improve the initial stiffness of the connection, allowing a rigid connection behavior to be exhibited according to Eurocode 3. The strength of the connections is influenced by the failure mode, and is further affected by the relative resistance of each element.

(4) The SCBB and the corresponding connections have been proved to achieve the basic standard of field weld-free construction of steel and composite buildings in high seismic regions. The potential application of such connections is envisaged in the future.

ACKNOWLEDGEMENTS

The research presented in this paper was sponsored by the National “Twelfth Five-Year” Plan for Science & Technology Support Program through Grant No. 2015BAL03B01-2.

REFERENCES

[1] BS EN 1993-1-8:2005. Eurocode 3: Design of Steel Structures - Part 1-8: Design Of Joints. British Standards, 2005.

[2] Mourad S, Ghobarah A, Korol R M. “Dynamic Response of Hollow Section Frames with Bolted Moment Connections”. Engineering Structures, 1995, 17(10):737-748.

[3] Mourad S, Korol R M, Ghobarah A. Design of extended end-plate connections for hollow section columns. Canadian Journal of Civil Engineering, 1996,23(1):277-286.

[4] Harada Y, Arakaki T, Morita K. Structural behaviour of RHS column-to-H beam connection with high strength bolts. Steel Structures, 2002,2:111-121.

[5] Yeomans N F. Rectangular hollow section column connections using the Lindapter Hollo-Bolt. Tubular Structures VIII, 1998.

[6] SHS Jointing: Flowdrill & Hollo-Bolt. British Steel Tubes & Pipes,Corby, 1997.

[7] Elghazouli A Y, Málaga-Chuquitaype C, Castro J M, et al. Experimental monotonic and cyclic behaviour of blind-bolted angle connections. Engineering Structures, 2009,31(11):2540-2553.

[8] Málaga-Chuquitaype C, Elghazouli A Y. Component-based mechanical models for blind-bolted angle connections. Engineering Structures, 2010,32(10):3048-3067.

[9] Tizani W, Al-Mughairi A, Owen J S, et al. Rotational stiffness of a blind-bolted connection to concrete-filled tubes using modified Hollo-Bolt. Journal of Constructional Steel Research, 2013,80:317-331.

[10] Tizani W, Wang Z Y, Hajirasouliha I. Hysteretic Performance of a New Blind Bolted Connection to Concrete Filled Columns under Cyclic Loading: An Experimental Investigation. Engineering Structures, 2013, 46(1):535-546.

[11] Lee J, Goldsworthy H M, Gad E F. Blind bolted T-stub connections to unfilled hollow section columns in low rise structures. Journal of Constructional Steel Research, 2010, 66(8):981-992.

[12] Lee J, Goldsworthy H M, Gad E F. Blind bolted moment connection to unfilled hollow section columns using extended T-stub with back face support. Engineering Structures, 2011, 33(5):1710-1722.

[13] ONESIDE brochure. Ajax Engineered Fasteners - BN012 data sheet, 2002. www.ajaxfast.com.au

[14] GB/T228.1-2010. Metallic materials – Tensile testing – Part 1: Method of test at room temperature. Chinese National Code, 2010.

[15] ANSI/AISC 341-10. Seismic Provisions for Structural Steel Buildings. American National Standard, 2010

[16] CECS102:2002. Technical Specification for Steel Structure of Light-weight Buildings with Gabled Frames. China Association for Engineering Construction Standardization, 2002.

Braced Frame Connection with Square CFT Columns Penetrated by Gusset Plates

Peng Wang#1
South China University of Technology
Guangzhou, China
pwang1987@126.com

Jianrong Pan#2*
South China University of Technology
Guangzhou, China
ctjrpan@scut.edu.cn

Jingmin Liang#3
South China University of Technology
Guangzhou, China
897864197@qq.com

Huashen Xie#4
South China University of Technology
Guangzhou, China
1450093791@qq.com

Zhan Wang#5
South China University of Technology
Guangzhou, China
wangzhan@scut.edu.cn

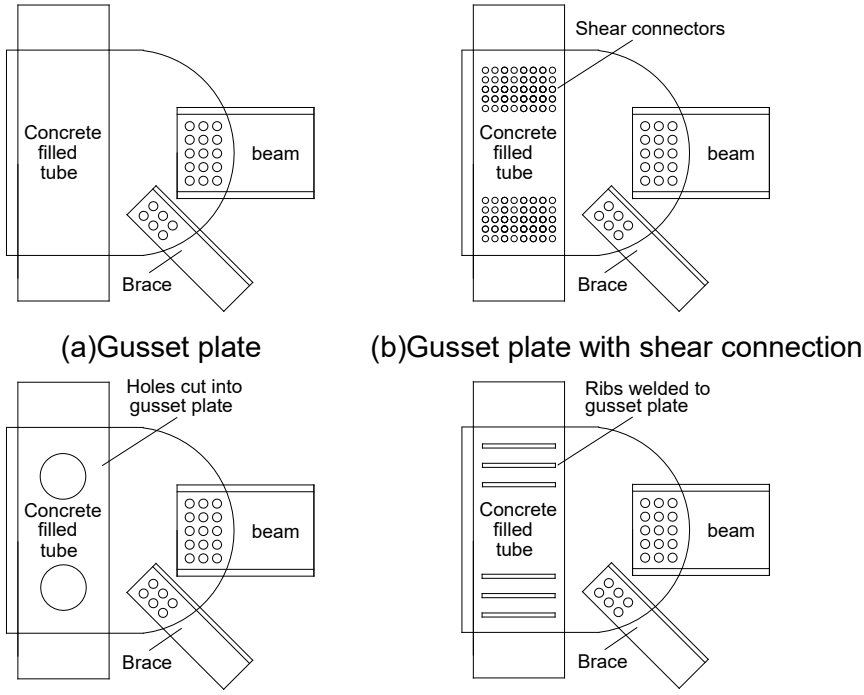
ABSTRACT

This paper describes an investigation into the behavior of braced frame connections with square CFT columns, comprised of a penetrating gusset plate. Four simplified connections with different construction details of the gusset plates were subjected to compressive load. The force transferring mechanism between steel and concrete and the composite action in the column were investigated. The experimental results revealed that the forces between steel and concrete with penetrating brace frame connections were delivered through the bearing caused by the edge of gusset plate, of the ribs or a hole added to the plate into the concrete infill. The construction details including with ribs or a single hole significantly enhanced the efficiency of force transmission and the composite action level in the column. The penetration braced frame connections with square CFT columns assure that square CFT column and composite connection are adequate to develop the required resistance for a wide range of braced frame systems.

INTRODUCTION

Braced frames with CFT columns are stiff, strong and economical structural systems for the reason that concrete-filled tube columns provide large axial stiffness and bracing system provides substantial lateral strength and stiffness. Therefore, a wide range of brace-beam-column (BBC) connection types have been used to connect braces and beams to composite columns in braced frames with CFT columns, such as penetration connection and internal diaphragm connection.

Braced frames with CFT columns usually require large diameter tubes, and the design bond stress of this column is usually too small to satisfy the shear transfer demands. Penetration connection is one kind of the viable BBC connections to improve the shear transfer capacity of most CFT columns. Penetrating gusset plate connections aid in the force transferring by adding direct bearing of steel on concrete, and this bearing mechanism could transfer forces between the steel and concrete readily. There are several ways to achieve the penetrations of connection, and the economical constructions of gusset plate penetrations are illustrated in Figure 1. The connection gusset plate fits within slots in the steel tube during fabrication and then welded to the tube. This type of steel-to-steel connection type is made for the beam and brace attachments, and it permits quick and economical fabrication.



(a)Gusset plate (b)Gusset plate with shear connection

(C)Gusset plate with holes (d)Gusset plate with ribs

Fig.1- Typical braced frame connections with CFT columns penetrated by gusset plates

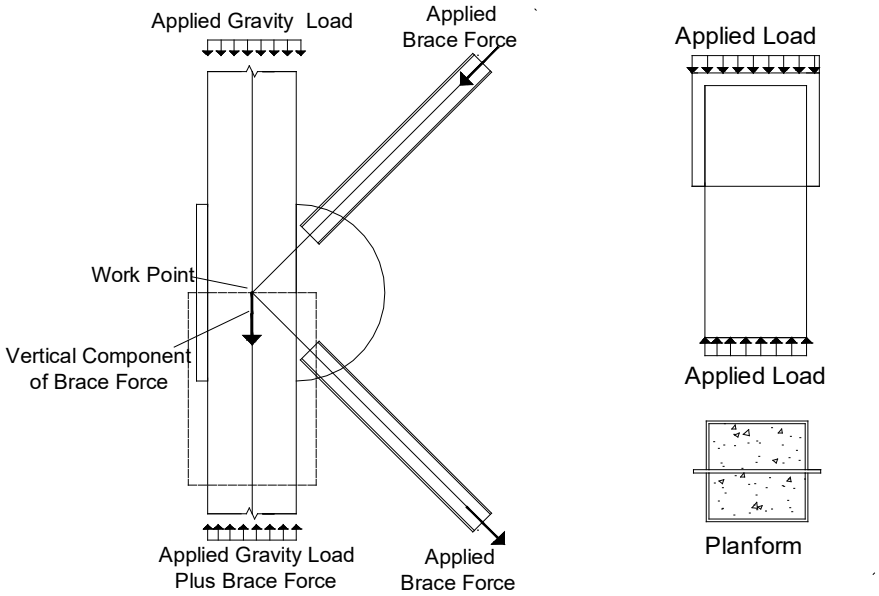
Both circular and square CFT columns are widely used in recent years. Nevertheless, more research studies have been conducted on circular CFT columns and connections. A series of non-linear analyses (MacRea, Kimura and Roeder 2003) and experimental studies (MacRae, Roeder, Gunderson and Kimura 2003) were completed to evaluate the behavior of

penetration connections of circular CFT columns. The results showed that penetration connections of circular CFT columns in braced frames have enhanced the composite action effect between steel and concrete and is revealed the law of load transfer and distribution between steel plate and concrete. Design guidance is obtained from these studies results.

Braced frames with square CFT columns have more regular shape and better adaptability to construction. However, little research has been carried out on the penetration connections of braced frames with square CFT columns. This limits the generalization of braced frame with square CFT columns. In this paper, experiments were conducted on the basis of simplified braced frame connection with square CFT columns penetrated by gusset plates. The connection behavior was discussed and the composite action of each specimen was evaluated.

CONNECTION SIMPLIFIED

The common actual braced frame connections with square CFT columns penetrated by gusset plates as show in Figure 2(a), would be difficult and expensive to carried out experiment with realistic boundary conditions. Therefore, a simplified connection could be used instead of the actual braced frame connection to be tested. Figure 2(b) shows how the simplified connection relates to the prototype one. The simplified one represents the bottom half of a gusset plate penetrated through a square CFT column, which is used to transfer the downward brace force shown in Figure2 (a) into the concrete infill. This force is represented in the experimental tests by a uniform vertical load applied at the top of the gusset plate. Due to symmetry in the connection, the upper half of the connection prototype would have the same behavior for an upward brace force. This simplified method has been proved to be viable (Gunderson 2003).



(a)Brace-Beam-Column connection idealization

(b)Simplified CFT connection test setup

Fig.2 – Simple frame connection

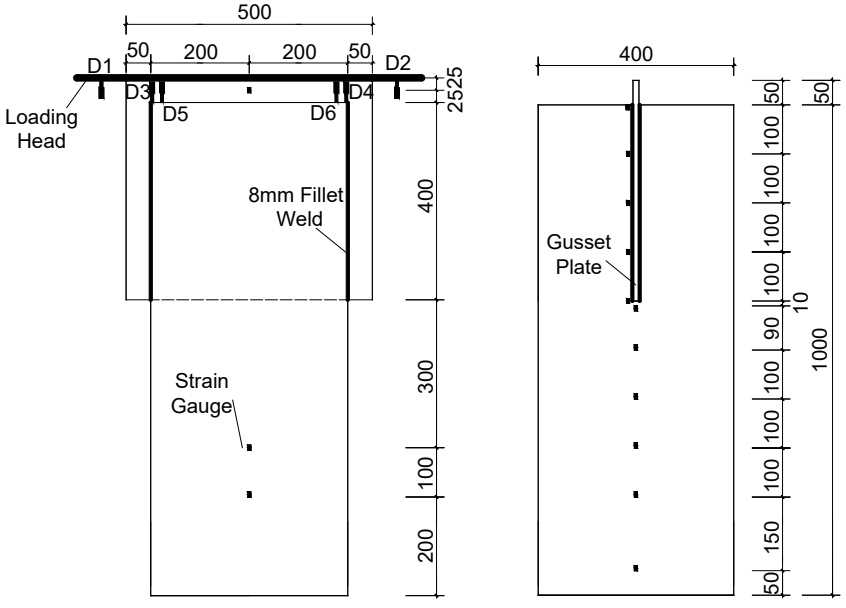
EXPERIMENTAL PROGRAM

Test specimens

The experimental study of simplified connection was carried out to determine the effectiveness of each connection detail in transferring forces from the gusset plate to the concrete infill and the tube, as well as the level of composite action of each connection type.

Four specimens were designed and built to simulate practice employed in common prototype square CFT-BBC connections. For the standard specimen with plain gusset plate, as shown in Figure 3, the simplified column adopted in test was 1000mm in height and 400mm in width. The gusset plate fits within slots in the tube, which were cut to a depth of 400mm and width of 2mm plus the gusset plate thickness. The projection of the gusset plate above the tube was approximately 50mm, which was used for loading. The gusset plate was welded on the outside of each side of the tube all the way around by using 8mm fillet welds. The construction details of each specimen are showed in Table 1.

The elastic modulus, yield strength and ultimate strength of the steel used were determined by the material test before the connection test, providing relevant basis for test loading analysis. Tension tests were carried on steel coupons cut from the tube and plate in the connection tests. These included 9 steel coupons (three for each steel tube and plates) were tested quasi-statically under monotonic tension to determine the stress-strain properties, the mean values of three same specimens were summerised in Table 2, besides, three standard concrete cylinders for the conrete slab were air cured beyond 28 days, the average compression strength of concrete cylinders was 30.8Mpa.



(a)Front view (b)Lateral view

Fig.3 – Typical test specimen dimensions and strain gauge instrumentation

Tab.1 – Details of each specimen

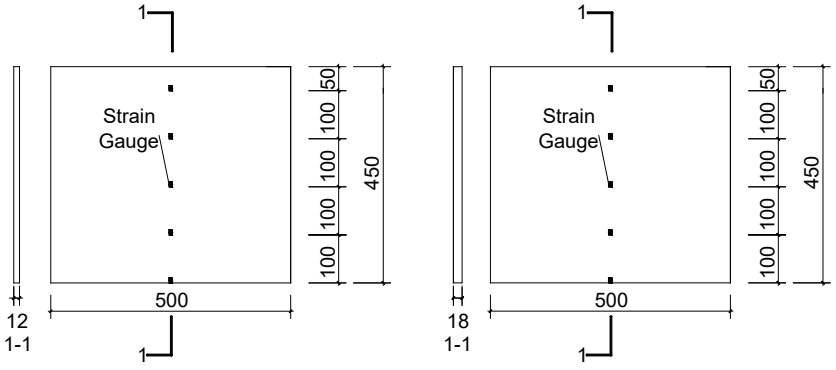
Specimen Number	Steel Tube Size (mm)	Plate Thickness (mm)	Plate Detail
SJ-1	400×10×400	12	Plain
SJ-2	400×10×400	18	Plain
SJ-3	400×10×400	12	Single Hole:
SJ-4	400×10×400	12	6 Solid square ribs

Tab.2 –Mechanical properties for the structural steels

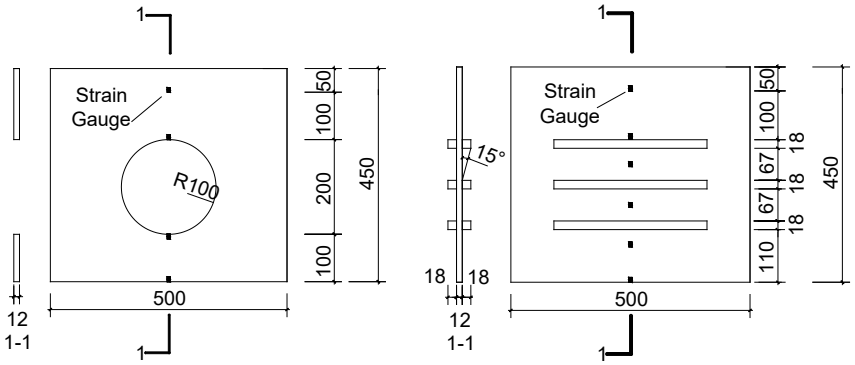
Material Sample	Thickness (mm)	Yield Stress f_y (MPa)	Ultimate Stress f_u (MPa)	Elasticity Modulus E_s(10^5MPa)
Plate-18mm	17.92	400	550	2.07
Plate-12mm	11.59	440	580	1.88
Tube	9.49	440	580	1.89

Test set-up and instrumentation

As shown in Figure 3, the displacement instruments were set on the loading device and both the top of the steel tube and the concrete infill, used to measure the loading displacement and the slippage between the steel and concrete. The strain gauges were attached to the main part of the gusset plate and the steel tube, as shown in Figure 3 and Figure 4. The main contents of the test include: vertical load of the gusset plate, vertical displacement of the loading head, slippage between the steel and the concrete infill, strain of the tube and gusset plate.



(a)Plain:12mm (b)Plain:18mm



(c)Single hole (d)6 Solid square ribs

Fig. 4 – Gusset plate dimensions and strain gauge instrumentation

Loading procedure

As the monotonic loading test progressed, the axial load was applied to the gusset plate by 100kN each step until the yield of the gusset plate was achieved. Then, the load was applied down to 50kN each step and stopped when out-of-plane bucking occurred at the gusset plate.

EXPERIMENTAL BEHAVIOR

General Behavior

The load applied to the plate was transferred to the square steel tube through the welds and to the concrete by means of bearing and friction. Strain in the tube and concrete increased with greater applied load. The final state of the specimen showed that there was obvious plastic deformation in the top 50mm of the gusset plate, and the out-of-plane buckling emerged at the gusset plate. The contact surface between the square steel tube and the concrete was stripped.

Due to varying gusset plate thicknesses and eccentricities between the loading head and the gusset plate, the yield load and the ultimate load of each specimen differed. The yield load is defined as the load when the top 50mm of the gusset plate yielded and the ultimate load only indicates the maximum applied load that the gusset plate could carry during the loading process, and this value does not represent the failure in the connection. At the same load level, the test results between the individual specimens can be compared. The main parameters of the test result are summarized in Table3.

Tab.3 –Main parameters of test results

Specimen Number	Description	Yield Load F_y (kN)	Ultimate Load F_u (kN)	Max Displace (mm)	Max Slippage (mm)	Composite Action (%)
SJ1	Plain:12mm	2500	2950	7.10	0.342	47.5
SJ2	Plain:18mm	3500	4550	12.55	0.635	54.7
SJ3	Single hole	2100	2850	9.70	0.292	69.4
SJ4	6 Solid square ribs	2600	3200	10.50	0.185	85.4

Composite Behavior

The amount of composite action of specimen was described by the percentage of composite action, G_{pc}, which was computed according to Eq.1(a). The ε_{gauge} in Eq.1(a) is equal to the strain measured in the square steel tube during the experiment, ε_{steel} is the expected strain in the steel tube if there is no concrete and it is computed as $P/(A_{tube}E_{steel})$, where A_{tube} is the cross-section area of the tube, and E_{steel} is the elastic modulus of the steel of 189GPa, and P is the axial load on the test specimen. The strain expected in the specimen if it is to remain fully composite, ε_{comp}, is computed according to Eq.1(b) where A_{conc} is the area of concrete in the tube and E_{conc} is the elastic modulus of concrete.

Respectively, when ε_{gauge} is completely equal to ε_{steel}, the steel is carrying all of the force and the present composite G_{pc} is equal to 0%, and if ε_{gauge} is equal to ε_{comp}, then the present composite G_{pc} is equal to 100%. The percent composite values were initially greater than 100% in some cases because initial bond between the steel and concrete could have contributed to the amplified.

The precent composite G_{pc} was calculated from strain gauges at 200mm of the steel, from those 300mm of the steel, from the concrete strain 300mm, from the base and from displacements in the bottom 600mm of the specimen as shown in Figure3. The square steel tubes never reached their yield point within the lower 400mm, so the use of the maximum change in strain can be used to establish an average stress. The G_{pc} from the strain gauges at 200mm and 300mm of the steel were similar indicating little bond transfer in between these gauges. The G_{pc} from the concrete stress gauges and from the displacements at the bottom of the test specimen also indicated similar trends to those obtained from the steel strain gauges. The final composite action values for each specimen represent a weighted average of the four methods described above. As mentioned before, the composite action was high at the initial loading phase, and the design process mainly considers the elastic phase before the yield. Therefore, the average of percent composite action was calculated from the results during the load degree of 1000kN to the yield.

$$G_{pc}=\frac{\varepsilon_{steel}-\varepsilon_{gauge}}{\varepsilon_{steel}-\varepsilon_{comp}}\times 100\% \tag{1a}$$

$$\varepsilon_{comp}=\frac{P}{A_{tube}E_{steel}+A_{conc}E_{conc}} \tag{1b}$$

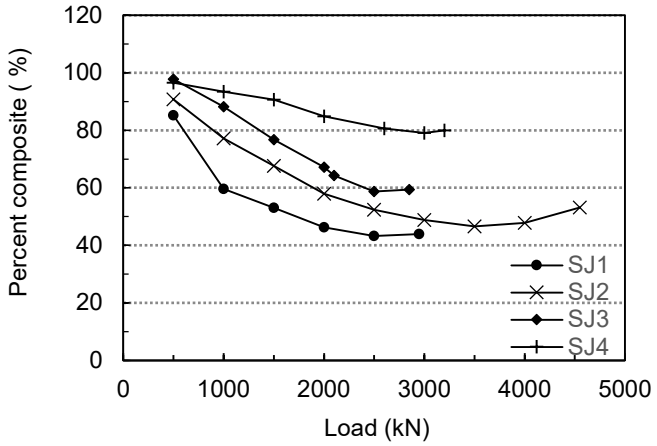


Fig.5 – Composite action

The average of percent composite action for each specimen was computed according to Eq.1(a), as shown in Table 3. The standard specimen SJ1 with 12mm plain gusset plate showed the lowest percent composite action with result of 47.5%. Specimen SJ2, with the thicker (18mm) gusset plate and greater bearing area, has a better composite action result of 55.03%. Specimen SJ3 had composite action of 69.4%, indicating that the gusset plate with a single hole was more effective than the simple plain gusset plate. When the gusset plate was welded six transverse ribs, the specimen SJ 4 possessed the best composite action of 85.4%, which turned out that the gusset plate with ribs made a remarkable contribution on the amount of composite action.

The percentage of composite action for each specimen at different levels of loading was illustrated in Figure5. The result curve generally decreases as chemical bond, friction and binding of the square CFT column were lost, but in some cases it slightly increased again possibly maybe due to the fact that the bearing became more significant.

Relative slippage between concrete and steel

The relative slippage between the concrete infill and the square steel tube was another index to indicate the composite performance of each specimen. These results demonstrate the effectiveness of each construction detail of the gusset plate to minimize slippage and increase the level of composite action. The slippage was measured at both the top of the steel tube and the concrete infill and represent slippage deformation in the tube. The results of the slippage are shown in Figure 6.

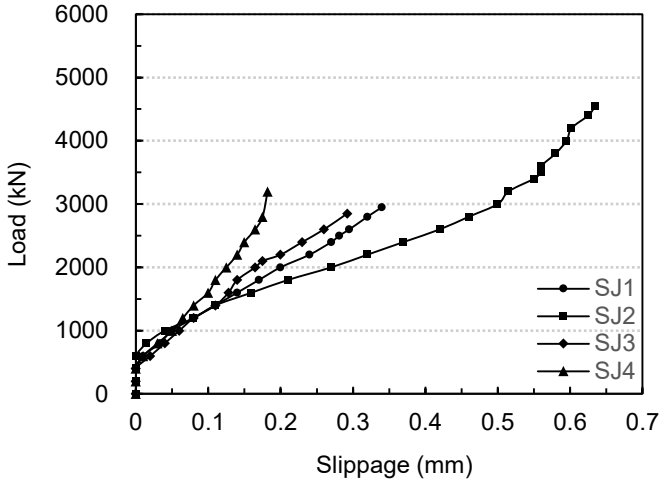


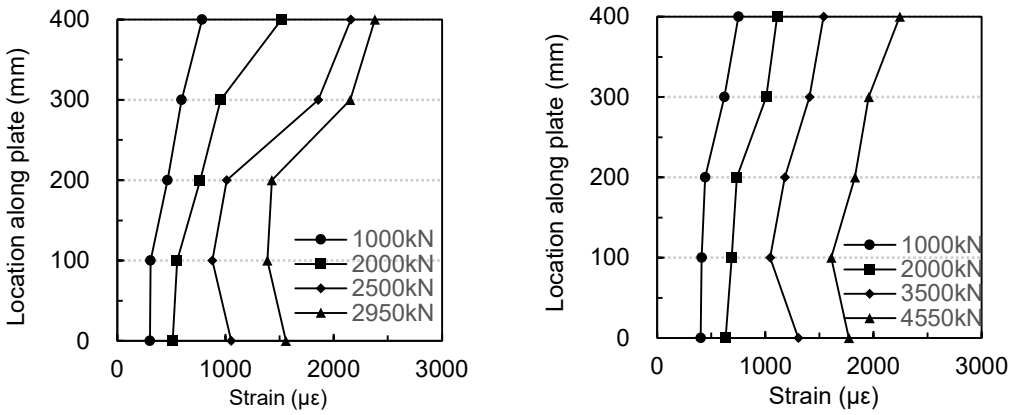
Fig.6 – Slippage between steel tube and concrete core

The slippage between the concrete and steel at the top of the square steel tube raised with increasing force and the relationship was approximately linear. The slippage results indicate that the level of composite action and point at which the bond connection between the steel and concrete breaks down. The graph reveals that all specimens had a slippage that was approximately equal to zero under 500kN. The transition point of the slope at 500kN suggests that the chemical bond between the concrete and steel has broken down. Friction controlled the slippage during the loading degree of 500kN to 1000kN. And then the mechanical transfer mechanisms such as bearing began to take over after approximately 1000kN. Since both the concrete and square steel tube were restricted at the base, the amount of slippage was limited.

The specimen SJ4 with ribs on the gusset plate exhibited the best result with the lowest slippages of 0.185mm, which was reduced by 46% compared with SJ1. Low levels of slippage was seen with ribs because they provide an increase area 6 times that of a plain plate and acted as a key to lock the concrete and steel together. The slippage of specimen SJ3 with a single hole cut into gusset plate was 0.292mm, which was reduced by 14% compared with SJ1. The hole cut into gusset plate increased the bearing area.

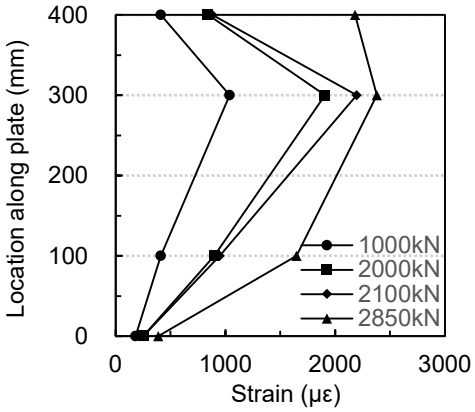
Strain Along the Plate

The effectiveness of the gusset plate details were analyzed by placing strain gauges along the mid-line location of the gusset plate, as showed in Figure4.The envelopes of results for 1000kN through the ultimate load of each specimen are showed in Figure7. The difference between the gauge readings along the plate provides an indication of the transfer of forces from the plate into the concrete.

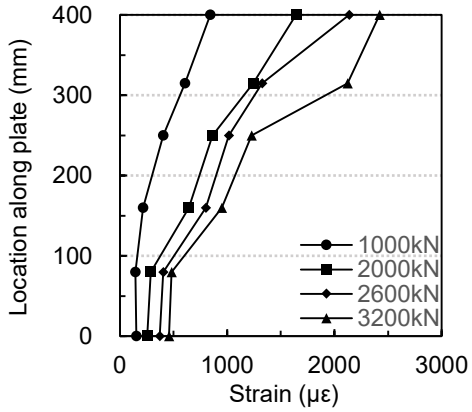


(a)SJ1

(b)SJ2



(c)SJ3



(d)SJ4

Fig.7 –Strain distribution along the plate

For the specimens with a plain gusset plate, SJ1 and SJ2, the force mainly transferred from the plate into concrete through chemical bond and friction before reach to the yield load. The curves are flat with small difference of strain between the top and the bottom, which means a little amount of force transferred into the concrete during this stage. When exceeding the yield load, the strain firstly decreased at the height of 400mm to 100mm and then increased at the bottom 100mm. It turns out that some force transferred into the concrete infill through directly bearing between the plate subface and the concrete infill.

The stain distribution along the plate for specimen SJ3, as seen in Figure7(c), firstly increased with the maximum value at the height of 300mm, the location of the top of the hole. Afterwards, the strain began to decrease obviously from the top to the end of the hole (at the height of 900mm to 700mm). The distribution of the strain represents that large amount of force had transferred into the concrete through the bearing area caused by the hole cut into the plate. Furthermore, the strain at the bottom 100mm of the gusset plate was not increased as described above for specimens SJ1 and SJ2, but showed a decreasing rule. It means the force at bottom of the gusset plate was significantly reduced.

For specimen SJ4 with 6 ribs welded on the plate, the strains above and below the ribs were slightly different at the loading degree of 1000kN. It was resulted of the small amount of initial

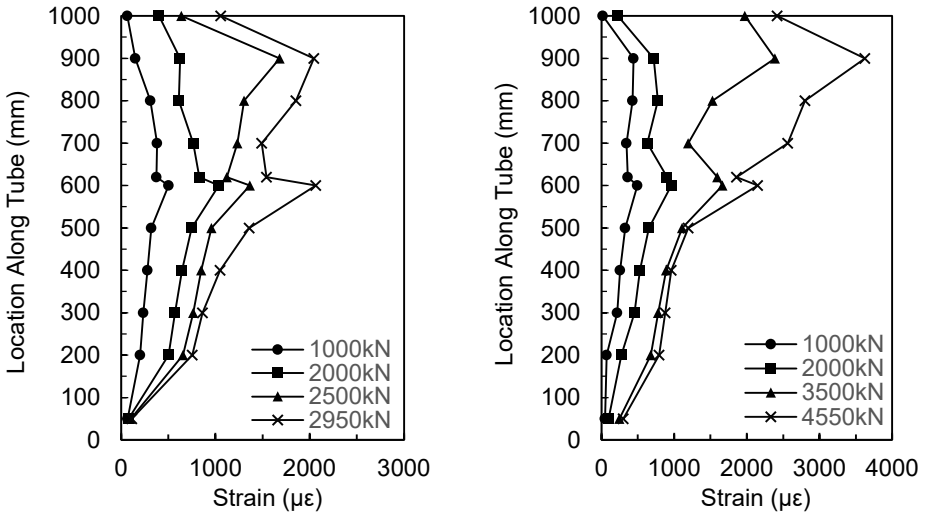
slippage between the steel tube and concrete. Nevertheless, the strain values above and below the ribs showed a shape decrease at the maximum loading degree, especially the difference of the top-most rib. The higher demands activated the top rib and allowed the forces to be transferred from the plate into the concrete.

Strain Along the tube

The strain distributions along the tube of the specimens, as seen in Figure8, have the same general shape, but it still shows some difference that caused by different gusset plate construction details.

At the height of 900mm close to the loading head, the strain of the steel tube had a large value and then decreased along the height of 900mm to 620mm, indicating that some force was transferred from the tube to the concrete during this height range. The strain at the height of 580mm, just under the gusset plate, was significantly increased because of the directly bearing between the plate subface and the steel tube. And then the strain distribution in the bottom 580mm height of the specimen showed a continuous decrease all the way down to the base of the tube. This was caused by a bond mechanism between the steel tube and the concrete infill that allowed the force to be transferred. Chemical bond, friction, and binding between the steel and concrete were all possible mechanisms that would allow the force transfer from the tube into the concrete infill.

At the loading degree of 1000kN and 2000kN, the strain distribution along the tube was similar for all specimens. At the yield loading degree and the ultimate loading degree of specimen SJ2, the sharp increase of strain along the tube as seen in Fig8(b) were due to localized yielding in the tube along the welds. The stains distribution of the tube of specimen SJ3 at the ultimate loading degree was significantly reduced at the height of 900mm-700mm. With more transfer bearing area on the plate caused by the ribs, the demand on the tube of SJ4 was much lower than SJ1. Moreover, the strain just under the gusset plate was also lower for SJ4 than for SJ1 with a plain gusset plate. This reflects a better composite action of specimen SJ4.



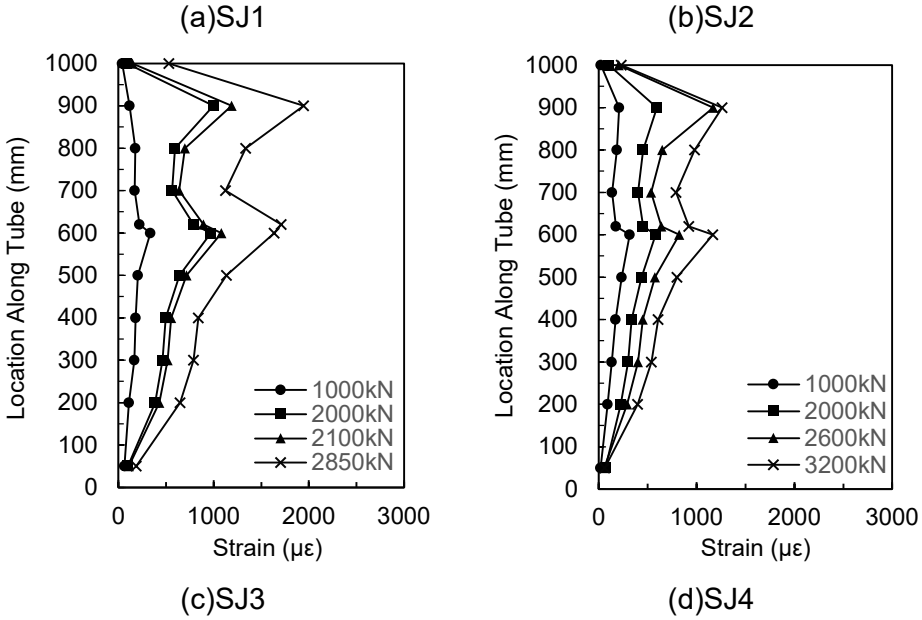


Fig.8. –Strain distribution along the tube

CONCLUSTIONS

According to the experimental study on the simplified connection of brace frames with square CFT columns penetrated by gusset plates, the efficiency of different construction details of the connection gusset plate in force transferring and composite action could be estimated through stain distribution, slippage, and the percentage of composite action. In general, the following conclusions can be drawn:

1. The penetrating gusset plain plate can effectively transfer the applied load to the square steel tube and the concrete infill resulted in a percent composite action value of 47.5%. The applied load transfers to the concrete infill through friction and bearing, while it transfers to the steel tube through the connection by the weld.
2. Increasing the thickness of the gusset plate was unable to improve the efficiency of the concrete infill at the height range of the gusset plate. However, it could offer a greater bearing area at the bottom between the gusset plate and the concrete, so as to improve the efficiency of the concrete in the bottom part of the specimen, and resulted in a better composite action value of 54.7% compared to the standard specimen SJ1.
3. The construction with a hole cut into the gusset plate could increase the bearing area between the gusset plate and the concrete infill at the height range of the gusset plate, and consequently increased the composite action from the value of the comparison specimen SJ1 47.5% to 69.4%.
4. Comparisons of the various connection details showed connection with transverse ribs welded on the gusset plate was the most effective in transferring force to the concrete infill of the column due to the ribs detail provided the largest bearing area close to the face of the gusset plate. The large transfer of force that occurred by the ribbed construction details resulted in the highest percent composite action values of 85.4%.

ACKNOWLEDGMENTS

This study was supported by the National Nature Science Foundation of China (51378009; 51378219; 51638009), the State Key Laboratory of Subtropical Building Science, South China University of Technology (2017ZB28).

REFERENCE

AISC. (1993). Load and resistance factor design specification for structural steel buildings, American Institute of Steel Construction, Chicago, USA.

Gunderson, Chad. (2002). “Braced frame connections with concrete-filled tube (CFT) columns.” MSCE thesis, Univ. of Washington, Seattle, USA.

Hajjar, J.F. (2008). “Composite steel and concrete structural systems for seismic engineering.” *Steel Construction*, 58(5–8):703-723.

Jingmin L. (2017). “Braced fame connections with square CFT Columns penetrated by gusset Plates.” MSCE thesis, South China Univ. of Technology, Guangzhou, China.

Macrae, G., Roeder, C.W., Gunderson, C., & Kimura, Y. (2004). “Brace-beam-column connections for concentrically braced frames with concrete filled tube columns.” *Journal of Structural Engineering*, 130(2), 233-243.

Macrae, G.A., Kimura, Y., & Roeder, C. (2004). “Effect of column stiffness on braced frame seismic behavior.” *Journal of Structural Engineering*, 130(130), 381-391.

Mckenry M.(2002) “Behavior of concrete filled steel tubes in concentrically braced frame.” MSCE thesis, Univ. of Washington, Seattle, USA.

Roeder, C.W. (1998). “Overview of hybrid and composite systems for seismic design in the United States.” *Engineering Structures*, 20(97), 355–363.

Roeder C.W., MacRae G.A., &Waters C.(2000). “Seismic behavior of steel braced frame connections to composite columns”. *Steel Connections IV Workshop.*

Roeder, C.W., Cameron, B., & Brown, C.B. (1999). “Composite action in concrete filled tubes.” *Journal of Structural Engineering*, 125(5), 477-484.

INFLUENCE OF COMPOSITE SLAB ON THE NONLINEAR RESPONSE OF EXTENDED END-PLATE BEAM-TO-COLUMN STEEL JOINTS

Roberto Tartaglia[1],
University of Naples 'Federico II'
Department of Structures for Engineering and Architecture
Naples, Italy
roberto.tartaglia@unina.it

Mario D'Aniello[2],
University of Naples 'Federico II'
Department of Structures for Engineering and Architecture
Naples, Italy
mdaniel@unina.it

Gian Andrea Rassati[3],
University of Cincinnati
Department of Civil and Architectural Engineering and Construction Management
Cincinnati OH, United States
gian.rassati@uc.edu

James Swanson[4],
University of Cincinnati
Department of Civil and Architectural Engineering and Construction Management
Cincinnati OH, United States
james.swanson@uc.edu

ABSTRACT

Extended end-plate connections are widely used in seismic resisting structures. Nowadays, this type of joints are prequalified as all-steel assemblies, namely disconnecting the slab from any protruding part of the connection in order to avoid composite behavior and to control the hierarchy of resistance between beam and column. However, the most of the building frames are designed considering steel-concrete composite slabs. The presence of the slab can strongly influence both the local and the global behavior of structure and the joint. Indeed, the presence of the composite slab increases both the stiffness and the strength of the joint thus affecting the beam-to-column hierarchy. The aim of this work is to investigate the influence of the composite slab on the joint response by means of finite element analyses. In particular, both the pure flexural capacity and the robustness behavior were investigated for two joint configurations, namely one fully steel, and the other considering also the composite slab with the corresponding reinforcements and shear connectors.

Keywords: composite, finite element analysis, beam-to-column joints, extended end-plate connection, prequalification.

INTRODUCTION

Nowadays, both AISC358-16 and EN1998-1-1 allow disregarding the interaction between the slab and the steel joint provided that the concrete slab is disconnected from any protruding part of the joint. Indeed, the current pre-qualification rules for steel beam-to-column joints (i.e. AISC358-16 in United States of America and those recently developed within the framework of Equaljoints project in Europe) have been developed for beam-to-column assemblies with disconnected slab in the zone of the connection. However, the presence of composite slab can influence both the response of qualified beam-to-column joints and the hierarchy of resistance between the beam and the column in moment resisting frames (MRF) behavior. Indeed, even though the concrete slab is locally disconnected both the continuity of the rebars and the presence of transverse beams connected to the joints can interact together with the steel joint. Therefore, several analytical and experimental studies have been carried out to evaluate the contribution of concrete slab to the behavior of steel joints [Aribert (2006), Leon (1998), Thermou (2004), Ciutina (2013), Lee (1989), and Simones (2001)]. The numerical response of composite joints has been also investigated by several Authors [Amadio (2011, 2017), Braconi (2008), Danku (2013), Salvatore (2005) Vasdravellis et al. (2009) Tartaglia et al. (2017b)], which demonstrated the effectiveness of Finite element (FE) numerical models in predicting the stiffness, strength, ductility, and energy dissipation capacity of composite joint assemblies. An example of the accurate interpretation of the experimental results by FEM was shown by Vasdravellis et al. (2009).

In light of these considerations, this paper describes and discusses the results of a preliminary FE study devoted to investigate the influence of composite slab on the inelastic response of steel joints subjected to both pure bending actions and catenary action induced by column loss scenario. Among the possible types of beam-to-column joint, this study focuses on extended stiffened end-plate bolted joints designed to behave as full strength according to the European prequalification procedure (i.e. according to EQUALJOINTS). In order to highlight the role of the slab, two different configurations were modeled, namely (i) all-steel joint without the presence of the slab, (ii) the joint with the presence of the slab, with code-compliant details to avoid theoretically the composite action between the joint and the slab. In this second configuration, the FE model takes into account the steel sheeting, the concrete deck, the shear connectors and the steel rebars.

The paper is organized into three main parts. The first part describes the investigated parameters and the design assumptions considered for the examined joint assemblies. The second part focuses on the modeling assumptions. The last part discusses the results of the finite element simulations.

Description of the investigated joints

The investigated beam-to-column joints are extracted from a set of reference buildings properly designed according to EN1998-1-1 and EN1993-1-1 (see Fig. 1a).

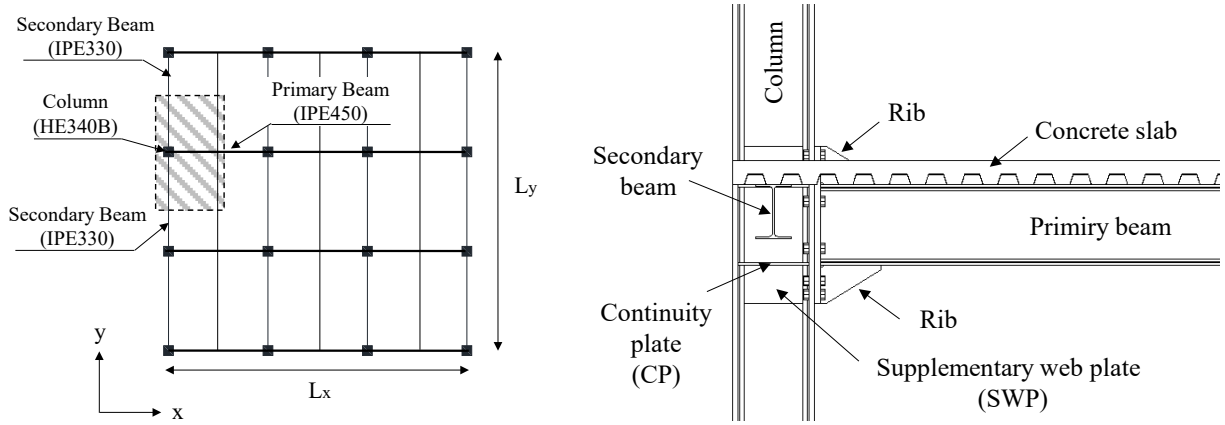


Figure 1: The reference structure and the features of the investigated joints.

The investigated assembly (see Fig. 1) consist in three beams connected to an external column (HE340B); the two beams in the Y direction (IPE330, hereinafter called secondary beam) were designed as composite with the slab according to EN1994-1-1. Contrariwise, the beam in the X direction (IPE450, hereinafter called primary beam) was designed as all-steel. The secondary beams were designed to resist solely gravity loads as well as their end-connections, which are made of bolted double cleats (see Fig. 2b) that were designed according to EN1993-1-8 to transfer all the shear force coming from the slab to the column.

Extended end-plate joint connects the primary beam to the column (see Fig. 2c). This joint was designed to resist seismic actions according to component method (EN1993-1-8), namely the joint was designed to guarantee the formation of plastic hinge in the beam without plastic engagement of the connection and column web panel. The geometrical features of the examined joints are reported in Tables 1 and 2.

The composite slab was properly designed according to EN1994-1-1 and EN1998-1-1 in order to carry the vertical loads and to behave as diaphragm under seismic event. The thickness of the concrete deck is equal to 75mm and A55-P600 G5 profiles sheeting with a depth equal to 55mm was used (see Fig. 3).

Table 1: Geometry of the end-plate connection.

Diameter		End-Plate						Rib	
Bolts	hole	h_{EP}	b_{EP}	t_{EP}	p_0	p_1	p_2	t_{Rib}	Slope
[mm]	[mm]	[mm]	[mm]	[mm]	[mm]	[mm]	[mm]	[mm]	[-]
30	33	870	280	25	50	75	180	20	40°

Table 2: Geometry of the double cleats connection.

Diameter		double cleat						
Bolts	Hole	h_{AP}	b_{AP}	t_{AP}	l_{AP}	e_0	e_1	e_2
[mm]	[mm]	[mm]	[mm]	[mm]	[mm]	[mm]	[mm]	[mm]
16	18	240	90	5	180	55	65	65

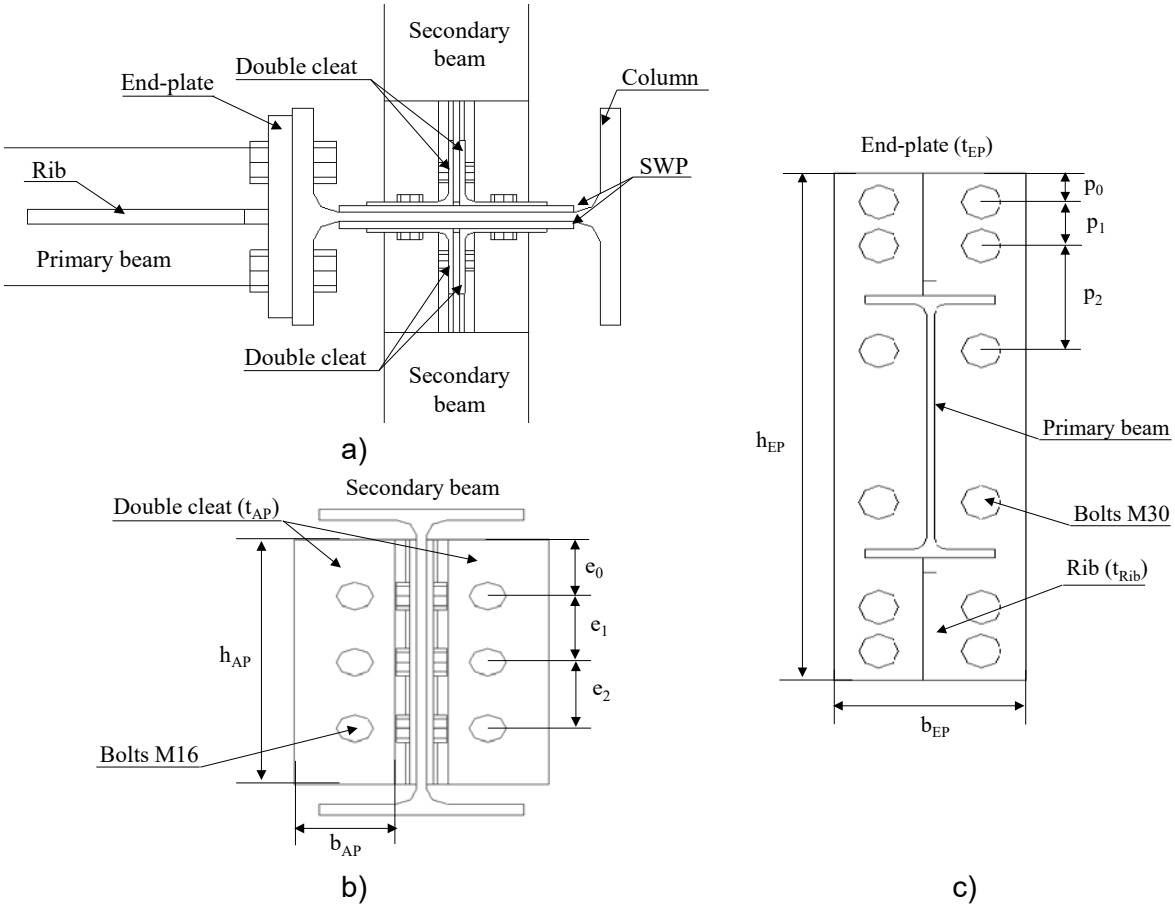


Figure 2: Connection geometry: a) planar view, b) angular connection and c) extended stiffens connection.

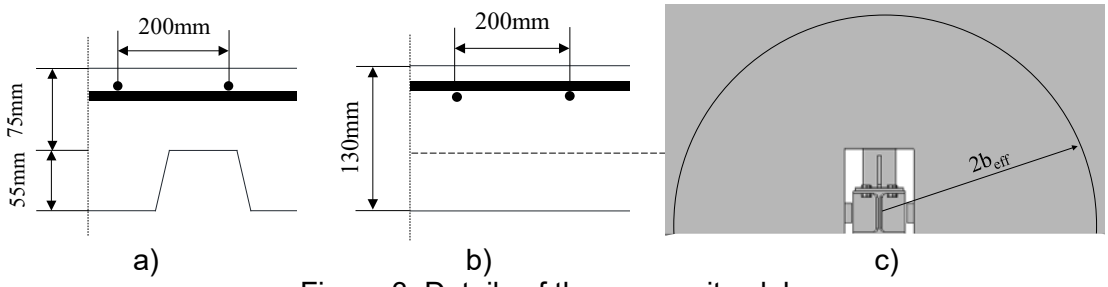


Figure 3: Details of the composite slab.

According to EN1994-1-1 pr. 7.4 in order to limit the crack opening on the concrete slab, it was assumed a mesh 200mmx200mm of ϕ10 steel rebars with a concrete cover of 30mm.

Shear connectors were used to guarantee the composite action between the slab and the beams. The distribution of the studs on the secondary beam is uniform with a spacing of 150mm to ensure a perfect connection.

For that concerns the primary beams, it should be highlighted that the MRF was designed with steel-only dissipative zones (concept c EN1998-1-1 pr. 7.1.2). Therefore, in order to prevent the involvement of the slab in the resistance of the dissipative zones, a circular area around the column with a radius equal to 2 times b_{eff} (where b_{eff} is the larger of the primary beams effective

widths) was maintained in accordance with EC8. In line with this hypothesis, also the connection between the slab and the column should be avoided; in particular a gap equal to 50 mm between the concrete and any protruding part of the connection was adopted.

THE FE MODEL

The influence of the concrete slab on the joint global behavior was investigated by means of numerical analyses performed in Abaqus 6.14.
Two finite element models (FEMs) were developed. The first model (ES-F-AS) (see Fig. 4a) was built disregarding the presence of the slab, but considering its contribution to the lateral torsional buckling with the introduction of additional constrains on the beams (as described by Tartaglia et al. (2018)). The second model (ES-F-WS) is more refined and it accounts for the concrete deck, the steel sheeting, the steel rebars and the shear connectors (see Fig. 4b and 4c).

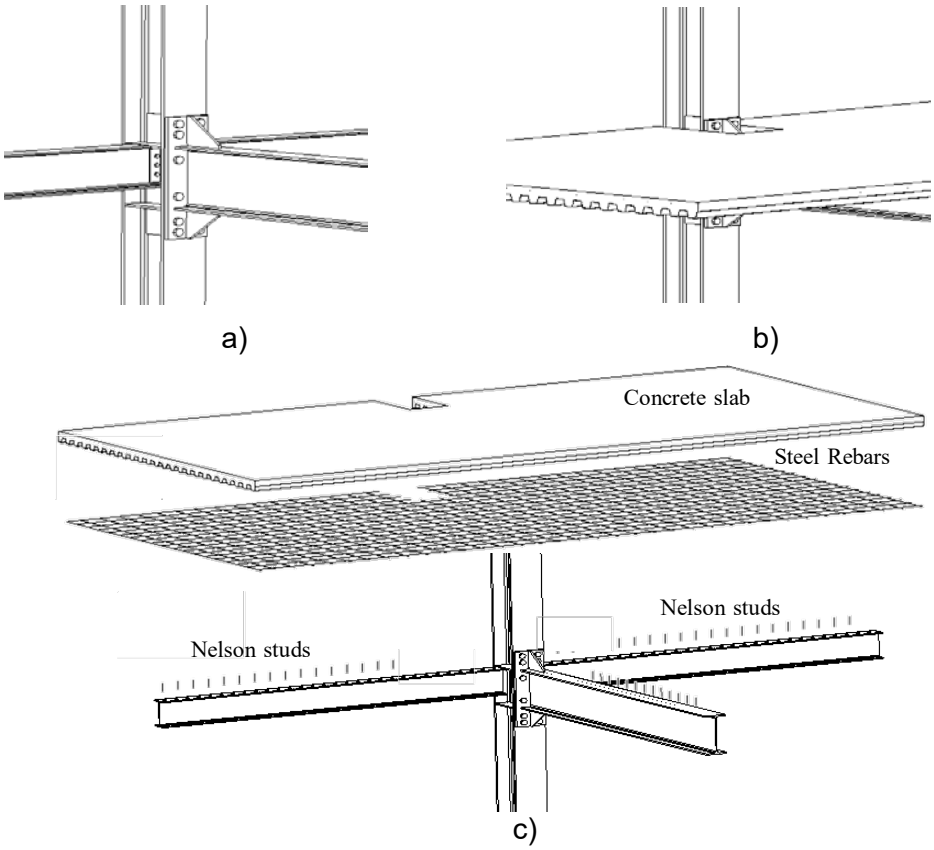


Figure 4: The two investigated models: a) ES-F-AS, b) and c) ES-F-WS.

Most of the model parts (beams, bolts, plates, stiffeners and concrete slab) were modelled using C3D8R (i.e. An 8-node linear brick, reduced integration, hourglass control) solid finite elements. Only the reinforcement and the shear connectors (in ES-F-WS model) were modelled by means of beam elements (B31 a 2-node linear beam in space) with their respective cross section in order to reduce the computational effort. The steel profiled sheeting was modelled by means of continuum shell elements (SC8R an 8-node quadrilateral in-plane general-purpose continuum shell, reduced integration with hourglass control, finite membrane strains) with the thickness of the real steel sheet (1 mm). The material properties were defined for each element individually in function of the adopted finite element (beam, shell or solid). Therefore, the material assumed

for the beams, the column and the stiffeners is an European S355 steel with average yield stress equal to $1.25F_y$, as recommended by EN1998-1-1, a steel density equal to 7850 kg/m^3 and a Young's modulus and Poisson ratio respectively equal to 210 GPa and 0.3. The plastic hardening was simulated using both nonlinear kinematic and isotropic hardening law on the basis of a set of coupon tests performed at University of Naples "Federico II". Shear connectors and steel deck have the same elastic properties but a simplified linear branch was considered for the post-yielding behavior. The mechanical behavior of the bolts was simulated as reported in Tartaglia et al. (2018). The material properties of the concrete were simulated using the concrete damage plasticity model proposed by Hillerborg et al. (1976). This model takes into account the reduction of the elastic stiffness caused by plastic straining both in tension and compression and it accounts as well for the stiffness recovery effects under dynamic loading conditions (Abaqus User's Manual, 2014). The characteristics of C25/30 concrete were defined in accordance with EN1992-1-1, i.e. density of 2500 kg/m^3, Young's modulus of 31GPa, and Poisson's ratio of 0.2. Table 3 summarizes the adopted material properties of all the introduced elements.

Explicit analyses were performed. A General Contact interaction was defined in order to simulate the model interactions (i.e. between the bolts and the column and end-plate).The Normal and Tangential Behavior were defined respectively introducing 'Hard Contact' and 'Penalty' friction formulation (with a coefficient equal to 0.3). In the ES-F-WS model the connection between the shear studs and the beams was modelled using Multi-point constraints (MPCs). Both the reinforcement and the shear studs were modelled with wire elements (respectively wire-truss and wire-beam) and embedded in the concrete, while the steel sheet was tied to the concrete slab.

Table 3: Material properties

Elements	Material	Yielding Strenght [N/mm2]	Ultimate strength [N/mm2]
Beams	S355	443.75	752.5
Column	S355	443.75	753.5
Stiffners	S355	443.75	754.5
Reinforcements	B450C	450	540
Shear connectors	SMD19105	235	360
Steel deck	A55-P600 G5	260	450
Bolts Seismic conn. (M16)	10.9	802.5	916.3
Bolts Angular conn. (M30)	10.9	802.5	916.3

Both ES-F-AS and ES-F-WS models have the same boundary conditions, with the only remarkable difference in the introduction of additional torsional constraints in the ES-F-AS model to prevent lateral torsional buckling in the beam. The mesh was adequately defined in function of both element type (solid, continuum shell and wire) and the expected stress concentration patterns. Moreover, the computational time/result quality ratio was analyzed in order to optimize the FEAs.

The bolt preloading was modelled as proposed by Pavlović et al. (2015), namely by applying a temperature variation, to simulate an artificial bolt shrinkage. Both the pure monotonic actions and the column loss scenario were applied at the primary beam extremity; in case of the seismic loads the vertical displacement was monotonically increase up to 6% joint rotation. For the analyses simulating the column loss scenario, the vertical displacement was increased up to a rotational level of 20% on the connection, while preventing the horizontal displacement.

RESULTS

In this paragraph, the results of the FEAs performed on both ES-F-AS and ES-F-WS are described in terms of moment rotation curve, yielding lines distribution and failure mode. As anticipated in the previous section, the influence of the composite slab, on the joint behavior, was investigated considering two possible scenarios: (i) monotonic bending and (ii) column removal.

Monotonic bending condition

The monotonic bending condition was examined in order to investigate the joint response when lateral forces (i.e. wind and earthquake) act on building frames. Moreover, due to the asymmetry of the ES-F-WS model, two monotonic analyses, considering both the hogging (ES-F-WS-M-) and the sagging (ES-F-WS-M+) moment, were analyzed.

As expected (see Fig. 5), despite the fact that the steel joint is disconnected from the slab, the moment rotation curves show a slight difference between the responses of the two models. With respect to the ES-F-AS, ES-F-WS presents an increase of capacity; indeed both the hogging and the sagging moment-rotation curves show an increase of resistance almost equal to 5%. These results confirm that, in spite of all the EN1994-1-1 and EN1998-1-1 rules being respected there is an interaction between the steel joint and the slab.

It should be noted that the increase of flexural capacity does not depend on the moment direction. Therefore, the resistant mechanism is not due to the direct interaction between the slab and the steel resistant joint. Instead, it depends on the torsional resistance of the secondary beam that offers an additional restraint to the slab.

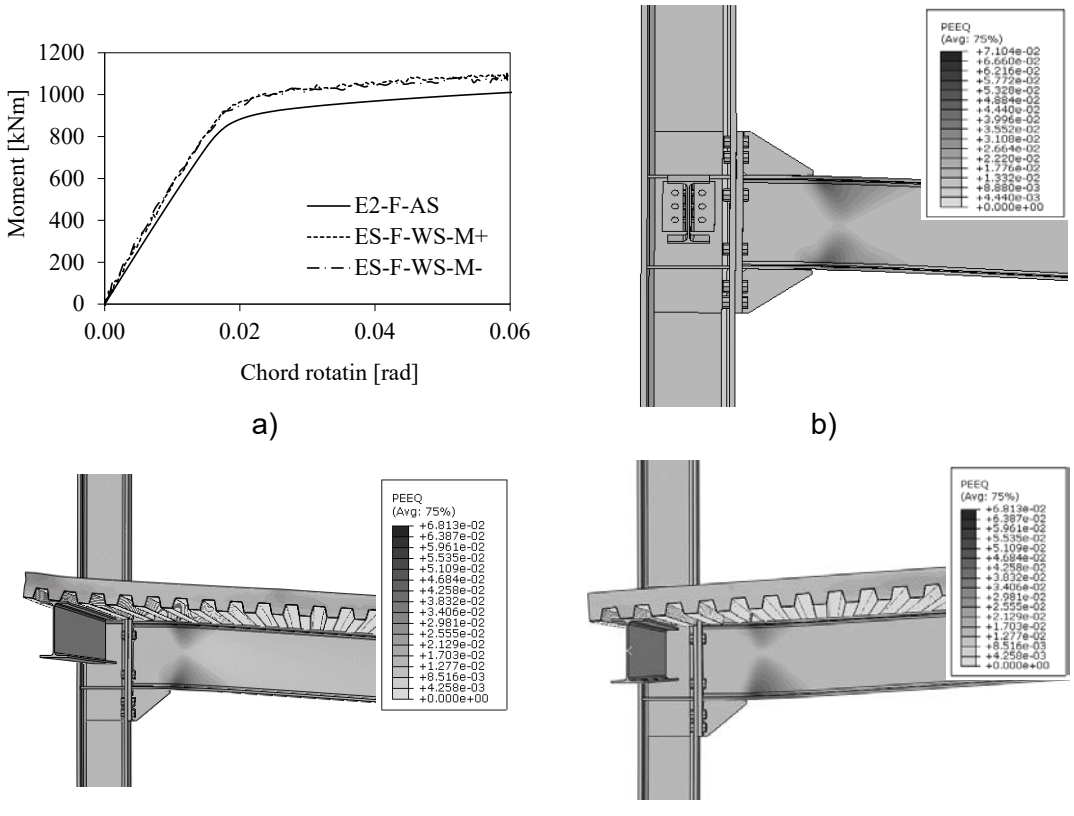
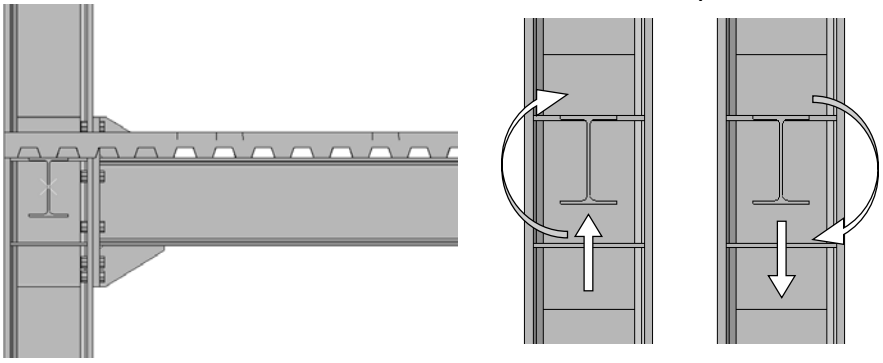


Figure 5: Seismic results in terms of Moment rotation curve (a) and PEEQ distribution (b, c and d).

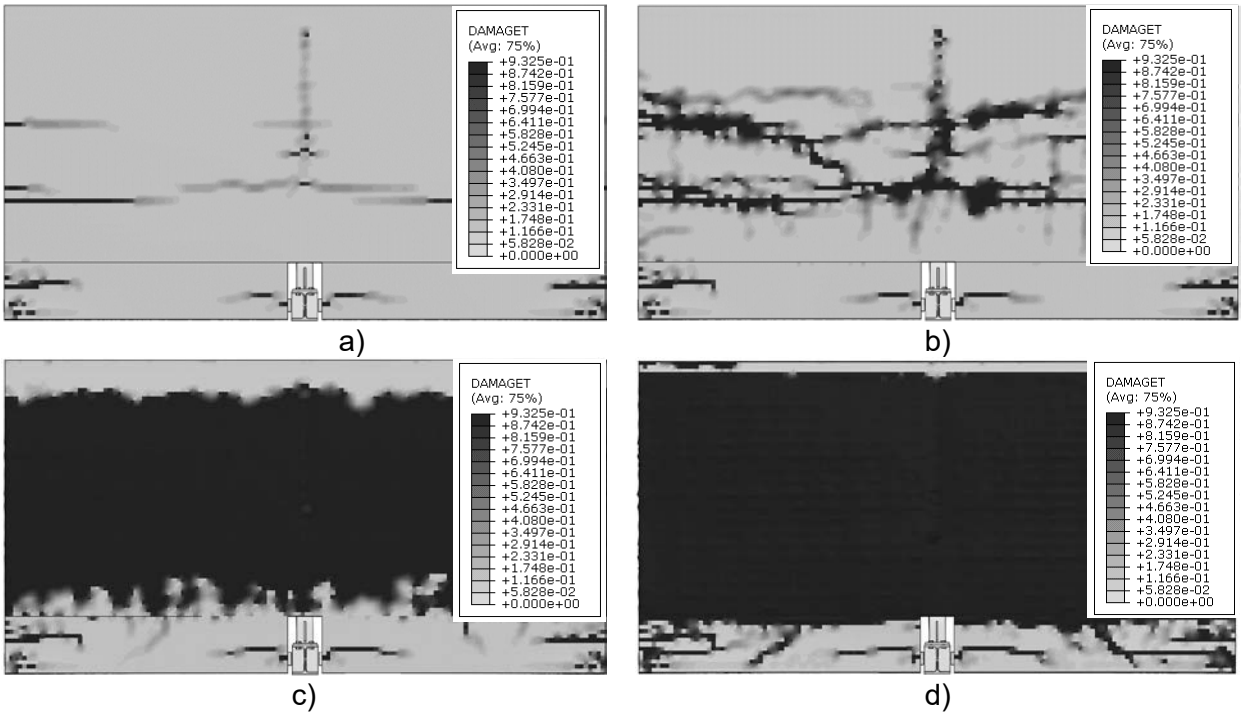
This observation is schematized in Fig. 6, where, for both hogging and sagging moment, it is reported the relation between the rotation and vertical displacement of the secondary beam with the slab induced displacements. Larger differences between the two models can be observed comparing their elastic stiffness. Indeed, as reported in Fig. 5a, both hogging and sagging moment show an increase of 15% in the case with the slab.
However, both the FE models show that the primary joint behave as full strength and the hierarchy of resistance between the beam and the column is not compromised.



a) b) c)

Figure 6: Torsional effect on the secondary beam in case of hogging (b) and sagging (c) moment

It is also interesting to note that both FE models show a similar value of the maximum plastic deformation (0.068 and 0.071 for ES-F-AS and ES-F-WS respectively) in the primary beam. Moreover, both models show a small contribution of the column and the bolts to the global dissipated energy equal to 3.5% and 2% respectively.



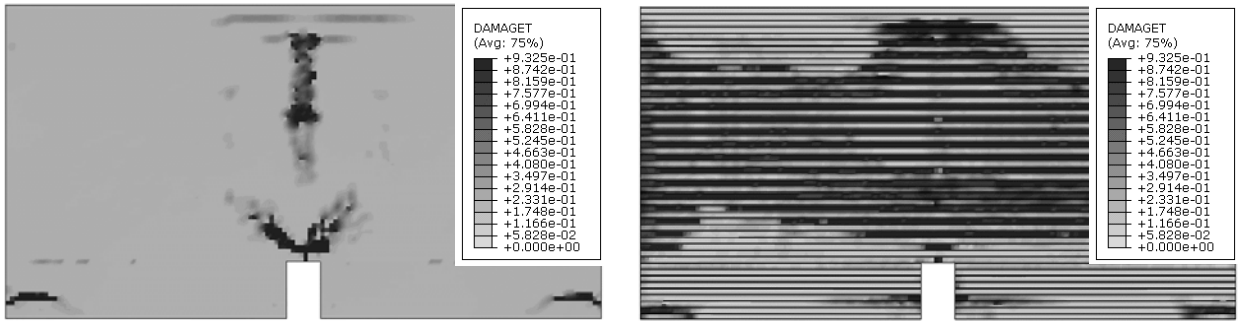
a) b)

c) d)

Fig. 7: The development of the tension damage on the ES-F-WS subjected to hogging moment at: 2% (a), 3% (b), 4% (c) and 6% (d) of chord rotation.

The tension damage (DAMAGET in Abaqus) on the concrete slab is reported in Figure 7. The first crack opening can be observed at 2% of rotation (see Figure 7a) where the damage distribution is mainly perpendicular to the primary beam axis around the shear studs. Increasing the rotation up to 3%, it can be observed (see Figure 7b) a larger distribution of the tension damage on the slab developing form the shear studs parallel to the primary beam. Finally, at 6% of chord rotation (see Fig. 7d) the distribution of the tension damage is almost uniform on the entire slab.

On the other hand, when the joint is subject to a sagging moment, the upper part of the slab will be in compression and no significant damage can be observed (see Fig. 8a). All the tension damage is in the lower part of the slab (see Fig. 8b).



a) b)

Figure 8: The ultimate tensional damage on the ES-F-WS subject to sagging moment.

Column loss scenario

The column removal scenario implies the loss of a column adjacent to the investigated joint. In this case, the rotation demand is larger than that imposed in the pure monotonic scenario. In addition, there is the development of the catenary action in the joint. Indeed, the presence of axial restraints and the large deformation regime substantially modify the local demand in the joint components as showed by Tartaglia et al. (2017a). Figure 9 show the moment-rotation response, where the moments are computed as the algebraic sum of the first order moment (i.e. the shear force at the tip of the cantilever beam by the corresponding shear length) and the second order contribution due to the catenary effects (i.e. the catenary action *N* multiplied by the deflection at the tip of the cantilever beam), which counterbalances the first order contribution (see Fig. 9b). Moreover, the evolution of normal action was plotted, in order to underline the great differences between the two FE models.

Indeed, the introduction of the composite slab strongly influences both the elastic stiffness (around 38%) and the bending capacity (around 33%) of the joint. A large part of these increments are due to the presence of the secondary beam (see Fig.10). Moreover, the presence of the slab strongly increases the beam resistance to the normal actions.

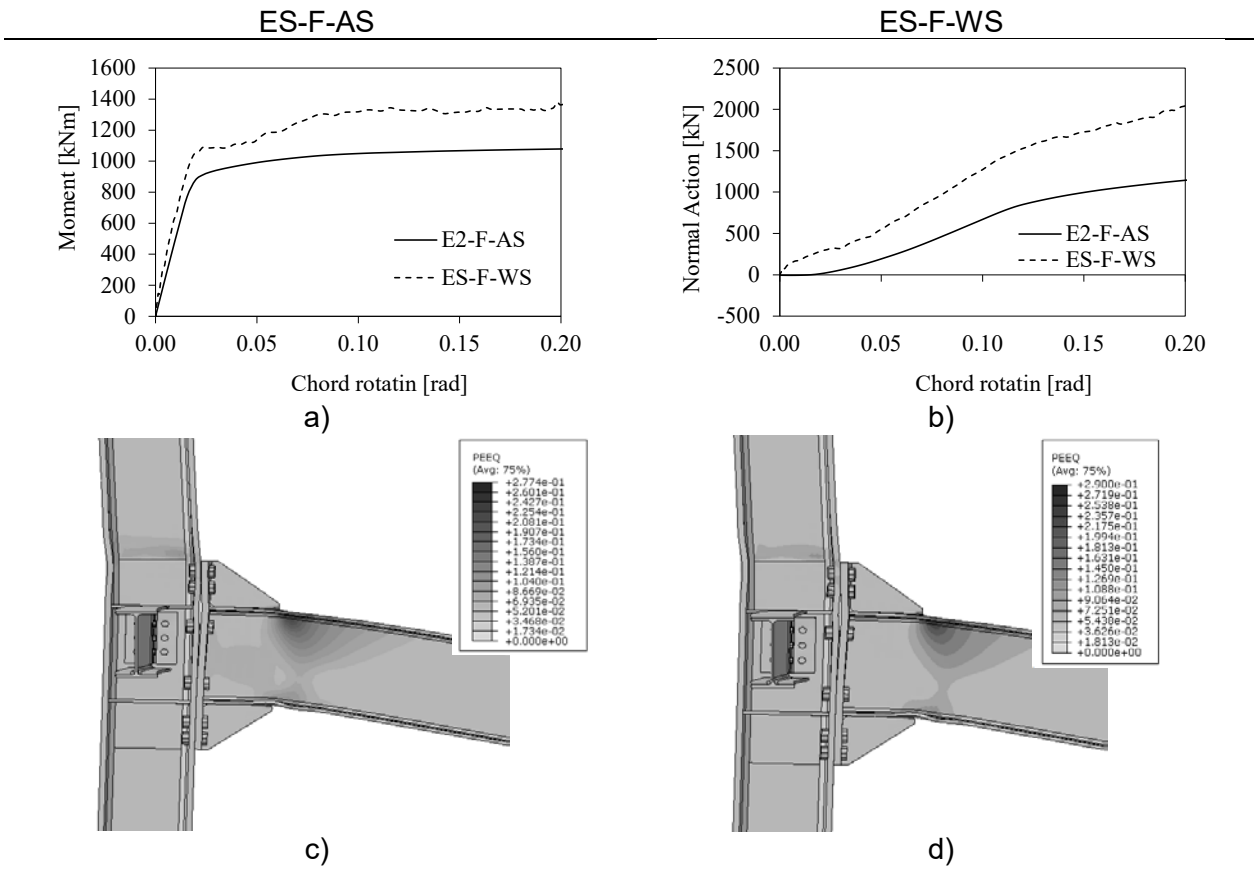


Figure 9: Column loss scenario results: Moment rotation curve (a), evolution of catenary action (b) and plastic deformation (PEEQ) (c and d).

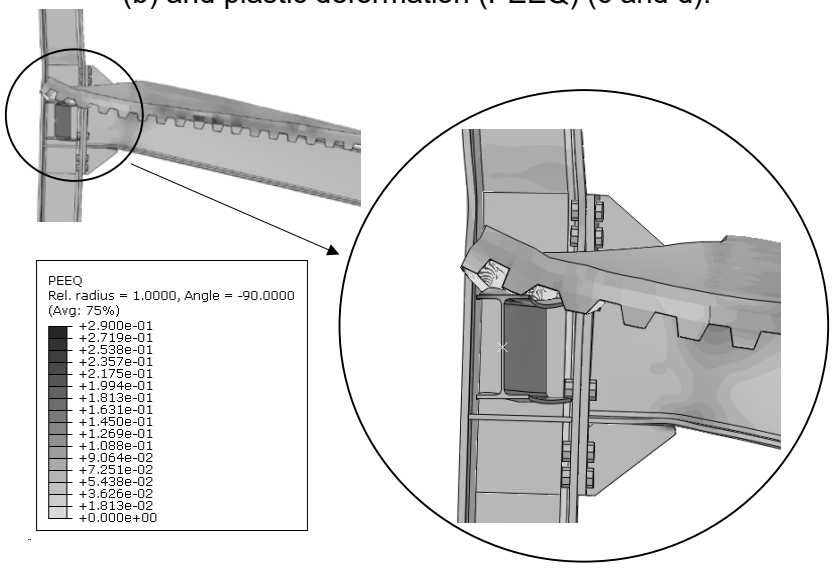


Figure 10: The influence of secondary beams on the concrete slab deformation.

CONCLUSIONS

In light of the results of the finite element simulations presented and discussed in the previous paragraphs, the following conclusions are drawn:

- A more refined model considering, not only the steel joint but also the presence of the concrete slab, the rebar, the shear connectors and the secondary beams, allows evaluating more accurately the joint behavior. In particular, the model with the slab (ES-F-WS) shows an increase of both elastic stiffness and bending capacity.
- The increase of elastic stiffness is mainly due to the presence of the concrete slab and its interaction with the steel joint. However, the increase of bending capacity is not due to the direct transfer of shear force between the primary beam and the slab, but from the torsional contribution of the secondary beams. Therefore, the modelling of secondary beams ensures a more accurate characterization of the joint ultimate capacity; indeed the underestimation of the joint capacity can modify the local hierarchy between the column and the beam and compromise the structural ductility.
- The FE models show that the examined details allows the formation of plastic hinge in the beam without interference with the slab.
- The influence of the slab is more evident when the column loss scenario is investigated. Indeed, despite the joints failure mode are similar, with the involvement of the column and the connection in the failure mechanism, both the bending capacity and the elastic stiffness differ due to the interaction between the secondary beam and the slab.

REFERENCES:

Amadio C, Bella M, Bertoni V, Macorini L. (2011). Numerical modeling and seismic assessment of steel and steel-concrete composite frames, the line 5 of the ReLUIS-DPC 2005–2008 Project, 409–448. Napoli, Italy: Doppiavoce.

Amadio C., Bedon C., Fasan M., Pecce M. R. (2017). Refined numerical modelling for the structural assessment of steel-concrete composite beam-to-column joints under seismic loads. *Engineering Structures* 138, 394–409. http://dx.doi.org/10.1016/j.engstruct.2017.02.037

Aribert J, Ciutina A, Dubina D. (2006). Seismic response of composite structures including actual behaviour of beam-to-column joints. *Composite Construction Steel Concrete*. V:708–17.

Braconi A, Bursi OS, Fabbrocino G, Salvatore W, Taucer F, Tremblay R. (2008). Seismic performance of a 3D full-scale high-ductility steel–concrete composite moment-resisting structure— Part II: test results and analytical validation. *Earthquake Engineering and Structural Dynamics*. 37:1635–55.

Cassiano D., D'Aniello M., Rebelo C., (2017) Parametric finite element analyses on flush end-plate joints under column removal. *Journal of Constructional Steel Research*, 137, 77–92.

Ciutina A., Dubina D. and Danku, G. (2013) Influence of steel-concrete interaction in dissipative zones of frames: I – Experimental study. *Steel and Composite Structures.* 15(3), 281-000. http://dx.doi.org/10.12989/scs.2013.15.3.281.

Danku G., Dubina D., and Ciutina A. (2013). Influence of steel-concrete interaction in dissipative zones of frames: II - Numerical study. *Steel and Composite Structures.* 15(3), 305-000. http://dx.doi.org/10.12989/scs.2013.15.3.305

Dassault (2014), Abaqus 6.14 - Abaqus Analysis User's Manual, Dassault Systèmes Simulia Corp.

EN 1993:1–1, Design of Steel Structures - Part 1–1: General rules and rules for buildings. CEN, 2005.

EN 1993:1–8, Design of Steel Structures - Part 1–8: Design of Joints. CEN, 2005.

EN 1994:1–1, Design of composite steel and concrete structures - Part 1–1: General rules and rules for buildings. CEN, 2005.

EN 1998-1, Design of Structures for Earthquake Resistance - Part 1: General Rules, Seismic Actions and Rules for Buildings. CEN, 2005.

EN 1992:1–1, Design of Concrete Structures - Part 1–1: General rules and rules for buildings. CEN, 2005.

EQUALJOINTS – European pre-QUALified steel JOINTS: RFSR-CT-2013-00021. Research Fund for Coal and Steel (RFCS) research programme.

Hillerborg A., Modeer M., and Petersson P-E. (1976). Analysis of crack formation and crack growth in concrete by means of fracture mechanics and finite elements. *Cement and Concrete Research*. 6, 773-782. Pergamon Press, Inc. Printed in the United States.

Lee S-J, Lu L-W. (1989) Cyclic tests of full-scale composite joint subassemblages. *Journal of Structural Engineering*. 115(8):1977–98

Lee J., and Fenves G.L. (1998). Plastic-Damage Model for cyclic loading of concrete structures. *Journal of Engineering Mechanics* 124(8) 892-900.

Leon, RT. (1998). Analysis and design problems for PR composite frames subjected to seismic loads. Engineering and structures 20(4-6) 364-71.

Pavlović, M., Heistermann, C., Veljković, M., Pak, D., Feldmann, M., Rebelo, C., Simões da Silva, L. (2015). Connections in towers for wind converters, part I: Evaluation of down-scaled experiments. *Journal of Constructional Steel Research.*

Salvatore W, Bursi OS, Lucchesi D. (2005). Design, testing and analysis of high ductile partial-strength steel–concrete composite beam-to-column joints. *Computers and Structures*. 83(28–30):2334–52.

Simões R, Simões da Silva L. (2001). Cyclic behaviour of end-plate beam-to-column composite joints. *Steel and Composite Structures*. 1(3):355–76.

Tartaglia R., D'Aniello M., (2017a) Nonlinear performance of extended stiffened end plate bolted beam-to-column joints subjected to column removal. *The Open Civil Engineering Journal*, 11, 3-15.

Tartaglia R., D'Aniello M., Rassati G.A., Swanson J., Landolfo R., (2017b). Influence of composite slab on the nonlinear response of extended end-plate beam-to-column joints. *Key Engineering Materials*, 763:818-825.

Tartaglia R., D'Aniello M., Zimbru M., Landolfo R., (2018) Finite element simulations on the ultimate response of extended stiffened end-plate joints. *Steel and Composite Structures.* 27(6):727-745.

Thermou GE, Elnashai AS, Plumier A, Doneux C. (2004). Seismic design and performance of composite frames. *Journal of Constructional of Steel Research*. 60:31–57.

Vasdravellis G, Valente M, Castiglioni CA. (2009). Behavior of exterior partial-strength composite beam-to-column connections: experimental study and numerical simulations. *Journal of Constructional Steel Research*. 65:23–35.

NUMERICAL INVESTIGATION OF MOMENT-RESISTING SLIM-FLOOR BEAM-TO-COLUMN CONNECTIONS

Cristian Vulcu, Rafaela Don, Adrian Ciutina, Dan Dubina
Politehnica University of Timisoara, Department of Steel Structures and Structural Mechanics
Timisoara, Romania
cristian.vulcu@upt.ro; rafaela.don@student.upt.ro; adrian.ciutina@upt.ro; dan.dubina@upt.ro

ABSTRACT

Slim-floor systems present various advantages: (i) additional floor-to-floor space; (ii) natural fire protection for steel beams; (iii) reduction of material consumption. Slim-floor solutions are currently used in non-seismic regions, and there are few studies that consider continuous or semi-continuous fixing of slim-floor beams. Consequently, a study was performed with the aim to develop reliable connections for slim-floor beams, which will ultimately be applicable to buildings located in areas with seismic hazard. The current paper presents the undertaken numerical procedures, and the outcome of the study. In a first stage, a finite element numerical model was calibrated based on a four point bending test of a slim-floor beam. Furthermore, a case study was performed in order to investigate continuous slim-floor beam-to-column connections. Two different types of connections were considered: (i) bolted end-plate, (ii) welded cover plate. The response was investigated considering both sagging and hogging bending moments.

INTRODUCTION

The structural solutions provided by the usage of composite elements are regarded as an effective method of enhancing structural performance. A series of advantages emerge as concrete, steel and additional components are integrated into a more resistant and ductile member (Arcelor-Mittal: "*Slim Floor an innovative concept for floors*"). In particular, the slim-floor building system is attractive to constructors and architects due to the integration of steel beams in the overall height of the floor, which leads to additional floor-to-floor space, used mostly for acquiring additional stories. The concrete slab offers natural fire protection to the steel beams, while the use of novel corrugated steel sheeting reduces the concrete volume, and replaces the secondary beams (for usual spans of steel structures).

Slim-floor solutions are currently used mostly in non-seismic regions – Hauf (2010) & Braun et al. (2014), and there are few studies that consider continuous or semi-continuous fixing of slim-floor beams. Malaska (2000) showed that the semi-continuous joining of slim-floor beams improves the flexural stiffness of slim-floor beams and allows for the use of shallower beam and floor sections, and for a better performance of beams under service conditions, by reducing cracking, deflections and vibrational problems. Wang et al. (2009) and Bernuzzi (1995) showed that in case of increasing gravitational loads, the continuous fixing of the slim-floor beams may lead to ductile plastic hinges, both at beam-ends and middle spans. In contrast, the usual seismic behavior rely on increased frame lateral stiffness and failure mechanisms by dissipation of seismic input energy, through the plasticization of dissipative elements or connections. Consequently, in the case of Moment-Resisting-Frames (MRF) or dual frame configurations considering MRF contribution, the beams or the beam-to-column joints of MRF will dissipate energy through plastic hinges. Therefore, the application of slim-floor beam systems in seismic zones should consider moment-resisting connection with columns, thus developing hogging bending, too. However, certain aspects characteristic for slim-floor systems should be considered (see Fig. 1):

- the concrete slab encases the top steel flange and needs one layer of hogging reinforcement;
- the natural bonding and/or the concrete dowels contribute significantly to the steel-to-concrete connection. In many cases there is no need for additional connectors;
- the bottom part of steel profile is generally larger than the top flange, in order to accommodate the concrete supporting system: shallow decking or precast concrete slabs;

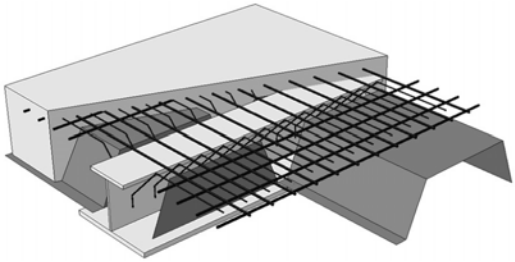


Fig. 1 Slim-floor system.

The current paper presents a study performed with the aim to develop reliable connections for slim-floor beams, with a view to the use in buildings located in areas with seismic hazard. The paper presents the numerical investigations undertaken and the outcome of the study. In a first stage, a finite element numerical model was calibrated based on a four point bending test of a simply supported slim-floor beam. Furthermore, a case study was performed in order to investigate continuous slim-floor beam-to-column connections. Two different types of connections were considered: (i) bolted end-plate, (ii) welded cover plate. The response was investigated considering both sagging and hogging bending moments.

FEM CALIBRATION OF A SLIM-FLOOR BEAM

Research background

The numerical analysis of slim-floor beam-to-column joints is based on an initial calibration of a finite element (FE) numerical model based on the experimental investigation conducted by Hauf (2010) on a four-point bending test of a slim-floor beam. This phase was needed due to the lack of data regarding continuous connections for slim-floor beams. This also represented a comparison basis which appropriately checked the accuracy of the beam-to-column connection models. This information became crucial with regard to the behavior of a composite element, the steel-to-concrete friction coefficient, the modeling procedure, the importance of “concrete dowels” and reinforcement, the meshing techniques and interactions.

Calibration of the numerical model

The calibration of the numerical model was performed based on the data available in Hauf (2010). This study presents the experimental testing of an 8 m long slim-floor assembly, represented by a 4-point-load arrangement, as shown in Fig. 2. The various components of the slim-floor beam are presented in Fig. 3. The complete technical information (e.g. geometry, boundary conditions, materials, etc.) is available in: Hauf (2010), Braun et al. (2014) and Braun et al. (2015). The numerical investigation was performed by means of the Abaqus v6.13 finite element modelling software. It is to be noted that the measuring units adopted for the definition of the geometry, material properties and loading conditions were millimeters (mm) and Newtons (N).

The material characteristics are defined within the numerical model for the following: concrete (C30/37), structural steel (S355) and reinforcement bars (S450), based on the real mechanical characteristics provided by the authors. The elastic behavior of the steel elements is described by: Young’s modulus E=210000 N/mm^2 and Poisson’s ratio v=0.3, whereas the plastic behavior

is illustrated in Fig. 4a. The input characteristics for the concrete elastic domain are: Young's modulus E=32500 N/mm^2 and Poisson's ratio v=0.2. The plastic domain behavior is defined by the stress-strain curve shown in Fig. 4b, without considering the tensile resistance.

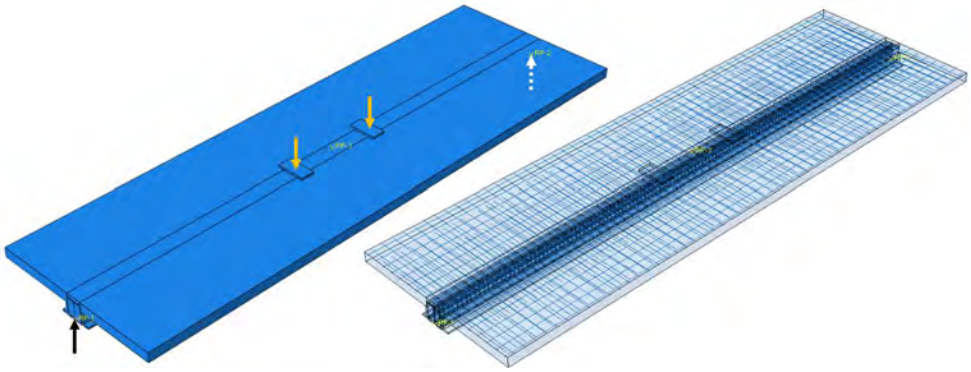


Fig. 2 Slim-floor beam – 3D view: static scheme; reinforcing bars arrangement.

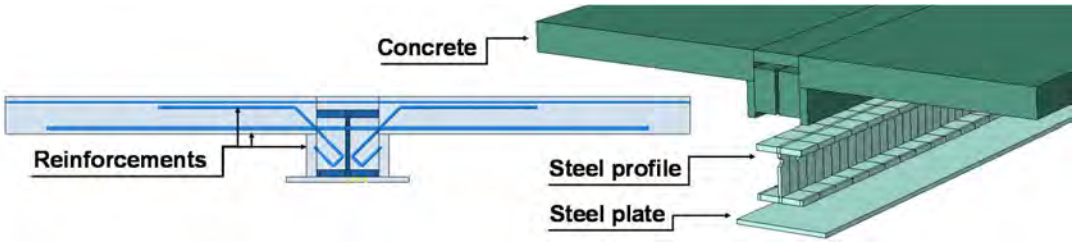


Fig. 3 Slim-floor beam components: reinforcing bars, concrete deck, steel profile, and steel plate.

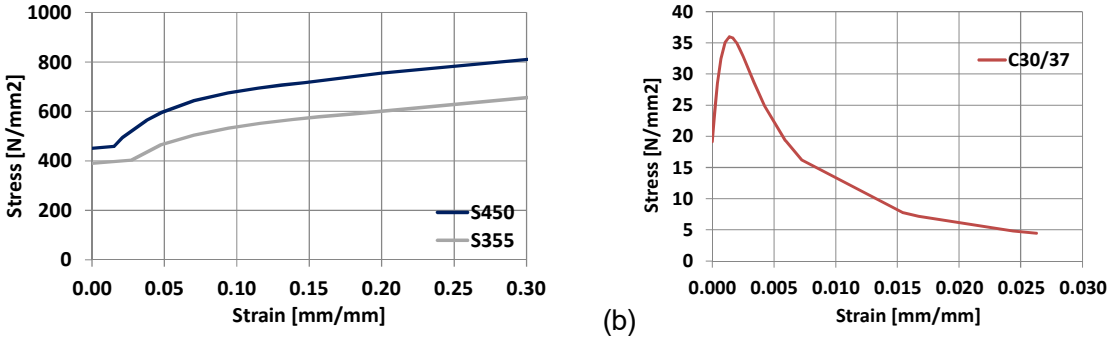


Fig. 4 Material model: (a) true stress - true strain curve for structural steel (S355) and reinforcing bars (S450); (b) stress-strain relationship for concrete.

Three types of interactions were used in this numerical model: embedded, tie and rigid body. In order to replicate the interface behavior of steel and concrete, an interaction law (and contact) was defined with a normal and tangential behavior. The normal behavior was assigned by "hard contact", which allows for surface separation. The tangential behavior was characterized by "penalty" with a friction coefficient in amount of v=0.6. The reinforcement was connected to the concrete part using the embedded constraint.

The "Dynamic Explicit" type of analysis was considered, due to the large amount of contact surfaces (e.g. between the steel profile and the surrounding concrete). Contact problems are more easily solved by using the "Dynamic Explicit" analysis, in contrast to the "Static General" analysis. In terms of the finite element type, the following have been used: (i) B31 for reinforcing

bars; (ii) C3D8R for steel profile, steel plates, concrete dowel and concrete. The approximate global size of finite elements / mesh was considered as follows: reinforcing bars (30 mm), concrete slab (23 mm), concrete dowel (12 mm), steel profile (13 mm), bottom steel plate (18 mm), lateral steel plate (13 mm). An overall view of the meshed assembly is shown in Fig. 5.

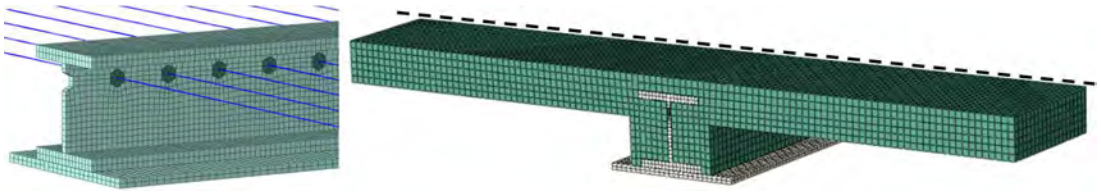


Fig. 5 Overall assembly view: mesh discretization.

Calibration results

The results of the numerical investigation are presented in terms of "bending moment – vertical displacement" curve (M-δ) in Fig. 6a. The deformation of the slim-floor beam model is illustrated in Fig. 6b. As can be observed, the numerical model is able to accurately reproduce the response of the tested specimen, in terms of both initial stiffness and composite assembly's capacity. Being justified by the symmetrical loading and boundary conditions, the response is illustrated only for the left side. The stress distribution and the plastic strain are also presented for the following components: concrete (Fig. 7a), steel profile (Fig. 7b), reinforcing bars (Fig. 7c).

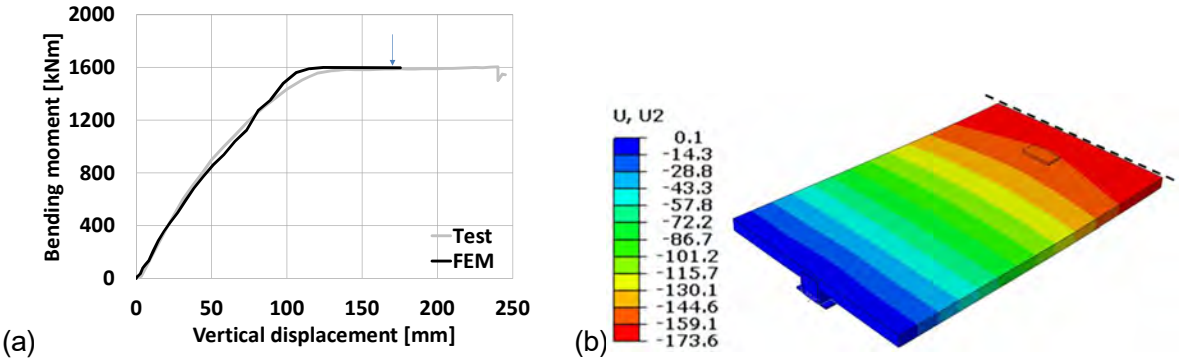


Fig. 6 Bending moment–vertical displacement curve (M-δ), Vertical displacement.

It can be easily observed in Fig. 7b that large plastic deformations (strain) appear in the steel profile's bottom flange, including the welded steel plate, similarly to the real failure mode.

Fig. 7a shows the stress distribution and the plastic strain that correspond to the concrete slab. Following the maximum bending formation, maximum stresses are logically concentrated in the middle of the span. However, in addition to the mid-length stress concentration, longitudinal yielding appears nearby the supports, justified by the presence of the shear force, absent between the two loading points.

Fig. 7c shows the stress distribution and the plastic strain in reinforcement bars. The maximum values are found in the middle of the span. An important aim of the numerical simulation was to involve the reinforcing bars and steel meshes in the load transfer mechanism. The inclined bars contribute to a large extent to the load transfer mechanism by connecting the concrete slab to the concrete located between the steel profile's flanges, thus preventing the separation of the two. Moreover, the reinforcing bars that pass through the web perforations, together with the effect of concrete dowels, contribute to the composite action of the assembly.

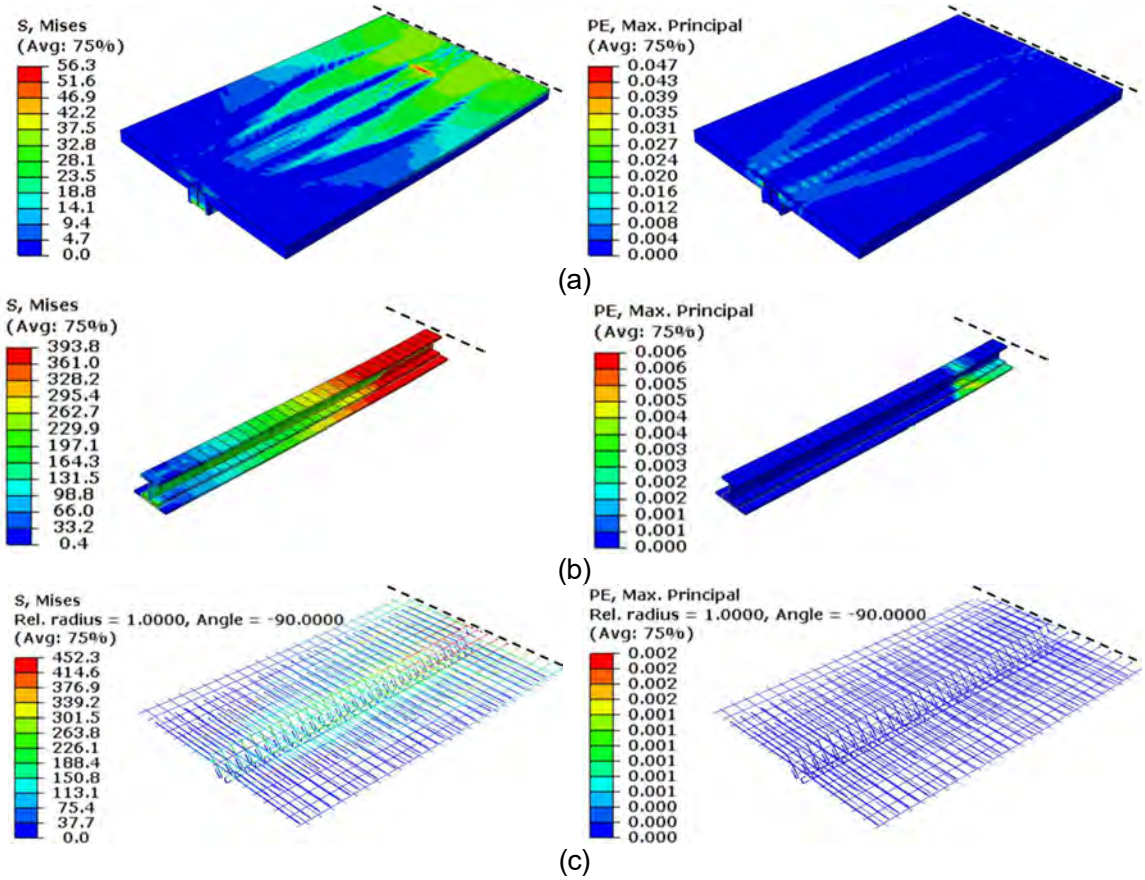


Fig. 7 Mises stress distribution and plastic strain in: (a) concrete, (b) steel profile, (c) reinforcing bars and meshes.

Concluding remarks

The calibration of the slim-floor beam has allowed setting various parameters related to the FE modelling. Moreover, the numerical investigation has also allowed for the assessment of the load transfer and the failure mechanism. In particular, the assembly failure mechanism resided in the formation of a plastic hinge in the mid span, justified by the large plastic deformations of the steel profile and the steel plate.

The FE calibration of the behavior of the slim-floor beam model leads to some important modeling features:

- the finite element investigation of the slim-floor assembly implies modeling both the transverse and the longitudinal reinforcing bars, as well as the inclined reinforcing bars. The adding of reinforcement bars to the model may improve the overall behavior of the assembly by enhancing its load bearing capacity. The overall involvement of the reinforcing bars and steel meshes in the load transfer mechanism is evident in this case;
- the inclined bars emphasize great significance in the load transfer mechanism by connecting the concrete slab to the concrete located between the steel profile flanges, thus preventing the separation of the two. The reinforcing bars that go through the web perforations, together with the concrete dowels, contribute to the composite action of the assembly.

NUMERICAL INVESTIGATION OF SLIM-FLOOR BEAM-TO-COLUMN CONNECTIONS

Configuration of the joint models

Based on previous calibration, six beam-to-column joint models were developed. Table 1 offers an overview of the joint models, and shows for each model the following information: (i) abbreviation, (ii) steel grade, (iii) concrete slab, (iv) transversal and longitudinal reinforcement, (v) inclined reinforcement, (vi) connection type.

Table 1 Investigated beam-to-column joint assemblies with slim-floor beams.

Nr.	Abbrev.	Steel	Concrete slab	T+L* reinforcement	Inclined Reinforcement	Connection
1	M1-S	S355	NO	NO	NO	Bolted end-plate
2	M2-SC	S355	YES	Ø6/100	NO	Bolted end-plate
3	M3-SC	S355	YES	Ø6/100	Ø6/100	Bolted end-plate
4	M4-SC	S355	YES	Ø10/100	Ø6/100	Bolted end-plate
5	M5-SC	S355	YES	Ø10/100	Ø6/20	Bolted end-plate
6	M6-SC	S355	YES	Ø10/100	Ø6/20	Welded cover plate
*T+L presence of the transversal and longitudinal reinforcement bars.						

The numerical models of the joints were developed based on an iterative process. E.g., in order to assess the importance of adding concrete and reinforcement bars to an assembly, the first model (M1-S) only includes steel elements. The models developed later included the concrete slab and different types of reinforcement.

Fig. 8 shows the configuration of the investigated beam-to-column joint model assemblies. In particular, the T-shape joint assembly (see Fig. 8ab) is composed of a slim-floor beam and a steel column. With a view to a better visualization of the joint components, the joint assembly in Fig. 8a has been disassembled into components in Fig. 8b to Fig. 8g.

The concrete slab integrating the steel beam and the reinforcement (transversal, longitudinal and inclined) has an effective width of 1200 mm and a height of 70 mm (computed according to the current EN 1994-1 (2004) conditions) and surrounds the column over a width of 450 mm. The concrete in the bottom troughs has been ignored in the analysis and consequently not modeled. It is to be noted that the reinforcement present in M3-SC to M6-SC models satisfy the reinforcement connection requirements of the Annex C of EN 1998-1-1 (2004).

The steel column profile is an HEB500, while the steel beam is composed by a bottom steel plate (Pl-20x390x1300 mm) welded to a half of an IPE450 profile. The column length is of 3200 mm, while the beam length is 1300 mm. An additional web plate and continuity plates have been used in the column web panel. Transversal, longitudinal and inclined reinforcement has been used for the concrete slab (see Fig. 8 c-d-e). The continuity of longitudinal reinforcing bars is assured around the column (Fig. 8d). It is to be noted that the usual diameter of reinforcement bars for slabs is Ø=6 mm, which justifies the choice of the first diameter used in the study (see Table 1). Moreover, the longitudinal reinforcing bars have been included in order to contribute to the negative bending moment capacity within the connection zone.

The connection between the slim-floor beam and the column is realized as: (i) bolted extended end-plate connection (Fig. 8d), (ii) welded cover plate connection (Fig. 8g). The bolted connection is realized using an extended end-plate and five bolt rows of M22-Gr.10.9 bolts (see Fig. 8d), while the welded connection is realized using cover plates (see Fig. 8g).

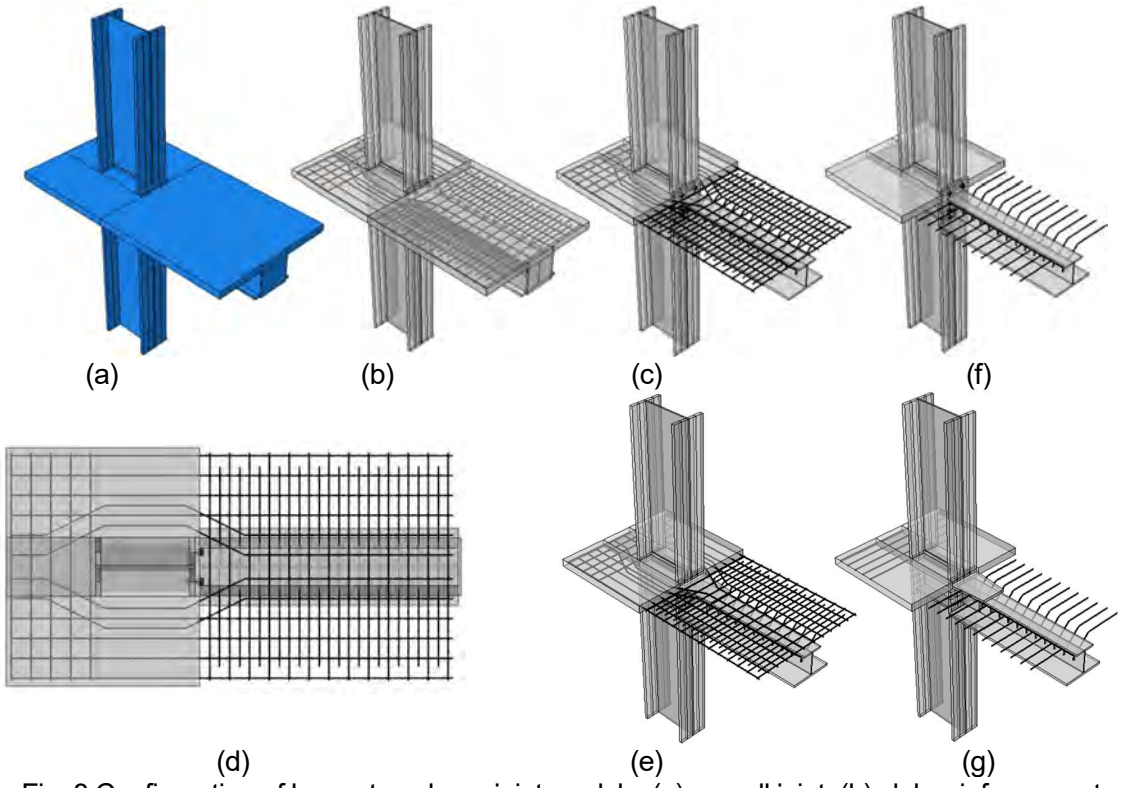


Fig. 8 Configuration of beam-to-column joint models: (a) overall joint, (b) slab reinforcement, (c)/(d)/(e) steel beam and reinforcement (longitudinal and transversal), (f)/(g) bolted end-plate / welded cover plate connection and inclined reinforcement.

Modelling procedure

The numerical investigations of the slim-floor beam-to-column joint assemblies (see Fig. 8) were performed by means of the Abaqus v6.13 software. Finite beam elements have been used for the reinforcement, and solid elements for the other components (bolts, plates, concrete, etc.). For the definition of the geometry and mechanical characteristics, millimeters and Newton's have been used as measuring units. The material characteristics have been defined for the following nominal characteristics: concrete (C30/37), structural steel (S355), bolts (H.R.10.9), and reinforcement bars (S400), by considering both elastic and plastic properties. Fig. 9 illustrates the true stress – true strain curves (except for the elastic deformation) for bolts (Gr.10.9), reinforcement (S400) and structural steel (S355). The material model for bolts has been defined based on a previous calibration of a T-stub characterized by failure mode 3 (i.e. bolt failure) – see Dubina et al. (2015). For all steel elements, the elastic modulus for steel has been taken as 210000 N/mm^2, and the Poisson coefficient was 0.3. The material model behavior used for concrete is shown in Fig. 4b.

A "Dynamic Explicit" type of analysis has been adopted, justified by the complex contacts between the various parts of the joint assembly (i.e. concrete, steel beam, bolts, end-plate, and column). For the contact between the various parts of the joint assembly, a contact law was defined with normal and tangential properties. The normal behavior was assigned through "hard contact", which allows for surface separation. The tangential behavior was characterized by "penalty", with a friction coefficient in amount of v=0.6. The connection between the reinforcement and the concrete slab was defined by using the "embedded region" constraint type. The discretization of the components was performed by using: (i) B31 finite element types for the reinforcing bars, (ii) C3D8R finite elements for the rest of the components. The global mesh size was adapted to

different FE: reinforcing bars – 20 mm; concrete – 17 mm; steel profile – 12 mm; bottom steel plate – 14 mm; column – 16 mm; end plate – 12 mm; column web plate and stiffeners – 14 mm; bolts – 7 mm. The discretization of the beam-to-column joint assembly / components is illustrated in Fig. 10. Boundary conditions were specified for the column and the beam: (i) at the top and the bottom ends of the column, a simple and respectively a fixed support were defined; (ii) at the tip of the beam, the load was applied in displacement control, which resulted in a positive or negative bending moment within the connection zone.

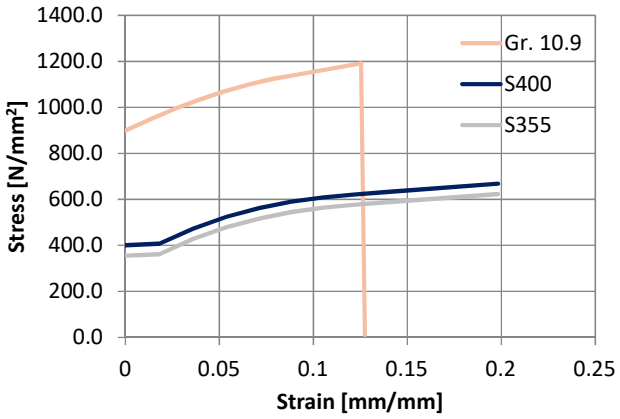


Fig. 9 True stress - true strain curve for steel (S355), reinforcement bars (S400) and bolts (Gr.10.9).

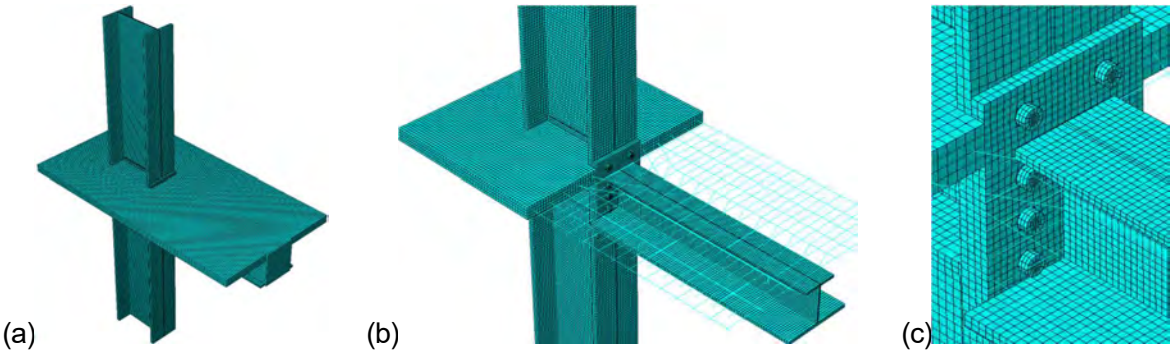
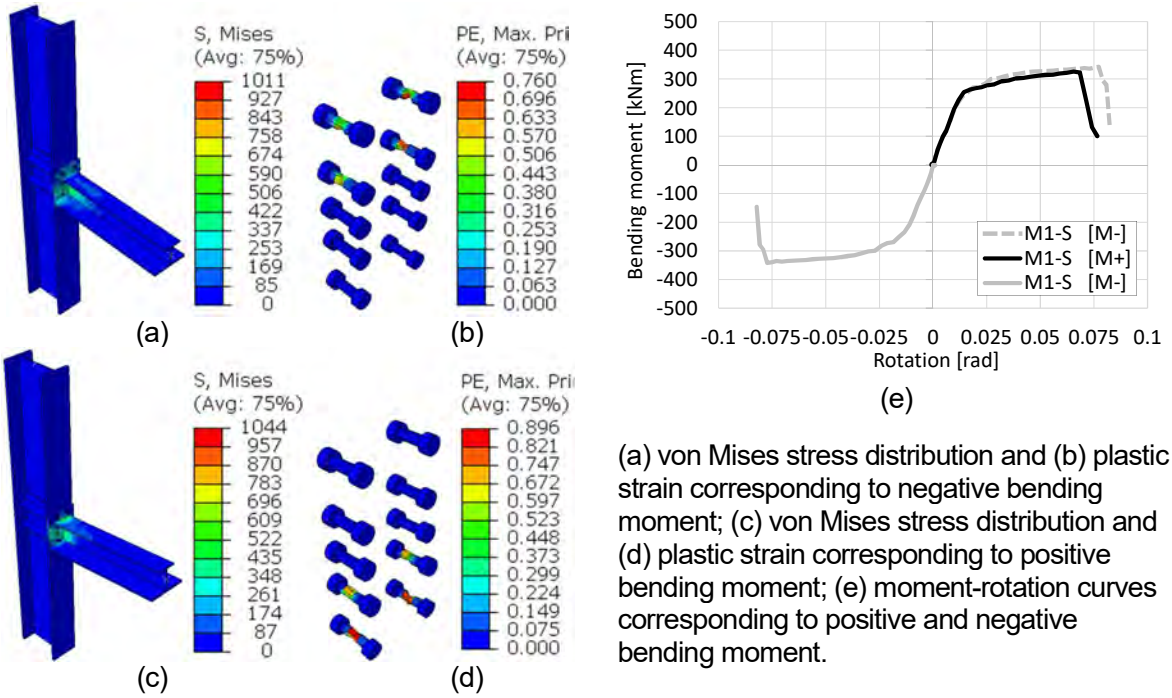


Fig. 10 Discretization of the beam-to-column joint assembly / connection.

Numerical result

The numerical models of the six beam-to-column joint assemblies were subjected to negative and positive bending moments. The numerical program allowed assessing the response in terms of moment-rotation curve, stress distribution and plastic strain. The failure mechanism was obtained, and from the comparison of moment-rotation curves, the influence of each parameter was assessed. In order to reach a uniformity of the results, the bending moments and the rotations were computed at the column face.

The response of the M1-S joint assembly is illustrated in Fig. 11. Under negative bending moment (Fig. 11a), the upper two bolt rows showed large plastic deformation (Fig. 11b), while under positive bending moment (Fig. 11c), the lower two bolt rows failed (Fig. 11d). Consequently, under both loading conditions, the failure mode was similar. The corresponding moment-rotation curves are presented in Fig. 11e. The comparison showed identical stiffness but with slightly higher capacity under negative bending, justified by the slightly un-symmetrical positioning of the bolt rows.



(a) von Mises stress distribution and (b) plastic strain corresponding to negative bending moment; (c) von Mises stress distribution and (d) plastic strain corresponding to positive bending moment; (e) moment-rotation curves corresponding to positive and negative bending moment.

Fig. 11 Response of M1-S joint assembly.

Fig. 12 shows the response of the M2-SC and M3-SC joint configurations in terms of moment rotation-curve (positive and negative). From the comparison between M1-S and M2-SC (see Fig. 12a), it can be observed that the presence of the reinforced concrete slab led to increased capacity and stiffness. Under a positive bending moment, the lever arm increased due to the presence of the concrete slab (70 mm thick above the upper beam flange). Under a negative bending moment, although there was an obvious increase of the initial stiffness, the longitudinal reinforcement within the slab (subjected to tension) slightly increased the capacity. The M2-SC model showed a separation between the concrete deck and the concrete within the beam flanges. This confirmed the importance of the inclined reinforcement that connected the two regions.

From the comparison between M2-SC and M3-SC (see Fig. 12b), it can be observed that the presence of the inclined reinforcement (Ø6/100 mm) led to a slight increase of capacity under a negative bending moment. Moreover, it was observed that the separation effect between the two concrete regions (i.e. the concrete slab and the concrete within steel flanges) was reduced.

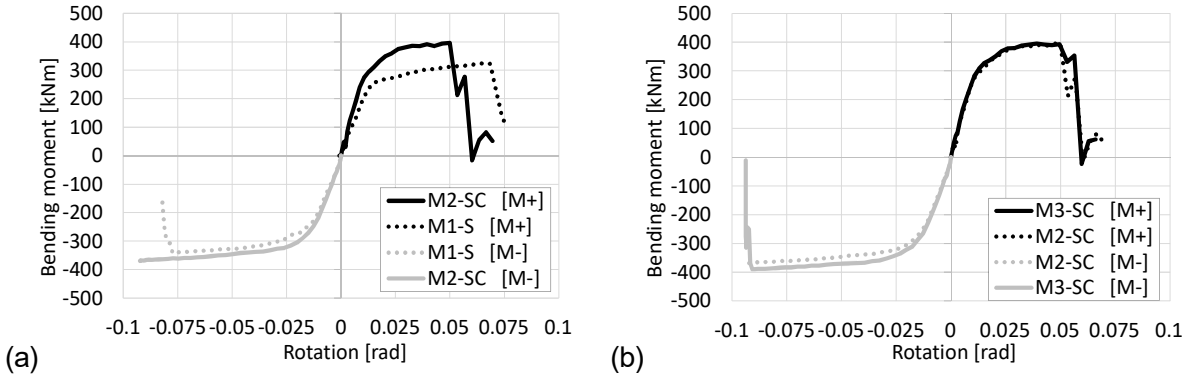
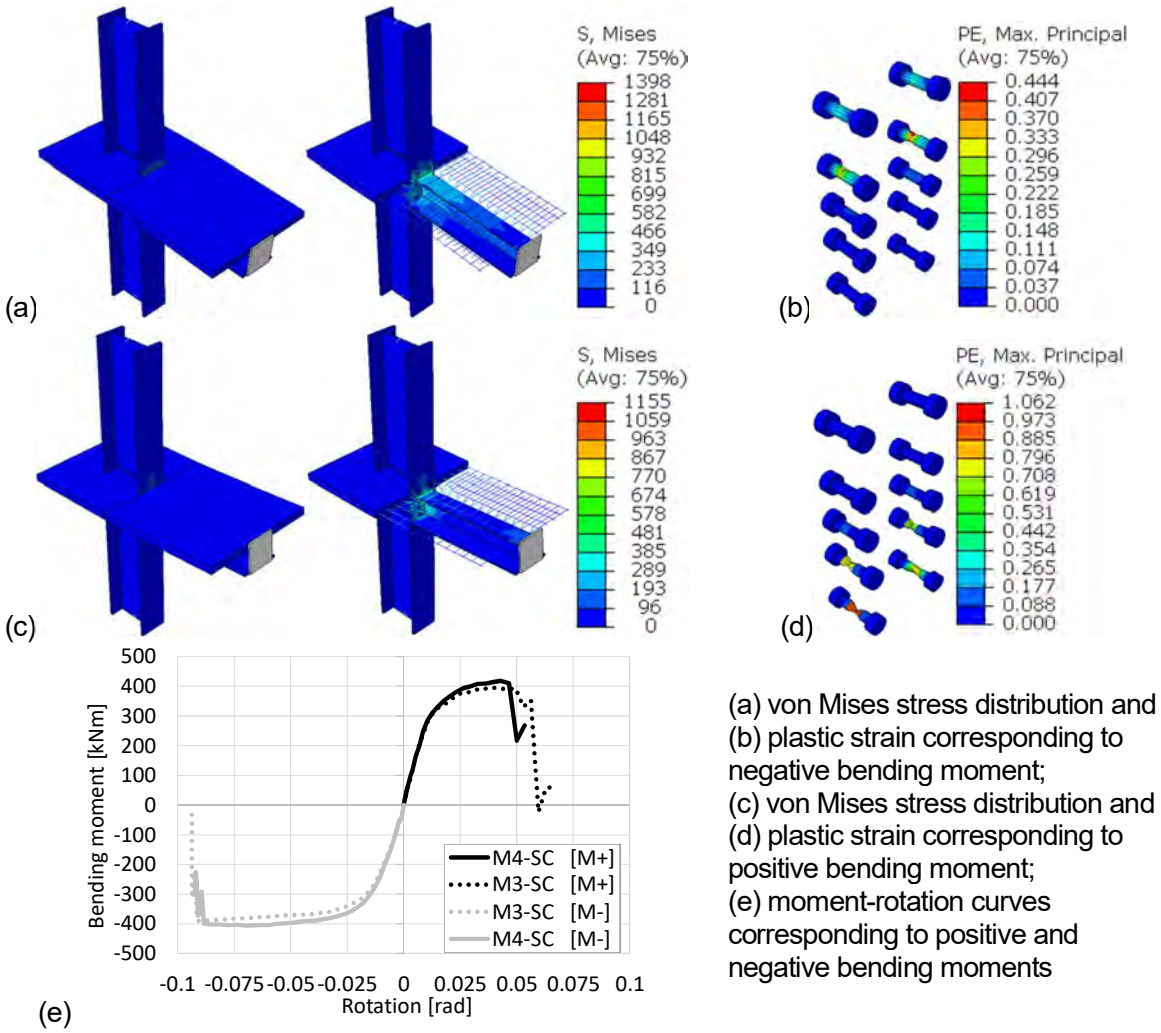


Fig. 12 Moment-rotation curves under positive and negative bending moment: (a) comparison between M2-SC and M1-S assembly; (b) comparison between M3-SC and M2-SC assembly.

In the case of the M4-SC joint configuration, the longitudinal and the transversal reinforcement was increased to Ø10/100 mm (see Table 1). The response of the M4-SC joint assembly is illustrated in Fig. 13. Under both loading conditions, the failure modes were similar, i.e. failure of bolts under tension. The corresponding moment-rotation curves are shown in Fig. 13e. The comparison showed slightly higher stiffness and capacity under a positive bending moment. A higher ductility corresponds to the negative bending moment, due to the presence of the reinforced concrete slab.

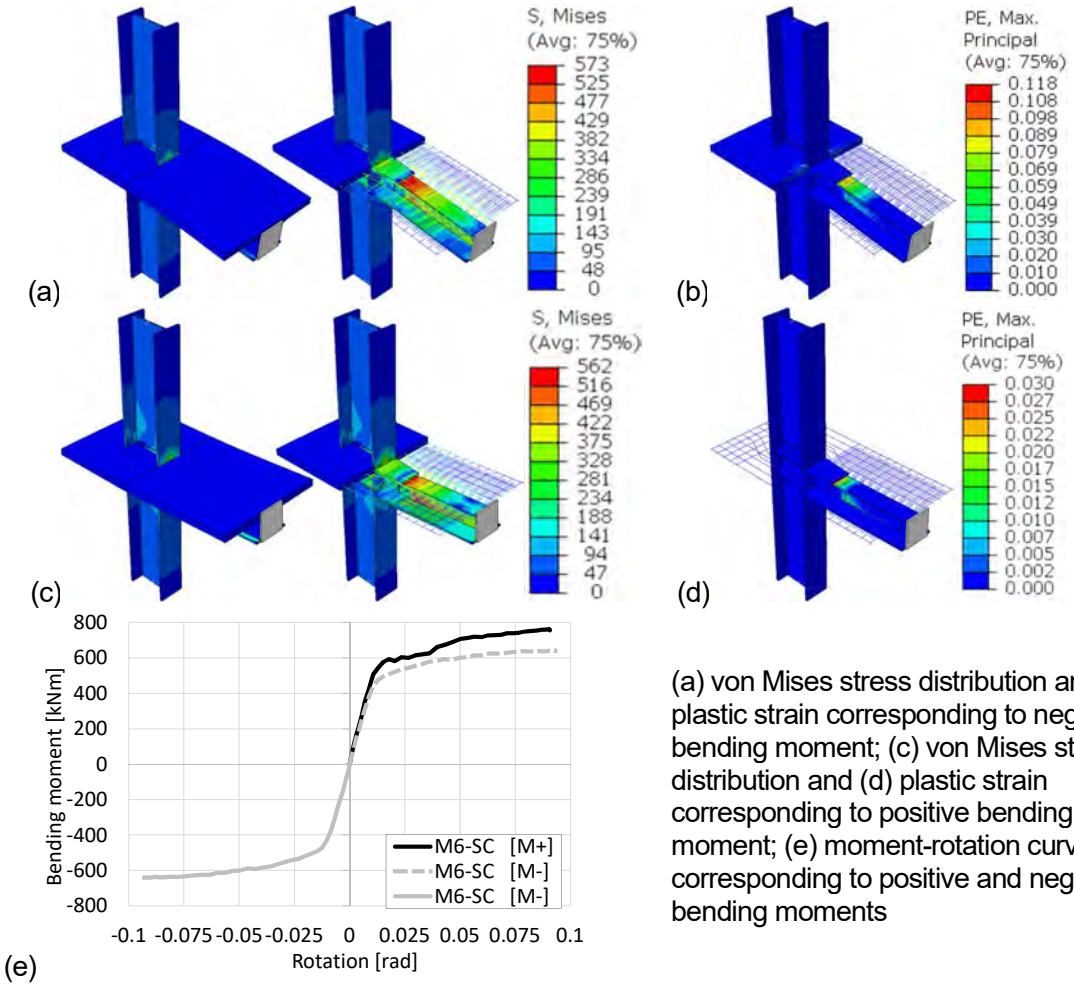


(a) von Mises stress distribution and (b) plastic strain corresponding to negative bending moment; (c) von Mises stress distribution and (d) plastic strain corresponding to positive bending moment; (e) moment-rotation curves corresponding to positive and negative bending moments

Fig. 13 Response of the M4-SC joint assembly.

From the comparison between M4-SC joint model and M3-SC, respectively M5-SC – it was observed that a higher amount of reinforcement led to a slightly higher capacity. For the same amount of longitudinal and transversal reinforcement, the increase of the inclined reinforcing bars did not improve the response significantly.

Fig. 14 shows the response of the M6-SC joint assembly (with welded cover plate connection). Under negative and positive bending moments (see Fig. 14a / Fig. 14c), large plastic deformations developed in the steel profile (see Fig. 14b and Fig. 14d), i.e. the failure mechanism consisted in the formation of a plastic hinge in the slim-floor beam. The presence of the concrete slab led to a slightly higher capacity under positive bending moment (Fig. 14e).



(a) von Mises stress distribution and (b) plastic strain corresponding to negative bending moment; (c) von Mises stress distribution and (d) plastic strain corresponding to positive bending moment; (e) moment-rotation curves corresponding to positive and negative bending moments

Fig. 14 Response of the M6-SC joint assembly.

Fig. 15a shows an overview with regard to the response of three investigated joint assemblies. The lowest stiffness and capacity corresponds to the bare steel joint (M1-S), and the highest corresponds to the slim-floor beam-to-column joint with welded cover plate connection (M6-SC).

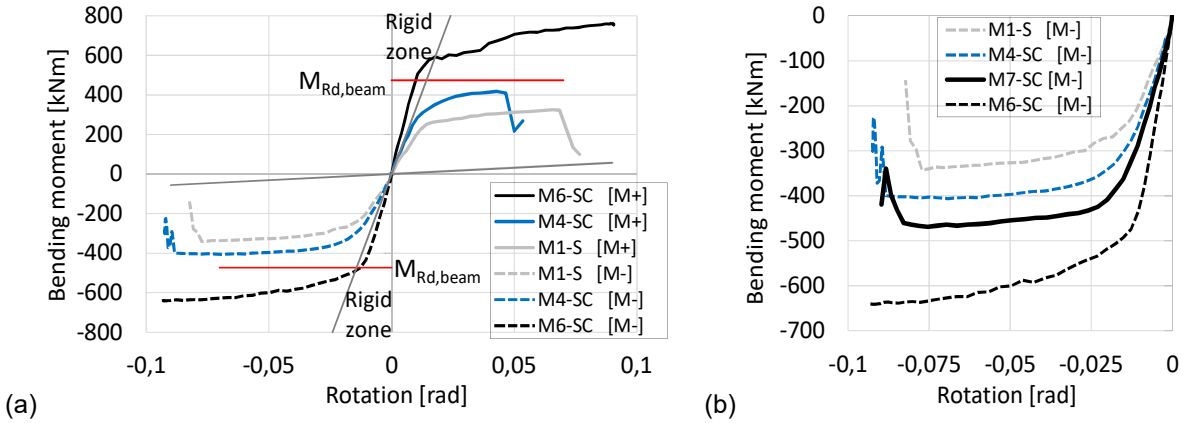


Fig. 15 (a) Overview of slim-floor beam-to-column joint response; (b) Influence of the increased amount of longitudinal reinforcement (in an additional joint model ***M7-SC***) compared to M4-SC.

CONCLUSIONS

The current study has been performed with the aim to develop reliable connections between slim-floor beams and columns – with a view to the application in structures located in seismic zones. In a first stage, a numerical model was calibrated based on a four point bending test of a slim-floor beam. Furthermore, a case study was performed in order to investigate two types of continuous slim-floor beam-to-column connections: (i) bolted end-plate, (ii) welded cover plate. The numerical calibration of the slim-floor beam allowed assessing the load transfer and the failure mechanism (plastic hinge at mid span). It proved the feasibility and the performance of the steel-concrete connection, i.e. reinforcing bars passing through the profile web and thus forming concrete dowels. The FEM investigation on slim-floor beam-to-column joints have shown that:

- The influence of the concrete slab is effective in sagging bending when it contributes to the global increase of both the stiffness and the bending capacity. In hogging, its influence is negligible and the connection is practically based on the steel components;
- For the modeled cases, the bolted end-plate connections can provide only limited resistance and stiffness due to the limited height, leading to semi-continuous joints (semi-rigid and partial resistant). Further studies are intended in order to observe their applicability in the case of dual frames in different seismic zones. In order to achieve continuous joints, welded cover plate connections (M6-SC type) may be a solution;
- The failure mode of the end-plate steel joint assembly was represented by the failure of bolt rows in tension (brittle failure). The presence of the reinforced concrete slab led to a limited increase in capacity and stiffness. The inclined reinforcement contributed to the load transfer mechanism by connecting the concrete slab to the concrete within flanges. A significant increase in longitudinal reinforcement will lead to a higher capacity under a negative bending moment (see M7-SC in Fig. 15b). In contrast, the failure mode of M6-SC joint assembly was represented by the formation of a plastic hinge in the slim-floor steel beam.

Based on existing studies and on the current study, it is proven that the slim-floor beams may be adapted to Seismic-Resistant Structures and the key-aspect is related to the behavior of slim-floor beam-to-column joints. Future research activities will involve experimental investigations as well as structural numerical investigations, in order to assess the applicability of such systems.

REFERENCES

Abaqus v6.13 [Computer software]. Dassault Systèmes, Waltham, MA.

Arcelor Mittal, “Slim-floor - innovative concept for floors”. Long Carbon Europe Sections & Merchant Bars.

Bernuzzi C., Gadotti F., Zandonini R., (1995). Semi-continuity in slim floor steel–concrete composite systems, 1st European Conference on Steel Structures. Eurosteel 1995.

Braun M., Obiala R., Odenbreit C., Hechler O., (2014). „Design and Application of a new Generation of Slim-Floor Construction”, 7th European Conf. on Steel & Composite Structures, Naples, Italy.

Braun M., Obiala R., and Odenbreit C., (2015). Analyses of the loadbearing behaviour of deep-embedded concrete dowels, CoSFB. Steel Construction, 8: 167–173. doi:10.1002 / stco.201510024.

Dubina D., et al. (2015). “High strength steel in seismic resistant building frames.” Final Rep. Grant No. RFSR-CT-2009-00024, RFCS Publications, European Commission, Bruxelles, Belgium.

EN 1994-1-1 (2004). “Eurocode 4: Design of composite steel and concrete structures—Part 1: General rules and rules for buildings”. Brussels, Belgium.

EN 1998-1-1 (2004). “Eurocode 8: Design of structures for earthquake resistance—Part 1: General rules, seismic actions and rules for buildings.” Brussels, Belgium.

Hauf G., (2010). Trag- und Verformungsverhalten von Slim-Floor Trägern unter Biegebeanspruchung.

Malaska M., (2000). Behaviour of a Semi-Continuous Beam-Column Connection for Composite Slim Floors, Ph.D. Thesis, Espoo, Finland, ISBN 951-22-5224-4.

Wang Y., Yang L., Shi Y., Zhang R., (2009). Loading capacity of composite slim frame beams, Journal of Constructional Steel Research 65 (2009) 650–661.

Improved Beam-to-Column Connection for Partially Encased Composite Structure

Yiyi Chen
Tongji University
Shanghai, China
yiyichen@tongji.edu.cn

Guanghong Chuan
Tongji University, China
rabbit_chuan@163.com

Jie Li
Tongji University
Shanghai, China
tongjilijie@163.com

ABSTRACT

For partially encased composite (PEC) structural frames the connection is one of the key issues. In Eurocode, there are recommended configurations of the connection which can be considered as rigid or semi-rigid, but is more apt to fit the requirement under monotonic loads. In this paper, an improved beam-to-column connection based on Eurocode configurations is suggested. Loading tests on the proposed connection specimens are carried out. The test designs two basic situations, one is the failure of connection, to observe the damage mechanism and to evaluate the resistance of the connection, the other is the failure of PEC beam, to check whether the proposed connection can guarantee the bending strength and ductility of the beams. Test results show that the proposed connection possesses expected load capacity, satisfied deformability and enables the connected beam to develop fully plastic deformation, therefore, the improved connection is suitable for resisting cyclically reversed moments in earthquake.

1 Introduction

Partially encased composite (PEC) structure possesses many advantages, one of which is the possibility to pre-fabricate members in workshop. This advantage has been paid more attention in recent several years, and PEC structure is considered a potential structural system for modern construction industrialization in China.

For pre-fabricated structures, the connection is a key issue. In Eurocode [1], there are several recommended configurations of the beam-to-column connections by bolt joint. However, those connections are typical pin connection or the one with asymmetrical moment resistant capacity. With the configuration of upper extended end plate of beam, the connection can afford the resistance against the moment induced mainly by gravity load, but relatively weak capacity to the moment reversed. If the designer tends to make the connection resist beam end moment in

two directions, which is the demand of moment resisting frames, the connection details recommended by Eurocode need to be improved.

PEC members including columns, beam-columns and beams have been extensively studied, covering variety of load patterns [2-10] in recent three decades, however, few public literatures concern the behavior of PEC beam-to-column connections, neither does the hysteretic behavior of them.

In this paper, an improved bolt beam-to-column connection based on Eurocode configurations is suggested. The target of the improvement is to enable the connection resist cyclically reversed moment during earthquake. An extended end-plate out of the beam section in upper and low edges with the possible arrangement of bolts is detailed designed. Loading tests are carried out. The tests aim at two targets, one is to investigate the failure mechanism of connection, the other is to check the capacity of the connection to allow development of full plastic moment at beam end. The test results are reported in the paper.

2 Configuration and constructional detail of improved PEC connection

2.1 Conventional configurations of PEC beam-to-column connection

Figure 1 shows the conventional configurations of PEC beam-to-column connection. All of them are with bolt joint, which makes construction on site free of weld. However, as for the connection performance, three of them could be taken as pin connection if only PEC beam is considered (Figure 1a, b and d). The else one using beam end plate (Figure 1c) can resist moment induced mainly by gravity load. Though all the connections together with the above slab have the capacity to resist beam end moment, for reversed bending action in earthquake the resistance may not be deemed enough.

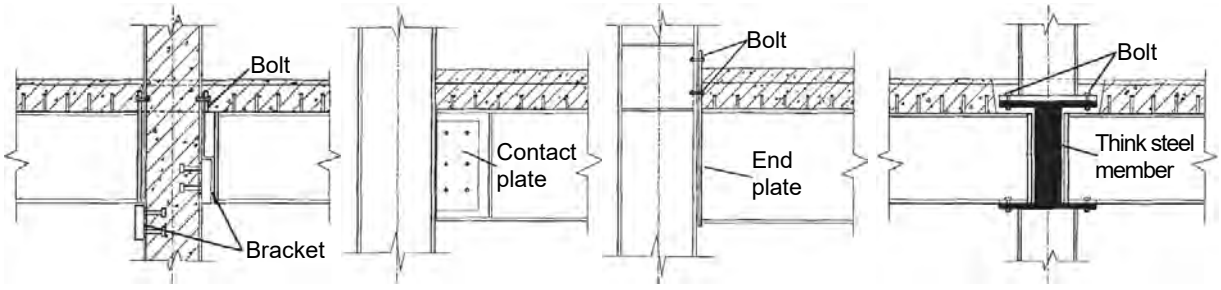


Fig 1 – Conventional configurations of PEC beam-to-column connection

2.2 Objectives of the connection improvement and its details

The next aspects are set as the objectives of the connection improvement:
(1) To make the connection possessing the capacity against cyclically reversed moment at beam end.
(2) To facilitate the assembling operation on construction site.
(3) To maximum the precast concrete part in PEC members.
As the result, the improved connection as shown in Figure 2 is adopted.

The end plate on beam is extended in two sides, instead of the one as shown in Figure 1c where the plate only extends in upper side. Furthermore, the extended part is reinforced by pair of triangular ribs so that it has enough stiffness and resistance against moment.

High-strength bolts are to be used for convenience in site assembling. Two possible arrangements of the bolts are considered. In case of the beam with narrow flange, bolts in middle shall arranged outside the PEC beam section as shown in Figure 2b, while in case of the wide beam, bolts in middle can be within the profile of PEC beam section.

In the latter case, a separating plate near beam end (Figure 2d) is designed to leave operation space for bolt installation on site. For the other part of the beam except for the operation space concrete is able to be cast in workshop in advance. The same countermeasures are also taken for PEC column. A pair of horizontal separating plates is welded to the H steel above and beneath the stiffeners of panel zone, as referred in Figure 2a. Within the scope of two separating plates and steel flanges, concrete shall be cast after the bolts are tightened in erection. For the main body of the column, however, the concrete shall be precast in workshop, so the casting concrete work on site is remained in a small amount.

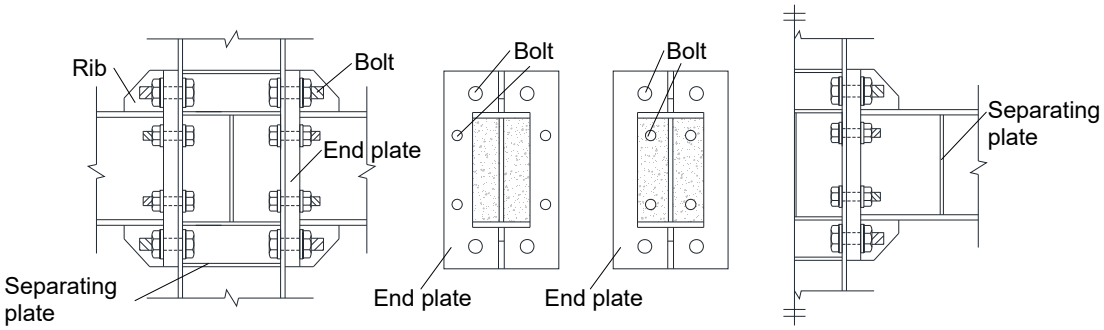


Fig 2 – Configuration of improved connection

3 Experimental programs

3.1 Design and fabrication of specimens

To realize the test purpose, i.e., to investigate the failure mechanism of connection and to check whether the connection allows beam end to develop fully plastic deformation, the specimens were designed in two expected failure modes, one is failure of connection and the other is failure of beam.

The specimen is formed in crucial configuration as shown in Figure 3. There are total six specimens. The specimen code is composed of 2 letters and 2 numbers. The letters indicate the expected failure mode and load condition in test. The first letter J or M refers to connection failure mode or member failure mode, respectively, and the last letter C refers to cyclic load pattern. The digits in specimen code indicate the configuration details. The first digit number 1 or 2 refers to the middle bolts between H steel flanges inside or outside the concrete of PEC beam (Figure 2b&2c), while the second digit number 1 or 2 denotes whether horizontal reinforcement bars in panel zone exist or not. The parameters of the specimens are shown in Table 1.

There are two basic types of PEC sections. One with the relatively stocky steel element and shear stud, longitudinal rebar and stirrup is recommended by current Eurocode (Figure 4a), and the other is featured with relatively thin steel element and free from stud and stirrup (Figure 4b). In this research, the latter is adopted. Built-up steel section is used. For the specimens designed as connection failure mode (J series), the steel column web in joint region is replaced with 4 mm thick plate, and its steel plate is shifted into Q235 with normal yield strength of 235 MPa lower than the column body adopting Q345 with normal yield of 345 MPa.

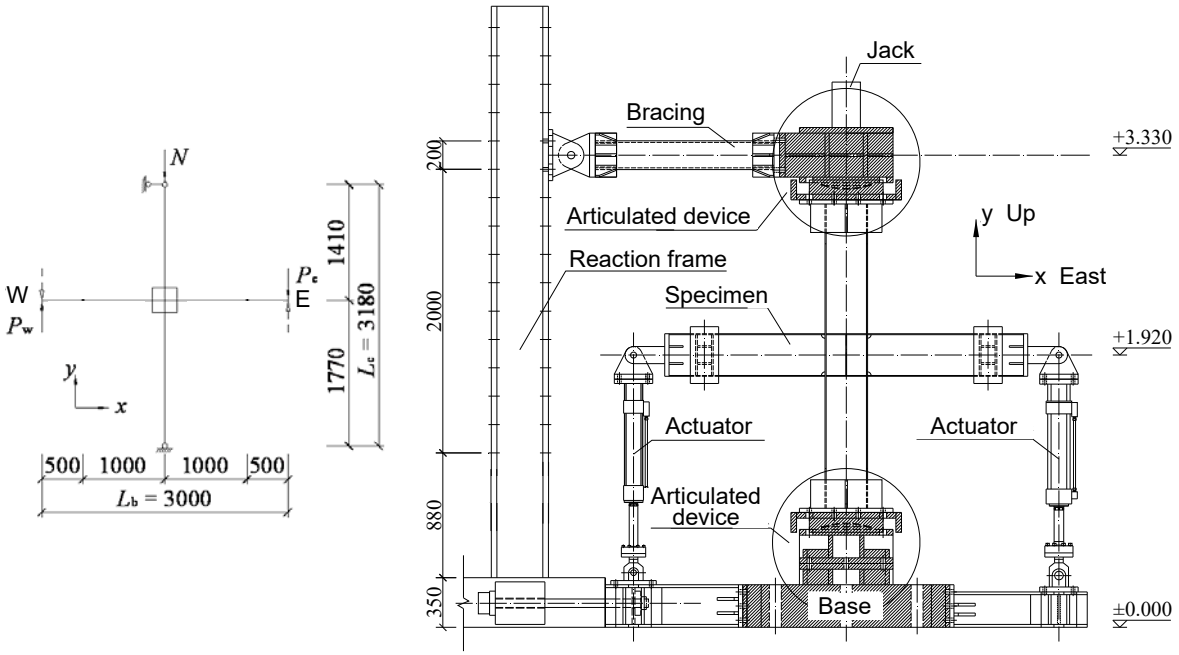


Fig 3 – The test specimen and loading set up

Table 1 – Parameters of specimens

Code	J11-C	J12-C	J21-C	J22-C	M11-C	M22-C
Section of steel beam	B1		B2		B3	B4
B_b/t_{bf} (steel beam flange)	4.6		5.6		12	14.5
Steel grade (steel beam)	Q345				Q235	
Section of steel column	C1				C2	
B_c/t_{cf} (steel column flange)	16.2				16	
Steel grade (steel column)	Q345				Q345	
α, (panel aspect ratio)	100				50	
Steel grade (panel zone)	Q235				Q345	

Note: The section of B1 through B4 is H200×100×8×10, H200×120×8×10, H200×100×4×4, H200×120×4×4, respectively, and section of C1 and C2 is H200×200×6×6, H200×200×8×6, respectively. The panel zone aspect ratio is defined as $(h_c+h_b)/t_{cw}$, where, h_c, h_b and t_{cw} are the depth of column and beam section, as well as column web thickness, respectively.

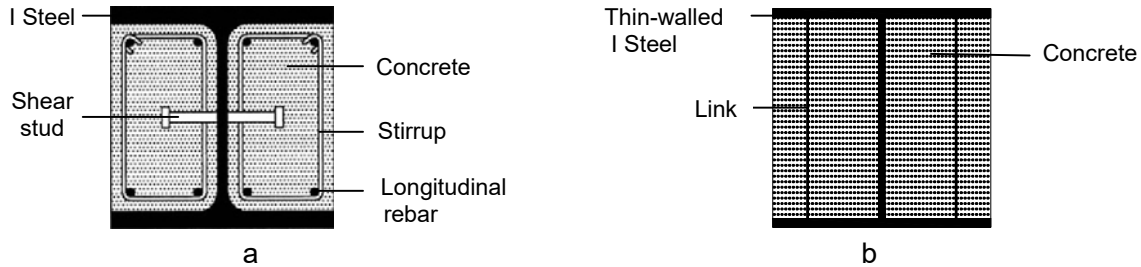


Fig 4 – Typical PEC sections

Steel beam is connected to the steel column flange by 10.9 grade high strength bolts through extended end plate. Eight bolts are used in one joint face, four of them outside the beam flanges are M22 with shank diameter of 22mm, and remained four between the beam flanges are M16 with shank diameter of 16mm.

In joint regions including the area surrounded by separating plates in beam and its end plate, and the area surrounded by horizontal separating plates in column together with column flanges, the concrete shall be cast on site in the practical engineering construction. For the test specimens, however, after the assembling of column and beam steel by pre-tensioned high strength bolts, the whole specimen is cast from one side to the other side, thus no formwork is needed.

3.2 Loading set up and protocol

The loading set up is shown in Figure 3. The base and top of specimen column are pin connected. The base is on a ground reaction beam and the top links to a horizontal bracing. An oil jack on top applies axial load on specimen column, and keeps constant load equal to 0.2 times of yield force of PEC column during the test. A pair of actuators is set on the two beam ends to produce cyclic moment and shear. Figure 5 shows the loading protocol which is referred to ATC-24 [11]. In the figure, Δ refers to the beam tip displacement, while Δ_y is the yield displacement which is determined by the previous monotonic loading tests. After the capacity peak, three cycles are enforced for each displacement amplitude, in order to study the effect of gradual concrete damage and local buckling of steel flanges.

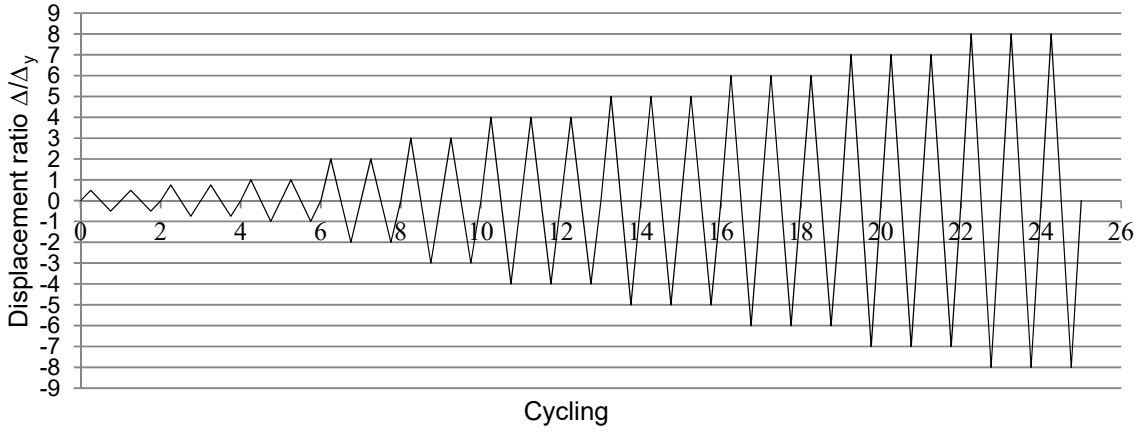


Fig 5 – Loading protocol

3.3 Arrangement of transducers and strain gauges

The bending deformation of PEC beam and shear deformation of panel zone are mainly concerned. To obtain the deformation precisely, rigid movement and incline of the specimen are removed from the measured data by arrangement of the monitoring transducers.

Strain gauges are arranged in panel zone and the beam flanges near its fixed end.

4 Test results

4.1 Mechanical properties of steel and concrete used for specimens

Mechanical properties of steel and concrete used for specimens are obtained by tensile steel coupons and compressive concrete cubes respectively. The data of steel which relate to specimen nonlinear behavior are listed in Table 2, where each datum is the average value of three coupons. And the compressive strength of concrete is listed in Table 3. Each datum is also the average value of three concrete cubes. By the table, the strength of concrete cast in one batch can be represented by the average value.

Table 2 – Mechanical properties of steel material

Steel grade	Plate thickness or rebar diameter (mm)	Applied element	fy (MPa)	fu (MPa)	Δ (%)
Q235	4	Panel zone, beam flange	297	445	31.0
	20	End plate of beam	274	436	31.5
Q345	6	Column flange and web	355	514	30.5
	8	Column and beam web	373	532	29.0
	10	Beam flange	379	555	30.0
	18	End plate of beam	387	566	28.0
HPB300	6	Link between flanges and rebar	596	657	-

Table 3 – Compressive strength of concrete (in MPa)

Specimen code	J11-C	J12-C	J21-C	J22-C	M11-C	M22-C	Average	Standard deviation
Side A cast firstly	38.8	41.3	39.1	43.2	43.6	41.2	40.6	2.39
Side B cast secondly	31.5	37.2	37.9	36.9	41.6	39.1	37.5	2.09

4.2 Damage evolution observed

Table 4 briefly summarizes the observed phenomena during the tests.

Table 4 – The observed phenomena of damage of specimen

Δ/Δ_y	J11-C	J12-C	J21-C	J22-C	M11-C	M22-C
±0.50	CB1	CB1			CB1, CB2	CB1
±0.75	CJ1	CB2, CJ1	CB1, CJ1	CB1, CJ1		
±1.00	CJ2	CJ2				
±2.00	CJ3	CB3, CJ3	CJ2	CJ2,CJ3	CB3, CJ1	CB2, CJ1, SB1
±3.00	SJ1, U1, U2	CJ4, U1, U2	CJ3, CJ4, U1	U1, U2,	SB1, SB2	CB3, CB4
±4.00	SJ2, CJ4	SJ1	SJ1, U2	SJ1, CJ4	CB4, U1,U2	U1, U2
±5.00		SJ2	SJ2		SB3, SB4 Loading stopped	SJ6, Loading stopped
±6.00				SJ2		
±7.00	SJ3, SJ4, loading stopped	SJ4	SJ3, SJ4, SJ5, loading stopped	SJ3, Loading stopped		
⩾8.00		SJ3, SJ5, Loading stopped				

The following symbols are used to represent the typical damage: CB1, Concrete tiny flaw in beam at or near its fixed end; CB2, Concrete flaw through whole beam depth; CB3, Concrete cracking through whole beam depth; CB4, Concrete dropped off from beam; SB1, Slightly buckling of beam flange; SB2, Severe buckling of beam flange; SB3, Visible buckling of beam web; SB4, Fracture of beam flange; CJ1, Concrete tiny flaw in joint zone; CJ2, Declined concrete cracking appearing in joint zone; CJ3, Concrete cracked severely in joint zone; CJ4,

Concrete dropped off from/squeezed out of joint zone; SJ1, Severe shear deformation of panel zone; SJ2, Opening largely between beam end plate and column flange; SJ3, Penal zone steel buckling visible; SJ4, Link welding spot cracked; SJ5, Panel zone plate cracking visible; SJ6, Fracture of end plate rib weld; U1, Ultimate load; U2, Peak load in second cycle obviously below that in first cycle.

Figure 6 and Figure 7 show the appearance of the typical failure modes.



(a) General view (b) Concrete filled in joint zone dropped off (c) Opening between column flange and beam end plate (d) Buckling and fracture of panel zone

Fig 6 – Typical damage of J-series specimens with connection failure mode



(a) General view (b) concrete cracking and steel flange buckling (c) Steel flange fracture

Fig 7 – Typical damage of M-series specimens with beam failure mode

By Table 4, it is known that it is common the tiny flaw of beam concrete due to bending appeared at first for all specimens when the relative deformation was about 0.5~0.75%, but the damage of J-series specimens then shifted to the connection, they underwent the crack and drop off of concrete in joint zone, the opening and closing cyclically of beam end plate and column flange, the local flexural deformation of column flange and buckling of panel zone after concrete squeezed out of. However, for the M-series specimens the main damage remained in the beams, though the joint zone concrete developed small flaw and fine cracking in the later process. The residual deformation shown in Figure 6a and Figure 7a exhibit the different features of final status of these two series specimens.

4.3 Loading-deformation curves

Figure 8 and Figure 9 display the typical load-deformation curves of the J-series specimens represented by J11-C which are designed as connection failure mode and M-series represented by M11-C which are beam failure mode. In each figure, the left one shows beam shear force

versus its tip displacement while the right one is the beam shear force versus the panel zone distortion. By the figures, we can read that (1) The non-linear deformation of specimen J11-C is mainly due to the deformation of joint zone. It can be deduced by comparison the two cyclic curves of Figure 8. On the contrary, non-linear deformation of specimen M11-C is contributed almost by beam because the curve of shear force versus panel zone deformation keeps almost linear as shown in Figure 9b. Of cause in this case no noticeable damage of column was observed in the test. (2) The specimen J11-C reaches its ultimate when its beam slope is about 0.03, while in the case of specimen M11-C its ultimate is corresponding to beam slope of 0.045 and the resistance keeps a short plateau till to the rotation of 0.055. (3) Specimen resistance degrades remarkable in the following cycle after the specimen reaches its ultimate, because the concrete damage evolutes severely. The curves of other specimens show similar features as these two specimens.

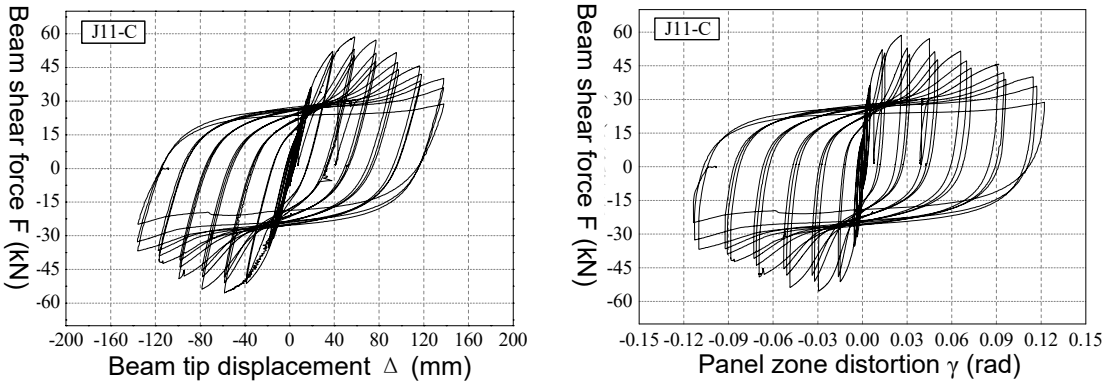


Fig 8 – Loading-displacement curves of J11-C

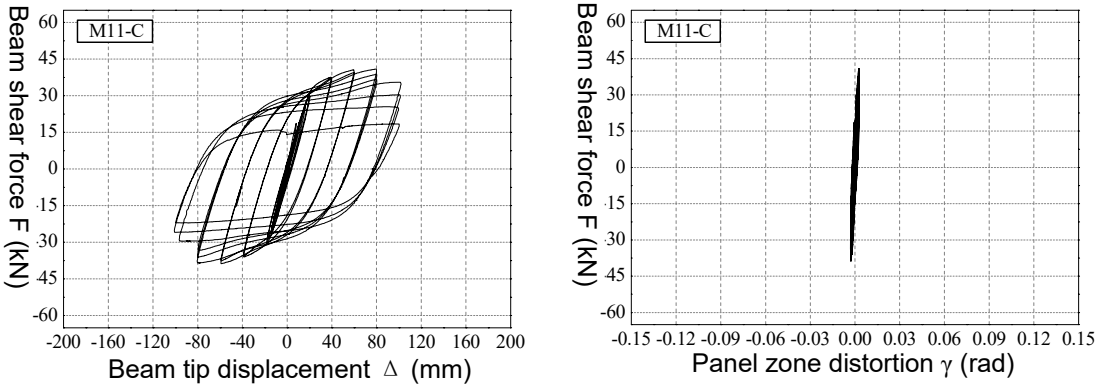


Fig 9 – Loading-displacement curves of M11-C

4.4 Ultimate, deformability and energy dissipation of specimens

Table 5 shows the ultimate recorded in tests. By figure 8 and 9, it is known that there are two peak values in reversed cyclic loading for each specimen. However, the two peaks are quite proximate with the diversity less than 5%, so the average of the two peaks denoted as F_{UT} is taken as the tested ultimate of specimen. The data are listed in Table 5.

As comparison, the predicted resistance $F_{UJ,pre}$ corresponding to the connection failure mode and $F_{UB,pre}$ corresponding to beam failure mode are listed too. The predicted resistance of connection is the minimum of those corresponding to end-plate failure, bolt failure and joint zone

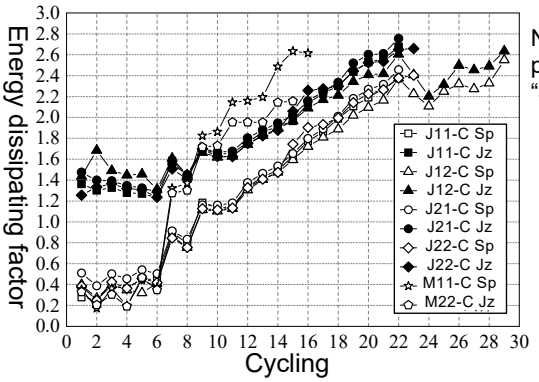
failure. The former two can use the available equations [12], but the last one is suggested by this study. The joint zone is mainly subject to shear force induced by beam end moment as well as the axial load on column top. The resistance is computed based on the following assumptions, (1) The shear stress on panel zone uniformly reaches yield strength of steel, i.e. in fully plastic deformation, (2) The column flange, horizontal stiffener, separate plates and rebar if existing act as rigid bar but with two end springs developing full plastic moment, (3) The concrete in the joint zone plays a role of inclined compressive stub, and (4) The ratios of axial stress due to axial load on column in steel and concrete is the same. There several possible failure modes and the resistance of each failure mode is computed. The minimum of them is determined as the resistance of the connection. By this resistance, the corresponding beam end load $F_{UJ,pre}$ is predicted. The moment capacity of beam is computed too, according to the equations recommended by Eurocode [1], and then converted into the beam tip load $F_{UB,pre}$. It can be seen by Table 5 that the computed resistances predict the capacity of specimens very well, and thus by the prediction it is possible to identify the failure mode.

Two ductility factors of the specimen are presented in Table 5. One is by the beam flexural deformation, denoted as δ_S, the other is by the joint zone shear deformation, denoted as δ_J. In both cases, the yield formation is identified in the same method: make the envelope curve of cyclic loading-deformation loops, draw initial elastic stiffness line through original point, and intersect the line to the horizontal level against ultimate load, then take the deformation corresponding to the crossover point as yield deformation. And the ultimate deformation to stipulate the ductility factor is the deformation when the resistance of specimen falls into 85% of its ultimate. By Table 5, it can be seen that no matter what failure mode is predominant, the ductility factor is quite good. For the J-series in which connection failure mode is predominant, Table 5 lists the ductility factors based on joint zone shear deformation. It shows that joint zone possesses relatively great deformability.

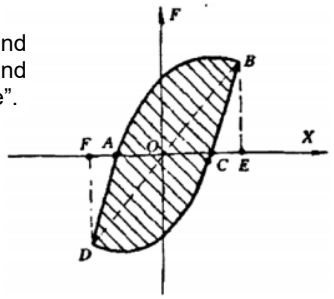
Table 5 – Summary of key data of the test

Key data	J11-C	J12-C	J21-C	J22-C	M11-C	M22-C
F_{UT} (kN)	57.0	58.1	57.5	58.9	39.9	46.7
$F_{UJ,pre}$ (kN)	55.2	55.2	55.2	55.2	70.8	70.8
$F_{UB,pre}$ (kN)	74.0	74.4	85.4	85.3	29.4	33.0
δ_S	4.14	4.14	4.05	4.13	5.21	4.50
δ_J	14.6	19.2	11.3	13.6	-	-

Figure 10a shows the dissipated energy of specimens and joint zones for per cycle, presented in the form of energy dissipating factor. The factor is computed by the surrounded area of load-deformation loop per cycle, as shown in Figure 10b with shadow, divided by the double triangular area (ΔOBE+ΔODF in Figure 10b). The figure includes the factors computed by whole specimen and by joint zone only for J-series. As general tendency, the energy dissipating factors increase with the increase of cycle numbers. But with the resistance deterioration in the second and third cycle in a given displacement amplitude, the factor should display a certain decrease. However, during the loading process, the actuator could not be controlled precisely, thus the followed deformation might exceed the previous amplitude. So the predicted 'decrease' does not show clearly in the figure. On the other hand, we can find in the J-series that the dissipating factor of joint zone is far greater than the specimen factor at the beginning. It is due to the damage concentration on joint zone but no big nonlinear behavior of the specimen at this stage.



Note: "Sp" in the legend presents "Specimen", and "Jz" presents "Joint zone".



The *i*th displacement amplitude

a b

Fig 10 – The energy dissipating factors

5 Brief discussions

The ultimate of the specimens can be well predicted based on the assumption of completely plastic capacity, which implies the fact that the beams and connections of specimens possess satisfied plastic capacity. Considering J-series specimens with large panel aspect ratio of 100, we know that the filled concrete in joint zone together with vertical rib strengthen the steel panel effectively. Premature local buckling can be prevented and the plastic deformability can be developed. The test also exhibits that the configuration of bolt connection with extended end plate by rib stiffened guarantees the full plastic capacity and rotation deformability of beam member, which indicates that the improved connection is appropriate to for moment resisting frame in PEC structures.

The ductility factors of the specimens obtained by tests show that the improved connection itself has quite good deformability, thus can be adopted in seismic design.

Construction details vary in the specimens, including the location of middle row bolts inside or outside the filled concrete, with or without the horizontal reinforced rebar in joint zone to confine the infilled concrete. Tests show that they have no substantial influence on the specimen behavior, especially on the resistance, ductility factor and energy dissipating factor. It shall provide more freedom for design.

6 Summary

The improved beam-to-column connection for PEC frames was proposed in order to resist inverse moments on beam end in potential earthquake. The constructional details were considered.

The cyclic loading tests on the proposed connection were carried out through six specimens to check its performance in the situations of connection failure mode predominated or beam failure mode predominated.

The test shows that the well designed connection can make the beam develops full plastic capacity and deformability. On the other hand, the connection can develop its ultimate till large non-linear deformation. Thus it can be concluded that the improved connection can be used in PEC frame for seismic design.

More study is still expected to make the classification of connection performance corresponding different seismic design requirement.

Acknowledgement

This research is partly supported by the Key Research and Develop Project of MST of China (Grant No. 2016YFC0701603)

Reference

[1] European Committee for Standardization (2004). *Design of composite steel and concrete structures，Part 1-1：General rules and rules for buildings*(EN 1994-1-1).Retrieved from https://www.cen.eu/

[2] Chicoine T，Tremblay R，Massicotte B，Ricles J，Lu L W. (2007). Behavior and strength of partially encased composite columns with built up shapes．*Journal of Structural Engineering*，128（3）：279~288. doi:10.1061/(ASCE)0733-9445(2002)128:3(279)

[3] Chicoine T，Massicotte B，Tremblay R． (2003). Long term behavior and strength of partially encased composite columns with built up shapes．*Journal of Structural Engineering*，129（2）：141~150. doi:10.1061/(ASCE) 0733-9445(2003)129:2(141)

[4] Oh M H, Ju Y K, Kim M H, et al. (2006). structural performance of steel-concrete composite column subjected axial and flexural loading. *Journal of Asian Architecture and Building Engineering* . 5(1): 153~160. Retrieved from https://www.jstage.jst.go.jp/article/jaabe/5/1/5_1_

153/_pdf.

[5] Chen Y Y，Wand T，Yang J，Zhao X Z. (2010). Test and numerical simulation of partially encased composite columns subject to axial and cyclic horizontal loads．*International Journal of Steel Structures*, 10(4)：385~393.doi: 10.1007/BF03215846

[6] Kindmann R, Bergmann R. (1993) Effect of reinforced concrete between the flanges of the steel profile of partially encased composite beams. *Journal of Constructional Steel Research*. 27(1-3): 107~122. doi: 10.1016/0143-974X(93)90009-H

[7] Nakamura S, Narita N. (2003) Bending and shear strengths of partially encased composite I-girders. *Journal of Constructional Steel Research*. 59(12): 1435~1453.doi:10.1016/S0143-974X(03)00104-4.

[8] Nardin S D, Debs A L H C E1. (2009) Study of partially encased composite beams with innovative position of stud bolts. *Journal of Constructional Steel Research*. 65(2): 342~350. doi: 10.1016/j.jcsr.2008.03.021

[9] Tsavdaridis K D，D’ Mello C，Huo B Y. (2013). Experimental and computational study of the vertical shear behavior of partially encased perforated steel beams．*Engineering Structures*，65：805~822. doi: 10.1016/j.engstruct.2013.04.025

[10] Muise J L． (2004). *Behavior of simple framing connectors to partially concrete encased H section columns*：(Master’s Thesis). University of Toronto, Toronto, Canada.

[11] Krawinkler H. (1992). Guidelines for cyclic seismic testing of components of steel structures. Report No. ATC-24, *Applied Technology Council*. Redwood City, CA.

[12] American Institute of Steel Construction (2010). *Specification for structural steel buildings*．(AISC．360-10). Retrieved from https://www.ansi.org/.

GIRDER-WALL CONNECTIONS USING CONCRETE ANCHORS IN COMPOSITE CONSTRUCTION

Jian Zhao
University of Wisconsin
Milwaukee, WI, USA
jzhao@uwm.edu

Bo Yang
Chongqing University
Chongqing, China
yang0206@cqu.edu.cn

ABSTRACT

Composite high-rise buildings usually benefit from concrete core walls and steel frames. Embedded connections are needed, which usually consist of a steel plate fixed to a number of headed anchor bolts/studs that are embedded in concrete. These connections can be subjected to complex loads in an earthquake; consequently, the seismic behavior of embedded connections is critical for the structural behavior.

Detailed design methods have been proposed for anchor reinforcement that can help single cast-in anchors to achieve ductile behavior under simulated seismic loading. Two reinforced anchors were installed in the plastic hinge zone of concrete columns. One was tested under monotonic loading while the other under cyclic loading. The tests indicated that well confined core concrete, even within plastic hinge zones, can support anchor connections. With the recommended anchor reinforcement, an innovative anchor connection between steel girders and concrete core walls is introduced for use in steel-concrete composite construction.

INTRODUCTION

Embedded anchor connections are used in composite structures with a concrete shear wall and a steel frame as shown in Figure 1. Embedded connections usually consist of a steel plate attached to several headed anchor bolts/studs or deformed bars that are embedded in concrete. These connections can be subjected to complex loads in an earthquake; therefore, the seismic behavior of embedded connections is critical for the structural behavior. Shake table tests of structure models in the literature have shown that the embedded connections are susceptible to damage in earthquakes, which in turn disturbs the desired structural performance (Gong et al. 2004; Zhou et al. 2012).

Seismic tests of cast-in anchors in plain concrete have shown unreliable seismic behavior (Petersen et al. 2011). The most common modes of anchor failure encountered in practice are anchor steel failure and concrete breakout failure. Anchor steel failure is caused by fracture of the anchor shaft in tension or shear while typical concrete breakout failure is shown in Figure 2: a concrete cone is broken away from the base concrete in which the connection is located. Concrete breakout failure occurs when anchors are located close to an edge or with small embedment depths. Breakout cracks usually originate from the anchor and propagate towards the reaction points in laboratory tests. A 35-degree crack propagation angle is assumed in design

(Fuchs et al. 1995), as shown by the regions encased in dashed lines in Figure 2.

Concrete breakout is a brittle failure mode and thus not preferred for anchors in seismic zones (Petersen et al. 2013a). Engineers can use steel reinforcement to improve the behavior of anchors likely controlled by concrete breakout. The existing anchor shear reinforcement recommended in ACI 318-14 code, mainly V-shaped hairpins wrapping around anchor shafts, may not be practical (Petersen et al. 2013b). In addition, tests have indicated that the existing anchor tensile reinforcement, in form of U-shaped hanger steel placed close to anchor bolts, can restrain concrete breakout failure; however, the desired anchor steel failure may not be achieved unless the concrete around the anchors are properly confined (Lin et al. 2013). In this paper, recommended anchor reinforcement was briefly introduced and applied to the anchor connections between concrete core walls and steel girders.

LITERATURE ON ANCHOR TENSION REINFORCEMENT

Existing studies

Hasselwander et al. (1974) conducted a series of tests on large-diameter (e.g., 1.75 in.), high-strength anchor bolts embedded near edges of concrete piers with edge distances ranging from one to six inches. The concrete piers contained No. 9 longitudinal bars at a spacing about five inches- and No. 4 stirrups. The anchor bolts were installed close to the longitudinal bars with an embedment depths of $15d_a$ (d_a is the embedment depth of the anchors); therefore the closest four to six longitudinal bars may be considered as the anchor reinforcement. The tests indicated that the longitudinal bars as anchor reinforcement did not ensure the load transfer from the anchor to the bars, and the anchors in only two specimens developed their yielding strength. Typical failure of the specimens started with cover concrete being pushed out near the anchor head and the concrete crushed above the large-size anchor heads.

Kotani et al. (2006) tested 0.5-in. [13-mm] bolts embedded 6.7 in. [170 mm] in narrow footing beams typically used for residential houses. No. 3 stirrups with a spacing of 12 in. [305mm] were used in four out of sixteen specimens. The closest two stirrups located roughly $0.9h_{ef}$ from the anchor did not restrain the breakout failure though an increase of 24 percent in anchor capacities and 100 percent increase in peak displacements were observed. Note that the concrete between the anchors in tension and the compression flange of the steel column was not protected with stirrups and surface reinforcement; therefore, the desired load transfer mechanism was not achieved.

Lee et al. (2007) tested five groups of four anchors with large diameters and deep embedment depths. One group of anchors were reinforced with four No. 8 U-shaped hairpins and another group with eight No. 8's. The vertical hairpins were divided into two groups, one group located within $0.2h_{ef}$ and the other $0.35h_{ef}$ from the anchor bolt. The No. 8 bars were assumed fully developed below the anchor head through a length of $14d_b$ with hooked ends, which is slightly smaller than the code-specified development length. The vertical hairpins were not proportioned to carry the anchor steel capacity in tension. Anchors with four hairpins developed two times the capacity of unreinforced anchors while the tests of the anchors with eight hairpins were terminated before the anchor capacity was clearly achieved.

Closed stirrups were provided in one of the two tension tests of shear studs for use in composite construction by Saari et al. (2004). The reinforced specimen contained No. 3 stirrups at a spacing of 3.5 in., which, along with longitudinal bars at all corners, formed a reinforcing cage around the studs. Concrete failure occurred to the unreinforced anchor while steel fracture occurred to the reinforced anchor with capacity increase about 100 percent.

Design Recommendations

Building codes and design guidelines allow engineers to use steel reinforcement to avoid concrete

breakout failure in design (ACI 318-14; Zhao and Lin 2017). The recommended anchor reinforcement usually consists of U-shaped hairpins. The existing design methods assume that the concrete breakout similar to that in plain concrete occurs before anchor reinforcement carries the design load. The recommendations on the design of anchor tension reinforcement are summarized in Figure 3. Note that the groups of two anchors in tension in Figure 3 can be the part of a four-anchor connection subjected to a moment from the connected steel element. U-shaped hairpins are typically recommended. In general, two design methodologies have been adopted: 1) concrete breakout cone forms before reinforcement within a certain range from the anchor bolts carry the tension force; 2) the load transfer from the anchor bolt to nearby reinforcement can be treated as that between spliced deformed bars or visualized using strut-and-tie models (STMs).

The existing anchor reinforcement recommended in ACI 318-14 code mainly consists of U-shaped hanger steel, placed close to the anchor in tension. The reinforcing bars embedded in the breakout cone, as shown in shaded areas in Figure 3, are assumed to provide tensile resistance. The U-shaped hairpins are required to be within a distance equal to half of the embedment depth ($0.5h_{ef}$) as illustrated in Figure 3c. This effective range is increased in CEN/TS (2009) to $0.75h_{ef}$. In addition, stirrups in beams within $1.0h_{ef}$ from the anchors can be counted as reinforcement for anchors according to a CEB report (1997).

Proposed Anchor Tension Reinforcement

Zhao and Lin (2017) evaluated the existing anchor reinforcement using experimental tests. Compared with the anchors embedded in plain concrete, a capacity increase ranging from 20% to 130% was observed in the tests of reinforced anchors. However, the expected steel fracture was not achieved mainly due to the lack of confining reinforcement. Splitting cracks developed, and the concrete around the anchor head lost its confinement and crushed prematurely, resulting in anchor pullout failure.

Based on these observations and other tests in the literature, recommendations for anchor tension reinforcement were proposed (Petersen et al. 2013b). The proposed reinforcement, as illustrated in Figure 4 includes: 1) load-carrying reinforcement in the direction of the anchors; 2) crack-controlling reinforcement in all directions that has a limited edge distance; and 3) local confining reinforcement near the anchor head if side-face blowout may control the failure. In addition, the tensile load on the anchors eventually needs to be transferred to the rest of the structure. Sufficient reinforcement, such as stirrups and surface bars, is needed to ensure proper load transfer. Note that with the concrete confined around the anchor, it is expected that the concrete will distribute part of the tensile force to the rest of structure.

The load-carrying reinforcement should be proportioned to carry a force equal to the design tensile capacity of the anchor bolt. The nominal yield strength of steel should be used in the calculation. The load-carrying reinforcement should be implemented using small-diameter closed stirrups. The stirrup width should be small yet satisfy the bending radius requirements. The depth of the stirrups should be large enough such that the vertical legs are fully developed for the tension load at both sides of the anchor head. Two stirrups should be placed next to the anchor shaft, where the crack in concrete may initiate above the anchor head under a tensile load. Rather than placing all bars within a small distance from the anchor, closely spaced stirrups with a center-on-center spacing of 2 to 3 in. [50-75 mm] can extend $1.0h_{ef}$, where h_{ef} is the embedment depth of the anchor, from the anchor bolt, as shown in Figure 4. Although the development length requirements for the anchor reinforcement can be satisfied through the interaction between the closed stirrups and corner bars, it is recommended that the closed stirrups are at least $8.0d_b$ from the anchor head.

The crack-controlling reinforcement is needed to cross all possible splitting cracks. Considering the load transfer from the anchor head to the load-carrying reinforcement: a strut-and-tie model

can be established with the struts conservatively assumed from the anchor head to the outmost load-carrying stirrups. The rest crack-controlling reinforcement can be determined considering the load transfer from the load-carrying reinforcement to the rest of the structure. All crack-controlling reinforcement should be proportioned using a steel stress of $0.6f_y$, and implemented using small diameter bars evenly distributed with a small and practical spacing in two orthogonal directions. The crack-controlling reinforcement should be properly developed. In addition, the closest four stirrups, as the load-carrying reinforcement, can be encased by three or four closed hoops in the transverse direction near the anchor head if the anchors are close to a free side surface (Figure 4). This is to better confine the concrete that is subjected to large compressive stresses above the head.

EVALUATION OF REINFORCED ANCHORS IN TENSION

The key role of anchor reinforcement, in addition to carrying the forces from the anchors, is to protect concrete around the anchors from splitting, breaking out, and crushing. This understanding of the related behavior has led to alternative designs and detailing for anchor reinforcement (Petersen and Zhao 2013). The tests in this study (Zhao 2014) were conducted to verify the proposed reinforcement for anchors placed in plastic hinge zones.

A total of three column specimens were used for single anchors in tension. The column height (h) was designed as 5 ft. [1.52 m] from the top face of the base block, which is close to that of a half story height. The column base block had a dimension of 48x20 in. [1220x508 mm] and a height of 17 in. [432 mm] as shown in Figure 5. Two tie-down holes were created using embedded PVC tubes. The tie down points were 3 ft apart following the hole pattern in the strong floor of the UWM Structures Laboratory. The horizontal loads were applied to the top of the column at 62 in. [1.57 m] from the base through a steel loading block.

Eight No. 5 bars (ASTM Grade 60) were provided as the longitudinal reinforcement for the columns. The concrete cover was 1.5 in. [38 mm], typical for RC members. A section analysis indicated that the column had a nominal moment capacity about 60 k-ft [81.3 kN-m]. This corresponded to about 12 kips [2.7 kN] at the top of the column. The actual loading capacity can be higher due to strain hardening of the bars. The shear design for the column for this load led to No. 4 [13-mm] ties at a spacing of 6 in. [150 mm], as illustrated in Figure 3. Additional ties were provided within the plastic hinge zone (the length of the plastic hinge zone l_p=1.5h=18 in. [457 mm]), as shown by shaded regions in Figure 5. The plastic hinge length of 1.5h was used because longitudinal bars yielded within this range (Lin et.al 2013).

The test anchors were made from 3/4 in. [19 mm] diameter ASTM A193 Grade B7 threaded rods (f_{ya}=105 ksi [724 MPa] and f_{uta}=131 ksi [903 MPa]). The net tensile area ($A_{sa,N}$) and the net shear area ($A_{sa,V}$) for the 3/4-in [19-mm] threaded rods are 0.334 in.^{2} [215 mm^2]. The test anchor, if fully developed, would take an ultimate tension load of 43.8 kips [195 kN], which is within the capacity of the MTS Model 244.31, actuator used in the study. A plate washer (1.5×1.5 in. [38x38 mm]) and a hex nut were tack welded to the end. The net bearing area (A_{brg}) was 1.8 in.^{2} [1161 mm^2], sufficient to carry the tensile load without causing pulling out failure as observed previous tests (Petersen et al. 2013b). The concrete compressive strength (f_c') was assumed as 4000 psi [27.6 MPa] and the maximum bearing strength $6.0f_c$' was used in design of the head plate (ACI 318-14).

The required anchor reinforcement for the 3/4-in. [19-mm] anchors in tension was found to be 0.73 in.^{2} [471 mm^2] Two additional No. 4 [13-mm] ties (with four stirrups legs as anchor reinforcement) were used, and located 2-in. [50-mm] from the test anchor, as shown in Figure 3. The needed anchor shear reinforcement was found to be 0.44 in.^{2} [284 mm^2] The two No. 4 [13-mm] ties next to the anchors were deemed sufficient, considering other ties within the plastic hinge zone.

The columns were expected to develop flexural cracks under lateral loads, especially in the plastic hinge zones. The cracks could propagate rather arbitrarily, passing the anchors, when the column develops inelastic behavior. In this case, concrete bearing strength can be significantly reduced. Therefore, three No. 4 [13-mm] U-shaped hairpins were placed near the anchor in the vertical plane, as shown in Figure 5. These hairpins were expected to confine the concrete from flexural cracking near the anchor heads. This local crack-controlling bars were slightly more than the calculation using a strut-and-tie model (ACI 318-14).

Ready mixed concrete with Wisconsin Department of Transportation Type A-FA mixture was used. The target concrete compressive strengths for the normal strength concrete was 4000 psi [27.6 MPa]. The hardened concrete had a compressive strength of 5800 psi at 28 days, and the compressive strength went up 6900 psi [47.6 MPa] at about 84 days, when the tests were conducted. The No. 5 [16 mm] reinforcing steel with a nominal yield strength of 60 ksi [414 MPa] were used as longitudinal reinforcement. The measured yield strength was 65 ksi [448 MPa], and the ultimate strength 101 ksi. [696 MPa].

The column specimen was fixed to the strong floor of the testing laboratory using two high-strength threaded rods. One MTS Model 244.31 actuator was used to apply a reversed cyclic displacement at the top of the column. The lateral load was applied to the column at 62 in. above the base block. Another MTS Model 244.31 actuator was used to apply tensile/shear forces to the anchors. The centerline of this actuator was located at the height of the test anchor. In order to minimize the relative displacement between the reaction frame and the specimen, a shoring frame was placed in between the reaction frame and the specimen. Strain gages and linear potentiometers were used to monitor the behavior of the test columns and the anchors.

The columns were subjected to reversed cyclic displacements. The displacement history included groups of three cycles with the following peak displacements: $\pm\Delta y$. $\pm 2\Delta y$, $\pm 3\Delta y$, $\pm 4\Delta y$, $\pm 6\Delta y$, and beyond $\pm 8\Delta y$. Loading rates for displacement cycles were kept at 0.24 in./min [6 mm/min] throughout the tests. The anchors were loaded after the columns were subjected to the entire cyclic loading history and developed damage in the plastic hinge zones.

The behavior of the two single anchors subjected to tension is shown in Figure 6. The load vs. displacement behaviour of Specimen T2 demonstrated that the steel ductile failure was achieved. Unlike normal sharp drop after peak load, the anchor steel had a relative long descending range. It may have been attributed to slow energy release rather than sudden energy release in a typical coupon tests, in which rigid loading devices are typically used.

The comparison of the load vs. displacement curve at the monotonic loading (T2 test) and cyclic loading in this case (T3 test) in Figure 6 indicated that the load curve followed the monotonic path closely till the failure. The small difference was mainly caused by upward orientation of the anchor in this case (T3) that may cause an additional small bending as well as governing tension on the anchor shaft when the anchor was subjected to tension, thus leading to the slightly low load path and final capacity. The difference may also have come from variations built in experimental tests.

The anchor remained steady at the load level of 44 kips [196 kN] without too much additional displacement. According to potential failure modes, the column will be able to take 61.8 kips [275 kN] before a flexural failure occurs. With the diagonal cracks path, the anchor tension force was again transferred to the rest of the column through the dry friction. The sliding surface was along a flexural crack above the base, which was opened before the tension force was applied to the anchor. This was slightly different from the monotonic loading in T2. According to the monotonic loading curve in T2, the anchor at a commanded displacement of 0.58 in. [14.7 mm] at 43 kips [191 kN], however, was compatible to that of 0.6 in. [15.2 mm] at the same loading level. This means that the column was stable without obvious degradation under cyclic loading and can still carry more loads.

The load vs. anchor displacement for both T2 and T3 confirmed that the anchors can be installed

in the plastic hinge zone when suitable anchor reinforcement is provided, as stated in Zhao and Lin (2017). These tests of anchors installed in the plastic hinge zones of RC columns also indicated that well confined concrete core can support anchor connections. With the proposed anchor reinforcement, the anchors can develop their full tensile capacities.

CONCEPT OF EMBEDDED CONNECTION AND RELATED LITERATURE

The proposed embedded connection is illustrated in Figure 7. The design is based on the existing research in the literature and the results of this study.

Girder-wall connections have a limited embedment depth, potential prying action from the plate deformation, and damaged concrete affect the seismic performance of embedded connections. The proposed connection thus seeks to mitigate these issues. Specifically, the available embedment length can be limited by the wall thickness, especially for the connections on the side faces of a wall, as illustrated in Figure 1. The tensile capacity of the connection in such situations is controlled by concrete breakout failure according to the current design regulations (ACI 318-14) if anchor reinforcement is not properly provided. It is proposed to use the newly developed anchor reinforcement consists of a group of closely spaced stirrups (rather than U-shaped hairpins) with a goal to confine concrete near the anchor heads. In addition, crack-controlling reinforcement was provided along all faces of concrete to restrain the concrete from splitting.

Girder-wall connections have a limited plate thickness as limited by practical applications. In most connections, a shear tab is welded to the embedded plate, and the forces are transferred from the shear tab to the anchor bolts/deformed bars through the embedded plate. Prying occurs when the stiffness of the embedded plate is not sufficient, which causes an increase in the tensile force. The bending deformation of the embedded plate also causes uneven distribution of tensile forces among the anchor bolts/deformed bars. Premature failure occurs in both cases. It is proposed to add stiffeners onto the back of the embedded plate to increase its stiffness, to minimize the prying action on the anchor bolts, and to evenly distribute the resulting tensile forces among the anchor bolts/deformed bars subjected to tension.

Girder-wall connections may be embedded in concrete experiencing extensive damage. Concrete walls may develop cracks, especially in lower stories of a complex building structure (as shown in Figure 1) when subjected to an earthquake. It is proposed to use the cracking controlling reinforcement similar to that used in this study.

The proposed girder-wall connections require extensive experimental verification before being used in practice. The design of anchor reinforcement may follow Appendix A. A prefabricated reinforcement cage, as shown in Petersen (2011) may benefit the construction.

SUMMARY

Two tests were conducted to verify the proposed reinforcement for anchors in tension. The single anchors were installed in the plastic hinge zone of concrete column specimens. Despite large cracks and concrete spalling occurred to the concrete within the plastic hinge zones, ductile steel fracture was achieved in all tests. The successful tests indicated that well confined core concrete, even within plastic hinge zones, can support anchor connections. The test also confirmed that the anchor reinforcement should confine concrete, restrain concrete from splitting cracks, and distribute loads from the anchor to the rest of the structure/structural element.

A new girder-wall connection is proposed based on the anchor tension reinforcement verified in this study. Special reinforcing cage will be used to confine the concrete around the girder-wall connections, and transfer tensile loading from the connection to the concrete. Stiffeners will be used to distribute the tensile loading from the connection to the anchors. The stiffeners will also serve as shear keys such the anchors can be designed for tension only. This connection needs

experimental verification before being used in practice.

REFERENCES

1. American Concrete Institute (ACI), “Building Code Requirements for Structural Concrete (ACI 318-14).” Farmington Hills, MI, 2014.
2. European Committee for Standardization, “Design of fastenings for use in concrete - Part 4-2: Headed Fasteners,” CEN/TS 1992-4-2, Brussels Belgium, 2009.
3. Comité Euro-International du Béton (CEB), “Fastenings to Concrete and Masonry Structures: State of the Art Report.” Thomas Telford Service Ltd., London. 1997.
4. Fuchs, W.; Eligehausen, R.; and Breen, J., “Concrete capacity design approach for fastening to concrete.” *ACI Structural Journal*, 1995, 92(1), pp.73-94.
5. Gong, Z., Lu, X., Lu, W., Li, P., Yang, S., Zhao, B. (2004) Shaking Table Model Test of a Hybrid High-Rise Building Structure, *Earthquake Engineering and Engineering Vibration*, Vol. 24, No. 4. pp.99-105. (in Chinese).
6. Hasselwander, G.; Jirsa, J.; Breen, J.; and Lo, K., "Strength and Behavior of Anchor Bolts Embedded Near Edges of Concrete Piers," Research Report 29-2F, Center for Transportation Research, the University of Texas at Austin, TX, 1974.
7. Kotani, H.; Matsushita, K.; Kajikawa, H.; Wu, D., “Experimental Study on Pull out Behavior of Anchor Bolt for Small Buildings (Footing With Singly Arranged Reinforcing Bars),” Summaries of technical papers of Annual Meeting Architectural Institute of Japan. C-1, Structures III, 2006, pp. 99-100. (in Japanese)
8. Lee, N.; Kim, K.; Bang, C.; and Park, K., "Tensile-Headed Anchors with Large Diameter and Deep Embedment in Concrete," ACI Structural Journal, Vol. 104, No. 4, 2007, pp. 479-486.
9. Lin, Z., Luke, B., Shahrooz, B., and Zhao, J. "Headed Anchors in Plastic Hinge Zone of Reinforced Concrete Members." Final Report (Volume III) for Project - Behavior and Design of Cast-in-Place Anchors under Simulated Seismic Loading. University of Wisconsin, Milwaukee, WI, 2013.
10. Lin, Z.; Petersen, D.; Zhao, J. and Tian, Y., “Simulation and Design of Exposed Anchor Bolts in Shear,” *International Journal of Theoretical and Applied Multiscale Mechanics.* 2011; 2(2), pp. 111-29.
11. Petersen, D., “Seismic Behavior and Design of Cast-in-Place Anchors,” MS Thesis, University of Wisconsin, Milwaukee, WI, 2011.
12. Petersen, D. and Zhao, J. "Design of Anchor Reinforcement for Seismic Shear Loads." ACI Structural Journal. Vol. 110, No. 1, pp.53-62, 2013.
13. Petersen, D., Lin, Z., and Zhao, J. "Reinforcement for Headed Anchors." Final Report (Volume I) for Project - Behavior and Design of Cast-in-Place Anchors under Simulated Seismic Loading. University of Wisconsin, Milwaukee, WI, 2013a.
14. Petersen, D., Lin, Z., and Zhao, J. "Reinforcement for Headed Anchors." Final Report (Volume II) for Project - Behavior and Design of Cast-in-Place Anchors under Simulated Seismic Loading. University of Wisconsin, Milwaukee, WI, 2013b.
15. Saari, W.; Hajjar, J.; Schultz, A.; and Shield, C., “Behavior of Shear Studs in Steel Frames with Reinforced Concrete Infill Walls,” Journal of Constructional Steel Research, Vol. 60, No. 10, 2004, pp. 1453-1480.
16. Shahrooz, B.; Tunc, G.; and Deason, J., "Outrigger Beam–Wall Connections. II: Subassembly Testing and Further Modeling Enhancements," Journal of Structural Engineering, Vol. 130, No. 2, 2004, pp. 262-270.
17. Zhao, J. and Lin, Z. "Design of Anchor Reinforcement for Seismic tension Loads." *Engineering Structures*. (in review).

18. Zhao, J. 2014, "Seismic behavior of single anchors in plastic hinge zones of RC columns," Tenth U.S. National Conference on Earthquake Engineering Frontiers of Earthquake Engineering July 21-25, 2014 Anchorage, Alaska.
19. Zhou, Y., Yu, J., Lu, X., and Lu, W. (2012) "Shaking table model test of a high-rise hybrid structure building with steel frame-concrete core wall." *Earthquake Engineering and Engineering Vibration*, Vol. 32, No. 2, pp. 98-105. (in Chinese).



Fig. 1 - Complex structures using embedded connections

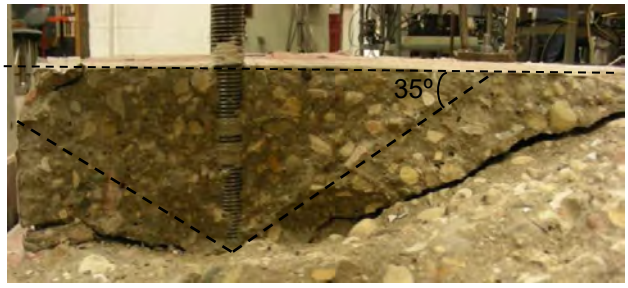


Fig. 2 - Typical concrete breakout failure of cast-in-place anchor bolts.

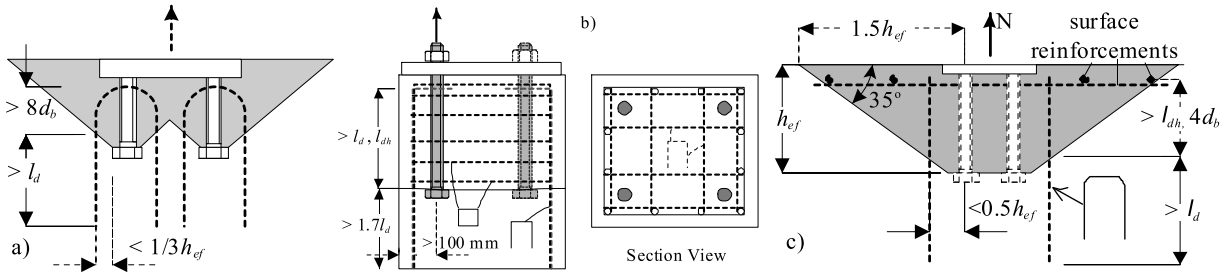


Fig. 3 - Existing reinforcement schemes for anchors in tension.

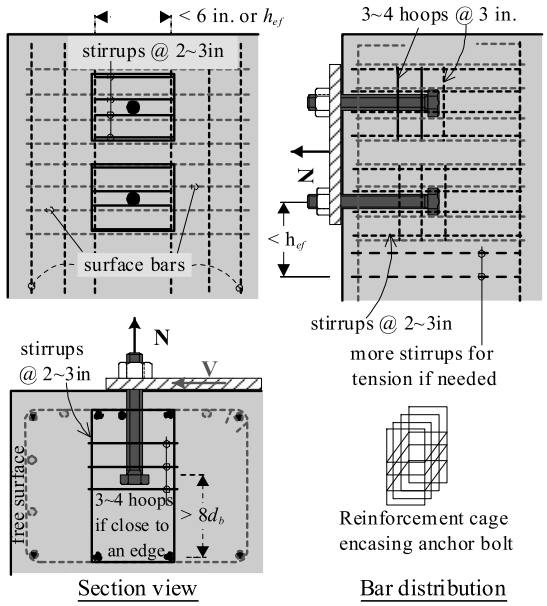


Fig. 4 - Proposed anchor tension reinforcement.

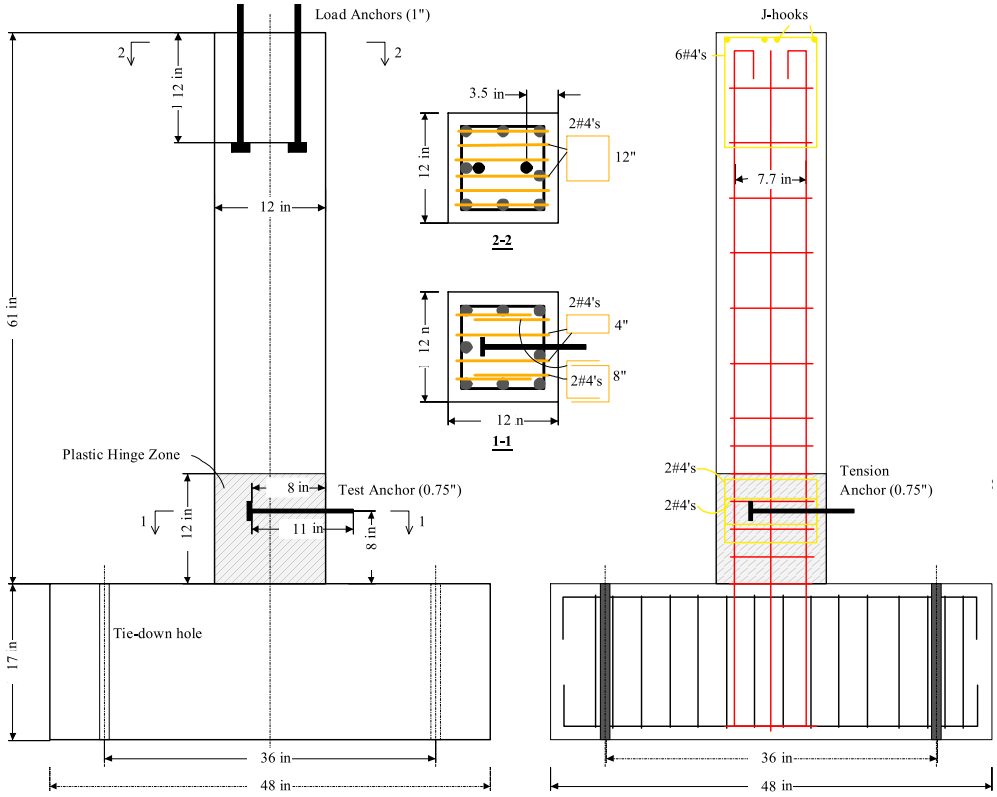


Fig. 5 - Dimension and reinforcement of tension specimens (1 in. = 25.4 mm)

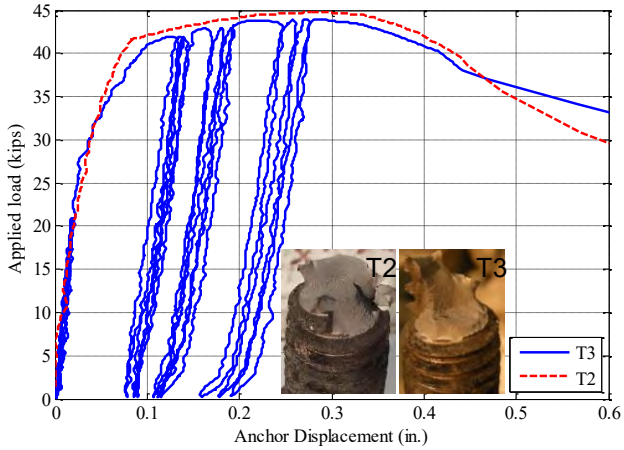


Fig. 6 - Anchor bolts in plastic hinge zone under tensile loading (1 in. =25.4 mm; 1 kip=4.5 kN)

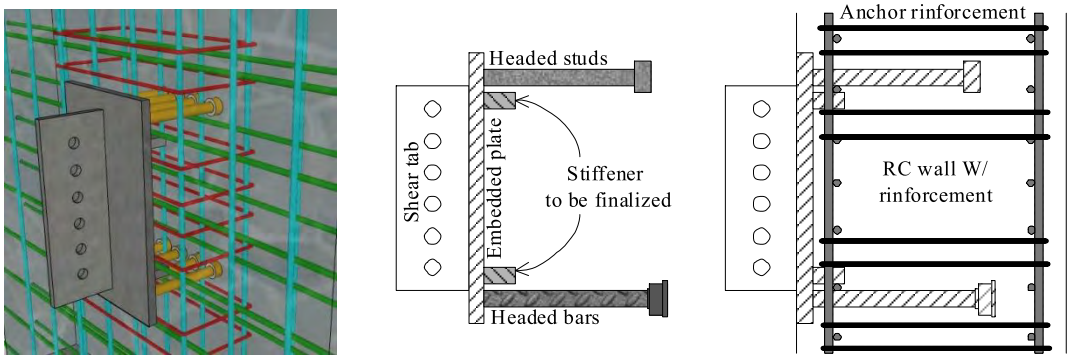


Fig. 7 - Concept of proposed innovative embedded connection

Appendix: Proposed Revision for Anchor Tension Reinforcement

17.4.2.9 — Anchor tension reinforcement

17.4.2.9.1 Anchor tension reinforcement shall be designed either by 17.4.2.9.2 for anchors and anchor groups in mass concrete, or 17.4.2.9.3 for anchors and anchor groups close to concrete edges.

17.4.2.9.2 Where anchor reinforcement is developed in accordance with 25.4 on both sides of the breakout surface, the design strength of the anchor reinforcement shall be permitted to be used instead of the concrete breakout strength in determining φN_n. A strength reduction factor of 0.75 shall be used in the design of the anchor reinforcement.

17.4.2.9.3 anchor tension reinforcement shall include 1) load-carrying reinforcement in the direction of the anchors; 2) crack-controlling reinforcement in all directions that has a limited edge distance; and 3) local confining reinforcement near the anchor head if side-face blowout may control the failure. The area of load-carrying reinforcement shall be determined by

$$A_{sa} = \frac{f_{uta} A_{se,N}}{f_{yt}} . \qquad (17.4.2.9.3)$$

where the limitation of $1.9f_{ya}$ on f_{uta} shall not be applied. The value of f_{yt} shall satisfy 20.2.2.4.

R17.4.2.9 — Anchor tension reinforcement

R17.4.2.9.1 Two design approaches for proportioning anchor reinforcement are included in 17.4.2.9.1. The provisions of 17.4.2.9.2 are similar to those of the 2011 Code. Section 17.4.2.9.3 allows an alternative design, in which closed stirrups and crack-controlling bars confine concrete around the anchors. The confined concrete along with the reinforcement transfers the tensile load to the structure.

R17.4.2.9.2 Same as the existing wording.

R17.4.2.9.3 With a goal to confine concrete in front of anchors and to prevent concrete breakout, the anchor reinforcement consists of closely spaced stirrups, corner bars, and crack-controlling bars distributed along all concrete faces as illustrated in Fig. R17.5.2.9.3.

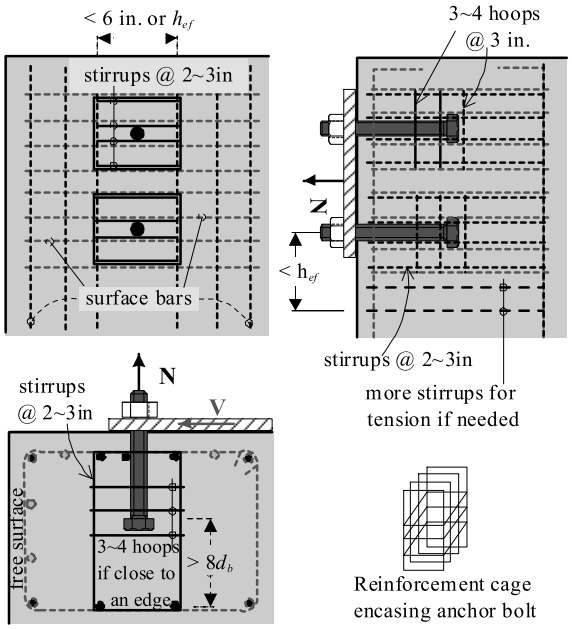


Fig. R17.4.2.9.3—anchor reinforcement for tension.

The load-carrying reinforcement should be proportioned to carry a force equal to the design tensile capacity of the anchors, and implemented using small-diameter closed stirrups. The closely

spaced stirrups with a center-on-center spacing of 2 to 3 in. can extend up to $1.0h_{ef}$ from the anchor bolt.

The design of the crack-controlling reinforcement can use two strut-and-tie models: one describing the load transfer from the anchor head to the load-carrying reinforcement, and the other describing the load transfer from the load-carrying reinforcement to the rest of the structure.

Crack-controlling reinforcement are necessary crossing all possible cracks. All crack-controlling reinforcement should be proportioned using a steel stress of $0.6f_y$, and implemented using small diameter bars evenly distributed with a small and practical spacing in two orthogonal directions. In addition, the anchors and the load-carrying reinforcement close to the anchor can be encased by three or four closed hoops in the transverse direction near the anchor head if the anchors are close to a free side surface. With the anchor tension reinforcement, anchor shaft fracture is expected if other failure modes in 17.4 do not control the anchor behavior.

The quasi-static cyclic tests of the reinforced anchors in tension, conducted at the University of Wisconsin, Milwaukee showed insignificant capacity reduction. Therefore no capacity reduction is needed for reinforced anchors subjected to cyclic tensile loading

STEEL-TO-CONCRETE JOINTS WITH LARGE ANCHOR PLATES UNDER SHEAR LOADING

Dipl.-Ing. Jakob Ruopp
University Stuttgart, Germany
jakob.ruopp@ke.uni-stuttgart.de

Prof. Dr.-Ing. Ulrike Kuhlmann
University Stuttgart, Germany
sekretariat@ke.uni-stuttgart.de

ABSTRACT

In industry and plant engineering especially, high flexibility is required at joints between steel and concrete. According to current standards, the maximum number of fasteners is limited to an arrangement of 3 x 3 anchors on an anchor plate. The load-carrying behaviour of large anchor plates under tension, shear and restraining forces was investigated within the scope of the research project “Large Anchor Plates with Headed Studs for Highly Stressed Constructions in Industry and Plant Engineering”. This paper describes the research results obtained at the University of Stuttgart for large anchor plates under shear loading. Findings for large anchor plates under tension and restraining forces were mainly investigated at the University of Kaiserslautern (Scholz et al., 2016).



Fig. 1 – Test setup for shear loading

The shear behaviour and distribution of forces within the anchor plate are crucial issues in the development of a design concept for steel-to-concrete joints with large anchor plates. The influence of different parameters, such as the dimensions of the anchor plate, the embedment depth of the headed studs or the eccentricity of the shear force, have been studied in several test series. Supplementary reinforcement was placed close to the headed studs in tension to strengthen the load-carrying capacity of the joint. The distribution of the shear forces has been assessed by means of numerical investigations together with the influence of further parameters such as concrete strength and reinforcement ratio. With regard to the load distribution within the anchor plate, elastic and plastic design approaches have been taken into account. Based on these studies, an efficient design model has been developed for steel-to-concrete joints with large anchor plates and a higher number of fasteners than originally permitted.

1. INTRODUCTION

Recently, hybrid building technology, where both materials, steel and concrete, are used according to their properties and their most suitable application, has spread among buildings and industrial practice, such as steel frames connected to column bases on foundations, or steel or composite beams joined to the concrete walls of staircases. Recently, several design concepts have been developed for steel-to-concrete joints within national and international research projects. Design approaches based on the component method have gained acceptance, where concrete and steel components are considered simultaneously.

In industry and plant engineering, large forces have to be transferred from structural steel elements to concrete elements such as walls or foundations. As a consequence of this, large anchor plates are required which enable the activation of a sufficiently large concrete volume to support these loads. However, current design rules limit load-carrying capacities due to the limitation of nine fasteners per anchor plate and the elastic design concept, which is the dominant method for the design of fastenings. Therefore, the resistance of an anchor plate is limited, which leads to complicated load distribution arrangements over several single anchor plates or solutions in pure concrete that avoid the “difficult” interface between steel and concrete. The scope of the research project was the development of a design model for large anchor plates with more than nine headed studs per anchor plate. Tests under normal, shear and restraining forces were conducted within the scope of the project (Figure 1).

2. STATE OF THE ART AND DESIGN CONCEPTS

The design concept for large anchor plates was developed based on the component method (Jaspart, 1991; Wald et al., 2008; Kuhlmann et al., 2012) which distinguishes between different failure modes based on a characterized structural behaviour of the single components. In an overall design concept, steel components according to EN 1993-1-8 and concrete components according to EN 1992-4 are considered simultaneously. In addition to the load-carrying capacity of the joint, the load-deformation behaviour can be determined for the whole joint.

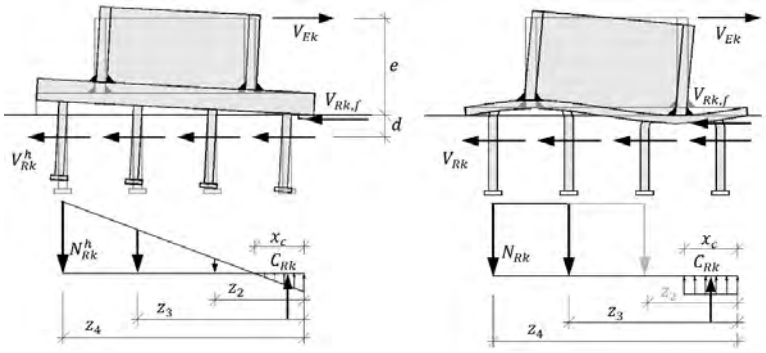


Fig. 2 – Elastic (left) and plastic (right) distribution of forces

In the design of the joint, it is possible to strengthen certain, more flexible components, thus achieving ductile behaviour of the joint. For example, if the thickness of the anchor plate is varied, the flexible behaviour of the anchor plate, which is considered within the T-stub under tension and compression according to EN 1993-1-8, can come into play. On the other hand, higher resistances for some concrete failure modes can be reached if, for example, supplementary reinforcement is placed next to the headed studs in tension and the interaction between concrete and reinforcement is considered according to recent approaches (Berger, 2015; Kuhlmann et al., 2012; Kuhlmann et al., 2015).

The more detailed analyses of the load-carrying behaviour of the single components, their individual stiffnesses and their interaction enable assumptions to be made regarding the loading side

for the distribution of loading which are significant for the design of anchor plates. Internal forces such as normal, shear and bending forces are distributed among the rows of headed studs according to an elastic design concept (EN 1992-4) if the anchor plate can be assumed to be sufficiently rigid (Figure 2). As part of the elastic design concept, it is assumed that all fasteners have the same stiffness. Load redistributions in the area of the anchor plate should not be considered, as the fastener carrying the maximum load is critical for the load-carrying capacity of the anchor plate. The elastic design concept is mainly used for the design of fasteners because it is especially suitable for concrete failure modes. Due to the reduced deformation capacity of the pure concrete components, load redistributions are neglected. Plastic redistributions among the rows of headed studs may be taken into account if brittle concrete failure modes are excluded. In the case of flexible anchor plates, a non-linear distribution of forces is possible, based on the requirement of a technical report referenced by EN 1992-4.

A plastic design concept was derived for anchor plates with several rows of fasteners within the scope of the first investigations of the ductile behaviour of steel-to-concrete joints (Cook et al., 1989). Besides the non-linear distribution of normal forces, this concept allows shear forces to be distributed according to the utilization factor based on the interaction equations of each row. This is contrary to the elastic approach, where the shear forces are distributed equally among the rows. Limiting cases for the distribution of shear forces may be derived from equilibrium conditions for different eccentricities. With a large eccentricity of the load, for example, the whole shear force can be carried by friction. For smaller eccentricities, shear loads are carried by friction and by a contribution of the rows of fasteners on the loaded side, and in the case of very small eccentricities, the shear force is distributed equally among the rows of fasteners. An improved approach was developed for plastic design in (Lotze et al., 1997). For a full utilization based on the interaction of normal and shear forces, sufficient deformability should be available at the anchor plate and its fasteners.

3. EXPERIMENTAL INVESTIGATIONS

3.1 GENERAL

Firstly, experimental investigations were carried out to gather information on the behaviour of large anchor plates under shear loading and to apply these results as validation for further numerical investigations. In a second step, an analytical design model that takes into account the load distribution in the steel-to-concrete joint was developed based on the experimental and numerical studies (Kuhlmann et al., 2016; Kurz et al., 2016). Fourteen tests were carried out on large anchor plates under shear loading without edge effects. Steel-to-concrete joints, e.g. in walls, were considered for these configurations as the full concrete volume can be activated without any influences of the edges.

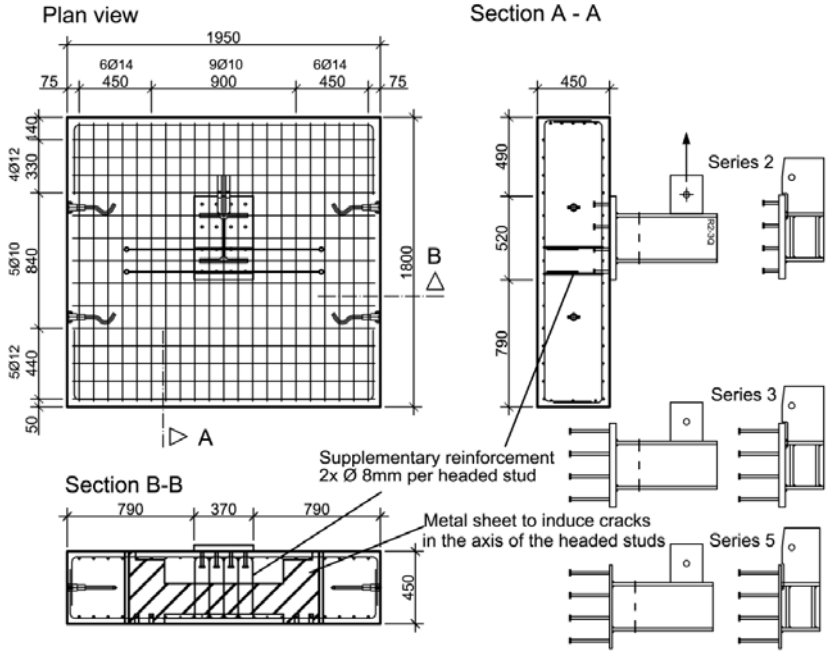


Fig. 3 – Reinforcement plan of test specimen R2-3Q and configuration of anchor plates for the other test series

The following parameters were varied within the specified limits:

- Eccentricity e (80 and 1000 mm)
- Thickness of anchor plate t_{ap} (15 and 40 mm)
- Length of headed stud h_n (100 and 250 mm)
- Cracked and uncracked concrete
- Reinforcement ratio of supplementary reinforcement (1 ø8 mm and 2 ø8 mm)

By varying the parameters given in Table 1, concrete and steel failure modes were planned beforehand and achieved in testing. In order to identify the influence of the different parameters, a testing matrix was chosen in a way that reference tests had been defined from which the other tests differed by only one single parameter. Thus, the influence of the various single parameters could be clearly identified.

Table 1 – Test parameters of shear tests

Test	Headed stud	Eccentricity e [mm]	Thickness of anchor plate [mm]	Supplementary reinforcement per headed stud	Concrete state
B3-Q	SD16/100	80	40	1 ø8 mm	cracked
R2-1Q	SD16/100	1000	40	2 ø8 mm	uncracked
R2-2Q	SD16/100	80	40	2 ø8 mm	uncracked
R2-3Q(1)	SD16/100	1000	40	2 ø8 mm	cracked
R2-3Q(2)	SD16/100	1000	40	2 ø8 mm	cracked
R2-4Q(1)	SD16/100	80	40	2 ø8 mm	cracked
R2-4Q(2)	SD16/100	80	40	2 ø8 mm	cracked
R3-1Q	SD16/250	1000	40	2 ø8 mm	uncracked
R3-2Q(1)	SD16/250	1000	40	2 ø8 mm	uncracked
R3-2Q(2)	SD16/250	1000	40	2 ø8 mm	cracked
R3-3Q	SD16/250	80	15	2 ø8 mm	uncracked
R5-1Q	SD16/250	1000	15	2 ø8 mm	uncracked
R5-2Q	SD16/250	1000	15	2 ø8 mm	uncracked
R5-3Q	SD16/250	80	15	2 ø8 mm	uncracked

The tension loading on the headed studs on the unloaded side of the anchor plate was influenced by the variation of the eccentricity. In tests with a large eccentricity, higher tension forces were obtained due to the resulting higher bending moment at the anchor plate. For this reason, different values of eccentricity were used. In addition, the thickness of the anchor plate was varied in order to determine the influence of a flexible anchor plate.

Where a concrete cone developed due to tension loading on the headed studs, these forces could be tied back by supplementary reinforcement, and, as a consequence, the load-carrying capacity of the related concrete failure modes increased. The supplementary reinforcement was placed next to the headed studs as shown in Figure 3 based on previous research results (Kuhlmann et al., 2012). In test B3-Q, one leg of a stirrup was placed next to the headed stud, whereas one stirrup with two legs per headed stud was considered in all other tests. In addition, several tests were performed in cracked concrete. Metal sheets were placed near the headed studs in tension and a crack width of approx. 0.3 mm was achieved on the axis of the two rows of headed studs on the unloaded side (Figure 3).

3.2 LOADBEARING BEHAVIOUR AND FAILURE MODES

The tests under shear load were conducted at the Materials Testing Institute, University of Stuttgart (Materialprüfanstalt Universität Stuttgart). To verify the analytical model, different failure mechanisms, such as concrete or steel failure, were initiated by varying the parameters given above (Figure 4).

Concrete pry-out failure was observed in the series with short headed studs, for tests with small and large eccentricity (Figures 4a and 4c). An elastic distribution of the normal forces was present in these tests, as the deformation of the anchor plate itself was very small. The cross-section of the anchor plate remained plane and no plastic deformations occurred. The embedment depth of the supplementary reinforcement in the concrete cone was small in comparison to the tests with long headed studs. Nonetheless, the supplementary reinforcement was activated. In the test with a smaller reinforcement ratio (B3-Q), the load-carrying capacity was 20 % lower (Figure 5b) than in the test with high reinforcement ratio (R2-2Q). In the test series with cracked concrete, the load-carrying capacities were reduced by 20 % compared with the reference tests (Figures 5a and 5b).

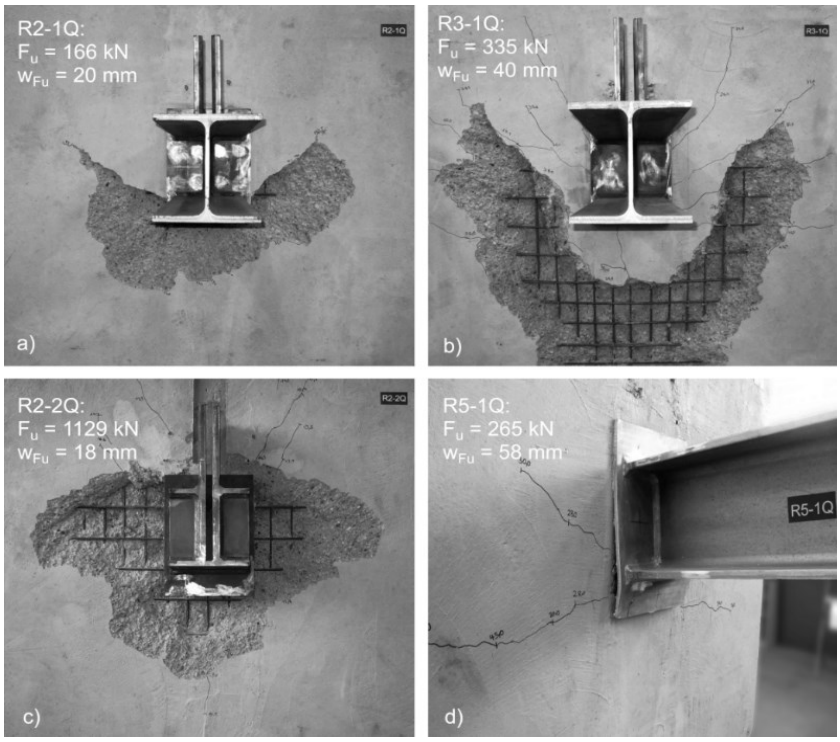


Fig. 4 – Failure mechanisms of shear tests with large anchor plates

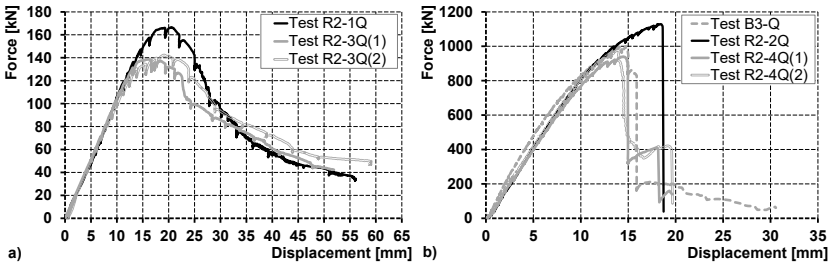


Fig. 5 – Load-deformation curve of test series 2 with a) large eccentricity and b) small eccentricity

The tests with longer headed studs and a thicker anchor plate (Figure 4b) resulted in a pry-out failure with a large concrete cone. The supplementary reinforcement was activated and the yield stress of the reinforcement was reached. In the tests with a small eccentricity, high shear forces occurred and the joint failed due to the headed studs shearing off. The influence of the pre-induced cracks was negligible, as many radial cracks developed in cracked and uncracked concrete. Only small deformations of the thick anchor plate were measured in these tests. In the rows of headed studs in tension, plastic redistributions occurred, measured by the strain gauges, due to the large uplift on the unloaded side of the anchor plate.

In the tests with thin anchor plates, the influence of the thickness of the anchor plate was observed by means of the development of yielding mechanisms (Figure 4d). In the tests with a large eccentricity, yielding mechanisms developed in the tension zone of the anchor plate. At maximum load, a

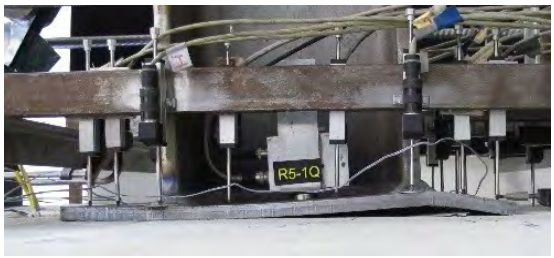


Fig. 6 – Yielding mechanism within the anchor plate at maximum load

mixed failure occurred due to yielding in the anchor plate and yielding in the headed studs (Figure 6). In the tests with small eccentricity and thin anchor plate, the headed studs sheared off at the base of the shaft similar to the tests with a thick anchor plate.

3.3 LOAD DISTRIBUTION OF NORMAL FORCES

One of the main goals of the experimental investigations was to determine the distribution of normal forces in the different rows of headed studs by varying the eccentricity of the shear force. To do that, strain gauges were attached to the shafts of the headed studs, to the supplementary reinforcement and to the top of the anchor plate. The stresses were evaluated by means of strains. In the rows of headed studs, the strain gauges were located according to a chessboard pattern. They were attached to the middle of the shaft in order to avoid the influence of the bending. The forces in the rows of headed studs were determined as mean values of the results measured by the strain gauges based on the mechanical properties of the material. An elastic distribution of normal forces was monitored in the tests with short headed studs and concrete failure modes. On the other hand, in the tests with long headed studs, plastic redistribution was measured towards the intermediate rows of studs. Compression forces were determined up to the maximum load in the first row in all tests with large eccentricity (Figure 7). The values measured by the strain gauges for large anchor plates and short headed studs comply with the definition of load distribution within anchor plates according to (Eligehausen et al., 2006), which assumes an elastic distribution of forces for brittle failure modes such as concrete pry-out failure. An elastic distribution of forces was determined in the tests with short headed studs (Figure 7a). Plastic redistribution among the rows of headed studs was observed for ductile failure modes such as steel failure in test R5-1Q (Figure 7b).

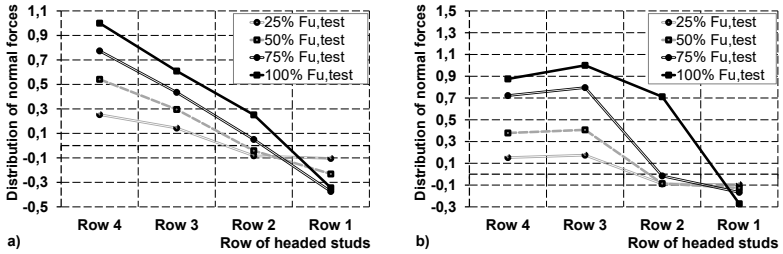


Fig. 7 – Load distribution of normal forces: a) test R2-1Q and b) test R5-1Q

4. NUMERICAL INVESTIGATIONS

The aim of the numerical investigations of the shear tests was to recalculate the maximum loads and the failure modes of the tests. Based on the tests, the numerical model was validated and the load distributions in the anchor plate evaluated – specifically, the distribution of shear forces among the rows of headed studs. In addition, parameter studies were conducted. The investigations of the anchor plate considered various parameters, including thickness, headed stud embedment depth and shear force eccentricity. The numerical results allowed also the enlargement of the database

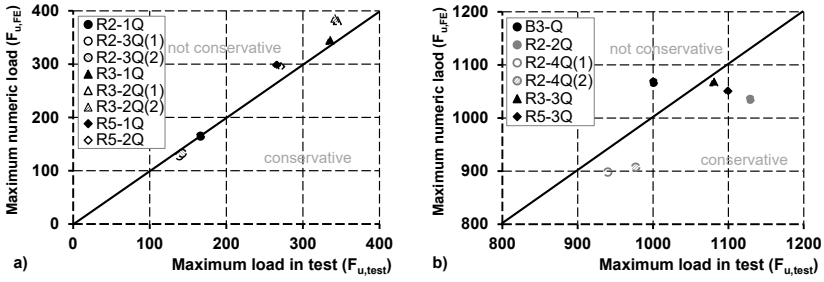


Fig. 8 – Comparison of maximum loads of FE model and test results for a) large eccentricity and b) small eccentricity

for the validation of the analytical model. The non-linear FE program MASA (Macroscopic Space Analysis) was used for the numerical studies as it permits modelling of the localized damage behaviour in the concrete of the shear joints (Ožbolt 2014). Good correlation was observed between the maximum loads from the tests and the numerical results. Figures 8a and 8c compare large and small eccentricities. The numerical model was also able to reproduce the load-carrying behaviour of all different failure modes such as steel and concrete failure for the same assumptions concerning boundary and modelling conditions. The non-linear behaviour of the steel was considered by the von Mises yield criterion and the damage behaviour of the concrete by the microplane model implemented in MASA.

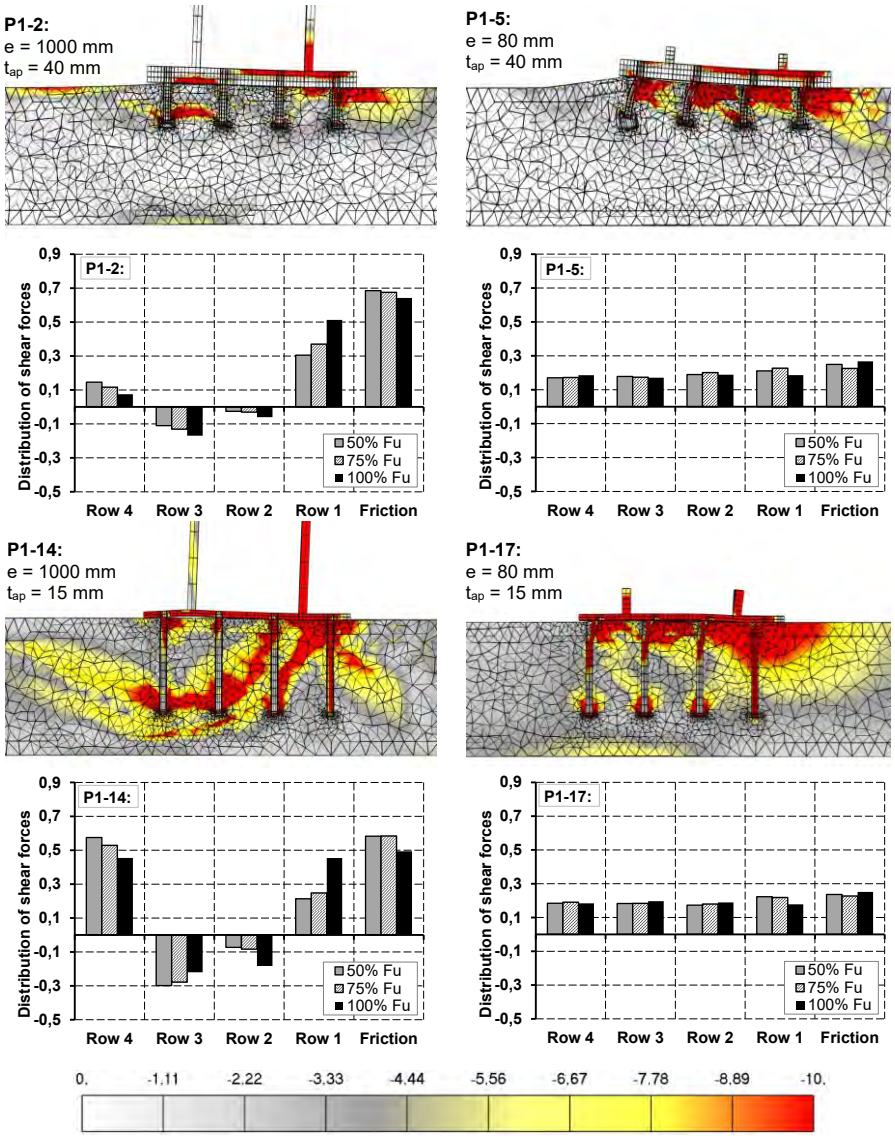


Fig. 9 – Principal compressive stresses in N/mm² and load distribution of shear forces within the different rows of studs for different eccentricities and anchor plate thicknesses

A number of parametrical studies were performed in order to examine the load-carrying behaviour of the anchor plates and to quantify the influence of different factors such as geometry and material properties. The parameters were selected so that the upper and lower values were validated by test results and the database was enlarged by parameter studies for values in between those boundaries. In addition, parameter studies were also conducted beyond the configurations of the test specimens. The concrete strength and the reinforcement ratio were varied in addition to varying the parameters eccentricity and anchor plate thickness. The studies of the influence of eccentricity and anchor plate thickness are shown in the following. A detailed description of all parameter studies is given in the final research report (Kurz et al., 2016).

The distribution of shear forces among the different rows of headed studs was quantified by the numerical investigations, because in the tests, it was not possible to determine the shear force per stud in a similar way as for the normal forces. Therefore, the nodal forces, derived from the numerical calculations, were summarized in a section through the base of the headed studs in

the different rows and compared with each other. The distribution of shear forces is illustrated in Figure 9 by the principal compressive stresses in the concrete. The results of the different principal compressive stress plots are scaled equally to the range between 0 and -10 N/mm² in order to be able to compare the plots with each other. Varying the eccentricity of the shear force has an influence on the load distribution of the tensile forces on the unloaded side and in the distribution of the shear forces, since large deformations occur due to the tension uplift of the anchor plate in the area of the T-stub (P1-2 and P1-14). High shear forces were determined in the shafts of the headed studs, especially with a thin anchor plate. For the studies with large eccentricities, a high contribution by the friction forces was determined for the shear capacity due to the comparatively compressive forces at the anchor plate. In these cases the shear force is mainly transferred by friction and the first row of studs. The distribution of the shear forces, determined in numerical studies with a small eccentricity, is approximately similar for thick and thin anchor plates. The shear force is distributed equally among the rows of headed studs (P1-5 and P1-17). The observations of the load distribution of the shear force, based on the numerical studies, are generally in line with the current plastic design concept for steel-to-concrete joints. However, high tensile and shear forces may occur due to membrane effects in the tension zone of the anchor plate. These effects require a common design concept for steel and concrete components.

5. COMPONENT MODE FOR STEEL-TO-CONCRETE JOINTS

5.1 GENERAL

In the design concept of the component method, the design resistances of the single components are compared with their actual loading accordingly. In addition, interaction equations due to loading in different directions have to be considered. Within the scope of a design concept for steel-to-concrete joints under shear loading, simplifications have to be considered, especially for anchor plates with a higher number of headed studs due to the high degree of static indeterminacy. A simplified analytical design model is proposed for steel-to-concrete joints with large anchor plates. In this model the tensile forces in the rows of headed studs on the unloaded side are assembled into one resultant tensile force. The analytical design model for the tension component has been calibrated and verified by test results under normal forces at the University of Kaiserslautern (Scholz et al., 2016). On the loading side, an elastic design concept with brittle failure mechanisms may be considered as well as a plastic design concept with load redistributions corresponding to the large deformations of the steel components.

5.2 SINGLE COMPONENTS FOR TENSION AND SHEAR

The component model for the steel-to-concrete joints is based on existing design concepts for the failure modes of the single components. The concrete capacity design (Fuchs et al., 1995; Eligehausen et al., 2006; EN 1992-4) for the current concrete components is expanded by more current approaches that consider the reinforcement near the fasteners (Berger, 2015; Kuhlmann et al., 2012; Kuhlmann et al., 2016).The analysis of the concrete components have to consider, on one hand, the fastener with the highest load and, on the other, the group failure mechanisms. Simplified design approaches were developed (Kurz et al., 2016), where the resistances of the supplementary reinforcement and the concrete are combined. For the steel components within the anchor plate, the T-stub model for tension and compression loading (Wald et al., 2008; EN 1993-1-8) is considered, which has been extended by newer concepts for T-stubs with several rows of bolts (Couchaux et al., 2015).

5.3 COMPONENT MODEL FOR LARGE ANCHOR PLATES UNDER SHEAR

In the following, an analytical design model is proposed for steel-to-concrete joints under shear loading which considers the different requirements and assumptions concerning the load distribution and the resistances depending on the different failure mechanisms. The eccentric loading of a steel-to-concrete joint is split into a bending moment for the definition of the normal components and into a pure shear force for the determination of the shear components, see Figure 10. This subdivision is applied to all failure modes. Of course, both loading directions are considered for the interaction equations.

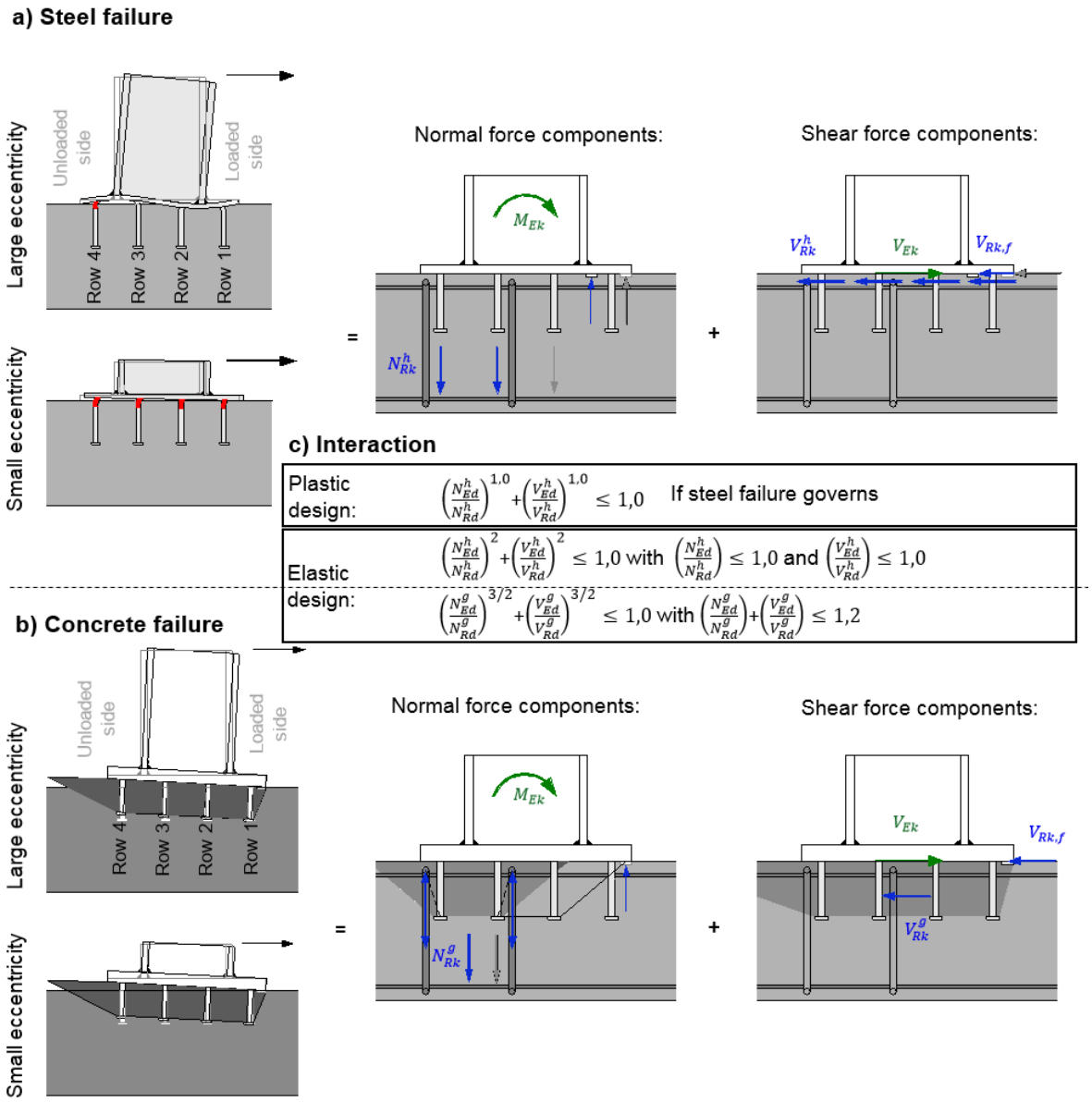


Fig. 10 – Design approach for large anchor plates under shear loading: a) load distribution for steel failure, b) load distribution for concrete failure and c) interaction formulas for tension and shear forces

Furthermore, the steel and concrete failure mechanisms are differentiated. Therefore, it is possible to distinguish between a single failure of the most heavily loaded fastener for steel failure and a group failure for concrete failure. In contrast to EN 1992-4, the components of the reinforcement

are associated with the group failure mode because the recent approach for the load-carrying capacity of the reinforcement considers the interaction between steel and concrete. So the resistance of the concrete cone is considered for the strength of the characteristic concrete component which should only be determined by considering the group of fasteners. For the tensile components, increases of the resistance are considered due to the overlap of the compression and tension zones (Zhao 1994). If elastic distribution of normal forces is assumed, effects due to an eccentric loading are included in the calculation of the tensile resistance for concrete failure (EN 1992-4). Within the scope of the plastic design concept, if brittle failure mechanisms can be excluded, the loading may be distributed equally among the rows of headed studs assuming plastic deformations. The tensile loading may be assigned to the rows of headed studs on the unloaded side for steel failure mechanisms, and the shear force that cannot be carried by the friction components is assigned to the first row of studs (Figure 10).

The normal forces in the rows of headed studs on the unloaded side are determined based on the equilibrium of vertical forces and moments around the compression zone (Figure 2). The internal forces can be distributed within the anchor plate according to Figure 10 for the different failure modes. The plastic design concept can be applied, if steel failure is the governing failure mode and the interaction equations for the plastic design given in Figure 10 are considered. Initially, an assumption is made for the depth and location of the compression zone and the number of rows of headed studs in tension. Within an iterative calculation, the assumption is reviewed and probably updated. A step-by-step procedure for designing the steel-to-concrete joints under shear loading and a general procedure are given in the project report (Kurz et al., 2016). In addition to a simplified design model according to (Kurz et al., 2016), where the tension loading is only assigned to the two rows of headed studs on the unloaded side, a more detailed model implemented in design software is described. Consequently, load redistributions and the flexible anchor plate can be considered based on the displacement method using the stiffness of the headed studs (Kuhlmann et al., 2012).

5.4 VERIFICATION OF THE COMPONENT MODEL

For the tests with large eccentricity, the results from the analytical design model for the different failure modes agree sufficiently well with the maximum test loads. The actual failure modes are also reproduced by the design concept (Figure 11a). The comparison between the results of the design model and the tests with small eccentricity show a conservative approach to the load-carrying capacities (Figure 11b). For the tests with small eccentricity and short headed studs, the resistance of the concrete pry-out failure is the governing failure mode in the analytical design model. As the supplementary reinforcement in the area of the headed studs cannot yet be considered within the model for pure shear, increases in the load-carrying capacity of this component will be possible in the future development of an improved model. The database for validating the analytical model was enlarged with the help of the numerical parameter studies. Further influences of different parameters were considered. In addition to the validation of the analytical model

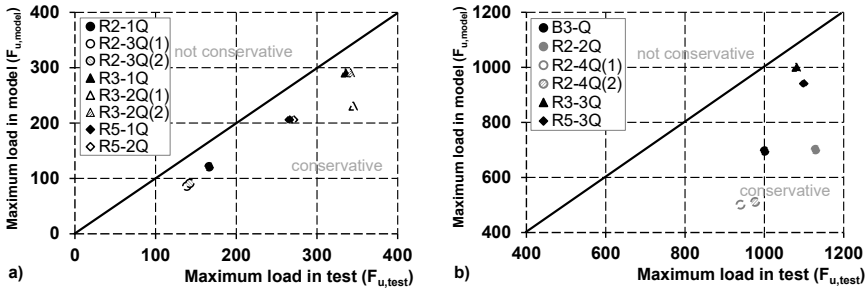


Fig. 11 – Comparison of maximum loads of the analytical model and the experimental results for a) large eccentricity and b) small eccentricity

in comparison to the 14 test results, approx. 90 additional numerical investigations were used for verification (Kurz et al., 2016).

6. CONCLUSIONS

Results of a research project were presented, where design models for large anchor plates under shear, tension and restraining forces had been generated. These models were developed based on experimental and numerical investigations for normal and restraining forces (Scholz et al., 2016) and shear forces. One aim of the project was to determine the load distribution of forces at the different rows of studs on the anchor plate, measured in the tests by strain gauges on the shafts of the headed studs and obtained by numerical calculations. Besides the embedment depth of the headed studs, other parameters were varied such as eccentricity, thickness of anchor plate and the reinforcement ratio of the supplementary reinforcement. In addition, tests were performed in cracked and uncracked concrete. Extensive numerical parameter studies were performed in order to enlarge the database of the tests and to determine the distribution of shear forces among the rows of headed studs. The numerical models were validated by the test results. The distribution of shear forces among the rows of headed studs could be quantified based on the numerical studies. The load-carrying behaviour and the influence of different parameters were examined with the help of the experimental and numerical studies. It might be possible to expand existing design concepts (EN 1992-4; EN/TR 1992-4) for large anchor plates if the requirements of an elastic or plastic design are considered consequently. Therefore, the resistances of the different failure modes of the single steel and concrete components (EN1993-1-8; EN 1992-4; EN/TR 1992-4) were used and extended by recent approaches to take into account the supplementary reinforcement according to (Berger, 2014; Kuhlmann et al., 2012). Further studies of the load-carrying behaviour of large anchor plates were performed (Ruopp 2018). Edge effects are not yet considered in the design model and have to be conservatively estimated by applying all loads to the row of headed studs close to the edge. Further numerical and experimental investigations have to be carried out for large anchor plates with edge effects in order to estimate the load-carrying behaviour and the load redistributions.

7. ACKNOWLEDGEMENTS

This IGF project of the Deutscher Ausschuß für Stahlbau (DASt) was funded by the AiF within the scope of the cooperative Industrial Research Programme (IGF) by the Federal Ministry for Economic Affairs and Energy based on a decision by the German Bundestag. The authors would like to take this opportunity to express their gratitude to all supporters of their research. Special thanks go to the industry partners Köster & Co. GmbH and Rau-Betonfertigteile GmbH & Co. KG for supplying the test specimens. Moreover, the authors would like to thank the project partners from the University of Kaiserslautern for the good cooperation and the Materials Testing Institute, University of Stuttgart (MPA), for their support regarding the tests.

REFERENCES

Berger, W. (2015). *Trag- und Verschiebungsverhalten sowie Bemessung von Kopfbolzenverankerungen mit und ohne Rückhängebewehrung unter Zuglast (Load-displacement behaviour and design of anchorages with headed studs with and without supplementary reinforcement under tension load)*. PhD thesis, Institute of Construction Materials, University of Stuttgart.

Cook, A.; Klingner, R. (1989): *Behavior and Design of Ductile Multiple-Anchor Steel-to-Concrete Connections*. Research Report CTR 1126-3, University of Texas at Austin.

Couchaux, M.; Demonceau, J.-F.; Weynand, K. (2015). *Calcul d'un assemblage par platine comportant quatre boulons par range*. Revue Construction Métallique 2.

EN 1993-1-8 (Eurocode 3): *Design of steel structures – Part 1-8: Design of joints*, Dec 2005.

EN 1992-4 (draft, Eurocode 2): *Design of concrete structures – Part 4: Design of fastenings for use in concrete* (not yet published).

EN/TR 1992-4: *Design of fastenings for use in concrete – Plastic design of fastenings with headed and post-installed fasteners*, Oct 2013 (not yet published).

Eligehausen, R.; Mallée, R.; Silva, J. F. (2006). *Anchorage in Concrete Construction*, Ernst & Sohn, Berlin.

Fuchs, W.; Eligehausen, R.; Breen J. E. (1995). *Concrete Capacity Design (CCD) Approach for Fastening to Concrete*. ACI Structural Journal 92. pp. 73–94.

Jaspart, J.-P. (1991). *Étude de la semi-rigidité des noeuds poutre-colonne et son influence sur la résistance et la stabilité des ossatures en acier.* PhD thesis, University of Liège.

Kuhlmann, U.; Hofmann, J.; Wald, F.; da Silva, L.; Krimpmann, M.; Sauerborn, N. et al. (2012). *New Market Chances for Steel Structures by Innovative Fastening Solutions between Steel and Concrete (INFASO)*. Final report, Report EUR 25100 EN, European Commission.

Kuhlmann, U.; Hofmann, J.; Wald, F.; da Silva, L.; Krimpmann, M.; Sauerborn, N. et al. (2015). *Valorisation of Knowledge for Innovative Fastening Solutions between Steel and Concrete (INFASO+)*. Final report, EUR 27745 EN, European Commission.

Kuhlmann, U.; Ruopp, J. (2015). *Anschlüsse zwischen Stahl und Beton – Anwendung in der Praxis (Steel-to-Concrete Joints – Practical Application)*. Bauingenieur 90, No. 12, pp. 583–593.

Kuhlmann, U.; Ruopp, J. (2016) *Large Anchor Plates with Headed Studs for Highly Stressed Constructions in Industry and Plant Engineering under Shear Loading*. Test report, research project AiF/IGF-Nr. 17654, Deutscher Ausschuß für Stahlbau (not published).

Kurz, W.; Kuhlmann, U.; Scholz, J.; Ruopp, J. (2016). *Large Anchor Plates with Headed Studs for Highly Stressed Constructions in Industry and Plant Engineering*. IGF Project, Deutscher Ausschuß für Stahlbau (DASt), final report.

Lotze, D. Klingner, R. E. (1997). *Behavior of Multiple-Anchor Connections to Concrete from the Perspective of Plastic Theory*. PMFSEL Report No. 96-4, University of Texas at Austin, pp. 10–17.

Mishaxhiu, N. (2014). *Steel-to-Concrete Joints – Development of a FE-Model for Large Anchor Plates with Concrete Failure Mechanisms*. Master thesis, No. 2015-10X, Institute of Structural Design, University of Stuttgart.

Ožbolt, J. (2014). *MASA – Microplane Analysis Program, Institute of Construction Materials*, University of Stuttgart.

Ruopp, J. (2019). *Studies on Steel-to-Concrete Joints under Shear and Moment Loading with Large Anchor Plates or Various Edge Influences (working title)*. PhD thesis, Institute of Structural Design, University of Stuttgart.

Rybinski, M.: (2014). *Komponentenmethode für Ankerplatten mit Kopfbolzen unter einachsiger Beanspruchung (Component method for anchor plates with headed studs under uniaxial loading)*. PhD thesis, Institute of Structural Design, University of Stuttgart.

Scholz, J.; Kurz, W. (2016). *Anschlüsse zwischen Stahl und Beton mit Zwangsbeanspruchung (Steel-to-concrete joints with restraining forces)*. Stahlbau 85, pp. 811–821.

Tschemmernegg, F.; Huber, G.; Huter, M.; Rubin, D. (1997). *Component Method and Component Tests. Development of Building Constructions in Mixed Structures*. Stahlbau 66, pp. 624–639.

Wald, F.; Sokol, Z.; Steenhuis, M.; Jaspart, J.-P. (2008). *Component Method for Steel Column Bases*. HERON 53, No. 1/2.

Zhao, G. (1994). *Tragverhalten von randfernen Kopfbolzenverankerungen bei Betonbruch (Loadbearing behaviour of fastenings with headed anchors at concrete failure remote from edge)*. PhD thesis, Institute of Construction Materials, University of Stuttgart.

Seismic column base connections: experiments, simulations, component and building models, and design implications

Amit M Kanvinde
Department of Civil and Environmental Engineering
University of California
Davis, California
kanvinde@ucdavis.edu

ABSTRACT

Column base connections in steel frames usually require attachment of a steel column to a concrete footing, either through anchor rods attached to a base plate, or through embedment of the column into the footing. In either case, their response is controlled by complex interactions between the steel and concrete components of the connection. Results from numerous studies on these connections over the last decade are presented. These studies, conducted primarily in an earthquake-engineering context, include: (1) experiments on exposed base plate as well as embedded column connections, (2) finite element simulations, (3) methods for strength and stiffness characterization, (4) component hysteretic models, and (5) nonlinear time history simulations of buildings incorporating base connection response. Cumulatively, these studies have resulted in an improved physical understanding of base connection response and tools to design as well as simulate them. Key results from each of these studies are summarized, along with integrative insights from all of them. These insights have implications for connection detailing, as well as philosophies for designing safe and economical structures in seismic regions that leverage beneficial aspects of connection response while considering possible weaknesses. Areas for future research are identified.

INTRODUCTION

Connections between steel columns and concrete footings transfer moments, axial, and shear forces from the entire structure into the foundation. Their design and construction takes numerous forms, depending on the structural system they belong to (e.g., moment vs braced frames), and the magnitude or type of forces they must resist. Broadly, these may be classified as exposed type (Figure 1a), in which a base plate is anchored to the footing, or embedded type (Figure 1b), in which the lower portion of the column is embedded into the footing. The former is appropriate for low-rise moment or braced frames, whereas taller frames usually require some degree of embedment for force and moment transfer, since an impractical number (or size) of anchor rods is required in an exposed type connection.

This paper describes research on various aspects of these connections conducted over the last decade, focusing on the work done in the author's research group. These aspects include (1) load resisting mechanisms, and strength and deformation characteristics, (2) stiffness of these connections, and (3) implications of connection response on structural performance. The research described here includes a comprehensive program of testing (>30 experiments), finite element

simulations for connection response, model development of strength and stiffness, and finally frame simulations to examine the effect of base connection flexibility on structural response. The paper begins by briefly reviewing some of the early research on these connections, before describing developments over the last decade. The paper concludes by summarizing research needs for the future.

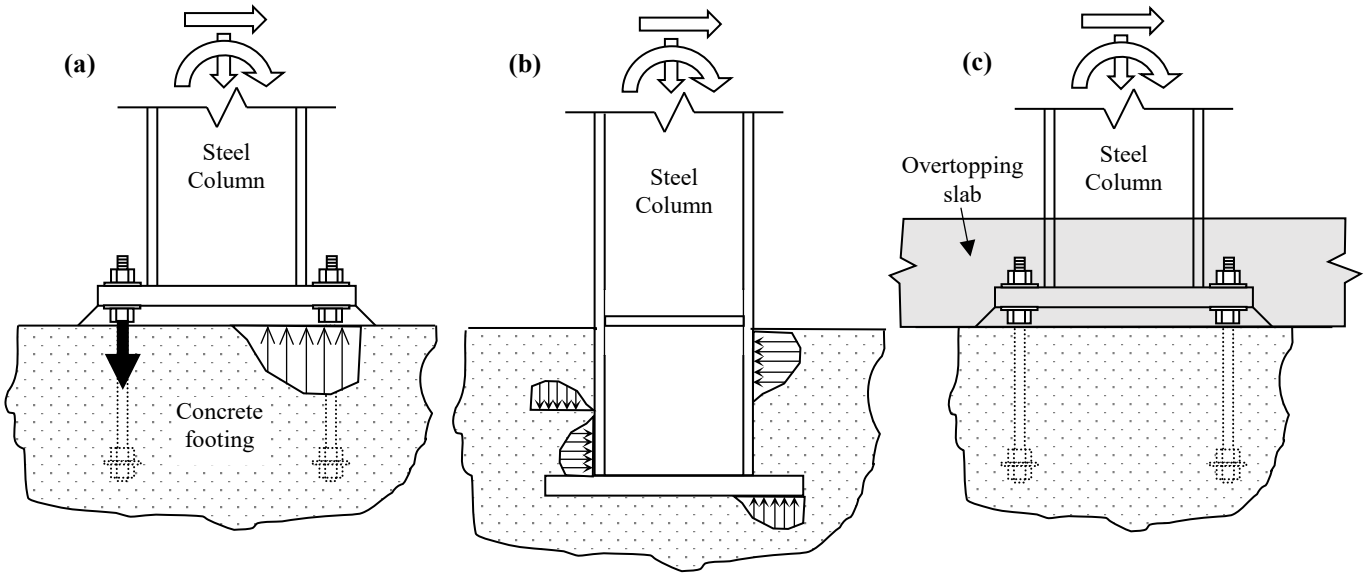


Figure 1 – Column base connections and force transfer mechanisms: (a) exposed with base plate and anchor rods, (b) deeply embedded, and (c) shallowly embedded due to overtopping slab

PRIOR RESEARCH ON COLUMN BASE CONNECTIONS

The American Institute of Steel Construction's (AISC) Steel Design Guide One (Kloiber & Fisher, 2006) along with the Seismic Design Manuals published by AISC (AISC, 2010) and the Structural Engineers Association of California (SEAOC, 2012) are primary references for the design of base connections. These documents represent the synthesis and culmination of research conducted over the last five decades. This includes experimental research by (Burda & Itani, 1999), (Astaneh & Bergsma, 1999), and analytical research by (Ermopoulos & Stamatopoulos, 1996), and (Pertold, Xiao, & Wald, 2000). For an exhaustive list see (Grauvilardell, Lee, Hajjar, & Dexter, 2005). A key part of Steel Design Guide One is the "Drake-Elkin Method," (Drake & Elkin, 1999) for the design of exposed base plate connections under axial compression and flexure. The method is based on assuming a pre-determined stress distribution (based on the concrete or grout failure stress) under the base plate under applied loads (illustrated schematically in Figure 1a) and then performing design checks on various parts of the connections. These include checking the base plate in flexure on the tension and compression side of the connection, and checking the anchor rods for tensile yielding. The design guide also provides guidance for designing base plates subjected to pure compression.

Research described in this paper focuses on details, and aspects of response not directly addressed by Design Guide One and preceding work. Specifically, the following issues are discussed:

1. Strength and deformation capacity of base connections: For exposed base connections, this involves: (a) experimental verification of the methods described in Design Guide One in a cyclic loading dominated seismic context, (b) examination of the response excluded from Design Guide One, and yet commonly used in construction, i.e., exposed base connections

with more than 2 rows of anchor rods (see Figures 2b and c), and embedded base connections (Fig 1b), and (c) examination of shear-transfer mechanisms in base connections.

2. Flexibility of base connections: Even if designed to meet strength requirements (i.e., designed to remain elastic under imposed loading), the base connections have significant flexibility. This paper described models developed to characterize this flexibility.
3. Implications for building performance and design: Flexibility in the base connections results in force redistribution and change in building seismic performance. This paper describes findings from time history simulations that assess these effects. Additionally, the paper examines whether dissipative characteristics of the column bases may be used in an advantageous manner for seismic design.

Each of the points above constitutes one section of the paper. Within each broad theme, different details are discussed along with appropriate references.

STRENGTH AND DEFORMATION CAPACITY OF BASE CONNECTIONS

As discussed in the preceding section, the strength of column base connections was examined for different types of details, and for different mechanisms (i.e., axial force and moment, or axial force and shear).

Exposed Base Plate Connections: Figure 2 shows the different types of exposed base connections tested by the author's group over the last decade. These include the following:

1. Exposed base plate connections with a standard 4 bolt pattern similar to that addressed in Design Guide One subjected to combinations of axial compression and shear – see Figure 2a.
2. Exposed base plate connections with two types of 8 rod patterns subjected to axial compression and shear (Figure 2b and 2c); these are not addressed by Design Guide One, yet commonly used. Specifically, the 8-rod pattern shown in Figure 2b is commonly used for square HSS (Hollow Steel Section) cantilever columns for mezzanines. Testing for points 1 and 2 is summarized in (Gomez, Kanvinde, & Deierlein, Exposed column base connections subjected to axial compression and flexure, 2010), and (Kanvinde, Higgins, Cooke, Perez, & Higgins, 2014).
3. Exposed base plate connections subjected to axial tension, compression and shear; see (Gomez, Kanvinde, Smith, & Deierlein, 2009).

In addition, Finite Element simulations were conducted to examine conditions not directly evaluated by the experiments; these included base plates of different thicknesses, as well as base connections subjected to biaxial bending and axial compression (see Figure 3).

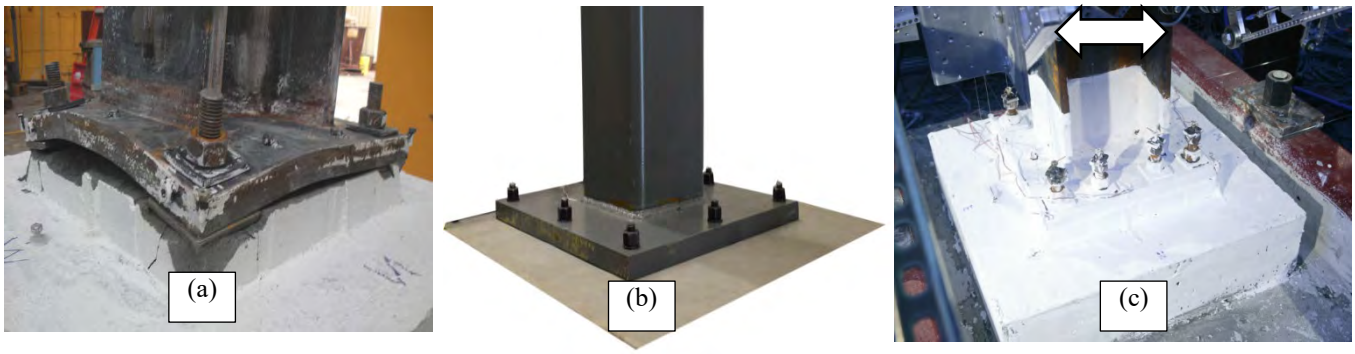


Figure 2 – Alternate anchor rod patterns: (a) 4-rod pattern addressed by Design Guide One (b, c) 8-rod patterns

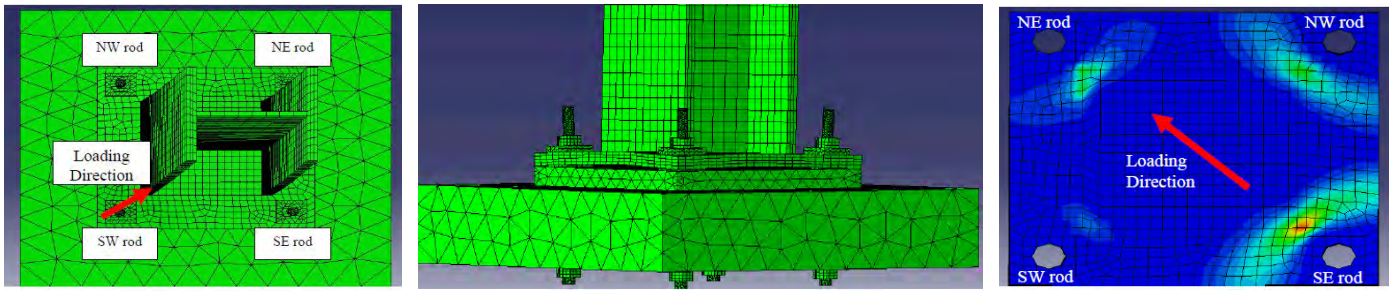


Figure 3 – Finite element model of base plate subjected to biaxial bending, indicating interaction of loading directions and high stress near corner

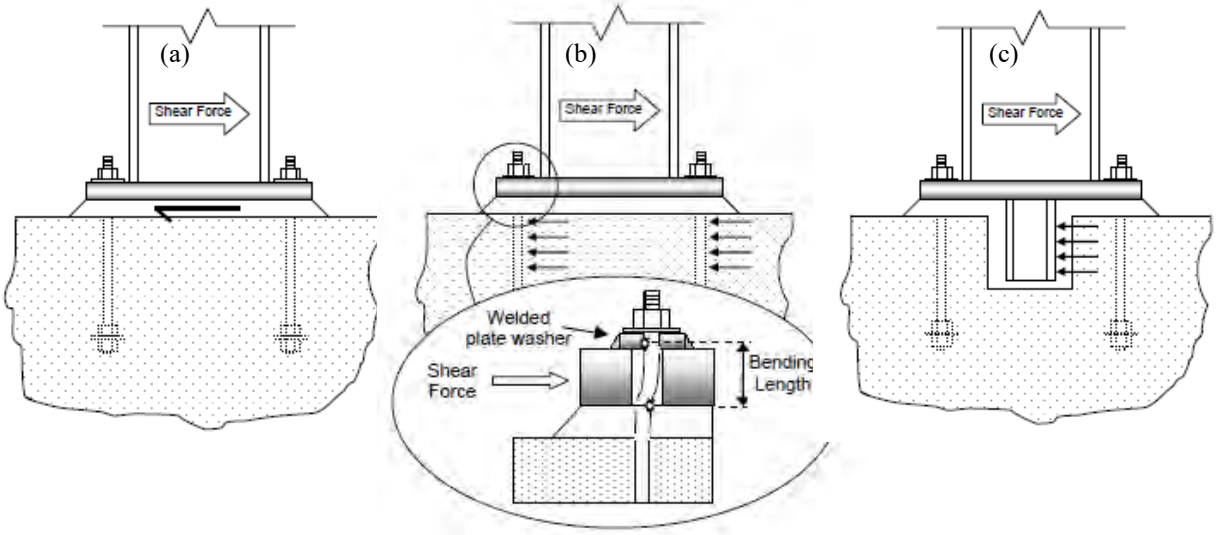


Figure 4 – Shear transfer mechanisms (a) Friction (b) Anchor rod bearing and (c) Shear key bearing

The primary findings pertaining to the strength of exposed base plate connections are summarized below:

1. Design Guide One is generally appropriate for characterizing the strength of exposed base plate connections with a 4-rod pattern (or more specifically two rows of rods in the direction of bending). Measurements indicate that the stress blocks assumed in the Drake and Elkin method appropriately represent the true stresses. However, it is noted that a check of base plate yielding on the compression side (see limit states discussed earlier) is not necessary, since it is a highly ductile limit state that does not affect the strength of the connection. Consequently, disregarding this design check reduces conservatism of the method.
2. Design Guide One is ill-equipped to characterize the strength of base plates with the 8-rod pattern. Specifically, it cannot address the static indeterminacy that arises due to the presence of multiple rows of anchor rods in tension. For some cases, such as the one shown in Figure 2c it is conservative, because it does not count the reserve strength provided by the additional anchor rods. However, in some cases, such as the one shown in Figure 2b where three anchor rods are present in a row, it may be unconservative, because it cannot characterize the unequal distribution of tensile forces among the anchor rods within a row (the central rod carries a disproportionately high fraction of the load). The work by Kanvinde et al., (2014), Gomez et al., (2010) suggests methods to address these (Figure 2b and Figure 2c) situations.
3. Three shear transfer mechanisms for exposed base plates were examined; these include (1) friction between base plate and grout, which is available when there is net compression, (2)

anchor rod bending, and (3) an embedded shear key. Figure 4 shown illustrates these schematically. It was determined that currently used approaches (as outlined in Design Guide One) are appropriate to characterize strength for the first two mechanisms, but may be quite unconservative for the shear-key bearing mechanism, since is disregards the size-effect in concrete. This may be addressed through other approaches, e.g., the Concrete Capacity Design method (Fuchs et al., 1995) which explicitly incorporates this effect.

4. The finite element simulations (similar to the one shown in Figure 3) confirm the above points, but additionally indicate that exposed column base plates are subject to an interaction in bending moments acting in the major and minor axes of the column, since the anchor rods carry tension corresponding to both these moments. Currently, no approaches are available for characterizing this interaction.

Embedded Column Base Connections: Current design guidance for Embedded Column Base connections is limited to the AISC Seismic Design Manual, which adapts test results for similar connections (e.g., steel link beams embedded in concrete shear walls) to develop strength equations for these connections. The professional practice has relied on these and similar (e.g., approaches using design equations for steel-concrete composite moment connections) for design of such connections. However, embedded column base connections are quite different as compared to any of these, for various reasons. These include the presence of axial force in the steel column as well as a high degree of confinement for the concrete in the bearing region ahead of the column flange. Grilli et al., (2017 – in press) tested 5 full-scale embedded base connections, in which the lowest portion column was embedded into a footing. These connections were subjected to combinations of axial compression, tension, flexure and shear. The tests reveal that the base moment and shear is resisted through a combination of three mechanisms, which are illustrated schematically in Figure 5: (1) bearing stresses between the column flanges and the concrete footing – Figure 5a, (2) the development of a concrete panel, which along with the column web resists the panel zone shear – Figure 5a, and (3) resistance to uplift of the embedded base plate – Figure 5b. The former two mechanisms act in series with each other (i.e., carry forces that are in equilibrium with each other), and together in parallel with the third (uplift mechanism). Grilli and Kanvinde (2017) present a strength characterization method for these connections; the method has two steps. First, the applied moment must be decomposed into the moment carried by mechanisms (1) and (2) above, and the moment carried by mechanism (3). Second, limit states associated with each mechanism must be identified, and the strengths corresponding to each must be aggregated into the connections strength. This process is not unlike that for composite steel beam-concrete column moment connections, as described in the design guide for composite connections (ASCE, 1994).

Column shear transfer in embedded base connections is relatively facile, and unlikely to result in a limit state by itself. However, the column shear is included into the calculation of the bearing stresses carrying the moment.

Barnwell (2015) conducted experiments on shallowly embedded column connections, in which the embedment of the base plate is incidental (rather than for strength), and arises from an overtopping concrete slab – see Figure 1c. In these, it was determined that the overtopping slab results in an increase in moment capacity, albeit the dominant resistance mode is still resistance to overturning of the base plate.

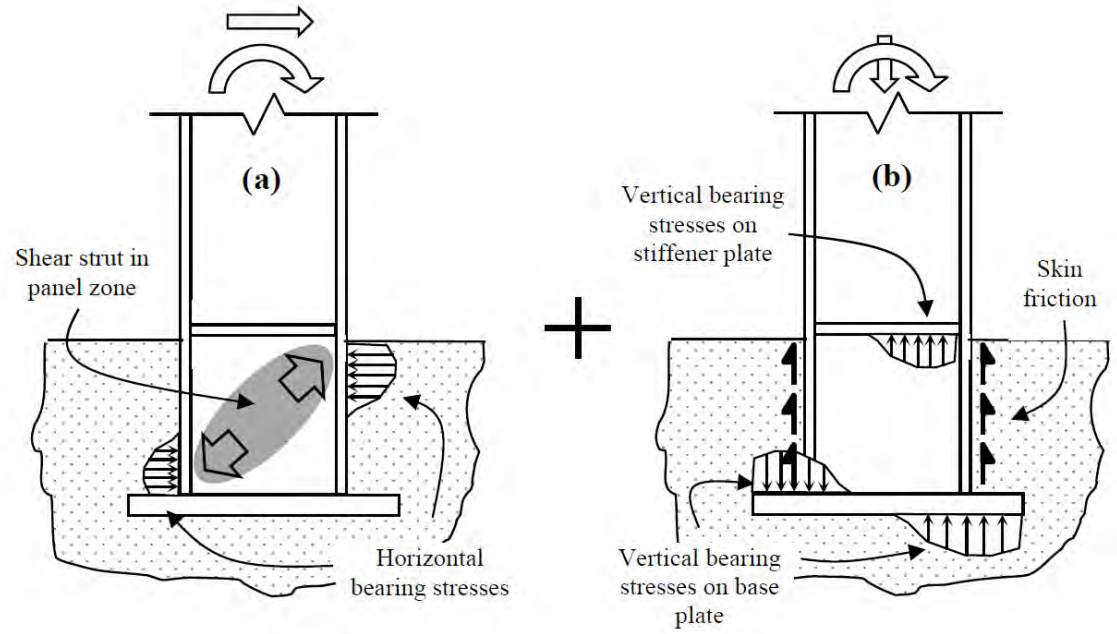


Figure 5 – Force transfer mechanisms in embedded base connections: (a) bearing on column flanges and panel zone shear (b) restraint to base plate uplift and skin friction

Figure 6 shows representative plots of moment-rotation curves for the exposed and embedded base connections. Two points may be noted from the figures. First, the connections show significant dissipative capacity, along with large ductility, with rotations in the range of 3-10% for almost all the specimens tested. Second, the specimens show significant rotational flexibility – this is uniformly observed even when these connections are designed to be stronger than the attached column or provided with an embedment to achieve base fixity. The implications of both these observations for design are discussed in upcoming sections.

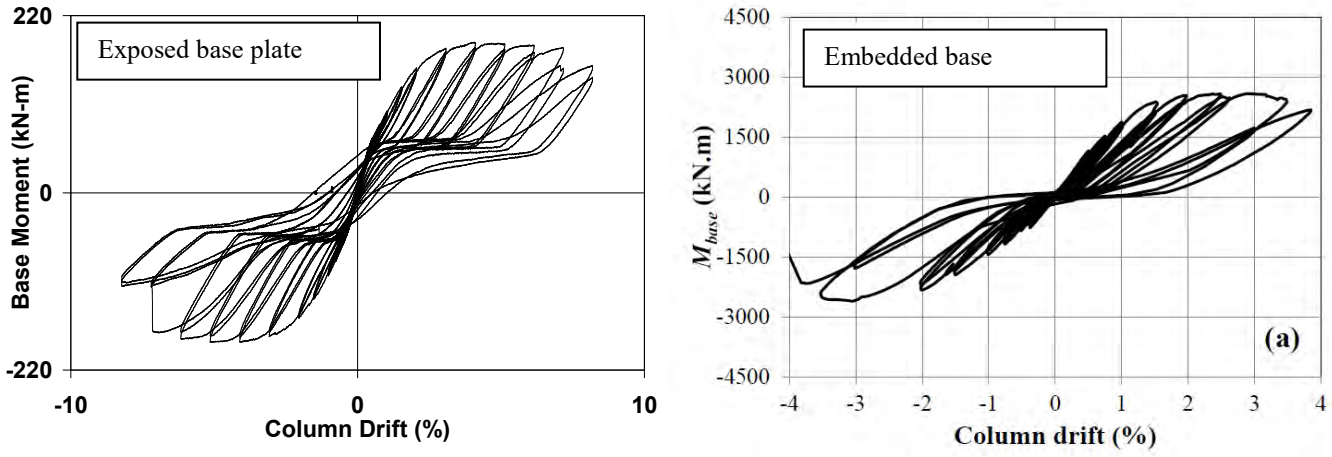


Figure 6 – Representative load-deformation graphs from exposed and embedded base connections, showing deformation capacity and dissipation

FLEXIBILITY OF BASE CONNECTIONS

Referring to the previous section, base connections (whether embedded or exposed) show significant rotational flexibility, such that elastic rotations of the base connection may approach 0.01 radians (which is on the order of yield drift in moment frames). However, these connections are usually modeled as fixed or pinned in structural simulation; this has the potential of mischaracterizing structural response. To address this, recent research by authors as well as others (Tryon, 2016; Trautner et al., 2015) has focused on the development of methods to determine the flexibility of base connections. Some of these approaches are briefly outlined here:

1. Kanvinde et al., (2012) proposed a method for characterizing the rotational flexibility of exposed base connections. This approach decomposes the deformations in the base plate into those from the concrete, anchor rod, and base plates (under a given axial force and moment), and then enforces compatibility to determine connection rotation. Since the method leverages the Design Guide One approach for strength characterization to determine stresses in concrete, anchor rods, and base plate, it requires only a modest amount of effort to compute base flexibility once the base plate has been designed. Figure 7 below shows the assumed deformations in this method.
2. Torres Rodas et al., (2017 – in press) present a method for characterizing the flexibility of embedded column base connections. The approach reflects physical insights developed during the tests on Embedded Column Bases by Grilli et al., (2017 – in press). The method considers deformations of several components within the connection, including bending and shear deformations of the embedded column, in addition to bearing deformations of the concrete adjoining the embedment. To resolve the internal indeterminacies of stress distribution within the connection, the method relies on stress distributions established for the strength model (Grilli and Kanvinde, 2017) discussed earlier. As a result, in a manner similar to the flexibility method for the exposed base connections, it retains a degree of simplicity and commonality with the strength model. Tryon (2016) presents a similar method for shallowly embedded base connections.

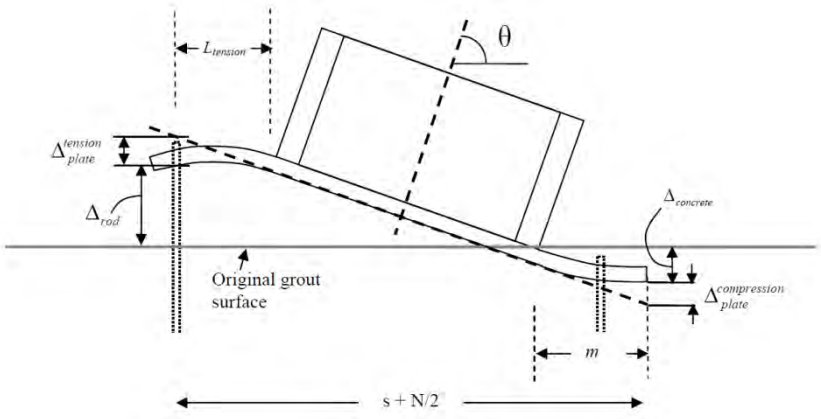


Figure 7 – Deformation contributions to exposed base plate connections

The models above may be used for simulating base connections in buildings, to estimate forces/moments for design, or they may be used for parametrically examining the effect of base flexibility on generic building response to inform general design approaches and philosophies.

The next section discusses the implications of base connection response (as observed in this and the previous section) on the seismic response of moment frame structures.

IMPLICATIONS FOR BUILDING RESPONSE AND DESIGN

Zareian and Kanvinde (2013) conducted a parametric study to examine the effect of column base flexibility on the seismic response of steel moment frames. To this end, the response of four frames (2, 4, 8 and 12-story) designed as per current code was investigated through static pushover simulations and sophisticated nonlinear response history simulations including collapse simulation. For each frame, a range of base fixities was examined, including realistic values that were determined for the as-designed base connections using the models summarized in the previous section. The results indicate that a reduction in base stiffness (with respect to the fixed base assumption, which is commonly used for mid- to high-rise frames, if the base is designed to be stronger than the column), lowers the point of inflection in the first story columns, greatly increasing moment demands at the top of the column. The results in concentration of deformations in the first story (i.e., a soft-story mechanism), undermining the performance in three ways: (1) significant increase in deformation demands, (2) decrease in system ductility, and (3) significant reduction in collapse-capacity, i.e., the median ground motion intensity associated with sidesway collapse. For the 4-, 8- and 12-story frames, this suggests that the expected response of frames is significantly worse than is implied by simulations and design approaches that assume a fixed base condition.

From a design perspective, the primary implication is that for mid- and high-rise buildings, the characterization of base stiffness is critical, and simulating the bases as fixed results in estimates of response that are significantly unconservative. On the other hand, for low-rise frames, the bases are generally modeled as pinned. This assumption is conservative since it discounts the base stiffness, moving the inflection point to the bottom and greatly increasing the column moment demands (with respect to the true condition). This may result in oversized first story columns.

Referring to prior discussion, almost all base connections tested in literature have significant rotation capacity (drifts in the range of 3-10%), even if not specifically detailed to be a ductile connection. Even if it is argued that the rotation capacity may be artificially high in well-constructed lab tests, it still is significant, especially when compared to rotation capacity requirements for other “ductile” connections such as beam column connections. Despite the available rotation capacity in base connections, they are often designed to remain elastic and force the plastic hinge into the lower end of the column (SEAOC, 2012).This means that the bases are designed for moments on the order of 1.1RyMp of the connected column. There are two significant issues with this:

1. Requiring the bases to remain elastic (i.e., designing for high moment) entails significant cost in terms of detailing (additional anchor rods, deeper embedment, thicker plates, more reinforcement). This may be unnecessary, given the potentially high deformation capacity of the base connections.

2. Tests on columns and W-sections show that plastic hinges in columns actually may have lower deformation capacities (~2% - Lignos and Krawinkler, 2013) even compared to bases, owing to phenomena such as local or lateral torsion buckling.

In summary, the current design philosophy for column bases may be backwards, i.e., protecting the potentially ductile base connection (often at high expense) while forcing yielding into a potentially less ductile component (the column). As outlined in this article, there is significant established knowledge regarding the component response of base connections, which have resulted in the fortuitous finding about the ductility. This knowledge may be used to develop a more rational design philosophy for frames that fully leverages this ductility (and dissipation) to result in economical and safer design.

SUMMARY AND RESEARCH NEEDS

This paper summarizes recent studies on the response of column base connections and its effect of structural performance. These studies have been focused on understanding strength limit states (under a variety of loadings), and then developing design considerations, i.e., strength models and detailing guidelines for these connections. A secondary outcome of these studies has been the understanding of the flexibility and hysteretic/ductility characteristics of these connections to inform the design of frames that use these connections. The research has focused on three different types of details:

1. Exposed base plate connections, in which a base plate is anchored to a concrete footing using anchor rods. These are the primary focus of Steel Design Guide One, and are feasible for low-rise buildings.
2. Deeply embedded base connections, in which the column is embedded into the concrete footing to achieve moment resistance. These are preferred for mid-high rise frames, and no design guidance is available for them.
3. Shallowly embedded base connections, which arise when exposed base connections are overlaid by a concrete slab on grade. These are common in low-rise frames for lateral systems and in high rise frames for gravity systems, providing lateral resistance in each case.

The state of research on each of these is at a different stage in terms of its maturity, documentation in design guides and documents, simulation methods, and adoption into design and construction practice. Despite this unevenness within the research on base connections, the main observation is that research on column bases (when considered as a whole) is significantly less mature than that on other connections such as welded beam column connections (due to the focus on these after the Northridge earthquake). Future research on these connections has the potential to significantly enhance the economy, performance, and safety of steel framed structures. Some particularly important research needs are outlined below:

1. Characterization of seismic performance, and the development of strength models for bae connections subjected to biaxial bending.
2. The development of dissipative and replaceable/repairable base connection technologies to enhance structural performance, and methodologies to design structures that take advantage of these technologies.
3. To enable point 2 above, the development of hysteresis models that can simulate the nonlinear/dissipative characteristics of these connections
4. Examination of configurations (especially of embedded base connections) that have not been tested, noting that only 5 deeply embedded base connections (reflecting US practice) have been tested so far.

ACKNOWLEDGMENTS

The author thanks the numerous organizations and individuals who contributed to this work. Major sponsors include: The American Institute of Steel Construction, Charles Pankow Foundation, National Science Foundation via the NEES Berkeley Equipment site. Material and fabrication donations were obtained from Herrick Steel of Stockton, CA; Gayle Manufacturing of Woodland, CA; and Transbay Steel of Napa, CA. The author also thanks the support staff at the NEES Berkeley equipment site, and the UC Davis laboratory. Students working on these projects include Ivan Gomez, David Grilli, Ryan Cooke, and Santos Jordan. Collaborators include Greg Deierlein of Stanford University, Paul Richards of Brigham Young University, Rick Drake of Fluor Corporation, Jim Malley of Degenkolb Engineers, Kevin Moore and Paul Cordova, both of Simpson Gumpertz and Heger, and Geoff Bomba of Forell Elsesser Engineers.

REFERENCES

AISC. (2010). Seismic Design Manual. Chicago, IL: American Institute of Steel Construction.

American Society of Civil Engineers (1994), “Guidelines for Design of Joints Between Steel Beams and Reinforced Concrete Columns,” Journal of Structural Division, ASCE, 1994, 120(8), 2330-2357.

Astaneh, A., & Bergsma, G. (1999). Cyclic Behavior and Seismic Design of Steel Base Plates. ASCE Structures Congress (pp. 409-414). Irvine, CA: American Society of Civil Engineers.

Barnwell, N. (2015). “Experimental Testing of Shallow Embedded Connections Between Steel Columns and Concrete Footings,” Masters Thesis, Brigham Young University.

Burda, J. J., & Itani, A. M. (1999). Studies of seismic behavior of steel base plates. Report No CCEER 99-7, Center of Civil Engineering Earthquake Research. Reno, NV: University of Nevada, Reno.

Drake, R., & Elkin, S. (1999). Beam Column Base Plate Design. Engineering Journal, 36(1) 29-38.

Ermopoulos, J., & Stamatopoulos, G. (1996). Mathematical Modeling of Column Base Plate Connections. Journal of Constructional Steel Research, 36(2) 79-100.

Fuchs, W., Eligehausen, R. and Breen, J.E. (1995), “Concrete Capacity Design (CCD) Approach for Fastening to Concrete,” ACI Structural Journal, Vol. 92, No. 1, pp. 73–94.

Gomez, I. R., Kanvinde, A. M., & Deierlein, G. G. (2010). Exposed column base connections subjected to axial compression and flexure. Chicago, IL: American Institute of Steel Construction.

Gomez, I. R., Kanvinde, A. M., Smith, C. M., & Deierlein, G. G. (2009). Shear Transfer in Exposed Column Base Plates. Chicago, IL: American Institute of Steel Construction.

Grauvilardell, J. E., Lee, D., Hajjar, J. F., & Dexter, R. J. (2005). Synthesis of Design, Testing, and Analysis Research on Steel Column Base Plate Connections in High-Seismic Zones. Minneapolis, MN: University of Minnesota.

Grilli, D.A., Jones, R., and Kanvinde, A.M., (2017 - in press). "Seismic Performance of Embedded Column Base Connections Subjected to Axial and Lateral Loads," Journal of Structural Engineering, ASCE.

Grilli, D.A., and Kanvinde, A.M., (2017). "Embedded column base connections subjected to seismic loads: Strength model," Journal of Constructional Steel Research, Elsevier, 129, 240-249.

Kanvinde, A.M., Grilli, D.A., and Zareian, F. (2012). “Rotational Stiffness of Exposed Column Base Connections – Experiments and Analytical Models,” Journal of Structural Engineering, ASCE, 138(5), 549-560.

Kanvinde, A. M., Higgins, P., Cooke, R. J., Perez, J., & Higgins, J. (2014). Column base connections for hollow steel sections: seismic performance and strength models. Journal of Structural Engineering, ASCE.

Kloiber, L., & Fisher, J. (2006). Steel Design Guide One, Base Plate and Anchor Rod Design (2nd Edition). Chicago, IL: American Institute of Steel Construction.

Lignos, D.G., Krawinkler, H. (2013). “Development and Utilization of Structural Component Databases for Performance-Based Earthquake Engineering”, ASCE, Journal of Structural Engineering, Vol. 139 (NEES 2), 1382-1394.

Pertold, J., Xiao, R. Y., & Wald, F. (2000). Embedded Steel Column Bases – I. Experiments and Numerical Simulation. Journal of Constructional Steel Research, 56(3) 253-270.

SEAOC. (2012). Special Moment Frame Base Connection Design Example 8. 2012 IBC SEAOC Structural/Seismic Design Manual Vol 4, Examples for Steel-Frame Buildings; 255-280. Sacramento, CA: Structural Engineers Association of California.

Torres Rodas, P., Zareian, F., and Kanvinde, A.M., (2017 – in press). “Rotational stiffness of deeply embedded column base connections,” Journal of Structural Engineering, American Society of Civil Engineers.

Trautner, C., Hutchinson, T., Grosser, P., and Silva, J. (2015). "Effects of Detailing on the Cyclic Behavior of Steel Baseplate Connections Designed to Promote Anchor Yielding." Journal of Structural Engineering, 10.1061/(ASCE)ST.1943-541X.0001361, 04015117.

Tryon, J.E., (2016). “Simple models for estimating the rotational stiffness of steel column to footing connections,” Masters Thesis, Brigham Young University.

Zareian, F., and Kanvinde, A.M.,(2013). “Effect of Column Base Flexibility on the Seismic Safety of Steel Moment Resisting Frames,” Earthquake Spectra, Earthquake Engineering Research Institute, 29(4), 1-23.

MOMENT-ROTATION CHARACTERISTICS FOR DECONSTRUCTABLE FLUSH END PLATE COMPOSITE JOINTS

Mark A. Bradford
m.bradford@unsw.edu.au

Abdolreza Ataei
a.ataei@unsw.edu.au

Xinpei Liu
xinpei.liu@unsw.edu.au

Centre for Infrastructure Engineering & Safety, School of Civil & Environmental Engineering
UNSW Sydney, NSW 2052, Australia

Abstract

A 3-D finite element modelling of flush end plate semi-rigid beam-to-column composite joints is described. The joints comprise of deconstructable post-installed friction-grip bolted shear connectors. The moment-rotation characteristics for these prototype joints subjected to a hogging bending moment with the influence of partial shear connection is investigated using ABAQUS, including material and geometric non-linearities. The accuracy and reliability of the numerical formulation are verified against experimental data, and a parametric study is conducted. Moment-rotation models for deconstructable flush end plate beam-to-column composite joints are proposed from these results.

INTRODUCTION

Steel-concrete composite beam-to-column partial strength joints are widely used in medium-sized steel-framed buildings, because they provide rapid construction solutions and possess excellent structural performance. The efficiency of a composite joint lies in ensuring composite action between the concrete slab and the steel beam. This composite action between these two components is normally achieved by using headed stud shear connectors welded to the top flange of the steel beam and embedded into a cast ***in-situ*** concrete slab. However, the deconstruction of this system and reuse of its components is almost impossible, and this produces environmentally-intrusive waste and CO_2 emissions.

One method of providing composite action between the concrete slab and steel beam to improve the structural behaviour of composite joints is to connect these two components with post-installed tensioned friction-grip bolted shear connectors (PFGBSCs). The innovative friction and bearing mechanisms for this connection have been shown to enable the composite beams and joints to be deconstructed easily at the end of their service life. In addition, the use of precast a concrete slab instead of a cast ***in-situ*** concrete slab can decrease the construction time and improve the quality of composite construction significantly. Therefore, using PFGBSCs in lieu of welded stud shear connectors improves the sustainability of composite construction significantly.

Surprisingly little research has been reported on beams and joints with PFGBSCs, especially from the perspective of deconstruction, and previous work has been reviewed by Ataei (2015). Whilst necessary for validation purposes, physical experimental studies of composite connections are very

expensive and time-consuming, and accordingly, considerable research momentum is gathering on using finite element (FE) simulations. A numerical model to simulate the behaviour of a composite beam with PFGBSCs was developed by Kwon, Engelhardt and Klinger (2012) using a FE technique. Liu, Bradford and Lee (2014) developed a 3-D FE model to study the ultimate strength and load-slip characteristics of PFGBSCs in beams with geopolymer concrete slabs, while Liu, Bradford, Chen and Ban (2016) proposed a 3-D FE model to investigate the behaviour of composite beams with PFGBSCs.

This paper presents a 3-D FE model using ABAQUS software to investigate the structural behaviour of semi-rigid beam-to-column composite joints with deconstructable PFGBSCs, precast concrete slabs and a strengthened I-section steel column. The detailed FE model developed includes all the pertinent connection components, in which material and geometrical non-linearities as well as the non-linearity of the interface contacts are incorporated. The accuracy and the reliability of the model are verified against experimental data reported elsewhere as well as test results obtained from full-scale laboratory tests conducted in this study. An extensive parametric evaluation is conducted, and existing prediction and design models are extended to elucidate the significant parameters for a composite joint with PFGBSCs and a precast concrete slab, including the initial rotational stiffness, rotation capacity and moment capacity.

FINITE ELEMENT MODELLING

Contact Modelling

There are several different components of the deconstructable beam-to-column composite joints: the steel beam, steel column, bolts in connection zone, bolt shear connectors, concrete reinforcing bars, flush end plate, steel beam and column stiffeners and the interaction between them should be taken into consideration in the modelling. The contact between these components was represented using the surface-to-surface contact interaction technique as shown in Fig. 1. One surface was taken as a master surface and the other a slave. Normal and parallel to the interface plane, HARD and PENALTY options were used respectively, with a friction coefficient of 0.45 (Ataei, Bradford & Liu 2016) for the interface between the steel beam and precast concrete slab and a friction coefficient of 0.25 for the other interactions. To be consistent with the experimental set-up, the holes in the steel column and flush end plate were modelled with a 1 mm clearance and could slip during loading. The TIE option was used to define the contact between the flush end plate-steel beam, while the EMBEDDED option was used to embed the reinforcement into the slab. Finally, non-linear springs were used to simulate the PFGBSCs, in which the results from push-out tests on M16 and M20 PFGBSCs (were used to characterise the load-slip behaviour of the bolt shear connectors and to represent their behaviour in the composite joints. The same location of the shear connectors was considered for the position of the springs as shown in Fig. 3.

Meshing, boundary conditions and restraints

A 3-D element was employed to simulate all components of the composite joint, in which truss elements (T3D2) with a linear approximation of the displacement and eight-node linear hexahedral solid elements with reduced integration and hourglass control (C3D8R) were used for modelling of the steel bars and the other components, respectively. The mesh used for each component of the composite joint was chosen based on an extensive sensitivity analysis conducted beforehand. Fig. 3 shows the mesh for the components in the joint.

Due to the symmetrical geometrical properties and applied loading, only half of each specimen about an axis of symmetry was modelled and the associated symmetric boundary conditions were considered on the plane of symmetry, as illustrated in Fig. 4. All nodes along the middle of the precast concrete slab, steel column web, column stiffeners and longitudinal reinforcing bars were

restrained from moving in the ***X*** direction and against rotation in the ***Y*** and ***Z*** directions. As the bottom of the steel column was fixed and restrained from displacing and rotating, all nodes at the bottom surface of the steel column were so restrained in the ***X***, ***Y*** and ***Z*** directions.

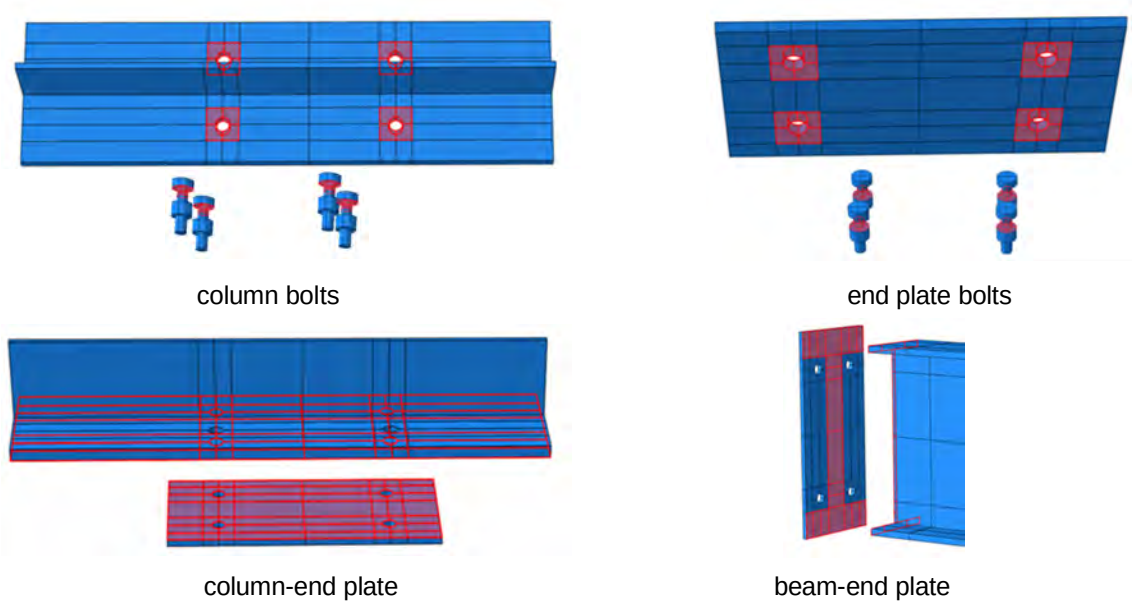


Fig. 1 – Contact surfaces between joint components

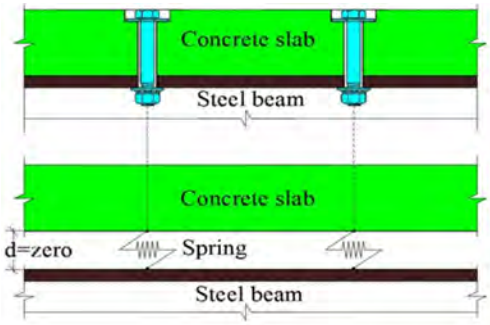


Fig. 2 – Simulation of PFGBSCs

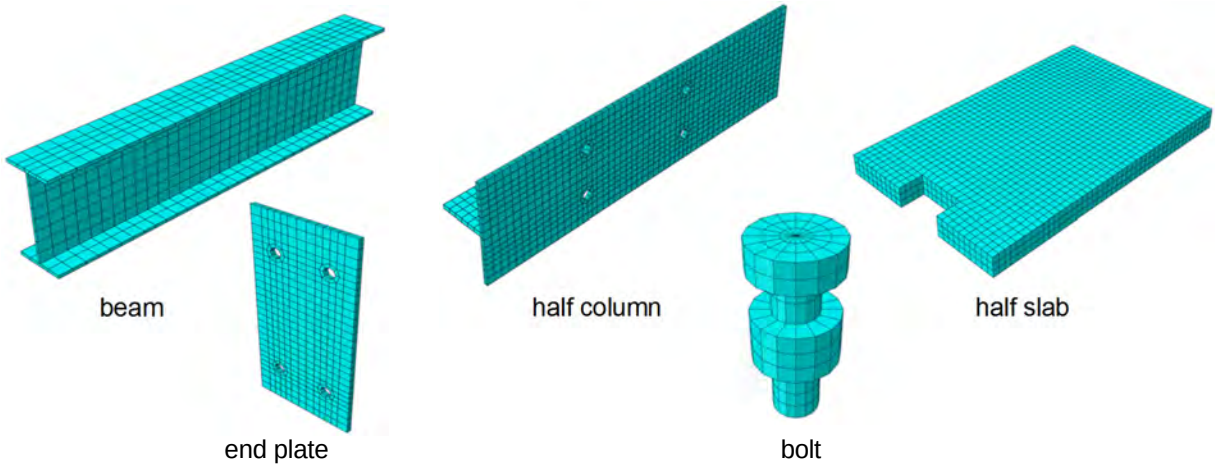


Fig. 3 – FE mesh for joint components

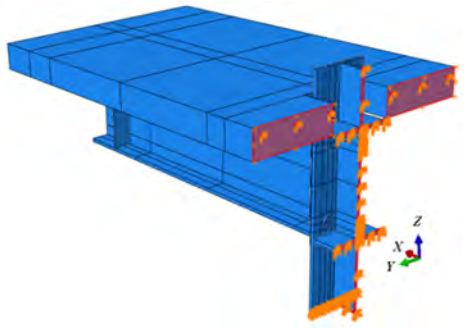


Fig. 4 – Half composite joint and boundary conditions

Material constitutive relationships

The relationship proposed by Carreira and Chu (1985) which has also been used in related studies was employed to simulate the behaviour of the concrete in compression. For concrete in tension, a linear–elastic representation followed by a linear softening branch was adopted. The tensile stress was assumed to increase linearly to 10% of its compressive strength. After cracking in the concrete, the stress declines to zero at strain of about 10 times its failure strain. The plasticity damage concrete feature available in ABAQUS was employed for this study.

To simulate the properties of all steel components used in the FE modelling, a multi-linear elastic-plastic curve was adapted. The values of the key parameters such as the yield strength, modulus of elasticity, ultimate strength and ultimate strain were determined and calibrated based on the laboratory material tests conducted in the experimental study (Ataei, 2015; Ataei, et al., 2016).

COMPARISON WITH EXPERIMENTAL RESULTS

Ataei et al. (2016) conducted three full-scale beam-to-column joint tests (CJ1 and CJ2 being composite; SJ3 being plain steel) designed and constructed in a cruciform arrangement to simulate the internal joint in a semi-rigid frame. All specimens consisted of a 460UB82.1 beam and a 250UC89.2 column. The reinforcement ratio in the precast concrete slab of the both composite joints was 0.9%. A total of 12 post-installed bolted shear connectors of Grade 8.8 M20 bolts (6 bolts per shear span) were used in pairs to connect the precast concrete slab to the steel beams. A 12 mm thick flush end plate and four Grade 8.8 M24 bolts were used to connect the composite beam to the steel column. Both composite joints and were designed with full shear connection. Subsequently, to investigate the influence of the partial shear connection on the behaviour of the composite joints, specimen CJ4 was designed and constructed by the authors in this study with partial shear interaction, in which a total of 8 post-installed bolted shear connectors of Grade 8.8 M16 bolts (4 bolts per shear span) were used in pairs. A 10 mm thick flush end plate was welded to the ends of the steel girders and four M24 Grade 10.9 bolts were used for connecting the steel girders to the columns. The purpose for this connection arrangement was to alter the failure mode from fracture of the bolts in the tension zone of the connection to fracture of the longitudinal reinforcement bars. Figs. 5 and 6 show the arrangement of the experimental setup and the failure mode of specimen CJ4. The moment versus rotation responses predicted by the FE models compared with the experimental results are shown in Fig. 7, and Table 1 compares the initial stiffness, rotation capacity, moment capacity and the final slip at the end of the beam obtained from both the FE modelling and the tests. Generally, good agreement between the experimental results and the FE predictions at the global level is evident.

PARAMETRIC STUDY

Shear connection ratios (SCRs) of 34%, 54%, 67%, 101%, 108%, 162%, 170% and 162% were considered to investigate their effect at the interface between the precast concrete slab and the steel beam. The ratio of the shear connection between the steel beam and precast concrete slab

was obtained by changing the number and size of shear connectors and their spacing along the composite beam length.



Fig. 5 – Experimental setup and instrumentation for CJ4



Fig. 6 – Failure mode of specimen CJ4

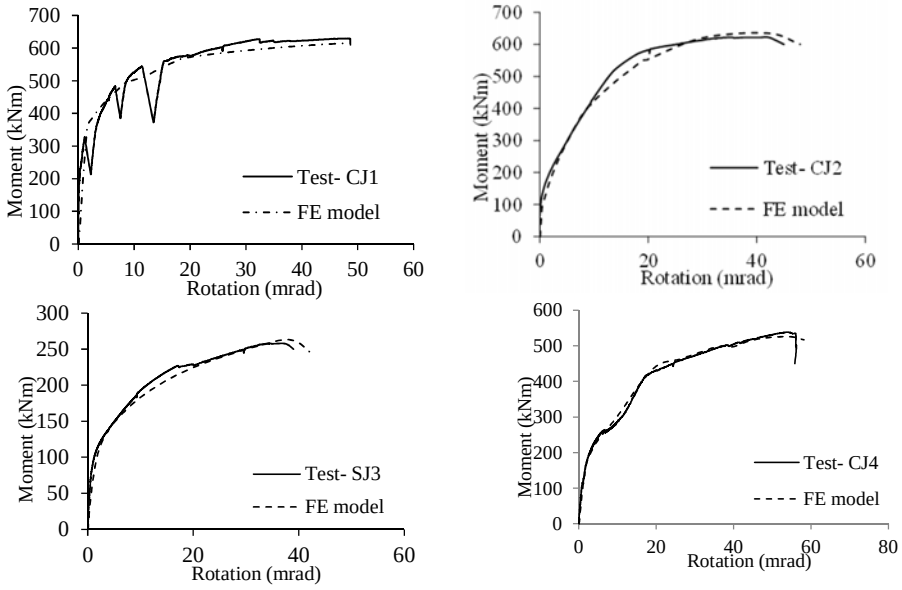


Fig. 7 – Comparison of tests and numerical model

The comparison of the moment-rotation relationships for different SCRs are shown in Table 2 and Fig. 8. As the SCR increases above a certain level (54%), the initial stiffness increases significantly, but, the increase in initial stiffness is accompanied with a significant reduction in the rotation capacity. A composite joint using a shear connection ratio of 34% shows limited ductility and strength, due to fracture of the bolted shear connector. In this case, the plastic strain may not be mobilised in the longitudinal reinforcing bars and the shear connector may fracture before the reinforcing bars yield. It can be concluded that a minimum level of shear connection ratio (about 50%) should be provided to prevent fracture of the bolted shear connectors.

Table 1 – Comparison of test results and FE predictions

Specimen	Initial stiffness (kNm/mrad)			Rotation capacity (mrad)			Moment Capacity (kNm)			Failure mode	
	Test	Model	Ratio	Test	Model	Ratio	Test	Model	Ratio	Test	Model
CJ1	135	130	0.96	44	48	1.09	630	614	0.97	BF	BF
CJ2	44	43	0.98	42	42	1.00	622	635	1.02	BF	BF
SJ3	32	30	0.94	38	40	1.05	256	259	1.01	BF	BF
CJ4	87	87	1.00	54	55	1.02	538	525	0.98	RBF	RBF
Average			0.97			1.04			1.00		
Standard deviation			0.02			0.03			0.02		

Notes: RBF= reinforcing bar fracture, BF= Bolt fracture.

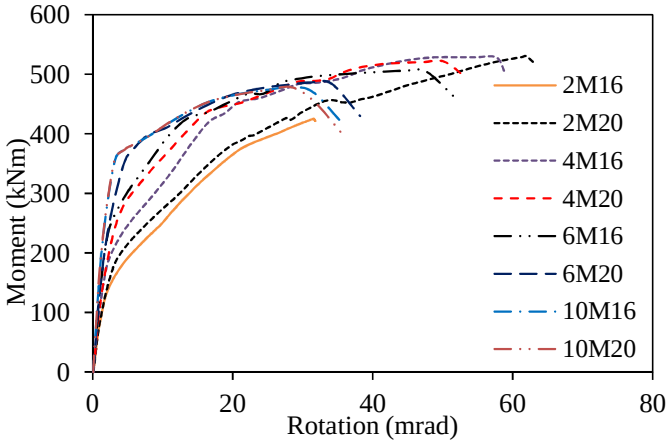


Fig. 8 – Effects of degree of shear connection on moment-rotation response

Table 2 – Effects of degree of shear connection

Model	Degree of shear connection	End slip	Initial stiffness	Rotation cap.	Moment Cap.	Failure mode
		mm	kNm/mrad	mrad	kN.m	
2M16	34	13.0	46	31	422	BSCF
2M20	54	11.7	52	62	530	RBF
4M16	67	6.5	73	57	529	RBF
6M16	101	4.0	85	45	506	RBF
4M20	108	5.3	70	50	521	RBF
6M20	162	1.4	88	31	486	RBF
10M16	170	0.5	111	28	479	RBF
10M20	270	0.5	114	28	479	RBF

Notes: RBF= reinforcing bar fracture, BSCF= Bolted shear connector fracture.

Further parametric studies were conducted on the effects of shear connector spacing, slab reinforcement ratio, bolt sizes, end plate thickness and grade, column steel grade, beam steel

grade, concrete slab thickness and column flange thickness and the results are presented in Tables 3 to 11 respectively.

Table 3 – Effect of shear connector spacing

Model	Degree of shear connection	Longitudinal spacing (mm)	End slip	Initial stiffness	Rotation cap.	Moment cap.	Failure mode
			mm	kNm/mrad	mrad	kN.m	
6M16	101	550	4.0	85	45	506	RBF
4M20	108	1100	5.3	70	50	521	RBF
10M16	170	275	0.5	111	28	479	RBF
6M20	162	550	1.4	88	31	486	RBF

Table 4 – Effect of slab reinforcement ratio

Model	Rein. Ratio %	End slip mm	Initial stiffness kN.m/mrad	Rotation cap. mrad	Moment Cap. kN.m	Failure mode
RR0.36	0.36	1.4	62	31	340	RBF
RR0.43	0.43	3.2	69	35	377	RBF
RR0.51	0.51	4.5	70	39	416	RBF
RR0.60	0.60	5.4	72	42	456	RBF
RR0.70	0.70	6.5	73	57	529	RBF
RR0.80	0.80	8.0	73	58	589	RBF
RR0.91	0.91	9.0	74	60	602	RBF
RR1.03	1.03	13.0	75	38	573	BSCF
RR1.16	1.16	13.0	75	32	548	BSCF
RR1.29	1.29	13.0	75	32	548	BSCF
RR1.43	1.43	13.0	76	32	548	BSCF

Table 5 – Effects of bolt size

Model	t_{ep}/d_b	End slip	Initial stiffness	Rotation capacity	Moment Capacity	Failure mode
		mm	kNm/mrad	mrad	kNm	
12 mm bolt	0.83	6.4	58	22	345	BF
14 mm bolt	0.71	7.0	65	27	404	BF
16 mm bolt	0.63	7.0	65	38	436	BF
18 mm bolt	0.56	7.0	66	43	465	BF
20 mm bolt	0.50	7.0	68	44	492	BF
22 mm bolt	0.45	6.5	73	51	520	RBF
24 mm bolt	0.42	6.5	73	57	529	RBF
26 mm bolt	0.38	6.0	74	56	548	RBF
28 mm bolt	0.36	6.0	82	58	556	RBF
30 mm bolt	0.33	6.0	97	56	562	RBF

Notes: RBF = reinforcing bar fracture, BF = Hollo-bolt fracture.

Table 6 – Effect of end plate size

Model	t_p/d_b	End slip	Initial stiffness	Rotation cap.	Moment Cap.	Failure mode
		mm	kNm/mrad	mrad	kNm	
6mm end plate	0.25	6.5	27	49	480	FEPF
8mm end plate	0.33	6.5	56	49	507	RBF
10mm end plate	0.42	6.5	73	57	529	RBF
12mm end plate	0.50	5.0	93	55	544	RBF
14mm end plate	0.58	4.5	112	53	568	BF
16mm end plate	0.67	4.5	128	55	596	BF
18mm end plate	0.75	4.5	146	54	620	BF
20mm end plate	0.83	4.5	158	51	642	BF
22mm end plate	0.92	4.5	170	48	658	BF
26mm end plate	1.10	4.5	185	38	665	BF
30mm end plate	1.25	4.5	196	36	665	BF

Table 7 – Effect of steel grade of end plate

Model	f_y	End slip	Initial stiffness	Rotation cap.	Moment Cap.	Failure mode
		mm	kN.m/mrad	mrad	kN.m	
S235	235	7.0	65	62	489	RBF
S345	345	6.5	73	58	529	RBF
S460	460	6.5	73	57	548	RBF
S550	550	6.5	73	56	565	RBF
S690	690	6.0	73	55	580	RBF
S800	800	5.5	73	54	588	RBF
S960	960	5.5	73	53	599	RBF

Table 8 – Effect of steel grade of column

Model	f_y	End slip	Initial stiffness	Rotation cap.	Moment Cap.	Failure mode
		mm	kNm/mrad	mrad	kNm	
S235	235	7.0	73	60	519	RBF
S345	345	6.5	73	57	529	RBF
S460	460	6.0	73	57	545	RBF
S550	550	6.0	73	57	546	RBF
S690	690	6.0	73	57	545	RBF
S800	800	6.0	73	57	547	RBF
S960	960	6.0	73	57	549	RBF

Table 9 – Effect of steel grade of beam

Model	f_y	End slip	Initial stiffness	Rotation cap.	Moment Cap.	Failure mode
		mm	kN.m/mrad	mrad	kN.m	
S235	235	7.0	73	55	490	RBF
S345	345	6.5	73	57	529	RBF
S460	460	6.0	73	59	546	RBF
S550	550	6.0	73	59	548	RBF
S690	690	6.0	73	59	549	RBF
S800	800	6.0	73	59	550	RBF
S960	960	6.0	73	59	550	RBF

Table 10 – Effect of slab thickness

Model	End slip	Initial stiffness	Rotation cap.	Moment Cap.	Failure mode
	mm	kNm/mrad	mrad	kNm	
80 mm Slab	11.0	53	63	526	RBF
120 mm Slab	6.5	73	57	529	RBF
160 mm Slab	5.7	85	55	559	RBF
200 mm Slab	5.6	97	52	577	RBF
240 mm Slab	5.4	121	49	598	RBF
280 mm Slab	5.0	142	46	616	RBF
320 mm Slab	5.0	167	44	635	RBF

Table 11 – Effect of column flange thickness

Model	t_{fc}	End slip	Initial stiffness	Rotation cap.	Moment Cap.	Failure mode
		mm	kNm/mrad	mrad	kNm	
10 mm flange	10	7.0	36	62	500	RBF
14 mm flange	14	6.5	53	60	527	RBF
18 mm flange	18	6.5	73	57	529	RBF
22 mm flange	22	6.0	77	57	546	RBF
26 mm flange	26	6.0	83	57	546	RBF
30 mm flange	30	6.0	86	57	546	RBF

DESIGN MODEL

A design model was proposed by Ahmad and Nethercot (1997) for determining the initial stiffness of a composite joint, which for a stiffened column web reduces to

$$S_j = \frac{h_{bsc}h_{rb}\left(\frac{1}{k_b}\right) + h_b^2\left(\frac{1}{k_{rb}} + \frac{1}{k_{bsc}}\right)}{\left(\frac{1}{k_{rb}} + \frac{1}{k_{bsc}}\right)\left(\frac{1}{k_b}\right)}, \quad (1)$$

where k_b = stiffness of top row of bolts, k_{rb} = stiffness of reinforcing bars, k_{bsc} = stiffness of shear connectors, with other parameters being defined in Fig. 9. The parametric study was used to evaluate this design model, with 53 analyses producing an average ratio of Eq. (1) to the FE results of 0.93 and a standard deviation of 0.38.

Anderson and Najafi (1994) proposed an expression for the moment capacity of a joint as

$$M_j = F_{rb}(h_{rb} - 0.5t_{fb}) + F_b(h_b - 0.5t_{fb}), \quad (2)$$

if $F_{rb} + F_b \leq F_{fb}$, and from

$$M_j = F_{rb}(h_{rb} - 0.5t_{fb}) + F_b(h_b - 0.5t_{fb}) - (F_{rb} + F_b - F_{fb})(0.5y_c + 0.5t_{fb}) \quad (3)$$

if $F_{rb} + F_b > F_{fb}$, in which the dimensions and actions are shown in Fig. 9. In addition, $y_c = (F_{rb} + F_b - F_{fb})/(t_{fb}f_{yb})$ denotes the depth of the web in compression. The parametric study was again used to evaluate the predictions of this design mode, with 53 analyses producing an average ratio of the model to FE results of 1.00 and a standard deviation of 0.13.

CONCLUSIONS

A 3-D FE model was developed using ABAQUS to simulate the structural performance of beam-to-column composite joints with deconstructable PFGBSCs and precast concrete slabs. The FE models were verified against experimental data reported elsewhere. In addition, a full-scale laboratory test specimen having deconstructable flush end plate composite semi-rigid joint and precast concrete slab was tested to investigate the influence of the partial shear connection on the behaviour of the composite joints. The FE results were also compared with the test results obtained from this test. An extensive parametric study was then conducted using the validated FE modelling. Finally, some existing prediction and design models were extended to predict the fundamental parameters for a composite joint with PFGBSCs and a precast concrete slab including the initial rotational stiffness, rotation capacity and the moment capacity. The FE modelling was shown by comparison with test results to be accurate. A parametric appraisal of design models for the initial

stiffness and moment capacity of two design procedures was carried out using the FE model, and these were shown to be relatively accurate for the deconstructable joints proposed.

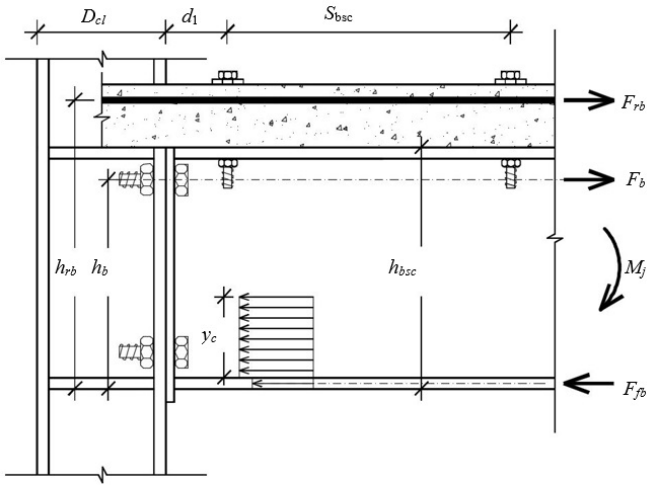


Fig. 9 – Actions and dimensions for design model

REFERENCES

Anderson, D., & Najafi, A. A. (1994). Performance of composite connections: major axis end plate joints. ***Journal of Constructional Steel Research 31***:31–57.

Ataei, A. (2016). A low-carbon deconstructable steel-concrete composite framed system with recyclable beam and slab components. PhD Thesis. School of Civil and Environmental Engineering, The University of New South Wales, Sydney, Australia.

Ataei, A., Bradford, M. A., & Liu, X. (2016). Experimental study of flush end plate beam-to-column composite joints with precast slabs and deconstructable bolted shear connectors. ***Structures 7***, 43-58.

Carreira, D. J., & Chu, K. H. (1985). Stress-strain relationship for plain concrete in compression. ***ACI Structural Journal 82***, 797-804.

Kwon, G., Engelhardt, M. D., & Klinger, R. E. (2012). Parametric studies and preliminary design recommendations on the use of postinstalled shear connectors for strengthening noncomposite steel bridges. ***Journal of Bridge Engineering, ASCE 17***(2), 310-317.

Lee, S. S. M., & Bradford, M. A. (2013). Sustainable composite beam behaviour with deconstructable bolted shear connectors. Composite Construction VII, Palm Cove, Queensland, Australia.

Liu, X., Bradford, M. A., & Lee, M. S. S. (2014). Behavior of high-strength friction-grip bolted shear connectors in sustainable composite beams. ***Journal of Structural Engineering, ASCE***. http://dx.doi.org/10.1061/(ASCE)ST.1943-541X.0001090.

Liu, X., Bradford, M. A., Chen, Q.J., & Ban, H. (2016). Finite element modelling of steel–concrete composite beams with high- strength friction-grip bolt shear connectors. ***Finite Elements in Analysis and Design108***, 54-65.

THE INFLUENCE OF A COMPOSITE SLAB ON THE SEISMIC BEHAVIOR OF MOMENT RESISTING FRAMES

Roberto Tartaglia[1],
University of Naples 'Federico II'
Department of Structures for Engineering and Architecture
Naples, Italy
roberto.tartaglia@unina.it

Mario D'Aniello[2],
University of Naples 'Federico II'
Department of Structures for Engineering and Architecture
Naples, Italy
mdaniel@unina.it

Gian Andrea Rassati[3],
University of Cincinnati
Department of Civil and Architectural Engineering and Construction Management
Cincinnati OH, United States
gian.rassati@uc.edu

James Swanson[4],
University of Cincinnati
Department of Civil and Architectural Engineering and Construction Management
Cincinnati OH, United States
james.swanson@uc.edu

ABSTRACT

Moment resisting frames (MRFs) are widely used for steel structures in seismic areas. However, MRFs are characterized by large lateral deformability that can impair the structural performance. In the case of all steel MRFs, the influence of composite slabs is generally disregarded when structural analyses are carried out at the design stage. However, it can be convenient to take into account their stiffening effect on the steel beams of the MRFs, even though the beam-to-column assemblies are designed with disconnected slabs. Therefore, in this paper the influence of composite slabs on the seismic response of MRFs has been investigated by means non-linear analyses.

Keywords: Moment resisting frame, composite, finite element analysis, beam-to-column joints, extended end-plate connection.

INTRODUCTION

Moment resisting frames (MRFs) are largely used for steel multi-story low and medium rise buildings in seismic areas. However, this structural system can be characterized by large lateral deformability, thus being highly sensitive to second-order P-Delta effects. When the slab is disconnected from the joint zone, MRFs are designed and calculated as all-steel, namely disregarding the stiffening role of the composite slab, which can be beneficial to reduce the lateral deformability. In addition, even in the case of dual systems where lateral forces are shared between a moment frame and a braced frame, the presence of the slab can have a beneficial effect on the global structural behavior. Finally, the presence of the composite slab can positively influence the joint behavior (Aribert 2006, Leon 1998 and Thermou 2004).

Moreover, a recent numerical study (Tartaglia et al. 2018a) on composite joints demonstrates that even though a protected zone around the column is maintained, there is a beneficial influence of the slab to the joint behavior.

The main object of this work is investigating by means of finite element analysis the influence and the advantages coming from considering the presence of the concrete slab in the MRF structural behavior even if there is no direct connection with the steel joints. To this end, in the FE model, developed in Seismostruct (SeismoStruct 2016), the real beam to column joint behavior was introduced by properly calibrated nonlinear links. The link behavior was calibrated on the experimental tests for the all steel joint (AS) while the calibration of the composite joint was done with respect to previous Abaqus (Dassault 2014) simulation results (Tartaglia et al. 2018a).

The paper is organized into three main parts: the definition of the designed structures and their geometrical characteristics, the introduction and the calibration of the nonlinear link in the Seismostruct model and the presentation of both the results of the static and the dynamic nonlinear analysis.

DESIGNED STRUCTURES

Eight MRFs were designed according to both EN1993-1-1 and EN1998-1-1 to investigate the influence of the concrete slab on the structural response. All structures have six floors with a story height of 3.5m, with the exception of the first floor, which is 4.5m. The same square plan with three bays for both directions and with two MRF systems along the X and four concentrically braced systems in the Y direction were considered (see Fig. 1).

The structures were alternatively designed considering two beam span lengths (6 and 8 meters) and two peak ground accelerations (0.35g and 0.45g). Furthermore, two structural typologies were investigated: an all steel solution (AS) and a partially composite solution (CS). In the former case (AS), the presence of the slab was completely neglected at design stage and only the steel structure was considered in the calculation and verification of the frames. In the second case (CS), the presence of the collaborating slab was accounted for even if the joints were still considered as all-steel, namely the hierarchy between the beam and the column was evaluated neglecting the contribution of the slab. To be consistent with this assumption, the portion of the ends of the beam at a distance equal to $2b_{eff}$ (effective length as defined in EN1994-1-1) from the column face was considered without shear stud. Therefore, the stiffening effect of the slab was accounted for only in the inner segments of beams were fully composite action was guaranteed by the presence of shear studs (see Fig. 2).

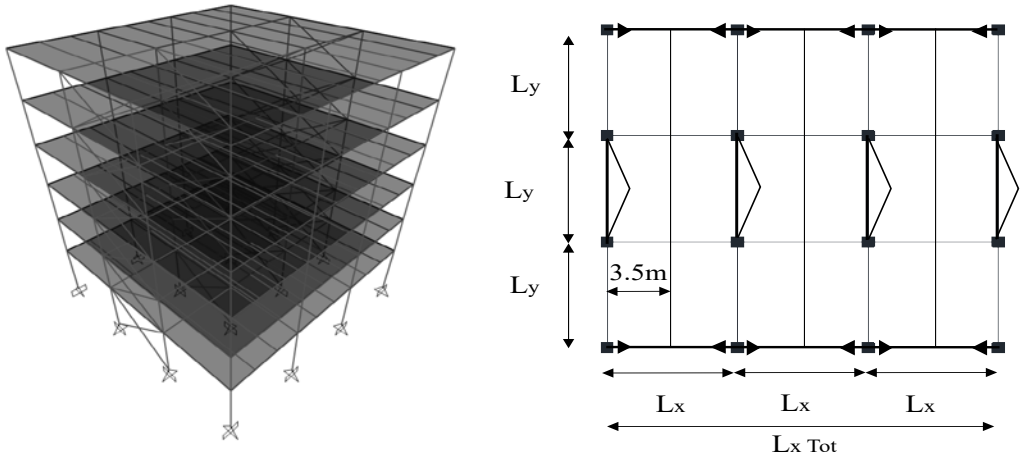


Fig. 1: The reference structure and the joint components descriptions.

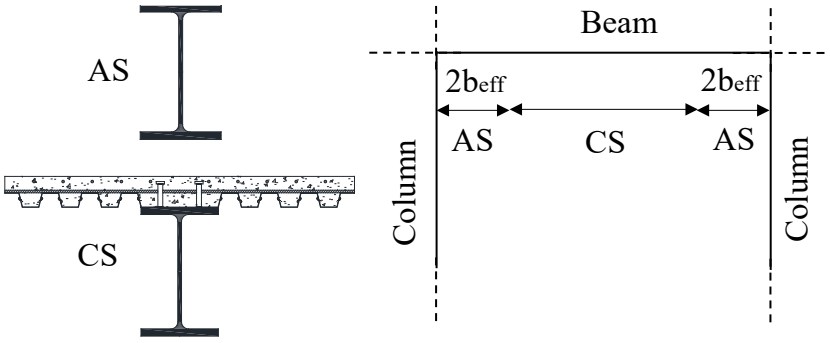


Figure 2: Cross sections considered in the design phase.

The cross sections of the designed frames are summarized in Table 1, where only the profiles of the first two bays are reported due to the structural symmetry.

For all the investigated cases, the most restrictive limitation was the deformability at the serviceability limit state. Indeed, the maximum interstorey drift ratio permitted by EN1998-1-1 is equal to 1% for buildings having nonstructural fixed elements or that cannot interfere with the structural deformation. This limitation significantly influenced the response of the frames designed, as also shown in Tartaglia et al. (2018b).

The presence of the slab, even if it is not collaborating with the steel elements in the protected zone (EN1994-1-1), increases the structure's lateral stiffness. Indeed, as shown in Table 1, accounting for the contribution of the slab allows the designers reducing the size of steel profiles. For instance, 6-5-8-0.45 structures (the buildings with 8m of span and designed for 0.45g) show a great reduction of the dimensions of the columns along the entire height of the structure with the only exception of the external column (first bay) at fifth and sixth storey.

Table 1: Structural elements cross section

Storey	First bay				Second bay			
	6-5-6-0.35							
	Column		Beam		Column		Beam	
	All Steel	Composite	All Steel	Composite	All Steel	Composite	All Steel	Composite
I	***HE500M***	***HE400M***	IPE550	IPE550	HE550M	HE450M	IPE550	IPE550
II	***HE500M***	***HE400M***	IPE550	IPE550	HE550M	HE450M	IPE550	IPE550
III	***HE450B***	***HE360B***	IPE500	IPE500	HE500M	HE400M	IPE500	IPE500
IV	***HE450B***	***HE360B***	IPE500	IPE500	HE500M	HE400M	IPE500	IPE500
V	***HE360B***	***HE340B***	IPE400	IPE400	HE450B	HE360B	IPE400	IPE400
VI	***HE360B***	***HE340B***	IPE400	IPE400	HE450B	HE360B	IPE400	IPE400
	6-5-6-0.45							
	Column		Beam		Column		Beam	
	All Steel	Composite	All Steel	Composite	All Steel	Composite	All Steel	Composite
I	HE500M	HE500M	IPE600	IPE600	HE600M	HE600M	IPE600	IPE600
II	HE500M	HE500M	IPE600	IPE600	HE600M	HE600M	IPE600	IPE600
III	HE500B	HE500B	IPE550	IPE550	HE500M	HE500M	IPE550	IPE550
IV	HE500B	HE500B	IPE550	IPE550	HE500M	HE500M	IPE550	IPE550
V	HE450B	HE450B	IPE400	IPE400	HE500B	HE500B	IPE400	IPE400
VI	HE450B	HE450B	IPE400	IPE400	HE500B	HE500B	IPE400	IPE400
	6-5-8-0.35							
	Column		Beam		Column		Beam	
	All Steel	Composite	All Steel	Composite	All Steel	Composite	All Steel	Composite
I	***HD400X393***	***HE550M***	IPE750x173	IPE750x173	***HD400X422***	***HD400X393***	IPE750x137	IPE750x137
II	***HD400X393***	***HE550M***	IPE750x173	IPE750x173	***HD400X422***	***HD400X393***	IPE750x173	IPE750x173
III	HE550B	HE550B	IPE600	IPE600	***HD400X393***	***HE550M***	IPE600	IPE600
IV	HE550B	HE550B	IPE600	IPE600	***HD400X393***	***HE550M***	IPE600	IPE600
V	HE400B	HE400B	IPE500	IPE500	HE550B	HE550B	IPE500	IPE500
VI	HE400B	HE400B	IPE500	IPE500	HE550B	HE550B	IPE500	IPE500
	6-5-8-0.45							
	Column		Beam		Column		Beam	
	All Steel	Composite	All Steel	Composite	All Steel	Composite	All Steel	Composite
I	***HD400X744***	***HD400X678***	IPE750x173	IPE750x173	***HD400x818***	***HD400x744***	IPE750x173	IPE750x173
II	***HD400X744***	***HD400X678***	IPE750x173	IPE750x173	***HD400x818***	***HD400x744***	IPE750x173	IPE750x173
III	***HD400x551***	***HD400x467***	IPE750x147	IPE750x147	***HD400X744***	***HD400X678***	IPE750x147	IPE750x147
IV	***HD400x551***	***HD400x467***	IPE750x147	IPE750x147	***HD400X744***	***HD400X678***	IPE750x147	IPE750x147
V	HE450M	HE450M	IPE600	IPE600	***HD400x551***	***HD400x467***	IPE600	IPE600
VI	HE450M	HE450M	IPE600	IPE600	***HD400x551***	***HD400x467***	IPE600	IPE600

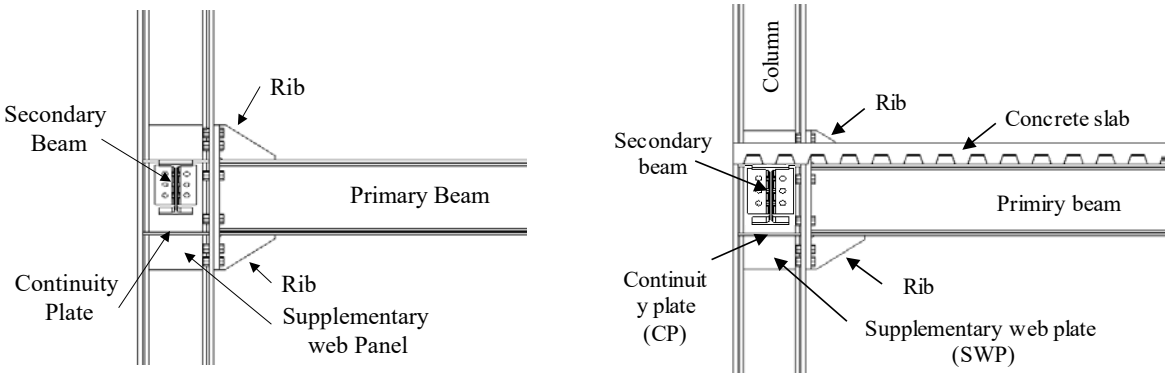
Table 2: Interstorey drift displacement

Storey	6-5-6-0.35		6-5-6-0.45		6-5-8-0.35		6-5-8-0.45	
	AS	CS	AS	CS	AS	CS	AS	CS
I	0.62%	0.68%	0.64%	0.69%	0.82%	0.82%	0.69%	0.72%
II	0.85%	0.85%	0.88%	0.90%	0.96%	0.96%	0.95%	0.95%
III	0.91%	0.92%	0.97%	0.95%	1.00%	0.95%	0.95%	0.97%
IV	0.86%	0.86%	0.93%	0.90%	0.99%	0.94%	0.84%	0.88%
V	0.89%	0.96%	1.00%	0.97%	0.96%	0.94%	0.82%	0.85%
VI	0.71%	0.72%	0.88%	0.84%	0.75%	0.73%	0.62%	0.61%

JOINT PERFORMANCE

Extended stiffened beam-to-column joints were adopted in all the designed structures (see Fig. 3a). Indeed, this type of joints can guarantee an adequate resistance and ductility in seismic areas allowing the formation of plastic hinges at the beam extremities, while remaining in the elastic range, even though the beam plastic hinges may experience large overstrength, as shown by Tartaglia et al. 2018c. All joints were designed according to the recent procedure developed within the EQUALJOINTS research project.

Two types of joints were considered in the modelling phase: an all steel solution (modelling only the steel joint) and a composite solution (modelling both the steel joint and the concrete slab (see Fig. 3 a and b respectively)).

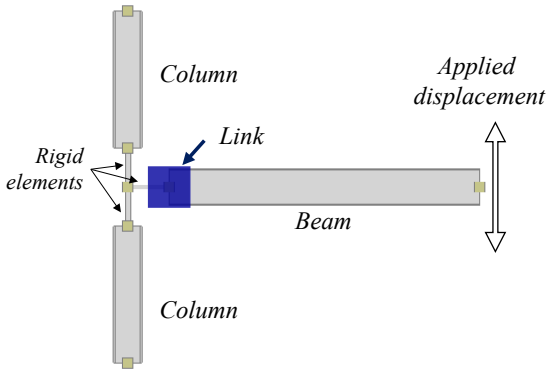


a) b)

Figure 3: Introduced joint typologies and geometry.

Therefore, in order to simulate the realistic behavior of the beam-to-column joint, a nonlinear link was introduced in the structural model. In the case of all steel solution the link behavior was calibrated on the results obtained within the EQUALJOINTs research project. In particular, as show, in Fig 4 a and b, the experimental test on a full strength joint was calibrated using the Seismostruct software modelling the real joint dimension by rigid elements and concentrating all the joint nonlinearity in a link. A smooth nonlinear spring element was used to simulate the joint response. As it can be noted this model can satisfactorily overlap the experimental test result.

In the composite structure, the composite slab gives an appreciable contribution to the joint behavior. Indeed, as reported by Tartaglia et al. (2018a) the slab influences both the elastic stiffness and the ultimate joint capacity (by 15% and 20% respectively).



a)

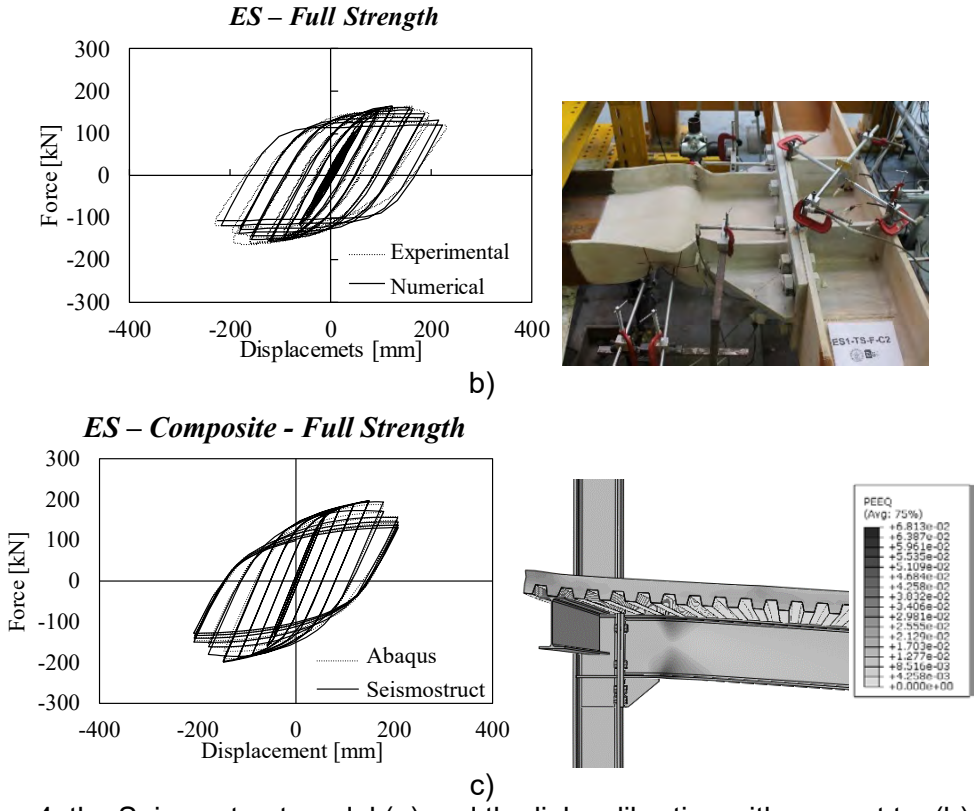


Figure 4: the Seismostruct model (a) and the link calibration with respect to: (b) the experimental test, for the all steel joint and (c) the Abaqus prediction, for the composite solution

RESULTS

Nonlinear static analysis

Nonlinear static analyses were performed considering two force distributions: proportional to the first vibration mode (FM) and uniform (U). Figure 5 shows for all the investigated structures the pushover curves in terms of base shear versus top displacement. As it can be observed, despite the structures were designed to have a comparable lateral stiffness (see Table 2), the presence of the composite slab increases the elastic stiffness. On the other hand, some differences can be noted in terms of maximum capacity. Indeed, the maximum structural capacity depends not only on the link resistance, but also on the distribution of the plastic hinges.

For instance, CS-6-5-6-0.35 (a structure with the composite slab) shows a lower capacity with respect to AS-6-5-6-0.35 (the corresponding all steel structure) (see Fig. 5a). In both structures, the first plastic hinges appear at the base of the columns at the first floor. It is worth noting that the EN1998-1 design procedure, with the stringent drift limitation imposed often results in structures forming plastic hinges at the base, although the strong-column weak-beam principle is respected. In this case, the AS structure has a larger column with a corresponding larger resistance. A similar behavior can be observed in Fig. 5b, indeed in this case both the AS and CS structures have the same steel profile; therefore, no appreciable differences can be pointed out in terms of ultimate capacity. Differently from these cases, the CS-6-5-8-0.35 structure shows an increase not only in terms of lateral stiffness, but also from the capacity point of view (see Fig.5c).

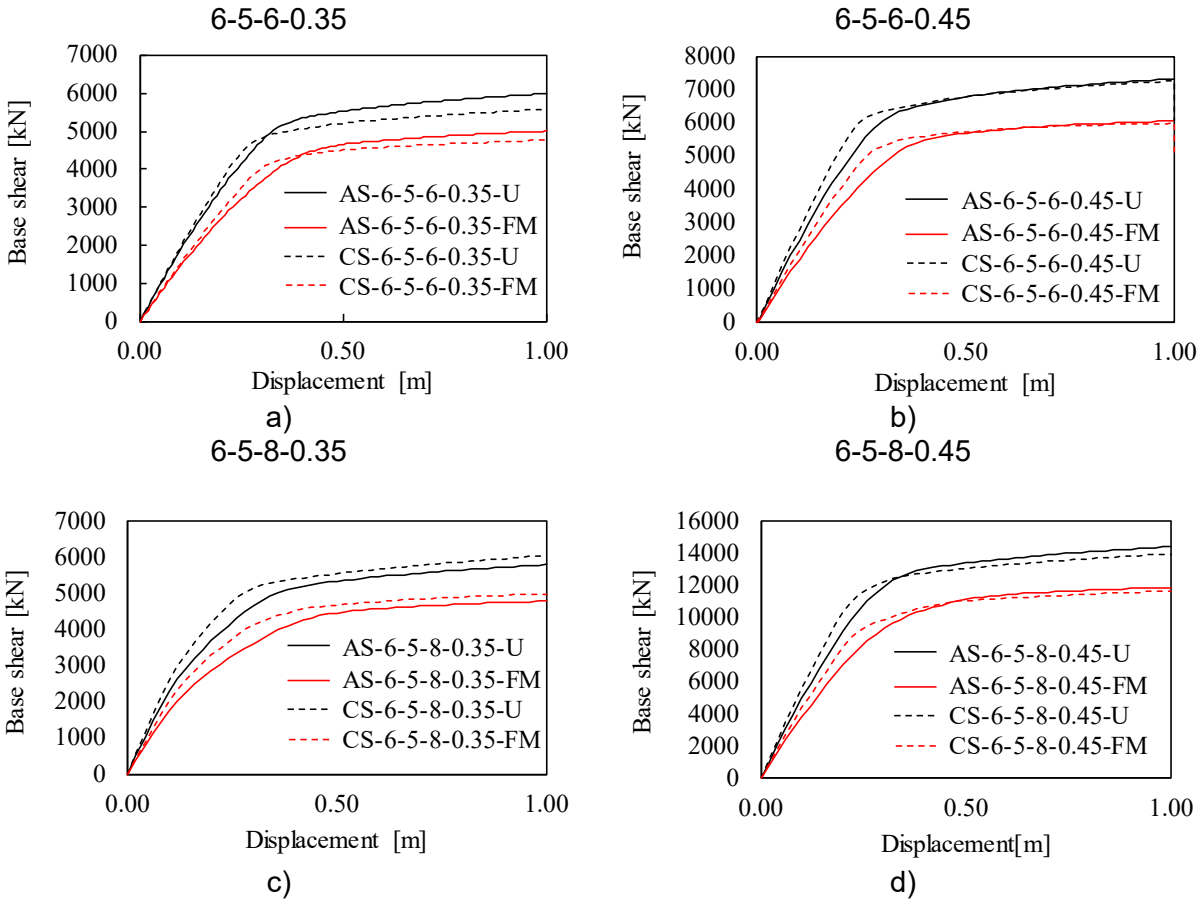


Figure 5: Pushovers results in terms of base shear top displacement.

Nonlinear dynamic analysis

The structural seismic performances were also evaluated by means of nonlinear dynamic analyses considering three limit states according to EN1998-1 : damage limitation (DL), significant damage (SD) and near collapse (NC). A set of 14 natural earthquake acceleration records were considered (see Table 3 and Fig. 6) to perform the dynamic time history analyses on the examined cases. The records were obtained from the RESORCE ground motion database (Akkar et al., 2014); all the spectra were scaled to match the elastic acceleration spectrum provided by EN 1998-1 (see Fig. 6). Moreover, since all the structures were analyzed in plane, the acceleration scaling factor was increased by a factor equal to 1.3 in order to take into account possible torsional effects. Furthermore, to evaluate the residual deformations, all records were fictitiously extended by 10 seconds with zero acceleration.

The transient interstorey drift ratios along the frame height presented in Fig. 7 reveal that for all three EC8 limit states the requirements of EC8 are fully satisfied with an overall response mostly in the elastic range for each limit state. Indeed, for all design methodologies, at the DL limit state, the structures remain elastic, as expected. Considering that, for SD and NC limit states, transient interstorey drift limits are 2.5% and 5% respectively, results show significantly lower values, within ranges between 0.35% and 0.43% for SD, and 0.48% and 0.57% for the NC limit state. This might be due to the highly restrictive design controlled by drift limits and stability criteria for all the cases.

Table 3: Basic data of the selected ground motions

Earthquake name	Date	Station Name	Station Country	Magnitude Mw	Fault mechanism
Alkion	24.02.1981	Xylokastro-O.T.E.	Greece	6.6	Normal
Montenegro	24.05.1979	Bar-Skupstina Opstine	Montenegro	6.2	Reverse
Izmit	13.09.1999	Yarimca (Eri)	Turkey	5.8	Strike-Slip
Izmit	13.09.1999	Usgs Golden Station Kor	Turkey	5.8	Strike-Slip
Faial	09.07.1998	Horta	Portugal	6.1	Strike-Slip
L'Aquila	06.04.2009	L'Aquila - V. Aterno - Aquila Park In	Italy	6.3	Normal
Aigion	15.06.1995	Aigio-OTE	Greece	6.5	Normal
Alkion	24.02.1981	Korinthos-OTE Building	Greece	6.6	Normal
Umbria-Marche	26.09.1997	Castelnuovo-Assisi	Italy	6.0	Normal
Izmit	17.08.1999	Heybeliada-Senatoryum	Turkey	7.4	Strike-Slip
Izmit	17.08.1999	Istanbul-Zeytinburnu	Turkey	7.4	Strike-Slip
Ishakli	03.02.2002	Afyon-Bayindirlik ve Iskan	Turkey	5.8	Normal
Olfus	29.05.2008	Ljosafoss-Hydroelectric Power	Iceland	6.3	Strike-Slip
Olfus	29.05.2008	Selfoss-City Hall	Iceland	6.3	Strike-Slip

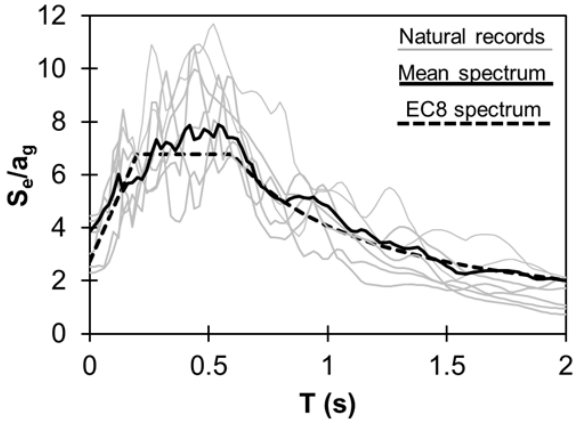
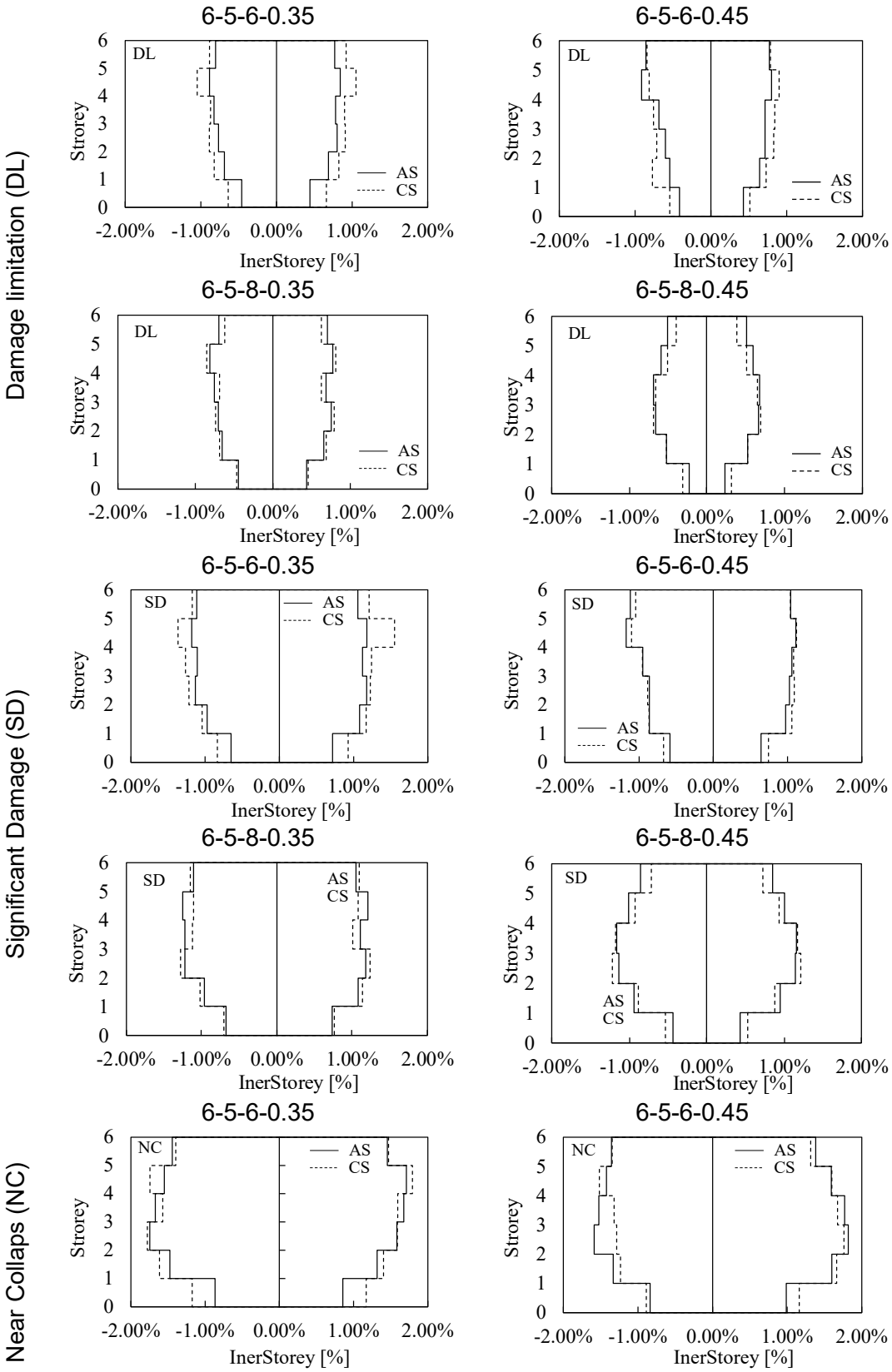


Figure 6: Comparison between natural records and EC8 design spectrum


Damage limitation (DL)
Significant Damage (SD)
Near Collaps (NC)
6-5-6-0.35
6-5-6-0.45
6-5-8-0.35
6-5-8-0.45
DL
SD
NC
AS
CS
Strorey
InerStorey [%]
-2.00%
-1.00%
0.00%
1.00%
2.00%

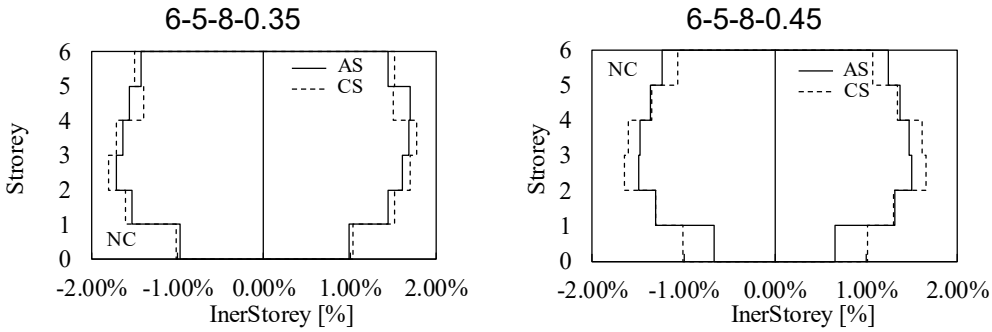


Figure 7: Interstorey drift at DL, SD and NC for all the investigated structures

The composite structures showed a more rigid global behavior than the all-steel cases (see Fig 5). However, no appreciable differences can be noted either in terms of displacement distribution along the height or in terms of values, with respect to the all steel solution. Indeed, observing the results reported in Fig. 7, it is not possible to recognize an overall difference between the responses of the AS and CS structures.

Comparing the pushover analyses with the IDA curves obtained considering the maximum drift in correspondence of the maximum base shear, it can be observed that the structures, for most of the fourteen ground motions, remain elastic (see Fig.8). In all the investigated cases, the stiffness results of IDAs are bounded within the two pushover curves (considering the two force distributions previously introduced) and show an elastic behavior of the structures even for the larger scaling factor (1.73).

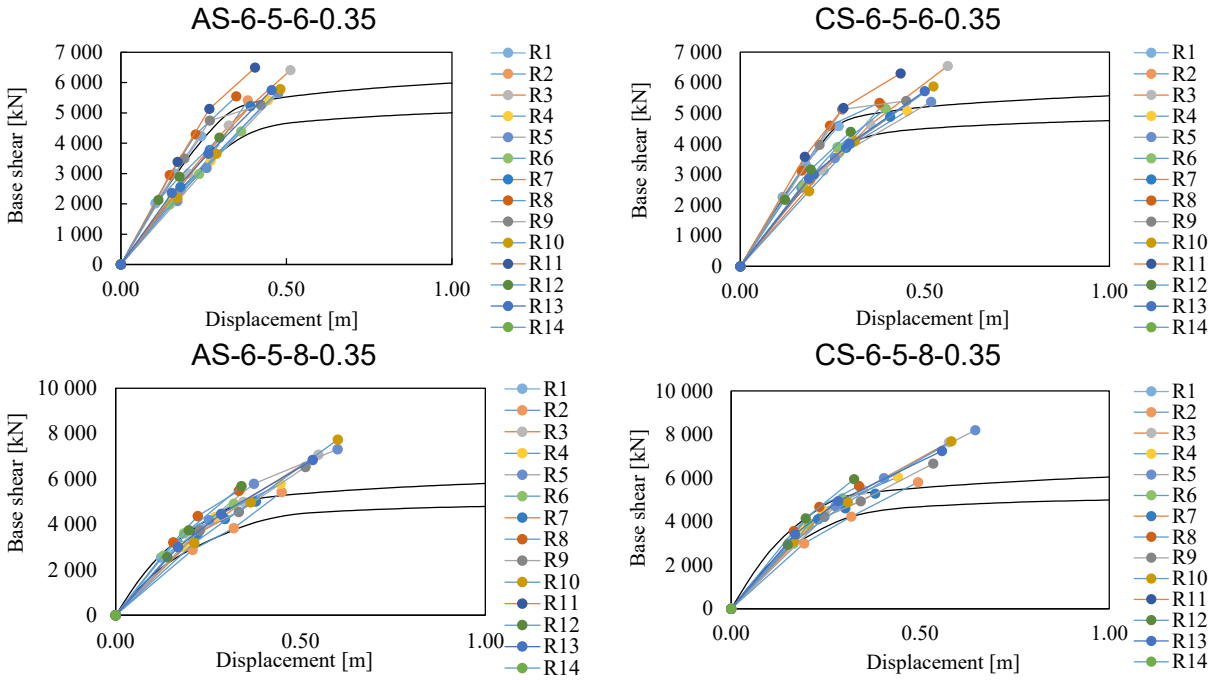


Figure 8: Comparison between pushover and IDAs curves for both the AS-6-5-6-0.35 and CS-6-5-6-0.35 structures.

CONCLUSIONS

In light of the results presented and discussed in the previous paragraphs, the following conclusions are drawn:

- A refined structural model considering also the presence of the concrete slab in the middle part of the beam allows properly accounting for the lateral stiffness of the structure. Indeed, if the presence of the slab is accounted for in the design phase, the size of the element cross section can be reduced as well as the costs.
- The non-linear link element defined in Seismostruct can adequately calibrate the real joint behavior. Indeed, by the introduction of a zero-length link between the joint and the beam it is possible to replicate the results of experimental tests and the ones coming from more sophisticated models.
- The concrete slab has an important role in the definition of the local beam-to-column joint behavior, even if all the EC1994-1-1 prescriptions for decoupling the steel joint from the slab are respected.
- All investigated composite structures show a larger lateral stiffness with respect to the all steel solution; however, from the resistance point of view, only when the plastic hinges are active at the beam end, a consistent increment of capacity can be observed.
- The highly restrictive limitation lead to a design controlled by drift limits, indeed, all the investigated structures show, for all the three limit states required by the EC1998-1-1, an elastic behavior, also for a scaling factor equal to 1.73.

REFERENCES:

Akkar S., Sandıkkaya M.A., Şenyurt M., Azari Sisi A., Ay B.Ö., Traversa P., Douglas J., Cotton F., Luzi L., Hernandez B., Godey S. (2014). Reference database for seismic ground-motion in Europe (RESORCE). *Bulletin of Earthquake Engineering*. 12(1):311-339.

Aribert J, Ciutina A, Dubina D. (2006). Seismic response of composite structures including actual behaviour of beam-to-column joints. *Composite Construction Steel Concrete*. V:708–17.

Dassault (2014), Abaqus 6.14 - Abaqus Analysis User's Manual, Dassault Systèmes Simulia Corp.

EQUALJOINTS – European pre-QUALified steel JOINTS: RFSR-CT-2013-00021. Research Fund for Coal and Steel (RFCS) research programme.

EN 1993:1–1, (2005) Design of Steel Structures - Part 1–1: General rules and rules for buildings. CEN.

EN 1998-1, (2005) Design of Structures for Earthquake Resistance - Part 1: General Rules, Seismic Actions and Rules for Buildings. CEN.

EN 1994:1–1, (2005) Design of composite steel and concrete structures - Part 1–1: General rules and rules for buildings. CEN.

EN 1993:1–8, (2005) Design of Steel Structures - Part 1–8: Design of Joints. CEN.

Leon RT., (1998). Analysis and design problems for PR composite frames subjected to seismic loads. *Engineering and structures* 20(4-6):364-71.

“SeismoStruct (2016) – A computer program for static and dynamic nonlinear analysis of framed structures,” available from http://www.seismosoft.com.

Tartaglia R., D'Aniello M., Rassati G.A., Swanson J., Landolfo R. (2018a). Influence of composite slab on the nonlinear response of extended end-plate beam-to-column joints. *Key Engineering Materials* 763:818-825.

Tartaglia R, D'Aniello M., Di Lorenzo G., De Martino A., (2018b). Influence of EC8 rules on p-delta effects on the design and response of steel MRF. *Ingegneria sismica* 35(3):104-120.

Tartaglia R., D'Aniello M., Zimbru M., Landolfo R., (2018c). Finite element simulations on the ultimate response of extended stiffened end-plate joints. *Steel and Composite Structures*,27(6):727-745.

Thermou GE, Elnashai AS, Plumier A, Doneux C., (2004). Seismic design and performance of composite frames. *Journal of Constructional of Steel Research*. 60:31–57.

CONCRETE-FILLED STEEL TUBE DUAL LATERAL-FORCE RESISTING SYSTEM

Johnn P. Judd, Ph.D., S.E.
Assistant Professor, Department of Civil and Architectural Engineering
University of Wyoming
Laramie, Wyoming
jjudd5@uwyo.edu

Nipun Pakwan
Graduate Research Assistant, Department of Civil and Architectural Engineering
University of Wyoming
Laramie, Wyoming
npakwan@uwyo.edu

ABSTRACT

A dual lateral-force resisting system consisting of a primary lateral-force resisting system and secondary concrete-filled steel tube (CFT) gravity column system is presented in this paper. The dual CFT system concept relies on the primary system to supply the main lateral strength, while the inherent lateral strength in the gravity framing system, augmented with the additional robustness of CFT columns, then provides additional lateral strength. To illustrate the concept, the seismic performance of 4-story office buildings with perimeter steel moment frames was predicted and compared to the performance of the buildings employing a dual CFT system using square HSS gravity columns. The analyses predicted that buildings with the dual CFT system were 22–68% less susceptible to seismic collapse depending on the ductility of the primary moment frame and the orientation of the gravity columns, compared to buildings with only the moment frame.

INTRODUCTION

Dual lateral-force resisting systems have two key characteristics that may enhance seismic performance compared to single systems. First, dual systems explicitly provide increased redundancy, allowing load to be transferred through alternate paths that are intended as part of the design, instead of unintentional redistribution of load. Second, dual systems may provide added safety against collapse and added resistance to structural and non-structural damage. The latter characteristic is the motivation for the dual system explored in this study.

The potential for the gravity framing system to act as a dual or “reserve” lateral-force resisting system has been recognized for several years. The effectiveness of the dual approach using the gravity framing system depends on several factors, such as building height, structural configuration, location of column splices, and beam-to-column connection details (Flores et al., 2014; Judd et al., 2016). Depending on these factors, gravity framing may help reduce residual story drift (Eatherton and Hajjar, 2011), improve collapse safety (Flores et al., 2014; Elkady and Lignos, 2015), and improve serviceability (Judd and Charney, 2014). For a dual system that

involves a steel moment frame (MF), a previous study (Judd et al., 2016) suggested that the gravity system needs to be capable of resisting at least 10% of the prescribed seismic forces in order to be effective. In many cases, the lateral capacity contribution of a conventional gravity framing system can be modest, on the order of 10–30% percent of the lateral-force resisting system. Furthermore, soft-story mechanisms can limit the global collapse resistance.

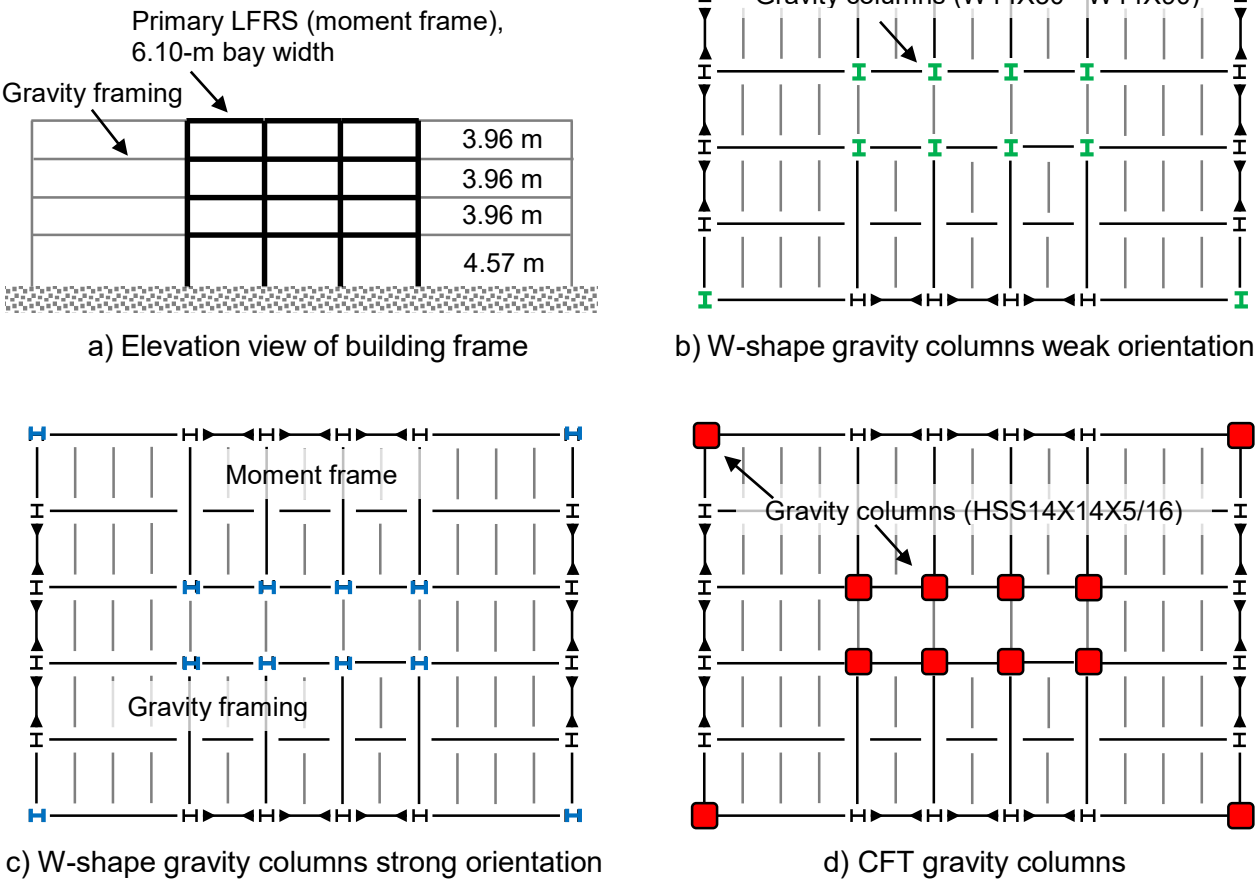
Concrete-filled steel tube (CFT) gravity columns may provide a pragmatic approach to increase the lateral strength of the gravity framing system and to improve the global collapse mechanism. Prior research (e.g. Hajjar, 2000; Denavit et al., 2016) has demonstrated that CFT columns can have significant flexural strength, axial compression strength, significant strength when subjected to combined axial and flexure loads, and may contribute to cost-effective construction. Perhaps more important in the context of a gravity framing system, CFT columns have excellent resistance in two orthogonal directions, compared to wide-flange (W-shape) sections.

The objective of this analytical study was to explore the potential of a dual CFT system concept. The dual CFT system concept relies on the primary system to supply the main lateral strength and stiffness. The inherent lateral strength in the gravity framing system, augmented with the additional robustness of CFT columns, then provides additional lateral strength. In this study, two types of primary lateral-force resisting systems were considered: (1) a non-ductile steel MF, and (2) a ductile steel MF. One type of CFT gravity column was considered: square HSS with a steel minimum yield stress, F_y equal to 317 MPa (46 ksi) and a concrete compressive strength, f_c' equal to 34.5 MPa (5 ksi). Rectangular and circular HSS and high-strength steel and concrete were not considered in this study. Gravity beam to-column connections use a single plate (shear tab) welded to flange or CFT wall. The seismic performance of 4-story office buildings with perimeter steel MFs was then predicted and compared to the performance of the buildings employing a dual CFT system using an adaptation of the FEMA P-695 methodology (FEMA, 2009a).

METHODOLOGY

The example building plan (Figure 1) was based on steel MF archetype buildings designed for the ATC-76 project (NIST, 2010). The building has perimeter moment frames, a 6.10-m (20-feet) bay length, a 4.57-m (15-feet) first story height measured to the top of the beam, and a 3.96-m (13-feet) upper story height (Figure 1a). Two types of MFs were evaluated for the primary lateral-force resisting system. First, a non-ductile MF designed for the highest spectral accelerations corresponding to Seismic Design Category (SDC) B for stiff soil (“site class D”, shear wave velocity equal to 183-366 m/s) was evaluated. The non-ductile MF used fully-restrained directly-welded flange connections. Second, a ductile MF designed for the highest spectral accelerations corresponding to SDC C for stiff soil was evaluated. The ductile MF was a Special Moment Frame (SMF) with reduced beam sections. Both types of MFs used columns fixed at the base.

The gravity framing system was designed for a 4.31 kN/m^2 (90 psf) dead load and a 2.39 kN/m^2 (50 psf) live load. The roof and floor of the buildings used a 140-mm (5.5-inch) composite slab and gravity framing beams spaced at 3.05 m (10 feet) on center connected to girders with shear tab connections. The gravity framing wide flange (W-shape) columns were pinned at the base and spliced 1.22 m (4 feet) above the third floor. The W-shape columns were oriented with the weak axis in the same direction as the moment frames (Figure 1b), and with the strong axis in the moment frame direction (Figure 1c). In this way, the influence of the gravity system column orientation was bounded for this building layout. Member sizes for the lateral-force resisting system and for the gravity framing system are provided by Judd (2015). Gravity columns varied from a W14X30 to a W14X90. For the dual CFT system (Figure 1d), W-shape columns were replaced with HSS14X14X5/16 steel tubes with ASTM A500 Gr. B steel, F_y equal to 317 MPa (46 ksi), and filled with un-reinforced concrete, with f_c' equal to 34.5 MPa (5 ksi).



a) Elevation view of building frame

b) W-shape gravity columns weak orientation

c) W-shape gravity columns strong orientation

d) CFT gravity columns

Fig. 1 – Building plan.

A model of the building was made using *OpenSees* (PEER, 2015). A perspective view of the model is shown in Figure 2. Beams and columns were modeled using an assembly of linear elastic elements and zero-length nonlinear springs, to simulate the formation of plastic hinges in the reduced section of the beams, plastic hinges at the top or bottom of columns, and shear yielding of the column panel zone. Second-order effects were included by modeling the gravity framing explicitly (instead of using a leaning column), and by using a "corotational" coordinate transformation (where the local element coordinate system continuously rotates).

The moment-rotation behavior of non-ductile MF beam-to-column connections (Figure 2a) and shear tab beam connections (Figure 2b) was modeled using the `Pinching4` and `MinMax` uniaxial materials in *OpenSees*, with load-deformation parameters based on empirical and test data, e.g. FEMA P-440A (FEMA, 2009b) and FEMA 355D (FEMA, 2000). (See Judd and Charney, 2016.)

The moment rotation behavior of ductile MF beam-to-column connections was modeled using the `bilin` material implementation of the modified Ibarra-Medina-Krawinkler bilinear model (Ibarra and Krawinkler, 2005), with load-deformation parameters based on a statistical analysis of experimental test data of bare steel RBS connections. The effect of composite action between the moment frame and slab was not included, but was considered in a related study (Judd, 2016).

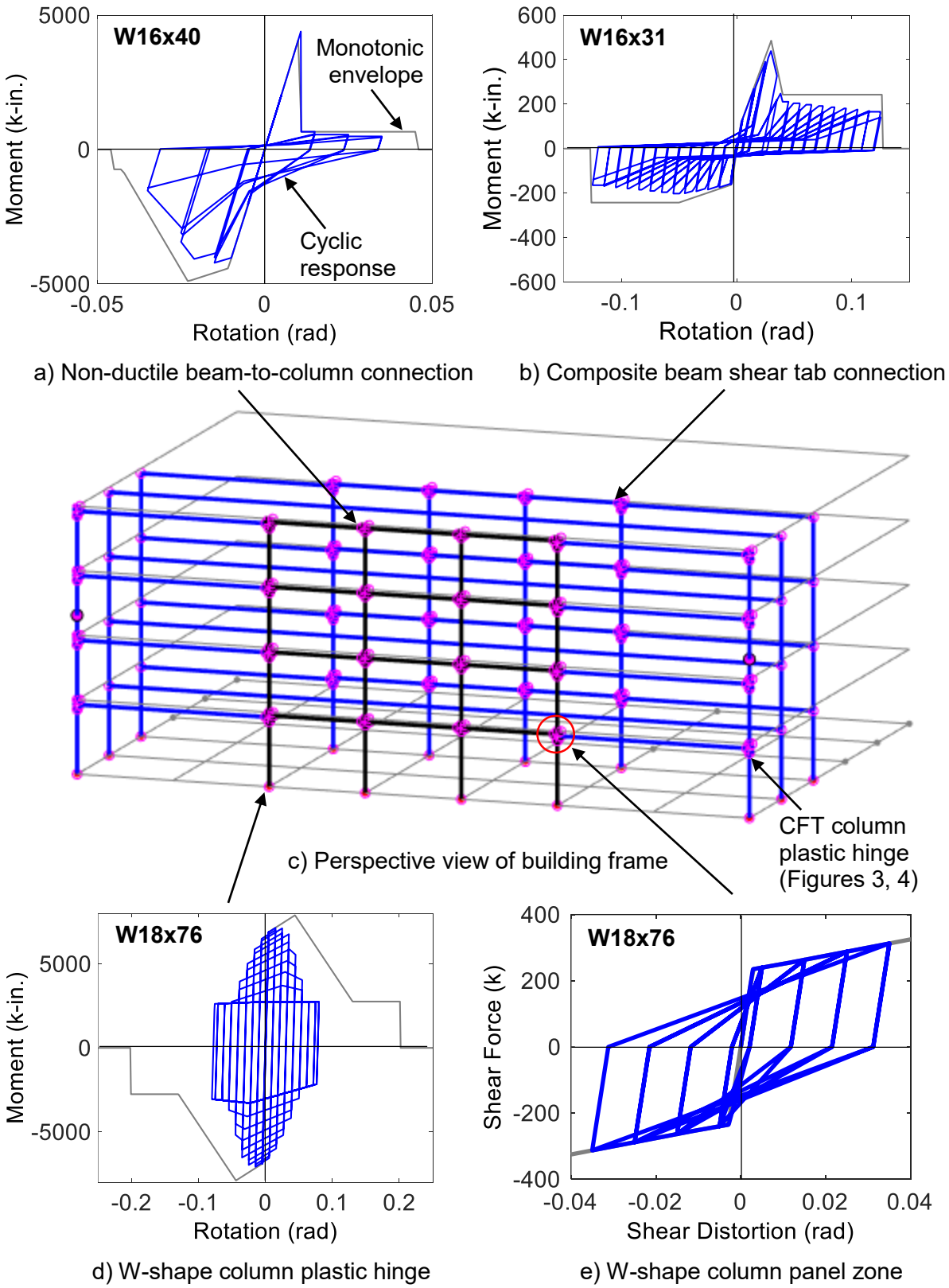


Fig. 2 – Analytical model of building frame

W-shape column plastic hinge behavior (Figure 2d) was modeled similarly to ductile MF connection behavior, except column strength was reduced to account for axial load interaction. The reduction in flexural strength was approximated using AISC 360-16 Equations H1-1a and H1-1b (AISC, 2016) and a constant axial load determined resulting from the gravity load plus half the lateral load calculated in a nonlinear static "pushover" analysis.

W-shape column panel zones were modeled using a form of the Krawinkler model that combines the contributions of the column web and the column flanges (Charney and Marshall, 2006). Shear-distortion behavior (Figure 2e) was modeled using the `hysteretic` material (a tri-linear envelope curve and bilinear hysteresis behavior). Column splices were idealized as pinned connections with no rotational constraint. The effect of the splice location and strength has been considered in a related study (Flores et al., 2014).

CFT column plastic hinge behavior (Figure 3) was modeled using the `BoucWen` material, with load-deformation parameters based on a parametric study of square CFT columns subjected to cyclic loading (Skalomenos et al., 2014). This modeling approach was selected over other models (e.g. Varma et al., 2005; Tort and Hajjar, 2010; Denavit and Hajjar, 2014), primarily due to the computational efficiency of the concentrated plasticity model and the numerical robustness of the `BoucWen` material when subjected to cyclic load and load reversal. In the `BoucWen` material, based on the Baber and Noori (1985) implementation, the force, σ versus deformation, ε relationship is defined as the sum of a linear part and a hysteretic part (Equation 1).

$$\sigma = \alpha k_o \varepsilon + (1-\alpha) k_o z \quad (1)$$

In Equation 1, *z* represents the hysteretic deformation, k_o is the elastic stiffness, and α is the ratio of the post-yielding to elastic stiffness. The hysteretic deformation variable z accounts for degradation using Equation 2. For square CFT sections, α is equal to 0.02 and k_o is calculated based on the effective stiffness, EI_{eff} (AISC 360-10, Equation I2-13).

$$\dot{z} = \left[\frac{A - |z|^{\eta}[\beta \, \mathrm{sgn}(\dot{\epsilon} z) + \gamma] v}{\eta}\right] \dot{\epsilon} \quad (2)$$

In Equation 2, the parameters γ and β control the shape of the hysteretic loop, n controls the transition from linear to nonlinear behavior. For square CFT sections, γ and β are equal to $0.25/\varepsilon_y$ where ε_y is the yield deformation accounting for axial-flexure interaction (Figure 4) based on the plastic stress distribution method (Method 2 in Commentary, AISC 360-16). The parameters A, v, and η control the stiffness and strength degradation via Equations 3 to 5, respectively.

$$A = (A_o - \delta_A e) \quad (3)$$

$$v = (1 + \delta_v e) \quad (4)$$

$$\eta = (1 + \delta_\eta e) \quad (5)$$

In the preceding equations, A_o is an amplitude factor, and δ_A, δ_v, and δ_η are strength and stiffness degradation parameters. For square CFT sections, A_o is equal to $1/\varepsilon_y$, δ_A is equal to 0.0, and δ_v and δ_η are calculated using equations 6 and 7, respectively, where b and t are the width and thickness of the HSS section in meters, respectively, and F_y and f_c' are expressed in MPa (Skalomenos et al., 2014). Finally, the rate parameter, e is defined by Equation 8.

$$\delta_v = A_o \exp\left[-4.5008 - 11.2683\, b + 4.9987\times10^{-4}(b/t)^2 - 50.8341/\sqrt{F_y}\right] \quad (6)$$

$$\delta_\eta = A_o \exp\left[-17.7959 + \frac{3.9012}{\sqrt{b}} - \frac{730.0289}{(b/t)^2} + 0.2583\sqrt{F_y/f_c'}\right] \quad (7)$$

$$\dot{e} = (1-\alpha) k_o \dot{\epsilon} z \quad (8)$$

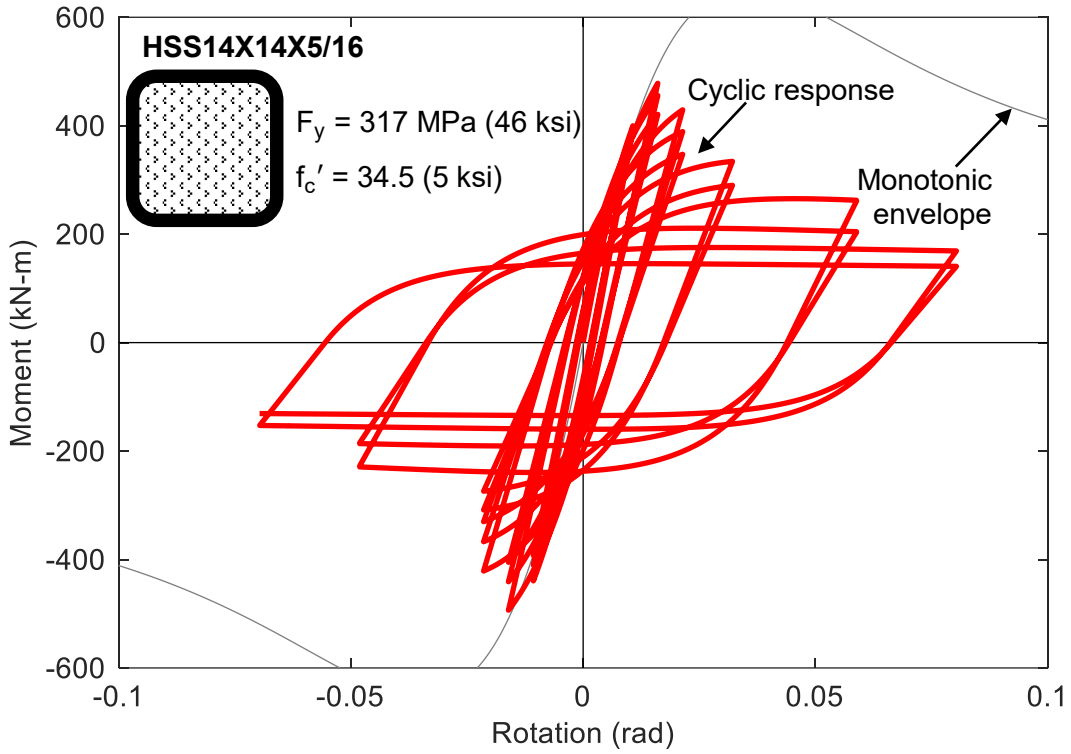


Fig. 3 – CFT column plastic hinge

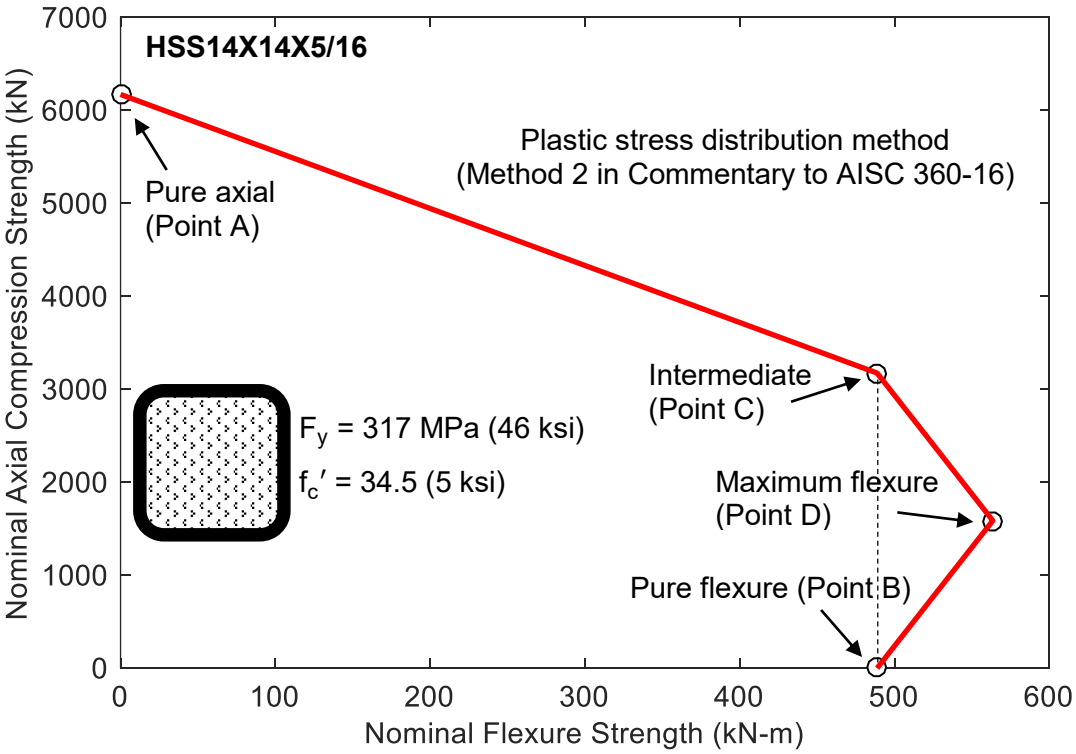


Fig. 4 – Interaction diagram for CFT column

The seismic performance of the buildings with the dual CFT system compared to "conventional" buildings (with W-shape columns in a strong or weak orientation) was evaluated using a sequence of analyses. An initial pre-load (gravity) analysis was followed by an Eigen-value analysis to determine the periods and modes of vibration of the building. The computed fundamental period of vibration was used for both referencing spectral accelerations. The gravity and vibration analyses were then followed by two pushover analyses: a first pushover analysis to estimate axial loads in columns, and a second pushover analysis to account for axial-flexure load interaction.

Incremental nonlinear dynamic response history analyses (IDA) were conducted using the FEMA P-695 Far-Field normalized ground motion set. Damping was explicitly modelled by the component hysteresis. Artificial "Rayleigh" damping was not added. The model was subjected to the set of ground motions, incrementally scaled in intensity with respect to the target SDC spectrum, S_{aMCEl} until the ground motions caused the building model to collapse in a side-sway mechanism. The collapse fragility was determined by fitting individual collapse points (spectral acceleration at the reference period and corresponding probability of collapse for a one scaled ground motion record) with a curve, assuming a lognormal cumulative distribution function. The median collapse margin ratio (ACMR) was increased to account for spectral shape ("SSF" factor) and the total dispersion in collapse capacity, β_{Total} based on record-to-record dispersion measured in the incremental dynamic analyses, β_{RTR} and epistemic dispersion due to design, test data, and modeling uncertainty (Judd, 2015).

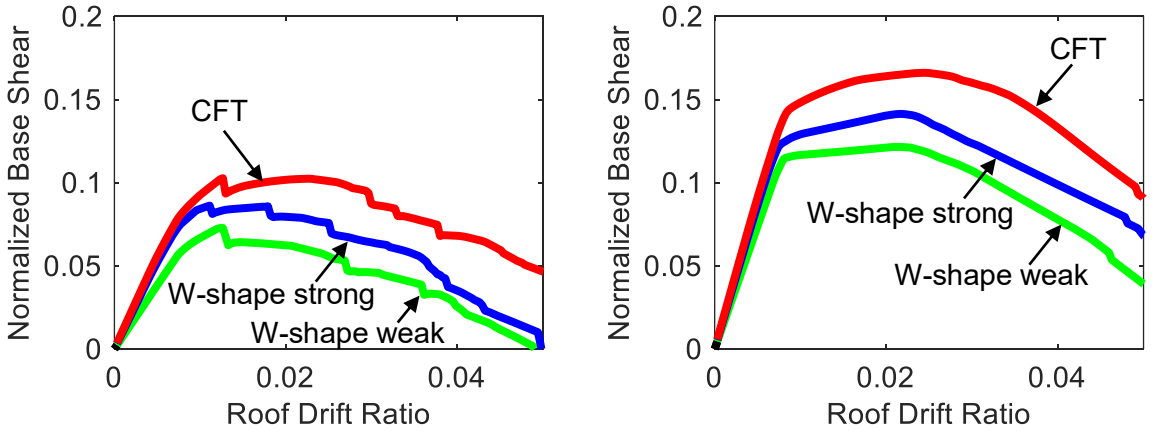
RESULTS

The results are summarized in Table 1, relative to the maximum spectral accelerations in SDC D for purposes of comparison with other seismic systems. As in prior studies (e.g. Judd, 2016), the computed fundamental period, T_1 was higher than empirical equations used to ASCE 7, but in line with the values calculated in the ATC-76 project. The buildings with a non-ductile MF were 7–19% stiffer compared to the conventional buildings, depending on the orientation of the gravity columns. Buildings with a ductile MF were 6–13% stiffer.

The effective base shear coefficient, C_s is given relative to SDC D_{max}. Since the MFs were designed for SDC B_{min} and SDC D_{min}, the building "over-strength," Ω is less than 1.0. The dual CFT system increased Ω observed in the pushover analyses (Figure 5) by up to 40%. The CFT columns also provided more over-strength compared to orienting W-shape gravity columns in the strong direction. The period-based ductility, μ_T of the building with the CFT columns increased.

Table 1. Collapse safety evaluation, relative to SDC D_{max}.

Building Gravity column	T_1 (s)	Static Pushover			Dynamic IDA					
		C_s	Ω	μT	S_{aMCE} (g)	SSF	ACMR S_{aDmax}	β_{RTR}	β_{Total}	P_c | S_{aDmax}
Non-ductile moment-frame buildings designed for SDC B_{min}										
W-shape weak	2.32	0.21	0.35	3.01	0.39	1.33	0.81	0.34	0.63	63%
W-shape strong	2.01	0.21	0.41	3.72	0.45	1.38	1.01	0.34	0.63	49%
CFT	1.87	0.21	0.49	4.60	0.48	1.27	1.08	0.34	0.63	38%
Ductile moment-frame buildings designed for SDC D_{min}										
W-shape weak	1.73	0.08	1.54	4.75	0.52	1.44	1.40	0.30	0.43	22%
W-shape strong	1.60	0.08	1.80	4.92	0.56	1.45	1.73	0.32	0.44	11%
CFT	1.51	0.08	2.11	5.40	0.60	1.48	1.85	0.29	0.42	7%

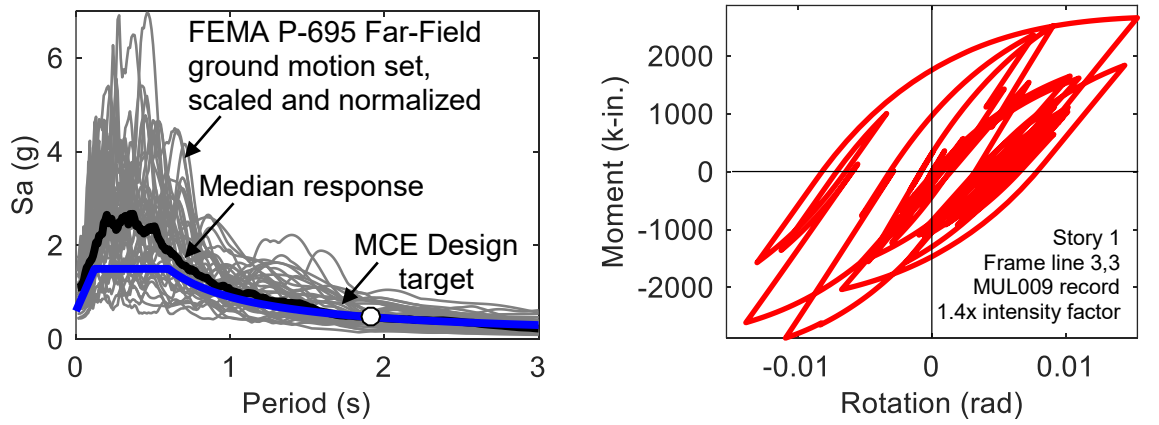


a) Non-ductile MF designed for SDC B_{min} b) Ductile MF designed for SDC D_{min}

Fig. 5 – Nonlinear static pushover response

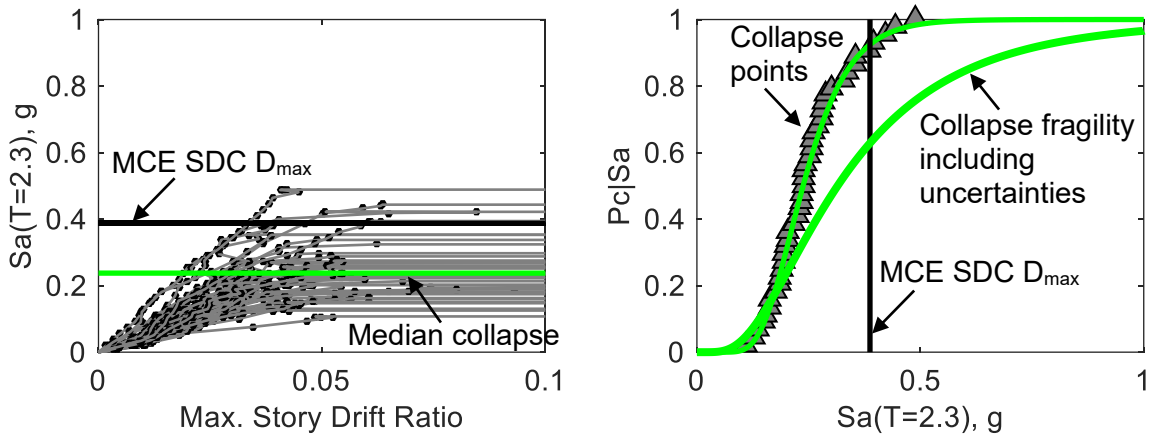
Figure 6a shows a representative response spectrum for the FEMA P-695 Far-Field ground motion set, normalized, scaled and anchored to the computed fundamental period of vibration of the building. Note that in the FEMA P-695 procedure, there is record-to-record dispersion at all periods, including the target period. Figure 6b shows a representative behavior of a CFT column.

The results of the IDA are shown in Figure 7 for the non-ductile MF buildings and in Figure 8 for the ductile MF buildings, relative to the maximum spectral accelerations in SDC D. A comparison of the results for the weak orientation (Figure 7a and Figure 8a) and the strong orientation (Figure 7b and Figure 8b) show that the dual CFT system is more effective at increasing the median collapse capacity than orienting all the W-shape columns in the strong direction. Furthermore, it should be noted that such an arrangement would produce a building with weak columns in the orthogonal (transverse) direction of the building. As a result of added stiffness due to the CFT columns, buildings with a dual CFT system were subjected to slightly higher spectral accelerations (see Table 1, column 6 for example). Notwithstanding the increase in spectral accelerations caused by the increased stiffness, by employing the dual CFT system the probability of collapse given the MCE-level ground motions ($P_c | S_{aMCEI}$) was 22–40% lower for the non-ductile MF buildings and 36–68% lower for the ductile MF buildings.

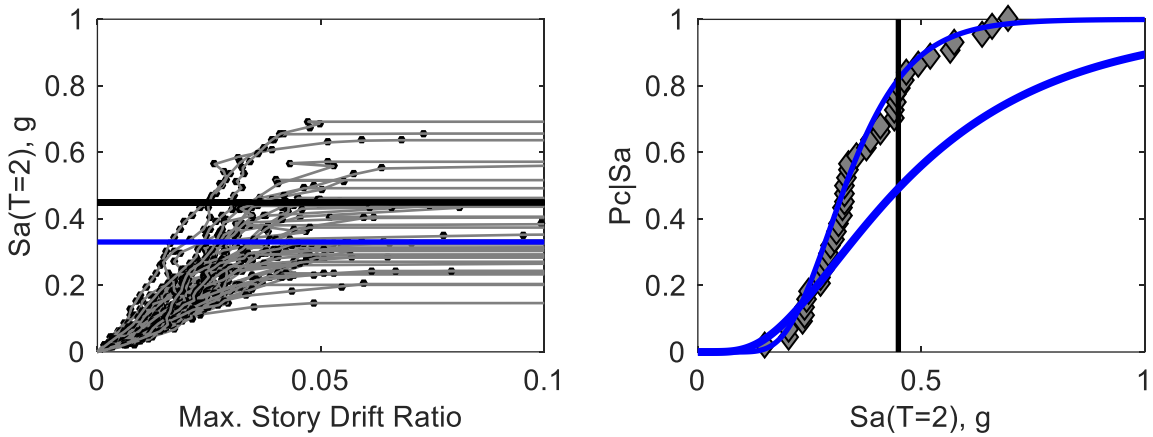


a) Scaled response spectrum b) CFT moment-rotation behavior

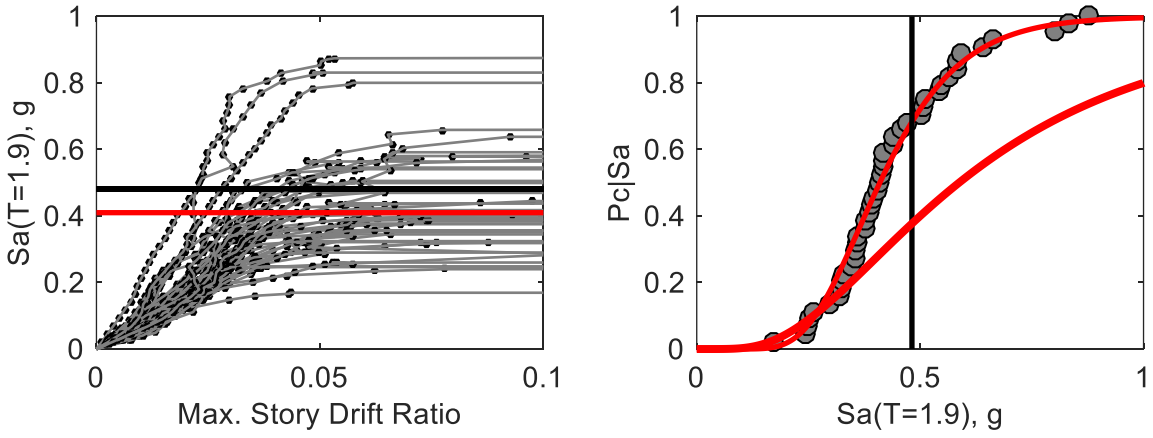
Fig. 6 Representative response for non-ductile SDC B_{min} with CFT gravity columns



a) W-shape gravity columns oriented in weak direction

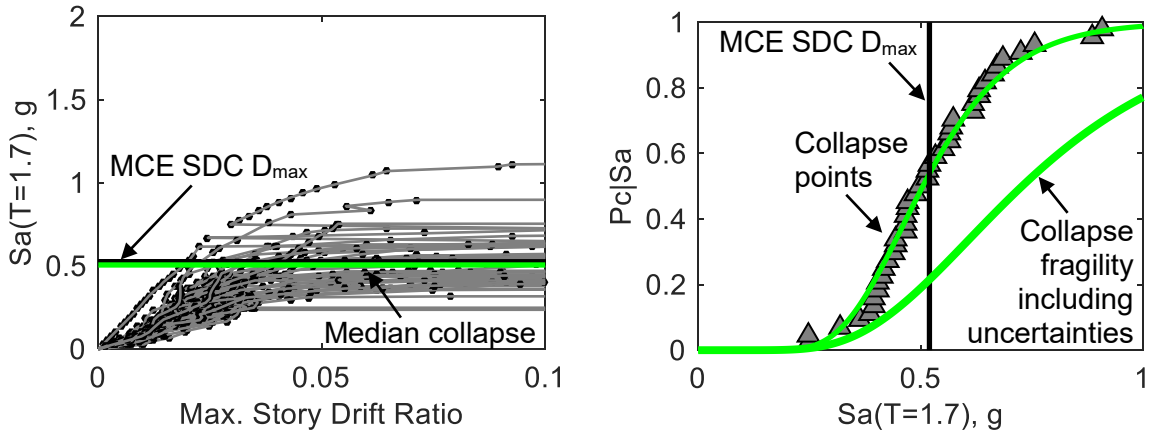


b) W-shape gravity columns oriented in strong direction

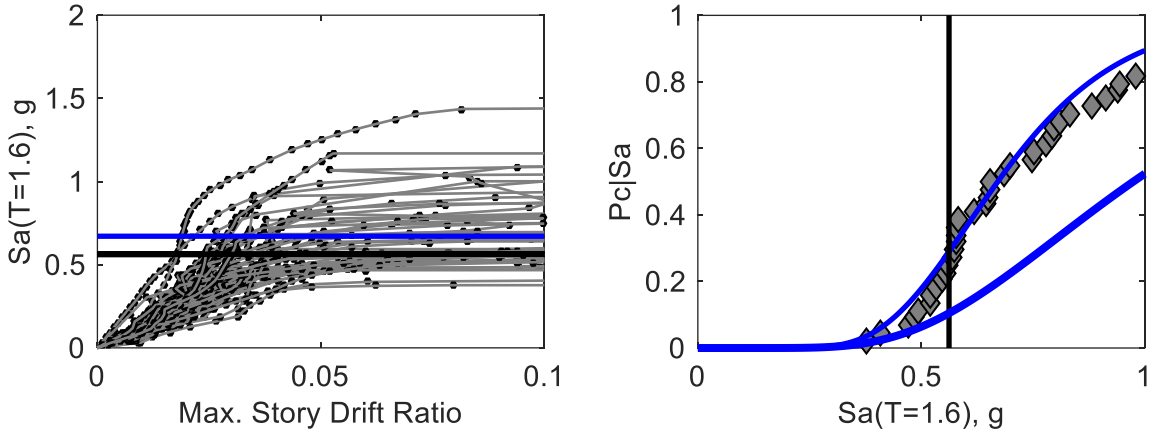


c) CFT gravity columns

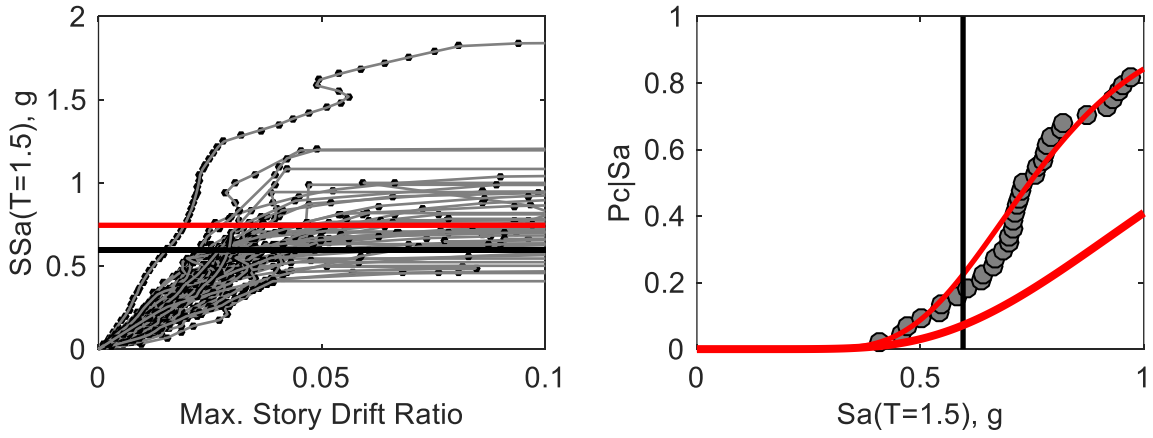
Fig. 7 – Non-ductile MF designed for SDC B_{min} IDA response



a) W-shape gravity columns oriented in weak direction



b) W-shape gravity columns oriented in strong direction



c) CFT gravity columns

Fig. 8 – Ductile MF designed for SDC D_{min} IDA response

CONCLUSIONS

The potential for using a primary MF system to supply the main lateral strength and stiffness, and the gravity framing system augmented with the additional robustness of CFT columns to provide additional lateral strength was explored in this study. The results indicated that the 4-story buildings with a non-ductile MF, and HSS14X14X5/16 columns with F_y equal to 317 MPa (46 ksi) and filled with 34.5-MPa (5-ksi) concrete, had a 22–40% lower probability of seismic collapse, compared to the conventional buildings with W-shape gravity columns, depending on the orientation of the W-shape column. Buildings with a ductile MF and the CFT columns had a 36–68% lower probability of seismic collapse.

Future research is underway to expand the scope of the study to consider a range of HSS sections, high-strength steel and high-strength concrete, and to examine the effect of the dual CFT system in a broader range of building heights, both low-rise and tall buildings. In this study, the CFT columns did not significantly change the global collapse mechanism of the building. Thus, one goal of the ongoing research is to reconfigure the CFT columns in an effort to develop a "stiffened spine" that inhibits story-drift concentrations that can lead to a soft-story mechanism, and thereby increase the global collapse resistance of the buildings. Another objective of the ongoing research is to examine the seismic performance of the dual CFT system in terms of repair costs, repair time, and business downtime by using the FEMA P-58 (FEMA 2012) framework. Finally, the implications for construction of the proposed system and the potential for application of the concept to building retrofit and rehabilitation need to be evaluated before implementation of the dual CFT system in actual buildings.

REFERENCES

AISC (2010). *Specification for structural steel buildings*. ANSI/AISC 360-10, American Institute for Steel Construction (AISC), Chicago, Illinois.

AISC (2016). *Specification for structural steel buildings*. ANSI/AISC 360-16, American Institute for Steel Construction (AISC), Chicago, Illinois.

Baber, T.T., Noori, M.N. (1985). "Random vibration of degrading, pinching systems." *Journal of Engineering Mechanics*, Vol. 111, No. 8, 1010–1026.

Charney, F.A., Marshall, J.A. (2006). "Comparison of the Krawinkler and Scissors models for including beam–column joint deformations in the analysis of moment resisting frames." *Engineering Journal*, Vol. 43, No. 1, 31–48.

Denavit, M.D., Hajjar, J.F. (2014). *Characterization of behavior of steel-concrete composite members and frames with applications for design*. Report No. NSEL-034, Department of Civil and Environmental Engineering, University of Illinois at Urbana-Champaign.

Denavit, M.D., Hajjar, J.F., Perea, T., Leon, R.T. (2016). "Seismic performance factors for moment frames with steel-concrete composite columns and steel beams." *Earthquake Engineering and Structural Dynamics*, Vol. 45, No. 10, 1685–1703.

Eatherton, M.R., Hajjar, J.F. (2011). "Residual drifts of self-centering systems including effects of ambient building resistance." *Earthquake Spectra*, Vol. 27, No. 3, 719–744.

Elkady, A., Lignos, D.G. (2015). "Effect of gravity framing on the overstrength and collapse capacity of steel frame buildings with perimeter special moment frames." *Earthquake Engineering and Structural Dynamics*, Vol. 44, No. 8, 1289–1307.

FEMA (2000). *State of the art report on connection performance*. FEMA-355D, Federal Emergency Management Agency, Washington, D.C.

FEMA (2009a). *Quantification of building seismic performance factors.* FEMA P-695, Federal Emergency Management Agency (FEMA), Washington, D.C.

FEMA (2009b*). Effects of strength and stiffness degradation on seismic response*. FEMA P-440A, Federal Emergency Management Agency (FEMA), Washington, D.C.

FEMA (2012). *Seismic performance assessment of buildings, volume 1—methodology*. FEMA P-58-1. Federal Emergency Management Agency (FEMA), Washington, D.C.

Flores, F.X., Charney, F.A., Lopez-Garcia, D. (2014). "Influence of the gravity framing system on the collapse performance of special steel moment frames." *Journal of Constructional Steel Research*, Vol. 101, No. 10, 351–362.

Hajjar, J.F. (2000). "Concrete-filled steel tube columns under earthquake loads." *Progress in Structural Engineering and Materials*, Vol. 2, No. 1, 72–81.

Ibarra, L.F., Krawinkler, H. (2005). *Global collapse of frame structures under seismic excitations*. Technical Report No. 152, The John A. Blume Earthquake Engineering Research Center, Department of Civil Engineering, Stanford University, Stanford, California.

Judd, J.P. (2015). *Multi-hazard performance of steel moment frame buildings with collapse prevention systems in the central and eastern United States*. Ph.D. dissertation, Civil Engineering. Virginia Polytechnic Institute and State University, Blacksburg, Virginia.

Judd, J.P. (2016). "Seismic collapse risk of steel-concrete composite moment-frame buildings." *International Colloquium on Stability and Ductility of Steel Structures*, Timișoara, România.

Judd J.P., Charney, F.A. (2014). "Seismic performance of buildings designed for wind." *Structures Congress*, Boston, Massachusetts, 2342–2354.

Judd J.P., Charney F.A. (2016). "Seismic collapse prevention system for steel-frame buildings." *Journal of Constructional Steel Research*, Vol. 118, 60–75.

Judd J.P., Charney, F.A., Flores, F.X. (2016). "The influence of gravity framing on the performance of steel buildings subjected to seismic loads." *International Workshop on Connections in Steel Structures (CONNECTIONS VIII)*, May 24–26, Boston, Massachusetts.

NIST (2010). *Evaluation of the FEMA P-695 methodology for quantification of building seismic performance factors*. NIST GCR 10-917-8, National Institute of Standards and Technology (NIST), Gaithersburg, Maryland.

PEER (2015). Open Systems for Earthquake Engineering Simulation (*OpenSees*), version 2.4.6. Pacific Earthquake Engineering Research Center (PEER), University of California, Berkeley, California.

Skalomenos, K.A., Hatzigeorgiou, G.D., Beskos, D.E. (2014). "Parameter identification of three hysteretic models for the simulation of the response of CFT columns to cyclic loading." *Engineering Structures*, Vol. 61, 44-60.

Tort, C., Hajjar, J.F. (2010). "Mixed finite-element modeling of rectangular concrete-filled steel tube members and frames under static and dynamic loads." *Journal of Structural Engineering*, Vol. 136, No. 6, 654–664.

Varma, A., Sause, R., Ricles, J.M., Li, Q. (2005). "Development and validation of fiber model for high-strength square concrete-filled steel tube beam-columns." *ACI Structural Journal*, Vol. 102, No. 1, 73–84.

An Introduction to Coupled Composite Core Wall Systems for High-Rise Construction

Amit H. Varma
Professor, Lyles School of Civil Engineering, Purdue University
West Lafayette, IN, USA
ahvarma@purdue.edu

Zhichao Lai
Postdoctoral Research Associate, Lyles School of Civil Engineering, Purdue University
West Lafayette, IN, USA
laizhichao@gmail.com

Jungil Seo
Research Engineer, Lyles School of Civil Engineering, Purdue University
West Lafayette, IN, USA
seo2@purdue.edu

ABSTRACT

This paper introduces the latest innovation in steel-concrete composite structures, namely, coupled composite core wall systems that are being developed for high-rise building applications as an efficient alternative to address issues associated with conventional concrete construction. The system consists of concrete filled – composite plate shear walls (CF-CPSWs) that are coupled together using steel beams or composite members. The CF-CPSWs consist of a concrete wall sandwiched between two steel faceplates. The faceplates are anchored to the concrete using stud anchors, and connected to each other using tie bars. The steel modules are pre-fabricated in the shop, and shipped to the site for erection, assembly, and concrete casting. Construction schedule is expedited by the pre-fabricated steel modules (from the shop), which also serve as the stay-in-place permanent formwork during casting.

A research program focusing on the lateral load (wind and seismic) behavior, analysis and design of the coupled core wall system and its individual components including the core walls, coupling beams, and beam-to-wall connections is currently ongoing. This paper summarizes preliminary results from the first sub-task of the research program, which focuses on the testing and numerical analysis of the individual core walls. The paper includes the proposed tentative test matrix, specimen details, and results from pre-test numerical analysis of the specimens using detailed 3D finite element models. The paper discusses the expected behavior (stiffness, strength, and ductility of the specimens), the effects of parameters such as the flange-to-web plate thickness ratio, and the axial load ratio. These results are used to finalize the test matrix.

INTRODUCTION

Coupled reinforced concrete (RC) shear walls have been widely used around the world in high-rise buildings as the primary lateral force resisting system for both wind and seismic applications. Some of the challenges associated with coupled RC core wall systems include rebar congestion

(for high rise buildings), and construction schedule due to formwork placement, removal, and concrete hardening, and the delays associated with discontinuity between the concrete core wall and the steel outrigger and belt truss system (when used). Recently, there has been increasing interest in the use an innovative coupled composite plate shear wall (CPSW) system as an alternative to address these issues associated with coupled RC core walls.

A concrete filled-composite plate shear wall (CF-CPSW) consists of a concrete wall sandwiched between two steel faceplates. The faceplates are connected to each other using regularly spaced tie bars, and anchored to the concrete infill using the ties or additional stud anchors. The steel faceplates serve as the primary reinforcement for the concrete wall, and no other additional rebar is needed or provided. Additionally, the steel faceplates serve as stay-in-place formwork for construction activities and concrete casting. The steel modules consisting of the steel plates, ties, stud anchors etc. are fabricated in the shop, and shipped to the field for erection, assembly of several such modules, and eventually casting of concrete.

Concrete-filled composite plate shear walls (CF-CPSWs) offer a potential alternative to reinforced concrete walls for high rise buildings because of the following reasons (Varma et al. 2015): (i) The steel modules can be pre-fabricated in the shop, which reduces the construction schedule associated with assembling and tying rebar cages. (ii) The steel faceplates serve as permanent formwork, which further reduces construction schedule. (iii) High reinforcement ratios such as 2% or more can be achieved relatively easily using steel faceplates. (iv) Rebar congestion issues are reduced by eliminating rebar cages. (v) Better concrete placement can be achieved using conventional or self-consolidating concrete.

In high rise buildings, these CF-CPSWs can be coupled together using steel beams or composite members (concrete filled steel tubes). As compared to conventional coupled RC shear walls, coupled CPSW have several potential advantages including: (i) higher stiffness and strength due to the use of steel faceplates that can achieve higher reinforcement ratios without congestion issues, (ii) better seismic performance due to the synergistic interaction between the steel and concrete materials, namely, confinement of the concrete by the steel, and local buckling restraint to the steel plate provided by the concrete infill, and (iii) construction schedule efficiency due to modular construction techniques, prefabrication and erection of steel modules, and continuity during construction of the steel belt truss and outriggers when needed.

A research program focusing on the lateral load (wind and seismic) behavior, analysis and design of the coupled core wall system and its individual components including the core walls, coupling beams, and beam-to-wall connections is currently ongoing. This paper summarizes preliminary results from the first sub-task of the research program, which focuses on the testing and numerical analysis of the individual core walls. The paper includes the proposed tentative test matrix, test setup, and pre-test numerical analysis of the specimens using detailed 3D finite element models.

This monotonic and cyclic flexural behavior of the proposed CPSW specimens are analyzed using detailed 3D nonlinear finite element (FEM) models built and analyzed using ABAQUS. The models are used to evaluate the effects of flange-to-web plate thickness ratio and axial load ratio, which were used to finalize the details of the specimens in the matrix. The detailed FEM models include various behavioral complexities such as: (i) yielding, local buckling, and fracture of the steel plates, (ii) concrete cracking and crushing, and (iii) cyclic stiffness degradation and recovery.

BACKGROUND

The lateral load behavior of CF-CPSWs, including their lateral force-displacement behavior and ductility, has been evaluated recently by many researchers. However, the focus has been on the in-plane shear behavior of squat walls for nuclear structures (Seo et al., 2016), and the in-plane flexural behavior of wall piers with or without boundary elements (Ramesh, 2013, Alzeni and Bruneau 2014, Kurt et al. 2016). Research on the lateral load behavior of coupled CF-CPSW core wall structures is somewhat limited. Figure 1 shows an example of a typical coupled CF-CPSW core wall structure. As shown, it consists of two individual core walls connected by coupling beams along the height of the structure. The individual core walls consist of two or more CF-CPSWs connected together to make either C, U, T, or I shapes.

There are some unique challenges that need to be addressed and resolved for coupled CF-CPSW core wall structures. For example, (i) the lateral load behavior including the stiffness, strength and drift capacity of the individual core walls, (ii) the effects of axial force on the lateral load behavior of individual core walls, (iii) the detailing of the connections between the individual CF-CPSWs comprising the core wall, (iv) the design of the coupling beam and the detailing of its connections to individual core walls, (v) the influence of coupling ratio on the lateral load behavior and design optimization of the coupled core wall system. Some of these unique challenges have been investigated and addressed for concrete core wall structures (El-Tawil et al., 2010) and included in AISC 341-16 (2016)for hybrid coupled core wall structures.

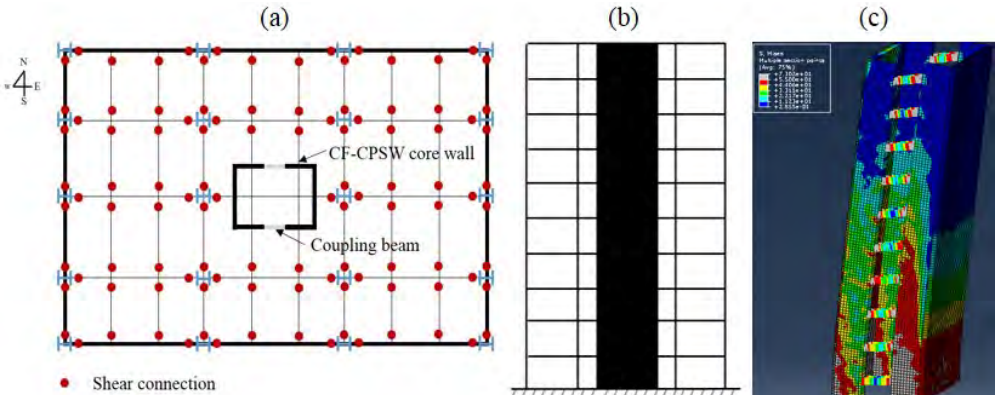


Fig.1 - Schematic of coupled CF-CPSW core wall structure: (a) structural plan, (b) elevation, and (c) simulated deformed state

EXPERIMENTAL PROGRAM

Figure 2 shows an idealized coupled shear wall system deformed under lateral loading, which causes a global over turning moment (OTM). The coupled system resists the OTM by developing an axial force couple ($\Sigma V_{beam,j}$ over the lever arm L) as well as flexural moment resistances in the individual walls (m_1 and m_2). The contribution of the axial force couple ($\Sigma V_{beam,j}$) to resisting OTM is defined as the coupling ratio (CR) and it can be calculated using Eq. (1). CR=0 implies that no coupling beams are present or the two individual shear walls are disconnected. CR=100% is the theoretical case where the coupling beam length is zero.

$$CR = \frac{L\sum V_{beam,j}}{L\sum V_{beam,j} + m_1 + m_2} = \frac{L\sum V_{beam,j}}{OTM} \quad (1)$$

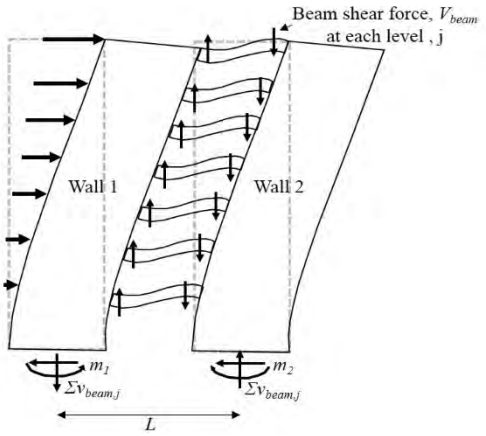


Fig. 2 - Deformed coupled shear wall system

The axial force couple ($\Sigma V_{beam,j}$) is applied to the individual shear wall (in addition to gravity loads) that vary during an earthquake. The axial compression force acting on the individual shear wall can potentially reduce the ductility of the wall due to concrete crushing failure and the axial tension force acting on the individual shear wall can reduce the stiffness and the shear capacity of the wall.

To evaluate (i) the structural performance of CF-CPSW and (ii) the effects of the axial force, six scaled tests will be conducted. The six CF-CPSW specimens (see Figure 3) will be subjected to cyclic quasi-static lateral loading as well as axial loading. The test specimens are 1/3-1/4 scale models of the bottom four-stories of the prototype walls. The test specimens have a wall aspect ratio of approximately 3. The proposed tentative test matrix for the CF-CPSW specimens is presented in Table 1. As shown, the primary parameter is the degree of axial compression force (10, 20, and 30% of the axial load capacity, $A_g f'_c$). The influence of axial compression force on the structural behavior (stiffness, strength, and drift capacity) of the uncoupled CF-CPSW core wall can be investigated by comparing the test results of the four specimens. In addition, the influence of the plate slenderness ratio (s_{stud}/t_p and s_{stud}/t_p) will be considered.

Table 1 – Tentative Test matrix

Specimen	***H, in***	***L, in***	***P, %$A_g f'_c$***	**t_{sc}, in**	**t_p, in**	**s_{stud}/t_p**	**s_{tie}/t_p**	**ρ_t**
CW-42-55-10	108	36	10	9	0.1875	-	24.0	0.55%
CW-42-55-20	108	36	20	9	0.1875	-	24.0	0.55%
CW-42-55-30	108	36	30	9	0.1875	-	24.0	0.55%
CW-42-14-20	108	36	20	9	0.1875	-	48.0	0.14%
CW-42-14-20	108	36	20	9	0.1875	-	48.0	0.24%
CW-42-24-20	108	36	20	9	0.1875	24	48.0	0.14%

Figure 4 shows a schematic view of the CF-CPSW core wall test setup with the specimens. As illustrated in the figure, the cyclic lateral loading will be applied at the top of the specimens using a set of hydraulic actuators. The compressive axial force will be applied to the specimens using

another set of hydraulic actuators. The lateral loading history will be developed based on the validation testing requirements prescribed in AISC 341-16 (2016).

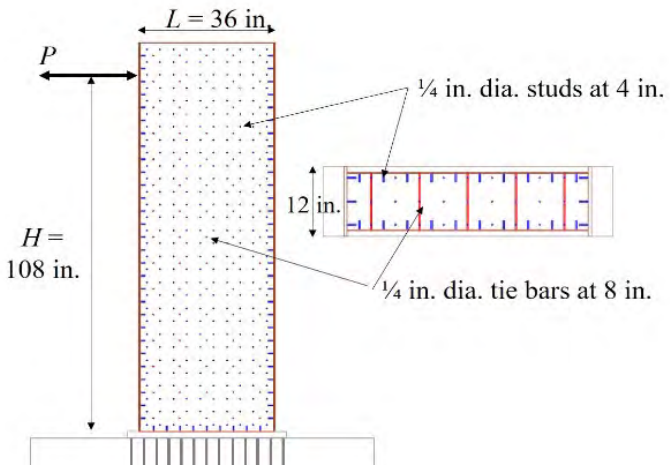


Fig. 3 - Typical test specimen

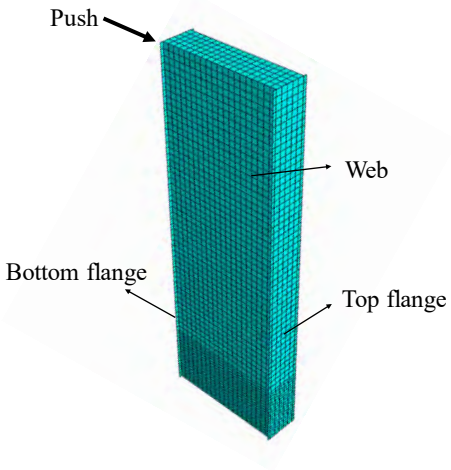


Fig. 5 - Typical FEM model

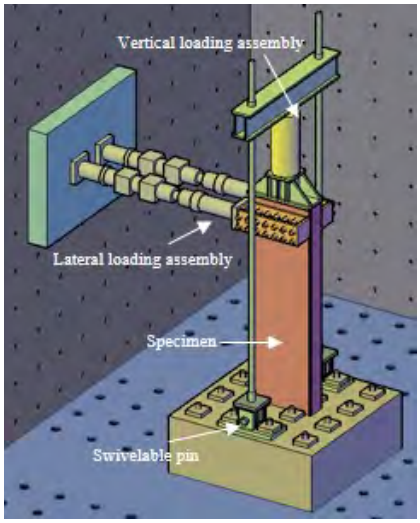


Fig. 4 - Schematic view of test setup

DETAILS OF SCALED SPECIMEN AND FEM MODELS

The height of the scaled CPSW is 120 in, the width is 40 in, and the thickness is 10 in. Tie bars were spaced 8 in. to develop composite action between the steel plates and the concrete infill. The diameter of the tie bars is 0.5 in. The resulting tie bar reinforcement ratio is 0.31%. The yield stress of the steel plates and tie bars is 50 ksi, and the compressive strength of the concrete infill is 6 ksi.

The FEM models were developed using ABAQUS (2016). Details of the FEM models include the element types, contact interaction, steel and concrete material models (including steel fracture and concrete cyclic damage), geometric imperfections, boundary conditions, and the analysis method. These details are similar to those developed by the authors for CFT members

in Lai and Varma (2017), and are briefly summarized as follows. Figure 5 shows the typical FEM model used in the analysis.

The steel face plates were modeled using four-node shell elements with reduced integration (S4R). The concrete infill was modeled using eight-node solid elements with reduced integration (C3D8R). The tie bars were modeled using two-node beam elements (B31). The connections between the tie bars and steel face plates were modeled using connector elements (CONN3D2). The axial and interfacial shear behavior of the connections were defined by specifying the corresponding force-displacement behavior of the connector elements. In this research, the axial behavior was assumed to be linear elastic (stiffness = E_sA_t, where A_t is the cross-section area of the tie bars). The shear behavior was defined using the model proposed by Ollgaard et al. (1971).

EFFECT OF FLANGE-TO-WEB THICKNESS RATIO

The developed FEM models were used to evaluate the effect of flange-to-web thickness ratio on the monotonic and cyclic behavior of the CPSW specimen. The flange-to-web thickness ratios were varied by changing the flange thickness (0.1875, 0.375, and 0.5 in) while keeping the web thickness constant at 0.1875 in. No axial load was applied during this evaluation.

Monotonic analysis and behavior

Three monotonic analyses were conducted to investigate the effect of flange-to-web thickness ratio on the strength and stiffness of CPSW. Figure 6 shows the resulting moment-displacement curves. The displacement reported in this figure represented the lateral deflection at the free end. As shown, the flexural stiffness and strength increase as the flange thickness increases. This figure also shows that the flexural strengths of all three members are greater than the corresponding plastic moment strengths M_p calculated based on AISC 360-16 (2016). This indicates that all three members can develop the plastic moment capacity.

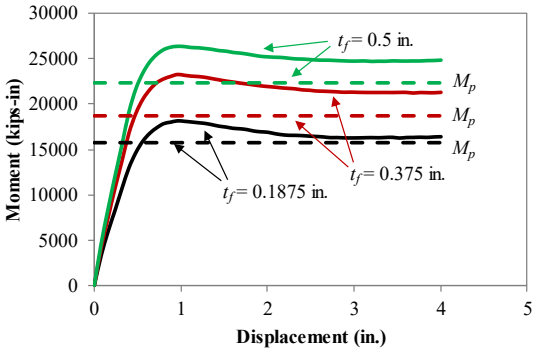


Fig. 6 - Effect of flange thickness on the monotonic moment-displacement curve from analysis

Cyclic analysis and behavior

Three cyclic analyses were conducted to investigate the effect of flange-to-web thickness ratio on the cyclic behavior and ductility of CPSW. Cyclic lateral loading was applied at the free end of the wall using the loading history shown in Figure 7. As shown, three elastic cycles were applied each at $0.5M_y$ and $1.0M_y$, where M_y is the moment corresponds to the first yield. After

that, three inelastic cycles were applied each at $1.0\Delta_y$, $2.0\Delta_y$, $3.0\Delta_y$, and $4.0\Delta_y$, where Δ_y represents the lateral displacement at the loading locations corresponding to the plastic moment (M_p). Δ_y, M_y, and M_p were obtained from corresponding monotonic analysis.

The analyses indicated that the failure modes for all three members are similar, i.e., local buckling of the flange and web at the base occurred first, followed by the fracture at these locations. Table 2 summarizes the loading cycles during which local buckling and fracture occurred. As shown, local buckling first occurred at $1.0\Delta_y$ push cycle. When the flange thickness is 0.1875 in., local buckling occurred at the flange first; while when the flange thickness is 0.375 or 0.5 in., local buckling occurred at the web first. Table 2 also indicates that increasing the flange thickness has negligible influence on the ductility (fracture occurred during the first 4.0 push and pull cycle for all specimens).

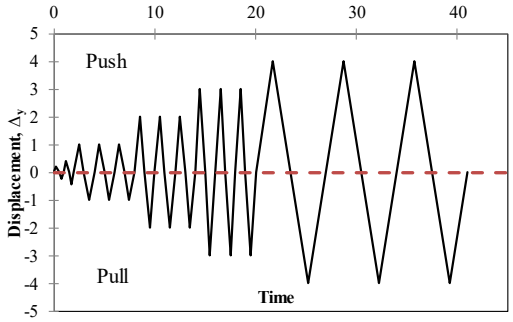


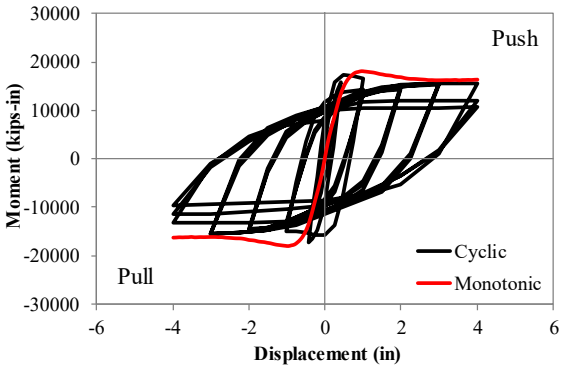
Fig. 7 - Loading history

Table 2 Summary of loading cycles during which local buckling and fracture occurred (CPSW with different flange thickness)

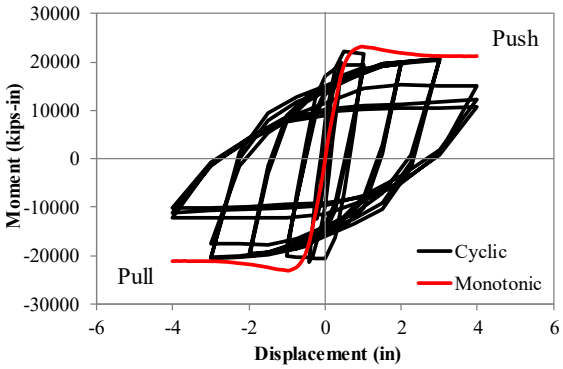
No.	Flange thickness	First appearance of local buckling	Initial Fracture
1	0.1875	Top flange at the base, first $1.0\Delta_y$ push cycle	Top flange at the base, first $4.0\Delta_y$ pull cycle
2	0.375	Web at the base close to the top flange, first $1.0\Delta_y$ push cycle	Bottom flange at the base, first $4.0\Delta_y$ push cycle
3	0.5	Web at the base close to the top flange, first $1.0\Delta_y$ pull cycle	Top flange at the base, first $4.0\Delta_y$ pull cycle

Figure 8 shows the cyclic load-displacement behavior of the walls. As shown, the cyclic behavior of all three walls was very good during the elastic cycles. There were no local buckling distortions, bulging or fracture during elastic loading cycles. During the first $1.0\Delta_y$ push cycle, local buckling developed at the base in the top and bottom flanges. The local buckling resulted in the about 9% loss of strength. After that, local buckling propagated into the webs. The local buckling increased during the $3.0\Delta_y$ cycles and resulted in fracture of the flanges in the first $4.0\Delta_y$ push and pull cycle. The fracture developed and spread to the webs during the second

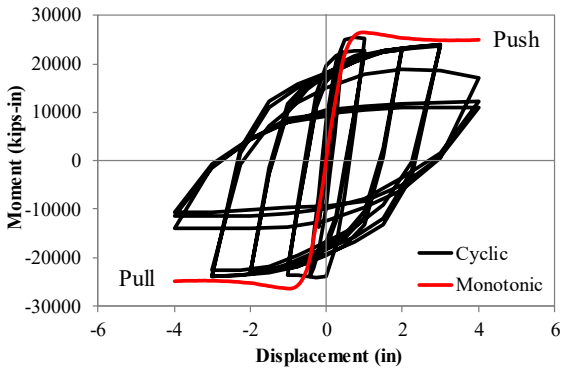
and third 4.0Δ_y push and pull cycle. Figure 8 indicates that the flange-to-web thickness ratio has negligible influence on the ductility (all three walls have a ductility of 3, the wall is assumed to remain its ductility if its strength loss is less than or equal to 20%). Figure 8 also includes the monotonic load-displacement behavior from the monotonic analysis. As shown, the monotonic load-displacement curve is similar to the envelope obtained from the cyclic analysis. Based on all these results, the flange thickness of 0.1875 in. was selected for all further evaluation and the design of the specimens identified in the tentative test matrix of Table 1.



(a) Flange thickness = 0.1875 in



(b) Flange thickness = 0.375 in.



(c) Flange thickness = 0.5 in.

Fig. 8 - Effect of flange thickness on the cyclic moment-displacement behavior from analysis

EFFECTS OF AXIAL LOAD RATIO

The developed FEM models were used to evaluate the effect of axial load ratio on the monotonic and cyclic behavior of CPSW. Five axial load ratios were used (-0.1, 0, 0.1, 0.2, and 0.3). The axial load ratios were varied by changing the applied axial load. The flange and web plate thickness was kept constant at 0.1875 in.

Monotonic analysis and behavior

Five monotonic analyses were conducted to investigate the effect of axial load ratio on the strength and stiffness of CPSW. Figure 9 shows the resulting moment- displacement curves. This figure indicates that as the axial load increases, the flexural stiffness and strength increase,

and the post-peak response becomes more negative. This figure also includes the plastic moment strengths M_p [calculated based on AISC 360-16 (2016)] of the wall without any axial load applied. As shown, when the axial load ratio is greater or equal to 0, the CPSW have flexural strengths greater than M_p. When the axial load ratio is equal to -0.1 (in tension), the CPSW have flexural strength close to M_p (98%).

Figure 10 compares the beam-column strength of CPSW with the beam-column interaction curve calculated using AISC 360-16 (2016) for filled composite columns. As shown, the beam-column strength of CPSW can be reasonably estimated using these AISC design equations.

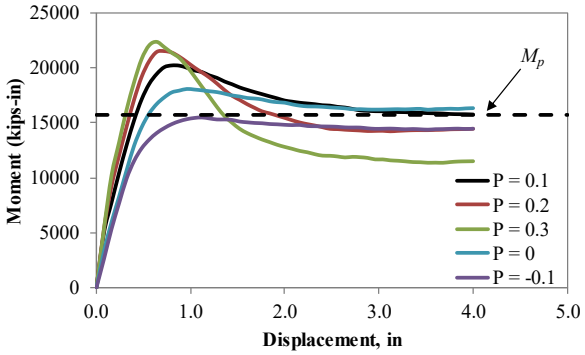


Fig. 9 - Effect of axial load ratio on the monotonic moment-displacement curve from analysis

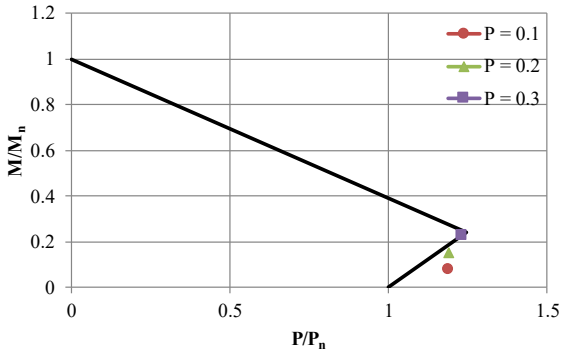
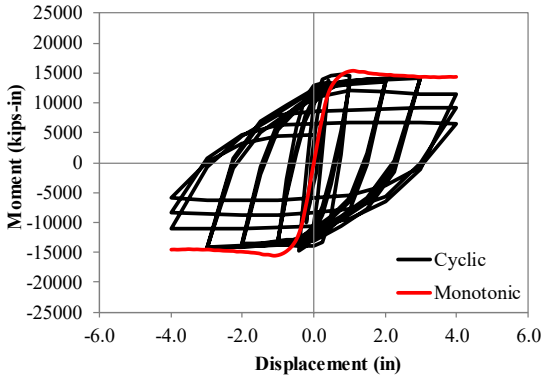


Fig. 10 - Comparisons of the analytical beam-column strength of CPSW with the beam-column interaction curve calculated using AISC 360-16

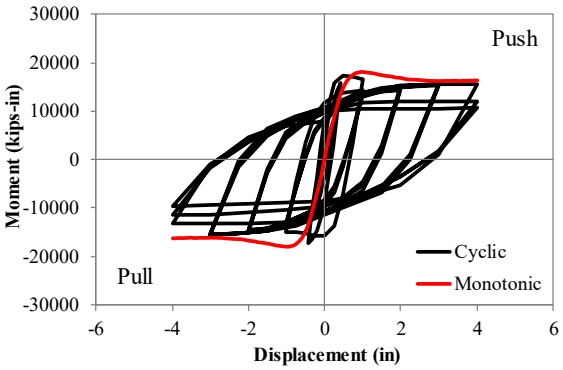
Cyclic analysis and behavior

Five cyclic analyses were conducted to investigate the effect of the axial load ratio on the cyclic behavior of CPSW. The loading history as shown in Figure 7 was applied. The analyses indicated that the failure modes of all walls are similar, i.e., local buckling of the flanges and webs occurred at the base, followed by the fracture at these locations. Table 3 summarizes the loading cycles during which local buckling and fracture occurred. As shown, increasing the axial load ratio does not have significant effect on the initiation of local buckling; however, it delays the initial fracture. When the axial load ratio is less than or equal to 0.1, initial fracture occurred at the first 4.0Δy push and pull cycle; when the axial load ratio is 0.2, initial fracture occurred at the third 4.0Δy push cycle; when the axial load ratio is 0.3, there is no fracture.

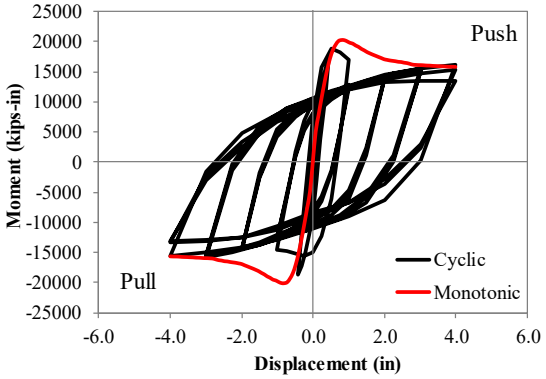
Figure 11 shows the cyclic load-displacement behavior of the walls. As shown, the cyclic behavior of all walls was very good during the elastic cycles. There were no local buckling distortion, bulging or fracture during elastic loading cycles. During the first $1.0\Delta_y$ push and pull cycle, local buckling developed at the base in the top and bottom flanges. After that, local buckling propagated into the webs. The local buckling increased significantly during the 3.0 and 4.0 Δ_y loading cycles.



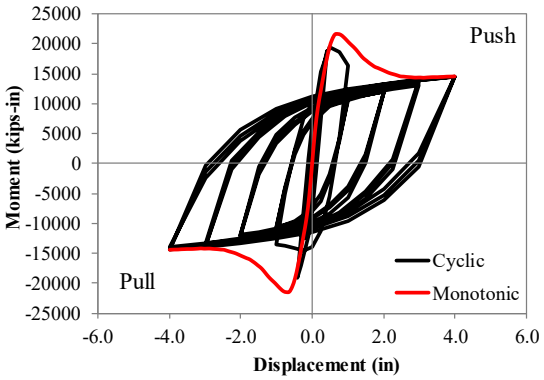
(a) Axial load ratio = -0.1



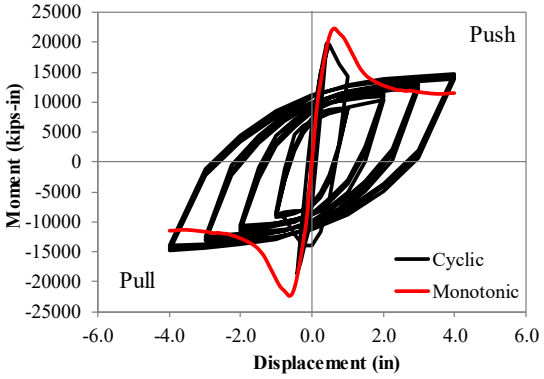
(b) Axial load ratio = 0



(c) Axial load ratio = 0.1



(d) Axial load ratio = 0.2



(e) Axial load ratio = 0.3

Fig. 11 - Effect of axial load ratio on the cyclic moment-displacement behavior from analysis

When the axial load ratio is less than or equal to 0.2, the local buckling resulted in the fracture of flange and web plate in the $4.0\Delta_y$ loading cycles. After $3.0\Delta_y$ loading cycles, the local buckling resulted in the loss of strength of 3.4%, 10%, 17.2%, 29%, and 33.7% for walls with the axial load of -0.1, 0, 0.1, 0.2, and 0.3, respectively. This indicates that ductility decreases as the axial load ratio increases (the wall is assumed to remain its ductility if its strength loss is less than or equal to 20%). Figure 11 also includes the monotonic load-displacement behavior from the monotonic analysis. As shown, the monotonic load-displacement curve is similar to the envelope obtained from the cyclic analysis.

Table 3 - Summary of loading cycles during which local buckling and fracture occurred (CPSW with different axial load ratio)

No.	Axial load ratio	First appearance of local buckling	Initial Fracture
1	-0.1	Bottom flange at the base, first $1.0\Delta_y$ pull cycle	Bottom flange at the base, first 4.0Δy push cycle
2	0	Top flange at the base, first $1.0\Delta_y$ push cycle	Top flange at the base, first $4.0\Delta_y$ pull cycle
3	0.1	Top flange at the base, first $1.0\Delta_y$ push cycle	Top flange at the base, first $4.0\Delta_y$ pull cycle
4	0.2	Top flange at the base, first $1.0\Delta_y$ push cycle	Top flange at the base, third $4.0\Delta_y$ push cycle
5	0.3	Top flange at the base, first $1.0\Delta_y$ push cycle	No fracture

CONCLUSIONS

Concrete filled – composite plate shear walls (CF-CPSW) are being evaluated as an alternative to reinforced concrete shear walls in high rise building construction. This paper presented the preliminary results from the first sub-task of an extensive research program focusing on the lateral load (wind and seismic) behavior, analysis and design of coupled CF-CPSW core wall structures for high rise buildings. A tentative test matrix focused on evaluating the lateral load behavior of individual CF-CPSWs was proposed and pre-test analyses were conducted using 3D finite element models accounting for the complexities of behavior including local buckling, concrete crushing, steel yielding and fracture, etc.

The results from the pre-test analyses were used to detail the specimens in the tentative test matrix. These results indicate that: (i) the lateral load behavior and strength of CF-CPSW specimens will be governed by their in-plane flexural response and plastic moment capacity. (ii) The plastic moment capacity and the axial load-moment capacity (P-M) interaction of CF-CPSW specimens can be estimated using provisions for filled composite members in AISC 360-16. (iii) Increasing the thickness of the flange plate increases the flexural strength, but does not have a significant influence on ductility. (iv) Increasing the axial load level increases the flexural stiffness and strength, but reduces the ductility, particularly for axial load levels greater than 20%. (v) The failure modes of specimens subjected to cyclic loading will be similar, i.e., local buckling of the flange and web at the base, followed by steel plate fracture at these locations.

ACKNOWLEDGMENTS

The research project discussed in this paper has been funded by the Charles Pankow Foundation and American Institute of Steel Construction. The opinions and findings discussed in this paper represent the preliminary thoughts of the authors alone.

REFERENCES

ABAQUS. (2016). *ABAQUS Version 6.16 Analysis User's Manuals*. Providence, RI, USA: Dassault Systemes Simulia Corporation.

AISC 341-16. (2016). *Seismic provisions for structural steel buildings*. Chicago, IL, USA: AISC.

AISC 360-16. (2016). *Specification for structural Steel buildings*. Chicago, IL, USA: AISC.

Alzeni, Y., & Bruneau, M. (2014). Cyclic inelastic behavior of concrete filled sandwich panel walls subjected to in-plane flexure. In *10th National Conference on Earthquake Engineering* (pp. 1–7). Anchorage, Alaska, USA: Frontier of Earthquake Engineering.

El-Tawil, S., Harries, K. a., Fortney, P. J., Shahrooz, B. M., & Kurama, Y. (2010). Seismic design of hybrid coupled wall systems: state of the art. *Journal of Structural Engineering*, *136*(7), 755–769.

Kurt, E. G., Varma, A. H., Booth, P., & Whittaker, A. S. (2016). In-plane behavior and design of rectangular SC Wall piers without boundary elements. *Journal of Structural Engineering*, *142*(6), 4016026.

Lai, Z., & Varma, A. H. (2017). Seismic behavior and modeling of circular concrete partially filled spirally welded pipes (CPFSWP). *Thin-Walled Structures*, *113*, 240–252.

Ollgaard, J. G., Slutter, R. G., & Fisher, J. W. (1971). Shear strength of stud connectors in lightweight and normal weight concrete. *AISC Engineering Journal*, (Aprl).

Ramesh, S. (2013). *Behavior and design of earthquake–resistant dual–plate composite shear wall systems [Dissertation]*. Purdue University.

Seo, J., Varma, A. H., Sener, K., & Ayhan, D. (2016). Steel-plate composite (SC) walls: In-plane shear behavior, database, and design. *Journal of Constructional Steel Research*, *119*, 202–215.

Varma, A.H., Malushte, S., Lai, Z. (2015). "Modularity and Innovation Using Steel-Plate Composite (SC) Walls for Nuclear and Commercial Construction." *Proceedings of the 11th International Conference: Advances in Steel-Concrete Composite Structures (ASCCS)*, At Beijing, China, Dec. 2015, http://dx.doi.org/10.13140/RG.2.1.4665.4804

IN-PLANE CYCLIC TESTING OF CONCRETE FILLED SANDWICH STEEL PANEL WALLS WITH AND WITHOUT BOUNDARY ELEMENTS

Michel Bruneau
SUNY Distinguished Professor, University at Buffalo
Department of Civil, Structural, and Environmental Engineering, 212 Ketter Hall,
Buffalo, 14260, NY, USA
Email: bruneau@buffalo.edu

Yasser Alzeni
Assistant Professor, Alexandria University
Department of Structural Engineering
Alexandria, Alexandria Governorate 11432, Egypt
Email: yasser_alzeni@azizmi.com

ABSTRACT

This paper presents results from an experimental study investigating the in-plane cycling inelastic flexural behavior of Concrete Filled Sandwich Steel Panel Walls (CFSSP-Walls) that are composed of two steel skin plates interconnected by tie bars, with the space between the skin plates filled with concrete. CFSSP-Walls with and without circular boundary elements were tested. All of the walls were able to exceed their theoretical plastic moment capacity, calculated assuming a full plastic stress distribution of the cross section. The tested specimens exhibited stable ductile behavior up to 3% drift (and beyond in some conditions). Local buckling of the steel skin led to minor degradation in flexural strength. Fracture of the skin plates eventually developed as the ultimate failure mode.

INTRODUCTION

Concrete-Filled Sandwich Steel Panel Walls (CFSSP-Walls) are being considered by practicing engineers for construction in seismic regions of the USA, including as ductile flexural walls in high-rise applications. Their appeal is that they are envisioned to be highly ductile, redundant, of high strength, and easy and rapid to construct (overcoming the congestion of reinforcement details that can be encountered in ordinary reinforced concrete walls, and because the steel shell can be used as formwork). Beyond accelerated construction and ductile seismic performance, use of a CFSSP-Wall instead of a conventional reinforced concrete wall in building applications can translate into thinner walls with resulting greater leasable space. However, at the time this research was conducted, there was a critical lack of knowledge on the in-plane cyclic inelastic behavior of such CFSSP-Walls, which, in spite of all the positive attributes of the structural system, was an impediment to implementation in seismic regions.

To help understand the in-plane flexural behavior of such walls, in the current study, four specimens with and without boundary elements were subjected to cyclic inelastic loading. Performance was evaluated in terms of ductility and lateral load carrying capacity. The results of this experimental work are presented here.

Note that at the time this research was conducted, the terminology “walls with boundary elements” was used by the authors to refer to the presence of a distinct structural shape wider than the rest of the wall (namely, a full HSS here), by opposition to the case where a simple closure plate (square or half-circular) is used at the end of the wall (referred to here as “walls without boundary elements”). This terminology is kept here to ensure consistency with the information contained in the full research report (Alzeni and Bruneau 2014), because changing the names of specimens and terminology here would only serve to confuse the readers referring to this report. However, the AISC 341-16 seismic provisions published more recently use the term “boundary elements” to encompass both types of walls tested here, and the term walls “without boundary elements” refer to those that do not have such cap plates (built, for example, using formwork at their ends to contain the concrete within the wall during the pour).

LITERATURE REVIEW

The type of composite wall considered here consists of sandwich steel panels filled with concrete. These have been used in many applications. Past research on that structural system has largely focused on walls subjected to out-of-plane loading and/or non-cyclic behavior (e.g., Wright (1998), Hossain and Wright (1998)). Sener et al (2015) summarized the experimental data base of out-of-plane flexural tests conducted on SC walls under different loading configurations, and different design parameters. Also, some of the past research has been conducted in relation to the Bi-Steel sandwich system that has been developed as flooring system, beams, columns, and walls system used in some non-seismic regions (Bowerman et al. 1999).

Limited research has been conducted on the in-plane inelastic cyclic response of CFSSP-Walls. Eom et al. (2009) conducted in-plane cyclic testing of three individual flexural walls and two coupled walls having rectangular and T-shaped cross-sections, representing 1/3 and 1/4 scale models of the first stories of a 30 story prototype. The tested specimen showed premature failure in the corner welding of the rectangular section and different methods were used to strengthen the walls, which were retested and (in some cases) able achieve estimated peak loads and develop reasonable ductile performance. Epackachi et al (2014) tested four CFSSP-Walls having an aspect ratio of one, but having no cap plate at the cross-section ends. Under in-plane cyclic loading, the tested walls were able to reach their yield moment (equal to M_y) and failed in a flexural mode, while the hysteretic loops exhibited significant pinching. Kurt et al (2016) tested eight CFSSP-Walls without boundary elements under cyclic lateral loads, where the walls had an aspect ratio between 0.6 and 1.0; the lateral load capacity of the tested walls were governed by the in-plane flexure capacity of wall cross section at the base. Seo et al. (2016) used a mechanics based model (MBM) to present the fundamental in-plane shear force-shear strain of the SC walls, the results were compared to the results of the experimental data base and an estimated value for the strength reduction factor was introduced.

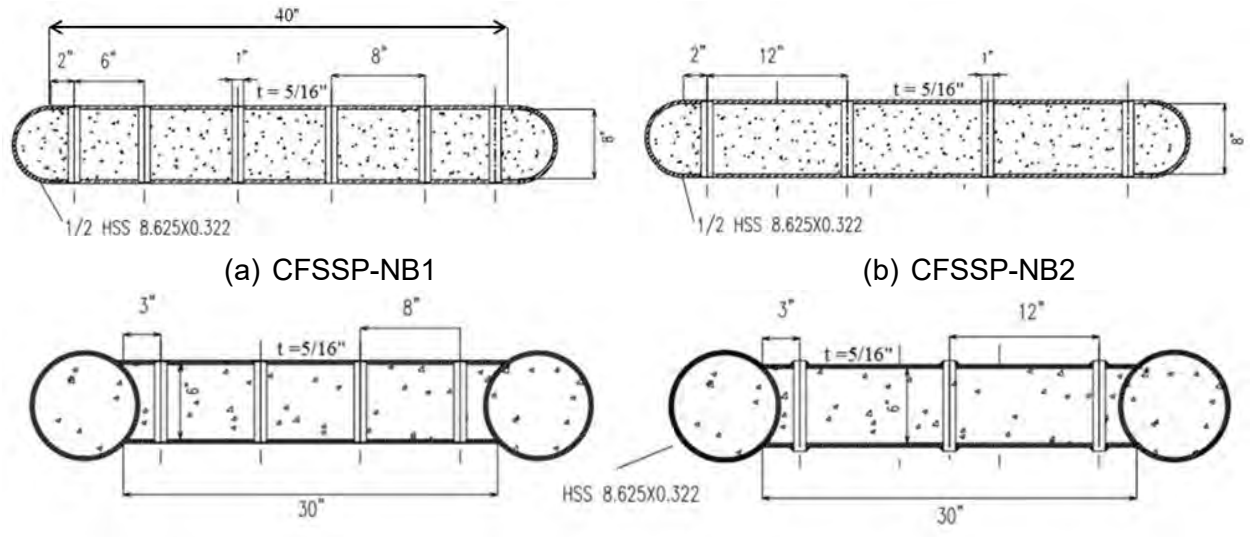
Most importantly, at the time the tests reported below were conducted (in 2012), there existed only limited data available on the inelastic cyclic behavior of flexural CFSSP-Walls.

EXPERIMENTAL PROGRAM

Four large scale CFSSP-Wall specimens were designed as cantilever walls fixed to a reinforced concrete footing. The CFSSP-Walls tested as part of this research program were meant to be representative of implementation in commercial buildings as cantilevering walls surrounded by gravity frames, where the floor is tied to the walls through seismic collectors. Note that the findings from this research cannot be directly extrapolated to designs for walls having T or C

plan cross-section, or other more complex configurations, for which additional research is recommended.

The tested specimens were divided over two groups, with cross-section properties shown in Figure 1. In the first group, identified by the label NB, the CFSSP-Walls have no boundary elements and their cross section is composed of double web skin plates having thickness, *t*, of 8 mm (5/16") and web width, *b*, of 1016 mm (40"), connected through circular tie bars spaced equally in both horizontal and vertical direction at a spacing, *S*, equal to 203.2 mm (8") and 304.8 mm (12") for specimens CFSSP-NB1 and CFSSP-NB2 respectively, corresponding to *S/t* ratio of 25.6 and 38.4. The cross-section is closed at its ends by half HSS sections; these were used instead of square ends in order to avoid premature failure of the cross section's corner welds due to concentration of stresses that has been observed in prior research on composite rectangular sections (e.g., Eom et al. 2009; El Bahey and Bruneau 2011; Ge and Usami 1996; Usami and Ge 1994; Kawashima and Unjoh 1997). Both specimens of Group NB have the same outer dimensions, plate thicknesses, and total width and height. Specimen CFSSP-NB1 and CFSSP-NB2 have a total width, *W*, 1235.1 mm (48.625") (skin plates plus two half-HSS 8.625×0.325) and total thickness, t_t, of 219.1 mm (8.625"). For specimens in Group NB, the tie bars were welded to the web skin plate using plug welding: tie bars having a total length equal to (t_t - t_s) were positioned to span the distance between the steel web plates center lines, and the remaining half thickness of the plate on each side was filled with welding material to create the plug weld. The tie bars had a diameter of 25.4 mm (1")and were designed to remain elastic throughout the test.



(a) CFSSP-NB1 (b) CFSSP-NB2

(c) CFSSP-B1 (d) CFSSP-B2

Figure 1. Tested specimens of CFSSP Walls

The second group of tested specimens, identified by the label B, are CFSSP-Walls having boundary elements (i.e., complete structural shapes) consisting of concrete filled round HSS section. The walls' cross section consists of HSS columns and of double web skin plates having a width, *L*, of 762 mm (30"), a thickness, t_s, of 8 mm (5/16"), and connected through tie bars spaced equally in both horizontal and vertical direction at a spacing, *S*, of 203.2 and 304.8 mm (8" and 12") for specimens CFSSP-B1 and CFSSP-B2, respectively, corresponding to *S/t* ratios of 25.6 and 38.4 (i.e., the same values used for the NB specimens). The Specimen CFSSP-B1 tie bars were connected to the web plate using plug welding as described for the Group NB

specimens. However, for specimen CFSSP-B2, tie bars were assembled differently. Bars having a total length of (t_t+2t_s) where used. As such, when installed, the tie bars protruded a distance of 8 mm (5/16") beyond the steel web plate on each side, and were fillet welded to the web steel plates.

The approach taken to determine the vertical and horizontal spacing of the tie bars, w_1 and w_2, respectively, such as to similarly prevent the skin plates from experiencing local buckling before yielding, was to consider the plate as similar to the case where a compression flange in concrete filled section is subjected to uniform compression and have simply supported edges for which Wright (1995) showed that the *S/t* ratio should be less or equal to 37 to ensure ductile behavior. Also, as an alternative and simpler approach, considering the plate as an idealized fixed ends column and setting the critical stress equal to the yield nominal yield stress of the web plate, a *S/t* value of 43 was obtained. Note that the limit would be 25 according to Zhang et al. (2014) based on their review of the effect of shear connectors design on composite action in such walls and the maximum steel plate slenderness needed to prevent local buckling of the steel plates prior to yielding.

For the CFSSP-Walls tested in this research, for a maximum 304.8 mm (12 in.) spacing of tie bars and web plates thickness of 7.94mm (5/16 in.), the corresponding maximum *S/t* ratio used for the specimens was 38.4. This is approximately equal to the above value for plates having simply supported edges.

The diameter of the tie bars should be selected such that they can provide adequate stiffness to control local buckling of the web plates, resist the shearing force transferred between the reinforced concrete core and the steel skin plate, and have adequate strength to resist the tensile force that develops during formation of the plastic mechanism created during inelastic buckling of the web skin plate.

Tensile force in the tie was calculated from the yielding of the web skin plate during buckling after the CFSSP-Wall has attained its plastic moment capacity. When the web plates buckle, plastic hinging of the skin plates forms as shown in Figure 2. Due to formation of this plastic mechanism, plastic moment capacity of the plates is reached at the plastic hinges locations. Although no shear forces proper develop at the end of each buckled segment, and analogy can be made to convert the axial forces in equilibrium into equivalent shear forces that induce tension forces on the tie bars. Accordingly, using this approximation, the minimum diameter of the tie bar was calculated by the following equation:

$$d_{\min} = 1.59 t_s \sqrt{\left(\frac{w_2}{w_1}\right)\left(\frac{F_{y,plate}}{F_{y,tie\cdot bars}}\right)}$$

Ties diameter was then selected to be conservatively greater than the value obtained by this equation, as no guidance existed at the time the specimens were designed and the authors wished to prevent tie-failure in this experimental program (past experiments have showed the undesirable rapid wall strength and stiffness degradation (e.g., Ramesh et al. 2013) that occurs when ties fail). Note that an adapted version of this equation eventually provided part of the tie design requirements specified in Section H7 of AISC-341-16. The welding between the tie bars and the skin plates (either plug welds or fillet welds, depending on the specimen) was sized to resist the same calculated tensile force in the tie bars.

The concrete used for the four specimens was self-consolidating regular strength (27.6 Mpa; 4 ksi) concrete (SCC), with a slump of 76.2 mm. The steel used for the HSS was ASTM A252 Gr 3 and for the steel web plates was ASTM A572 Gr.50. Detailed information on material

properties obtained from steel coupons and concrete cylinders are provided in Alzeni and Bruneau (2014).

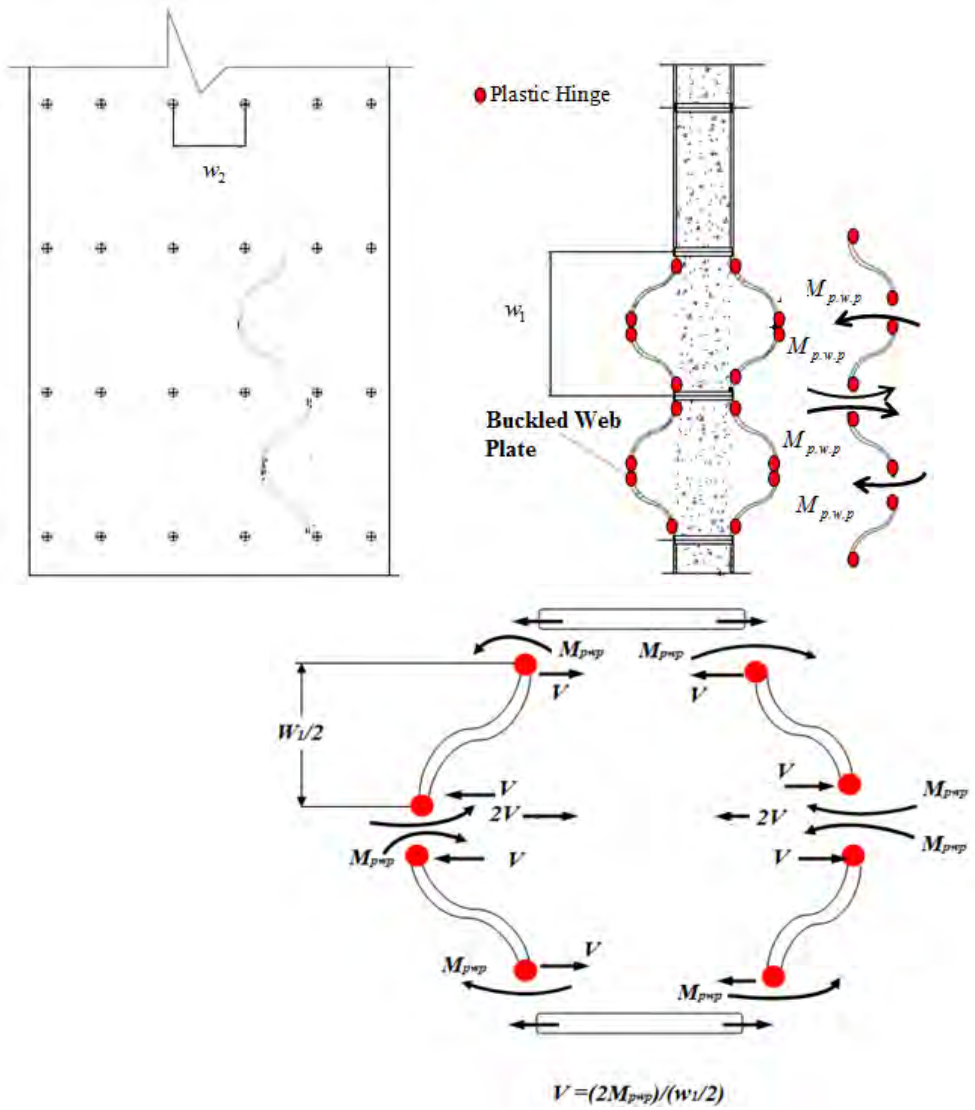


Figure 2. Forces exerted on tie bars due to web local buckling

TEST SET-UP AND LOADING PROTOCOL

The tested specimens were 3048 mm (120”) tall cantilever type walls (providing an aspect ratio of 2.5) fixed to a reinforced concrete base, itself connected to the strong floor of the lab using pre-tensioned DYWIDAG bars. Details on the wall connection to the footing and actuator connection details are provided in Alzeni and Bruneau (2014). Lateral loading was applied at the top of the specimens by a servo-controlled actuator. Two bracing trusses were used to avoid out-of-plane motion of the wall. Specimens were subjected to quasi-static displacement cycles following the ATC 24 loading protocol, with three displacement cycles at each displacement step, up to a displacement equal to three times the yield displacement, and two cycles at each displacement magnitude after that. The yield displacement, δ_y, was initially defined here as the displacement at which the extreme steel fibers of the CFSSP-Wall skin plate starts to yield. The values of δ_y were obtained from push over analyses done using the

finite element models (in ABAQUS), considering a fixed base model. Information on calibration of the finite element model is provided in Alzeni and Bruneau (2014). The specimens were subjected to cyclic displacements per this protocol until substantial fracture in the steel web plates and the HSS part of the CFSSP-Wall specimens occurred.

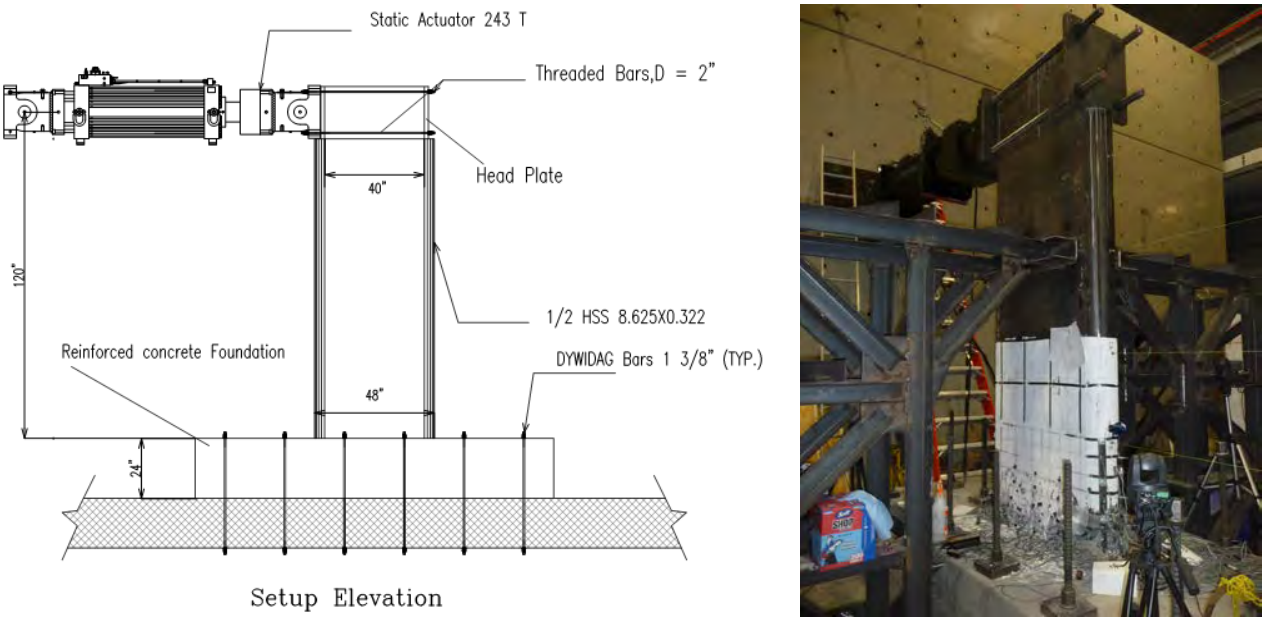


Figure 3: Test set-up

EXPERIMENTAL RESULTS

Only minor differences in response were observed in the cycling inelastic response of the 4 specimens. Observations are summarized here for specimen CFSSP-NB1, representative of typical behavior. Thorough description of the detailed hysteretic response of all specimens is presented in Alzeni and Bruneau (2014, 2017).

At 0.6% drift, strain gages on the specimen indicated the onset of yielding. Some flaking of white wash paint was noted, especially in parts of the HSS. There was no visual evidence of local buckling. At 1.2% drift the entire base of the wall seemed to be yielding, but there was still no observed local buckling. Local buckling was first observed at 1.8% drift. This buckling was located on the web plate of the specimen, on one side of the wall, between the first and the second row of tie bars from the base. The half HSS part of the section did not buckle at this drift level. At 2.4% drift, the half HSS end of the cross-section developed local buckling at a location equivalent to between the first and the second row of ties above the footing (Figure 3). Minor fractures appeared in some of the plug welds on the first row of tie bars.

At 3%, some of the tie bars plug welds fractured around the perimeter of the tie bars. During cycling, fractures also started to propagate from the circumference of the first tie bar in the first row towards the half HSS. The crack propagated by about 3/4 of an inch. At 3.6% drift, a first crack developed in the HSS part of the cross-section, on the face of the buckled wave in the half HSS. Testing stopped after a few cycles at this 3.6% drift value, as the wall fractured over 18 inches of its base, in a plane passing through the center line of the first row of tie bars (Fig. 4).



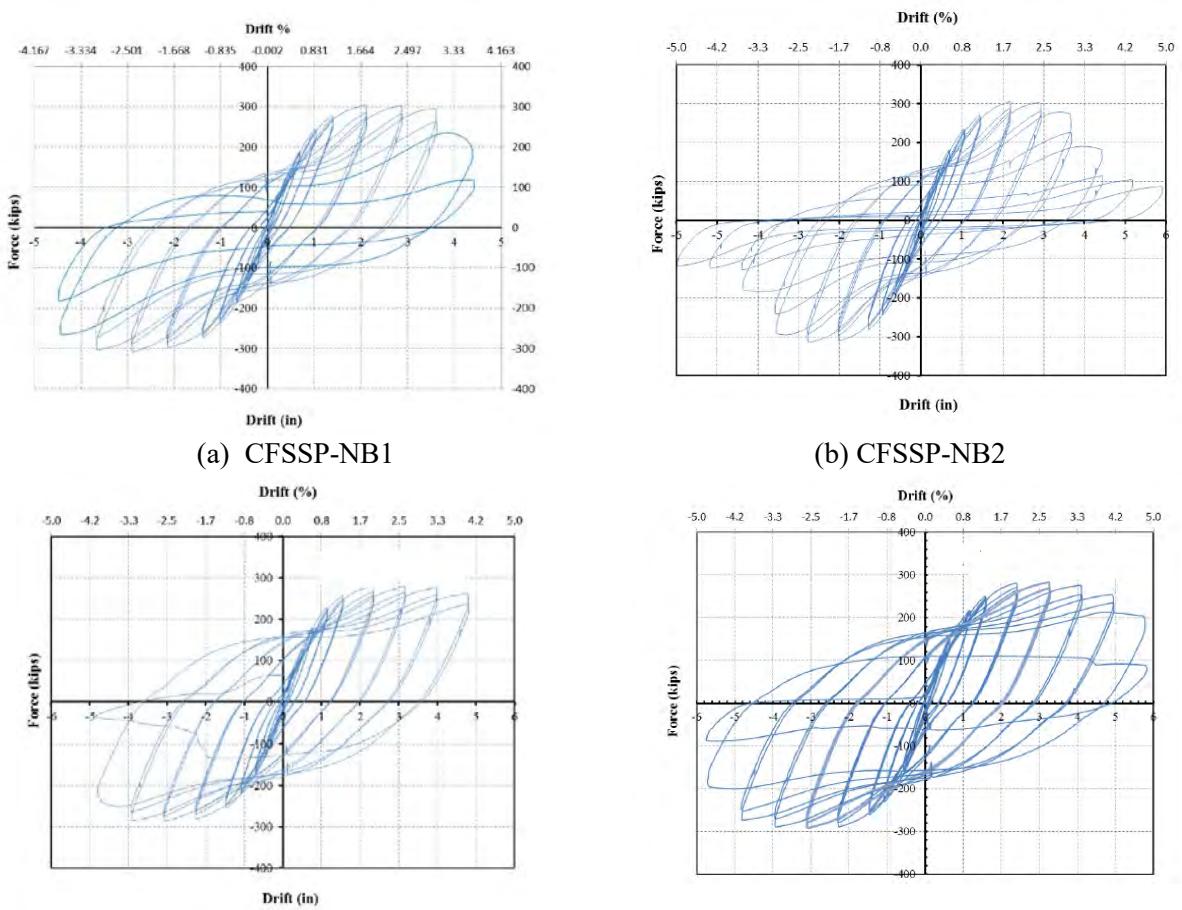
Figure 3: The Local Buckling of the HSS Part at 2.4% Drift



Figure 4: Fracture of the CFSSP-NB1 Specimen East Side at 3.6% Drift

The experimentally obtained lateral load versus top displacement relationships for all specimens are shown in Figure 5. The corresponding yield displacement, δ_y, maximum displacement, maximum strength compared to M_p calculated based on coupon values, and dissipated energy are summarized in Table 1. The displacement ductility reported in that Table was calculated based on a definition of δ_y established by considering an equivalent bilinear system. The maximum displacement was defined as the post-peak displacement where the strength degrades to 80% of the peak value. Results indicate that the wall exhibited ductile behavior up to significant drifts (considering that walls are stiff structural elements expected to develop relatively small drifts during an earthquake). Experimental results (in Table 2) also indicated that all wall tested were able to develop their plastic moment computed using cross-section analysis and actual material properties.

Note that for the B-type specimens, larger drifts were required to produce the same limit states. Significantly, for the specimen CFSSP-B2 having filled-welded ties: cracks initiating along the plug welds was first observed at 3.3% drift, with major fracture and progressive loss of strength developing around 4% drift.



(a) CFSSP-NB1 (b) CFSSP-NB2

(c) CFSSP-B1 (d) CFSSP-B2

Figure 5: Experimentally Obtained Hysteretic Behavior of Specimens

Table 1. Evaluation of Test Data

Specimens	*Max* Δ_u	*Max.drift* Δ_u/h (%)	*Yield.displ.* Δ_y (mm)	*Ductility* Δ_u/Δ_y	$\mu_{,(1^{st}\ yield)}$ Φ_{max}/Φ_{y1}	$\mu_{,(bi\text{-}linear)}$ Φ_{max}/Φ_{yb}	*Dissipated Energy* (kN-m)
CFSSP-NB1	104.1	3.4%	20.3	5.13	14.44	7.74	1349
CFSSP-NB2	93.2	3.0%	25.4	3.67	12.88	6.54	1821
CFSSP-B1	121.9	4.0%	22.9	5.33	14.98	8	1595
CFSSP-B2	127	4.16%	22.9	5.50	11.06	5.55	1965

***** At the point beyond M_{max} where strength has dropped to $0.8M_{max}$

Table 2. Load Carrying Capacity of the CFSSP-Walls

Specimens	*Max* M_{max} (kN-	*Estimated,* (kN-m)	*Ratio*	*Drift %* M_p	*Drift %* M_{max}
CFSSP-NB1	41330.9	36200.2	1.13	1.20	1.80
CFSSP-NB2	41352.2	36200.2	1.13	1.20	1.80
CFSSP-B1	38042.1	30998.2	1.22	1.0	2.0
CFSSP-B2	38749.2	30998.2	1.25	1.0	2.67

LOCAL BUCKLING AND FAILURE MODES

All specimens developed a similar ultimate behavior, with local buckling developing during ductile response while sustaining a lateral load with minimal strength degradation up to large drifts. Fracture in all specimens developed upon repeated cycles of local buckling of the steel web plate and of the HSS, and accelerated by fracture of the welding between the tie bars and skin plate. However, in all cases, the vertical weld between the steel webs and the (half or full) HSS sections remained intact. Note that, in all cases, the cracks that developed in the metal after the development of local buckling only propagated upon development of larger drifts. This made it possible for the specimens to survive up to the large drifts recorded. Arguably, whether the crack propagation behavior would be different under dynamic loading is unknown at this time and could be the subject of future research. However, evidence collected during large-scale experiments of moment-resisting connections that fractured during the Northridge earthquake (Bruneau et al. 2011) suggested that result from dynamic response might not be significantly different from that those from pseudo-static testing. Review of the videos recorded during the experiments showed that for Specimen CFSSP-B2, fracture started independently on the HSS at a different location, and that the wall would have failed at the same drifts even if fracture had not developed slightly earlier at the ties. This indicates that using a different welded or bolted detail for the tie bar to skin plate connection would not have significantly improved the behavior of the tested walls beyond what was obtained for specimen CFSSP-B2 (provided that the tie bars in all cases are designed to have adequate strength and stiffness).

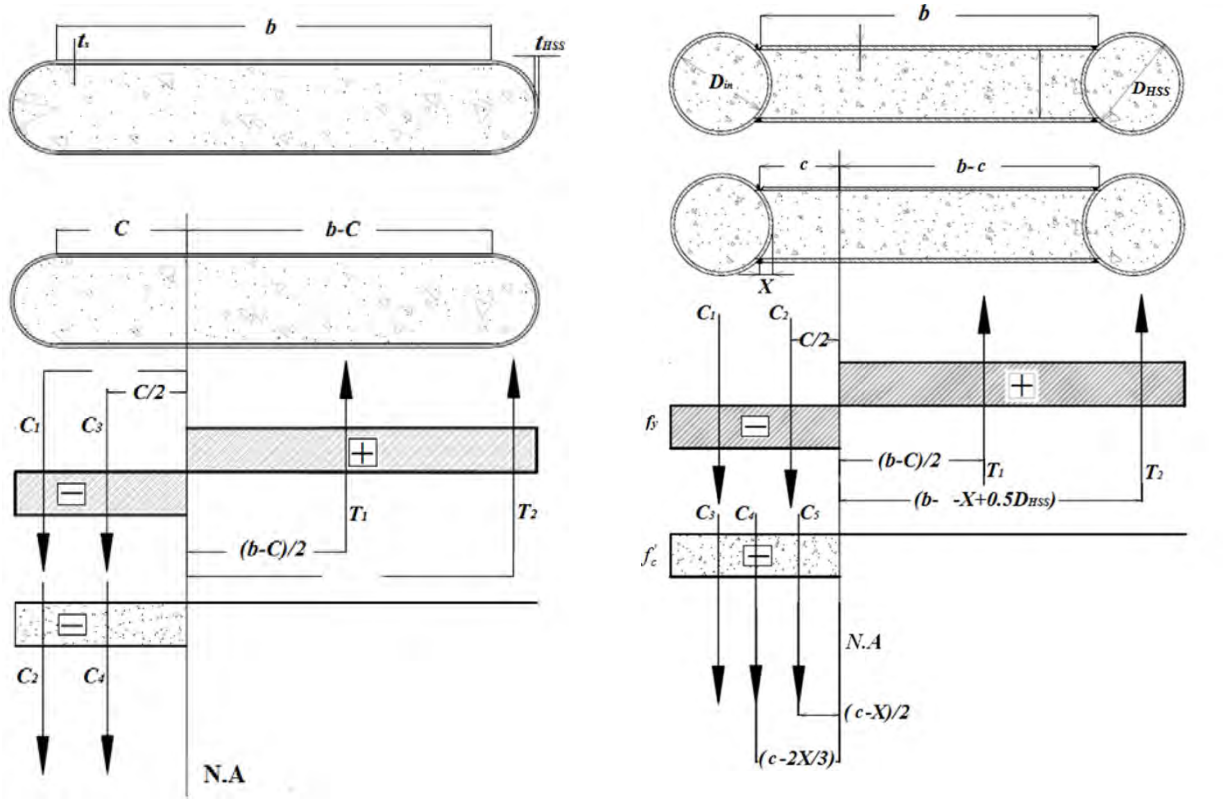
DUCTILITY EVALUATION

The four of the tested specimens were able to sustain their strength up to drifts higher than 3%. Displacement ductility ratio, μ_D, was calculated based on the ratio between the maximum

displacement, Δ_{max} (corresponding to 80% of the peak load) and the yield displacement, Δ_y (calculated from the idealized elastic-perfectly plastic envelope curve). Table 1 presents the ductility ratio values for the tested specimens. Displacement ductility exceeded 5.0, except for specimen CFSSP-NB2 which reached a value closer to 4 (i.e., 3.67). Also, curvature ductility for the tested specimens was also calculated from the experimentally recorded rotations, θ. Two curvature ductility values were calculated; one based on yield curvature defined from the idealized elastic-plastic envelope of the resulting moment curvature hysteretic curves; another based on yield curvature defined by first yield at the extreme fiber of the HSS boundary element. Further details on curvature calculation are presented in Alzeni and Bruneau (2014, 2017).

LOAD-CARRYING CAPACITY

The plastic moment capacity of the CFSSP-Walls was calculated using simple plastic theory principles, considering that the steel parts of the cross-section has fully yielded on both the tension and compression sides of the plastic neutral axis, and that the concrete on the compression side has reached fc' (neglecting any reduction factors), as shown in Figure 6. The closed-form expressions that were derived to calculate the corresponding plastic moments (Alzeni and Bruneau 2014, 2017) have been included in AISC-341-16, and match the stress blocks below. No factors were used to modify this calculated nominal plastic strength.



(a) CFSSP-NB cross-section (b) CFSSP-B cross-section

Figure 6. Schematic Diagram for stress distribution used to calculate M_p

SUMMARY AND CONCLUSIONS

Four cantilever CFSSP-Walls, with and without boundary elements, were tested in order to evaluate their seismic performance. In walls without boundary elements, the cross-section was closed at its ends by half HSS sections; full HSS columns were used at the ends of the cross-section for walls with boundary elements. HSS sections met the AISC compactness requirements for moderate ductility, and spacing of ties was limited to 38 times the web plate thickness.

The tested walls were able to attain their plastic moment capacity, M_p, and all exhibited a ductile behavior through cyclic excursions with limited strength degradation up to 3% lateral drift. Local buckling of the steel web plates and/or the round HSS part of the cross section occurred only after the tested walls reached their M_p. Behavior of the specimens having a closer tie spacing of 25 times the web plate thickness was not significantly different. Note that M_p here was calculated by assuming that the steel has reached F_y in tension and compression on respective sides of the wall's neutral axis, and that the concrete over the entire compressed part of the wall has reached f_c' (using values from steel coupons and concrete cylinders).

In all of the tested walls, fracture started in the steel web, after local buckling, typically initiating at the location of the connection between the tie bar and the web plate and propagating to the rest of the wall. In specimen CFSSP-B2, that had tie bars fillet welded to the skin plates and that exhibited an improved ductility, fracture simultaneously initiated in the HSS at a location independent from the steel web, which suggests that methods to connect the tie bars that would further delay fracture there would not, alone, enhance ductile behavior beyond that observed for specimen CFSSP-B2.

ACKNOWLEDGMENTS

This work was supported by the AISC (American Institute for Steel Construction), and Egyptian Ministry of Higher Education. However, any opinions, findings, conclusions, and recommendations presented in this paper are those of the authors and do not necessarily reflect the views of the sponsors.

REFERENCES

AISC-341 (2016). "Seismic Provisions for Structural Steel Buildings." American Institute of Steel Construction, Chicago, Illinois.

Alzeni, Y., Bruneau, M. (2014). "Cyclic Inelastic Behavior of Concrete Filled Sandwich Panel Walls Subjected to in plane Flexure." Technical report MCEER, 14-009, Buffalo, NY.

Alzeni, Y., Bruneau, M., (2017). "In-Plane Cyclic Testing of Concrete Filled Sandwich Steel Panel Walls with and without Boundary Elements", ASCE Journal of Structural Engineering, Vol.143, No.9.

Bruneau, M., Uang., C.M., Sabelli, R. (2011). "Ductile Design of Steel Structures - 2nd Edition", McGraw-Hill, New York, NY, 921p.

Bowerman, H., Gough, M., and King, C. (1999). "Bi-Steel Design and Construction Guide", British Steel Ltd, Scunthorpe, U.K.

El-Bahey, S., and Bruneau, M. (2011). "Bridge piers with structural fuses and bi-steel columns. I: Experimental testing." Journal of Bridge Engineering, 17(1), 25-35.

Eom, T.-S., Park, H.-G., Lee, C.-H., Kim, J.-H., and Chang, I.-H. (2009). "Behavior of double skin composite wall subjected to in-plane cyclic loading." Journal of Structural Engineering, 135(10), 1239-1249.

Epackachi, S., Nguyen, N.H.,Whittaker, A.S.,and Varma, A.H.(2014).”In-plane seismic behavior of rectangular steel-plate composite wall piers” Journal of Structural Engineering, 04014176(9), 1-9.

Ge, H. and Usami, T. (1996). ”Cyclic Tests of Concrete-Filled Steel Box Columns.” J. Struct. Eng., 122(10), 1169–1177.

Kawashima, K., Unjoh , S. (1997). “The Damage of Highway Bridges in the 1995 Hyogo-Ken Nanbu Earthquake and its Impact on Japanese Seismic Design”, Journal of Earthquake Engineering, Vol. 1, No. 3, Pp. 505-541

Kurt, E.G., Varma, A.H., Booth, P.N., and Whittaker, A., (2016). "In-plane Behavior and Design of Rectangular SC Wall Piers Without Boundary Elements." ASCE Journal of Structural Engineering, J. Struct. Eng. Vol. 142, Issue 6, 10.1061/(ASCE)ST.1943-541X.0001481, 04016026.

Hossain, K. A., and Wright, H. D. (1998). "Performance of profiled concrete shear panels." Journal of Structural Engineering, 124(4), 368-381.

Ramesh, S., Kreger, M.E., Bowman, M.D., (2013). “Behavior and Design of Earthquake-ResistantDual-Plate Composite Shear Wall Systems”, Report submitted to Charles Pankow Foundation, http://www.pankowfoundation.org/grants.cfm?prodonly=1 (project RGA#06-06).

Sener, K., Varma, A.H., and Ayhan, D. (2015). "Steel-Plate Composite SC Walls: Experimental Database and Design for Out-of-Plane Flexure." Journal of Constructional Steel Research, Vol. 108, May, pp. 46-59, Elsevier Science.

Seo, J., Varma, A.H., Sener, K., and Ayhan, D. (2016). "Steel-Plate Composite (SC) Walls: In-Plane Shear Behavior, Database, and Design." Journal of Constructional Steel Research, Elsevier Science, Volume 119, Pages 202-215.

Usami, T. and Ge, H. (1994). ”Ductility of Concrete-Filled Steel Box Columns under Cyclic Loading.” J. Struct. Eng., 120(7), 2021–2040.

Wright, H. (1995). "Local stability of filled and encased steel sections." Journal of Structural Engineering, 121(10), 1382-1388.

Wright, H. (1998). "Axial and Bending Behavior of Composite Walls." Journal of Structural Engineering, 124(7), 758-764.

Zhang, K., Varma, A.H., Malushte, S., and Gallocher, S. (2014). "Effects of Shear Connectors on the Local Buckling and Composite Action in Steel Concrete Composite Walls." Nuclear Engineering and Design, Special Issue on SMiRT-21 Conference, Vol. 269, pp. 231-239, Elsevier Science.

Cyclic Shear Behavior of Steel-Plate Composite Walls for High-Rise Buildings

Xiaodong JI[1], Xiaowei CHENG[2], Xiangfu JIA[3]

[1]Tsinghua University, Beijing 100084, CHINA ,E-mail: jixd@mail.tsinghua.edu.cn
[2]Tsinghua University, Beijing 100084, CHINA, E-mail: cxw15@mails.tsinghua.edu.cn
[3]Tsinghua University, Beijing 100084, CHINA, E-mail: jiaxiangfu@foxmail.com

ABSTRACT

Steel-plate composite walls are composed of steel plate with reinforced concrete encasement on both sides (referred to as “single-plate composite (SPC) walls”) or a concrete infill sandwiched in between two steel faceplates (referred to as “double-skin composite (DSC) walls”). This paper presents a series of experimental tests, including 2 SPC and 3 DSC wall specimens, conducted to investigate cyclic shear behavior of the composite walls used for high-rise buildings. All wall specimens had a shear-to-span ratio of 1.2, and were designed with a reinforcement ratio of approximately 6.0%. The specimen was designed with flange walls to enforce in-plane shear failure in the web wall. The test results indicate that the DSC walls had the shear deformation capacity 20% larger than the counterpart SPC walls, as the faceplates prevented spalling of crushed concrete. In addition, shear strength design formulas specified in various codes are verified using a large volume of test data.

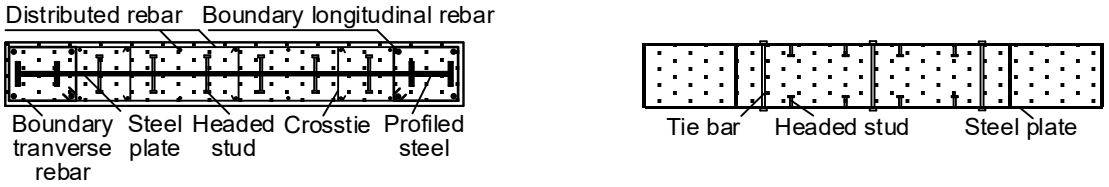
Keywords：Composite walls; Seismic applications; Experimental; Cyclic shear behavior; Shear strength; Design formulas

INTRODUCTION

With quick urbanization in past two decades, a large number of high-rise buildings have been constructed in China. Most of the super-tall buildings adopt core wall-frame-outrigger system or core wall-mega frame system, where the core walls carry a large portion of base shear forces and overturning moments induced by earthquake actions. To meet the extremely large shear force demand and ensure the flexural ductility of the walls in the lower stories, steel-plate composite walls are developed as a promising alternative to reinforced concrete (RC) walls.

Two types of steel-plate composite walls have seen increasing use for high-rise buildings in China. As shown in Figure 1, the first type is composed of steel plate with reinforced concrete encasement on both sides, referred as “single-plate composite (SPC) walls”, and another type consists of a thick concrete infill sandwiched by two steel faceplates on the exterior surfaces, referred as “double-skin composite (DSC) walls”. Use of steel plate significantly increases the

shear strength of the walls, and thus translates into thinner walls with resulting greater usable space. A statistical analysis of steel-plate composite walls for a large number of high-rise buildings indicates that most composite walls are designed with a relatively high steel reinforcement ratio of 6 to 8%. Besides, those walls are usually subjected to a high axial force ratio due to large gravity force of super-tall buildings.



(a) Single-plate composite (SPC) wall (b) Double-skin composite (DSC) wall

Fig. 1 Typical cross-section of steel-plate composite walls

Recently, a number of experimental tests and numerical studies (e.g., Eom et al. 2009, Ji et al. 2013, Nie et al. 2013, Wang et al. 2017) have been conducted on the steel-plate composite walls for high-rise buildings. While these studies focus on the in-plane flexural behavior of slender composite walls, experimental data of the cyclic in-plane shear behavior of the composite walls used for high-rise buildings is limited.

This paper presents a series of quasi-static tests used to examine the cyclic shear behavior of steel-plate composite walls. Section 2 describes the experimental program. The test results are detailed in Section 3. Finally, this study evaluates design equations for calculating the in-plane shear strength of the composite walls from various codes by comparing them with test data.

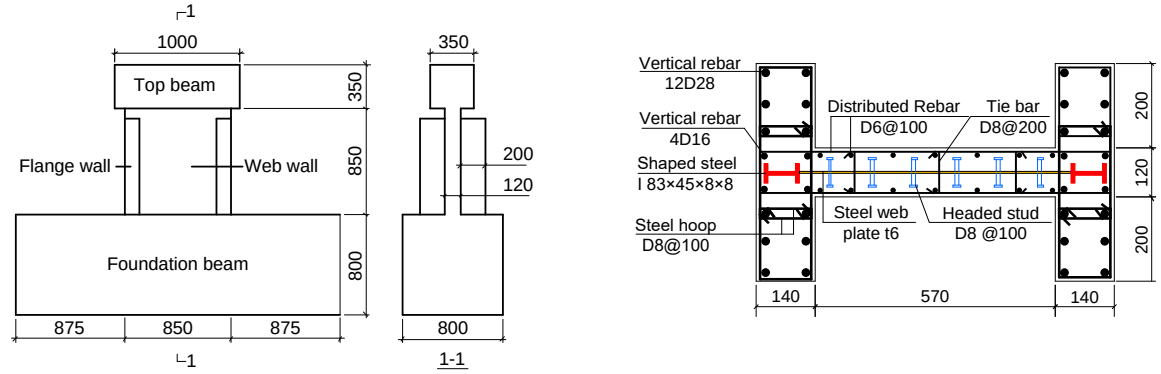
EXPERIMENTAL PROGRAM

TEST SPECIMENS

The test specimens were designed to represent the structural walls in the lower stories of a high-rise building, and were fabricated at approximately one-third scale to accommodate the capacity of the loading facility. A total of five wall specimens were tested, including two single-plate composite walls (labeled as SPCW1 and SPCW2) and three double-skin composite walls (labeled as DSCW1 through DSCW3). The specimens were designed with an I-shaped section, where the web wall primarily resists in-plane shear and the flange walls resist the overturning moment. The in-plane flexural strength of the wall specimen was designed to significantly exceed its in-plane shear strength, which enforces pure in-plane shear behavior and failure in the web wall. Figure 2 shows the overall geometry, structural layout, and reinforcement details for the specimens. The specimens were cast integrally with a large foundation beam and a loading beam. As shown in Figure2(a), the flange walls were intentionally disconnected from the top beam to limit the possible shear contribution induced by the secondary bending moments of the flange walls and for easy installation of loading threaded bars. All steel plates and rebar were securely anchored to the

foundation beam, and those in the web wall were extended into the top beam.

As shown in Figure 2(b), the SPC web wall have steel plate thickness, t_p, equal to 6 mm for the specimens. The steel reinforcement ratio, t_p/T, of the SPC web wall is equal to 4.9%, where T denotes the thickness of web wall. The steel plate was connected to the I-shaped steel embedded at its two edges by complete-joint-penetration (CJP) groove welds. Headed studs (diameter = 8 mm, length = 40 mm) were used to provide shear transfer between steel plate and RC encasement. D6 (diameter = 6 mm) steel rebar were placed as horizontally and vertically distributed reinforcement of the wall web with a spacing of 100 mm, corresponding to a reinforcement ratio of 0.9%. Thus, the total steel reinforcement ratio of SPCW web wall was 5.8%. Heavy longitudinal reinforcement was intentionally designed in the boundary elements and flange walls to ensure large flexural strength of the wall specimens. The boundary transverse rebar and web crossties were threaded through holes on the steel plate.



(a) Overall geometry dimension

(b) Cross section of SPCW1 & SPCW2

(c) Cross section of DSCW1& DSCW2

(d) Cross section of DSCW3

Fig. 2 Geometry and reinforcement of wall specimens

The DSC web wall had faceplate thickness, t_p, equal to 4 mm for those specimens. The steel reinforcement ratio, $2t_p/T$, of the DSC web wall was equal to 6.4%. As shown in Figure 2(c), Specimens DSCW1 and DSCW2 used a typical combination of shear studs and tie bars, to develop composite action between steel faceplates and concrete infill, and to prevent local buckling of steel faceplates. Table 1 presents the details of the connections. The faceplate

slenderness ratio (i.e., the ratio of the stud spacing s over the steel faceplate thickness t_p) was equal to 25, which satisfies the AISC N690s1-15 slenderness limit of $1.0\sqrt{E/f_y}$ for non-slender steel faceplates to prevent local buckling before yielding. The steel faceplates of the DSC flange walls were intentionally thickened to 8 mm to ensure large flexural strength of the overall wall specimen. The web faceplates were welded to the flange faceplates using CJP groove welds. U-shaped rebar was used to provide the bond shear strength along the interface between the steel plate of the flange wall and the concrete infill of the web wall by the shear-friction mechanism (Ji et al. 2013).

Specimen DSCW3 was identical to Specimens DSCW1 and DSCW2, with the exception that it used a novel connector for developing composite action and for tying the faceplates together, as shown in Figure 2(d). Vertical stiffeners were welded to the faceplates using fillet welds and they were connected to each other using a series of tie battens (Nie et al. 2013). The ratio of the stiffener spacing (s) over the steel faceplate thickness (t_p) was 37.5, which is greater than the AISC N690s1-15 slenderness limit.

Table1 Design parameters of wall specimens

Spec. no.	Stud/stiffener spacing (mm)	Tie bar/plate spacing (mm)	Plate slenderness ratio	Steel reinforcement ratio	Total axial force (kN)	Axial force ratio n
SPCW1	100	—	16.7	5.8%	1243	0.16
SPCW2	100	—	16.7	5.8%	2486	0.29
DSCW1	100	200	25	6.4%	1389	0.16
DSCW2	100	200	25	6.4%	2779	0.31
DSCW3	150	80	37.5	6.4%	2779	0.31

The strength grade of the concrete in the wall specimens is C50, with the nominal cubic compressive strength f_{cu} equal to 50 MPa. The cubic strength of concrete $f_{cu,t}$, measured on the day of specimen testing, was equal to 56.0 and 63.8 MPa for Specimens SPCW1 and SPCW2, and 47.6, 52.7 and 50.5 MPa for Specimens DSCW1 through DSCW3, respectively. The axial compressive strength of the concrete was taken as $f_{c,t} = 0.76f_{cu,t}$ according to the Chinese code.

All the steel plates used for the specimens had a strength grade of Q235 (the nominal yield strength f_y = 235 MPa). All rebar had a strength grade of HRB400 ($f_{y,d}$ = 400 MPa). Table 2 summarizes the properties of the steel plate and rebar measured from standard coupon tests and standard rebar tensile tests.

Table 2 Material properties of steel plate and rebar

Plate or rebar	Plate thickness t_p or diameter D(mm)	Yield strength $f_{y,t}$ (MPa)	Ultimate strength $f_{u,t}$ (Mpa)	Elongation δ (%)
Plate	6	281.3	424.9	30.2
	8	302.1	450.8	37.3
Rebar	8	424.0	636.0	9.5
	16	442.2	610.7	10.0
	28	445.0	623.2	10.6

Note: The elongation of steel plate was measured after rupture along a 50-mm gauge length including the fracture zone, while the elongation of rebar is the uniform elongation (i.e., the measured strain corresponding to the peak stress of the rebar).

In accordance with the Chinese technical specification for concrete structures of tall building JGJ 3-2010, the axial force ratio for composite walls can be calculated using Eq. (1).

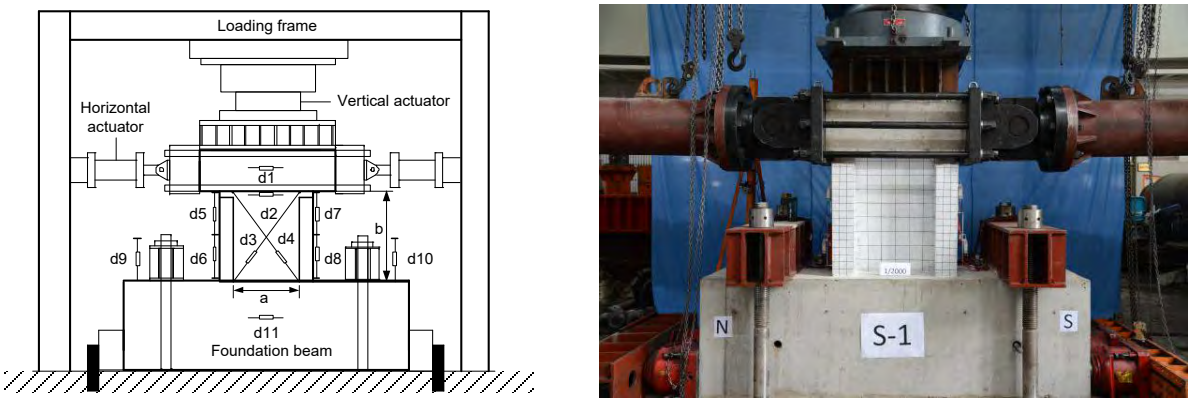
$$n = \frac{N}{f_c A_c + \sum f_y A_s + \sum f_p A_p} \quad (1)$$

where, n denotes the axial force ratio, N denotes the axial force applied on the wall, f_c denotes the axial compressive strength of the concrete, f_y and f_p denote the yield strength of embedded steel profile and steel plate, respectively, and A_c, A_s and A_p denote the cross-sectional areas of concrete, steel profile and steel plate, respectively.

As the flange walls of the specimens were disconnected from the top beam, the axial force was applied primarily to the web wall in the upper portion of the specimen. However, the axial force could generally spread and transfer to the flange walls in the lower portion of the specimen. Preliminary finite element analysis indicated that the web wall resisted an average of approximately 77% of the applied axial force. The axial force ratio for the web walls was calculated using Eq. (1), and the approximate proportion (77%) of the applied axial force, the measured dimensions of the web wall and the actual strength of steel and concrete materials. Specimens SPCW1 and DSCW1 had a moderate axial force ratio of 0.16, while Specimens SPCW2, DSCW2 and DSCW3 had a high axial force ratio of 0.29.

TEST SETUP AND INSTRUMENTATION

Figure 3 shows the test setup. The axial force was first applied and maintained constant during the test. The lateral cyclic loading was applied in displacement-control using two actuators. The first three cycles were applied in the elastic range of response. Three levels of drifts were included, i.e. 0.05%, 0.1% and 0.2%, and one cycle was performed at each level. After the specimen reached the estimated yield drift of 0.4%, the lateral displacement was increased with increments of 0.4% drift, and two cycles were repeated at each drift level. The test was terminated when the specimen failed completely due to crushing of the concrete.



(a) Sketch of test setup (b) Photograph of test setup

Fig. 3 Test setup

Instruments were used to measure loads, displacements and strains in the specimen. Figure3 (a) shows the layout of linear variable differential transformers (LVDTs) mounted on the specimens. Strain-gauge rosettes were mounted on the steel plate and steel profile to measure the strains. The strains in a few horizontally and vertically distributed rebar, boundary longitudinal rebar, shear studs and tie bars are also monitored.

EXPERIMENTAL RESULTS

HYSTERETIC RESPONSES

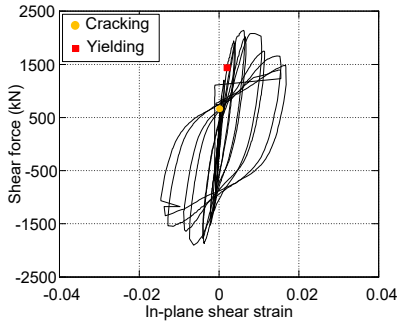
Using the data measured by a pair of diagonal LVDTs d3 and d4 (see Figure 3(a)), the in-plane shear deformation Δ_{sh} and average shear strain γ of the web wall were estimated as follows

$$\Delta_{sh} = (\delta_3 - \delta_4)\sqrt{a^2 + b^2} / 2ab \tag{2}$$

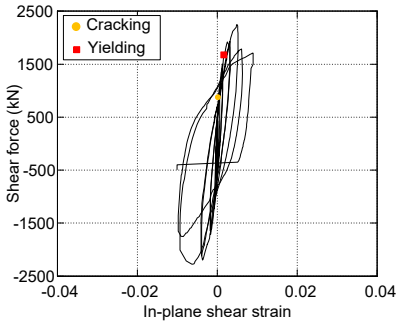
$$\gamma = \Delta_{sh} / b \tag{3}$$

Where, δ_3 and δ_4 denote the deformation measured by LVDTs d3 and d4, and *a* and *b* denote the clear length and height of the web wall as shown in Figure 3(a).

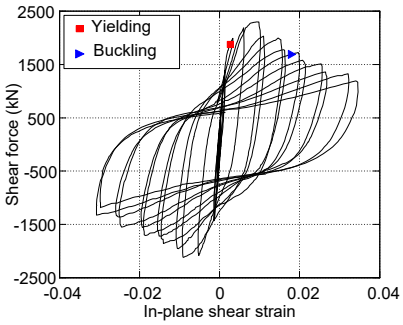
Figure 4 shows the hysteresis curves of in-plane shear force versus the average shear strain calculated by Equations (2) and (3). Figure 5 shows the envelope curves of the specimens. As the faceplates of the DSC wall specimens can prevent the spalling of the concrete, they showed more ductile behavior than the SPC wall counterparts. As Specimens SPCW2 and DSCW2 were subjected to higher axial force, they showed a faster decrease of the post-peak strength than Specimens SPCW1 and DSCW1, respectively. Specimen DSCW3 that used vertical stiffeners and tie plates for connecting two faceplates exhibited stable hysteretic loops up to very large shear strain of approximately 3%.



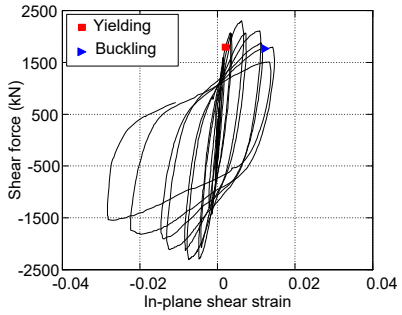
(a) SPCW1



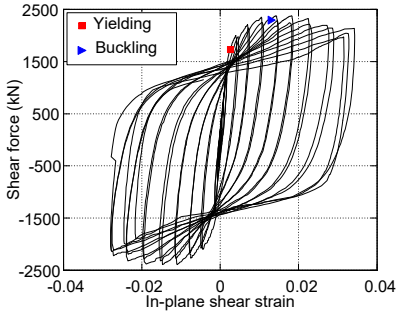
(b) SPCW2



(c) DSCW1



(d) DSCW2



(e) DSCW3

Fig. 4 Hysteretic loops of lateral force versus in-plane shear strain of specimens.

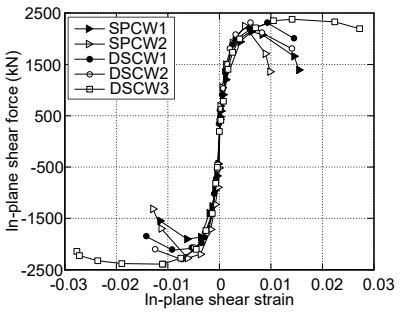


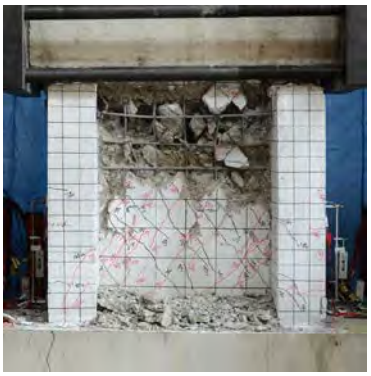
Fig. 5 Envelope curves of lateral force versus in-plane shear strain of specimens.

DAMAGE AND FAILURE MODE

Analysis of the data from the strain-gauge rosettes indicated the yielding of steel plates occurred at approximately 0.20 to 0.25% shear strain. For the SPC wall specimens, a large number of crisscross diagonal cracks induced by cyclic shear loads developed and subdivided the web wall into a series of concrete segments separated by inclined cracks. The cyclic reversal led to spalling of some concrete segments at approximately 0.7%, followed by buckling of steel rebar and steel plate. For the DSC wall specimens, local buckling of faceplates was observed at 1.8% shear strain for Specimen DSCW1 and at 1.2% for Specimens DSCW2 and DSCW3. In the end, the concrete infill crushed at the location where the faceplates buckled. More details of the damage and failure of the DSC wall specimens can be found in Ji et al. 2017. Figure 6 shows the failure mode of the wall specimens. Note that the damage of concrete was mainly concentrated in the upper portion of the web wall where the axial force was larger than the lower portion.

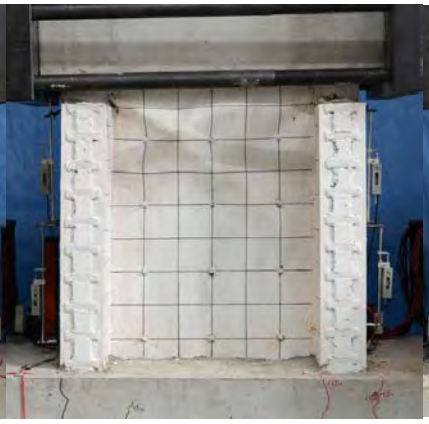


(a) SPCW1



(b) SPCW2







(c) DSCW1 (d) DSCW2 (e) DSCW3

Fig. 6 Failure photographs of the wall specimens

SHEAR STRENGTH AND DEFORMATION CAPACITIES

Table 3 summarizes the shear strength and deformation capacities of the specimens. The yield load V_y corresponds to the yielding of steel plates as measured by the strain-gauge rosettes. The yield shear strain γ_y is the average shear strain measured by diagonal LVDTs corresponding to the yield load V_y. The ultimate shear strain γ_u is defined as the post-peak shear strain corresponding to the lateral load that is 85% of the peak load. As Specimen DSCW3 did not show obvious strength degradation until complete failure, its ultimate shear strain was defined to be the maximum level of shear deformation sustained for at least one full cycle of loading prior to failure of the wall. The ductility factor is calculated as $\mu_\gamma = \gamma_u/\gamma_y$.

The following observations are made from Table 3. (1) The ultimate shear strain of Specimens DSCW1 and DSCW2 was 36% and 34% larger than that of Specimens SPCW1 and SPCW2, respectively. The increased shear deformation capacity of the DSC walls is attributed to the fact that the faceplates can prevent the spalling of the concrete and offer somewhat confinement to the infilled concrete. (2) The increase of the axial force ratio from 0.16 to 0.30 led to a slight increase of the maximum shear strength by 5 to 10%, while it resulted in a significant decrease of the ultimate shear strain by 27% for both SPCW and DSCW specimens. (3) The vertical

stiffeners and tie plates appeared to provide more effective restraint to the faceplates, and consequently DSCW3 had a significantly larger ultimate shear strain than other specimens.

Table 3 Shear strength and deformation capacities of wall specimens

Spec. No.	Yield shear strain γ_y (%)	Yield shear strength V_y (kN)	Peak shear strain γ_p /%	Peak shear strength V_p (kN)	Ultimate shear strain γ_u /%	Ductility ratio μ_γ
SPCW1	0.21	1435	0.63	2021	1.13	5.4
SPCW2	0.17	1676	0.55	2260	0.83	4.9
DSCW1	0.27	1878	0.93	2212	1.54	5.7
DSCW2	0.22	1797	0.68	2306	1.12	5.1
DSCW3	0.26	1735	1.25	2387	3.09	11.9

DESIGN FORMULAS OF SHEAR STRENGTH

DESIGN FORMULAS FOR SINGLE-PLATE COMPOSITE WALLS

Per the AISC 341-10 provisions, the shear strength of SPC walls is estimated as the yield shear strength of the steel plates only, neglecting the shear contribution provided by RC encasement, which is given by

$$V = 0.6 f_p A_p \tag{4}$$

Where, f_p denotes yield strength of steel plate, A_p denotes cross-section area of steel plates. Note that, the web of boundary steel profiles is taken as a portion of steel plate in the calculation of shear strength.

Chinese technical specification for concrete structures of tall buildings (JGJ 3-2010) estimates the in-plane shear strength of SPC walls by superposing the in-plane shear strength of steel plates V_s and shear strength of RC encasement V_c, given by

$$V = V_s + V_c \tag{5-a}$$

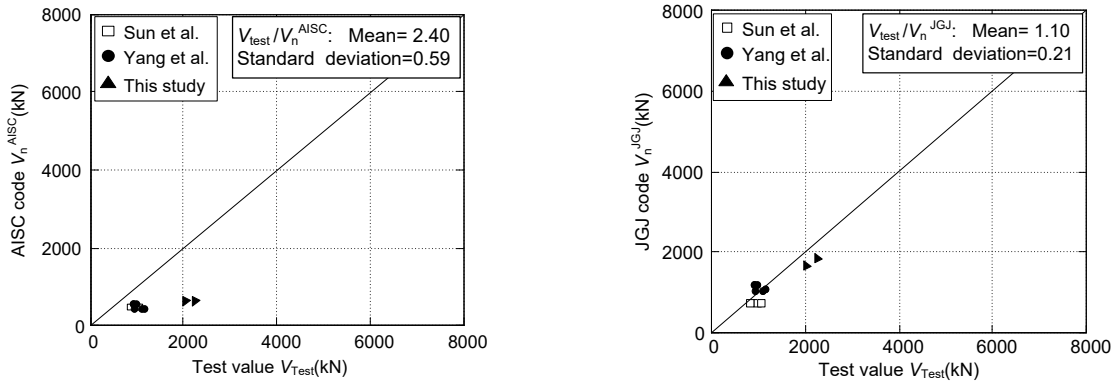
$$V_c = \frac{1}{\lambda - 0.5}\left(0.5 f_t b_w h_{w0} + 0.13 N\right) + f_{yv}\frac{A_{sh}}{s} h_{w0} \tag{5-b}$$

$$V_s = \frac{0.6}{\lambda - 0.5} f_p A_p \tag{5-c}$$

In these equations, f_t denotes tensile strength of the concrete; f_{yv} denotes yield strength of horizontally distributed rebar; f_p denotes yield strength of steel plate; b_w denotes thickness of the web wall; h_{w0} denotes effective depth of the wall; A_{sh} denotes cross-sectional area of the horizontally distributed rebar within spacing s; A_p denotes cross-sectional area of the steel plate (the web of boundary steel profiles is taken as a portion of steel plate in this calculation); λ denotes shear-to-span ratio of the wall (the value of λ is assumed to be equal to 1.5 if it is smaller than 1.5); and N denotes axial compressive force applied to the wall web.

A number of data from past tests (Sun et al. 2008; Yang et al. 2010) and from this test program

was used for validation of shear strength design formulas. A total of 12 SPC wall specimens are considered, of which the steel reinforcement ratio varies from 4.1 to 6.2%, and the axial force ratio varies from 0.16 to 0.29. Figure 7 shows the comparison between the calculated values per the design equations and the test results. It indicates that the JGJ 3-2010 code equations provide a reasonable estimation on the in-plane shear strength of SPC walls. The mean and standard deviation for the ratio of V_{test}/V_n equal to 1.10 and 0.21, respectively. However, the AISC 341-10 equation significantly underestimates the in-plane shear strength capacity of SPC walls, as it neglects the shear contribution of RC encasement.



(a) AISC 341-10 (b) JGJ 3-2010

Fig. 7 Verification for design formulas of shear strength for SPC walls

DESIGN FORMULAS FOR DOUBLE-SKIN COMPOSITE WALLS

The design equations in U.S. code AISC N690s1-15 are based on the mechanics-based model (MBM) theory, and further simplified as shown in Eq. (6-a). In this equation, κ is a calibration factor calculated using Eq. (6-b). The values of $\bar{\rho}$ in Eq. (6-b) are calculated using Eq. (7-c), and they vary from 0.01 to 0.04. In these equations, f_c and f_p denotes the concrete compressive strength and the yield strength of steel faceplates in MPa, respectively.

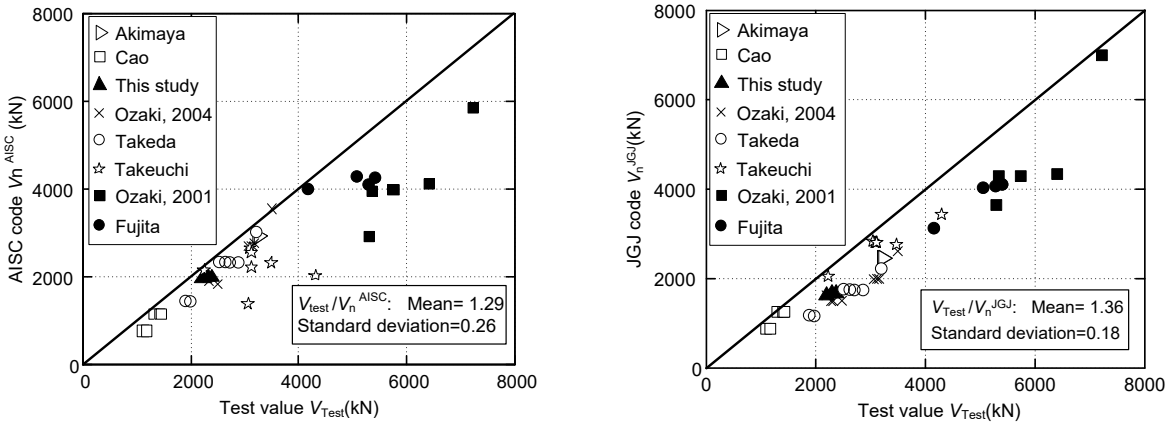
(7-a) $$V_n^{AISC} = \kappa f_p A_p$$

(7-b) $$\kappa = 1.11 - 5.16\bar{\rho} \le 1.0$$

(7-c) $$\bar{\rho} = \frac{1}{83}\frac{f_p A_p}{A_c\sqrt{f_c}}$$

The JGJ 3-2010 formulas for estimating the shear strength of DSC walls are similar as those for SPC walls (Eq. 5), except for removing the shear contribution of horizontally distributed rebar.
Test data on DSC walls are collected from past tests (Akiyama et al. (1991), Takeda et al. (1995); Takeuchi et al. (1998), Fujita et al. (1998), Ozaki et al. (2001) and (2004), Cao et al. (2013)) and from this test program. A total of 42 test specimens are considered, of which the steel

reinforcement ratio varies from 1.3 to 6.4%, and the axial compressive force ratio varies from zero to 0.31. Figure 8 shows the comparison between the calculated values per the design equations and the test results. The figure indicates both AISC N690s1-15 and JGJ 3-2010 code equations provide reasonable and conservative assessment of the in-plane shear strength of DSC walls.



(a) AISC N690s1-15 (b) JGJ 3-2010

Fig. 8 Verification for design formulas of shear strength for DSC walls

CONCLUSIONS

This paper presented a series of quasi-static tests on cyclic shear behavior of steel-plate composite walls for high-rise buildings. The following conclusions are drawn from this study.

(1) DSC wall specimens have approximately 35% larger shear deformation capacity than SPC wall specimens, as the faceplates of DSC walls prevent the spalling of the concrete.

(2) Increasing the axial ratio from 0.16 to 0.30 slightly increased the shear strength of the steel-plate composite walls, with it led to over 20% decrease in the shear deformation capacity.

(3) The DSC wall specimen with vertical stiffeners and tie plates connecting the two faceplates had the ultimate shear strain reaching 3%, significantly larger than the DSC wall specimens with headed shear studs and tie bars as connectors.

(4) Analysis of the test data of 12 SPC wall specimens indicates that the JGJ 3-2010 design formulas provides reasonable estimates of the shear strength of SPC walls, while the AISC 341-10 formula significantly underestimates the shear strength.

(5) Analysis of the test results of 42 DSC wall specimens indicates that the design formulas of AISC N690s1-15 and JGJ 3-2010 can provide reasonable and conservative estimates of the shear strength of DSC walls.

REFERENCE

AISC (American Institute of Steel Construction). (2015). “Specification for safety-related steel structures for nuclear facilities including supplement no. 1.” *AISC N690s1-15*, Chicago.

ANSI/AISC (American Institute of Steel Construction). (2010). Seismic provisions for structural steel buildings. *ANSI/AISC 341-10*, Chicago.

Akiyama, H., Sekimoto, H., Fukihara, M., Nakanishi, K., & Hara, K. (1991). A compression and shear loading test of concrete filled steel bearing wall. In *Transactions of the 11th international conference on structural mechanics in reactor technology.*

CMC (China Ministry of Construction). (2010). “Technical specification for concrete structures of tall building.” *JGJ 3-2010*, Beijing. (in Chinese).

Cao, W., Yu C., Dong, H., Qiao, Q., Li, H., & Zhang, Y. (2013). Experimental study on seismic performance of composite shear walls with double steel plates under different constructions. *Journal of Building Structures, 34*, 186-191 (in Chinese).

Eom, T. S., Park, H. G., Lee, C. H., Kim, J. H., & Chang, I. H. (2009). Behavior of double skin composite wall subjected to in-plane cyclic loading. *Journal of Structural Engineering*, *135*(10), 1239-1249.

Fujita, T., Funakoshi, A., Akita, S., Hayashi, N., & Matuso, I. (1998). Experimental Study on concrete filled steel structure: Part16 Bending Shear Tests (effect of bending strength). *Summaries of Technical Papers of Meeting Architectural Institute of Japan,*1121-1122.

Ji, X., Jiang, F., & Qian, J. (2013). Seismic behavior of steel tube–double steel plate–concrete composite walls: Experimental tests. *Journal of Constructional Steel Research*, *86*, 17-30.

Ji, X., Cheng, X., Jia, X., & Varma, A. H. (2017). Cyclic In-Plane Shear Behavior of Double-Skin Composite Walls in High-Rise Buildings. *Journal of Structural Engineering*, *143*(6): 04017025.

Nie, J., Hu, H. H., Fan, J., Tao, M., Li, S., & Liu, F. (2013). Experimental study on seismic behavior of high-strength concrete filled double-steel-plate composite walls. *Journal of Constructional Steel Research*, *88*, 206-219.

Ozaki, M., Akita, S., Niwa, N., Matsuo, I., & Usami, S. (2001). Study on steel plate reinforced concrete bearing wall for nuclear power plants part1; shear and bending loading tests of SC walls. *Transaction of the 16th International Conference on Structural Mechanics in Reactor Technology*, Washington DC, Paper ID: 1554.

Ozaki, M., Akita, S., Osuga, H., Nakayama, T., & Adachi, N. (2004). Study on steel plate reinforced concrete panels subjected to cyclic in-plane shear. *Nuclear Engineering and Design*, *228*(1), 225-244.

Sun, J., Xu, P., Xiao, C., Sun, H., & Wang, C. (2008). Experimental study on shear behavior of steel plate-concrete composite wall. *Building Structure, 38*(6), 1-7 (in Chinese).

Takeda, T., Yamaguchi, T., Nakayama, T., Akiyama, K., & Kato, Y. (1995). Experimental study on shear characteristics of a concrete filled steel plate wall. In *Transactions of the 13. International conference on structural mechanics in reactor technology.*

Takeuchi, M., Narikawa, M., Matsuo, I., Hara, K., & Usami, S. (1998). Study on a concrete filled structure for nuclear power plants. *Nuclear Engineering and Design*, *179*(2), 209-223.

Wang, B., Jiang, H., & Lu, X. (2017). Seismic performance of steel plate reinforced concrete shear wall and its application in China Mainland. *Journal of Constructional Steel Research*, *131*, 132-143.

Yang, X. (2010). Experimental research on shear behavior of high-strength concrete steel composite walls. (Master Dissertation). *China Academy of Building Research*, Beijing, China. (in Chinses)

Experimental Study on the Seismic Performance of New Hybrid Coupling Wall Subassemblies with Replaceable Steel Coupling Beam

Yang Liu (corresponding author)
Associated Professor of Structural Engineering, College of Civil Engineering, Huaqiao University
Xiamen, China
E-mail: lyliuyang@hqu.edu.cn

Hao Lin
Postgraduate of Structural Engineering, College of Civil Engineering, Huaqiao University
Xiamen, China
E-mail: linhao425@163.com

Zixiong Guo
Professor of Structural Engineering, College of Civil Engineering, Huaqiao University
Xiamen, China
E-mail: guozxcy@hqu.edu.cn

Hongsong Hu
Professor of Structural Engineering, College of Civil Engineering, Huaqiao University
Xiamen, China
E-mail: huhs@hqu.edu.cn

Bahram M. Shahrooz
[a] Professor of Structural Engineering, Dept. of Civil and Architectural Engineering
Construction Management, Univ. of Cincinnati, Cincinnati, U.S.
[b] Distinguished Professor, College of Civil Engineering, Huaqiao University
Xiamen, China
E-mail: shahrobm@ucmail.uc.edu

ABSTRACT

Coupled shear wall is an efficient and promising lateral load resistant system. Significant accomplishments have been achieved in understanding the seismic performance and load carrying mechanism of coupled wall systems with different components, e.g., reinforced concrete (RC) walls with RC coupling beams, or RC walls with steel coupling beams. To further improve seismic performance and rapid function restoration after earthquakes, a new hybrid system consisting of steel plate composite structural wall piers and replaceable steel coupling beams was investigated. Three half-scale subassemblies having different details were designed, fabricated, and tested under cyclic loading. All three subassemblies used steel coupling beams with the same span/depth ratios, but had different details. Two subassemblies with replaceable steel coupling beam components were repaired in situ after being loaded up to 2% chord rotation, and were subsequently loaded up to 10% chord rotation to study the seismic performance of the specimens after repair. The results showed that the new hybrid subassemblies exhibited satisfactory performance in terms of achieving the required strength and stiffness, excellent ductility, and stable hysteretic behavior. The performance of the repaired specimens was nearly the same as their counterparts before repair, indicating acceptable fuse details that can be replaced.

INTRODUCTION

Various experimental programs have been conducted to address the interaction between steel coupling beams and reinforced concrete structural walls in a hybrid coupled wall system. Past research showed that properly designed and detailed steel coupling beams provided outstanding strength, stiffness, ductility, and appreciable energy dissipation. In spite of excellent performance of steel coupling beams, post-event repair would be costly or not feasible because of significant inelastic deformations to which coupling beams are subjected. An innovative coupling beam with a replaceable mid-span "fuse" was studied in a past project [Fortney et al. 2006]. This design concept is based on concentrating the damage due to seismic loads in specially detailed components, which can be removed and replaced after earthquakes allowing in situ repair of the structure. In response to seismic excitation, steel coupling beams are expected to dissipate energy in a manner similar to the response of shear links in eccentrically braced frames (EBFs). The idea of a mid-span fuse is analogous to a replaceable link in EBFs [Fortney et al. 2007]. The basic premise for coupling beams with a mid-span fuse coupling is that all inelastic deformations are concentrated in the fuse.

The main objective of the research presented in this paper is to further enhance the performance of steel coupling beams by providing post-event replaceability without costly repair of the wall pier and the coupling beam connections. This objective was achieved by designing the beam such that all of the inelastic damage would be concentrated in the middle of the steel coupling beam, i.e., where the fuse is located. The goal is to restore the resistance of the structures after a seismic event. This paper is focused on the experimental component of the reported research.

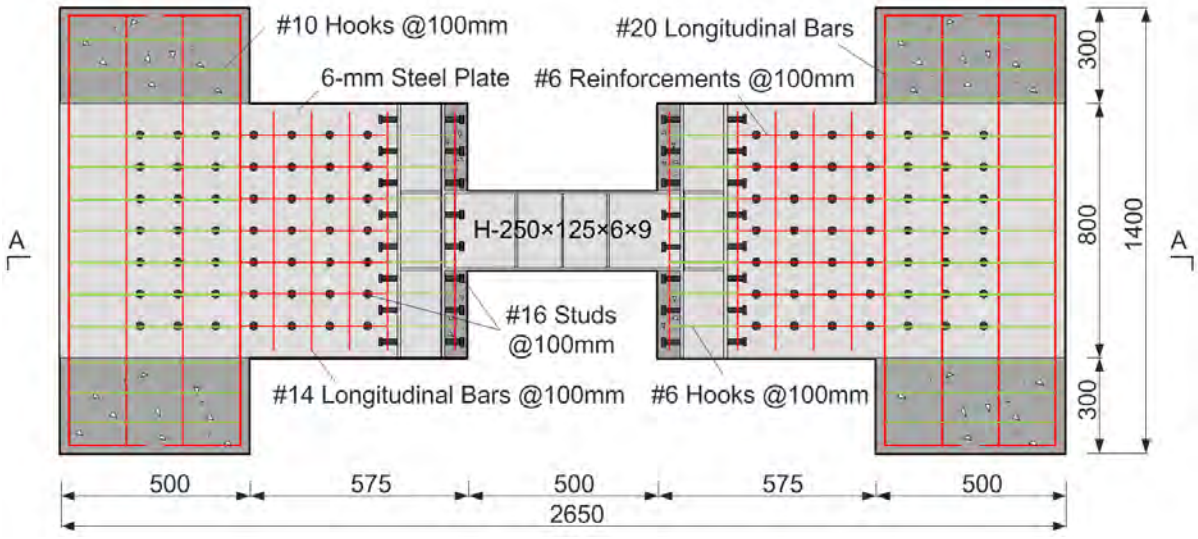
EXPERIMENTAL PROGRAM

TEST SPECIMENS

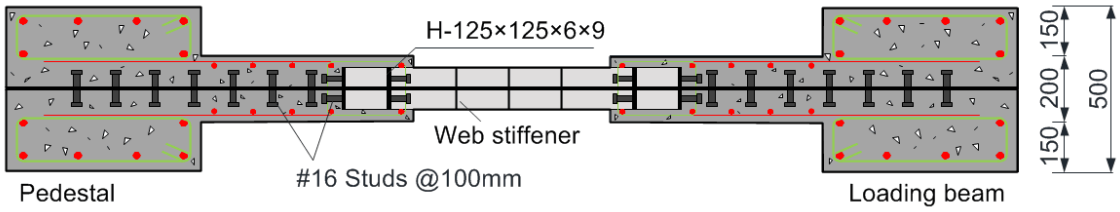
Five specimens were fabricated and tested (Table 1). One specimen without a replaceable fuse was tested as benchmark. The reinforcement details of all the specimens were the same, as shown in Figure 1. The test variables were the connection details between the fuse and the rest of the coupling beam that was detailed to remain elastic, see Figure 2. The composite wall piers consisted of structural steel boundary elements welded to "shear plates". The steel boundary elements were H125×125×6×9. The elastic segments of the steel coupling beams were embedded in the wall piers and welded to encased steel boundary elements. As seen from Table 1, the thickness of flanges, webs, and end plates in the elastic components were made thicker than those in the fuse in order to prevent damage in the portions that are not meant to be replaced. High strength 16-mm diameter bolts (Grade 10.9) were used to connect the end plates of the "fuses" and the elastic components of the coupling beams. The ultimate strength of the bolts was 1000MPa with the yield strength to ultimate strength ratio of 0.9. Shear stud connectors were used on both sides of the steel plates and the flanges of the boundary elements to ensure sufficient bond between the steel and concrete. The diameter and nominal length of the studs were 16mm and 60mm, respectively.

MATERIAL PROPERTIES

All the specimens were cast at the same time using concrete from a single ready-mix truck. The average 28-day compressive strength was 45.7MPa, as determined by testing cubes. The maximum aggregate size was 10mm, selected to ensure good consolidation around the embedded components. The horizontal reinforcement of the wall piers and stirrups in the loading beam and pedestal were 6-mm diameter deformed bars. The diameter of the longitudinal reinforcement in the wall piers was 14mm. The thickness of the steel plate and stiffeners were 6mm. The measured material properties were shown in Table 2.

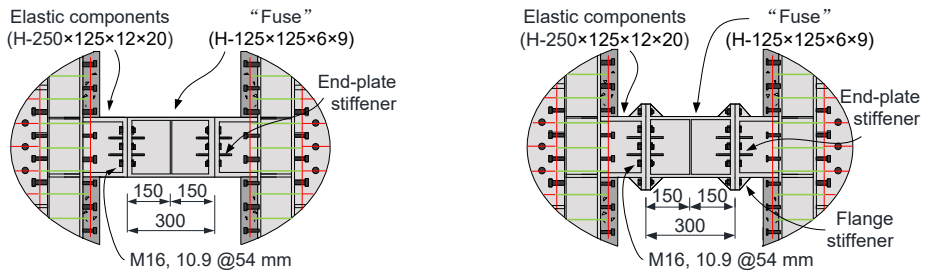


(a) Elevation view



(b) Plan view

Fig. 1 - Reinforcement details of specimens (all dimensions are in mm)



(a) Replacement detail A (b) Replacement detail B

Fig. 2 - Replacement details of the steel coupling beams

Table 1 - Parameters of specimens

Specimen I.D.	Fuse or coupling beam	Elastic component	Span/depth	Replacement detail
SCB-2	H250x125x6x9	---	2.0	---
FCB-1	H250x125x6x9	H250x125x12x20	2.0	A
FCB-1-1*	H250x125x6x9	H250x125x12x20	2.0	A
FCB-2	H250x125x6x9	H250x125x12x20	2.0	B
FCB-2-1*	H250x125x6x9	H250x125x12x20	2.0	B

* with a new fuse

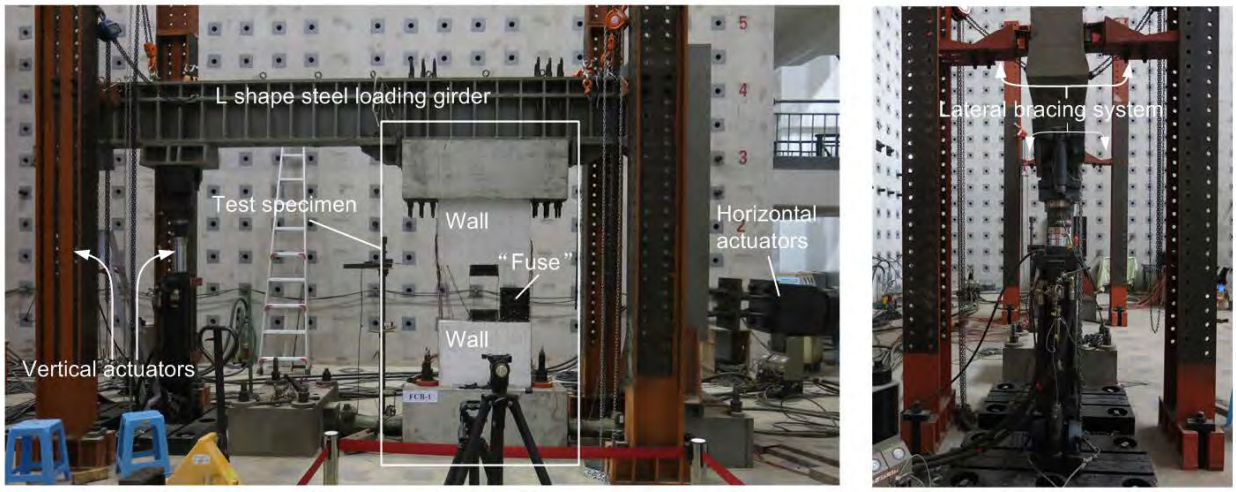
Table 2 - Material properties of reinforcement steel

d(mm)	f_y(MPa)	f_u(MPa)	E_s(MPa)	ε_y ($\times 10^{-6}$)
6	625	630	2.0×10^5	3125
14	455	595	2.0×10^5	2275
6*	295	595	2.0×10^5	1475

Note: d is the diameter of the steel bar; * the thickness of the steel plate; f_y is the yield strength; f_u is the ultimate strength; E_s is the elastic modulus; ε_y is the yield strain.

EXPERIMENTAL SETUP

The test setup was shown in Figure 3. The specimens consisted of four parts: steel coupling beam, composite wall piers, loading beam, and pedestal. For loading convenience, the specimens were rotated 90 degrees such that the coupling beam was vertically placed, and the loading beam was bolted to a rigid L-shaped loading girder. Three actuators were used to simulate the loading and boundary conditions expected in coupled wall buildings. The specimen was loaded horizontally with a 1000kN hydraulic actuator to create a lateral drift between the ends of the coupling beam. Two 500kN hydraulic actuators were attached to the steel L-shaped girder to ensure lateral drift without any rotation in the coupling beam. To guarantee lateral stability of the loading system, the L-shaped loading girder was laterally braced at three points.



(a) Front view (b) Side view

Fig. 3 - Test setup

All the specimens were loaded similarly following a series of cyclic displacements with increasing amplitudes. The selected loading protocol is shown in Figure 4. Specimen SCB-2 was loaded up to a drift angle of 0.1 rad. Specimens FCB-1 and FCB-2 were first loaded up to a drift angle of 0.02 rad. After conducting 3 cycles at this displacement amplitude, loading was stopped with zero horizontal load. The small drift angle and termination of loading simulated in situ replacement of the fuse following a moderate earthquake. The procedure for replacing the fuse was shown in Figure 5. The residential displacements of FCB-1 and FCB-2 with zero lateral load were maintained with the three actuators described above. After installing new fuses, specimens FCB-1-1 and FCB-2-1 were loaded up to drift angle of 0.1, with the ending states of the previous loading history for specimen FCB-1 and FCB-2 taken as their starting point from 0 drift, respectively.

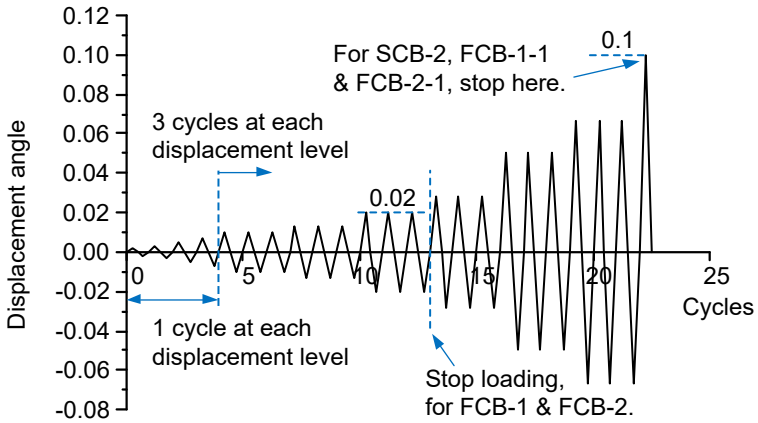
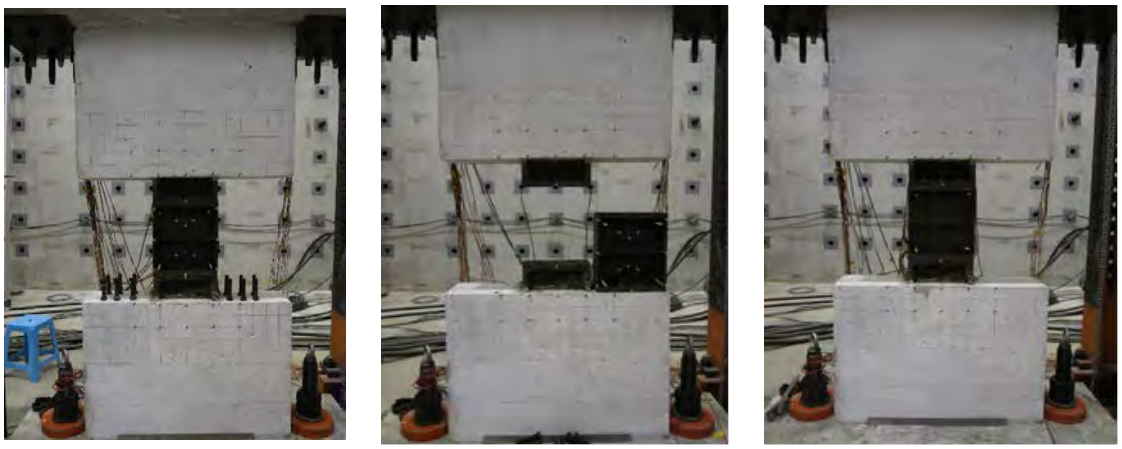


Fig. 4 - Horizontal loading history



(a) Remove bolts (b) Disassemble “fuse” (c) Replace “fuse”

Fig. 5 - In situ replacement process

EXPERIMENTAL RESULTS

DAMAGE AND CRACK PATTERN

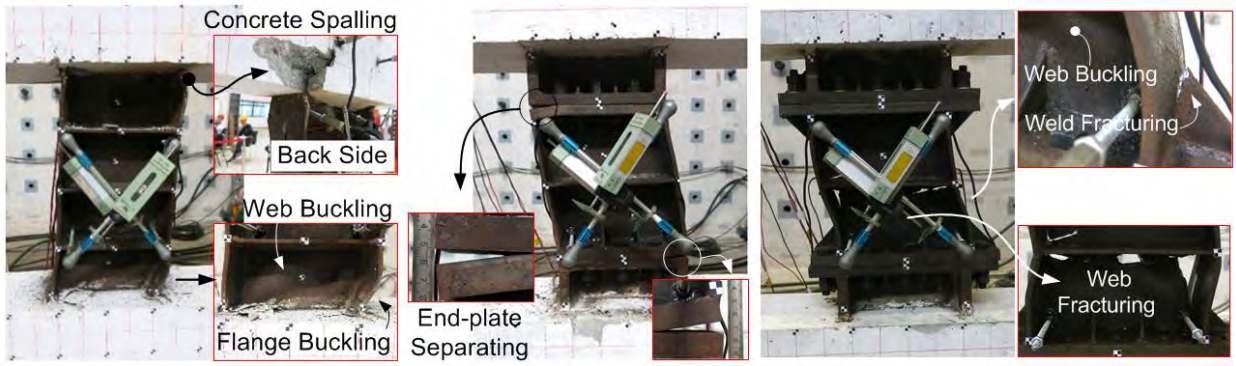
The typical failure modes of the specimens were shown in Figure 6. For specimen SCB-2, some minor cracks on the wall piers were observed at small drift angles (around 0.003 rad.). The flanges of the steel coupling beam yielded during the first cycle of drift angle of 0.01 rad. The flanges of the steel beam began to separate from the concrete of the wall piers at drift angle of 0.02 rad. Buckling of the flanges was observed at the first cycle of drift angle of 0.05 rad, and became progressively severe during the following loading stages. Localized spalling of concrete at the edge of the top wall pier occurred at the first cycle of drift angle of 0.1 rad. Local buckling of the web was observed at the last cycle of drift angle of 0.1 rad, and diagonal tension fields began to propagate at the bottom end of the steel coupling beam. A slight strength degradation was detected only during the last loading cycle.

For specimens FCB-1, no discernable cracks were detected until the drift angle reached 0.01 rad. Some minor cracking occurred at the beam-wall interface, and the web of the fuse began to yield due to diagonal tension. At drift angle of 0.02 rad, there was a 1.5mm gap between the end plates, and the maximum tension strain in the fuse web was 17251με ($11.7\varepsilon_y$), suggesting considerable plastic deformation in the fuse.

For small drift angles, there was no major difference between FCB-1-1 and FCB-1. As the displacement amplitudes increased, the gap between the end plates and the plastic strain in the fuse web became larger. The developing gap and the reversed loading weakened the resistance of the coupling beam, as evident by several sudden drops of the horizontal load and loud noises due to slippage between the end plates. This phenomenon was clearly seen from the hysteretic curve shown in Figure 7(b). For safety reasons, FCB-1-1 was monotonically loaded from drift angle 0.05 up to 0.1 rad., which was the maximum intended drift angle. No weld fracture or strength degradation was observed. It should be noted that Detail "A" used in FCB-1 is not expect to provide significant moment transfer.

For specimens FCB-2, no major issues were observed except for a few minor cracks in the wall piers. The maximum tension strain of the "fuse" web was 9701με (6.6 ε_y).

For specimen FCB-2-1, no gap between the end plates was observed during the entire loading history, mainly because of the connection details (Figure 2b) that could transfer moment between the fuse and the rest of the coupling beam. Initiation of weld fracture in the flange stiffener was detected at drift angle of 0.05 rad. The fuse flanges buckled during the first cycle of drift angle of 0.05 rad, and the fuse web-stiffener weld began to fracture at the third cycle of drift angle of 0.067 rad. After completing three cycles of 0.1 drift angles, there was a sudden drop in the horizontal load due to web fracture at the web-flange interface and propagation of fracture in the web-stiffener weld, at which loading was stopped. The final failure mode of specimen FCB-2-1 is shown in Figure 6(c).



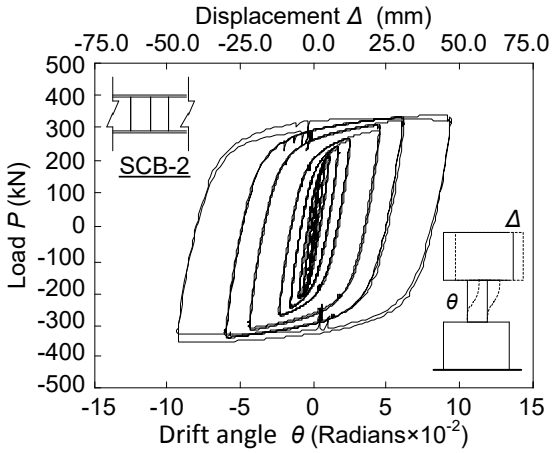
(a) SCB-2 (b) FCB-1-1 (c) FCB-2-1

Fig. 6 - Failure modes of specimens

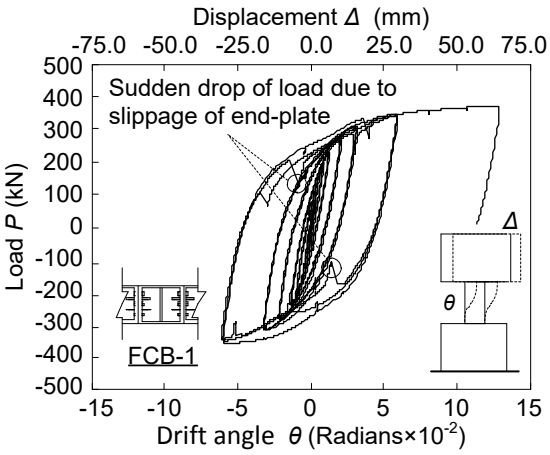
HYSTERETIC RESPONSE

The load (P)-drift angle(θ) hysteretic curves of all the specimens were plotted in Figure 7. The curves of specimen SCB-2 were stable and showed very good energy dissipation characteristics. Only slight strength degradation was detected for the second cycle of 0.1 rad drift angle at which the web began to buckle. The hysteretic performance of specimen FCB-1-1 below drift angle of 0.02 rad was almost identical to that of FCB-1 (Figure 7(d)), suggesting that replacing fuses would be feasible after moderate earthquakes, and the performance would be satisfactory. For specimen FBC-2, equipment failure negatively impacted the hysteretic performance. As a result, the responses of this specimen and FCB-2-1 were slightly different (Figure 7(e)). It was, nevertheless, possible to demonstrate that the seismic performance of the coupling beam could be recovered after replacing the fuse. The effects of excessive opening of the end plates in FCB-1-1 was evident by a number of sudden load drops (Figure 7(c)). For specimen FCB-2-1, the connection between the fuse and the elastic components was modified by extending the ends plates above and below the flanges and using flange stiffeners. The hysteretic performance

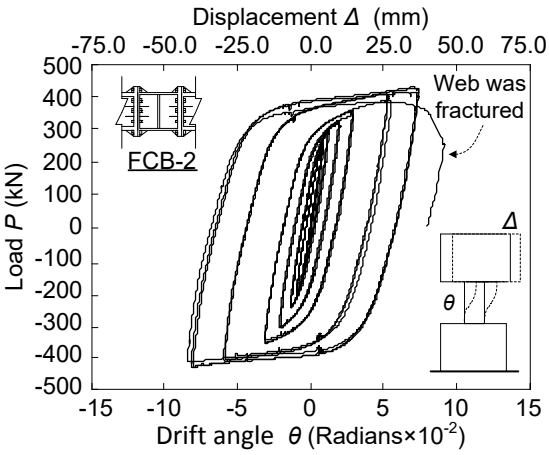
of FCB-2-1 was, accordingly, improved remarkably in comparison to specimen FCB-1-1 and was nearly similar to that of specimen SCB-2. As stated before, specimen moment transfer in specimen FCB-1-1 was not expected to be large. The initial stiffness of specimen FCB-2-1 was higher than SCB-2, because of the thicker web and flange of the elastic components in FCB-2-1.



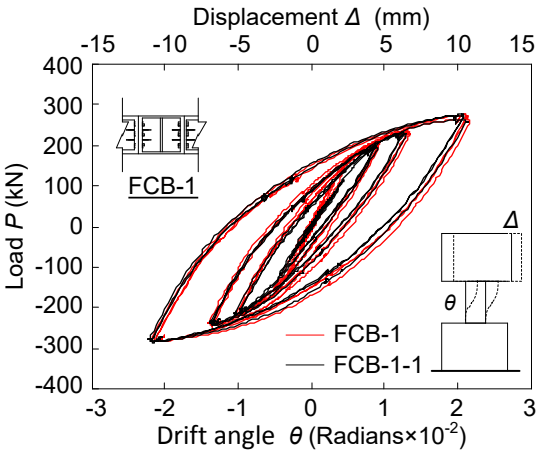
(a) SCB-2



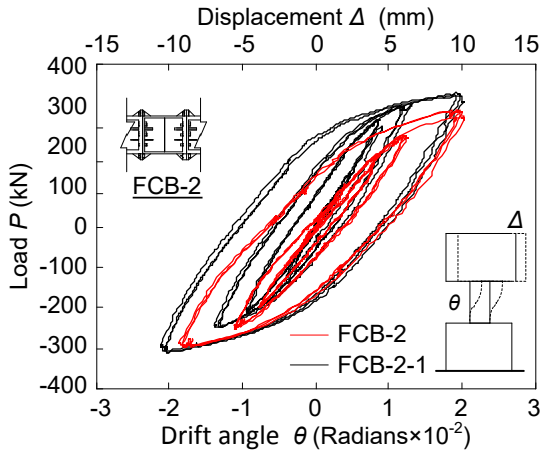
(b) FCB-1-1



(c) FCB-2-1



(d) FCB-1 (replaced)



(e) FCB-2 (replaced)

Fig. 7 – Hysteretic curves of load – displacement angle.

SKELETON CURVE

Skeleton curves of all the specimens were shown in Figure 8, and the characteristic points of the curves were summarized in Table 3. The yield point of the skeleton curve was determined graphically. The strength of the specimen maintained an upward trend during the loading process. The ultimate capacity of specimen SCB-2, FCB-1-1, and FCB-2-1 was 332.6kN, 370.4kN, and 424.2kN in forward loading, respectively. The repaired specimens exhibited nearly identical strength with their former counterpart specimens, which indicate the reasonable details of replacement for the steel coupling beams. The maximum strength of specimen FCB-1-1 and FCB-2-1 were 11.4 % and 27.5% higher than that of SCB-2, respectively. The higher capacities are attributed to the smaller span-to-depth ratio of the fuses in FCB-1-1 and FCB-2-1.

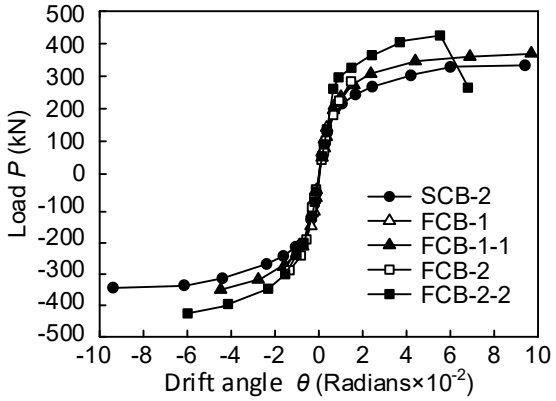


Figure 8 - Skeleton curves of specimens

Table 3 - Load and displacement angle at characteristic points of the skeleton curves

No.	P_y/kN	θ_y /rad	P_m/kN	θ_m /rad
SCB-2	231.3	0.00139	332.6	0.00936
FCB-1-1	275.5	0.00157	370.4	0.00965
FCB-2-1	325.3	0.00147	424.2	0.00551

Note：P_y and P_m are yield load and peak load, respectively; θ_y and θ_m are drift angle at yield load and peak load, respectively.

ENERGY DISSIPATION CHARACTERISTICS

As seen from Table 4, the dissipated energy, expectedly, increased with an increase in the drift angle. Specimens FCB-1-1 and FCB-2-1 dissipated more energy than SCB-2 up to 0.05 rad., which was not the maximum drift angle for cyclic loading of SCB-2. These dissipated energies suggest the adequacy of the selected details.

Table 4 - Dissipated energy (kJ) at different story drift angles

Specimen No.	story drift angles					Total dissipated energy before θ=0.05
	0.010	0.013	0.020	0.029	0.050	
SCB-2	1.89	4.35	10.93	21.44	54.88	93.50
FCB-1-1	1.38	3.49	9.90	20.45	51.81	87.03
FCB-2-1	1.34	3.97	11.33	23.67	66.05	106.37

The equivalent viscous damping coefficient mainly reflects the “fullness” of the hysteresis curve, calculated according to Eq. 1.

$$h_e = \frac{1}{2\pi} \frac{S_{ABC} + S_{CDA}}{S_{OBE} + S_{ODF}} \quad (1)$$

Where, S_{ABC}, S_{CDA} are the areas surrounded by the hysteresis loops filled with vertical lines in Figure 9, and S_{OBE}, S_{ODF} are the areas of the corresponding triangles.

Table 5 summarized the equivalent viscous damping coefficients at different drift angles. As the drift angle increased, the equivalent viscous damping coefficient, expectedly, increased, indicating that the plastic energy dissipation of the specimen became larger. As mentioned before, there were several sudden slippages of the end plates in specimen FCB-1-1 during the loading process. These slippages caused some "up and downs" in the hysteretic curves; hence, the equivalent viscous damping coefficient of FCB-1-1 was slightly lower than the other specimens. However, in general, the equivalent viscous damping coefficients of all specimens were not significantly different.

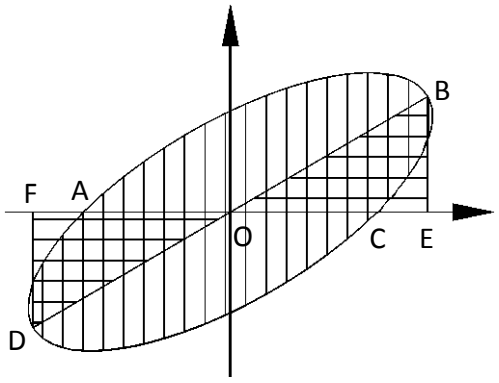


Fig. 9 - Hysteretic loop

Table 5 - Equivalent viscous damping ratios at different story drift angles

No.	story drift angles				
	0.010	0.013	0.020	0.029	0.050
SCB-2	0.16	0.22	0.29	0.35	0.33
FCB-1-1	0.11	0.17	0.25	0.31	0.39
FCB-2-1	0.09	0.17	0.27	0.33	0.43

STIFFNESS CHARACTERISTICS

The degradation of peak-to-peak stiffness against drift angle was plotted in Figure 10. The initial

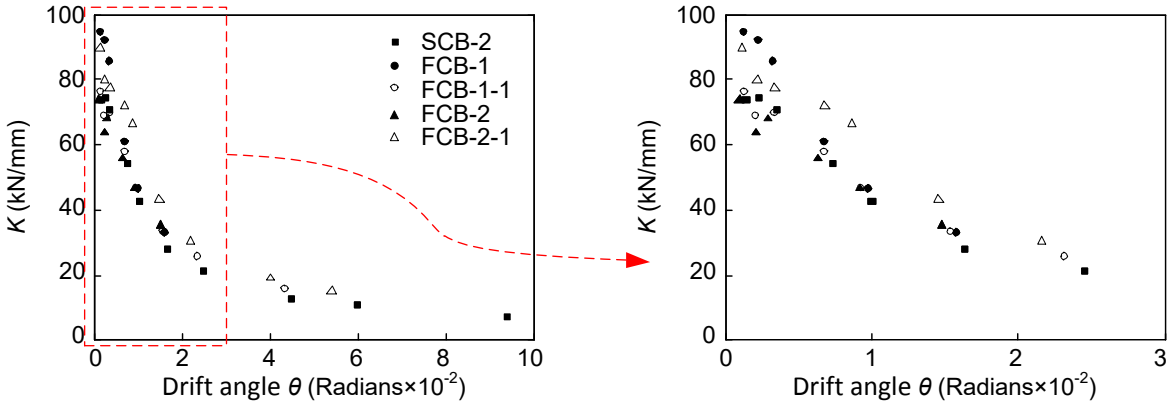


Fig. 10 - Stiffness degradation curve

stiffness of all specimens, expectedly, degraded with an increase in the drift angle. No significant differences in the trend of the data were observed in general. The initial stiffness of specimen SCB-2 was lower than the other four specimens, because the thickness of flanges and web in this specimen were smaller than their counterparts in the specimens with a mid-span fuse.

CONCLUSIONS

Subassemblies consisting of two steel plate composite wall piers and a steel coupling beam with a mid-span fuse were tested to evaluate the seismic performance of this system, and to examine the feasibility of replacing the fuse. The following conclusions can be drawn based on this research:

1) The specimens exhibited satisfactory performance, including: high strength and stiffness, excellent ductility, and stable hysteretic behavior.
2) Based on the experimental results, both of the selected fuse details performed well in terms of recovering the seismic performance after subjecting the specimen to a maximum drift rotation angle of 0.02 rad. and replacing the fuse. The initial stiffness of the specimens with fuses was higher than that with a single steel coupling beam, because of the thicker flanges and webs in the elastic components of the former specimens.
3) The steel coupling beam with replacement detail “A” experienced some sudden slippages between the end plates under large rotation angles, which led to temporary loss of load carrying capacity, and degradation of energy dissipation capacity. It should be noted that the selected detail is not expected to offer a large level of moment transfer. This problem was successfully resolved using replacement detail “B”.
4) No significant damage was observed in the wall piers, especially for the specimens with fuses. It is concluded that the selected replacement details offer an effective method to limit the entire plastic damage within the fuse.

ACKNOWLEDGMENTS

Ph.D. Candidate H. Chen from Huaqiao University gave a great help on the modification of the pictures in this paper. The author sincerely appreciates his help. This work was funded by the National Natural Science Foundation of China (Grant No. 51378228 and 51878304), which is greatly acknowledged.

REFERENCES

Gong, B., & Shahrooz, B. M. (2001). Concrete-steel composite coupling beams. i: component testing. Journal of Structural Engineering, 127(6), 625-631.

Gong, B., & Shahrooz, B. M. (2001). Concrete-steel composite coupling beams. ii: subassembly testing and design verification. Journal of Structural Engineering, 127(6), 632-638.

Harries, K. A. (2001). Ductility and deformability of coupling beams in reinforced concrete coupled walls. Earthquake Spectra, 17(3), 457-478.

Wu, Y., Xiao, Y., & Anderson, J. C. (2009). Seismic behavior of pc column and steel beam composite moment frame with posttensioned connection. Journal of Structural Engineering, 135(11), 1398-1407..

El-Tawil, S., Fortney, P., Harries, K., Shahrooz, B., Kurama, Y., Hassan, M., & Tong, X. (2010). Recommendations for seismic design of hybrid coupled wall systems. American Society of Civil Engineers, Virginia.

Mansour, N., Christopoulos, C., & Tremblay, R. (2011). Experimental validation of replaceable shear links for eccentrically braced steel frames. Journal of Structural Engineering, 137(10), 1141-1152.

Farsi, A., Keshavarzi, F., Pouladi, P., & Mirghaderi, R. (2016). Experimental study of a replaceable steel coupling beam with an end-plate connection. Journal of Constructional Steel Research, 122, 138-150.

Li, X., Lv, H. L., Zhang, G. C., & Ding, B. D. (2015). Seismic behavior of replaceable steel truss coupling beams with buckling restrained webs. Journal of Constructional Steel Research, 104, 167–176.

Eljadei, A. A., & Harries, K. A. (2015). On the use of fixed point theory to design coupled core walls. Engineering Structures, 102, 61–65.

Bengar, H. A., & Aski, R. M. (2016). Performance based evaluation of rc coupled shear wall system with steel coupling beam. Steel & Composite Structures, 20(2), 337-355.

Ji, X., Wang, Y., Zhang, J., & Okazaki, T. (2017). Seismic behavior and fragility curves of replaceable steel coupling beams with slabs. Engineering Structures, 150(2017), 622–635.

Ji Xiaodong, Wang Yandong, Ma Qifeng, & Okazaki Taichiro. (2017). Cyclic Behavior of Replaceable Steel Coupling Beams. Journal of Structural Engineering, 143(2), 04016169.

Fortney, P. J., Shahrooz, B. M., & Rassati, G. A. (2006). The Next Generation of Coupling Beams. International Conference on Composite Construction in Steel and Concrete (pp.619-630).

Fortney, P. J., Shahrooz, B. M., & Rassati, G. A. (2007). Large-scale testing of a replaceable “fuse” steel coupling beam. Journal of Structural Engineering, 133(12), 1801-1807.

NUMERICAL INVESTIGATION OF COMPOSITE DETACHABLE SHORT LINKS

Mariana Zimbru[1],
University of Naples 'Federico II'
Department of Structures for Engineering and Architecture
Naples, Italy
mariana.zimbru@unina.it

Mario D'Aniello[2],
University of Naples 'Federico II'
Department of Structures for Engineering and Architecture
Naples, Italy
mdaniel@unina.it

Aurel Stratan[3],
Politehnica University of Timișoara, Department of Steel Structures and Structural Mechanics
Timișoara, Romania
aurel.stratan@upt.ro

Raffaele Landolfo[4]
University of Naples 'Federico II'
Department of Structures for Engineering and Architecture
Naples, Italy
landolfo@unina.it

Dan Dubină[5]
Politehnica University of Timișoara, Department of Steel Structures and Structural Mechanics
Timișoara, Romania
dan.dubina@upt.ro

ABSTRACT

Eccentrically braced frames (EBF) equipped with replaceable short links are effective seismic resisting systems due to their ductility and ease of repair in the aftermath of an earthquake. Several existing studies revealed that short links can develop shear overstrength (i.e. V_u/V_p, where V_u is the ultimate shear strength and V_p the corresponding plastic resistance) larger than the value recommended in EC8 (i.e. V_u/V_p =1.5). In particular, the presence of axial restraints is one of the factors responsible for the higher shear overstrength owing to the development of catenary actions in the link at large rotational demands. Another source of shear overstrength is the composite slab that can resist the shear distortion together with the short link. Full scale pseudo-dynamic experimental tests on a 3D EBF carried out within the DUAREM project (Ioan et al, 2016) allowed investigating the response of detachable links with two different arrangements: (i) steel solution – the link was uncoupled from the slab (ii) composite solution – the slab runs over the link and is connected to the beam. In this paper, the second set of composite detachable links are analyzed by means of finite element simulations with the aim to evaluate the shear overstrength and the level of axial force developed by the links.

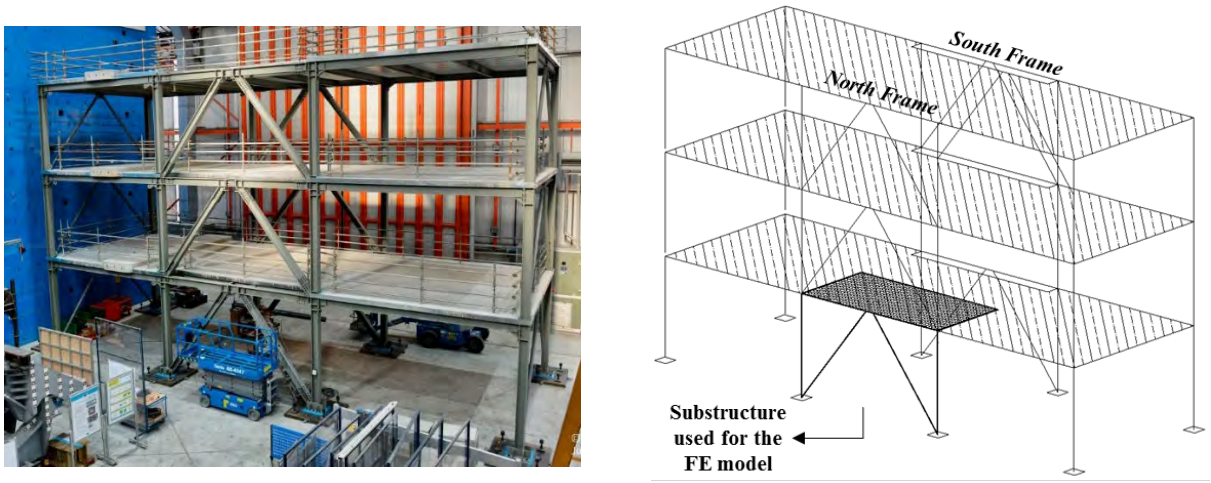
Keywords: Seismic design, replaceable links, composite, finite element analysis.

INTRODUCTION

Structural systems that allow fast and simple repair solutions in the aftermath of important seismic events often represent the design target in seismic areas. The research carried out in the past decades led to the development and improvement of traditional structural systems and design strategies that can nowadays be re-adapted into innovative systems that satisfy the previously mentioned objective. Among the large variety of steel structural schemes, eccentrically braced frames (EBFs) are generally considered the rational compromise between the large stiffness of the braced structures and the ductility that is typically provided by moment resisting frames (MRFs). Indeed, with rough simplification, the braces guarantee lateral stiffness and the links provide ductility and dissipative capacity. Since the links are the dissipative fuses, several studies have been carried out to investigate the possibility to replace this component (Mansour et al., 2008; Ioan et al., 2013). These studies highlighted the key role of the link end connections that should guarantee the possibility to detach and to replace the damaged links. It is trivial to recognize that the link connections must be designed with adequate overstrength. The presence of axial restraints can induce catenary actions developing into the links to which corresponds shear overstrength larger than $1.5V_p$, being V_p the plastic shear of the link (Azad & Topkaya 2017). The possibility to replace damaged links also depends on the residual lateral displacements after the seismic event. Dubina et al., (2008) and Bosco et al, (2017) highlighted that dual-eccentrically braced frames (D-EBFs), namely EBFs combined with some MRF spans, are effective to minimize the residual drifts. Buildings designed with composite links had an overall good performance during the Christchurch earthquake sequence of 2011-2012, showing limited residual drifts (Clifton et al., 2012). Indeed, early in the development of EBFs, Ricles and Popov (1987) highlighted the influence of the slab on the strength and stiffness of the structural typology. Furthermore, Ciutina et al. (2013) and Danku et al. (2013) demonstrated that simply disconnecting the slab from the dissipative zones in D-EBFs does not lead to a response governed solely by the steel element, on the contrary, the overall strength and stiffness are improved while the ductility is preserved.

Within the DUAREM project, Ioan et al. (2016) carried out full scale pseudo-dynamic experimental tests on D-EBFs with very short links that demonstrated the effectiveness of the reparability of D-EBFs with detachable shear links. In particular, these tests also focused on the link-to-slab interaction. In particular, the experimental mockup (see Figure 1a) was conceived with two different types of link-to-slab details, one per side of the prototype. Indeed, one of the perimeter frames was detailed as an all-steel solution without slab interaction (i.e. South frame in Figure 1b) and the frame on the opposite side was detailed with full-composite girder with Nelson studs distributed on the braced span except for the link (e.g. North frame in Figure 1b). These arrangements allowed to examine the interactions between the link and the slab as well as the feasibility of the repair in case of slab damage.

In order to investigate the influence of the slab at the local level on the damage pattern as well as the development of shear and axial overstrength, finite element models of the DUAREM composite links were developed and the numerical results are described and discussed in this paper. The numerical simulations allowed to deepen the interpretation of the results obtained experimentally, but also provided a basis for potential theoretical developments for the design of composite links.



a) Experimental mock-up b) Sub-structuring of the numerical model

Fig. 1 – The DUAREM mockup

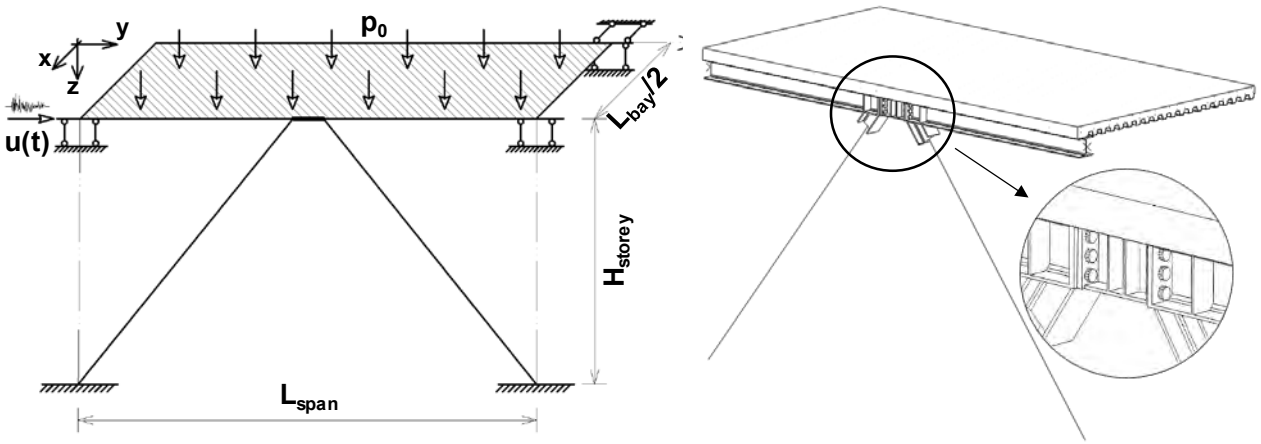
THE FE MODEL

Finite element analyses (FEAs) were performed using Abaqus/Explicit software. The geometry of the FE model (Figure 2a and b) was extracted from the sub-structuring of the full-scale frame tested within the DUAREM research project (Ioan et al., 2016). Although the structure was a 3 storey D-EBF, only two models are required because the geometrical characteristics of the 1st and 2nd storey link and connection are identical, while all other parts (beams, braces) are identical throughout the entire building. Table 1 and Figure 2c detail the main geometrical features of the links. The links were designed with two web stiffeners, in accordance with the EC8 rules. As it can be observed in Figure 1a and b, the South frame (the all-steel solution) has the slab fully disconnected from the link and the beam containing it, while the North frame (the composite solution) has the slab running over the link and connected to the beam of the EBF bay by means of shear studs. Figure 1b schematically depicts the mockup and the substructure used for the numerical model (highlighted in grey for the first-floor model S1).

Table 1 – Link geometrical properties

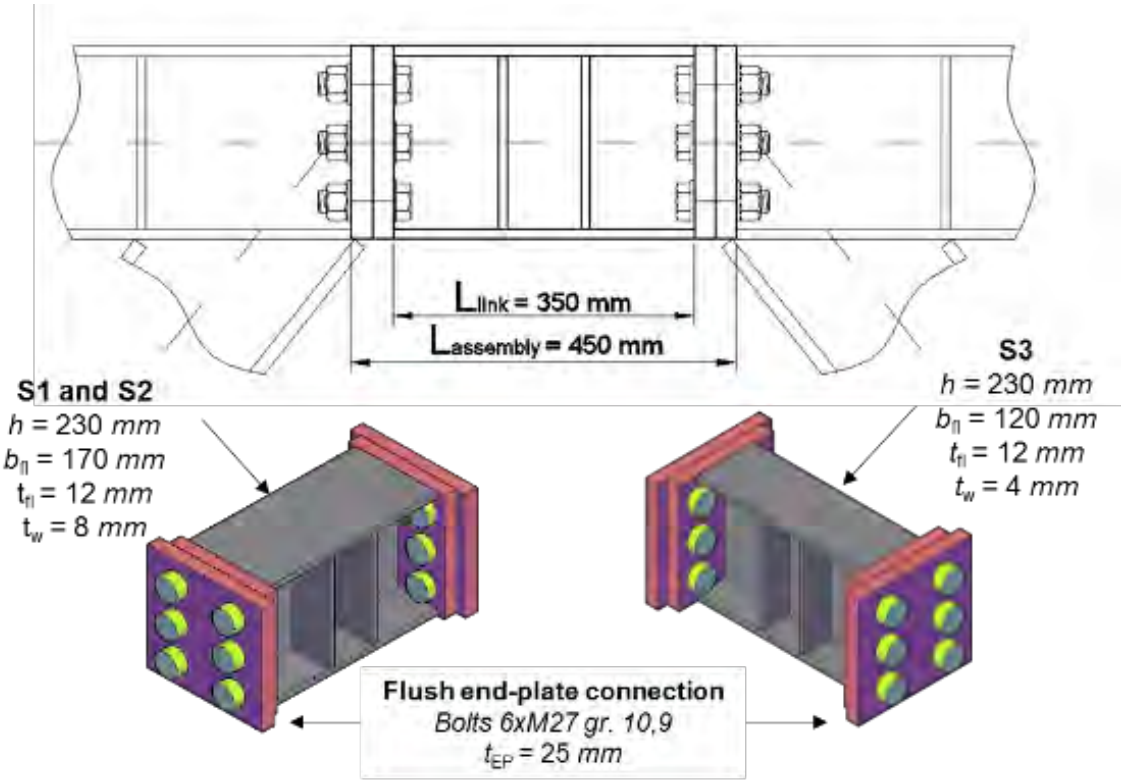
Specimen	Link length (e_{link})	Assembly length ($L_{assembly}$)	Height (h)	Width (b_{fl})	Flange thickness (t_{fl})	Web thickness (t_w)
	[Mm]	[mm]	[mm]	[mm]	[mm]	[mm]
S-1	350	450	230	170	12	8
S-2	350	450	230	170	12	8
S-3	350	450	230	120	12	4

The entire span containing the link and half transverse bay are modelled as depicted in Figure 2a. The model includes the link connected to the adjoining beams, the braces and the secondary beams perpendicular to the plane of the frame. The concrete slab, steel deck, reinforcement and Nelson studs were modelled with their corresponding experimental geometrical features and material properties (Ioan et al., 2016).



a) Static scheme

b) The FE model



c) Links and connections geometrical characteristics

Fig. 2 – Sub-structure geometry and boundary conditions

In order to reduce the computational effort, the following modelling assumptions were adopted:

- The reinforcement bars, the Nelson studs and the braces were modelled by means of beam elements (B31 a 2-node linear beam in space, with 6 DOF per node) with their respective cross-section. The brace segment in the immediate vicinity of the beam was modelled as a solid part, for a better representation of the transfer of forces between the two elements.

- The steel deck was modelled by means of continuum shell elements (SC8R an 8-node quadrilateral in-plane general-purpose continuum shell, reduced integration with hourglass control, finite membrane strains, with 3 DOF per node) with the thickness of the real steel sheet (0.8 mm).

The other parts (steel beams, link, bolts, plates, stiffeners and concrete slab) were modelled using C3D8R (8-node linear brick, reduced integration with hourglass control, with 3 DOF per node) solid finite elements.

The material properties were defined for each element individually, function of the material (steel, concrete) and the type of finite element adopted (beam, shell or solid). S355 steel is used for steel beams, braces, end-plates and stiffeners. The steel density (7850 kg/m^3) and nominal elastic properties in terms of Young's modulus (210 GPa) and Poisson ratio (0.3) were considered. The nonlinear stress-strain curves were obtained from the tensile coupon tests sampled from the members constituting the mockup. The plasticity was modelled with the combined isotropic-kinematic hardening law. S235 steel was used for the links and different properties were assigned to their flanges and webs, corresponding to the results of coupon tests. The reinforcement bars, the Nelson studs and steel deck properties have similar elastic properties but for the post-yielding behavior, a simplified linear branch was considered, with the respective strength and strain limits. Table 2 summarizes the adopted properties of the elements.

The bolts of the flush end-plate connections at the link ends were M27 HV grade 10.9. Their mechanical behavior was simulated in accordance with Tartaglia et al. (2018, 2019). The slab material property was simulated using the concrete damage plasticity model proposed by Hillerborg et al. (1976). This model takes into account the reduction of the elastic stiffness caused by plastic straining both in tension and compression and it accounts as well for the stiffness recovery effects under dynamic loading conditions (Abaqus User's Manual, 2014). The characteristics of C25/30 concrete were defined in accordance with Eurocode 2, i.e. density of 2500 kg/m^3, Young's modulus of 31GPa, and Poisson's ratio of 0.2.

Table 2 – Material properties

	Type	Material	Yield strength	Ultimate strength	Elongation
			[MPa]	[MPa]	[%]
Link Flanges		S235	260	453	31
Web link S1		S235	296	473	29
Web link S3		S235	296	460	23
Reinforcement	610HD mesh	B450C	450	540	15
Studs	SMD19105	S235	235	360	15
Steel deck	A55 – P600 G5	S250	260	450	15

Explicit analyses were carried out. Hence, a General Contact interaction was defined for the entire model. The global property in terms of Normal and Tangential Behavior was defined as 'Hard Contact' and using the 'Penalty' friction formulation, respectively. Multi-point constraints (MPCs) were used to define the connection between the shear studs and the beams, the beam and solid part of the braces and the secondary and main beams. The steel sheet was tied to the concrete slab. The reinforcements and the shear studs were embedded in the concrete.

The nature of the analysis dictates also the way the bolt preloading is defined. The clamping action of the bolts was applied by inducing artificially the shrinkage of the shanks through a temperature variation in the bolt. The permanent load was applied as distributed pressure on the entire top surface of the slab, with a magnitude of 5 kN/m^2 (which is the value applied during the tests).The boundary conditions were defined based on the scheme in Figure 2. The lateral actions were imposed as monotonically increasing displacement applied at the main beam ends, along the slab edge, and except for the displacement along the y-axis, all other DOFs are restrained. The braces were fully restrained while the boundary conditions at the end of the composite slab (in the section at the mid-bay) allow the displacement along the y-axis (the direction in which the lateral action is applied) and restrain all other DOFs. The mesh was adequately defined for each element type (solid, continuum shell and beam) and considering seed sizes that can provide optimum time/quality ratios. In total, each model had approximately 100000 solid elements, 20000 shell elements and 6000 beam elements.

Previous analyses on all-steel link assemblies were conducted in order to calibrate the numerical model. As depicted in Figure 3, good agreement between the experimental and numerical response was obtained (Zimbru et al., 2017).

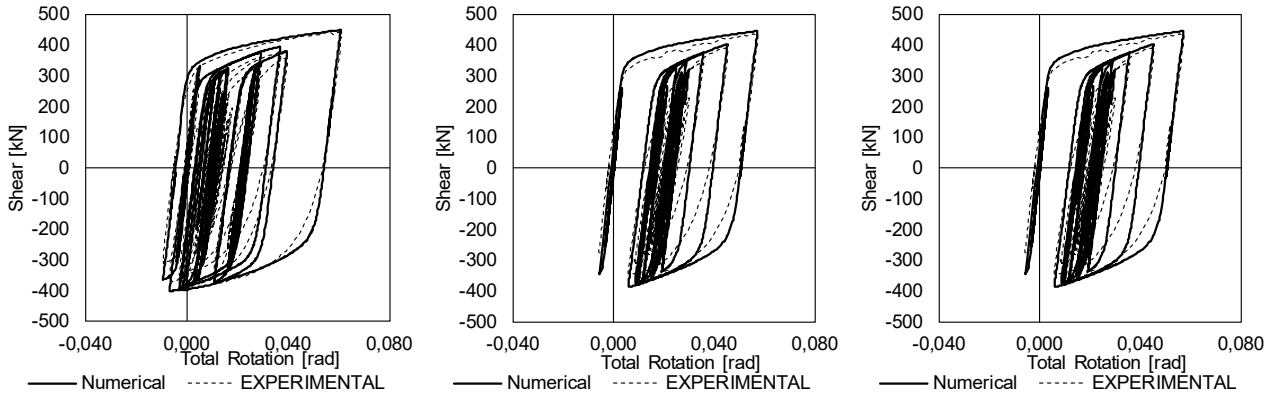


Fig. 3 All-steel (South Frame) Experimental vs Numerical Shear Force-Rotation Curves

RESULTS

The numerical results of the composite link assemblies were compared with the output obtained in previous investigations of all-steel links (Zimbru et al., 2017) in order to assess the accuracy of the current model. The comparison is made in terms of link forces (V_{link}, N_{link}), thus disregarding the slab contribution for the composite model. Figure 4 shows that the shear strength (a) and axial force (b) developed in the link of the composite model (North frame) have very close values to the ones of the forces in the all-steel link (South frame). Furthermore, the numerical model is able to replicate the initial stiffness and plastic shear capacity.

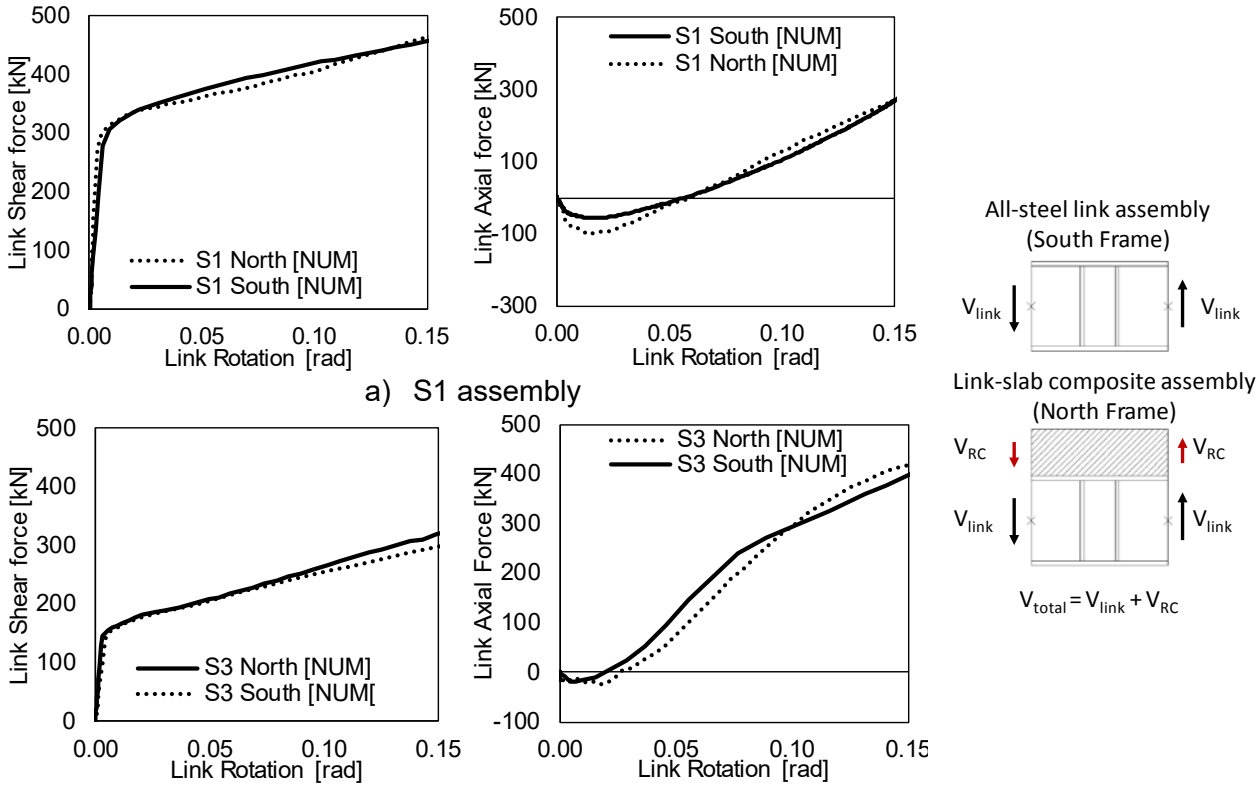
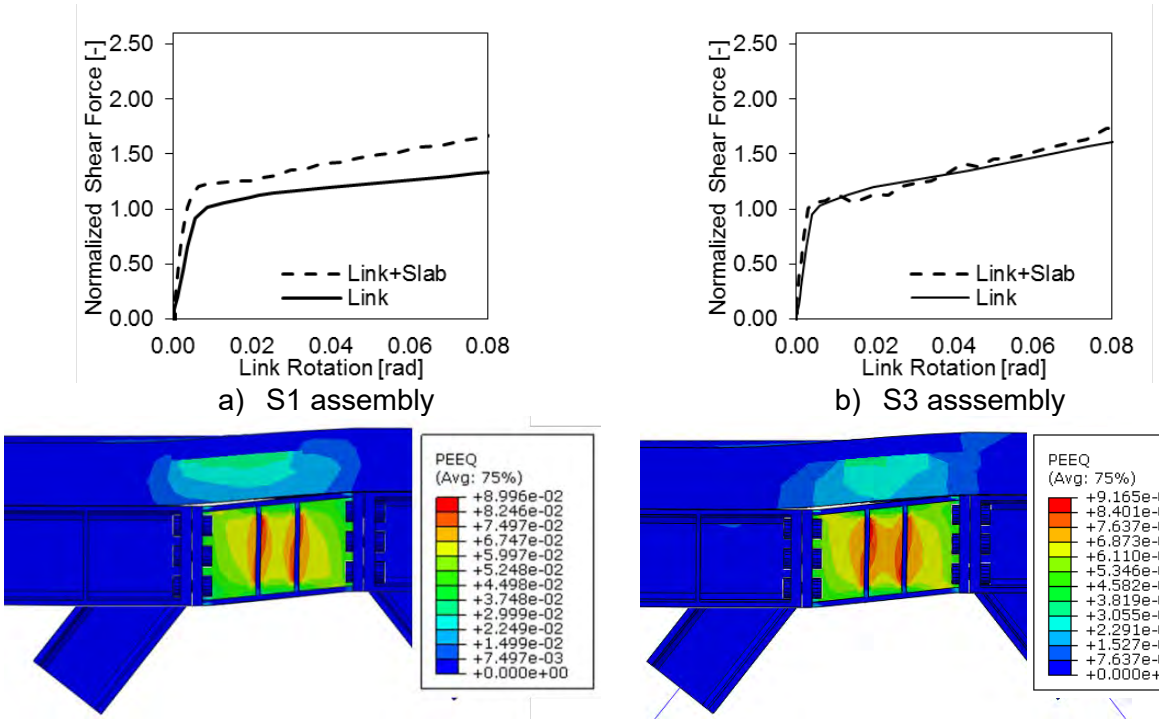


Fig. 4 – Comparison between the shear (V_{link}) and axial force (N_{link}) developing into the all-steel (South) and the composite (North) links

The link-to-slab assembly develops larger shear forces, as it can be seen in Figure 5a and b, and in particular for S1, the contribution of the slab can be clearly distinguished as the difference between the total shear and the link shear. Overstrength after reaching the plastic strength can also be noticed for both links. Indeed, as depicted in Figure 5, the link-to-slab assembly indicates shear overstrength values larger than those exhibited by the all-steel links. The numerical results confirm that the slab contributes to the shear strength of the link by resisting shear in parallel. In particular, the peak shear overstrength at 0.08 rad is about 1.7 for both link-to-slab assemblies. This finding, in line with those of Ciutina et al., 2013, highlights the need to revise the capacity design rules in order to guarantee the effectiveness of the capacity design rules.

Figure 5c and d depict the equivalent plastic strain (PEEQ) distribution in the two link-slab assemblies at 8% of link rotation. It is possible to observe the large concentration of damage in both link and slab, confirming thus the development of the composite action.



a) S1 assembly b) S3 asssembly

c) S1 assembly d) S3 assembly

Fig. 5 – Normalized link and total shear force (a and b) and PEEQ distributions (c and d)

In order to evaluate analytically the contribution of the RC slab to the response of the link-slab assembly, it was assumed that the two elements work in parallel (given that no shear studs are placed on the link, but only on the beams of the frame), and the ultimate bending capacity of the slab was evaluated. Under this assumption, two possible mechanisms for achieving the shear capacity of the slab were alternatively considered: (i) the shear capacity corresponding to the flexural failure of the slab and (ii) the shear capacity of the RC slab. For the first scenario, Figure 6 briefly describes the static scheme of the models and the cross-section of the slab for the evaluation of the bending moments (the slab flexural capacity at the left - M_{left} - and right - M_{right} - end of the link differ as the section is not symmetric under sagging and hogging bending) and the corresponding shear ($V_{slab,M}$). Meanwhile, for the evaluation of the RC shear capacity ($V_{slab,Rd,c}$), the recommendations of Eurocode 2 were used.

Table 3 shows the values analytically calculated, while Figure 7a and b depict the comparison with the values obtained from the FE analysis. It can be observed that for assembly S1, the link-to-slab assembly shows an increase of shear capacity with respect to the bare steel profile and that the analytical prediction matches perfectly the numerical curve, i.e. evaluating the shear capacity as the sum of the link shear strength and slab shear capacity gives a good approximation. However, for the case of S3 (i.e. the shorter link), the initial plastic shear strength is achieved by means of the steel link alone, while the shear capacity developed at 8% of link rotation (the value that is used for the capacity design of non-dissipative members) is also influenced by the slab.

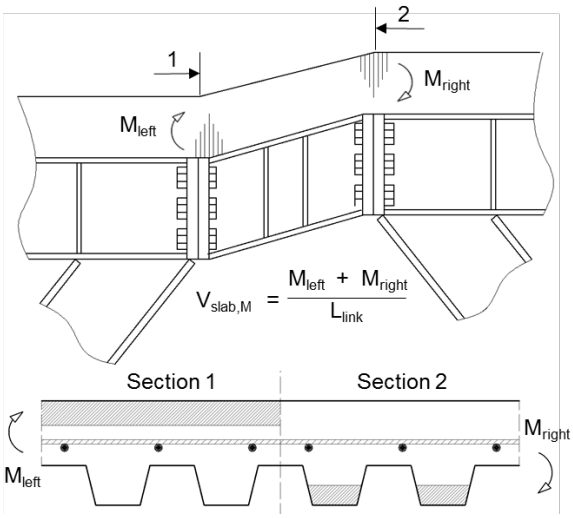


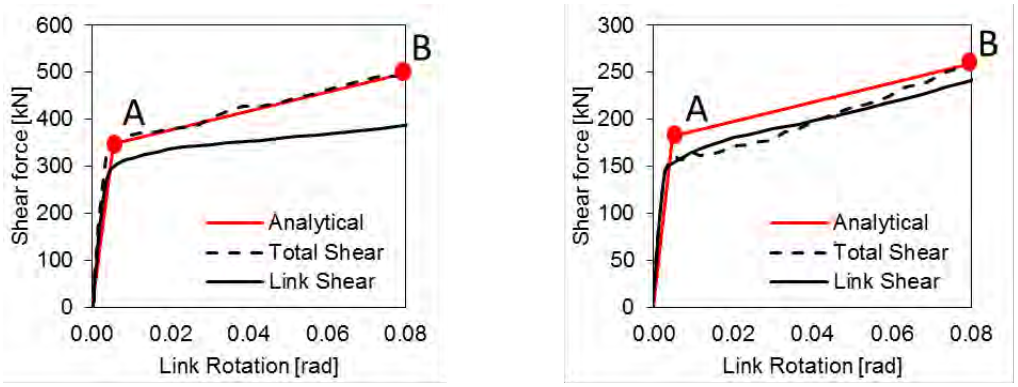
Fig. 6 – Increase of shear capacity due to the flexural hinging of the slab

Table 3 Summary of resistance contribution of the RC slab

	b_{eff}	$V_{slab,M}$	$V_{slab,Rd,c}$	$V_{y,link}$	V_A	V_B
	m	kNm/m	kN	kN	kN	kN
S1	0.40	54	49	290	350	499
S3	0.40	54	49	145	194	266

Where:

b_{eff} is the effective width of the RC slab calculated according to EC4
$V_{slab,M}$ is the shear contribution of the RC slab considering its ultimate flexural resistance (see Figure 5)
$V_{slab,Rd,c}$ is the shear resistance of the RC slab evaluated according to Eurocode 2
$V_{y,link}$ is the shear capacity of the steel link
V_A is the shear capacity of the link-slab assembly obtained by summing up $V_{y,link}$ and the minimum between $V_{slab,M}$ and $V_{slab,Rd,c}$
V_B is the shear capacity of the link-slab assembly at 8% link rotation obtained considering 1.5 $V_{y,link}$ (where 1.5 is the shear overstrength coefficient according to Eurocode 8) and the minimum between $V_{slab,M}$ and $V_{slab,Rd,c}$.



a) S1 b) S3

Fig. 7 – Shear from the all-steel link and the link-to-slab assembly

Figure 8 depicts the tensile damage distribution in the RC slab of S1 model for varying link rotation levels. As it can be expected, the damage increases as the rotational demand increases. In particular, when the link deforms inelastically it pushes the floor slab out of plane. The distribution of the tensile damage into the slab at 0.08 rad link rotation is far from the damage recognizable into a composite beam, but it transversally involves the deck with the formation of yield lines oriented with the imposed deformation. This finding is in line with the observations presented by Clifton et al. (2012).

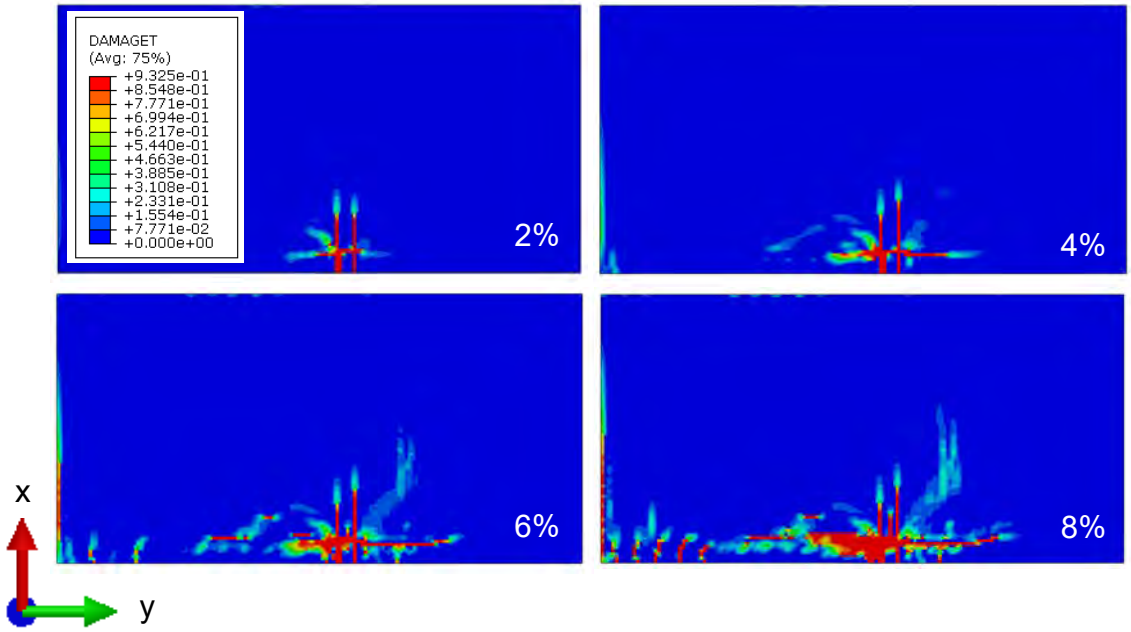


Fig. 8 – Top view of the tension damage distribution in the slab of S1 assembly

CONCLUSIONS

In light of the results of the finite element simulations presented and discussed in the previous paragraphs, the following conclusions are drawn:

- The shear and the axial forces developing into the steel links of the North frame (the link-to-slab system) do not differ from those exhibited by the all-steel assemblies. This result confirms that the design strength of link end-connections does not depend on the slab.
- The reinforced concrete slab brings a significant contribution to the dissipative mechanism but with the downside of significant damage in the slab, not only in the area above the link but also spreading along the beam containing the link.
- The link-to-slab assemblies may develop larger shear strength than the all-steel links. This implies that this increase of strength should be properly accounted for the capacity design of braces.
- During the experimental pseudo-dynamic tests, the level of damage observed was reduced, at the maximum link rotation of 6%. However, it can be observed from the numerical analyses that damage increases in the affected areas and spreads to new ones when the link rotation exceeds the rotation of 8%. The significant level of damage

in the slab leads to a proportional increase in repair costs in the aftermath of the design earthquake.

- The mechanisms leading to additional shear capacity owed to the RC slab need to be further investigated and proper rules for the definition of the effective width (b_{eff}) need to be developed.

REFERENCES:

Azad, K.S.. & Topkaya, C., (2017). “A review of research on steel eccentrically braced frames” Journal of Constructional Steel Research, 128, 53-71

Bosco, M., Marino, E.M., Rossi, P.P. (2017). A design procedure for dual eccentrically braced-moment resisting frames in the framework of Eurocode 8. *Engineering Structures*, 130, 198-215.

Ciutina, A., Dubina, D. and Danku, G. (2013) Influence of steel-concrete interaction in dissipative zones of frames: I – Experimental study. *Steel and Composite Structures.* 15(3), 281-000. http://dx.doi.org/10.12989/scs.2013.15.3.281

Clifton G.C., Nashid H., Ferguson G, Hodgson M., Seal C., Bruneau M., MacRae G.A. and Gardiner S. (2012). Performance of Eccentrically Braced Framed Buildings In The Christchurch Earthquake Series of 2010/2011. *Proceedings. of 15th WCEE*, Lisbon, Portugal, September 24-28.

Danku, G., Dubina, D., and Ciutina, A. (2013). Influence of steel-concrete interaction in dissipative zones of frames: II - Numerical study. *Steel and Composite Structures.* 15(3), 305-000. http://dx.doi.org/10.12989/scs.2013.15.3.305

Dassault (2014), Abaqus 6.14 - Abaqus Analysis User's Manual, Dassault Systèmes Simulia Corp.

Dubina, D., Stratan, A., Dinu, F. (2008). Dual high-strength steel eccentrically braced frames with removable links. *Earthquake Engineering and Structural Dynamics*, 37, 1703–1720.

EN 1998-1, Design of Structures for Earthquake Resistance - Part 1: General Rules, Seismic Actions and Rules for Buildings. CEN, 2005.

EN 1993:1–8, Design of Steel Structures - Part 1–8: Design of Joints. CEN, 2005.

EN 1992:1–1, Design of Concrete Structures - Part 1–1: General rules and rules for buildings. CEN, 2005.

Hillerborg, A., Modeer, M., and Petersson, P-E. (1976). Analysis of crack formation and crack growth in concrete by means of fracture mechanics and finite elements. *Cement and Concrete Research*. 6, 773-782. Pergamon Press, Inc. Printed in the United States.

Ioan, A., Stratan, A., Dubina, D. (2013). Numerical simulation of bolted links removal in eccentrically braced frames*. Pollack Periodica* 8(1), 15-26.

Ioan, A., Stratan, A., Dubină, D., Poljanšek, M., Molina, F.J., Taucer, F., Pegon, P., Sabău, G. (2016). Experimental validation of re-centring capability of eccentrically braced frames with removable links. *Engineering Structures*, 113, 335–346.

Mansour, N., Shen, Y., Christopoulos, C., Tremblay, R. (2008). Experimental evaluation of nonlinear replaceable links in eccentrically braced frames and moment resisting frames. *The 14th Conference on Earthquake engineering*, Beijing, China, October 12-17.

Ricles, J. M. and Popov, E. P. (1987). Experiments on eccentrically braced frames with composite floors. Berkeley, California, Earthquake Engineering Research Center, University of California: 324 pp

Tartaglia, R., D'Aniello, M., Zimbru, M., Landolfo, R. (2018). Finite element simulations on the ultimate response of extended stiffened end-plate joints. *Steel and Composite Structures*, 27(6), 727-745. DOI: 10.12989/scs.2018.27.6.727

Tartaglia, R., D'Aniello, M., Rassati, G.A. (2019). Proposal of AISC-compliant seismic design criteria for ductile partially-restrained end-plate bolted joints. *Journal of Constructional Steel Research* 159, 364-383.

Zimbru, M., D'Aniello, M., Stratan, A., Landolfo R., and Dubina, D. (2017) Finite element modelling of detachable short links. Eccomas Proceedia COMPDYN (2017) 790-801, doi: 10.7712/120117.5457.17470

DIRECT ANALYSIS FOR STRUCTURES MADE OF HIGH STRENGTH STEEL

Si-Wei Liu[1], Siu-Lai Chan[1*] and Tian-Ji Li[2]

[1] Department of Civil and Environmental Engineering,
The Hong Kong Polytechnic University, Kowloon, Hong Kong.

[2] Shanghai Construction No.5 (Group) Co., Ltd. Shanghai, China

*Corresponding Author: Email: ceslchan@polyu.edu.hk

ABSTRACT

Buckling curves for high strength steel are not easily obtainable because of limited resources in testing the members under high loads, resulting in difficulty for engineers to design structures made of high strength steels. This paper proposes a method based on direct analysis (DA) method for design of high-strength steel members and frames allowing explicit modeling of residual stresses such that numerical simulation analysis and design can be conducted as substitutes of full-scale physical tests. A section analysis technique based on quasi-Newton iterative scheme is adopted to take into account the effects of residual stress with the geometrical imperfections measured. Residual stress for the welded box-sections and H-sections fabricated by high-strength steel are measured and adopted for illustration. To complete the consideration of buckling and second-order effects, the initially crooked with arbitrarily-located-hinge (ALH) element is introduced. A fiber hinge model using the sectional strength-iteration surfaces is used for modeling of material yields. Several examples are employed to verify the accuracy and validity of the proposed approach. This paper is to contribute to the formulation of a versatile numerical procedure to account for residual stresses and geometric imperfections separately for design of high-strength steel members and frames where physical tests are expensive.

Keywords Direct analysis, high strength steel, imperfections

INTRODUCTION

Direct analysis (DA) for steel structure design is a new trend for design of modern structures without assumption of effective length. However, most design codes only contain clauses for use steel with strengths ranging from 235MPa to 460MPa, the current design formulae based on the linear assumption is not directly applicable to design of high-strength steel members and frames.

DA allows the use of plastic hinge or plastic zone. Generally speaking, the former is efficient but less accurate than the latter. This paper proposes a method of using plastic zone to generate yield surface for plastic hinge so the advantages of both methods are retained. Further, the suggested method allows separated considerations of residual stress so it can deal with DA of high strength steel from the basic principle.

The applications of high-strength steel constructions is becoming more important and was initiated since 1990s such as projects of Sony Center in Berlin, Latitude Tower in Sydney, Star City in Darling Harbour of Sydney, NTV Tower in Tokyo, JR East Main Office in Tokyo, Landmark Tower in Yokohama, Tokyo Skytree and Beijing National Stadium and CCTV New Building. Many benefits were observed in practice regarding the structural efficiency, constructional speed and so on.

The use of high-strength steels can significantly reduce member size and increase safety margin, but the stability problems could be more acute. Geometrical initial imperfections and the residual stress are two major factors for structural and member design. Initial geometric imperfections exist in all steel members and frames and they are critical in stability design. In addition, residual stress could reduce the ultimate capacity of compression members via the degradation of stiffness and yielding, and decrease the fatigue endurance of members under cyclic loading. Further, residual stresses have an obvious influence on the ultimate load capacity for flame-cut welded box and H-columns (Ziemian 2010)

Analyses and design by the beam-column elements are considered to be the most efficient in practice, and this approach has been extended to practical design in recent years. In the present study, the curved

arbitrarily-located-hinge (ALH) element, proposed by Liu et al. (2014a, 2014b), is employed and the initial member curvature associated with P-δ and P-Δ effects are directly modeled in an incremental-iterative numerical procedure.

Material yielding is another major factor controlling the ultimate load and overall stability of a framed structure when one uses DA for design. An approach using the plastic fiber hinge model is proposed in the present study. The material yielding on hinge locations is modeled by a gradually softening spring. Contrary to the traditional or refined plastic hinge model where the empirical and simplified linear interaction equations are commonly adopted for yield surface of sections, the present sectional yield surface is constructed by a plastic fiber hinge model which could consider residual stresses directly and analytically rather than empirically.

To generate the sectional yield surfaces, the cross-section analysis technique is required and this method has been extensively studied since the 1960s. Numerous researchers have proposed equations for yield surfaces and the present study uses a more rigorous procedure of quasi-Newton interactive scheme, where the steel sections are automatically divided into several fibers in calculating the stress resultant of a cross section.

The residual stress models are vital and available for the analysis and have been investigated by experiments [see, for examples, Usami and Fukumoto (1984) and Rasmussen and Hancock (1995)]. In this paper, two distributed patterns of residual stress for the welded box-sections and H-sections fabricated by high-strength steel are discussed. The section analysis technique based on the Quasi-Newton iterative scheme with explicit consideration of the residual stresses is elaborated. To consider second-order effects associated with initial imperfections, the curved arbitrarily-located-hinge (ALH) element is adopted. A plastic fiber hinge model using the sectional strength-iteration surfaces is introduced for reflecting the yield behavior. Finally, two examples are given for verifying the accuracy and validity of the proposed method.

ASSUMPTIONS

In the present study, the following assumptions are taken for analysis of the beam-column members and their cross sections. (1) Strains in the element are small, but the large deformations are achieved using the incremental tangent stiffness method; (2) Euler-Bernoulli hypothesis is assumed and the strain distribution along the cross section is linear; (3) Second-order effects including the P-Δ and P-δ deformations are considered; (4) Material yielding on the critical section is reflected by the plastic fiber hinge; (5) Loads are conservative and applied on element nodes; and (6) Warping and beam lateral-torsional buckling are not considered.

BEAM-COLUMN ELEMENT FORMULATIONS

The important parameters such as initial imperfections, large deflection and material yielding, are required to be simulated in the numerical procedure. In the present study, the arbitrarily-located-hinge (ALH) element shown in **Fig. .** below proposed by Liu et al. (2014a, 2014b) is used and should be referred for details.

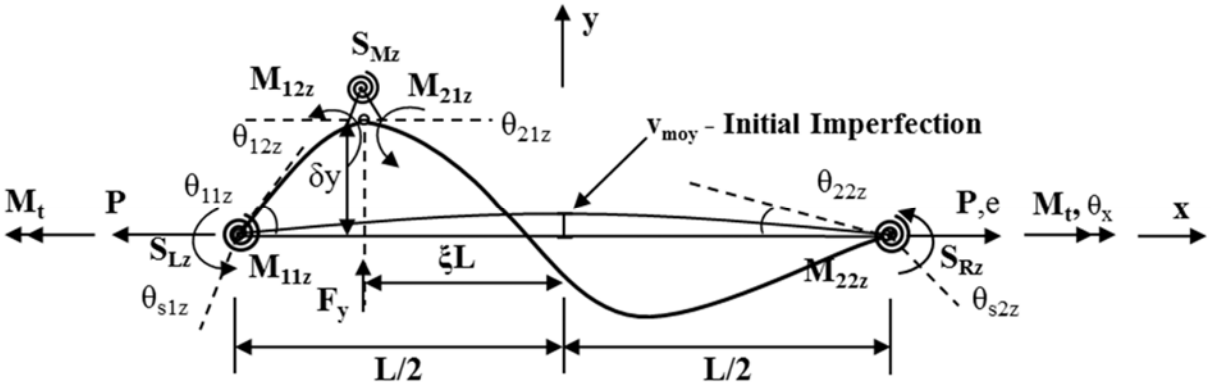


Fig 1 The beam-column element

PLASTIC ZONE MODEL

Plastic analysis is required to form a yielding function to monitor the process of the sectional plastification. The plastic fiber hinge method is derived from the refined plastic hinge approach proposed by Chan and Chui (1997). Contrary to the traditional lumped plasticity or refined plastic

hinge methods, which assume the simplified criteria to examine the material yielding on hinge locations, the proposed model employs the analytical and rigorous sectional yield surfaces to control the hinge stiffness.

YIELD SURFACES

For any steel sections under a given axial-load, the corresponding moments can be computed by the presented sectional analysis method. The sectional yield surface, adopted to describe the axial force and related moments of section, is outlined below (see **Fig. 2**).

The outermost boundary is a failure surface shown in **Fig. 2**. The ultimate state of a section is described by these data points that induce failure of steel sections. The surface is necessary for determining the individual load-bearing capacity in traditional design of steel structures.

Initial yield surface is also a basic strength control criterion for plastic analysis. Within this surface generating from a specific load combination, the corresponding section maintains elastic. When generating initial yield surfaces, all fibers of a section will be monitored and the onset of strains beyond the elastic limit is also detected. The internal force and moments are calculated through the integration of stresses along the cross-section. Subsequently, sectional capacity can be obtained from the initial yield condition.

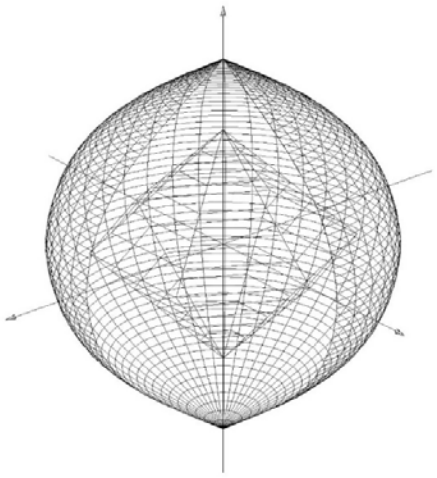


Fig.2 Initial yield and failure surfaces

Yield and Plastic Moments

The whole strength interaction space is divided into failure and initial yield surfaces in three zones as shown in **Fig. 3**. These zones are named as the elastic, elasto-plastic and plastic hardening zones. The hinge stiffness is determined according to the current loading position in the strength interaction space. When the load point lies inside the elastic zone, the section reminds elastic and the hinge stiffness is infinitely large, which means no plastic deformation is formed at the hinge location. Once the loads go into the elasto-plastic zone, the partially yielding on the critical section begins and the hinge stiffness decreases. If the load exceeds the failure surface, the corresponding section will be fully yielded and the hinge stiffness is set to a small value. The elastic and plastic moments are defined as minimum moment causing yield and maximum moment capacity, which are further used to update the hinge stiffness.

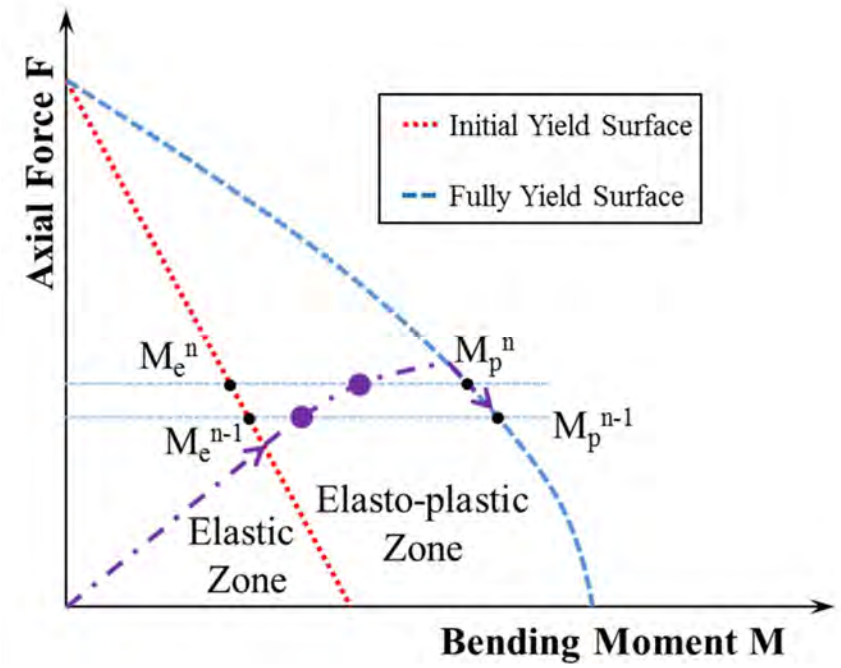


Fig.3 Initial yield and failure surfaces

Hinge stiffness

As aforementioned, the degradation in hinge stiffness reflects the material yielding on hinge sections. The formulations for calculating the spring stiffness *S*, are written as,

$$S = 10^{+10}\frac{EI_0}{L}, \text{ for } M_i^{\zeta} \le M_{\text{er}}^{\zeta} \tag{1}$$

$$S = \frac{EI(\zeta)}{L}\left|\left(M_{\text{pr}}^{\zeta} - M_i^{\zeta}\right)/\left(M_i^{\zeta} - M_{\text{er}}^{\zeta}\right)\right| \text{ for } M_{\text{er}}^{\zeta} < M_i^{\zeta} < M_{\text{pr}}^{\zeta} \tag{2}$$

$$S = \frac{EI(\zeta)}{L}\rho, \text{ for } M_i^{\zeta} \le M_{\text{er}}^{\zeta} \tag{3}$$

where $EI(\zeta)/L$ is the bending stiffness in the current iteration; the elastic and plastic moment capacities at the current axial force are given by M_{er}^{ζ} and M_{pr}^{ζ}.

Cross section analysis

The sectional yield surfaces, i.e. yield and plastic surfaces, are generated by the some rather standard procedures as locations of neutral axis, determination of axial force and moment resistance by a summation process of stresses which can include residual stresses directly below.

$$\sigma_i = f(\varepsilon_i) \tag{4}$$

$$\varepsilon_i = \varepsilon_{ai} + \varepsilon_{ri} + \phi_i v_i \tag{5}$$

in which σ_i is the direct stress, ε_i is the total strain, ε_{ai} is the axial strain; ε_{ri} is the residual strain, φ_i is the curvature and v_i is the distance.

And the bending moments can be obtained from Eqs. (4) and (5) through the following summation process.

$$M_z = M_u\cos\theta_n - M_v\sin\theta_n = -\left(\sum_{i=1}^{n}\sigma_i A_i v_i\cdot\cos\theta_n + \sum_{i=1}^{n}\sigma_i A_i u_i\cdot\sin\theta_n\right) \tag{6}$$

$$M_y = M_u\sin\theta_n + M_v\cos\theta_n = -\sum_{i=1}^{n}\sigma_i A_i v_i\cdot\sin\theta_n + \sum_{i=1}^{n}\sigma_i A_i u_i\cdot\cos\theta_n \tag{7}$$

$$N_x = \sum_{i=1}^{n}\sigma_i A_i \tag{8}$$

in which M_u, M_v and N_x are the bending moments and axial force and M_z and M_y are the global moments referred to the geometrical centroid.

EXAMPLES

Two examples are selected to demonstrate the accuracy and applicability of the proposed method. **Example 1 - High-strength welded box columns of Q460**

A box-section column fabricated by Q460 high-strength steel under axial compression are analyzed and compared the analysis results with the test data reported by Wang et al. (2014). The geometric dimensions of the box-column are shown in **Figs. 4** (a) and (b) below.

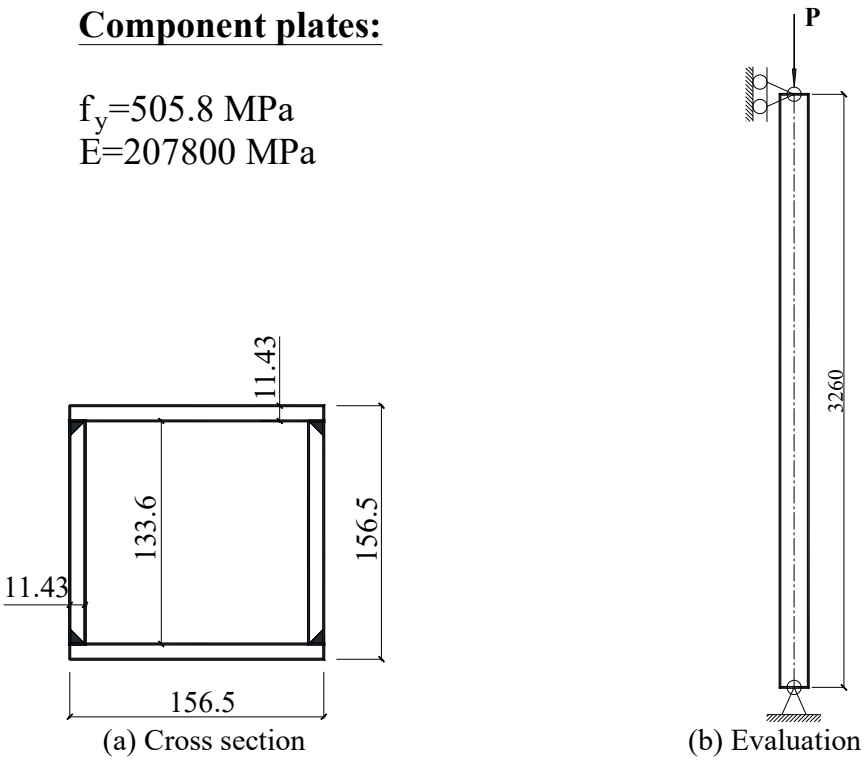


Fig. 4 Box-section column

The data of material properties and initial geometric imperfections are measured and given by Wang et al. (2014) with the actual yield strength 505.8 MPa, the elastic modulus 207.8 GPa and the initial deflection is L/666. Distributed model of residual stresses on the section selects the rectangular shape pattern recommended by Wang et al. (2012). The ratio of tensile residual stress to yield stress is 0.678 and of compressive residual stress to yield stress is 0.195.

Fig. 5 illustrates the comparison of the results obtained in the proposed analysis method with the test results. The ultimate capacity of the column derived by the presented method is 2701 kN that is close to the experimental value (2591 kN) but the deflection or stiffness is less accurate with the theory larger. The numerical result indicates an acceptable performance of this method in tracing the nonlinear behavior of high-strength steel box-columns. Thus, the proposed method accounting for residual stress and geometrical imperfections separately is further employed in DA of the following example.

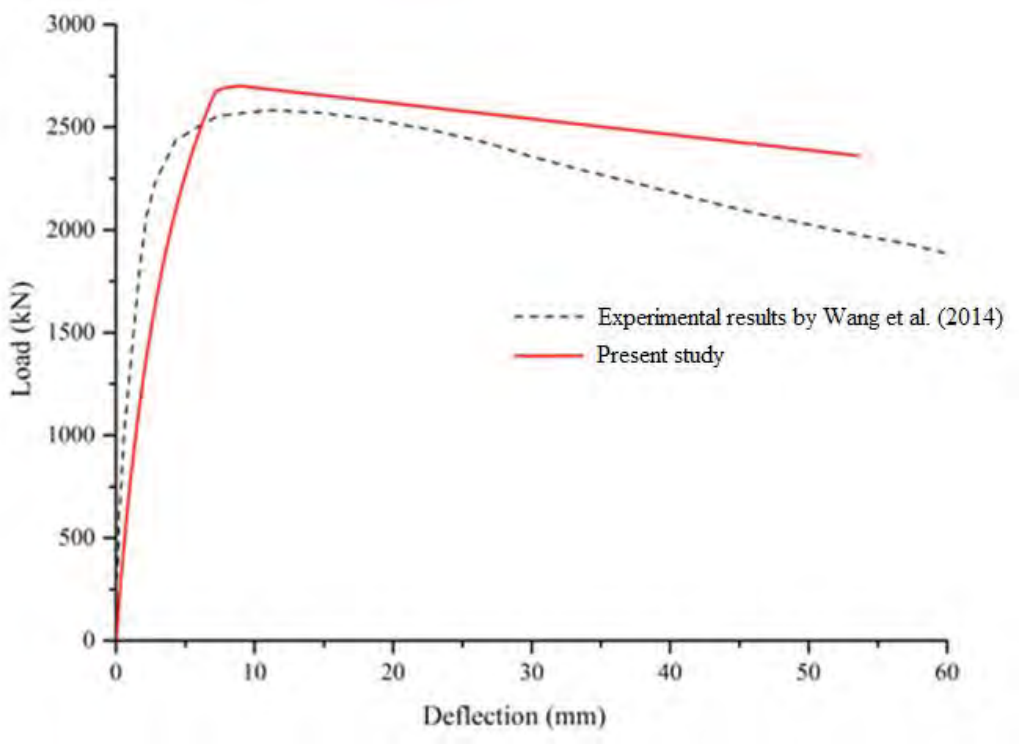


Fig.5 Comparison with test results

Example 2 - Two-story spatial steel frame with different steel grades

In the example, a two-story and two-bay spatial steel frame with I-sections for both beams and columns is introduced in **Fig. 6**, which is originally presented and analyzed by the Finite Element Method (FEM) by Cuong et al. (2007). The sectional dimension of beams and columns in the frame is H150×160×10×6.5. The yielding strength, elastic modulus and shear modulus are 350 MPa, 221 GPa and 85 GPa. The concentrated load P acting on the nodes is 80 kN. The geometrical imperfections of

the frame from the original publication is simulated by nodal coordinates. The imperfections of individual members are excluded in the analysis. In order to explore the behavior of high-strength steel in frames, grade Q460 and Q690 are adopted in this spatial frame. The nominal yield stress for Q460 and Q690 are 460 MPa and 690 MPa, respectively.

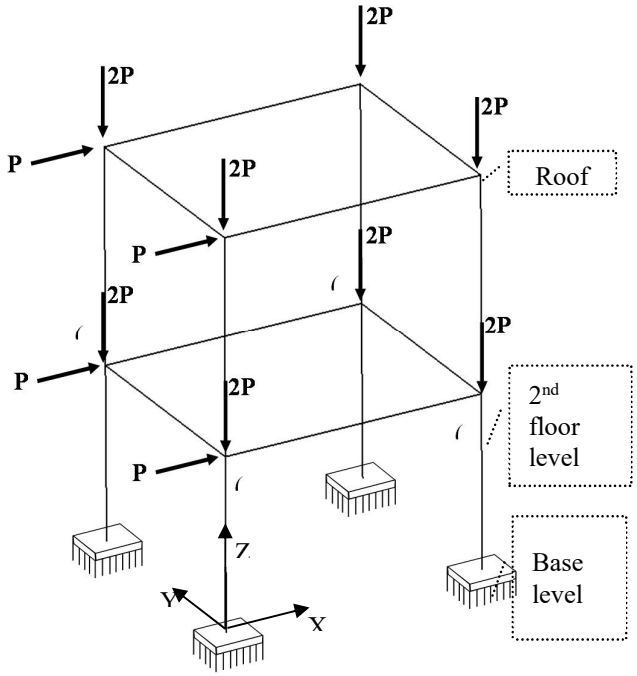


Fig.6 The studied 3-dimensional frame

Fig. 7 shows load-displacement curves at the roof and 2nd floor levels for three steel grades. It can be seen that the ultimate load factors obtained by the present study and the FEM are similar and equal to 0.92 and 0.94 respectively. It suggests that the presented analysis method possesses high accuracy for direct analysis of spatial steel frames. The failure load factors for steel grade Q460 and Q690 are 1.13 and 1.5, respectively. It is concluded that the ultimate capacity of high-strength steel members is considerably higher than ordinary steel members under the same sectional dimension and loading cases. It also indicates that utilizing high-strength steel can significantly reduce the section size, material

consumption and construction costs because of lighter weight as well as increase in usable floor area which is an important factor in cities with high land cost. All these make a significant contribution to economical benefits and resource-saving.

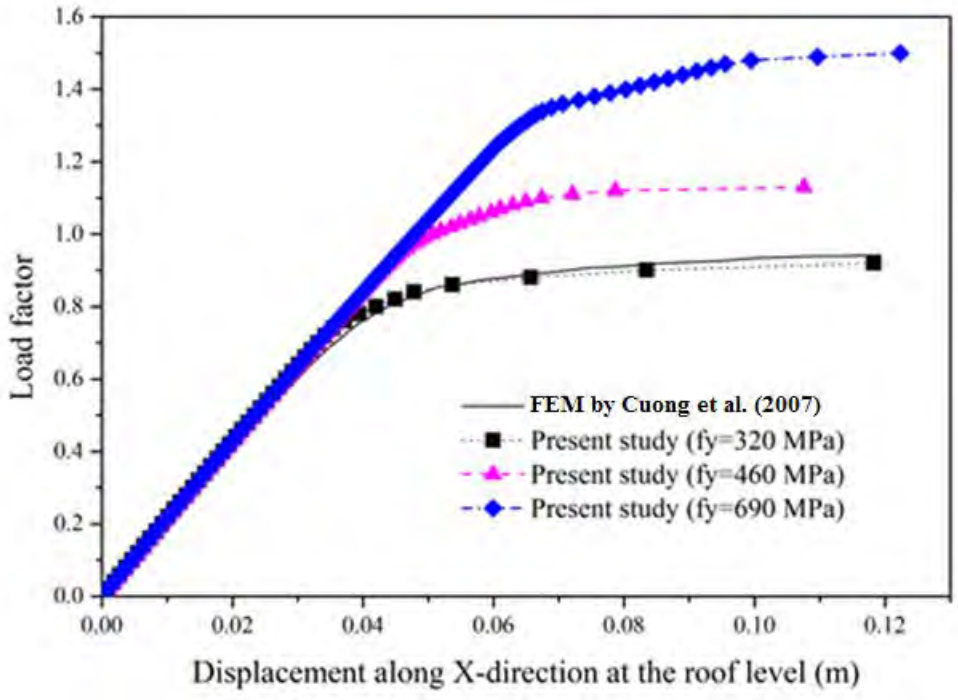


Fig.7 The results using different steel grades

Conclusions

In this paper, a new direct analysis method is proposed for advanced analysis and design of high-strength steel members and frames. The sectional analysis technique with quasi-Newton iterative scheme is exploited to consider the residual stress effects, and suitable for arbitrary steel sections. The second-order effects related to initial geometrical imperfections can be modeled by the curved ALH element. A plastic fiber hinge method is used to reflect the yielding behavior of members. The major advantage is to abandon the needs utilizing the approximate buckling curves in specifications. Additionally, the consideration of residual stresses by constructing interaction curves could avoid the scenario that their effects are overestimated or underestimated in practical design owing to the simplified clauses in codes for residual stress consideration.

Acknowledgements

The authors are grateful to the financial supports by the Research Grant Council of the Hong Kong SAR Government on the project “Second-order and Advanced Analysis of Arches and Curved Structures (PolyU 152012/14E)” and “Second-Order Analysis of Flexible Steel Cable Nets Supporting Debris (PolyU 152008/15E)” and support by Innovation and Technology Fund of the Hong Kong SAR Government for the project “Development of an energy absorbing device for flexible rock-fall barriers (ITS/059/16FP)”.

References

Chan, S. L. and P. P. T. Chui (1997). "A generalized design-based elastoplastic analysis of steel frames by section assemblage concept." Engineering Structures 19(8): 628-636.

Liu, S.-W., Y.-P. Liu and S.-L. Chan (2014a). "Direct analysis by an arbitrarily-located-plastic-hinge element—part 1: planar analysis." Journal of Constructional Steel Research 103: 303-315.

Liu, S.-W., Y.-P. Liu and S.-L. Chan (2014b). "Direct analysis by an arbitrarily-located-plastic-hinge element—part 2: spatial analysis." Journal of Constructional Steel Research 103: 316-326.

Ngo-Huu, C., S.-E. Kim and J.-R. Oh (2007). "Nonlinear analysis of space steel frames using fiber plastic hinge concept." Engineering Structures 29(4): 649-657.

Rasmussen, K. J. R. and G. J. Hancock (1995). "Tests of high strength steel columns." Journal of Constructional Steel Research 34(1): 27-52.

Usami, T. and Y. Fukumoto (1984). "Welded box compression members." Journal of Structural Engineering **110**(10): 2457-2470.

Wang, Y.-B., G.-Q. Li, S.-W. Chen and F.-F. Sun (2014). "Experimental and numerical study on the behavior of axially compressed high strength steel box-columns." Engineering Structures 58: 79-91.

Wang, Y. B., G. Q. Li and S. W. Chen (2012). "The assessment of residual stresses in welded high strength steel box sections." Journal of Constructional Steel Research 76: 93-99.

Ziemian, R. D. (2010). Guide to stability design criteria for metal structures, John Wiley & Sons.

PERFORMANCE OF COMPOSITE BEAMS IN FIRE: PRE-TEST ANALYSIS OF FULL-SCALE EXPERIMENTS

Joseph A. Main, Fahim Sadek, Jonathan M. Weigand, Jian Jiang,
Lisa Choe, Selvarajah Ramesh, Matthew S. Hoehler, Mina Seif, John Gross

Engineering Laboratory, National Institute of Standards and Technology
100 Bureau Drive, Gaithersburg, MD 20899

joseph.main@nist.gov, fahim.sadek@nist.gov, jonathan.weigand@nist.gov, jian.jiang@nist.gov,
lisa.choe@nist.gov, selvarajah.ramesh@nist.gov, matthew.hoehler@nist.gov,
mina.seif@nist.gov, john.gross@nist.gov

ABSTRACT

This paper presents results from pre-test analysis of a full-scale, 42 ft (12.8 m) span, composite beam with double-angle connections, under uniform gravity loading simulated using six equally spaced concentrated loads, and subjected to a 4000 kW compartment fire followed by a period of cooling. This configuration corresponds to the first in a series of fire tests on composite beams to be performed in the National Fire Research Laboratory, with varying steel gravity connection types and slab restraint conditions. The beam, connections, and composite slab are modeled using a reduced-order, shell-element-based modeling approach that enables coupled thermal-structural analysis by using the same finite element mesh for the heat transfer and structural analyses. This approach includes (i) realistic fire-induced thermal loads, (ii) temperature-dependent thermal and mechanical material properties, (iii) layered shell elements for the framing members and connections, and (iv) a newly developed reduced-order modeling approach for the composite slab on steel decking.

INTRODUCTION

In current engineering practice in the United States, fire protection of structures is measured by fire endurance duration and is achieved through prescriptive requirements specified based on standard fire tests. Standard fire tests (ASTM E119, 2016 or ISO 834, 2014) typically characterize fire-performance through furnace testing of isolated components or small subsystems. These tests do not provide an accurate representation of structural performance in actual fires (Phan et al. 2010). Steel buildings subjected to structurally significant fires experience thermal assault comprising elevated temperatures and thermal gradients, which may induce both temperature-dependent degradation of material mechanical properties and loads in the composite slab, steel framing, and connections that were not accounted for in the structural design. The framing members and connections in the structure may be subjected to large compressive forces induced by restraint against thermal expansion, followed by large deflections, rotations, tensile forces, and potential destabilization. Similarly, the composite slab

may also be subjected to large compressive forces due to restrained thermal expansion, which might exacerbate the potential for heat-induced explosive spalling of concrete. In addition, thermal contraction during cooling can lead to the development of large tensile forces. Properly accounting for the complex interactions between the framing members, composite slab, and connections presents significant challenges that require thorough examination from both experimental and analytical perspectives. New computational tools and design approaches are needed for evaluating the response of structural systems to realistic, uncontrolled fires.

The paper is focused on a recently-developed computational modeling approach for combined thermal-structural analysis of composite floor systems that adequately accounts for the relevant behaviors and failure modes of structural members, connections, and composite slab subjected to fire loading. The reduced-order, shell-element-based, computational modeling approach allows the same finite element mesh to be used for both the thermal and structural analyses. This analysis approach is applied to a series of composite beam tests, to be conducted at the National Fire Research Laboratory (NFRL), to provide pre-test predictions of the specimens' response and ultimate capacity.

This paper presents preliminary results from pre-test analysis of a full-scale, composite beam with welded-bolted double-angle connections (angles welded to the column flange and bolted to the beam web), under uniform gravity loading simulated using six equally spaced concentrated loads and subjected to a 4000 kW compartment fire. This configuration represents the first in a series of composite beam specimens that will be tested in the NFRL, with varying gravity connection types and slab restraint conditions. These pre-test predictions are an essential aspect of the NFRL's test program because they are used to: (i) help with planning of experiments and instrumentation layout, (ii) estimate when failure may occur to help ensure safe execution of tests, and (iii) evaluate accuracy of current modeling approaches. Due to the innumerable uncertainties in the analyses, the pre-test analyses will provide the "mean-case" response based on best-estimate values of the models' input parameters, along with a range of expected responses when accounting for the various sources of uncertainties.

COMPOSITE BEAM TESTS

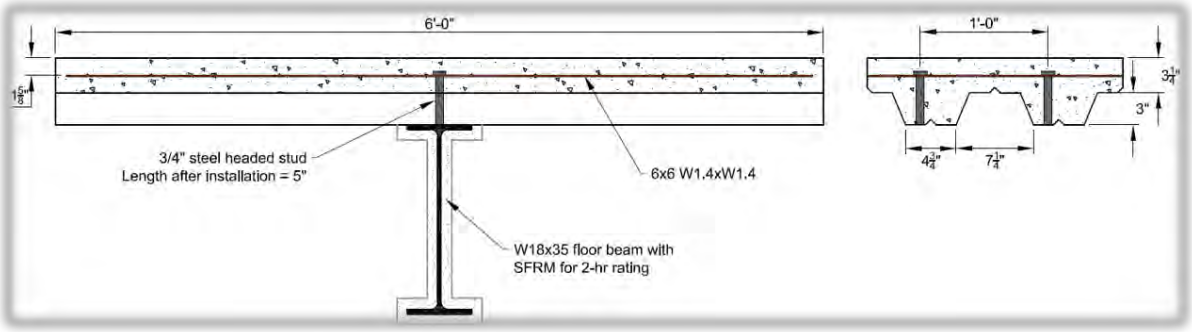
The NFRL at the National Institute of Standards and Technology (NIST) (Bundy et al., 2016) is a unique facility that enables research on the response of real-scale structural systems to realistic fire and mechanical loading under controlled laboratory conditions. Using this new facility, NIST is conducting full-scale structure-fire experiments on composite floor systems in multi-story steel framed buildings, that are intended to provide the technical basis and data necessary to advance performance-based design of structures subjected to significant fires, validate physics-based computational models to predict the fire-performance of structures, and evaluate approaches to measure structural deformations in the composite floors. Composite floor systems were selected for this experimental program due to their widespread use in U.S. building construction and because of the significant challenges inherent in modeling the complexities of their response under fire loading, such as the interactions between the gravity connections, concrete slab, metal deck, and shear studs.

As part of this testing program, the NFRL is testing five 42 ft (12.8 m) span composite beam subassemblies subjected to combined structural and fire loading. Each composite beam specimen consists of a lightweight concrete slab cast on top of profiled steel decking acting compositely with a steel beam via steel shear studs. The concrete slab has a thickness of 3.25 in (82.6 mm) above the top of the decking, with embedded 6×6 W1.4/1.4 welded wire mesh reinforcement having a 6 in × 6 in (152 mm × 152 mm) grid spacing with wire cross-sectional area of 0.014 in^2 (9.0 mm^2) placed at mid-depth of the 3-1/4 in (82.6 mm) topping

slab. The width of floor slab is 6 ft (1.83 m), see Figure 1. The minimum specified compressive strength of the concrete is 4000 psi (27.6 MPa), and the measured 28 day compressive strength was 6588 psi (39.2 MPa). Polypropylene fibers were used in the concrete mix to mitigate potential for explosive spalling of the concrete slab under fire. The 20 gage galvanized Vulcraft 3VLI20 steel decking (ASTM A653 Grade 33) has a thickness of 0.0358 in (0.91 mm) with 3 in (76.2 mm) deep ribs spaced at 12 in (305 mm) on-center. Steel headed shear studs (ASTM A108) with a diameter of 3/4 in (19 mm) and length of 5-3/16 in (132 mm), are installed at 12 in (305 mm) intervals to develop composite action between the beam and the slab.

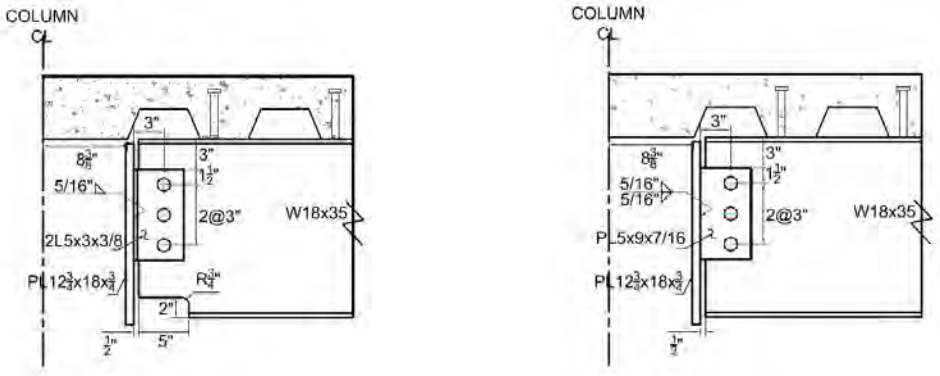
The centerline-to-centerline span between columns of the composite beam specimen is 42 ft (12.8 m) and the distance between the bolt lines of the shear connections is 40 ft (12.2 m). The floor beams are W18×35 sections and the columns are W12×106 sections; both are made of ASTM A992 steel with a minimum yield strength of 50 ksi (345 MPa). The beams are thermally insulated using 5/8 in (16 mm) thick Southwest 5MD sprayed fire-resistive material (SFRM), resulting in a 2 hour fire rating of the floor system. The beams are connected to the supporting steel columns using one of the following gravity connections:

1. Double angles bolted to the beam web and welded to the column (Figure 2(a)), with three rows of 3/4 in (19 mm) diameter A325 high-strength bolts and L5×3×3/8 angles. The angles are welded to a sacrificial plate, measuring 12-3/4 in × 18 in × 3/4 in (324 mm × 457 mm × 19 mm), on the columns using 5/16 in (8 mm) fillet welds; or
2. Single plate shear connection with a 9 in × 5 in (229 mm x 114 mm) shear plate with a thickness of 7/16 in (11 mm). The shear plate is welded to a sacrificial plate, measuring 12-3/4 in × 18 in × 3/4 in (324 mm × 457 mm × 19 mm), on the columns using 5/16 in (8 mm) fillet welds and bolted to the beam web using three rows of 3/4 in (19 mm) diameter A325 high-strength bolts (Figure 2(b)). The shear plate uses A36 steel.



3.

4. Fig. 1 – Composite beam specimen and floor slab geometry.



(a) (b)

5. Fig. 2 – (a) Welded-bolted double-angle connection; (b) single-plate shear connection.

The test setup is shown schematically in Figure 3. The composite floor slab extends to the centerlines of the support columns where it is supported on girders which approximate rigid vertical support. Two restraint conditions are considered along the short edges of the composite floor slab: free and fixed. The long edges of the floor slab are braced to prevent twisting of the test specimen while allowing for vertical displacement (i.e., the concrete slab is permitted to deflect with the beam, but is not allowed to twist transverse to the axis of the floor beam). The supporting columns are braced, as shown in Figure 3, to provide horizontal stiffness and resistance to thermal expansion.

During the fire tests, uniform gravity loading (representative of the service gravity loading condition) is applied via six equally-spaced concentrated loads along the centerline of the beam using three water-cooled beams (shown in blue in Figure 3). The water-cooled beams are loaded at their ends using hydraulic actuators located below the test floor and controlled to maintain a constant and equal load in each actuator throughout the duration of the test.

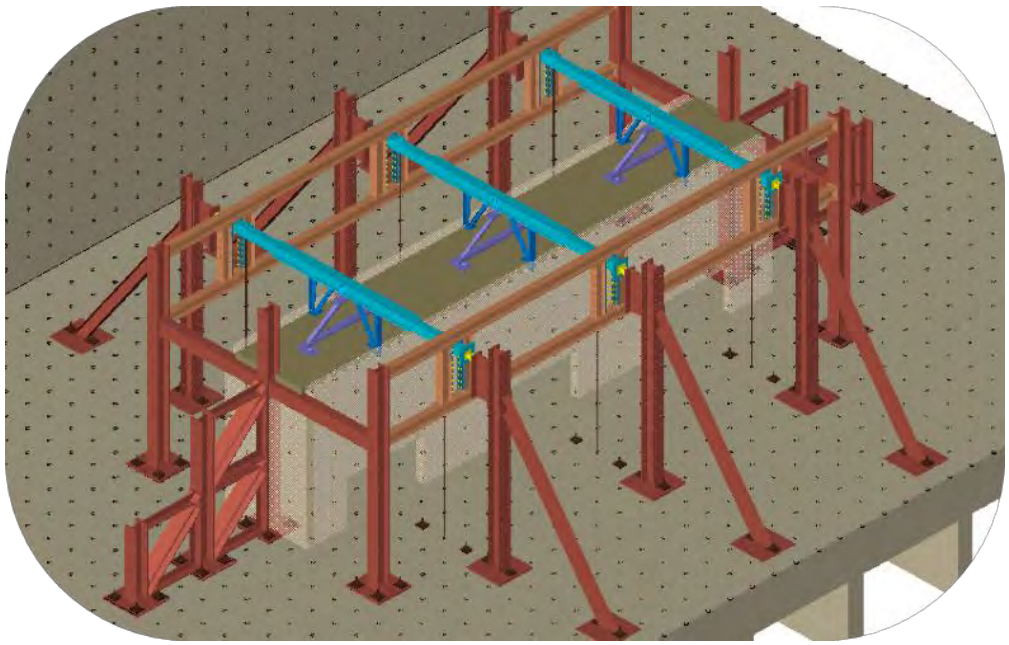


Fig. 3 – Composite beam test setup.

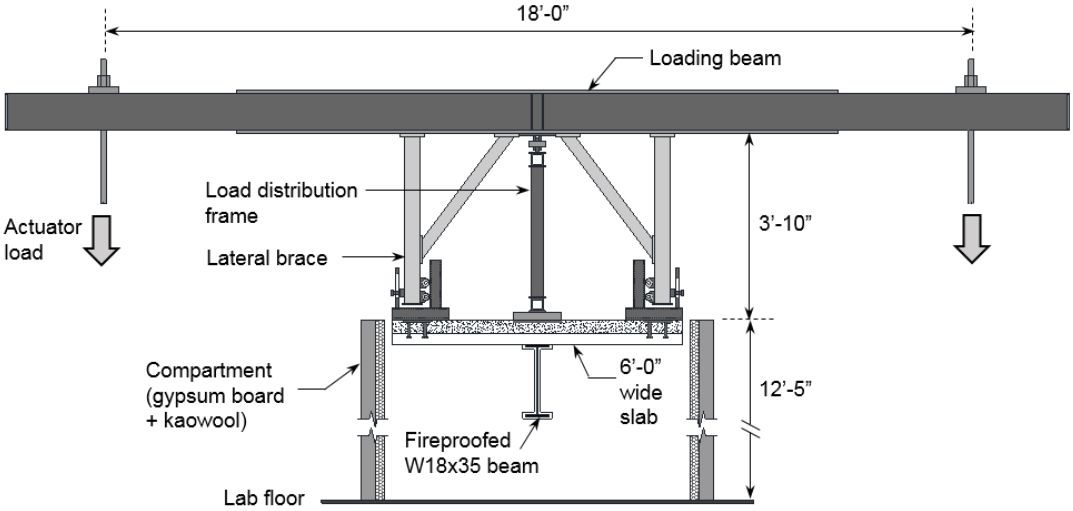


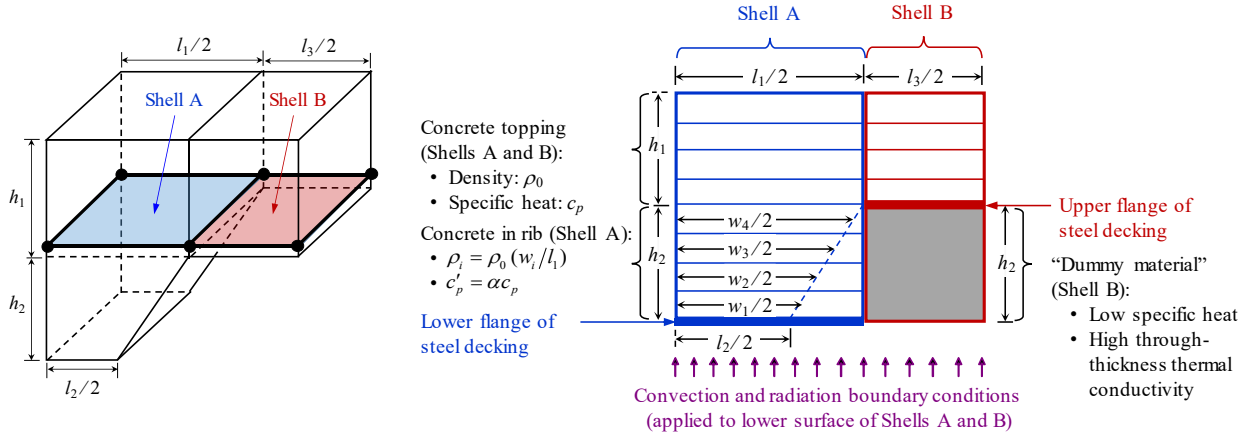
Fig. 4 – Configuration of fire compartment and load-distributing frame.

The thermal load and resulting structural temperatures will be developed and controlled using three 3.5 ft × 5 ft (1 m × 1.5 m) natural gas burners distributed along the centerline of the composite beam specimen. The heat release rate (HRR) of each burner will be held constant at 1333 kW (for a total of 4 MW) for 3.5 hours to achieve an upper layer gas temperature of 900 °C. The heating will be followed by a 30 min period of passive cooling. Walls constructed from gypsum board and lined with thermal ceramic blanket (Kaowool) will be used to confine the fire below the test specimen, as shown in Figure 4. Ventilation for inlet air and outgoing combustion products is provided through a 26.6 ft^2 (2.47 m^2) total area of openings distributed along the bottom portion of the walls.

COMPOSITE SLAB MODELING AND VALIDATION

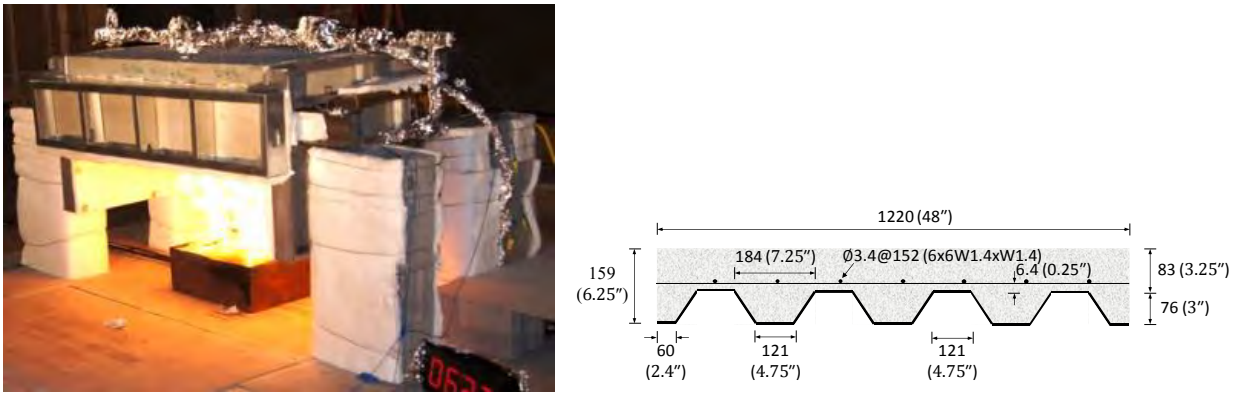
Prior to developing the pre-test model of the composite beam specimens, a significant effort was made to develop and validate a reduced-order, shell-element-based modeling approach for the composite slab (Jiang et al., 2017), in which a layered composite shell formulation with distinct structural material, thermal material, and thickness was specified for each layer. Distinct layers were specified for the steel decking and the welded wire mesh reinforcement, with multiple layers representing concrete specified through the thickness of the slab. The periodic geometry of the slab was captured using alternating strips of shell elements representing the thick portions (Shell A) and thin portions (Shell B) of the composite slab, as illustrated in Figure 5.

Heat input from the web of the steel decking had a significant influence on the temperature distribution within the thick portion of the slab. In this reduced-order modeling approach, the specific heat of concrete in the rib of the steel decking was modified to indirectly account for the additional heat input through the decking web, since only thermal loading on the upper and lower flanges of the decking can be explicitly modeled in the layered shell approach. Reducing the specific heat increases the thermal diffusivity, thereby increasing the rate of heat flow through the rib. An optimum ratio of the modified specific heat (c'_p) in the rib to the actual value (c_p) was determined by Jiang et al. (2017), based on the thickness of the upper continuous portion of the slab, h_1, relative to the thickness of the rib, h_2.



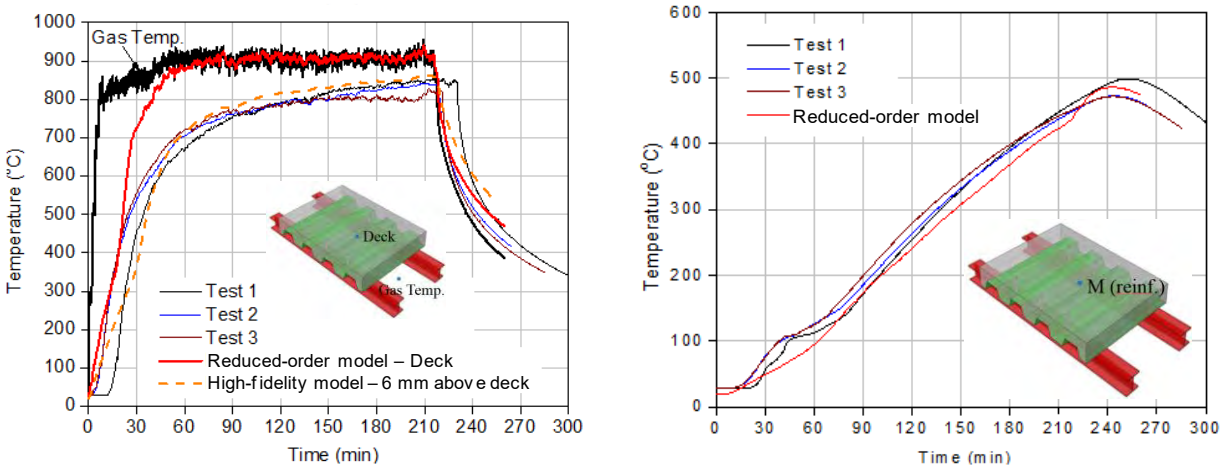
(a) (b)

Fig. 5 – (a) Representation of composite slab using alternating strips of shell elements, and (b) layered-shell representation of thick and thin portions of composite slab.



(a) (b)

Fig. 6 – Exploratory composite slab tests: (a) setup and (b) geometry. Dimensions in mm (in).



(a) (b)

Fig. 7 – Comparison of measured and computed temperatures of from the thick portion of composite slabs: (a) steel decking; (b) reinforcement.

The accuracy of the reduced-order composite slab modeling approach was evaluated against three exploratory fire tests on small composite slabs supported by two W5x19 steel beams tested at the NFRL, shown in Figure 6. The slabs were 4 ft (1.22 m) long and 3 ft (0.91 m) wide, and were heated from beneath the steel decking with a natural gas burner. Similar to the full-length composite beam specimens, the slabs used Vulcraft 3VLI decking, with a 3.25 in (83 mm) concrete topping on 3 in (76 mm) deep ribs. Lightweight concrete was used with a measured density of 129 lb/ft^3 (2068 kg/m^3) and measured moisture content of 9.2 %. The thermal conductivity and specific heat of concrete at ambient temperature were measured as 2.1 W/(m·K) and 938.7 J/(kg·K), respectively. The temperature-dependent thermal properties of the concrete were based on Eurocode 4 (EN 2005), scaled per the measured values at ambient temperature. The convection and radiation boundary conditions used in the heat transfer analysis were consistent with those used by Jiang et al. (2017).

Figure 7 presents a comparison of measured and computed temperature histories of the steel decking and reinforcement in the thick portion of the slab (Point M). The difference between the measured and computed temperatures of the decking (nearly 200 °C difference at 60 minutes) may be partially attributable to the mounting of the thermocouple on the top surface of the

decking, which resulted in the thermocouple being partially embedded in concrete. Some temperature lag relative to the steel decking would thus be expected, because of the steep temperature gradient in the concrete slab near the decking. To investigate this effect, high-fidelity finite element analyses were performed using the approach presented by Jiang et al. (2017), and Figure 7(a) shows the computed temperature history at 1/4 in (6 mm) above the decking (the first solid-element node in the concrete above the decking), which agreed well with the temperature measured by the thermocouple. Another factor that may have contributed to the lower measured temperature of the steel decking is debonding of the decking from the concrete slab, which was observed after the tests. This debonding would have disrupted the heat transfer between the decking and the concrete and may have contributed to the lower temperatures measured by the thermocouple on the top surface of the decking. The predicted temperature of the reinforcement (Figure 7(b)) agreed well with the test results. Retardation of heating due to evaporation at 100 °C can be observed in the measured results in Figure 7(b). The effect of moisture content is accounted for in the models through an increase in the specific heat between 100 °C and 200 °C (Jiang et al. 2017), which does not capture the plateau at 100 °C seen in the measured data. However, this discrepancy between the measured and computed results is not significant.

The structural response of the reduced-order composite slab modeling approach has been validated previously for composite floor systems subjected to column loss (Main and Sadek, 2012; Main et al. 2015). Further validation under combined thermal-structural loading is ongoing. The concrete, steel decking, and welded wire reinforcement were all modeled using temperature-dependent stress-strain curves and thermal expansion coefficients based on Eurocode 2 (EN 1992-1-2, 2005). Spalling of concrete at elevated temperatures was not considered in the modeling.

PRE-TEST COMPOSITE BEAM MODEL

The beam, connections, and composite slab on steel decking were modeled using a reduced-order shell-based modeling approach that enabled coupled thermal-structural analysis by using the same finite element mesh for the heat transfer and structural analyses (Figure 8). This approach includes (i) realistic fire-induced thermal loads generated using the Fire Dynamics Simulator (FDS), (ii) temperature-dependent thermal and mechanical material properties to account for the degradation of material characteristics, strength, and stiffness at elevated temperatures, (iii) temperature-dependent layered shell elements for the framing members and connections, and (iv) the newly developed reduced-order shell-based modeling approach for the composite slab on steel deck described above. The model used the measured concrete strength and expected properties (yield strength of 55 ksi (379 MPa)) for the A992 steel. The steel decking and welded wire mesh materials were modeled as elastic-perfectly plastic with yield strengths of 45 ksi (310 MPa) and 75 ksi (517 MPa), respectively.

The NIST Fire Dynamic Simulator (FDS) was used to estimate the thermal loads that the specimen would experience during the fire, using a computational fluid dynamics model of the compartment and the composite floor. These thermal loads were transferred to the model for thermal analysis via convective and radiative heat transfer boundary conditions, assuming a uniform temperature in the upper gas layer. The maximum upper gas layer temperature predicted using FDS was approximately 1650 °F (900 °C). The gas temperature history is presented subsequently with the analysis results.

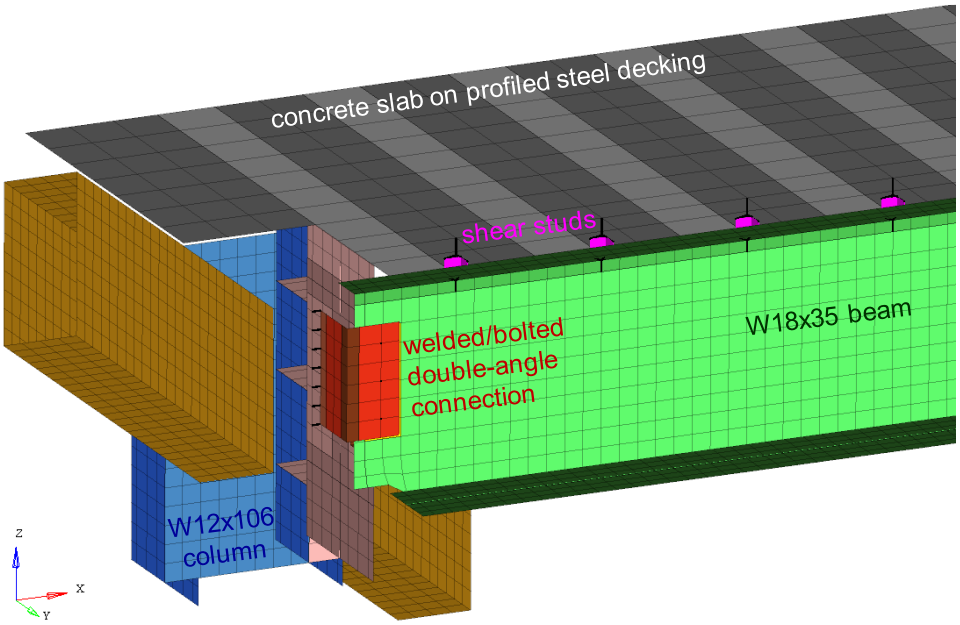


Fig. 8 – Details of composite beam shell-based modeling approach.

The boundary conditions in the model were specified to represent those of the composite beam tests. In the analysis presented in this paper, the bases of two end-columns were modeled as fixed; the column restraint conditions will be updated based on stiffness test of the column bracing system prior to the experiments. The gravity loads were applied to six steel loading plates in contact with the top surface of the composite slab (Figure 9), with the gravity loads transferred to the steel beam through contact interfaces between the loading plates, the slab, and the top flange of the beam. Consistent with the applied gravity loading scheme, the loading plates were free to rotate with the slab, but were permitted to translate only in the vertical direction. Lateral displacements of both slab edges were restrained through contact with vertical steel plates at 1/6, 1/2, and 5/6 of the beam span.

Each shear stud was modeled using a solid hexahedral element (Figure 10(a)), which provided the same load-slip behavior for relative shear of the top and bottom surfaces in any direction. Rigid-body constraints were used to tie solid elements to the respective nodes on the beam flange and the composite slab. The shear studs were heated through thermal contact with the top surface of the beam's top flange. The load-slip response of the solid elements (representing the shear studs) at ambient temperature was calibrated to achieve a target load-slip behavior based on Ollgaard et al. (1971). Degradation in the strength and stiffness of the shear studs at elevated temperatures was determined based on data from high-strength bolts (Figure 10(b)). The temperature-independent slip at shear stud failure, at peak load, was based on Dara (2015).

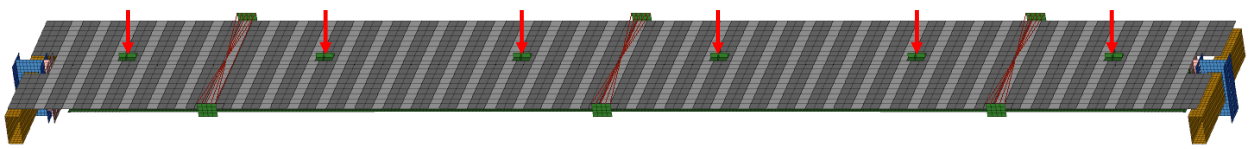
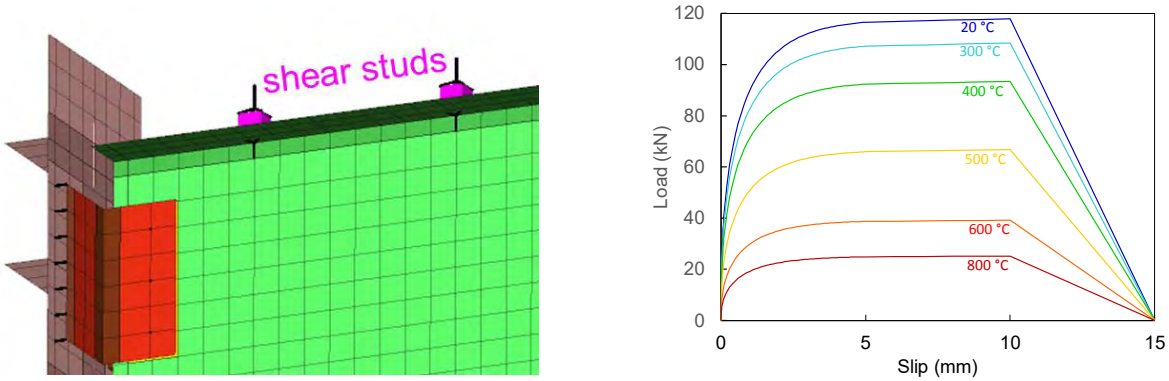


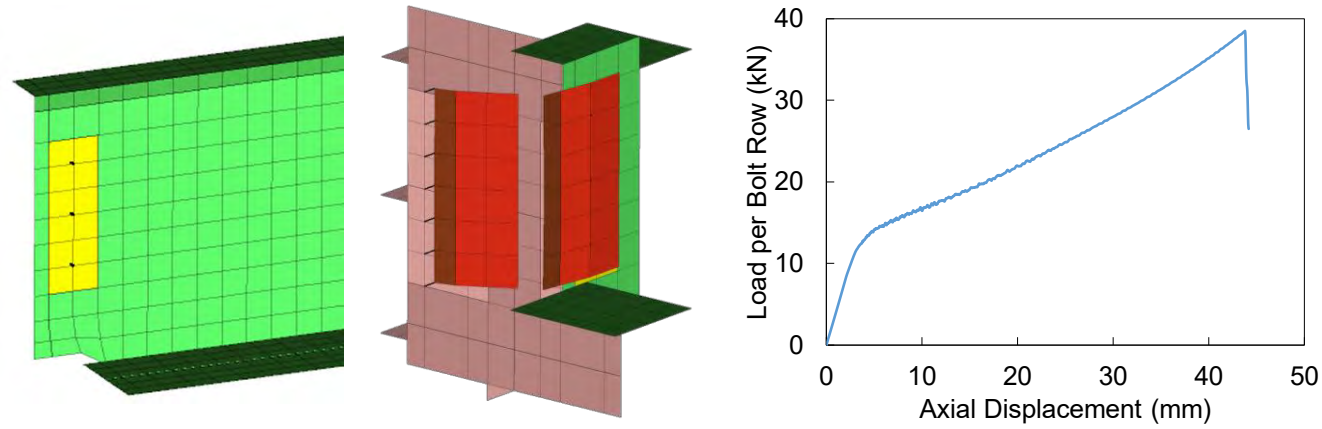
Fig. 9 – Overview of 42 ft (12.8 m) composite beam model. Vertical arrows correspond to locations of applied gravity loads.



(a) (b)

Fig. 10 – (a) Solid hexahedral element representing shear studs, and (b) temperature-dependent shear stud load-displacement behavior (1 kN = 0.225 kip; 1 mm = 0.0394 in).

The welded-bolted double-angle connections were modeled using a relatively coarse mesh of shell elements. The behavior of the connections was modeled by calibrating the temperature-dependent material models of the shell elements in the beam web and the angles to achieve target capacities and load-displacement responses. Specifically, the stress-strain curves of the shell elements in the beam web local to the connection (Figure 11(a)) were used to capture bolt shear and bearing-induced deformations of bolt holes, and the stress-strain curves of the shell elements in the angles (Figure 11(b)) were calibrated to model angle opening. Figure 11(c) shows the tensile load-displacement response of a single bolt row of the welded-bolted angle connection at ambient temperature. A triaxiality-dependent erosion criterion was calibrated to represent tearing of the angles at their heel or welded edge. Heat transfer between angles, beam, and column plate was modeled using surface-to-surface thermal contact.



(a) (b) (c)

Fig. 11 – Welded-bolted web angle connection: (a) shell elements in beam web local to the connection, (b) shell elements representing the angles, and (c) ambient temperature tensile load-displacement response of a bolt row of the connection (1 kN = 0.225 kip; 1 mm = 0.0394 in).

RESULTS FROM COMPOSITE BEAM PRE-TEST ANALYSIS

Preliminary results from the pre-test analysis of the full composite beam are presented herein, with no sprayed fire resistive materials, to illustrate the capabilities of the modeling approach. The first analysis was considered push-down loading at ambient temperature, with the gravity

loads increased until failure. The structural analysis was conducted using an explicit numerical scheme. The results in this section present the mean-case response based on a best estimate of the models' input parameters. The thermal and structural analyses, however, are subject to many sources of uncertainties, including uncertainties associated with the ambient and elevated-temperature mechanical properties of the steel and concrete, input temperature time-history, and restraint conditions. Analysis of uncertainties is currently underway to first identify the most influential parameters that affect the response using design of experiments methodology, and then to bound the analysis results by providing a range of responses for two cases: most severe and least severe.

Figure 12 shows the results of the structural analysis under push-down loading. As the vertical loading on the beam increased, the beam deflected, inducing rotations at the double-angle connections. The abrupt increase in horizontal load at approximately 9 in (229 mm) of vertical displacement at midspan corresponded to binding of the beam web against the column (Figure 13(a)). The ultimate capacity of the composite beam was associated with failure of shear studs and failure of the connections by tearing of the angles at their welded edges. Failure occurred at a vertical displacement of 16.9 in (429 mm) at midspan and a peak vertical load of 24.3 kip (108 kN) per loading point.

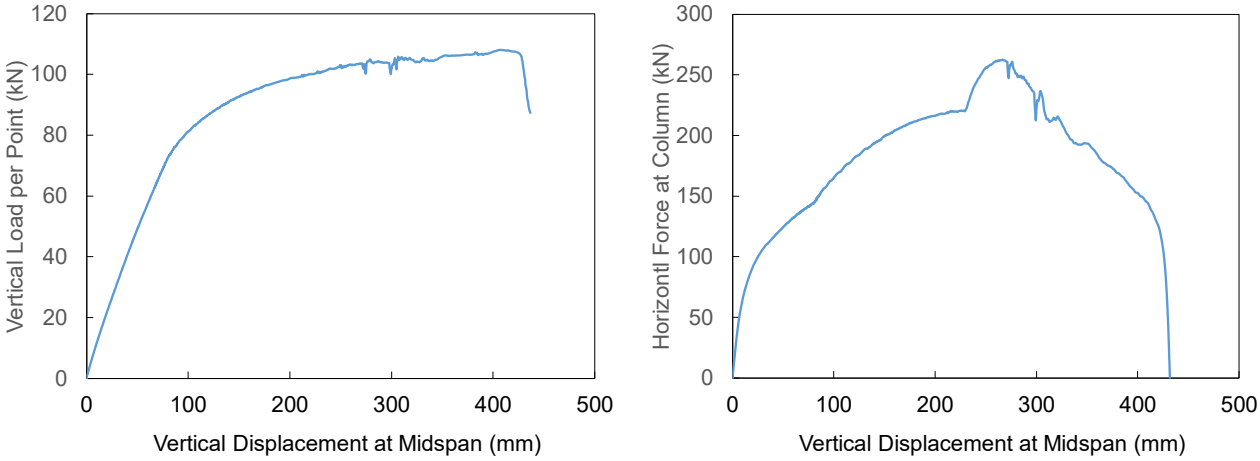


Fig. 12 – Analysis results for ambient-temperature push-down loading: (a) vertical load per loading point; (b) horizontal force at exterior columns (1 kN = 0.225 kip; 1 mm = 0.0394 in).

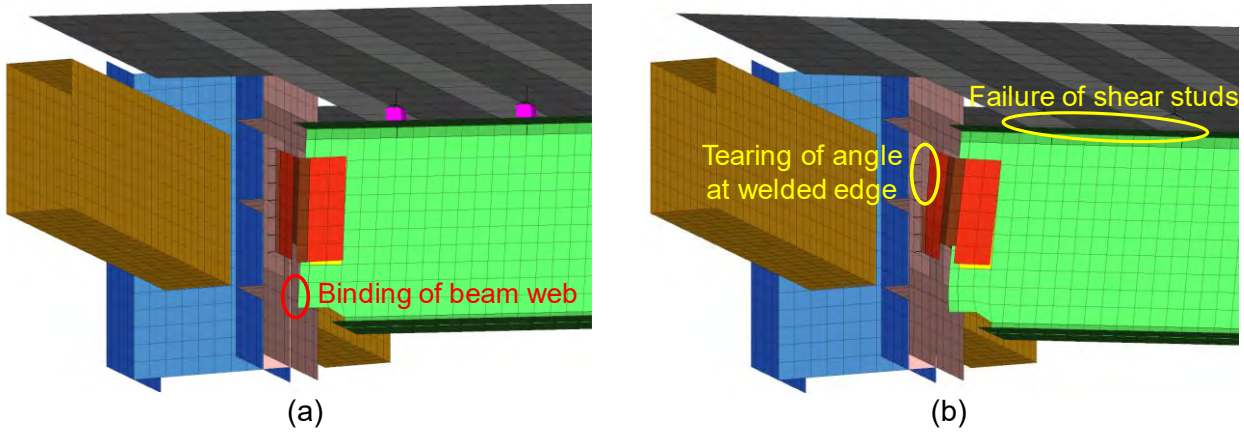


Fig. 13 – Analysis results for ambient-temperature push-down loading: (a) Binding of beam web on column flange; (b) failure of shear studs and tearing of angles at welded edge.

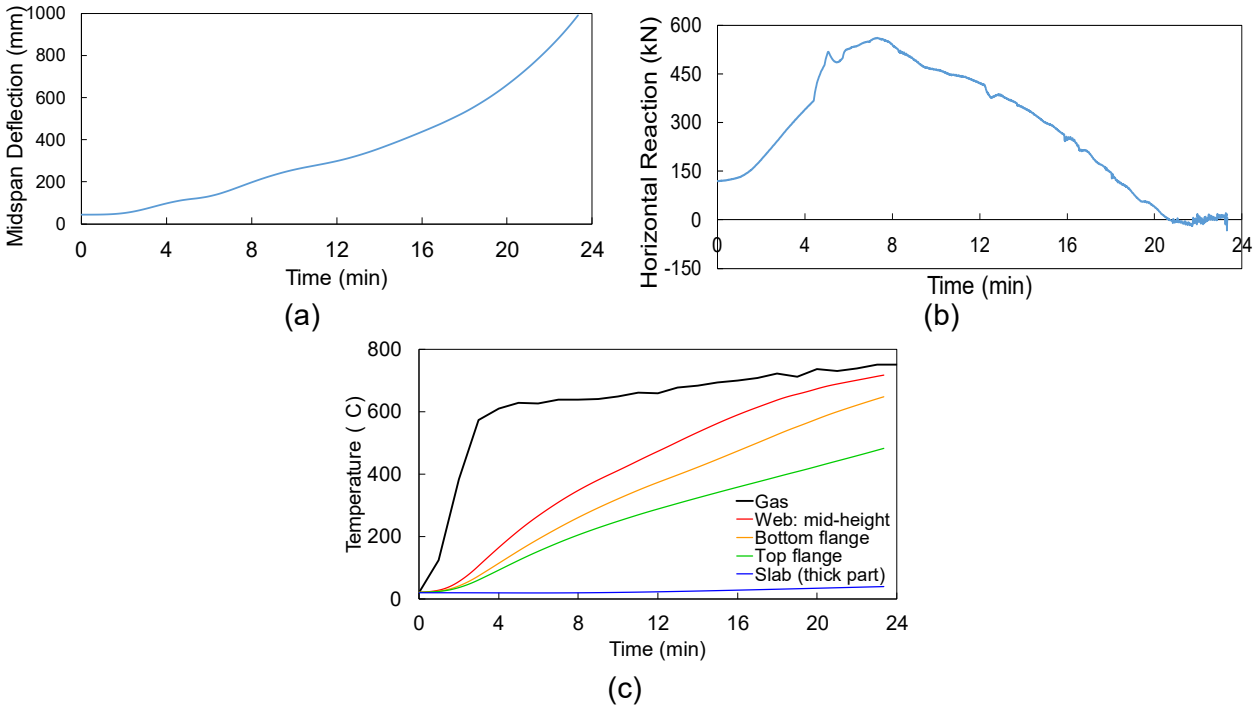


Fig. 14 – Thermal-structural analysis results: (a) midspan deflection, (b) horizontal force at exterior columns, and (c) temperature distribution (1 kN = 0.225 kip; 1 mm = 0.0394 in).

In the second pre-test analysis, the gravity loading of 10 kip (45 kN) per loading point was gradually increased prior to heating and then held constant during the heating. The thermal loads were applied to the exposed surfaces using convective and radiative boundary condition, based on the average temperature time-history for the upper gas layer obtained from the FDS simulation of the fire (Figure 14(c)). The analysis was performed using implicit thermal and explicit structural analyses. To overcome the computational costs associated with running explicit structural analyses over a long duration, the thermal and structural analyses were performed on different time scales, with a 4.4 hour (16,000 s) fire duration corresponding to a duration of 16 s (16,000 ms) in the structural analysis. Thus, different base units were used in defining properties for thermal materials (N, m, s) and structural materials (N, m, ms). This 16 s duration for the structural analysis was sufficient to ensure a quasi-static response prior to failure, with the kinetic energy remaining less than 5 % of the external work.

The results of the combined thermal-structural analysis are shown in Figure 14. The abrupt increase in the horizontal reaction after about 4.5 minutes of heating (at a midspan deflection of 4.4 in (112 mm)) was due to binding of the beam web on the column flange. The binding was due to the combined effects of temperature-induced thermal expansion of the beam and rotation of the beam ends at the web angle connections. As the heating continued, the binding force on the beam flange increased, initiating local buckling of the beam web after about 15.5 minutes of heating at a midspan displacement of 16.2 in (411 mm), after which the horizontal reaction at the columns decreased and the midspan deflection increasing more rapidly. Failure of the unprotected composite beam occurred after only about 20 minutes.

SUMMARY

This paper presented preliminary results from pre-test analysis of a full-scale 42 ft (12.8 m) span composite beam with double-angle connections, subjected to (i) push-down analysis under uniform gravity loading and (ii) constant uniform gravity loading and a 4000 kW

compartment fire. Results from the push-down analysis showed that failure of the shear studs, along with nearly simultaneous rupture of the welded-bolted double-angle connections, limited the capacity of the composite beam. Results under uniform gravity loading and heating showed that beam binding due to thermal expansion in the beam was sufficient to induce localized web buckling in the beam, which in turn decreased the horizontal resistance of the composite beam. The unprotected beam failed after only about 20 minutes of heating. This paper also introduced a reduced-order modeling approach for thermal and structural analysis of composite slabs on steel decking, which represents the periodic profile of the composite slab using alternating strips of layered shell elements. The performance of this reduced-order approach for heat transfer analysis was validated against full-scale composite slab subassembly tests subjected to real fires. Discrepancies between measured and computed temperatures of the steel decking may have been influenced by debonding of the decking, but good agreement was observed between the measured and computed temperatures of the reinforcement.

DISCLAIMER

Certain commercial entities, equipment, products, or materials are identified in this document to describe a procedure or concept adequately. Such identification is not intended to imply recommendation, endorsement, or implication that the entities, products, materials, or equipment are necessarily the best available for the purpose.

REFERENCES

ASTM International (2016), “ASTM Standard E119-16a Standard Test Methods for Fire Tests of Building Construction and Materials”, Standard E119-11a, ASTM International, West Conshohocken, PA.

Bundy, M., Hamins, A., Gross, J., Grosshandler, W., Choe, L. (2016). “Structural fire experimental capabilities at the NIST National Fire Research Laboratory”, Fire Technology, 52(4), 959–966.

Dara, S. (2015). “Behavior of the Shear Studs in Composite Beams at Elevated Temperatures.” Ph.D. Dissertation, The University of Texas at Austin, TX.

EN 1992-1-2. (2005). Eurocode 2 Design of concrete structures: Part 1.2: General rules, Structural fire design, European Committee for Standardization (CEN), Brussels.

EN 1994-1-2. (2005). Eurocode 4 Design of composite steel and concrete structures: Part 1.2: General rules, Structural fire design, European Committee for Standardization (CEN), Brussels.

ISO (2014), “Fire-resistance tests – Elements of building construction” Standard ISO 834-11, International Organization for Standardization, Geneva, Switzerland.

Jiang J., Main J.A., Sadek F., Weigand J.M. (2017). “Numerical Modeling and Analysis of Heat Transfer in Composite Slabs with Profiled Steel Decking.” NIST Technical Note 1958, National Institute of Standards and Technology, Gaithersburg, MD.

Main, J.A., Weigand, J.M., Johnson, E., Francisco, T., Liu, J., Berman, J.W., and Fahnestock L.A. “Analysis of a Large-Scale Composite Floor System Test under Column Loss Scenarios.” Proceedings of the 2015 ASCE/SEI Structures Congress, Portland, Oregon.

Main, J.A. and Sadek, F. (2012). “Robustness of steel gravity frame systems with single-plate shear connections.” NIST Technical Note 1749, Gaithersburg, MD.

Ollgaard, J.G., Slutter, R.G., and Fisher, J.W. (1971). “Shear strength of stud connectors in lightweight and normal weight concrete.” *Engineering Journal*, AISC, 8(2), 55-64.

Phan, L.T., McAllister, T.P., Gross, J.L., and Hurley, M.J. (2010). “Best Practice Guidelines for Structural Fire Resistance Design of Concrete and Steel Buildings.” *NIST Technical Note 1681*, National Institute of Standards and Technology, Gaithersburg, MD.

TOWARDS AN ENGINEERING METHOD FOR FIRE DESIGN OF CONCRETE-FILLED STEEL TUBE COLUMNS WITH SOLID STEEL CORE

Martin Neuenschwander
ETH Zurich
Institute of Structural Engineering
Zurich, Switzerland
neuenschwander@ibk.baug.ethz.ch

Markus Knobloch
Ruhr-Universität Bochum
Institute of Steel, Lightweight and Composite Structures
Bochum, Germany
markus.knobloch@rub.de

Mario Fontana
ETH Zurich
Institute of Structural Engineering
Zurich, Switzerland
fontana@ibk.baug.ethz.ch

ABSTRACT

Concrete-filled steel tube columns with solid steel core are innovative pre-fabricated composite columns with outstanding structural fire behavior, allowing slender designs under high loading without additional fire protection. Their singular structural behavior in fire stems conceptually from their specific design of beneficial composite action between the different structural components (steel tube, concrete infill and solid steel core). These structural, economic and architectural advantages make these columns appealing for use in high-rise building practice. However, due to their high load-bearing capacity, experimental investigations of their structural behavior in fire are substantially hampered by test facility limits and cost. Based on the findings of a previous combined experimental and numerical study using cutting-edge engineering methods, the paper develops the grounds for a novel approach towards a simplified fire design method that is suitable for practitioners and needed for further dissemination of this innovative type of composite column in building practice.

INTRODUCTION

Concrete-filled steel tube columns with solid steel core are pre-fabricated innovative composite columns that consist of a circular outer steel tube, a concentrically placed solid steel core and concrete infill in between. This type of composite column is most suitable for use in high-rise building practice, because of its high load-bearing capacity and the fact that exceptional fire resistances can be reached without additional fire protection. The singular structural fire behavior is based on an innovative design of composite action between the different components of the column (steel tube, concrete, steel core). A gradual load-redistribution process from the outer more quickly degrading components (steel tube, concrete) to the inner thermally shielded steel core enables the long-standing stability and strength of such composite columns in the case of a fire. However, the advantage of the high load-bearing capacity in turn hampers experimental

Table 1 – Summary of specimen properties of fire test series [4].

Fire test	D_{tube} [mm]	t [mm]	D_{core} [mm]	t_c [mm]	L [mm]	$\bar{\lambda}_{20°C}$ [-]	$N_{pl,20°C}$ [kN]	$N_{R,20°C}$ [kN]	P_0 [kN]	μ [-]	t_f [min]	End Condition
1	133.0	4.0	60.0	32.5	3540	1.515 a)	1876.4 a)	579.6	85	0.16	94	Pinned-Pinned
2	219.1	4.5	110.0	50.1	3600	0.687 a)	4911.0 a)	3497.2 a)	2000	0.57	24	Pinned-Fixed
3	219.1	4.5	110.0	50.1	3600	0.687 a)	4911.0 a)	3497.2 a)	1500	0.43	169	Pinned-Fixed
4	219.1	4.5	150.0	30.1	3600	0.652 a)	6638.5 a)	4972.5 a)	1900	0.38	179	Pinned-Fixed

a) According to Eurocode 4, calculated with experimentally established mean values of material properties

investigations. The compilation of an extended fire test database that would be needed for the development of simplified fire design methods for such columns, is therefore not only very costly but also partially infeasible due to capacity limits of test facilities. Considering the potential of today's advanced numerical methods, it appears therefore appealing to strive to substitute costly fire tests of concrete-filled steel tube columns with solid steel core with numerical simulations, and develop on the basis of such numerically compiled databases simplified fire design methods that are needed to further disseminate this innovative type of composite column in high-rise building practice.

In the case of ordinary concrete-filled steel tube columns this strategy has been followed by several researchers in the past few years. This lead to the development of several simplified fire design methods [1-3], which were derived from databases of simulated fire tests that were compiled with numerical models considering temperature-dependent code material models and non-varying nominal boundary conditions. However, the first comprehensive experimental and numerical study on the fundamental structural fire behavior of concrete-filled steel tube columns with solid steel core [4-8] showed that replacing fire tests using this approach is not suitable for this column type. This paper presents and validates an alternative modeling approach that is suitable to numerically extend a sparse experimental fire test database of concrete-filled steel tube columns with solid steel core for the purpose of developing a simplified fire design method.

PREVIOUS RESEARCH

A combined experimental and numerical research project on the fundamental structural fire behavior of concrete-filled steel tube columns with solid steel core has been recently accomplished at ETH Zurich [4-8]. The experimental part of the project consisted of a series of four full-scale ISO Standard fire tests with pre-loaded columns of different cross-sectional type, nominal boundary conditions and load ratios as summarized in Table 1. The test series was performed in the structural fire lab of the Materials Testing Institute in Brunswick in Germany. A detailed description of the test setup, the results of the fire tests and of the post-test examination of the specimens is comprehensively documented in [8]. Moreover, the temperature-dependent constitutive behavior of the different materials of the full-scale composite column specimens was established with an extensive experimental program performed at ETH Zurich [5-7]. The program encompassed strain-rate controlled steady-state tensile tests at elevated temperatures of the tube and the core steels, and strain-rate controlled steady-state cyclic compression tests at elevated temperatures of the concrete. The numerical part of the project consisted of a comprehensive Finite-Element-Method (FEM) modeling study on the simulation of the complex thermo-mechanical behavior of this type of composite columns in fire and the feasibility of replacing costly full-scale fire tests with such numerical simulations [8]. The study showed that a best-calibrated model can accurately reproduce the behavior observed in full-scale fire tests,

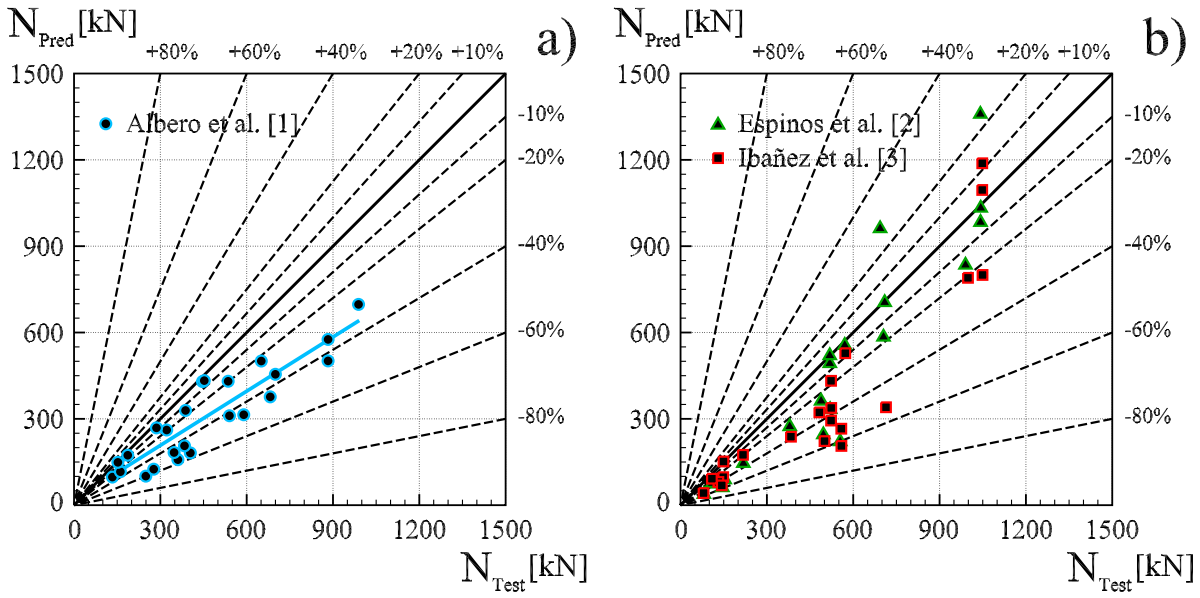


Fig. 1 – Predictive capacity of available simplified fire design methods for ordinary concrete-filled steel tube columns: fire design method of [1] against test data of [10] and [11] (a) and fire design methods of [2] and [3] against NRCC data [12].

when considering experimentally established temperature-dependent material behavior and influences of the test-setup that are varying over the course of the test time. When neglecting the varying influences of the test-setup by using a model with non-varying nominal boundary conditions however the comparison with the test data becomes inconsistent and allows only for a conditional validation of such a model. This observation is exactly the starting point of the follow-up research project on simplified fire design methods for concrete-filled steel tube columns with solid steel core that will be presented in this paper, because this observation impedes a straightforward application of the methodology that was used successfully in the case of ordinary concrete-filled steel tube columns.

SIMPLIFIED FIRE DESIGN METHOD

Simplified design methods in structural engineering traditionally idealize the load-carrying behavior of structural members by conceptual mechanical models that have been derived on the basis of experimental observations. The effectiveness of such methods for engineering practice lies within the relative simplicity of predicting the capacity of a given structural member for a design. Usually this is achieved by sacrificing some accuracy for the benefit of conceptual simplicity and/or ease of use in engineering practice. Often, the general range of applicability of such methods is however restricted by the extent of the experimental database on the basis of which they have been developed.

In structural fire design, the extent of available experimental databases is especially limited. This is because experimental investigations are costly, often restricted by the capacity of test facilities, and very complex and difficult to conduct in order to give meaningful results. In order to provide the grounds for the development of simplified fire design methods, it appears therefore promising, using advanced numerical methods to extend existing experimental databases or to compile numerical ones instead. One strategy to achieve this goal consists of validating in a first step a numerical model against selected tests from a given experimental database. Typi-

cally, a numerical model is used that considers temperature-dependent code material models (e.g. Eurocode or ASCE) and non-varying nominal boundary conditions. In a second step, a comprehensive numerical database is compiled by performing extended parametric studies with the validated model. It is noteworthy to realize that this strategy implicitly assumes that such a selectively validated model can be arbitrarily generalized, completely irrespective of specific conditions of the underlying validation tests. Using this strategy, several research projects have successfully proposed simplified fire design methods for ordinary concrete-filled steel tube columns in the past few years [1-3], among which the most recent and comprehensive one [1] is evaluated to eventually substitute the currently suspended simplified fire design method (Annex H) of Eurocode 4 [9]. Figure 1 illustrates the predictive capacity of these simplified fire design methods with respect to test data. Figure 1a shows with round markers the results obtained with the method of [1] when predicting the tests of [10] and [11], whereas Figure 1b gives with triangular and square markers respectively the results when using the methods of [2] and [3] to predict the NRCC data [12]. It follows from Figure 1a that the proposed new method which will eventually be considered in Eurocode 4 gives very conservative results with the linear trend-line almost coinciding with the -40%-deviation line and the markers of the four lowest predicted values almost lying on the -60%-deviation line. Despite the advantage of a wide range of applicability of this method including many different cross-section types (square, rectangular, tubular and elliptical), high slenderness ratios and very large eccentricities, the sheer conservativeness of the method gives rise for debate.

It is a generally recognized issue that the results of fire tests with identical structural members and nominally identical test conditions can vary greatly depending on the test facility. There are two main sources of influence that can explain the different behavior. The first can be assigned to deviations in the fire exposure leading to different heating histories of a test member and finally different structural behavior. However, considerable research effort has been undertaken in this field that mitigated the problem and allowed achieving a high level of consistency among different fire test labs through suitable standardization. The second source of influence is the concrete implementation of a member's nominal test boundary conditions, which is not standardized and naturally varies, as every test lab has its own best solution. However, not only the aspect of the concrete implementation of boundary conditions should be taken into account, but also how they possibly vary over the course of a fire test. Despite that this is a generally accepted issue, very little research effort has been undertaken thus far to understand this possible source of influence and especially, to assess its relevance for the conception of simplified fire design methods.

Just very recently, this problem has been addressed for the first time with the case of concrete-filled steel tube columns with solid steel core [8]. The study showed that the complex behavior in fire of such composite columns (varying in cross-section type, slenderness and load ratios) can be accurately simulated when considering not only experimentally established temperature-dependent constitutive material behavior but also test-setup specific influences via varying boundary conditions. In contrast, when using non-varying nominal boundary conditions the simulations compared inconsistently and overall poorer with the test data. This is illustrated in Figure 2 that compares the model responses obtained with varying boundary conditions and non-varying nominal boundary conditions (blue dashed and red dotted lines respectively) against the deformation-time histories of the axial displacement, $u(t)$, and the lateral deflection, $w(t)$, of two different fire tests of [4] (black solid lines). In some cases, as the one shown in Figure 2a, the model yielded also with non-varying nominal boundary conditions robust and reasonably conservative predictions of the fire resistance, whereas in other cases, as the one illustrated in Figure 2b, the non-varying nominal boundary conditions triggered in the model a local failure mechanism that was however never observed in the tests, and lead to excessively conservative predictions of the fire resistance (30 minutes versus 169 minutes in the test).

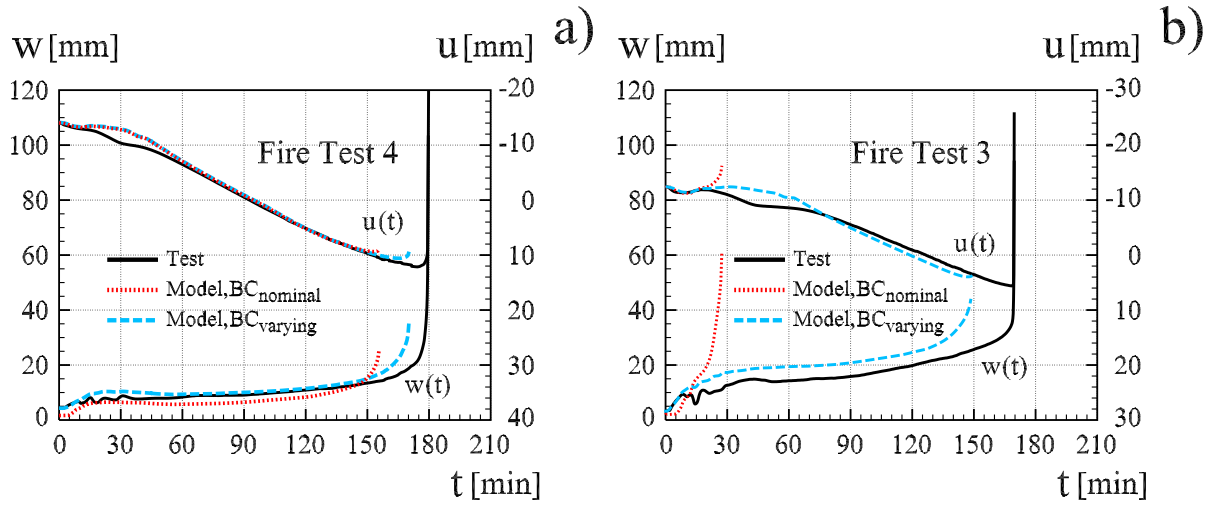


Fig. 2 – Influence of boundary conditions when modeling concrete-filled steel tube columns with solid steel core: model responses versus test data of fire test 4 (a) and fire test 3 (b).

In the framework of simplified fire design methods this finding shows two things: It suggests first that a different strategy than the one using non-varying nominal boundary conditions is needed when compiling a numerical database for concrete-filled steel tube columns with solid steel core, and second that a suitable alternative strategy consists of considering test-setup specific influences via varying boundary conditions. Such an alternative strategy adapts the spirit of the well-established principle – "built into a structure as tested" – of traditional experiment-based structural fire engineering to today's situation, where combined experimental and numerical methods are used, and especially advanced numerical methods partially allow replacing fire tests by simulations. In the context of replacing fire tests with numerical simulations, the aforementioned principle then rather reads – "simulated as tested" – which specifically includes also the simulation of boundary conditions and their varying character over the course of a fire test. This novel strategy allows compiling a numerical database that has the character of an extended experimental database of a specific test-setup and excludes potentially over-conservative simulation results that are related to non-varying nominal boundary conditions. Finally, resulting simplified fire design methods from such a numerical database are also conceptually more suitable for engineering practice, because the configurations in which composite columns are used in real structures are closer to the varying boundary conditions of fire test-setups than they are to the non-varying nominal boundary conditions of purely numerical simulations.

Using this novel approach, the present study aims at computing for different fire ratings the slender buckling strength of concrete-filled steel tube columns with solid steel core of different length, in order to extend the experimental database of [4] without the need of additional costly fire tests in the same lab. A simplified cross-section independent fire design tool can then be derived when the resulting database is transformed into the format of normalized slender buckling strength curves.

NUMERICAL EXTENSION OF EXPERIMENTAL DATABASE

This section in detail presents, how a sparse database of fire tests of concrete-filled steel tube columns with solid steel core can be extended to a numerical database, by using the novel strategy that was outlined in the preceding section. In a first step, a numerical model is developed that simulates a reference test from the fire test database at hand (fire test 4 of [4] in the

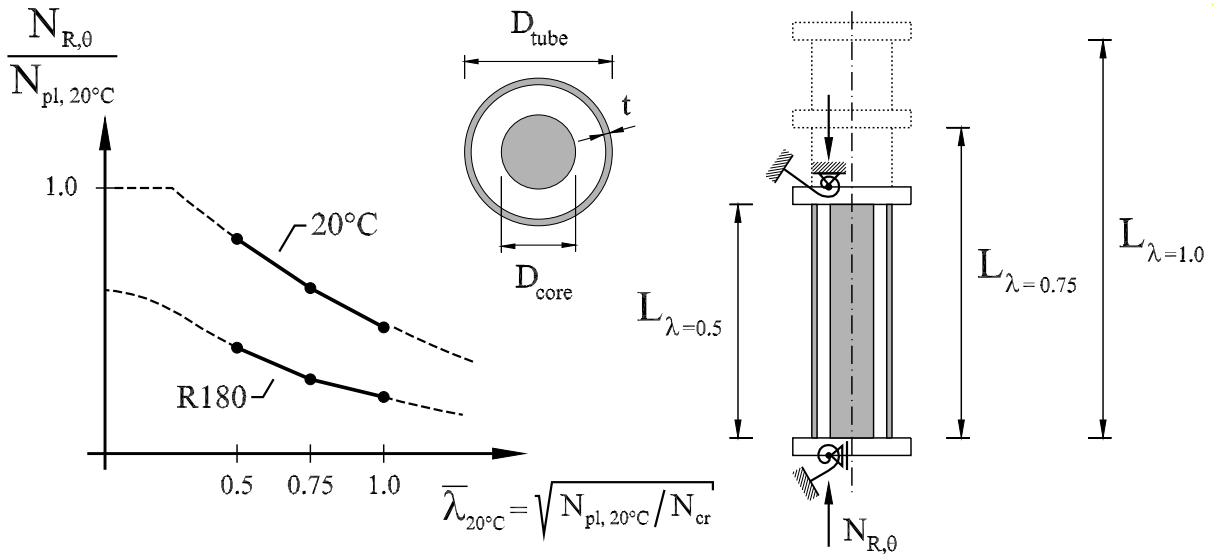


Fig. 3 – Schematic illustration of numerical extension of experimental database.

present case). Test-setup specific influences on the reference test specimen and its interaction with the test rig are considered in the model by means of varying boundary conditions that are calibrated such that the model response compares reasonably well with the measured global deformation-time histories of the reference fire test. The calibrated model is then used to compute at slenderness ratios that are relevant for design practice the corresponding points on the slender buckling strength curves of given fire ratings, as illustrated in the schematic graph of Figure 3. For every such point, an iterative calculation procedure is necessary to find the preload a column of the given slenderness ratio can withstand for the time of the fire rating. The slenderness ratio is varied in the model by changing only the length of the reference test specimen (Figure 3), whereas the cross-sectional type and the boundary conditions remain unchanged. Finally, the resulting relative slender buckling strength curves are then compared against the results of two other fire tests that have not been used to calibrate the varying boundary conditions (fire test 2 and 3 featuring different cross-sectional type but identical nominal test boundary conditions as the reference test), in order to validate the slender buckling curve approach of the proposed simplified fire design method.

The section is organized in three subsections: The first subsection describes in brief the FEM model that was used in order to simulate additional fire tests on the test rig on which the reference test had been performed. The second subsection presents the calibration procedure that was used to develop the non-varying boundary conditions that incorporate the characteristics of the simulated test rig. The third subsection finally presents the simulation results and discusses the validation of the simplified fire design method that can be derived on the basis of the simulations.

Table 2 – Summary of meshing parameters.

$\bar{\lambda}_{20°C}$	L	Elements axial direction			Elements tangential direction			Elements radial direction		
		q_{ore}	$q_{concrete}$	q_{tube}	m_{core}	$m_{concrete}$	m_{tube}	n_{core}	$n_{concrete}$	n_{ube}
[-]	[mm]	[-]	[-]	[-]	[-]	[-]	[-]	[-]	[-]	[-]
0.50	2692	112	178	202	9	18	28	3	2	2
0.75	4038	168	266	302	9	18	28	3	2	2
1.00	5384	224	356	404	9	18	28	3	2	2

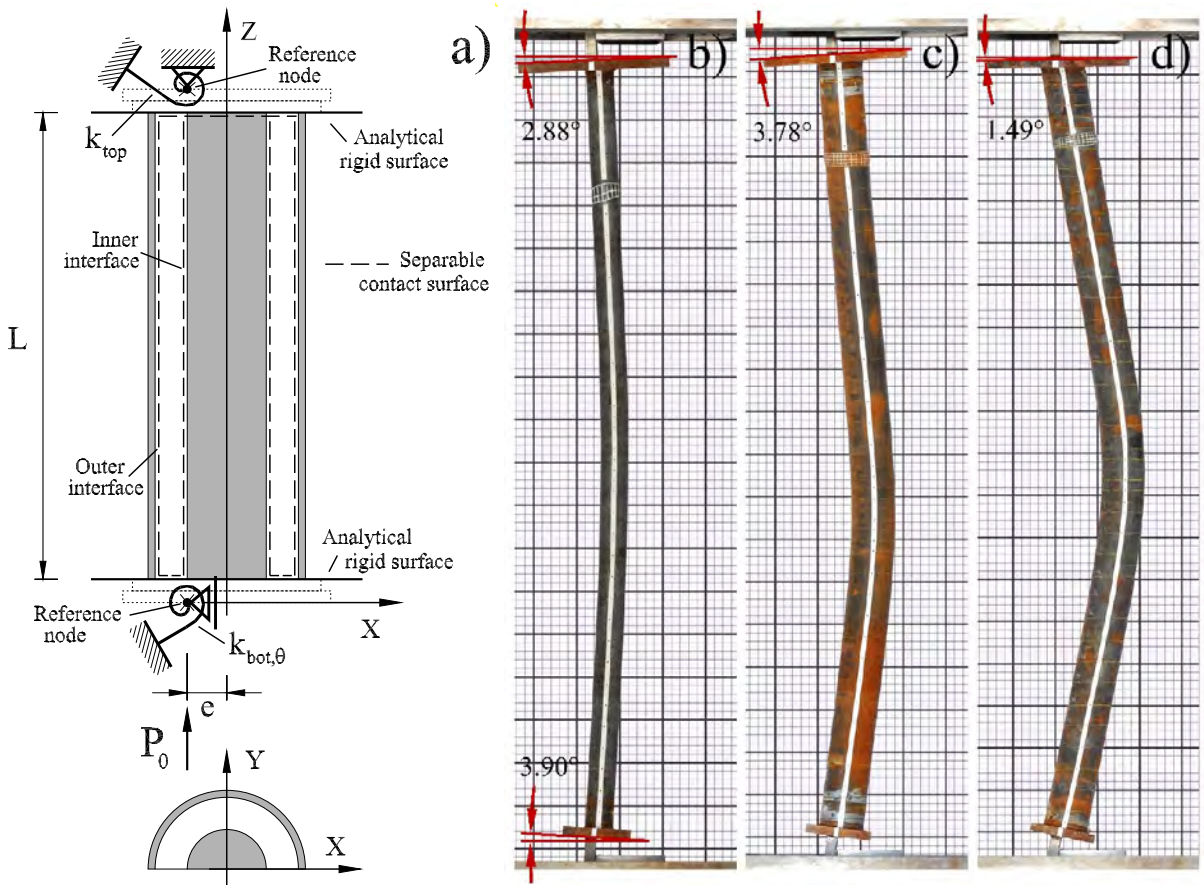


Fig. 4 – Schematic diagram of numerical model (a), column specimen after fire test 1 with a fire resistance of 94 minutes (b), fire test 2 with a fire resistance of 24 minutes (c) and fire test 4 with a fire resistance of 179 minutes (d).

Numerical model

A three-dimensional model of the column of the reference fire test (fire test 4) with geometric cross-sectional properties according to Table 1 was build using the implicit FEM code ABAQUS Standard. This subsection summarizes only the most relevant model features, as a detailed description is available in [8]. Exploiting the radial symmetry of the cross-section allowed modeling only half of the column as shown in the schematic diagram of Figure 4a that indicates also the orientation of the model with respect to the global axis system. The different components of the column were modeled independently with continuum elements of reduced integration (C3D8R elements of the ABAQUS library) in the case of the steel core and the concrete infill, and with continuum shell elements (SC8R elements) in the case of the steel tube. The steel-concrete interfaces between the components were idealized by means of separable contacting surfaces with a temperature-independent Coulomb friction model as mechanical interaction ($\mu_f = 0.1$). The end plates at the bottom and the top of the column were represented by analytical rigid surfaces. The eccentric loading condition of the test setup ($e = 10$ mm) was considered by offsetting in global X-direction the reference nodes of the analytical rigid surfaces, in which also the pre-load as well as the boundary conditions were prescribed. The data of the elevated-temperature material testing program performed at ETH Zurich [5-7] was considered as constitutive input data in the concrete damaged plasticity model and the classical metal plasticity model of ABAQUS Standard. Experimentally established temperature-dependent thermal expansion of the steel [7]

was considered, whereas for the concrete the relation according to Eurocode 4 [4] was used. Moreover, residual stresses resulting from the cooling phase after hot-rolling were considered in the steel core according to the computed distributions by [13], whereas residual stresses and strains due to cold-forming of the steel tubes were neglected.

The simulation of the fire tests was performed as a sequentially coupled thermal stress analysis consisting of two steps. In the first step, the temperature-time histories of the nodes in the column model were computed with a heat transfer analysis. The heat transfer from the gas in the furnace following the ISO Standard temperature-time curve to the column specimen was modeled with convective and radiative boundary conditions using a convection coefficient, $h = 25$ W/m^{2}K and a resulting emissivity, $\varepsilon = 0.7$. The heat transfer across the outer steel-concrete interface between the steel tube and the concrete was modeled as a gap conductance with an effective heat transfer coefficient, $k_{gap} = 100$ W/m^{2}K, to account for a thermally induced air-gap, whereas perfect contact was assumed for the inner interface between the concrete and the steel core. The predictive capacity of this heat transfer model has been validated with temperature recordings from tests of columns of two different cross-sectional types and fire exposure times up to three hours in [8]. In the second step, the fire tests were simulated by incrementally applying to the nodes of the pre-loaded columns the temperature-time histories from the previous heat transfer analysis while simultaneously ensuring static equilibrium of the heated column until eventual failure.

Calibration of varying boundary conditions

This subsection presents the simplifying mechanical modeling assumptions that were developed to represent via varying boundary conditions the concrete implementation of the nominal boundary conditions and their changing nature over the course of the reference fire test (fire test 4). The starting point for this development constituted the comparison between the simulation results that were obtained with a model using non-varying nominal boundary conditions and the test recordings. The two deformation recordings that appeared to be difficult to track with the model were the lateral deflection, $w(t)$, and the rotation of the bottom end plate, $\varphi(t)$. Figure 5a and 5b respectively show with dotted red lines the predicted courses of these two deformations over the test time, t, in comparison to the test recordings that are given with black solid lines. The graphs in Figure 5 show two principle differences between the model response and the behavior observed in the test. First, it follows that at the start of the fire exposure at t=0 minutes the lateral deflection and the rotation of the bottom end plate are predicted significantly smaller than actually measured. Second, it is apparent that the predicted rotation of the bottom end plate starts increasing significantly after 60 minutes of fire exposure, whereas in the test the rotation remained stable over a more extended period of time. The observed deviations in the model response can be attributed to the boundary conditions, because the influence of the material behavior is already accurately captured in the model through experimentally established constitutive calibration data at ambient and elevated temperature. In the next two paragraphs, these deviations will be discussed in relation to the test end conditions of the column specimen.

From the first observation of Figure 5 follows that the nominally fixed upper end of the column was in reality compliant in the test-setup. Assuming that the test rig remains elastic and at ambient temperature during the fire test, the upper boundary condition was modeled as an elastic rotational restraint with a constant spring stiffness, $k_{top} = 1.85$ kNm/mrad (Figure 4a). The stiffness of the spring was calibrated by matching the initial lateral deflection, w_0, and the bottom end plate rotation, φ_0, of the model with the test recordings. This modeling approach implicitly considers that the relative degree of rotational restraint by a test rig varies during the course of a fire test, because it depends on the stiffness ratio between the test rig and the specimen. The longer a fire test takes, the greater a specimen's temperature-induced degradation of stiffness

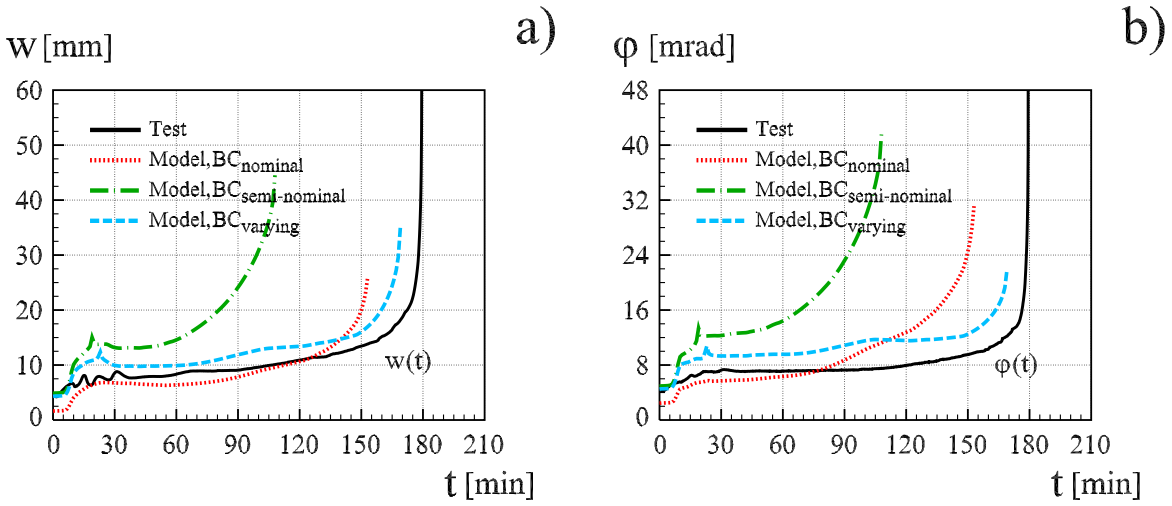


Fig. 5 – Calibration of boundary conditions with reference fire test: simulated lateral deflection-time histories (a) and rotation-time histories of bottom end plate (b).

and strength and in turn the higher the rotational restraint exerted by the test rig that remains in contrast elastic and at ambient temperature. Figures 4c and 4d clearly illustrate this behavior with the measured residual rotation of the nominally fixed upper end of the specimen of fire test 2 (Figure 4c, fire resistance $t_f = 24$ minutes) that is significantly greater than in the case of fire test 4 (Figure 4d, fire resistance $t_f = 179$ minutes) which lasted in contrast almost 3 hours. However, considering in the model only the nominally fixed upper end with an elastic restraint and keeping at the bottom end of the column the nominally perfect hinge naturally gives too conservative predictions of the fire resistance, as shows Figure 5 with the green dash-dotted lines obtained with this modeling approach of semi-nominal boundary conditions.

From the second observation of Figure 5 can be concluded that frictional effects must have been present in the nominally pinned boundary condition at the bottom end of the column that increased with increasing temperature. Additional support for this explanation gives Figure 4b that shows the only test specimen of [4] that was tested with nominally pinned boundary conditions at both ends (fire test 1). Despite the symmetric nominal boundary conditions, the residual end plate rotation at the top was significantly smaller than at the bottom. Comparison with the temperature recordings in close vicinity to the column's bottom and top end showed that the smaller residual rotation at the top correlated with higher temperatures and the greater residual rotations at the bottom with lower temperatures. This observation indicates that the rocker-bearing type of implementation of the hinge in the test-setup exhibited with increasing temperature higher frictional effects that can be associated with deformations in the rocker-bearing [4]. In order to capture this influence, the non-varying nominally pinned boundary condition at the bottom of the column was replaced in the model by a rotational spring with temperature-dependent stiffness, $k_{bot,\theta}$, (Figure 4a) that was calibrated such that the simulated deformation-time history of the bottom end plate rotation compared reasonably well with the test readings. The resulting temperature-dependent characteristics of the rotational spring are displayed in Figure 6c.

Figure 4 finally shows that the readings from the reference fire test (black solid lines) can be predicted reasonably well (blue dashed lines), when using an engineering modeling approach that considers via varying boundary conditions the compliance of the test rig and temperature-dependent frictional effects in the nominally pinned boundary condition of the concrete test-setup.

Results and validation of simplified fire design method

The model with calibrated varying boundary conditions of the preceding subsection was used to simulate a series of fire tests with columns of identical cross-sectional type and nominal boundary conditions as the reference fire test. Within the simplifying mechanical modeling assumptions about the test-setup, such a simulated fire test series replaces an extended costly program on the test rig in the structural fire laboratory of the Materials Testing Institute of Brunswick in Germany. The goal of this simulation series was to compile the data for a simplified tabular design tool that predicts the slender buckling strength of concrete-filled steel tube column with solid steel core for a given fire rating. The simulation program was set up in such a way that it provided slender buckling strength curves at ambient temperature and for ISO fire ratings of 30, 60 90, 120 and 180 minutes that cover most design situations of building practice. Discrete values of the slender buckling strength curves were computed at slenderness ratios $\bar{\lambda}_{20°C}$ of 0.5, 0.75 and 1.00, covering the range that is relevant for building practice. The different slenderness ratios at ambient temperature were realized by changing in the model only the length of the column. Table 2 summarizes the respective column lengths and mesh parameters that were used in the simulation program and Figure 6a displays the resulting simplified fire design tool on the basis of normalized slender buckling strength curves, whose development will be discussed next. Each discrete value on the slender buckling strength curves was calculated iteratively by adjusting the pre-load. A pre-load was accepted as the slender buckling strength of a given fire rating, $N_{R,\theta}$, when the column resisted not more than 30 seconds longer than the required

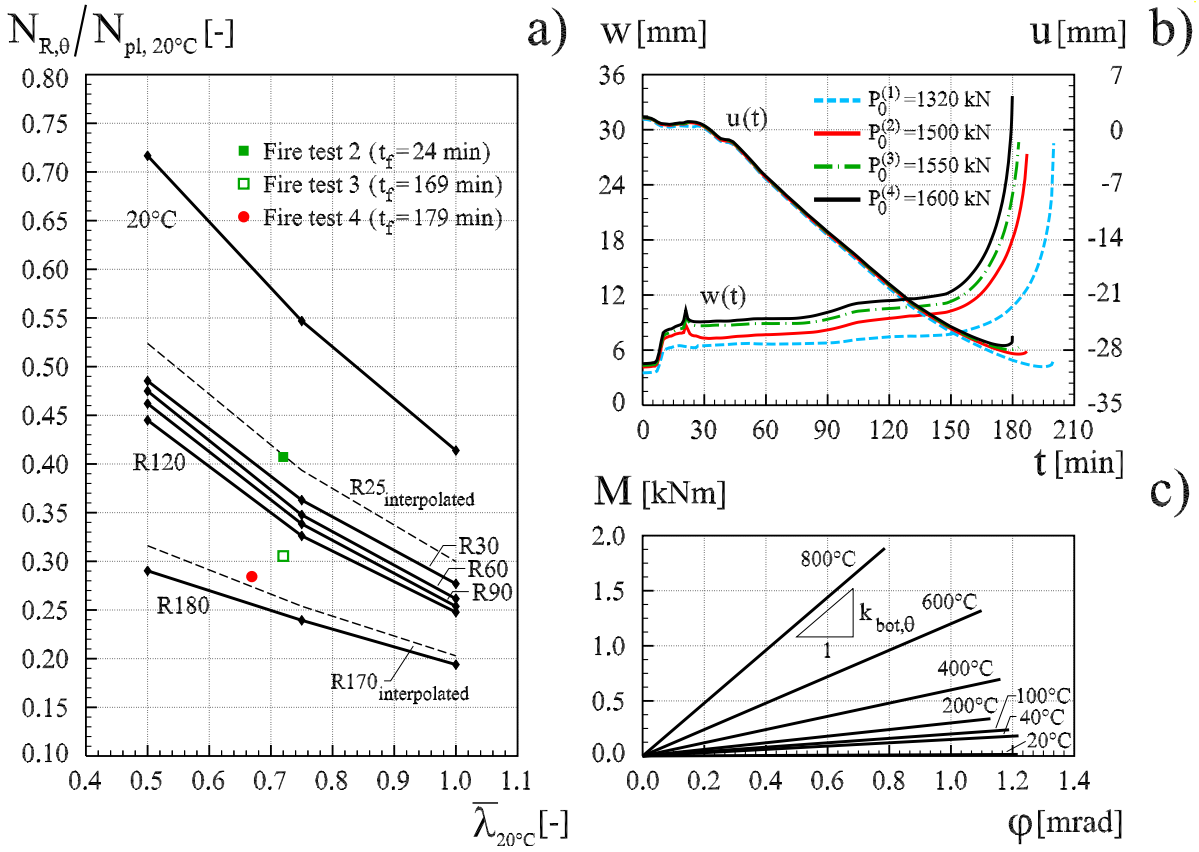


Fig. 6 – Results and validation of method: normalized slender buckling strength curves for given fire ratings (a), iteration procedure (b), and temperature-dependent spring stiffness (c).

time of the respective fire rating. Figure 6b illustrates this iteration procedure with the specific results of a column of slenderness ratio of 0.75 and a fire rating of 180 minutes. The resulting slender buckling strengths were then normalized with respect to the plastic cross-sectional capacity at ambient temperature, $N_{pl,20°C} = 6683.5$ kN (Table 1). Plotting the normalized slender buckling strength, $N_{R,\theta}/N_{pl,20°C}$, against the slenderness ratio at ambient temperature, $\bar{\lambda}_{20°C}$, as shown in Figure 6a, finally provides a simplified fire design tool for concrete-filled steel tube columns with solid steel core that is independent of the cross-sectional type and therefore suitable for design practice. Moreover, the tool allows to determine for a given design of a column at ambient temperature the slender buckling strength for a required rating of ISO fire exposure, without involving any heat transfer calculations.

Figure 6a includes besides the computed normalized slender buckling strength curves also those test results of [4], namely fire tests 2 to 4 (Table 1) that fall into the range of slenderness ratios that are covered by the design tool. The results of fire test 2 and 3 are both given with a square marker (filled and unfilled respectively), to indicate that their specimens were of identical cross-sectional type, whereas the result of fire test 4 (the reference fire test) of different cross-sectional type is indicated with a round marker. It is apparent in Figure 6a that the marker of fire test 2, in which a fire resistance of, $t_f = 24$ minutes was reached, almost coincides with the linearly interpolated slender buckling strength curve of the design tool for a fire rating of 25 minutes. In the case of fire test 3 (t_f=169 minutes) however, the tool's prediction is conservative in a similar degree as in the case of fire test 4 (t_f=179 minutes), which can be seen in Figure 6a by comparing the corresponding markers of the test results with the respective interpolated slender buckling strength curves of the design tool. In the case of fire test 3, a better comparison could be reached, by improving the calibration of the temperature-dependent rotational spring with the reference fire test, without compromising the excellent predictive capacity of the design tool at lower fire ratings.

For two reasons, fire test 2 and 3 are especially suitable to validate the simplified fire design tool. First, because unlike the reference fire test they have not been used to calibrate the varying boundary conditions, and second, because they have been performed with column specimens of another cross-sectional type than the one of the reference fire test. The comparison of the results of fire test 2 and 3 with the tool's predictions (Figure 6a) therefore confirm the soundness of the proposed approach of modeling the test-setup specific influences on a specimen during a fire test by means of varying boundary conditions, and validate the suitability of using a method that is independent of the cross-sectional type such as a normalized slender buckling strength curve.

CONCLUSIONS AND OUTLOOK

A novel modeling approach to extend sparse experimental fire test databases of concrete-filled steel tube columns with solid steel core has been presented that considers test-setup specific influences on the specimen during a fire test by means of varying boundary conditions. Using this novel approach normalized slender buckling strength curves for given fire ratings of 30, 60, 90 120 and 180 minutes were calculated at slenderness ratios of 0.5, 0.75 and 1.0 that can be used as a preliminary tabular fire design tool (Figure 6a). From the tool's validation by fire tests that have not been used in the calibration of the varying boundary conditions, the following conclusions and recommendations for future research can be drawn:

- Normalized slender buckling strength curves are conceptually suitable as a simplified fire design method for this type of composite column.

- Varying boundary conditions constitute a valid engineering approach to appropriately consider complex test-setup specific influences on a specimen during a fire test when compiling a numerical database for the development of a simplified fire design method.
- Further successful dissemination of this innovative type of composite column in high-rise building practice depends on the development of a simplified fire design method that is supported by a numerical database, which reliably excludes over-conservative model predictions that are related to non-varying nominal boundary conditions.

REFERENCES

[1] V. Albero, A. Espinos, M.L. Romero, A. Hospitaler, G. Bihina, C. Renaud, Proposal of a new method in EN1994-1-2 for the fire design of concrete-filled steel tubular columns, Eng. Struct. 128 (2016) 237-255.

[2] A. Espinos, M.L. Romero, A. Hospitaler, Simple calculation model for evaluating the fire resistance of unreinforced concrete filled tubular columns, Eng. Struct. 42 (2012) 231-244.

[3] C. Ibañez, J.V. Aguado, M.L. Romero, A. Espinos, A. Hospitaler, Fire design method for concrete filled tubular columns based on equivalent concrete core cross-section, Fire Saf. J. 78 (2015) 10-23.

[4] M. Neuenschwander, M. Knobloch, M. Fontana, ISO Standard fire tests of concrete-filled steel tube columns with solid steel core, J. Struct. Eng. (2016) 10.1061/(ASCE)ST.1943-541X.0001695, 04016211.

[5] M. Neuenschwander, M. Knobloch, M. Fontana, Suitability of the damage-plasticity modelling concept for concrete at elevated temperatures: Experimental validation with uniaxial cyclic compression tests, Cem. Con. Res. 79 (2016) 57-75.

[6] M. Neuenschwander, M. Knobloch, M. Fontana, Generic model stress-strain relationship for concrete in compression at elevated temperatures, ACI. Mat. J. 114 (2017) 3-14.

[7] M. Neuenschwander, M. Knobloch, M. Fontana, Elevated temperature mechanical properties of solid section structural steel, Constr. Build. Mat. in press.

[8] M. Neuenschwander, M. Knobloch, M. Fontana, Modeling thermo-mechanical behavior of concrete-filled steel tube columns with solid steel core subjected to fire, Eng. Struct. 136 (2017) 180-193.

[9] CEN (European Committee for Standardization), Eurocode 4: Design of composite steel and concrete structures – Part 1-2: General rules – Structural fire design, EN 1994-1-2, Brussels, Belgium, 2008.

[10] A. Espinos, M.L. Romero, E. Serra, A. Hospitaler, Circular and square slender concrete-filled tubular columns under large eccentricities and fire, J. Constr. Steel Res. 110 (2015) 90-100.

[11] A. Espinos, M.L. Romero, E. Serra, A. Hospitaler, Experimental investigation on the fire behaviour of rectangular and elliptical slender concrete-filled tubular columns, Thin-Walled Struct. 93 (2015) 137-48.

[12] T.T. Lie, M. Chabot, Experimental studies on the fire resistance of hollow steel columns filled with plain concrete, Internal Report No. 611, Inst. for Res. in Constr., National Research Council of Canada (NRCC), Ottawa, Canada, 1992.

[13] G. Hanswille, M. Lippes, Composite columns made of high-strength steel and high-strength concrete, Stahlbau 77 (2008) 296-307 (in German).

FIRE BEHAVIOR OF BLIND-BOLTED CONNECTIONS TO CONCRETE FILLED TUBULAR COLUMNS UNDER TENSION

Dr.-Ing. Ana M Pascual
ampascualpastor@gmail.com

Prof. Dr.-Ing. Manuel L Romero
Universitat Politècnica de València, Spain
mromero@mes.upv.es

ABSTRACT

The blind-bolts allow the connection of steel girders to tubular columns preventing the problems derived from welding in construction and its maintenance. The behavior of this type of connections at room temperatures has been covered in several researches. Nonetheless, its performance in fire is unknown. The aim of this work is to gain insight into the behavior of the blind-bolted connection exposed to the standard fire curve ISO834 and pull-out load.

With that purpose, a thermo-mechanical numerical model using the Finite Element Method has been developed. The simulation is a sequentially coupled analysis. The study includes the comparison between the fire capacity of the connection to a Hollow Steel Section (HSS) column and to a Concrete Filled Tubular (CFT) column and the assessment of the performance in terms of fire resistance time.

1. INTRODUCTION

The advantages of CFT columns have been widely demonstrated. Concrete infill enhances the structural behavior of the HSS tubes, increases the strength of the column and prevents local buckling of the steel tube. The steel tube provides a confinement to the concrete and improves its strength and stiffness. Additionally, the insulation and heat sink effect of concrete make them more resistant under fire conditions.

However, the use of CFT is restricted because of the design of the connection since there is a lack of suitable simple methods for its structural analysis. In that respect, the component method in Eurocode 3 Part 1.8 (EN 1993-1-8, 2004) permits to obtain analytically the main structural characteristics of joints by assembling springs of the contributive parts. But, the components involved in HSS and CFT columns are still not defined (Da Silva et al., 2003; Lopes et al., 2013; Pitrakkos & Tizani, 2013).

The bolted connection to tubular columns requires the use of blind-bolts, able to be tightened from one side of the tube. Up to now, several blind-bolt systems have been developed, as a rule, these systems provide shear connections. However, some bending moment can be transmitted by the connections under a suitable design, as it has been proved by many researches (France et al., 1999a, 1999b, 1999c; Lee et al., 2010).

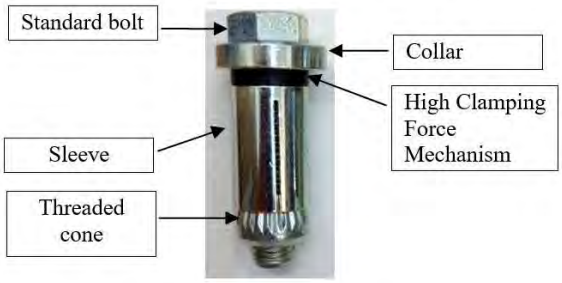


Fig. 1 – Hollo-bolt.



Fig. 2 – Extended Hollo-bolt.

Among the different fastener systems, the present investigation deals with the Hollo-bolt system by (Lindapter, 2012) (Figure 1) and the Extended Hollo-bolt (Figure 2). The latter is a modified version of the Hollo-bolt developed in the University of Nottingham (Ellison & Tizani, 2004; Pitrakkos & Tizani, 2013) in order to transmit bending moment. The Hollo-bolt consists basically of three elements: a standard bolt, a sleeve with four slots and a cone with a threaded hole where the bolt is screwed, Figure 1. It has an easy installation: first, the piece is inserted through clearance holes of the elements to join, then, the bolt is tightened causing the cone to move against the inner face of the tube and the sleeve's legs expand until the total clamping force is transmitted.

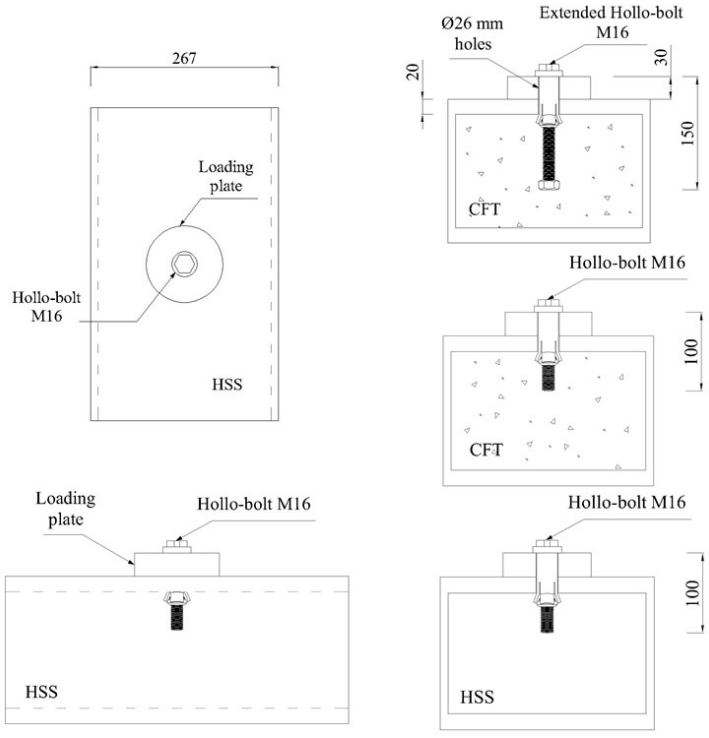


Fig. 3 – Connection of a single blind-bolt from tests (Pitrakkos & Tizani, 2013).

The Extended Hollo-bolt (EHB) is similar to the Hollo-bolt (HB) but with a longer shank ended in a screwed nut (Figure 2) to reduce the stress concentration in steel tube and distributing it within concrete in order to improve the stiffness connection. Tests in full scale connections (Tizani et al., 2013) and pull-out tests (Pitrakkos & Tizani, 2013) have given evidence of the Extended Hollo-bolts to provide a certain stiffness and a subsequent semi-rigid behavior.

Several investigations have been developed to characterize the blind-bolted connections to tubular columns at ambient temperature, however, no researches have been found related to their fire performance. Traditionally, connections under fire have been assumed to be colder than the elements jointed, due to its lower section factor A/V (exposed area A of the element per unit of length divided by V volume of the element per unit of length), the same protection as the rest of elements is therefore used. But, in several catastrophic fires (NIST, 2008) the failure of the connection has been pointed out as the cause of the structural collapse, hence the awareness of the limited understanding of connection fire performance and the necessity of the oversight of the forces caused by the beams during the fire.

First studies on the connection fire performance were on steel connections (Al-Jabri et al., 2006) (Yu et al., 2011) (Huang et al., 2013). The fire behavior of connections beam to CFT in realistic structures were studied by (Ding & Wang, 2007), who considered five different types of joints, and (Elsawaf et al.,2011). They demonstrated the importance of the connection flexibility and strength if the full capacity of the beam is aimed. Reverse channel connections highlighted due to their desirable ductility, being the objective also of the research of (Lopes et al., 2013).

Some of the aforementioned studies on the fire performance of bolted connections assumed concrete filled tubular columns but none of them included blind-bolted connections and their fire behavior. The thermal analysis of blind-bolted connections was covered by the authors in previous research (Pascual et al., 2015a). The aim of the work here reported is to assess the thermo-mechanical response of blind-bolted moment-resisting connections, specifically on the tension zone. For that, FE analysis of the connections to HSS and CFT are developed, with Hollo-bolts and with Extended Hollo-bolts. Thus, the role of the concrete infill and the bolt anchorage within the concrete can be observed by comparison between the different types of connections.

2. FE MODELLING OF THE CONNECTION UNDER FIRE

2.1 INTRODUCTION

Three-dimensional numerical models of the connection were elaborated using the FEA package ABAQUS. In the absence of tests of the blind-bolted connections under fire and pull-out forces to validate the FE model, the thermal and the mechanical parts were validated separately. The research covers two connections: single blind-bolt and T-stub connection, and three cases for each: using Hollo-bolt system to connect a plate with an unfilled tube column (HSS), the same blind-bolt but in a filled tube (CFT) connection and the Extended Hollo-bolt in a CFT. The geometry of the connections analyzed can be seen in Figure 3 and Figure 4.

2.2 VALIDATION OF THE NUMERICAL THERMAL MODEL

The thermal behavior of blind-bolted connections was studied by the authors in a previous work (Pascual, 2015; Pascual et al., 2015a), through experiments and FEA that permitted the calibration of the thermal FE model. Twelve unloaded small-scale specimens were tested under

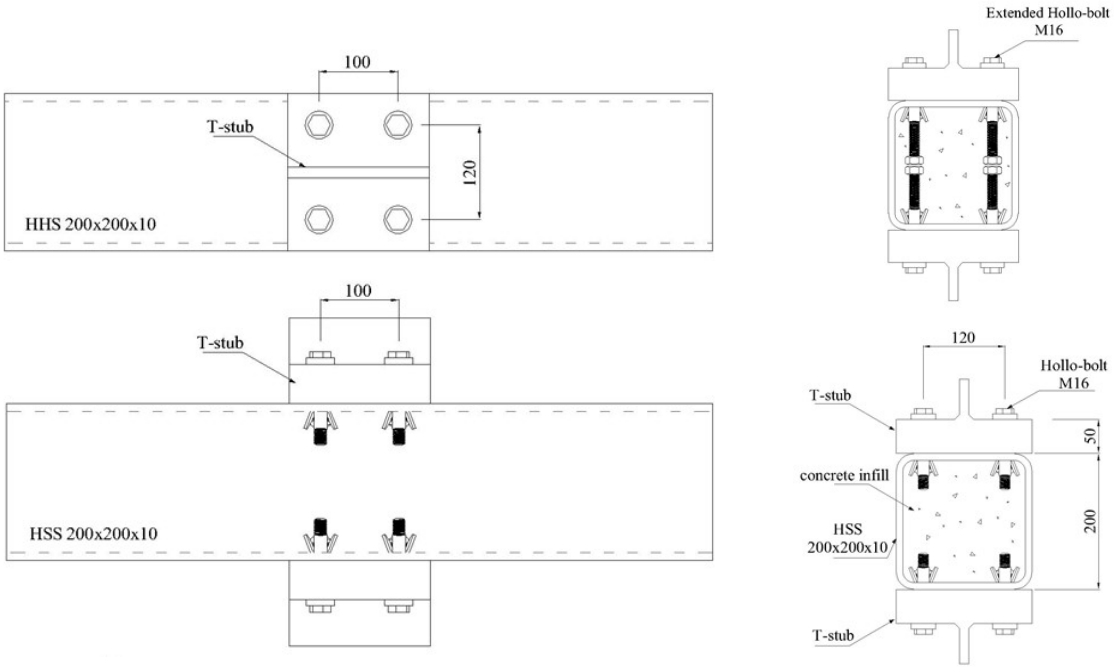


Fig. 4 – Double T-stub connection to a HSS 200x200x10 from tests (Ellison & Tizani, 2004)

the standard fire curve ISO834 in a gas furnace. The program was organized in 4 series of 3 different sections. Each series included 3 types of connections: Hollo-bolt in HSS, Hollo-bolt in CFT and Extended Hollo-bolt in CFT. The difference between the series was the dimension of the column section: 150x150 and 8mm tube thickness (Series 1), 220x220 and 10mm tube thickness (Series 2), 250x150 and 10mm tube thickness (Series 3) and 350x150 and 10mm tube thickness (Series 4). Measurements of temperature were taken at different positions of the bolt and across the concrete section. In parallel, three-dimensional numerical models for the connections were developed to simulate the pure heat transfer problem. The thermal properties of the material and interactions were calibrated through comparison with the experiments.

The accuracy of the FE simulations to represent the thermal behaviour of the connection was assessed by comparing the temperature-time curves numerically calculated and the ones measured by the thermocouples in the laboratory. A good correlation (Pascual, 2015; Pascual et al., 2015a) was observed and consequently the FE model was set to study other parameters.

2.3 VALIDATION OF THE NUMERICAL MECHANICAL MODEL

Before modelling the two configurations (Figure 3 and Figure 4) that are representative of the tension area of a connection I-beam to CFT column and due to the complexity of the interactions and non-linear behavior, other connections were modelled. The objective was to ensure with a large number of simulations the adequacy of the final models used for the thermo-mechanical analysis, starting from simpler models with standard bolts and only steel elements and finishing with complex models of the blind-bolted connection to concrete filled steel columns. Table 1 shows a summary of the calibration work, where the authors of the tests, the type of connection

and elements connected are specified, additionally the ratio maximum load from tests to maximum load from the finite element analysis is in the last column of the table.

Table 1 – List of connections of the calibration work (Pascual, 2015)

Calibration test (authors)	Type of connection	Type of bolt	Beam	Beam/Column	$\xi=M_{u,test}/M_{u,FEM}$ ($N_{u,test}/N_{u,FEM}$)
Jaspart & Bursi, 1998	2 T-stub	M12 grade 8.8	IPE 300	IPE 300	0.93
Janss et al., 1987	Flush endplate	M16 grade 10.9	IPE 300	HEB160	1.01
Wang et al., 2010	2 T-stub	M16 grade 8.8	I-section t=15 mm	I-section t=15mm	0.98
Wang et al., 2010	2 T-stub	HB16 grade 8.8	I-section t=25 mm	I-section t=25mm	1.02
Mesquita et al., 2010	Flush endplate	HB20 grade 8.8	IPE 330	SHS 200x200x8	0.90
Tizani et al., 2013	Flush endplate	EHB16 grade 8.8	356x171x67	CFT 200x200x12.5 (f_c=40N/mm^2)	1.05
Tizani et al, 2013	Flush endplate	EHB16 grade 8.8	457x152x52	CFT 200x200x10 (f_c=40N/mm^2)	0.99
Tizani et al, 2013	Extended endplate	EHB16 grade 8.8	356x171x67	CFT 200x200x10 (f_c=40N/mm^2)	1.05
Tizani et al, 2013	Flush endplate	EHB16 grade 8.8	457x152x52	CFT 200x200x8 (f_c=40N/mm^2)	0.96
Tizani et al., 2013	Flush endplate	EHB16 grade 8.8	356x171x67	CFT 200x200x8 (f_c=40N/mm^2)	1.05
Tizani et al., 2013	Flush endplate	EHB16 grade 8.8	457x152x52	CFT 200x200x12.5 (f_c=40N/mm^2)	1.05
Tizani et al, 2013	Flush endplate	EHB16 grade 8.8	356x171x67	CFT 200x200x10 (f_c=40N/mm^2)	1.08
Tizani et al, 2013	Flush endplate	EHB16 grade 8.8	356x171x67	CFT 200x200x10 (f_c=60N/mm^2)	1.07

The adequate correlation with the experiments led to the modelling of the two connections, Figure 5 and Figure 6, whose definition was based on the experiments used for the validation (Ellison & Tizani, 2004; Pitrakkos & Tizani, 2013).

The first connection under study consisted of a single blind-bolt clamping a loading frame plate and the tube column, Figure 3. The tensile force was transmitted to the blind-bolts through the rigid loading frame plate, 30mm thick. The tube column was not strictly a real commercial HSS, it was an arrangement of plates that worked similarly and where the upper plate was 20mm thick.

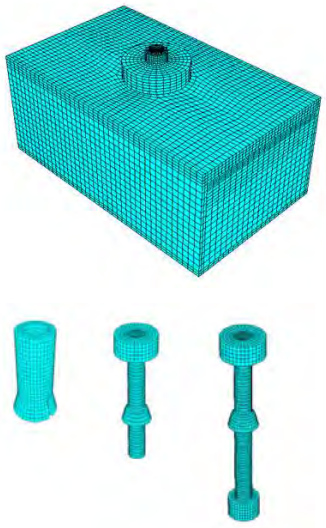


Fig. 5 – FE model of the single blind-bolt connection.

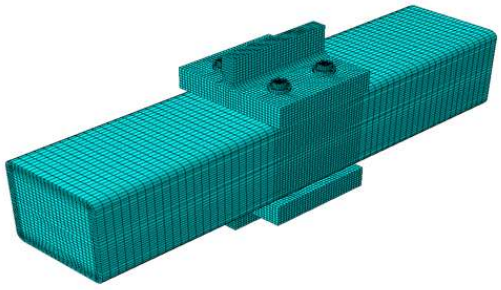


Fig. 6 – FE model of the T-stub connection.

The thickness of the plates was designed in order to behave in the elastic range and in consequence, all attention was focused on blind-bolts performance which controlled the behavior of the connection. Eight specimens from (Pitrakkos & Tizani, 2013) were modelled, they covered different types of bolt (standard bolt, Hollo-bolt and Extended Hollo-bolt), types of column (HSS and CFT), bolt grade and concrete resistance.

The second connection involved two T-stubs bolted to opposite sides of a HSS 200x200x10 S375 taken from (Ellison & Tizani, 2004), Figure 4. As in the specimen with the single blind-bolt the main interest was concentrated on the blind-bolt behavior, so thickness of T-stub flanges was 50 mm. Load was applied by pulling out the upper T-stub while the bottom one was fixed. Two specimens were calculated and validated, considering the connection to a concrete-filled tubular (CFT) column with the two different fastener systems: the Hollo-bolt and the Extended Hollo-bolt.

The definition of the FE model for both connections followed essentially the same criteria, Figure 5 and Figure 6 depict the model of each connection. They were symmetrical about the vertical planes, so only quarter of the specimens was simulated in order to reduce the computational cost.

The fastener was modelled in the tightened state, i.e. assuming the sleeve shape and fastener cone position after the torque application. Hollo-bolt was simplified into two parts: the first one included the standard M16 grade 8.8 and the fastener cone, the second one represented the sleeve in the expanded state. The shank length was 100mm in the single blind-bolted connections and 120mm length in the double T-stub connections. The Extended Hollo-bolt was similarly modelled (Figure 5), by means of the two parts, but taking into account the longer shank (150mm long for both connections) and a nut attached at the end. For the sake of simplicity, the screw thread in the bolt shank was not considered, nor the hexagonal shape of the bolt head and nut.

The analysis procedure attempted to reproduce the actual execution steps of the specimen. In the first stage and before the concrete fill took place, the torque was applied using the ABAQUS “bolt load” function. In the second step, the concrete was inside the tube and the tension load was transmitted through the loading frame plate or the upper T-stub as a static displacement. The failure took place when the velocity of the deformation increased abruptly, which coincided with the lack of equilibrium in the system and the loss of convergence of the Newton’s method.

Three-dimensional eight-noded solid elements with reduced integration (C3D8R) were employed for all the parts in the connection. Mesh density was finer in areas where higher stress gradient occurred, i.e. around blind-bolts, where most interactions happened.

Due to the multiple and different parts in contact, the complexity of the numerical model resided to a greater extent in the interactions definition. A total of 9 contacts were tackled:

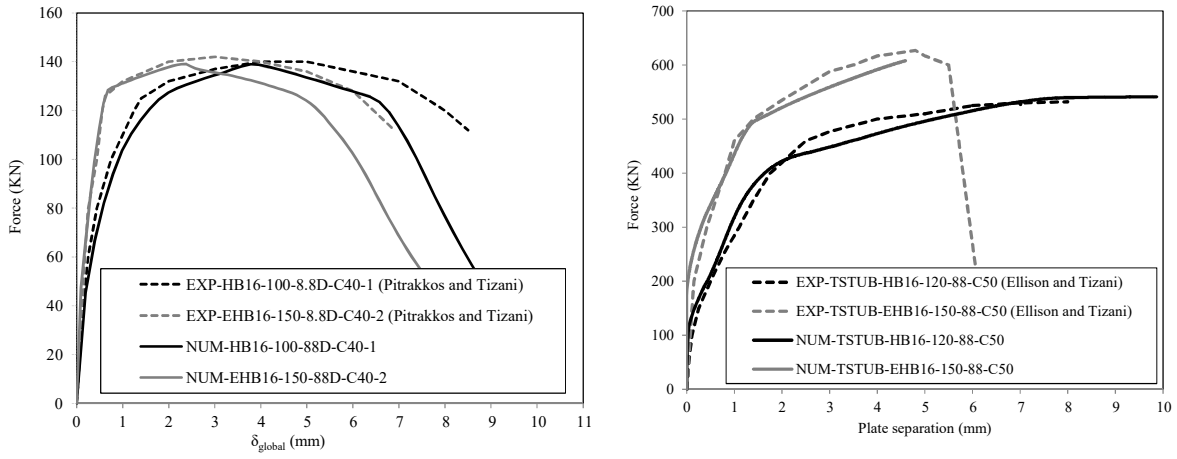
- Contacts between steel surfaces: headbolt to plate/T-stub flange, sleeve to plate/T-stub flange hole surface, sleeve to tube column hole surface, sleeve to fastener cone and external face of tube column to plate/T-stub flange.
- Contacts between steel and concrete surfaces: internal face of the steel tube column to concrete, sleeve to concrete, shank to concrete and nut to concrete (Extended Hollo-bolt).

Interactions were defined as surface to surface contact with finite sliding formulation. In normal direction, “hard” contact behavior was used, whereas in the tangent direction the Coulomb friction model was employed. By means of the friction coefficient (μ), coulomb friction law relates the maximum shear stress in the surfaces with the pressure between them, it was assumed μ=0.25 in the interaction steel-concrete. Eventually, μ=0.25 was used in steel-steel contacts except for sleeve to fastener cone interaction and sleeve to tube hole where was necessary to increase the sticking area increasing the friction coefficient, otherwise slippage of surfaces introduced bolt motion and made the convergence difficult.

The plasticity model for steel behavior was isotropic multiaxial with the Von Mises yield surface. Linear behavior was defined through Young's modulus (E) and Poisson ratio's (v). Standard bolts that formed the fastener system were high strength steel M16 (16mm diameter) grade 8.8. Strain-stress curve was defined by means of the data from tests used for the validation (Ellison & Tizani, 2004; Pitrakkos & Tizani, 2013). Sleeve specifications are provided by (Lindapter, 2012). Sleeve length depends on the total thickness to fasten, i.e. the plate plus the tube thickness. In the single blind-bolted connections (30+20= 50mm) 63mm sleeve length was prescribed and 84mm in T-stub connections (10+50=60mm). Regarding sleeve strength, 430MPa are indicated in the catalogue, although values of yield and ultimate strength from experimental data available in the literature (Liu et al.,2012) were finally adopted. In a similar way, structural steel for tube section was of grade S355 but again values of strength were extracted from data test on analogous tubes (Tizani et al., 2013). The true stress-strain curve was applied.

The concrete damaged plasticity model was selected to define the yielding part of the concrete. The parameter values that described the yield surface and plastic flow were obtained from literature (ABAQUS). For the dilation angle (φ), which defined the dilatancy in plasticity, 30º and 15º were used, due to the negligible effect of the confinement there was no difference between the two values. The ratio (K), which informed about shape of the deviatory plane, was 0.66. The other three parameters that complete the model definition were: eccentricity (ϵ=0.1), ratio of initial equibiaxial compressive stress to initial uniaxial yield stress (f_{b0}/f_{c0}=1.16) and viscosity parameter (0.01). The damaged plasticity model permitted the definition of the plastic regimen under compression and tension. For concrete compression, the stress-strain hardening and softening curve was obtained from (EN 1992-1-1, 2004). The post failure tension behavior was defined by stress-fracture energy law (FIB 2010. Model Code 2010). Concrete of grade C40 was used in specimens with a single blind-bolt, and C50 in the double T-stub connections.

Eight single connections and two double T-stub connections were simulated and compared with experimental tests with a good correlation of the curves force-plate separation, Figure 7.



a) b)

Fig. 7 – Comparison of force-displacement curve between experiments and FEA (Pascual, 2015b; Pascual et al., 2015) for a) single connection; b) T-stub connection.

2.4 DESCRIPTION OF THE THERMO-MECHANICAL MODEL

Once the suitability of the mechanical and thermal numerical models to capture the connections behavior was proved, the fire analysis was carried out. The two blind-bolted connections

representatives of the tension area in moment-resisting connections were studied under tensile load and elevated temperatures: the single blind-bolted connection and the double T-stub connection to the tube column, Figures 3 and 4. Three cases were conducted for each one: with HB and HSS column, HB and CFT column, and EHB and CFT column. The geometry of the connections defined for the analysis at room temperature was maintained.

Sequentially coupled thermal-stress analysis were carried out, following the recommendations of (Espinos et al., 2010). In this type of analysis the stress-strain solution depended on the temperature field but not the opposite. Conversely, in a fully coupled analysis, the mechanical and thermal response affect each other, the stress and thermal analysis are simultaneous. The latter procedure is closer to reality, but at the expense of high computational cost and convergence problems, the accuracy improvement is not worth noting.

In a sequentially coupled thermal-stress analysis two finite element models are needed: a thermal model and a mechanical model. First, the pure heat transfer model was computed. Temperature-time curves were obtained for each node and kept to be applied to the mechanical model as a prescribed thermal load after the axial loading. Afterwards, the mechanical model for the stress-deformation was developed. Before tensile load application, the stress produced in the steelworks by tightening the bolts was input as an initial state. In the following stage, and taking into account that the tube is filled with concrete, load was applied. Finally, the temperature field kept was input onto the mechanical model while the load was propagated.

3. FIRE PERFORMANCE OF THE CONNECTION

3.1 FAILURE MODE

The plate and tube thickness were designed in order to focus the attention on the fire resistance consequence of the fastener system. Depending on the type of connection, the failure was governed by the shank of the bolt or by the sleeve. In case of being dominated by the sleeve, strength was lower but flexibility higher.

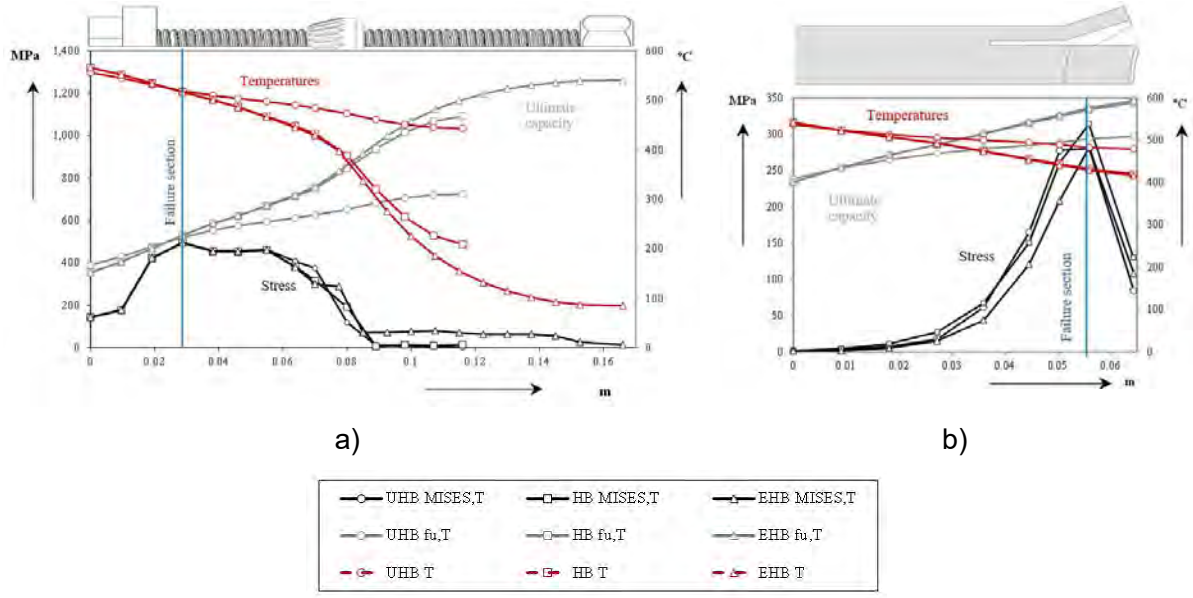


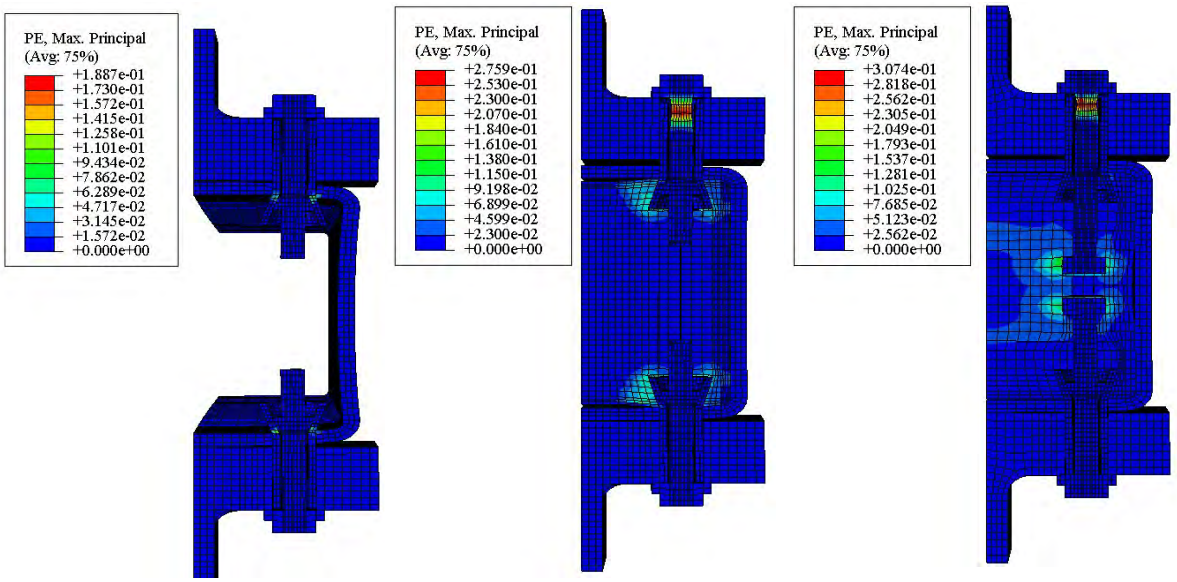
Fig. 8 – Mises stress (MISES,T), ultimate steel strength ($f_{u,T}$), and temperatures (T) along a) shank for the three cases of the single blind-bolted connections at connection failure; b) sleeve for the three cases of the single blind-bolted connections at connection failure.

Figures 8a and 8b compare Mises stresses along the shank bolt and the sleeve with their respective steel strength capacity (f_u), immediately before the collapse and for the three types of connections. They show the part of the connection (shank or sleeve) that reached the ultimate capacity and indicate the section where failure was assumed and which is the same for all of the connections. For the shank bolt, the critical section was next to the bolt head (Figure 8a), where temperature was highest and steel strength is consequently lowest. Meanwhile, in the sleeve, the highest stresses were concentrated around the folded section, Figure 8b. Figures 8a and 8b include a second axis that reflects the temperature along both parts. It can be observed that fracture occurred around 500ºC, when steel strength decrease became more significant and was reached by Mises stress.

In the HB connection to the HSS column, sleeve and shank failed at the same time, Figure 8a and 8b. However, in connections to CFT columns (HB and EHB) the failure was dominated by the shank fracture, due to the fact that stresses distributed through the concrete reducing sleeve deformation. Finally, the ultimate strength capacity of the shank bolt was reached in all of the three connection types.

The FE model of the double T-stub bolted connections permitted to gather more data to understand the connection fire performance. Thickness of the T-stub flange was designed to eliminate any influence on the behavior, however, the tube thickness was significantly lower than in the single blind-bolted connections, so its effect should not be totally neglected.

Figure 9 shows the deformed shape at failure of the double T-stub connections at elevated temperatures. Concrete prevented the deformation of the tube column that took place in the HSS, as it occurred at room temperature. Plastic deformation is also depicted in Figure 9, which helped for the detection of the failure mode for each type of connection. In the connection to the unfilled column, stress on the sleeve governed the failure whereas the shank did not present plastic deformations (Figure 9a). In the case of CFT columns, bolt shank reached its ultimate capacity and dominated the connections collapse, although high plastic strains were also observed in the sleeve and the concrete (Figure 9b and 9c).



a) HSS connection b) HB to CFT column c) EHB to CFT column

Fig. 9 – Plastic strain in double T-stub connections to tube column at failure.

3.2 FIRE RESISTANCE RATING

The Fire Resistance Rating (FRR) indicates the time in minutes that the connection is capable of sustaining the loads before failure. The single blind-bolted connections were calculated under different load levels with regard to the maximum load supported at room temperature, in order to know its influence on the FRR. Table 2 shows that FRR increased by 11 minutes for the three connections types when load level decreased from 50% to 20% load level. Expectedly, as the load level was lower, the FRR improved. Moreover, it is worth noting that unprotected connections to CFT columns reached 36 min of FRR when 20% loaded.

The effect of concrete on bolt temperature can be observed from Figure 8a by inspecting the area of the bolt directly in contact with concrete, starting from 0.08m along the shank length. However, the shank bolt fracture occurred next to the exposed area of the bolt, so concrete influence was not as remarkable as it was expected. Connections to CFT gained 4-5min (16-20%) of FRR compared with HSS connections, Table 2. The heat sink effect of concrete was assumed to be more important in case of thinner tube and plate.

On the other hand, there were no differences in FRR between the Hollo-bolt and the Extended Hollo-bolt connection to CFT, Table 2. Similarly, it was attributed to the fact that the fracture took place next to the head of the bolt and the bolt anchorage within the concrete did not reduce stress nor temperature in that section.

Table 2 – FRR for single blind-bolted connections and T-stub connections. Load level influence for single blind-bolted connections.

Specimen index	Load level	FRR	$FRR_{HB/EHB}$-FRR_{UHB}	
	%	min	min	%
UHB16-100-8.8D-L50	50	20.55		
UHB16-100-8.8D-L40	40	23.15		
UHB16-100-8.8D-L20	20	30.78		
HB16-100-8.8D-C40-L50	50	24.68	4.13	20.12
HB16-100-8.8D-C40-L40	40	27.01	3.87	16.71
HB16-100-8.8D-C40-L20	20	35.60	4.82	15.67
EHB16-150-8.8D-C40-L50	50	24.70	4.15	20.21
EHB16-150-8.8D-C40-L40	40	27.14	4.00	17.27
EHB16-150-8.8D-C40-L20	20	35.63	4.85	15.77
T-UHB16-120-8.8D	50	17.78		
T-HB16-120-8.8D-C50	50	22.15	4.37	24.55
T-EHB16-120-8.8D-C50	50	22.05	4.27	23.99

4. CONCLUSIONS

This research is a numerical study on the fire performance of blind-bolted connections to CFT and HSS in the tension zone of moment-resisting connections. In the absence of fire experiments to validate the thermo-mechanical model, the mechanical part of the problem was corroborated at room temperature with tests on the same connections, whereas the validation of the heat transfer was accomplished in a preceding research by the authors (Pascual et al., 2015a).

The objective was to provide data to gain insight into tensile loaded blind-bolted connections in fire and to assess the effect of concrete infill and the anchorage of the blind-bolt. Two types of connections were analyzed, a single blind-bolt connecting a plate to a tube column and a double T-stub connection to a tube column. The type of column (HSS and CFT) and the type of fastener system (HB and EHB) were the variables considered for each connection. The fastener system was the element that governed the connection failure due to the thickness of the plate or T-stub

flange and the tube, but depending on the connection and temperatures, the sleeve or the bolt shank were determinant. The conclusions from the study are the following:

- Concrete filling the tube column resulted in 16-20% enhancement in FRR for the connection with the single blind-bolt compared with connections to unfilled columns, and around 25% for the double T-stub connections. In connections to HSS, the failure was shared by the sleeve and the shank of the fastener. For the connections to CFT columns the shank bolt of the fastener system decided the connections collapse, where stresses in the sleeve were lower due to the concrete.

- The anchorage of the shank bolt into the concrete provided by the EHB did not represent an increase in the FRR compared with the HB in connections to CFT. Failure of the shank was located next to the bolt head where neither temperature nor stress were directly affected by the anchorage.

REFERENCES

Al-Jabri, K. S., Seibi, A., & Karrech, A. (2006). *Modelling of unstiffened flush end-plate bolted connections in fire*. Journal of Constructional Steel Research, 62(1-2), 151-159.

Bursi, O. S., & Jaspart, J. P. (1998). *Basic issues in the finite element simulation of extended end plate connections*. Computers & Structures, 69(3), 361-382.

EN 1992-1-1 (2004). *Eurocode 2: Design of concrete structures. Part 1-1: General rules and rules for buildings*. Brussels, Belgium: Comité Européen de Normalisation.

EN 1993-1-8 (2004). *Eurocode 3: Design of steel structures. Part 1-8: Design of joints*. Brussels, Belgium: Comité Européen de Normalisation.

Da Silva, L. S., Neves, L. F. C., & Gomes, F. C. T. (2003). *Rotational stiffness of rectangular hollow sections composite joints*. Journal of Structural Engineering, 129(4), 487-494.

Ding, J., & Wang, Y. C. (2007). *Experimental study of structural fire behavior of steel beam to concrete filled tubular column assemblies with different types of joints*. Engineering Structures, 29(12), 3485-3502.

Elsawaf, S., Wang, Y. C., & Mandal, P. (2011). *Numerical modelling of restrained structural subassemblies of steel beam and CFT columns connected using reverse channels in fire*. Engineering Structures, 33(4), 1217-1231.

Ellison, S., & Tizani, W. (2004). *Behavior of blind bolted connections to concrete filled hollow sections*. The Structural Engineer, 82, 16-17.

Espinos, A., Romero, M. L., & Hospitaler, A. (2010). *Advanced model for predicting the fire response of concrete filled tubular columns*. Journal of Constructional Steel Research, 66(8-9), 1030-1046.

FIB 2010. Model Code 2010. Lausanne, Switzerland: Fédération Interantionale du Béton.

France, J. E., Davison, J. B., & Kirby, P. A. (1999a). *Moment-capacity and rotational stiffness of endplate connections to concrete-filled tubular columns with flowdrilled connectors.* Journal of Constructional Steel Research, 50(1), 35-48.

France, J. E., Davison, J. B., & Kirby, P. A. (1999b). *Strength and rotational response of moment connections to tubular columns using flowdrill connectors*. Journal of Constructional Steel Research, 50(1), 1-14.

France, J. E., Davison, J. B., & Kirby, P. A. (1999c). *Strength and rotational stiffness of simple connections to tubular columns using flowdrill connectors*. Journal of Constructional Steel Research, 50(1), 15-34.

Huang, S. S., Davison, B., & Burgess, I. W. (2013). *High-temperature tests on joints to steel and partially-encased H-section columns*. Journal of Constructional Steel Research, 80, 243-251.

Janss, J., Jaspart, J. P., & Maquoi, R. (1987). *Experimental study of the non-linear behavior of beam-to-column bolted joints*. In: Proc. of a State-of-the art workshop on connections and the behavior, strength and design of steel structures. Elsevier Applied Science Publishers, 26-32.

Lee, J., Goldsworthy, H. M., & Gad, E. F. (2010). *Blind bolted T-stub connections to unfilled hollow section columns in low rise structures.* Journal of Constructional Steel Research, 66(8-9), 981-992.

Lindapter (2012). Type HB- Hollo-Bolt. Cavity fixings 2, Product brochure. Lindapter International, UK. 41-43.

Liu, Y., Málaga-Chuquitaype, C., & Elghazouli, A. Y. (2012). *Response and component characterisation of semi-rigid connections to tubular columns under axial loads*. Engineering Structures, 41(0), 510-532.

Lopes, F., Santiago, A., Da Silva, L. S., Heistermann, T., Veljkovic, M., & Da Silva, J. G. (2013). *Experimental behavior of the reverse channel joint component at elevated and ambient temperatures. International Journal of Steel Structures*, 13(3), 459-472.

Mesquita, A., Da Silva; L.S., & Jordao,S. (2010). *Behavior of I beam SHS column steel joints with Hollo-bolts: An Experimental Study*. In: Proc. 13th International Conference on Tubular Structures XIII. The University of Hong Kong.

National Institute of Standards and Techology (NIST). *Final Report on the collapse of the World Trade Center building 7*. USA: National Institute of Standards and Technology (2008).

Pascual, A. M., Romero, M. L., & Tizani, W. (2015a). *Thermal behavior of blind-bolted connectios to hollow and concrete filled tubular columns*. Journal of Constructional Steel Research, 107, 137-149.

Pascual, A. M., Romero, M. L., & Tizani, W. (2015b). *Fire performance of blind-bolted connections to concrete filled tubular columns*. Engineering Structures, 96, 111-125.

Pascual, A. M. (2015). *Fire Behavior of blind-bolted connectios to concrete filled tubular columns under tension*. Dissertation. Department of Construction Engineering and Civil Engineering Projects, Universitat Politècnica de València.

ABAQUS. ABAQUS User´s Manual. Providence. Rohde Island, USA. Dassault Systèmes. Simulia Corporation. ABAQUS vs 6.6. ABAQUS/Standard Version 6.6.

Pitrakkos, T., & Tizani, W. (2013). *Experimental behavior of a novel anchored blind-bolt in tension*. Engineering Structures, 49, 905-919.

Tizani, W., Al-Mughairi, A., Owen, J. S., & Pitrakkos, T. (2013). *Rotational stiffness of a blind-bolted connection to concrete-filled tubes using modified Hollo-bolt*. Journal of Constructional Steel Research, 80(0), 317-331.

Wang, Z. Y., Tizani, W., & Wang, Q. Y. (2010). *Strength and initial stiffness of a blind-bolt connection based on the T-stub model*. Engineering Structures, 32(9), 2505-2517.

Yu, H., Burgess, I., Davison, J., & Plank, R. (2011). *Experimental and Numerical Investigations of the Behavior of Flush End Plate Connections at Elevated Temperatures*. Journal of Structural Engineering, 137(1), 80-87.

ROBUSTNESS DESIGN AND POSSIBLE COLLAPSE MECHANISMS OF BUILDING FRAMES IN A FIRE

Kei KIMURA
Nippon Steel & Sumitomo Metal Corporation
Futtsu, Japan
kimura.ze8.kei@jp.nssmc.com

Fuminobu OZAKI
Nagoya University
Nagoya, Japan
ozaki@dali.nuac.nagoya-u.ac.jp

Ryoichi KANNO
Nippon Steel & Sumitomo Metal Corporation
Futtsu, Japan
kanno.kx4.ryoichi@jp.nssmc.com

ABSTRACT

For fire safety design, conventional prescriptive design has been rapidly changing to more flexible and economical performance-based design. In this design approach, extensive research has been conducted on robustness to make full use of inherent structural resistance. This paper first reviews and summarizes the past and ongoing research activities on structural robustness design for fire resistance of floors and frames. A frame collapse mechanism that provides structural resistance even in the case of semi-rigid frames is proposed. In the proposed mechanism, resistance against gravity loading can be provided largely by the flexural resistance of floor systems above the localized fire zone. With a simple limit analysis technique, the increased resistance of a multi-storied frame is calculated and demonstrated, revealing that a substantial number of the columns may also be unprotected in addition to the floor joists by floor robustness design already established. The resisting mechanism proposed in this study for building frames has not been fully verified experimentally; therefore, further studies are required.

INTRODUCTION

Fireproofing materials such as sprayed vermiculite can increase the fire resistance of structural steel members and their thickness can be determined easily based on the required fire resistant rating. Recently, this conventional prescriptive design has been rapidly changing to performance-based design that can enable more flexible and economical design. In this design approach, there have been extensive research activities on “robustness” or “redundancy” to make full use of the inherent structural resistance. One of the representative examples is a series of research activities in Europe on the membrane action of a composite floor slab under increasing temperature (Wang et al., 1996), (Bailey et al., 2000), (Nadjai et al., 2011). The design guidelines for the membrane action have been proposed so that floor joists can remain unprotected against fire (SCI, 2006), (Vassart et al., 2012). Another example is frame robustness research that takes into account the whole frame resistance when some columns lose their load resisting capacities due to fire (JSSC, 2005). This research is currently limited to

the frames designed to protect against earthquakes, whose beam-column connections are fully rigid.

This paper first reviews and summarizes the past and ongoing research activities on structural robustness design under fire from both floor and frame resistance perspectives. By focusing on the latter frame case, one possible frame collapse mechanism that can provide structural resistance of semi-rigid frames is proposed. In the proposed mechanisms, the resistance against gravity loading may be provided largely by the flexural resistance of floor systems above the localized fire zone. Applying a simple limit analysis technique, the increased resistance of a multi-storied frame is calculated.

OVERVIEW OF FIRE RESISTANT DESIGN IN JAPAN

Before discussing the robustness design, an overview of fire resistant design of steel buildings in Japan is presented to ascertain the technological advancements in fire design. In Japan, the most common method of increasing the fire resistance is to use fireproofing materials. One representative example is sprayed vermiculite having high thermal insulation performance; however, there are disadvantages in using it. For example, the working environment is difficult and unhealthy, and regular maintenance is required because of its quality deterioration. As a result, the use of other materials such as gypsum board, blanket or intumescent material has increased; however, there still is a strong need to reduce the fireproofing work in Japan due mainly to the problem of the growing labor shortage.

In 1988, fire resistant (FR) steel was developed in Japan. FR steel is a carbon steel that includes alloys such as Cr and Mo in order to increase the strength at high temperature (Sakumoto et al., 1992), (Sakumoto et al., 1994). FR steel has a yield stress at 600°C that is equal to or larger than 2/3 times the design strength at ambient temperature as shown in Figure 1. Due to this improved performance, FR steel has been applied in many car parks and atriums in Japan as shown in Figure 2.

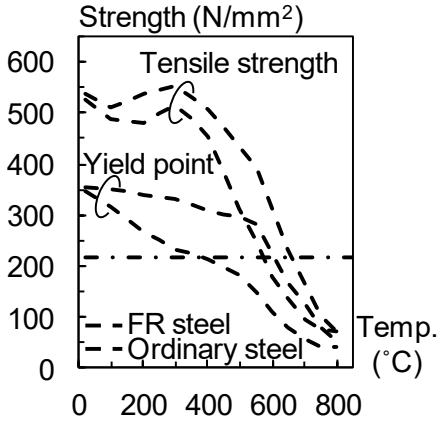


Fig. 1 – Mechanical properties of FR steel at high temperature



(a) A car park



(b) An atrium

Fig. 2 – Examples of FR steel application

A performance-based design method for fire safety has been developed in Japan since the 1980s as shown in Figure 3. A series of research activities on the structural fire resistance of steel frames were conducted from 1982 to 1987 and the first design method was proposed by the Building Center of Japan (BCJ, 1989). Since then, further active studies on the behavior of steel members and frames at elevated temperature have been conducted. The Architectural

Institute of Japan (AIJ) published a recommendation for the fire-resistant design of steel structures (AIJ, 1999) and then a verification method for fire resistant performance was issued for design practitioners by the Japanese government in 2001. Note that in the same period, Eurocode3 for the structural fire design of steel structures was published in European countries.

In line with the rest of the world, conventional prescriptive design has been rapidly changing to a more flexible and economical performance-based design in Japan. Along with this trend, there has been interesting research conducted recently on the methodology in which stress redistribution is taken into consideration for steel frames in a fire. This research conducted in Japan is intended largely to remove the fire protection in some of the columns. In Europe, there has been similar research activity, but the stress redistribution has been considered not on the frames but on the floor slabs.

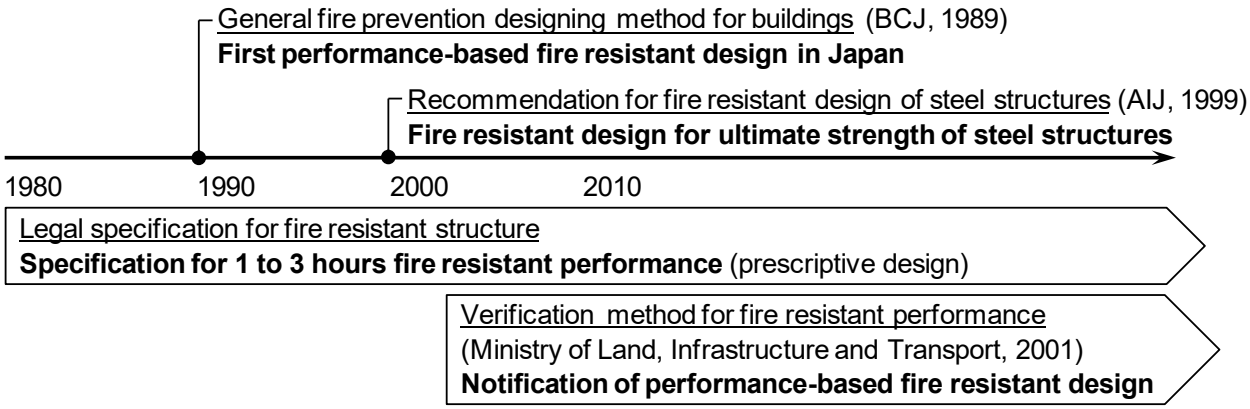


Fig. 3 – Timelines of fire resistant design in Japan

ROBUSTNESS DESIGN

The structural behavior of a steel frame in a fire changes over time due to the reduction of the material strength and the thermal expansion of the structural members. Figure 4 shows the behavioral process (Stages 1 to 3) in the fire of a steel frame with no fire protection from the fire initiation until the complete collapse.

Stage 1: Continuing heat input by fire increases the temperature of the structural members.
Stage 2: Decrease in material strength at high temperature reduces the member strength.
Stage 3: Increase in the number of damaged members reduces the stability of the whole frame.

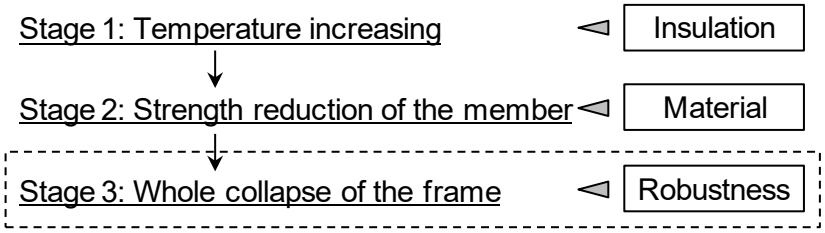
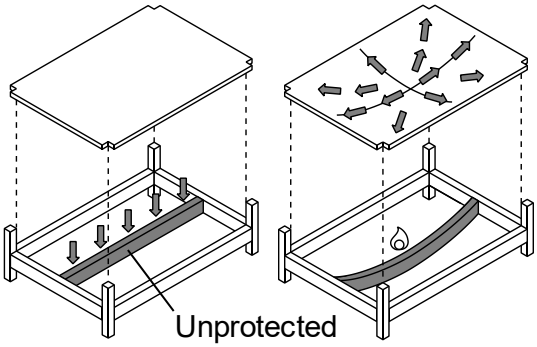


Fig. 4 – Process to total collapse of frame and preventing solutions

There are solutions to secure the safety of the frame in fire. Heat insulation such as sprayed mineral fiber is the most common solution for Stage 1. Another solution is to use a special steel material such as FR steel, which can be categorized as a solution for Stage 2. For Stage 3, one

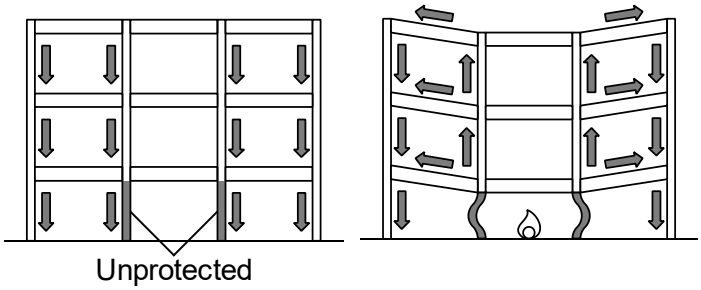
has to consider the stress redistribution in the frame and structural elements, because in this stage, the members and elements in the frame lose their strength. The design for this stage is based on an observation that one member or element did not cause the entire collapse of the frame. This solution for Stage 3 is called “robustness design” and may be defined as a design that considers the ultimate resistance of a frame or a structural element until its collapse.

In Europe, there are design guidelines for floor robustness, through which fireproofing materials of floor joists can be partially omitted as shown in Figure 5. This is possible by considering the load-bearing capacity of floor slabs when the slabs undergo large deflections and exhibit a membrane action. On the other hand, in Japan, a design methodology for frame robustness has been proposed so that fireproofing materials of the columns can be partially omitted as shown in Figure 6. This design is possible by considering the load redistribution over the entire frames when some of the columns lose their strength. Both floor and frame robustness designs will be discussed more in detail after the next sections.



(a) At ambient temp. (b) In a fire

Fig. 5 – Load-bearing mechanisms of floor at ambient and high temperatures



(a) At ambient temp. (b) In a fire

Fig. 6 – Load paths in frames at ambient and high temperatures

FLOOR ROBUSTNESS

The fire resistant performances of concrete slabs and steel beams (joists) are evaluated separately by standard fire tests with small-scale specimens because these tests are simple and safe. In reality, however, a composite floor slab consisting of a reinforced concrete slab and steel joists shows higher performance than isolated standard fire tests. Historically, observations after some real fires have deepened the understanding on how multi-story steel buildings behave in a fire and the knowledge obtained has had a large impact on the design of the composite floors in a fire.

In 1996, a series of fire tests on an eight-story steel building were conducted in the UK at the Building Research Establishment’s Cardington Laboratory (Wang, 1996). It provided valuable information on the behavior of a steel frame in a real fire. After this landmark test, focusing on composite floors with unprotected steel joists at elevated temperatures, a series of fire tests and numerical analyses were further conducted to evaluate the load-bearing capacity of the floors.

The results clarified that even when the unprotected steel joists lost their strength, the vertical load was resisted through the reinforced concrete slab by so-called tensile membrane action at high temperature. The resistant mechanism is shown in Figure 7 (Bailey and Moor, 2000). Both tension and compression zones were formed in the slab as the slab deflection became large, providing a stable tensile membrane action to gain resistance against the vertical load. Design guidelines considering this membrane effect have been proposed with simple design models such as the one shown in Figure 8 (Bailey and Moor, 2000). The guidelines enabled steel joists

underneath the floor slab to remain unprotected against fire. Bailey and Moor (Bailey and Moor, 2000) also indicated that the aspect ratio and the amount of deflection of the slab affected the strength as shown in Figure 9. In addition, a trial evaluation of slab and beam resistances during a fire was conducted as shown in Figure 10, showing that the beam had a quick loss of its strength while the slab gained its strength gradually due to the membrane action as the fire progressed. Depending on the beam and floor joist arrangement in frame design, this floor robustness design would make it possible to omit around 30% of the fire protection applied to all the beams and floor joists.

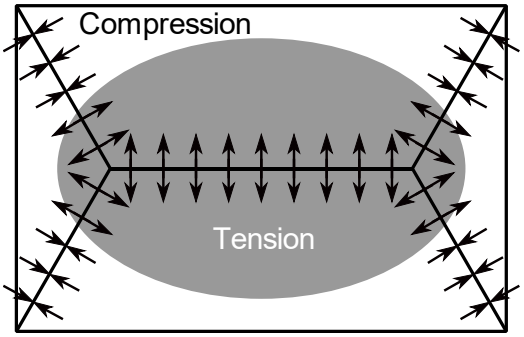


Fig. 7 – Compression and tension zones for tensile membrane action

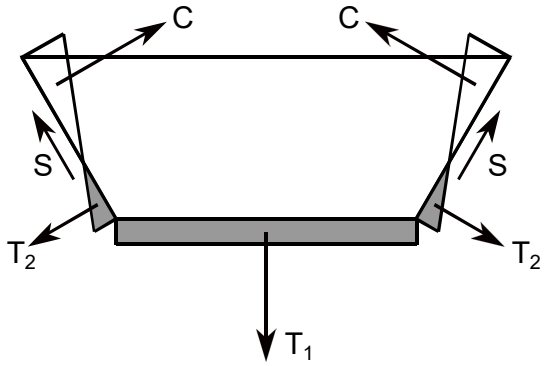


Fig. 8 – In-plane force equilibrium

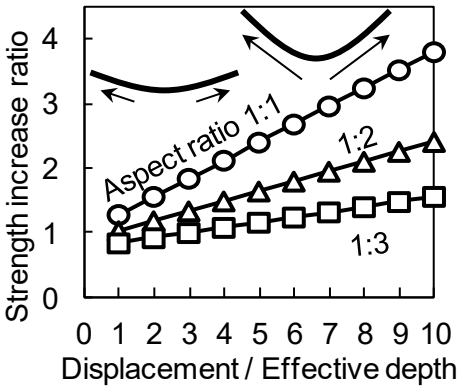


Fig. 9 – Strength increase ratio for a composite slab

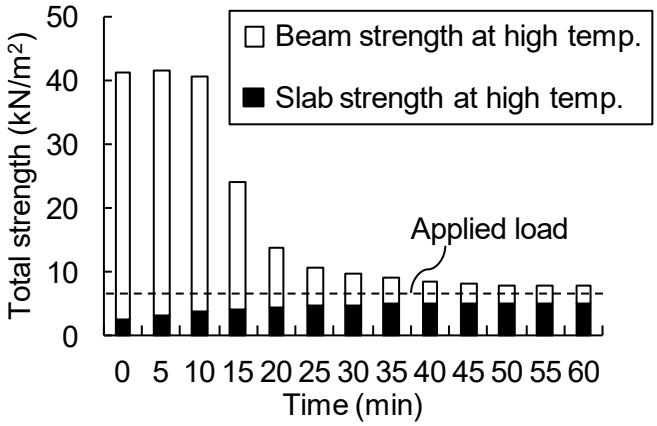


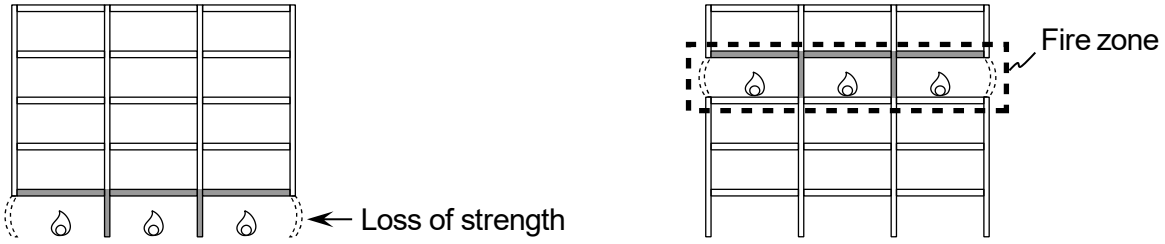
Fig. 10 – Trial evaluation for a composite slab with unprotected beams in a fire

FRAME ROBUSTNESS

The loss of the strength of heated columns does not immediately trigger overall frame collapse in a fire. In particular, for rigid steel frames, the high capacity of stress redistribution against gravity loading can be expected. Considering this stress redistribution, the Japanese Society of Steel Construction (JSSC) proposed a frame robustness design in Japan that rendered some of the columns in a steel frame unprotected against fire (JSSC, 2005).

Figure 11 (a) shows the concept of the frame robustness design. Considering a steel frame with fire protection where a fire occurs on the first floor and the exterior columns on the same floor are rendered unprotected, the exterior columns could remain unprotected if the remaining columns and the upper frame above the floor are stable and have sufficient strength to support the entire gravity load. When the frame becomes unstable and collapsed, the exterior columns must be protected against fire. Various column combinations can be checked through this way

to determine the best unprotected column combination that gives the largest unprotected area. As shown in Figure 11 (b), when story fire compartments are fully effective and fire does not spread to other stories, the columns on each floor can be evaluated separately from the second story to the fifth story to determine the best unprotected column combination in the entire frame. This is the idea and basic procedure for the frame robustness design.



(a) Robustness design for the first floor (b) Robustness design for the other stories

Fig. 11 – Frame robustness design at high temperature

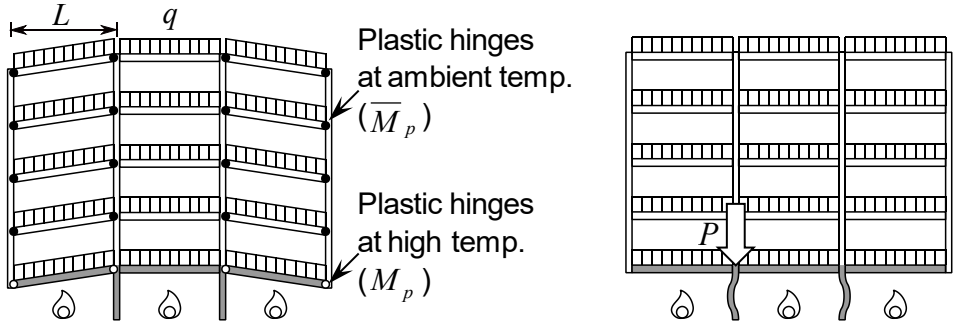
Figure 12 shows the collapse modes of a five-story steel building frame, assuming unprotected exterior columns on the first floor lose their strength at high temperature (JSSC, 2005). There are two types of modes: beam collapse mode (Figure 12 (a)) and column collapse mode (Figure 12 (b)). The following design formulae can be derived for both collapse modes:

$$\sum \frac{1}{2} qL^2 < \sum 2\,\bar{M}_p + 2M_p \tag{1}$$

$$P < N_{cr} \tag{2}$$

where

q : distributed load on the girders
L : length of the girder
M_p : full plastic moment of the girder at the fire story at high temperature
$\bar{M}_p$: full plastic moment of the girder at the upper stories at ambient temperature
P : vertical load applied to a protected column at the fire story
N_{cr} : axial strength of a protected column at the fire story at high temperature



(a) Beam collapse mode (b) Column collapse mode

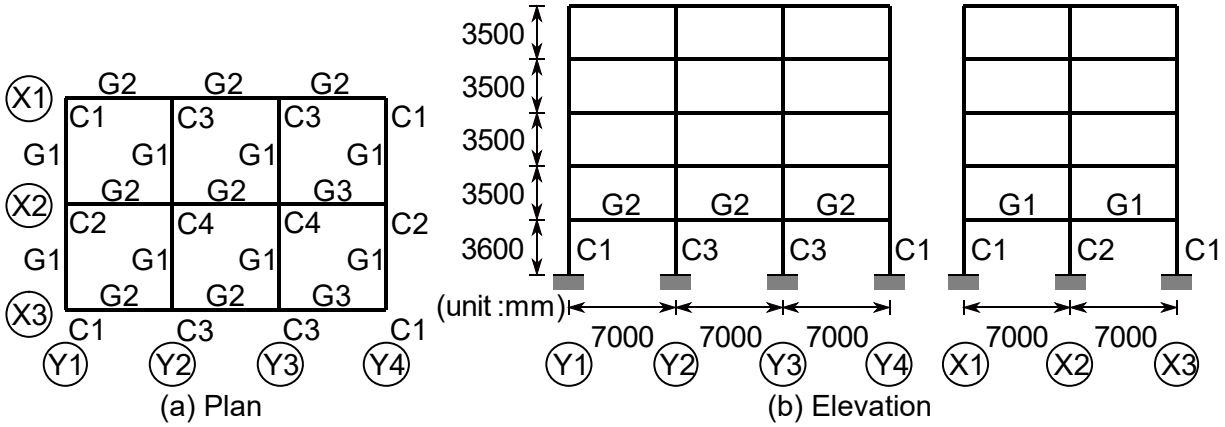
Fig. 12 – Two types of collapse mode

Eqn. (1) is a formula obtained assuming that the distributed gravity load above the first floor is resisted by the remaining frame. In Japan, the seismic design requires that the beam be weaker than the column; therefore, applying the principle of virtual work to the plastic hinges shown in Figure 13 (a), Eqn. (1) can be obtained as a condition in which the entire frame is stable. On the other hand, Eqn. (2) is a formula that checks if the remaining columns on the first floor have

sufficient strength to support the vertical load above the first floor. If both formulae of Eqns. (1) and (2) are satisfied, the entire frame with unprotected exterior columns on the first floor is stable. Thus, fire protection rendered to the exterior columns on the first floor could be omitted. Various unprotected column combinations would be checked not only for the first floor but also for the above floors one by one to obtain the best unprotected column combination in the entire frame.

DESIGN EXAMPLE OF FRAME ROBUSTNESS

A design example for the column robustness is shown in Figure 13, which was reported by the Building Research Institute (BRI) in Japan (BRI, 2008). The building was a typical five-story office building in Japan, designed against earthquakes based on the seismic design code in Japan. Tables 1 and 2 show the sections of the columns and beams together with material types (JIS standard) and their material strengths *F*. In this building, beams were fully-rigidly connected to columns with full penetration welding; therefore, the strength of the connections was the same as or larger than the full plastic moment of the beam. Note in the strength calculations through Eqns. (1) and (2) that the full plastic moment of the beams and the axial strength of the columns were assumed to be given by those calculated at ambient temperature, considering fire protection rendered to the members.



(a) Plan (b) Elevation

Fig. 13 – Building for design example

Figure 14 shows a comparison between the beam and column collapse modes. The horizontal axis is the ratio of the resistance to the external force, called the safety index in this study. Referring to Eqns. (1) and (2), the left hand side terms correspond to the external force whereas the right hand side terms provide the resistance. As Figure 14 shows, the column collapse mode was more stable than beam collapse mode because the safety index became large. This is because the building was designed primarily against earthquakes.

In Japan, the overall beam collapse mechanism is generally preferred to increase the energy dissipating capacity while the local story collapse mechanism is avoided. As a result, steel frames are generally designed so that column strength is higher than beam strength such as a 50% increase in the column. This is why the column collapse mode is more stable for seismically designed frames. This means, in turn, that the beam collapse mode is the dominant mode of failure for the frame robustness design and checking the column strength may not be necessary. As shown in the beam collapse mode in Figure 14, the upper stories were less stable than the lower stories, because the number of beams to be resisted became fewer as the designed story moved upward.

Table 1 – Sections for column

Story	C1, C2, C3, C4 (BCR295)
5	□-400x400x12
4	□-400x400x12
3	□-400x400x12
2	□-400x400x14
1	□-400x400x16

(BCR295 : F=295N/mm²)

Table 2 – Sections for beam

Story	G1 (SN400B)	G2 (SN400B)	G3 (SN400B)
R	H-500x200x10x16	H-450x200x 9x14	H-488x300x11x18
5	H-500x200x10x16	H-500x200x10x16	H-500x200x10x16
4	H-488x300x11x18	H-500x200x10x16	H-500x200x10x16
3	H-488x300x11x18	H-500x200x10x16	H-500x200x10x16
2	H-488x300x11x18	H-488x300x11x18	H-488x300x11x18

(SN400B : F=235N/mm²)

(Size : H-Depth x Width x Web thickness x Flange thickness (unit : mm))

Figures 15 and 16 show the effect of the location of unprotected columns on the beam collapse mode. As shown in Figure 16, the exterior columns had less effect on the entire stability (strength) of the building frame. This is because the exterior columns supported smaller gravity loads than the interior columns. This comparison indicates that the exterior columns become more preferable to omit the fire protection than the interior columns. As a result of the frame robustness design for the building considered, it is possible that the exterior columns can be unprotected while the interior columns remain protected. Overall, approximately 50% of the fire protection rendered to the entire columns would be omitted in this design example.

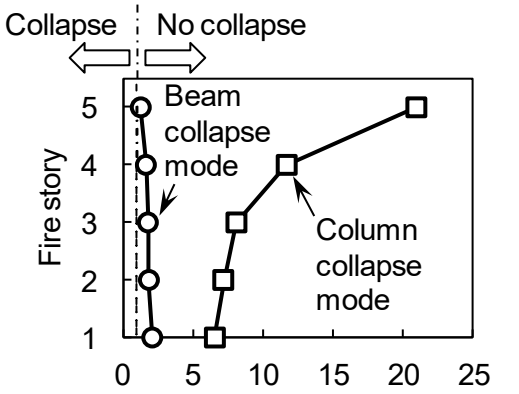
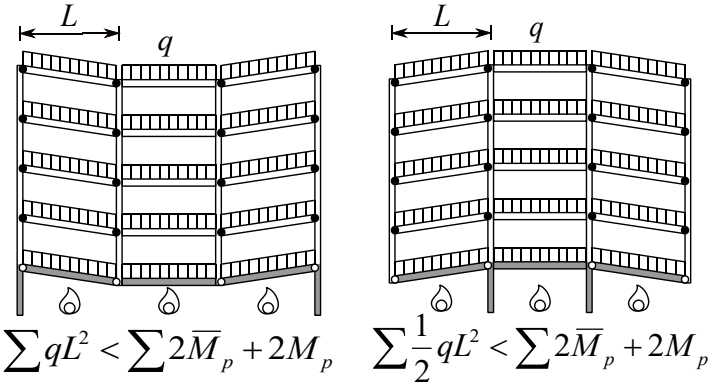


Fig. 14 – Comparison of robustness



(a) Loss of inner columns (b) Loss of outer columns

Fig. 15 – Difference due to unprotected column location

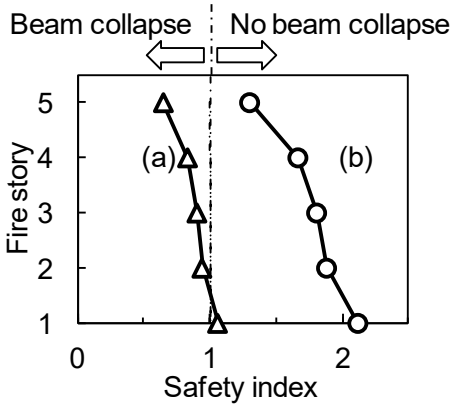


Fig. 16 – Comparison of robustness

POSSIBLE FRAME COLLAPSE MECHANISMS FOR SEMI-RIGID FRAMES

In the case of seismic resistant buildings, some columns can be unprotected because of the relatively large ultimate capacity of the building frame. This large capacity can be attributed mainly to the rigid connections between the columns and beams as shown in Figure 17 (a). On the other hand, in the case of non-seismic resistant buildings, the load-bearing capacity

becomes smaller because of the smaller strength of semi-rigid connections. In particular, the strength of the beam collapse mode decreases to a large degree in the case of semi-rigid connections. Therefore, buildings with semi-rigid connections do not expect much from the frame robustness.

One possibility for increasing the frame robustness even in the case of semi-rigid frames might be to consider the flexural resistance of floor slabs as shown in Figure 18. As the figure shows, the floor slabs might play an important role in stress redistribution in a building in a fire. Figure 19 shows the possible simplified collapse mechanisms in the case of semi-rigid frames when one exterior column in the fire zone lost its strength. Figure 19 (a) is the case where the floor slab contribution is not considered whereas Figure 19 (b) is the case where the floor flexural resistance is directly considered.

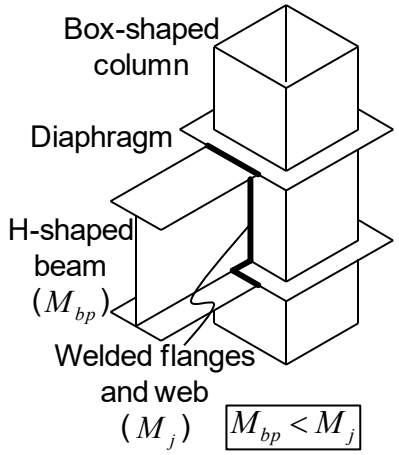
For the mechanism shown in Figure 19 (a), external works, W_{ex}, and internal works, W_{in}, are given by the following equations:

$$W_{ex} = \sum \frac{1}{3} w A_f \theta_x l_x \tag{3}$$

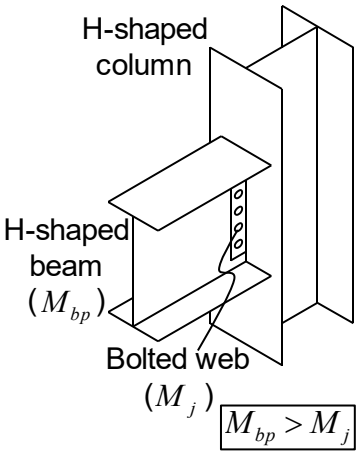
$$W_{in} = \sum \left(2M_{jx}\theta_x + 2M_{jy}\theta_x \frac{l_x}{l_y} \right) \tag{4}$$

where

w : distributed load applied over the floor
A_f : floor area
θ_x : virtual rotation angle of the beam in the x-direction
l_x : beam length in the x-direction
l_y : beam length in the y-direction
M_{jx} : resisting moment strength of beam-column connection in the x-direction
M_{jy} : resisting moment strength of beam-column connection in the y-direction



(a) For seismic design



(b) For non-seismic design

Fig. 17 – Typical beam-to-column connection details

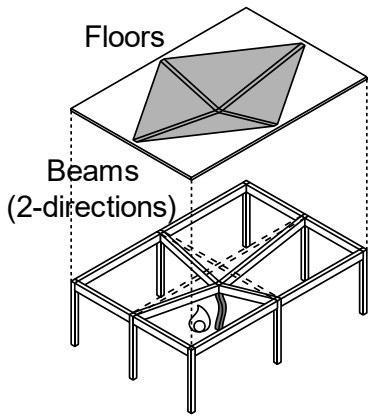
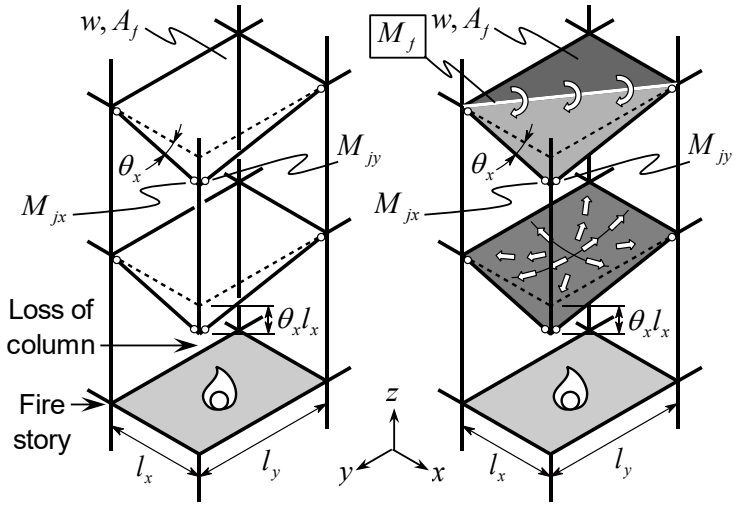


Fig. 18 – Proposed mechanism for non-seismic design

In Eqn. (3), the external work can be summed up in all the upper stories above the fire zone. The internal work in Eqn. (4) is calculated by adding all the works conducted at plastic hinges formed in the upper stories above the fire zone. When $W_{ex} < W_{in}$ is satisfied, the mechanism shown in Figure 19 becomes stable and the exterior column is unprotected against fire. The mechanism in Figure 19 (a) is theoretically possible, but as described previously, the strength of

M_{jx} and M_{jy} is generally quite small. Therefore, in reality the without-floor mechanism may not be stable and effective for frame robustness design.



(a) Without floor (b) With floor

Fig. 19 – Simple design models for frames with semi-rigid connections

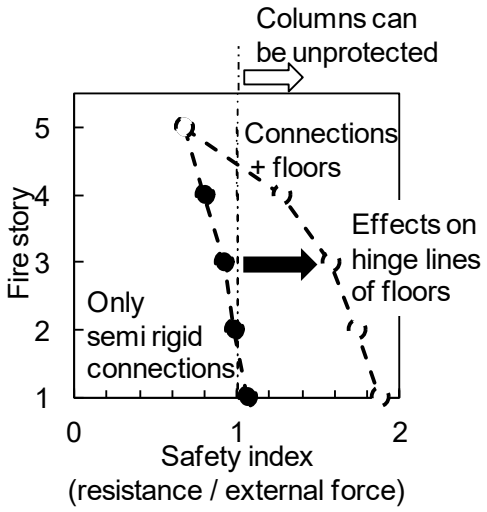


Fig. 20 – Difference in safety index due to floor resistance consideration

For the mechanism having the floor contribution shown in Figure 19 (b), plastic yield lines might be formed in the upper floors at ambient temperature. Note that the yield line resistance may not be considered in the floor directly exposed to a fire (the floor just above the fire zone). Instead, the floor may have a different mode of collapse, that is, the membrane collapse that was described in floor robustness. For the mechanism shown in Fig. 19 (b), Eqn. (4) can be modified to the following, by adding a term related to internal works by floor bending:

$$W_{in} = \sum\left(2M_{jx}\theta_x + 2M_{jy}\theta_x\frac{l_x}{l_y}\right) + \sum\left(M_f\frac{l_x^2+l_y^2}{l_y}\theta_x\right) \quad (5)$$

where

M_f : plastic bending strength of the floor per unit width

TRIAL DESIGN CONSIDERING PROPOSED FRAME ROBUSTNESS

A trial evaluation based on frame robustness design was conducted for a semi-rigid building frame. The building considered was similar to the five-story building shown in Figure 14, except that the beam-column connections were semi-rigid. Note that the floor slabs on each story are assumed to be made of composite floor slabs, consisting of steel decks with a depth of 50 mm and of lightly reinforced concrete with a thickness of 90 mm above the top of the decks. The following assumptions were made in this trial design:

- The plastic strength of the connections is given by 0.2 times the beam plastic moment.
- The plastic bending strength of the floor is given for negative bending around the weak axis.

For the first assumption, the ratio of the resistant moment of the connections to the full plastic moment of the beams generally varies depending on the type of connections, but conservatively the value of 0.2 was assumed. For the second assumption, the anisotropy of the floor due to composite slabs or the presence of floor joists could have an effect on the bending strength of the floor but it was disregarded by using the weak axis properties.

Figure 20 shows the results of the trial evaluation for the semi-rigid frames shown in Figure 19. The vertical axis is the story number subjected to fire and the horizontal axis means the ratio of W_{in} to W_{ex} (safety index). As for the no floor case shown in Figure 19 (a), the safety indices were smaller than 1.0 for most of the stories, which means that the omission of the fire protection for the corner columns would be quite limited. On the other hand, as for the floor case (Figure 19 (b)), the safety indices became larger than 1.0 for all the stories except the fifth one, meaning that the majority of the corner columns would be unprotected. Regarding the fifth story shown in Figure 20, there was no strength increase due to the floor because the floor above the story was directly exposed to the fire and the flexural resistance might be very small.

Figures 21 and 22 show the effects of the column locations on the safety index. There were three types of column locations considered as shown in Figure 21. Case (c) was for a corner and the results have already been shown in Figure 20. Case (b) was for a side column and Case (a) was an inner column. Figure 22 shows all the results together and the side column from the first to the third floor would be unprotected. In addition, the interior column from the first to the second floor would be unprotected. The reason that the inner column had lower safety indices was because the tributary area (shaded area in Figure 21) for the floor load was larger. This resulting larger load lowered the safety of the column compared to the other column cases. As seen in the above, the safety index is affected not only by the location but also by the applied load of the column.

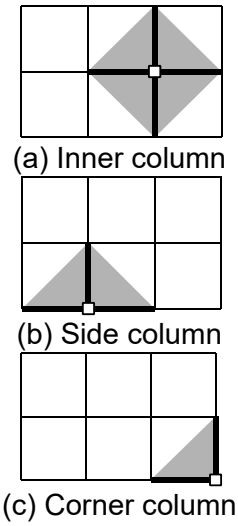


Fig. 21 – Considered locations of unprotected column

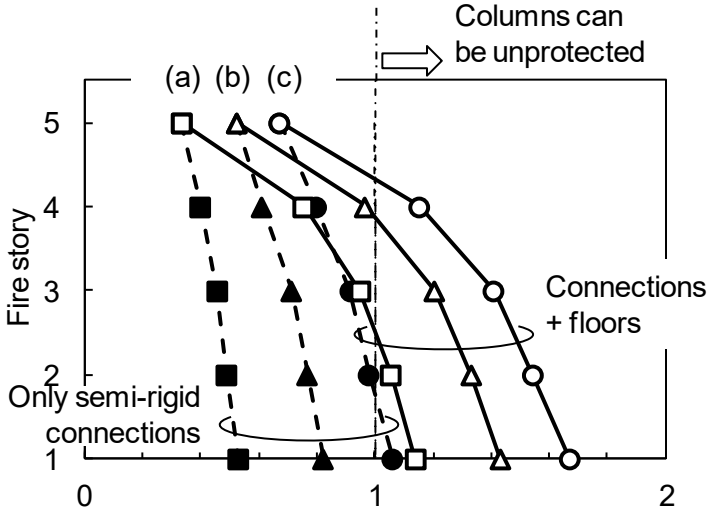


Fig. 22 – Effects of location of unprotected column

Figure 23 shows a possible unprotected column combination obtained by conducting the safety check of the column one by one in the entire building frame, where the floor slab resistance was considered. As Figure 23 shows, approximately 30% of the columns would be unprotected against fire, resulting in more economical design than the design considering only floor robustness. Note in this trial design that the omission of the fire protection would obviously be increased if the flexural resistance of the floor slabs is increased. Overall, frame robustness design considering floor flexural resistance could increase the number of unprotected columns even for buildings with semi-rigid connections. It should be noted, however, that floor resistance in the frame robustness design needs to be verified by experiments and/or numerical analyses. This hypothetical design methodology thus requires further study in the future.

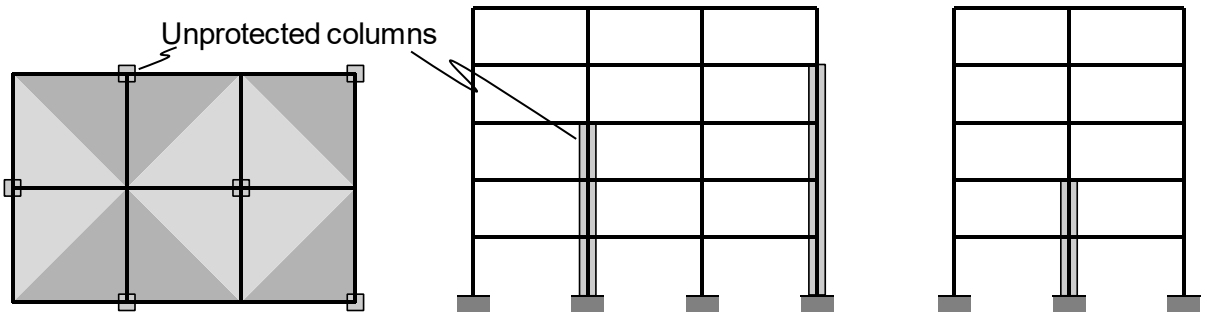


Fig. 23 – Possible unprotected column combination based on frame robustness design

CONCLUSIONS

This paper reviewed and summarized the past and ongoing research activities on structural robustness design under fire from both floor and frame resistance perspectives. By focusing on the latter frame case, one possible frame collapse mechanism that can provide structural resistance even of semi-rigid frames was proposed. In the proposed mechanism, the resistance against the gravity load might be provided largely by the flexural resistance of floor slabs above the localized fire zone. Applying a simple limit analysis technique, the robustness resistance of a multi-storied frame with semi-rigid connections was calculated and demonstrated, which realized that approximately 30% of the columns might also be unprotected in addition to floor joists due to the membrane action already proposed in the past. The resisting mechanism proposed in this study for building frames is not fully verified at present by experiments and/or numerical analyses; therefore, further studies are obviously required in the future.

REFERENCES

Architectural Institute of Japan (AIJ) (1999). *Recommendation fire resistant design of steel structures* (in Japanese).Bailey, C.G. & Moore, D.B. (2000). The structural behavior of steel frames with composite floor slabs subject to fire, Part1: Theory & Part2: Design. *The Structural Engineer*, 78(11), 19-33.

Building Center of Japan (BCJ) (1989). *General fire prevention designing method for buildings* (in Japanese).

Building Research Institute (BRI) (2008). *Manual for design and fabrication of cold-formed square steel tube* (in Japanese).

Japanese Society of Steel Construction (JSSC) (2005). *Guidelines for collapse control Design – Construction of steel buildings with high redundancy-, Part1: Design & Part2: Research.*

Nadjai, A., Bailey, C.G., Han, S.H., Vassart, O., Zhao, B., Hawes, M., Franssen, J.M. & Simms, I. (2011). Full scale fire test on a composite floor slab incorporating long span cellular steel beams. *The Structural Engineer*, 89(21), 18-25.

Sakumoto, Y., Yamaguchi, T., Ohashi, M. & Saito, H. (1992). High-temperature properties of fire-resistant steel for buildings. *Journal of Structural Engineering*, 118(2), 392-407.

Sakumoto, Y., Yamaguchi, T., Okada, T., Yoshida, M. & Saito, H. (1994). Fire resistance of fire-resistant steel columns. *Journal of Structural Engineering*, 120(4), 1103-1121.

Steel Construction Institute (SCI). (2006). *Fire safe design: A new approach to multi-storey steel framed buildings* (P288).

Vassart, O. & Zhao, B. (2012). *Membrane action of composite slab in case of fire: Background document & Design guide* (Edition 2012-1).

Wang, Y.C. (1996). Tensile membrane action in slabs and its application to the Cardington fire tests. *Proceeding of the second Cardington conference*. (pp. 55-67). England.

PROGRESSIVE COLLAPSE ANALYSIS OF COMPOSITE STEEL FRAMES UNDER ELEVATED TEMPERATURE

Hussam Mahmoud, Ph.D.
Department of Civil and Environmental Engineering, Colorado State University,
Fort Collins, USA
Hussam.Mahmoud@colostate.edu

Chao Qin
Department of Civil and Environmental Engineering, Colorado State University,
Fort Collins, USA
Chao.Qin@colostate.edu

ABSTRACT

Collapse analyses of buildings under fire are relatively lacking. Recent events, particularly the 9/11 terrorists attack, have spiked interest in assessing the full collapse behavior of buildings under fire. In this study, a 3D numerical model of a composite steel frame is developed, and its performance evaluated under fire up to and including collapse. The frame is a hybrid 6-story building with moment, gravity, and concentrically braced frames. The building is subjected to the ASTM E119 standard fire curve for two different scenarios – first-floor corner compartment fire and whole first-floor fire. The results show that the full structural response including the collapse mechanism during fire events can be predicted with reasonable accuracy using advanced numerical finite element analysis. The results also show collapse initiation to be triggered following the failure of few columns, as opposed to one column, highlighting the importance of the analysis for performance-based engineering.

INTRODUCTION

Since the Broadgate Phase 8 fire in London and the subsequent Cardington fire tests in the 1990s, researchers have begun to experimentally investigate and understand the behavior of steel-framed building structures in fire (British Steel 1999, Newman et al. 2000). Interest

in full system analysis of structures under fire was re-energized in 2001 following the collapse of the Twin Towers and World Trade Center 7 (WTC-7) due to terrorist attacks. These high impact events and early tests have prompted extensive finite element (FE) modelling to investigate the full behavior of steel framed buildings under fire loading. Due to the extensive computational demand, resulting from the high level of material inelasticity and geometrical nonlinearity, 2D FE modeling was viewed as an attractive alternative than 3D models. However, 2D models are limited in that they dismiss key behavioral features including participation of all system components in the load carrying mechanisms, particularly at large deformations. Various studies have been conducted to evaluate the local behavior and global performance of steel framed structures under fire (Memari and Mahmoud 2014, Liew and Ma 2004, Gu and Kodur 2011, Wang and Moore 1995, Huang et al. 2000). Agarwal and Varma (2013) conducted a qualitative assessment of the importance of gravity columns on the stability of a typical steel building subjected to corner compartment fire. The study, however, included only early stage of failure without simulating progressive collapse. Jiang, et al. (2014) studied the collapse mechanisms of 2D steel braced frames exposed to single and multi-compartment fires, while capturing large deformations. Similar to previous studies, the analysis provided valuable insight on the behavior but did not include progressive collapse of the system.

In the above-mentioned analysis, collapse or global instability of the structure was not evaluated through explicitly modeling progressive collapse of the frames, instead assessment of stability was generally evaluated through either monitoring of simulation convergence or by assessing the limits of column interaction equations. The lack of convergence while to some extent could be related to system instability due to P-Δ effects, this is not always the case as highlighted in Mahmoud et al. (2015). Therefore, modeling progressive collapse explicitly can eliminate the speculations as to the reasons for the lack of convergence in numerical FE models.

Currently there are two studies in the literature by Sun et al. (2012) and Gann (2008) where collapse analysis of 2D and 3D frames, respectively, under fire was conducted. In a study by

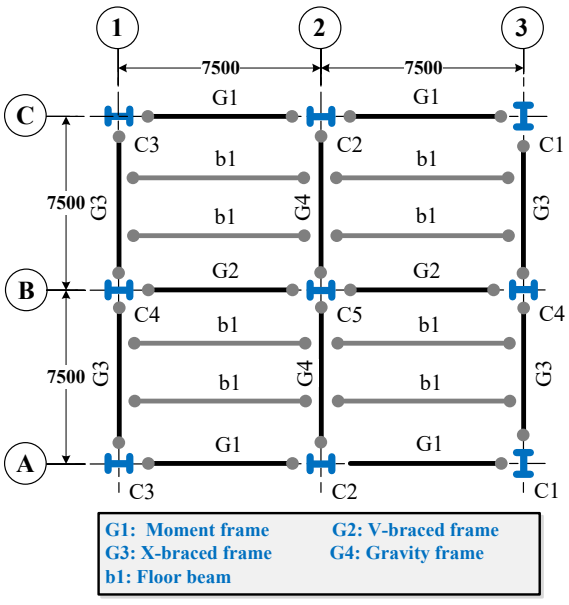
Sun et al. (2012), a robust static–dynamic procedure to capture collapse mechanisms of braced 2D steel-framed structures under was proposed. The study, while it provided notable advances, did not include failure of connections or fracture of elements. The study by Gann (2008) pertained to the National Institute of Standards and Technology (NIST) investigation of the collapse of WTC-7 and included assessment of the full 3D progressive failure of the building. This was realized through incorporating material inelasticity, geometric nonlinearity, contact between the collapsing structural elements, and element erosion based on defined failure criterion.

Clearly, previous studies provided substantial knowledge pertaining to the large inelastic response of steel frames under fire. However, apart from the WTC-7 analysis (Gann 2008), the studies stopped short of modeling the entire system progressive collapse, which requires simulating element separation and fracture as well as contact between the fractured elements and collapsed floors. To that end, this study aims to build upon existing knowledge to evaluate the progressive collapse mechanisms of a 3D six-story steel building. In the simulations, complete connection failures and interaction between all elements are modeled in order to capture the progressive failure of the system.

STRUCTURAL CONFIGURATION

The structure is 2-bay (15 m) by 2-bay (15 m) square (7.5m each bay) six-story building with a height of 22.38 m and is shown in Figure 1 (Foutch et al. 1986). The first story is 4.5 m in height while the remaining stories are 3.4 m each. The girder-to-column connections in the frame axis A, B, and C are fully welded moment connections. In addition, the frame at axis B is a Concentrically Braced Frame (inverted V). The pin connection between the girders and the columns and beams and girders at frame line 1, 2, and 3 are shear tab connections. The exterior frames 1 and 3 contains X-braces in each span. The columns, girders, and beams are wide-flange sections, sized as shown in Figure 1, and made with A36 steel material. The brace members are rectangular HSS made with A500 Grade B steel. Shear studs are utilized to achieve composite action between the slabs and the beams and girders. The slab is made of lightweight concrete with nominal thickness of 90 mm and 165 mm. The concrete

reinforcement bars are 6 mm in diameter on a 100 mm grid with a nominal minimum cover of 29 mm.



Column sections

Story #	C1	C2	C3	C4	C5
6-5	W10x49	W10x33	W10x33	W10x33	W12x40
4-3	W12x65	W12x53	W10x39	W10x60	W12x72
2	W12x79	W12x65	W12x50	W12x79	W12x106
1	W12x87	W12x87	W12x65	W12x106	W12x136

Frames beam sections

Floor #	G1	G2	G3	G4
6	W16x31	W16x31	W18x35	W21x50
5	W16x31	W18x35	W18x35	W21x50
4	W18x35	W18x35	W18x35	W21x50
3	W18x35	W18x40	W18x35	W21x50
2	W18x40	W18x40	W18x35	W21x50

Floor beam and bracing sections

Story #	b1	B1	B2
5-6	W16x31	ST-4x4x3/16	ST-4x4x3/16
4	W16x31	ST-5x5x1/4	ST-4x4x3/16
2-3	W16x31	ST-6x6x1/4	ST-4x4x3/16
1	W16x31	ST-6x6x1/4	ST-4x4x3/16

Fig. 1 - Plan view and member designation of the modeled building

FINITE ELEMENT MODELING APPROACH

All models used in this study were developed and analyzed using the general-purpose FE program ABAQUS (Simulia 2014). Line elements were utilized for the beams and columns and shell elements for the slabs. The density of ASTM A36 steel was assumed to be 7800 kg/m^3. The tensile strength of the A36 steel was set to 250MPa and the Poisson's ratio to 0.26. The brace members were cold formed rectangular HSS tubes of ASTM A500 B steel with a specified yield stress of 315 MPa. The density of ASTM A500 B steel is around 7850 kg/m^3. The stress-strain properties of the steel were modeled as elastic perfectly plastic. The Johnson-Cook constitutive damage model (1985) was selected for inclusion of damage initiation in the material model. The temperature-dependent mechanical and thermal properties were adopted from European code as shown in Figure 2 (Eurocode 2005). In this study, the Young's modulus of the concrete was set to 15 GPa and the density to 2400 kg/m^3. The conductivity of concrete was 0.5 W/mK. A yield stress of the 6 mm steel reinforcing bars of 398 N/mm^2 was used. Because concrete is a good thermal insulation material, the temperature-dependent mechanical properties of concrete and reinforcing steel were

neglected in the study. For modeling the concrete slabs, the concrete damage plasticity (CDP) constitutive model was implemented in Jankowiak and Lodygowski (2005).

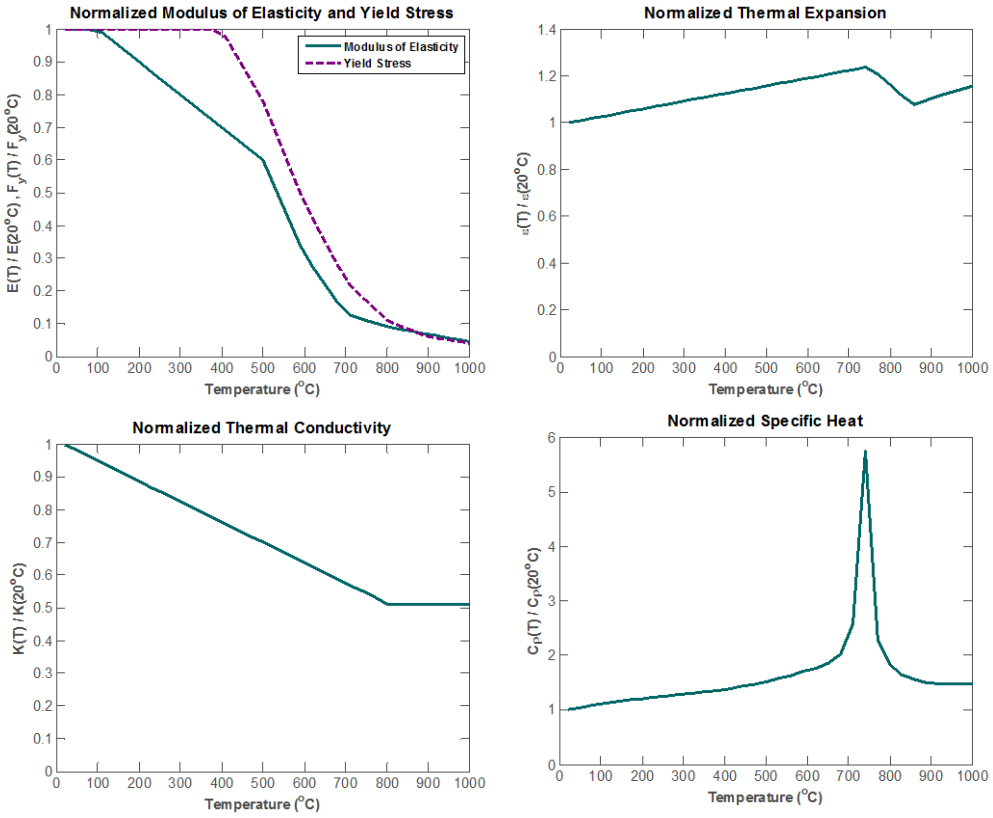


Fig. 2 - Temperature-dependent mechanical and thermal properties of steel

For moment connections, a spring is used with rotational stiffness, k_θ, determined from the stiffness matrix of a fixed-fixed beam as $k_\theta = \frac{4E_T I}{L}$ where E_T is Young's Modulus as a function of temperature. The plastic moment, M_p, as a function of temperature (T) is $M_p(T) = F_y(T) * Z_x$, which is used is used to represent the plasticity of the fully weld connection; where $F_y(T)$ is the yield stress as a function of temperature and Z_x is the plastic section modulus. Failure of the connection is specified when a rotation value of 0.06 radians. It is important to note that while the rotation at peak capacity is constant, the peak strength is not and is function of $F_y(T)$ as noted above.

A component-based model for shear tab connection subjected to fire was developed by Sarraj (2007). In this model, the whole connection is treated as a group of springs representing each bolt row in addition to bearing springs representing the two connected

plates. The initial stiffness of a shear connection is denoted as, K_i, which is composed of three parts as noted in Rex and Easterling (2003) and modified in this study to include temperature effect:

$$K_i = \frac{1}{\frac{1}{K_{br}}+\frac{1}{K_b}+\frac{1}{K_v}} \quad (1)$$

where,

K_{br} is the bearing stiffness, K_b is the bending stiffness and K_v is the shear stiffness and can be found using the following equations.

$$K_{br} = \Omega(T) t_p f_y (d_b/25.4)^{0.8} \quad (2)$$

$$K_b = 32E(T) t_p (L_e/d_b - 0.5)^3 \quad (3)$$

$$K_v = 6.67G(T) t_p (L_e/d_b - 0.5) \quad (4)$$

where,

$\Omega(T)$ is a parameter obtained by curve-fitting parameter as a function of temperature; t_p and f_y are plate thickness and yield strength, respectively; d_b is the bolt diameter, $E(T)$ is the elastic modulus of the plate, L_e is the plate edge distance, and $G(T)$ is the shear modulus of elasticity.

The bolt shear stiffness can be represented using the proposed temperature dependent expression.

$$K_{bv} = \frac{0.15G(T)A_s}{d_b} \quad (5)$$

where,

G_T is the temperature dependent shear modulus; A_s is the cross-section area of the bolt; and d_b is bolt diameter.

FIRE SCENARIOS, LOADING AND RESULTS

Total dead loads of 4.3 kN/m^2, 3.6 kN/m^2, and 1.4 kN/m^2 were used for the floor, roof, and exterior wall areas, respectively. The live loads for the floor and roof areas were 2.8 kN/m^2

for the slabs and the beams and 1.8 kN/m^2 for the girders. The load combination for the fire analysis is set to $D + 0.5L$, where *D* is dead load, *L* is live load, which is based on the work by Ellingwood and Corotis (1991). Two fire scenarios were utilized in the study and included a contained corner compartment fire on the first floor and a whole first floor fire. Figure 3(a) shows a rendered view of the corner fire case while Figure 3(b) shows a rendered case of the whole floor fire. The standard ASTM E-119 time-temperature curve, shown in Figure 3(c) was utilized in this study.

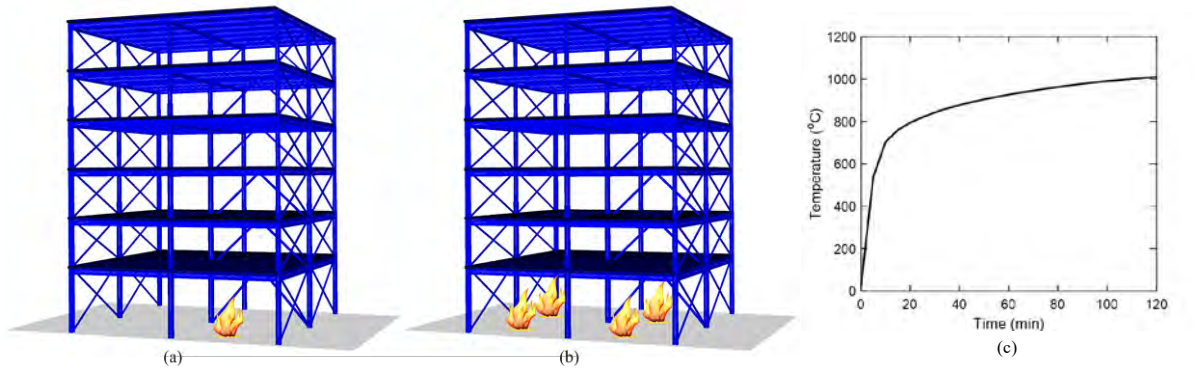
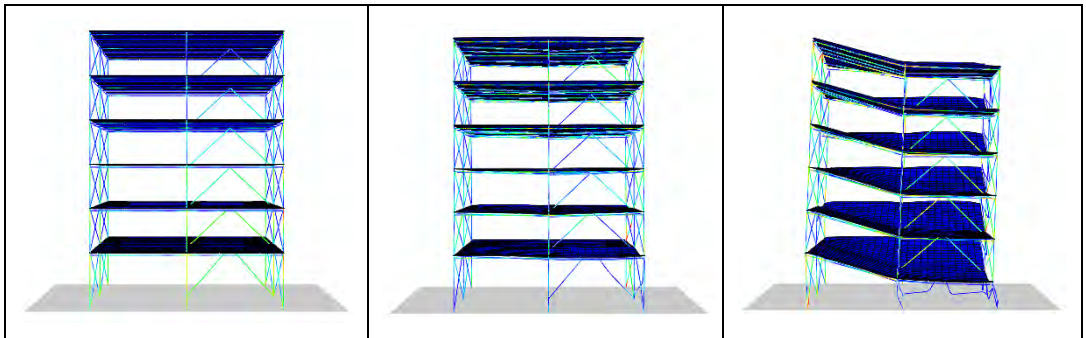


Fig. 3 – (a) fire Case 1, (b) fire Case 1, and (c) ASTM E119 Standard fire curve

For Case 1 (single corner compartment fire in Figure 4), when the step time was at 20 min, the temperature reached 773.5°C on the time-temperature curve, and the global response of the entire structure at this stage was marked by substantial deformation of the concrete slab. At this point, the entire corner bay collapsed and started to drag other floors with it, causing notable twist in the entire structure combined with lateral deformation. At 40 min (860.6°C), the building lost its ability to sustain any loading as marked by the additional lateral and vertical downward deformation of the entire structure. The substantial unbalanced forces resulted in several fractures of braces in the first two floors.



Step Time=0 sec	Step Time=10 min	Step Time=20 min

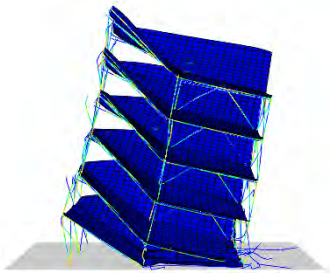
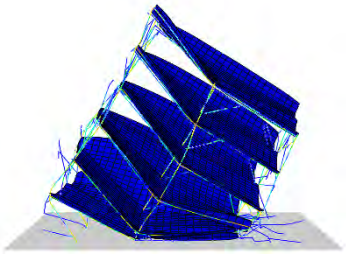
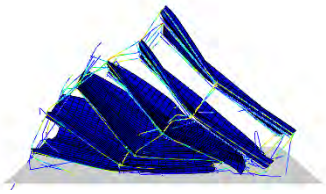
Temperature=20℃	Temperature=704℃	Temperature=773.5℃
		
Step Time=30 min Temperature=843℃	Step Time=40 min Temperature=860.6℃	Step Time=50 min Temperature=909.4 ℃

Fig. 4 - Collapse Sequence for Case 1

For Case 2, (whole floor fire in Figure 5), when the step time was at 20 min, the temperature reached 773.5°C on the time-temperature curve, and the global response of the entire structure at this stage was marked by substantial deformation in the columns of the first floor. At this point, progressive collapse of the entire frame was initiated and progressed as shown in Figure 5.

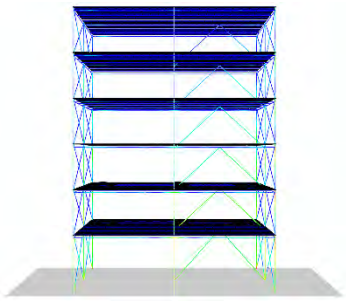
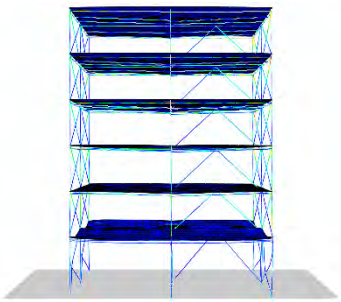
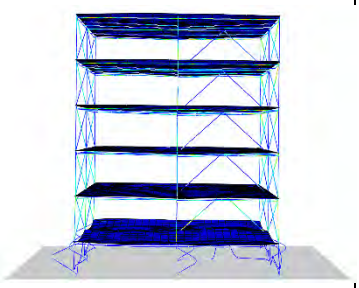
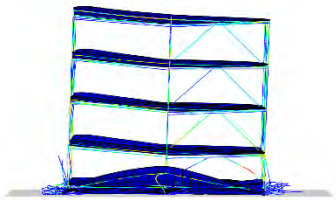
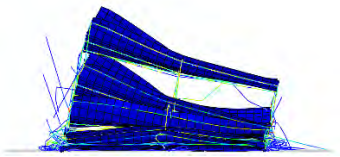
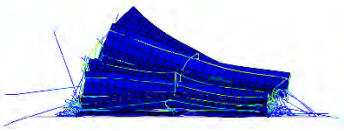
		
Step Time=0 sec Temperature=20℃	Step Time=10 min Temperature=704℃	Step Time=20 min Temperature=773.5℃
		
Step Time=30 min Temperature=843℃	Step Time=40 min Temperature=860.63℃	Step Time=50 min Temperature=909.37℃

Fig. 5 - Collapse Sequence for Case 2

In addition to the global collapse sequences, the displacement of each column at the element nodes at the first-floor height were extracted from the results as shown in Figure 6(a) and (b)

For Case 1, at 700°C, the columns of the heated compartment started to move downward with their maximum displacement being reached at around 820°C to 840°C. The columns which were not directly subjected to fire started to displace downwards at 842°C. The whole first floor reached its displacement limit when it was in contact with the ground at 927°C. This is depicted in Figure 6(a). For Case 2, a small upward displacement was observed initially due to thermal elongation of the steel. When the temperature reached 700°C, the structural steel lost more than half of its strength and the entire floor started to displace vertically downward as shown in Figure 6(b) through equal displacement of all columns. Full contact with the ground is reached at 823°C.

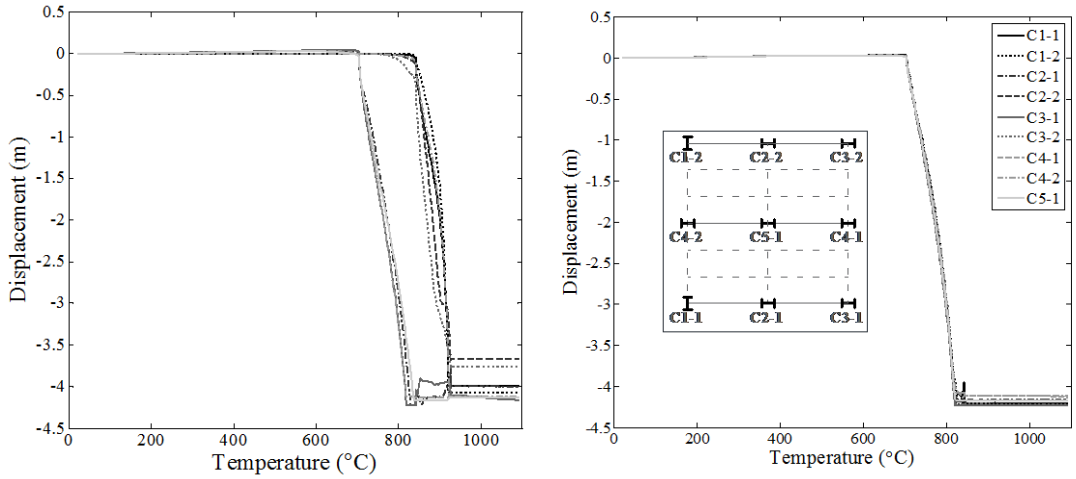


Fig. 6 - Vertical Displacements of First Floor Columns (a) Case 1 and (b) Case 2

Assessment of the column interaction equations is shown in Figure 7(a) and (b) for Case 1 and Case 2, respectively. As shown in both figures, various columns violate the interaction equation at as low of a temperature as 200ºC. Specifically, for Case 1 one column exceeded the interaction equation at about 200ºC and a total of three columns at about 400ºC. For Case 2, one column exceeded the interaction equation at about 200ºC and a total of six columns at about 400ºC. This is well below the temperature of approximately 700ºC at which global collapse was triggered for both frames. This indicates that the ASIC Specifications pertaining to individual column buckling could be overly conservative in determining the limit state for an entire system performance.

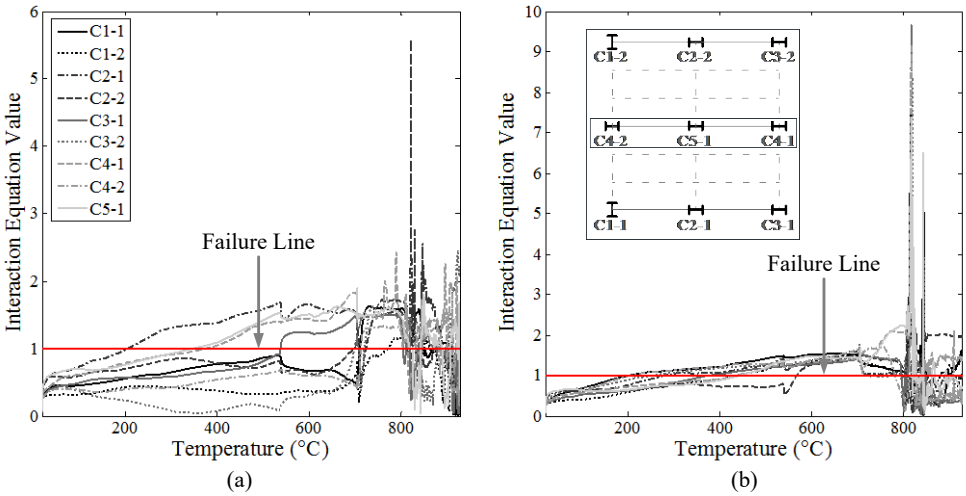


Fig. 7 - Vertical Displacements of First Floor Columns (a) Case 1 and (b) Case 2

SUMMARY AND CONCLUSION

In this study, detailed FE models of 3D six-story steel building structures were created and utilized for collapse simulations. This was realized through employing detailed FE simulations to assess the behavior of individual members such as girders, beams, columns and braces as well as the whole system response that is controlled by the interaction between the various elements and components. The 6-story building system was subjected to the ASTM E-119 Standard fire curve. Two different scenarios were evaluated including a first-floor corner compartment and whole first floor.

The main findings and general conclusions obtained from this study are summarized in the following key points.

- In first floor corner compartment fire cases, the building models was shown to twist, lean towards the compartment in which the fire is applied, and laterally sway.
- In the full first floor fire cases, failure of the building progressed straight downwards, and no visible twist was observed during collapse.
- The interaction equation values for all columns was exceeded and in some cases at low temperature.

REFERENCES

Agarwal, A, and Varma, A. (2013). Fire Induced Progressive Collapse of Steel Building Structures: The Role of Interior Gravity Columns. *Engineering Structures*, 58, 129-140.

British Steel. (1999). The Behavior of Multi-Story Steel Framed Buildings in Fire. A report by the European Joint Research Program. Retrieved from http://www.mace.manchester.ac.uk/project/research/structures/strucfire/DataBase/References/MultistoreySteelFramedBuildings.pdf

Ellingwood, B. and Corotis, R. (1991). Load Combinations for Buildings Exposed to Fires. *Engineering Journal*, 28 (1): 37–44.

En, Cen. (2005). Eurocode 3: Design of Steel Structures, Part 1.2: General Rules—Structural Fire Design. London: British Standards Institution. Vol. 2.

Foutch, D., Roeder, C., and Goel, S. (1986). Preliminary Report on Seismic Testing of A. Full-Scale Six-Story Steel Building.

Gann, R. (2008). NIST NCSTAR 1A: Final Report on the Collapse of World Trade Center Building 7, Federal Building and Fire Safety Investigation of the World Trade Center Disaster. (2008). National Institute of Standards and Technology, Gaithersburg, MD.

Gu, L. and Kodur, V. (2011). Role of Insulation Effectiveness on Fire Resistance of Steel Structures under Extreme Loading Events. *Journal of Performance of Constructed Facilities*, 25(4): 277–86.

Huang Z, Burgess I, and Plank, R. (2000). Three-Dimensional Analysis of Composite Steel Framed Buildings in Fire. *Journal of Structural Engineering*, 126(3):389–97.

Jiang, J., Guo-Qiang L., and Usmani, A. (2014). Progressive Collapse Mechanisms of Steel Frames Exposed to Fire. *Advances in Structural Engineering,* 17(3): 381-398.

Jankowiak, T and Lodygowski, T (2005). Identification of Parameters of Concrete Damage Plasticity Constitutive Model. *Foundations of Civil and Environmental Engineering,* 6(1): 53-69

Johnson, G. and Cook, W. 1985. Fracture Characteristics of Three Metals Subjected to Various Strains, Strain Rates, Temperatures and Pressures. *Engineering Fracture Mechanics* 21(1): 31–48.

Memari, M. and Mahmoud, H, 2014. Performance of Steel Moment Resisting Frames with RBS Connections under Fire Loading. *Engineering Structures*, 75, 126–138.

Mahmoud, H., Ellingwood, M. and Memari, M. (2015). Challenges and Alternative Approaches for Simulating the Response of Steel Structures Exposed to Fire", Second International Conference on Performance-based and Life-cycle Structural Engineering (PLSE), Brisbane, Australia, 9-11 December.

Newman, G., Robinson, J., and Bailey, C. (2000). Fire Safe Design: A new Approach to Multi-Story Steel-Framed Buildings. *Steel Construction Institute*.

Rex, C. and Easterling, S. (2003). "Behavior and Modeling of a Bolt Bearing on a Single Plate." *Journal of Structural Engineering*, 129(6): 729 - 800.

Richard Liew, J. and Ma, K. (2004). Advanced Analysis of 3D Steel Framework Exposed to Compartment Fire. *Fire and Materials*, 28:253–267.

Sarraj, M. (2007). The Behaviour of Steel Fin Plate Connections in Fire. PhD thesis, University of Sheffield.

Simulia *v6.14*, (2014). Dassault Systems, Providence, RI. (www.simulia.com).

Sun, R., Huang, Z., and Burgess, I. (2012). The Collapse Behaviour of Braced Steel Frames Exposed to Fire. *Journal of Constructional Steel Research*, 72: 130–42.

Wang Y. and Moore, D. (1995). Steel Frames in Fire: Analysis. Engineering Structures, 17(6): 462–72.

PROGRESSIVE COLLAPSE:
THE CASE OF COMPOSITE STEEL-CONCRETE FRAMES

Riccardo Zandonini[1] riccardo.zandonini@unitn.it, Nadia Baldassino[1] nadia.baldassino@unitn.it,
Fabio Freddi[2] f.freddi@ucl.ac.uk, Giacomo Roverso[1] giacomo.roverso@unitn.it

[1]Department of Civil, Environmental and Mechanical Engineering, University of Trento
Trento, Italy

[2]Department of Civil, Environmental and Geomatic Engineering, University College of London
London, UK

ABSTRACT

Residual strength and alternate load paths are two fundamental design strategies to ensure adequate resistance against progressive collapse of structures. This paper presents an experimental study carried out on two full-scale steel and concrete composite frames to investigate their structural behaviour in case of a column collapse. The study focusses on the redundancy of the structure as provided by the beam-slab floor system as well as by the ductile beam-to-column joints. The specimens were ground floor sub-frames 'extracted' from two reference buildings designed in accordance to the Eurocodes. The frames have the same overall dimensions, but a different, symmetric and asymmetric, configuration of the column layout. In both tests, the collapse of an internal column was simulated. The paper presents the main features of the frames and the principal outcomes of the test on the symmetric frame.

INTRODUCTION

In the last decades, important and numerous studies have been conducted about the collapse of structures caused by accidental loss of columns. The interest in studying the effects of extreme loading conditions has being triggered by a few catastrophic events occurred in recent years since the Ronan Point Building case (UK, 1968). These tragic events lead many countries to include, in their design codes [1-6], integrity and structural robustness requirements in order to design a *robust* structure. As to design principles, the Eurocode 0 [7] prescribes that "a structure shall be designed and executed in such a way that it will not be damaged by events such as explosion, impact and the consequences of human errors, to an extent disproportionate to the original cause". As to design practice, the Eurocode 1-7 [4] provides several strategies to design structures against accidental events. In particular, strategies for identified accidental actions and strategies for limiting the extent of localised failure are specified.

Column loss in a building is one of the most common and effective damage scenario recommended for progressive collapse investigations. The collapse of vertical members causes dynamic effects, large deformations of the floor system and high rotation in the beam-to-column connections. The collapse of an extensive part of the structure can be avoided if the damaged part is able to redistribute loads to the undamaged parts so that a new stable equilibrium configuration is achieved. In the context of alternate load paths, the ductility offered by the joints and the 3D performance capabilities of the floor system represent essential factors for a robust structural response. In order to improve the knowledge about progressive collapse and to study the effects that a column loss causes to a structure, 3D full-scale experimental tests are the most comprehensive approach. On the other hand, these experiments are very complex and expensive, and, to date, very few experimental data are available.

Recently, the 'RobustImpact' research project [8] studied the robustness of composite steel-concrete frames affected by accidental actions. This European research project, aimed at developing a new robust design approach against impact loading, is based on the residual strength and the alternate load path method. Analytical, numerical and experimental activities were planned and accomplished (Figure 1) to get insight into different issues of robustness.

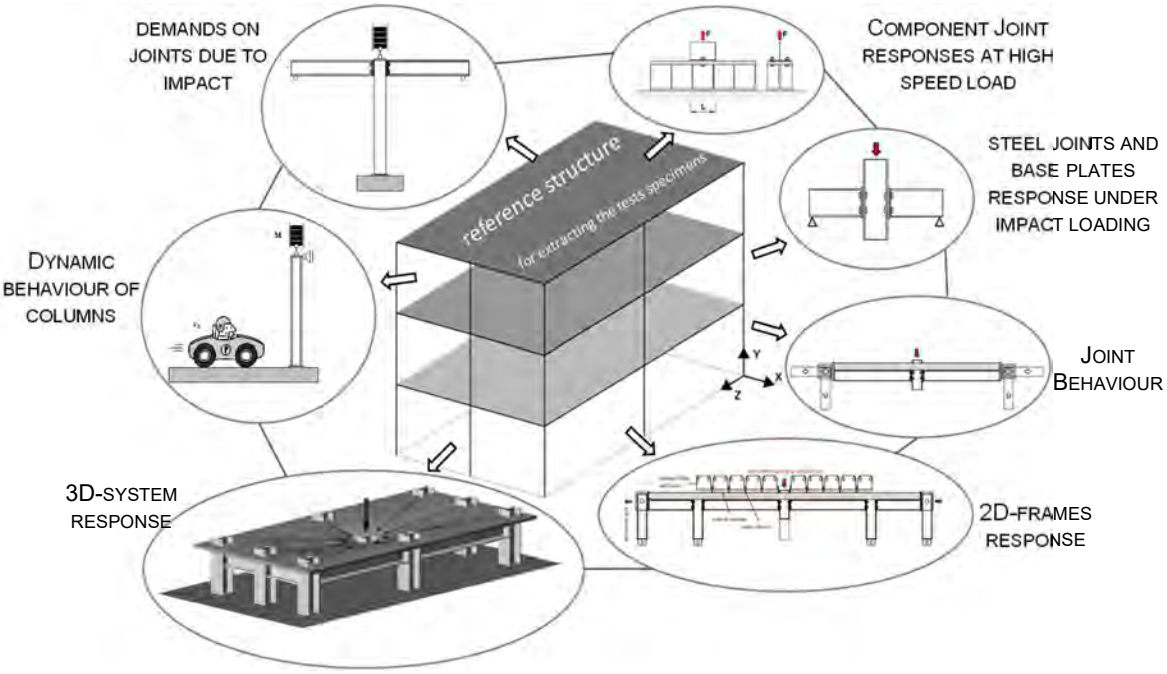


Fig. 1 – Issues investigated in the Robustimpact project (after [8])

Within this project, the University of Trento activity focused on the contribution provided by the concrete slab and by the beam-to-column joints. For a better insight into the mechanisms of force redistribution in the structures, two experimental tests were conducted on 3D full-scale steel and concrete composite structures 'affected' by the loss of an internal column. The specimens had the same geometric and structural properties, but two different column layouts. This paper presents the main features of the experimental study, with particular reference to the main outcomes of the first 'symmetric' test.

THE REFERENCE STRUCTURES

Two 'typical' five-storey steel and concrete office buildings were selected as reference structures. In particular, two different columns layouts were investigated: the first configuration is symmetric with respect to both the plan X and Y axes (Figures 2-3), while the second one is symmetric only with respect to the Y axis. The structures were named as "*Symmetric*" and "*Asymmetric*", respectively.

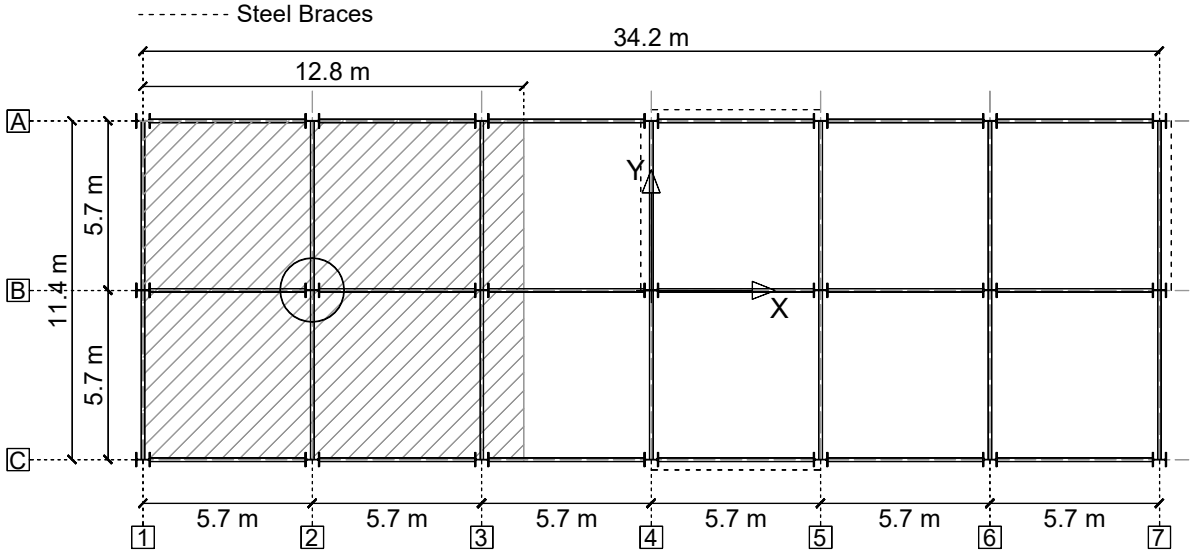
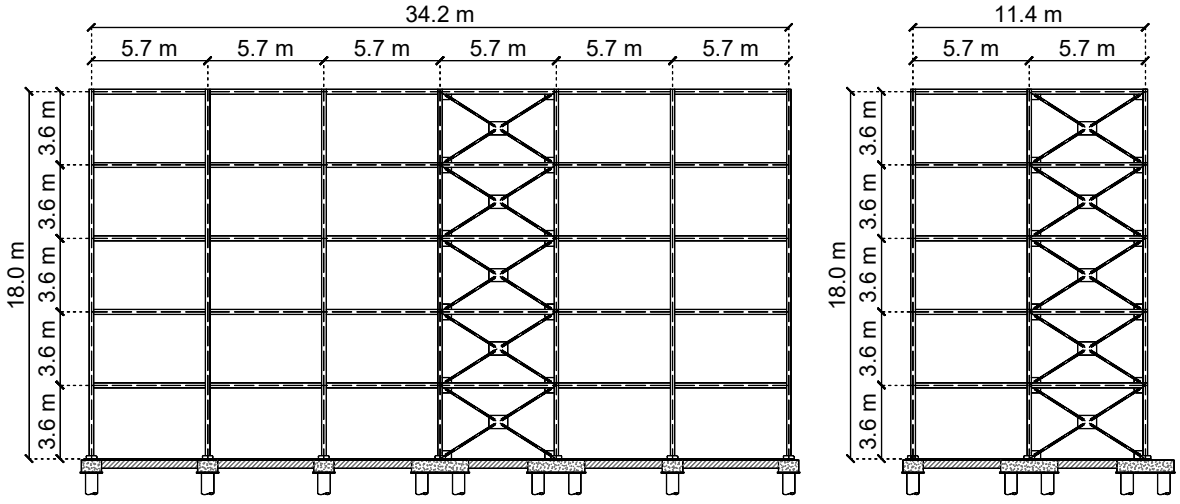


Fig. 2 – The plan view of the symmetric reference building



a) Y-direction b) X-direction

Fig. 3 – Elevation views

The design was based on the Eurocodes rules [9-13]. The aim was to study frame systems, where no detail was affected by seismic design rules. Bracings were hence designed under

wind loads only. Besides, structural design aimed at getting, for both structures, the same section of the structural elements. In particular, columns were HEB220, steel beams IPE240 and concrete slab thickness 150 mm. In absence of previous studies on progressive collapse of composite frames, it was decided to have fully composite beams. Beam-to-column joints (Figure 4), the same in both structures, were bolted flush-endplates designed according to the component method as in the Eurocode [12]. Structural steel grade S355, rebars grade B450C, bolts class 10.9 and concrete C30/37 were the materials selected for the structural elements and joints.

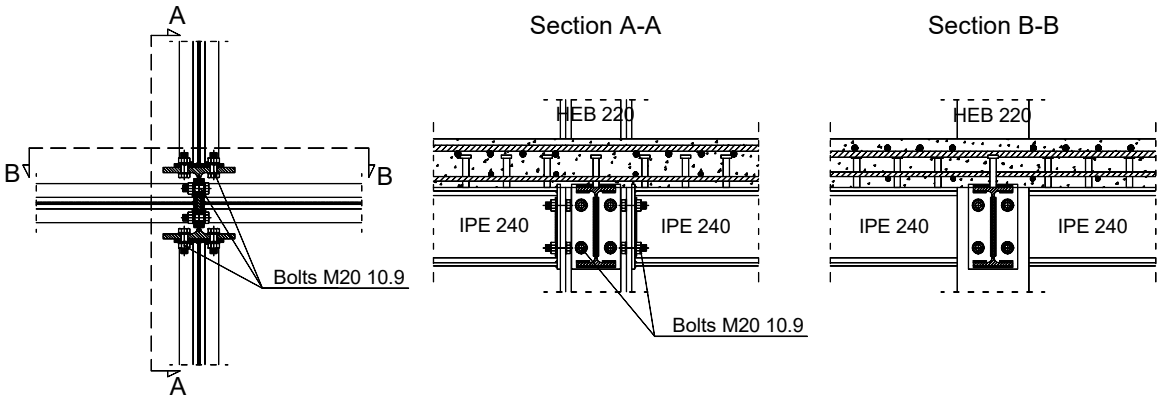


Fig. 4 – Beam-to-column internal joint

THE SUB-STRUCTURES

The tests were performed on full-scale 2x2 bays sub-frames 'extracted' from the first floor of the corresponding reference building, as illustrated by the dotted area in Figure 2. The circle individuates the column that was removed during the test. Plan view and cross section of the symmetric specimen are reported in Figure 5.

Finite element analysis of the full-frames and of the sub-frames provided the background to the design of the experimental test and, in particular, the lateral restraining system that connects the specimen to the counter-walls of the laboratory. The goal of the analyses was to mimic in the test the presence of the bracing system and of the remaining part of the reference structure. They pointed out the need for extending the columns up to approximately the point of contra-flexure between the first and second floor. A set of trusses, pinned to the top of the sub-frame columns (called 'crowning beams') were also required to adequately account for the influence of the upper stories of the reference structure. As to the sub-frame restraining system, three different options, as illustrated in Figure 6, were considered in the analysis. In Option 1 and 3, only the steel beams are restrained while the slab is not connected to the reaction wall. The presence of the bracings in the full-frame prevents from any significant longitudinal displacement and hence, the relevant d.o.f. U1 is fully restrained in the sub-frame. This d.o.f. is left free at the central beam (B in Figure 6) where the vertical and lateral displacements (U2 and U3) are restrained. Besides, in Option 1, the end rotations of beams A and C about both principal axes (R2 and R3) are restrained, and the central beam's end is restrained against rotations R2 and R3. In the Option 2, in addition to the restraints of the Option 1, also the parts of the slab adjacent to the lateral beams are connected, for a width of 0.5 m, to the reaction wall, restraining all the translational degrees of freedom. Option 3 is similar to Option 1 but all the rotations are released. Comparing the results in terms of deformations and internal forces with the ones obtained from the analysis of the corresponding full-frame, option 3 was then

selected, where all the lateral restraints are made up by truss elements connected to the steel frame. More details about the design of the lateral restraining system can be found in [14].

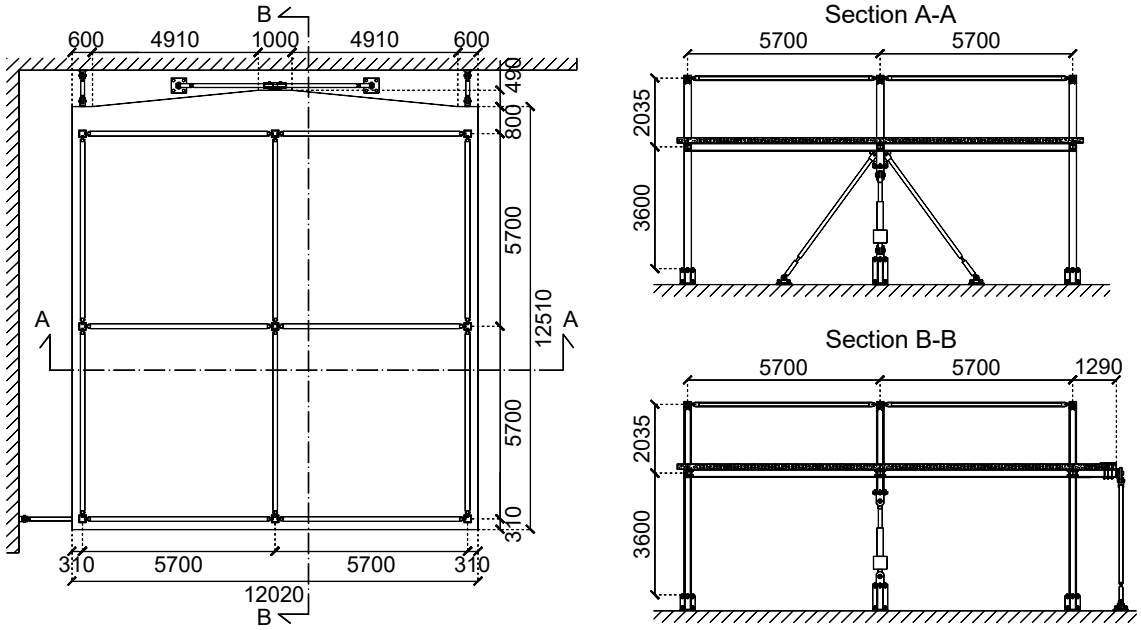


Fig. 5 – Plan view and sections of the symmetric sub-frame (measures in mm)

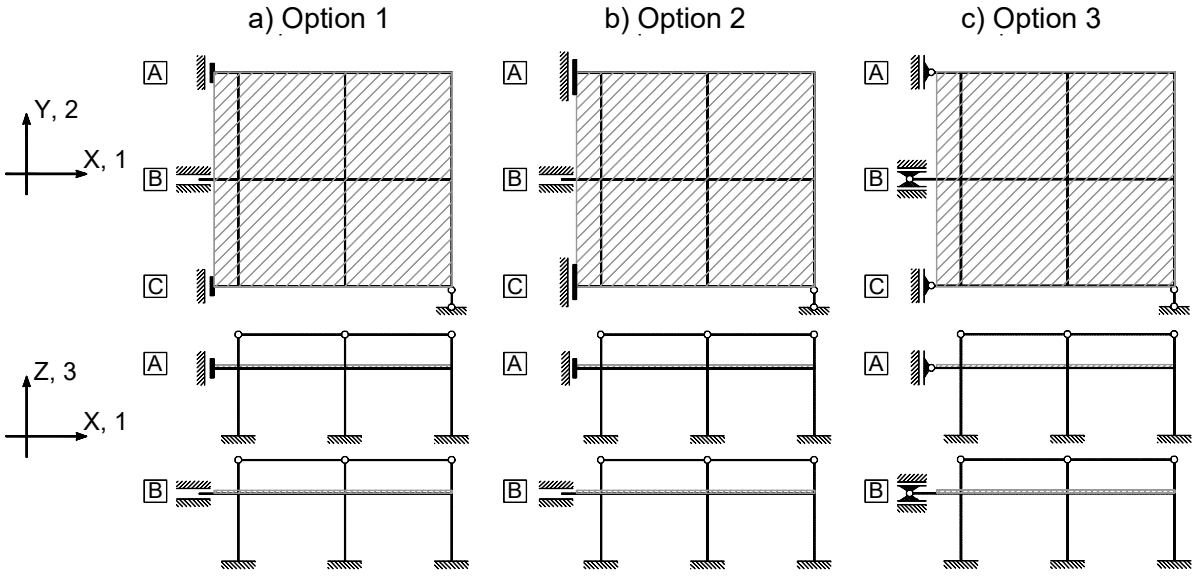
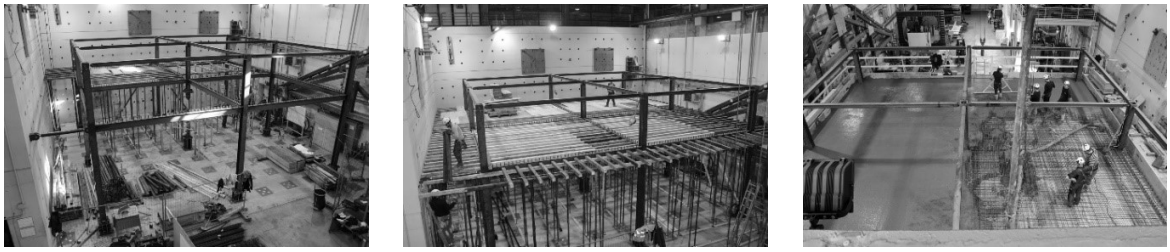


Fig. 6 – Lateral restraints options

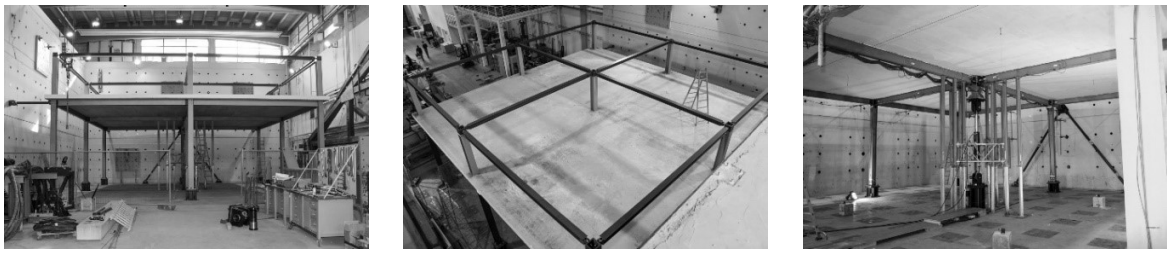
The specimens were built inside the Laboratory of Materials and Structures Testing of the University of Trento. The construction of the frame started with the erection of the steel skeleton and the formwork installation (Figure 7a-b). The reinforcement bars were then positioned and

the concrete poured (Figure 7c). Figure 8a-b shows the symmetric specimen completed, while Figure 8c shows the 'central column' that was replaced by a hydraulic jack in order to simulate the collapse. During the constructional phases, the central beams were held in position by using a provisional propping system, which was removed when the hydraulic jack was activated.



a) b) c)

Fig. 7 – The constructional phases



a) b) c)

Fig. 8 – The specimen

THE MATERIALS

Compression and splitting tests on concrete samples were performed according to the criteria of [15] and [16] respectively. During the casting phase, 18 cubes (150 mm side) and 15 cylinders (150 mm diameter and 300 mm height) were prepared. In order to appraise the evolution of the concrete compression resistance, tests on cubes were performed at age, from casting, of 7, 28 and 102 days (e.g. the time of the full-scale test), while splitting tests on cylinders were conducted at ages of 28 and 102 days. Table 1 reports the measured concrete properties.

Table 1: Concrete properties

	Concrete's age (days)	n. of tests	Average cube compressive strength (MPa)	Average tensile splitting strength (MPa)
Cubes	7	3	43.83	-
	28	9	56.47	-
	102	6	65.74	-
Cylinders	28	6	-	3.81
	102	9	-	4.25

As to steel, Table 2 and 3 report the yield stress, the ultimate tensile strength and the elongation at failure of rebars and structural steel, respectively.

Table 2: Rebars steel properties

Rebar's diameter (mm)	Yield stress (MPa)	Ultimate tensile strength (MPa)	A_{gt} (%)*
10	496	586	10.5
16	523	631	9.4

*A_{gt} total extension at maximum force

Table 3: Structural steel properties

Component	Yield stress (MPa)	Average yield stress (MPa)	Ultimate tensile stress (MPa)	Average ultimate tensile stress (MPa)	A (%)*
Column HEB220	300	303.3	441	440.3	34.9
	306		442		34.5
	304		439		36.1
Beam IPE240	383	409.3	537	540.7	28.2
	391		541		27.0
	454		544		33.3

*A permanent deformation of the gage length after fracture

THE MEASUREMENT SET-UP

The specimen was extensively instrumented to maximise the information gained from the experiment. Due to the complexity of the frame response, the most important parameters to be measured during the test were carefully identified. The attention was focused on the response of the columns, beams and joints. In particular, strain gauges were installed to measure the strain state at the columns base, at the mid-span of the internal and external beams and near the central column in the internal beams. From the readings of the strain gauges, it was possible to obtain some parameters such as the average axial strain and the curvature of the section, and consequently, assuming the material in the elastic range, the axial force and the bending moment. Strain gauges to measure the axial strain were also installed in the truss restraining elements, in the crowning beams and in some reinforcement bars in the vicinity of the central column. Displacement transducers and inclinometers were installed in correspondence of the beam-to-column connections to measure the joints' rotation. Further transducers enabled to monitor the torsional rotation of the external beams and the rotation of the external columns in correspondence of the beams' joints. At the central node of the frame, a wire transducer measured the vertical displacement and a load cell the force acting on the central column. Furthermore, the vertical displacements at the centre of the slab panels were monitored. Instruments' signals were logged at a frequency of 2 Hz. Figure 9 provides the layout of the instrumentation set-up, and Table 4 lists the instruments together with the related parameters. In Figure 9, the letters identify the columns (column A, column B,…), the beams between columns (beam AB, beam BC, ...), the lateral restraints (br. A, br. G, br. I, br. HG and br. HI). Furthermore, P1, P2, P3 and P4 are the points where the transducers measuring the vertical displacements of the slab panels were located.

THE TESTING PROCEDURE

The test plan comprises the following steps:

1. activation of the hydraulic jack and removal of the propping system;
2. application of the vertical loads. At this aim, bags filled with sand were placed on the slab reproducing a uniform distributed load of 8.80 kN/m^2 to approximate the factored

design load, including finishes, partitions and live loads (Figure 10a). This load is not the Code recommendation for checks against progressive collapse, but it makes possible studying the floor capability of transfer loads in nonlinear range (catenary action, membrane action, joint ductility). The bags were placed on two layers: the first one is distributed uniformly on the slab, the second one is placed on a reduced area as shown in Figure 10b;

3. simulation of the column removal by reducing the pressure of the hydraulic jack down to zero (velocity=1.4 mm/min);
4. stabilization of the specimen;
5. application, by means of the actuator, of a tensile force in displacement control mode (velocity = 1.50 mm/min) incremented up to 'collapse'.

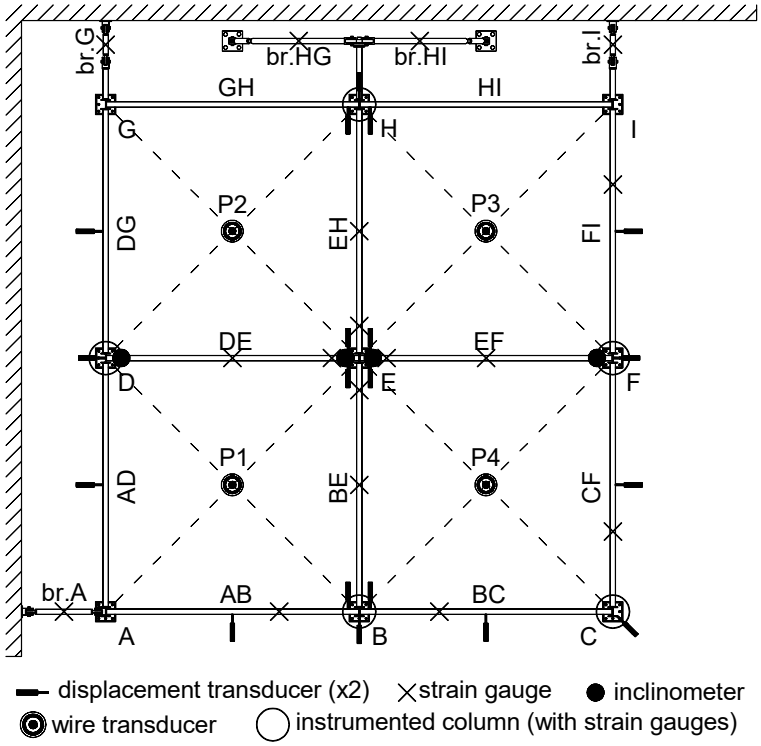


Fig. 9 – The measurement set-up

THE MAIN RESULTS

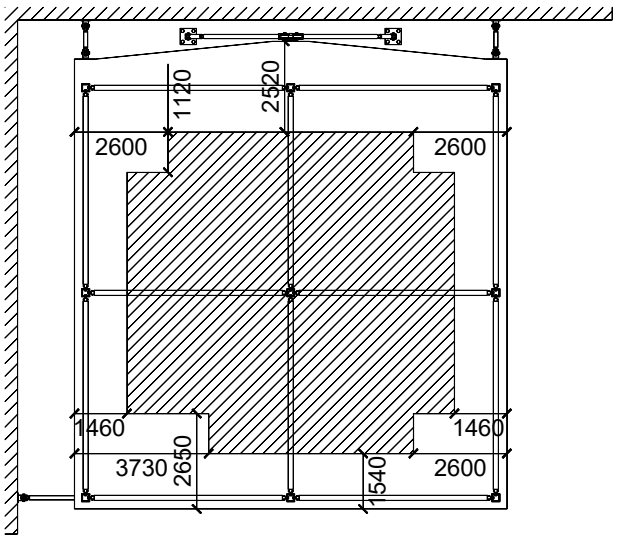
The deflection of the central node is plotted in Figure 11 with respect to the load measured by the load cell (in the graph positive values of the load mean compression). The central column was completely lost at a central node displacement of about 165 mm, which corresponds to 1/33 of the beam span. The load carried by the central column (E) has redistributed in the other columns as shown in Table 5. As a result, columns B, D and F carried about twice the axial force acting before the column removal. The axial force increase in column H was the greatest due to the nearby restraining truss system. At the contrary, the corner column C unloaded due to the effect of the concrete slab action. The test was ended when, under the applied tension force, the connection between the central column E and the beam EH 'failed' (Figure 12). The

failure was associated with the fracture of the two bolts of the bottom row of the joint c (see Figures 13a and 14a). This occurred for a vertical displacement of approximately 300 mm (1/18 of the beam span) and a corresponding applied force of 300.85 kN. At this stage, the column H was the most stressed, while columns B, D and F are stressed almost at the same level (see Table 5). The slab effect 'maintains' the corner column C axial force basically constant.

Table 4: Instruments and parameters measured

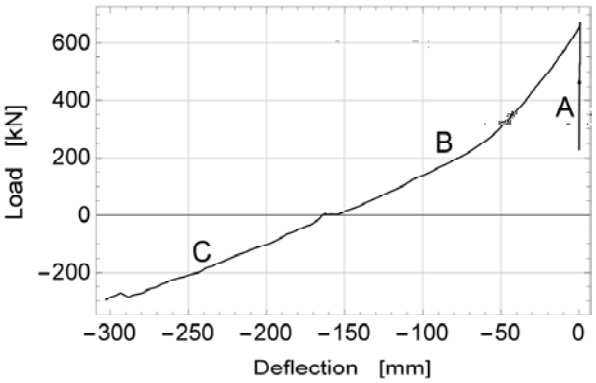
Structural element	Instrument	Parameter measured	Parameter deduced
Columns	Strain gauges at the base	Average axial strain	Axial force
		Curvature (strong-weak axis)	Bending moments
	Displacement transducers at the beam level	Rotation	
Internal beams	Strain gauges at mid-span and near the central column	Average axial strain	Axial force
		Curvature (strong axis)	Bending moment
External beams	Strain gauges at mid-span	Axial strain	Axial force
	Displacement transducers at mid-span	Torsional rotation	
Crowning beams	Strain gauges at mid-span	Axial strain	Axial force
Lateral restraints	Strain gauges at mid-span	Axial strain	Axial force
Reinforcement bars	Strain gauges near the central column	Axial strain	Axial force
Joints	Displacement transducers	Rotation	-
	Inclinometers	Rotation	-
Slab panels	Wire transducer	Deflection	-
Hydraulic jack (central column)	Load cell	Axial load	-
	Wire transducer	Vertical displacement	-





a) b)

Fig. 10 – Vertical loads on the slab (measures in mm)



Test phases:

A: Application of the vertical load

B: Column removal

C: Application of the tensile force

Fig. 11 – Load-deflection relation of the central node



Fig. 12 – The specimen at the end of the test

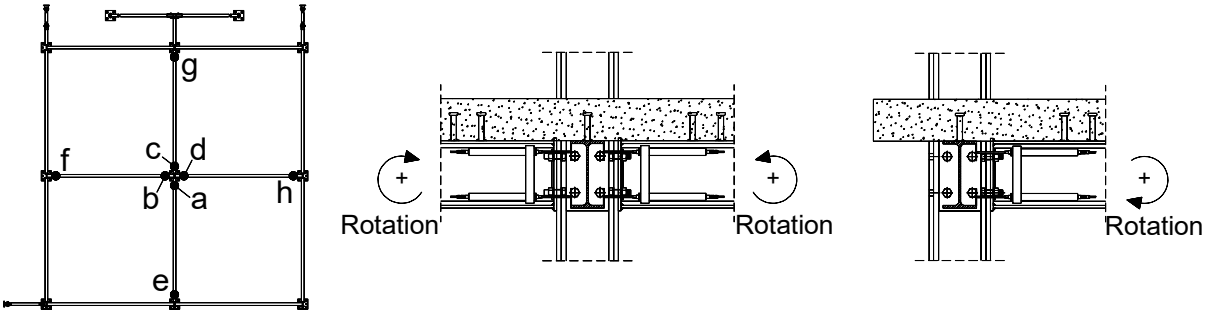
Table 5: Axial force in the columns (kN)

Column	End of the loading phase	End of the column removal	End of the test
E	669.89	2.64	-300.85
B	143.82	319.08	373.08
C	58.01	49.49	63.01
D	148.99	285.07	330.83
F	151.63	308.04	365.02
H	212.07	546.84	635.54

Both central and external beam-to-column joints experienced important deformations at the end of the test. In particular, the following phenomena occurred: at the central node, significant plastic deformations of the endplate of the beams BE and EH (Figure 14b-c); in the vicinity of the external column H (Figure 15a), instability of the bottom flange of the beam EH; in the web panel of column B, shear deformation in correspondence of the connection with the beam BE (Figure 15b); at external columns D and F (Figure 15c), horizontal cracks in the slab. Figure 16 reports the connections rotation with respect to the load applied on the hydraulic jack (Joint f rotation is not reported due to an instrument malfunction). The substantial rotational demand is apparent.

Focusing on the internal beams, Figure 17 reports the axial force (normalised on the yield force of the steel section) near the central node and at the beam mid-span. As a first appraisal of the response, near the central node (Figure 17a) the axial force evolved from negative to positive due to the change of the bending moment sign during the column removal. In correspondence

with the beam mid-span (Figure 17b), the steel section remains in tension during all the duration of the test. The process of passing from a negative to a positive bending moment at the central node was pointed out as well by the evaluation of the axial strains in the instrumented reinforcement bars near the central column E. During the application of the tensile force by the actuator, the rebars registered a significant axial force increase, and, at the end of the test, some bars reached the yielding force.



a) Joints position b) Central joints c) External joint

Fig. 13 – Joints position and positive rotation assumption



a) Central node b) Connection a c) Connection c

Fig. 14 – Central connections at collapse (see Figure 13a)



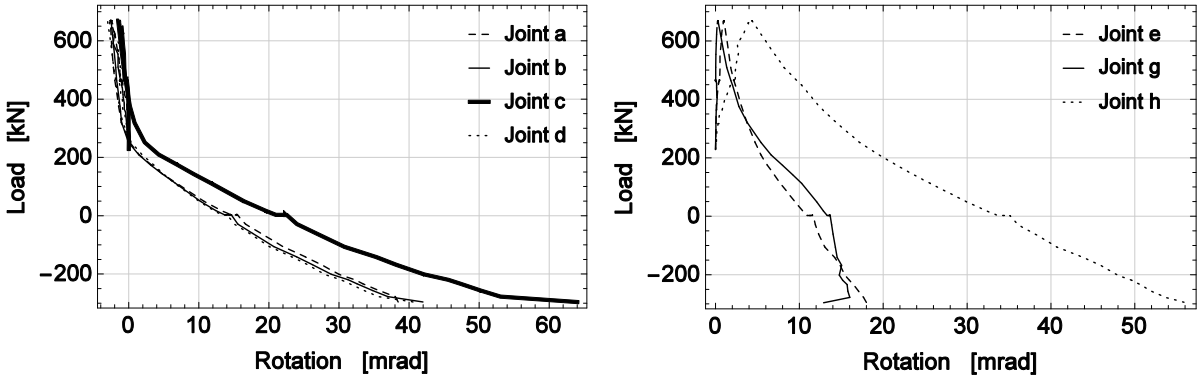
a) Connection g b) Connection e c) Joint f

Fig. 15 – External connections at collapse (see Figure 13a)

CONCLUSIONS

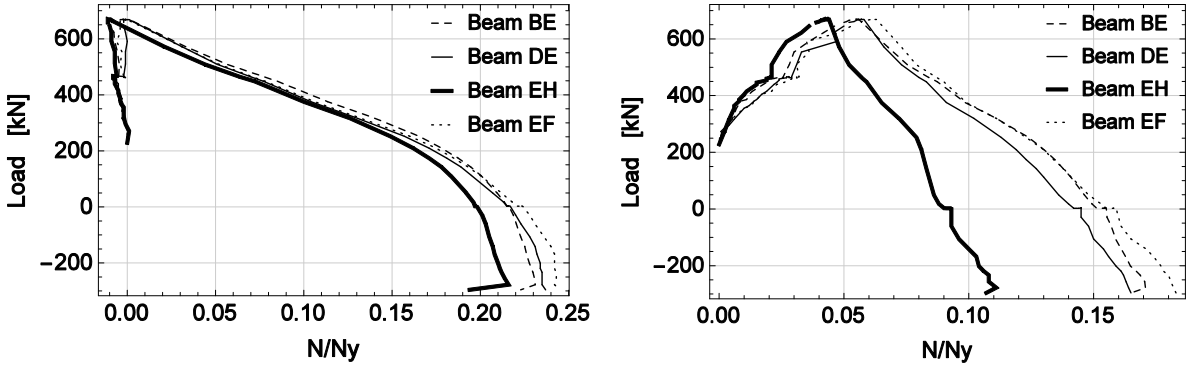
This paper presents the main results of an experimental test performed at the University of Trento on a full-scale steel and concrete composite structure subjected to a column loss. It enables investigating the importance of the joints' ductility and the role of the concrete slab for

allowing the forces redistribution in the structure associated to the alternate loading path activated after the column loss.



a) Internal connections b) External connections

Fig. 16 – Connection rotation



a) Near the central node b) At the beam mid-span

Fig. 17 – Axial force in the central beams

The full-scale specimen was ‘extracted’ from the first floor of a reference building designed in accordance with the Eurocodes. The central column collapse was simulated by replacing the column with a hydraulic jack that was kept inactive before the beginning of the loading. The test was carried out with the following sequence: the hydraulic jack was first activated and the propping system removed, the vertical loads were then applied on the slab and the column removal was simulated reducing the pressure of the jack down to zero. Finally, with the aim of appraising the structural residual strength, an incremental tension force was applied at the central node up to the ‘frame collapse’ associated with the failure of a central joint.

The results reported in this paper pointed out that the joints, designed as ductile, enable achievement of very high rotations. Joint ductility is provided by plastic deformations, mainly of the end-plate and the column web in shear. Local beam buckling and horizontal cracks of the outstanding slab at external joints should be considered in design in order to ensure adequate ductility.

Despite the collapse was associated with joints' failure, the key role of the slab for ensuring loads and forces redistribution from the damaged to the undamaged parts of the structure is apparent. The cracking pattern on the top side of the concrete slab revealed the formation of 'compressive rings' typical in slabs where the membrane forces are activated.

ACKNOWLEDGMENTS

The test was made possible by the grant from the Research Fund for Coal and Steel of the European Community (Contract number No. RFSR-CT-2012-00029). The Authors also gratefully acknowledge the work by the technicians of the Structural Testing Laboratory of the University of Trento: Stefano Girardi, Marco Graziadei and Alessandro Banterla.

REFERENCES

[1] GSA, Progressive collapse analysis and design guidelines for new federal office buildings and major modernization projects, General Service Administration, USA, 2003.
[2] DoD, Unified Facilities Criteria (UFC): Design of building to resist progressive collapse, Unified Facilities Criteria (UFC) 4-023-03, Department of Defense, USA, 2009.
[3] Office of the Deputy Prime Minister. The building regulations 2000, part A, schedule 1:A3, disproportionate collapse, London, UK, 2004.
[4] EN 1991-1-7, Eurocode 1: Actions on structures – part 1-7: General actions – Accidental actions, European Committee for Standardization, Brussels, 2006.
[5] BS, BS5950: Structural use of steelwork in buildings, part 1: code of practice for design – rolled and welded sections, British Standard Institute, London, UK, 2001.
[6] BS, BS6399: Loading for buildings, part 1: code of practice for dead and imposed loads, British Standard Institute, London, UK, 1996.
[7] EN 1990, Eurocode 0: Basis of structural design, European Committee for Standardization, Brussels, 2004.
[8] European Commission - Research Programme of the Research Fund for Coal and Steel. Robust impact design of steel and composite building structures – 'RobustImpact'. Grant Agreement number RFSR-CT-2012-00029. Document in press.
[9] EN 1991-1-1, Eurocode 1: Actions on structures – part 1-1: General actions, densities, self-weight, imposed loads for buildings, European Committee for Standardization, Brussels, 2002.
[10] EN 1992-1-1, Eurocode 2: Design of concrete structures – part 1-1: General rules and rules for buildings, European Committee for Standardization, Brussels, 2004.
[11] EN 1993-1-1, Eurocode 3: Design of steel structures – part 1-1: General rules and rules for buildings, European Committee for Standardization, Brussels, 2005.
[12] EN 1993-1-8, Eurocode 3: Design of steel structures – part 1-8: Design of joints, European Committee for Standardization, Brussels, 2005.
[13] EN 1994-1-1, Eurocode 4: Design of composite steel and concrete structures – part 1-1: General rules and rules for buildings, European Committee for Standardization, Brussels, 2004.
[14] R. Zandonini, N. Baldassino, F. Freddi. Robustness of steel-concrete flooring systems - An experimental assessment, Stahlbau, 83 (9), 608-613, 2014.
[15] EN 12390-3:2009, Testing hardened concrete – Part 3: Compressive strength of test specimens.
[16] EN 12390-6:2009, Testing hardened concrete – Part 6: Tensile splitting strength of test specimens.

Concrete Filled Steel Tubes for Bridge Applications

Charles W. Roeder
Professor, Department of Civil Engineering, University of Washington
Seattle, WA 98115-2900 USA
croeder@uw.edu

Dawn E. Lehman
Professor, Department of Civil Engineering, University of Washington
Seattle, WA 98115-2900 USA
delehman@uw.edu

ABSTRACT

Concrete filled steel tubes (CFST) are composite members that are used in many countries, but with limited use in the US. Bridge construction uses steel tubes filled with reinforced concrete (RC) for pile and drilled shaft foundations, but they are designed as RC members where composite behavior is neglected. Steel tubes have been used for jacketing upgrades or stay-in-place formwork for RC bridge piers. Recent research at the University of Washington funded by the CALTRANS, WSDOT, and others focused on using the composite behavior of circular CFST for accelerated seismic construction of deep foundations and bridge piers. Research has evaluated the behavior of large diameter circular CFST members and their connections. Connections with good seismic performance and suitable for economical and rapid construction were developed. Deep foundations encounter high shear and moment demands due to lateral spreading and liquefaction of soils, and this has also been investigated. This research is summarized.

INTRODUCTION

CFST is widely used for bridge construction in Asia, but its use is limited in the US. US bridge engineers sometimes have serious preconceptions and misconceptions that have limited the use of CFST. Bridge construction in the US is inherently different than in Asia because of differences in construction costs and practices. As a result, design and construction practices that are practical and economical in other countries may not be viable for US construction. Nevertheless, CFST offers potential advantages for US bridge construction, because of its high strength, stiffness and ductility, and because of the accelerated construction that can be provided by CFST. This paper reviews the current use of CFST in US bridge construction, recent research into the use of CFST in bridges and potential future applications of these composite members.

CFST IN BRIDGE CONSTRUCTION

Composite CFST construction has had limited use in US bridge construction, steel tubes filled with RC with no composite behavior with the steel tube have been used more frequently. Three seismic applications of steel tubes with RC infill are noted in US bridge construction. First, older RC bridge piers suffer severe damage during earthquake load as illustrated in Figure 1, and jacketing for seismic retrofit of reinforced concrete bridge piers with inadequate shear reinforcement, confinement, or rebar splice and development lengths have been done to ensure improved seismic performance. Extensive research has been performed on this issue (Priestley et al. 1994), because increased pier resistance from composite action increases the seismic demands on foundations and other parts of the structure. Jacketing confines the concrete but avoids shear stress transfer (and the resulting composite resistance) between the RC column and the steel tube. In addition, the steel tube is stopped short of connecting elements to limit force and moment transfer.



Fig. 1. Seismic damage to an RC bridge pier



a) Inserting the steel tube



b) Inserting the reinforcing cage

Fig. 2. Deep drilled shaft foundations

Bridges in the US employ a range of foundation types. Spread footings are often the most economical, but bridges designed for seismic loadings may require deep foundations due to large seismic design forces and soft, weak soil deposits. Pile foundations may use precast concrete piles, steel H-piles, or steel tube piles, and these piles are a second major application of steel tubes filled with RC fill. Pile-to-pile cap connections in bridge design often are simple embedded shear resisting connections, which may develop limited flexural resistance that is neglected in design. Steel tube piles offer significant advantages, and they are commonly used today. The tubes can be driven or vibrated into place, cleaned of soil for a portion of their depth. A reinforcing cage may be inserted into the pile to provide a calculable flexural resistance and increased stiffness and end bearing capacity of the pile, but the composite behavior of CFST usually is neglected in design. The reinforcing cage may also extend into the pile cap to provide shear and moment transfer at the pile-to-pile cap connection.

Drilled shaft foundations are a third application of steel tubes filled with RC for bridge design. The shafts may be 2 to 4m in diameter and more than 80 to 90m in depth in seismic regions. A steel tube frequently is inserted into the shaft to hold back loose soil and facilitate construction (see

Figure 2a), and a steel reinforcing cage is inserted into the tube as shown in Figure 2b before the tube is filled with concrete. The resistance of the shaft is evaluated as a RC member with no consideration of the composite action or the steel tube.

Bridge engineers often confuse these 3 noncomposite applications with CFST, and US design specifications probably contribute to this misinterpretation. Composite CFST design provisions have historically evolved in 3 major US design specifications. The AISC and ACI specifications are focused on steel and concrete buildings, respectively, (AISC 2010, ACI 2011) and they consider the composite behavior of CFST. The AASHTO specifications are focused on bridge design (AASHTO 2016), and these provisions historically lie between the AISC and ACI provisions. However, there is substantial differences between CFST provisions in ACI and AISC, and a brief comparison is justified.

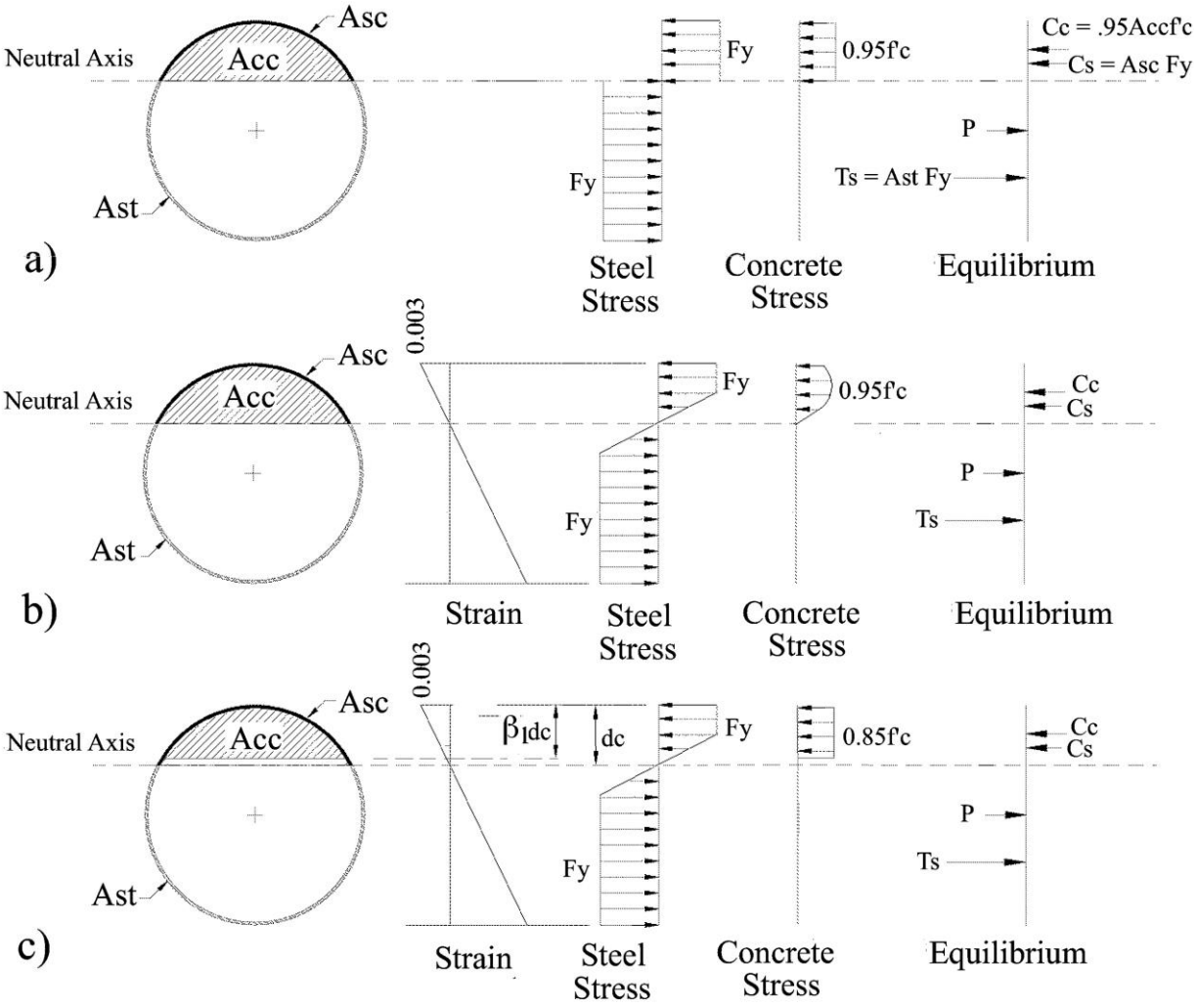


Fig. 3. Evaluation models for CFST; a) AISC plastic stress distribution method, b) AISC strain compatibility, c) ACI strain compatibility

The AISC and ACI specifications provide specific methods for predicting the flexural and axial resistance of circular CFST. AISC (2010) permits both the plastic stress distribution method (PSDM) (see Figure 3a) and the strain-compatibility (SC) (see Figure 3b) methods. The ACI provisions recognize only the SC method as illustrated in Figure 3c. For the PSDM, the section

develops the full yield stress of the steel in tension and compression and a uniform compressive stress of $0.95f'_c$ in the concrete of circular CFST in compression where f'_c is the specified compressive strength of the concrete. Equilibrium is applied over the cross section for each possible neutral axis location to develop axial load-bending moment interaction curves, which are affected by the slenderness, D/t, of the tube. Smaller D/t values result in larger resistance due to larger area of steel. Larger D/t values significantly increase bending moment for modest axial loads due to the increased contribution of the concrete fill in compression. However, the total resistance is smaller, since the concrete contributes more to the resistance. Bishop (2009) evaluated these alternate methods, compared design predictions to past experimental results, and showed that the PSDM is conservative and consistently provides more accurate predictions of circular CFST resistance. He showed that the experimental moment capacity of circular CFST was 1.24 times the measured moment capacity in prior experiments with a standard deviation of 0.18. The SC method has considerable appeal, since it is the basis of reinforced concrete design, and it is also provides a measure of curvature and deformation of the member at various load levels. However, Bishop showed that it is not a particularly reliable model for CFST, because it requires a strain or deformation limit to establish the resistance. He showed that the experimental moment capacity of CFST was 1.64 time the ACI SC prediction, because the 0.003 mm/mm strain limit was employed, and the standard deviation was 1.17. This great scatter was caused because the .003 strain limit for concrete was proposed to control spalling of concrete members, and spalling cannot occur in CFST due to the confinement provided by the steel tube.

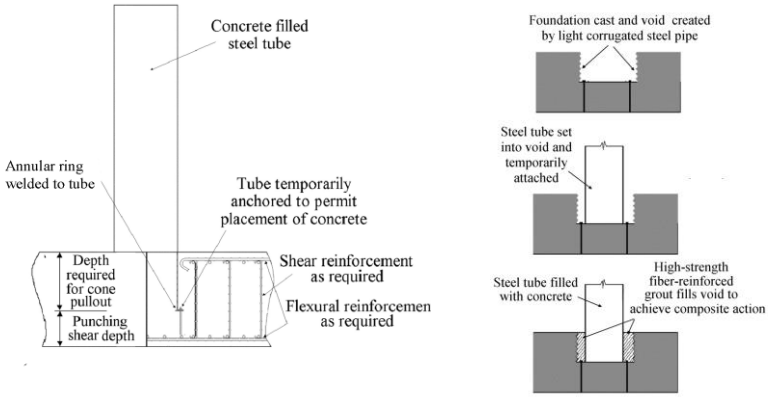
The AISC SC method employs a linear strain distribution, a bilinear steel material curve, a parabolic unconfined concrete material behavior, and equilibrium to determine axial and flexural capacity as shown in Figure 3b. The maximum strain in the extreme compression fiber of the concrete (which is within the tube) is still 0.003 mm/mm, and so this method also provides a much more conservative estimate of behavior. Bishop explored other methods of limiting strain, curvature or other deformation with the SC method. Other limits such as a strain limit in the steel or curvature of the member resulted in greater accuracy and smaller standard deviation, but they also produced a significant number of unconservative predictions of CFST resistance.

RECENT EXPERIMENTAL RESEARCH ON CFST FOR BRIDGE CONSTRUCTION

Some recent developments have changed the prospects for using CFST in bridge design. First, bridge construction has recently focused on accelerated and more economical construction without resulting in reduced structural performance. CFST clearly offers benefits in this realm because they provide good structural performance with reduced cost and field construction time by eliminating formwork, shoring, and internal reinforcement. Further, CFST elements offer greater resistance with significantly less weight and material than RC members, because the steel tube provides greater confinement to the concrete and reinforces the concrete at the optimal location. As a result, significant savings in material may result.

Research clearly shows that circular CFST provides better performance than rectangular CFST because circular tubes better confine the concrete fill and increase the shear stress transfer (bond stress) between the tube and the concrete fill. However, US engineers often use rectangular CFST, because they believe that connections are easier due to the flat steel surfaces provided by the tube. Recently, significant research has been performed on circular CFST connections with large diameter tubes suitable for bridge construction. Two CFST column-to-footing or CFST pile-to-pile cap connections have been developed as shown in Figure 4 (Lehman and Roeder 2012). Both connections employ an annular ring (see Figure 5) at the end of the tube to develop connection resistance. The annular ring has the same thickness and yield stress as the wall of the tube and extends a distance 8 times the thickness into the fill and the encasing concrete.

Figure 4a shows a cast-in-place embedded connection where the annular ring is temporarily supported on a lift or pedestal and then cast into the footing or pile cap. Construction labor issues in US may result in a preference for the recessed grouted foundation connection illustrated in Fig. 4b. The footing is cast with a recess formed by a light gauge corrugated steel tube. The CFST tube with its annular ring is placed into the recess and grouted with high strength reinforced grout. The tube is then filled with concrete, and construction proceeds as with other connections. In addition, three CFST column-to-precast cap beam connections illustrated in Fig. 6 have been developed to facilitate the use of precast pier caps with CFST pier columns and to further enhance accelerated bridge construction (Stephens et al. 2014).

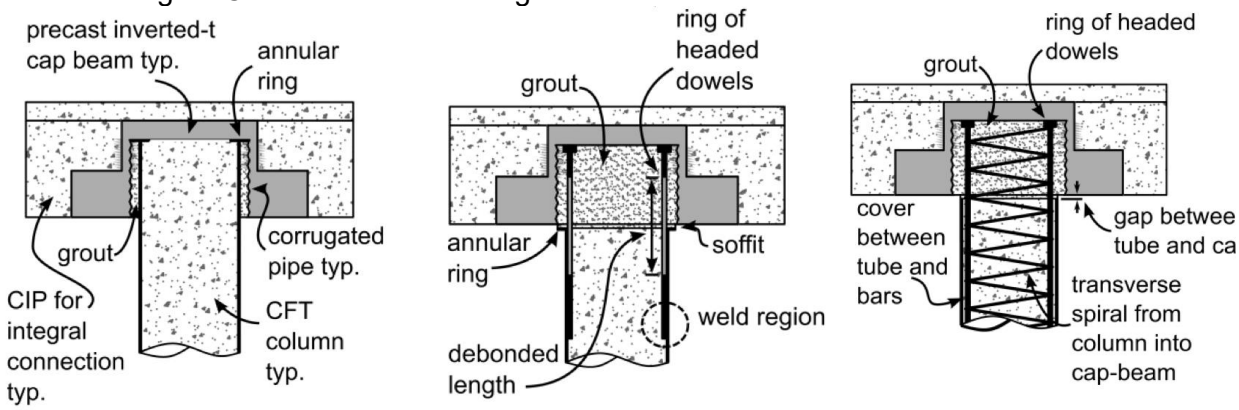


a) Embedded connection b) Grouted connection



Fig. 5 Annular Ring

Fig. 4. CFST column to footing connection



a) Embedded connection b) Welded dowel connection c) RC connection

Fig. 6. CFST column to precast cap beam connections

Eighteen foundation connection specimens were built and tested under cyclic lateral load in the setup illustrated in Fig. 7 (Lehman and Roeder 2012). The connection performance is strongly influenced by footing thickness and embedment depth, since they relate to punching shear and cone pullout of the tube in flexure, and these issues were a focus of the research. Specimens with shallow embedment depths cause significant damage to the reinforced concrete footing or pile cap as shown in the lateral force-story drift plot and photo of Figures 8a and 8b. This shallow embedment depth provides enough resistance to yield the tube and nearly develop the full plastic capacity of the composite section, but the connection loses much of this moment capacity result in virtually no damage to the footing as shown in Figure 8e, and they develop and maintain the full plastic capacity of the composite member through large inelastic deformations with no deterioration in resistance as shown in Figure 8a. Local buckling of the tube occurs after large inelastic deformations as shown in Figure 8d, and after multiple cycles of large inelastic

deformation. The cyclic plastic strains due to straightening and rebuckling of walls of the tube ultimately lead to ductile tearing. The concrete inside the tube is well confined, and no damage to the concrete fill occurred until after severe local buckling of the tube. After severe local buckling, crushing of the concrete in this local area of the buckle occurs, and the concrete in this zone is large pulverized and may pour out of the tear. The required embedment depth and footing thickness required for punching shear were established from this research.

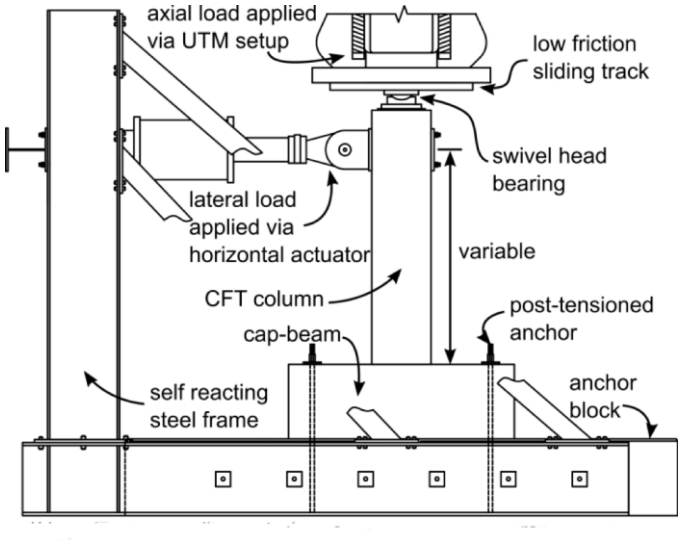
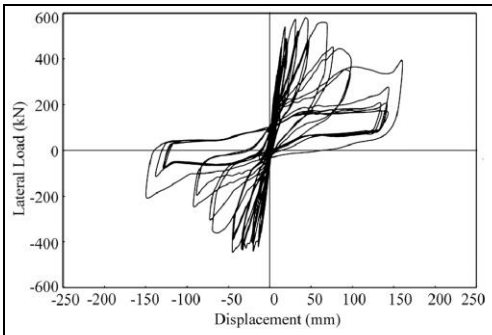


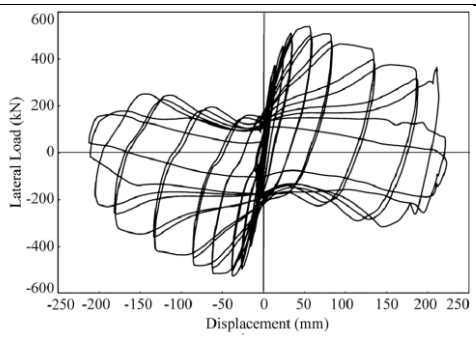
Figure 7. Test Setup.



a) Force – displacement with shallow embedment



b) Photo of footing damage with shallow embedment



c)Force – displacement with adequate embedment



c) Local buckling of tube



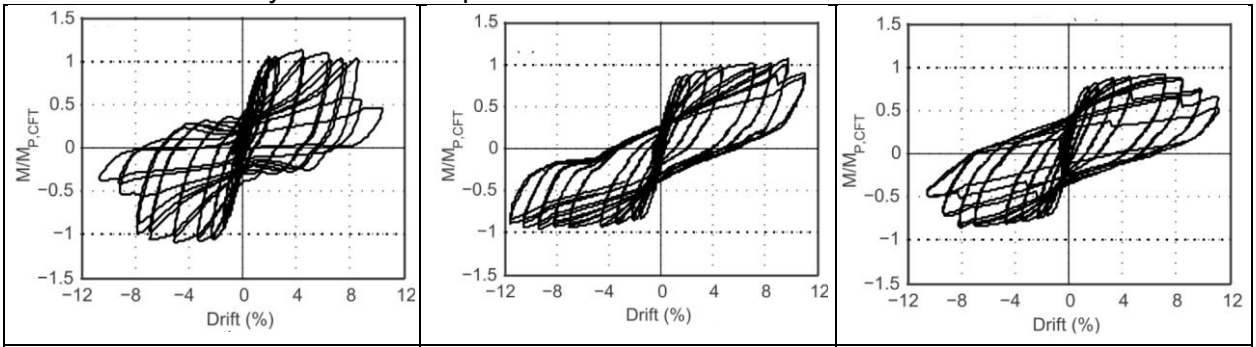
e) Photo of footing and connection at end of test

Fig. 8 Typical test results for CFST foundation connections

Calculations show that CFST bridge piers can be constructed with 30% to 40% less material and weight than an RC pier of equivalent strength and stiffness. Further, CFST piers provide better seismic performance than the heavier RC member. The CFST member is rapidly constructed because the steel tube is fabricated off site, is quickly erected, and supports construction loads during erection and subsequent placement and curing of the concrete fill. Creep and shrinkage of the concrete is minimized with CFST construction compared to RC construction (Lehman et al. 2013). Environmentally friendly construction practices such as cement replacement can be employed, because the steel tube supports construction loads during the long period required for the concrete to gain its full strength with these alternate materials. Reinforcement or shear connectors are usually not required within the steel tube, and no shoring or formwork is required. Fabrication is quite simple since it consists of forming and cutting the tube and welding an annular ring to the end of the tube. CFST pier columns can be constructed in days rather than weeks or months required for RC bridge piers. The lighter weight of the steel tube eliminates the need for heavy cranes required with other accelerated construction methods.

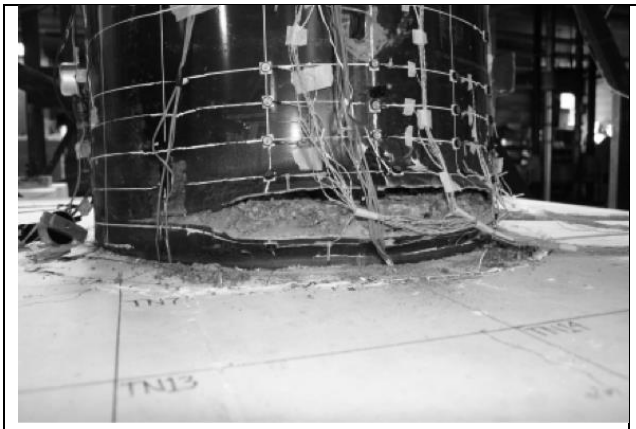
The CFST pier column-to-precast cap beam connections are divided into three broad categories: (1) the embedded connection (see Figure 6a), (2) the welded dowel connection (see Figure 6b), and (3) the RC connection (see Figure 6c). Eight CFST pier column-to-precast cap beam connections were tested under cyclic inelastic deformation in either the longitudinal or transverse directions of the bridge pier. The longitudinal and transverse directions are different, because the bending moment is either parallel or normal to the axis of the axis cap beam, respectively.

The embedded connection (Figure 6a) is a logical extension of the grouted-recessed foundation connection (see Figure 4b). A recess is formed in the precast cap beam. The recess of the precast cap beam is placed over the CFST column and its annular ring, and is grouted into the recess with reinforced grout. This connection develops the full resistance of the CFST as illustrated in lateral force-story drift plot of Fig. 9a, and it supports all construction loads without temporary shoring. As with the foundation connection, the embedment depth is important, because this relates to potential cone pullout and damage to pier cap. The required width of the cap beam is important to the economy, esthetics, and performance of the connection, and it was also investigated. The ultimate failure of this connection is again associated with plastic deformation of the composite member, local buckling of the steel. and tearing of the steel in the local buckled region after numerous cycles of large inelastic deformation as shown in Fig. 10a. The embedded connection develops the full strength of the CFST column, and it has high stiffness and excellent ductility and inelastic performance.

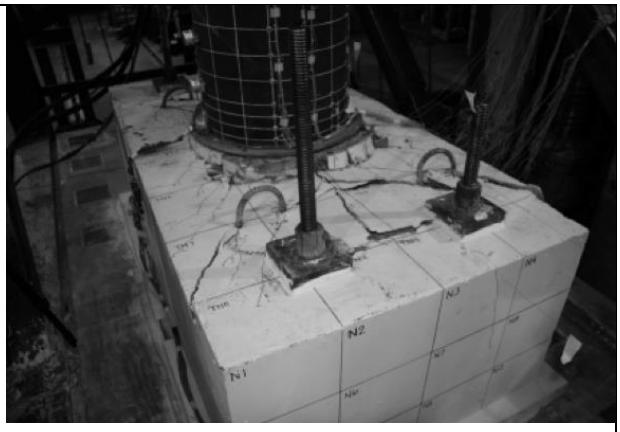


a) Embedded connection	b) Welded dowel connection	c) RC connection

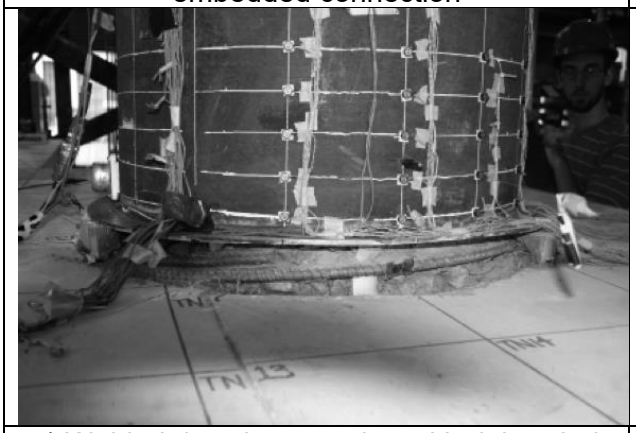
Fig. 9. Force-deflection behavior of precast pier cap connections



a) Tear in tube after cyclic local buckling of embedded connection



b) Footing damage cause by welded dowel connection with no debonding



c) Welded dowel connection with debonded bars



d) Fracture of reinforcing bars and spiral in RC connection

Fig. 10. Photos of typical precast pier cap connection behavior

The welded dowel and RC connections shown in Figures 6b and 6c were developed because bridge engineers may prefer a weaker connection to limit the seismic demands on other structural elements. Their strength depends upon the size and spacing of the rebar, which are limited by the inside perimeter of the tube. The welded dowel connection will normally be significantly stronger than a RC connection, because the reinforcing bar is entirely within the steel tube for the welded dowel connection and concrete cover is not required. The steel tube does not extend into the pier cap with either the welded dowel or the RC connection. Figure 6b, shows a welded dowel connection with debonded reinforcing bars, since debonded bars provide better inelastic performance (see Figure 9b) with little damage to the pier cap (see Figure 10c) increase the inelastic deformation capacity and reduce the damage to the pier cap. Dowel bar connections with bonded bars were tested and significant damage to the pier cap as shown in the photo of Figure 10b. The actual behavior of unbonded RC and welded dowel connections is a rocking behavior due to the large axial deformations of the unbonded bars, and significant separation between the tube and the cap beam were noted as illustrated in Figures 10c and 10d. The resistance of the welded dowel connection in Fig. 9b is fairly close to that of embedded connection, because the internal reinforcement had 87% of steel area of the tube but the yield

stress of the rebar was 45% larger than that of the tube. While the resistance of this welded dowel connection is greater than that possible with a RC column (see Figure 9c) due to the larger effective diameter of the rebar and the better confinement of the steel, the resistance of welded dowel connections is smaller than that of a CFST embedded connection, because it is difficult to weld adequate rebar into the tube to develop the resistance of the tube. The RC connection also had large inelastic deformation that was limited to yielding in the longitudinal rebars and grout in the soffit region. The RC connection was weaker and more flexible than the embedded CFST connection. Its stiffness was 69% of the stiffness of the embedded CFST of identical size and properties. Significant damage to internal longitudinal bars and spiral reinforcing were noted in these specimens. Buckling and fracture of the bars were also noted (see Figure 10d).

The placement and design of the welds joining the reinforcing bars to the inside of the tube was a critical issue for the welded dowel connection. A flare bevel weld was designed to develop the tensile strength and inelastic deformation capacity of the reinforcing bar, and an experimental study of this weld was completed prior to testing of the full connections to assure that the performance goals were achieved. The primary test parameters included rebar size, weld strength, bonding or debonding the dowels from the concrete, and the embedment depth of the bar into the steel tube. Weld strengths ranging from 80% to 120% of the dowels strength and embedment depths of $16d_b$ and $24d_b$ were evaluated. The bars were pulled to failure using a hydraulic ram placed into a self-reacting system. The failure mode in all tests was characterized by dowel yielding followed by strain hardening and fracture of the steel bar. Debonding the reinforcing decreased the visible concrete damage, and no damage to the tubes in the weld region was observed in any of the tests. Design and placement of the weld was completed in accordance with American Welding Society (AWS) Bridge Welding Code (AASHTO/AWS 2010).

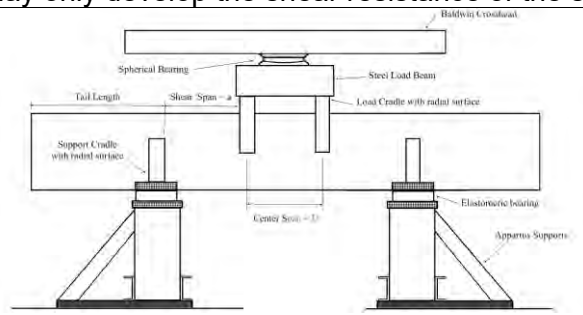
The welded dowel and RC connection have substantial penalties with regard to accelerated construction. The embedded CFST connection easily supports the weight of the cap beam, girders, and construction equipment during erection, and so shoring is not required. However, welded dowel connections cannot support the weight of the cap beam, and therefore shoring or other support system is required to support the pier cap while the cap is grouted into place and while the grout cures. It is possible that clamp supports may be applied to the CFST column to support the pier cap with the RC and welded dowel connections. Additional data and information these tests may be found elsewere (Stephens, Max T. et al. 2016 and Stephens, Max. et al. 2016).

The prior research focused on work done to develop economical and practical connections for CFST piles, drilled shafts, bridge piers and columns. The shear force demands on foundation and substructure elements are quite large for piles and drilled shafts subjected to earthquake loading. Since bridges are commonly built on deep soil deposits, foundation design is often concerned with liquefiable layers of soil that may introduce lateral spreading or movement during large earthquakes. Movements of this type may cause large shear forces in piles and drilled shafts, and there is great interest in establishing the shear capacity of CFST under different applications and load conditions.

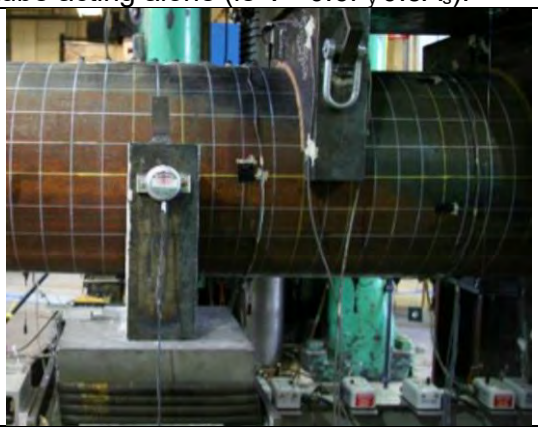
The Washington State Department of Transportation funded a study to address this issue. A few prior shear tests had been performed (Xu et al. 2009, Xiao et al 2012, and Nakahara and Tokuda 2012), but these prior tests were on moderately small diameter tubes under idealized conditions. Actual piles and drilled shafts are of much larger size and the actual applications may have dirt or contamination inside the tube, inaccurate geometric placement and other concerns. This research study evaluated larger tubes and tubes reflecting current field conditions. Figure 11 shows the test setup and deformation of one of the test specimens failing in shear.

It should be emphasized that shear and flexure are related, since shear is the derivative of the moment diagram. Hence, shear force can be limited by flexural resistance, by failure in composite action due to inadequate shear stress transfer between the steel tube and the concrete fill induce

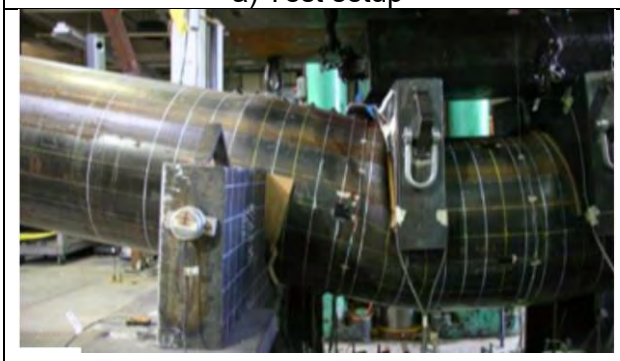
failure, or by a true shear strength failure of the composite CFST member. This distinction does not appear to be recognized some of the prior research studies, and this distinction was a major focus of this research. The experimental study considered tubes that were 500 mm in diameter, with wall thickness of 12.5 or 16 mm, and yield stress of 350 to 490 MPa. The shear span, a (see Fig. 11a), had to be quite small to obtain a shear failure (usually a< 0.375D). Further, shear stress transfer is required to develop the shear resistance of the composite CFST member. Hence, the tail length in the specimens (see Figures 11a and 11b) were important. Specimens without adequate tail length or with poor shear stress transfer between the steel tube and concrete fill may only develop the shear resistance of the steel tube acting alone (ie $V \approx 0.6F_y 0.5A_s$).



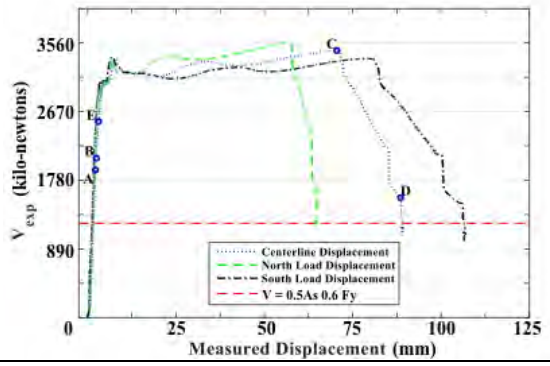
a) Test setup



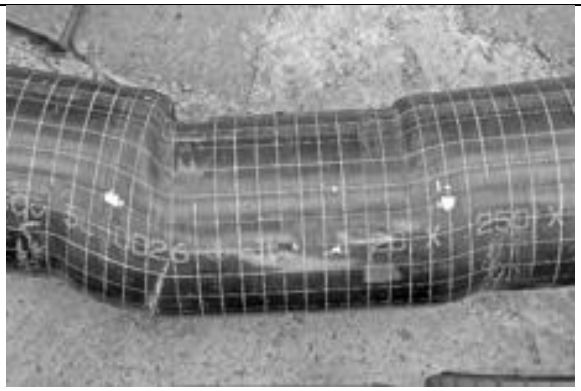
b) Photo of test specimen



c) Photo of test specimen after significant shear deformation



d) Typical shear force-deformation behavior



e) Deformation and ultimate tearing of shear controlled CFST



f) Concrete cracking of fill inside a shear controlled CFST

Fig 11. Shear tests of CFST members

Twenty two large scale specimens were tested, and all three behaviors were obtained. Figure 11d is the force deflection behavior of a CFST specimen truly failing in shear. The shear resistance of these specimens is significantly larger than 2 times the shear resistance of the bare steel tube. Specimens failing through flexure or through inadequate tail or development length have significantly smaller shear force. Figure 11e shows the severe shear strains in the steel tube with this true shear failure mode. The deflections were extremely large compared to the short shear span, and the ultimate failure was ductile tearing of the steel tube where the tear initiated from the shear span of the specimen. The concrete fill clearly contributed to this large shear resistance. Much of the contribution was provided by the concrete fill retaining the shape and cross section of the tube. However, large shear strains and severe shear cracking occurred in the shear span as shown in Figure 11f. Very limited cracking occurred in the concrete located in the central flexural span of the specimens as shown in the figure.

SUMMARY AND CONCLUSIONS

This has been a brief overview of the use of CFST in US bridge construction. It is clear that the use of CFST in bridge construction is less advanced in the US than in many other countries. Nevertheless, significant advances have been made in recent years, and it is expected that the use of CFST in US bridge construction will increase significantly in the future. The primary usage of CFST has been and will likely continue to be for piles, drilled shafts and bridge pier columns. Connections suitable for seismic design of bridge pier columns have been discussed. These connections are practical and economical and they facilitate accelerated bridge construction. A recent study on the shear resistance of CFST was summarize. It is shown that the shear resistance of CFST is very large, and that the shear failure is a very ductile failure mode.

ACKNOWLEDGEMENTS

Research was sponsored by the Army Research Laboratory (Cooperative Agreement Number DAAD19-03-2-0036 through Advanced Technology Institute), by the California Department of Transportation (CALTRANS) (Agreements 59A0641 and 65A0446) and the Washington State Department of Transportation (WSDOT) (Agreement T1461). The views and conclusions contained in this document are those of the authors and should not be interpreted as representing official policies, either expressed or implied, of the Army Research Laboratory, the US. Government, CALTRANS or WSDOT. The U.S. Government is authorized to reproduce and distribute reprints for Government purposed notwithstanding any copyright notation heron. The authors gratefully acknowledge the financial support of these organizations. In addition, the advice and assistance provided by Ron Bromenschenkel, Michael Cullen, and Peter Lee of the CALTRANS, Bijan Khalighi of WSDOT, and Jon Tirpak of the Advanced Technology Institute and the Vanadium Technology Partnership.

REFERENCES

American Association of State Highway and Transportation Officials (AASHTO) (2012) AASHTO LRFD Bridge Design Specifications, Washington, D.C.

American Association of State Highway and Transportation Officials (AASHTO) (2014) AASHTO LRFD Bridge Construction Specifications, 3rd Edition with 2010 through 2014 Interims, Washington, D.C.

American Concrete Institute (ACI) (2011) Building Code Requirements for Structural Concrete (ACI 318-11), Farmington Hills, MI

American Institute of Steel Construction (AISC) (2010). Specification for Structural Steel Buildings, AISC, Chicago, Illinois.

American Welding Society (AWS) (2010) "Bridge Welding Code," *AASHTO/AWS D1.5:2010 Standard*, Miama, FL.

Bishop, E. (2009) Evaluation of the Flexural Resistance and Stiffness Models for Circular Concrete-Filled Steel Tube Members Subjected to Combined Axial-Flexural Loading, *a thesis submitted in partial fulfillment of the Master of Science in Civil Engineering Degree*, University of Washington, Seattle, December 2009.

Lehman, D.E. and Roeder, C.W. (2012) "Foundation Connection for Circular Concrete Filled Tubes," *Journal of Constructional Steel Research*, Vol. 78, November 2012, pgs. 212-25, Elsevier.

Lehman,D.E., Kuder, K., Gunnarsson, A.K., Roeder, C.W., and Berman, J.W. (2013) "Circular Concrete Filled Tubes for Improved Sustainability and Seismically Resilience", *Journal of Structural Engineering*, ASCE, Reston, VA, ISSN 0733-9445/B4014008(12).

Moon, J., Lehman, D.E., Roeder, C.W., and Lee, H-E (2013) "Evaluation of Embedded Concrete Filled Tube (CFT) Column-to-Foundation Connections," *Engineering Structures*, Vol. 56, pgs 22-35, Elsevier.

Moon, J., Lehman, D.E., and Roeder, C.W. (2012) "Strength of Circular Concrete Filled Tubes (CFT) with and without Internal Reinforcement Under Combined Loading," *Journal of Structural Engineering*, ASCE, Reston, VA, DOI:10.1061(ASCE)ST1943-541X.000078.

Moon, J., Roeder, C.W., Lehman, D.E., and Lee, H-E (2012) "Analytical Modeling of Bending of Circular Concrete-Filled Tubes," submitted for publication review, Engineering Structures, Elsevier.

Nakahara, H., and Tokuda, S., (2012). "Shearing Behavior of Circular CFT Short Columns," *Proceedings of 10th International Conference on Steel Concrete Composite and Hybrid Structures*, Singapore, pgs 362-369.

Priestley, M.J., Seible, F., and Xiao, Y. (1994) "Steel jacket retrofitting of reinforced concrete bridge columns for enhanced shear strength; test results and comparison with theory," *ACI Structural Journal*, Vol 91, pp 537-551.

Roeder, C.W., and Lehman, D.E. (2012) "Initial Investigation of Reinforced Concrete Filled Tubes for use in Bridge Foundations," Washington State Dept. of Transportation Report WA-RD 776.1, Olympia, WA.

Roeder, C.W., Lehman, D.E., Stephens, M. (2014) "Concrete Filled Steel Tubes for Accelerated Bridge Construction," *Transportation Research Record No. 2406, Vol. 1*, Washington, DC, pgs 49-58.

Roeder, C.W., Lehman, D.E., and Bishop, E. (2010) "Strength and Stiffness of Circular Concrete Filled Tubes," ASCE, *Journal of Structural Engineering*, Vol 136, No. 12, pgs 1545-53, Reston, VA.

Stephens, M. T., Berg, L. M, Lehman, D.E. and Roeder, C.W. (2014) "Circular concrete filled tube bridge pier connections for accelerated bridge construction," *Proceedings: 2014 National Accelerated Bridge Construction Conference*, Miami, FL, pgs 354-363.

Stephens, Max. T., Lehman, Dawn E., and Roeder, Charles W. (2016) "Design of CFST column-to-foundation/cap beam connections for moderate and high seismic regions," *Engineering Structures,* Vol. 122, pgs 323-337.

Stephens, Max, Berg, Lisa, Lehman, Dawn E. and Roeder, Charles W. (2016) "Seismic CFST Column-to-Precast Cap Beam Connections for Accelerated Bridge Construction," *Journal of Structural Engineering*, ASCE, Reston, VA, DOI: 10.1061?(ASCE)ST.1943-541X.0001505.

Xiao, C., Cai, S., Chen, T., and Xu, C., (2012). "Experimental study on shear capacity of circular concrete filled steel tubes," St*eel and Composite Structures*, Vol 13, No 5, pgs 437-449, Techno Press.

Xu, C., Haixiao, L., and Chengkui, H, (2009). "Experimental study on shear resistance of self-stressing concrete filled circular steel tubes," *Journal of Constructional Steel Research,* Vol 65, pgs 801-807, Elsevier.

HOT-DIP GALVANIZING IN STEEL AND COMPOSITE BRIDGE CONSTRUCTION

Dieter Ungermann
TU Dortmund University, Institute of Steel Construction
Dortmund, Germany
dieter.ungermann@tu-dortmund.de

Svenja Holtkamp
TU Dortmund University, Institute of Steel Construction
Dortmund, Germany
svenja.holtkamp@tu-dortmund.de

Dennis Rademacher
ArcelorMittal Europe – Long Products
Esch-sur-Alzette, Luxemburg
dennis.rademacher@arcelormittal.com

ABSTRACT

This paper summarizes the most important results of the finished FOSTA research project P835 on the use of hot-dip galvanizing for steel and composite bridge construction, where the corrosion protection duration and the influence of hot-dip galvanizing on the fatigue behavior of steel were examined. Based on these results the range of application of the hot-dip galvanizing shall be transferred to the innovative shear connector of composite dowel strips in composite bridges. After some basic information about the composite dowel strip, the first results and planned studies of the current FOSTA research project P1042 will be presented, which shall allow the safe application of hot-dip galvanizing to composite dowel strips with cyclic loads. Finally, the first hot-dip galvanized “PreCoBeam” bridge is presented, which combines the economic advantages of hot-dip galvanizing and composite dowel strips.

INTRODUCTION

Steel components in steel and composite bridge construction are usually protected against corrosion by organic coatings. Comprehensive research during the last years showed that hot-dip galvanizing of steel members in bridge structures allows significant economic and ecological advantages. It could be demonstrated that the first corrosion protection can last over a bridge’s lifetime of 100 years, even in an environment with a high corrosivity, so that no major maintenance measures of the corrosion protection are necessary. Several studies demonstrate that almost the same initial costs for the first corrosion protection can be expected in comparison to the costs of usual organic coating systems.

Bridges, however, are subject to cyclical loading and require a proof against material fatigue in accordance with (EN 1993-1-9, 2010). Thus, an application of hot-dip galvanizing was not

possible until recently, as the rules for fatigue design are only valid on non-galvanized details and the influence of the hot-dip galvanizing on the fatigue strength of steel components had previously not been studied sufficiently. With the results of many fatigue tests with hot-dip galvanized specimens in the frame of the recently finished research project P835 (Ungermann, et al., 2014), now these economic and ecological advantages can be applied for steel and composite bridge constructions and significant cost savings can be obtained. The results enable the design of bridges in accordance with the regulations of (EN 1993-1-9, 2010) for frequently appearing details in bridge construction.

Parallel to this research another innovative solution to increase the efficiency of composite bridges has been developed. Starting with several research projects and first application in 2003, composite dowel strips offer a very economical solution for the shear connection between steel girder and concrete slab in composite bridge constructions. Continuous improvement and further development finally led to a general technical approval (Allgemeine bauaufsichtliche Zulassung Z-26.4-56, 2013) by DIBt in Germany. Many bridges containing this new technology are built meanwhile, not only in Germany.

To combine the economic cost savings of this new technology of shear connection with the economic and ecological advantages of hot-dip galvanizing during the lifecycle, a research project was launched with the aim to analyze the effects of the hot-dip galvanizing on the fatigue resistance of flame cut composite dowel strips and furthermore to enable a simplified evidence of absence of cracks according to DASt-Guideline 022 (DASt-Richtlinie 022, 2009, revised 2016). This paper presents the first results as well as the experiences of the first bridge project with hot-dip galvanized composite dowel strips in Germany.

HOT-DIP GALVANIZING

CORROSION PROTECTION DURABILITY

The durability of corrosion protection of zinc coatings in the atmosphere depends on its layer thickness as well as the corrosivity of the environment. A classification of the environmental conditions based on the atmospheric loading is given in so-called corrosivity categories (C1 low to C5 high) with corresponding zinc abrasion rates in the first year in (ISO 12944-2, 1998). An annual abrasion rate for long-term behavior of the zinc coatings in the atmosphere can be calculated according to (ISO 9224, 2012) and thereby enables to determine the durability of the corrosion protection of a structure or the required zinc layer thickness for a desired protection period. To assess the current corrosiveness of different atmospheric environments exposure tests of standard samples were carried out on six bridges in Germany by the Institut für Korrosionsschutz Dresden GmbH, beginning in May 2011 (Ungermann, et al., 2014). Based on a comparison with test data of corrosion measurements at four of these bridges in 1983, partly significant improvements of corrosivity due to lower atmospheric pollution were identified. Individual local effects, e.g. caused by de-icing salt, can lead to higher removal rates and should be taken into account. The identified, location-specific corrosivity enables to determine the theoretically possible corrosion protection duration of hot-dip galvanized steel and composite structures under current conditions. These studies (Ungermann, et al., 2014) showed that a theoretically protection duration of 80 to even 100 years can be achieved with a thickness of zinc coating > 200 µm at corrosion category C4. This is nearly equal to the target service life of a steel or composite bridge construction. However, the exact zinc layer thickness is difficult to plan, since it depends on several factors. Thus, the silicon content of the steel has a great influence on the zinc layer thickness, which also increases with a longer dipping time. In bridge construction usually a steel with a high silicon content (>0.2%) is used. In combination with large component thicknesses and thereby necessary longer dipping times in the zinc bath (maximum dipping time

according to DASt-Guideline 022 (DASt-Richtlinie 022, 2009, revised 2016)), zinc coating thicknesses of more than 200 µm are common in bridge construction, but should be checked prior to the construction of the bridges by using work samples. Hence, significant cost savings during the lifetime can be achieved, as 2 - 3 renewals would be required with an organic coating in the same period.

FATIGUE RESISTANCE

In addition to the static design, bridges are exposed to cyclical traffic loads and therefore require a proof against material fatigue according to the European design standards (EN 1993-1-9, 2010), (EN 1993-2, 2010) and (EN 1994-2, 2010). For this purpose a classification of the construction into fatigue detail categories is necessary, which are assigned to normalized fatigue strength curves (S/N curves) in (EN 1993-1-9, 2010). Galvanized components are not covered by the standard, though not explicitly excluded. However, since the notch types were derived from experimental investigations on construction details generally carried out on non-galvanized test specimens, they could not be safely applied to hot-dip galvanized components. Accordingly, the proof against material fatigue for hot-dip galvanized constructions based on current standards could not be provided until recently.

In order to close these gaps and enable the use of hot-dip galvanizing in bridge construction, the research project FOSTA P835/IGF-No. 351/ZBG (Ungermann, et al., 2014) investigated the fatigue behavior of typically used notch details. For the basic proof of the applicability of hot-dip galvanizing in steel and composite bridge construction, comparative large and small-scale tests of non-galvanized and hot-dip galvanized components corresponding to the most important notch details according to EN 1993 for bridge sections with small and medium spans were carried out at TU Dortmund University and MPA Darmstadt. The results of the small scale tests were confirmed by corresponding and complementary large-scale tests to consider the actual fatigue effects of the details. Thereby, an investigation of the isolated influence of the zinc coating on the cyclic load bearing capacity of structural steel was possible, additionally to the determination of hot-dip galvanized detail categories based on (EN 1993-1-9, 2010).

The results of comparative fatigue tests of small scale samples with the main intention to identify the influence of hot-dip galvanizing on fatigue strength and classified in non-galvanized state into detail category 125 according to (EN 1993-1-9, 2010), are exemplary shown in Figure 1. Both, different steel grades as well as various cutting processes (water jet cutting, flame cutting, milling) are included in the evaluation of the test results according to the background document of EN 1993-1-9 (Sedlacek, et al., 2007). The evaluation proofed the detail category 125 for the non-galvanized specimens, represented as black dots, but the hot-dip galvanized samples, shown as gray triangles, had to be classified one detail category lower at category 112.

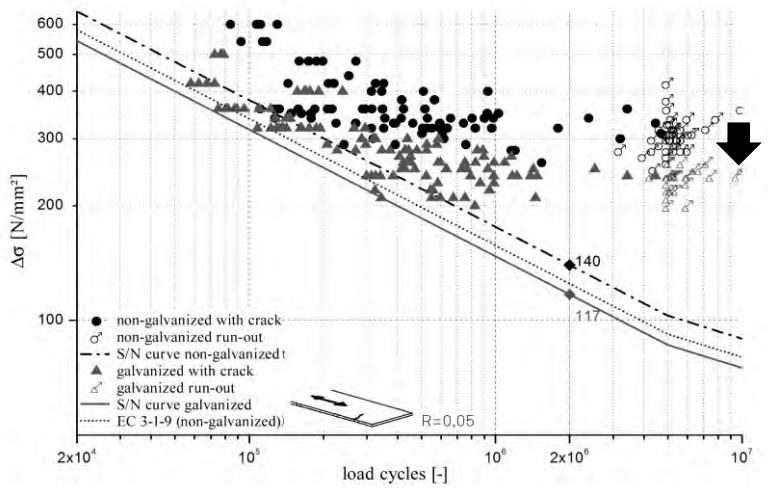


Fig. 1. - Comparison of non-galvanized (detail category 125) to hot-dip galvanized small scale specimens (Ungermann, et al., 2014)

In a direct comparison of non-galvanized to hot-dip galvanized samples, a reduced fatigue limit was observed for all examined details, compare Figure 1. The average reduction was around 20% to 30%. Shrinkage cracks which are already existing in the unloaded initial state in the δ_1-phase of the iron-zinc alloy layer were found responsible for the decreasing fatigue strength. As seen in Figure 2 these micro-cracks grow into the base material under cyclic load due to stress peaks causing premature fatigue crack initiation (Ungermann, et al., 2014).

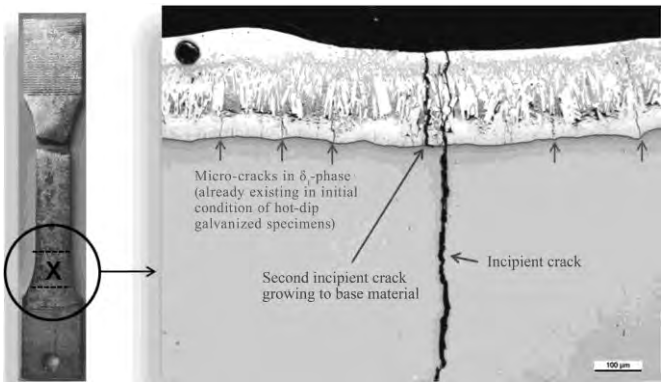


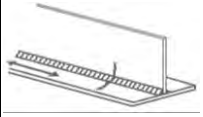
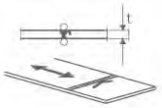
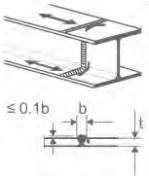
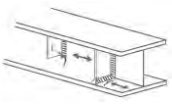
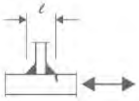
Fig. 2. - Metallographic section of micro-cracks and fatigue cracks (Ungermann, et al., 2014)

All conducted fatigue tests, including component-like, batch galvanized test samples with geometrical and structural imperfections as manufacturing tolerances or residual welding stresses, were statistically evaluated according to the Commentary to Eurocode 3 (Sedlacek, et al., 2007). The results clearly show that the detail categories defined in (EN 1993-1-9, 2010) for non-galvanized steel components cannot be transferred directly to hot-dip galvanized steel components. In fact, some of them must be reduced by a maximum of one category to account for the influence of hot-dip galvanizing. Some normative detail categories could although be confirmed, especially in already low classifications due to geometrical notching effects. But this

reduction of detail category does not inevitably lead to the need for an enlargement of the cross sections, because the fatigue check is often not decisive for the dimensioning.

On the basis of all test results a table of detail categories for hot-dip galvanized steel complementary to the standard of (EN 1993-1-9, 2010) have been compiled, which is shown in Table 1. The fatigue check according to the well-known procedure can thus also be applied for galvanized components and hence the advantages of the hot-dip galvanizing can be used for steel and composite bridges easily.

Table 1 - Detail categories of tested hot-dip galvanized construction details (Ungermann, et al., 2014) (Ungermann, et al., 2015)

Detail category	Construction detail		Description *
140			Plates, flats and rolled sections with rolled or milled edges NOTE: The fatigue strength curve associated with category 140 is the highest. No detail can reach a better fatigue strength at any number of cycles
112			Material with machine gas cut or water jet cut edges with shallow and regular drag lines Machine gas cut with cut quality according to EN 1090
100			Manual longitudinal fillet weld
80			Manual longitudinal fillet weld over manual transverse butt weld
100		Size effect for $t > 25$ mm: $k_s=(25/t)^{0,2}$	Transverse butt weld in plates and flats
80		Size effect for $t > 25$ mm: $k_s=(25/t)^{0,2}$	Transverse butt weld in rolled sections with height of weld convexity not greater than 10% of weld width
80		Size effect for $t > 25$ mm: $k_s=(25/t)^{0,2}$	Transverse butt weld in plates, flats, rolled sections and welded plate girders with height of weld convexity not greater than 20% of weld width
80		$\ell \leq 50$ mm 	Vertical stiffeners welded to a rolled section or plate girder
80 (m=8)			Welds under shear loading: Stud shear connectors for composite application

* Requirements for execution in accordance with identical detail in EN 1993-1-9

The general feasibility was proved with the first application of hot-dip galvanizing for a composite road bridge in Germany, where the theoretical research results were subjected to an in-situ test. This bridge was completed in summer 2016.

COMPOSITE DOWEL STRIPS

GENERAL BASICS

Composite dowel strips are very efficient composite connectors, which are used mainly for composite bridges of small and medium spans. Composite dowel strips have been continuously developed by various research projects over the last few years. Recently, in 2013, a general technical approval by DIBt in Germany was issued for non-galvanized composite dowel strips with clothoid and puzzle shape. This general technical approval Z-26.4-56 (Allgemeine bauaufsichtliche Zulassung Z-26.4-56, 2013) regulates the scope, production and design basis as well as the determination of load-bearing capacity and the fatigue check.

The composite dowel strip is produced by autogenous flame cutting or a method which leads to equivalent properties in terms of load bearing capacity and fatigue resistant. Generally, hot rolled sections are cut in the middle of its web, producing two beams with composite dowels necessary for transferring the longitudinal shear forces. By the elimination of the upper steel flange and thus the reduction of steel consumption in areas which contribute only slightly to stiffness and load bearing capacity (Figure 3b, Figure 3c), composite dowel strips offer economic and product-technical advantages compared to other connectors as shear studs respectively conventional prefabricated composite beams with composite dowels strips welded on the upper flange (Figure 3a). Further economic applications are T-beam cross-sections with external dowel strips functioning as external reinforcement (see Figure 3c).

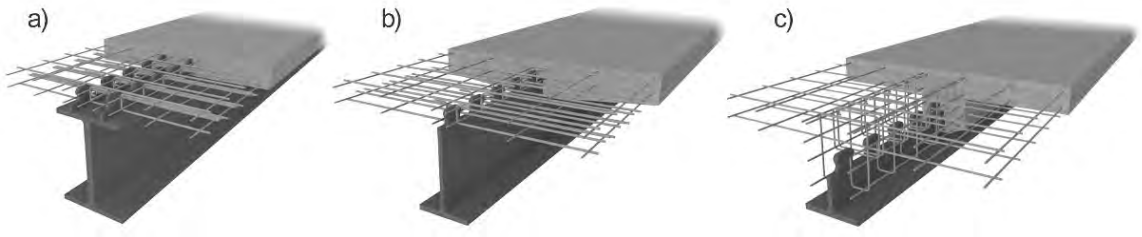


Fig. 3 - Examples of application of composite beams with composite dowel strips in bridge construction (Allgemeine bauaufsichtliche Zulassung Z-26.4-56, 2013)

The calculation of composite beams with composite dowel strips is carried out according to the limit state design of (EN 1992), (EN 1993) and (EN 1994) supplemented by the German general technical approval (Allgemeine bauaufsichtliche Zulassung Z-26.4-56, 2013). Under cyclic loads, steel and concrete fatigue has to be verified as well as a rigid shear connection has to be ensured, whereby the individual components influence each other. (Gündel, et al., 2014)

The procedure for the fatigue check of the steel strip is given in the approval (Allgemeine bauaufsichtliche Zulassung Z-26.4-56, 2013) in accordance with the local stress concept of (EN 1993-1-9, 2010). The local stress (L) resulting from the transmission of the longitudinal shear force of the considered dowel and the global stress (G) from the bending action of the composite beam determine the stress amplitude at the maximum spot. These stresses are calculated by

multiplying the nominal stresses (taking account of both the local and global stress effect) with stress concentration factors from equation (1).

$$\Delta\sigma = k_{f,L} \cdot \frac{\Delta V \cdot S_y}{I_y \cdot t_w} + k_{f,G} \cdot \left(\frac{\Delta N}{A} + \frac{\Delta M}{I_y} \cdot z_D \right) \quad (1)$$

where $k_{f,L,CL} = 7{,}3$; $k_{f,G,CL} = 1{,}5$ (Clothoid)

$k_{f,L,PZ} = 8{,}6$; $k_{f,G,PZ} = 1{,}9$ (Puzzle)

These stress concentration factors were derived from finite element calculations and verified by strain measurements in push-out and beam tests (Feldmann, et al., 2012). Depending on the cutting quality of the flame cut surfaces, detail category 125 or 140 according to (EN 1993-1-9, 2010) applies on the resistance side.

HOT-DIP GALVANIZING OF COMPOSITE DOWEL STRIPS

The regulations of the German general technical approval for composite dowel strips (Allgemeine bauaufsichtliche Zulassung Z-26.4-56, 2013) do not include the use of hot-dip galvanizing for cyclic loaded components. In principle, the fatigue check is conceivable with the table of detail categories for hot-dip galvanized steel on the basis of (EN 1993-1-9, 2010), which has been derived within the research project P835 (Ungermann, et al., 2014), see Table 1. However, the specific influences from complex geometry, production-induced residual stresses and the load-bearing behavior of the dowel strip were not taken into account in the underlying tests. In order to reliably exploit the economic advantages of hot-dip galvanizing for composite bridges with composite dowel strips and to provide a fatigue check by means of extended scientific certifications, the fatigue behavior of the hot-dip galvanized composite dowel strips is investigated within a current research project FOSTA P1042/IGF-No. 18624N (Feldmann, Kühne, Ungermann, & Holtkamp, exp. 2019). While maintaining the design concept for fatigue resistance of the general technical approval (Allgemeine bauaufsichtliche Zulassung Z-26.4-56, 2013) as described in the previous section, a new detail category for flame-cut, hot-dip galvanized composite dowel strips is to be determined for the fatigue check according to (EN 1993-1-9, 2010) or the classification according to Table 1 is to be confirmed.

Initially, numerous extensive numerical studies at the RWTH Aachen University investigated the stresses of the composite dowel strips occurring during the hot-dip galvanizing. For this, the immersion of large steel girders with clothoid geometry and the most unfavorable dipping parameters according to the limits of DASt-Guideline 022 (DASt-Richtlinie 022, 2009, revised 2016) as a dipping angle of 0° and a dipping speed of 0.8m/min (both not used in practice) was simulated by applying a temperature of 450°C, corresponding to the usual temperature of a zinc bath. The numerical model was validated by measurements of the temperature distribution inside the web and measurements of strains at one dowel during the galvanizing process of four 7m long beams with dowel shape, see (Feldmann, Kühne, Ungermann, & Holtkamp, exp. 2019). As small scale samples allow a better and simpler experimental procedure for the planned fatigue tests than only doing full scale component tests, the numerically determined stresses of beams with typical bridge profiles occurring during the galvanizing process had to be transferred

subsequently to small scale samples of heavy plates. Numerous investigations have shown that the reduction to a dowel strip of heavy plate and thus the removal of the flange and the lower web height, which has an influence on the magnitude of the resulting stresses, can be compensated by dipping the dowel strips upside-down. With a web height of 270mm, this procedure offers similar strains in the critical point of the dowel's ground as girders with unfavorable profiles for bridge constructions.

To analyze the influence of hot-dip galvanizing on the fatigue strength of composite dowel strips a large number of experimental investigations will be carried out at TU Dortmund University. Initially, comparative fatigue tests of small scale samples with clothoid dowel shape and steel grades S355 and S460 will be performed in non-galvanized finish and galvanized finish realized by dipping upside-down. At this stage the samples are tested as dowel strips without concrete slab. The experimental set-up is designed in such a way that the load results in stresses similar to those from real loading. The maximum load from the "global" stress occurs at a similar position to the maximum stress during hot-dip galvanizing. The numerical investigation of the experimental set-up and the investigations to determine the point of failure of the small-scale specimen will be extensively presented in the final report (Feldmann, Kühne, Ungermann, & Holtkamp, exp. 2019). In order to take into account the interaction between the steel dowel and the concrete slab and to investigate a possible interference or influence of the zinc layer to the composite effect, additional cyclic push-out tests, similar to the standard test set-up according to (EN 1994-1-1, 2010), appendix B, will be carried out. Thereby the specimens' stresses correspond to the "local" bearing behavior of the composite beams. For the final verification of a preliminary S/N curve, determined by small scale sample experiments, four-point bending tests on large composite beams with component-like dimensions and with welded composite dowel strips and halved rolled sections (see Figure 3a, Figure 3b) will be carried out. This combines both, the global and local bearing behavior. Thereby previously excluded effects can be taken into consideration. While maintaining the described design concept based on the general technical approval of composite dowel strips (Allgemeine bauaufsichtliche Zulassung Z-26.4-56, 2013), the possibly new S/N curve and the subsequent defined detail category of the flame cut, hot-dip galvanized composite dowel strips for the fatigue check according to (EN 1993-1-9, 2010) will permit a scientifically verified application of hot-dip galvanizing for composite dowel strips in future composite bridge constructions.

Additionally to the fatigue studies, the research project examines a classification of the composite dowel strips into a detail class according to DASt-Guideline 022 "Hot-dip galvanization of load-bearing steel structure components" (DASt-Richtlinie 022, 2009, revised 2016), which has to be applied in Germany for batch galvanizing of structural steel components. This guideline was developed by extensive research since 2005, as an accumulation of heavy crack-damage cases during or after galvanizing of large supporting steel components occurred in the period from 2000 to 2007 in Germany. During the dipping process of steel components the high temperature changes and restraint effects due to the component geometries result in potentially large transient stresses and local plastic deformations (Pinger, 2009). Due to design and production high residual stresses occur additionally in many bridge details such as flame cut composite dowel strips. In unfavorable conditions, an overlapping of these stresses can lead to small micro cracks or even to the failure of whole components. Therefore, the DASt-Guideline 022 (DASt-Richtlinie 022, 2009, revised 2016) defines requirements for material and process parameters to reduce these effects and avoid crack initiation. A simplified procedure with classification into a construction class, a detail class and therefrom resulting confidence zone allows determining the necessary tests for the galvanized construction to ensure absence of cracks. Since no classification of the composite dowel strip is possible in an existing detail class, the influence of various unfavorable process and geometrical parameters on the stresses of the composite dowel strips occurring during the hot-dip galvanizing are analyzed with the developed numerical models at RTWH

Aachen University. Thus, the general applicability of the hot-dip galvanizing for composite dowel strips shall be ensured.

FIRST APPLICATION - A GALVANIZED PRECOBEAM BRIDGE IN HALLE-OSENDORF

The Elster-Bridge Osendorf (Germany) is the first “PreCoBeam” bridge with hot-dip galvanized steel structure. This bridge combines the economic and ecological advantages of prefabricated composite beams (PreCoBeams) with composite dowel strips with those of hot-dip galvanizing. It therefore results in an extremely economic construction, both in production and in service life (Seidl, Danders, Gunkel, Rademacher, & Pinger, 2017). The bridge is located in Halle-Osendorf and transfers a rural road across the Weisse Elster to a nature reserve. The single-span frame bridge with twin-girder cross-section and a span length of 21 m (see Figure 4) replaces an old three-span structure that was damaged by a flood.

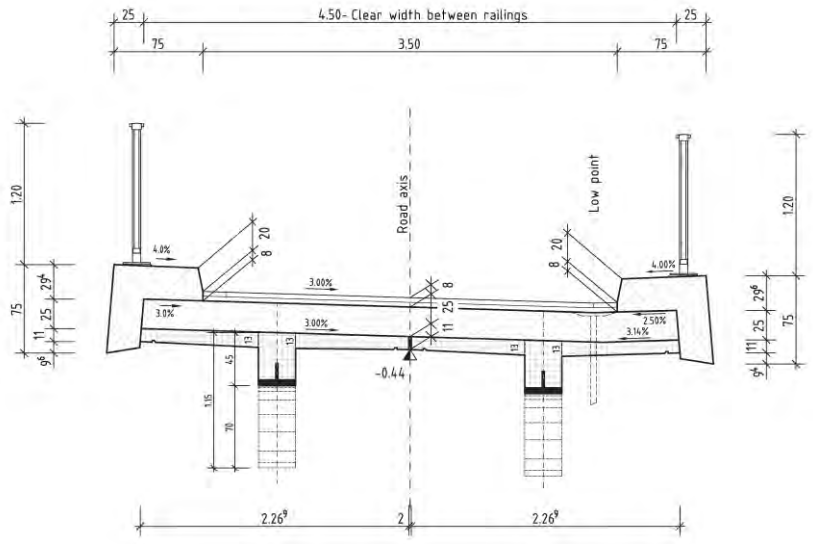


Fig. 4 - Cross-section with two PreCoBeams and in-situ concrete (© SSF Ingenieure AG) (Seidl, Danders, Gunkel, Rademacher, & Pinger, 2017)

The rolled sections (HD320x300, steel grade S355ML), cut into halves with composite dowel shape, are used as an external reinforcement of the T-beams (see Figure 3c). After the flame cutting the edges and surfaces of the steel teeth were ground. The halved beams were subsequently cambered by cold forming with a pitch of 1.08 m, which could still be measured without changing after galvanization at 450°C. The construction height is 0.70 m in mid-span and 1.40 m at the abutments of the bridge, resulting in a slenderness of l/30 respectively l/15.

For transport reasons, the approximately 20.4 m long halved beams were divided into 2 beams each. With total lengths of approximately 10.2 m they complied with the maximum zinc bath lengths and could be galvanized without problems. The galvanizing was carried out according to DASt-Guideline 022 (DASt-Richtlinie 022, 2009, revised 2016) close to the construction site in Landsberg/Halle. The necessary length of immersion time was derived from preliminary tests, so that finally mean layer thicknesses of at least 350 µm could be measured on the flange bottoms of the four rolled profiles (see Figure 5). These thicknesses ensure a theoretical corrosion protection period of >100 years, see (Ungermann, et al., 2014). The cut surfaces of the dowel

geometry gained significantly lower layer thicknesses. As they are finally completely enclosed in concrete, this has no adverse effects in terms of durability (corrosion), but has a positive effect on the fatigue behavior.



Fig. 5 - Cooling of galvanized beams (Seidl, Danders, Gunkel, Rademacher, & Pinger, 2017)

After hot-dip galvanizing each two 10.2 m long pieces had to be connected again to one beam by welding. To avoid high efforts to remove zinc around the intended site joints, the areas close to the weld preparation were protected by a special lacquer before galvanizing. Thus zinc deposit could be prevented. According to the procedure (Ungermann, et al., 2014), which was developed for site joints of galvanized bridge components, at first residues of the lacquer at the beam ends were removed, subsequently the joints were welded and the weld seams ground flush. The areas around the joint were blasted, spray-galvanized and sealed.

After pouring the concrete of the PreCoBeam into the prepared formwork and hardening of the concrete, the prefabricated beams with external reinforcement were lifted in place. Finally the deck slab was completed by in-situ concrete (Figure 6).



Fig. 6 - PreCoBeam in final position before adding in-situ concrete for the slab (© SSF Ingenieure AG) (Seidl, Danders, Gunkel, Rademacher, & Pinger, 2017)

In addition to the very long, maintenance-free service life of the steel components due to the galvanizing, the high robustness of the zinc coating enables to resist the usual mechanical stresses occurring during transport and installation without damage. Thus, the construction

process does not have to be interrupted or delayed for necessary repair work on the corrosion protection system. The use of hot-dip galvanized steel components therefore supports the essential advantages of the composite construction with regard to short construction times.

SUMMARY

The finished research project P835 (Ungermann, et al., 2014) revealed that hot-dip galvanizing has great advantages with regards to life cycle costs and durability of steel and composite bridges and can easily be applied with moderate modifications, amongst others due to the reduction of fatigue strength for hot-dip galvanized details. Their cause was detected in micro-cracks in the zinc layer emerging during the hot-dip galvanizing and growing to the base material under cyclic loading.

Furthermore, several investigations in recent years have contributed to an innovative shear connector, the composite dowel strip, which is regulated in a general technical approval in Germany (Allgemeine bauaufsichtliche Zulassung Z-26.4-56, 2013).

To combine and take advantage of both developments by enabling the safe and scientifically proven application of hot-dip galvanizing for composite dowel strips, the presented research is carried out in the current FOSTA research project P1042 (Feldmann, Kühne, Ungermann, & Holtkamp, exp. 2019), with particular consideration of the fatigue behavior. The fatigue resistance will be examined by small-scale tests of not embedded dowel strips and push-out tests. Experiments on large composite beams shall finally verify the new derived S/N curve of flame cut, hot-dip galvanized composite dowels for the fatigue check according to (EN 1993-1-9, 2010). Furthermore, numerous numerical investigations examine the stresses on the composite dowel strip occurring during the hot-dip galvanizing process, in order to determine the geometry of the small scale samples and, on the other hand, to define a detailed class according to DASt-Guideline 022 (DASt-Richtlinie 022, 2009, revised 2016) by means of parameter studies.

The first-time use of hot-dip galvanizing at a prefabricated composite bridge with dowel strips (PreCoBeam) has shown that the application is basically possible and can be realized without any problems, considering certain design and process parameters.

NOTE

This report was written for Composite Construction CVIII in 2017. The research project P1042 has now been completed. The final research results can be found in the final report, which is expected to be published in 2019.

ACKNOWLEDGEMENTS

Both the research project P835 (IGF-No. 351/ZBG) and the research project P1042 (IGF-No. 18624N) were carried out with the financial support of the Arbeitsgemeinschaft industrieller Forschungsvereinigung „Otto von Guericke“ e.V. (AiF) Cologne, Germany and funding from the German Federal Ministry for Economy. Many thanks to these supporting committees. Also many thanks to Forschungsvereinigung Stahlanwendung e.V. (FOSTA) and Gemeinschaftsausschuss Verzinken e.V. (GAV) for their supervision and support. Furthermore, many thanks to the project partners, the involved industry companies and the project support committee of both projects for their support.

The first bridge with hot-dip galvanized precast composite beams with dowel strips (PreCoBeam) was initiated by SSF Ingenieure AG and the municipality of Halle (Germany). The realization of

the hot-dip galvanized steel construction was carried out by ArcelorMittal Europe - Long Products and Voigt & Schweitzer on behalf of OST Bau - Osterburger Strasse-, Tief- und Hochbau GmbH.

REFERENCES

Allgemeine bauaufsichtliche Zulassung Z-26.4-56. (2013). Verbunddübelleisten (coposite dowel strips). Berlin: Deutsches Institut für Bautechnik (DIBt).

DASt-Richtlinie 022. (2009, revised 2016). *Guideline for hot-dip-zinc-coating of prefabricated loadbearing steel components.* Deutscher Ausschuß für Stahlbau DASt.

EN 1992. (n.d.). Eurocode 2: Design of concrete structures.

EN 1993. (kein Datum). Eurocode 3: Design of steel structures.

EN 1993-1-9. (2010). Eurocode 3: Design of steel structures - Part 1-9: Fatigue. Brussels: European Committee for Standardization (CEN).

EN 1993-2. (2010). Eurocode 3: Design of steel structures - Part 2: Steel bridges. Brussels: European Committee for Standardization (CEN).

EN 1994. (kein Datum). Eurocode 4: Design of composite steel and concrete structures.

EN 1994-1-1. (2010). Eurocode 4: Design of composite steel and concrete structures - Part 1-1: General rules and rules for buildings. Brussels: European Committee for Standardization (CEN).

EN 1994-2. (2010). Eurocode 4: Design of composite steel and concrete structures – Part 2: General rules and rules for bridges. Brussels: European Committee for Standardization (CEN).

Feldmann, M., Gündel, M., Kopp, M., Hegger, J., Gallwoszus, J., Heinemeyer, S., . . . Hoyer, O. (2012). *Neue Systeme für Stahlverbundbrücken - Verbundfertigteilträger aus hochfesten Werkstoffen und innovativen Verbundmitteln, research report FOSTA P804.* Düsseldorf.

Feldmann, M., Kühne, R., Ungermann, D., & Holtkamp, S. (exp. 2019). *Ermüdungsfestigkeit feuerverzinkter Verbunddübelleisten im Verbundbrückenbau, IGF-No. 18624N, FOSTA P1042.*

Gündel, M., Kopp, M., Feldmann, M., Gallwoszus, J., Hegger, J., & Seidl, G. (2014). Die Bemessung von Verbunddübelleisten nach neuer Allgemeiner bauaufsichtlicher Zulassung. *Stahlbau 83*(2), 112-121.

ISO 12944-2. (1998). Paints and varnishes - Corrosion protection of steel structures by protective paint systems - Part 2: Classification of environments. Beuth Verlag.

ISO 9224. (2012). Corrosion of metals and alloys – Corrosivity of atmospheres – Guiding values for the corrosivity categories. Berlin: DIN Deutsches Institut für Normung e. V.

Pinger, T. (2009). *Zur Vermeidung der Rissbildung an Stahlkonstruktionen beim Feuerverzinken unter besonderer Berücksichtigung der flüssigmetallinduzierten Spannungsrisskorrosion, dissertation.* RWTH Aachen University.

Sedlacek, G., Hobbacher, A., Nussbaumer, A., Müller, C., Stötzel, J., & Schäfer, D. (2007). *Commentary to Eurocode 3 - EN 1993-Part 1-9 - Fatigue.* unpublished: RWTH Aachen University.

Seidl, G., Danders, A., Gunkel, F., Rademacher, D., & Pinger, T. (2017). Elster bridge Osendorf – a hot-dip galvanized composite bridge with external reinforcement. *Stahlbau 86*(2).

Ungermann, D., Rademacher, D., Oechsner, M., Landgrebe, P., Simonsen, F., Friedrich, S., & Lebelt, P. (2014). Design of hot-dip galvanized bridges, Proceedings of 7th European conference on steel and composite structures. *Eurosteel 2014, Napoli*, 741-742.

Ungermann, D., Rademacher, D., Oechsner, M., Landgrebe, R., Adelmann, J., Simonsen, F., . . . Lebelt, P. (2014). *Feuerverzinken im Stahl- und Verbundbrückenbau, IGF-No. 351/ZBG, research report FOSTA P835.* Düsseldorf.

Ungermann, D., Rademacher, D., Oechsner, M., Simonsen, F., Friedrich, S., & Lebelt, P. (2015). Feuerverzinken im Brückenbau – Teil 1: Zum Einsatz feuerverzinkten Baustahls bei zyklisch beanspruchten Konstruktionen. *Stahlbau 84*(1), pp. 2-9.

Operational testing of composite railway bridges with innovative composite dowels

Daniel Pak
Universität Siegen, Chair of Steel and Steel-Composite Construction
Siegen, Germany
pak@bau.uni-siegen.de

Maik Kopp
RWTH Aachen University, Division 10.2 - Construction Management
Aachen, Germany
maik.kopp@zhv.rwth-aachen.de

Günter Seidl
Fachhochschule Potsdam, Chair of Steel and Steel-Composite Construction
Potsdam, Germany
seidl@fh-potsdam.de

ABSTRACT

Composite dowels are increasingly used as shear connectors, especially for prefabricated composite bridges. Advantages compared to headed studs are in particular an increased strength, a sufficient deformation capacity even in high strength concrete and a simple application in steel sections without upper flange. In Germany composite dowels are designed according to a national technical approval available for any design office and construction company. In 2012, the VFT Rail® system, adopting these composite dowels, was approved in accordance with CEN and railway standards by the German Federal Railway Office (EBA) for operational testing. Due to positive experiences gained during operation, two additional bridges were designed by SSF Ingenieure AG and brought into operation in 2014 by the German railway Deutsche Bahn (DB). To survey those bridges, a monitoring campaign was set up, investigating (among others) the stress distribution between concrete and composite dowels. The results are presented in this paper.

1. Composite dowels with clothoid shape as shear connectors for railway bridges

Composite dowels are shear connectors for composite beams, which consist of openings in steel plates, cast with concrete. They are either made of steel plates welded on the upper flange of steel beams or fabricated directly out of the web of steel beams. Up to 2013, they were used for road and railway bridges in Germany with approvals in the individual case. In 2013, the national technical approval Z-26.4-56 (Deutsches Institut für Bautechnik DIBt, 2013) was issued, allowing for a design of composite dowels in the regular case. In parallel, the prefabricated composite bridge type VFT Rail® with composite dowels in clothoid shape was approved by the German Federal Railway Office (EBA) for operational testing, based on the same design principles. The first composite bridge structure using external reinforcement was put into operation by the German Railway Company DB Netz AG on the railway link Bingen-Saarbrücken, crossing the river Simmerbach (Seidl, Mensinger, Koch & Hugle, 2012). Two years later, two additional railway bridges with the same cross section were designed by SSF Ingenieure AG and brought into operation in Upper Bavaria (Germany).

2. VFT railway bridges

2.1. Design requirements

In the case of railway bridge replacements, the clearance below the bridge is often widened and the span increased. Therefore, the construction height of the new superstructure is of central importance. To address this problem, new bridge types have been developed within the framework of a project initiated by Germany's railway infrastructure provider DB Netz AG: these bridges are designed to meet the requirements for replacement in existing networks with regard to a slender design, manufacturing process, traffic flow and maintenance. As a result, two bridge types with external reinforcement (composite dowels), either with direct rail fastening or with a ballast bed, were developed by SSF Ingenieure AG (Germany) (Seidl, Mensinger, Koch & Hugle, 2012), whereas the one with direct rail fastening is discussed in this paper.

2.2. Design principles and construction

The superstructure of the VFT railway bridge (VFT Rail®) with direct rail fastening is designed as a simply supported composite beam. Composite action between concrete and steel girders (which act as external reinforcement) is realized by composite dowels (geometry MCL250/115 (Seidl, Mensinger, Koch & Hugle, 2012), Figure 1, right). Shear reinforcement is placed in cut-outs between the steel dowels according to (Deutsches Institut für Bautechnik DIBt, 2013).

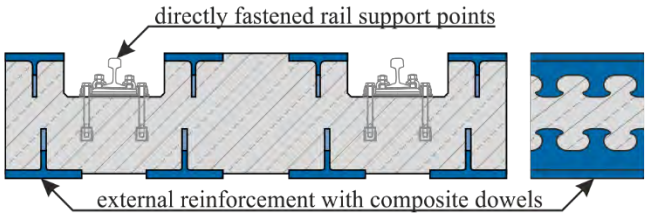


Fig. 1 – transverse cross section (left) VFT-Rail® with rail support points directly fastened to the superstructure and composite dowel and longitudinal cross section (right, depicting the clothoidal shape of the dowels)

Each single rail is taken by a recessed concrete channel to increase the effective height of the cross section (Figure 1, left). The steel-reinforced track channels are furthermore acting as derailment guard. As a result, the concrete pressure zone is reduced by 40%; the pure concrete cross-section is no longer able to take the compressive stresses even if high-strength concrete is used. Therefore the compression zone is strengthened by external reinforcement as well, which furthermore results in an increase of stiffness of the superstructure. The superstructure is completely prefabricated; the prefabricated accompanying paths are subsequently fixed to the structure to reduce the installation weight. Due to prefabrication, the quality of the structure is high. Quality deficiencies can (if necessary) be remedied in the factory already and are therefore decoupled from the time pressure of the track possession period (Seidl, Mensinger, Koch & Hugle, 2012).

Due to concrete shrinkage, state II (cracked concrete) builds up over the concrete's cross section. Therefore, for design purposes shear forces are assigned to the concrete and bending forces to the structural steel.

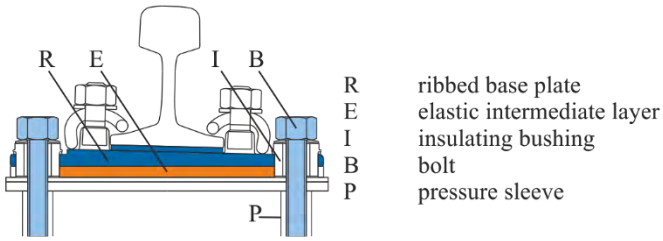


Fig. 2 – Structure of adjustable rail support point system Krupp ECF

The elastic, adjustable rail support system Krupp ECF (ThyssenKrupp GfT Gleistechnik, 2006) is used to fasten the rails directly to the composite girder (Figure 1, left and Figure 2). Each rail support point is anchored by means of two bolts that are braced to pressure sleeves embedded in the precast concrete. Lining plates are used to compensate vertical tolerances.

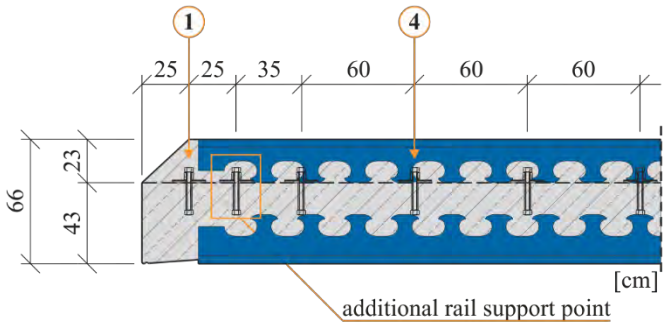


Fig. 3 – Pattern of rail fasteners at the end of superstructure

The rail support points are placed in a regular pattern of 60 cm. Next to the transition between superstructure and backfilling, an additional point is placed to reduce the compressive forces in this region (Figure 3). The regular distance of 60 cm is continued on the ballast bed in front of the bridge. To reduce differential settlements in that region, wide B90 concrete sleepers are placed in front and behind the bridge structure. The rail support points are adjustable in position and height to compensate for superstructure tolerances.

A possible maintenance replacement of the first four rail support points needs to be ensured according to the approval for operational testing. Therefore, the first four rail support points are fixed by means of stainless steel bolts, fixed to the superstructure. The type of fixation depends on the specific type of rail support fixation. One solution requires the steel bolts to be screwed into nuts that are fixed at the end of pressure sleeves, embedded in the superstructure. Another solution calls for screwing threaded rods into friction welded stainless steel sleeves, anchored in the VFT concrete girder.



Fig. 4 – VFT Rail® bridges constructed in Germany (left: crossing the river Simmerbach, middle / right: Upper Bavaria)

The first VFT Rail® bridge was built in 2012 in the course of railway track 3511 between Bingen and Saarbrücken (Germany) (Figure 4, left) (Feldmann et al., 2012). It replaced two existing steel troughs with ballast bed, which had reached their live span. After successful operation of this bridge, the approval for an extended operational testing of the VFT-Rail® system was granted by the German Federal Railway Office (EBA) in 2013 (Eisenbahnbundesamt, 2013). Three years later, two additional bridges of the same type came into operation in Upper Bavaria (Germany) (Figure 4, middle and right). The start of operation of all three bridges was accompanied by measurement campaigns, conducted by RWTH Aachen University; the results of the strain measurements performed at the steel dowels of the two Bavarian bridges are discussed within the scope of this paper. The measured values are compared to values calculated according to the general technical approval Z-26.4-56, which is summarized shortly in the next section.

3. Design of composite dowels according to German general technical approval

Within the scope of the national technical approval Z-26.4-56 (Deutsches Institut für Bautechnik DIBt, 2013), the design of composite dowels in clothoid (CL) and puzzle (PZ) shape to be used under sagging and hogging moment is regulated (Kathage et al., 2016). The geometry can be scaled in dependence of the distance of the openings between 150 and 500mm with a plate thickness between 6 and 40mm. Structural steel grades S235, S355 and S460 are covered. The steel dowels have to be fabricated by gas cutting or a cutting-process which is similar in terms of strength and fatigue. For fatigue loading, the quality has to meet the requirements for detail category 125 or detail category 140, respectively, according to EN 1993-1-9.

The verification of the longitudinal shear connection has to be proofed in accordance with EN 1994-1-1, whereas an equal spacing is also allowed for steel sections without upper flange, taking into account additional design constraints.

Three possible failure modes under static loading are governed by the technical approval. Particularly for small openings and large steel plate thicknesses, the dominating failure mode is double shearing of the concrete dowel. For composite members with low distances between concrete dowel and concrete surface, the ductile failure mode “concrete pry-out” governs, which is similar to the concrete pry-out of anchors subjected to shear forces. For small plate thicknesses and low steel strength, ductile steel failure can occur. In beam-type sections with thin webs and composite dowels as external reinforcement, another non-ductile failure mode can occur. In that case splitting tensile forces can exceed the concrete tensile stress, which results in a horizontal crack at the height of the composite dowel.

The fatigue design concept comprises steel fatigue, concrete fatigue and securing of a rigid shear joint.

Regarding concrete fatigue design, it is distinguished between the loss of bearing capacity due to trickling of crushed concrete out of the composite joint and cyclic concrete pry-out of

composite dowels with insufficient concrete cover subjected to high upper loads. To guarantee for a rigid shear connection between the steel and the concrete section, the strain shift between steel and concrete section is used as criterion for a relevant degradation of the composite joint.

The steel fatigue design is based on the geometric stress approach. On the resistance side the fatigue strength is described by the fatigue strength curve of detail category 125 (machine gas cut edges having shallow and regular draglines) or of detail category 140 (machine gas cut edges with subsequent dressing) in accordance with EN 1993-1-9.

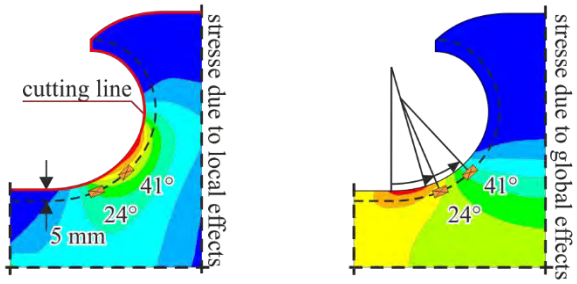


Fig. 5 – Calculated stress distribution (schematic, left: “L”ocal loading due to shear force acting at steel dowel, right: “G”lobal loading due to axial deformation of the external reinforcement due to bending of the composite section)

On the load side, the geometric stress amplitude is calculated. Therefore, it has to be distinguished between two possible maximum stress distributions. On the one hand, a stress maximum occurs in the upper region of the clothoid due to (“L”ocal) shear forces acting at the steel dowel (Figure 5, left). On the other hand, a stress maximum occurs close to the base of the dowel, caused by (“G”lobal) axial deformation of the external reinforcement due to global bending (Figure 5, right).

However, a simple prediction of the actual position of the relevant hot-spot and the resulting geometric stress amplitude is not possible, as both effects interfere, based on the position of the steel dowel as well as the position of the loading. Therefore, the geometric stress amplitude is calculated conservatively as the sum of those stresses, even though they do not occur at the same position (Feldmann et al., 2014) (Mensinger, 2010).

The geometric stresses are not calculated by the designer directly; in fact they are determined by an amplification of nominal stresses, defined as longitudinal shear stresses (“L”ocal) and normal stresses (“G”lobal) at the dowel base (eq. 1).

$$\Delta\sigma = \left| k_{\mathrm{f,L}} \cdot \frac{\Delta V \cdot S_{\mathrm{y}}}{I_{\mathrm{y}} \cdot t_{\mathrm{w}}} \right| + \left| k_{\mathrm{f,G}} \cdot \left(\frac{\Delta N}{A} + \frac{\Delta M}{I_{\mathrm{y}}} \cdot z_{\mathrm{D}} \right) \right| \qquad (1)$$

The stress amplification factors $k_{\mathrm{f,L}}$ and $k_{\mathrm{f,G}}$ were calculated and verified experimentally for both dowel shapes using different numerical models:

- for clothoidal shape “CL” of the steel dowel: $k_{\mathrm{f,L,CL}} = 7.3$ and $k_{\mathrm{f,G,CL}} = 1.5$
- for puzzle “PZ” shape of the steel dowel: $k_{\mathrm{f,L,PZ}} = 8.6$ and $k_{\mathrm{f,G,PZ}} = 1.9$

On the safe side for the determination of stresses due to global bearing behavior the influence of tension stiffening can be neglected (cracked section). For stresses due to longitudinal shear transfer, the more unfavorable value from calculations with a cracked and an un-cracked section should be used.

To exclude low cycle fatigue the geometric stress amplitude is limited to $2 \cdot f_{\mathrm{y}}$ and the upper geometric stress is limited to $1.3 \cdot f_{\mathrm{y}}$.

In compliance with the approval for operational testing, the rail operator made the long-term measurement of these strains in the steel girders of the three VFT Rail® bridges conditional. The measurements allowed for a confirmation of considerations underlying the design of the composite dowel and for a confirmation of correct application of rules based on stress concentration factors respectively. In the following, the monitoring concept for the bridges constructed in Upper Bavaria is described, followed by a discussion of measurement results.

4. Monitoring concept

For measurement of strains in the composite dowels of all bridges (Figure 1, right), strain gauges were applied and connected by wire during prefabrication of the composite elements in the workshop.

The measurements were performed as short-term measurements, allowing for a high-frequency (1000 Hz) recording of short-term loading caused by single train crossings. These temporary measurements were performed three times during a period of half a year.



Fig. 6 – “Stop-run” of single locomotive

For the first measurements a single locomotive of known weight (load per axle = 216 kN) came to stop every single meter on the VFT-Rail® girder for at least one minute (Figure 6). The data recorded during this “stop-run” was used to check precisely the monitoring analysis tools as well as the correct implementation of data into the evaluation routines. All following measurements were performed during regular train crossings.

5. Local stresses in external reinforcement

5.1. Determination of design values

The internal forces needed for the determination of design stresses were determined by means of a framework model. The section stiffness was calculated according to elasticity theory for state I (uncracked concrete, Figure 7, left) as well as for state II (cracked concrete in tension zone, Figure 7, right). In the case of state II, tension stiffening was disregarded (cracked concrete not contributing to stiffness, Young’s modulus of cracked concrete set to $E_c = 0$). In the region of compression, concrete action was considered with non-reduced Young’s modulus. For the determination of the tension zone’s height, neutral axis $z_{i,total}$ = 37.9cm from state I was considered without iteration. In both cases, next to external reinforcement, conventional internal reinforcement (32 x Ø32) was taken into consideration as well. Especially in state II, the influence of this so-called redundancy reinforcement on the total stiffness of the cross section could not be disregarded.

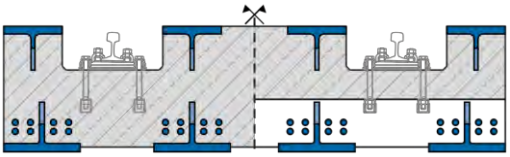


Fig. 7 – Cross section for state I (left) and state II (right), rail support point drawn in for illustration purposes only

Internal bending moment *M* as well as internal shear force *V* were determined in the monitored sections for different load positions. Therefore, the loading of a single axle was applied step-wise to the framework model with a step-size of 0.1m. Based on these internal forces, nominal normal stresses were calculated at the inner side of the upper and lower flanges, at the web as well as at the base of the steel dowel (close to the stress hot-spot).

The stress calculation in the flanges as well as in the web was based on the global bending moment only. An amplification due to local stress concentration had not to be considered in this region; the stress amplification factor $k_{\mathrm{f,G}}$ was set to 1.0. The calculation of stresses in the region of the steel dowel was performed in compliance with the procedure given in the general technical approval (Deutsches Institut für Bautechnik DIBt, 2013) as described in chapter 3, based on the global bending moment as well as on internal shear forces. The stress amplification due to structural effects as well as local bending of the steel dowel (caused by internal shear forces) was considered by means of the stress amplification factors $k_{\mathrm{f,G,CL}}$ and $k_{\mathrm{f,L,CL}}$ (eq. 1).

5.2. Field measurements

5.2.1. Test set-up and measurement

The strain gauges were applied at one pair of outer external reinforcement (lower steel girder G7 and associated upper steel girder G3) of the VFT-Rail® girder (Figure 8).

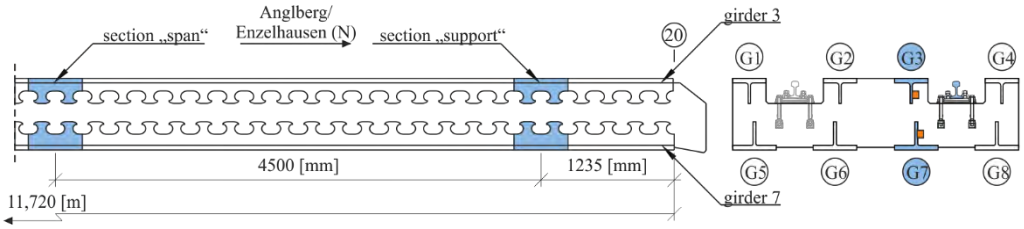


Fig. 8 – Measurement sections at superstructure of the VFT rail bridge

In axial direction, two measurement sections were defined. On the one hand, the position of the section close to the bearings (section “support”) had to be chosen in a way to allow for measurement of high shear forces in the composite section. On the other hand, local effects due to the load transfer into the bearings had to be minimized. Therefore, the section “support” was defined at a distance of about 0.875m to the bearing axis around the 5th and 6th steel dowel. The section “field” was defined in mid-field around steel dowel 23 and steel dowel 24, as in this section the highest bending moments and deformations occurred (Figure 8).

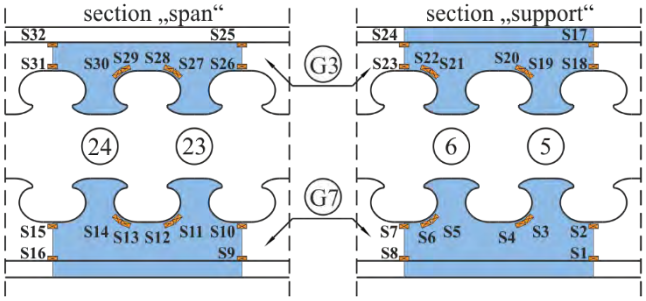


Fig. 9 – Position of strain gauges

In the two measurement sections (Figure 8) strain gauges were applied at the flanges and the web (Figure 9). The strain gauges placed at the flanges and at the web allowed for the determination of the linear strain distribution over the cross section. Additional strain gauges were applied close to the hot-spots (Figure 5, Figure 9). Based on experiences gained in former research projects (Feldmann et al., 2014) (Feldmann, Hegger, Hechler & Rauscher, 2007) (Heinemeyer, 2011) the position of these strain gauges was chosen at an angle of 24° and 41° to measure the maximum strains occurring in that region.



Fig. 10 – Strain gauges in hot-spot region (steel dowel 6) (left), protected strain gauges, covered with 2-component adhesive (PS-adhesive) and permanent elastic cement (AK22)

However, it was not possible to measure the maximum strain at the actual hot-spot directly, as it always occurs directly at the cutting line. Therefore, the strain gauges were applied in a distance of 5mm to the cutting line, which still covers the predicted hot-spot region (Figure 10, left). As the stress concentration factors as given in the general technical approval do not reflect exactly the stresses measured there, they were adopted to the actual measurement position.

The strain gauges were applied prior to casting in the workshop. In total 32 conventional steel strain gauges (R = 100 Ohm) were applied to the steel girders of the bridge (Figure 9). As all strain gauges were covered by concrete, special care needed to be taken prior to casting regarding the protection of the gauges. Therefore, all strain gauges were covered by a 2-component adhesive (PS-adhesive) after application of the signal wires. After hardening, this adhesive formed a stiff protective cover. Finally, a layer of permanent elastic cement (AK22) was applied, which minimized the risk of the gauges to be pulled off due to concrete pressure (Figure 10, right). Furthermore, all signal wires were placed inside elastic ducts, placed in the radius of the steel profiles and leading to one of the abutments of the bridge structure (axis 20, Figure 8).

5.2.2. Measurement results

Within the scope of this paper, selected results of the strain measurements of the second bridge constructed in Upper Bavaria (Germany) are discussed. Therefore, the strains measured are transformed into stresses. At first, results are presented gained by measurement of strains at flanges, web and within the hotspot region during the stop-runs of the diesel electric locomotive. These results are compared with the theoretic characteristic values determined according to the national technical approval (whereas the stress concentration factors are adopted to the actual measurement position). Afterwards the strain values recorded during regular train crossings are checked to identify time-dependant effects.

Undisturbed region: flange of lower external reinforcement (stop-run)

In Figure 11 the strains on the inner side of the flange (S1, S8, S9, S16, see Figure 9 for exact location) are compared to the theoretic characteristic values. The stresses are plotted over position of the first axis of the train on the bridge. The single measurement sections (section “field”: green and blue, section “support”: yellow and orange) can be clearly identified. The highest strains in each region are measured when the axis is placed at the position of the particular section, which complies with the bending moment influence line.

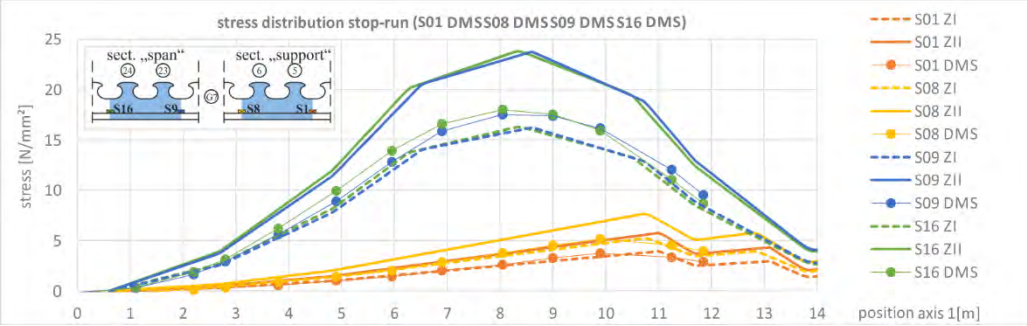


Fig. 11 – Measured strains / stresses on the inner side of the flange (lower external steel girder, points) compared to calculated stresses for state I (dashed line) and state II (solid line)

A comparison of the measured values to the theoretical values of state I (uncracked concrete, dashed lines) shows, that the measured strains / stresses exceed the characteristic design values slightly in mid-field (Figure 11). This leads to the conclusion that cracking of the concrete occurred in the section’s tension zone, redistributing the stresses to the structural steel. However, all measured values are situated clearly below the characteristic design values for state II (cracked concrete, solid lines, Figure 11).

Undisturbed region: web of lower external reinforcement (stop-run)

The strains measured in the web (S2, S7, S10, S15, see Figure 9 for exact location) show the same behaviour during train crossing as the strains measured at the flange (Figure 12). The stresses in the web are by 35% lower than the corresponding stresses in the flange, which can be attributed (amongst others) to the smaller lever arm to the neutral axis. All values are increased compared to the theoretic values of state I (uncracked concrete), which again shows that state II (cracked concrete) governs and needs to be considered during design.

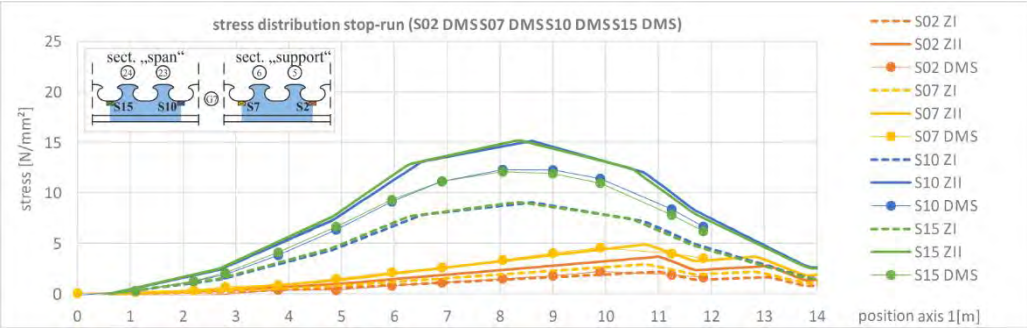


Fig. 12 – Measured strains / stresses at web of lower external reinforcement, compared to calculated values for state I (dashed line) and state II (solid line)

Hot-spot region: steel dowel of lower external reinforcement (stop-run)

Stresses due to global bending of the composite girder and stresses caused by local bending of the steel dowel superimpose within the region of the so-called hot-spot at the foot of the dowel. Furthermore, the stresses are increased due to geometric notch effects. In mid-field, global bending still governs the stress state (Figure 13), whereas strain gauges S12 and S13 show distinctively higher values as strain gauges S11 and S14. On the one hand, this can be attributed to the slightly larger lever arm. On the other hand, this confirms the prediction that the stress state is governed by global effects at mid-field, yielding an increase of stresses at the position of the lower strain gauge (measuring hot-spot strains / stresses due to global effects, compare Figure 5).

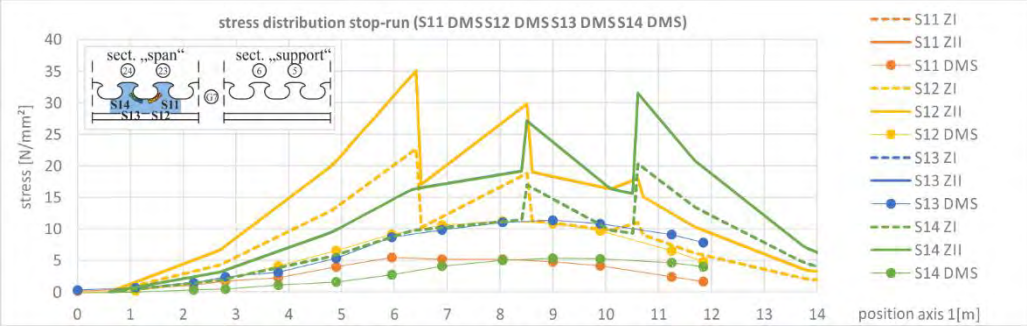


Fig. 13 – Measured strains / stresses within the region of the hot-spot, lower external reinforcement, compared to calculated values for state I (dashed line) and state II (solid line)

The characteristic design values exceed the measured values, as for design the stress sums of global and local stress are taken into account on the safe hand side. However, neglecting the local effects (bending of the steel dowel due to shear forces) leads to an underestimation of the stresses measured in the hot-spot region, which shows the necessity of stress superposition. It is further recalled that for design, the hot spots not only at midfield and at the bearings have to be investigated to find the critical cross section, but all other hot spots in between as well.

Time dependency, stresses in flange of lower external reinforcement (regular traffic)

To check the development of the measured values over time, the crossing of scheduled trains is recorded as well. The first measurement of strains caused by the diesel electric locomotive during normal operations (Figure 14) shows a very good agreement with the values obtained during the stop-run (Figure 11). The gliding mean value of all strains /

stresses measured is situated close the curve of state I (uncracked concrete), which corresponds to the results discussed before. The measurement performed six months later (Figure 15) does not show a distinctive change of strain / stress magnitude.

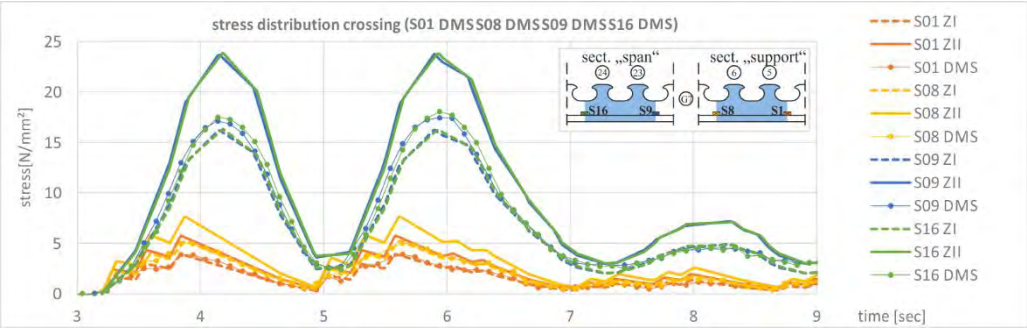


Fig. 14 – Stresses in lower flange, 1st measurement (03/11/2014), diesel electric locomotive and bulk freight wagons (empty)

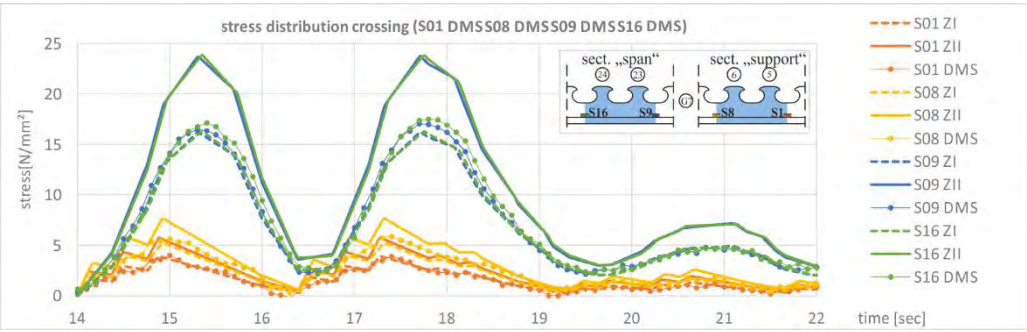


Fig. 15 – Stresses in lower flange, 3rd measurement (08/05/2015), diesel electric locomotive and bulk freight wagons (empty)

It can be concluded that there is a good correlation between calculated characteristic stresses and measured strains / stresses. Together with the evaluation of results in the region of the hot-spot, this leads to the conclusion that the given design concept and safe-sided design rules based on stress concentration factors (Deutsches Institut für Bautechnik DIBt, 2013) is applied correctly.

6. Conclusions and outlook

Since 2013, the national technical approval Z-26.4-56 regulates the design and application of such composite dowels in Germany, reflecting the consistent continuation of the standardization development for composite dowels. However, the validity of that approval expires in May 2023. For the future, provisions are made to include these design rules into EC4. The successful realization of the VFT Rail® bridges in Simmerbach (Germany) (Feldmann et al., 2012) and Bavaria (Germany), combined with the confirmation of the applicability of state of the art calculation methods by monitoring measures proved the applicability, reliability and readiness for the market of the new bridge type. Furthermore the results again show that the given design concept and design rules based on stress concentration factors are significantly safe-sided. For inclusion of these design rules into EC4, they might be slightly modified to allow for an even more economic design.

REFERENCES

Deutsches Institut für Bautechnik DIBt. (2013). Allgemeine Bauaufsichtliche Zulassung, Verbunddübelleisten, Z-26.4-56. Berlin.

Eisenbahnbundesamt. (2013). Erweiterung der Zulassung zur Betriebserprobung vom 06.12.2010 der Bauart VFT-Rail der SSF Ingenieure AG zur Verwendung in Strecken der Eisenbahn des Bundes mit zulässigen Geschwindigkeiten bis 160 km/h. Bonn.

Feldmann, M., Hegger, J., Gündel, M., Kopp, M., Gallwoszus, J., Heinemeyer, S. & Hoyer, O. (2014). P804 - Neue Systeme für Stahlverbundbrücken – Verbundfertigteilträger aus hochfesten Werkstoffen und innovativen Verbundmitteln. VERBUND-DÜBEL-LEISTEN. Düsseldorf: FOSTA - Forschungsvereinigung Stahlanwendung e. V.

Feldmann, M., Hegger, J., Hechler, O. & Rauscher, S. (2007). P621 - Untersuchungen zum Trag- und Verformungsverhalten von Verbundmitteln unter ruhender und nichtruhender Belastung bei Verwendung hochfester Werkstoffe,. Düsseldorf: FOSTA - Forschungsvereinigung Stahlanwendung e. V.

Feldmann, M., Pak, D., Kopp, M., Schillo, N., Wirth, T., Mensinger, M. & Koch, E. (2012). Eisenbahnüberführung Simmerbach. Stahlbau, 81, pp. 737-747. doi:10.1002/stab.201201610

Heinemeyer, S. (2011). Zum Trag- und Verformungsverhalten von Verbundträgern mit Puzzleleisten und ultrahochfestem Beton (doctoral dissertation). Aachen, Germany: RWTH Aachen University.

Kathage, K., Feldmann, M., Kopp, M., Pak, D., Gündel, M., Hegger, J. & Gallwoszus, J. (2016). Composite Dowels as Shear Connectors for Composite Beams—Background to a New German Technical Approval. Composite Construction in Steel and Concrete VII, (pp. 593-606).

Mensinger, M. (2010). Gutachterliche Stellungnahme G 1008 Low Cost Bridge: Beurteilung der Konzepte zum Nachweis der statischen Tragfähigkeit und der Ermüdungssicherheit der Verdübelung der externen Bewehrung des neuartigen Brückentyps "Low Cost Bridge". München.

Seidl, G., Mensinger, M., Koch, E. & Hugle, F. (2012). Projektbericht Eisenbahnüberführung Simmerbach - Pilotbrücke in VFT-Rail Bauweise mit externer Bewehrung. Stahlbau, 81, pp. 100-107.

ThyssenKrupp GfT Gleistechnik. (2006). Oberbauhandbuch. Bochum.

Integral vs. Seismic Control in Composite Deck Bridges

Uwe E. Dorka
University of Kassel
Kassel, Germany
uwe.dorka@uni-kassel.de

Andrea Klarendic
University of Kassel
Kassel, Germany
andrea.klarendic@uni-kassel.de

ABSTRACT

This paper presents a study that compares an integral design for a typical elevated road consisting of a composite deck and rc piers, with a Hyde System design, where force limits can be controlled during an earthquake (seismic control concept). There is no question that an integral bridge can be designed safely for modern code requirements. But the definition of robustness requires a minimal functionality after an extreme event and a speedy recovery, especially for elevated roads and railroads. During such events, design ground motions are exceeded and additional hazards are triggered like tsunami, landslides and fires.

Focusing on an extreme ground motion, this study compares the remaining functionality, reparability and recovery time to full functionality for both designs of the elevated road mentioned before. The 2011 M_W 9.0 Tohoku scenario is used. It is the current basis for seismic risk studies in the Osaka Bay area.

Keywords: seismic control, integral bridges, Hyde System, emergency functionality, Tohoku event

1. INTRODUCTION

More and more integral bridges are being built today, whose evolution dates back to late 1930s. The first known integral bridge in the United States is the Teens Run Bridge in Ohio, which was built in 1938. In the 1960s they started to spread around the world. They are either reinforced or pre-stressed concrete bridges, like the Naibekoshinai River Bridge in Japan built in 1996, or a composite deck bridges made of concrete slabs and steel girders, like the A27 Brochampton Road Bridge in the United Kingdom built in 2001, which is similar to the bridge studied in this paper. The world's longest known integral bridge is the FAS 50 over Happy Hollow Creek built in 1997 with a total length of 358 m (Burke Jr, 2009). These are all integral bridges where a solid connection is provided between piers and superstructure and abutments and superstructure, replacing the usual bearings.

On the other hand, bridges with seismic control require a "seismic link" where forces or force limits can be controlled during an earthquake (Dorka, 2004). In the NATO Science-for-Peace project "Seismic upgrading of Bridges in South-East Europe by Innovative Technologies" (ISUbridge) a 3-span model of a deck bridge was placed on the shaking table at IZIIS, Skopje (“Figure 1”, Dorka & Ristic, 2013). The controllable friction device UHYDE-*fbr* (“Figure 2”, Dorka, 1995) was placed between piers and deck. With it the behavior of various passive devices were simulated (stiff-plastic, bi-linear, base isolation type, viscous, acceleration dependent, stiff-plastic device failure). The bridge model was tested under sine- sweep excitations and the records from the Ulcinj-Albatros and EL-Centro earthquakes. It was shown that forces in the piers were under control: Especially the stiff-plastic control devices effectively limit the forces and protect the piers, even if the devices are overloaded and fail (Dorka, 2014). Thus robustness was added, which is especially important for elevated roads where the failure of one pier eliminates the functionality of the whole road.



Fig. 1 – Model of a 3-span deck bridge on the shaking table at IZIIS, Skopje (Dorka & Ristic, 2013)

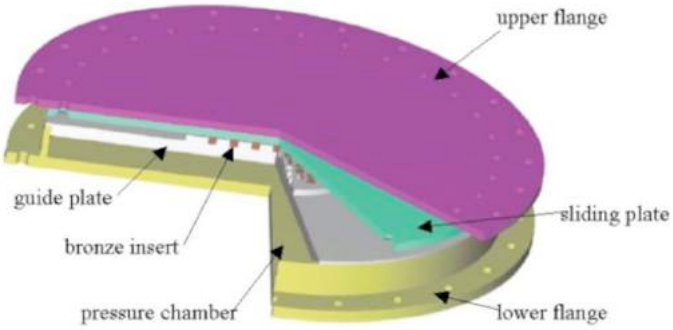


Fig. 2 – Schematic representation of patented bi-directional semi-active friction device UHYDE-*fbr*. The friction force is controlled by pressurized air (Dorka, 1995).

Integral bridges cannot have such links, so seismic control is not applicable. This raises the question: Which concept is superior in earthquake prone regions?

2. STRUCTURAL CONTROL

In this paper, structural control is understood as the *control of selected response variables, such as displacements or their time derivatives (velocities, accelerations) and/or forces, of a structure subjected to dynamic loading* (Dorka, 2004). Such control of a structure can be achieved, if the structural system is properly selected. Rigid-body motion control systems appear to be the ones most suitable for seismic actions: They minimize the kinetic and potential energies (and therefore displacements and forces) and allow for the control of forces in the links between the rigid bodies. Four such systems have been suggested so far for buildings (“Figure 3”).

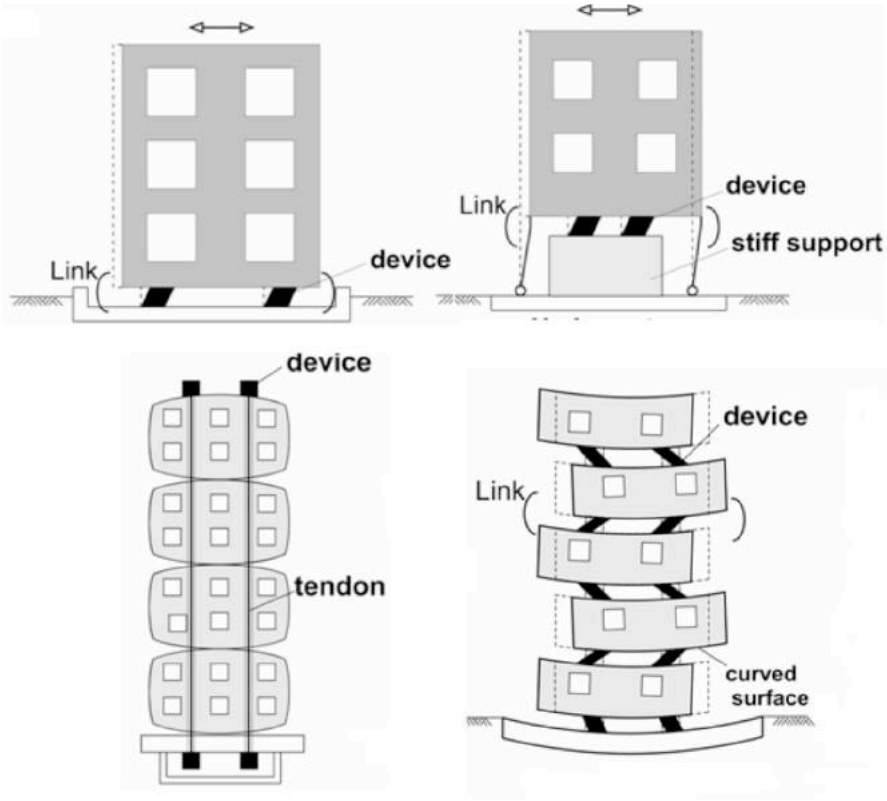


Fig. 3 – Structural concepts suitable for seismic control: Base Isolation, Hysteretic Device System, Tendon System, Pagoda System (Dorka, 2004)

It is evident that a deck bridge has a structural concept that naturally suits a Hysteretic Device Systems, where deck and piers are rigid bodies. The link between them is ideal for providing seismic control (control of force limits) by placing suitable devices there.

In general control devices can be passive, active or semi-active.

Passive control devices do not require any external energy source and are activated by the motion of the structure. They should not be confused with “dampers” or dissipators” as described in (Housner et al., 1997) and (Symans & Constantinou, 1999), because the conversion of mechanical energy into (harmless) heat is not their primary purpose: It is the control of forces, especially force limits! Therefore, friction or metal-yielding based devices provide better controllability than viscous or base-isolation devices, which do not have a force limiting hysteresis.

Active control devices can provide full controllability of forces throughout the earthquake, but are expensive, use large amounts of external energy, require a sophisticated electronic sensing and control system and need extensive maintenance. This makes them unsuitable for almost all earthquake related applications where their action may be only required a couple of times in several decades.

Halfway between passive and active control lies semi-active control in which a certain key parameter of the control device is controlled. Semi-active control devices require an external energy source to operate, but the energy needed is significantly smaller than for active devices, which makes them less expensive and more attractive. They can improve controllability in comparison to passive devices and have the potential to achieve the performance of a fully active system for certain applications. Such devices include variable-orifice fluid dampers, controllable friction devices (like the UHYDE-*fbr*, " Figure 2"), variable-stiffness devices, controllable tuned liquid devices, electro-rheological and magneto-rheological devices and controllable impact devices (Housner et al., 1997; Symans & Constantinou, 1999).

3. COMPOSITE BRIDGE SELECTED FOR THIS STUDY

A composite bridge typical for a 4-lane elevated road has been selected for this comparative study. Only two spans (70 m each) were modeled in order to study the interaction of one pier with the deck, which is the critical detail for both, the integral and the seismic controlled bridge.

The superstructure is made of a typical concrete slab and 2 steel I-shaped girders, as shown in "Figure 4". The deck slab has a variable height: 24 cm at cantilever ends, 46 cm at joints with steel girders and 34 cm in the middle. Two girders at axial distance of 10.8 m are 3.2 m in height in total. Flange width is 1.0 m at the bottom and 0.9 m at the joints with the slab, with thickness of 10 cm.

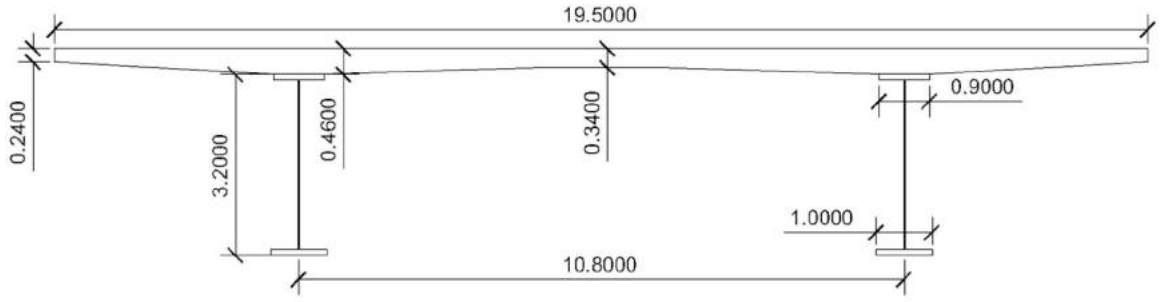


Fig. 4 – Selected typical cross section of the composite bridge

According to CSI Knowledge Base, there are several ways of modeling composite behavior (Computers and Structures, 2010). Different approaches are shown in "Figure 5". Composite action in these bridges is modeled using frame insertion points as in 'Model 4', where frames and shells are drawn at the elevation of deck centroid.

This ´Model´ showed better full composite behavior (full connection through the span length) than the ones with body constraints or fixed links, which is the reason why is it chosen.

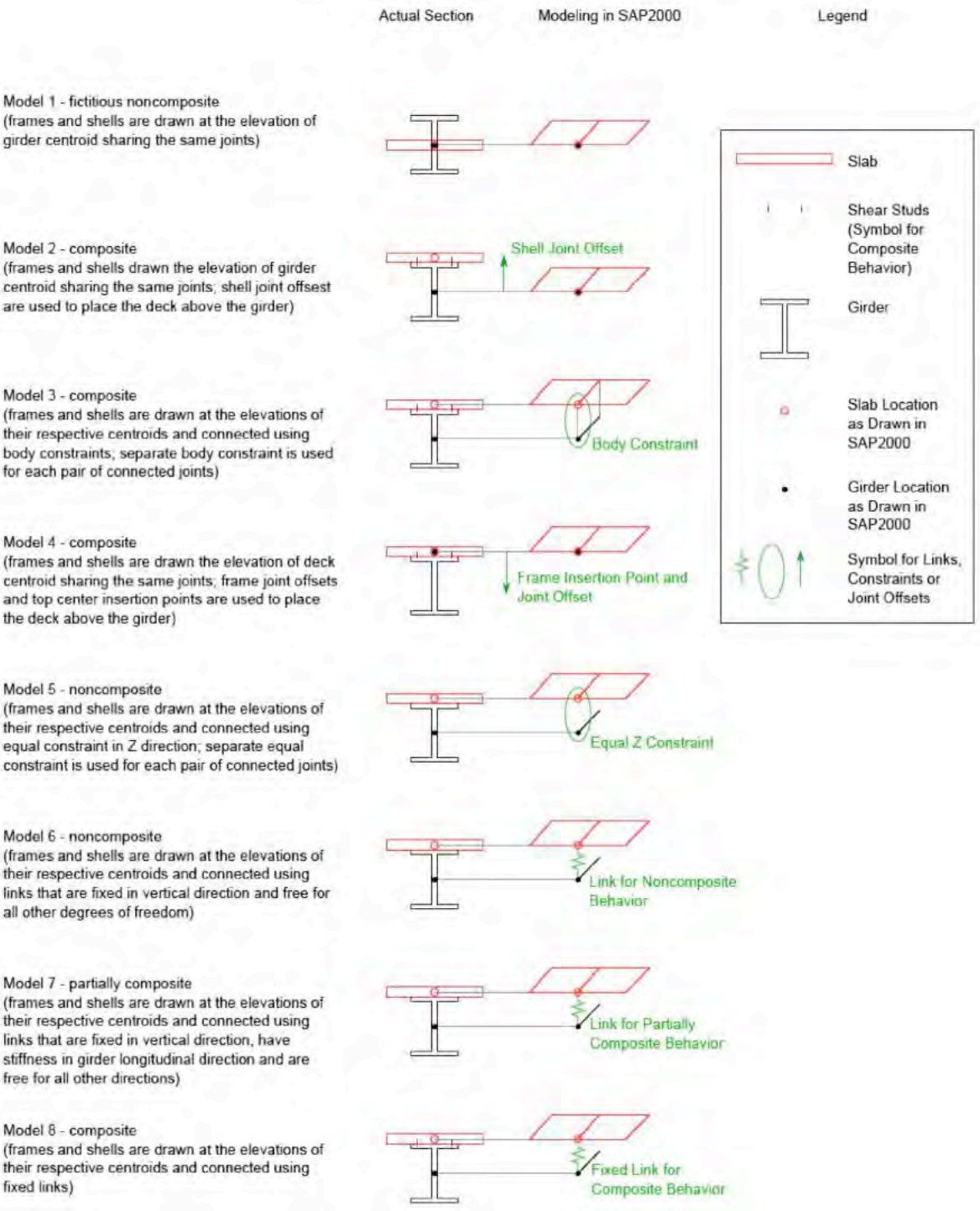


Fig. 5 – Approaches to modeling composite behavior (Computers and Structures, 2010). Model 4 is selected in this study

The superstructure is supported by piers in the middle and abutments on both ends. Piers are formed out of two round columns, each 120 cm in diameter, spaced at 10.8 m just below the steel girders. Height of the piers is a typical 6 m. Abutments are designed as walls at the ends of the bridge, 2.5 m wide and 4 m high.

All the steel elements were designed with steel grade S355. Piers, abutments and cross beam were designed with concrete grade C35/45, slab and transverse girder were designed with concrete grade C45/55.

Both (integral and seismic control) bridges have been analyzed using SAP2000 v15.

4. THE INTEGRAL BRIDGE

To achieve integral behavior in this bridge, the piers are fixed at the top to the transverse girder, which connects and stiffens the longitudinal steel girders. The width of the transverse girder is 1.5 m. Abutments are extended to the top end and connected with the concrete slab. "Figure 6" shows the model as defined SAP2000.

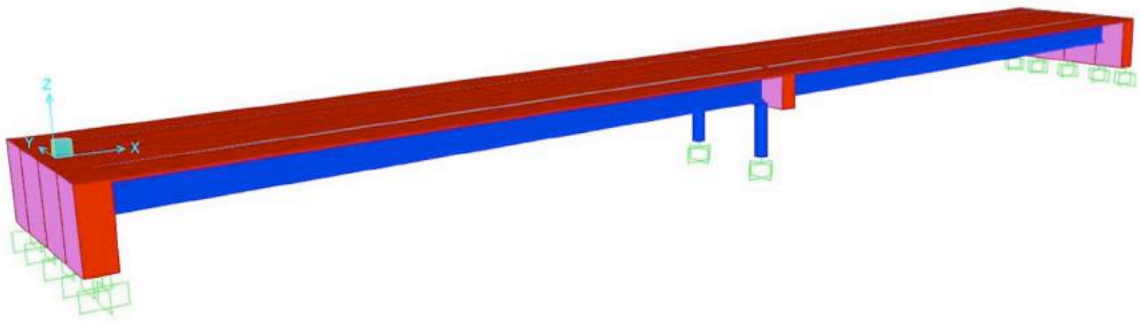


Fig. 6 – Integral bridge

5. THE BRIDGE WITH SEISMIC CONTROL (HYDE-SYSTEM)

In this bridge piers have a cross beam 1.5 m in width and 1.2 m in height on top providing a link to the superstructure where elastomeric bearings are placed underneath the two steel beams and a passive control device in the middle. Bearings and control device are connected directly to the steel girders and concrete deck, respectively. "Figure 7" shows the model as defined in SAP2000.

Bearings are modeled as linear links with the stiffness of 828 kN/mm in vertical direction and 11.3 kN/mm in both horizontal directions. These values are taken from technical specifications of elastomeric bearing pads made by Trelleborg Engineered Systems (Trelleborg, 2009).

The seismic control device is modeled in SAP2000 as *Plastic (Wen) link*, which is based on the hysteretic behavior proposed by Wen (Wen, 1976), with nonlinear behavior in both horizontal directions. The stiffness of this plastic link is 140 kN/mm and the yield force is 200 kN. These values are selected to achieve the desired performance for the design earthquake, which requires linear behavior throughout the structure (except in the control device) and no exceedance of the design displacement limit for the control devices.

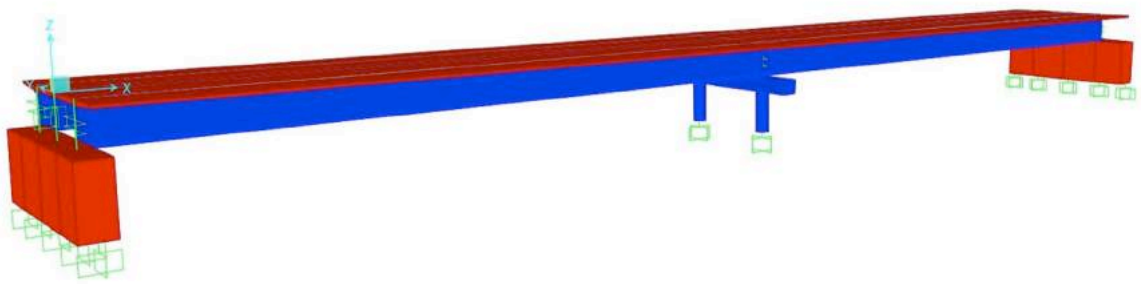


Fig. 7 – Bridge with passive seismic control

6. EARTHQUAKE DATA

All earthquake data used in analyzing these bridges was obtained from NIED Database via the Strong-motion Virtual Data Center (National Research Institute for Earth Science and Disaster Resilience, 2011).

The bridges were subjected to the records from the 2011 M_W 9.0 Tohoku earthquake. The data was collected from the Oshika MYG011 station, whose hypocentral distance from the earthquake is 81.3 km. Three directions were recorded as shown in "Figure 8". Direction N-S of the earthquake captured the maximal acceleration of 9.21 m/s^2, which is applied to the ´x directions´ of both bridges. In the E-W direction the maximum acceleration was 6.88 m/s^2, which is applied to the ´y directions´. Lastly, the station recorded the maximal acceleration of 2.54 m/s^2 in the U-D direction, which is applied in the ´z directions´ of the bridges. The duration of the recorded earthquake is 300 s, but for the purposes of this study the 20 s of the second wave (80 – 100 s) were sufficient, where the biggest accelerations occurred.

7. RESULTS

By looking at the stress in both bridges and comparing them, one can see the differences between the behavior of the integral bridge and the controlled bridge. The integral bridge shows excessive stresses in the whole slab, especially in the region where the slab is connected to the transverse girder and abutments ("Figure 9") indicating serious damage in these locations.

The bridge with seismic control shows significantly smaller stresses in general ("Figure 10"). Moments in the plate are essentially negligible (±45 kN-m), as oppose to moments in the plate of an integral bridge.

First simple estimate gives rough values of a yield moment for concrete piers 5940 kN-m, and of a full plastic capacity 10080 kN-m.

Moments in the piers of both bridges are shown in "Figure 11" and "Figure 12".

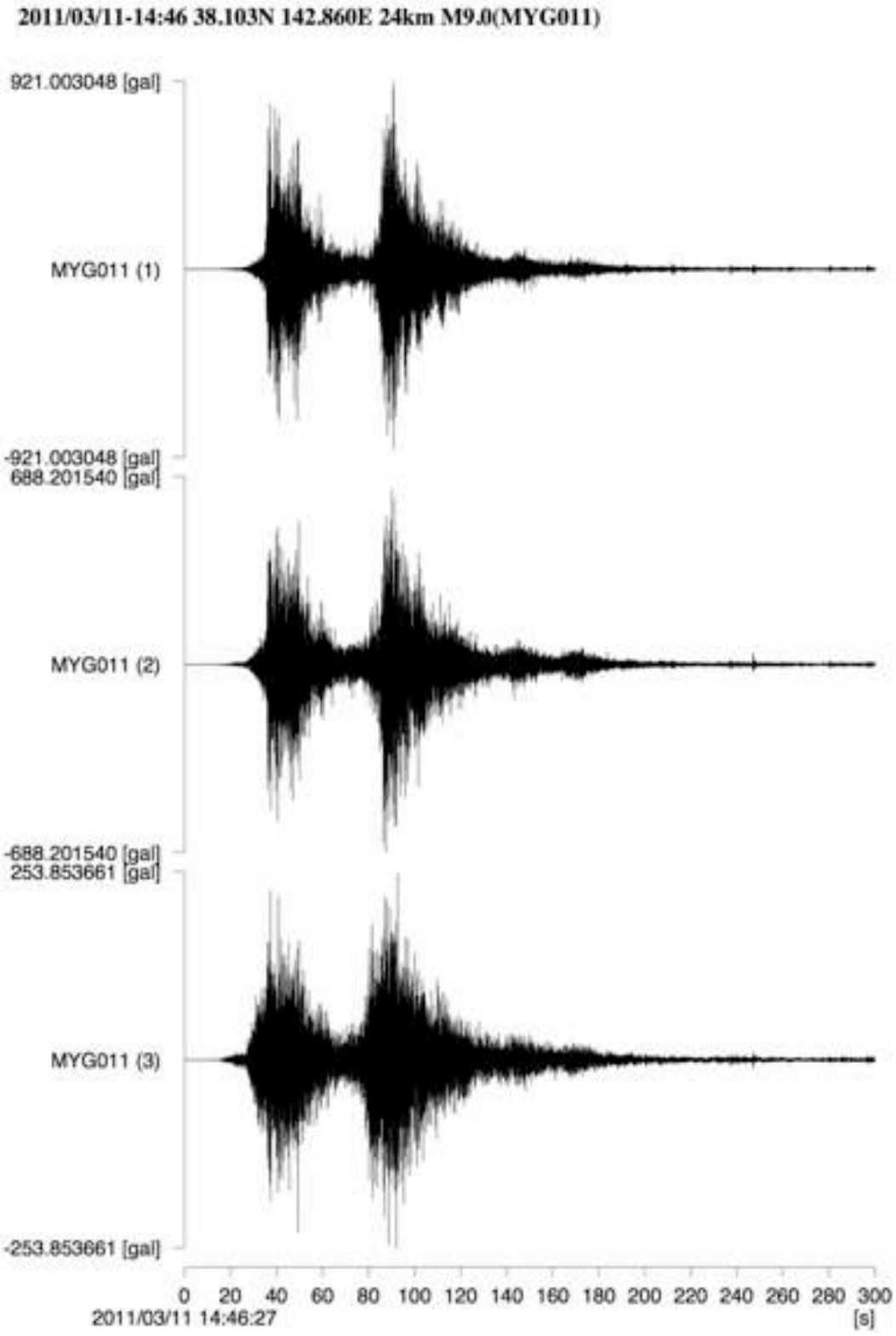


Fig. 8 – Earthquake data, recorded acceleration (National Research Institute for Earth Science and Disaster Resilience, 2011)

The full moment capacity is not reached, but the integral model with the maximum moment in the pier around 9040 kN-m is close to reaching the capacity limit, and is well into the plastic behavior. Moments in the piers of the bridge with seismic control stay well within the elastic zone, with its maximum moment of 4740 kN-m. This is 2 times smaller than the moment in the integral bridge.

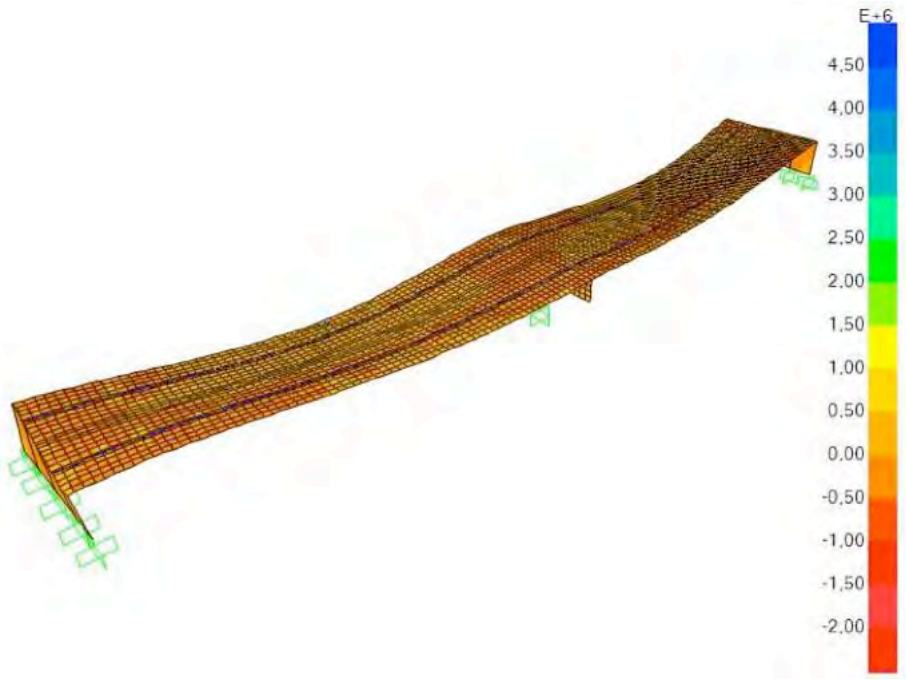


Fig. 9 – Moments in the integral bridge (N-m)

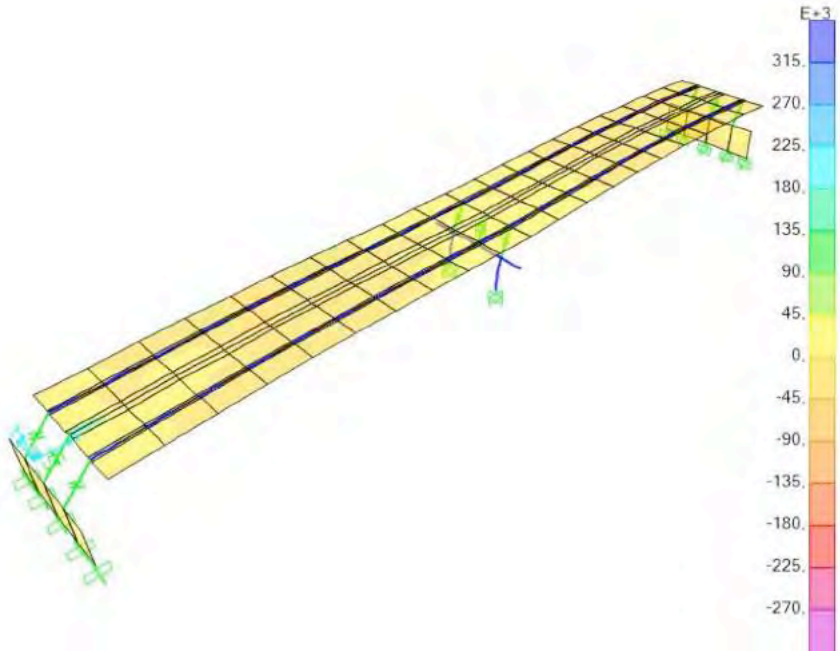


Fig. 10 – Moments in the controlled bridge (N-m)

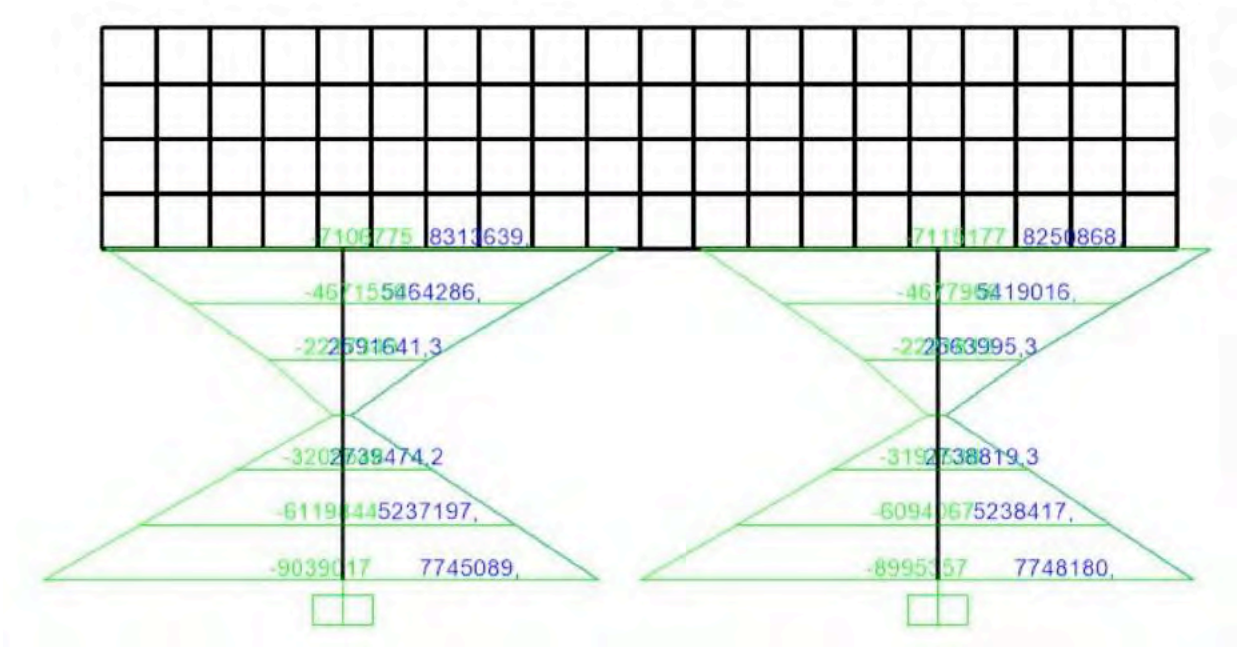


Fig. 11 – Moments in the piers (integral bridge, N-m)

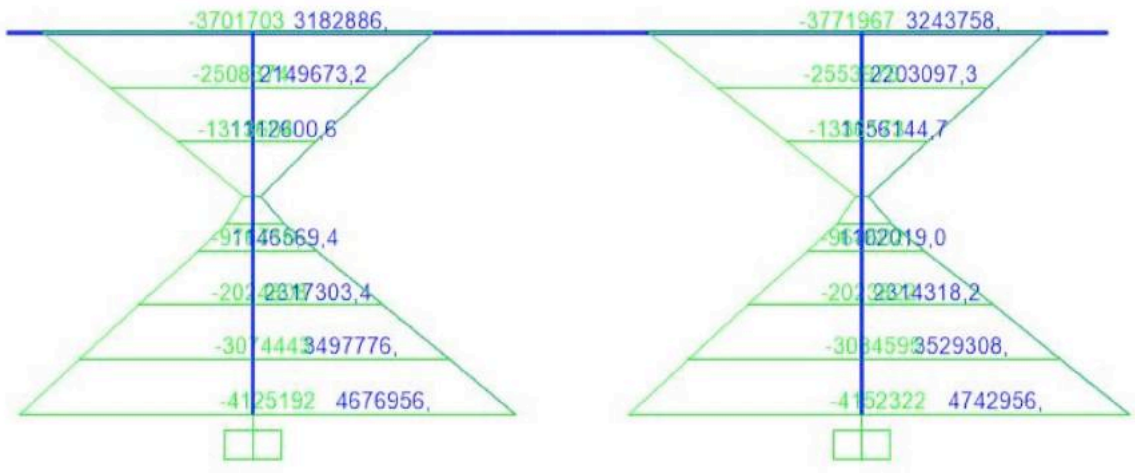


Fig. 12 – Moments in the piers (controlled bridge, N-m)

The hysteresis loop of the modeled seismic control device is shown in the “Figure 13”, which shows the well-controlled limit force in the link (200 kN). Displacement of the deck ranges between -100 mm to +80 mm.

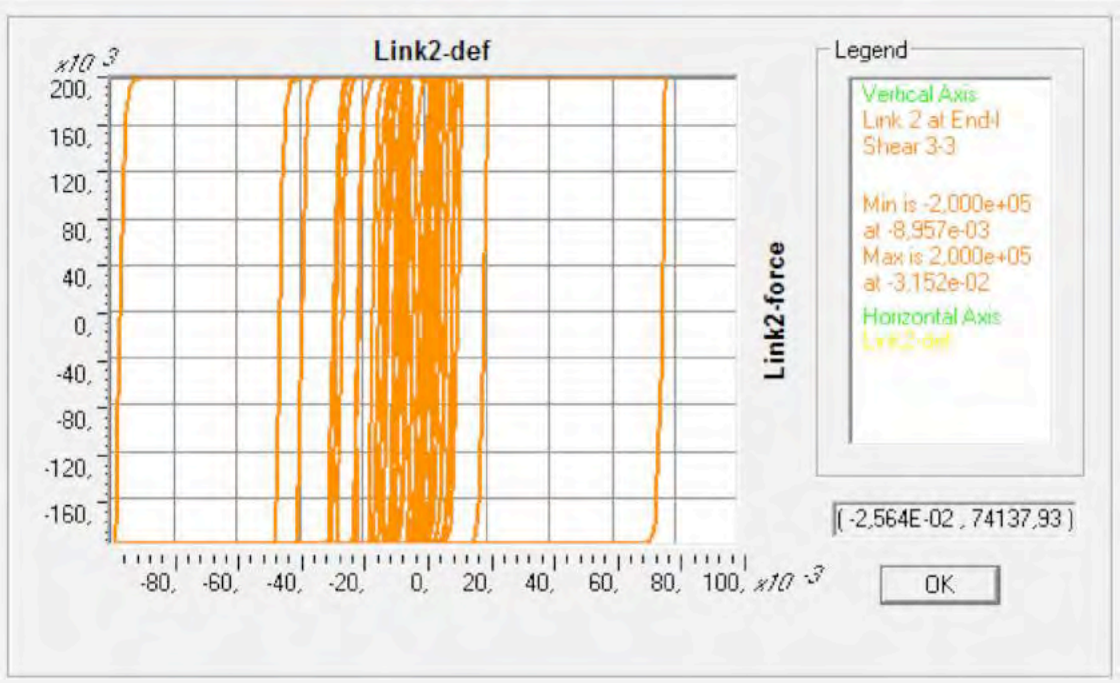


Fig. 13 – Hysteresis loop of the control device (force in N, deformation in m)

8. POST-QUAKE FUNCTIONALITY

This study has shown that an integral composite bridge is most likely going to experience severe damage in and around the piers during an extreme earthquake, most likely causing failure and collapse. This bridge is likely to lose its functionality. Reconstruction is going to be extensive and time-consuming, in the meantime causing severe problems to the functioning of the road network. In some familiar cases, like the 1994 Northridge and 1995 Kobe earthquakes, pier failures shut down entire road networks, with reconstruction taking several years.

For the bridge with seismic control it is highly unlikely that deck and piers will be damaged to a degree that functionality is severely reduced. The passive seismic device in the link is clearly capable of saving the piers from collapsing. Under more extreme conditions, some cracking of the deck may occur, if the displacements in the link become excessive and the superstructure slips off the bearings. But even under such conditions, the piers are protected (as the ISU-bridge experiments have shown: Dorka, 2014) and emergency functionality is unlikely to be lost. This kind of damage is also much easier and faster to repair than in the integral case, where some piers have likely collapsed.

All in all post-quake functionality of damaged bridges is little understood and needs further research.

9. CONCLUSIONS

Two composite bridges, an integral and a seismic controlled one, were compared in order to study their behavior and assess their post-quake functionality under an extreme earthquake event. The 2011 Tohoku scenario was used for this purpose. Both bridges where

meant to represent a typical elevated road with hundreds of piers, although only one pier was modeled in order to study the effect of such an extreme event on this vital connection between superstructure and pier: If this fails, and especially if the pier collapses, the whole road looses its functionality.

The study shows that the integral bridge is clearly in danger of sustaining heavy damage in and around this vital detail. This damage may occur in the deck as well as in the piers, which may even collapse. This can easily result in a total loss of functionality (one collapsed pier is enough) and extended repair and reconstruction works. The integral bridge is therefore not a robust structural concept suited for elevated roads in earthquake prone regions.

More robust structural systems must be used for bridges and elevated roads in such regions, and seismic control concepts (like the Hyde-system studied here) are capable of providing this for composite bridges within traditional, cost-effective bridge concepts. This even opens the way for retrofitting such bridges without excessive interference: With the necessary link already in place, only a suitable control device must be inserted to provide the necessary robustness.

10. REFERENCES

Burke Jr, M. P. (2009). *Integral and Semi-Integral Bridges.* Chichester: Wiley-Blackwell.

Computers and Structures, Inc. (8. January 2010). *CSI Knowledge Base*. Retrieved November 1, 2016 from CSI America: https://wiki.csiamerica.com/display/kb/Home

Dorka, U. E. (1995). *Patentnr. 5456047.* United States.

Dorka, U. E. (2004). Erdbebensicherung durch Structural Control. *Stahlbau 73, Heft 9* , 661-667.

Dorka, U. E. (1994). Hysteretic device systems for earthquake protection of buildings. *5th US Conference on Earthquake Engineering* (S. 775-785). Chicago: EERI.

Dorka, U. E. (2014). Seismic control for elevated roads. *Building materials and structures* , 9-20.

Dorka, U. E., & Ristic, D. (2013). *Seismic Upgrading of Bridges in South-East Europe by Innovative Technologies; ISUbridge (SfP Project Number 983828); Final Report.* Skopje: The NATO Science for Peace and Security Programme.

Housner, G., Bergman, L., Caughey, T., A.G., C., Claus, R., Masri, S., et al. (1997). Structural control: Past, present and future. *ASCE Journal of Engineering Mechanics* (123(9)), 897-971.

National Research Institute for Earth Science and Disaster Resilience. (11. March 2011). *NIED: Database.* Retrieved December 8, 2016 from NIED: National Research Institute for Earth Science and Disaster Resilience: ftp://www.kyoshin.bosai.go.jp/knet/3comp/2011/03/20110311144600/MYG0111103111446.ta r.gz

Symans, M. D., & Constantinou, M. C. (1999). Semi-active control systems for seismic protection of structures: a state-of-the-art review. *Engineering Structures* (21(6)), 469-487.

Trelleborg. (25. November 2009). *Engineered Products: Trelleborg.* Retrieved November 1, 2016 from Trelleborg AB: http://www.trelleborg.com/en/engineered-products/products--and-- solutions/bearings

Wen, Y.-K. (1976). Method for Random Vibration of Hysteretic Systems. *Journal of the Engineering Mechanics Division, Vol. 102 (2)* , 249-263.

AUTHORS' INDEX

Abspoel, R. 239
Agarwal, A. 274
Aggelopoulos, E. 74
Alzeni, Y. 643
Ataei, A. 597
Ayyad, H. 274

Baldassino, N. 762
Barcewicz, W. 322
Bradford, M. 597
Broschart, Y. 132
Bruneau, M. 643
Burgan, B. 74

Cao, Y. 474
Chan, S. 690
Chen, H. 169
Chen, Y. 502, 550
Cheng, X. 655
Chhabra, A. 38
Choe, L. 702
Chuan, G. 550
Ciutina, A. 62, 538
Clayton, P. 217
Cordova, P. 486

Dai, X. 181
D'Aniello, M. 526, 607, 678
Deierlein, G. 486
Denavit, M. 369, 381
Don, R. 538
Donahue, S. 217
Dorka, U. 812
Dubina, D. 538, 678

Easterling, S. 286
Eatherton, M. 286
Eggert, F. 310
Engelhardt, M. 217

Fargier-Gabaldon, L. 486
Feldmann, M. 144
Fleischman, R. 274
Fontana, M. 714
Freddi, F. 762

Gajda, J. 132
Gajewski, M. 322
Garcia, M. 381
Garlock, M. 358
Geißler, K. 346
Gizejowski, M. 322
Gordon, J. 13
Gross, J. 702
Guo, F. 206
Guo, Z. 169, 450, 667

Hajjar, J. 251, 381
Han, L. 462
Han, X. 474
Hanya, K. 334
Hauf, G. 194
Hee Kang, W. 86
Helwig, T. 217
Hicks, S. 62, 86, 98
Hiroshima, S. 334
Hjiaj, M. 416
Holtkamp, S. 787
Hooper, J. 1
Hou, C. 462
Hu, H. 667
Hüttig, L. 25

Inamasu, H. 428

Jeon, C. 440
Ji, J. 474
Ji, X. 655
Jia, X. 655
Jian, X. 502
Jiang, J. 702
Judd, J. 619

Kang, W. 98
Kanno, R. 334, 738
Kanvinde, A. 428, 586
Keo, P. 157, 416
Kim, D. 440
Kimura, K. 738
Kitaoka, S. 334
Klarendic, A. 812
Klemencic, R. 1
Knobloch, M. 714
Kopp, M. 144, 800
Korpas, G. 346
Kostadinova, N. 346
Kuhlmann, U. ...109, 194, 310, 574
Kurz, W. 132, 346

Lai, Z. 392, 631
Lam, D. 181
Landolfo, R. 678
Lee, H. 404
Lehman, D. 775
Leon, R. 381
Lepourry, C. 157
Li, G. 206
Li, J. 550
Li, M. 502
Li, T. 690
Liang, J. 513
Liao, Y. 450
Liew, R. 50
Lignos, D. 428
Lin, H. 667
Liu, S. 690
Liu, X-J. 450
Liu, X-P. 597
Liu, Y. 169, 450, 667
Lu, Y. 450

Mahmoud, H. 750
Main, J. 702
Mathias, N. 13
Mazeika, A. 38
Morgen, B. 1
Neuenschwander, M. 714

Nguyen, Q. 416
Nijgh, M. 263

O'Brien, P. 286
Odenbreit, C. 62
Ozaki, F. 738

AUTHORS' INDEX

Pak, D. 800
Pakwan, N. 619
Palas, F. 157
Pan, J. 513
Park, H. 404
Parra-Montesinos, G. 486
Pascual, A. 109, 726
Pavlovic, M. 263
Perea, T. 381

Qin, C. 750

Rademacher, D. 787
Raichle, J. 109
Ranzi, G. 228
Rassati, G. 526, 607
Ricles, J. 274
Roeder, C. 775
Romero, M. 726
Roverso, G. 762
Ruiz-Sandoval, M. 381
Ruopp, J. 574

Sadek, F. 702
Sarkisian, M. 13
Sause, R. 274
Schäfer, M. 298
Schorr, J. 194
Seidl, G. 800
Seif, M. 702
Selvarajah, R. 702
Seo, J. 631
Shahrooz, B. 169, 450, 667
Sheehan, T. 181
Shim, C. 440
Shimada, Y. 121
Somja, H. 157, 416
Stark, J. 239
Stratan, A. 678
Stroetmann, R. 25
Swanson, J. 526, 607
Szczerba, R. 322

Takada, K. 334
Tartaglia, R. 526, 607, 678

Uang, C. 274
Ungermann, D. 787
Uy, B. 86, 98

Varma, A. 392, 631
Veljkovic, M. 263
von Arnim, M. 263
Vulcu, C. 538

Wang, L. 251
Wang, P. 358, 513
Wang, W. 502
Wang, Y. 50
Wang, Z. 513
Webster, M. 251
Weigand, J. 702
Williamson, E. 217
Wolters, K. 144

Yamada, S. 121
Yang, B. 561
Yang, H. 1
Yang, Z. 206
Ye, Y. 169
Yong, D. 50
Yoshida, F. 334
You, T. 474

Zandonini, R. 762
Zhang, J. 13
Zhang, X. 206
Zhao, J. 561
Zimbru, M. 678

KEYWORD INDEX

ambient vibration 381
analytical..... 392, 98, 121, 228, 263, 274, 346, 369, 416, 526, 607, 619, 702, 714, 750, 812
analytical/experimental 286
anchor connections 561
anchorage.....574
beam test.....263
beam-column connection 550
blast behavior 762
blind bolts 502, 726
bracing design 334
bridge applications.....98, 775, 787, 800, 812, 358,
buckling design formula.....334
buckling restrained bracing...440
buckling restraining effect.....334
buildings 86
closed profiled sheeting.....206
ComFlor.....210, 239
composite action.....513
composite beams 298, 132, 334, 346
composite beams and trusses 13, 62, 74, 121, 157, 181, 194, 251, 263, 310, 574, 702
composite bridges 787
composite columns....13, 50, 74, 369, 381, 392, 404, 416, 440, 450, 513, 714
composite construction...86, 561
composite dowel strips 787
composite joints.....597
composite links.....678
composite slab and metal deck.....217
composite slabs.....206, 239
composite steel-concrete beams.....322
composite structural systems 1, 13, 38, 74, 194, 251, 286, 322, 346, 428, 440, 486, 513, 526, 550, 574, 607, 619, 750, 762, 800
composite structure 169
composite walls 1, 74, 631, 643, 655
concrete anchors.....561
concrete-filled RHS/SHS column 502
concrete-filled square steel tube.....513
concrete-filled steel tube (CFST).....462
concrete-filled tubes 775
concrete-filled tubular columns 726
connected towers 38
connections 502, 702
constitutive model.....50
construction schedule..... 631
corrosion.....462
coupled systems.....631
cyclic shear behavior..... 655
database.....392
decks and slabs.....62, 206, 228, 274, 286, 607
deconstructable 597
deep deck.....239
deep foundation..... 775
deformation limits 474
demountability 263
design.....392
design for deconstruction 263
design formulas 655
design method.....450
details of gusset plate.....513
direct analysis.....690
distortional instability 322
drilled shafts 775
ductility.....310
ecological balance..... 25
effective flexural rigidity 381
effective stiffness 381, 416
elastic flexural rigidity 381
elastic stiffness 381
elevated temperatures.....702
embedded column base connections 428
encased columns.....381
engineering model.....144
environmental product declarations 25
Eurocode 2 416
Eurocode 4 .....298, 416
Experimental..... 50, 132, 157, 181, 206, 251, 263, 310, 404, 486, 513, 574, 586, 643, 655, 714, 787
experimental analysis.....762
experimental data collection...474
experimental investigations....322
experimental study 550, 667
experimental tests 144
fastening technology.....574
fatigue resistance 787
finite element analysis (FEA) 450, 597, 334, 678, 726, 206, 462
finite element model 169, 538
finite element shell model.....322
fire.....358
fire behavior.....702, 714, 750
fire resistance 726
floor membrane action..... 738
floor systems 25
force transferring mechanism 513
frame collapse mechanism...738
friction-grip bolts 597
geometrical imperfections.....322
gravity framing connections..217
headed studs 574
headed studs close to the edge.....109
high strength concrete 392
high strength steel 392, 690
high-rise buildings.....50
hot-dip galvanizing.....787
hybrid columns 416
hybrid coupling walls 667
impact.....462
imperfections 690
injection bolt.....263

KEYWORD INDEX

innovative hybrid members...416
innovative hybrid system 631
large-scale testing 217
lateral stiffness.....631
lateral strength..... 631
lateral-torsional buckling.....334
life-cycle analysis (LCA) 462
linked towers.....38
load slip behavior.....310
longitudinal shear resistance 239
Mexico 381
m-k method.....239
moment magnification 416
moment resistance 298
moment-resisting connections 538
non-seismic building frames.738
numerical simulations.....144
office and commercial buildings 25
parametric studies 206
partial shear method.....239
performance based design... 440
performance based fire safety design 738
performance levels 474
piers and superstructure connection 812
piles 775
pin-structures.....144
plastic design.....298
post-welding residual stresses 322
prediction methods 263
project.....1, 13, 38, 194
project descriptions.....586, 38, 194
push-out test.....157, 169, 263
recommendations for design and execution 263
regressive analysis.....474
reinforced concrete.....416
reliability.....392
replaceable component 450
replaceable details.....667
replaceable links.....678
resins 263
robustness 762, 738
second-order effect.....416
seismic.....217
seismic applications.....13, 121, 274, 440, 502, 526, 550, 586, 619, 643, 655, 775, 812
seismic behavior...538, 631, 667
seismic design 678
seismic engineering.....561
shear buckling 358
shear connections 109
shear connectors.....62, 132, 144, 157, 169, 181, 194, 206, 263, 310, 787, 800
shear strength.....655
slim-floor beams 538
small-scaled.....144
SRC columns.....381, 474
stability of steel columns..... 428
standards and specifications.....62, 74, 86, 98, 228, 310, 369, 404, 486, 762, 800
static shear capacity.....144
steel 358
steel and composite constructions 25
steel columns.....428
steel coupling beams.....667
steel slit damper 450
steel-concrete connections 561, 574
structural redundancy..... 738
sub-assemblage experiments 334
sustainability.....25
tall buildings.....561
ultimate capacity.....206
ultra-high strength concrete....50
U-shaped steel beam 157
validation of numerical model.....322
welded plate girders 322
wind behavior 631

VIRGINIA TECH™

Smarter. Stronger. Steel.

American Institute of Steel Construction
312.670.2400 | www.aisc.org

P705-20